ARO 22564.1-66-CF

Proceedings of the
Fifteenth International Symposium on
Shock Waves and Shock Tubes
Berkeley, California, July 28-August 2, 1985

Edited by

Stanford University

OCT 1 0

86

REPORT DOCUMENTATION PAGE

1a. REPORT SECURITY CLASSIFICATION	1b. RESTRICTIVE MARKINGS
Unclassified	AD73026

2a. SECURITY CLASSIFICATION AUTHORITY	3. DISTRIBUTION / AVAILABILITY OF REPORT
2b. DECLASSIFICATION / DOWNGRADING SCHEDULE	Approved for public release; distribution unlimited.

4. PERFORMING ORGANIZATION REPORT NUMBER(S)	5. MONITORING ORGANIZATION REPORT NUMBER(S)
	ARO 22564.1-EG

6a. NAME OF PERFORMING ORGANIZATION	6b. OFFICE SYMBOL (If applicable)	7a. NAME OF MONITORING ORGANIZATION
Stanford University		U. S. Army Research Office

6c. ADDRESS (City, State, and ZIP Code)	7b. ADDRESS (City, State, and ZIP Code)
Stanford, CA 94305	P. O. Box 12211 Research Triangle Park, NC 27709-2211

8a. NAME OF FUNDING / SPONSORING ORGANIZATION	8b. OFFICE SYMBOL (If applicable)	9. PROCUREMENT INSTRUMENT IDENTIFICATION NUMBER
U. S. Army Research Office		DAAG29-85-C-0079

8c. ADDRESS (City, State, and ZIP Code)	10. SOURCE OF FUNDING NUMBERS			
P. O. Box 12211 Research Triangle Park, NC 27709-2211	PROGRAM ELEMENT NO.	PROJECT NO.	TASK NO.	WORK UNIT ACCESSION NO

11. TITLE (Include Security Classification)

Shock Waves and Shock Tubes

12. PERSONAL AUTHOR(S)

dited by Daniel Bershader and Ronald Hanson

13a. TYPE OF REPORT	13b. TIME COVERED	14. DATE OF REPORT (Year, Month, Day)	15. PAGE COUNT
Final	FROM 1 Feb 85 TO 31 Jan 86	September 1986	915

16. SUPPLEMENTARY NOTATION

The view, opinions and/or findings contained in this report are those of the author(s) and should not be construed as an official Department of the Army position, policy, or decision, unless so designated by other documentation.

17. COSATI CODES			18. SUBJECT TERMS (Continue on reverse if necessary and identify by block number)
FIELD	GROUP	SUB-GROUP	Shock Waves, Shock Tubes, Hook-Method Spectroscopy, Shock-Heated Gases, Gases

19. ABSTRACT (Continue on reverse if necessary and identify by block number)

papers were presented

The Fifteenth Proceedings consist of a record number of papers—110, delivered in 32 sessions, including eight plenary sessions for the invited lectures. Principal among these was the Paul Vieille Memorial Lecture presented by John Sandeman of the Australian National University, titled "The Application of Hook-Method Spectroscopy to the Diagnosis of Shock-Heated Gases." The contributed papers are divided into nine categories. Their titles reflect the broad scope of the subject. Of special interest were the presentations by David Russell (USA) and Koichi Kambe and co-workers (Japan) dealing with an important new medical advance—the nonintrusive destruction of kidney stones by underwater focused shock waves. Several of the papers reflect the recent and continuing interest in shock wave phenomena in 'dusty' gases and other multiphase and heterogeneous systems, including chemically reactive configurations.

20. DISTRIBUTION / AVAILABILITY OF ABSTRACT	21. ABSTRACT SECURITY CLASSIFICATION
☐ UNCLASSIFIED/UNLIMITED ☐ SAME AS RPT. ☐ DTIC USERS	Unclassified

22a. NAME OF RESPONSIBLE INDIVIDUAL	22b. TELEPHONE (Include Area Code)	22c. OFFICE SYMBOL

DD FORM 1473, 84 MAR — 83 APR edition may be used until exhausted. All other editions are obsolete.

Shock Waves and Shock Tubes

Proceedings of the
Fifteenth International Symposium on
Shock Waves and Shock Tubes
Berkeley, California, July 28-August 2, 1985

Edited by
Daniel Bershader and Ronald Hanson
Stanford University

Preface

Systematic study of shock wave phenomena began after the Second World War. The history of the subject is intertwined with that of the development and utilization of the shock tube. In its several forms, that device has proved to be a most versatile and resilient tool for the investigation of shock-wave-related problems covering a wide variety of fields both in fundamental science and in applied technology. Hence the phrase "Shock Tube Symposium" as a title for the earlier biennial meetings. The expanded breadth of subject areas currently associated with shock wave phenomena now warrants, we feel, the modified title "Shock Waves and Shock Tubes."

The first of these symposia was a small meeting at M.I.T. in 1957, generated by Mr. R. Birukoff, a scientist with the U.S. Air Force sponsoring organization. Ten years later in Freiburg, Germany, the Sixth Symposium took on a fully international character, owing especially to the earlier planning efforts of Dr. H. Schardin of the West German government. Subsequent meetings have been held in many parts of the world. The Sixteenth Symposium will take place in Aachen, West Germany, in 1987.

The International Symposium on Shock Waves and Shock Tubes clearly is the most important meeting dealing with shock wave physics and related physical, chemical, and biological science and technology. The world's leading investigators in the field of shock waves and shock tubes normally attend and present their reports at these meetings, and the Proceedings of these symposia are a unique archival resource. Much of the material is not available in any other journal or compendium.

The Fifteenth Proceedings consist of a record number of papers—110, delivered in 32 sessions, including eight plenary sessions for the invited lectures. Principal among these was the Paul Vieille Memorial Lecture presented by John Sandeman of the Australian National University, titled "The Application of Hook-Method Spectroscopy to the Diagnosis of Shock-Heated Gases." The contributed papers are divided into nine categories as detailed in the Contents. Their titles reflect the broad scope of the subject. Of special interest were the presentations by David Russell (USA) and Koichi Kambe and co-workers (Japan) dealing with an important new medical advance—the nonintrusive destruction of kidney stones by underwater focused shock waves. Several of the papers reflect the recent and continuing interest in shock wave phenomena in "dusty" gases and other multiphase and heterogeneous systems, including chemically reactive configurations. The papers on shocks in condensed matter reflect the growing participation in these symposia by researchers investigating shocks in solids and liquids. The contents also reveal that the classic areas of shock interactions and propagation and of experimental methods continue to receive considerable attention, with the result that new and fruitful concepts are being introduced. Shock wave phenomena associated with chemical problems played a prominent role at this meeting, owing probably, in part, to its juxtaposition with the Tenth International Colloquium on the Dynamics of Explosions and Reactive Systems, which took place in Berkeley during the following week. Finally, we note the increased application of the methods of computational fluid dynamics to shock wave problems, as evidenced by several papers.

The Symposium was regarded as highly successful. Apart from the high technical quality of the contributions, the success of the meeting was made possible only by the efforts of many people, to all of whom the Executive Committee is most grateful. It is a particular pleasure to acknowledge the dedicated help of Teresa Storm, the Symposium Administrator, as well as the important contributions of Ilse Gluckstadt Bershader, organizer and leader of the Companions' Program, and of Vadim Matte, Michael Mandella, Eileen Javar, Frank Robben, Ray Whittaker, and Peggy Little, all of whom helped with several phases of the preparation and implementation. Charles Treanor played a key role in coordinating the preparation of the Program/Abstract booklet. We are most appreciative, as well, of the generous efforts of all members of the Papers Committee assembled by Robert Dannenberg. In addition, thanks are due to several members of the International Advisory Committee for their constructive suggestions with respect to the program. And we are grateful to William Carver of Stanford University Press for his expertise in coordinating the publication of this volume.

Finally, the Executive Committee is surely indebted (and we know that the Symposium participants join us in this sentiment) to the organizations that provided the needed financial support for the Symposium and the publication of these Proceedings: the U.S. Defense Nuclear Agency, the National Science Foundation, the U.S. Army Research Office, NASA-Ames Research Center, Calspan Corporation, TRW Corporation, and Physics International Company.

Stanford, California

Daniel Bershader
Ronald Hanson

Contents

Part I: Plenary Lectures

Part II: Shock Propagation and Interactions

Part III: Shock-Generated Chemical Kinetics

Part IV: Shock Computation, Modeling, and Stability Problems

Part V: Shock Wave Aerodynamics

Part VI: Experimental Methods

Part VII: Shocks in Multiphase and Heterogeneous Media

Part VIII. High Energy Gas Excitation and Wave Phenomena

Part IX: Technical Applications and Shocks in Condensed Matter

Part I
Plenary Lectures

The Application of Hook-Method Spectroscopy to the

Diagnosis of

Shock-Heated Gases

R.J. Sandeman

Department of Physics and Theoretical Physics
Australian National University, Canberra. Australia.

The history of the hook method and allied interferometric techniques which employ the dispersion of atomic media is described together with an explanation of the formation of the fringes along the spectrum and the reason for their hooked appearance about an absorption line. The peculiar advantages of these techniqes, which has proved itself as an important and accurate method of measuring oscillator strengths, is discussed from the point of view of obtaining populations of energy states in a gaseous medium. Examples of its application to the study of shock waves and shock-like produced plasmas are given. Other experiments which employ dispersion methods are also described concluding with possibilities of more novel applications.

Introduction

Hook-method spectroscopy uses the dispersion behaviour of a medium close to an absoption line. It is not restricted to gases, but the applications discussed here concern gases or vapors for which the absoption lines are the spectral transitions of the constituents of the medium. The method arose in 1910 when Roschdestvenski (perhaps accidentally) placed a plane-parallel glass plate into the reference arm of his interferometer when he was studying the dispersion surrounding the sodium D-lines and observed that the previously hyperbolic-shaped fringes turned into ones which appeared "hook-shaped". (These fringes are still hyperbolic but are now asymptotic to axes which are at an acute angle - rather than orthogonal - to each other.) Previously, Wood[1] and particularly Ladenburg[2] and co-workers had studied the dispersive behaviour in sodium vapour and in gases using interferometers coupled with spectrographs without this important inclusion of the glass plate. They used a technique devised by Puccianti[3] in 1901 which involved plotting the fringe positions near the line and was less accurate and more complicated.

Roschdestvenski's St Petersberg thesis was published in Annallen der Physik in 1912[4]. Ladenburg saw the utility of his simple technique and published three papers in succession in 1928 the latter two with Kopfermann, which dealt with anomalous dispersion in discharges in neon[5]. In Russia also the method was rapidly adopted for the measurement of oscillator

---

[†] At that time *anomalous dispersion* was used to describe the fact that, on the blue side of an absorption line the refractive index is less than one although the *dispersion* there is still "normal" i.e., the refractive index increases with decreasing wavelength (or increasing frequency). The dispersion is only truly anomalous (increasing refractive index with increasing wavelength) inside the half-width points of the absorption profile. Despite this, reference to anomalous dispersion is still used in general to indicate that one is using the behaviour of the refractivity close to an absorption line rather then "within" it.

strengths in particular (e.g. Prokofiev 1924[6]) but also for obtaining information concerning populations of states in discharges. This work has continued to the present day.

The first application of the method to the diagnostics of shock waves was in 1961 by Dunaev Tumakaev and Shukhtin[7]. They used the hook method to measure the population of energy states before and after shock waves through Hg vapour and from these deduced temperatures assuming a Boltzmann distribution. In 1965 Tumakaev and Lasovskaya added a framing camera and obtained time resolved data in the Hg vapour shock tube. In 1975 they also reported the use of a dye-laser light source (giving μsecond time resolution) for hook-method determinations of the populations of the excited states behind shock waves in xenon[8].

At the Eighth International Shock tube Symposium in London in 1971, Parkinson[9] reported on the work he and his colleagues were conducting using the hook-method to obtain oscillator strengths for iron and subsequently nickel and chromium in which the shock tube enabled these elements to be prepared in atom form (with some ions also) through dissociation of their carbonyls in a heat bath of argon.

In Japan, Fukuda's group at the University of Kyoto adopted the hook method for both oscillator strength measurements and for diagnostic purposes in discharges. They obtained excellent time resolution (circa 5 nanosecond) by employing a nitrogen-laser-pumped dye laser, operating in broad-band mode, for the light source[10].

Techniques allied to the hook method have been considered and of these "spectral-line interferometry" as proposed by Measures[11] of UTIAS is possibly the most important. It is two-wavelength interferometry (does not require a spectrograph) with one source wavelength chosen outside the region of dispersion due to the spectral line, while the other is chosen within its influence.

Lately the hook method has been used to obtain the population in a lasing transition in which there is a population inversion[12]. Increasingly it is becoming more common as a tool in discharges where the other methods of emission or absorption spectroscopy are not seen as applicable because of problems associated with optical depth or with thermodynamic equilibrium. Marlow[13] and Huber[14] have both published reviews of the hook method.

Dispersion and anomalous dispersion

In the application of interferometry to gas flows shock waves etc., the measured quantity is the phase shift between the recombined test and reference beams. The phase difference is due to the difference in the retardation of the two beams. which for gaseous media, depends linearly on the column density of the medium traversed. The absorption and retardation of an electro-magnetic radiation field (the source beam) at a particular frequency is modelled by considering the interaction of the oscillating electric field of the source with all the natural oscillations (electric-dipole transitions) in the atoms or molecules of the medium. Each transitions can be represented as a classical harmonic oscillation. of the transition electron in the local electric field of the atom or molecule. After making approximations restricting the density of the medium, so that both the extinction coefficient k (non-dimensional form of the absorption coefficient) and the refractivity n-1 are small compared to unity, then

$$n - 1 = \sum_{ij} r_o N_i f_{ij} \lambda_{ij}^3 (\lambda - \lambda_{ij}) / \{4\pi[(\lambda - \lambda_{ij})^2 + (\gamma_{ij}/2)^2]\}.$$

Here r_o is a constant, λ_{ij} is the wavelength of the transition and λ that of the source radiation while γ_{ij} is the full width at half maximum of the line profile (here in units of wavelength) and is obtained from the damping constant of the oscillating electron. The population of the lower level of the transition is N_i and f_{ij} is the so called oscillator strength (f-value) introduced by Ladenburg

(1921)[15] as the number of "dispersion electrons", as a fraction of the N_i, which are effective in the interaction at the oscillator frequency. The f-value is an atomic constant which in general must be measured, although recently there has been some success in calculation using quantum mechanics.

For a wavelength close to particular transition (λ-λ_{ij} small) then the contribution of all the other transitions is virtually a constant background and the local variation in the refractivity (dispersion) is due solely to the local oscillation. The behaviour of the extinction coefficient and the refractivity is shown in figure 1.

The region of anamolous dispersion is apparent. Also shown is the Sellmeier approximation to the refractivity, which assumes that the damping constant is zero (the spectral line has zero width). This has a hyperbolic dispersion and it is a good approximation for wavelengths more than five times the half-width at half maximum of the absorption line profile. It is this fact - that from the far wings to reasonably close to line centre, the refractivity is independent of various broadening mechanisms - which gives refractivity methods of measurement such power and utility. Both Doppler broadening and collisional broadening change the refractivity close to the line. However the above statement is still true for a large range in the ratio of the Lorentzian to Gaussian widths and for distances larger than five Doppler half-widths.
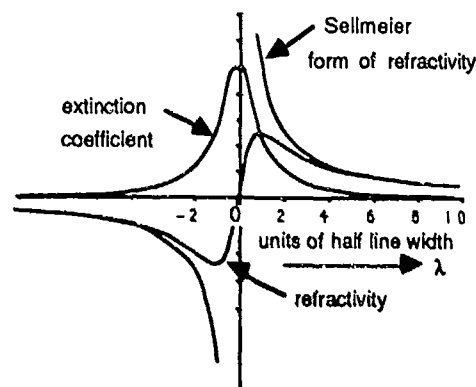
Figure 1: Dispersion and absorption near a spectral line.

Both Marlow[13] and Measures[11] showed this theoretically, while Blendstrup, Bershader and Landhoff[16] measured the resonance refractivity and absorption of sodium vapour and so confirmed it experimentally. They also measured refractivities of the order of 5×10^3 larger than the value for air (as an example of normal interferometry) at STP of 2.3×10^{-4}, before the fringe visibility became too small. They suggested that enhanced flow visualisation might be achieved by using resonance refractivity, as with spectral-line interferometry.

In his paper on this last topic, Measures took into account both Doppler and collisional broadening and derived expressions which can be used to choose the two wavelengths - one close, the other far from the line - for two-wavelength interferometry. Subtraction of these two interferograms gives the distribution of the integrated population (along the ray path) in the lower state of the spectral line. The potential of this technique has increased with advances in narrow-band pulsed and c-w dye lasers. Obviously one needs both high spectral resolution of the two light sources and accuracy in knowing their wavelengths with respect to the line centre. Blendstrup et al.[16] pointed out that in a situation where the background density is too small to produce a measurable fringe shift on a normal inteferogram, a measurable interferogram might be obtained by working with a narrow-band light source tuned close to a spectral line. (Preferably the line should arise from an energy level near to the ground state of the test gas, but if that is not possible then an included species would have to be used). This is a form of "super interferometry" and it need not be restricted to interferometry since a Schlieren or shadowgraph system would respond equally well[17]. Interpretation of fringe shifts would require some care because the population of the lower state depends on the local temperature as well as the density but for flow visualization alone that may not matter.

Hook formation

Hook-interferometry couples the interferometer with a stigmatic spectrograh in order to observe the dispersion behaviour close to spectral lines (figure 2).
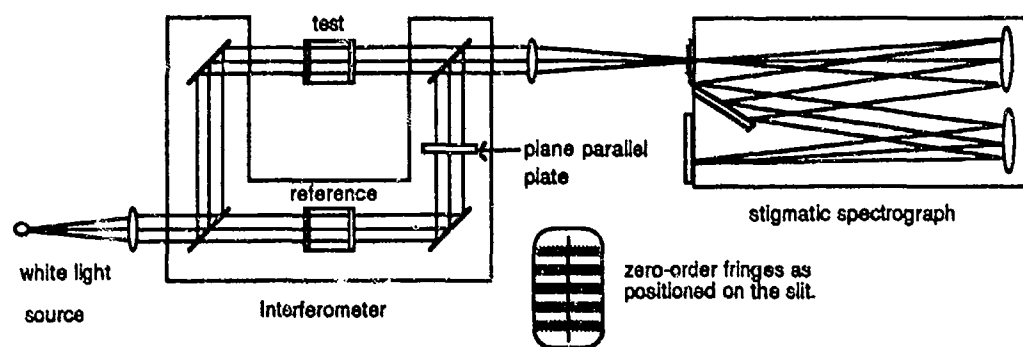
Figure 2: Set up for hook interferometry.

A light source which has a continuum structure over the observational bandwidth is therefore required. "White-light" fringes (near-zero path difference) are focussed to cross the entrance slit of the spectrograph and consequently appear as nearly horizontal fringes across the spectrum. The interferometer is then adjusted to place a large optical path in the reference beam , commonly with a glass or fused silica plate or a low dispersion air path; the test beam being unchanged. The fringes dissapear from the entrance slit but on the spectrum they appear as slanted fringes whose wavelength separation depends on the size of this path difference.

A diagram may be constructed to illustrate this[13] (figures 3 and 4).
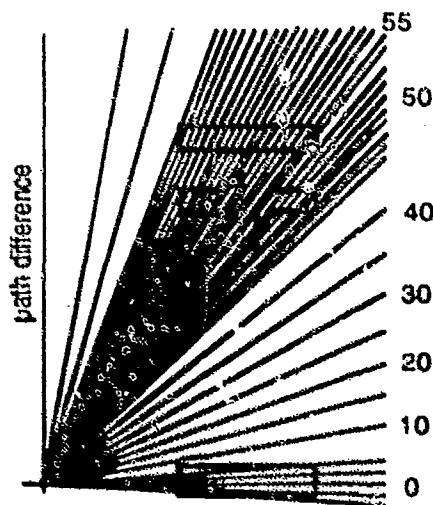
Figure 3: Fringe formation
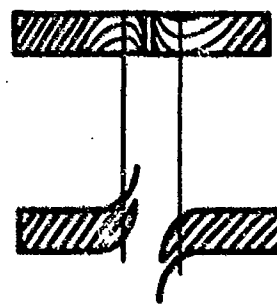
Figure 4: Hook formation

The abscissa is wavelength (as on the spectrum) and the ordinate, path difference in units of wavelength. Fringes are single wavelengths apart so they appear on this diagram as straight lines from the origin of slope p say, where p is the "order" of particular fringe (its number in order from the zero fringe - the wavelength axis). White-light fringes crossing the spectrograph slit appear on this diagram (on the image plane) as a rectangular box crossing the abscissa, as wide as the bandwidth of the spectrograph and as high as the number of fringes on the slit. The introduction of the optical path in the reference beam moves this box to high order on the diagram. The fringes thus appear on the spectrum as they do in the box. The box remains rectangular only if the optical path is

free of dispersion, otherwise it follows the dispersion curve. In this case the box has to be transformed to a rectangle so that the true shape of the fringes may be seen on the image plane of the spectrograph.

If the test atoms are introduced with their local dispersion (figure 1), the outline of the "box" follows the shape of the local dispersion curve (the opposite to that in figure 1, because an increase the reference beam path is taken as positive). Note that the slope (p) of some fringes can become equal to the local slope of the dispersion curve. When this box is transformed to a rectangle (figure 4), these points have zero slope on the spectrum and the fringes form the characteristic "hooked" appearance. At these points therefore,

$$p = d(n-1)l \, / \, d\lambda = r_o \int N_i \, dl \, f_{ij} \, (\lambda_{ij})^3 \, / \, \{4\pi(\lambda_h - \lambda_{ij})^2 \},$$

where the Sellmeier form of the refractivity has been used and $\int N_i \, dl$ is the integrated column population along the ray path through the test medium of length l and λ_h is the wavelength at the hook positions. If there is background dispersion, as would be introduced by using a glass plate for the large optical path in the reference beam, and this is κ say, then

$$p = \kappa + d(n-1)l \, / \, d\lambda,$$

or;

$$p - \kappa = K = r_o \int N_i \, dl \, f_{ij} \, (\lambda_{ij})^3 \, / \, \{4\pi(\lambda_h - \lambda_{ij})^2 \},$$

K is called the "hook constant" although it does vary across the spectrum, however it can usually be taken to be constant over the line dispersion. The magnitude of K can be obtained simply by measuring the separation of the fringes well away from the influence of the spectral line. The required quantity, $\int N_i \, dl \, f_{ij}$ (abbreviated to Nfl), therefore can be obtained directly from two measurements;
   (1) the wavelength separation of the hooks about the spectral line,
   (2) the wavelength separation of the (undisturbed) fringe system away from the spectral line and interpolated to the value at the line itself, if necessary.

In principle this is an easy and simple technique. There is control on how far from the line centres the hooks appear, by choosing the size of the optical path placed in the reference beam. Thus in general, it is possible to ensure that the Sellmeier form for the refractivity is valid at the hook positions. An increase in the Nfl product at constant K, pushes the hooks further from the line centre - proportional to the square root of the change in Nfl. This means that the method has a large dynamic range - covering some eight orders of magnitude in Nfl. By employing new techniques of measurement at small hook widths[18], its lower limit can just overlap the higher sensitivity of absorption at the line centre and, as already pointed out, it does not suffer the problems associated with optical depth or broadening. The major difficulties arise in the instrumentation: requiring an interferometer, a spectrograph of reasonably high resolving power with a plate factor approaching 1 Å/mm and a "white-light" source of high spectral brightness.

Spatial resolution

If one is not concerned with spatial resolution, which implies that the test atoms have uniform column density over the field of view of the interferometer, the source may be imaged onto the spectrograph slit and the fringes of the interferometer localised (focussed) onto the source with an f-number chosen to ensure that the spectrograph is used to its full resolution. In this way maximum use is made of the intensity of the light source. Some five fringes along the length of the spectral line are sufficient to obtain a good estimate for the hook width. On the other hand if spatial resolution is required (or necessary) along the length of the slit then particular attention needs to be paid to the design of the optics.

In some interferometers, but particularly in the Mach-Zehnder type, the fringes may be localised to a plane which may be placed within the test atoms. This is of course necessary in normal

interferometry in order to obtain spatial resolution across the field of view. It is possible to do the same in the case of hook-interferometry by localising the interferometer fringes within the test atoms as before and imaging the slit of the spectrograph onto the same plane. If the population of the lower state of the transition varies along the slit, then this will appear as a variation in the width of the hooks along the spectral line in the image plane of the stigmatic spectrograph (e.g., see figures 6,9). In this case the number of fringes required across the slit depends on the magnitude of the population gradient in that direction, and on the resolution.

Because the slit is usually only 50 micron or less wide and say 15 to 20 mm long, while interferometers operate with closely collimated light beams, the brightness of the light source is crucial in obtaining good contrast fringes. One often has to restrict the collimated area of the beam in the interferometer (e.g. make it slit-like) and perhaps relax the collimation itself to some degree in order to maintain the resolution of the spectrograph by ensuring that the grating is fully covered.

Experiments

1. Channelled spectra

This is an application of the instrumentation required for hook measurements but uses a low resolution spectrometer covering a wide bandwidth. It is mentioned here because it is a true dispersion measurement. In order to obtain electron density distributions behind shock waves it is common to use two-wavelength interferometry. This is because free electrons have a very different refractivity to atoms. Not only is it negative, but the dispersion is also anomalous over the visible spectrum. Two-wavelength interferometry provides effectively two equations to solve for the population of the free electrons from the background. The idea in using a channelled spectrum is to do mutilple-wavelength-streak interferometry over a small spatial region confined to the about a mm or so along the spectrometer slit. The interferometer is set up as for a hook spectrum but with an infinite fringe system on the slit. The spectrum is now crossed by a vertical fringe system (parallel to the slit) and one observes the so called channelled spectrum. In the fringe-formation picture the "box" has zero height (<< one fringe high) so as the optical path increases vertical fringes take the place of the slanted ones in the previous case.

This fringe system is then swept in time along the slit axis during the passage of the shock. Each fringe is shifted by the normal density change toward the red, corresponding to an increase in the optical path in the test beam with the larger shift in the blue region. Free electrons shift the fringes to the blue with the larger shift in the red. Therefore, there are as many equations to obtain the electron density from the normal dispersion components as the number of fringes, with an improvement in accuracy due to statistical averaging. Also the fringes increase in order number by one, in progression toward the blue and this extra information is also useful in the analysis.
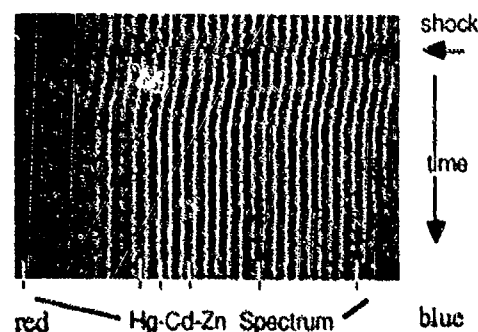
Figure 5: Channelled spectrum

It is necessary to be careful that spectral lines do not locally perturb the fringe shift because of their dispersion. The technique has been used in our laboratory to measure electron densities behind strong shock waves[19] and as far as I know we are the only ones to use channelled spectra for this purpose, although the method is commonly employed in other applications. For example, to measure dispersion in solid state crystals etc.

2.Temperature distributions along the stagnation streamline on a blunt body in shock tunnel flows.

Our first attempt at using the hook method in shock applications applied it to the stagnation streamline within the shock layer on a cylindrical body in high enthalpy flow in nitrogen in the T3

shock tunnel at ANU[20]. The spectrometer available at the time had a focal length of 0.5 metre which restricted the ultimate sensitivity considerably. The spectral region was chosen in order to observe the resonance and 1ev lines of atomic chromium which was expected to exist as an impurity in the test gas, due to the high temperatures which occur in the stainless steel reservoir after shock reflection. Chromium is useful as an element for hook studies because three resonance transitions originating at the ground-state lie in the 425nm- 429nm region and seven lines originating from energy levels close to 1ev above the ground state lie between 430nm - 439nm. Consequently almost all of these lines can be photographed in one exposure (figure 9). We were able to see the ground state chromium density before the shock wave and follow its changes along the streamline to the body as in figure 6.
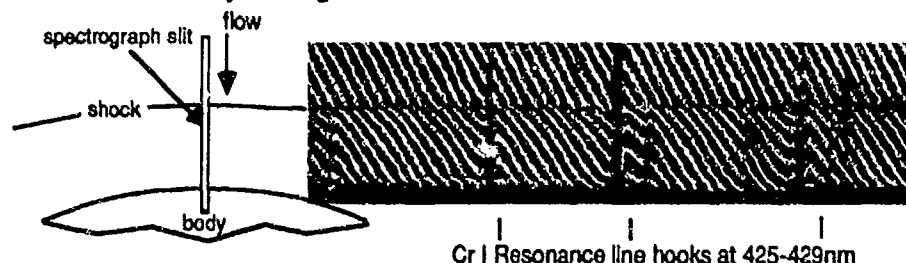
Figure 6: Hooked spectrum along stagnation streamline

The 1ev lines however were only hooked between the shock wave and the body surface. An excitation temperature was obtained for the chromium 1ev level by assuming a Boltzmann distribution between the ground and these levels. The temperature distribution deduced did in fact agree with the calculated temperature distribution within the shock layer although the error bars were rather large. The light source for this work was an exploding copper wire with a pulse time of some 50μsec which was quite adequate for this work.

3. Shock stability
Our laboratory has had a long interest in the problems associated with the stability of shock waves in real gases using normal interferometry for diagnosis. One difficulty which occurred in the inerpretation of the interferograms was that at the higher shock speeds we could detect the shock wave but the sensitivity was too low to observe the mixing front between the test and driver gases. It was neccessary to determine whether the observed instabilities in the shock wave were intrinsic behaviour or arose from disturbances of a nearly coincident mixing front.

Because we considered that the driver gas would be contaminated with sodium vapour but the shocked-test gas, by taking normal precautions, should be relatively clean; we decided to attempt spectral-line streak interferometry close to the Na-D2 line. A cw-ring dye laser of some 15 MHz bandwidth (1.7×10^{-4} Å) provided the light source and was tuned to 5889.20Å (line centre at 5889.95Å) and 5868.36Å for the off line case. The wavelengths were measured with a wavemeter accurate to better than 0.01Å. The photographs showed no enhancement at the shock wave itself (as we had hoped) but some enhancment of the "oscillations" in the fringes some distance from the shock front (figure 7a, 7b), but were still not conclusive concerning the mixing front position.

Figure 7a: Source λ=5868.36Å   Figure 7b: λ=5889.20Å   Figure 7c: λ=5889.95Å
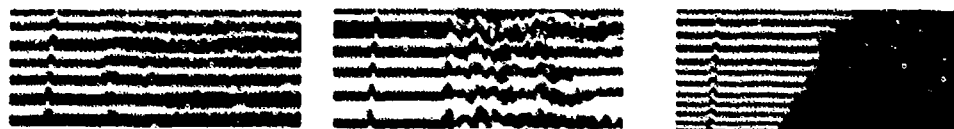
As we tuned closer to the line centre however we noticed that the absorption was beginning to reduce the fringe contrast until when we tuned right on line centre they disappeared completely[21]

(figure 7c). In this case therefore, since we were interested only in flow visualisation, absorption at the line centre was the most sensitive and conculsive.

4. Metastable populations in ionising shocks.

Recently Mishin et al.,[22] suggested that the type of instability observed firstly by Glass and co-workers[23], which begins in the ionisation cascade behind ionising shock waves in argon could be initiated by a sudden release of energy into the gas similarly to the behaviour in detonations. The mechanism they propose for this exothermic reaction is that metastable atoms could be excited to a high excitation temperature by atom-atom collisions[24] in the non-equilibrium region behind the frozen shock and could reach high over-populations. These would be then be converted to highly excited molecular ions by associative ionisation and subsequently, deactivated by superelastic collisions thus releasing their energy as kinetic energy. The important link in this chain is the production of the metastables directly behind the shock.

They, and also Yushchenkova[24] separately, supported their arguments with two experiments; one in a low density argon plasma stream in which shocks could be produced over a body and the other in shock waves produced by colliding two supersonic streams. However in both cases a high concentration of metastable atoms was *artificially* introduced. For normal shocks into argon their mechanism requires a high population of metastable atoms to be produced before the ionisation region. This is in contradiction to the model proposed by Oettinger and Bershader[25] for example, which predicts no significant population of the metastable levels until after the ionisation cascade.

We set out to check this mechanism directly by monitoring the two argon, $1s_3$ and $1s_5$, metastable level populations using the hook-method, in both the stable and unstable cases. The slit was imaged to lie along the shock tube axis thus providing spatial resolution. Initially when observing the 6965.43 Å line ($1s_3$ - $2p_2$, f-value = 0.029), we used a nitrogen laser- pumped dye laser (dye =nile blue) with a pulse time of 5 nanoseconds, timed to position the slit at various distances behind the shock wave. This transition gave a sensitvity of 1.9×10^{13} metastables cm^{-3} with a 1 metre spectrograph.
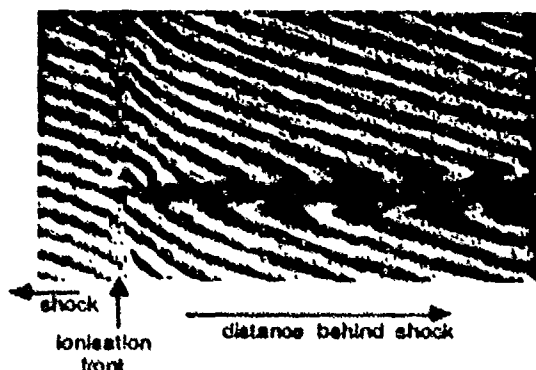
Figure 8a: Spatially resolved hook spectrum of the 7635.11 line of argon for an unstable shock M=14.4
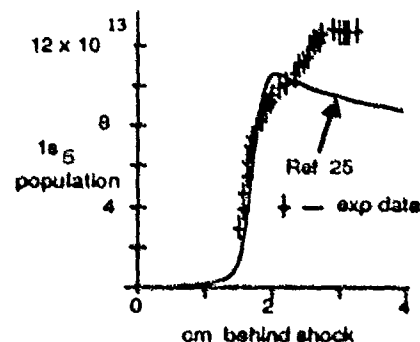
Figure 8b: Population of the $1s_5$ metastable level from 8a and ref 25.

Subsequently we changed to the 7635.11Å ($1s_5$ - $2p_6$, f= 0.239) and 7724.2 ($1s_3$ - $2p_2$, f=0.341) lines to obtain the improved sensitivity through the higher f-values. In order to obtain sufficient brightness at these higher wavelengths, we employed fluorescence from the dye (DOTC) pumped by a flash-lamp pumped dye laser (Rhodamine 640) with a pulse time of 1 micro-sec. The output of the Rh 640 covers the absorption band of the DOTC.

The result of our observations (figure 8) is that no metastable population exists in the non-equilibrium region above our lower limit of 2×10^{12} cm^{-3} (no hooks). This is some 10^{-4} times smaller than that required by the exothermic theory. On the other hand we did observe population of the metastables after the cascade front, to a value which is in very good agreement with the accepted models[25]. We will be publishing a full account of this work and the data shortly.

5. Temperature distributions behind shock waves in helium argon and nitrogen.

An interest in the use of the hook-method as a means of determining the distribution of temperatures has prompted a series of experiments using spatial resolution along the slit behind normal shock waves and within the Mach stem region in pseudo-steady Mach reflection. Time resolution of 5 nanosecond was obtained by using the nitrogen laser to pump a fluorescing dye source. The dye in this case was stilbene giving an output covering the chromium resonance lines and those from the 1ev level. A fluorescing source is preferred over a dye laser source because it does not exhibit the strong random-spectral structure which can seriously degrade the quality of the hook photographs.The pulse was timed so that the shock, in both the above cases, would appear on the slit (figure 9).

Cr I resonance lines $E_1=0$ Cr I excited state lines $E_i = 1ev$
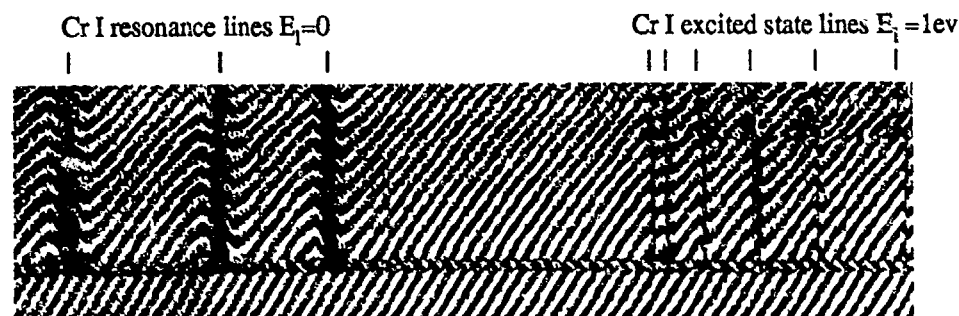
Figure 9: Hooked spectrum behind a Mach 16 shock wave in N_2, taken on a medium dispersion spectrograph. $T_{meas} = 5917 \pm 60$ K. $T_{calc} = 6500$ K.

$Cr(CO)_5$ was mixed with the test gas in concentrations of up to 0.3%. Even at this level however it was found that dissociation of the carbonyl and excitation of its products lowered the temperatures by some 3% below those expected for the equilibrium gas behaviour without the carbonyl. The temperature was obtained by calculating the population of the ground and 1ev states from the hook measurements and assuming a Boltzmann distribution over those states. This was then compared with the temperature calculated for the real gas with known thermodynamic information concerning the carbonyl and its products. The measured CrI excitation temperatures agreed with these predictions within the error range (±2%) to temperatures up to 6000K. Then they began to be sytematicaly lower (see figure 9). At temperatures above 7000-8000 K in argon the carbonyl is photo-dissociated ahead of the shock and ionised behind it, which reduces the effectiveness of the technique as a diagnostic. Relaxation rates are affected also of course.

This success prompted us to attempt to obtain temperature distributions within Mach stem regions of pseudo-steady Mach reflection for near perfect gas conditions.The spectrograph slit was imaged at four locations from the wall, three of these between the wall and the triple point, the other just outside. The light was the 5 nanosec nitrogen pumped dye laser and it was also timed to place the slit correctly in successive shots. A spectrograph of 5 m focal length improved the resolution over the normal shock work above. Figure 10 presents results which have been read to provide early results for this presentation.

The wedge angle is 15 degrees and the initial shock Mach number is 7.7 into argon at a pressure of 40 torr.
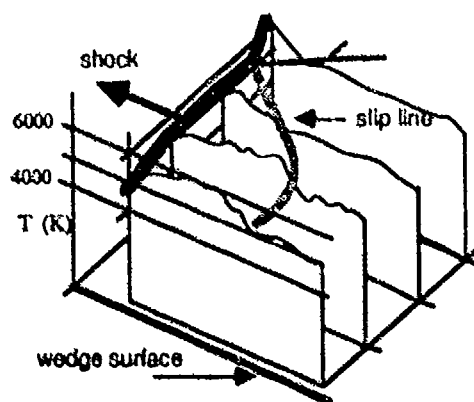
Figure 10: Temperature distributions in pseudo-steady Mach reflection.

6. Time development of the population distribution of alkaline earth elements following sudden excitation of the resonance line (a light-shock).

An illustration of the use of spectral-line interferometry is provided by another experiment in which a laser beam, tuned to the resonance line of atoms in a vapour column, is used to suddenly saturate that transition (a form of light shock). This work followed an initial experiment in sodium vapour in which the pumped-column was rapidly and completely ionised[26]. Our interest was to study the behaviour outside the pumped column. Accordingly we have set up a barium vapour source which produces a disc of vapour some 6 cm in diameter and 1cm thick (figure 11).

The central 1mm core of the vapour is irradiated with a flash-lamp pumped laser, tuned to the 5535Å resonance line of the Ba I. The cw-ring laser is tuned near to transitions out of the excited states of the atom and ion and is the light source for a Michelson interferometer. Vertical fringes in the vapor, are imaged on to the slit of a sweep camera and give spatial resolution normal to the pumped column. A wavemeter of 0.3 GHz accuracy gives the ring-laser wavelength and therefore its separation from the line centre. The sweep is begun prior to the firing of the flash-lamp laser.
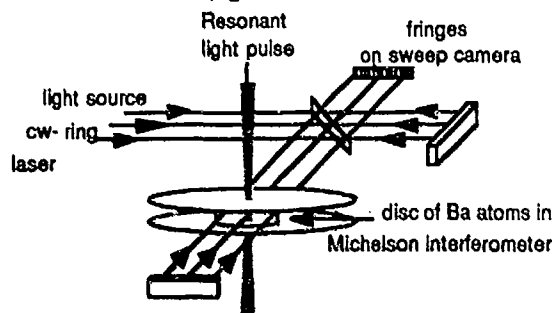
Figure 11: Spectral-line interferometry
on "light-shocked" Ba atoms.
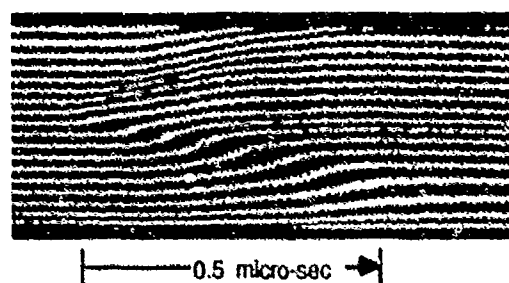
Figure 12a: Spectral-line interferogram of the 6s5d $^1D_2$ - 5d6p $^1P_1$ 5826.27Å line of Ba I vapour, c-w ring dye laser 15MHz bandwidth, detuned 5.8 GHz from line centre.
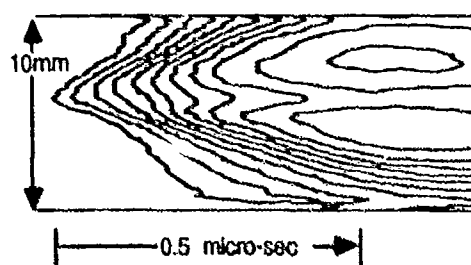
Figure 12b: Contours of column population, $\lambda/4$ apart, corresponding to an $\int Ndl = 8 \times 10^{16}$ cm^{-2}. The pump laser beam is 1mm wide at the 'peak' and lasts for 0.5 µsec.

The resulting interferogram (figure 12a) is digitised and analysed using a two-dimensional Fourier transform procedure[27] to extract the phase distribution. We then unravel this into radial population distributions via an Abel inversion process. Figure 12b shows the integrated column population contours before the inversion procedure.

Novel procedures

The high brightness, short pulse times, bandwidth control and tunability of modern laser sources has opened up new possibilites in applying spectral-line dispersion and absorption methods to shock and plasma diagnostics. Their spectral range, restricts the transition wavelengths and thus the atoms which can be used in such experiments. For example, the important resonance lines of the gases commonly used in shock tube experiments are still beyond the reach of laser or pseudo-laser sources of sufficient power to act either as a light source or an excitation source

(excluding perhaps synchrotron radiation). When such sources become available (I assume that they will), then direct access to these transitions would enable us to probe the collisional processes, particularly in non-equilibrium regions.

A better knowledge of the collisional processes involved throughout the relaxation region would seem to be paramount to our understanding of shock behaviour. One way perhaps of observing these is to perturb the local population rapidly (e.g. the light shock) and follow the decay of the perturbation back to the former situation. Lasers can provide sufficient power to saturate a transition and produce temporarily an infinite excitation temperature between the levels. Monitoring the flourescence from the upper state can give these decay rates, but we have found this method unsuccessful using sodium as a tracer, because of insufficient information concerning the initial sodium population. A dispersion method such as hook- or spectral-line interferometry, which can measure populations directly, if used in conjunction with flourecense techniques, could be very useful in this regard. In particular spectral line interferometry, as used in the last experiment above could map the spatial, as well as the temporal distribution of the disturbed populations beginning from an initially small pumped region.

References
1. R.W. Wood, *Phil Mag.*, **8**, 298 (1904). (see R.W. Wood, Physical Optics, Dover (1964).)
2. R. Ladenburg, *Ann. d. Phys.*, **38**, 249 (1912).
3. L. Puccianti, *Mem. Spettrosc. It.* **33**, 133 (1904).
4. D. Roschdestvenski, *Ann. d. Phys* . **39**, 307 (1913).
5. R. Ladenburg, *Zeit. f. Phys.*, **48**, 15 (1926).
   H. Kopfermann and R. Ladenburg, *Zeit. f. Phys.*, **48**, 26 and 51 (1926).
6 V.K. Prokofiev, *Trudy Gos. Optic. Ins* ., 3(25), 1 (1924).
7. Yu. A. Dumaev, G.K. Tumakaev, and A.M. Shukhtin, *Sov. Phys -Tech. Phys.*, **6**, 815 (1962).
8. G.K. Tumakaev and V.R. Lasovskaya, *Zh. Tekh. Fiz.*, **43**, 2008 (1973).
9. W.H. Parkinson, *Proc. 8th. Int. Shock Tube Symposium*, 5-8 July London (1971).
10. K. Miyazaki, Y Ogata, T. Fujimoto and K. Fukuda, *Japan J. App. Phys.*, **13**, 1866 (1974).
11. R.M. Measures, *Appl. Opt.* **9**, 737 (1970).
12. I. Smilanski, L.A. Levin and G. Erez, *Opt. Lett.*, **5**, 93 (1980).
13. W.C. Marlow, *Appl. Opt.* **6**, 1715 (1967).
14. M.C.E. Huber, *Progress in Gas Dynamic Research by Optical Methods:* D.S. Dosanjh, Ed. Plenum N.Y. 85 (1971).
15. R. Ladenburg, *Zeit. f. Phys*,. **4**, 451 (1921).
16. G. Blendstrup, D. Bershader and P.W. Langhoff, *AIAA Jour.* **16**, 1106 (1978).
17. R.J. Sandeman, *Proc. 8th. Int. Shock Tube Symposium*, 5-8 July London (1971).
18. R.J. Sandeman, *Appl. Op.* **18**, 3873 (1979).
19. P. Meier and R.J. Sandeman, *Proc 10th Int . Shock Tube Symposium*, 14-16 July, Kyoto (1975).
20. H.G. Hornung and R.J. Sandeman, *J. Phys. D. Appl. Phys.*, **7**, 920 (1974).
21. A.F.P. Houwing and R.J. Sandeman, *Proc. 14h. Int. Shock Tube Symposium*, 19-22 Aug. Sydney (1983).
22. G.I Mishin, A.A.P Bedin, N.I. Yushchenkova, G.E. Skvortsov and A.P. Ryazin, *Zh Tekh. Fiz.* **51**, 2315 (1981).
23. M.P.F. Bristow and I.I. Glass, *Phys. Fluids*, **15**, 2066 (1972).
24. N.I. Yushchenkova, *Zh. Tekh. Fiz.*, **6**, 1283 (1980).
25. P.E. Oettinger and D. Bershader, *AIAA Jou.*, **5**, 1625 (1967).
26. T.B. Lucatorto and T.J. McIlrath, *Phys. Rev. Lett.* **37**, 428 (1976).
27 D.J. Bone, H. -A. Bachor and R.J. Sandeman, to be published.

CONDENSED MATTER AT HIGH SHOCK PRESSURES

W. J. Nellis, N. C. Holmes, A. C. Mitchell, H. B. Radousky, and D. Hamilton

Lawrence Livermore National Laboratory
University of California
Livermore, California 94550

Experimental techniques are described for shock waves in
liquids: Hugoniot equation-of-state, shock temperature
and emission spectroscopy, electrical conductivity, and
Raman spectroscopy. Experimental data are reviewed and
presented in terms of phenomena that occur at high
densities and temperatures in shocked He, Ar, N_2, CO,
SiO_2-aerogel, H_2O, and C_6H_6. The superconducting
properties of Nb metal shocked to 100 GPa (1 Mbar) and
recovered intact are discussed in terms of prospects for
synthesizing novel, metastable materials. Ultrahigh
pressure data for Cu is reviewed in the range 0.3-6TPa
(3-60 Mbar).

I. INTRODUCTION

Significant advances in shocked, condensed matter have been made in
recent years through diagnostic development, specimen fabrication, and
theory. The nature of this work is summarized in the proceedings of recent
Topical Conferences on Shock Waves in Condensed Matter.[1,2] General areas of
concentration have been the properties of fluids and solids at high densities,
temperatures, and strain rates and the nature of materials processed and
recovered from high dynamic pressures. In this paper the main emphasis will
be on dense fluids at shock pressures up to 100 GPa (1 Mbar), compressions up
to 5-fold over initial liquid density, and shock temperatures up to 10,000K.
At such extreme conditions several phenomena occur including molecular
repulsion, rotation, vibration, and dissociation, electronic and molecular
ionization, and chemical decomposition and reaction. Examples from the
literature will be reviewed and new results will be presented to illustrate
these phenomena.

The properties of dense molecular fluids at high pressures and
temperatures have three principal applications: the equation of state and
chemistry of high explosives, the nature of the interiors of the outer planets
(Jupiter, Saturn, Uranus, and Neptune), and hydrodynamic applications. The
relation between these areas and shock-compression studies was discussed
previously.[3]

II. EXPERIMENTS

The experiments are performed using shock waves generated by the impact
of planar projectiles onto planar target specimens. While, historically,
strong shock waves have been generated using high explosives,[4] in recent
years most research has utilized impactors launched by light-gas guns.[5]
Maximum impact velocities are 2 and 8 km/s for single-stage and two-stage
light-gas guns, respectively. A Ta impactor at 2 and 6 km/s achieves shock
pressures in Al of 30 and 200 GPa. respectively. Gas guns have several
advantages over explosive shock generators. Shock strength is simply tuneable
by choice of impactor material and velocity, shock-wave profile is simply
tuneable by choice of impactor thickness and design, shock pressures twice as
large as with plane wave explosive systems are available, and facilities are
operated in a conventional laboratory setting. The current state of temporal

and spatial resolution for shock-wave diagnostics means that gun facilities
can now be scaled down substantially without compromising the ability to
perform novel and diverse research with a well characterized and simply
tuneable shock driver.

The experiments discussed here were performed using a two-stage light-gas
gun described previously.[6-8] The two driving media or stages are gunpowder
reaction products and H_2 gas. The gunpowder drives a heavy piston which
compresses the H_2 gas. When the H_2 pressure reaches ~ 100 MPa (1 kbar)
a rupture valve opens and the compressed gas accelerates a light (~ 15g)
projectile to velocities up to 8 km/s along a smooth bore launch tube. Strong
shock waves are generated by impact of projectile onto target positioned about
0.5m beyond the muzzle of the launch tube. Projectile velocity is measured in
free flight between muzzle and target by a flash radiograph system. A more
detailed description of two-stage gun operation and shock-wave diagnostics is
available.[9]

The fundamental measurement is equation of state which determines the
pressure, density, and specific internal energy achieved in shock compression
experiments. These experiments are based on the Rankine-Hugoniot relations
and shock impedance matching.[9] The measured quantities are impactor
velocity, shock velocity, and initial density. The method is described
elsewhere for single- and double-shocked liquids.[10,11] Having measured the
equation of state, other properties can be measured to study the nature of the
state; for example, shock temperature, electrical conductivity, and Raman
spectra. In these experiments the impactor velocity is also measured and the
state achieved is obtained by shock impedance matching using the previously
determined equations of state. Figures 1a and 1b illustrate experimental
configurations for single and double-shock Hugoniot experiments. In the
former, shock velocity is measured in the liquid, and in the latter it is
measured in an anvil behind the liquid.

A shock temperature or emission spectrum measurement in a transparent
liquid is illustrated in Fig. 1c. Radiation emitted from the shock front
exits the unshocked portion of the specimen and is directed to either a
6-channel time-resolved pyrometer[12,13] or to a spectrograph and
1000-channel, time-integrated, gated, linear diode array.[14] For simple
dense fluids like Ar, both molecular dynamics and continuum mechanics
calculations indicate that the shock front is about 10 Å and < 10^{-12}s
thick.[15,16] Thus, for simple shocked fluids the emission spectra are fit to
graybody or blackbody spectra and the assumption is made that the temperature
so derived is characteristic of equilibrated shocked material emitting light
from behind the shock front through an optically thin shock front. For more
complex fluids, for example those undergoing chemical reactions, the shock
front can be optically thick, so that the equilibrium temperature is not
observed while nonequilibrium spectral features might be.

A two-probe electrical conductivity experiment for a shocked liquid is
illustrated in Fig. 1d.[17] A current is established in the shunt resistor,
and the time-resolved voltage across the electrodes in parallel with the shunt
resistor is measured as the shock transits the electrodes. The cell
resistance versus known electrical conductivities is calibrated in separate
experiments prior to the shock experiment.

The microscopic nature of shocked fluids can be investigated by pulsed
Raman spectroscopy, which measures the distribution of molecular vibrational
frequencies. The experimental arrangement is illustrated in Fig. 2. Light
from a 10 ns 0.2J KrF (284 nm) laser pulse is incident normally on a specimen
of shocked liquid. Light from spontaneous Raman scattering, 10^{-10}J total,
is viewed at 45^0 off axis, dispersed by a spectrograph, and recorded on a
gated, linear diode array.[18] The laser light is focussed several mm behind
the shock front and so this technique requires that the shocked specimen
remain transparent.

In the case of transparent, brittle, solid specimens, like silica aerogel, the configuration for an equation-of-state experiment in which shock velocity is measured is shown in Fig. 3.[19] Because the shock front radiates strongly in the visible, the stepped rear surface is coated with $\sim$ 1000 Å of Au to absorb thermal radiation until shock breakout at the coated surface. By temporally streaking the optical emission from the coated, stepped surface, the transit time of the shock across the step height can be measured. This technique is similar to that used previously to measure transit times for laser-driven shock waves in metals.[20] The shock temperature is measured by using a simple, uncoated specimen disc and sending light emitted from the shock front to a pyrometer or spectrograph.

Several additional measurements are made in shocked solids, including time-resolved interface velocity measurements by optical interferometry,[21,22] the generation of dynamic, planar, isentropic compression waves by graded-density impactors,[23] the detection of phase transitions by both the measurement of longitudinal sound speeds[24] and shock temperatures,[25] and flash X-ray diffraction from crystals in the shock state.[26,27]

In addition to the diagnostic developments major advances have resulted from specimen fabrication. For example, in order to investigate the high-density regime of molecular fluids, higher-density liquid specimens were shocked, rather than gases. In order to liquify most small molecules at atmospheric pressures, cryogenic temperatures are required. Thus, each specimen holder was a small cryostat[10,28,29] - a different one for each experiment. States of high-temperature matter in expansion relative to crystal density have been studied because of the recent availability of fine-grained, transparent, porous SiO_2 aerogel having $\sim$ 100 Å pore size.[19] The fine pore size means that the material is uniform and equilibrium will be achieved much faster than the time scale of the experiments. However, this material is extremely brittle and requires vacuum holders and diamond cutting tools to achieve the required micron surface flatness. Dynamic isentropic compression is now possible because of the development of impactors with linearly varying density (shock impedance) produced by careful sedimentation of metallic powders in an epoxy-like matrix.[23] These examples illustrate the importance of special materials and fabrication techniques in this field.

III. THERMAL EQUILIBRIUM

Shocked condensed matter is generally in thermal equilibrium during the measurements owing to the high densities and temperatures. For example, liquid N_2 shocked to 30 GPa[10] has a density of 2 g/cm^3 (4 x 10^{22} N_2/cm^3) and a shock temperature of $\sim$ 6000K.[30] Assuming the mean free path between collisions is a molecular diameter and that molecular velocity is thermal, then the intermolecular collision time is $\sim$ 10^{-13}s. The N_2 molecular vibration time is $\sim$ 10^{-14}s. The shock front width or equilibration time in shocked dense Ar is $\lesssim$ 10^{-12}s.[16] All these times are much less than the time resolutions of the diagnostic systems which are $\sim$ 10^{-9}s and the duration of the experiments which are 10^{-7}-10^{-6}s. Of course, phenomena which require longer than the experimental lifetime could produce deviations from thermal equilibrium. At the conditions considered here, however, examples of nonequilibrium behavior are difficult to identify unambiguously and are most likely to occur in chemically reacting systems.

IV. RESULTS

Equation-of-state experiments have been performed in the last few years for most small molecules including He,[29] H_2 and D_2,[28] N_2,[10,31] O_2,[10] air, Ar,[10,32] Xe,[33] CO,[11] CH_4,[11] C_6H_6,[34] n-C_4H_8 (polybutene).[34]

NH_3 [17] and H_2O.[17] The maximum pressures and densities, which our group has achieved in these shocked liquids, are listed in Table I. The corresponding calculated and, in some cases, measured maximum temperatures are in the range 5,000-30,000 K.

Shock temperature measurements have been performed for a number of these fluids: H_2O,[13] NH_3,[35] Ar,[36] N_2,[36] C_6H_6,[34] and n-C_4H_8.[34] Temperature is an important thermodynamic parameter because it provides information about the distribution of internal energy between thermal and internal degrees of freedom. In the case of C_6H_6 and possibly n-C_4H_8 the radiating temperatures from the shock fronts are substantially lower than the temperatures calculated theoretically assuming chemical equilibrium. This difference suggests that the radiating temperatures are not representative of shocked matter in thermal and chemical equilibrium behind the shock front.[34]

The electrical conductivity has been measured for shocked H_2O,[17,37] NH_3,[38] N_2,[39] O_2,[39] and C_6H_6.[39] The purpose is to determine the magnitude and mechanisms of electrical conduction and in so doing to possibly obtain information about the nature of the fluids which cannot be obtained from state variables. For example, the high conductivity of shocked H_2O indicates a significant amount of H_2O molecules are chemically ionized above 20 GPa shock pressure.[37] This proposal motivated the Raman spectroscopy measurements described below in order to look for ionic species like OH^- and H_3O^+. The electrical conductivities of shocked N_2 and O_2 are even higher than for H_2O and electrons are probably the dominant conduction mechanism.

The spontaneous Raman spectra of shocked water has been measured from 7-26 GPa[18] to try to identify molecular and ionic species from spectral features. At 26 GPa water is compressed two-fold and heated to 1700 K. The stimulated Raman scattering from shocked benzene has been measured at 1.2 GPa, indicating the existence of the molecular state at this shock pressure.[40] The emission spectrum of benzene has been measured to 59 GPa to try to identify chemical species in or close to the shock front.[14]

V.   DISCUSSION

Intermolecular repulsion is the dominant effect at high densities and temperatures. The rare gases are the simplest materials to study in this respect, because the physical properties are determined solely by the repulsive potential, provided electronic excitation is negligible. The He Hugoniot data are interpreted only in terms of an effective pair potential, the calculated shock temperatures as large as 20,000 K being much smaller than the ionization potential.[29]

For Ar the upper limit of the "cold" range is a single-shock pressure of 36 GPa, a compression of 2-fold over initial liquid density, and a calculated temperature of 12,000 K. The pair potential derived from Ar shock-wave data is in excellent agreement with pair potentials derived from molecular-beam scattering data, indicating that two-body interactions dominate in the dense fluid. The pair potential derived from Ar shock-wave data has the exponential-six form:[41]

$$\phi(r) = \epsilon \left\{ \left[\frac{6}{\alpha - 6} \right] \exp \left[\alpha(1 - r/r^*) \right] - \left[\frac{\alpha}{\alpha - 6} \right] \left(\frac{r^*}{r} \right)^6 \right\} , \qquad (1)$$

where r is the intermolecular distance. The Ar Hugoniot data are shown in Fig. 4. Curve D was calculated using only the potential of Eq. (1) and agrees with the data below 36 GPa. At higher pressures the data fall well below Curve D. Agreement with the data is achieved by taking into account electronic excitation and the density dependence of the electron energy gap.[32] A similar result was obtained for Xe.[33] A fundamental conclusion of the rare gas study is that high shock temperature is a very useful probe of the electronic structure at high density and pressure.

The shock-compression data for non-polar molecules can be calculated using the potential of Eq. (1) scaled via corresponding states and by taking into account molecular vibrational and rotational degrees of freedom. The energy parameter ϵ is scaled on critical temperature and the distance parameter r^* on the cube root of critical volume. The procedure is valid systematically to a compression of 2.5 times liquid density for N_2, CO, Xe, O_2, CH_4, and CO_2.[41]

The Hugoniot data for liquid N_2[10,31,42] and CO are shown in Fig. 5. N_2 and CO are isoelectronic, they have virtually identical critical points, and in these experiments they had the same initial density, 0.81 g/cm^3. Thus, they are expected to have the same Hugoniot curve by the arguments in the preceding paragraph. The curve through the data up to 15 and 30 GPa for CO and N_2, respectively, was calculated using a potential scaled from Ar via corresponding states[41] and is in excellent agreement with both the N_2 and CO data. This agreement is evidence that N_2 and CO retain their molecular structure up to 30 and 15 GPa, respectively. Deviations from molecular behavior are interpreted as decomposition in both. In the CO case a large number of product molecules are probably formed by chemical reaction. Nitrogen probably undergoes a dissociative phase transition. In fact, double-shock points for nitrogen starting from 20-25 GPa lie above the principal Hugoniot in pressure-volume space. This is the only known material in which this has been observed and is evidence that these points are in a phase transition region. Comparison with theory indicates that the shock temperature is driving the diatomic to monatomic transition in nitrogen at lower pressures than required at room temperature. Above 70 GPa the two Hugoniot curves merge again and atom density appears to dominate over the chemical nature.

Hugoniot data for silica aerogel are shown in Fig. 6. This aerogel is initially 20-fold expanded relative to α-quartz density. Although the specimens were shock-compressed 6 to 7-fold, the material is still 3-fold expanded relative to crystal density. In an experiment shocked to 6.7 GPa a shock temperature of 10,800 K was measured. Thus, these experiments access a new regime for accurate laboratory measurements on high-temperature expanded-volume states of glass. This material has several important potential uses. It can be a very low shock-impedance equation-of-state standard. It can be used to generate and study few-eV inertially-confined plasmas, as for shocked gases.[43] Its equation of state may be used to understand cratering phenomena because SiO_2 is a major geological material.

Water is a complicated fluid in that the H_2O molecule is polar and the intermolecular potential is not spherically symmetric. Intermolecular H-bonds have a strong influence on the structure of water, especially at low pressures. The electrical conductivity of shocked water is quite large, about 20 (ohm-cm)$^{-1}$ from 30-60 GPa.[17] This conductivity has been interpreted in terms of ionization: $2 H_2O \rightarrow OH^- + H_3O^+$. The high conductivity indicates that significant, if not total, ionization does occur.

In order to identify the chemical species in shocked water, spontaneous Raman spectroscopy experiments were performed in the shock pressure range 7.5-26 GPa. Only a broad OH-stretch band is observed at all pressures. A spectrum for 11.7 GPa is shown in Fig. 7. No definite indications of OH^- or H_3O^+ ions are observed based on the positions of their vibrational bands at ambient. The position of the OH-stretch band is virtually independent of shock pressure and the shape of the OH-stretch band changes in such a way as to indicate the destruction of intermolecular H-bonds, as would be expected. These bonds have a characteristic energy of $\sim$ 1000 K and the shock temperature is about 1,700 K at 26 GPa. The analysis seems to indicate that the H_2O molecule remains the dominant scattering component with increasing pressure. The H_3O^+ ion is not observed because its presence is associated

with hydrogen-bonded H_2O complexes which are destroyed at these conditions. Absence of H_3O^+ means that OH^- and H^+ are most probably the conduction mechanism in strongly shocked water. Evidently, the hydroxyl ion cannot be distinguished from H_2O at high shock pressures.

Chemical decomposition and reaction occurs in shocked hydrocarbons. Benzene, for example, has the distinct volume collapse of a phase transition in its Hugoniot curve at 13 GPa.[44] Optical absorption experiments show that benzene retains its molecular nature up to 13 GPa.[45] The volume collapse at 13 GPa has been interpreted by the formation of dense carbon phases.[34,46] The emission spectra from shock fronts in benzene have been measured in the range 22-59 GPa.[14] A spectrum at 50 GPa is shown in Fig. 8. The spectrum has a broad graybody thermal component with nonequilibrium features superimposed. Features in the spectral range are coincident with the Swann bands for the C_2 molecule and provide the first spectral evidence for the formation of carbon phases in shocked hydrocarbons.

High dynamic pressure is also used to synthesize new materials. For example, stoichiometric Nb_3Si with a high superconducting transition temperature T_c = 18 K has only been synthesized by processing a nonsuperconducting phase at 100 GPa (1 Mbar) shock pressures.[47] In order to develop the experimental and computational techniques to process materials at 100 GPa shock pressures and recover them for investigations of material structure and physical properties, Nb metal was recently recovered intact from peak dynamic pressures in the range 60-120 GPa.[48] Pressure and effective-plastic-strain histories were calculated using a finite element hydrodynamic computer code. Recovered specimens were characterized by X-ray diffraction, metallography, Vicker's hardness, and T_c. The maximum change observed in a T_c of 9.18 K for the unshocked specimen was 0.035 K in the specimen shocked to a maximum pressure of 0.6 Mbar. Shock processing V_3Si at 100 GPa depresses its T_c by 1.8 K from the initial value of 16.4 K.[49] These results indicate that shock-induced defects and disorder have a relatively weak effect on the T_c of equilibrium phases and suggest that shock-synthesized metastable superconductors might have T_c's close to intrinsic values for the ordered material.

Finally, shock-impedance-match experiments have been performed at ultrahigh pressures using two-stage guns to accelerate impactors to 8 km/s, chemical explosives to drive impactors to 15 km/s, and strong shock waves generated in proximity to underground nuclear explosions.[50-56] At ultrahigh pressures nuclear-explosive-driven experiments are the only ones that provide the required accuracy because of the long shock transit times and steady profile of the shock wave. The Hugoniot data for Cu is summarized in Fig. 9, which is a plot of shock velocity versus mass velocity. The data in this figure span the shock pressure range 0.3-6 TPa (3-60 Mbar). At lower pressures the data fit a linear shock velocity-mass velocity relation, shown as the solid line, which extends up to 1.5 TPa. At higher pressures the data deviates systemmatically below the extrapolation of the linear fit, which is probably indicative of a transition to Thomas-Fermi behavior at pressures above 10 TPa. The smooth nature of the data are striking considering the variety of techniques that were employed over the $\sim$ 25 years in which this data was accumulated.

ACKNOWLEDGEMENT

REFERENCES

1. "Shock Waves in Condensed Matter-1981," edited by Nellis, W. J., Seaman, L. and Graham, R. A., American Institute of Physics, 1982.
2. "Shock Waves in Condensed Matter-1983," edited by Asay, J. R., Graham, R. A. and Straub, G. K., Elsevier Science Publishers, 1984.
3. Nellis, W. J., "Shocked Fluids at High Densities and Temperatures," in Shock Waves in Condensed Matter-1983, edited by Asay, J. R., Graham, R. A. and Straub, G. K., Elsevier Science Publishers, 1984, p. 31.
4. Taylor, J. W., "Thunder in the Mountains," in Shock Waves in Condensed Matter-1983, edited by Asay, J. R., Graham, R. A. and Straub, G. K., Elsevier Science Publishers, 1984, p. 3.
5. "Shock Waves in Condensed Matter-1981," edited by Nellis, W. J., Seaman, L. and Graham, R. A., American Institute of Physics, 1982, pp. 613-712.
6. Jones, A. H., Isbell, W. M. and Maiden, C. J., "Measurement of the Very-High-Pressure Properties of Materials Using a Light-Gas Gun," Journal of Applied Physics, Vol. 37, Aug. 1966, p. 3493.
7. Mitchell, A. C. and Nellis, W. J., "Diagnostic System of the Lawrence Livermore National Laboratory Two-Stage Light-Gas Gun," Reviews of Scientific Instruments, Vol. 52, Mar. 1981, p. 347.
8. Mitchell, A. C., Nellis, W. J. and Monahan, B., "Enhanced Performance of a Two-Stage Light-Gas Gun," in "Shock Waves in Condensed Matter-1981," edited by Nellis, W. J., Seaman, L. and Graham, R. A., American Institute of Physics, 1982, p. 184.
9. Nellis, W. J., "Measurements at Ultra-High Dynamic Pressures," in "High Pressure Measurement Techniques," edited by Peggs, G. N., Applied Science Publishers, 1983, p. 69.
10. Nellis, W. J. and Mitchell, A. C., "Shock Compression of Liquid Argon, Nitrogen, and Oxygen to 90 GPa (900 kbar)," Journal of Chemical Physics, Vol. 73, Dec. 1980, p. 6137.
11. Nellis, W. J., Ree, F. H., van Thiel, M. and Mitchell, A. C., "Shock Compression of Liquid Carbon Monoxide and Methane to 90 GPa (900 kbar)," Journal of Chemical Physics, Vol. 75, Sept. 1981, p. 3055.
12. Lyzenga, G. A. and Ahrens, T. J., "Multiwavelength Optical Pyrometer for Shock Compression Experiments," Reviews of Scientific Instruments, Vol. 50, Nov. 1979, p. 1421.
13. Lyzenga, G. A., Ahrens, T. J., Nellis, W. J. and Mitchell, A. C., "The Temperature of Shock-Compressed Water," Journal of Chemical Physics, Vol. 76, June 1982, p. 6282.
14. Johnson, M. L., Nicol, M. F. and Holmes, N. C., to be published.
15. Klimenko, V. Y. and Dremin, A. N., "Structure of a Shock Wavefront in a Liquid," in "Detonatsiya," edited by Breusov, O. N., Academy of Sciences of USSR, 1978, p. 79.
16. Hoover, W. G., "Structure of a Shock-Wave Front in a Liquid," Physical Review Letters, Vol. 42, June 1979, p. 1531.
17. Mitchell, A. C. and Nellis, W. J., "Equation of State and Electrical Conductivity of Water and Ammonia Shocked to the 100 GPa (1 Mbar) Pressure Range," Journal of Chemical Physics, Vol. 76, June 1982, p. 6273.
18. Holmes, N. C., Nellis, W. J., Graham, W. B. and Walrafen, G. E., to be published.
19. Holmes, N. C., Radousky, H. B., Moss, M. J., Nellis, W. J. and Henning, S., "Silica at Ultrahigh Temperature and Expanded Volume," Applied Physics Letters, Vol. 45, Sept. 1984, p. 626.
20. Trainor, R. J., Shaner, J. W., Auerbach, J. M. and Holmes, N. C., "Ultrahigh-Pressure Laser-Driven Shock-Wave Experiments in Aluminum," Physical Review Letters, Vol. 42, April 1979, p. 1154.

21.   Barker, L. M. and Hollenbach, R. E., "Interferometer for Measuring High
      Velocities of Any Reflecting Surface," Journal of Applied Physics, Vol.
      43, Nov. 1972, p. 4669.
22.   Durand, M., Laharrague, P., Lalle, P., Le Bihan, A., Morvan, J. and
      Pujols, H., "Interferometric Laser Technique for Accurate Velocity
      Measurement in Shock Wave Physics," Reviews of Scientific Instruments,
      Vol. 48, March 1977, p. 275.
23.   Barker, L. M., "High-Pressure Quasi-Isentropic Impact Experiments," in
      "Shock Waves in Condensed Matter-1983," edited by Asay, J. R., Graham, R.
      A. and Straub, G. K., Elsevier Science Publishers, 1984, p. 217.
24.   McQueen, R. G., Hopson, J. W. and Fritz, J. N., "Optical Technique for
      Determining Rarefaction Wave Velocities at Very High Pressures," Reviews
      of Scientific Instruments, Vol. 53, Feb. 1982, p. 245; Brown, J. M. and
      McQueen, R. G., "Melting of Iron Under Core Conditions," Geophysical
      Research Letters, Vol. 7, July 1980, p. 533.
25.   Radousky, H. B., Ross, M., Mitchell, A. C. and Nellis, W. J., "Shock
      Temperatures and Melting in CsI," Physical Review B, Vol. 31, Feb. 1985,
      p. 1457.
26.   Johnson, Q., Mitchell, A. C. and Smith, I. D., "Flash X-ray Tube for
      Diffraction Studies on a Two-Stage Light-Gas Gun," Reviews of Scientific
      Instruments, Vol. 51, June 1980, p. 741.
27.   Johnson, Q. and Mitchell, A. C., "Flash X-ray Diffraction Studies to 100
      GPa," in "High Pressure Science and Technology," Vol. 2, edited by Vodar,
      B. and Marteau, Ph., Pergamon, 1980, p. 977.
28.   Nellis, W. J., Mitchell, A. C., van Thiel, M., Devine, G. J., Trainor, R.
      J. and N. Brown, "Equation-of-State Data for Molecular Hydrogen and
      Deuterium at Shock Pressures in the Range 2-76 GPa (20-760 kbar),"
      Journal of Chemical Physics, Vol. 79, Aug. 1983, p. 1480.
29.   Nellis, W. J., Holmes, N. C., Mitchell, A. C., Trainor, R. J., Governo,
      G. K., Ross, M. and Young, D. A., "Shock Compression of Liquid Helium to
      56 GPa (560 kbar)," Physical Review Letters, Vol. 53, Sept. 1984, p. 1248.
30.   Johnson, J. D., Shaw, M. S. and Holian, B. L., "The Thermodynamics of
      Dense Fluid Nitrogen by Molecular Dynamics," Journal of Chemical Physics,
      Vol. 80, Feb. 1984, p. 1279.
31.   Nellis, W. J., Holmes, N. C., Mitchell, A. C. and van Thiel, M., "Phase
      Transition in Fluid Nitrogen at High Densities and Temperatures,"
      Physical Review Letters, Vol. 53, Oct. 1984, p. 1661.
32.   Ross, M., Nellis, W. and Mitchell, A., "Shock-Wave Compression of Liquid
      Argon to 910 kbars," Chemical Physics Letters, Vol. 68, Dec. 1979, p. 532.
33.   Nellis, W. J., van Thiel, M. and Mitchell, A. C., "Shock Compression of
      Liquid Xenon to 130 GPa (1.3 Mbar)," Physical Review Letters, Vol. 48,
      March 1982, p. 816.
34.   Nellis, W. J., Ree, F. H., Trainor, R. J., Mitchell, A. C. and Boslough,
      M. B., "Equation of State and Optical Luminosity of Benzene, Polybutene,
      and Polyethylene Shocked to 210 GPa (2.1 Mbar)," Journal of Chemical
      Physics, Vol. 80, March 1984, p. 2789.
35.   Radousky, H. B., Mitchell, A. C. and Nellis, W. J., to be published.
36.   Voskoboinikov, I. M., Gogulya, M. F. and Dolgoborodov, Yu. A.,
      "Temperatures of Shock Compression of Liquid Nitrogen and Argon," Soviet
      Physics Doklady, Vol. 24, May 1979, p. 375.
37.   Hamann, S. D., "Properties of Electrolyte Solutions at High Pressure," in
      "Modern Aspects of Electrochemistry," No. 9, edited by Conway, B. E. and
      Bockris, J. O'M., Plenum, 1974, p. 126.
38.   Kovel, M. I., "The Shock Wave Hugoniot and Electrical Conductivity of
      Liquid Ammonia in the Pressure Range 45-282 kbar," Lawrence Livermore
      National Laboratory Report UCRL-51367, March, 1973.

39. Hamilton, D., Mitchell, A. C., and Nellis, W. J., to be published.
40. Schmidt, S. C., Moore, D. S., Schiferl, D. and Shaner, J. W., "Backward Stimulated Raman Scattering in Shock-Compressed Benzene," Physical Review Letters, Vol. 50, Feb. 1983, p. 661.
41. Ross, M. and Ree, F. H., "Repulsive Forces of Simple Molecules and Mixtures at High Density and Temperature," Journal of Chemical Physics, Vol. 73, Dec. 1980, p. 6146.
42. Zubarev, V. N. and Telegin, G. S., "The Impact Compressibility of Liquid Nitrogen and Solid Carbon Dioxide," Soviet Physics Doklady, Vol. 7, July 1962, p. 34.
43. Fortov, V. E., "Shock-Wave Production of a Non-Ideal Plasma," Soviet Physics JETP, Vol. 44, July 1976, p. 116.
44. Dick, R. D., "Shock Wave Compression of Benzene, Carbon Disulfide, Carbon Tetrachloride, and Liquid Nitrogen," Journal of Chemical Physics, Vol. 52, June 1970, p. 6021.
45. Yakusheva, O. B., Yakushev, V. V. and Dremin, A. N., "The Opacity Mechanism of Shock-Compressed Organic Liquids," High Temperatures-High Pressures, Vol. 3, 1971, p. 261.
46. Yakusheva, O. B., Yakushev, V. V. and Dremin, A. N., "Relation Between Loss of Transparency by Carbon Compounds under High Dynamic Pressures and Anomalies on the Impact Compressibility Curves," Russian Journal of Physical Chemistry, Vol. 51, 1977, p. 973.
47. B. Olinger and L. R. Newkirk, "Bulk A15, High T_c Nb_3Si Synthesized by Shock Compression," Solid State Communications, Vol. 37, Aug. 1981, p. 613.
48. Nellis, W. J., Moss, W. C., Radousky, H. B., Mitchell, A. C., Summers, L. T., Dalder, E. N., Maple, M. B. and McElfresh, M., "Superconducting Critical Temperatures of Niobium Recovered from Megabar Dynamic Pressures," Lawrence Livermore National Laboratory Report UCRL-92742, June, 1985.
49. Stewart, G. R., Olinger, B. and Newkirk, L. R., "Degradation of Superconductivity in A15 V_3Si by Explosive Compression," Physical Review B, Vol. 31, March 1985, p. 2704.
50. Altshuler, L. V., Kormer, S. B., Bakanova, A. A., and Trunin, R. F., "Equation of State for Aluminum, Copper, and Lead in the High Pressure Region," Soviet Physics JETP, Vol. 11, Sept. 1960, p. 573.
51. Altshuler, L. V., Bakanova, A. A. and Trunin, R. F., "Shock Adidabats and Zero Isotherms of Seven Metals at High Pressures," Soviet Physics JETP, Vol. 15, July 1962, p. 65.
52. Trunin, R. F., Podurets, M. A., Moiseev, B. N., Simakov, G. V. and Popov, L. V., "Relative Compressibility of Copper, Cadmium, and Lead at High Pressures," Soviet Physics JETP, Vol. 29, Oct. 1969, p. 630.
53. Trunin, R. F., Podurets, M. A., Simakov, G. V., Popov, L. V. and Moiseev, B. N., "An Experimental Verification of the Thomas-Fermi Model for Metals Under High Pressure," Soviet Physics JETP, Vol. 35, Sept. 1972, p. 550.
54. Mitchell, A. C. and Nellis, W. J., "Shock Compression of Aluminum, Copper, and Tantalum," Journal of Applied Physics, Vol. 52, May 1981, p. 3363.
55. Ragan, C. E., "Shock-Wave Experiments at Threefold Compression," Physical Review A, Vol. 29, March 1984, p. 1391.
56. Mitchell, A. C., Nellis, W. J., Heinle, R. A., Repp, G. W., Moriarty, J. A., Ross, M. and Holmes, N. C., to be published.

Table 1. Summary of shock-compression experiments for fluids. T_0 is initial temperature, ρ_0 is initial density, ρ_{max} is maximum density, and P_{max} is maximum shock pressure.

Liquid	T_0 (K)	ρ_0 (g/cm^3)	ρ_{max} (g/cm^3)	P_{max} (GPa)[a]
Helium	4	0.12	0.68	56
Deuterium	20	0.17	0.96	76
Hydrogen	20	0.07	0.23	10
Nitrogen	77	0.81	2.8	82
Oxygen	77	1.2	3.3	86
Carbon Monoxide	77	0.81	3.0	69
Methane	111	0.42	1.6	92
Benzene	295	0.89	2.4	70
Polybutene	295	0.89	2.7	210
Argon	87	1.4	3.8	91
Xenon	165	3.0	9.6	130
Ammonia	230	0.69	1.8	64
Water	295	1.0	3.5	220

a 1 GPa = 10 kbar.
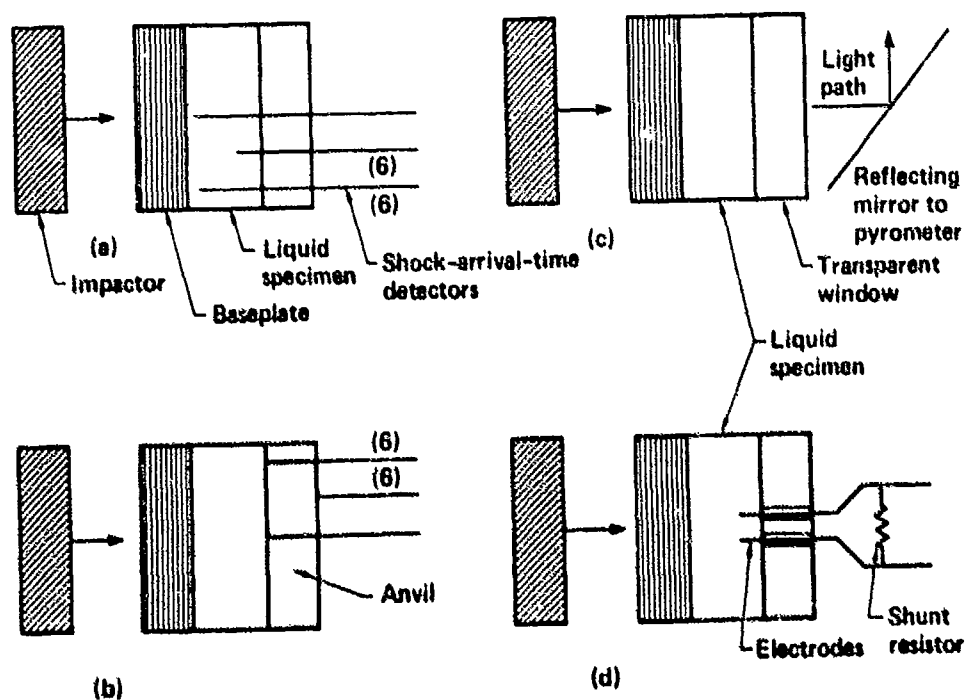
Figure 1. a) Schematic of single-shock equation-of-state experiment.[10] b) Double-shock equation-of-state experiment.[11] c) Shock temperature[13] or emission spectroscopy[14] for transparent liquid specimen. d) Electrical conductivity experiment.[17]
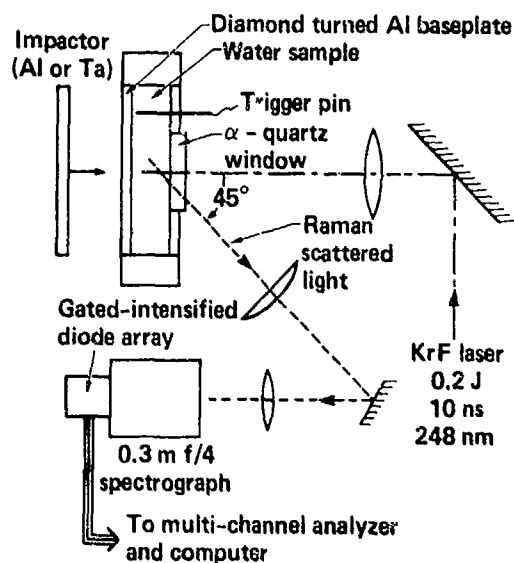
Figure 2. Schematic of pulsed, spontaneous, Raman scattering experiment in shocked water.[18]

Figure 3. Schematic of equation-of-state (top) and shock temperature (bottom) experiments for shocked transparent silica aerogel. At top, Au coating screens thermal radiation from a streaking camera until shockwave reaches rear surfaces of stepped target. At bottom, light emitted from the shock front is sent to a pyrometer during transit time of shock through specimen.[19]

Figure 4. Hugoniot data for shocked liquid Ar.[10] Curve A was calculated taking into account interatomic repulsion and electronic excitation across volume-dependent electron energy gap. Curve D was calculated neglecting electronic excitation.[32]
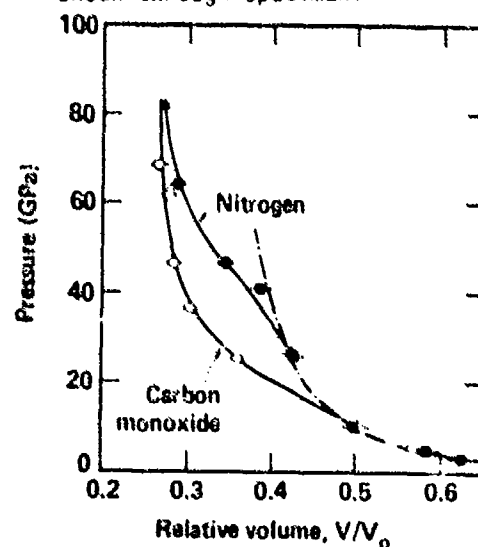
Figure 5. Hugoniot data for shocked liquid N_2[10,31,42] and isoelectronic CO.[11] Dash-dot curve is theory[41] for both molecular N_2 and CO. Initial volume of both is 34.7 cm³/mole.
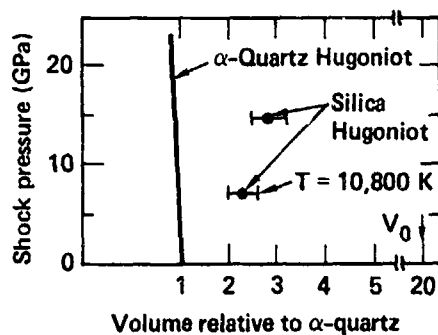
Figure 6. Hugoniot data for
silica aerogel, which is porous
SiO_2 expanded 20-fold relative
to α-quartz density.[19]
Although aerogel is compressed
substantially, the final
densities are still less than
crystal density. Indicated
temperature was measured
pyrometrically.

Figure 7. Spontaneous Raman
spectrum from water shocked to 11.7
GPa[18] using system in Fig. 2.
Spectrum is sum of two gaussian
components shown.

Figure 8. Emission spectrum from
benzene shocked to 50 GPa.[14]
Features labelled A, B, C are
coincident with the Swann bands for
C_2 molecule.
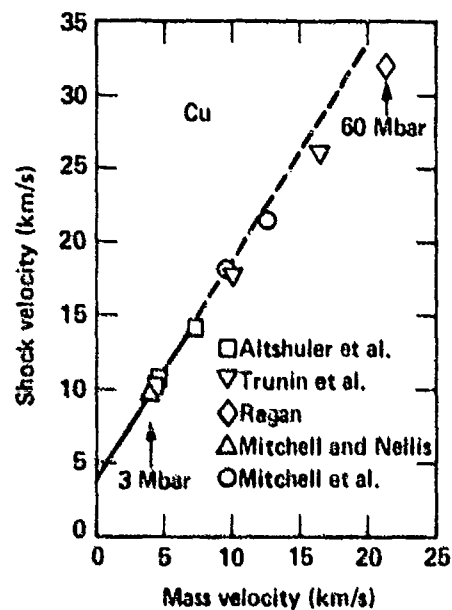
Figure 9. Shock velocity versus
mass velocity for Cu spanning
range 0.3-6 TPa (3-60 Mbar).[50-56]

A REVIEW OF SHOCK WAVES AROUND AEROASSISTED ORBITAL

TRANSFER VEHICLES

Chul Park

NASA Ames Research Center
Moffett Field, California

Aeroassisted orbital transfer vehicles (AOTVs) are a
proposed type of reusable spacecraft that would be used
to transport cargoes from one Earth-bound orbit to
another. Such vehicles could be based on the proposed
Space Station and used to transport commercial satel-
lites from the Space Station to geostationary orbits or
to polar orbits and return. During a mission, AOTVs
would fly through Earth's atmosphere, thus generating
aerodynamic forces that could be used for decelerating
the vehicles or changing their direction. This review
of published AOTV research findings was concerned with
the shock-wave-induced, high-temperature airflows that
would be produced around these vehicles during atmo-
spheric flight. In the survey, special emphasis was
placed on the problems of (1) the chemical physics of
multitemperature, ionizing, nonequilibrium air flows,
and (2) the dynamics of the flows in the base region of
a blunt body with complex afterbody geometry.

INTRODUCTION

Starting about 1970, near-Earth space became a realm not only for scien-
tific exploration but also for commercial enterprises. Artificial satellites
are used not only for telecommunications, but also, for example, in making
weather and crop forecasts; detecting crop-destroying insects and diseases;
finding new Earth resources, such as natural gas or oil; detecting shipwrecks
and forest fires; and space manufacturing. These satellites are in various
orbits, ranging from a low-Earth-orbit (LEO) a few hundred kilometers to a
geosynchronous-Earth-orbit (GEO) 35,000 km above the ground. Delivering satel-
lites from the ground to these various orbits became a profitable commercial
activity, and, in some instances, it has been shown that retrieving defunct
satellites could also be done profitably.

Various nations have developed different rocket vehicles for the purpose
of carrying such satellite cargoes. Two best known such vehicles are the U.S.
Space Shuttle and Ariane of European Space Agency.[1] The Space Shuttle and
Ariane are expected to deliver (respectively, with the anticipated upgrading),
about 30,000-kg and 4,500-kg payloads to LEOs.

To transfer such payloads to different orbits, additional propulsion is necessary. The payload that can be delivered to a GEO will be determined principally by the specific impulse of the rocket engine of the upper stage vehicle. For purposes of this review, a specific impulse of 350 sec, or equivalently, an enhaust velocity V_1 of 3430 m/sec, will be assumed. In the interest of simplicity, equatorial launches will be assumed also.

To transfer from a LEO to a GEO, one must follow an elliptic orbit with perigee and apogee coinciding with the LEO and GEO, as shown in figure 1. In order to transfer from the circular orbit at LEO to the the elliptic transfer orbit, a velocity increment ΔV ($=V_f - V_i$) of 2,573.9 m/sec is necessary. After reaching the GEO, there must be another velocity increment ΔV of 1,489.0 m/sec in order to stay in the circular orbit. The well-known rocket equation relates the velocity increment ΔV to the required mass of fuel.[2] For the case under consideration, the mass ratios become

$$\text{For perigee burn : } M_i/M_f = 2.118 \tag{1}$$

$$\text{For apogee burn : } M_i/M_f = 1.544 \tag{2}$$

$$\text{The mass ratio product} = 2.118 \times 1.544 = 3.270 \tag{3}$$

where M_i is the initial mass, which includes the mass of the expended fuel, and M_f is the final mass.

At present, the upper stage vehicles used for this purpose are expendable (see fig. 1(a)). This is becoming expensive because of (1) the cost of manufacturing and testing, and (2) relatively high insurance premiums because of low reliability. By making the upper-stage vehicle reusable, one could eliminate both these problems and achieve a considerable commercial advantage. Such a conceptual vehicle, operating solely on rocket engines for producing ΔV's, as depicted in figure 1(b), is referred to as orbital transfer vehicle (OTV).[3] The OTVs suffer from one serious handicap, however. After delivering the payload to the GEO, the OTV must now expend the mass ratio of 3.270, in order to descend to the LEO. This mass ratio requirement greatly reduces the true payload capacity of the OTV.

The idea of aeroassisted orbital transfer vehicle (AOTV) was initiated to alleviate this difficulty.[4,5] An AOTV would be equipped with an aerodynamic surface that would produce drag (and some lift, if possible) and withstand whatever heat to which it would be exposed. On return from the GEO, the AOTV would dive into Earth's atmosphere and skip out of it as shown schematically in figure 1(c). In doing so, the vehicle would be decelerated by drag, an operation referred to as aerobraking. A small course adjustment would be necessary after the vehicle skipped out of the atmosphere, but it could be accomplished by using only a very small amount of fuel. By this operation, the mass ratio required for the return trip is reduced from 3.27 to about 1.55, an advantage of a factor greater than 2. We can call this class of AOTV low-lift AOTVs or aerobraking AOTVs.

An OTV and AOTV have three different applications: (1) delivery of
payloads from LEO to GEO, (2) retrieval of payloads from GEO to LEO, and
(3) excursions to GEO in which no transfer of payload takes place. By
adding and multiplying the numbers given in equations (1) to (3), one obtains
the payload capacities for these three functions, as shown in table 1. As
shown in the table, an AOTV can improve the payload capacity considerably over
that of an OTV The maximum mass of the AOTV at the time of atmospheric entry
is of the order of 10,000 kg. Detailed calculations of this type have been
carried out by various authors in recent years and are available in the open
literature.[6-12]

Another reason for proposing an AOTV is for changing orbital inclina-
tion angle with respect to the equator.[4,5] For instance, for a satellite
in an equatorial orbit at the altitude of 150 km with a circular velocity
of 7,768 m/sec to change to a polar orbit, the required ΔV is
$1.4142 \times 7,768 = 10,986$ m/sec. If this ΔV is achieved entirely by burning
rocket fuel, the required mass ratio is 22.60. If the vehicle is to return
from the polar orbit back to the equatorial orbit, the required mass ratio is
$22.60 \times 22.60 = 605.4$. Such a large mass ratio requirement could be reduced if
the vehicle could utilize aerodynamic lift. Assuming that the vehicle had an
aerodynamic lifting surface, it could dive into the atmosphere with an expendi-
ture of a small amount of fuel. The vehicle would fly in a highly banked atti-
tude so as to produce a large sidewise force. This operation is referred to as
aeromaneuvering.[4] For this type of vehicle, a large L/D is preferred, and it
can be designated a high-lift AOTV, or an aeromaneuvering AOTV.[13]

Unlike the aerobraking AOTV, the benefits of an aeromaneuvering AOTV are
not easy to predict for missions involving large orbital-plane-angle changes
because there are too many arbitrary parameters that affect the payload calcu-
lation (little such information appears in the open literature).[4,8,9] Hence,
no attempt will be made here to assess the benefits of the high-lift AOTV for
this kind of application. Since there is no reason for the AOTVs to land on
the ground, the most economic way of operating them would be to base them in
space--on the proposed Space Station[14] or on some similar space structure.

FLIGHT REGIMES

One of the most critical components of the AOTV is the aerodynamic surface
(the aerobrake for the low-lift AOTV or the lifting surface for the high-lift
AOTV). The aerodynamic surface will be subject to heat transfer from the hot
shock layer flow around it. Such a surface must not only withstand the heat
but be chemically unaffected by atomic oxygen that exists in the shock-layer
flow. Presently, such materials are used on the Space Shuttle Orbiter.[15,16]
These materials can withstand heat-transfer rates of the order of 200 kW/m^2.
For this review, therefore, it will be assumed that the tolerable heat-transfer
rate is 200 kW/m^2.

In order to roughly define the regime of flight of the AOTVs, we will
assume the AOTV to be a sphere. Equations of motion of such a body are well
known.[17] We will assume that the AOTV is returning from the GEO, and that its
mass is 10,000 kg, a typical maximum value seen in table 1. After the vehicle

skips out of the atmosphere, we will assume that its new apogee will be 200 km above the ground. As a trial value, we will assume the radius of the sphere to be 10 m. The convective heat-transfer rate to the stagnation point of such a vehicle can be calculated easily using an existing technique.[18]   Figure 2 shows the results of the calculation. As seen here, this vehicle approximately satisfies the maximum allowed heat-transfer limit of 200 kW/m^2. Its perigee is approximately 80 km. For an AOTV, there exists an implicit relationship between the flight density and the nose radius imposed by the fact that the velocity decrement through the aerobraking flight be the desired value.[18]   This leads to

$$q_c = \text{const} \times V^{3.15}R^{-1.5}$$

This shows that the convective heat-transfer rate is relatively sensitive to the choice of nose radius. Conversely, the flight density is also sensitively affected by the nose radius. The flight regimes are, therefore, fairly narrowly defined. The flight regimes are shown in table 2 at the perigee for an aerobraking AOTV with zero lift. More detailed analyses of the trajectories and the associated flight regime parameters have been performed analytically.[19]

CHEMICAL KINETICS AND RADIATIVE HEAT-TRANSFER RATES

The shock standoff distance for a sphere is a function of the density ratio across the normal shock wave, or, equivalently, a function of the effective specific heat ratio (see, e.g., ref. 20) which is determined by the chemical state in the shock layer. Because an AOTV flies through a low density regime, the flow in the shock layer is most likely in the state of chemical relaxation. There is one well-known standardized computer program that computes chemical reactions for a one-dimensional inviscid flow.[21]   Unfortunately, such existing programs assume that all internal modes of energy (rotation, vibration, electronic excitation, and electron translational) are in equilibrium with the translational mode of the heavy particles. It is well known that rotational temperature equilibrates with translational temperature very quickly.[22]   Vibrational excitation is somewhat slower, but in the environments encountered in past space missions, it was usually faster than the rates of dissociation.[23]   For the AOTV, however, the translational temperature behind the shock is over 40,000 K. Here, vibrational relaxation and dissociation are likely to proceed simultaneously.

It is known also that electron kinetic temperature interacts strongly with the vibrational modes of a molecule.[24]   The equilibration between the electron translational temperature and heavy-particle translational temperature is slow because of the large mass disparity between them.[25,26]   This causes the electron translational temperature to deviate from the heavy-particle translational temperature. Recent studies show that the low electronic states of atoms and molecules are easily excited to their Boltzmann values on impact by electrons.[25]   As a result, for the purpose of approximately determining the total energy contents in the electronic excitation mode, one may assume the electronic excitation temperature to be the same as the electron translational temperature.

For these reasons, the chemical reactions in the shock layer over an aerobraked AOTV requires, in general, the recognition of three different temperatures: heavy-particle translational and rotational, vibrational, and electronic excitation and electron translational.[26] If the flow conditions were such that the interaction between the electron translational energy and vibrational excitation is allowed to proceed frequently, then one could further assume that the vibrational temperature and the electron-electronic temperature are the same, leading to a two-temperature situation.[27-29]

To compute the reacting flows under this two- or three-temperature environment, reaction rate coefficients must be expressed in terms of these different temperatures. At present, very little is known of this multitemperature description of rate coefficients, although work is in progress in an effort to understand the phenomena.[30]

This problem can be approached from a purely experimental viewpoint. Unfortunately, however, even the experimental data are contradicting and confusing. Beginning in the late 1950s and continuing until about 1970, shock tubes were operated to observe the flow behavior behind strong shock waves.[31,32] Shock velocities in excess of 10 km/sec have been generated in such facilities. The free-stream densities in such tests were, however, typically 5 to 10 times higher than those given in table 2. In all such tests, it was found that the radiation intensity was zero at the shock wave, rose to a peak, and decayed and approached a plateau. The distance to the peak, the distance to the equilibration point, and the peak intensity value have been measured over a wide range of conditions.

The peak intensity was seen to be between about 2 and 15 times stronger than the plateau values, depending on the wavelength.[31] This phenomenon became known as nonequilibrium overshoot, or nonequilibrium enhancement, of radiation. These quantities were found to approximately obey the so-called binary scaling law.[31,32] That is, the distances were inversely proportional to the gas density, and the intensity was proportional to density. As a result, the radiation integrated over the distance became approximately independent of the flow density.

Until recently, there has not been any serious effort to quantitatively explain the observed data. Most recently, an effort was made to understand the observed phenomena, using the best available computing techniques. To do so, however, the form of dependence of various reaction rates on vibrational and electron-electronic temperatures had to be assumed.[28] The results of such calculations are given in reference 28. Reference 28 shows that we are not yet able to quantitatively explain the observed nonequilibrium radiation enhancement phenomenon.

In addition to the shock-tube experiments, flight experiments were conducted in the early years to investigate the chemical kinetic behavior in the shock layer over a reentry vehicle. Those flight-test projects are named Fire (refs. 33,34), Apollo (ref. 35), PAET (Planetary Atmospheric Experiment Test) (ref. 36), and RAM (Radio Attenuation Measurement)-C (refs. 37-41). In both the Fire and Apollo experiments, the total radiation power incident on the

stagnation region was measured, using several different instruments. In the
PAET experiment, a multiple of narrowband monochromators were installed to
measure the radiation incident on the stagnation region. In RAM-C test, micro-
wave experiments (attenuation, reflection, and phase shift) were conducted to
determine the behavior of electrons in the shock layer.

However, the results of these flight tests did not lead to any definite
explanation or conclusion. In the case of Fire and Apollo, the radiative
heat-transfer rates measured near an altitude of 80 km were much lower than
those deduced from the shock-tube experiments. This observed phenomenon
prompted a hypothesis known as "collision-limiting,"[33-35] that is, that there
are not enough collisions to maintain the population of the highly excited
states at low densities. This explanation was accepted in the days of Apollo
and was used in the design of Apollo missions. In retrospect, however, this
"collision-limiting" theory is flawed. The concept is based on the assumption
that the excitation of atoms and molecules occurred mostly through collisions
of atoms and molecules. In recent years, it became known that electrons are
many orders of magnitude more efficient in electronically and vibrationally
exciting atoms and molecules.[25] Using the available data on electron-impact
excitation rates, one finds that the collision-limiting phenomenon occurs at
altitudes of about 100 km (see ref. 25), instead of 80 km.

An alternative explanation of the observed low radiation intensity in Fire
and Apollo is the effect of boundary-layer growth, which is known as the "trun-
cation" hypothesis.[31] According to this hypothesis, the profile of electron
temperature may develop a thick, cool boundary layer near the wall owing to the
high thermal conductivity of the electron gas. The electron temperature bound-
ary layer may have grown so thick that it may extend almost to the shock wave,
thereby preventing the occurrence of nonequilibrium overshoot in electron and
vibrational temperatures. That is, the rise in radiation intensity is "trun-
cated" by the cool, electron boundary layer.

The PAET experiment[36] confirmed that the observed radiation at a
selected wavelength (390 nm) was higher than the equilibrium value. Unfor-
tunately, however, the experiment did not measure the global (integrated
over the entire wavelength range) radiation. Also, the flight speed was
considerably lower than that of AOTV. Analysis is in progress to explain
quantitatively the values obtained in the PAET test, and has met with partial
success.

The results of the RAM-C test have been analyzed by several investi-
gators.[37-41] Each investigator was able to explain a portion of the data
produced. However, there is no unifying analysis that explains all aspects
of the data.

These uncertainties about chemical kinetics have a serious implication for
the design of an aerobraked AOTV. Presently, the radiative heat-transfer rate
q_r is uncertain to within the range

$$40 \leq q_r \leq 400 \text{ kW/m}^2$$

A computer program named HF730 was written in 1969 that allows differences among translational, rotational, vibrational, and electron temperatures.[42] However, this program assumed a Boltzmann distribution of internal states at these given temperatures. In the nonequilibrium flow under consideration, the internal state populations are governed not by the Boltzmann relation but by one known as the "quasi-steady-state" relationship, which states that the sum of all electronic transitions into a state is approximately equal to the sum of all transitions going out of the state.[25] A new computer program named NEQAIR (ref. 25) has been written by incorporating this principle into the HF730 program. The NEQAIR program requires a large set of excitation rate-coefficient values, only some of which are presently available; however, work is in progress in all these areas.

STABILITY, GUIDANCE, AND CONTROL

The velocity and flight angle at the time of atmospheric entry of an AOTV can be different from the planned values because of errors in the operation of the main rocket engines, both in thrust and in direction. In order to correct for any such errors, the vehicle must be maneuvered while in the atmosphere. Also, it became known in recent years that the density of the atmosphere in the altitudes of interest can vary over a wide range.[17,43] An aerobraking AOTV must maneuver to fly through the desired densities. For these reasons, an AOTV requires a small amount of lift.

To provide a finite lift and be stable is not so easy for an AOTV, because the center of gravity (c.g.) will vary widely depending on the mission and on the amount of fuel remaining in the tanks. The c.g. variation will affect the pitching stability parameter most severely. The primary consideration in the design of an aerobraked AOTV is to have an acceptable pitching stability at all possible c.g. locations at the highest allowed angle of attack. The roll angle will be controlled by the use of small rocket engines known as reaction control system (RCS) engines. The effective average angle of attack and L/D can be lowered by alternating the bank angle between a positive and a negative value. A course change can be accomplished also by maintaining a fixed bank angle. In this way, the vehicle has a two-parameter control in its maneuvering.

How an aerobraked AOTV can negotiate an atmosphere with greatly varying density is yet to be determined.[17] It would be highly desirable to know the density distribution before the atmospheric flight, and that possibility is presently under study.[44] A multiple atmospheric pass is suggested as one way of reducing the effect of density uncertainty.[7,8,11]

EXAMPLES OF PROPOSED DESIGNS

Ballute

In this design, the aerobrake consists of a balloon-like elastic gas bag, inflated to the shape of a blunt body. Its size will be varied by controlling the pressure inside the gas bag.[45] The main advantage of this design is that it could be the lightest and cheapest to make of all the options.

There are, however, two potential problems with the ballute. The first is that the variation of drag coefficient produces only one-degree-of-freedom control. The second possible problem concerns the question of static stability when the ballute is deformed as a result of an asymmetric external pressure distribution. No study has yet been made of the aerodynamic characteristics of a ballute that is only partially inflated and that is set at a finite angle of attack. Common sense would predict that the windward side would depress inward owing to the increased shock-layer pressure there, while the lee would bulge out because of the decreased pressure there. This will tend to produce a moment that will increase the angle of attack, leading to a static instability. To avoid the occurrence of such static instability, the location of the c.g. may have to be compromised.

Conical Lifting Brake

In this concept, the aerobrake consists of a sphere-cone, which resembles spacecraft of past NASA missions.[46] The configuration currently favored uses a 70° cone with the sphere radius equal to the frustum radius. The 70° cone was selected because it showed the largest range of allowable c.g. locations.[47] The stress on the components occurs only in one direction: the direction of rocket thrust and the direction of the aerodynamic drag coincide approximately. The main potential problem of this design concerns the yet unknown phenomenon which somehow increases both pressure and heat-transfer rates in the base region at a finite angle of attack.[48]

Raked Cone

The raked cone is an ellipsoidal body truncated strongly asymmetrically.[12] The fuel tanks are split into two (or more) parts and are placed far apart. By controlling the relative amounts of fuel in each tank, the vehicle could adjust its trim angle of attack. The thrust line of the main engines is nearly perpendicular to the direction of flight. Its optimum L/D is about 0.3, the highest of all existing designs. The high L/D makes it possible to fly at the highest negative L/D, thereby at altitudes substantially higher than 80 km.

There are two problems associated with the raked cone. The first is the difficulty in placing the c.g. on the thrust line of the main rocket engines; depending on the mass and dimensions of the payload and the amount of fuel remaining in the tanks, the c.g. point may vary over a wide range. The second problem is that the structures must withstand stresses in two directions: the direction of the thrust line when the engines are firing, and the direction of flight during atmospheric deceleration.

FLUID MECHANICS OF BASE FLOW

In both the conical lifting brake and the raked cone, the payload may have to be carried in the base region to form a protruding afterbody. Convective and radiative heat-transfer rates to the base region of a reentry vehicle have been studied over the years.[49-52] It is known that both convective and radiative heat-transfer rates increase with base pressure. In most past reentry vehicles, the base pressure was quite small, that is, of the order

of 1% of that of the front stagnation point value.[52] As a result, the base
heat-transfer rates were also usually very small. One cannot necessarily
expect this to be the case for an AOTV. The experimental data taken in a
hypersonic wind tunnel with a conical lifting brake[48] show that both pressure
and convective heat-transfer rates can be very high over certain portions of
the afterbody when the vehicle is at a finite angle of attack.

In order to understand the nature of the flow in the base of a conical
lifting brake, an effort is presently being made to study the phenomenon in a
different type of facility. At Ames Research Center, scale models of such
vehicles are flown in a hypersonic, free-flight range, and shadowgraph pictures
are taken of the flow field around the flying models. The results are being
analyzed with the help of computational fluid dynamics.[53] A significant dif-
ference is appearing between the base flow field of this type of AOTV and that
without a protruding afterbody.[54] The computed flow field shows that there are
two recirculating regions in the flow rather than one: one between the aero-
brake and the afterbody, and the other behind the afterbody. The first recir-
culating region resembles a two-dimensional separated flow produced by a back-
ward-facing step,[53,54] and the second is an axisymmetric base flow. It is
known that the two-dimensional separated flow over a backward-facing step pro-
duces a recirculating region pressure which is substantially higher than in the
base of an axisymmetric body without protruding afterbody.[52,54] Thus, one sees
a possibility of relatively high base pressure for the AOTV, which may cause
high convective and radiative heat-transfer rates.

CONCLUSIONS

Aeroassisted orbital transfer vehicles are useful for two purposes: they
can carry satellite payloads between GEOs and the Space Station, and between
near-equatorial orbits and near-polar orbits on a reusable basis. Because of
its reusability, high reliability resulting from the reusability, and substitu-
tion of aerodynamic forces for a rocket engine burn, the AOTVs can introduce a
substantial advantage in commercial utilization of space. The flight regimes
of the vehicle are defined relatively narrowly from the various practical con-
straints; the regimes are such that nonequilibrium vibrational excitation,
dissociation, and ionization will proceed simultaneously in the shock layer
over the vehicle. Present understanding of these chemical kinetic phenomena is
poor. The requirement that these vehicles may have to carry their cargo in the
base region, as a protruding afterbody, introduces a unique fluid-mechanical
problem of base flow.

REFERENCES

1. Jane's All the World's Aircraft. Jane's Publishing Co., Vol. 1981-1982,
    London, England, 1982, pp. 690-691.

2. Hill, P. G.; and Peterson, C. R.: Mechanics and Thermodynamics of Propul-
    sion. Addison-Wesley Publishing Co., Reading, Mass., 1965, p. 371.

3. Garland, S.: Integration Becomes the Name of the OTV Game. Aerospace
    America, vol. 22, no. 8, Aug. 1984, pp. 70-73.

4. Walberg, G. D.: A Survey of Aeroassisted Orbit Transfer. J. Spacecraft &
    Rockets, vol. 22, no. 1, Jan.-Feb. 1985, pp. 3-18.

5. Howe, J. T.: Introductory Aerothermodynamics of Advanced Space Transpor-
    tation Systems. J. Spacecraft & Rockets, vol. 22, no. 1, Jan.-Feb. 1985,
    pp. 19-26.

6. Menees, G. P.: Thermal-Protection Requirements for Near-Earth Aeroas-
    sisted Orbital-Transfer Vehicle Missions. Progress in Astronautics and
    Aeronautics, Vol. 96, H. F. Nelson, ed., AIAA, New York, N.Y., 1985,
    pp. 257-285.

7. Menees, G. P.; Park, C.; and Wilson, J. F.: Design and Performance Analy-
    sis of a Conical Aerobrake Orbital-Transfer Vehicle Concept. Progress in
    Astronautics and Aeronautics, Vol. 96, H. F. Nelson, ed., AIAA, New York,
    N.Y., 1985, pp. 286-308.

8. Menees, G. P.; Davies, C. B.; Wilson, J. F.; and Brown, K. G.: Aero-
    thermodynamic Heating Analysis of Aerobraking and Aeromaneuvering Orbit-
    Transfer Vehicles. Progress in Astronautics and Aeronautics, Vol. 96,
    H. F. Nelson, ed., AIAA, New York, N.Y., pp. 338-360.

9. Menees, G. P.; Wilson, J. F.; Davies. C. B.; and Brown, K. G.: Aero-
    thermodynamic Heating and Performance Analysis of a High-Lift Aeromaneu-
    vering AOTV Concept. AIAA Paper 85-1060, Williamsburg, Va., 1985.

10. Powell, R. W.; Naftel, J. C.; and Stone, H. W.: Performance Evaluation of
     the Atmospheric Phase of an Orbital Transfer Vehicle. AIAA Paper 84-0405,
     Reno, Nev., 1984.

11. Rehder, J. J.: Multiple Pass Trajectories for an Aeroassisted Orbital
     Transfer Vehicle. Progress in Astronautics and Aeronautics, Vol. 96,
     H. F. Nelson, ed., AIAA, New York, N.Y., 1985, pp. 186-197.

12. Scott, C. D.; Reid, R. C.; Maraja, R. J.; Li, C. P.; and Derry, S. M.: An
     AOTV Aeroheating and Thermal Protection Study. Progress in Astronautics
     and Aeronautics, Vol. 96, H. F. Nelson, ed., AIAA, New York, N.Y., 1985,
     pp. 309-337.

13. Davies, C. B.; and Park, C.: Optimum Configuration of High-Lift Aero-
     maneuvering Orbital Transfer Vehicles in Viscous Flow. AIAA
     Paper 85-1059, Williamsburg, Va., 1985.

14. Beggs, J. M.: Space Station: The Next Logical Step. Aerosp. Am.,
     vol. 22, no. 9, Sept. 1984, pp. 47-52.

15. Korb, L. J.; Morant, C. A.; Calland, R. N.; and Thatcher, C. S.: The
     Shuttle Orbiter Thermal Protection System. Ceramic Bulletin, vol. 60,
     no. 11, Nov. 1981, pp. 1188-1193.

16. Leiser, D. B.; Smith, M.; and Goldstein, H. E.: Developments in Fibrous Refractory Composite Insulation. Ceramic Bulletin, vol. 60, no. 11, Nov. 1981, pp. 1201-1204.

17. Cerimele, C. J.; and Gamble, J. D.: A Simplified Guidance Algorithm for Lifting Aeroassist Orbital Transfer Vehicles. AIAA Paper 85-0348, Reno, Nev., 1985.

18. Park, C.: A Review of Shock Waves Around Aeroassisted Orbital Transfer Vehicles. NASA TM-86769, June 1985.

19. Desautel, D.: Analytical Characterization of AOTV Perigee Aero-thermodynamic Regime. Progress in Astronautics and Aeronautics, Vol. 96, H. F. Nelson, ed., AIAA, New York, N.Y., 1985, pp. 230-253.

20. Park, C.: Calculation of Radiation from Argon Shock Layers. J. Quant. Spectrosc. Radiat. Transfer, vol. 28, no. 1, July 1982, pp. 29-40.

21. Bittker, D. A.; and Scullin, J.: General Chemical Kinetics Computer Pro-gram for Static and Flow Reactions, with Application to Combustion and Shock-Tube Kinetics. NASA TN D-6586, 1972.

22. Bird, G. A.: Molecular Gas Dynamics. Clarendon Press, Oxford, England, 1976, p. 186.

23. Flagan, R. C.; and Appleton, J. P.: Excitation Mechanisms of the Nitrogen First-Positive and First-Negative Radiation at High Temperature. J. Chem. Phys., vol. 56, no. 3, Feb. 1972, pp. 1163-1173.

24. Lee, J-H.: Electron-Impact Vibrational Excitation Rates in the Flowfield of Aeroassisted Orbital Transfer Vehicles. AIAA Paper 85-1035, Williams-burg, Va., 1985.

25. Park, C.: Calculation of Nonequilibrium Radiation in the Flight Regimes of Aeroassisted Orbital Transfer Vehicles. Progress in Astronautics and Aeronautics, Vol. 96, H. F. Nelson, ed., AIAA, New York, N.Y., 1985, pp. 395-418.

26. Lee, J. H.: Basic Governing Equations for the Flight Regimes of Aero-assisted Orbital Transfer Vehicles. Progress in Astronautics and Aero-nautics, Vol. 96, H. F. Nelson, ed., AIAA, New York, N.Y., 1985, pp. 3-53.

27. Park, C.: Radiation Enhancement by Nonequilibrium in Earth's Atmo-sphere. J. Spacecraft & Rockets, vol. 22, no. 1, Jan.-Feb. 1985, pp. 27-36.

28. Park, C.: Problems of Rate Chemistry in the Flight Regimes of Aero-assisted Orbital Transfer Vehicles. Progress in Astronautics and Aero-nautics, Vol. 96, H. F. Nelson, ed., AIAA, New York, N.Y., 1985, pp. 511-537.

29.   Park, C.: On Convergence of Computation of Chemically Reacting Flows.
      AIAA Paper 85-0247, Reno, Nev., 1985.

30.   Jaffe, R. L.: Rate Constants for Chemical Reactions in High-Temperature
      Nonequilibrium Air. AIAA Paper 85-1038, Williamsburg, Va., 1985.

31.   Allen, R. A.; Rose, P. H.; and Camm, J. C.: Nonequilibrium and Equilib-
      rium Radiation at Super-Satellite Reentry Velocities. Research
      Report 156, AVCO-Everett Research Laboratories, Everett, Mass., Sept.
      1962.

32.   Arnold, J. O.; and Whiting, E. E.: Nonequilibrium Effects on Shock-Layer
      Radiometry during Earth Entry. J. Quant. Spectrosc. Radiat. Transfer,
      vol. 13, no. 9, Sept. 1973, pp. 861-870.

33.   Cauchon, D. L.: Project Fire Flight 1 Radiative Heating Experiment. NASA
      TM X-1222, 1966.

34.   Cauchon, D. L.: Radiative Heating Results from the Fire 2 Flight Experi-
      ment at a Reentry Velocity of 11.4 Kilometers per Second. NASA TM X-1402,
      1967.

35.   Lee, D. B.; and Goodrich, W. D.: The Aerothermodynamic Environment of the
      Apollo Command Module during Super-Orbital Entry. NASA TN D-6792, 1972.

36.   Whiting, E. E.; Arnold, J. O.; Page, W. A.; and Reynolds, R. M.: Composi-
      tion of the Earth's Atmosphere by Shock-Layer Radiometry during the PAET
      Entry Probe Experiment. J. Quant. Spectrosc. Radiat. Transfer, vol. 13,
      no. 9, Sept. 1973, pp. 837-859.

37.   Evans, J. S.; Schexnayder, C. J.; and Huber, P. W.: Computation of Ioni-
      zation in Re-Entry Flowfields. AIAA J., vol. 8, no. 6, June 1970,
      pp. 1082-1089.

38.   Nerem, R. M.; and Dilley, J. F.: An Analysis of Re-Entry Flight Measure-
      ment of Shock Layer Microwave Radiation. AIAA J., vol. 8, no. 7, July
      1970, pp. 1295-1301.

39.   Adams, J. C., Jr.: Shock Slip Analysis of Merged Layer Stagnation Point
      Air Ionization. AIAA J., vol. 8, no. 5, May 1970, pp. 971-973.

40.   Kang, S. W.: Nonequilibrium, Ionized, Hypersonic Flow over a Blunt Body
      at Low Reynolds Number. AIAA J., vol. 8, no. 7, July 1970, pp. 1263-1270.

41.   Kang, S. W.; Dunn, M. G.; and Jones, W. L.: Theoretical and Measured
      Electron-Density Distributions for the RAM Vehicle at High Altitudes.
      AIAA Paper 72-689, Boston, Mass., 1972.

42. Whiting, E. E.; Arnold, J. O.; and Lyle, G. C.: A Computer Program for a Line-by-Line Calculation of Spectra from Diatomic Molecules and Atoms Assuming a Voigt Profile. NASA TN D-5088, 1969.

43. Talay, T. A.; White, N. H.; and Naftel, J. C.: Impact of Atmospheric Uncertainties and Real Gas Effects on the Performance of Aeroassisted Orbital Transfer Vehicles. Progress in Astronautics and Aeronautics, Vol. 96, H. F. Nelson, ed., AIAA, New York, N.Y., 1985, pp. 198-229.

44. Menees, G. P.; Park, C.; Wilson, J. F.; and Brown, K. G.: Determination of Atmospheric Density Using a Space-Launched Projectile. AIAA Paper 85-0327, Reno, Nev., 1985.

45. Woods, W. C.; Andrews, D. G.; and Bloetscher, F.: Experimental Evaluation of an Inflatable Ballute for Application to Aeroassisted Orbital Transfer Vehicles. AIAA Paper 84-0409, Reno, Nev., 1984.

46. Intrieri, P. F.; De Rose, C. E.; and Kirk, D. B.: Flight Characteristics of Probes in the Atmosphere of Mars, Venus, and the Outer Planets. Acta Astronautica, vol. 4, no. 7-8, July-Aug. 1977, pp. 789-799.

47. Davies, C. B.; and Park, C.: Aerodynamics of Generalized Bent Biconics for Aeroassisted, Orbital-Transfer Vehicles. J. Spacecraft & Rockets, vol. 22, no. 2, Mar.-Apr. 1985, pp. 104-111.

48. Shih, P. K.; and Gay, A.: Low Lift-to-Drag Aerobrake Heat Transfer Test at Mach 10. Progress in Astronautics and Aeronautics, Vol. 96, H. F. Nelson, ed., AIAA, New York, N.Y., 1985, pp. 378-394.

49. Murphy, S. N. B.; and Osborn, J. R.: Base Flow Phenomena with and without Injection: Experimental Results, Theories, and Bibliography. Progress in Astronautics and Aeronautics, Vol. 40, S. N. B. Murphy, ed., AIAA, New York, N.Y., 1979, pp. 345-367.

50. Park, C.: Modeling of Radiative Heating in Base Region of Jovian Entry Probe. Progress in Aeronautics and Astronautics, Vol. 69, W. B. Olstad, ed., AIAA, New York, N.Y., 1980, pp. 124-147.

51. Shirai, H.; and Park, C.: Shock-Tube Studies of Radiative Base Heating of Jovian Probe. Shock Tubes and Waves, Proceedings of the 12th International Symposium on Shock Tubes and Waves, A. Lifshitz and J. Rom, eds., Magnes Press, The Hebrew University, Jerusalem, 1980, pp. 419-428.

52. Brant, D. N.; and Nestler, D. E.: Development of an Afterbody Radiative and Convective Heating Code for Outer Planet Probes. Progress in Astronautics and Aeronautics, Vol. 64, R. Viskanta, ed., AIAA, New York, N.Y., 1979, pp. 345-367.

53. Lombard, C. K.; Vankatapathy, E.; and Bardina, J.: Forebody and Base Flow
     of a Dragbrake OTV by an Extremely Fast Single Level Implicit Algorithm.
     AIAA Paper 84-1699, Snowmass, Colo., 1984.

54. Chapman, D. R.; Kuehn, D. M.; and Larson, H. K.: Investigation of Sepa-
     rated Flows in Supersonic and Subsonic Streams with Emphasis on the Effect
     of Transition. NACA Technical Report R-1356, 1957.

TABLE 1.- PAYLOAD AND MASSES OF THE UPPER STAGE VEHICLE, IN kg, UNDER THE
MOST IDEAL CONDITIONS, STARTING FROM AN EQUATORIAL LOW-EARTH-ORBIT AT
150 km, WITH A ROCKET ENGINE WITH A SPECIFIC IMPULSE OF 350 sec

		Space Shuttle upper stage			Ariane
		Expendable	OTV	AOTV	Expendable
Mass at takeoff from LEO assumed		30,000			4,500
Type		Expendable	OTV	AOTV	Expendable
Mass of hardware assumed		2,000	2,000	3,000	300
Delivery to GEO	Payload	7,174	2,634	4,542	1,442
	Reentry mass	0	2,000	3,000	0
Retrieval from GEO	Payload	0	1,160	8,349	0
	Reentry mass	0	3,160	11,349	0
Excursion to GEO	Payload	0	806	2,942	0
	Reentry mass	0	2,806	5,942	0

TABLE 2.- TYPICAL PERIGEE CONDITIONS FOR AEROBRAKED AOTV

Altitude, km..80
Convective heat-transfer rate q_o, kW/m^2.............200
Density ρ, kg/m^3.................................2×10^{-5}
Mean free path λ, m.............................4×10^{-3}
Nose radius R, m.......................................10
Reynolds number, $\rho VR/\mu$...........................1.5×10^5
Stagnation pressure p_s, atm.........................0.015
Velocity, V, km/sec....................................9
Viscosity μ, kg/(m·sec)............................1.2×10^{-5}
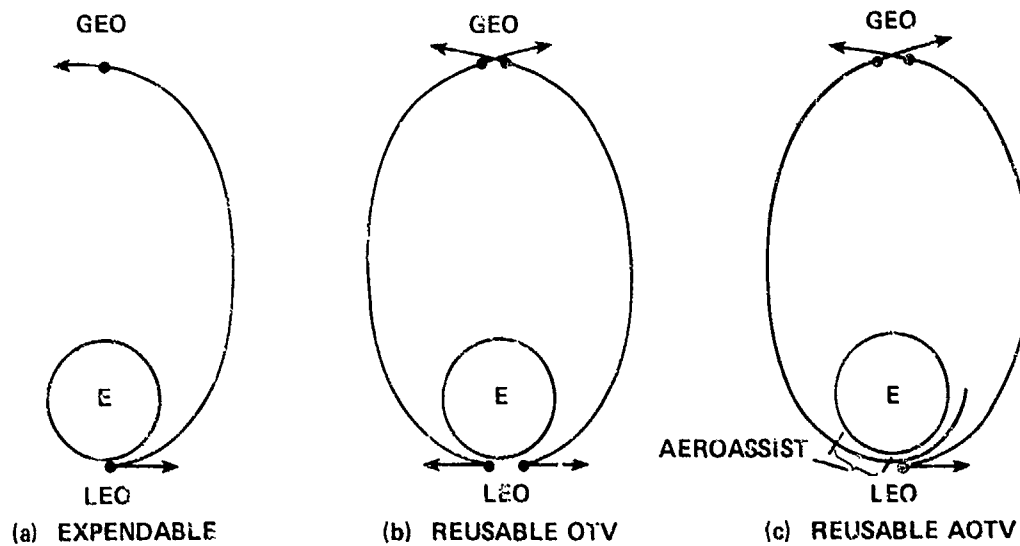
Fig. 1   Three different modes of transferring payloads from LEO to GEO.
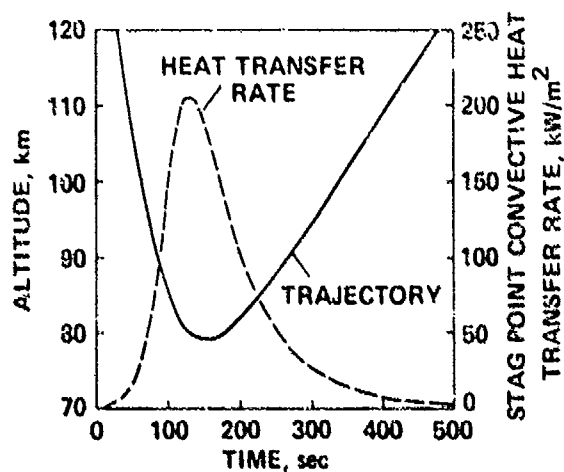
Fig. 2   Flight trajectory and stagnation point in convective heat-transfer rates for a spherical aerobraking AOTV with nose radius of 10 m, mass of 10,000 kg, on return from a GEO.

SHOCK WAVE FOCUSING PHENOMENA

H. Grönig

Stoßwellenlabor, Institut f. Luft- u. Raumfahrt, RWTH Aachen,
W. Germany

The focusing of shock and blast waves is of interest in a
variety of fields. Well-known examples are the wave systems
of manoeuvring supersonic aircrafts. Shock waves with non-
planar fronts occur when plane waves travel through inhomo-
geneous media or by reflection on curved boundaries. Weak
waves with concave fronts converge to focal points or cau-
stics. In stronger waves nonlinear effects become important
leading to Mach reflections. Usually regions of high energy
density are produced by the focused waves. These have been
used e.g. to initiate detonations, to produce very strong
shock waves and rare reaction products. In a recent applica-
tion the focusing of underwater blast waves has been used
for fracturing of kidney and gall stones.
The studies presented in this review concentrate on the fo-
cusing of weak shock waves reflected on curved boundaries.
The random-choice-method has been applied to different two-
dimensional cases with good agreement in both, the location
of the gas dynamic focus and the pressure amplitude. Fo-
cusing of blast waves produced by short-duration sparks af-
ter reflections on ellipsoids in air and water have also
been studied experimentally and numerically. Using a ruby-
laser-stroboscope together with a shadowgraph technique and
a rotating mirror camera cylindrical converging shock waves
in a Kantrowitz-type shock tube have been produced. Conver-
ging longitudinal waves in lucite plates are observed by
time-resolved interferometry and compared with several nume-
rical methods; there is evidence of Mach-reflection in PMMA.

1. Introduction

It is well known that non-planar shock waves having a concave front in the
propagation direction converge with a subsequent production of high values of
the state variables in some regions. This sort of shock focusing has been de-
monstrated by Perry and Kantrowitz[1] more than thirty years ago by some spec-
tacular schlieren photographs obtained in a small shock tube device where it
was possible to produce cylindrical converging shock waves. Theoretically the
problem of cylindrical and spherical converging shock waves of infinite
strength has been dealt with by Guderley[2] more than forty years ago. A conside-
rable number of papers has been published since then on different problems re-
garding focusing waves, both experimentally and theoretically, so that it is
hardly possible to mention most of them; some of them which are mainly and
closely connected to our own work will be cited.

Hemispherical converging strong shock waves have been generated in a special
explosion chamber by Glass and Sharma[3] to produce diamonds and neutrons. An
experimental and theoretical study on the behaviour of the medium near focus
has been performed by Saito[4] for the experimental setup just mentioned. Various
kinds of explosions and detonation waves have been focused; one of these is
shown in Fig. 1; it is the detonation chamber proposed and tested by Terao[5].
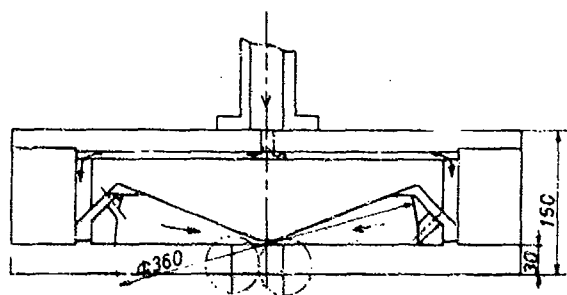
Fig.1:
Schematic diagram of the
detonation chamber of
Terao[5].

Here the detonation is initiated in a tube; the detonation wave then expands as
a cylindrical outgoing wave and, after turning through a passage of numerous
holes, it is focused by conical or spherical walls to the center of the cham-
ber. Experimental studies on the stability of converging cylindrical shock
waves have been performed by Wu et al.[6]. An extension of Perry's and Kantro-
witz[1] work has been presented by Takayama et al.[7] recently, regarding also the
stability of cylindrical converging shock waves. In this work the shock wave is
guided by a smooth transition through the annular part of the shock tube until
it reaches the cylindrical gap where it is focused. By using holographic inter-
ferometry Takayama et al.[7] have succeeded in studying the details of the fo-
cusing process. Our own studies have been concentrated on several geometries:
first: focusing on ellipsoidal reflectors; secondly: plane two-dimensional and
rotationally symmetric reflectors similar to the experiments of Sturtevant and
Kulkarny[3], and thirdly focusing of cylindrical shock waves by means of a geome-
try essentially similar also to Perry and Kantrowitz[1]. As media gases and wa-
ter, but also lucite plates have been used.
The experimental results have been compared mainly with numerical calculations
using the random-choice-method (RCM) recommended by Glass[9] in his Paul Vieille
Memorial Lecture four years ago on this Symposium. Studies of focusing of blast
waves in air from an ellipsoidal reflector were carried out by Holl[10] using for
numerical comparison Whitham's shock dynamics[11] in a modified version due to
Davies and Guy[12]. In view of the recent applications of underwater shock waves
to fracture kidney stones these studies have been extended to axially symmetric
experiments by Müller[13]. These experiments have been compared with numerical
calculations of Olivier[14] applying the RCM also to the focusing of weak under-
water shock waves.
In the case of the focusing of cylindrical shock waves a comparison is possible
with Takayama's previous work[7], an additional experimental work which was car-
ried out in close cooperation with Takayama at Aachen and a very recent study
by Kleine[15] using a schlieren system and a ruby-laser-stroboscope making it
possible to produce series of photographs of each experiment. In a further stu-
dy focusing of weak compression waves in lucite plates has been performed by
Henckels[16] using the reflected shock wave at the end wall to initiate the
pulse; time resolved interferograms and shadowgraphs were compared with results
of several calculation methods. To increase the amplitude of these waves small
pellets of explosive have been applied revealing the occurrence of Mach reflec-
tion in PMMA in the course of the interaction of two cylindrical waves both
generated at the same time.

2. Focusing by concave reflectors

2.1 Medium air

In the studies performed by Holl[10] ellipsoidal reflectors were use. A weak
blast wave is produced by a fast capacitor discharge across a spark g   ocated

in the far focus of the ellipsoid. Figure 2 shows the principal experimental setup. The electrodes of the spark gap are embedded in a flat plate to produce an undisturbed hemispherical blast wave. This wave encounters an ellipsoidal
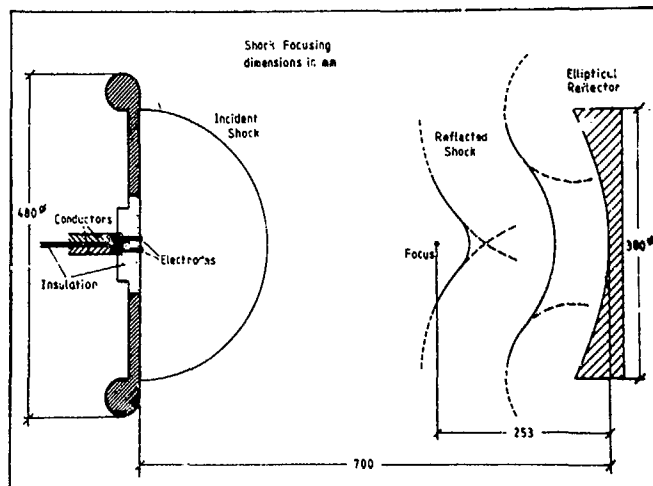
Fig. 2:
Experimental setup for focusing of weak blast waves (Holl[10]).

reflector with axial symmetry and, after reflection, the wave front is converging to the second focus. The fronts were photographed by means of a single shot spark schlieren system; pressure histories were recorded by Kistler pressure gauges. Figure 3* shows series of schlieren photographs; in Fig. 3a the wave has acoustic strength ($M_0 = 1.0068$), and the focusing occurs according to geometrical acoustics. The field of view is 178 mm in diameter, and the waves are moving from left to right. M_0 is the Mach number immediately after reflection. When the center part of the wave reaches the focal region it steepens up and accelerates. Thereby a Mach stem is formed and further focusing is prevented. Surprisingly, this Mach stem shrinks beyond the focus, and finally the wave leaves the focal region crossed and folded as predicted by geometrical acoustics. If the plane of symmetry is considered as an ideal reflecting wall the whole process corresponds to a transition from Mach to regular reflection[17]. Figure 3b* shows the focusing for a moderately weak wave. The height of each photograph corresponds to 67 mm. Here a deeper reflector (80 mm in diameter) is used located 80 mm closer to the spark gap. No wave crossing is observed here beyond the focus but the Mach stem length is continuously increasing. The geometry corresponds more to Whitham's shock dynamics[18]; the Mach stem, however, is not bent convex as predicted by shock dynamics but straight as usually observed. There is a transition Mach number that separates these two fundamental cases. Depending on the convergence ratio d/f of the reflector it is found to lie between 1.05 and 1.10 in agreement with the value determined by Sturtevant and Kulkarny[8]. The location of the wave fronts and the pressures on different positions on the axis of symmetry have been calculated by a time stepping scheme proposed by Davies and Guy[12] and Fong and Ahlborn[19] which is based on the CCW theory. The wave front (its upper half only) is divided up into 100 straight elements for each of which the normal shock relations hold. The variations of the ray tube areas are taken into account by Chisnell's channel formula[20]. The results of these calculations are compared with pressure measurements on the axis in Fig. 4. Here the pressure amplification of the shock jump on the axis of symmetry referred to the pressure jump on the reflector surface is plotted with respect to the distance x from the reflector apex normalized with its focal length f. For moderately weak blast waves the pressure at focus is overestimated as the calculation does not allow for the reflected branches of the Mach reflection and the expansion waves behind the

*Photographs are arranged following the references

shock front. Consequently the central part of the wave accelerates too much and overshoots beyond the focus just as Whitham has predicted. Figure 5 shows the upper halves of the calculated and observed wave patterns at succesive times. Near the focus and in the outermost parts deviations from the experimentally observed wave positions may be noted, the reason being the same as just given above.
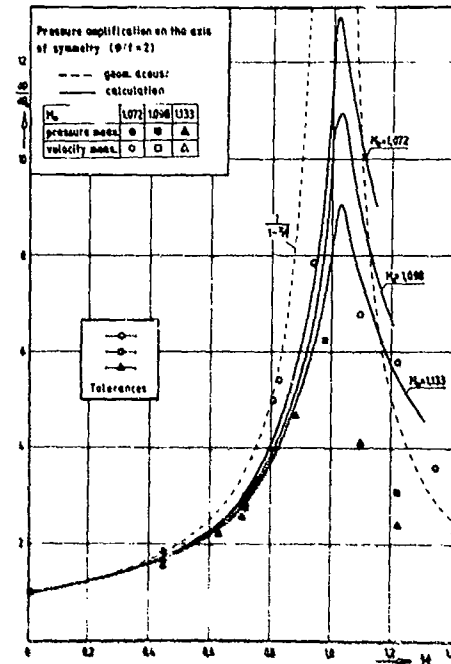
Fig. 4: Focusing of moderately weak waves; measured and calculated pressure amplification of the shock jump on the axis.
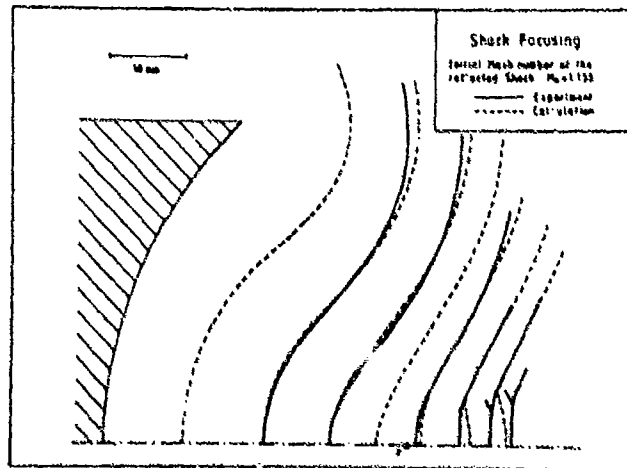
Fig. 5: Focusing of moderately weak waves ; comparison between experiment and calculation.

Because of the difficulties occurring near the focal region when applying the CCW method, two-dimensional RCM was applied to the cases of plane and axially symmetrical parabolic reflectors for plane incident waves and to ellipsoidal reflectors for point explosions originating in either one of the both focal points. The basic equations for unsteady two-dimensional plane or axially symmetrical inviscid motions of a non-heat-conducting compressible fluid are solved numerically using the method of Glimn[21] and Chorin[22] . The RCM is essentially an explicit numerical scheme that repeatedly solves a one-dimensional Riemann or shock tube problem between grid points to obtain the solution at the next time level (Igra & Gottlieb[23]). For the numerical solution of the two-

dimensional homogeneous equations the operator-splitting technique introduced to the RCM by Sod[24] is also used in the study of Olivier[14,25] . Special attention has been given by Olivier to the influence of the random number generator and of the passive velocities. Random-number generators, which yield smooth solutions in one-dimensional cases, may exhibit large fluctuations especially near boundaries in two-dimensional problems. The handling of the passive velocities has also an influence on the solution: they may be regarded as passive scalars (Chorin[22], Colelia[26]) or as constants (Olivier[14]). By using mean values of the passive velocities a certain smoothing is achieved without affecting the steepness and amplitude of the focal pressure signature for weak shock waves.

As a test for the numerical calculations the shock tube experiments of Sturtevant and Kulkarny [8] are used for comparison. They measured the pressure history in the focal region of a parabolic cylinder with its axis of symmetry coinciding with the shock tube axis. Figure 6 shows the comparison between the experimentally obtained pressure history as a solid line and the result of the corresponding RCM calculation. The time scale is 50 μs /div and the vertical
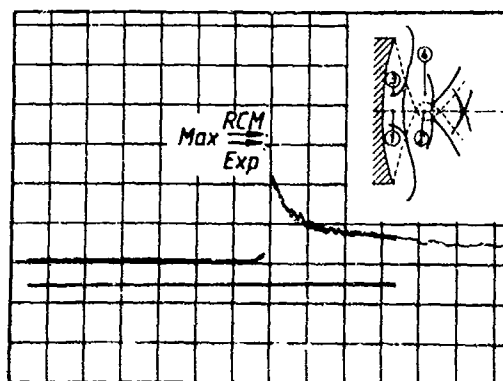
Fig. 6: Comparison between RCM[14]
and experiment[8].

scale 0.4 bar/div. Location 2 refers to a spot very close to the geometrical focus; initial shock Mach number is 1.1. Due to the steep pressure rise which cannot be resolved from the printed oscillogram the maximum measured pressure has been obtained from Fig. 9 of Sturtevant's and Kulkarny's paper[8] showing the maximum pressures during the focusing process. Maximum calculated and measured pressure are indicated by arrows.

Very recently the same problem was treated by Saito et al.[27] and Nishida et al.[28] applying, however, in their numerical calculation the piecewise-linear-method (PLM) proposed by Colella and Glaz[29]. Due to the smoothing by interpolation, the finite difference calculation and additional dissipative terms the flow field is free from oscillations and fluctuations. The location of the focus is also in very good agreement with the experimental results of Sturtevant and Kulkarny[8]. In Fig. 7 two pressure fields calculated by Nishida et al.[28] are shown at two successive instants of time. After shock reflection at the parabo-
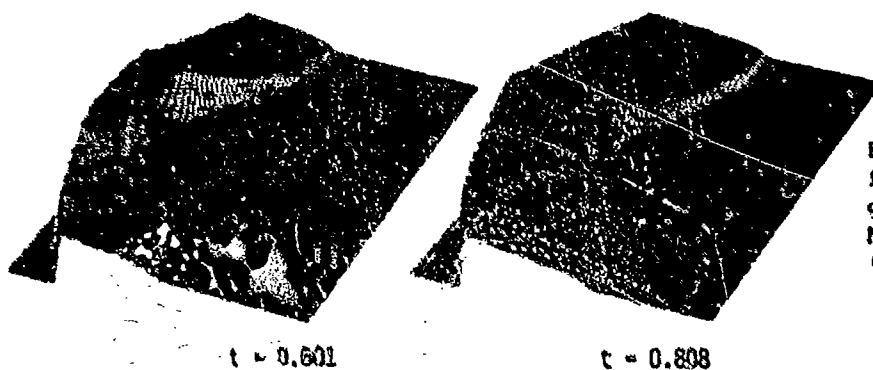
Fig. 7: Pressure
fields of converging shock wave,
M_0 = 1.13
(Nishida et al.[28]).

t = 0.601   t = 0.808

lic surface two pressure peaks appear in the reflected front close to the trip-
le points where the converging center of the reflected wave meets the reflected
waves from the corners. This conclusion is confirmed by the RCM calculations of
Olivier[14] and the discussion of Sturtevant[18]. Also generally the gasdynamic
focus is found to lie inside the geometric focal distance, approaching the geo-
metric focus as the strength of the incident shock becomes weak. With decrea-
sing depth of the reflector the gasdynamic focus again leaves the geometric one
in the direction of the reflector. The PLM has been also very recently applied
by Takayama[30] in calculating isopycnics of the shock reflection at a plane cir-
cular reflector and of the subsequent focusing process in order to compare them
with infinite fringe holographic interferograms.

2.2 Medium Water

With the application of focused underwater shock waves for fracturing kidney
and gall stones experimental and numerical studies of focusing of waves in wa-
ter have been of great interest worldwide. One the of first papers on quantita-
tive measurements of shock focusing by ellipsoidal reflectors is that of
Takayama[31] et al. presented at the last Shock Wave Symposium. To initiate the
shock waves they use lead azide pellets with laser ignition. By means of a
double exposure holographic interferometer it has been possible to deduce the
pressure distribution in the flow field. Comparison has been made with the one-
dimensional RCM for calculating the radial pressure field of the micro-explo-
sions.
Our own experiments are performed in a water basin where the shock wave is
initiated by a short-duration underwater spark in a similar setup as with
Holl's experiments[10] in air. After reflection of the wave at an ellipsoidal
reflector the wave is focused in the focal point closer to the reflector. The
pressure field is studied by means of pressure gauges having an upper frequency
of about 10 MHz and a spatial resolution of about half a millimeter, they have
been developed by Müller and Platte[13].
The two-dimensional RCM was also applied by Olivier[25] to the focusing problem
by ellipsoids taking both the closer and farther focus as origin of the wave.
For not too extended ellipsoids the numerical results are in good qualitative
agreement with the experiments, both those by Takayama[31] and our's[25].

3.   Focusing of cylindrical waves in air

In the study described in this section a similar setup has been used as des-
cribed by Perry and Kantrowitz[1]. The experimental arrangement is shown in Fig.
8. The shock tube has an inner diameter of 300 mm and a 1:10 cone is mounted
inside leaving an annular ring 50 mm wide close to the end wall. The gap be-
tween the bottom of the cone and the end wall has a width of 10 mm. Shadow-
graphs have been taken by Kleine[32] using a ruby-laser-stroboscope and a high-
speed rotating-mirror camera which allow to take photos with time intervals
from 2.5 up to 3.5 μs. Thus it is possible to visualize the whole time history
of a cylindrical shock wave being focused in a single experiment. Experiments
have been performed covering a Mach number range of $M_0 = 1.1$ up to 2.1 with
nitrogen as driven and helium as driver gas. The slender cone cuts out an annu-
lar shock wave which is bend 90^0 degrees at the sharp edge of the cone but is
also reflected a few tens of microseconds later forming almost a new cylindri-
cal shock tube, the reflected region being the new driver.
In Fig. 9 series of shadowgraphs are shown for an initial shock of Mach
number $M_0 = 1.3$ and 2.1 , resp. Obviously an initial asymmetry of the conver-
ging shock is greater with the higher Mach number. Behind the incident shock a
number of waves may be seen originating from multiple reflections and diffrac-
tion during the shock forming process. At the lower Mach number of $M_0 = 1.3$ the

field of view. This vortex ring breaks down rather soon.

All the shocks being observed in these experiments tend to approach a somewhat curved triangular shape which is believed to be due to the design of the supporting system of the cone.
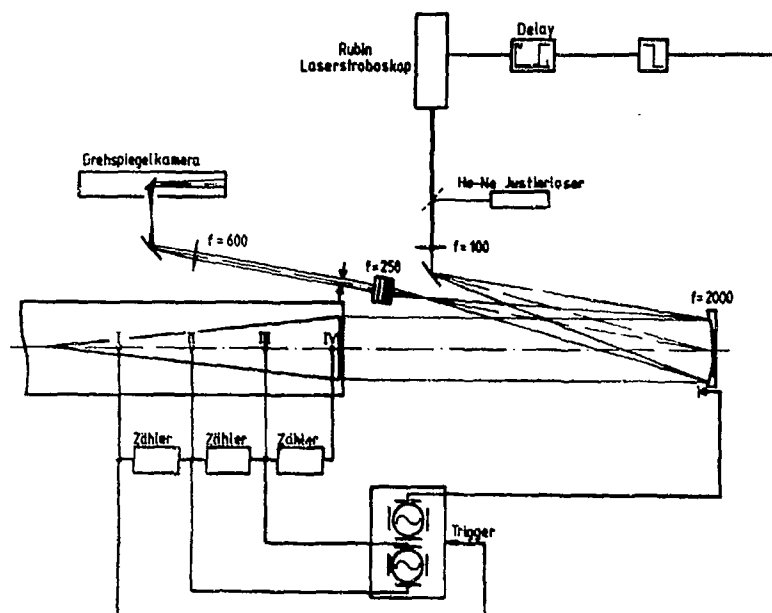
Fig. 8: Experimental setup for time resolved shadowgraphs of converging cylindrical shocks.

The cone is mounted by three pairs of struts at equi-angles of $120°$. The two marks are 100 mm apart. At small shock diameters of about 5 mm the shortcomings of the shadow method are obvious; due to the large density gradients nearly all of the incident light is deflected leaving the center almost dark. Thus the process of actual shock focusing and instability cannot be observed in detail that way. A rather strong and 'long-living' vortex at the center of implosion indicates the final instability of the converging wave.

Picture series taken at the maximum frequency possible with this continuously writing rotating mirror camera (400 kHz) indicate that the actual focusing process takes place within a space of nanoseconds (Fig. 10[*]). Mean velocities of the shock wave were measured and plotted in Fig. 11 in comparison with analytical approaches, the reference point for both, the Guderley and CCW curve, being the experimental point closest to the center. The quite large discrepancies far from center are believed to be due to the multiple reflections after the bending of the incident shock. Olivier[25] compared the results with a one-dimensional RCM calculation and found almost complete agreement with Guderley for the higher Mach number. Pressure measurements were also performed close to the center. Agreement exists between the measured pressure history and that obtained by integrating the numerically calculated one over the pressure sensitive surface of 3.2 mm in diameter for the used Kistler gauge as shown in Fig. 12.

In previous studies Takayama et. al.[7] used an almost similar shock tube, however, with a smooth bending section for the shock and a different number of struts to support the cone. He obtained a number of infinite fringe holographic interferograms which clearly revealed an instability mode of four as shown in Fig.13[*] for $M_o = 1.1$. Recently by the cooperation of Prof. Takayama we were able to set up at the Stoßwellenlabor a system for interferometric holography which is shown in Fig. 14. Figure 15[*] shows an interferogram comparable to that

of Fig. 13[*] also just before focusing where obviously a triangular shape domi-
nates.
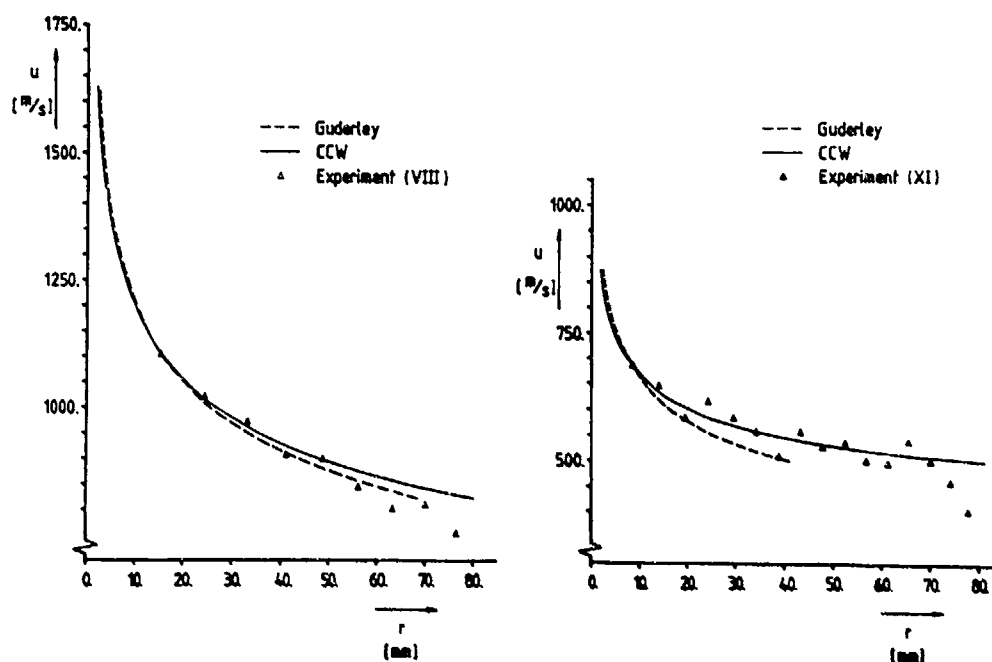
Fig. 11: Velocity of imploding shock versus distance from center:
M_0: (a) 2.1, (b) 1.3. Similarity coefficient 0.8276 (-0.038; + 0.031)
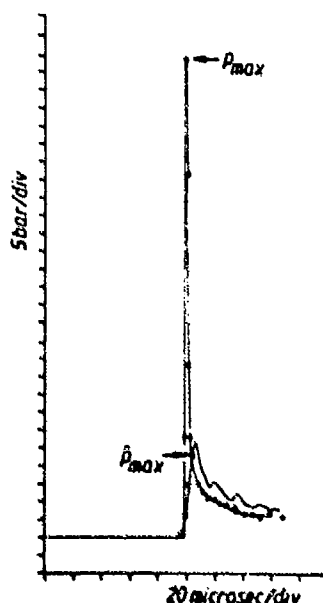
Fig. 12: Measured (—) and
computed (ooo) pressure
history near focus for
M_0 ($r=100$ mm) = 1.35;
xxx integrated over the
gauge area.

At higher Mach numbers these deviations from a cylindrical shape are still more
striking. The conclusion from these experiments is that the final instabilities
of a cylindrical shock wave may be caused by disturbances far away from the
center of implosion and that probably a low number of instability modes is more
persisting than instabilities of higher modes.

Film Holder

Spherical Mirror
d = 200 mm,
f = 2.000 mm

L

L

L

BS

9:1 Beam Splitter

M

300 mm diameter
Shock Tube

M

Holographic Ruby Laser

0   1 m   2 m

M
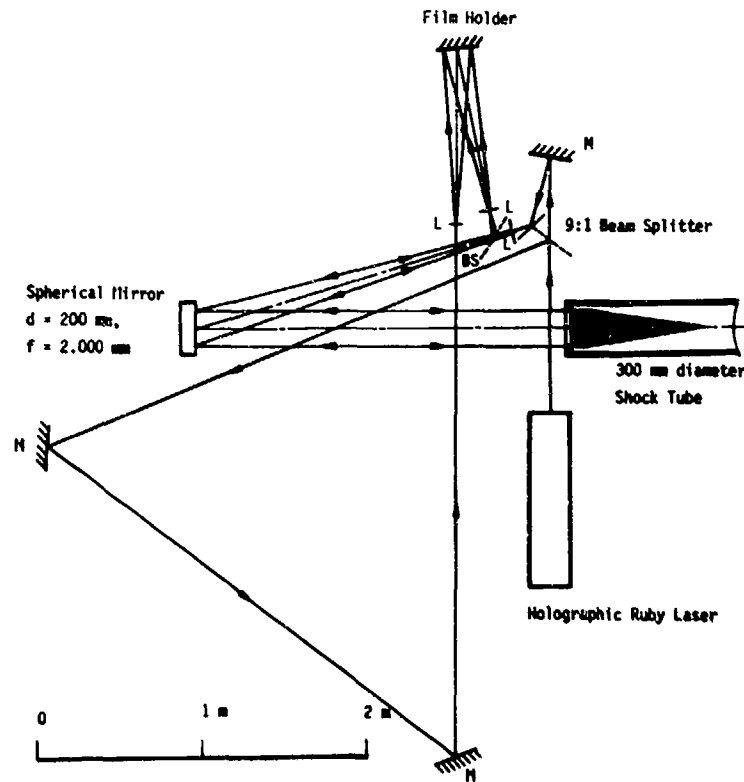
SCHEMATIC DIAGRAM OF OPTICAL ARRANGEMENT

Fig. 14: Schematic diagram of holographic system.

Gardner et al.[33] use the CCW approach to study analytically and numerically the stability of imploding shocks; for sufficently large amplitudes they note that linear behaviour breaks down and the solution develops into a kink form of the shock waves. Yu[34] makes an asymptotic expansion of the CCW equations near focus and shows that the loci of small perturbations for converging cylindrical shock waves are logarithmic spirals. An analytical approach to the problem of cylindrically converging shock (and detonation) waves has been recently developed by Matsuo[35].

4. Focusing of stress waves in solids

For the study of focusing of stress waves in lucite plates (PMMA) two experimental setups have been used: using the reflected shock at the end wall and small pellets of explosive. The both cases by means of a Mach-Zehnder interferometer, the ruby laser stroboscope and the rotating mirror camera a series of interferograms has been obtained for each experiment.
Figure 16 shows a plane incident wave train of three longitudinal compressive pulses embedded in a dispersive wave[36]. The pulses are generated by repeated reflection of transversal waves at the front and rear side of the plate. The change of the width of the plate measured by the shift of the interference fringes is shown in Fig. 17 as a function of the distance[16]. The measured variation is compared with calculations performed by Raatschen[37] using a two-
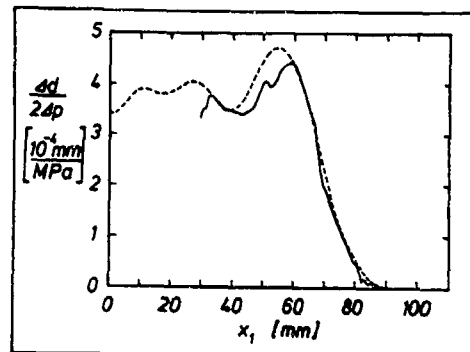
Fig. 17: Variation of plate's
thickness: experiment and me-
thod of characteristics .

dimensional characteristic method. The focusing experiments by means of a cir-
cular lucite plate have most recently also compared with the RCM applied to
longitudinal and transversal stress waves in solids. Here linear and nonlinear
stress-strain relations are taken into account and to our best knowledge the
Riemann problem has been solved in this case for the first time[38]. Figure 18
shows the two-dimensional stress field for the instant of focusing of a longi-
tudinal wave at the circular boundary.
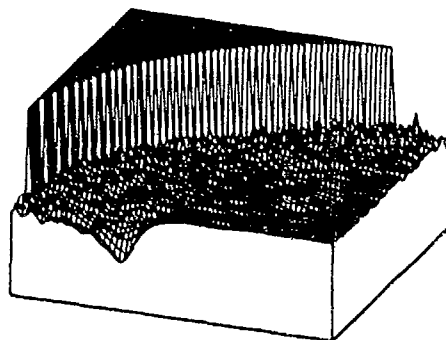
Fig. 18: Focusing of longitudinal
wave (RCM[38]).

To increase the stress pulses in the PMMA plates beyond the limit of the re-
flected shock tube pressure small pellets of explosive have been used by
Henckels et al.[39].Using the classical arrangement of Ernst Mach with the simul-
taneous explosion of two pellets, Mach reflection could be observed as shown
in the shadowgraph of Fig. 19 ; an analytical assessment similar to that given
by Holl et al.[40] for water confirms this experimental result.

5. Conclusion

A number of studies have been reviewed regarding the focusing process of con-
cave shock waves in gases, fluids and solids. Experiments by time-resolved op-
tical methods are in agreement with numerical calculations using different ap-
proaches; two-dimensional RCM and PLM seem to complement rather than to com-
pete with each other. RCM has successfully been applied to the focusing process
in PMMA plates, too. Mach reflection, finally, has also been observed in PMMA
plates.

Acknowledgements

References

1. Perry, R.W., Kantrowitz, A.: The production and stability of converging shock waves, J. Appl. Phys. 22, 1951, pp. 878-886.
2. Guderley, G.: Starke kugelige und zylindrische Verdichtungsstöße in der Nähe des Kugelmittelpunktes bzw. der Zylinderachse , Luftfahrtforsch. 29, Lfg. 9,1941 S. 302-312.
3. Glass, I.I., Sharma, S.P.: Production of diamonds from graphite using explosive-driven implosions, AIAA J. 14, 1976, pp. 402-404.
4. Saito, T.: An experimental, analytical and numerical study of temperatures near hemispherical implosion foci. UTIAS Report No. 260, Dec. 1982.
5. Terao, K.: Temperatures in imploding detonation waves. Jap. J. Appl. Phys. 23 , 1984, pp. 27-33.
6. Wu, J.H.T., Neemeh, R.A., Ostrowski, P.P.: Experimental studies of the production of converging cylindrical shock waves. AIAA J. 18, 1980, pp. 47-48.
6a. Wu, J.H.T., Neemeh, R.A., Ostrowski, P.P., Elabdin, M.N.: Production of converging cylindrical shock waves by finite element conical contractions. In: Ahlborn, B., Hertzberg, A., Russell, D. (Eds.): Shock Tube and Shock Wave Research, Univ. Wash. Press, Seattle 1978, pp. 107-114.
7. Takayama, K., Onodera, O., Hoshizawa, Y.: Experiments on the stability of converging cylindrical shock waves, Theor. and Appl. Mech., 32, 1984, pp. 117-127.
8. Sturtevant, B., Kulkarny, V.A.: The focusing of weak shock waves , J. Fluid Mech. 73, 1976, pp. 651-671.
9. Glass, I.I.: Beyond three decades of continuous research at UTIAS on shock tubes and waves, Treaner, C.T., Hall, J.G. (Ed's.): Shock Tubes and Waves. State Univ. New York Press, Albany, 1982, pp. 3-20.
10. Holl, R.: Wellenfokussierung in Fluiden, Doctoral Thesis, RWTH Aachen 1982.
10a. Holl, R., Grönig, H. (Appendix by Olivier, H.) Focusing of weak blast waves, Archer, R.D., Milton, B.E. (Ed's.): Shock Tubes and Waves. New South Wales Univ. Press, Sydney 1983, pp. 563-570.
11. Whitham, G.B.: A new approach to problems of shock dynamics, Part I, Two-dimensional problems, J. Fluid Mech. 2, 1957, pp. 145-171.
12. Davies, P.O.A.L., Guy, T.B.: The prediction of weak diffracting and reflecting wave patterns, ZFW 19, 1971, pp. 339-347.
13. Müller, M., Platte, M.: Einsatz einer breitbandigen Piezodrucksonde auf PVDF-Basis zur Untersuchung konvergierender Stoßwellen in Wasser. ACUSTICA, in press 1985.
14. Olivier, H.: Zweidimensionale Instationäre Stoßwellen. Anwendung der Random-Choice-Methode. Doctoral Thesis, RWTH Aachen 1985.
15. Kleine, H., Takayama, K. Grönig, H.: Stability of cylindrical, converging shock waves, to be published.
16. Henckels, A.: Experimentelle Untersuchung instationärer Wellen in Scheiben, Doctoral Thesis, RWTH Aachen 1985.
17. Ben-Dor, G., Takayama, K., Kawauchi, K.: The transition from regular to Mach reflection and from Mach to regular reflection in truly nonstationary flows, J. Fluid Mech. 100, 1980, pp. 147-160.
18. Sturtevant, B.: Propagation of Shock Waves in Nonuniform Media. Lecture series presented at the Stoßwellenlabor, RWTH Aachen, Oct./Nov. 1982.

19.   Fong, K., Ahlborn, B.: Stability of converging shock waves, Phys. Fluids 22, 1979, 416-421.

20.   Chisnell, R.F.: The motion of a shock wave in a channel, with applications to cylindrical and spherical shock waves, J. Fluid. Mech. 2, 1957, pp. 286-298.

21.   Glimm, J.: Solution in the large for nonlinear hyperbolic systems of equations, Comm. Pure Appl. Math. 18, 1965, pp. 697-715.

22.   Chorin, J.A.: Random choice solution of hyperbolic systems, J. Comp. Phys. 22,1976, pp. 517-533.

23.   Igra, O., Gottlieb, J.J.: Interaction of a rarefaction wave with an area reduction, Archer R.D., Milton, B.E. (Ed's): Shock Tube and Waves. New South Wales, Univ. Press, 185-195, Sydney 1983.

24.   Sod, G.A.: A numerical study of a converging cylindrical shock, J. Fluid Mech. 83, 1977, pp. 785-794.

25.   Olivier, H. , Grönig, H.: Two-dimensional shock focusing and diffraction in air and water, 15th Int. Symp. on Shock Tubes and Waves, Berkeley 1985.

26.   Colella, P.: Glimm's method for gas dynamics, SIAM J. Sci. Stat. Comp. 3, 1982, pp. 76-110.

27.   Saito, T., Nakagama, T., Nishida, M.: Note on the focusing of shock waves. Presented at the Annual Meeting of Jap. Soc. Aeron. and Astron., April 1985 in Japan.

28.   Nishida, M., Nakagawa, T., Kikuyama: Numerical calculations of the flow-field with shock focusing: Preprint to be published, 1985.

29.   Colella, P., Glaz, H.M.: Efficient solution algorithms for the Riemann problem for real gases, Lawrence Berkeley Laboratory, LBL- 15775, 1983.

30.   Takayama, K.: Stability of converging cylindrical shock waves. Presented at the Colloquium of the Sonderforschungsbereich 27 "Wellenfokussierung", RWTH Aachen, July 3 and 4, 1985.

31.   Takayama, K., Esashi, H., Sanada, N.: Propagation and focusing of spherical shock waves produced by underwater microexplosions. In Archer, R.D., Milton, B.E. (Ed's): Shock Tubes and Waves, New South Wales Univ. Press, Sydney 1983, pp. 553-562.

32.   Kleine, H.: Shadowgraphs of converging cylindrical shock waves. Studienarbeit, Stoßwellenlabor, RWTH Aachen, July 1985.

33.   Gardner, J.H., Book, D.L. , Bernstein, I.R.: Stability of imploding shocks in the CCW approximation, J. Fluid Mech., 114, 1982, pp. 41-58.

34.   Yu, Sh.: Asymptotic solution near focus of a two-dimensional shock and instability near axis of a cylindrical shock with CCW approach, Z. Naturf. 39a, 1984, pp. 1011-1022.

35.   Matsuo, H.: Cylindrically converging shock and detonation waves. Phys. Fluids 26, 1983, pp. 1755-1762.

36.   Henckels, A., Grönig,H.: Experimental studies of stress waves in elastic plates with curved boundary. Pichal M.(Ed.): Optical Methods in Dynamics of Fluids and Solids. Springer-Verlag, Berlin, Heidelberg, 1985, pp. 143-149.

37.   Raatschen, H.-J.: Institut für Mechanik, RWTH Aachen, private communication, 1984.

38.   Esser,B.: Random-Choice-Verfahren zur Berechnung nichtlinearer Wellen in elastischen Scheiben. Presented at the Colloquium of the Sonderforschungsbereich 27 "Wellenfokussierung", RWTH Aachen, July 3 and 4, 1985.

39.   Henckels, A., Takayama, K., Grönig, H.: Study of Mach Reflection in PMMA Plates. 15th Int. Symp. on Shock Tubes and Waves, Berkeley, 1985.

40.   Holl, R., Takayama, K., Higashino, F.: Generation, propagation and reflection of underwater shock waves. Japan National Shock Wave Symposium in Tokyo, 1983, pp. 44-47.

a) 0   60   120   230 μs

b) 0   43   57   66   89   92 μs
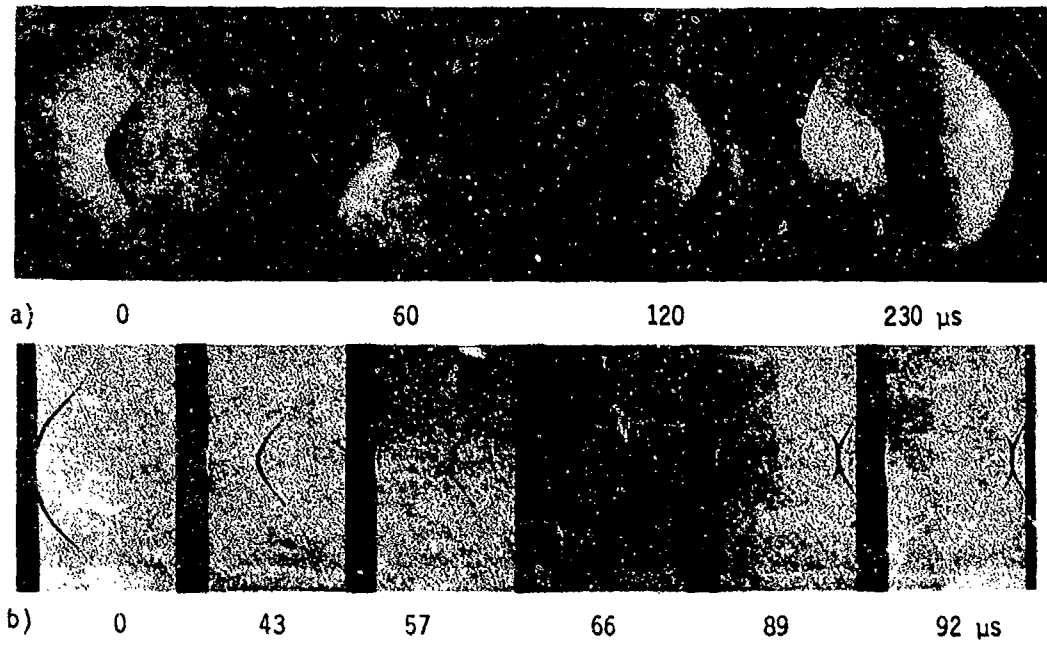
Fig. 3: Wave focusing in air. M_0 (a) 1.0068 ,   (b) 1.072

a)   0   42.5   59.5   68   119 μs

b)   0   25.5   59.5   76.5   144 μs
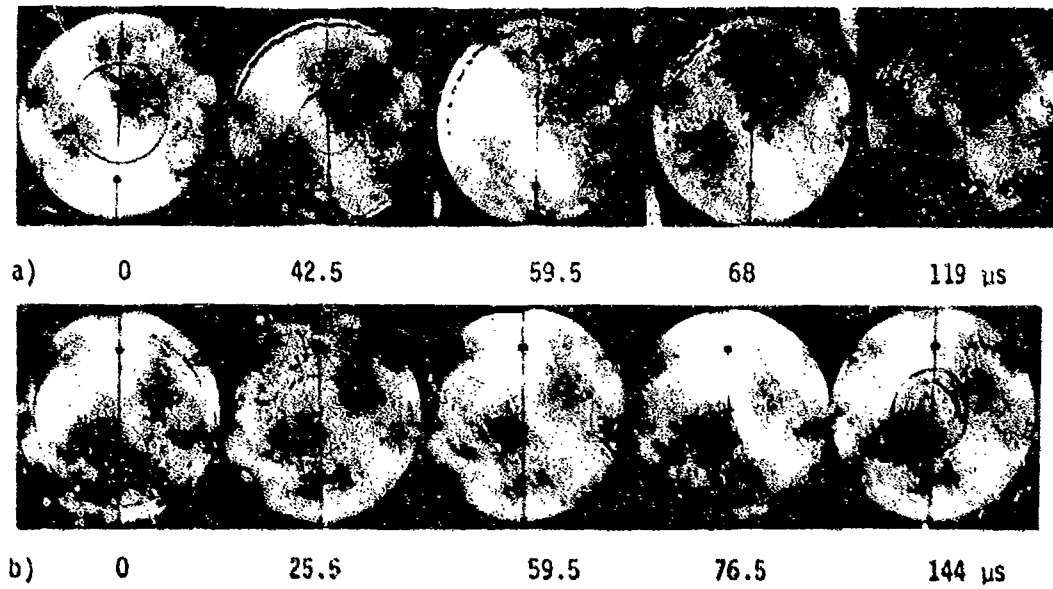
Fig. 9: Series of shadowgraphs of a single experiment M_0 (a) 1.3 , (b) 2.1 .
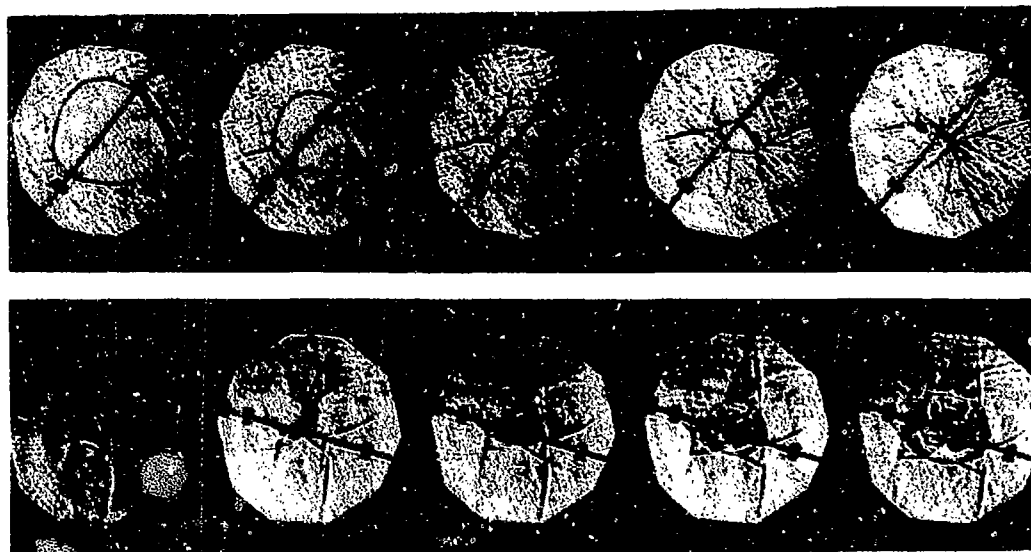
Fig. 10:   Successive shadowgraphs with $\Delta t = 2.5 \, \mu s$; M_o: (a) 1.3 , (b) 2.1

40 mm

Fig. 13:   Infinite fringe holographic interferogram of converging cylindrical shock $M_o = 1.1$ (from Takayama et al.[7]).

Fig. 15:   Infinite fringe holographic interferogram; $M_o = 1.3$.
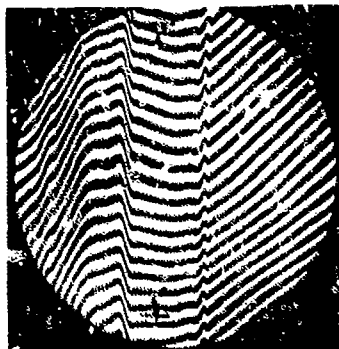
Fig. 16:   Interferogram of wave propagation in a PMMA plate.

Fig. 19:   Mach reflection in a PMMA plate.

SHOCK DYNAMICS OF NONINVASIVE FRACTURING OF KIDNEY STONES

David A. Russell

Department of Aeronautics and Astronautics
University of Washington, Seattle, WA 98195

A review is provided of the snock dynamics of extracor-
poreal shock-wave lithotripsy. Methods of predicting
blast wave redirection, focusing, and coupling are pre-
sented and discussed. Experiments were carried out using
a Q-switched ruby laser to initiate waves inside an
ellipsoidal reflector attached to a water tank. Piezo-
electric gages provided maps of peak pressure, and human
kidney stones were suspended in the target zone and frac-
tured. General agreement with prediction is found and
areas for further study identified.

1. INTRODUCTION

Extracorporeal shock-wave lithotripsy is the newest and most promising
treatment for kidney-stone disease. Originated in West Germany, the technique
is now well documented[1], and more than 12,000 patients have been treated
worldwide. Figure 1 illustrates the essential fluid mechanical features. A
sudden deposition of energy at a point inside a water-filled reflector creates
a spherical blast wave which is redirected through a water bath and targeted
onto the brittle calculus inside the patient. The technique is based on the
fact that tissue and muscle have similar transmission characteristics to water,
that a local refocusing of the shock occurs, that the applied pulse is short
compared to the wave transit time through the stone, and that the stones have a
tensile strength generally agreed to be only 5-50 atm. Hundreds of separate
shocks are applied until the calculus is spallated into fragments which pass
naturally. The technique is noninvasive, with obvious advantages over percu-
taneous stone removal or open surgery.

The shock dynamics of extracorporeal shock-wave lithotripsy present inter-
esting challenges to the shock physicist, and are the subject of the present
paper. While the German work uses electric arcs, the energy source is not of
concern here as long as delivery is effectively symmetric and instantaneous.
At issue is the reconvolution of the initial spherical blast wave to an exter-
nal focus, and the resultant stresses induced in the target. As illustrated by
Fig. 1, most of the original spherical blast will undergo reflection. For an
ellipsoid this reflected wave is a segment of a spherical surface centered at
the second focus, if the wave speed is constant and wall reflection perfect. A
particular interest is the degree to which the refocusing process can be
treated acoustically and the significance of nonlinear effects.

The following section reviews basic analysis used in the study, and is
followed by a description of the experimental setup. Both are then applied to
the wave generation, reflection, diffraction, and coupling processes implicit
in Fig. 1, and conclusions are offered.

2. SHOCK PROCESSES

The Tait relation connecting the pressure, p, and density, ρ,

$$\frac{p+B}{B} = \left(\frac{\rho}{\rho_0}\right)^n \qquad (1)$$

is used as the equation of state for water. B, a weak function of entropy, is taken to be constant with value of 3000 atm. The exponent, n, is a constant at 7.15, and ρ_0 is a reference density at standard conditions. Note that Eq. 1 has the form of an isentropic perfect gas for p increased by B.

Equation 1 may be used with 1-D continuity and momentum to yield the shock jump conditions. For B/p_1, $Z \gg 1$ these take the approximate form:

$$\frac{\rho_2}{\rho_1} = 1+\epsilon; \quad \frac{u_2}{c_1} = \epsilon; \quad \frac{U_S}{c_1} = 1 + (\frac{n+1}{4})\epsilon; \quad \frac{c_2}{c_1} = 1 + (\frac{n-1}{2})\epsilon$$

$$\text{(2)}$$

$$\text{where } \epsilon = \frac{p_1}{B} \frac{Z}{n} \text{ with } Z = \frac{p_2}{p_1}$$

Here u_2 is the velocity following a shock travelling at speed U_s into undisturbed fluid, c is the speed of sound, and conditions 2 are behind the shock while 1 are in front. It is readily shown that a weak wave originating a specific distance behind a shock will overtake it in a distance of $[(n+1) \epsilon/4]^{-1}$ original spacings.

Superposition of a uniform velocity in the plane of the shock, together with the wall boundary-condition leads to the exact oblique-shock reflection solutions of Fig. 2. As shown in the insert, the oblique shock I reflects as R. The figure indicates the nonideal nature of the reflection process as a function of Z across I and the incidence angle β. Reflections to the right of the dashed line are Mach reflections.

The change in average strength of a shock travelling down a converging 1-D channel of arbitrary cross-section may be approximated by integrating the result of the wave interaction with a differential area change[2]. This has been repeated for water, using Eqs. 1 and 2 and steady area-change relations[3]. If K(Z) is assumed constant, the simple relation

$$A(Z-1)^{1/K} = \text{cons't} \tag{3}$$

is obtained. K is found to be equal to 1/2 in the acoustic limit, increasing by 1% for Z = 100 and 6% for Z = 1000; this contrasts with a 20 -30% reduction for ideal air at Z = 100.

Often the effective channel or stream-tube cross section area is not known a priori. The theory of geometrical shock dynamics[4] uses a description similar to geometrical acoustics, with coordinates in the shock front and on rays normal to it. Again assuming that the local cross-sectional area determines the shock Mach number and hence Z, geometric considerations lead to characteristic equations for axially symmetric flow:

$$\frac{\partial(\theta+\omega)}{\partial\eta} = -\frac{\sin m \sin \theta}{r}$$

$$\text{(4)}$$

$$\frac{\partial(\theta-\omega)}{\partial\zeta} = \frac{\sin m \sin \theta}{r}$$

Here θ is the local angle of the ray and r the normal distance off the axis of symmetry. The equivalents to the Prandtl-Meyer function and Mach angle in supersonic flow, ω and m, have been worked out for water[3]; approximations based on Eqs. 2 and 3 were found to give inaccurate results. The η and ζ directions are at local angle $\theta+m$ and $\theta-m$ respectively.

The calculation procedure for Eq. 4 requires inicial data along a shock surface with boundary conditions at its edge. Each characteristic mesh point then gives the shock properties when at that point. Three separate cases were calculated for Fig. 3, each with an initial spherical shock segment having R/D = 2, where R is the radius of curvature and D the shock diameter, and a constant Z=1 edge boundary condition. The ordinate is the centerline shock strength normalized by the initial value, and the abscissa is the dimensionless distance travelled. The shocks can be expected to strengthen as they converge, with linear acoustics predicting infinite amplitude at x/D=2. However, an expansion wave from the Z=1 boundary must propagate inward from the shock edges. The result is an earlier peak at a reduced value, these effects depending on the initial Z and the shock shape. The solid lines on Fig. 3 are for uniform initial Z-profile, the dashed line for a conical distribution with Z = 100 at the peak and 1 at the edge.

Figure 4 was calculated[5] for weak normal waves incident on a 1-D slab of elastic material in water. The ordinate is the amplitude of the reflected and transmitted waves shown in the insert, ratioed to that for the incident wave. It is plotted versus the acoustic impedance, ρc, of the elastic material relative to water. When these are equal the incident wave is transmitted unchanged. A strong reflected wave off the first surface of the reflector of Fig. 1 requires materials with high relative ρc; very small values of ρc correspond to gas bubble and air interface interactions. Spallation depends on the amplitude of the reflected wave off a back surface. A material in vacuum must preserve the boundary condition of zero stress at a free surface, and this requires that a compression wave perfectly reflect as a tension wave. Figure 4 shows that the presence of the water bath increases Ar_2/A_i to 0.15-0.25 for abscissa values between 1.5 and 8, a range which should encompass all stone targets.

Figure 5 is an x-t diagram of the stress field induced in the 1-D elastic slab of material for the particular case of a compression wave with a trapezoidal profile in time impacting on the left. The slab boundaries are the extreme left and right dashed lines. The solid lines represent the stress in the material at that x-location, with tension to the left. The figure is for a relative ρc of 5; thus from Fig. 4, the amplitude of the initial stress at the front surface is 0.3 of the applied pressure, and the reflected tension wave is 0.7 of that. All waves travel in the x-t plane with slope given by the elastic wave speed, c. The stress at any point on the figure is the sum of the contributions from left and right running waves, and these reduce each time an interface is met. Peak tensile stress first appears at the x-location immediately behind the back surface, where the plateau of the weakened reflected wave has just cleared the last of the incident one. Fracture will occur if this stress exceeds the stone strength. For a pulse characterized by an instantaneous rise followed by a linear fall to zero over time δ_t, the location of this first maximum is given by $c\delta_t/2$.

3. EXPERIMENTAL SETUP

Figure 6 is a schematic of the experimental arrangement. A 50 J capacitive discharge between electrodes in water gave erratic results, and was replaced as the energy source by a 3J 30nsec single-pulse ruby laser (Apollo Model 5). The multi-mode 2-cm diameter beam was focused through a flat window by a movable uncoated f=2 in air lens. It then passed through a 1.25-cm diameter hole in the reflector, itself attached to a 30x30x30 cm water tank made of plexiglas. The reflector was a hollow half-ellipsoid with minor and semi major axes of 12.7 cm, resulting in an eccentricity of 0.866 and wall to focal-point

distance of 1.7 cm. It was machined at full 12.7 cm depth out of aluminum.
Some measurements were also made with a higher eccentricity brass ellipsoid
with a window at right angles to that shown on Fig. 6. The laser beam could be
passed directly through the side of the box through various uncoated glass
lenses producing focal lengths of 3.8, 4.5, and 12.5 cm in water. The tank
water was continuously run through an external filter; use of distilled water
was not necessary, however some temperature control was required in order to
avoid air supersaturation.[1]

A calorimeter (Scientech 38-0101) was used to measure energy delivered
through the optics. Information on breakdown volume in the water was obtained
by exposing film behind various neutral-density filters. Pressure was recorded
with piezoelectric gages (Kistler 603A, PCB 111A22) connected to a 50 Mhz stor-
age oscilloscope (Tektronix 7000 series) triggered off the laser firing cir-
cuit. Fracturing experiments were carried out by suspending stone samples on a
thread at the experimentally-determined second focal point.

The pressure gages were calibrated with a solenoid switched volume. A
HeNe laser was passed through the ruby laser optics to insure allignment with
the reflector axis. Film burn patterns were used to check ruby laser mode and
diameter, while pinholes in thin tape targets located the actual focus in the
water. All spacial peak-pressure profiles were obtained by moving a single
gage for a series of runs each 30 seconds apart, finishing with a test repeat
of the first point. The results were found to be independent of gage used and
repeatable to within the reading accuracy of the oscilloscope.

A typical pressure trace is shown on Fig. 7. The gage was located on the
centerline at the exit of the ellipse, and 0.7J was delivered to the focal
point. As anticipated by Fig. 1, the trace shows the initial blast wave fol-
lowed at a time corresponding to wave travel over twice the wall to focal-point
distance by a reinforced reflected wave. The higher frequency oscillations
appear to be due to thickness-mode ringing. The rise time of both pulses is
seen to be 1 μsec, a limit imposed by the elastic wave transit-time through the
gage sensor. Recent numerical and experimental results[6] yield a pressure-
profile for a blast wave in water which can be approximated by an instantaneous
jump followed by a linear fall off to a low value at 10% of the shock-to-origin
distance. Based on this, a 1 μsec actual profile width was estimated for Fig.
7, and it was calculated[7] that the measured peak pressure was low by as much
as a factor of 2. Recent measurements with miniature 50 nsec PVDF gages[8]
appear to confirm this factor.

4. APPLICATION

Figure 8 collects peak pressure measurements versus r, the distance from
laser breakdown, for unconfined blast waves in water. The 4.3 cm focal-length
lens assembly was mounted in the tank wall for these experiments, and the pres-
sure gage was lined up perpendicular to the laser axis. The curves are label-
led with the value of E, the energy delivered through the optics.

The solid lines are the best fit to the data and correspond to the p (E,r)
expression shown on the figure with K = 2.1 (10)^5 in atm and cm units. Little
laser energy passed beyond the breakdown region and thus the process was ener-
getically similar to chemical explosions. Early chemical explosions in the
sea[9] gave an E exponent of 0.33, with the bracketed quantity raised to the
1.13 power; a more recent study of chemical microexplosions[6] found values of
0.33 and 1.15 respectively. An $E^{1/3}/r$ dependence can be argued for weak waves
on dimensional grounds[9].

The high E-dependence of Fig. 8 may be connected with departures from sphericity in the blast at higher E. While p-measurements parallel to the optical axis were identical to the perpendicular ones at 0.3J, they were 30% low at 1.4J. Rather than a submillimeter sphere, photographs of the breakdown at 1.0J revealed a conical region of light 0.4 cm long, indicating multiple site initiation. Not surprisingly, the pressure perpendicular to the optical axis was reduced further when the 12.5 cm optics were used.

From Eq. 2, U_s for the blast wave exceeds the acoustic speed by only 1% for $Z = 100$. When the wave reflects, Fig. 2 shows that the angle could be increased by a few percent. This might be accommodated by opening the reflector less rapidly, however it will be shown that the shock strength falls off rapidly near the wall. The maximum value of incident β for the 0.866 ellipsoid occurs at the exit and is less than 60°; thus the figure shows that regular reflection occurs throughout for $Z < 500$.

Fig. 9 presents peak pressures in the reflected wave obtained from traces such as Fig. 7. These are plotted versus radial off-axis position for a series of 0.7J runs with the gage located in the exit plane, and located 5cm further out. The exit profile is peaked at the center, falling to a low value as r approaches the ellipsoid edge at 6.35cm. The peak is amplified and sharpened at the farther out station. The dashed lines on Fig. 9 are for a model based on simplified shock dynamics and the ellipsoid geometry. It is referenced to a measured blast-wave peak pressure of 45 atm at the bottom of the ellipse for E = 0.7J. The strength of the wave at other points of impingement is approximated by the inverse radius ratio. From that point, the shock strength is found by applying Eq. 3 to the area change between two conical surfaces with apex at the second focal point and differential angle apart. Both the height of this region and its circumference around the axis decrease as the focus is approached, as may be inferred from the insert on Fig. 9. The model shows agreement with the general trends in the experiments. Note that a pure optical intensity analogy would show a much sharper peak.

Figure 10 presents the peak pressures measured along the axis of symmetry for the same 0.7J case as Fig. 9. The first dashed line is the location of the reflector exit plane, while the second is the geometrical focal point. The lines connecting the data of Fig. 10 suggest a maximum amplification of only 2 from the exit peak pressure, with this occuring on a broad shoulder ahead of the geometrical focus, and followed by a rapid drop. These effects are qualitatively explained by the discussion of shock diffraction leading to Fig. 3. As the bottom of the ellipsoid at $x = -12.7$cm is struck by a 45 atm blast, the peak amplification from this reference is 3. A further sharpening of the radial profile from the $x = 5$cm data of Fig. 9 can be expected at the focus, so that the full-width at half-maximum is less than the 1.4cm shown.

Kidney stones were suspended at the peak location indicated on Fig. 10 and fractured to sub millimeter size by applying hundreds of shocks produced by a nominal 1.5J of laser energy delivered to the water. With a δ_t of 1 µsec, maximum tensile stress should first appear at a depth of 1 mm for c double the sound speed in water. Fig. 10 indicates a peak pressure of 150 atm at 0.7J. Scaling with energy from Fig. 6 and using a factor of 0.2 from Fig. 4 leaves a peak tensile stress in the stone of 40 atm, close to the maximum strength mentioned in the Introduction. The expected factor of 2 higher actual peak pressure would allow this strength to be met at even shallower depths. However, it should be noted that particles were frequently observed to be dislodged from the front of the target stone, and complex fracture mechanisms may exist.

5. CONCLUSIONS

An overview of the shock dynamics of the noninvasive fracturing of kidney stones has been presented. It was shown that, for conditions of interest, a particular half ellipsoid reflector will project an external peak pressure of 3 times the strength of the original blast wave intercepted at its base. The peak is sharply focused in space and time at a location upstream of the geometric focus. A tensile stress of 15-25% of this pressure can be expected for stones targeted at that point.

It has been found that a simple stream tube model explains features of the reflection process, while shock dynamics predicts the diffraction and focusing that occurs after leaving the reflector. Numerical solution of the full inviscid equations of motion could increase the precision of the shock predictions and provide information about the flow evolution, but these would need improved instrumentation for verification. Among other questions needing study are non-ideal energy deposition including bubble dynamics, disturbances caused by electrodes and windows, transmission through impurities and bio tissue, diffraction around and stresses induced in 3-D targets, failure mechanisms, and nonisotropic stone characterization.

ACKNOWLEDGEMENTS

REFERENCES

1.   Chaussy, Ch., et al "Extracorporeal Shock Wave Lithotripsy," Karger Munich) 1982.

2.   Chisnell, R. F., "The Motion of a Shock Wave in a Channel, with Applications to Cylindrical and Spherical Shock Waves," Journal of Fluid Mechanics, Vol. 2, 1957, p. 286.

3.   Dao, S. C., "Geometrical Shock Dynamics," thesis, Master of Science in Aeronautics and Astronautics, University of Washington, 1983.

4.   Whitham, G. B., "A New Approach to Problems of Shock Dynamics," Journal of Fluid Mechanics, Vol. 5., 1952, p. 363.

5.   Kolsky, H., "Stress Waves in Solids," Dover Publications, New York, 1963.

6.   Takayama, K., Esashi, H., and Sanada, N., in Shock Tubes and Waves, New South Wales University Press, 1983, p. 553.

7.   Charko, R. E., "Laser Shock Wave Lithotripsy," thesis, Master of Science in Aeronautics and Astronautics, University of Washington, 1984.

8.   Keilman, G., private communication, International Biomedics, Inc., Mercer Island, Washington.

9.   Cole, R. H., "Underwater Explosions," Princeton University Press, Princeton 1948.
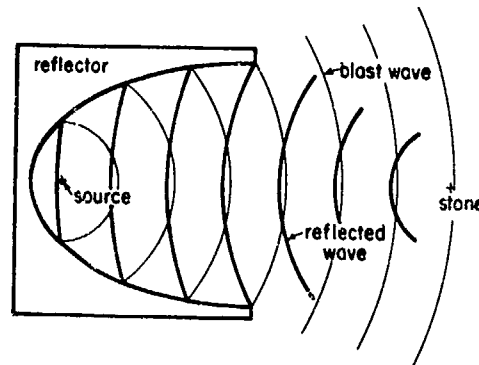
Fig. 1   Schematic of wave motion
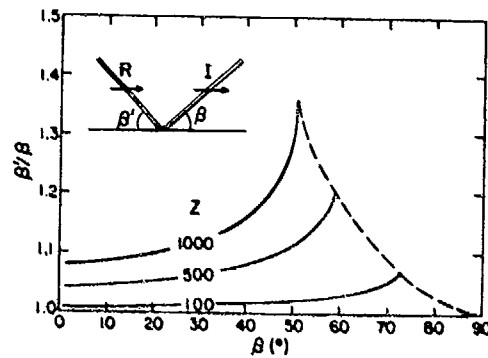
Fig. 2   Oblique shock reflection in water.
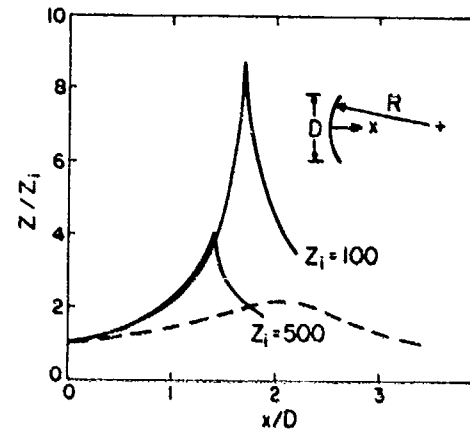
Fig. 3   Centerline amplification of spherical shock segment in water $R/D = 2$.   Solid lines are for uniform Z_i, dashed conical.
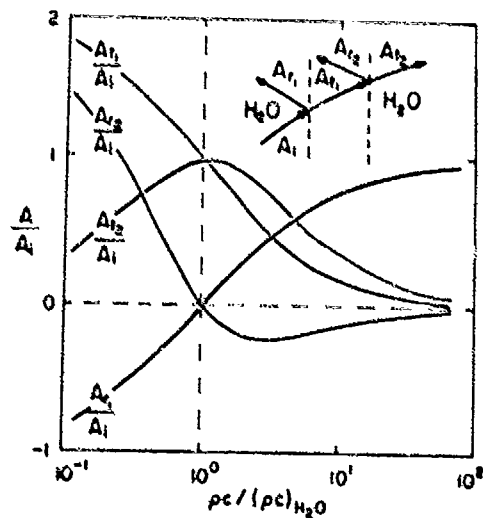
Fig. 4   Wave transmission and reflection from surfaces of 1-D elastic solid in water.
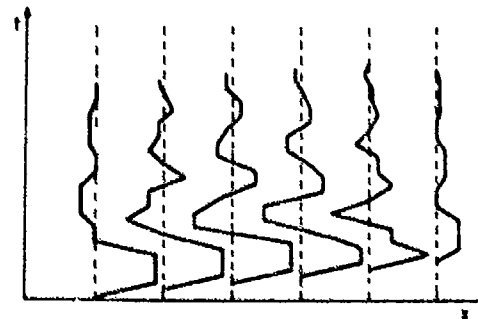
Fig. 5   x-t diagram showing stress distribution in elastic solid. Trapezoidal pulse applied; $\rho c/(\rho c)_{H_2O} = 5$.
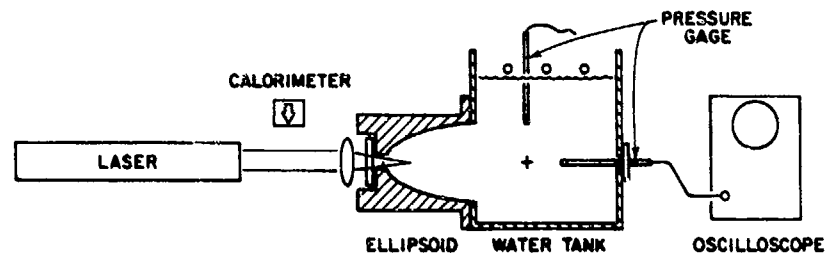
Fig. 6 Experimental setup.
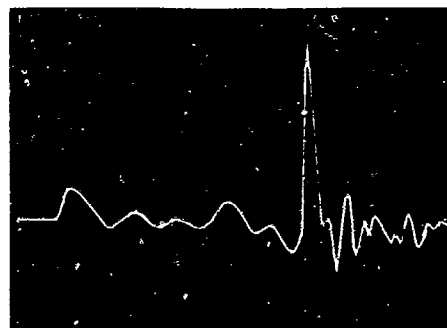
Fig. 7 Pressure trace on reflector at exit. Horizontal scale 5 µsec/div.

$$p = k\left(\frac{E^{0.48}}{r}\right)^{1.17}$$
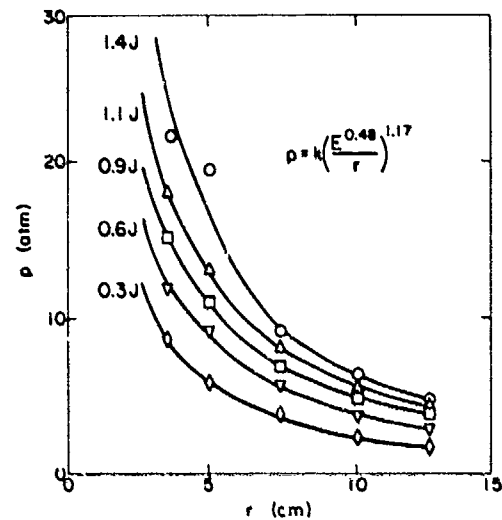
Fig. 8 Peak pressure versus distance from unconfined laser breakdown in water.

○ x = 0 cm
△ x = 5 cm
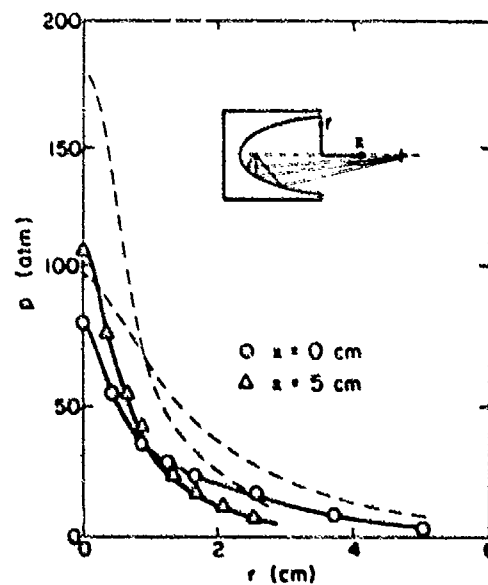
Fig. 9 Peak pressure normal to reflector axis. 0.7J input; dashes are for model
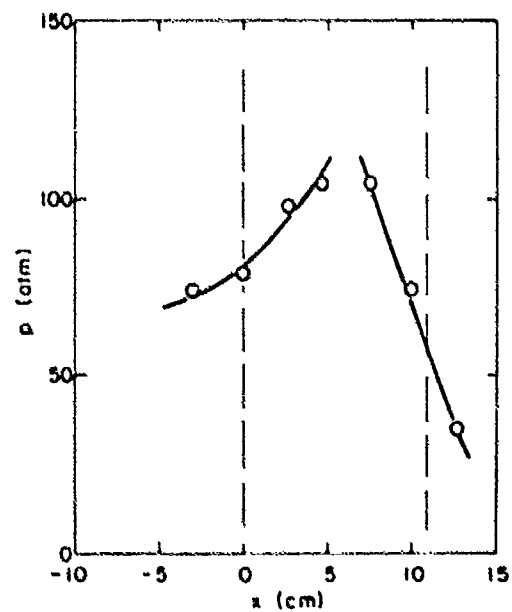
Fig. 10 Peak pressure along reflector axis. 0.7J input.

REALISTIC NUMERICAL SYNTHESES OF SHOCK-EXCITED

MOLECULAR SPECTRA

R.W. Nicholls, M.W.P. Cann and J.B. Shin

Centre for Research in Experimental Space Science
York University, 4700 Keele St.,
North York, Ontario, Canada M3J 1P3

Realistic numerical synthesis of molecular spectra is a
powerful diagnostic research tool. It has been widely
applied to many laboratory, atmospheric, and astrophysic-
al circumstances. Synthetic spectrum programmes for
specific applications, and of great flexibility now
exist. An example is given of spectral synthesis of the
high temperature high pressure O_2 spectrum applicable to
shock wave and combustion situations.

1. INTRODUCTION

For many years spectroscopy has been an important diagnostic tool for the
study of physical conditions of gases in astrophysical, atmospheric and labor-
atory circumstances, including shock wave and combustion phenomena. In princ-
iple intensity measurements on well identified emission and/or absorption spec-
tral features of atomic and molecular species can provide information on
species concentrations (number densities), and on the degree of excitation, be-
cause both emission intensities and relative absorptions are proportional to
species concentrations. Knowledge of relative concentrations of various levels
of excitation allows for the determination of "temperatures" (gas kinetic,
rotational, vibrational, electronic, excitation etc.) which characterize the
gas when local thermodynamic equilibrium conditions exist, as is often the case
in shock wave excitation processes.

In optically thin circumstances direct diagnostic interpretation of
emission or absorption intensities of individual spectral features, or light
fluxes in radiometer pass bands is fairly straightforward. There are however
experimental circumstances for which simple diagnostic methods are not appro-
priate. For example in the transient high pressure, high temperature conditions
which occur in shock waves, the number densities are often sufficiently high
that optically thick conditions occur. The emission spectrum is then controlled,
(see equation 4a below) by the absorption coefficient[1]. The temperature and
collision frequencies are often sufficiently high that Doppler and collision
broadening of spectral features also occur. These effects have a significant in-
fluence on the appearance of a spectrum and on which features lie in radiometer
pass bands. They call for special methods of diagnostic interpretation. While
the widths of non-overlapped broadened lines can be used in some circumstances
for diagnostic purposes, the principal effect of line broadening on the appear-
ance of molecular spectra is partial or total merging of adjacent lines. This
can make unambiguous identification of spectral features difficult.

In such cases it is very useful to be able to compare an experimental
spectrum profile with a realistically calculated synthetic profile, the form of
which is controlled by the relevant input data on the temperature and pressure
in the source. Over the past three decades therefore, numerical spectral syn-
thesis methods of increasing power and flexibility have been developed and used
for diagnostic purposes in astrophysics, atmospheric science and chemical
physics. Synthetic spectra can be used not only for diagnostics but also to aid
the identification and analysis of complex molecular spectra.

2. THE PRINCIPLES OF SPECTRUM SYNTHESIS

Spectrum synthesis is based on the well known equations (1a and 3a) for spectral emission and absorption intensities. The integrated power of an emission spectral feature arising from transitions between an U(pper) and a L(ower) level is:

$$I_{UL} = K \; N_U \; A_{UL} \; E_{UL} \tag{1a}$$

where K is a constant which takes account of units, optical collection geometry and instrumental response, N_U is the species number density in the upper state U, A_{UL} is the Einstein A coefficient or transition probability per particle per second, and E_{UL} is the energy quantum involved.

For diatomic molecular spectra, in equation (1a)

$$E_{UL} = hc/\lambda_{UL} = hc \; \nu_{UL} \tag{1b}$$

$$A_{UL} = (64\pi^4/3hc^3) \; \nu_{UL}^3 \; R_e^2(\bar{r}_{v'v''}) \; q_{v'v''} \; S_{J'J''} \tag{1c}$$

$$N_U = (N/Q) \; \exp(-E_U/kT) \tag{1d}$$

$$\text{where } \nu_{UL} = \nu_{oo} + \Delta G_v + \Delta F_J \tag{1e},$$

is the wavenumber of the spectral feature which is determined by the spectral structure constants in the vibrational (G(v)) and rotational (F(J)) eigenvalues[2]. R_e is the electronic transition moment of the transition, $\bar{r}_{v'v''}$ is the r-centroid and $q_{v'v''}$ is the Franck Condon factor of the band in question and $S_{J'J''}$ is the Hönl-London factor for the band line[3]. Often in shock tube spectroscopy the conditions approach local thermodynamic equilibrium, and the Boltzman equation (1d), (in which Q is the partition function, N is the total number density of the species and E_U is the upper level energy) can be used to predict the species population. If the species of interest are thermally formed by chemical reactions in the shock wave, thermochemical methods have to be used to estimate N and its variation with T.

Equation (1a) can now be written as a function of ν to show how contributions from the profiles of a number of lines contribute to the intensity at wavenumber ν.

$$I(\nu) = K \; \sum_i N_U \; R_e^2(\bar{r}_{v'v''}) \; \nu_{v'J'v''J''}^4 \; q_{v'v''} \; S_{J'J''} \; b(\nu) \tag{2}$$

where $b(\nu)$ is the line profile function, and Σ is the summation over every feature which contributes to the profile at wavenumber ν. Numerical synthesis methods for emission spectra use this equation to calculate $I(\nu)$ at each of a number of closely spaced grid points in ν.

Similarly under optically thin conditions the spectral transmission of an absorbing slab is given by:

$$I/I_o = \exp(-\tau) \tag{3a}$$

where I_o is the incident flux and I is the emergent flux. τ is the optical depth, which when integrated over a spectral feature can be written:

$$\tau = N \; \sigma \; X \tag{3b}$$

where N is the number density of absorbers, σ is the cross section per absorber, and X is the path length. When N_i absorbers of type i contribute to the extinction at wavenumber ν, equation (3b) becomes

$$\tau = X \sum_i N_i \, \sigma_i(\nu) \tag{3c}$$

and $\sigma_i(\nu) = (8\pi^3/3hc) \, \nu \, R_e^{\,2}(\bar{r}_{v'v''}) \, q_{v'v''} \, \Sigma_{v'v''J'J''} \, S_{J'J''} \, b(\nu)$ (3d)

where $b(\nu)$ is the line profile function. Numerical synthesis methods for absorption spectra are based on these equations, and applications to the spectrum of oxygen are described in section 3 below. In the optically thick gases of shock-tube spectroscopy, the absorption cross section $\sigma(\nu)$ controls the emission spectrum through equations (4a,b,c)[1]. Spectrum synthesis of $\sigma(\nu)$ is thus of great importance in emission and absorption applications of shock tube spectroscopy. Equations (4a,b,c) are also used to predict the radiation flux through the passbands of shock tube radiometry[4,5].

$$I(\nu) = B(\nu,T) \, (1- \exp(-k'(\nu,T) \, X)) \tag{4a}$$

where $B(\nu,T)$ is the Planck function, and $k'(\nu)$ is the absorption coefficient with stimulated emission taken into account

$$k'(\nu,T) = k(\nu) \, (1-\exp(-h\nu/kT)) \tag{4b}$$

and $k(\nu) = \sum_i N_i \, \sigma_i(\nu)$ (4c)

In order to use equations (2), (3) and (4) to perform numerical spectrum synthesis it is necessary to:

i) Locate all line centres of the spectral features.

ii) Place a normalized line profile function $b(\nu)$ adjusted for each line appropriate to the physical conditions at each line centre.

iii)Adjust the amplitude of the profile to take account of transition probability and population factors.

iv) Select a closely spaced grid of ν-values, and at each grid point add the contributions from each line whose profile has a significant value at the point.

These procedures result in the high resolution synthetic spectrum which can be plotted. The line profile $b(\nu)$ normally takes account of combined collision (Lorentz) and Doppler (Gaussian) line shapes. A convolution of these is well represented by the Voigt profile for which algorithms exist[6,7]. In order to produce a synthetic spectrum plot for comparison with an experimental profile, the high resolution plot has to be degraded by convolution with an instrumental profile. A triangle function with a suitable half width can often be used for this purpose.

For spectral synthesis the following information is needed.

a) Molecular structure constants from which line centre locations may be accurately determined from equation (ie), or "look-up" tables of line centre locations. Firm molecular data are not always available, particularly for transitions between high quantum number levels, to enable line centres to be located accurately enough for adequate synthesis of high resolution spectra. The important compilation and assessment of molecular structure constants by Huber and Herzberg[8] is invaluable. It reveals cases where insufficient rotational constant information (nearly always derived from spectra excited in low temperature excitation sources, or in absorption) exists for adequate high resolution synthesis of the rotational features of high temperature shock excited spectra.

b) The transition probability constants: electronic transition moment $R_e(r)$, Franck-Condon Factors $q_{v'v''}$ and r-centroids $\bar{r}_{v'v''}$, Hönl-London Factors $S_{J'J''}$. Many measurements of electronic transition moments and band strengths $S_{v'v''} = R_e^{\,2}q$, for numerous band systems have been reported[9] in the literature. Tables of Franck-Condon factors and r-centroids have been published for many band systems. Numerous analytic and numerical molecular potentials have been

used and a number of programmes now exist for routine computation of Franck-Condon factors for realistic potentials (see eg[10]). Simple formulae for SHO Franck-Condon factors exist[11]. Many data on Hönl-London factors exist[12-15]. None of the data in the literature on any of these quantities should be adopted without critical scrutiny.

c) Line profile constants which determine the relative amounts of collision and thermal broadening which should be folded in to the Voigt profile. The constants needed are the half widths of the Lorentz and of the Gaussian effects. They depend on temperature, pressure and molecular structure constants as seen in equations (5a) and (5b).

d) Thermodynamic constants of the materials to allow for calculation of thermally excited populations of species and levels.

The earliest approach to spectrum synthesis was embodied in the concept of Band Models in which a statistical approach is taken to distribution of lines in a band and line profiles[16-19]. Band models are often used to describe intensity profiles of polyatomic molecular spectra.

In the 1960's there was great interest in the absorption and emission spectral properties of high temperature air. A number of laboratories developed synthetic spectrum codes to calculate the low resolution spectral absorption coefficient of heated air from the soft X-ray to IR, over a range of temperatures from 1000 to 200,000°K taking relevant molecular electronic and vibration-rotation, atomic photoionization and free-free transitions into account. The Spectral Absorption Coefficient of Heated Air (SACHA) code developed at the Lockheed Palo Alto laboratories is an example of such a spectral synthesis programme, in which low resolution calculations were made in 0.1ev bins for tabulation, plotting and calculation of Planck and Rosseland mean absorption coefficients[1,20-24].

The Atmospheric Optics laboratory of the AFGL has developed a most useful set of synthetic spectrum programmes for calculation of the spectral transmittance and radiance through the earth's atmosphere. AFGL also developed an important compilation of spectral line parameters; locations, strengths and widths of pertinent absorption lines of atmospheric molecules for use with some of their synthesis programmes. This massive compilation contains 120,000 lines of seven common atmospheric species and some trace species from the red end of the visible to the microwave region of the spectrum[25,26]. The best known of the synthesis programmes is the LOWTRAN series[27] for low spectral resolution calculations (20cm^{-1}). LOWTRAN uses a band model approach and has atmospheric modelling capabilities. For high resolution spectra the FASCOD1 programme is available[28]. It calls on the AFGL atmospheric line data set and speeds up the calculations by employing an approximate spectral line shape, Lorentz, Doppler or Voigt, based on a decomposition algorithm. It also includes atmospheric model features. Various AFGL reports refer to the HITRAN programme, used for precision line by line calculations in small spectral regions. Examples of its operations may be found in the high resolution spectra generated in small spectral regions around laser frequencies[29]. None of these programmes are yet applicable to the synthesis of shock excited spectra.

One of the first truly flexible programmes to calculate the intensity distribution of molecular spectra on a line-by-line basis was developed at the NASA Ames Research Center by Arnold, Whiting and Lyle[30,31]. It treats emission and absorption spectra from electronic transitions from diatomic molecules and some atoms on a line-by-line basis in the spirit of equations (2,3,4) above. It was developed for shock tube applications, specifically to radiometer pass band measurements[32,34]. The capability of this programme has been extended in our laboratories over the past decade and several new programmes have been written. They can be applied not only to shock excited spectra[35] but also to discharge excited spectra[36] astrophysical spectra[37] and to atmospheric transmission studies in the ultraviolet[38,39] infrared[40], and microwave[41] region of the spectrum.

An application of our programme to realistic synthesis of high temper-
ature high pressure O_2 spectra is discussed in the following section.

3. SYNTHESIS OF THE O_2 SPECTRUM BETWEEN 180 AND 300nm

When O_2 is subjected to shock wave or combustion conditions it can exper-
ience transient temperatures of some thousands of degrees and transient pres-
sures of some tens of atmospheres. As an example of a recent spectral synthesis
which has application to shock wave conditions, a review is given here of a
synthesis of the spectral absorption coefficient of oxygen between 180 and
300nm, for temperatures between 300 and 3000°K and pressures from 1 to 50atm.
The absorption coefficient was calculated at high resolution, and, for compari-
son with experiment, was then degraded to instrumental resolutions. The princi-
pal aspects of the work are given below. A more detailed discussion is given in
reference 42.

In the wavelength interval chosen, the O_2 absorption spectrum, which
originates from vibrational levels of the ground $X^3\Sigma$ state, has contributions
from bands and photodissociation continua of the Schumann-Runge ($X^3\Sigma-B^3\Sigma$),
Herzberg I($X^3\Sigma-A^3\Sigma$), Herzberg II($X^3\Sigma-c^1\Sigma$) and Herzberg III($X^3\Sigma-A'^1\Delta$) systems.
In addition, contributions are made to the absorption by a continuum of the
$(O_2)_2$ dimer. The three principal contributors to the absorption are, in order
of decreasing wavelength, from bands (300-250nm) and photodissociation con-
tinuum (250-180nm) of the Herzberg I system, and bands (200-180nm) and the
photodissociation continuum (195-180nm) of the Schumann-Runge system. The wave-
length ranges of these principal contributors are somewhat temperature-
dependent. The contributions from the Herzberg II and III systems are extremely
small. At the higher temperatures considered, account has been taken of absorp-
tion contributions from thermally excited lower vibrational levels up to $v'' =$
about 6. An objective selection procedure for these contributions is discussed
below. Input data used are as follows.

a) Molecular Structure constants: The constants from which line locations
were calculated were available in the literature[39,43].

b) Transition Probability constants: Electronic transition moments were
adopted from a critical review of the literature[39]. Franck-Condon factors (and
Franck-Condon densities for the photodissociation continua) were calculated by
use of the TRAPRB programme of Jarmain and McCallum[10] which first evaluates
Klein Dunham potentials for which vibrational wavefunctions are determined.
Hönl-London factors for effective singlet states were used[2].

c) Line profiles: The Voigt profile $b(v)$ was generated by Whiting's
approximation[6] which is economical in computer use. The profile is specified by
the effective Gaussian and Lorentzian half widths W_G and W_L given by:

$$W_G = 2v(2kT \ln2/mc^2)^{1/2} \text{ cm}^{-1} \qquad (5a)$$

$$W_L = aP(273.2/T)^s \text{ cm}^{-1} \qquad (5b)$$

and their ratio. P is pressure in atmospheres and T is the temperature in
degrees Kelvin. a is 0.3 and s is 0.7. Predissociation broadening was added to
W_L as appropriate.

d) Thermodynamic constants: Total number densities N of O_2 molecules were
interpolated from tables in the American Institute of Physics Handbook[44] for
all 28 pairs of temperature and pressure: T(°K) 3000,600, 1000(500)3000;
P(atm): 1,10,25,50. The relative populations in thermally excited vibrational
levels v'' of the $X^3\Sigma$ state were evaluated from equation (1d).

In making these calculations it is neither practical nor necessary to in-
clude all possible bands of the Schumann-Runge and Herzberg I systems in each
case for their strengths vary over many orders of magnitude. A preliminary
assessment therefore was made of the relative intensities of bands in each of
the v''-const progressions to assess which should be included in the

calculations. Figures 1 and 2 illustrate the results of this assessment for the Schumann-Runge system at temperatures of 300 and 3000°K. They are semi-logarithmic plots of relative band strengths vs wavelength. Bands which fall above the dotted line in each case were used in the calculations.

High resolution O_2 absorption coefficients are first calculated. Typical spectral segments are illustrated in Figures 3 and 4 in the 195 to 200nm range for temperatures of 300 and 3000°K respectively. Figure 4 clearly shows well separated lines of the (1,0), (2,0) and (3,0) bands consistent with the relative intensities of Figure 1. The spectrum of Figure 4 is much richer with interlaced features of many bands consistent with Figure 2. Spectra were calculated at an increment of between 4 and 5×10^{-5}nm with a total number of points between 2.5 and 5×10^{5}. At 300°K 3560 Schumann-Runge and 2297 Herzberg I lines were included. At 3000°K 23,948 and 7790 lines respectively were included. For comparison with typical experimental observations the spectra were degraded numerically by convolution with a triangular instrument function of full width at half maximum of 0.05nm which was stepped across the spectral range in increments of 0.0125nm. Examples of the resulting spectra are shown in Figures 5, 6 and 7 for 300, 1000 and 3000°K respectively. In each case the lower plot is for 1 atm pressure and the upper plot is for 50 atm. pressure. As temperature (and pressure) increase the spectral detail is quickly lost. At lower temperatures the absorption coefficient decreases by many decades with increase in wavelength across the spectral range while at high temperatures the decrease is only a few decades. To compare the results with those of the Lockheed SACHA study[23] the high resolution spectra were first degraded with a triangular instrument function of full width at half height of 1nm which is comparable to the bin width of the SACHA calculations. Figure 8 displays the comparison. The increased absorption predicted here arises from the inclusion of far more Schumann-Runge bands, the Schumann-Runge photodissociation continuum, the Herzberg I bands and the $(O_2)_2$ dimer continuum. Improved molecular constants were also used.

4. SUMMARY

The principles of numerical spectral synthesis have been reviewed and illustrated with reference to the high temperature-high pressure absorption spectra of O_2 in the ultraviolet.

5. ACKNOWLEDGEMENT

REFERENCES

1. Armstrong, B.H. and Nicholls, R.W., "Emission, Absorption and Transfer of Radiation in Heated Atmospheres", Pergamon Press, 1972.
2. Herzberg, G., "Spectra of Diatomic Molecules", Van Nostrand, 1950.
3. Nicholls, R.W., "Electronic Spectra of Diatomic Molecules", Chapter 7, pp325-393, "Electronic Structure of Atoms and Molecules" (ed. H. Eyring, D. Henderson and W. Jost), Academic Press, 1969.
4. Arnold, J.O. and Nicholls, R.W., "A Shock Tube Determination of the Ground State Dissociation Energy and Electronic Transition Moment for the CN Violet and Red Band Systems", pp340-351, Proceedings of the 9th International Shock Tube Symposium, (ed. D. Bershader and W. Griffith) Stanford University Press, 1973.
5. Cooper, D.M. and Nicholls, R.W., "Intensity Measurements of Seven Band Systems of C_2 between 2000A and 12,000A in Shock Waves through $A-C_2-H_2$ at

6000°K", pp696–703, Proceedings of 10'th International Shock Tube Symposium (ed. G. Kamimoto), Kyoto, 1975.

6. Whiting, E.E., "An Empirical Approximation to the Voigt Profile", Journal of Quantitative Spectroscopy and Radiative Transfer, Vol. 8, 1379–1384, 1968.

7. Armstrong, B.H., "Spectrum Line Profiles: The Voigt Function", Journal of Quantitative Spectroscopy and Radiative Transfer, Vol. 7, 61–88, 1967.

8. Huber, K.P. and Herzberg, G., "Constants of Diatomic Molecules", Van Nostrand-Reinhold, 1979.

9. Nicholls, R.W., "Transition Probability Data for Molecules of Astrophysical Interest", Annual Reviews of Astronomy and Astrophysics, Vol. 15, 197–233, 1977.

10. Jarmain, W.R. and McCallum, J.C., "TRAPRB, A Computer Programme for Molecular Transitions", University of Western Ontario, Department of Physics, London, Ontario, 1970 and Jarmain, W.R., "Journal of Quantitative Spectroscopy and Radiative Transfer, Vol. 11, 421–426, 1971.

11. Nicholls, R.W., "Model Studies on the Systematics and Interpolation of Franck-Condon Factor Arrays", Journal of Quantitative Spectroscopy and Radiative Transfer, Vol. 22, 481–492, 1982.

12. Tatum, J.B., "The Interpretation of Intensities of Diatomic Molecular Spectra", Astrophysical Journal Supplement, Vol. 14, 21–55, 1967.

13. Kovacks, I., "Rotational Structure in the Spectrum of Diatomic Molecules", Adam Hilger, 1969.

14. Whiting, E.E. and Nicholls, R.W., "Theory of Rotational Intensities in Diatomic Molecular Spectra", Astrophysical Journal Supplement, Vol. 235, 1–20, 1974.

15. Whiting, E.E., Patterson, J.A., Nicholls, R.W. and Kovacks, I., "Computer Checking of Rotational Line Intensity Factors for Diatomic Transitions", Journal of Molecular Spectroscopy, Vol. 47, 84–98, 1973.

16. Goody, R.M., "Atmospheric Radiation", Oxford, 1964.

17. Penner, S.S., "Quantitative Molecular Spectroscopy and Gas Emissivities", Addison Wesley, 1959.

18. Plass, G.N., "Models for Spectral Band Absorption", Journal of the Optical Society of America, Vol. 48, 690–703, 1958.

19. Kidd, K.G. and King, G.W., "Some Comments on Band Contour Methods", Journal of Molecular Spectroscopy, Vol. 40, 461–472, 1971.

20. Armstrong, B.H., Sokoloff, J., Nicholls, R.W., Holland, D.H. and Meyerott, R.E., "Radiative Properties of High Temperature Air", Journal of Quantitative Spectroscopy and Radiative Transfer, Vol. 1, 143–162, 1961.

21. Churchill, D.P., Hagstrom, S.A. and Landshoff, R.K.M., "The Spectral Absorption Coefficient of Heated Air", Journal of Quantitative Spectroscopy and Radiative Transfer, Vol. 4, 291–321, 1964.

22. Churchill, D.R. and Meyerott, R.E., "Spectral Absorption Coefficient of Heated Air", Journal of Quantitative Spectroscopy and Radiative Transfer, Vol. 5, 69–86, 1965.

23. Landshoff, R.K.M. and Magee, J.L. (Eds.), "Thermal Radiation Phenomena: Vol. 1 Radiative Properties of Air", Plenum 1969.

24. Landshoff, R.K.M. and Magee, J.L. (Eds.), "Thermal Radiation Phenomena: Vol. 2 Excitation and Non-Equilibrium Phenomena in Air", Plenum 1969.

25. Rothman, L.S., Gamache, R.R., Barbe, A., Goldman, A., Gillis, J.R., Brown, L.K., Toth, R.A., Flaud, J.M., Camy-Peret, C., "AFGL Atmospheric Absorption Line Parameters Compilation: 1982 Edition", Applied Optics, Vol. 22, 2247–2236, 1983.

26. Rothman, L.S., Goldman, A., Gillis, J.R., Gamche, R.R., Pickat, H.M., Pynter, R.L., Husson, N. and Chedlin, A., "AFGL Trace Gas Compilation: 1982 Version", Applied Optics, Vol. 22, 1616–1627, 1983.

27. Kneizys, F.X., Shettle, E.P., Gallery, W.O., Chetwynd, Jr. J.H., Abreu, L.W., Selby, J.E.A., Clough, S.A., Fenn, R.W., "Atmospheric Transmittance/Radiance Computer Code LOWTRAN 6" Air Force Geophysics Laboratory, AFGL-TR-83-0187, August 1, 1983.

28. Clough, S.A., Kneizys, F.X., Rothman, L.S., Gallery, W.O.,"Atmospheric Spectral Transmittance and Radiance: FASCOD1B", SPIE, Vol. 277, 152-166, 1981.

29. McClatchey, R.A., D'Agati, A.P., "Atmospheric Transmission of Laser Radiation: Computer Code LASER", Air Force Geophysics Laboratory, AFGL-TR-78-0029, Jan. 31, 1978.

30. Arnold, J.O., Whiting, E.E. and Lyle, G.C., "Line by Line Calculation of Spectra from Diatomic Molecules and Atoms Assuming a Voigt Profile", Journal of Quantitative Spectroscopy and Radiative Transfer, Vol. 9, 775-798, 1969.

31. Whiting, E.E., Arnold, J.O. and Lyle, G.C., "A Computer Program for a Line-by-Line Calculation of Spectra from Diatomic Molecules and Atoms Assuming a Voigt Line Profile", NASA TN D-5088, 1969.

32. Arnold, J.O. and Nicholls, R.W., "A Shock-Tube, Determination of the CN Ground State Dissociation Energy and the CN Violet Electronic Transition Moment", Journal of Quantitative Spectroscopy and Radiative Transfer, Vol. 13, 115-133, 1973.

33. Arnold, J.O. and Nicholls, R.W., "A Shock Tube Determination of the Electronic Transition Moment of the CN Red Band System", Journal of Quantitative Spectroscopy and Radiative Transfer, Vol. 12, 1435-1452, 1972.

34. Cooper, D.M. and Nicholls, R.W.,"Measurement of the Electronic Transition Moments of C_2 Band Systems", Journal of Quantitative Spectroscopy and Radiative Transfer, Vol. 15, 139-150, 1975.

35. Shin, J.R. and Nicholls, R.W., "Intensity Measurements on the ScO Blue-Green System Using Shock-Tube Radiometry", pp140-147, Proceedings of the 11th International Shock Tube Symposium (eds. B. Ahlborn and R. Russell) University of Washington Press, 1978.

36. Danylewych, L.L. and Nicholls, R.W., "Intensity Measurements and Transition Probabilities for Bands of the CN Violet System", Proceedings of the Royal Society of London, Vol. 360A, 557-573, 1978.

37. Danylewych, L.L., Nicholls, R.W., Neff, J.S. and Tatum, J.B., "Absolute Spectrophotometry of Comets 1973XII and 1975IX: Profiles of the Swan Bands", Icarus, Vol. 35, 112-120, 1978.

38. Cann, M.W.P., Nicholls, R.W., Evans, W.F.J. and McEwen, D.J., "Theoretical Simulation of Solar Ultraviolet Fluxes Measured on 8 July 1974 STRATOPROBE I Flights", Atmosphere, Vol. 14, 205-213, 1976.

39. Cann, M.W.P., Nicholls, R.W., Evans, W.F.J., Kohl, J.L., Kurucz, R., Parkinson, W.H. and Reeves, E.M., "High Resolution Atmospheric Transmission Calculations down to 28.7km in the 200-243nm Spectral Range", Applied Optics, Vol. 18, 964-977, 1979.

40. Cann, M.W.P., Nicholls, R.W., Roney, P.L., Blanchard, A. and Findlay, F.D., "Spectral Line Shapes for Carbon Dioxide in the 4.3µm Band", Applied Optics, Vol. 24, 1374-1384, 1985.

41. Cann, M.W.P. and Nicholls, R.W., "Theoretical Computations of the Microwave Transmittance and Emittance in the Earth's Atmosphere: Atmospheric Slant Path Calculations", 11th Quarterly Report pp39 DSS/AES Contract OFS81-00214.

42. Cann, M.W.P., Shin, J.B. and Nicholls, R.W., "Oxygen Absorption in the Spectral Range, 180-300nm for Temperatures to 3000K and Pressures to 50atm", Canadian Journal of Physics, Vol. 62, 1738-1751, 1984.

43. Creek, D.M. and Nicholls, R.W., "A Comprehensive Re-Analysis of the O_2 Schumann-Runge System", Proceedings of the Royal Society of London, Vol. 341A, 517-536, 1975.

44. Gray, D.E. (ed.) American Institute of Physics Handbook, 3rd Edn., McGraw Hill, 1972.
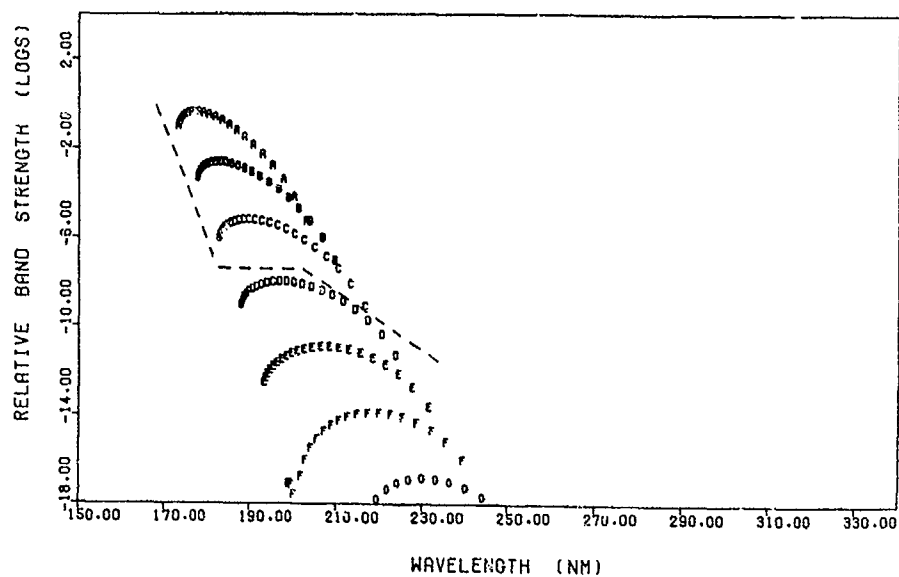
Figure 1.   Schumann-Runge Absorption Band Strengths (300°K) v"=0(A); 1(B); 2(C) etc.   used lie above broken line.
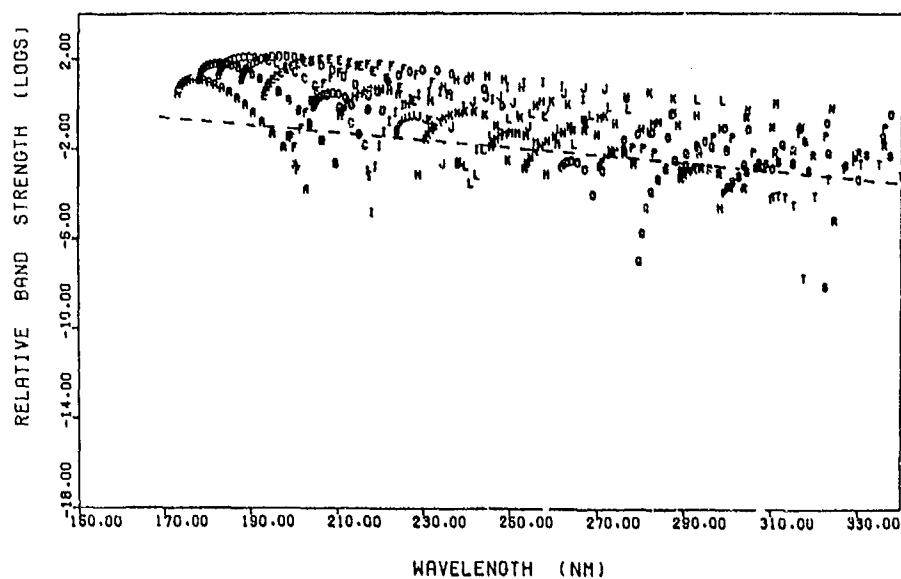
Figure 2.   Schumann-Runge Absorption Band Strengths (3000°K) See caption to Figure 1.
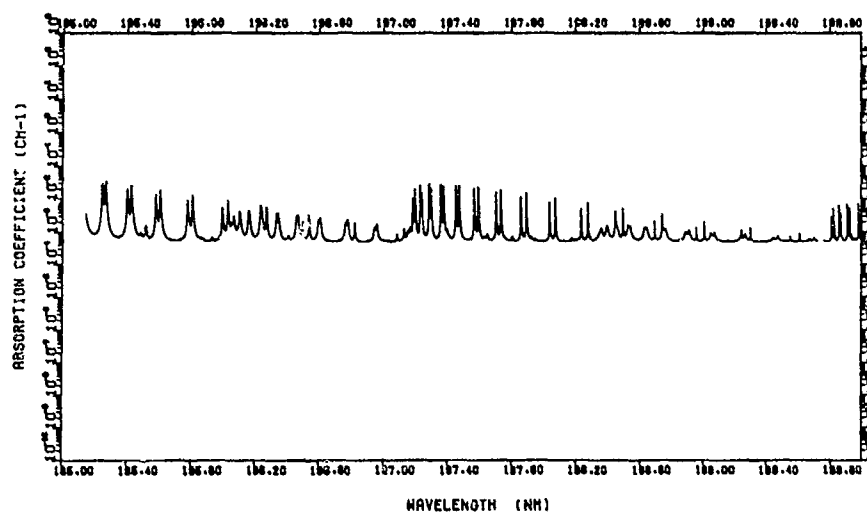
Figure 3. Synthesis of undegraded high resolution 300°K oxygen
absorption coefficient spectrum showing lines of the
(1,0), (2,0) and (3,0) Schumann-Runge Bands.
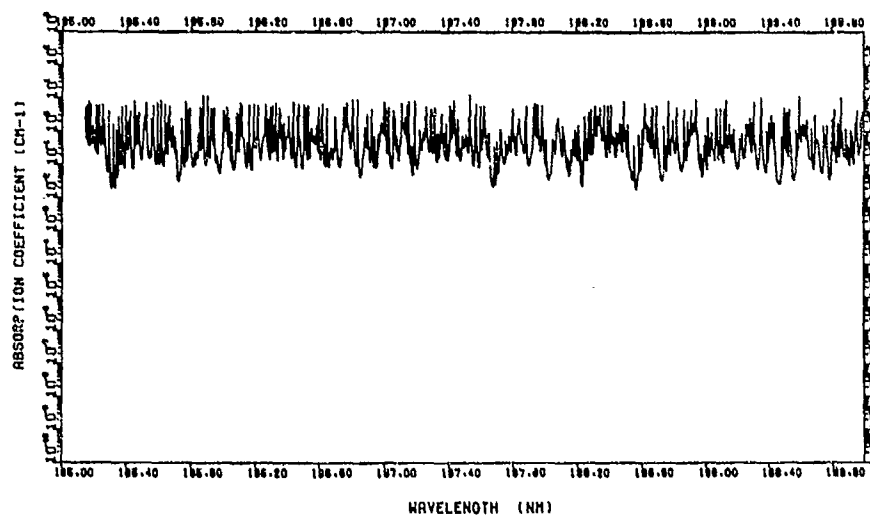
Figure 4. Synthesis of undegraded high resolution 3000°K oxygen
absorption coefficient spectrum.
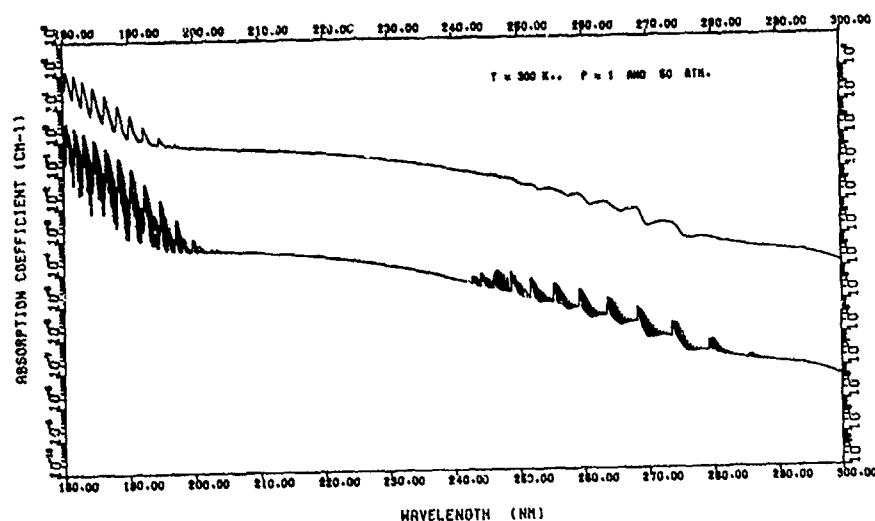
Figure 5. Synthesis of degraded 300°K oxygen absorption coefficient spectrum. Upper curve 50atm; Lower curve 1atm.
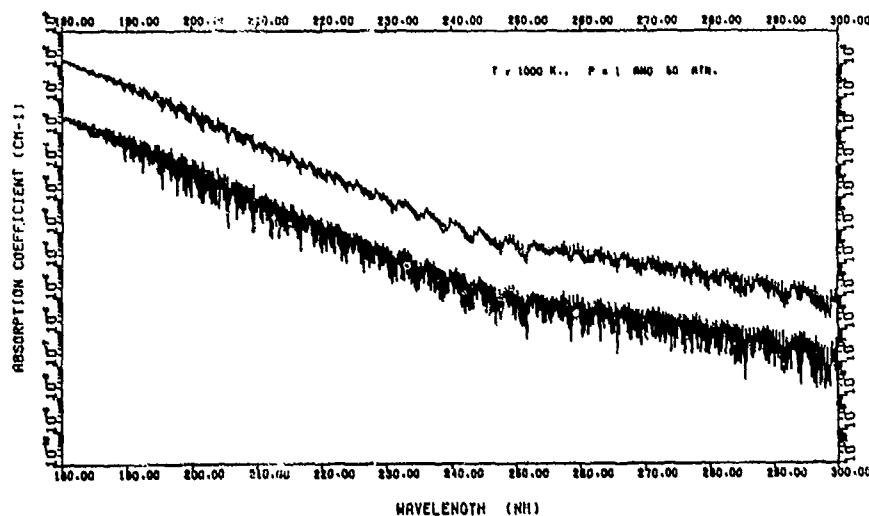
Figure 6. Synthesis of degraded 1000°K oxygen absorption coefficient spectrum. Upper curve 50atm; Lower curve 1atm.
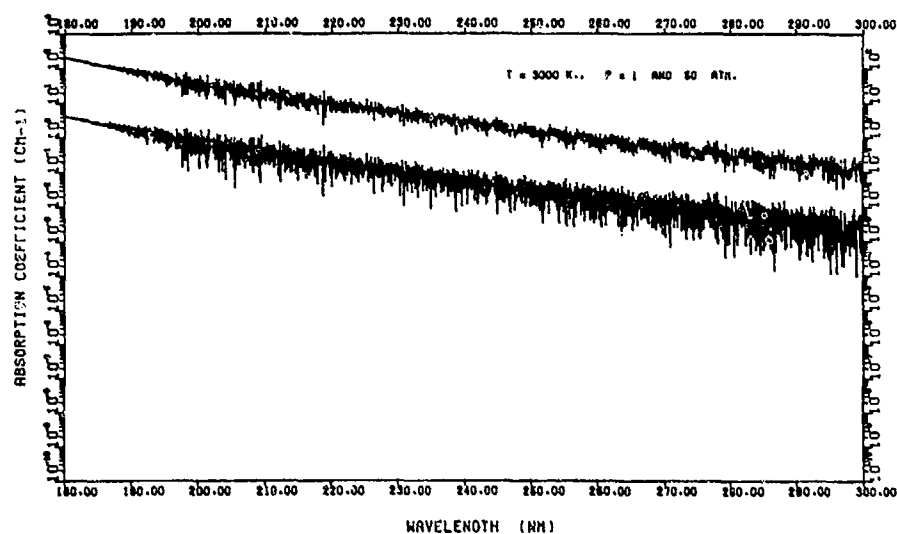
Figure 7. Synthesis of degraded 3000°K oxygen absorption coefficient
spectrum. Upper curve 50 atm. Lower Curve 1 atm.
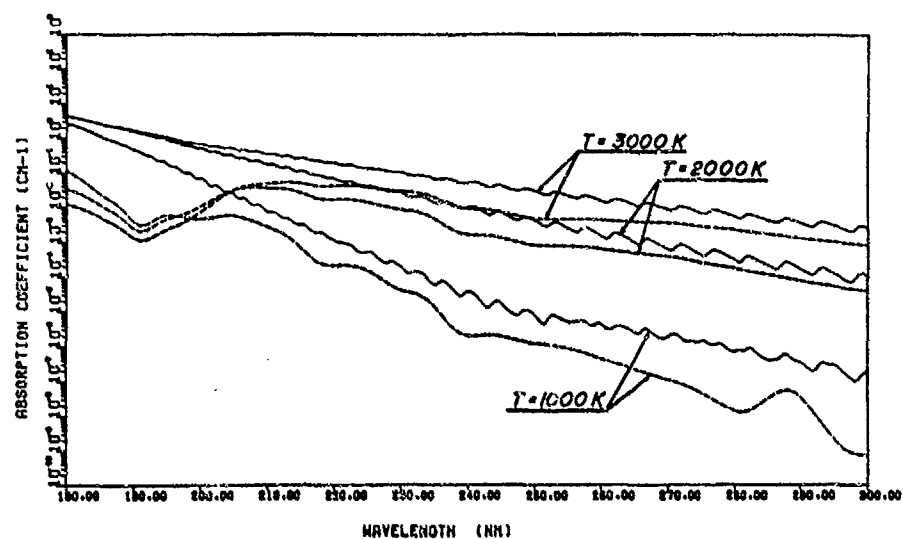
Figure 8. Comparision between the SACHA[23] (dotted), and the present
(full line) calculations of the spectral absorption
coefficient of Heated O_2

AUTO-IGNITION OF HYDROGEN BY A SHOCK-COMPRESSED OXIDIZER[*]

A.Sakurai
Tokyo Denki University,
Saitama, 350-03 Japan

In connection with the developement of diesel type hydrogen fueled engine as one of the problems for the future energy sources, nonsteady aspect of mixing and autoignition of hydrogen jets injected into the air heated by rapid compression are studied. The approach is in two ways. The first one deals with an idealized setup to get understandings of the basic features of the phenomenon, and experiments are performed with use of a conventional shock tube, where pressurized hydrogen gas is released almost instantaneously through a small hole at the endplate of the shock tube into a uniform air of high temperature and pressure produced by the reflection of shock wave at the endplate. The resluts are compared well with the corresponding numerical simulation. The next step is to study some more realistic features appearing in actual engines mostly through the measurement of ignition delay time on unsteady hydrogen jet in various experiments.

1. INTRODUCTION

Hydrogen is generally recognized as one of the most promising as a future fuel among the alternative energy sources which can be substituted for conventional fossile fuels. There have been numerous attempts to apply hydrogen to reciprocating engines, and recently a direct-injection type diesel engine has been recognized to be promising as a hydrogen-fueled engine because injecting hydrogen into the cylinder can prevent backfire and increase volumetric efficiency. It is important in predicting the performance characteristics of these engines to know the mixing process between hydrogen and high temperature oxidizer,and the combustion process from the ignition to flame formation. While extensive theoretical and experimental studies have been performed on the steady jet issued into the isothermal atmosphere, few studies on mixing and combustion processes have been performed. In the present study,attention is focoused on the nonsteady aspects of ignition of hydrogen jet injected into the air heated by rapid compression.

The approach to the subject is in two ways: The first one deals with an idealized setup of injecting a gas from a small hole into a uniform atomosphere to get thorough understandings of the basic features of the phenomenon, while the other studies the effects of actual situation such as non-uniformity of the air.

Two types of shock tubes-conventional and free piston-are utilized for the rapid compression of the air. Hydrogen gas is injected through a perforated end plate of a shock tube into the air compressed by the reflected shock wave or the free piston. Mixing process of the jet with the surrounding air is observed by sequential instantaneous schlieren photographs taken with microflash stroboscope. When the ignition occurs, the luminosity of the ignition kernel can be detected by a photomultiplier. In addition to the above , the pressure and velocity changes with time in the test section is recorded to an independent experiment and utilized for the time-resolved quantitative analysis. The characteristics of the jet flame in the final stage in the ignition process is necessary to be known and is examined by another independent experiment.

A numerical model for hydrogen jets undergoing chemical reaction is developed for the purpose of simulating the ignition process. It is utilized extensively for the first part of the investigation to supply the defficiencies of the information in the complementary of experimental measurements.

2.   INJECTION OF HYDROGEN INTO A UNIFORM AIR

It is reviewed in this section that the experiment and the numerical simulataion of an idealized situation,where pressurized hydrogen gas is released almost instantaneously through a small hole at the endplate of a conventional shock tube into a uniform air of high temperature and pressure produced by the reflection of shock wave at the endplate.

Experiment (Suzuki & Adachi)[1,4,9,10].   Figure 1 shows the experimental setup for conventional shock tube. The driver section is 1.65 m long and the driven section is 6.0 m. The required temperature of the air in a test section is achieved by presetting the pressure ratio.

Fuel gas stored in a chamber is injected through a small nozzle into the driven section by the rupture of the diaphram which separates the fuel chamber from the test section. Several pressure transducers(Kistler 603B) are flush-mounted on the shock tube wall in order to measure shock velocities and to trigger the driver circuit of the power supply of a pulsed-laser which ruptures the diaphram to inject fuel plume. The timing of the injection have to be regulated precisely, and it is set 0.5 ms after the arrival of shock wave at the end plate. The time reguired for fuel to issue from the end plate through a small nozzle is about 0.012 ms after laser beam is emitted for the pressure range measured.

Numerical simulation(Takayama, Taki, Fujiwara, Hayashi and Sakurai [1,2,5]). The equations of a chemically reactive, multi-component, axisymmetric, viscous, and heat conducting gas flow in a quasi-conservation form are utilized and a simplified one-step reaction model of three-body collision along with the reaction rate K [16] is employed as follows:

$$H_2 + \frac{1}{2}O_2 + M \text{--}>H_2O + M + q_r$$
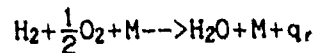
$$k = 8.76 \times 10^{15} T^{-1/4} \exp(-16900/T) \quad cm^{3/2} mole^{-3/2} sec^{-1}$$

where M represents the third body and q_r the exothermicity of the reaction. The chemical species appearing in the model are hydrogen, oxygen, nitrogen and H_2O, which are assumed to be perfect gases. The following expression is used for the mixture viscosity coefficient μ:

$$\mu = C_t \sum_i X_i \mu_i T^{1/2} \quad \text{g/cm/sec}$$

where μ_i is the viscosity coefficient of species i at the temperature T_0 and C_t a constant, representing the effect of turbulence and is assumed 1~30 to the present calculation. The heat conduction and mass diffusion coefficients are obtained assuming Prandtl's and Lewis' numbers as one.

The utilized numerical scheme is the explicit second-order MacCormack method, which is found effective for nonsteady phenomena containing both shock wave propagation and turbulent diffusion. The computer program is coded according to the following procedures: The basic equations are transformed to one-dimensional equations with respect to x(axial) and r(radial) directions using the time-splitting method, and then the transformed equations are discretized by the MacCormack method along with the FCT smoothing technique[14,15,16,18].

The boundary conditions are set in general to simulate the experimental situations, while some of them are changed for the convenience of actual computation. It is assumed that a hydrogen gas having the stagnation pressure 608 KPa and the temperature 300 K flows isentropically through a sonic throat, and spurts out through a hole on the end wall of a shock tube with the pressure 321 KPa, the temperature 250 K and the velocity 1202 m/s at the exit. The air is assumed to consist of nitrogen and oxygen, being initially at rest, of which the pressure p_i is 101 KPa while the temperature T_i is set to one of 300, 1000, and 1400 K.

As an example, the physical properties used in the calculation to the case of initial air temperature T_i = 1400 K are given in Table 1.

Jets.   As a preliminary investigation, the mixing of the oxydizer with fuel gas by using an inert gas in place of a fuel gas is examined.

A typical example of the schlieren photographs of the spurting gas is shown in Figure 2(a).

An advancing shock along with the reflected one can be seen in front of the spurting gas. Figure 3 shows the measured trajectries of propagating shock front and hydrogen jet.

Numerical simulation corresponding to this preliminary case of inert gas is performed under the condition that the air is initially in rest with its pressure and temperature of 101 KPa and 300K, so that no ignition can occure.

As an example of the results the density distributions at the instants of t = 40 and 90 μs are shown in figure 2(b), and compared with the corresponding experimental schlieren photographs.

The positions of the hydrogen jet and shock fronts obtained from the numerical calculation are plotted against various times and compared with those from the experimental measurements in Figure 3.

The propagation characteristics of the front shock wave represented by its pressure-distance relation at the center line as seen in Figure 3 is compared with that of ideal point source blast wave in Figure 4(Sakurai & Takayama [3]), where   is the reduced distance normalized by the factor $W^{1/3}$ with the equivalent energy value W determined for each case from the formula in Ref[17].

It is seen in Figure 4 that a salient feature of the flow field behind the shock can possibly be described by the one given by the point source theory.

The computed velocity and hydrogen density distributions as seen in Figure 5 reveal the structure of the hydrogen jet : The density is high in front and core regions of the hydrogen jet; whereas it is low in the circumferential region, where mixing of hydrogen and air strongly occurs; the velocity in the jet core is high and a vorticity appears in the expanding frontal region.

The pressure and velocity changes with time in the test section is recorded in an independent experiment (Kuniyoshi [19]) and utilized for the time-resolved quantitative analysis. An example of the velocity measurements is shown in Figure 6.

Ignition.   Ignition delay times obtained in the experiments are plotted in Figure 7, where the abscissa is the reciprocal of the oxydizer temperature T_5 behind the reflected shock. The delay time here is seen to be larger than that for the premixed gas, indicating that a certain amount of duration is needed for unsteady mixing before ignition.

The numerical simulation to this later stages of the phenomenon is less accurate in comparison with that for the previous case of initial stages. Nevertheless it can represent a feature of the ignition process, as seen in Figure 8, where the amount of H_2O generated is shown at 0.262 ms for the case of initial air temperature 1000K.

The amount of H_2O produced by the chemical reaction strongly varies depending on the initial air temperature ; for instance , approximately 10^{-5} g/cm^3 of H_2O is produced in the case of T_i = 1400 K, while it is reduced down to only $10^{-10} g/cm^3$ at T_i = 300 K.

The temporal behaviors of the temperature and H_2O density distributions are shown in Figure 9 to the case of T_i = 1400 K. It is seen that the region having a high temperature as well as a high rate of H_2O production advances to the right with the speed of approximately the one for the flame propagation of 3 m/s suggesting the start of ignition followed by the propagation of a flame front. In fact, the ignition delay time t_d = 150 μs for T_5 = 1400 K, determined from the experimental data given in Figure 7, is consistent with the time scale appearing in Figure 9.

3.   EXPERIMENTS ON VARIOUS EFFECTS

Results of experiments to investigate some more realistic features in actual engines are reviewed here.

The effect of the turbulence to the flame is examined by an independent experiment (Yoshida [19]) where a steady hydrogen jet flame surrounded by air flow of laminar or turbulent type is investigated. Typical example of the schlieren photograph of the jet flame is shown in Figure 10.

Piston compression. (Higashino, Shioneri & Sakurai [1,7,8,]). Effects of higher pressures in oxidizer are examined with use of a free piston shock tube. The pressure history is seen to be similar to that experienced in a cylinder of an actual reciprocating engine. Free piston shock tube consists of a steel driver section and a stainless steel driven section. The driver section is 1 m long and has a circular cross section of 70 mm in inner diameter. The driven section is 2 m long and has a circular cross section of 26.7 mm inner diameter. An aluminum test section of 65 mm long and 26 mm inner diameter is set at the end of the driven section to investigate ignition of hydrogen gas injected into it. A solenoidal valve is mounted at the center of the end plate to inject hydrogen gas. Four different sorts of pistons are tested. They are 0.01 kg and 0.022 kg teflon pistons, 0.099 kg duralmine and 0.029 kg steel pistons. Measurements of pressure and the emission of light due to the ignition are made with use of a piezo electric pressure gauge and photomultiplier.

Throughout the experiments, air is used not only as driver but also as driven gas. The ignition delay is defined as the duration required for the photomultiplier to detect a signal of a specific level from the fuel injection. Oxydizer temperature T_5 is calculated from the incident shock velocity measured with a universal counter. Moderately heavy piston is necessary to get a higher stagnation pressure in the test section and the piston of 0.022 Kg is used.

The experiments are carried out in the region near the ignition limit of 900 K, which is known as an autoignition temperature for premixed gas. The ignition of the hydrogen jet is determined by the obserbations in pressure change and self luminescence due to combustion. Typical traces on the synchroscope are shown in Figure 11. The upper and the lower traces show respectively the pressure and the light emission histories with time. The pressure jump and the light emission due to combustion can be observed in Figure 11(a), indicating injected hydrogen being ignited in this case. Whereas, in Figure 11(b), light emission is observed, but there is no jump in the presure, meaning that no steady combustion occurs in this case. Figure 12 shows the ignition delay time t_d , plotted against the reciplocal of the temperature Tm, which is the mean value of the temperature during the period between the instant of the injection and that of the ignition. The initial pressure in the test section in this case is 16 KPa and the 0.099 Kg piston is used. In the figure, the open and the closed circles correspond respectively to the cases of ignition during the compression process and the expansion process. These data expressed by the closed circles are qualitatively reasonable although these are some ten times higher than the usual values for premixed gases. Naturally, the reason of the difference can be attributed to the duration needed for unsteady mixing of hydrogen and air before ignition.

Interaction of jet with shock wave. (Ishii, Higashino, & Sakurai [11, 12, 13, 19]). The interaction phenomena of the jet with the shock wave is investigated in some detail in connection with the problem of the timing of fuel injection. Experiments are made with use of a nondiaphram shock tube at temperatures near ignition temperature limit. Experimental setup is as follows: The low pressure section is 4.5m long, has a square cross section of 40 x 40 mm^2 and has observation windows near the end plate. Hydrogen gas stored in commercial cylinder is injected into the test section through an orifice on the end plate of the shock tube. Injection is controlled by a solenoid valve in the pipe connectiong the gas cylinder to the shock tube. The valve is triggered by an electrical pulse and remained open for 54 ms. The flow rate of the hydrogen through the orifice of the end plate is about 2 cm^3/ms measured at STP. The fuel is injected into the test chamber for 8.5 to 11 ms before the reflection of the incident shock waves at the end plate. The strength of incident shock Mach nemers ranged between 2 and 3. Pressure change behind the incident and the reflected shock wave is measured with pressure tranceducers mounted on the side wall of the chamber. Although a uniform region of temperature and pressure is obtained behind a reflected shock wave in the test section the interaction of the jet with the shock wave can occur depending on the timing of injection. A typical schlieren photograph and a schematic of the interaction between the reflected shock wave and the jet are shown in Figure 13, and the trajectory of the apex A of the bow shock wave determined from successive schlieren photographs are shown in Figure 14. The maximum temerature at A estimated from its trajectory is two times higher than the value in the absence of the jet.

The ignition delay time for various spurting timings of hydrogen jet are determined from the photomultiplier output and plotted against various injection time t_s in Figure 15. The measured ignition delay time is several

times greater than the existing data for premixed gases. It is seen that ignition is controlled by the mixing process between hydrogen and air for higher temperature region. Whereas it is limited by reaction rates for the relatively low temperatures.

SUMMARY

Necessity for studing the nonsteady aspect of ignition of hydrogen jets in connection with R and D of a diesel type hydrogen engine as one of the problems of future energy sources is stressed.

A few different types of shock tubes as well as numerical simulation are utilized to clarify the mixing process between hydrogen and high temperature oxidizer and the ignition phenomena. The ignition delay time determined on various cases is roughly several times greater than the existing data for premixed gases.

REFERENCES

1. Research on Effective Use of Thermal Energy SPEY14,255-262(1985).
2. Takayama,F. and Sakurai,A.,Proc. 15th Conf. Japan Soc. Fluid Mech., 196-200, (1983), (in Japanese).
3. Sakurai,A. and Takayama,F.,J. of Phys. Soc. of Japan, 52, 2963-2964, (1983).
4. Suzuki,T. and Adachi,T., Ann. Rept. Heat Fluid Sci., 1, 203-218, (1983).
5. Sakurai,A. and Takayama,F., Preprint of Autumn Meeting of Japan Phys. Soc., 13a-R-12, (1983), (in Japanese).
6. Ishii,Y., Higashino,F., and Sakurai,A., Pre-print of J.S.M.E. on Heat Eng., 63-64, (1983), (in Japanese).
7. Higashino,F. and Shioneri,T., Preprint of J.S.M.E. Conf., 837-1, 291-294, (1983), (in Japanese).
8. Higashino,F., Shioneri,T., and Sakurai,A., Preprint of 927th J.S.M.E. Conf., 1-4, (1984), (in Japanese).
9. Suzuki,T. and Adachi,T., Res. Rept. of SECOM Sci. Tech. Fund., 55-61, (1984), (in Japanese).
10. Adachi,T. and Suzuki,T., ibid., 62-66, (1983), (in Japanese).
11. Ishii,Y., Higashino,F., and Sakurai,A., Preprint of 927th J.M.E.S. Conf., 1-4, (1984), (in Japanese).
12. Ishii,Y., Higashino,F., and Sakurai,A., Preprint of J.S.M.E. Hitachi Meeting, 1-4, (1983), (in Japanese).
13. Ishii,Y., Higashino,F., and Sakurai,A., Preprint of J.S.M.E. Conf., 843-2, 18-21, (1984), (in Japanese).
14. Boris,J.P. and Book,D.L., J. Computational Phys.,18,p.284-,(1975).
15. Rivard,W.C., Farmer,O.A., and Butler,T.D., Los Alamos Scientific Lab. Rept. La-5812, (1974).
16. Lewis,B. and von Elbe,G., Combustion, Flames and Explosions of Gases,Academic Press,(1961).
17. Jones,D.L., Phys. Fluid, 11 1664-,(1948).
18. Taki,S. and Fujiwara,T., Proc. 18th Symp.(Intern) on Combustion, 1617-, (1981).
19. Sakurai,A., Annual Report of Research on Effective Use of Thermal Energy p.88(1982); p.121(1983); p.70(1984).

Table 1.   Physical Properties
(Initial Air Temperature T_i = 1400 K)

Species	c_{pi} erg/g/K	μ_i g/cm/sec/$K^{1/2}$
N_2	1.23×10^7 (1400K)	1.06×10^{-5}
O_2	1.14×10^7 (1400K)	1.33×10^{-5}
H_2	1.60×10^8 (1400K)	1.33×10^{-5}
H_2O	3.09×10^7 (3000K)	6.47×10^{-6}
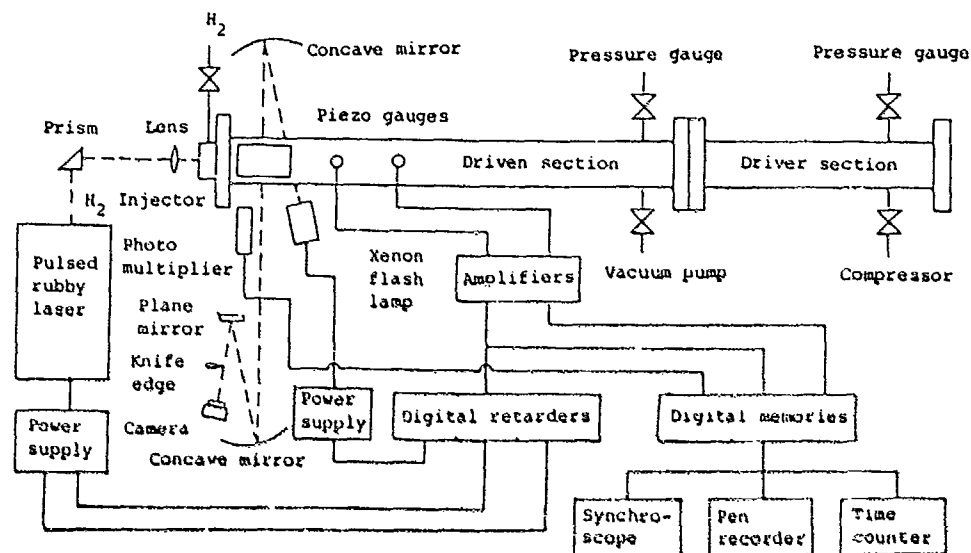
Fig.1 Schematic diagram of experimental apparatus of shock compression.

(b)   (a)
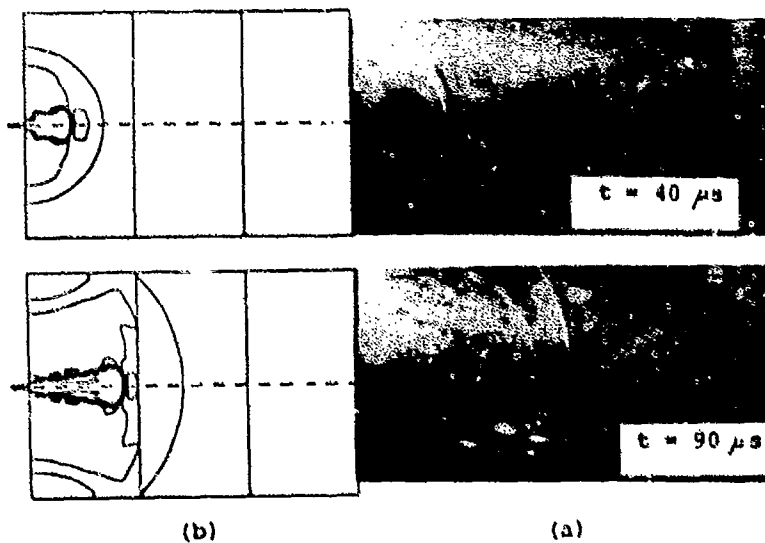
Fig.2. Density distributions obtained by schlieren photographs of the
experiment (a) and numerical simulation (b) at t=40 and 90 μs,
where the initial air temperature T_i = 300 K.
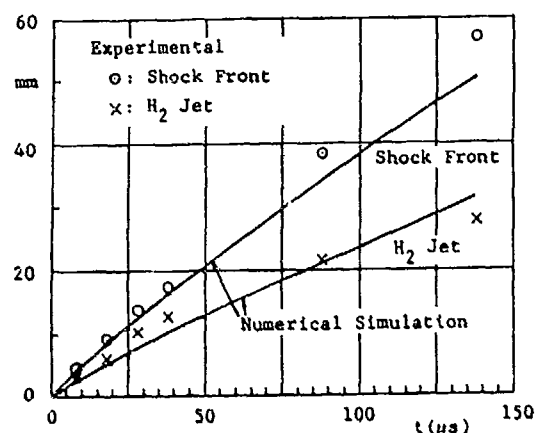
Fig.3.

Comparison of the positions of the hydrogen jet and the shock front versus time for the experimental results and the numerical ones.

Fig.4.

Experimental and numerical shock pressure-distance curves compared with that of ideal point source blast wave: O,x numerical --- experimental.
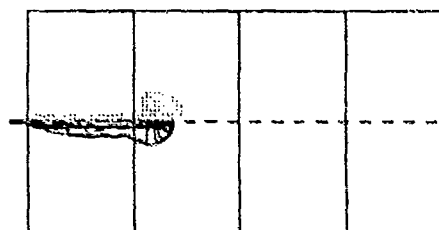
Fig.5.

Velocity and hydrogen density distributions for T_i=300K at t=143 μs in upper and lower half parts, respectively.   Dark region in the figure represents high density, and Δ is the contour interval.

Fig.6.

Velocity change with time measured on the central axis of jet at 3 mm from the center.
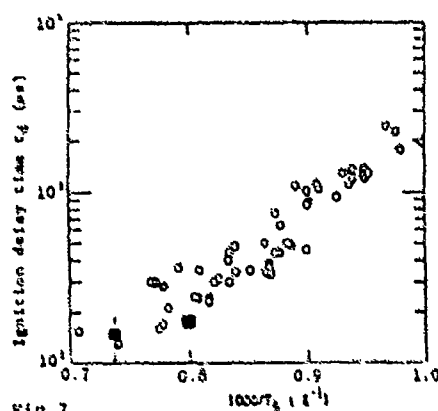
Fig.7.

Ignition delay time in a uniform temperature oxydizer. O and ■ denote the experimental and numerical results, respectively. T_d is the temperature behind a reflected shock wave.
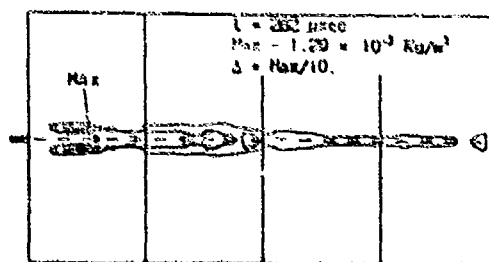
Fig.8.

H_2O distribution at 262 μs for initial air temperature 1000K. Δ denotes contour interval.

Temperature H_2O density

t = 80 μs

t = 140 μs
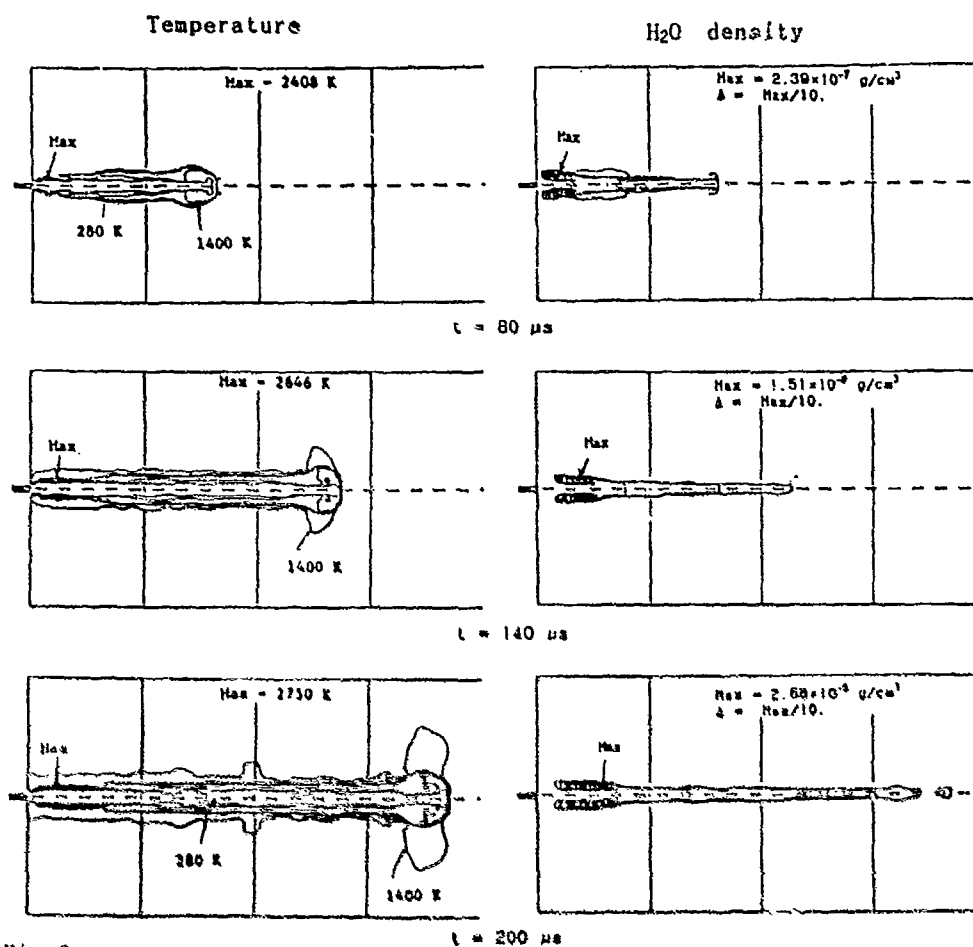
t = 200 μs

Fig.9.

Temperature and H_2O density distributions for T_i=1400K at t=80, 140 and 200 μs.
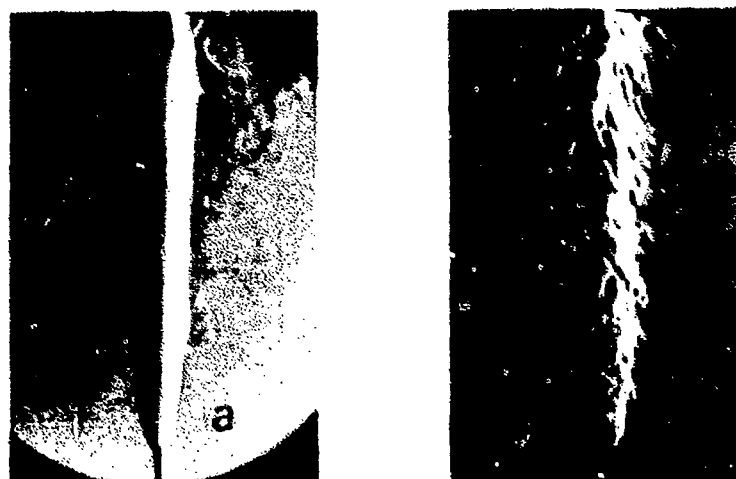
Fig.10. Typical schlieren photographs of steady hydrogen jet (a) laminar air flow, (b) turbulent air flow.
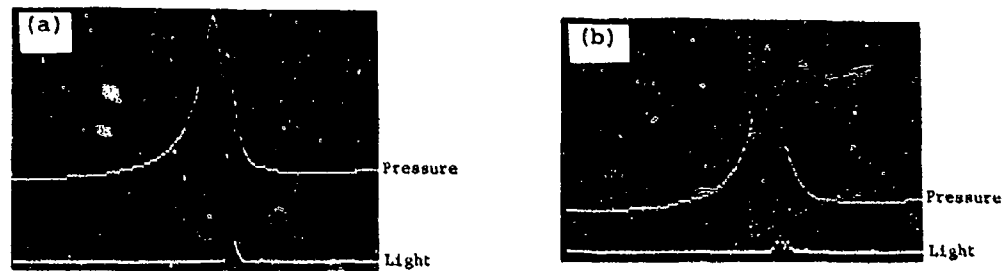
Fig.11. Pressure and light emission in the test section
(a) Ignited case   (b) Non-ignited
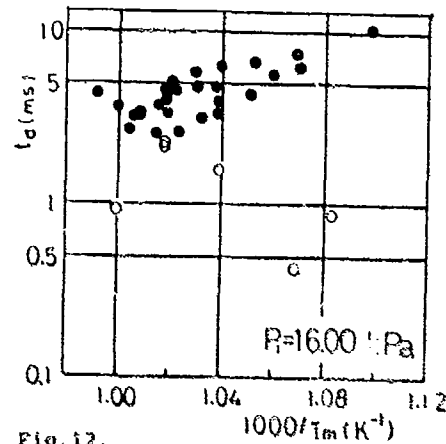
Fig.12.

Ignition delay time, t_d , versus
mean temperature, T_m in the test
test section.   0.099kg piston is used.
P_1 = 16 kPa.

(Higashino & Ishii)

Fig.11. Interaction of shock wave with jet.
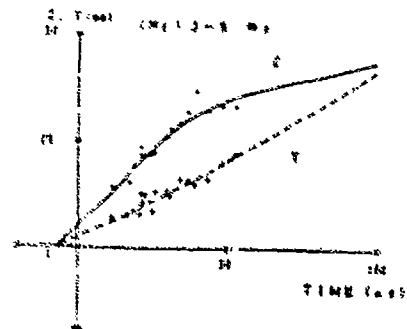
Fig.14.

Trajectries of reflected and bow
shock waves.

Fig.15.

Relation between ignition delay time
observed behind reflected shock wave &
hydrogen injection time t_s.
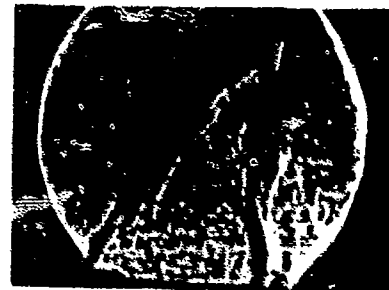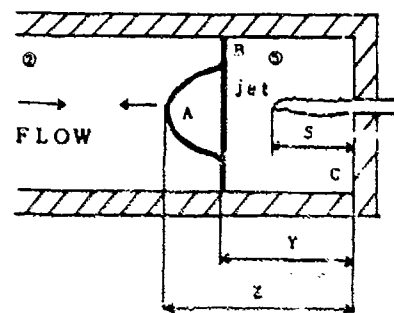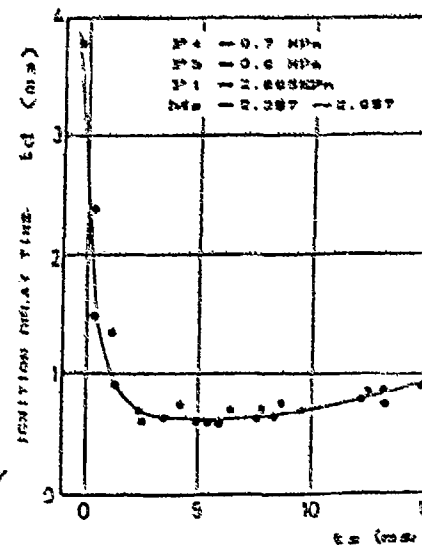
SHOCK WAVES IN HELIUM AT LOW TEMPERATURES

H. W. Liepmann and J. R. Torczynski

Graduate Aeronautical Laboratories
California Institute of Technology
Pasadena, CA 91125

Shock waves are a powerful probe of the physics, thermodynamics, and fluid mechanics of helium, particularly at low temperatures and moderate pressures. Gasdynamic shocks in helium vapor have attained Mach numbers around 40 with minimal side wall influence. When such shocks are incident upon the vapor-superfluid interface, measurements of reflected and transmitted wave strengths may be used to study the boundary conditions across the evaporating interface (not all are known). Transmitted pressure shock waves in the superfluid may cross phase boundaries, producing the (normal) liquid or solid phases. Temperature shock waves exist in the superfluid and are easily produced and observed, exhibiting some features similar to shocks in a fluid near its critical point. The relative velocities produced by strong temperature shocks (around 10 m/sec) are orders of magnitude larger than those in steady channel counterflow, so that these shock experiments shed new light on the mechanism that ultimately limits the counterflow. Moreover, since the relative velocity is both a dynamic and a thermodynamic variable of the superfluid, the chemical potential equation of state may be measured in previously inaccessible thermodynamic regions. Such shocks also provide a means of producing metastable liquid by crossing the vapor-superfluid coexistence curve without cavitation. Finally, the evaporating interface boundary conditions may be studied by schlieren photography of temperature shock waves impinging on the vapor-liquid interface from below.

1. INTRODUCTION

Several interesting features are apparent in the thermodynamics of helium at low temperatures and moderate pressures (see Figure 1.1). In common with other substances, He^4 has a liquid-vapor coexistence curve terminating in a critical point, with $T_c \approx 5.2$ K and $p_c \approx 2.3$ atm. However, unique to helium is the fact that the low-temperature/low-pressure condensed phase is not a solid. Rather, He^4 has two liquid phases, denoted He I, the higher temperature and rather ordinary liquid phase, and He II, the lower temperature superfluid phase. The coexistence curve around 2.2 K that separates these regions is called the $\lambda-line$, referring to the logarithmic shape of the specific heat anomaly, much like those occurring in some solid state phase transitions. Note that helium does not solidify under its own vapor pressure, a result of its large quantum mechanical uncertainty energy. Instead, pressures exceeding 25 atm are required to form the solid phase. Moreover, below 0.8 K the slope of the solid-liquid coexistence curve is slightly negative, so the *superfluid* phase has the lower entropy.

Shock waves may be produced in any of these thermodynamic regions although of principal interest here are the vapor and superfluid phases. Even at low temperatures, helium vapor is well characterized as an ideal gas, with $\gamma = 5/3$, away from the critical point. As such, it admits the standard gasdynamic shock waves. Superfluid helium, on the other hand, has *two* modes of wave propagation in the bulk fluid, as predicted by the *two-fluid model*.[1-4] which is discussed below. Like other liquids, superfluid helium admits pressure waves, referred to as *first sound*. However, in He II heat transport takes place by an internal convection process involving the relative motion of the two fluids, called *counterflow*. Just as first sound is associated with the mass flux and the pressure, the heat flux and the temperature give rise to another type of wave, called *second sound*. Large amplitude waves of either type steepen to form shocks, as noted by many investigators.[5-15]

2. GASDYNAMIC SHOCK WAVES

Shown in Figure 2.1 is a schematic diagram of the cryogenic shock tube.[7] Two features distinguish this shock tube from most others. First, the diaphragm consists of mylar wound between two spindles. This spool mechanism permits changing the diaphragm (up to 70 times) without opening the shock tube interior to the atmosphere, making operation of the cryogenic shock tube both economical and practical. More important, however, is the fact that the driven section of this shock tube is at a very low temperature although the driver section is at room temperature.

The advantages of a cryogenic driven section are seen from ideal shock tube theory. The "shock tube equation" is given by

$$\frac{p_4}{p_1} = \left[1 + 2\gamma_1(\gamma_1 + 1)^{-1}(M_s^2 - 1) \right]\left[1 - \frac{\gamma_4 - 1}{\gamma_1 + 1}\frac{a_1}{a_4}\frac{M_s^2 - 1}{M_s} \right]^{-2\gamma_4/(\gamma_4 - 1)} , \tag{2.1}$$

where regions 4 and 1 refer to the driver and driven sections, respectively, and $a_i^2 = \gamma_i R_i T_i$ gives the sound speed. As $\rho_4/p_1 \to \infty$, this equation has as its limit

$$M_s = \frac{1}{2}\frac{\gamma_1 + 1}{\gamma_4 - 1}\frac{a_4}{a_1} + \left[\left(\frac{1}{2}\frac{\gamma_1 + 1}{\gamma_4 - 1}\frac{a_4}{a_1} \right)^2 + 1 \right]^{1/2}. \tag{2.2}$$

For helium with $\gamma = 5/3$, this equation simplifies to

$$M_s = 2\left(\frac{T_4}{T_1} \right)^{1/2} + 2\left(\frac{T_4}{T_1} + \frac{1}{4} \right)^{1/2} \approx 4\left(\frac{T_4}{T_1} \right)^{1/2}. \tag{2.3}$$

Thus, with $T_4 \sim 300$ K and $T_1 \sim 3$ K, shock Mach numbers around 40 are not unreasonable.

As T_1 is decreased, the predictions of ideal-gas/ideal-shock-tube theory are more and more closely followed, as shown in Figure 2.2. This is because boundary layer effects at the side walls are minimized due to the reduced viscosity at low temperatures. Moreover, real gas effects such as radiation and ionization are unimportant for even the strongest of shocks. The gas temperature behind the shock is bounded by $T_2 \leqslant 2.5 T_4$, which is small when compared with temperatures corresponding to the above phenomena.

There are many areas of possible application[7] open to the cryogenic shock tube. One use in the study of superfluid helium involves reflecting gasdynamic shocks from the vapor-superfluid interface. Such an event,[8] shown in Figures 2.3-4, is of interest because one of the boundary conditions holding across the steadily evaporating interface is unknown — the reflected and transmitted wave strengths *cannot be calculated* without making an assumption about the unknown boundary condition. Thus, the problem can in principle be inverted by making shock strength measurements. As a postscript, if this type of a transmission-reflection experiment had been performed prior to the two-fluid ideas (it easily could have been), then the consequent unexpected *experimental* discovery of second sound would have pointed out the insufficiency of "one-fluid" dynamics to describe superfluid helium!

3. SHOCK WAVES IN SUPERFLUID HELIUM

3.1. The Two-Fluid Model

As mentioned above, when the temperature is lowered below 2.2 K, liquid helium undergoes a phase transition somewhat similar to Bose condensation. He II is often referred to as a *quantum fluid* since quantum mechanics is macroscopically important in its description. This can be seen by considering the ratio Q of the deBroglie wavelength Λ, the length scale of "quantum" effects, to the interatomic spacing d for molecules of mass m.

$$Q = \frac{\Lambda}{d} = \frac{\hbar}{d(mkT)^{1/2}} \tag{3.1}$$

For most liquids, m and T are both large, and d is typically at least a few Angstroms. Thus, Q is small. For helium at 2 K, Q is of order unity, so each atom interacts quantum mechanically with its neighbors.

The importance of quantum mechanics for He II is manifested in the need for the two-fluid model, which describes He II as being a mixture of two fluids, the *normal* and *super* components, having densities

ρ_n and ρ_s and velocities $\vec{v}_n$ and $\vec{v}_s$, respectively.[1-2] The total mass density of a fluid element is given by $\rho = \rho_n + \rho_s$, and its velocity is just the center of mass (CM) velocity $\rho\vec{v} = \rho_n\vec{v}_n + \rho_s\vec{v}_s$. Instead of ρ_n, ρ_s, $\vec{v}_n$, and $\vec{v}_s$, it is often more convenient to use ρ, ξ, $\vec{v}$, and $\vec{w}$, where $\xi = \rho_n/\rho$ is the normal mass fraction and $\vec{w} = \vec{v}_n - \vec{v}_s$ is the relative velocity. Note that $\vec{w}$ is a Galilean invariant. Also, w^2 is the thermo-dynamic variable that is canonically conjugate to ξ. The chemical potential is thus a function of *three* variables, $\mu = \mu(p,T,w^2)$ where $d\mu = \rho^{-1}dp - sdT - \frac{1}{2}\xi dw^2$. The equations of motion are the conservation equations for mass, momentum, and energy. However, since there are extra variables, there are additional equations constraining the motion. The superfluid equation states that elements of the super component are accelerated by gradients in the chemical potential. Also, $\vec{v}_s$ is constrained to be irrotational away from singularities (line vortices), with circulation quantized in multiples of h/m. See Landau and Lifshitz[1] or London[2] for full (and unsurpassed) accounts of the two-fluid model and Feynman[3] for a discussion of circulation quantization.

Since there are two components, two densities, two velocities, and so forth, there are two "sounds" or modes of wave propagation in the bulk fluid. *First sound* is a pressure-density-velocity wave, just ordinary sound. It is a useful and accurate approximation to assume that the coefficient of thermal expansion vanishes, so that ρ is independent of T and s is independent of p. Hence, perturbations in the temperature and relative velocity are virtually nil, so the two components move as one. The acoustic speed of first sound is then given by the familiar formula

$$a_1^2 = \left.\left(\frac{\partial p}{\partial \rho}\right)\right|_s,$$
(3.2)

with typical values around 230 m/sec. *Second sound* is just the reverse, involving temperature, entropy, and relative velocity. Perturbations in the pressure and CM velocity are very small for the reason given above, so there is no mass flux (the two components move oppositely) although there is a *heat* flux $\vec{q} = \rho_s sT\vec{w}$. The acoustic speed of second sound is

$$a_2^2 = \frac{\rho_s s^2 T}{\rho_n c_p},$$
(3.3)

which is typically around 20 m/sec although it vanishes at the λ-line.

3.2. Pressure Shock Waves

As demonstrated in Figure 2.3, pressure shock waves can be produced in superfluid helium. Weak first sound shocks are well described by the relations given by Khalatnikov.[4]

$$M = 1 + \frac{1}{2}A\frac{\Delta p}{\rho a_1^2}$$
(3.4)

$$A = \rho a_1^2 \left.\left(\frac{\partial}{\partial p}\right)\right|_s \ln(\rho a_1)$$
(3.5)

A, the steepening coefficient of first sound, is always positive, so only compression first sound shocks exist in superfluid helium.

Figure 3.1 shows phase diagram trajectories of a few shocks, produced as described in § 2. Note that the transmitted pressure shock starting from $T_o = 2.095$ K crosses the λ-line (state 6), so the λ-transition occurs within the shock front.[a] An $x-t$ diagram of this case verifies this fact — no transmitted temperature shock is produced. For two other cases, $T_o = 1.989$ K and 2.031 K, after the transmitted shock reflects from the shock tube end wall, it crosses the λ-line (state 7). When it intersects the transmitted temperature shock, the latter disappears since second sound does not exist in He I.

Phase changes to the solid are in principle possible but have not as yet been attempted. Heating of the fluid by pressure shocks is not a problem since these shocks are nearly isothermal (the very small temperature jump is actually *negative*). The most promising method of producing sufficiently strong shocks would probably employ a shock tube with an area variation rather than one with a higher performance driver (higher pressure, heated, and/or hydrogen).

3.3. Temperature Shock Waves

As mentioned above, in superfluid helium the relative velocity $\vec{w}$ forms a third thermodynamic variable along with the pressure p and the temperature T. It is impossible to produce large relative velocities with steady channel counterflow: wall effects restrict values of w to around 1 cm/sec for a tube of reasonable size. Temperature, or second sound, shock waves generate very large relative velocities and thus open new thermodynamic regions to exploration.

Generation of second sound shock waves is straightforward. Just as a mass flux is necessary for an ordinary shock, a heat flux is needed for a second sound shock: the heat flux is associated with the relative velocity ($q = \rho_s sTw$), just as the mass flux is associated with the CM velocity ($J = \rho v$). A "thermal piston" or heater is made by passing current through a thin film nichrome resistor (Joule heating), which has been vacuum-deposited on one of the shock tube end walls, an optically flat quartz substrate. Temperature waves are detected using superconducting thin films, typically located at the opposite end wall. These superconducting sensors are operated at the midpoint of the superconducting transition (see Figure 3.2) so that a small temperature perturbation gives rise to a large resistance perturbation. A biasing electromagnet placed behind the sensor allows the transition temperature to be shifted to the desired experimental temperature. These sensors operate in the MHz range, with typical sensitivities of 1 V/K. [They can be more sensitive — Roesgen[16] attained values around 1 kV/K.] Figure 3.3 shows an oscillograph from such a sensor of an initially rectangular temperature profile that has evolved into a shock front, a uniform region, and an expansion fan.

Nonlinear second sound was first observed by Osborne[5] and Dessler and Fairbank.[6] Weak second sound shock waves are predicted to obey the following equations of Khalatnikov.[4]

$$M = 1 + \frac{1}{2}B\frac{\Delta T}{T} \tag{3.6}$$

$$B = T\left[\frac{\partial}{\partial T}\right]_p \ln\left[\frac{a_2^3 c_p}{T}\right] \tag{3.7}$$

$$\frac{\Delta w}{a_2} = \frac{\rho c_p}{\rho_s s}\frac{\Delta T}{T} \tag{3.8}$$

A graph of B, the steepening coefficient of second sound, is shown in Figure 3.4. Away from the λ-line, B is positive, so second sound shocks in this region are temperature-raising. As the λ-line is neared, however, B becomes negative and large, so here the shocks are temperature-lowering. In this latter case, the shocks are akin to rarefaction shocks, commonly seen in fluids near their critical points. One can imagine an initially rectangular temperature pulse spanning the region from B positive to B negative. In this case shock waves form at both the leading and the trailing edges of the pulse. The resulting *double-shock* pulses[9,14] (see Figures 3.5-6) are a subtle and striking verification of the nonlinear two-fluid model using shock waves.

Turner examined the predictions of Khalatnikov for weak second sound shocks. At low heater powers he found that an initially rectangular finite amplitude temperature profile underwent the expected nonlinear evolution, as in Figure 3.3. Moreover, temperature jump and arrival time (Mach number) data was in quantitative agreement with Eqs. (3.6-7). For larger heater powers, Turner observed systematic deviations (see Figure 3.7), as well as modification of the temperature profile (see Figure 3.8). He found a bound on the relative velocity produced with second sound shocks, the so-called *shock limit*, shown in Figure 3.9.

$$w_{max} \propto \frac{\rho_s \kappa^3}{k_B T} \tag{3.9}$$

Here $\kappa = h/m$ is the quantum of circulation[3] of thermally nucleated quantized vortex rings.[10,11]

Torczynski confirmed the role of quantized vorticity generation in causing the shock limit.[15] Moreover, he demonstrated that this limiting phenomenon occurred only as the shock entered the fluid at the heater — a shock once produced could be arbitrarily and harmlessly strengthened away from the heater by using a shock tube with a converging conical channel[13] (see Figure 3.10). Indeed, no limitation on w away from the heater was found, even with an area change of 3:1. The strongest shocks produced in this way had temperature jumps of 87 mK and relative velocities exceeding 10 m/sec (at the small end of the channel),

based on the numerical results of Moody and Sturtevant.[12] These relative velocities are orders of magnitude larger than the observed steady counterflow values and are respectable when compared to $a_2 \approx 20$ m/sec and $v_L \approx 58$ m/sec (the Landau[1] criterion — a minimum velocity for momentum exchange between the *super* component and the wall it flows past).

The large relative velocities that can be set up with second sound shock waves strengthened away from the heater open the way to measure the relative velocity dependence of the chemical potential equation of state (recall § 3.1). The dependence of μ on p and T with $w = 0$ is well known from Maynard's data.[17] However, for large w, the functional form of $\mu = \mu(p,T,w^2)$ is not known. The approximation most often used is to set

$$\mu(p,T,w^2) = \mu(p,T,0) - \tfrac{1}{2}\xi(p,T,0)w^2 , \tag{3.10}$$

essentially keeping only the first term in a Taylor series expansion of the differential relation in § 3.1 (for example, Moody and Sturtevant[12]). The lack of an exact equation of state when w is large hinders precise numerical prediction of the state change produced by a shock wave. However, this problem may be inverted: the exact equation of state may in principle be determined by numerical analysis of Mach number and temperature jump data from second sound shocks of varying strengths and initial states.

Associated with a second sound shock wave are jumps in all thermodynamic quantities, not just the temperature. The pressure jump across a second sound shock is small and *negative*.

$$\Delta p \approx -\rho c_p T (\Delta T/T)^2 \tag{3.11}$$

This raises the possibility of using second sound shock waves to produce a phase change, but not by crossing the phase boundary usually considered, the λ-line. Since the pressure jump is negative, it is possible to cross the vapor-superfluid coexistence curve by a *decrease of pressure*. Table 3.1 shows a comparison of the pressure jumps of the strongest converging shocks and other relevant pressures.[13]

Table 3.1. Pressure jumps across strong second sound shocks.

T_o	p(SVP)	Δp(hydro)	p_o	Δp(Khal.)	Δp(Moody)
1.605	5.83	2.00	7.83	-4.65	-10.05
1.571	5.00	2.00	7.00	-4.96	-11.61
1.463	3.00	2.00	5.00	-5.55	-14.71

The Khalatnikov and Moody predictions are contrasted. The initial pressure for these experiments is about 2 Torr higher than the saturated vapor pressure because of the hydrostatic head, as indicated. In all cases, the coexistence curve is crossed, apparently without cavitation. Furthermore, the more exact numerical solutions of Moody suggest that tensile stress was put on the liquid. It is possible that this effect may be exploited to study a metastable liquid.

Second sound shock waves are also good probes of the evaporating vapor-superfluid interface. As stated above, not all of the boundary conditions across a steadily evaporating interface are known. This can be understood since there are extra dynamic and thermodynamic variables for He II which have no analog for the vapor. Thus, when a second sound shock of known strength impinges on the interface with a given angle of incidence, the strengths and angles of the transmitted and reflected shock waves *cannot be calculated*. Measurement of these wave strengths and angles provides a way to evaluate hypothetical boundary conditions. Figure 3.11 shows a schlieren photograph of a second sound shock wave reflecting from the vapor-superfluid interface.[14] A remnant of the incident second sound shock is barely visible where the reflected shock (the fine dark line) intersects the interface (the broad dark line) at the side wall. A gas-dynamic shock (the light line) is also transmitted into the vapor. This photograph nicely illustrates the sensitivity of angle measurements with respect to the nonlinearities involved. The reflected second sound shock travels into and is convected by the relative velocity field established by the incident shock. If this effect were ignored, the Mach number of the reflected shock based on the interface angle would be less than unity. Proper inclusion of this effect yields a reasonable value for the Mach number.

4. CONCLUSIONS

Shock waves are very useful in studying low-temperature helium. Gasdynamic shocks can have extremely high Mach numbers while avoiding many other difficulties associated with strong shocks and shock tubes. Both gasdynamic and second sound shocks can be reflected from the vapor-superfluid interface to probe the boundary conditions during evaporation. First sound and second sound shocks can be used to induce and study phase transitions. Finally, second sound shocks produce relative velocities orders of magnitude larger than other techniques, forcing helium into otherwise inaccessible thermodynamic states, and thus allow further measurements of the equation of state.

REFERENCES

1. Landau, L.D., and Lifshitz, E.M., *Fluid Mechanics*, Pergamon Press, Oxford, 1959, Ch. XVI.

2. London, F., *Superfluids Vol. II: Macroscopic Theory of Superfluid Helium*, John Wiley & Sons, Inc., New York, 1954, pp. 126-139.

3. Feynman, R.P., "Application of Quantum Mechanics to Liquid Helium", *Prog. in Low Temp. Phys.*, **1**, 1955, p. 17.

4. Khalatnikov, I.M., *An Introduction to the Theory of Superfluidity*, W.A. Benjamin, Inc., New York, 1965, Ch. 13.

5. Osborne, D.V., "Second Sound in Liquid Helium II", *Proc. Phys. Soc. (London)*, **64**, 1951, p. 114.

6. Dessler, A.J., and Fairbank, W.M., "Amplitude Dependence of the Velocity of Second Sound", *Phys. Rev.*, **104**, 1956, p. 6.

7. Cummings, J.C., "Development of a High-Performance Cryogenic Shock Tube", *J. Fluid Mech.*, **66**, 1974, pp. 177-187.

8. Wise, J.L., *Experimental Investigation of First and Second Sound Shock Waves in Liquid Helium II*, Ph.D. Thesis, Calif. Inst. of Tech., 1979.

9. Turner, T.N., "New Experimental Results Obtained with Second-Sound Shock Waves", *Proc. of 16th Int. Conf. on Low Temp. Physics*, North-Holland Publishing Company, Amsterdam, 1981, p. 701.

10. Turner, T.N., "Using Second-Sound Shock Waves to Probe the Intrinsic Critical Velocity of Liquid Helium II", *Phys. Fluids*, **26**, 1983, p. 3227.

11. Liepmann, H.W., and Laguna, G.A., "Nonlinear Interactions in the Fluid Mechanics of Helium II", *Ann. Rev. Fluid Mech.*, **16**, 1984, pp. 139-177.

12. Moody, D.M., and Sturtevant, B., "Shock Waves in Superfluid Helium", *Phys. Fluids*, **27**, 1984, p. 1125.

13. Torczynski, J.R., "Converging Second Sound Shock Waves in Superfluid Helium", *Phys. Fluids*, **27**, 1984, p. 1138.

14. Torczynski, J.R., Gerthsen, D., Roesgen, T., "Schlieren Photography of Second Sound Shock Waves in Superfluid Helium", *Phys. Fluids*, **27**, 1984, p. 2418.

15. Torczynski, J.R., "On the Interaction of Second Sound Shock Waves and Vorticity in Superfluid Helium", *Phys. Fluids*, **27**, 1984, p. 2636.

16. Roesgen, T., *Second Sound Scattering in Superfluid Helium*, Ph.D. Thesis, Calif. Inst. of Tech, 1985.

17. Maynard, J., "Determination of the Thermodynamics of He II from Sound Velocity Data", *Phys. Rev. B*, **14**, 1976, p. 3868-3891.

Figure 1.1. The phase diagram of He⁴.

Figure 2.1. The cryogenic shock tube.

Figure 3.1. States produced by pressure shock waves in regions 6, 7, and 8 (see Figure 2.3-4). In some instances phase transitions are induced.

Figure 2.2. A comparison of ideal-shock-tube theory to cryogenic shock tube experiments with four different driven temperatures.
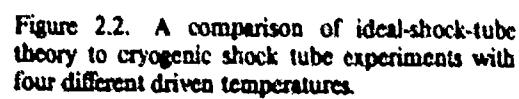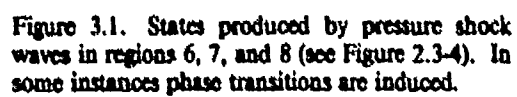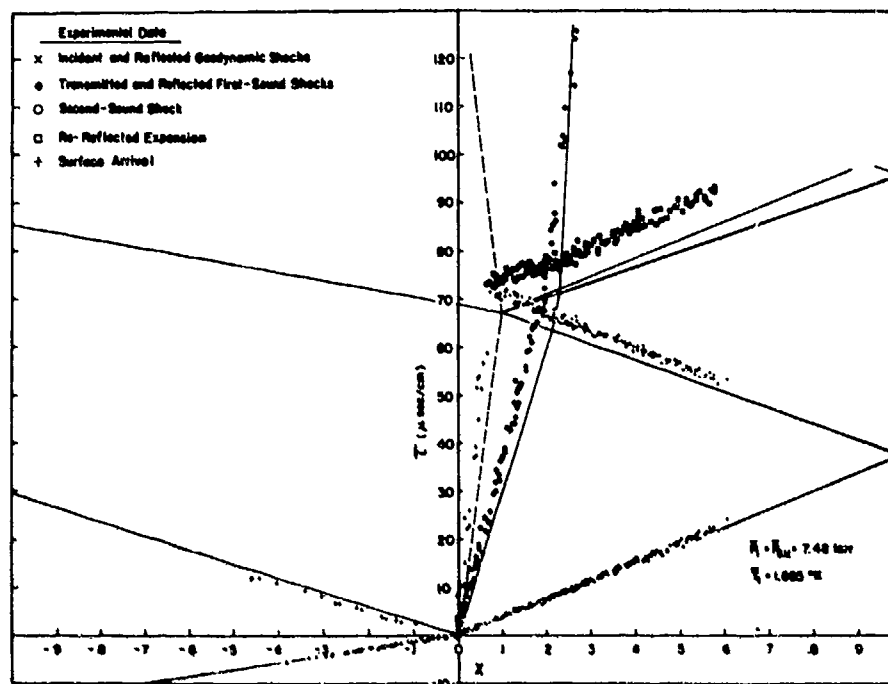
Figure 2.3. Typical wave diagram of shock waves obtained by reflecting a gasdynamic shock wave from the He II interface.

Figure 2.4. Schematic diagram of the above shock-interface experiment.
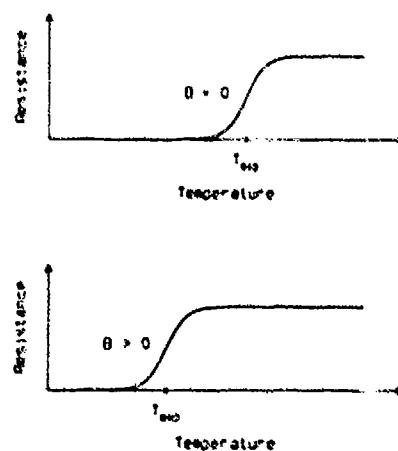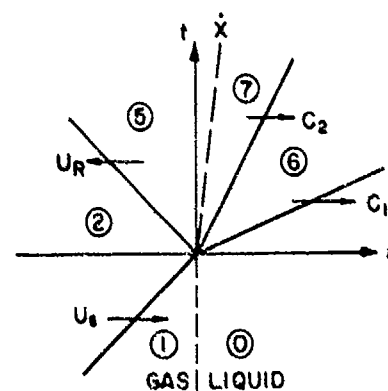
Figure 3.2. The variation of resistance with temperature of a typical superconductor. A magnetic field depresses the transition temperature.
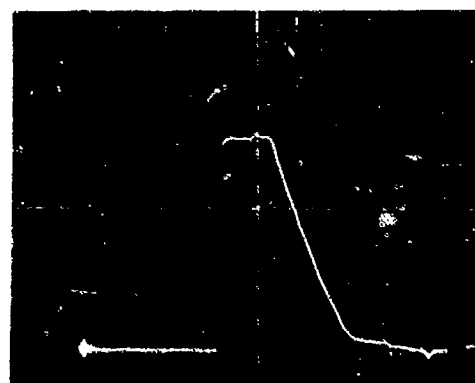
Figure 3.3. Oscillograph of a finite amplitude temperature wave, traveling from right to left.
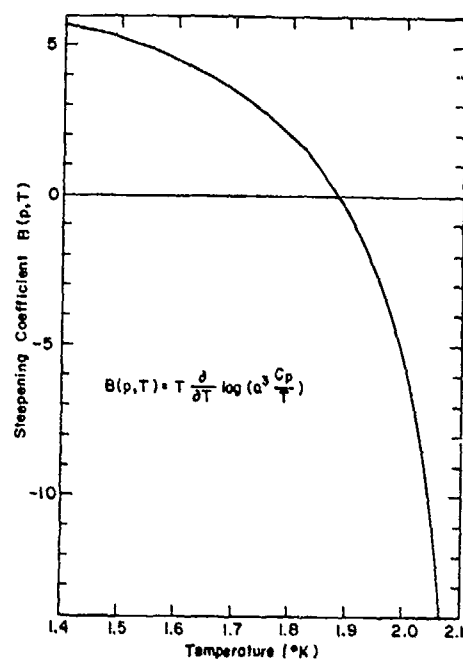
Figure 3.4. The steepening coeffient of second sound, $B(p,T)$, at saturated vapor pressure.
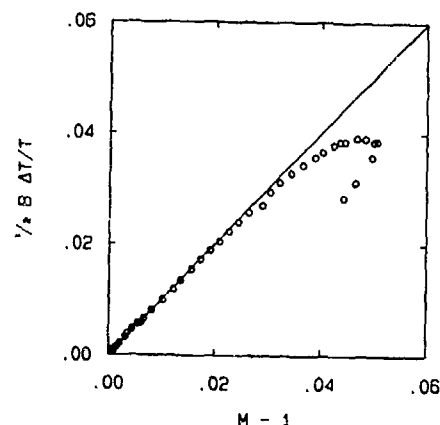
Figure 3.7. Second sound shock waves follow the Khalatnikov relation (the 45° line) until the shock limit is reached.

Figure 3.5. Below 1.884 K, B is positive, yielding temperature-raising shocks. Above 1.884 K, B is negative, yielding temperature-lowering shocks. A wave spanning 1.884 K will form shocks at both ends. Waves are traveling from right to left.

(a) Simple Formation   (b) Wave Modification

(c) Shock Limit   (d) Beyond the Shock Limit
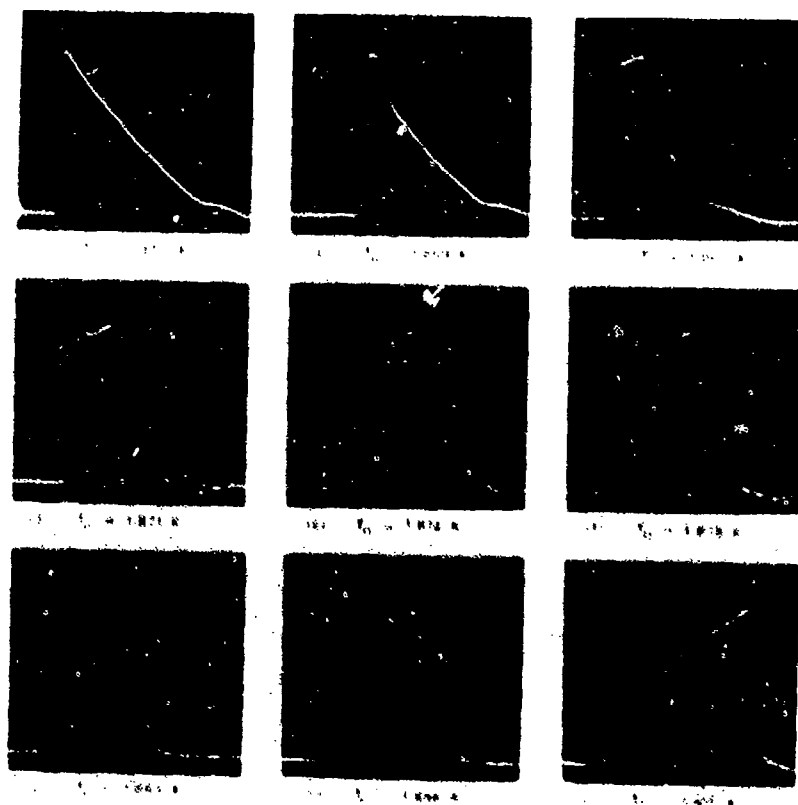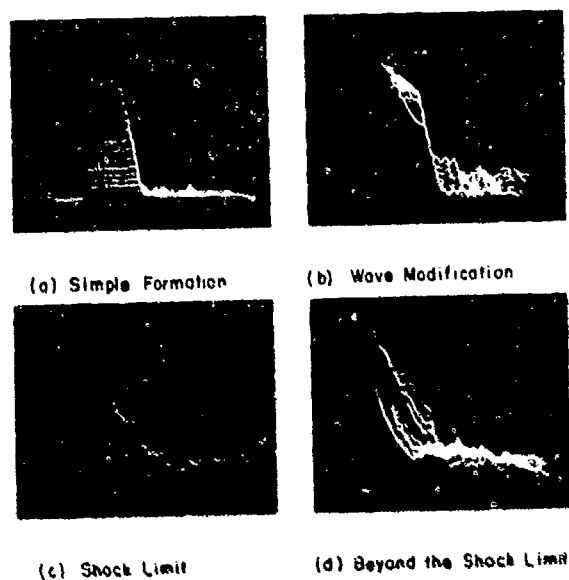
Figure 3.8. The waveforms of moderate strength shocks are trapezoidal as expected (see Figure 3.3). For shocks nearing the shock limit, the flow is degraded following the shock.
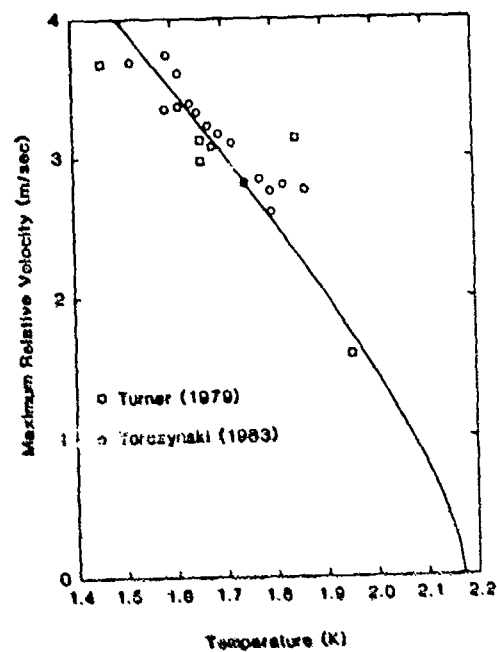
Figure 3.9. A plot of w_{max} vs. T. The solid curve represents the best fit of Eq. (3.9) to the data.

Figure 3.10. Spherical shock waves strengthen as they propagate into a conical channel.

Figure 3.11. Schematic diagram and schlieren photograph of a second sound shock wave hitting the interface obliquely.

Figure 3.6. A schlieren photograph of a double-shock profile, bending upward.

Part II
Shock Propagation and Interactions

THE REFLECTION OF A REGULAR REFLECTION OVER A SECONDARY RAMP

J.M. Dewey[1], G. Ben-Dor[2] and K. Takayama[3]

(1) Department of Physics, University of Victoria, Victoria, BC, Canada
(2) Department of Mechanical Engineering, Ben-Gurion University of the Negev, Beer Sheva, Israel
(3) Institute of High Speed Mechanics, Tohoku University, Sendai, Japan.

An analysis is presented of the various shock wave configurations which will occur when a regular reflection propagating along a straight wedge encounters a sudden increase or decrease in the slope of the wedge surface which changes from θ_w^1 to θ_w^2. It is shown analytically that three different reflection processes may be expected depending on the incident shock wave Mach number (M_i) and the two wedge angles (θ_w^1 and θ_w^2). The analytical predictions have all been verified experimentally.

1. INTRODUCTION

Regular reflection is one of the two major types of reflection of a shock wave over a solid surface[1]. In the case of an air burst explosion, for example, a spherical blast wave is generated. During the early stages of its interaction with the ground surface the reflection of the blast wave is regular (figure 1a). As the blast wave propagates outwards the reflection changes to a Mach reflection (figure 1b). Either reflection may encounter a sudden compressive on expansive change in the slope of the reflecting surface. To calculate the pressure distribution along such a surface an understanding of the interaction of a regular or a Mach reflection with a secondary wedge is of importance. The analysis to be presented aims at establishing both the reflection processes and final shock configurations of a regular reflection encountering a sudden increase or decrease in the slope of the wedge surface.

2. ANALYSIS

A compressive and an expansive double wedge are illustrated in figure 2. The slopes of the first and second wedges are θ_w^1 and θ_w^2, respectively, and the slope of the second wedge with respect to the first is

$$\Delta\theta_w = \theta_w^2 - \theta_w^1 \tag{1}$$

If $\Delta\theta_w > 0$ the double wedge is concave and if $\Delta\theta_w < 0$ the double wedge is convex. The reflection over any double wedge depends on three parameters: the incident shock wave Mach number, M_i, and the first and second wedge angles, θ_w^1 and θ_w^2, respectively. The phenomenon will be described in the (θ_w^1, θ_w^2) plane, but, since the phenomenon also depends on the incident shock wave Mach number, M_i, the (θ_w^1, θ_w^2) plane presentation is valid for a fixed value of M_i only.

The (θ_w^1, θ_w^2) plane is shown in figure 2. Equation 1 in this plane is described by straight lines with 45° slopes along which $\Delta\theta_w$ is constant. In the region above the line for which $\Delta\theta_w = 0$, $\Delta\theta_w > 0$ and the double wedge is concave. Below this line $\Delta\theta_w < 0$ and the double wedge is convex. Since the present paper is concerned with the reflection of a regular reflection over a secondary ramp only the region to the right of the line $\theta_w^1 = \theta^{det}$ will be considered (θ^{det} is the "detachment" wedge angle for a given incident shock wave Mach number, M_i, at which transition from regular to Mach reflection is expected to occur).

If $\theta_w^1 > \theta_w^{det}$ the incident shock wave reflects from the first wedge as a regular reflection[2]. This regular reflection propagates up the wedge until it encounters the leading edge of the second wedge and negotiates it.

Region 1

Since $\Delta\theta_w > 0$ the wedge is concave like. The incident shock wave reflects over the first wedge as a regular reflection ($\theta_w^1 > \theta_w^{det}$) and upon encountering the second compressive wedge the wave angles are changed but the reflection remains regular ($\theta_w^2 > \theta_w^{det}$).

The reflection process in this region is shown in figure 4 for $\theta_w^1 = 55°$ and $\theta_w^2 = 75°$ ($\Delta\theta_w = 20°$). The regular reflection over the first surface appears in figure 4a while the final regular reflection over the second surface is clearly seen in figure 4b.

Region 2

Unlike the previous case, here $\Delta\theta_w < 0$, and therefore the wedge is convex like. The incident shock wave reflects over the first compressive wedge regularly ($\theta_w^1 > \theta_w^{det}$). Upon encountering the second expansive wedge the wave angles are changed but the reflection remains regular ($\theta_w^2 > \theta_w^{det}$).

The reflection process in this region is shown in figure 5 for $\theta_w^1 = 65°$ and $\theta_w^2 = 50°$ ($\Delta\theta_w = -15°$). A shadowgraph of the regular reflection over the first surface is shown in figure 5a while a shadowgraph of the final regular reflection over the second surface is shown in figure 5b.

Subregions 1a and 1b, 2a and 2b

The pressure P_{rf} behind the reflected shock of the regular reflection over the first wedge is in general different from the pressure P_{rs} behind the reflected shock of the regular reflection over the second wedge. Thus when the regular reflection encounters the second wedge (compressive or expansive). The pressure at the reflection point suddenly changes from P_{rf} to P_{rs}. Such a sudden change in the pressure must be supported by "an unsteady wave of finite amplitude or a finite amplitude band of waves"[3]. We may therefore expect that the reflection point on the second wedge will be followed by either compression waves (or a shock wave) or expansion waves depending upon whether the transition caused a sudden pressure decrease or increase. Figure 6 shows the pressure ratio behind the reflection point of a regular reflection as a function of the reflecting wedge angle θ_w for a given incident shock Mach number. $M_i = 1.3$. The pressure ratio Pr/Po goes through a minimum at about $\theta_w = 60°$. Consequently, in the double wedge reflection process now being considered three pressure change behaviours are possible. If, in the example for $M_i = 1.3$, $\theta_w^1 = 50°$ and $\theta_w^2 = 60°$ then at transition from the first to the second wedge the pressure behind the reflection point suddenly drops. However, if $\theta_w^1 = 60°$ and $\theta_w^2 = 85°$ then at transition the pressure behind the reflection point suddenly increases. There could also be a case for which there is no pressure change at transition, e.g., $\theta_w^1 = 55°$ and $\theta_w^2 = 65.775°$. Thus, different flow patterns are to be expected behind the second reflection point according to these different pressure changes.

The added dashed line in figure 3 divides each region into two subregions 1a & b and 2a & b. In subregions 1a and 2b the reflection process involves a

transition from a high pressure regular reflection to a low pressure regular reflection (H → L) while in 1b and 2a the transition is from a low pressure regular to a high pressure regular reflection (L → H). Therefore in subregions 1a and 2b it is expected that the reflection over the second wedge will be followed by a shock or a compression wave, while in subregions 1b and 2a the second reflection is expected to be followed by an expansive wave.

Figure 6 indicates that for the given wedge angles combination of the experiment in region 1 there is a transition from a low pressure RR (figure 4a) to a high pressure RR (figure 4b). As mentioned earlier this sudden pressure drop behind the reflection point must be supported by a shock wave. This shock wave is clearly seen in figure 4b. For the experiment in region 2, the transition is from a high pressure RR (figure 5a) to a low pressure RR (figure 5b). Consequently, in this case the sudden pressure change is supported by a rarefaction wave (figure 5c).

Region 3

The double wedge is again convex like ($\Delta\theta_w < 0$). The incident shock wave reflects over the first wedge as a regular reflection ($\theta_w^1 > \theta_w^{det}$). Upon encountering the second expansive wedge the incident shock wave find itself propagating over a wedge angle $\theta_w^2 < \theta_w^{det}$ from which it can reflect only as a Mach reflection. Therefore the regular reflection terminates and transitions into a Mach reflection.

The reflection process in this region is shown in figure 7 for $\theta_w^1 = 60°$ and $\theta_w^2 = 30°$ ($\Delta\theta_w = -30°$). A shadowgraph of the regular reflection over the first surface is clearly seen in figure 7a. When the reflection point of this regular reflection encounters the sudden change in the slope of the surface it takes off to form a triple point of a Mach reflection. As can be seen from figure 7b, the formation of this Mach reflection is associated with a corner generated rarefaction wave. A clear Mach reflction over the second surface at a later time is shown in figure 7c.

3. CONCLUSION

The reflection process of a regular reflection over a compressive on an expansive corner has been analysed using the basic concepts of the reflection of a planar shock wave over a single wedge.

The analysis suggests three different reflection processes which have all been verified experimentally.

REFERENCES

1. Mach, E., "Uber Einige Mechanische Wirkungen des Electrischen Funkens", Akad. Wiss, Wien, Vol. 77, 1878; p. 819.
2. Neumann, J. von, Collected Works, Vol. 6, Pergamon Press, Oxford, 1963.
3. Henderson, L.F. and Lozzi, A., "Experiments on Transition of Mach Reflection", Journal of Fluid Mechanics, Vol. 68, 1975, p. 139.

Fig. 1 Blast Wave Reflection

Fig. 2. The (θ_w^1, θ_w^2) plane
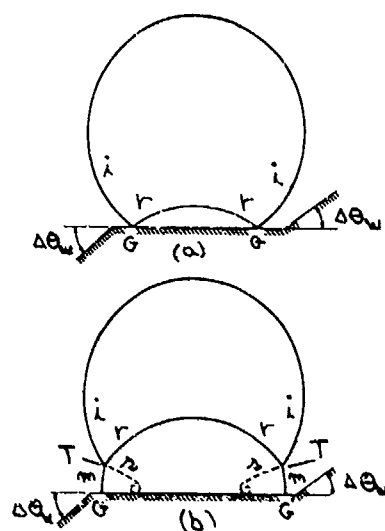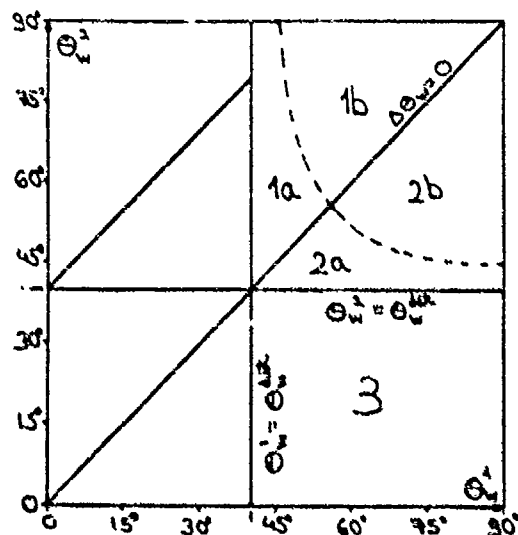
Fig. 3. Three regions of different reflection process of a regular reflection over a secondary expansive on compressive ramp.
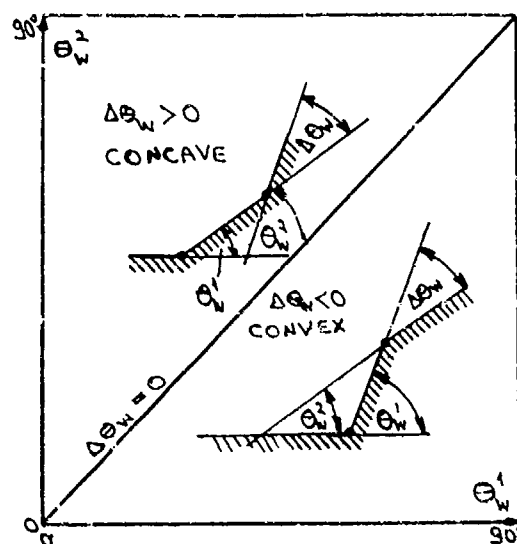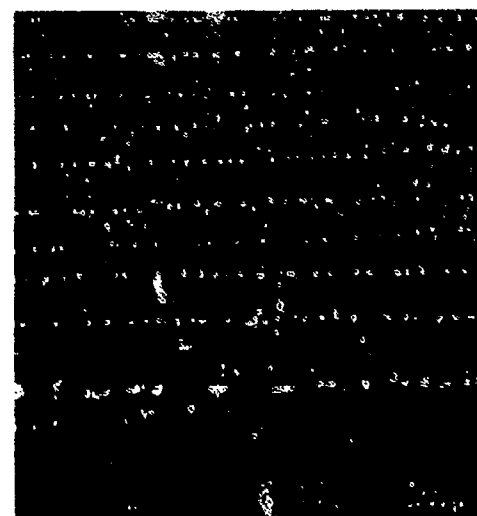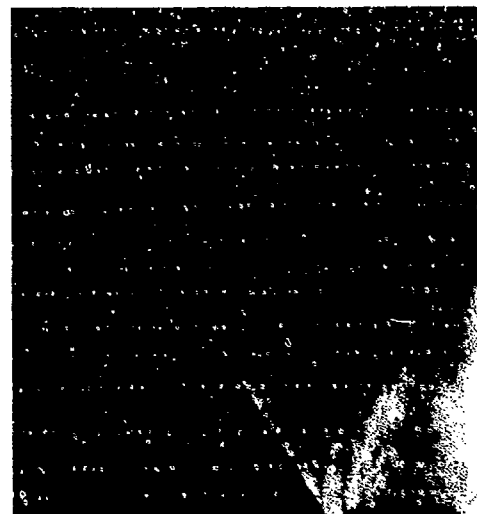
Fig. 4. Reflection process in region 1
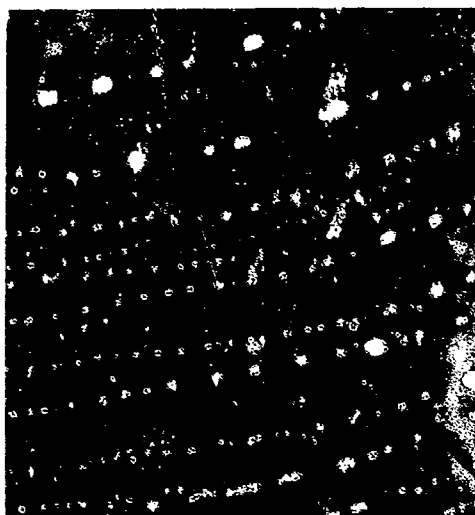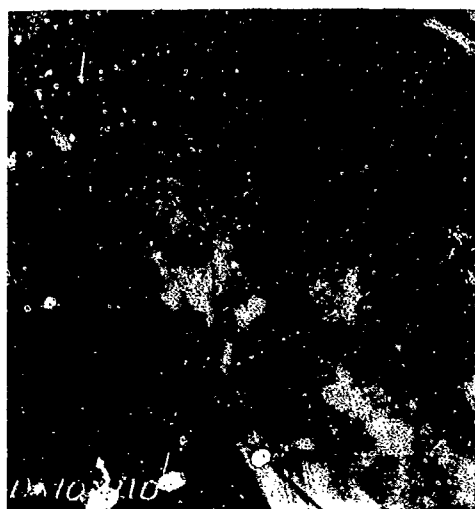
Fig. 5.   Reflection process in region 2
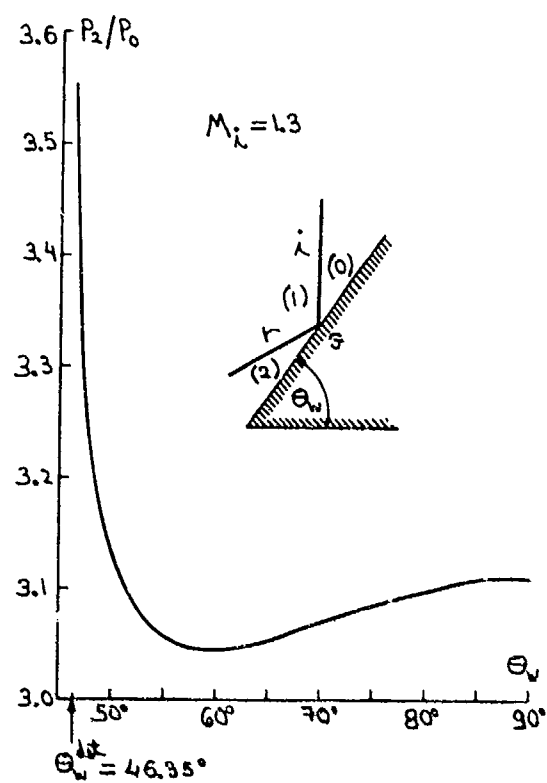
Fig. 6.   Pressure ratio across a regular reflection as a function of the reflecting wedge angle.
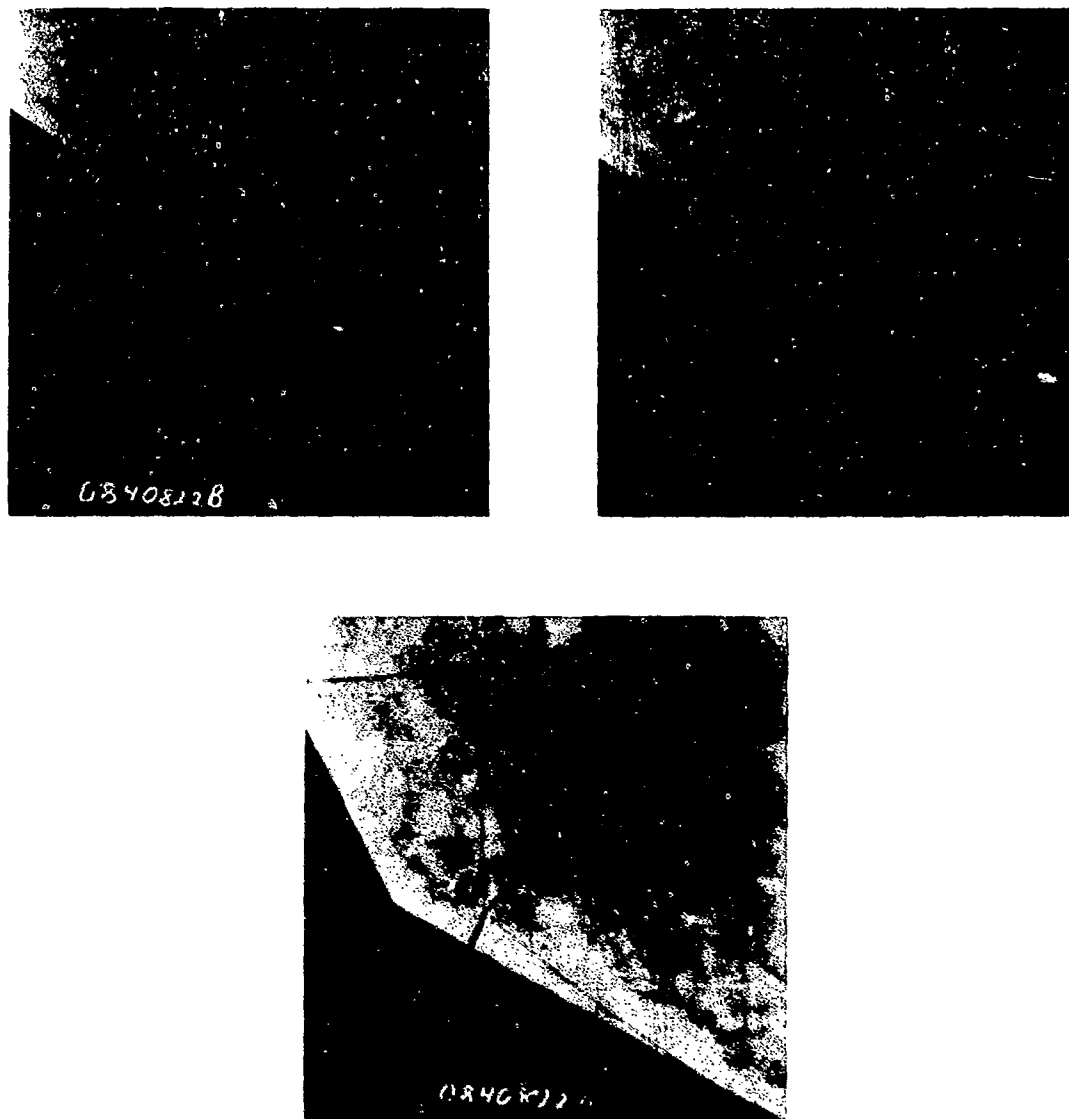
Fig. 7.   Reflection process in region 3

COLLISION OF MACH REFLECTIONS WITH A 90-DEGREE RAMP

J.-C. Li and I. I. Glass

Institute for Aerospace Studies
University of Toronto
Toronto, Canada

The collision of nonstationary oblique-shock-wave
Mach-reflections with a perpendicular ramp on a 20°-wedge was
investigated interferometrically and numerically. Single-Mach
reflection (SMR) in air, complex-Mach reflection (CMR) in air and
double-Mach reflection (DMR) in carbon-dioxide were studied at
incident shock Mach numbers M_s of 2.40, 3.94 and 5.77,
respectively. After the collision of the Mach stem with the
perpendicular ramp, very complex interactions occurred among
shock waves, nonstationary rarefaction waves, quasi-steady
expansion waves, contact surfaces and boundary layers. The
isopycnics were evaluated and are presented and discussed for the
various reflection processes.

Based on the self-similarity of the shock-wave-diffraction
process and the results of three-shock theory, a reasonable
treatment of discontinuous surfaces is given and combined with a
modified fluid-in-cell numerical method to solve the flow fields
for the SMR case. A comparison of the present numerical results
with the experimental and other current numerical data shows
reasonable agreement with the various flow isolines, especially
near the leading edge of the wedge.

1. INTRODUCTION

The interaction of a spherical blast wave with a planar surface, which
impedes the normal path of the blast wave, can be reasonably treated as an
oblique-shock-wave reflection over a wedge, providing the spherical flow has
developed enough to resemble its two-dimensional equivalent. The equivalent
wedge angle is geometrically related to the incident wave angle made between
the blast wave and the surface. If there are obstacles on the planar surface,
such as buildings or other structures on the ground, the phenomenon of
shock-wave diffraction becomes very complex. The observation and understanding
of this interaction are of importance not only to engineers interested in
blast-wave loading but also to aerodynamicists interested in the properties of
the flow field.

The simplest laboratory experiment that can be designed to study this
problem quantitatively is to use the shock-induced flow over a wedge with a
90°-ramp in a shock tube and utilizing infinite-fringe interferometric
techniques. A number of computational fluid dynamicists have tackled such
problems and made many improvements in the numerical simulation of
nonstationary oblique-shock-wave reflections (Ref. 1). If good agreement can
be obtained between the experimentally-measured isopycnics and those
calculated numerically, then it will lend confidence in the computational
methods for spherical flows generated by height-of-burst explosions, where
experimental results are not readily obtainable. Much more data can be

obtained numerically for flow-field quantities that are usually very difficult
to measure experimentally. Consequently, this would ultimately reduce the cost
of conducting complex blast wave experiments in the field.

2. ANALYTICAL CONSIDERATIONS

Regardless of the type of nonstationary oblique-shock-wave reflection,
the flow field generated by a wedge is self-similar with respect to time since
there is no characteristic length associated with the diffraction (Ref. 2).
The entire shock-wave diffraction pattern is amplified linearly with time.
Since the planar incident shock wave moves with a constant velocity, the
phenomenon of nonstationary oblique-shock-wave reflection can be considered to
be pseudo-stationary in the frame of reference attached to the reflection
point in regular reflection or the first triple point in Mach reflection.
Then the flow quantities can be assumed as uniform in each region near the
reference point and found from the oblique-shock-wave equations (Ref. 3). In
case of the collision with a 90°-ramp, the relations for the normal reflection
of a shock wave (Ref. 4) are added to evaluate the properties behind the
reflected Mach stem. It is reasonable to assume that the Mach stem is
perpendicular to the wedge surface (this is not always the case in practice
and leads to error in analytical expressions for the triple-point-trajectary
angle χ, see Ref. 5) and the properties immediately behind the Mach stem are
uniform.

In the present experiments, the highest incident shock Mach numbers in
air and CO_2 were less than 4 and 6, respectively. Dissociation and ionization
can be neglected for all of the present experiments (Ref. 5). The vibrational
relaxation length of nitrogen behind the incident shock wave is about 1 m for
the CMR experiments in air ($M_S \sim 3.9$, $P_0 = 2$ KPa and $T_0 \sim 300$ K) (Ref. 3). The
vibrational relaxation length of oxygen, however, is about 10 mm at the above
mentioned conditions (Ref. 3). It is reasonable for this case to treat air as
gas in which only oxygen is excited. For the SMR experiments in air ($M_S \sim 2.4$,
$P_0 = 6.67$ KPa and $T_0 \sim 300$ K) both nitrogen and oxygen can be treated as frozen.
For the DMR experiments in CO_2 ($M_S \sim 5.8$, $P_0 = 1.33$ KPa and $T_0 \sim 300$ K) the
vibrational relaxation length of CO_2 is about 0.2 mm, hence CO_2 behaves as an
equilibrium gas for vibrational excitation (Ref. 3).

3. EXPERIMENTAL METHODS AND RESULTS

The UTIAS 10 cm x 18 cm Hypervelocity Shock Tube was used to conduct the
experiments for the present study. Cold helium was employed as a driver gas.
Medical-grade air and commercially-available carbon-dioxide of purity
exceeding 99.8% were used as the test gases. The incident shock velocity was
obtained by measuring the traverse time between several Atlantic LD-25
piezoelectric pressure transducers flush-mounted in the wall of the channel.
The absolute error in calculating the incident shock Mach number can be
estimated by means of a procedure outlined in Ref. 6. For air the absolute
error is 0.03 at $M_S = 2.40$ and 0.06 at $M_S = 3.94$; for CO_2 it is 0.09 at
$M_S = 5.77$. Three different incident shock Mach numbers (2.40, 3.94 and 5.77)
were chosen to obtain SMR and CMR in air and DMR in CO_2. In the present
experiments, the scatter in the incident shock Mach numbers M_S ranged from
2.37 to 2.44 for SMR, and from 3.88 to 4.00 for CMR and from 5.69 to 5.86 for
DMR, owing to the non-repeatability of the bursting pressure of the
diaphragm.

A 23-cm dia field-of-view Mach-Zehnder interferometer in an infinite-
fringe mode was used to study the density field of the reflection pattern.

The values of density can be evaluated in regions near the first triple point. Just after the collision of the incident shock wave or the Mach stem with the ramp, the density behind the regular-reflected shock wave or a normally-reflected Mach stem can also be given. The densities in these particular regions were used as starting points to evaluate the isopycnics. For the purpose of this study, a 20°-wedge with perpendicular ramps having heights of 12.7 mm, 25.4 mm and 50.8 mm, respectively, was mounted at two locations in the shock tube to show clearly the change of the diffration patterns with time.

A series of infinite-fringes interferograms are presented in Figs. 1-7, along with their tabulated density values, to illustrate the process of the collision of a Mach reflection with the 90°-ramp. Before the collision of the Mach reflection with the ramp, the shock-wave-diffraction pattern, as shown in Figs. 1 and 2, is independent of the ramp. The flow field around the model is self-similar.

After the incident shock wave or the Mach stem impinges on the ramp, the flow field around the ramp becomes very complex and strongly dependent on the height of the ramp relative to the triple point. If on collision the Mach-stem height exceeds the ramp diagonal (e.g. Figs. 3, 4 and 5), the incident shock wave cannot impinge on the ramp and the Mach stem is divided into two parts. The lower part of the Mach stem is normally reflected from the ramp and diffracts around the upper corner of the ramp. The upper tail of the reflected Mach stem gradually weakens and finally catches up with the originally reflected shock wave. The upper part of the Mach stem continues on.

Just after the collision, between the ramp and the normally-reflected Mach-stem, there exists a stagnation region (region 4 in Fig. 3), in which the density, pressure and temperature have their highest values, until the nonstationary rarefaction wave fills the region. The rarefaction wave is generated by a large difference of pressure between the stagnation region and the one behind the upper Mach stem. In front of the ramp, the propagation of the rarefaction wave causes the originally-stagnant gas to be accelerated to supersonic speed. This is similar to the phenomenon observed in the driver of a shock tube. In order to be parallel to the top of the ramp, the flow behind the rarefaction wave has to turn to the top and be further accelerated through a Prandtl-Meyer expansion. Across the nonstationary rarefaction wave and the quasi-steady expansion wave, the density, pressure and temperature reduce to their minimum values in the vicinity of the upper corner of the ramp.

The interaction of the expansion wave with the upper Mach stem causes it to be curved but perpendicular to the top surface. The density and pressure behind the upper Mach stem is much higher than that near the upper corner of the ramp (see Figs. 3 and 4). A second shock wave is generated to match the pressures behind the upper Mach stem and the expansion waves. The second shock wave appears to be very sharp near where the density and pressure have their minimum values. It weakens gradually and becomes a compression wave far away from the top owing to the increasing pressure behind the expansion waves. As time goes on, the reflected Mach stem meets and interacts the slipstream (Figs. 3, 4). After the collision, the reflected Mach stem is transmitted and the contact surface is deflected. At same time, a shock wave can be reflected from the contact surface (Ref. 7). However, it is too weak to be seen owing to its interaction with the nonstationary rarefaction wave. An increase in density is observed in a narrow region behind the reflected Mach stem, perhaps owing to the vibrational-relaxation process of oxygen in air. It is seen that the rarefaction waves are no longer planar because of the different

temperatures and resultant sound speeds on the two sides of the slipstream. The wave propagation is faster in the higher temperature region adjacent to the ramp wall than in the other. This is why the isopycnics undergo a transition upward to higher density. A bifurcation of the reflected Mach stem appears near the isopycnic marked u (Fig. 4), as it interacts with the wall boundary layer.

After the collision of a DMR with the 12.7-mm high ramp (see   Fig. 5), the upper part of the reflected Mach stem S_5 collides the first reflected shock wave S_1 and the second reflected shock wave S_2. The second Mach stem S_6 passes through the expansion wave and weakens. The first contact surface C_1 is laminar initially and then becomes turbulent and interacts with the expansion wave E. The upper part of the first Mach stem S_3 is curved and may be bifurcated to ensure that it is perpendicular to the top of the ramp. The interaction of the reflected Mach stem S_4 with the boundary layer on the wedge surface is so strong that it generates a lambda-shock configuration. The temperature behind the reflected Mach stem S_4 is high and strongly nonuniform. The heat radiation causes the change in the temperature field ahead of the reflected Mach stem and generates an additional density pocket. There appears to be a shock-compression wave S_7 at the end of the expansion wave E to match the pressures behind the first Mach stem S_3 and expansion wave E and to have the flow parallel to the top surface.

If on collision the Mach-stem height is smaller than the ramp diagonal, the incident shock wave first collides with the ramp and it is also divided into two parts as shown in Figs. 6 and 7. The upper part continues on along the top of the ramp. The lower part, in general, interacts with the ramp as a regular reflection except for very large wedge angle. The regular-reflected shock-wave diffracts around the upper corner of the ramp. A nonstationary rarefaction wave and a quasi-steady expansion wave exist in the region surrounded by the regular-reflected shock-wave. The upper tail of the regular-reflected shock-wave gradually weakens owing to the interaction with the expansion waves. After the collision of a SMR with the ramp, a stagnation region (region 4 in Fig. 6) exists between the ramp and the normally-reflected Mach stem. The reflected Mach stem meets and interacts with the slipstream and gives rise to a transmitted shock, a deflected contact surface and a reflected shock, which appears too weak to reflect from the ramp surface (Ref. 7). Simultaneously, the regular—reflected shock-wave collides with the originally-reflected shock-wave and generates two transmitted shock waves. Again a shock-compression wave exists between the incident shock wave and the expansion wave.

For the DMR case (Fig. 7), the phenomenon is more complex. The protrusions P_1 and P_2 caused by heat radiation exist ahead of not only the reflected Mach stem S_3, but also the regular-reflected shock-wave S_4. The bifurcation of the reflected Mach stem S_3 is very clear. Between the ramp and the reflected Mach stem S_3, there exist some vortices affected by the strong rolling up of the first slipstream. The reflected Mach stem S_3 sweeps over the second Mach stem S_6 and the first reflected shock wave S_1. The first reflected shock wave S_1 is reflected from the ramp to form a new shock wave S_5.

4. NUMERICAL METHOD

The Euler equations of motion govern a nonstationary two-dimensional flow, that is, continuity, momentum and energy equations. These nonlinear partial differential equations can be written in terms of three independent

variables: time, t, plus two space dimensions, x and y. Under the assumptions of an inviscid, non-heat-conducting flow, these equations can be written in a Cartesian coordinate system (see Ref. 11 for details), and solved using a modified fluid-in-cell (FLIC) method.

5. RESULTS

Based on the foregoing numerical method, simulations were done for single-Mach reflection in perfect air. A set of contours for various properties were obtained and compared with the state-of-the-art numerical simulation performed by Glaz (Ref. 10). Very reasonable agreement was obtained for the wave system shapes and isolines of density, pressure, specific internal energy and velocity components along the x- and y-axes and along and normal to the wedge surface. As expected, the FLIC-method was not capable of handling the ramp problem. This was done in Ref. 10.

6. CONCLUSIONS

An interferometric study was made of the collision of Mach reflections with a 90-degree ramp. Before the collision of the Mach stem or the incident shock wave with the ramp, the flow phenomenon is self-similar; but not so after the collision. The height of the ramp relative to the triple point determines the type of reflection pattern. Because of the interactions among shock waves, nonstationary rarefaction waves, quasi-steady expansion waves, contact surfaces and boundary layers, the phenomenon becomes very complex. On the whole, the collision of the CMR with the ramp is similar to that of the SMR except for the different shapes of the reflected shock wave. However, for the collision of the DMR with the ramp, the vortices caused by the strong rolling up of the contact surface and the protrusions generated by heat radiation are also observed. Such flows can only be evaluated numerically by solving the Navier-Stokes equations and then comparing the simulations with the present interferograms.

Based on the self-similarity of the shock-wave-diffraction process, the solution of the three-shock theory, and a reasonable fit to the discontinuous surfaces, a modified fluid-in-cell (FLIC) numerical method was used to solve the flow field for the single-Mach-reflection case. Despite the simplifications made in the present numerical method, much information was obtained, such as, flow-field density, pressure, specific internal energy and velocity. A comparison of the present numerical results with the experimental isopycnics shows fair agreement, especially near the leading edge of the wedge. A comparison of the present simulation of the flow field with the more reliable state-of-the-art numerical-results of Glaz (Ref. 10) shows reasonable agreement for the various isolines. Further details can be found in Refs. 1, 9, 10 and 11.

REFERENCES

1. Glaz, H. M., Colella, P., Glass, I. I. and Deschambault, R. L., "A numerical, graphical and experimental study of oblique-shock-wave reflections", Univ. of Toronto, UTIAS Report No. 285 (1985); see also Proc. R. Soc., London, A 398, pp. 117-140 (1985).

2. Jones, D. M., Martin, P. M. E. and Thornhill, C. K., "A Note on the Pseudo-Stationary Flow behind a Strong Shock Diffracted or Reflected at a Corner", Proc. Roy. Soc., Sec. A, V. 209, p. 238 (1951).

3. Hu, T. C. J. and Shirouzu, M., "Tabular and Graphical Solutions of Regular and Mach Reflections in Pseudo-Stationary Frozen and Vibrational-Equilibrium Flows", Univ. of Toronto, UTIAS Report No. 283 (1985).

4. Glass, I. I. and Hall, J. G., "Shock Tubes", Handbook of Supersonic Aerodynamics, NAVORD Report 1488, V. 6, Sec. 18 (1959).

5. Shirouzu, M. and Glass, I. I., "An assessment of Recent Results on Pseudo-Stationary Oblique-Shock-Wave Reflections", Univ. of Toronto, UTIAS Report No. 264 (1982).

6. Ben-Dor, G. and Whitten, B. T.,"Interferometric Techniques and Data Evaluation Methods for the UTIAS 10 cm x 18 cm Hypervelocity Shock Tube", Univ. of Toronto, UTIAS Tech. Note No.208 (1979).

7. Jahn, R. G., "The Refraction of Shock Waves at a Gaseous Interface", J. Fluid Mech., V. 1, Part 5, pp. 457-489 (1956).

8. Gentry, R. A. Martin, R. E. and Daly, B. J., "An Eulerian Differencing Method for Unsteady Compressible Flow Problems", J. Comput. Phys., 1, pp. 87-118 (1966).

9. Deschambault, R. L. and Glass, I. I., "An Update on Non-Stationary Oblique Shock-Wave Reflections:Actual Isopycnics and Numerical Experiments", J. Fluid Mech., V. 131, pp.27-57 (1983).

10. Glaz, H, M. et al, Private communication (1984); see also: Glaz, H. M., Glass, I. I., Li, J.-C. and Walter, P., "Interaction of Oblique Shock-Wave Reflections in Air with Downstream Obstacles", presented at 10th Int. Colloquium on Dynamics of Explosions and Reactive Systems", University of California, Berkeley, Aug. 4-9, 1985.

11. Li, J.-C. and Glass, I. I., "Collision of Mach Reflections with a 90-Degree Ramp in Air and CO_2",Univ. of Toronto, UTIAS Report No. 290 (1985).

Fig. 1 Collision of SMR with a 90°-
ramp in air at $M_S=2.44$ and
$t=136$ μs, $\theta_w=20°$, $\ell=134$ mm,
$h=25.4$ mm, $P_0=6.67$ KPa,
$T_0=297$K, $\rho_0=7.82\times10^{-5}$ g/cm^3,
$\lambda=6943$A, $\Delta\rho/\rho_0=0.39$.

Fig. 2 Collision of DMR with a 90°-
ramp in CO_2 at $M_S=5.81$ and
$t=59$ μs, $\theta_w=20°$, $\ell=134$ mm,
$h=12.7$ mm, $P_0=1.33$ KPa,
$T_0=297$K, $\rho_0=2.38\times10^{-5}$ g/cm^3,
$\lambda=6943$A, $\Delta\rho/\rho_0=1.27$.

Fig. 3 Collision of SMR with a 90°-
ramp in air at $M_S=2.40$ and
$t=166$ μs, $\theta_w=20°$, $\ell=134$ mm,
$h=25.4$ mm, $P_0=6.67$ KPa,
$T_0=297$K, $\rho_0=7.82\times10^{-5}$ g/cm^3,
$\lambda=6943$A, $\Delta\rho/\rho_0=0.39$.

Fig. 4 Collision of SMR with a 90°-
ramp in air at $M_S=2.43$ and
$t=201$ μs, $\theta_w=20°$, $\ell=134$ mm,
$h=25.4$ mm, $P_0=6.67$ KPa,
$T_0=296$K, $\rho_0=7.84\times10^{-5}$ g/cm^3,
$\lambda=6943$A, $\Delta\rho/\rho_0=0.39$.

Fig. 5 Collision of DMR with a 90°-
ramp in CO_2 at $M_S=5.78$ and
$t=119$ µs, $\theta_w=20°$, $\ell=134$ mm,
$h=12.7$ mm, $P_0=1.33$ KPa,
$T_0=294K$, $\rho_0=2.40\times10^{-5}$ g/cm³,
$\lambda=6943A$, $\Delta\rho/\rho_0=1.26$.

Fig. 6 Collision of SMR with a 90°-
ramp in air at $M_S=2.38$ and
$t=159$ µs, $\theta_w=20°$, $\ell=134$ mm,
$h=50.8$ mm, $P_0=6.67$ KPa,
$T_0=296K$, $\rho_0=7.84\times10^{-5}$ g/cm³,
$\lambda=6943A$, $\Delta\rho/\rho_0=0.39$.

Fig. 7 Collision of DMR with a 90°-
ramp in CO_2 at $M_S=5.69$ and
$t=117$ µs, $\theta_w=20°$, $\ell=134$ mm,
$h=50.8$ mm, $P_0=1.33$ KPa,
$T_0=297K$, $\rho_0=2.38\times10^{-5}$ g/cm³,
$\lambda=6943A$, $\Delta\rho/\rho_0=1.27$.

MULTIPLE, INTERNAL CONICAL MACH REFLECTIONS

B. E. Milton

School of Mechanical and Industrial Engineering.
University of New South Wales, Sydney, Australia

D. Q. Duong

Department of Housing and Construction
Sydney, Australia

K. Takayama

Institute of High Speed Mechanics,
Sendai, Japan

Studies of shock wave Mach reflection processes in conical con-
tractions where the final wall angle is achieved in two equal steps
are reported in this paper. This is an approach to the examination
of shock movement into contoured nozzles and contractions. For
a given cone apex angle, a number of possible reflection patterns
have been identified depending on the primary cone length. A
computational method based on the ray-shock theory has been
developed from that for single cones. Experiments have been
carried out using pressure transducer measurements at the cone
centreline and holographic methods for internal axisymmetric flow
visualization. The calculations and experimental measurements
show good agreement and indicate that the major effect of the
primary cone is to increase the Mach stem length or its strength
depending on the reflection pattern. The flow visualization ex-
periments, still in the preliminary stage, confirm the anticipated
curvatures in both triple-point trajectories and Mach stem.

INTRODUCTION

Mach reflection processes have been extensively studied (from Smith[1] to, for example.
Henderson et al[2]) in the plane two-dimensional cases where a shock impinges on a wedge
of shallow angle and are generally well understood although many details require further
elucidation. In internal axisymmetric cases, a limited number of studies are available, these
being much more difficult because of the lack of suitable flow visualization techniques but are
important because the inward moving disturbances can develop very high pressures within
ductwork. The reinforcement of a shock wave in a convergence is essentially related to the
reflection patterns established during its progression through the contraction and the larger
axisymmetric area reduction is obviously of great significance when compared to the plane
two-dimensional case.

In the very early stages of a conical Mach reflection, the ratio of the duct radius to the
reflection pattern dimensions approaches infinity. At its onset, the reflection should therefore
be identical to that of a shock wave reflecting from a plane wedge. Thus, for a shock wave
moving into a conical nozzle or contraction of wall angle less than about 45°, a Mach reflection
should ensue. As the Mach stem progresses towards the centreline, the accumulation of
disturbances into the smaller area available should cause both the Mach stem and triple-point

trajectory to develop significant curvature. This problem has been studied computationally and experimentally by both Setchell et al[3] and Duong and Milton[4]. No internal flow visualization of this phenomenon has been available to date and the above curvatures have been imputed from the close correspondence of calculation and experimental measurements taken at certain limited positions (e.g. the centreline and the wall) by use of pressure transducers. Multiple Mach reflections arise when a second wedge or cone of increased angle is placed downstream of the first. This has been examined by Takayama et al[5] for two consecutive plane wedges and by Milton[6] for a plane wedge preceded by a radius. A study of a two cone configuration is a first step in examining shock interaction with a curved axisymmetric contraction.

In summary, this research aims

(i) to extend existing calculation procedures and experimental techniques to examine Mach reflection caused by two consecutively mounted cones

(ii) to examine the resulting internal axisymmetric Mach reflection processes using holographic techniques for flow visualization.

SHOCK REFLECTION PATTERNS WITHIN MULTIPLE CONES

The complete internal reflection pattern within a single cone has been previously explored[3,4] From the available calculations and experimental data, it appears to be similar to that occurring within an equivalent two-dimensional wedge shaped contraction except that the curvature in the triple-point trajectory in the conical case brings the centreline shock jump positions closer together allowing more reflections within the total length. By smoothing the entry to a plane two-dimensional area reduction, it has been shown[6] that the Mach stem length is increased. In the axisymmetric case, a similar smooth entry may be regarded as a series of truncated cones of increasing wall angle. For this study, two cones only are considered, each turning the wall direction in equal increments to the final value.

A number of reflection patterns are possible depending on the truncated length of the primary cone. When the shock impinges on the first corner, the triple-point trajectory (TP1) will be initially identical to that which would occur for a complete primary cone. The Mach stem from this reflection interacts with the second corner forming an additional triple-point trajectory (TP2). The major complexity occurs when the triple-point trajectories intersect giving two basic configurations which are readily identifiable. If the primary cone is less than a defined length, the triple-point trajectories intersect before reaching the centreline and a single, modified Mach stem should continue to progress downstream as in the plane two-dimensional case. If the primary cone exceeds this length, TP1 will reflect at the centreline and intersect TP2 further downstream. These two reflection configurations are shown on Figure 1 designated as *Types 1* and *3*. Also shown are the limiting cases for both the above giving a total of five configurations, arbitrarily classified here with increasing primary cone length as *Types 0, 1, 2, 3* and *4*. A *Type 0* pattern is that established when the primary cone is of zero length and is simply the single cone with half-apex angle equal to the total wall angle. This is the basic case with which comparisons can be made. *Type 2* is the case where the trajectories meet exactly on the centreline and it therefore separates the two basic cases. *Type 4* is the intersection which occurs when TP1, reflected from the centreline reaches the wall exactly at corner 2. Further increases in the primary cone length would result in a repeat of the above cases except that they would now be preceded by one complete cycle of reflections from corner 1.

COMPUTATIONAL SOLUTIONS

The computational scheme used here has been described previously[4] for single cones and

is based on the ray-shock theory (Whitham[7]). Little additional modification is required for the present study of shock interactions with two (or more) cones.

The major differences in treatment are due to the TP intersections as discussed previously. Figure 2 shows the ray POQ through the intersection point. For the flow above ray POQ, no addition to the basic scheme is required. That is, calculations proceed through TP1, entry Mach numbers to TP2 are calculated and the reflection after TP2 follows. Essentially each corner is a separate calculation. For *Type 2* configurations, this completes the two-corner part of the calculations, analysis then reverting exactly to that applied to a single cone. For *Types 1* and *3*, further assumptions are necessary. To start the calculations below ray POQ, the ray direction OQ and the Mach number at that point are taken from the calculations of the flow above it. This defines a boundary for the lower part of the flow field. The Mach number of the shock exiting from the reflection may now not be identical above and below OQ. This is particularly noticeable with *Type 3* configurations due to its additional re-reflection from the centreline. As two immediately adjacent sections of a shock cannot move in the same direction with different velocities an adjustment needs to be made to the direction of OQ, orienting it at a slightly lesser angle to the centreline.

(a) *Type 1* Reflections

Typical results are shown on Figure 3 ($M_o = 2.4$ $\gamma = 1.4$, 10°-20° cone). These results can be compared with those for a single 20° cone[4] and can be seen to be generally similar. The effect of the primary cone is to alter the position of the first triple-point trajectory, centreline intersection point moving it slightly upstream away from the cone apex. The length x from this point to the cone apex is plotted on Figure 4 for a range of cases and has been normalized against the equivalent single cone. It can be seen from the figure that the primary cone length is the major variable affecting x and hence the stem length. Incident shock Mach numbers in the range considered have only a small effect as does isentropic index. The two-step entry to a cone of larger semi-apex angle (i.e. in these cases 20° compared to 10°) results in a bigger percentage increase in Mach stem length at the centreline location. Thus a greater gain in shock strength should be achievable by a cone of gradual entry when that cone has a larger apex angle.

(b) *Type 3* Reflections

Results are shown on Figure 5. The first position on the centreline where both corners influence the shock front is now closer to the apex and is downstream of the initial TP1, centreline intersection. It is not until this point is passed that a general similarity to *Type 0* or *Type 1* reflections appears. In this region, further increase in primary cone length reduces the relative size of the Mach stem. However, the Mach stem now becomes progressively stronger due to the increasing influence of the re-reflection of TP1 from the centreline.

EXPERIMENTAL WORK

Pressure Transducer Measurements

The basic experimental work for this project was carried out in a 189 mm diameter shock tube described previously[4]. The test sections were a 5°-10° and a 10°-20° cone combination both with a primary cone length of 1.343 times the shock tube radius. Incident shock Mach numbers of $M_o = 1.47 \pm 0.02$ and 2.40 ± 0.02 in air were used. The technique for locating the shock wave was to use an upstream facing pressure transducer on the end of a stiff centreline probe inserted through the cone apex[4]. The probe was moved incrementally with each of a large number of runs repeated under the same initial conditions, thereby giving a full centreline assessment of shock strength. Jumps in strength indicated the arrival and re-reflection of a Mach stem at the centreline.

Results are given on Table 1. The length of the primary cone is such that these should be *Type 3* reflections. The first jump is due to the unmodified triple-point trajectory from the first corner while the second and later jumps are caused by the combined trajectories from both corners.

TABLE 1

Cone Combination (Primary Cone Length $\ell/R = 1.343$)	Incident Shock Mach No.	Jump No.	Distance From Apex x/L		Shock Mach No.	
			Measured	Calculated	Measured	Calculated
5°-10°	1.47	1	0.65	0.628	1.34	1.38
		2	0.55	0.529	–	2.20
	2.40	1	0.695	0.681	1.40	1.42
		2	0.555	0.559	–	2.60
10°-20°	1.47	1	0.43	0.408	1.44	1.50
		2	0.32	0.307	–	2.80
		3	0.09	0.069	–	3.60
	2.4	1	0.485	0.482	1.75	1.80
		2	0.35	0.340	2.23	2.60
		3	0.09	0.071	3.45	3.80

It can be seen that good agreement exists in the shock location. From Figure 6 it can be seen that a very rapid fall-off in Mach number exists on the centreline immediately following the second and third jump positions. The possible error in determining the Mach number is therefore very much higher than that in locating the shock. Hence, additional runs were required to fully explore the Mach number close to these positions. This was only carried out in the 10°-20° cone with $M_o = 2.4$ and so information on Mach numbers is limited. However, for the data obtained, the agreement is reasonable.

Flow Visualization Techniques

Flow visualization for internal axisymmetric Mach reflection is extremely difficult and has not been used previously. However, because of the expected complexity of the wave patterns, experiments have been commenced. These are still under development but preliminary material is available.

In order to render the shock waves visible within a conical contraction, two approaches using holographic methods were examined. These were:

(i)   An arrangement similar to a shadowgraph in which a parallel beam of light is passed through a transparent test section with an aspheric external surface. This maintains the light rays parallel to the original direction through the test section. This method has been described by Takayama and Onodera[8] and is referred to simply as holographic interferometry.

(ii) A diffuser is placed in the light path just before the test section, which uses a simple cylindrical external surface. This is referred to as real time holography.

For both methods pulsed light from a holographic ruby laser was used, split 60:40 between the object beam and the reference beam.

Holographic Measurements

With the first method, a simple cone of 10° semi-apex angle was machined into a transparent section with an aspheric outer surface similar to that previously reported [8]. The cone was connected to a 50mm diameter shock tube. For the real time holographic experiments, a multiple 10°-20° semi-apex angle cone (primary cone length $\ell/R = 0.532$) was machined

into similar transparent material and was connected to a 100mm diameter shock tube. Both shock tubes used air as the test gas with a Mach number $M_o = 1.75$ or 1.76 ± 0.03.

The holographic interferometric observation gives a clearer photograph with better spatial resolution but it requires test sections which are difficult to construct. With the real time holography, the position of the triple-point and the shape of the main shock front and Mach stem can be adequately observed. Results for the single 10° cone are summarized in Figure 7 and show a distinctly curved triple-point locus as predicted by the calculations. A slight backwards curvature in the Mach stem is also observable and corresponds to the increasing ray angle near the centreline. With the aspheric lens, the diffraction of the light rays slightly displace the shock along its axis. This has been calculated as 0.292R on the centreline. Calculations modified for this distortion are shown on Figure 7 where good agreement exists. The results for the multiple 10°-20° contraction are shown on Figure 8. There is again good agreement with experiment.

CONCLUSIONS

Computational techniques based on the ray-shock theory and used previously to calculate reflection patterns for a shock wave moving into a single cone have now been extended to multiple cone combinations. This allows examination of the effect of a gradual approach to the contraction and is a first step in the study of shock movement into contoured nozzles and contractions. For the double cone case, a number of different reflection patterns have been identified, the pattern depending on the primary cone length.

Experiments have now been carried out using centreline pressure transducer measurements for the double cones and holographic flow visualization methods for both double and single cones. Good agreement has been obtained with calculations, particularly at the highest Mach number tested. With the holographic methods, a transparent test section with a single 10° half-apex angle cone machined inside and an aspheric outer surface gave good clarity. However, diffuse, real-time holography allowed a simpler test section. Here, the clarity was reduced but the shock wave shapes and triple-point position could be adequately distinguished. These flow visualization techniques confirm the computational predictions that the triple-point trajectory has substantial curvature and the Mach stem a small curvature. These experiments are still in the preliminary stages and further data is required.

REFERENCES

1. Smith, L. G., "Photographic Investigation of the Reflection of Plane Shocks in Air," Rpt. 6271, Office of Scientific Research and Development, Washington D.C., November 1945.

2. Henderson, L. F. and Gray, P. M., "Experiments on the Diffraction of Strong Blast Waves," Proc. Roy. Soc., London, A377, 1981, pp. 363-378.

3. Setchell, R. E., Storm, E. and Sturtevant, B., "An Investigation of Shock Strengthening in a Conical Convergent Channel," J. Fluid Mech., 56, 3, 1972, pp. 505-522.

4. Duong, D. Q. and Milton, B. E., "The Mach Reflection of Shock Waves in Converging Cylindrical Channels," Experiments in Fluids, 3, 1985, pp. 161-168.

5. Takayama, K., Onodera, O. and Ben-Dor, G., "Holographic Interferometric Study of Shock Transition Over Wedges," Proc. Int. Congress of High Speed Photography and Photonics, Strasbourg, August 1984.

6. Milton, B. E., "Moving Shock Wave Behaviur in Area Contractions of Arbitrary Shape," Proc. 5th A'asian Conf. on Hyd. & Fluid Mech., Canterbury, New Zealand, December 1974, pp. 492-499.

7. Whitham, G. B., "A New Approach to Problems of Shock Dynamics, Part 1: Two Dimensional Problems," J. Fluid Mech., 2, 1957, pp. 145-171.

8.   Takayama, K. and Onodera, O., "Shock Wave Propagation Past Circular Cross Sectional 90° Bends," Shock Tubes and Waves, Proc. 14th Int. Symp. on Shock Tubes and Waves, Sydney, August 1983, pp. 205-212.
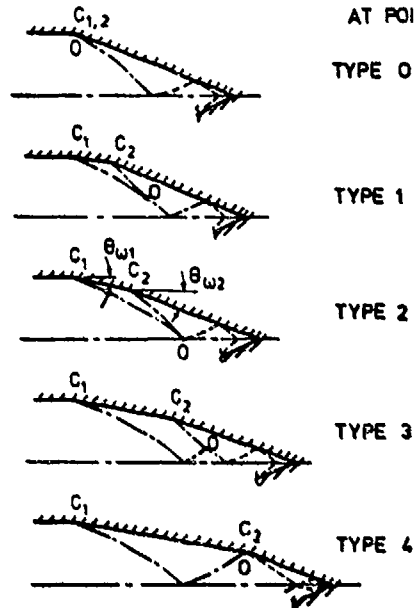
Fig. 1   Possible Reflection Patterns for a Two-Step Corner
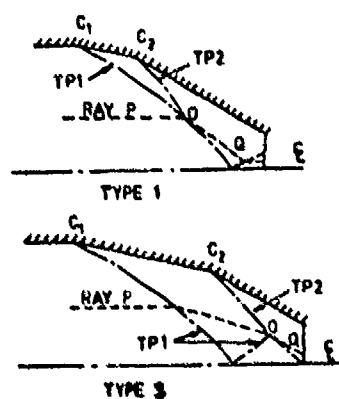
Fig. 2   Intersection Patterns of TP Trajectories for Calculation
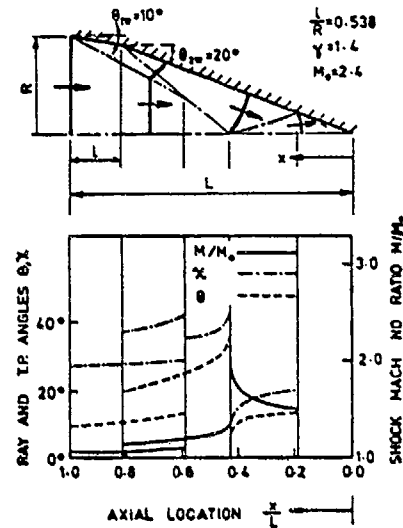
Fig. 3   Typical Results of Calculations. *Type 1*
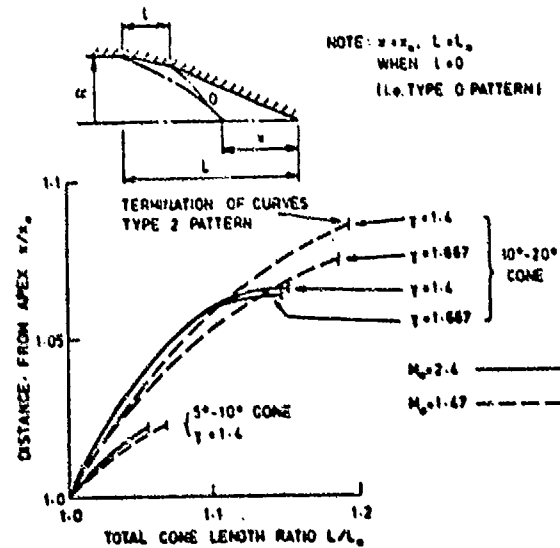
Fig. 4   Trends in Mach Stem Length, *Type 1*
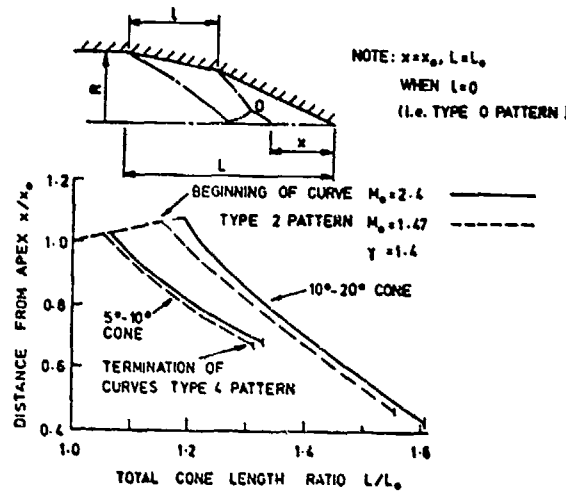
Fig. 5 Trends in Mach Stem Length,
Type 3
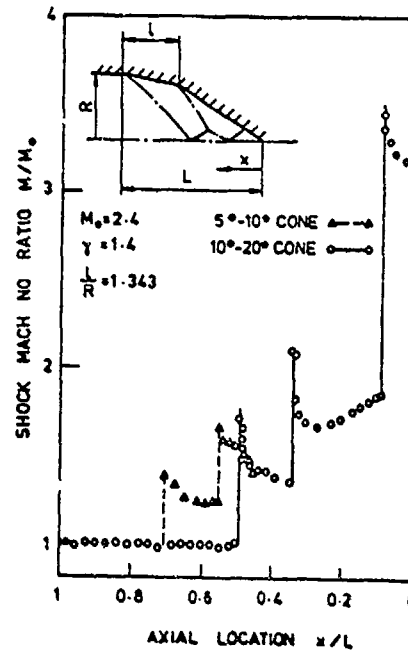
Fig. 6 Pressure Transducer
Measurements
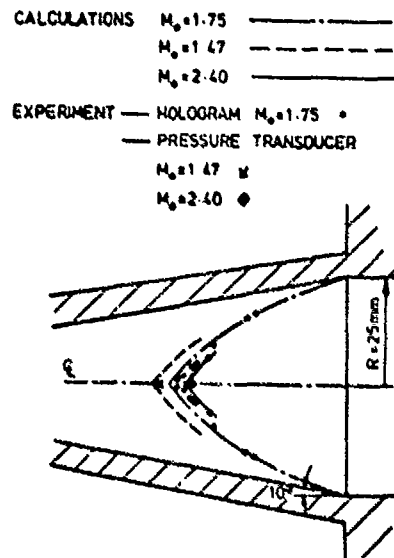
Fig. 7 Holographic Interferometry
Measurements in a Single Cone
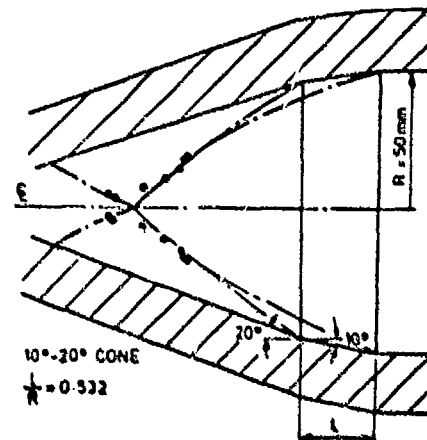
Fig. 8 Real Time Holographic
Measurements in a 10°-20° Cone,
Type 1

IRREGULAR SHOCK DIFFRACTION SYSTEMS

L.F. Henderson

Department of Mechanical Engineering
University of Sydney, Sydney NSW, 2006, Australia

A new criterion is proposed for the transition between
regular RR and Mach MR reflexion. It is based on the
minimum surface pressure condition which occurs for
example when a plane shock diffracts over a concave
corner. Although experiment indicates that the new
criterion is invalid for rigid adiabatic surfaces it
may possibly be relevant for liquid or flexible surfaces.
An exact expression is presented for it. A detailed
classification scheme and topological map in (ξ_i, θ_w)
coordinates is presented for the shock systems that
occur during diffraction.

I. INTRODUCTION

If a plane shock i of inverse strength $\xi_i \equiv P_o/P_1$ diffracts over a concave
corner of apex angle θ_w in a gas with ratio of specific heats γ then the pres-
sure P_2 on the surface of the ramp just downstream of the reflected shock r can
be calculated by the von Neumann theory[1] provided that the shock system is a
regular reflexion RR. Figure 1 shows that P_2 at first decreases with decreasing
θ_w (or increasing shock incidence $\omega_o = \pi/2 - \theta_w$) until it reaches a minimum
$P_2 = P_{min}$, but after that P_2 increases rather rapidly, so there is a sign change
of $\partial(P_2/P_o)/\partial\theta_w$ at $P_2 = P_{min}$. Subsequently the pressure reaches a maximum and
then a further decrease in θ_w will result in transition to an irregular reflex-
ion IR, such as a Mach reflexion.

In this paper we present an expression for the minimum pressure point and
propose it as a possible criterion for the onset of IR for the special case
when the reflecting surface is flexible. In addition we consider the sequence
of IR systems that occur as θ_w varies from $\pi/2$ to zero with constant (γ, ξ_i)

2. THE MINIMUM PRESSURE CONDITION

2.1 The condition

It is obtained from the RR theory by deriving $\partial(P_2/P_o)/\partial\omega_o = 0$. If
$\omega_o = \omega_{min}$ and $x \equiv \sin^2\omega_{min}$, the result is,

$$B_4 x^4 + B_3 x^3 + B_2 x^2 + B_1 x + B_o = 0 \qquad (1)$$

where,

$$B_4 \equiv 16\gamma(1-\xi_i)^2 \left[-(\gamma+1) + 2(\gamma+1)\xi_i + (3\gamma-1)\xi_i^2\right]$$

$$B_3 \equiv 32\gamma(1-\xi_i)^2 \left[(\gamma+1) + (\gamma-1)\xi_i\right]^2 \qquad (2)$$

$$B_2 \equiv 4\left[(\gamma+1) + (\gamma-1)\xi_i\right]^2\left[-(3\gamma^2+6\gamma+1) + 2(-\gamma^2+4\gamma+1)\xi_i + (\gamma+1)(\gamma-1)\xi_i^2\right]$$

$$B_1 \equiv 8\left[(\gamma+1) + (\gamma-1)\xi_i\right]^4$$

$$B_o \equiv -(3-\gamma)\left[(\gamma+1) + (\gamma-1)\xi_i\right]^4$$

2.2   The condition as a criterion for the onset of irregular reflexion

Suppose there is a hinge at the corner so that the pressure applied to the rigid sloping surface causes a clockwise torque T_i to be exerted about the hinge Figure 2. Suppose also that T_i is balanced by an equal and opposite torque T_e applied by the surroundings to the system. Finally let the walls be adiabatic. The system can now be regarded as a purely mechanical one because it may exchange virtual or actual work with its surroundings but not heat. When $\pi/2 < \theta_w < \theta_{min}$, then by Figure 1, $\partial(P_2/P_0)/\partial\theta_w < 0$. Hence if θ_w is reduced by $d\theta_w$ (for example by reducing T_e by dT_e) then the system will respond by reducing P_2/P_0, and restore the torque equilibrium. It is concluded that the system is stable. However, if $\theta_{min} > \theta_w > \theta_e$, then $\partial(P_2/P_0)/\partial\theta_w < 0$. The sign change means that an infinitesimal reduction in θ_w and T_e will now cause P_2/P_0 to increase so that $T_i > T_e$ and the system becomes unstable. This suggests that the regular reflexion should undergo transition at $\theta_w = \theta_{min}$, or $\omega_0 = \omega_{min}$, to some other system such as Mach reflexion. However, experiment does not support this. The discussion so far has ignored the effect of the corner signal cs, but as θ_w decreases the cs moves closer to the reflexion point and reduces the area over which the Pressure P_2 can act. So even though P_2 may be increasing there is a reduction in pressure on other parts of the surface. Experiment indicates that consequently there is a decrease in T_i to match that of T_e even when $\partial(P_2/P_0)/\partial\theta_w < 0$. These arguments are based on the assumption that the surfaces are rigid and adiabatic, and the conclusion could be different when these assumptions are invalid. For example, if a shock diffracts over a flexible or liquid surface so that conditions in region 2 could prevail locally, then the minimum pressure criterion might be relevant, especially if after transition to some other system one gets $\partial(P_2/P_0)/\partial\theta_w > 0$.

3.   CLASSIFICATION OF SHOCKS

3.1 Strong and weak shocks

The separating condition between strong and weak shocks will be defined as the coincidence of the sonic and mechanical equilibrium criteria, $\xi_i = \xi_{cr}^*$, some data is given in Table 1.

γ	5/3	7/5	9/7
ξ_{cr}^*	0.30375	0.37531	0.40855
$\omega_0^* = \omega_n^0$	37.680	40.374	41.612

TABLE 1.   Alternative separation condition between strong and weak incident shocks $H_2 = 1$

It has the important property that the flow downstream of the reflected shock r is sonic, $H_2 = 1$. Consequently, for weak shocks near transition the flow downstream is subsonic $H_2 < 1$, and for strong shocks it is supersonic $H_2 > 1$. The property $H_2 > 1$ is a necessary condition for the appearance of systems with additional waves such as for example double Mach reflexion DMR. The strong-weak boundary is plotted in Figure 3.

3.1 Forward and backward facing waves

It will also be convenient to classify the waves as belonging to either the forward or backward families. A wave is in the forward family if it

deflects the streamlines through the angle δ in the positive (anticlockwise) sense, and in the backward family when the deflexion is in the opposite sense. Here, i is always selected to be in the forward family. So r is always a backward facing shock in RR, Figure 2. In MR, r may be in either family, but the separating condition between the two families is when r is a normal shock, $\delta_1 = 0$, $\omega_0 = \omega_a$ say. After a lengthy calculation, a closed form expression can be obtained for it, namely a polynomial of degree 4 in $x \equiv \sin^2 \omega_a$. Exact expressions for its roots are,

(i) $x \equiv \sin^2 \omega_a = 1$, that is $\omega_0 = \omega_a = \pi/2$, which is trivial in that all three shocks i,r,s in MR coincide to form a single normal shock.

(ii)

$$x \equiv \sin^2 \omega_{g1} = \frac{[(\gamma+1) + (\gamma-1)\xi_1]^2}{2\gamma[(\gamma+1) + (\gamma+1)\xi_1 - 2\xi_1^2]} , \tag{3}$$

This root is also trivial because r degenerates to a Mach line, and i and s become a single plane shock. It corresponds to glancing incidence, $\theta_w = 0$, $\omega_0 = \omega_a = \omega_{g1}$ say, $M_1 = M_2 = 1$.

(iii) the other two roots may be obtained from,

$$G_2 x^2 + G_1 x + G_0 = 0, \tag{4}$$

where,

$$G_2 \equiv 2\gamma[(\gamma+1) + (\gamma-1)\xi_1](1-\xi_1)[(\gamma+1) + (\gamma+3)\xi_1] ,$$

$$G_1 \equiv -\{(\gamma+1)^2(3\gamma+1) + (\gamma+1)(\gamma^3+3\gamma^2+3\gamma-3)\xi_1 + (2\gamma^4+3\gamma^3-9\gamma^2-15\gamma+3)\xi_1^2 \tag{5}$$

$$+(\gamma^4+2\gamma^3-4\gamma^2+10\gamma-1)\xi_1^4\},$$

$$G_0 \equiv [(\gamma+1) + (\gamma-1)\xi_1]^3 ,$$

and where only the negative branch root is of physical significance, Figure 3.

4. IRREGULAR REFLEXION

For constant (γ,ξ_1) an irregular reflexion IR will appear whenever θ_w becomes small enough, or ω_0 large enough. The IR is typically some form of Mach, or other "non-specular" reflexion, Figure 3.

4.1 Weak shocks

For weak shocks $M_2 < 1$, after transition so the entire flow downstream of r is able to influence the triple point, and in particular the corner signal cs can always catch up with it. Because $M_2 < 1$, a single Mach reflexion SMR is expected after transition, with r backward facing. As θ_w decreases, r eventually becomes a normal shock as determined by equations (4) and (5), and beyond that it is forward facing, Figure 3. As θ_w continues to decrease the condition for sonic flow downstream is eventually attained $M_2 = 1$. This is a catch-up condition for the corner signal, but with the difference that r is forward facing, whereas r is usually a backward wave at catch-up. Beyond this condition $M_2 > 1$ and it becomes possible for other waves to appear, for example a fourth shock or an expansion wave[2,3], Figure 3. If θ_w decreases still further r approaches a Mach line degeneracy and this condition has been determined by Wuest[4]; after correcting and rewriting his result we get,

$$SIN^2\omega_w = \frac{\left[(\gamma+1)+(\gamma-1)\xi_i\right]\left\{(\gamma+1)+(3\gamma-1)\xi_i\pm(\gamma+1)\left[\left(1+\frac{\gamma-1}{\gamma+1}\xi_i\right)\left(1+\frac{\gamma+1}{\gamma-1}\xi_i\right)\right]^{\frac{1}{2}}\right\}}{2\gamma\left\{\left[(\gamma+1)+2(\gamma+1)\xi_i+(\gamma-3)\xi_i^2\right]\pm(\gamma+1)(1+\xi_i)\left[\left(1+\frac{\gamma-1}{\gamma+1}\xi_i\right)\left(1+\frac{\gamma+1}{\gamma-1}\xi_i\right)\right]^{\frac{1}{2}}\right\}} \,,$$

(8)

According to present theory the reflected shock r cannot exist when $\omega_0 > \omega_w$. Now the flow downstream of i is supersonic relative to i, whereas that downstream of the Mach shock s is subsonic. The only possibilities seem to be for r to be either replaced by a band of compression waves continuously distributed downstream of i, Figure 4, or for viscous effects to become significant. The incident and Mach shocks now form a single wave without any slope discontinuity, and the system will be called a "continuous wave reflexion" CWR. In such a system the contact discontinuity cd would be replaced by a continuously distributed band of vorticity. The existence of a CWR has not been definitely established by experiment, but a photograph from Henderson and Siegenthaler's paper[5] may be a CWR.

The final development is for the reflected waves to weaken until they all become degenerate at glancing incidence. The condition is given by equation (5). All these conditions are plotted in Figure 3.

4.2   Very weak and extremely weak shocks

With constant (γ,ξ_i) and for weak shocks, single Mach reflexion SMR occurs in the range $\omega_0{}^{*}{<}\omega_0{<}\omega_0{}^{**}$, that is between the catch-up conditions for the backward and forward facing reflected shock. Inspection of Figure 3 reveals that the range shrinks with increasing ξ_i and vanishes for some $\xi_i = \xi_\alpha$, $\omega_0 = \omega_\alpha$. This occurs when the condition for sonic flow downstream of RR coincides with the sonic condition downstream of SMR with r a forward facing shock, Table 2 and Figure 3.

γ	5/3	7/5	9/7
ξ_α	0.7953	0.7989	0.8010
$\omega_\alpha{}^0$	52.047	52.118	52.173

TABLE 2.   Condition for the coincidence of the sonic condition downstream of regular reflexion $M_2{=}1$, with the sonic condition downstream of single Mach reflexion $M_2{=}1$, when the reflected shock is also a forward facing wave

An incident shock will be defined as "very weak" when $\xi_i > \xi_\alpha$. It is clear from Figure 3 that there are no Mach reflexions for these shocks, the only possibilities are regular RR, from wave FWR or continuous wave CWR reflexions.

If ξ_i increases still further then the range of ω_0 for FWR also shrinks, and eventually vanishes at $\xi_i = \xi_\beta$, $\omega_0 = \omega_\beta$ say. This is at the coincidence of the sonic condition downstream of RR and the Wuest limit, Table 3 and Figure 3. For $\xi_i > \xi_\beta$ only RR and CWR are possible, and these might be called "extremely weak shocks."

γ	5/3	7/5	9/7
ξ_β	0.84024	0.8328	0.8268
$\omega_\beta^{\,0}$	55.12618	54.2932	53.7592

TABLE 3.   Condition for the coincidence of the sonic condition down-
stream of regular reflexion $M_2=1$, with the Wuest limit when
the reflected shock and the fourth wave are Mach line
degeneracies

4.3 Strong shocks

Strong shock diffraction has the property that near transition the flow
downstream is supersonic $M_2>1$. Evidently, this is a necessary condition for the
appearance of extra waves in the system. When M_2 is only just larger than one
then r is observed to develop a rapid change in its slope, a "kink" K Figure 4,
called a "complex Mach reflexion" CMR. For larger M_2 the change in slope at K
sharpens and an extra shock appears, to form a double Mach reflexion DMR. The
Mach number M_2 is variable downstream of r and according to Ikui et al[6] a CMR
changes into a DMR where $M_2 \geq 1$ at K.

For yet stronger shocks the vortex sheet from the primary triple point
moves forward and curls up tightly behind the Mach shock s Figure 4, causing s
to develop an inflexion point.[6,7,8,9] With experiments[7] in oxygen there is no
sign of the inflexion for $M_i = 7.1$, but there is for $M_i = 10.1$ and 11.7. In
freon 12 and with $M_i = 4.94$, there is an extra shock associated with the in-
flexion[9], and Colella and Glaz[10] found the same thing in their numerical studies
of $M_i = 8$ shocks in air. These will be called "hyper-Mach reflexions,"HMR.

If ω_0 increases beyond its value at, or near, transition it is found that
M_2 decreases. Eventually, the sonic condition is reached and after that $M_2 < 1$.
A strong irregular reflexion IR is then reduced to a single Mach reflexion,
Figure 3.

REFERENCES

1. Neumann, J. von. 1943. See, Collected Works, Vol. 6. 1963. Pergamon.

2. Guderley, K.G. 1962. The theory of transonic flow. Oxford: Pergamon Press.

3. Henderson, L.F. 1966. Aero. Quart. 17, 1-20.

4. Wuest, W. 1948. Z. Angew. Math. Mech. 28, 73-80.

5. Henderson, L.F. & Siegenthaler, A. 1980. Proc. R. Soc. A. 369, 537-555.

6. Ikui, T., Matsuo K., Aoki, T. & Kondoh, N. 1982. Bull. JSME, 25, 1513-1520.

7. Weynantes, R.R. 1968. Tech. Note Inst. Aerospace Studies, University of
    Toronto, UTIAS 126.

8. Law, C.K. 1970. Tech. Note Inst. Aerospace Studies, University of
    Toronto, UTIAS 150.

9. Semenov, A.H., Syshchikova, M.P. & Berezkina. M.K. 1970. Sov. Phys.
    Tech. Phys. 15, 795-803.

10. Colella, P. & Glaz, H.M. 1984. Paper read to the 4th Mach Reflexion
    Symposium, Tokyo and Sendai, Japan.

Figure 2. Reduction of the Diffracting System to a Mechanical System.
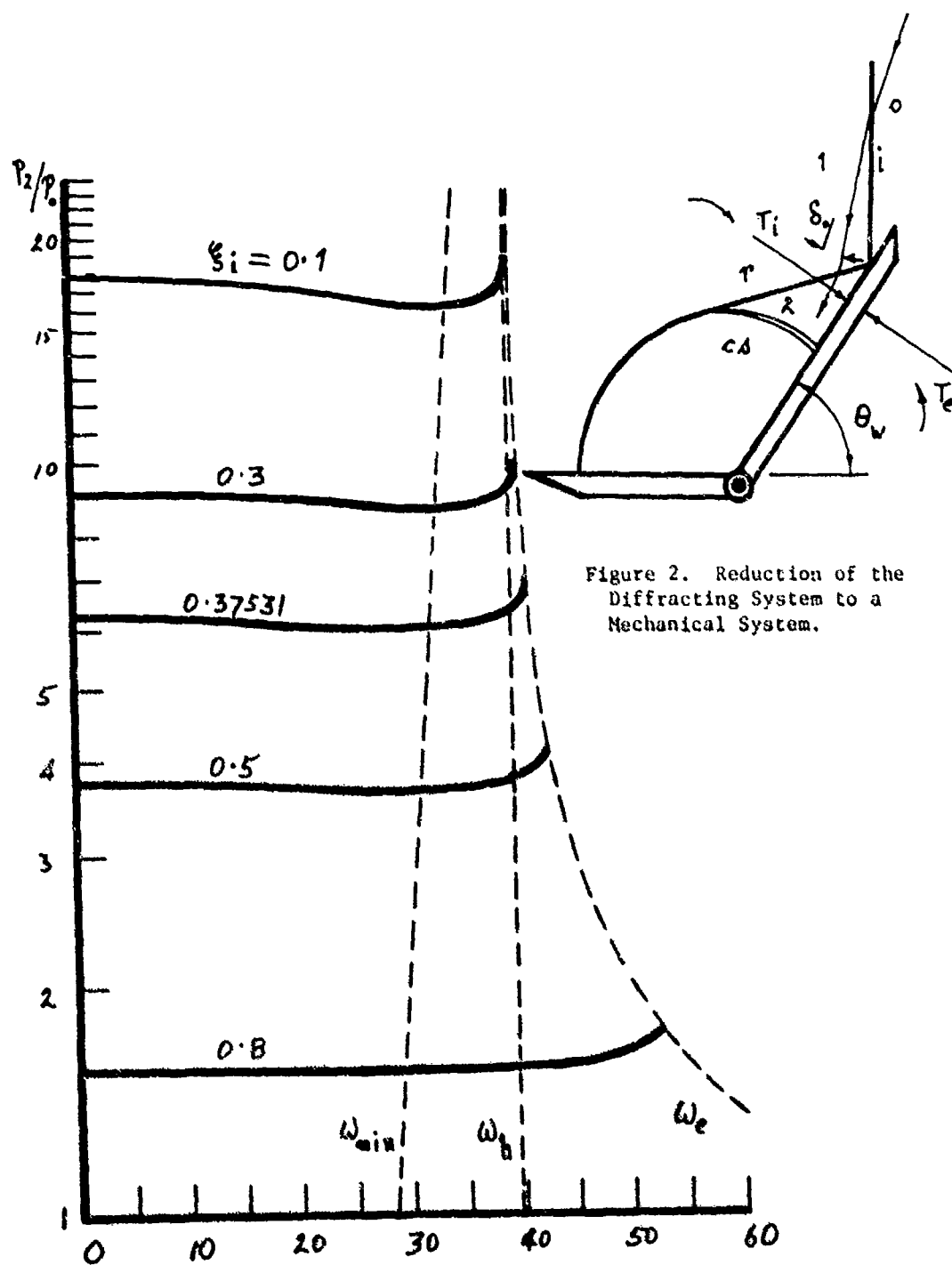
Figure 1. Surface Pressure Distribution on a Ramp Caused by a Regular Reflecting Diffracting Shock Wave.
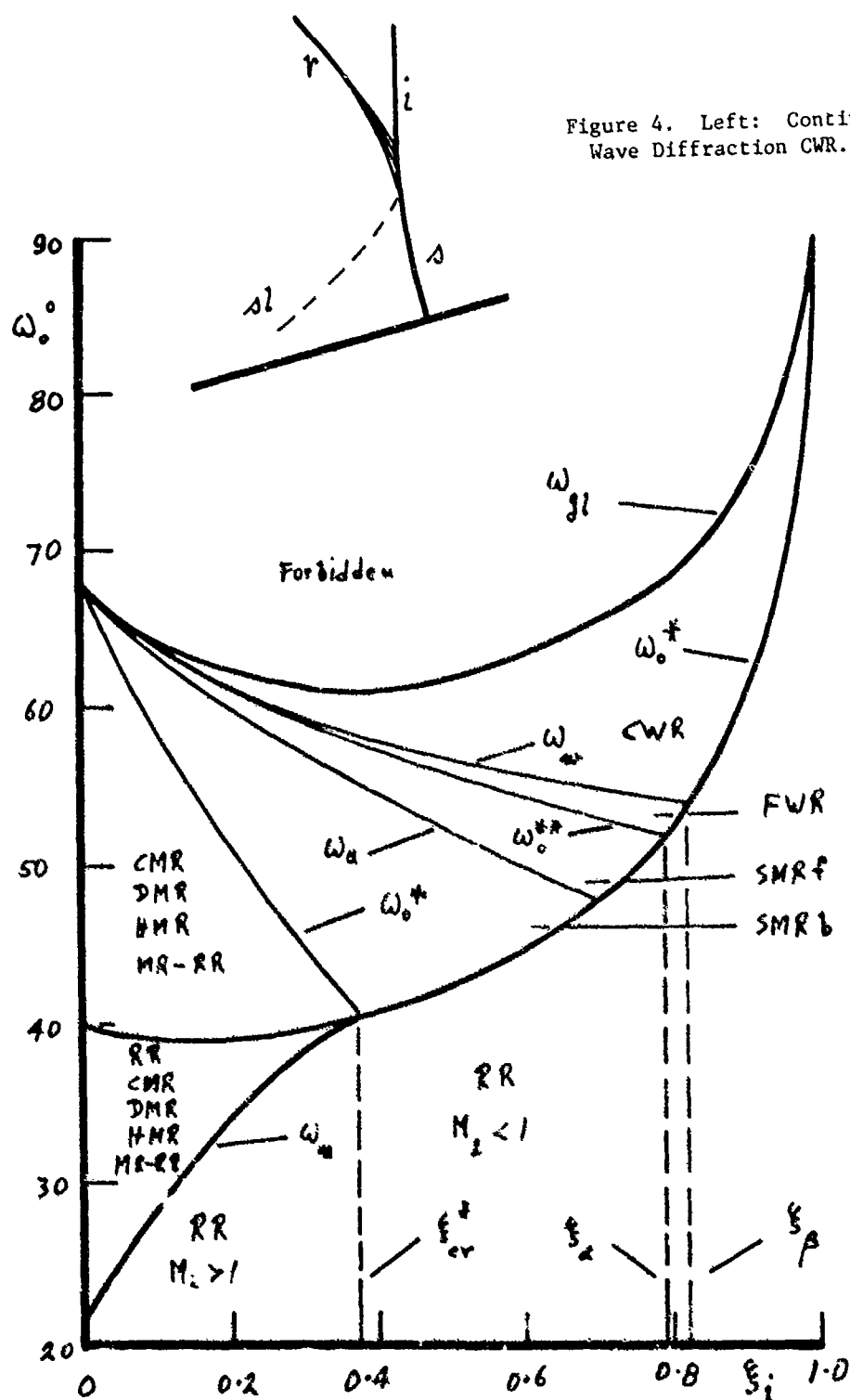
Figure 4. Left: Continuous Wave Diffraction CWR.

Figure 3. Topological Map for a Diffracting Shock Wave in a Monotonic Gas $\gamma = 5/3$

PSEUDO-STATIONARY MACH REFLEXION OF SHOCK WAVES

F. Seiler

Franco-German Research Institute Saint-Louis (ISL)
12, rue de l'Industrie, 68301 Saint-Louis. France

The pseudo-stationary oblique shock wave reflexion by a
wedge was numerically investigated by the direct Monte-
Carlo simulation technique. In this numerical study the
real gas flow is simulated at the molecular level by
using a large number of model particles following their
positions in phase space. In order to simulate the shock
reflexion from a wedge, a two-dimensional computational
model was set up. The incident shock wave is generated
by a piston, which is suddenly set in motion and then
moving into the flow at constant velocity. The incident
shock wave, simulated in a model gas of about 10000
particles, propagates down the gas and hits a wedge.
By oblique shock reflexion the reflected shock develops.
The calculations are carried out for a shock Mach number
3 and a monatomic gas with wedge angles from 30° up to
70°. The Monte-Carlo calculation results provide a full
picture of the variation of the most important flow param-
eters. The influence of the boundary layer on the reflect-
ed shock angle and the transition to Mach reflexion will
be discussed and compared with experimental data. It can
be seen that the boundary layer effect shifts the transi-
tion condition to higher incident shock angles. In addi-
tion, smaller reflected shock angles are produced.

1. INTRODUCTION

1.1 PHENOMENON

When a planar moving shock wave hits a reflecting wedge (Figure 1), the
incident shock wave (I) is reflected at the wedge surface and a reflected shock
wave (R) can be observed. Two fundamental types of shock reflexion appear. They
are regular reflexion (RR) and Mach reflexion (MR). The Mach reflexion can be
subdivided into single-Mach (SMR), complex-Mach (CMR) and double-Mach re-
flexions (DMR). The first to describe the phenomena of RR and SMR was E. Mach
in 1878. Since then detailed and thorough investigations of shock reflexion
have been performed by many researchers but until now its behaviour has not
been fully understood, especially the transition from regular to Mach re-
flexion of shock waves. The available theoretical descriptions of this pheno-
menon are in agreement with experiments only for relatively narrow ranges of
parameters.

The present paper has the aim to improve the understanding of the non-
stationary shock reflexion at a wedge with new numerical results, obtained by
a gaskinetic method, the so-called direct Monte-Carlo simulation technique [1]
Monte-Carlo calculations for the steady shock reflexion were already done by
Auld and Bird [2], showing that this gaskinetic method can also be applied under
a macroscopic aspect besides a microscopic one.

1.2 TRANSITION CRITERIA

With a Galilean transformation of the unsteady shock reflexion by a wedge
to the moving shock reflexion point P, the flow field can be considered as a

pseudo-stationary one. In this coordinate-system the wedge surface and the gas in region (1) move at speed u_1. The incident shock (I) deflects the flow towards the wall by an angle δ_2. Since the wall is impermeable, the flow must be deflected back parallel to the wall by the reflected shock (R). This process is best understood if pressure p is plotted against the deflexion angle δ as shown in Figure 2. The conditions upstream of the incident shock are represented by point 1 on the solid wave polar with $p = p_1$ and $\delta = 0$. The region downstream of the incident shock is denoted by point 2 with $\delta = \delta_2$. The point 3 behind the reflected shock lies on an appropriate dashed polar. As the wedge angle β_w decreases, i.e. the shock angle ζ_1 increases, δ_2 increases until the reflected shock reaches the maximum flow deflexion angle. This is the conventional criterion for the onset of Mach reflexion and is sometimes called the detachment condition. Mach reflexion becomes possible, where the point 3 just equals the pressure achieved from 1 through a normal shock. This smallest deflexion angle δ_2, at which Mach reflexion is theoretically possible was given by von Neumann, denoted as the von Neumann criterion [3]. Many experiments done in pseudo-steady flows support the detachment criterion, whereas some recent experiments in the steady case clearly support the von Neumann condition. Hornung et al. [3] advanced another criterion, that differs slightly from the detachment condition. They suggest, that regular reflexion (RR) terminates, when the flow behind the reflected shock becomes sonic with respect to the reflexion point P (sonic criterion).

1.3 BOUNDARY LAYER EFFECTS

Regular reflexion is theoretically not possible for shock angles $\zeta_1 > \zeta_{1,d}$. Some experimental results [3,4] indicate, that the transition occurs at significantly higher values $\zeta_{1,tr} > \zeta_{1,d}$ with $\zeta_{1,tr} - \zeta_{1,d}$ up to several degrees. Taking into account the viscosity and heat conduction, the flow field shown in Figure 3b can explain the modified transition conditions. Considering the regular reflexion in the reflexion point reference, a uniform flow with the velocity u_1 strikes the incident shock. After the shock reflexion the flow velocity is lower than u_1, but the wall velocity remains at u_1. The developing boundary layer acts as a mass sink and this displacement effect can be considered by a negative displacement thickness δ^*. Therefore the flow deflexion through the reflected shock is smaller than in the inviscid case. The p, δ map (Figure 3a) illustrates this boundary layer effect. The flow direction can have a component perpendicular to the wall with a small flow angle ϵ, determined by the growth of the displacement thickness. It is evident that this behaviour results in a transition shock angle $\zeta_{1,tr}$ shifted to larger values by an amount of approximately ϵ. Consequently the wedge angle $\beta_w = 90° - \zeta_1$ at which transition occurs moves to smaller values.

A further consequence of the boundary layer influence should result in a smaller reflected shock angle ζ_3, whereas experimentally the opposite has been observed [3].

2. DIRECT MONTE-CARLO SIMULATION

2.1 THEORETICAL DESCRIPTION

The flow field under consideration was numerically investigated by the direct Monte-Carlo simulation technique developed by Bird [1]. This method is a statistical one, which describes the behaviour of the gas flow on the molecular level. In this gaskinetic theory, the distribution function for the molecular velocities provides a statistical description of the gas pattern. The basic equation which describes the change of the distribution function is the Boltzmann equation. Bird [5] showed, that the Monte-Carlo calculation results are a solution to the Boltzmann equation.

In order to use this simulation technique for calculating the flow field under consideration, a two-dimensional computational model was set up as shown in Figure 4. The real gas flow in the physical space is simulated by some thou-

sands of particles, why this technique can only efficiently be used with a sufficiently large and fast computer. The velocity components and position coordinates are stored in the computer and are followed in time.

The simulation procedure starts with particles having a Maxwellian velocity distribution corresponding to thermodynamic equilibrium in the quiescent gas at the temperature T_1. These particles are uniformly distributed in space, which is subdivided in a sufficiently small network of cells. The simulation proceeds in discrete time steps. During these steps, the particles move according to their individual velocities and are reflected at the flow boundaries. At the wedge surface, the particles are reflected once specularly for simulating an inviscid gas flow and twice diffusely to simulate a boundary layer development at the wedge surface. In this case the moving gas particles are slowed down at the wedge and then take the wall temperature. At all the other boundaries specular reflection is always used. The incident shock wave is generated by a piston, which is suddenly set in motion and moves at constant velocity into the flow from left (see Figure 4). The shock wave propagates down the gas and impinges on the wedge surface. With proceeding time the incident shock wave climbs up the wedge and a reflected shock wave can be observed. At each time stop, representative collision pairs are selected randomly in each cell according to their relative speed. The collision process is calculated classically with the hard sphere model.

The macroscopic quantities, for example density, temperature etc. can be extracted by sampling and averaging over appropriate molecular quantities in each cell. Because the number of molecules considered is small, the fluctuations of the macroscopic quantities are significant. The fluctuations are reduced by averaging the computational results of about 35 independent calculation runs.

2.2 INPUT DATA

All calculations were carried out on a Bourroughs 7700 computer. The initial number of simulation particles within the whole flow field was 11500 for all runs. The initial cell size in ξ-direction was 2.3. The cell size in the η-direction has been enlarged with increasing distance from the wedge surface, beginning with a width of 2. In the simulation procedure all the lengths are normalized by the mean free path of the real gas particles. Since the cell size was chosen larger than the mean free path, a smearing effect of the shock wave profiles is produced. The cell size acts as a second characteristic length besides the mean free path, when the cell size is within the range or greater than the mean free path.

The shock reflexion was calculated for an incident shock Mach number of 3 for a perfect monatomic gas. The wedge angles are varied from 30° up to 70° with steps of 10°. The time counter in the simulation calculations was continued until the incident shock wave moved about 200 mean free paths on the wedge surface behind the leading edge.

3. CALCULATION RESULTS

The results of the Monte-Carlo calculations are given in Figure 5 by means of lines of equal density $\rho_n = (\rho - \rho_1)/(\rho_2 - \rho_1)$. The statistical scatter of the Monte-Carlo calculation results was eliminated by drawing smooth curves through the points representing the sampling results for the individual cells.

Without boundary layer for a wedge angle $\beta_w = 70°$ (Figure 5a) the density contours show a well established regular reflexion (RR). The reflected shock angle ζ_3 can be determined to be about 15°. The corresponding density contours for the case of $\beta_w = 60°$ can be seen in Figure 5b. Here, likewise RR occurs with an angle ζ_3 of approximately 25°. The two sets of contours without displacement effects in Figure 5c and 5d are for wedge angles of 50° and 40°, respectively. These wedge angles are both above the detachment criterion value

of $\beta_{w,d} = 54.2°$ at which Mach reflexion should appear. The two density fields referred look different from those of regular reflexion. The Mach stem can clearly be seen and increases in length going from $\beta_w = 50°$ to the picture with $\beta_w = 40°$. At both angles there appears a growing region of subsonic flow, viewed from the frame of reference of the reflexion point. The mentioned signs are characteristic ones for the Mach type reflexion nature. Therefore it can be suggested that Mach reflexion is present for both wedge angles. Besides, a kink in the outer density contours is established, as can be seen for complex Mach reflexion (CMR). It seems to be evident from Figure 5 that in these two cases CMR is present. For supporting this statement test calculations with many more model particles, smaller cell widths and a more realistic inter-molecular potential are necessary to be sure that no numerical instability effects may lead to the given Mach type reflexion interpretation of the Monte-Carlo simulation results. Finally on the left side of Figure 5e a well develop-ed single-Mach reflexion (SMR) can be seen, corresponding to $\beta_w = 30°$. A clear Mach stem is visible and the triple-point has significantly moved away from the wall. For the three Mach type cases ($\beta_w = 30°$, 40° and 50°) the triple-point trajectory angle χ can be determined to about 8.5°, 5° and 2.5°.

The results of the simulation calculation with boundary layer are given on the right side of Figure 5. The density results can be interpreted in such a way, that regular reflexion (RR) appears for wedge angles $\beta_w = 70°$, 60° and 50°. That means, that RR exists at a wedge angle of 50°, where Mach reflexion should be in question. As discussed before, the wall displacement effect of the boundary layer shifts the transition point to larger values of the shock angle ζ_1, i.e. to smaller wedge angles β_w, in agreement with the shown regular reflexion type for $\beta_w = 50°$. Likewise in agreement with the expected displace-ment effect, the reflected shock angles (for $\beta_w = 70°$, 60° and 50°: $\zeta_3 = 10°$, 15° and 25°) are smaller than for the calculated inviscid flow. For $\beta_w = 40°$, the reflexion type could not be determined exactly, because the density field contains elements of both, regular as well as Mach reflexion. There seems to exist a mixed reflexion type, pointing out that for smaller wedge angle Mach reflexion must occur. This is confirmed by the density picture for $\beta_w = 30°$. The triple-point trajectory angle χ has a value of about 4° below the angle without boundary layer. Regarding the density contours, the kink mentioned above is again visible, and so complex Mach reflexion (CMR) can be assumed.

In Figures 6 to 8 the temperature and velocity flow fields, calculated without boundary layer effect, are illustrated by means of lines of constant temperature $T_n = (T-T_1)/(T_2-T_1)$, constant $v_n (=v/u_2)$- and $u_n (=u/u_2)$-velocities. for wedge angles $\beta_w = 30°$ (MR) and 70° (RR). The temperature contours of Figure 6 are similar to the density contours of Figure 5 and give a represent-ative impression of the two different reflexion types of shock waves. Similar-ly, the v_n-velocity lines of Figure 7 show the regular and Mach type reflexion. The most significant differences can be seen on the u_n-velocity pictures (Figure 8). The step from RR to MR changes completely the u_n-velocity field. In the Mach type case behind the Mach stem, a region with relatively high u_n-velocities is formed, which seems to correspond to the flow field between the slipstream (S) and the Mach stem (M).

In Figure 9 the reflected shock angle ζ_3 is plotted against the wedge angle β_w. The solid line gives the solution of the oblique shock equations for the two shock configurations. It can be seen that the Monte-Carlo simulation results without boundary layer effects are slightly above the plotted two-shock solution, whereas the values with wall displacement are lower, in con-trast to measurements in argon, which have always given higher reflected shock angles.

The dependence of the triple-point trajectory angle χ on the wedge angle β_w is plotted in Figure 10. The calculation (solid line) just as the experi-mental points are given by Ben-Dor & Glass [6]. The results of the Monte-Carlo calculation, taken from the density contours of Figure 5, are also included in Figure 10. The points in the cases without boundary layer are in relatively

good agreement with the data of Ben-Dor & Glass. The simulation with boundary layer considerations shows a much lower value of χ.

The Monte-Carlo simulated reflexion type results are compared in Figure 11 with the non-stationary shock wave reflexion regions indicated by Ben-Dor & Glass [6] for monatomic gases in a M_S, β_w' map. The effective wedge angle β_w' of Figure 11 equals $\beta_w + \chi$ in the domains of SMR, CMR and DMR and β_w in the domain of RR, where $\chi = 0$. The points deduced from the calculations executed without displacement effects are well within the predicted regions, whereas those without wall displacement show a slight disagreement. These points are shifted to smaller effective wedge angles, i.e. the transition to Mach reflexion occurs at larger incident shock angles, which is in agreement with the considerations made about the displacement influence on the transition condition.

The domain of no reflexion (NR) disappears, when the vertical axis is transformed to the actual wedge angle β_w of Figure 12. In this more physical plane the quintessence is the same as before. The Monte-Carlo simulation without boundary layer agrees well with the given shock reflexion type domains [6], except for the point concerning a wedge angle $\beta_w = 30°$. Here, the simulation density contours show SMR, while CMR is predicted. But the deviation is relatively small. The boundary layer influence is also shown by the expected transition angle shifting. The simulation boundary layer calculations are supported by measurements of Hornung and Taylor [4], whose experimental incident shock angles ζ_1 lie up to 7° above the inviscid transition angle.

4. CONCLUDING REMARKS

The pseudo-stationary shock wave reflexion at the surface of a wedge has been calculated using the direct Monte-Carlo simulation technique. The calculations were carried out for monatomic perfect gases and a shock Mach number 3 with and without boundary layer development behind the reflected shock. Wedge angles β_w ranging from 30° to 70° with steps of 10° were considered. Following the detachment criterion, transition from regular reflexion (RR) to Mach reflexion (MR) occurs at a wedge angle of 54.2°. The inviscid calculations show RR for $\beta_w = 60°$ and MR for $\beta_w = 50°$, in agreement with the predicted transition. The boundary layer influence produces a smaller transition wedge angle, i.e. a higher incident shock transition angle ζ_1. For $\beta_w = 50°$ RR occurs. The shock transition angle, exceeding the detachment criterion is in agreement with the negative wall displacement effect of the boundary layer behind the reflected shock and is supported by several experimental results.

As theoretically predicted, the calculated reflected shock angles ζ_3 with displacement effect are below the results without wall displacement. This fact contradicts measured shock angles.

Furthermore, the Monte-Carlo calculations provide a full picture of the variation of all important flow parameters. The main interest of this study was a macroscopic description rather than a microscopic aspect. Therefore it was tolerated that the shock wave widths are affected by the cell sizes, which have been chosen larger than the mean free path. As a consequence, the shock widths resulted too large. In further simulation calculations it would be necessary to investigate the influence of the cell size and the number of particles per cell in order to make sure that these parameters do not affect excessively the results obtained. Furthermore, calculations should be carried out with a more realistic intermolecular potential and a more realistic interaction between the wedge surface and the gas particles, from which the boundary layer development depends.

extremely extensive computations during 1980-1981 at the "Institut für Strömungslehre und Strömungsmaschinen" of the University of Karlsruhe and is indebted to Prof. B. Schmidt of the same institute for his suggestions, support and criticisms received at various stages of the work.

REFERENCES

1.   Bird, G.A., "Molecular gas dynamics", Clarendon Press, Oxford, 1976

2.   Auld, D.J. and Bird, G.A., "The transition from regular to Mach reflexion", Proceedings of the 9th Fluid and Plasma Dynamics Conference, San Diego, California, 1976

3.   Hornung, H.G., Oertel, H. and Sandeman, R., "Transition to Mach reflexion of shock waves in steady and pseudosteady flow with and without relaxation", Journal of Fluid Mechanics, Vol.90, Part 3, pp.541-560, 1979

4.   Hornung, H.G. and Taylor, J.R., "Transition to Mach reflexion of shock waves. Part 1. The effect of viscosity in the pseudosteady case", Department of Physics, Australian National University

5.   Bird, G.A., "Direct simulation and the Boltzmann equation", Physics of Fluids, Vol.13, No.11, 1970

6.   Ben-Dor, G. and Glass, I.I., "Domains and boundaries of non-stationary oblique shock-wave reflexions. 2. Monatomic gas", Journal of Fluid Mechanics, Vol.96, Part 4, pp.735-756, 1980
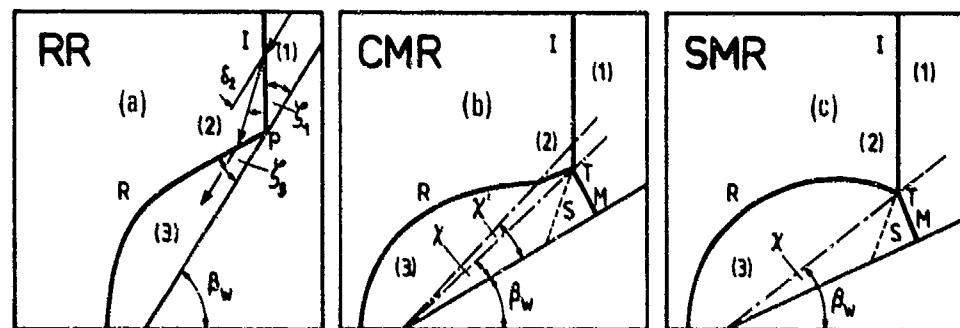
Figure 1. (a) Regular reflexion (RR), (b) Complex-Mach reflexion (CMR) and (c) Single-Mach reflexion (SMR) illustrations
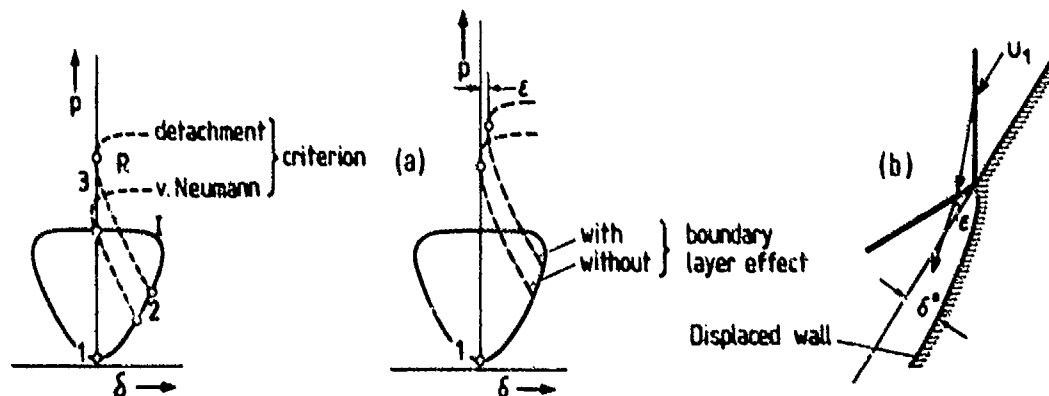
Figure 2. p, δ map

Figure 3. The wall displacement effect. (a) Effect on the p,δ map. (b) Displaced wall
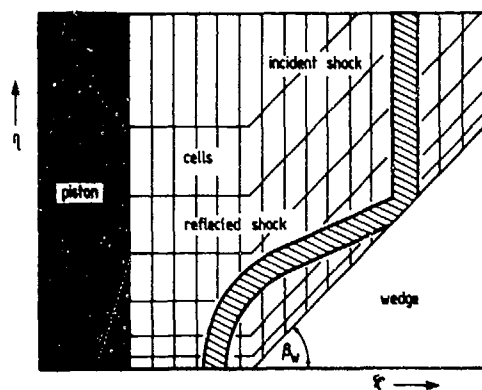
Figure 4.
Computational model

(a)

(b)
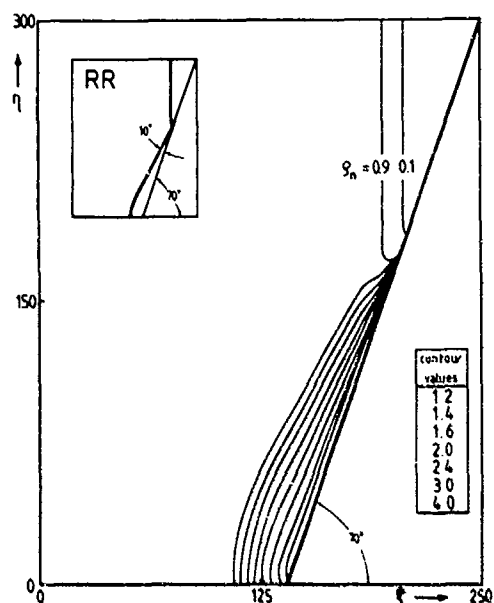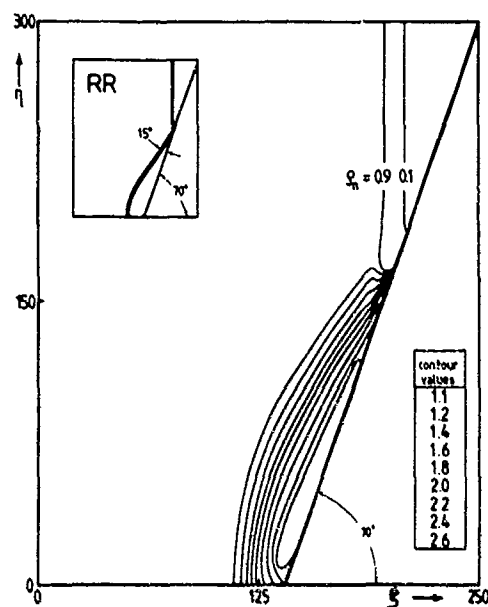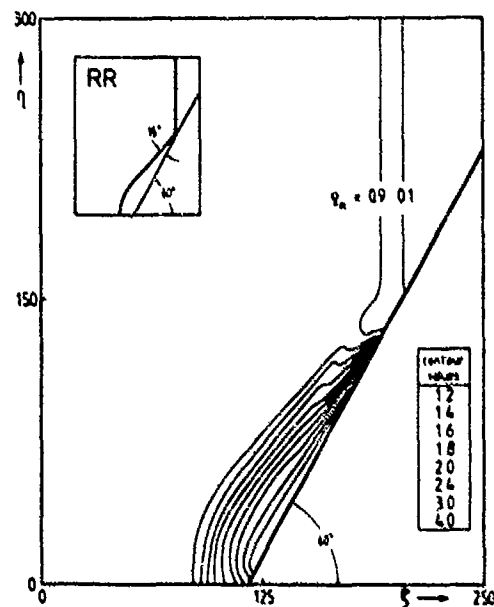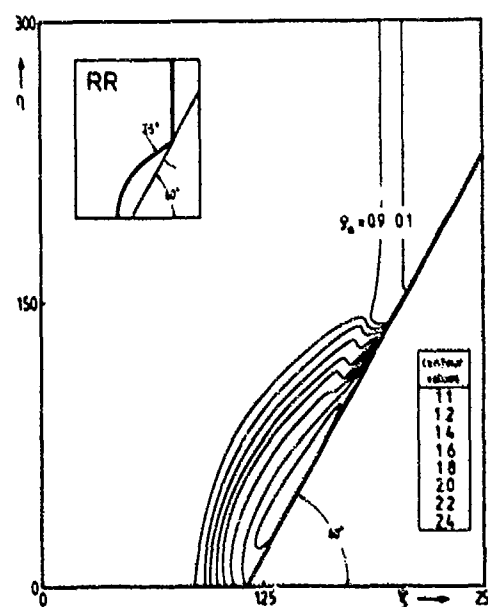
Without b.l.   Figure 5. For legend see page 137   With b.l.
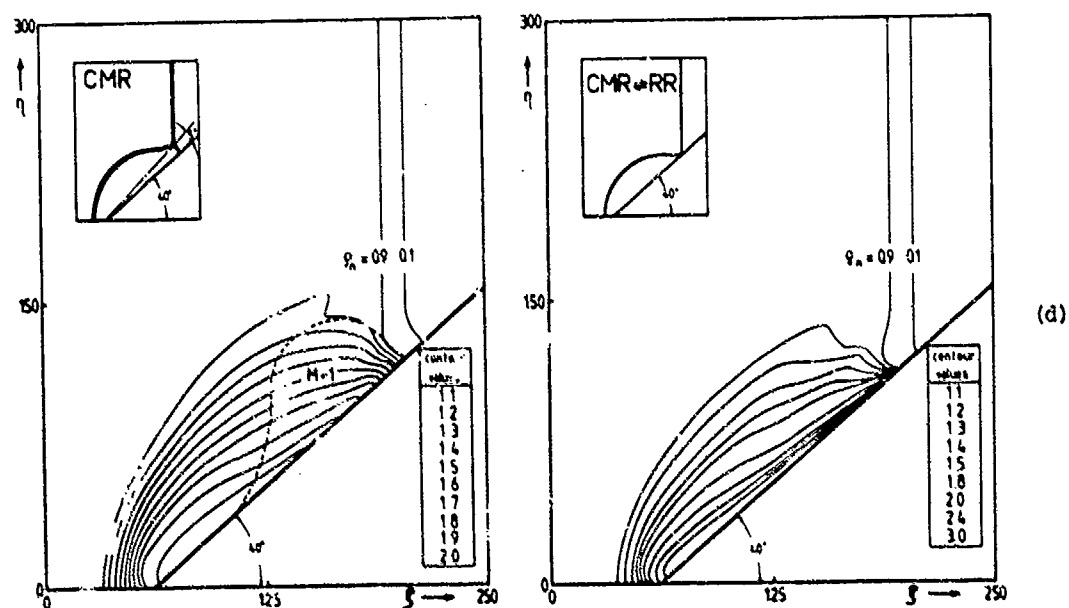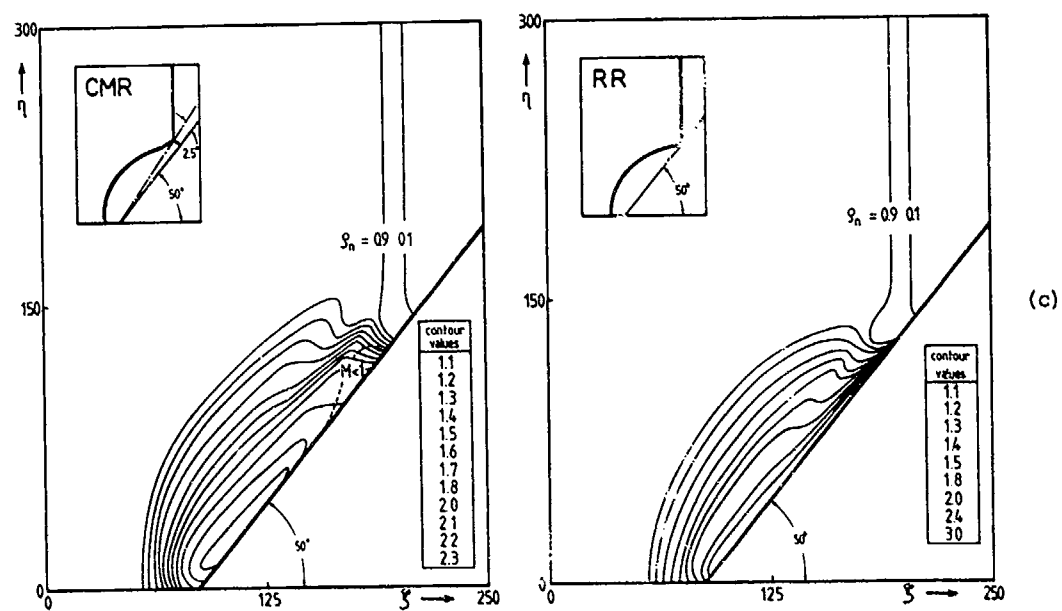
Figure 5. For legend see facing page

Without boundary layer   With boundary layer

Figure 5. Density contours from the simulation with and
without boundary layer

Figure 6.
Temperature contours
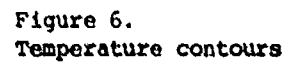
Figure 7.
v_n-velocity contours
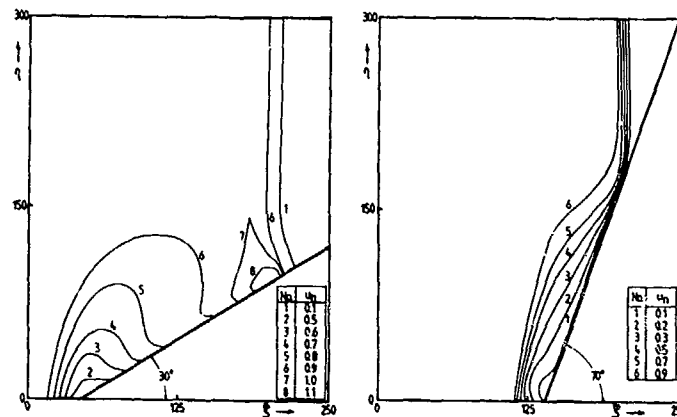
Figure 8.
u_n-velocity contours
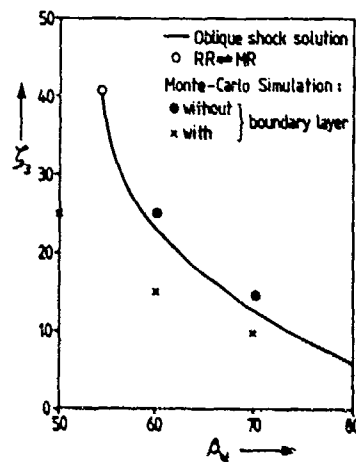
Figure 9. Re-
flected shock
angle ζ_3 as a
function of the
wedge angle β_w
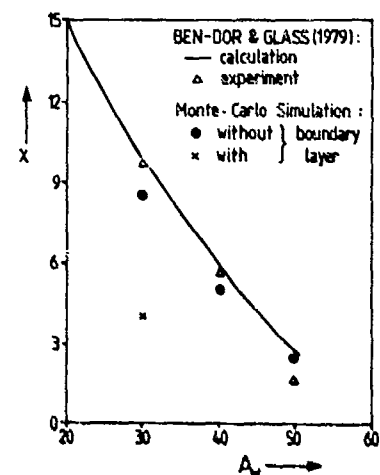
Figure 10.
Triple-point
trajectory
angle χ versus
wedge angle β_w
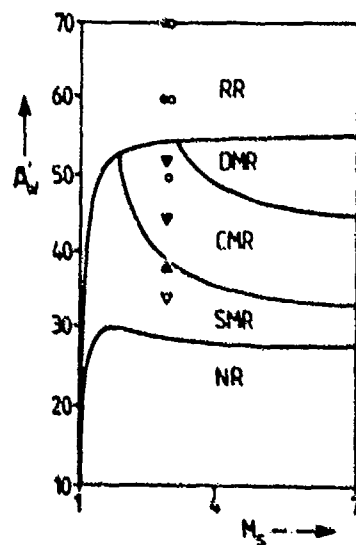
Figure 11. Regions of different oblique shock
wave reflexions given by Ben-Dor & Glass [6]

Simulation data with
boundary layer:
▽ CMR, △ SMR, ○ RR.
Data without bounda-
ry layer:
▼ CMR, ▲ SMR, ● RR
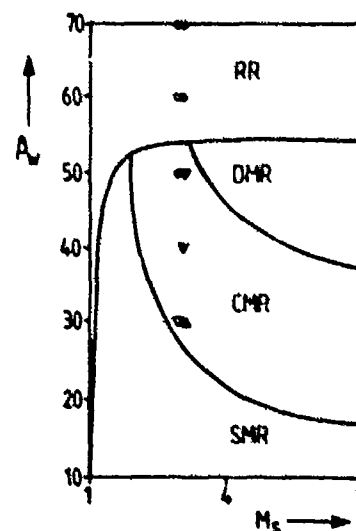
Figure 12. Domains of pseudo-
stationary shock wave reflex-
ions (Ben Dor & Glass [6])

ON THE EFFECTS OF SHOCK WAVE

REFLECTION IN A CONFINED SPACE

K.C. PHAN AND J.L. STOLLERY

COLLEGE OF AERONAUTICS
CRANFIELD INSTITUTE OF TECHNOLOGY
CRANFIELD, BEDFORD, ENGLAND

An experimental study has been made of a shock wave
discharging into a square box. The main aim of this
investigation was to simulate the firing of a shoulder-
launched weapon from a confined space. High levels of
shock amplification can result due to shock reflections
from the walls of the enclosure. In this study, a
series of measurements have been made of shock wave
reflect¹ons from boxes having various degrees of
confinement. The results of further tests in which some
of the walls were lined with foam are also included.
The records taken include schlieren pictures and pressure
signatures, with particular attention being paid to the
position corresponding to that of a gunner's ear.

1. INTRODUCTION

A shock wave emerging from a tube will attenuate as it expands spherically
into the surrounding atmosphere. However, if the expansion of the shock wave
is confined,the overall strength of the pressure wave established inside the
enclosure can be amplified, due to shock wave reflections from the walls. The
subsequent interactions between the emerging blast wave and the walls of the
room can produce excessive levels of blast that may be intolerable to the human
operator.

This paper describes an experimental study in which a simple, open-ended
shock tube is used to simulate the firing of a weapon in a confined space.
Compressed air was used as the driver gas to generate a shock wave which was
discharged into a wooden box. Pressure measurements were taken inside the box,
at a location close the shock tube exit. The results show how the reflected
shock overpressure depends on the degree of confinement, simulated by removing
various walls of the box. The effect of fitting a suppressor is also described.
Both the strength and the signature of the reflected shock waves are modified.
In addition, results are given for a series of tests in which the walls of the
box were covered with foam. The transient-behaviour of the reflected shocks is
reported.

2. EXPERIMENTAL ARRANGEMENT

(i)   The Shock Tube and the Model of a Confined Space

A simple open-ended shock tube, 32 mm internal diameter, was used through-
out this study. The initial pressure ratio across the diaphragm, (P_4/P_1) was
6.44 with air driving air, the driven air being initially at atmospheric pressure.
The measured initial incident shock Mach No. was 1.46 (the corresponding
theoretical shock Mach No. is 1.50).

Fig. 1 shows the general layout of the box which measured 640 x 640 x 640 mm internally. The open end of the shock tube was inserted through the front wall (FW) into the box. Provision was also made to simulate various conditions of confinement by making the roof (R), front wall (FW), and a side wall (SW) of the box removable. The three tube-in-box configurations tested are shown in Figs. 1a, b and c.

The configurations C2 and C3 were used to examine the effects of back wall and side wall proximity respectively.

(ii)   Pressure Transducer Deployment, Data Recording and Storage System

A Kulite pressure transducer was placed at a point representing the operator's ear position (point R_G in Fig. 1). The transducer was mounted in a flat circular (disc-like) housing, with its flat surface placed horizontally in the plane of the shock tube axis. The transducer output was stored in a DATA LAB, 4096 words x 10 bits transient recorder capable of a maximum sampling rate of 2 MHz. Permanent digital data were stored in cassette cartridges via a micro-computer.

3.   ANALYSIS OF EXPERIMENTAL RESULTS

(i)   Preliminary Assessment of the Pressure Variations Recorded at a Slow Sampling Rate

The process of shock wave reflection and re-reflection inside a box is complex and can last for a "long time", typically 100 ms in our case. In order to obtain some idea of the most important period within this timescale a few pressure signatures were taken at a slow sampling rate. Fig. 2 shows a pressure history at the point R_G of configuration C1, sampled at 20 µs per point (50KHz). It is clear, from Fig. 2 that (i) the maximum overpressure occurs 5 ms after the shock wave emerges from the exit, and (ii) the time between the start of the pressure pulse and the subsequent decay of pressure fluctuations to an insignificant value (usually taken as 1/10th of the peak value[1]) is about 80 ms. Blast assessment[2] of recoilless gun firings in a room gives values of this decay period ranging from 80 ms to 100 ms.

Because the sample rate limits the highest frequency component of the signal that is measurable, a faster rate of sampling is usually preferred. Since the interesting portion of the signal (Fig. 2) occurs within 5 ms of the initial shock emerging from the tube, it was decided to sample at a rate of 2 µs per point (500kHz). A typical shock wave rise-time is about 10 µs.

(ii)   Identificaiton of Pressure Pulses in a Fully Enclosed Box (Configuration C1)

The initial phase of development of the shock wave reflection pattern with time is sketched in Fig. 3. After the initial incident pressure pulse ΔP_I, the reflection pattern consists of reflections from the roof, floor, front, side and back walls. The identity of individual pulses is shown on the pressure-time record, see Fig. 4(ii). Comparison with the pressure signature obtained with no confinement (Fig. 4(i)), clearly shows the effects of multiple shock reflection.

Though each reflected pressure pulse, on its own, does not exceed the value of the incident pulse ΔP_I, unwanted shock coalescence can occur producing overpressures greater than ΔP_I. This is shown as ΔP_{max} in Fig. 4(ii). Between ΔP_I and ΔP_{max}, the pressure increase due to wave reflection from the roof (ΔP_R)

is greater than the other individual pressure pulses. This is because the transducer recording ΔP_R is mounted 'head on'. The effect of this becomes even more pronounced at higher incident shock conditions, such that the value of ΔP_R can exceed the initial incident pulse (ΔP_I). This implies that in the corresponding practical situation, a human operator, standing upright, firing a shoulder-launched weapon from inside a room would experience a very strong reflected pressure pulse from the side walls.

(iii) The Effects of Altering the Degree of Confinement in Configuration C1.

The various conditions of confinement were simulated by the removal of one or two faces of the box. Some of the results are given in the last column of TABLE 1, where ΔP_{max} denotes the maximum over-pressure fluctuations following the incident pressure pulse ΔP_I (ΔP_I = 2.381 kpa or 0.346 psi).

A set of pressure records is given in Fig. 4. As expected, the worst situation occurs when the box is complete, the measured ΔP_{max} exceeds the value of ΔP_I by 50%. As one or two walls are removed so ΔP_{max} is reduced. Among the one-wall-removed configurations, the reduction of ΔP_{max} with the front wall open is relatively small in comparison with the other conditions of confinement. This is because the strength of the expanding shock wave in the region upstream of the tube exit (towards the front wall) is weaker than in the downstream region. The most significant effect which influences the overall level of ΔP_{max} is the reflection of the stronger region of the incident shock from the top, side and back walls.

(iv) The Effect of Foam-Lined Inner Walls, Configuration C1 (Complete Box)

A number of investigations[3,4] have been made concerning shock wave reflection from foam materials. Our study examines the effect of foam-lined walls inside an enclosure. Some of the measured pressure signatures are shown in Fig. 5a. It is immediately evident that the reflected shock wave is being suppressed, incident energy being absorbed by the diffusion of mass flux through the interstices of the foam material.

A set of schlieren photographs, which show the incident shock wave reflecting from a solid and a porous surface, is given in Fig. 5b. Because the field of vision was limited by the size of the mirrors (12" diameter), these pictures were taken with the roof and floor moved closer together (210 mm instead of 640 mm).

(v) The Effect of Back Wall (BW) Proximity on ΔP_{R_G}*(Configuration C2)

For reasons of accessibility, the front-wall-open configuration was chosen for this investigation. Fig. 6a presents a pressure record obtained at the R_G position with the tube exit 100 mm from the back wall. The reflected shock from the back wall (ΔP_{BW}) is followed by a large pressure pulse (ΔP_B). Originally, this was thought to be due to the shock reflecting from the other surfaces of the box but subsequent tests, in which the roof and side walls were removed showed no marked improvement. These results suggested that the effect could only be due to the back wall alone.

Fig. 6b shows a sequence of schlieren pictures of events before and after the emerging shock impinges on to the back wall. From the pressure trace (Fig. 6a) the time intervals from the instant when the trigger pulse is received to the first three shocks are noted. These are;

* ΔP_{R_G} is an abbreviation for the pressure signature at the point R_G.

Event Registered	Time Interval of Event from Trigger Pulse
ΔP_I	760 µs
ΔP_{BW}	1270 µs
ΔP_{VR}	1800 µs

Comparing these events registered on the pressure record with the schlieren photographs shown in Fig. 6b, it is evident that the predominant large peak overpressure (ΔP_{VR}) is the result of the shock associated with the vortex ring[5,6] being reflected from the back wall. As the distance of back wall from the tube exit increases, the influence of the reflected vortex ring diminishes as shown by comparison with Fig. 4(ii).

(vii) The Effect of Side Wall (SW1) Proximity on ΔP_{R_G} (Configuration C3)

Table 1 summarises the results obtained by altering the lateral tube position with respect to the side walls. Some pressure records are shown in Figure 7a.

Condition of Confinement	($\Delta P_{max}/\Delta P_I$) at the point R_G				
	Position of tube from SW1 (x mm)				
	104 mm	160 mm	216 mm	272 mm	320 mm
Fully Enclosed	1.925	1.710	1.560	1.450	1.500
Roof Off	0.980	0.975	1.190	0.695	0.825
SW1 Open	1.000	1.265	1.050	0.910	0.875
FW Open	1.330	1.050	1.085	1.000	1.300
Roof Off, SW1 Open	0.350	0.675	0.450	0.570	0.625
Roof Off, FW Open	0.850	0.900	0.800	0.500	0.650

TABLE 1

In the case of a complete box, ΔP_{max} occurred about 3 6 ms from the instant the shock emerges from the tube (see Fig. 7a). Based on the time intervals estimated below it seems that ΔP_{max} mainly due to the reflection of the shock associated with the vortex ring. In addition, since the distance from the tube exit to the back wall (BW) remains constant at 480 mm, the time interval between ΔP_I and ΔP_{max} should remain the same for all cases of side wall proximity. This is confirmed by the pressure records shown in Fig. 7a. The difference in the *level* of ΔP_{max} is the direct effect of the proximity of the side wall (SW1), as shown in table 1.

Path of shock associated with the vortex ring	Estimated Speed	Time Interval
Tube exit to Back Wall (480 mm)	~225 ms^{-1} (estimate based on pressure records shown in Fig.7b)	~2.13 ms
Back Wall to R_G position (~5.3 mm)	~333 ms^{-1} (based on schlieren pictures shown in Fig. 6b)	~1.73 ms

(vii) The Reflections in an Enclosure from a Suppressed Emerging Shock Wave

Fig. 8(iii) shows a pressure history of the shock wave reflections due to a suppressed shock wave released in a fully enclosed confinement. Though the maximum overpressure level is less than ΔP_{max} with an unsuppressed emerging shock (see Fig. 8(i)), the emission of a series of weaker waves produced by the suppressor, makes a significant difference to the pressure histories. In

particular the silencer introduces significant pressure oscillations in the frequency range of 2 to 3 KHz. It has been suggested[7] that transient overpressure fluctuations around these frequencies can induce some losses in hearing sensitivity. However, these pressure fluctuations are influenced by the type of reflecting surface. Hence by lining the walls of the enclosure with a foam material, the induced overpressure fl ctuations can be eliminated as shown in Figs. 8(ii) and 8(iv).

4. CONCLUSIONS

This study has shown that a shock wave released in a confined space, can produce an overpressure level in excess of the initial incident overpressure (ΔP_I). As the walls of the confined volume are removed so the maximum overpressure is reduced. In some cases the level of overpressure fluctuations can fall below the initial incident pressure value.

When the shock tube exit is close to the back wall, the dominant feature of the reflection process is the behaviour of the shock associated with the vortex ring.

Lining the walls with a foam material casues a dramatic reduction of the overall level of overpressure flunctuations, as well as an elimination of the high frequency components of the pressure signature.

REFERENCES

1. Coles, R.R.A., Garinther, G.R., Hodge, D.C., Rice, C.G., "Hazardous Exposure to Impulse Noise". Jn. of the Acoustal Society of America. Vol. 43, No. 2, 1968, p.336.

2. Clare, P., "Blast Assessment of Recoilless Gun Firings". Technical Proceedings of the Blast Overpressure Workshop. TTCP-KTA-7 July 1983, RARDE, Fort Halstead, U.K.

3. Clarke, J.F. "Reflection of Weak Shock Waves from Absorbent Surfaces". Proc. Roy. Soc. A396 (1984).

4. Devereux, F. et al, "On Shock Reflection and Attenuation at Atmospheric Pressure". DREV TN-1871/70, Defence Research Establishment, Valcartier, Quebec, Canada.

5. Baird, J.P. "Interfometric Study of Supersonic Vortex Ring". University of New South Wales, Australia. Private Communication.

6. Phan, K.C., Stollery, J.L., "The Effect of Suppressors & Muzzle Brakes on Shock Wave Strength". 14th Int. Sym. on Shock Tubes & Waves, August 1983, Sydney, Australia.

7. Clayden, W.A., Hillman, A. "Some Recent U.K. Work on Noise from Shoulder-Launched Recoilless Weapons. 4th Int. Ball. Sym. 1978.

NOTATION

P_1 Ambient Pressure (14.7 psi).
P_2 Static pressure of the initial incident shock wave inside the tube.
P_4 Compres.ion Chamber (or driver) Pressure.
ΔP Overpressure relative to ambient
ΔP_I Initial incident static overpressure at the reference point, R_G.
C Calibre (= one diameter of shock tube, 32 mm)
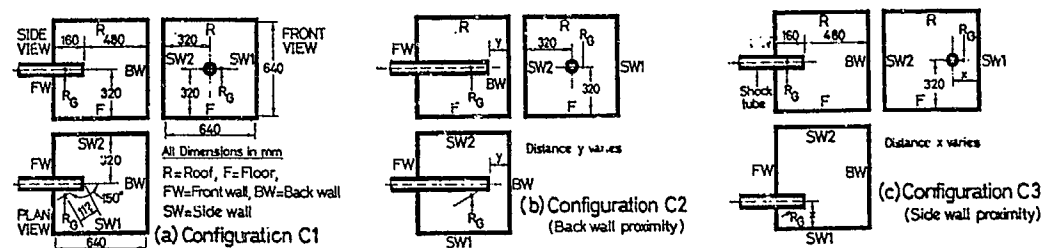
Figure 1 The general layouts of three tube-in-box configurations used to simulated the condition of confined space
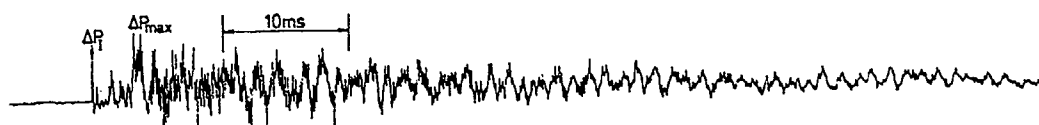
Figure 2 A pressure record taken at R_G position in the fully enclosed configuration, C1 (Data sampled at 20 microseconds per point or 50 Khz.)
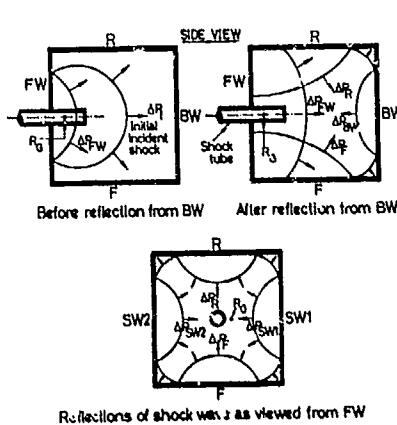
Figure 3 A sequence of representative sketches of the early development of shock wave reflection in a fully enclosed configuration.
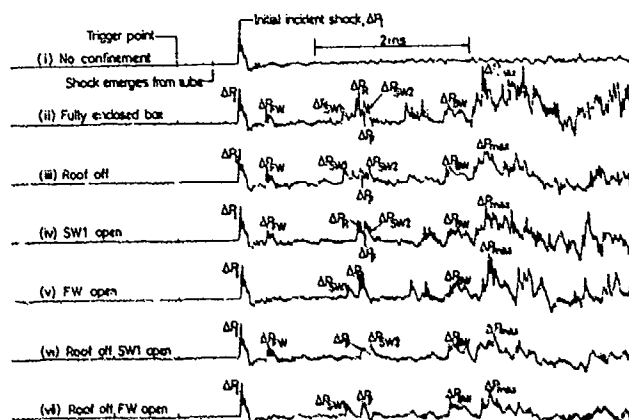
Figure 4 Examples of pressure signature at R_G position obtained in various conditions of confinement (C1 tube-in-box configuration).
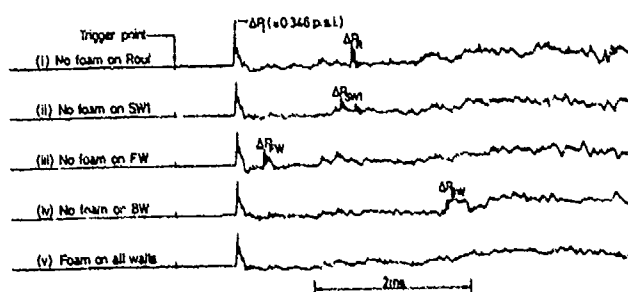
Figure 5a Pressure signatures at R_G position showing the effect of foam-lined walls (C1 configuration, foam thickness = 48mm PRETEX).
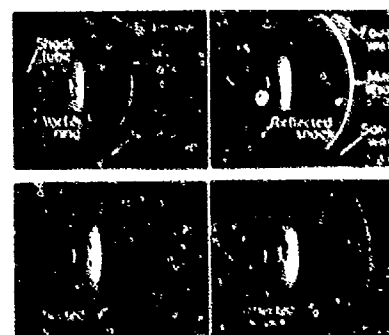
Figure 5b Schlieren pictures of shock wave reflection from a solid surface and a foam surface
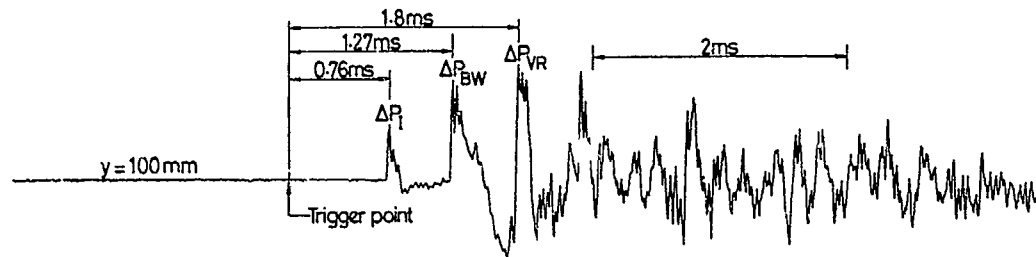
Figure 6a A pressure signature at R_G position on the effect of back wall proximity
(C2 configuration, y=distance of BW from tube exit, see Fig.1b)
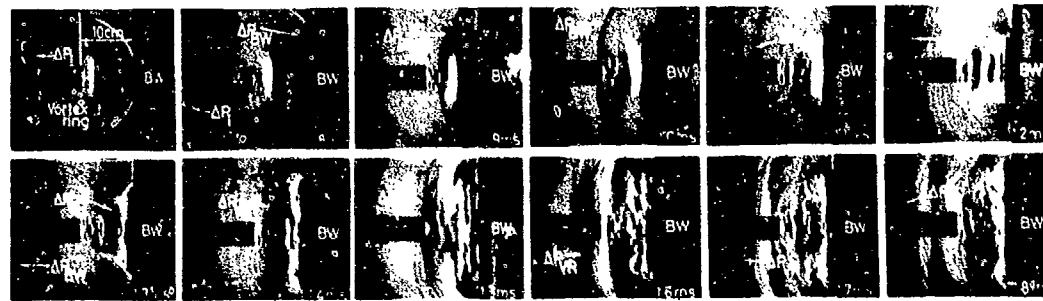
Figure 6b Schlieren pictures of shock wave reflection showing a sequence of events after the emerging
shock impinges onto a back wall (time interval is from trigger point)
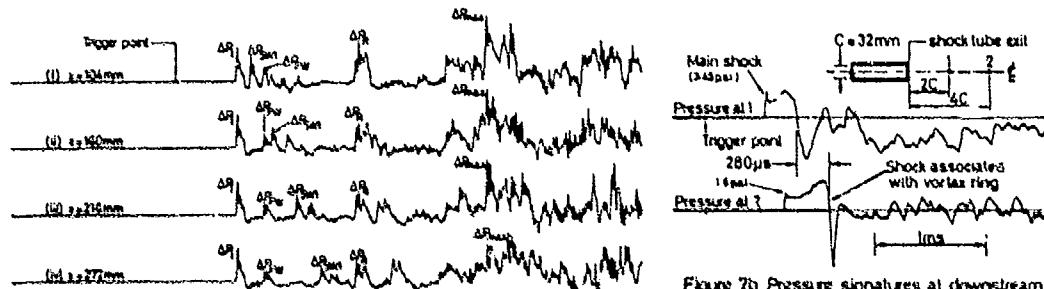
Figure 7a Some pressure records at R_G position showing the effect of side
wall (SW1) proximity (C3 fully enclosed configuration)
(z=distance from SW1 to shock tube axis, see fig.1c)

Figure 7b Pressure signatures at downstream
region along the tube axis
(No confinement)
(Trigger point to tube exit is 162mm)
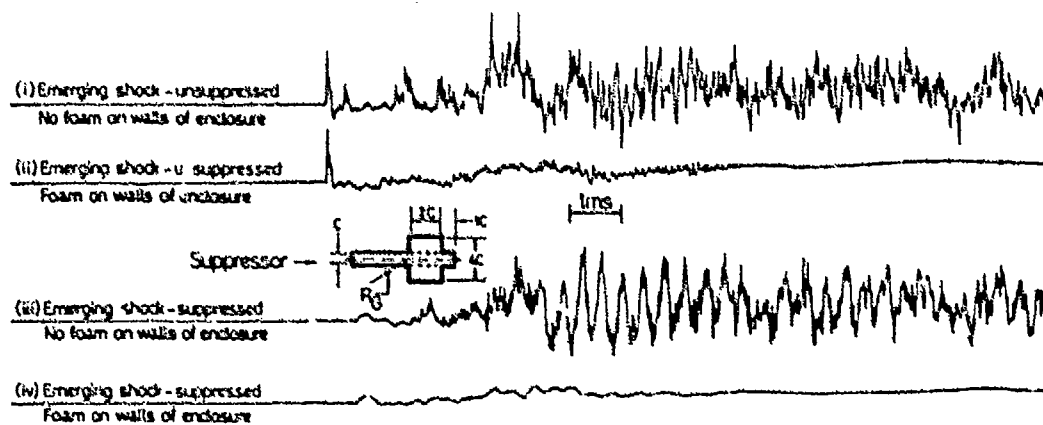
Figure 8 Pressure histories at R_G position of shock wave reflection from a suppressed and an unsuppressed
emerging shocks inside a fully enclosed confinement of C1 configuration

TRANSFORMATION OF A PLANE UNIFORM SHOCK INTO CYLINDRICAL OR SPHERICAL UNIFORM SHOCK BY WALL SHAPING

Y. SAILLARD, H. BARBRY, and C. MOUNIER

Commissariat à l'Energie Atomique

B.P. 27

94190 VILLENEUVE St GEORGES — FRANCE

A theoretical method is presented for the calcu-
lation of the wall shape of a shock tube, which changes an
initial plane shock of uniform strength into a cylindrical
or spherical shock of uniform strength in some solid angle
and without Mach reflections . This method uses Whitham's
theory of shocks in characteristic form . It has been nume-
rically treated and gives the complete shock evolution during
its propagation into the convergent section of the shock tube.
The nozzle geometry and shock amplifications theoretically
expected are indicated and one sample of numerical results
is given . .

INTRODUCTION

The decrease of the cross sectional area of a shock tube is known
to amplify the strength of a shock wave . The use of this gain in shock
strength to produce high pressures and temperatures has been noted by many
investigators. The rule of Chisnell[1] which connects the area contraction to
the change of the Mach number gives a theoretical estimate of this amplifi-
cation .

The wall shape of the shock tube is important for the determina-
tion of the value of the shock strength[2], and it seems necessary to use a
profile with a sufficiently gradual contraction in order to avoid formation of
Mach reflections .

The approximate theory describing the two or three dimensional beha-
viour of shock wave has been established by G.B. WHITHAM[3], by extending the
Chisnell's rule to infinitesimal ray tube . This theory has been used to define
some particular configurations of the wall apt to generate from an initial
plane shock a stronger converging shock . One possibility is to define the wall
shape by the condition of convergence at a single point of the disturbances on

the shock propagation direction and shock strength issued from the wall. In the two dimensional case and for a strong shock, the wall shape is a logarithmic spiral. It has been extensively studied[4,5,6,7] theoretically and experimentally. Another possibility, close to the previous one, is to prescribe the convergence of disturbances issued from the wall not at a single point but at the given final shock position (cylindrical or spherical)[9].

The shock which occurs from the previously defined wall shape has not uniform strength, and as a matter of fact the shock cannot strictly focus on a point. The result is a rather complicated implosion flow with strong disturbances. So, in order to have a symmetrical implosion it could be useful to obtain a circular shock (cylindrical or spherical) of uniform strength. Therefore, it is worthwhile finding a suitable wall shape which can change a plane shock into a cylindrical or spherical shock with uniform strength possibly limited to a certain angle without generating Mach reflection. This problem has risen and its possibility has been discussed recently[8]. A method is proposed here which gives it a solution and allows a numerical construction of the wall shape, in the frame of Whitham's theory.

SHOCK DYNAMICS

The geometry considered is two-dimensional ($\nu = 0$) or axisymmetric three-dimensional ($\nu = 1$). A shock at a point (x,y) is determined by $M(x,y)$ its Mach number and $\theta(x,y)$ the angle between the axis Ox (the axis of symmetry in the case $\nu = 1$) and its propagation direction. The rays are defined as the orthogonal trajectories of the successive positions of the shock, the wall of the shock tube is a particular ray. The set of equations describing the shock behaviour is[3].

$$(1) \begin{cases} \dfrac{\partial}{\partial x}\left[\dfrac{\sin\theta}{M}\right] - \dfrac{\partial}{\partial y}\left[\dfrac{\cos\theta}{M}\right] = 0 \\[2mm] \dfrac{\partial}{\partial x}\left[y^\nu \dfrac{\cos\theta}{A(M)}\right] + \dfrac{\partial}{\partial y}\left[y^\nu \dfrac{\sin\theta}{A(M)}\right] = 0 \end{cases} \quad \text{with}$$

$$(2) \begin{cases} A(M) = \exp\left[-\int_{M_1}^{M}\dfrac{u\,\lambda(u)}{u^2-1}\,du\right] \\[2mm] \lambda(u) = \left[1+2\mu+\dfrac{1}{u^2}\right]\left[1+\dfrac{2}{\gamma+1}\left(\dfrac{1-\mu^2}{\mu}\right)\right] \\[2mm] \mu = \sqrt{\dfrac{(\gamma-1)u^2+2}{2\gamma u^2-\gamma+1}} \end{cases}$$

γ is the ratio of the specific heats of the gas considered

Here $A(M)$ has been chosen so as to have $A(M_1) = 1$, M_1 is a typical Mach number of the solution. If the shock strength is uniform, $A(M)$ is proportional to the shock area.

If the shock is strong, $A(M)$ becomes (strong shock approximation) :

$$(3) \quad A(M) = \left[\dfrac{M}{M_1}\right]^n, \quad n = 1 + \dfrac{2}{\gamma} + \sqrt{\dfrac{2\gamma}{\gamma-1}}$$

The important point is that the system (1) is hyperbolic, and can be written in the following characteristic form :

$$(4) \quad \frac{d}{ds}\left[\theta \pm \omega(M) \pm \nu I\right] = 0 \quad \text{on the characteristic curves } C^{\pm} \begin{cases} \frac{dx}{ds} = \cos(\theta \pm m) \\ \frac{dy}{ds} = \sin(\theta \pm m) \end{cases}$$

$$\omega(M) = \int_{M_1}^{M} \sqrt{\frac{\lambda(u)}{u^2-1}}\, du \qquad \text{tg}\, m = \frac{1}{M}\sqrt{\frac{M^2-1}{\lambda(M)}} \qquad \frac{dI}{ds} = \frac{\sin\theta\, \sin m}{y}$$

The Riemman invariants $R^{\pm} = \theta \pm \omega(M) \pm \nu I$ are constant along the characteristics $C^{\pm}$. This formulation holds as far as the characteristics of a same family do not cross . If they cross it corresponds to the formation of a three shock Mach reflection . The characteristics represent the trajectories of the disturbances of the shock shape and strength which propagate on the shock, they allow to determine the domain where the solution is defined when θ and M are given on some curves of the (x,y) plane. It is this important property which will be used here .

DEFINITION OF THE SOLUTION

We seek a wall shape which transforms a plane shock of uniform strength into a cylindrical shock (two-dimensional geometry, $\nu = 0$) or a spherical shock (axisymmetric three dimensional geometry , $\nu = 1$) of uniform strength in a certain angle . The problem is symmetric, and the axis Ox is the plane of symmetry ($\nu = 0$) or the axis of symmetry ($\nu = 1$) . The final shock of circular shape DF and uniform Mach number M_1 is given within an angle θ_1 (Fig. 1) . The initial plane shock of uniform Mach number M_0 is given too, but its position is not known . The solution will be defined and numerically constructed from the final and initial shocks .

In addition to the data of final and initial shock strengths, we assume that the characteristics C^+ issued from the axis for $x_A \leq x \leq x_B$ converge on F, and that $\theta = 0$ on the axis, this last assumption is necessary to avoid formation of Mach reflection on the axis Ox . With these conditions the solution is perfectly determined as it will be established now by looking at the different regions separated by some particular characteristics (Figure 1) .

In the region I bounded by the characteristic C_1^+ : FB, the solution is well defined in terms of the final shock . As characteristics C^+ converge on F, this point is a singularity, M and θ are multivalued but they are related by the Riemann invariant along the characteristic C^- reduced into a point at F .

$$(5) \qquad \theta - \omega(M) = -\theta_1 - \omega(M_1)$$

The region II is connected by characteristics C^+ to F and by characteristics C^- to the region I, therefore the two quantities M and θ can be calculated owing

to the invariance of $R^{\pm}$ along $C^{\pm}$. The M values on the axis for $x_A \leq x \leq x_B$ can
be calculated too because the axis where $\theta = o$ is connected by a C^+ to region II,
and the solution in region III is determined. When M on the axis reaches the
initial Mach number M_o , this position defines the point A which is the issue
of the characteristic C^- propagating on the initial plane shock ($M = M_o$, $\theta = o$)
and coming from the wall . As M_1 and θ_1 are given all the values of M_o are not
permitted, M_B the value of M at point B which depends on M_1 and θ_1 is a maximum
for M_o . Finally, in the region IV connected by a C^+ to initial shock and by a
C^- to region II or III , the solution is determined, M, θ and consequently the
wall shape can be calculated .

There is a solution of particular interest, the solution which corresponds
to $M_o = M_B$, in this case A is in B and there is no singularity at F and conse-
quently no discontinuity for the shape of the wall at F . We call it regular
solution .

The method which has been given shows that the solution can be defined in
a coherent ways from characteristics theory, and allows a numerical calculation.But
it is not really a proof of its existence, indeed the characteristics of a same
family can possibly cross in region II III or IV . Only the effective numerical
calculation can ensure that crossing does not occur, giving then a strong presump-
tive evidence for the existence of the solution.

DISCRETISATION OF EQUATIONS AND NUMERICAL CALCULATION OF THE SOLUTION

It is now shown how the equations in characteristic form (4) has been
discretised to obtain numerically the theoretical solution . The final circular
shock of Mach number M_1 and position at radius R is given within
the angle θ_1 (Figure 1), the initial Mach number M_o is given too . In the
following the coordinates and the Mach number are respectively normalized by
R and M_1 .

Different methods are used according to the regions considered . In the
region I the solution is easily found to be a circular shock . In polar coordi-
nates (ρ, ϕ) with $x = \rho \cos\phi$, $y = \rho \sin\phi$ the solution given by :
$$\theta = \phi - \pi \quad , \quad \frac{dM}{d\rho} = -(\nu + 1) \frac{M}{\rho} \, tg^2 \, m \quad \text{with} \quad M (\rho = 1) = 1$$
is solved with a classical Runge-Kutta method of order 4 and a constant step $d\phi$
In the strong shock approximation, the solution can be written explicitely, the
characteristic C_1^+ is a logarithmic spiral $\rho = \exp\sqrt{n}(\phi + \theta_1 - \pi)$ and the
value of M at point B is : $M_B = \exp -(\nu+1) \, \theta_1 / \sqrt{n}$

In the region II or III(outside $x = o$) the solution is calculated at the

crossing of characteristics C^+ and C^-. Knowing the position and values (M, θ) at the intersection P of characteristics C^+_{k-1} and C^-_1 and at the intersection Q of characteristics C^+_k and C^-_{1-1}, the position and values at the intersection R of characteristics C^+_k and C^-_1 (figure 2) are obtained by solving the following system which is the discretised form of (4):

$$\left[\sin(\theta_P - m_P) + \sin(\theta_R - m_R)\right](x_R - x_P) - \left[\cos(\theta_P - m_P) + \cos(\theta_R - m_R)\right](y_R - y_P) = 0$$

$$\left[\sin(\theta_Q + m_Q) + \sin(\theta_R + m_R)\right](x_R - x_Q) - \left[\cos(\theta_Q + m_Q) + \cos(\theta_R + m_R)\right](y_R - y_Q) = 0$$

$$\theta_R = \frac{1}{2}\left[\theta_P + \theta_Q + \omega_Q - \omega_P + \nu(I_{PR} - I_{QR})\right] \;,\; \omega_R = \frac{1}{2}\left[\theta_Q - \theta_P + \omega_P + \omega_Q - \nu(I_{PR} + I_{QR})\right]$$

I_{PR} and I_{QR} are mean values of I on PR and QR not explicited here, M_R is obtained from ω_R by numerically reversing $\omega(M)$ given in (4)

This implicit system is solved by an iterative method. In fact only a few number of iterations are necessary to obtain a convergent solution for x_R, y_R, M_R, θ_R.

In the region IV the problem is the same and the discretisation of (4) is similar, excepted that P is the intersection of C^+_{k-1} and C^-_1, Q the intersection of C^+_k and C^-_{1+1}, R the intersection of C^+_k and C^-_1 (figure 3).

In region III, when the point R to be calculated is on the axis Ox (R at the intersection of C^-_1 and C^+_k) we obtain it from the point Q at the intersection of C^-_{1-1} and C^+_k by solving the system :

$$\frac{1}{2}\left[tg\,(\theta_Q + m_Q) + tg\,m_R\right]\left[x_R - x_Q\right] + y_Q = 0 \;\;,\;\; \omega_R = \theta_Q + \omega_Q - \nu I_{QR}$$

which is the discretisation of the Riemann invariant R^+ where we have used the condition $\theta = o$ on the axis . This implicit system is solved by an iterative method .

Using the above described discretisations, and choosing a step $d\phi$ defining the different points on C^+_1 , a step $d\theta$ for the values of θ at F, and an equal number of points on FA and AG, the solution is calulated successively in regions I, II, III and IV . The wall shape FG is obtained by calculating the ray $\frac{dy}{dx}$ = tg θ going by F. To check the numerical results, another method has been developped for the simple case of two- dimensional geometry and strong shock approximation . Skipping the details, it gives the solution in a semi-analytical form, and the agreement with the numerical solution is excellent .

RESULTS

The parameters defining the wall shape are the initial M_o and final M_1 shock Mach number, the angle θ_1 of the final circular shock, the type of geometry : $\nu = o$ (cylindrical final shock), $\nu = 1$ (spherical final shock), and the specific heat ratio γ . With these data specified, the successive positions of shock, the rays, the trajectories of characteristics, and the wall shape can be calculated.

In the strong shock approximation and for regular solution, the ratio M_o/M_1 and the convergent shock tube dimensions normalized by the radius R of final shock can be expressed analytically in terms of θ_1 and γ

$$\frac{M_1}{M_0} = e^{\frac{(\nu+1)}{\sqrt{n}}\theta_1} \quad , \quad \frac{y_o}{R} = [\theta_1 + \nu(2\sin\frac{\theta_1}{2} - \theta_1)] e^{\sqrt{n}\theta_1} \quad , \quad \frac{|x_o|}{R} = \sqrt{n}\ \frac{y_o}{R} + e^{\sqrt{n}\theta_1}$$

These quantities shown figure (4) are very sensitive to the values of θ_1, on account of exponential dependence. To have not prohibitive shock tube dimensions, it seems necessary to limit the angle of final convergent tube to $\theta_1 < 60°$. The regular solution, which is the solution corresponding to minimum values of y_o/R and $|x_o|/R$ for given θ_1, is certainly the most attractive to test experimentally .

The results of the program calculating the solution, tested for different values of parameters, show no irregular behaviour for the quantities and no crossing of characteristics. Therefore it can be assumed that the solution is likely to exist .

We present now figure 5 an example of regular solution calculated in the case : $\gamma = 5/3$, $\nu = 0$, $\theta_1 = 45°$, with strong shock approximation. The wall of the shock tube, the successive positions of shock at equal times and the characteristics are indicated . The coordinates of the wall are given Table 1 . The shock amplification is $M_1/M_0 = 1,452$.

It is worthwhile comparing the length of the nozzle obtained here with the length L of a logarithmic spiral corresponding to $\gamma = 5/3$ with the same initial cross section, the ratio x_o/L is about 1,6 . It means that the shock tube wall proposed here has a much less converging shape that the logarithmic spiral already tested experimentally[4,5,6], and the flow   can have a significant different behaviour .

REFERENCES

/1/ R.F. CHISNELL : J. Fluid Mech. 2, p. 286

/2/ G.A. BIRD : J. Fluid Mech. 5, p. 60

/3/ G.B. WITHAM : Part 1, J. Fluid Mech. 2, p145 ; Part 2, J. Fluid Mech. 5, p. 369

/4/ B.E. MILTON, R.D. ARCHER : AIAA Journal : 7 (1969), p. 779

/5/ B.E. MILTON, R.D. ARCHER : 8 th. Shock Tube Symposium (1971), p.55

/6/ J.W.T. Wu, R.D. ARCHER, S. MOLDER : 9 th. Shock Tube Symp. (1973), p.604

/7/ B.E. MILTON, R.D. ARCHER, D.E. FUSSEY : 10 th. Shock Tube Symp. (1975), p.348

/8/ L.Z. DUMITRESCU : 14 th. Shock Tube Symp. (1981), p. 196

/9/ J. LAU : CASI Trans. 4 (1971), p. 13

TABLE 1: Wall coordinates for regular solution, $\gamma = 5/3$, $\nu = 0$, $\theta_1 = 45°$

x/R	0.71	0.88	1.12	1.47	1.88	2.36	2.88	3.42	4.15	4.92	5.71	6.57	7.62	8.72	11.	13.88
y/R	0.71	0.87	1.13	1.44	1.61	1.88	2.15	2.39	2.67	2.93	3.16	3.38	3.59	3.77	4.01	4.11

FIGURE 1 : Schematic diagram of the solution

FIGURE 2 : Calculation of R

FIGURE 3 : Calculation of R

FIGURE 4 : M_1/M_o, $|x_o|/R$, y_o/R in terms of θ_1 for $\gamma = 5/3$

FIGURE 5 : Regular solution, for $\gamma = 5/3$, $\nu = 0$, $\theta_1 = 45°$, and strong shock approximation, with characteristics and successive shock positions
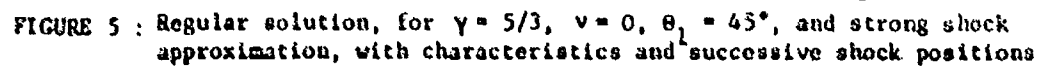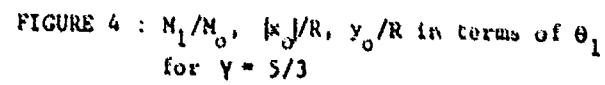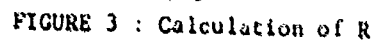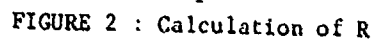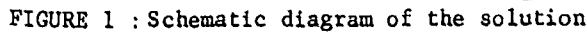
ON THE OCCURRENCE OF REGULAR REFLECTION OF SHOCKS
IN CONCAVE CORNER FLOWS

R. Niehuis, H. Schöler, H. Hornung

Deutsche Forschungs- und Versuchsanstalt für
Luft- und Raumfahrt e.V.
Institut für Experimentelle Strömungsmechanik
Bunsenstraße 10, D-3400 Göttingen
F.R. Germany

Reflection of oblique shock waves at plane walls or planes
of symmetry can either occur as a regular or a Mach reflec-
tion. The condition at which transition occurs from one
reflection type to the other is known for sufficiently
strong shock waves in two-dimensional flows. The shock
wave structure in concave corner flow is very similar to
the case of shock reflection in two-dimensional flows, if
viewed in appropriate plane sections. Concave corner flows
are therefore investigated in order to study the occurrence
of regular shock reflections in three-dimensional flows. So
far, only Mach reflections have been observed in such flows.
Regular reflections are shown to be possible for corner
flows by applying the transition criteria known from two-
dimensional flows. Experiments performed in a number of
corner geometries at different Mach numbers, confirmed the
theoretical results. Regular reflection was observed pro-
vided that the model is fitted with a slit in the corner.
The shock wave interaction was determined by means of opti-
cal tomography.

1. INTRODUCTION

In many practical cases of supersonic flow the problem arises that shock waves
generated at different components interact with each other in a complicated
way. Usually, shock reflection occurs and the flow becomes three-dimensional.

In two-dimensional supersonic flow, reflection of shock waves can occur either
as a regular reflection (r.r.) or a Mach reflection (M.r.), see Fig. 1. During
the last decade these two types of shock reflection have been studied inten-
sively in two-dimensional flows. An overview and introduction to the problem
with an extensive list of references is given by Hornung[1]. The conditions at
which transition between the two types of reflection takes place are known.

However, it is unknown to date whether these conditions are also applicable to
three-dimensional flows. Even the question whether r.r. is possible in three-
dimensional flows has not been answered finally. It is the purpose of this pa-
per to answer these questions.

The internal corner flow has been chosen to study the reflection of shock waves
in three dimensions. The corner is formed by two plane surfaces with sharp lea-
ding edges being symmetrically disposed about the free-stream direction. On the
windward side they generate attached shock waves interfering with each other.
Charwat and Redekopp[2] were the first to succeed in determining the shock wave
structure in such a corner by experiments. They found a structure sketched in
Fig. 2b. It consists of two planar shocks emanating from the leading edges
(wedge shocks), a corner shock that joins the two shocks, and two embedded

shocks. Due to the fact that the wedge shock is reflected at the plane of symmetry in a similar way as a M.r. in two-dimensional flow, we are going to call this a M.r. here, too. Subsequently, M.r. has been observed and reported also by other authors, e.g. Watson and Weinstein[3] and West and Korkegi[4]. The influence of the corner geometry on the corner flow field has been intensively investigated in systematical studies by Kipke and Hummel[5] and Möllenstädt[6]. They discovered further details of the flow structure like boundary layer separation and vortices. It is interesting to note, however, that in all these cases M.r. has been observed, i.e. a shock wave structure as sketched in Fig. 2b.

Beside this structure a different one is likely to occur, although it has not been observed so far. It is similar to a r.r. in two-dimensional flows, see Fig. 2a. In this special case the two wedge shocks interfere directly with each other without a corner shock. It will be shown that this kind of shock wave structure is possible, too, in corner flow.

2. THEORETICAL ANALYSIS

Consider a steady, inviscid, supersonic corner flow. Assuming that the shock waves are attached at the leading edges and planar up to the line of intersection, the flow problem depends on four independent parameters beside the gas constant γ, namely:

- M free-stream Mach number
- 2λ corner angle between the two plates,
- α angle of attack of the corner relative to the free-stream direction,
- ϕ sweep angle of the leading edges.

Provided that the flow is supersonic everywhere relative to the body, there exists a region in the vicinity of 0 in which the flow is "conical", i.e. where the components of all gradients along straight lines through 0 are zero. This result follows from the fact that in this region the flow has no information of a length scale (note that this would not be true if the leading edges were not sharp or if the flow were viscous). In the following we restrict the discussion to the conical flow region.

In the special case of r.r., Fig. 2a, it is possible to reduce the problem to one of plane flow as follows. Consider the line of intersection of the wedge shock with the plane of symmetry, i.e. the line OB. Let the plane P be perpendicular to this line and consider the velocity components in this plane. Since the direction OB is parallel to all the shock waves in the flow, these shock waves can only affect velocity components normal to the line OB. Hence, the conical flow of Fig. 2a can be generated by superimposing a uniform flow normal to the plane flow of plane P. Notice that this is not true in the case where a M.r. occurs, since no direction can be found which is parallel to all the shock waves.

So long as the reflection is regular, however, the superposition is valid. We therefore conclude that the criteria known from two-dimensional flows can be used to describe the failure of regular reflection, i.e. the transition from r.r. to M.r. in corner flows.

We restrict ourselves now to corner flows with cross-flow Mach numbers M_c ('= Mach number in plane P) larger than 2.4 (for air with $\gamma = 1.4$). In this case the transition from r.r. to M.r. occurs at a particular condition, the so-called von Neumann condition

$$\theta = \vartheta^*(M_c, \gamma),$$

where θ is the shock wave angle. This condition means that in steady flows the transition takes place when the pressure behind the reflected shock just equals the pressure which would be generated by a normal shock at the same free-stream conditions, see Hornung and Robinson[7]. R.r. occurs when θ < θ* is fulfilled. Otherwise M.r. will occur.

The cross-flow Mach number and the shock wave angle θ in the plane P can be calculated for a given corner geometry using the oblique shock relations. Knowing the cross-flow Mach number, the critical shock wave angle θ* can be determined by applying the von Neumann condition. Accordingly, we expect a r.r., such as in Fig. 2a, for θ < θ* and the M.r. of Fig. 2b otherwise.

Varying the geometrical parameters in a numerical study it turned out that r.r. is possible in corner flows. Fig. 3 shows an example for an air flow at M = 15.8 in a corner with unswept leading edges. Transition between r.r. and M.r. occurs at the plotted curve. In this plot the points indicate those geometries which have been investigated by Kipke and Hummel[5]. They observed M.r. in all cases, which agrees with our theory. Generally, it was found that all the corner geometries which have been investigated (in the literature known to the authors) and for which the cross-flow Mach number was larger than 2.4, are in agreement with the theory.

Since M.r. was observed in all these experiments our experiments were designed in order to verify whether r.r. is possible in corner flows.

3. EXPERIMENTS

A corner model was built with two plates consisting partly of glass in order to visualise the flow field inside the corner with optical methods. It was constructed in such a way that two of the geometrical parameters could be varied easily, namely the corner angle and the angle of attack. The model had a conically widening slit at the line where the two plates would join. This turned out to be necessary in order to avoid multiple shock reflections which eventually would suppress r.r., a phenomenon which has been discovered in earlier experiments.

Experiments were carried out in the DFVLR Ludwieg tube at Göttingen at a free-stream Mach number of 6 and a Reynolds number (based on the length of the leading edges, b = 80 mm) of 1.20 x 10^{6}. Additional experiments were performed in the DFVLR Trisonic Blow-Down Windtunnel at Cologne at a free-stream Mach number of 4 and a Reynolds number of 6.24 x 10^{6}. The shock structure in the corner was visualized by the Schlieren method in the Blow-Down Windtunnel and by a Schlieren Interferometer using two Wollaston prisms (for reference see Merzkirch[8]) in the Ludwieg tube for better resolution of the lower density. Both methods are sensitive to density gradients in the flow and yield a projection of the three-dimensional shock structure. The edges of shock wave surfaces appear as sharp lines on the projection. It is impossible to obtain information about the three-dimensional nature of the shock wave structure with a single projection. However, by recording a number of projections at different angular views, the shock wave structure can be reconstructed by means of tomography (tomography is a method to reconstruct a three-dimensional object in an arbitrary section by a number of projections).

In order to record projections at different angular views the model was rolled about the free-stream flow vector in an angle range of 90°. A total number of 30 different angles was recorded for each corner configuration. The shock wave structure in planes normal to the free-stream direction was reconstructed with two different tomographic methods. One is a graphical approach based on a simple back projection of the loci of the discontinuities, i.e. shock waves, seen

on the photographs. The other is a numerical method, which is called convolution-back projection in the literature. We used a similar algorithm as Shepp and Logan[9] with an identical filter function. The projections were prepared in such a way that for each recorded angular view a narrow Gaussian distribution function was superimposed at those loci where shock waves were seen and set to zero elsewhere. The projections generated in this manner were discretized and fed into the reconstruction algorithm.

4. RESULTS

Fig. 4 shows the result of a reconstruction for a slitted corner with unswept leading edges having a corner angle of $2\lambda = 68°$ and an angle of attack of $\alpha = 15.5°$. The free-stream Mach number is 4.0. Fig. 4a shows a perspective view on a plane normal to the free-stream direction. By projecting the ridge lines into the Y,Z-plane, see Fig. 4b, one recognizes that they represent the location of the shock waves. In this particular case it is a r.r.. The embedded shock waves have not been reconstructed for convenience, because the purpose of this work is to investigate the way the wedge shocks interact with each other. The earlier-mentioned slit in the corner can be seen clearly in Fig. 4b.

Fig. 5 summarizes all the corner geometries investigated and the type of shock reflection obtained. The two plotted curves indicate where transition from r.r. to M.r. occurs according to the theory. It has to be mentioned that the $M = 4$ curve in the plot starts at an angle of attack of 15°. This is due to the fact that for values smaller than 15° the cross-flow Mach number is smaller than 2.4. These cases have been excluded in the present theory. The experiments clearly confirmed the occurrence of r.r. in certain corner geometries. They fall into the range predicted by the theory. Generally, we found good agreement between experiment and theory, as shown in Fig. 5.

5. CONCLUSIONS

Previous investigations have only observed Mach reflection in corner flows. The present work has shown that:

1. The conical flow model allows the failure of regular reflection to be described by two-dimensional theory.

2. The conditions at which previous experiments were conducted all lie in the range where this theory predicts Mach reflection.

3. In the range where regular reflection is predicted, multiple reflection in the corner prevents it.

4. Multiple reflection may be avoided by opening the corner with a conically widening slit.

5. Transition from regular to Mach reflection with such a model was observed to occur at the condition predicted by the theory, using optical and tomographic techniques on a transparent model at two Mach numbers.

6. REFERENCES

1. Hornung, H.: "Regular and Mach Reflection of Shock Waves"; to be published in Ann. Rev. Fluid Mech., 1986.

2. **Charwat, A.F.; Redekopp, L.G.:** "Supersonic Interference Flow along the Corner of Intersecting Wedges"; AIAA Journal, Vol. 5, pp. 480, March 1967.

3. Watson, R.D.; Weinstein, L.M.: "A Study of Hypersonic Corner Flow Interactions"; AIAA Journal, Vol. 9, pp. 1280, July 1971.

4. West, J.E.; Korkegi, R.H.: "Supersonic Interaction in the Corner of Intersecting Wedges at High Reynolds Numbers"; AIAA Journal, Vol. 10, pp. 652, May 1972.

5. Kipke, K.; Hummel, D.: "Untersuchungen an längsangeströmten Eckenkonfigurationen im Hyperschallbereich, Teil I: Ecken zwischen ungepfeilten Keilen"; Z. Flugwiss., Vol. 23, pp. 417, Dec. 1975.

6. Möllenstädt, W.: "Untersuchungen an längsangeströmten Eckenkonfigurationen im Hyperschallbereich, Teil II: Ecken zwischen gepfeilten Keilen"; Z. Flugwiss., Vol. 8, pp. 405, June 1984.

7. Hornung, H.; Robinson, M.L.: "Transition from Regular to Mach Reflection of Shock Waves. Part 2. The Steady-Flow Criterion"; J. Fluid Mech., Vol. 123, pp. 155, 1982.

8. Merzkirch, W.: "Flow Visualization"; Academic Press, pp. 115, 1974.

9. Shepp, L.A.; Logan, B.F.: "The Fourier Reconstruction of a Head Section"; IEEE Trans. Nucl. Sci., Vol. NS-21, pp. 21, June 1974.
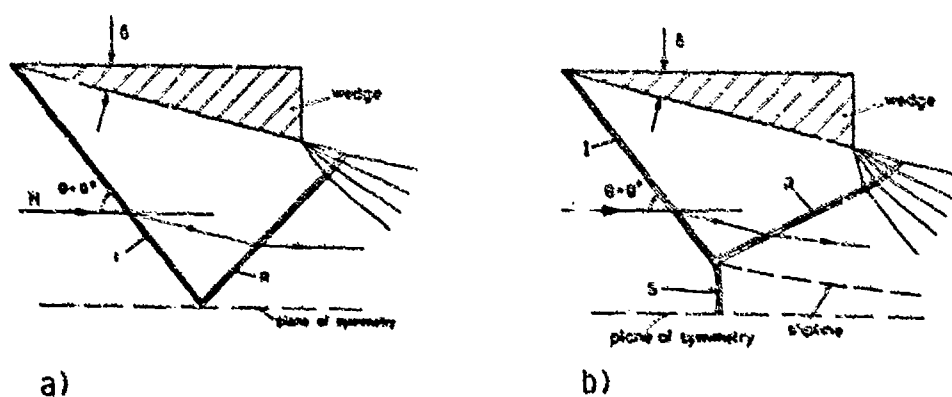
Figure 1: Shock wave reflection in steady two-dimensional supersonic flow; a) regular reflection (r.r.), b) Mach reflection (M.r.)
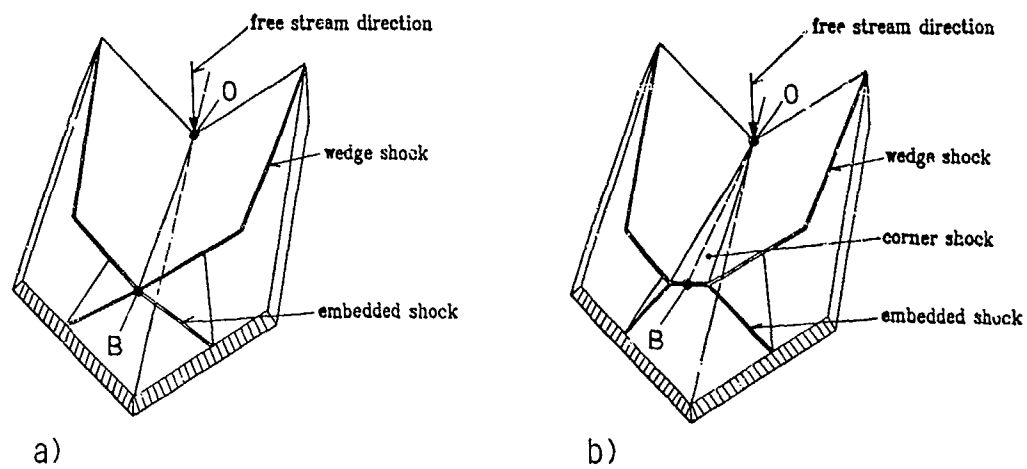
Figure 2:   Shock wave structure in supersonic corner flow
            a) r.r. type,   b) M.r. type
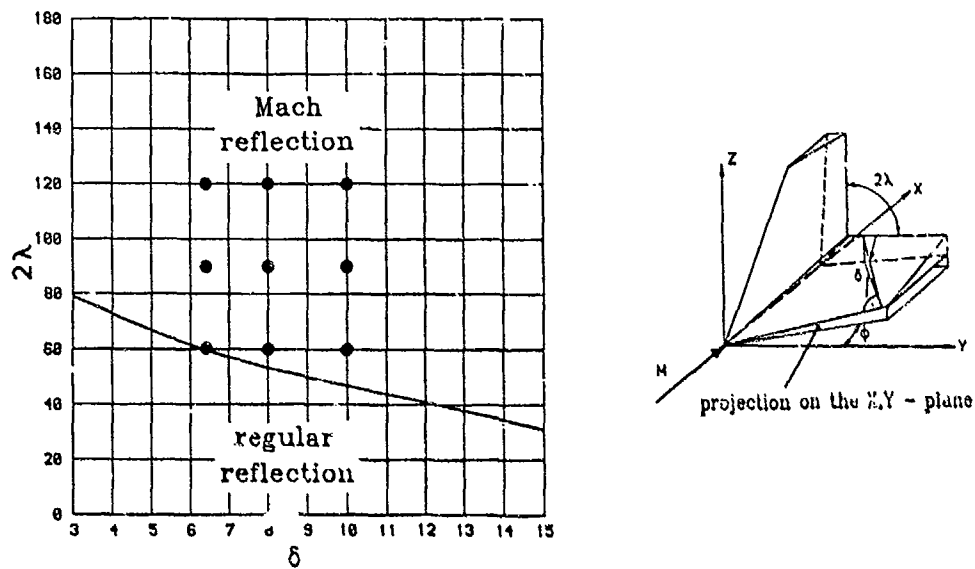
Figure 3:   Calculated occurrence of r.r. and M.r. in corner flows at M = 15.8
           and $\phi = 0°$; $\gamma = 1.4$ (• Experiments of Kipke and Hummel[5])

a)   b)
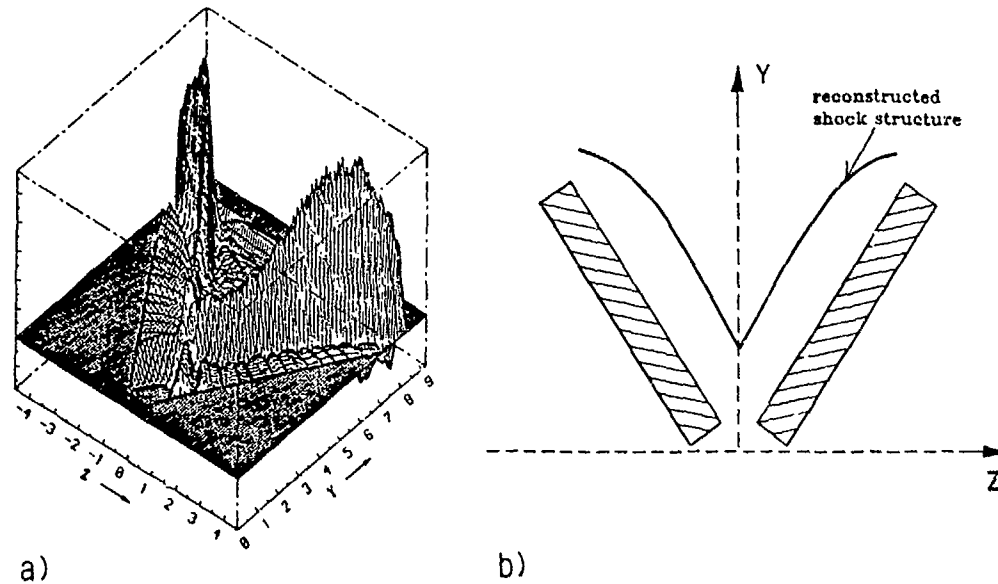
Figure 4:   Tomographic reconstruction of the shock wave structure of a corner
flow field in a plane normal to the free-stream direction.
$M = 4$, $\alpha = 15.5°$, $2\lambda = 68°$, distance from the apex: 53 mm, $\gamma = 1.4$;
a) perpective view on the plane,   b) reconstructed sectional shock
wave structure

● $M = 6$,   ▲ $M = 4$:   Mach reflection
◉ $M = 6$,   △ $M = 4$:   regular reflection
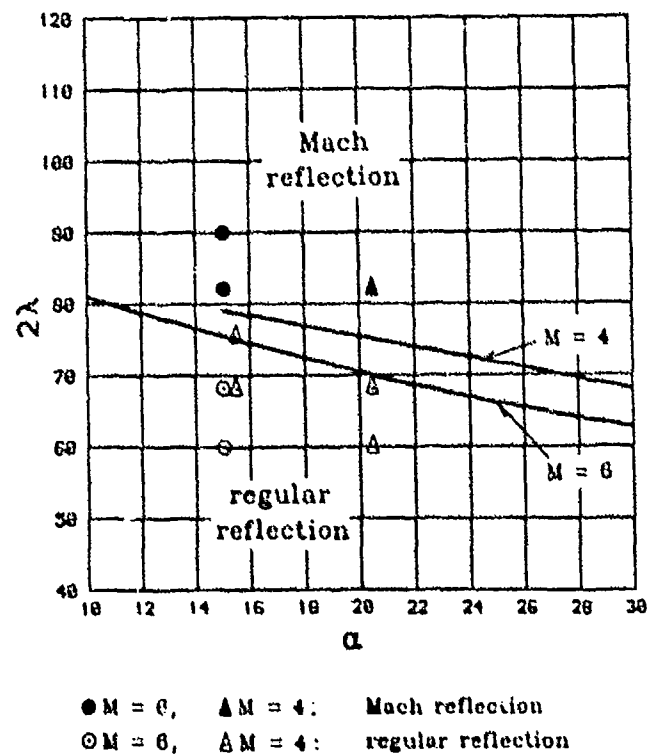
Figure 5:   Experimentally determined shock wave structure in corner flows com-
pared with theoretical calculations; $\gamma = 1.4$

EXPERIMENTAL STUDY OF SHOCK WAVE REFLECTION

IN A NARROW CHANNEL

J.Brossard, N.Charpentier

Laboratoire de Recherche Universitaire
Bourges, 18014, France

T.V.Bazhenova, V.P.Fokeev, A.A.Kalachev, A.I.Kharitonov

Institute for High Temperatures
Moscow, 127412, USSR

Shock wave reflection in carbon dioxide has been
studied in square and three different rectangular
channels with heights (lowest dimension of chan-
nel cross-section) comparable or less than the
height of bifurcation zone of reflected shock
wave. In this case secondary shock wave is formed
behind bifurcation zone and follows the reflected
shock. The influence of channel corners was found
to retard the point of boundary layer separation
in close proximity of channel ribs and entails the
disappearance of separation on narrow faces of the
channel when the opposite bifurcation zones close.
The specific feature of the pressure distribution
on lateral wall was found to depend on pressure
measurement position and is defined by the dimen-
sion of bifurcation zone. It is shown that pressure
in the point of boundary layer separation exceeds
by fifty percent the stagnation pressure of boun-
dary layer calculated from Mark criterium.

1. INTRODUCTION

The bifurcation of reflected shock wave is the subject of
many studies that is due to necessity of gas stete determination
near the end wall of shock tube.[1,3]
In all papers this gasdynamic phenomenon was examined as a
two-dimensional one without taking into account the effect pro-
duced by the side walls although all studies have been carried
out in tubes of square and rectangular cross-section. Influence
of corners in many cases could be discarded. Nevertheless the
singularity of flow near corners can be decisive on the entire
field of flow in sufficiently narrow channels when the dimension
of channel cross-section is comparable with the height of bifur-
cation zone. The complex flow near channel corner is hard to be
experimentally studied because this region is covered up by the
process of reflection on the channel axis. To be noted that pecu-
larities of the reflection with strongly pronounced bifurcation
and the filling by the bifurcation zone of the cross-section of
the channel were primarely mentioned by Strehlow and Cohen.[4]
In this paper the shock wave reflection was studied mainly
in carbon dioxide because in this case we have a more developed

form of bifurcation in comparison to bi-atomic gases, which gives
the opportunity to find out the complete structure of the flow.

2.   EXPERIMENTAL EQUIPMENT

The study of shock wave reflection was carried out in one-
diaphragm shock tube of conventional type of square cross-section
72x72 mm, length of driver section was 1.5 m, of driven section-
6.5 m. Driver gases were nitrogen and helium, driven gases were
carbon dioxide, nitrogen and air with initial pressure p_o in the
range of 5 - 35 mm Hg, Mach number M_S of incident shock wave
2.5 - 4. A four channel installation of Cranz-Schardin type[13]
with 230 mm diameter of light windows beam was used for optical
observation of the flow. In three channels schlieren-photographs
of shock reflection in different time were taken using light
source of 0,5 mcs duration. In the fourth channel schlieren
streak photograph was registered using light source of 1 ms
duration.

Piezo-gauges were used for pressure measuring on the shock
tube lateral surface near the end wall.

Sharp plates were placed in the experimental part of shock
tube in order to study the process of reflection in channels of
different cross-section. These plates cut out a part of the in-
cident shock wave. In fig.1 one can see the position of the
plates and piezo-gauges and image of slit of the photo-streak
camera. Four channels have been used with the width of 72 mm and
different height of 72 mm (A), 56 mm (13), 22 mm (C) and 8 mm (D).
The end wall of shock tube was movable (in channel A) which enabl-
ed one to alter the dimension between end-wall and window.

3.   EXPERIMENTS

In Fig.2 typical schlieren-photograph of reflection in CO_2
(channel A, p_o= 10 mm Hg, M_S = 3,57) and suitable scheme are
presented. Reflected shock wave moves from left to right with
velocity V_R , point of boundary-layer separation A and correspon-
ding line of separation A' on the window of shock tube move with
velocity V_A, gas flow entrained by incident shock wave moves with
velocity U_4. The front leg AR in the bifurcation foot forms an
angle φ with lateral wall, pressure behind front leg is p_A .
Rear leg RS and slipstream RT are parts of three-shock configura-
tion. Trajectory of point R is indicated by dashed line OR, dis-
tance of point R from the lateral wall, e.g. height of bifurcation
foot, increase linearly with the distance from the end wall,
further on its growth decreases and stops when stationary λ -con-
figuration is observed.

The experiments have shown the following features of the
reflection process. At the end plate of shock tube, vortex is
formed along the perimeter of shock tube cross-section. Its for-
mation at end wall is due to considerable velocity gradient
across slipstream RT, which is characteristic of gases with low
Γ (Γ -specific heat ratio). The second peculiarity, connected
with the influence of channel corner is deformation and retarda-
tion of boundary layer separation lines A' near channel corner.
The length of deformed part of line A' is of order of bifurcation
foot height. Line S' of end of the rear shock RS is deformed too.

The third peculiarity is the formation of the secondary shock wave F in flow core following the reflected shock R. In narrow channels this phenomenon is pronounced more clearly and the system of the consecutive shocks might be observed as it was found by Strehlow and Cohen.

The formation of F-wave coincides with the moment, when bifurcation zone takes the major part of the cross-section of the channel. The problem of the formation of the F-wave requires the consideration of the complex flow through the moving nozzle with deformed walls, formed by lines AS.

The line behind the shock F in Fig.2 corresponds to the back side of the slipstream RT, which marks the dimension of the bifurcation zone.

The behaviour of reflected shock in the narrower channels in illustrated by the schlieren-photographs in Fig.3. In this case the influence of the channel corners and bifurcation zones on the flow core is more pronounced and one can note follows. At the reflection in channel B the parameters of bifurcations on the side wall of the shock tube are equal to those on the sharp plate surface, although the boundary layer parameters are different in these cases. The difference between separation lines A' in N_2 and CO_2 can be seen for channel B. The shock wave reflection in CO_2 leads to the appearance of stronger disturbances and vortices behind reflected shock than in N_2.

In channel C the bifurcations closed. The influence of channel corners applies to the whole flow near narrow channel faces. This results in strong deceleration of the separation line A' and disappearing of boundary layer separation on the narrow faces. Reflected front transforms in a wedge-like surface, which can be asymetric.

In the narrowest channel D the reflected front transforms in one oblique shock wave. In Fig.4 streak-photographs and pressure oscillogramms for stations X and Y in channel A are presented. It can be seen that at station X the pressure grows jump-like up to the value P_λ at the moment of the passage of the separation point A. After that the pressure rests constant during about 50 mcs and then rises to the value of reflected shock pressure P_R. At the station Y pressure grows gradually (during about 1 ms) after passage of the point A, till the contact surface arrival, separating driven and driver gases in shock tube. The same was mentioned in study [14] for air and CO_2. Difference in piezogauges data is determined by the structure of bifurcation zone, registered by the mean of streak records. Near the end wall the bifurcation zone has a very small length, and takes 50 mcs to pass section X growing linearly. Mean while the reflected shock removes from the end wall, self similarity is breaking, eielding the deceleration of the back point of the separation zone, which isn't achieve section Y.

Searching streak records one can see that the secondary shock F arises in the case of well-developed bifurcation and in our case is not connected with interaction of reflected wave with contact surface as it was observed in study [15]. This fact can be seen in Fig.4 on the lower streak photograph, recieved with the observation window, being displaced from the end wall at 45 mm.

The sensitive characteristics of the bifurcation are the parameters of the front leg AR. In Fig.5 the variation of P_λ /P_1 is presented by the circles where P_λ is the pressure in the

separation point A under the front leg and P_4 - the pressure
behind incident shock wave. Open circles correspond to the measu-
rement in station X (distance from end plate is 25 mm), black
circle - for section Y (distance 85 mm), half-filled circle cor-
respond to measurement in section X, but with displaced end plate
(distance from the end plate 71 mm). The curves represent the
calculated values of the boundary layer stagnation pressure in
reflected shock coordinate system [4], curve 1 - calculated, using
velocity V_R from [16], 2 - for the average experimental velosity
V_R , in the channels A and B, measured in the sections X and Y,
3 - for V_R , calculated with γ =1.29. Curve 4 is P_λ /P_4 calcu-
lated from average experimental velosity V_λ . The experiments
show that the pressure P_λ in CO_2 at developed bifurcation is
about 50% over the values, yielding from Mark's model [1] . The
pressure near the end wall is independent from M_s for the range
of M_s = 2.5 - 4 and lower than the pressure at the distance
70-80 mm from the end wall.

Pressure P_λ can be obtained also from the front leg para-
meters. The experimental data: V_λ , front leg slope φ and velo-
sity of flow gives values P_λ /P_4 , represented in Fig.5 by hat-
ched region 5 (using [16]) and 6 (for γ = 1,29) for corresponding
sound velocity. The values of P_λ from front leg parameters are
coincident with the piezogauge-measured data.

Experimental values of P_R at the side wall of channel A can
not be applied as a state condition parameter near end wall, as
this was marked also in study [14] . The dispersion of P_R signifi-
cally exceeds typical experimental error.

CONCLUSION

As the result of presented study in CO_2, it has been shown
that the reflected shock-boundary layer interaction trends to
the formation of complex flow pattern with the secondary shock
wave behind reflected shock as the heights of bifurcation zones
become comparable with the height of channel. The influence of
the channel corners, resulting in separation point deceleration,
is more pronaunced at closing of bifurcation zones in narrow
channels. The pressure at separation point does not agree with
the calculated values using the Mark's model.

REFERENCES

1. Mark, H., "The Interaction of a Reflected Shock Wave with
    the Boundary Layer in a Shock Tube", JAS, Vol.24, N 4,
    April 1957, p.304.

2. Strehlow, R. and Cohen, A., "Limitation of the Reflected
    Shock Technique for Studying Fast Chemical Reactions and its
    Application to the Observation of Relaxation in Nitrogen and
    Oxygen", J. of Chem.Phys., Vol.30, N 1, 1959, p.257.

3. Dyner, H.B., "Density Variation due to Reflected Shock-
    Boundary-Layer Interaction", Physics of Fluids, Vol.9, N 5,
    May 1966, p.879.

4. Davies, L. and Wilson, Y.L., "Influence of Reflected Shock
    and Boundary-Layer Interaction on Shock-Tube Flows", Physics
    of Fluids, Vol.12, N 5, Pt.2, 1969, p.37.

5. Matsuo, K., Kawagoe, S. and Kage, K., "The Interaction of a
    Reflected Shock Wave with the Boundary Layer in a Shock Tube",
    Bull. JSME, Vol.17, N 110, August 1974, p.1039.

6. Sanderson, R.J., "Interpretation of Pressure Measurements
    behind the Reflected Shock in a Rectangular Shock Tube",
    AIAA J., Vol.7, N 7, July 1969, p. 1370.

7. Holder, D.W., Stuart, C.M. and North, R.Y., "Reflected Shock
    Tunnel", British Aeronautical Research Council Report, N 22,
    1961, p.891.

8. Honda, M., Takayama, K., Onodera, O. and Kohama, Y., "Motion
    of Reflected Shock Waves in Shock Tube", Proc. of the 10th
    Intern. Shock Tube Symp. Ed. G.Kamimoto, Kyoto University,
    Japan, 1975, p.320.

9. Bull, D.C. and Edwards, D.H., "An Investigation of the Ref-
    lected Shock Interaction Process in a Shock Tube", AIAA J.,
    Vol.6, N 8, 1968, p.1620.

10. Zhilin, Y.V., Bazhenova, T.V. and Gvozdeva, L.G.,"Bifurcation
    of the Shock Wave upon Reflecting from the End Wall of the
    Shock Tube", Archives of Mechanics, Vol.30, N 4-5, 1978,
    p.675.

11. Taylor, J.R. and Hornung, H.G., "Real Gas and Wall Roughness
    Effects on the Bifurcation of the Shock Reflected from the
    End Wall of a Tube", Proc. of the 13th Intern. Symp. on Shock
    Tubes and Waves, Ed. C.E.Treanor and J.G.Hall, State Univer-
    sity of New York Press, 1981, p.262.

12. Takano, Y., Miyoshi, S. and Akamatsu, T., "Reflection Proces-
    ses of Ionizing Shocks in Argon on an End Wall of a Shock
    Tube", Proc. of the 12th Intern. Symp. on Shock Tubes and
    Waves, Ed. by A.Lifshitz and J.Rom, The Magnes Press, The
    Hebrew University, Jerusalem, 1980, p.187.

13. Sukhorukikh, V.S., Kharitonov, A.I. and Sharov, Y.L., "The
    Cranz-Schardin Method in the Parallel Beams", Proc. of the
    15th Intern.Congress on High Speed Photography and Photonics,
    SPIE, San-Diego, 1983, p.534.

14. Dumitrescu, L.Z., Popescu, C., and Brun, R., "Experimental
    Studies of the Shock Reflection and Interaction in a Shock
    Tube", Proc. of the 7th Intern. Shock Tube Symp. Ed. by
    I.I.Glass, University of Toronto Press, 1969, p.751.

15. Matsuo, K., Kage, K. and Kawagoe, S., "The Interaction of a
    Reflected Shock Wave with the Contact Region in a Shock
    Tube", Bull. JSME, Vol.18, N 121, July 1975, p.681.

16. Lapworth, K.C., "Normal Shock-Wave Tables for Air, Argon,
    Carbon Dioxide, Carbon Monoxide, Hydrogen, Nitrogen, Nitrous
    Oxide and Oxygen", British Aeronautical Research Council,
    C.P. N 1101, London, 1970.

FIGURES CAPTIONS

Fig. 1. Scheme of rectangulare channels. All dimentions in mm.

Fig. 2. Bifurcation of reflected shock wave in channel A. CO_2 , p_0 = 10 mm Hg, M_s = 3,57. R - triple point, AR and φ - the front leg and its slope, RS and S' - rear leg and its back-line, RT - slipsteam, A and A' - point and line of boundary layer separation, F - secondary shock wave, V_R and V_λ - velocities of reflected shock and separation point.

Fig. 3. Schlieren photographs of reflection in different channels. 1 - channel B, N_2 , p_0 = 35 mm Hg, M_s = 2.59, 2 - CO_2 , p_0 = 12.5 mm Hg, M_s = 3.09, 3 - CO_2 , p_0 = 5 mm Hg, M_s = 5.56, 4 - channel C, CO_2 , p_0 = 45 mm Hg, M_s = 2.59, 5 - CO_2, p_0 = 10 mm Hg, M_s = 3,41, 6 - channel D, CO_2 , p_0 = 20 mm Hg, M_s = 3,25.

Fig. 4. Variations in pressure on the side wall of shock tube and streak photographs for shock wave reflection in CO_2 in channel A, p_0 = 10 mm Hg, M_s = 3.15. Upper record, pressure in section X; lower record - in section Y, sweep speed - 100 mcs/div. 1 - photo taken with oscillograms, arrows show the piezogauge positions; 2 - photo with F-wave more pronounced; 3 - photo with deplaced end wall by 45 mm. I.S. - incident shock C.S. - contact surface.

Fig. 5. Relationship between p_λ / p_1 and M_s in CO_2, channel A. 1,2,3,4 - boundary layer stagnation pressure[i] , using V_R from [16] (1), experimental values V_R (2) and V_R for γ = 1,29 (3); 4 - using measured V_λ . Open circles - p_λ / p_1 in section X, black circles - for section Y, half-filled circles - for section X with displaced end plate by 45 mm. 5,6 - calculated values p_λ / p_1 using experimental parameters of front leg with sound velosity from [16] (5) and for γ = 1,29 (6).
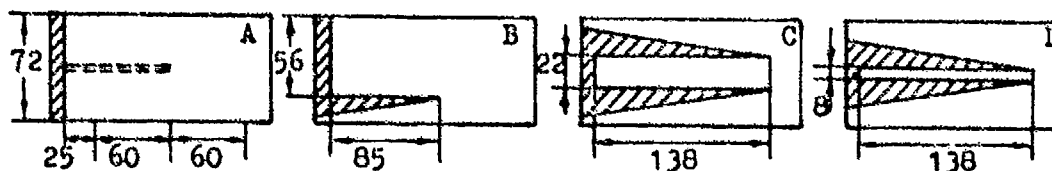
Fig. 1
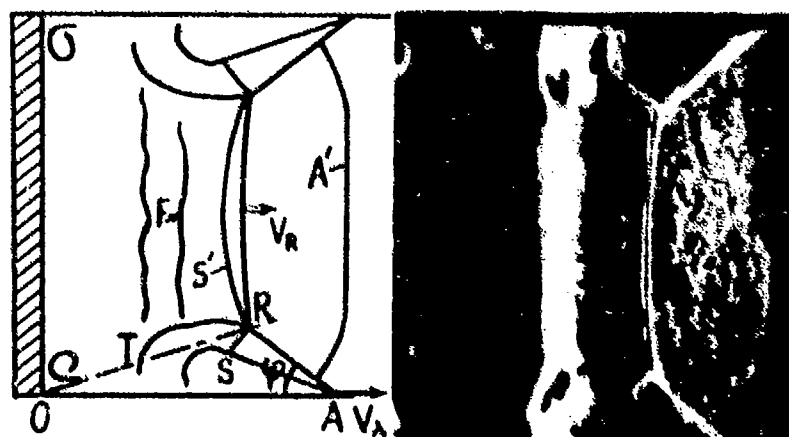
Fig. 2
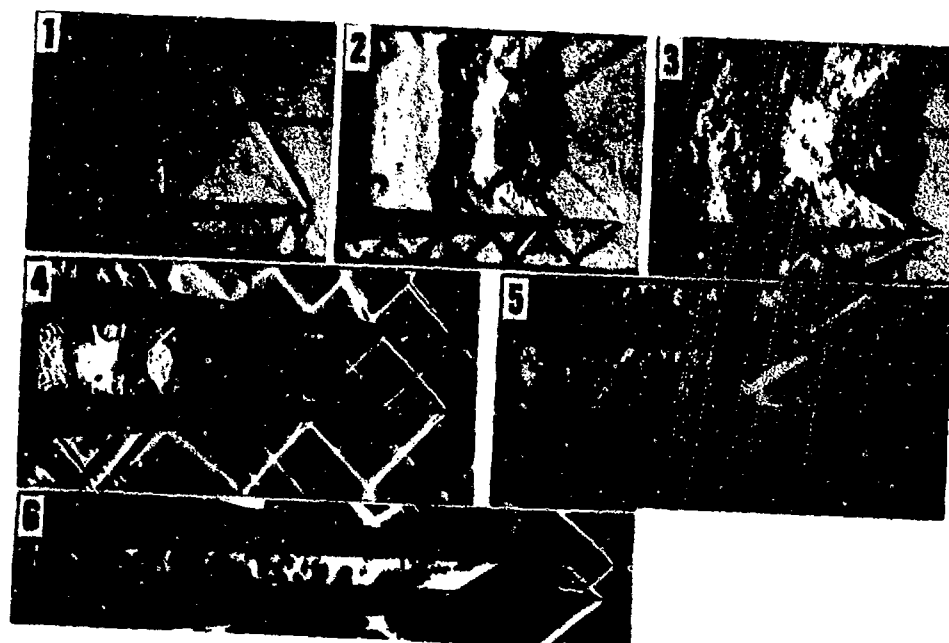
Fig. 3
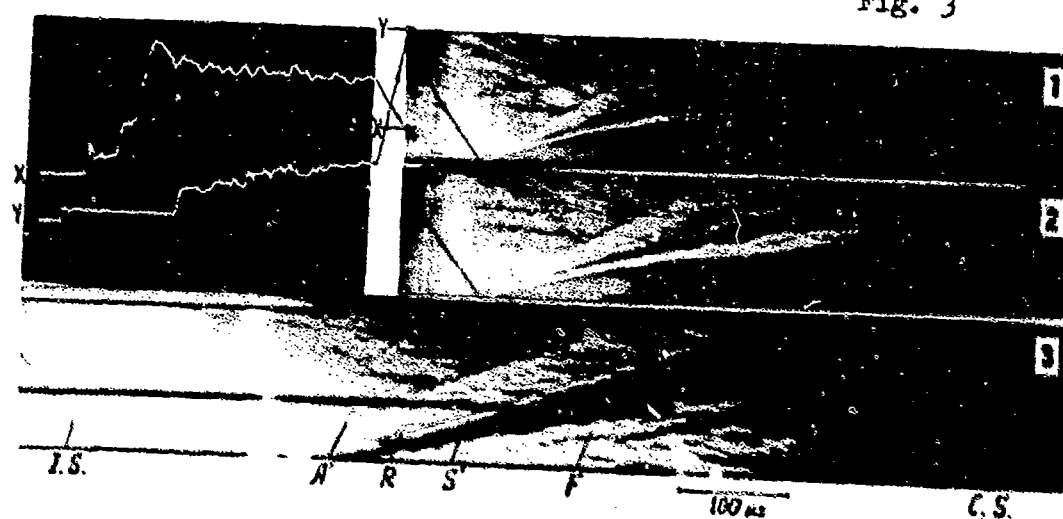
Fig. 4
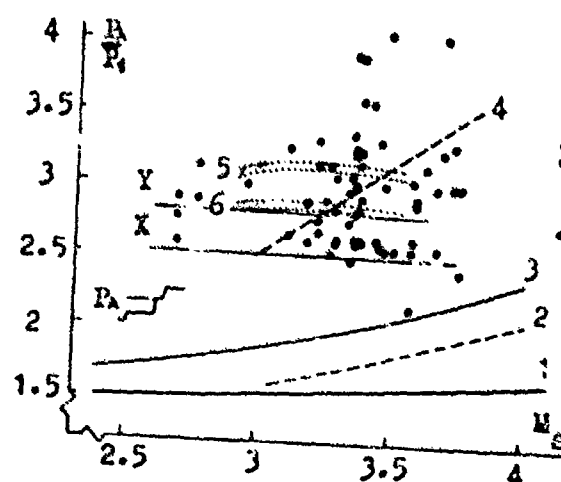
Fig. 5

AIR-INDUCED GROUND PRESSURE WAVES
IN GRANULAR SOIL MATERIALS

D. Hveding

Norwegian Defence Research Establishment,
P O Box 25, N-2007 Kjeller, Norway

The report deals with certain aspects of wave propagation
in and the dynamic reaction of a granular material when
subjected to an impulse load of long duration. The ex-
perimental set up generates uniaxially transmitted and
(normally) reflected pressure waves. The measuring tech-
nique and instrumentation are briefly commented. The
basis for a simple theoretical presentation of relations
of interest for the experiments is given. The main ex-
perimental results are summarized. Some of the theoreti-
cally predicted and the measured data are compared.

1. INTRODUCTION

A granular soil material (as sand) under an impulse load, can
be shown to be influenced by several factors that should be brought
into a set of equations in order to properly describe the dynamic
reaction of the material. Experiments concerning wave generation,
transmission and reflection for given sets of initial conditions
and recognizing the two (three) phase nature of granular materials,
should improve the basic understanding of the granular material
dynamics. This paper will present some results of our theoretical
and experimental investigations concerning air-induced ground pres-
sure waves in granular materials (sand). The experimental set up
was made geometrically simple and the test conditions were well
defined and made to match the theoretical assumptions as much as
possible. In particular a continuum theory for granular materials
will require material homogeneity (velocity fields) for the soil
dynamic experiments. Preliminary investigations were therefore done
in this and other problem areas.

2. LOADING SITUATIONS, EXPERIMENTAL SET UP

The study assumed a loading situation determined by an air-
shock wave sweeping over the horizontal surface of a uniform or
homogeneous semi-infinite granular material, Figure 1.1. The gene-
ral loading situation is, at each position assumed to be similar
to a one-dimensional (uniaxial) piston type of loading on the sur-
face, Figure 1.2, and will generate separate uniaxial pressure
waves in the sand with assumingly no interference by means of an
impulse transfer mechanism. The front position of these waves will
be represented by the wavefront line, which for increasing time is
propagated in the material in the horizontal direction. This is
indicated on Figure 1.2 for a constant and sweeping surface
loading. The paper will consider the loading situation over a
period that clearly reflects the dynamic reaction of the material.
A test container (Figure 1.2) connected to a 400 mm diameter
shocktube was filled with a well defined type of sand and compacted
in a special way so that the dry density of the bulk material was
close to constant in the volume. A stable but increasing moisture

content with depth could not be avoided. The different experiments were all performed on the same type of sand and with (close to) the same initial parameter data and air shock loading. The long duration air shock nominal strength, p_{21} = 2.5. Bulk material average dry density ρ_o = 1730-1780 kg/m^3. The moisture content close to the surface w ≈ 5% and bottom (z = 500 mm) w ≈ 10%. The grain diameter was mainly from d = 0.3 to 0.6 mm

3. TRANSDUCERS, INSTRUMENTATION

Transducer weight, size, shape, orientation and their mostly "free floating" contact condition with the sand particles are some of the important parameters to take into account in order to measure representative data for the pressure waves. Practical measuring problems and the complex dynamic behaviour of the grains determined the design and use of three different transducers with the necessary dynamic response to yield three independent groups of realistic data. The S-transducer was made as a 3 mm thick round disc placed as shown, Figure 2.1. It will measure the average side oriented grain pressure. From separate experiments it was possible to determine a factor k_1 that will correlate the normal average pressure-time (H-t) data referred to the average grain contact area to the measured side oriented grain pressure-time ($\overline{\sigma}$-t) data. The A-transducer was made small (<1 cm^3) and light weight (ca 2 g) and will respond to the real changes in the average grain motion induced by the uniaxial pressure wave. This transducer will thus give average grain acceleration-time ($\overline{a}_k$-t) and velocity-time ($\overline{v}_k$-t) data. The A-and S-transducers are placed in pairs in the center x-z volume (100 mm apart sideways) in a measuring point grid (up to 100 transducers), Figure 2.2. This gives a necessary measuring redundancy. The grid system was, however, primarely used to obtain a sufficient amount of travel time data (t_3, t_5) from which the wave front positions and the wave front velocities (C_z, C_{zR}) can be determined to a satisfactory degree of accuracy.

4. THEORY

The granular theory as developed by[1][2][3][4] has been applied to the experimental wave transmission. Generally the theory will provide a qualitative background for defining a reaction model that will include the general features of the measured results. A short presentation of certain relations of interest for the experimental situation will be given[5]. Major assumptions are:

1. The uniaxial loading situation results only in an irreversible compaction or distension of the uniformly distributed granular material made up of non-uniform grains
2. The wave propagation is uniaxial, the z-direction
3. The grains are incompressible, non-crushing and nonbending
4. The different cohesion forces are small, the main intergranular forces are based on frictional effects
5. Moisture and gas in the pore volume are ignored (mass- and pressure-wise), one will consider a one-phase material
6. Moisture content will influence the dynamic reaction of the granular material by changing the mobility of the grains
7. The wave front velocity (C_z) during the loading at each measuring point is constant
8. The dry-density $\rho_o(x,z,y)$ is assumed constant, grain pressure due to weight (σ_o) is neglected, constant temperature

9.   The continuous distribution of the grain volume will define
      the bulk material and the deformation field at each position

The granular material has the structure of a distributed body
which can be considered as a continuum. The density of the material
at any point (X_i) and time (t) can be expressed as

(4.1) $\rho(X_i,t) = \nu(X_i,t) \cdot \gamma(X_i,t)$

Any changes in the material density (ρ) will only be deter-
mined by the volume distribution function (ν) when the grain den-
sity function (γ) is constant. The variable ν is defined as

(4.2) $\nu = \dfrac{\text{GRAIN VOLUME } (V_i)}{\text{TOTAL VOLUME } (V)}$, $1 > \nu > 0$

Changes in ν will reflect the relative motion of the uniformly
distributed grains in a control volume as a result of a directed
grain compaction or distension and therefore of the pore volumes.
The parameter will define the average grain motion at each position
during a loading situation. This can formally be developed from a
theoretical kinematic point of view resulting in

(4.3) $\dfrac{\dot{\nu}}{\nu_0} = \dfrac{d\bar{v}_k}{dt} \cdot \dfrac{\bar{a}_k}{C_2}$ (4.4) $\dfrac{\dot{\nu}}{\nu_0} = \dfrac{\bar{a}_k}{C_2} + (\dfrac{\bar{a}_k}{C_2})^2$ (4.5) $\dfrac{\Delta\nu}{\nu_0} = \dfrac{\bar{v}_k}{C_2}$

These relations will give a direct connection between the
measureable average grain acceleration $\bar{a}_k$ and velocity $\bar{v}_k$ and the
ν-function and its time derivatives as a measure of the average
granular motion, assuming a constant $\nu = \nu_0$.

The dynamic reaction of or the thermo-kinetic process in the
material as represented by several dependent variables R_i, will be
assumed dependent on the initial value of the volume distribution
function (ν_0), changes in ν and the entropy changes (ζ) associated
with the process and given by

(4.6) $R_i = f(\nu_0, \nu, \dot{\nu}, \nu_0/\nu, \nabla\nu, \zeta)$

The formal thermodynamic procedure used to establish the con-
stitutive equations and the required restrictions for these to be
valid under the given assumptions, will not be given here[1,2,3].

Based on the above relations one can write the conservation
laws in terms of directly measureable parameters and thus in a
"simple way" express the effects of the granular material dynamics.
The conservation of mass will for the given conditions be expressed
by a relation similar to equation (4.3). The conservation of linear
monumentum will give an expression relating the pressure forces (S)
and the resulting changes in the average grain acceleration ($\bar{a}_k$).
Here S can only be determined by the variables expressed by R_i,
equation (4.1) and (4.6). The thermo-kinetic process will also
require a balance of forces. The intergranular forces that deter-
mine the compaction/distension of the material (h) can be related
to the measureable average grain pressure (H). This will depend
on $\nabla\nu$ and its time derivative. The body force g represents the
intergranular forces that are determined by fricitional effects and
are dependent on $\dot{\nu}$. These forces will have to be balanced by an
inertia force k expressing the dynamic effects of the relative
motion of the grains. It may be related to the mobility of the
grains and will be influenced by the initial parameter data. The k
will be a function of ν and ν_0, the other two variables are consti-

tutively related as given by R_{ij}, equation (4.6). The force balance equation will relate these parameters

$$(4.7) \quad \rho_0 \cdot \overline{\dot{k} \cdot \dot{\nu}} = \frac{dh}{dz} + g = H + g = B$$

By combining equation (4.7) with the linear momentum equation and substituting the pressure force S by B one finds that

$$(4.8) \quad B = \rho_0 \cdot \overline{\nu}_k \cdot C_z = H + g$$

Integrating equation (4.7) results in an expression for k or $k \cdot \dot{\nu}$ as function of the grain pressure B. For the given assumptions one can express the grain parameters (k and B) by the variable ν and its derivatives by using equation (4.5) and (4.8). The inertia term k will primarely be associated with the integrated effect of the grain compaction/distension ($\Delta\nu$) or the average uniaxial grain deformation ($\overline{d}_k$). The pressure term B will be proportional to $\overline{\nu}_k$ or $\Delta\nu$ for constant C_z and ρ_0. The equations can be used to show the parameteric relation for the front velocity C_z as

$$(4.9) \quad C_z^2 = \frac{dk}{d\nu} \cdot \frac{\dot{\nu}^2}{\Delta\nu} \cdot \nu_0 + k \cdot \frac{\ddot{\nu}}{\Delta\nu} \cdot \nu_0$$

This is a complex relation in spite of the simplifying assumptions. The constrained modulus M_ν can be expressed as

$$(4.10) \quad M_\nu = \frac{dB}{d\Delta\nu} = \gamma_0 \cdot C_z^2 = \frac{\dot{g}}{\dot{\nu}}$$

It was assumed that C_z was constant f ex over the impulse loading time (t_{gg}, Figure 3.6), consequently also M_ν and $B/\dot{\nu}$ (or $B/\overline{a}_k$, equation (4.3)), must be constant with the implications this will have for the parameters in the above equations and the possibility to determine different variables in an independent way.

Normally reflected uniaxial waves (from hard reflection surfaces) that can be considered superimposed on the transmitted (T) wave, can directly be represented by the given theory (f ex equation (6.2)). A granular reflection theory under development will express the dynamic reflection process in a similar way as above[10]. For the purpose of data comparison a theoretically based empirical expression is given by equation (6.3).

5. EXPERIMENTAL RESULTS

Some of the results concerning the transmitted (T) and the normally reflected (R) pressure waves will be presented[10]. The measuring point grid gave travel time data for the transmitted (t_3) and reflected (t_5) waves from which a series of wavefront curves (x-z-t) as shown on Figure 3.1 were obtained. These curves gave data for the wavefront velocity $C_z(z)$ for the T-and $C_{zR}(z)$ for the R-wavefront curves, Figure 3.2. Both wavetypes were uniaxial. The z-dependence of the front velocities were also influenced by changes in the effective density (ρ_e) of the material (f ex moisture). This will affect the grain inertia term (k) and grain mobility.

The grain pressure (S- and P-) tranducers and the accelerometers (A-transducer) gave consistent data that correlated well with each other and the travel time data. Figure 3.3 and 3.4 show typical or average amplitude-time histories representative for all the experiments where uniaxial wave data were measured. Characteristic average maximum amplitudes are presented on Figure 3.5 and 3.6. The

steep z-gradient of the maximum amplitudes without loosing the
general form for the amplitude-time curve is interesting. The re-
flected wave can be considered superimposed on the transmitted wave
as shown in Figure 3.3 and 3.4. Closer to the reflection surface
the loading situation becomes increasingly complex. On the surface
itself one has measured a large normal reflection pressure (H_R)
(typically 4-6 times the undisturbed transmitted wave right above
the surface) that remained high over a long period, Figure 3.4. The
reflected waves, after a short distance above the surface, show a
marked amplitude reduction (Figure 3.6) at the same time as the am-
plitude-time histories are changed ("stretched out"). The measured
results generally support the theoretical formulation of section 4
over and at a solid and rough reflection surface for an impulse
dominated wave loading. A few observations will be included [10]

1   The front velocities C_z and C_{zR} can be considered constant at
    each position over the loading times. Small and consistent
    deviations could be detected especially for the reflected wave
2   Measurements showed that the relation $T = B/\bar{a}_k$ = constant was
    generally valid, Section 4, also for the normally reflected
    waves over the reflecting surface
3   The g-term (equation 4.7) was small in relation to the normal
    grain pressure (H)
4   The moisture content and distribution influenced the wave
    transmission measureably
5   Only one type of pressure (compaction) wave was generated in
    the material, this is theoretically expected

6. THEORETICAL-EXPERIMENTAL DATA

An indication of how well the theoretical formulation can pre-
dict consistent measured data for defined initial parameters, will
be given by comparing calculated results using independent measure-
ments in connection with different theoretical relations. Some
sample calculations are shown below, the data are taken from the
presented figures, the previous sections and from different mea-
surements not presented. The calculations are made for positions
close to and on the reflecting surface, z = 450-500 mm, Figure
2.2^{10}. With reference to equation 4.8, Figure 2.2, section 3,
$B = H + g = H$, the normal maximum pressure for the transmitted and
normally reflected waves are given by

(6.1a, b) $H = \rho_o \cdot \bar{\eta}_k \cdot C_z = k_1 \cdot \bar{\sigma}$

(6.2a, b) $\Delta H_R = \rho_o \cdot \Delta\bar{\eta}_{kR} \cdot C_{zR} = k_1 \cdot \Delta\bar{\sigma}_R$

The k_1-factor is assumed constant over the loading time and
was determined by separate experiments. These data compare well
with values that can be obtained from a theoretical expression
assuming the condition given in section 5, point 2. The total
reflected pressure H_R may be given a theoretical-empirical form

(6.3a, b) $H_R = \rho_o \cdot \bar{\eta}_k \cdot (C_z + K(z)) \cdot C_{zR}) = k_1 \cdot \bar{\sigma}_R$

where $K(z)$ is a dynamic correction factor characteristic for the
reflection process close to and on the reflection surface. $K(z)$
decreases above the surface.

The constrained modulus H_v is calculated according to equation

(4.10) and must be considered as an average value over the loading time since C_z (and C_{zR}) can only be constant under certain conditions. The expression for C_z, equation (4.9), can for the test conditions be shown to reduce to the form (a_k term dominates)

(6.4) $\quad C_z^2 = k \cdot \dot{a}_k/\bar{v}_k \cdot \nu_0$ $\qquad\qquad$ (6.5) $\quad C_z = \dot{H}/\bar{a}_k \cdot \rho_0$

Equation (6.4) can be compared to an expression for C_z deduced from the linear momentum equation, equation (6.5). The inertia term can be estimated from equation (4.7). In general will C_z vary over the loading time (section 5, point 1).

By using corresponding, representative and independently measured data, one can calculate and compare the results given by the presented expressions. The following tables give some results

kN/m²	eq (6.1a)	eq (6.1b)	eq (6.2a)	eq (6.2b)	ρ_O = 1750kg/cm³
H	90	100	–	–	k_1 = 3.3
ΔH_R	–	–	102	100	C_{zR} = 450 m/s
Refl factor R = (ΔH_R+H)/H			~ 2	~ 2	C_z = 300 m/s

kN/m²	eq (6.3a)		eq (6.3b)	k_1 = 1.7
H_R	480	K = ⊤	510	ρ_O = 1750 kg/m³
R	~ 5	C_z = ͜͜0 m/s	~ 5	Refl factor R = H_R/H

The modulus (eq 4.10) M_v = 2600 · 300² = 235.10³ kN/m².
The front velocity C_z can be estimated by equation (6.4) and (6.5).

m/s	eq (6.4)		eq (6.5)	
C_z	350-270	$\dfrac{v_O}{a_k}$ = 0.65 max = 200 g	285	k_1 = 3.3 ρ_O = 1750 kg/m³

The calculated data are in fair agreement with the measured representative C_z = 300 m/s for z ~ 450-500 mm (Figure 3.2).

7. CONCLUSIONS

The study has shown that a simple granular theory based on grain dynamics can give a representative description of the dynamic reaction of a granular material and a first order approximation to the measured data. Acceptable agreement both qualitatively and quantitatively was obtained for the different parameters for the uniaxially transmitted and normally reflected pressure waves in the moist granular material. This was demonstrated for the impulse dominated grain compaction during the loading risetime. This situation will also imply that the experiments at each position will give a deformation field comparable to the theoretical requirements. For other time periods and loading situations, different grain dynamic forces (theoretically described) will make influential contributions in determining the reaction model for the material. The initial parameter data will be of importance since these affect the grain mobility. Various reflection geometries and a non-uniaxial wave propagation will introduce complicating factors. The study suggests that also these situations can be theoretically expressed based on the general granular theory and yield data representative of the measured results. Further work is planned and in progress for the purpose of determining the characteristics of dynamic reaction models for granular materials in a wider perspective. Here both simplified and direct expressions as well as computer programs will be of interest in order to determine the

loading function in connection with structural dynamics.

REFERENCES
1.   Goodman, M.A., "A continuum theory for the dynamical behaviour
     of granular materials", Dr. thesis, Tulane University, 1970.
2.   Goodman, M.A. and Cowin, S.C., "A continuum theory for granu-
     lar materials", Arch. Rat. Mech. Anal., Vol. 47, 1972, p.249.
3.   Nunziato, J.W. and Cowin, S.C., "A nonlinear theory of elastic
     materials with voids", Arch. Rat. Mech. Anal., Vol. 72, 1979,
     p.175.
4.   Cowin, S.C. and Nunziato, J., "Linear elastic materials with
     voids", J. Elasticity, Vol. 13, 1983, p.125-147.
5.   Truesdell, C., "The classical field theories", Handbuch der
     physik Band III/I, Springer Verlag, 1960.
6.   Coleman, B.D. and Noll, W., "The thermodynamics of elastic
     materials with heat conduction and viscocity", Arch. Rat.
     Mech. Anal., Vol. 13, 1963, p.167.
7.   Mindlin, R.D., "Microstructure in linear elasticity", Arch.
     Rat. Mech. Anal., Vol. 16, 1964, p.51.
8.   Toupin, R.A., "Theories of elasticity with couple-stress",
     Arch. Rat. Mech. Anal., Vol. 17, 1964, p.85.
9.   Krizek, J.R., "Rheologic behaviour of cohesionless soils sub-
     jected to dynamic loads", Trans. Soc. Rheology, Vol. 15:3,
     1971, p.491.
10. Hveding, D. "Several FFI/NOTAT concerning experiments and
     theoretical studies", f ex 83/4025, 84/4003, 85/4001, 84/4030,
     84/4031, Norwegian Defence Research Establishment (in Norw)
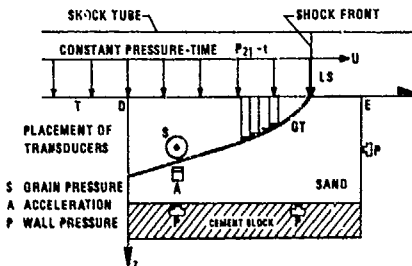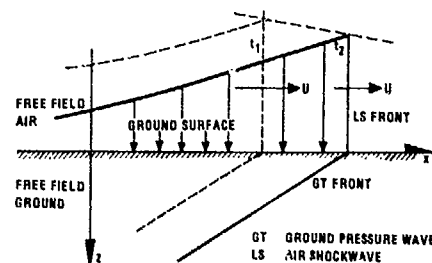
Figure 1.1   Ideal freefield
             loading situation

Figure 1.2   Loading situation,
             shocktube-testcontainer
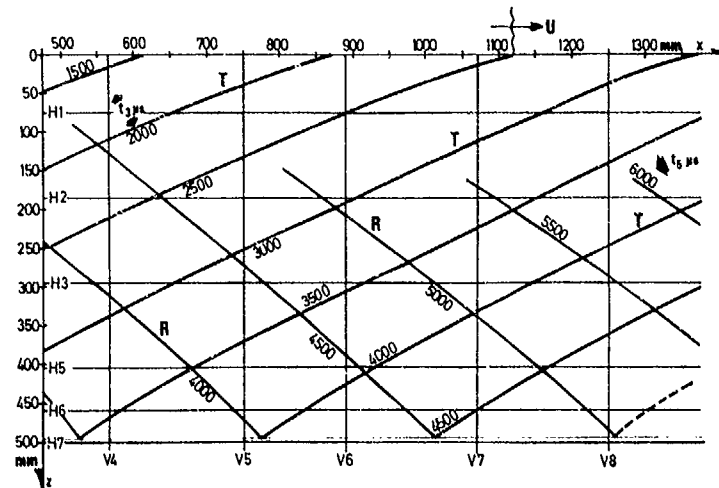
Figure 2.1   Transmitted and reflected   wavefront lines
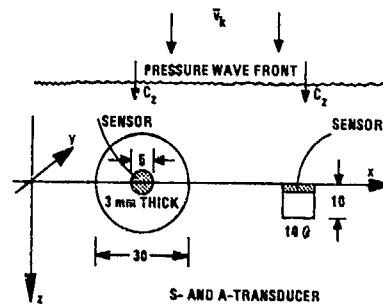
Figure 2.1   Transducer geometry
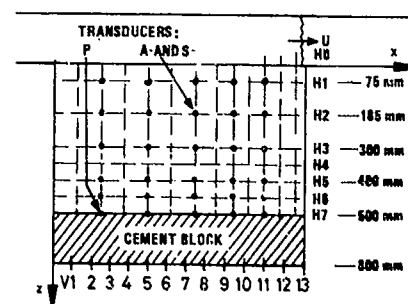
Figure 2.2   Measuring point grid
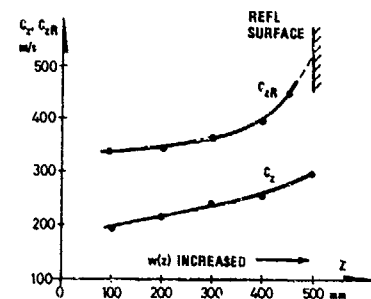
Figure 3.2   Representative
wavefront velo-
cities
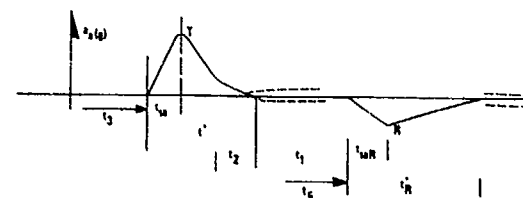
Figure 3.3   Representative acceleration-time curve for
all measured data

t_3 = travel time transmitted wave (T)

t_5 = travel time reflected wave (R)

t_{sa} = 30 – 50 μs

t^+ = 100-150 μs

t_{saR} = 50 -120 μs
t_{R^+} = 200 μs } incr. with decr. z
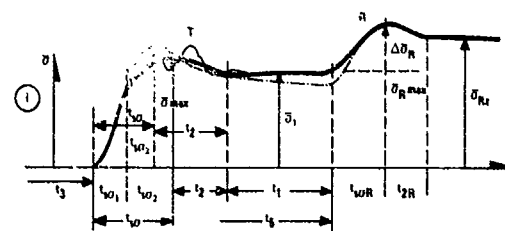
Figure 3.4   Representative grain pressure-time curve ($\bar{\sigma}$-t)
as measured in the sandvolume (I) and on the
rough cementblock bottom (II)

t_3 = travel time transmitted wave (T)

t_5 = travel time reflected wave (R)

t_{sa} = 90-130 μs (I)

t_{sa1} = 30-50 μs (I), t_2 > t_{sa2}

t_1 = dependent on z, σ_1 is near constant

t_{saR} = 80-180 μs, incr. with decr. z

$\Delta\bar{\sigma}_R$: tends to decrease with decr. z

$\bar{\sigma}_R$: normal refl. on bottom surface (II)
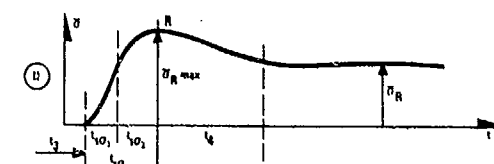
Figure 3.5   Representative max
acceleration
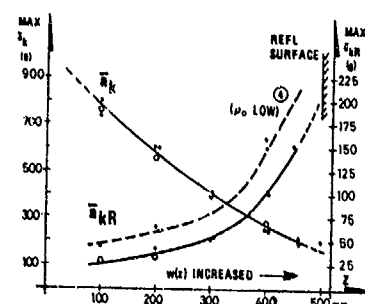
Figure 3.6   Representative max
grain pressure

WAVE AND THERMAL PHENOMENA

IN H.S.-TUBES WITH AN AREA CONSTRICTION

E. Brocher and M. Kawahashi[*]

Institut de Mécanique des Fluides
de Marseille, 1, rue Honnorat,
13003 Marseille, France

[*]Department of Mechanical Engineering
Faculty of Engineering, Saítama University
255 Shimo-Okubo, Urawa, 338 Japon

The propagation of waves in a Hartmann-Sprenger tube
having an area constriction is studied both theoretical-
ly and experimentally. It is found that there are seve-
ral possible modes of oscillations within the tube. The
observed mode depends on the diameter - and length -
ratios of the upstream and downstream parts of the tu-
be. The mode also depends on the Mach number of the ex-
citing jet. In the "first" mode, the shock wave genera-
ted in the upstream cavity is transmitted trough the
area change and strongly amplified. In higher modes, the
incident wave in the upstream cavity meets, near the
area change, a shock wave traveling in the opposite di-
rection in the downstream cavity. For a given total
length, the oscillation frequency cf the 3rd and 5th
modes are approximately 3 and 5 times the frequency of
the 1st mode, respectively. The thermal effects, essen-
tially due to repetitive shock heating, strongly depend
on the oscillation mode. In the 1st mode, the tempera-
ture steadily increases along the tube, with a steep
temperature gradient in the downstream cavity. In the
3rd mode, a steep temperature gradient is observed
near the area constriction whereas the temperature is
high and almost constant in the downstream cavity. The
influence of the shape of the joining section between
the upstream and downstream cavities has been investi-
gated. The highest shock intensities and thermal ef-
fects have been observed with a sinusoidal converging
section.

1. INTRODUCTION

At the 13th International Symposium on Shock Waves and Tubes, it was shown[1]
that a Hartmann-Sprenger tube (HS-tube) presenting a sudden change in cross
section could produce high amplitude pressure waves. The configuration studied
is shown in Fig. 1. A high speed jet flows out of a "needle" nozzle[2] and drives
flow oscillations within a tube with constriction. A simplified wave diagram
for the flow within the tube was proposed. A theoretical amplification was de-
rived and experimental values were in good agreement with the predicted ones.
Subsequently, it was found that several modes of oscillations are possible[3].
The wave diagram as well as the thermal effects are quite different for each mo-
de. This is important when one considers the H.S.-tube as an igniter for pyro-
technic compositions[4].

Linear acoustic theory gives some idea on the possible oscillation modes. However, it cannot predict which one of these modes will be observed. Also, because the oscillation amplitude is very large and can attain several bars, it is not surprising if one finds substantial deviation between measured and calculated frequencies. The agreement between numerical experimental values and computations made with the so-called FLIC-method (fluid-in-cell) is much better.

2. LINEAR THEORY

The basic scheme of the linear theory applied to the single-step H.S tube is as follows. The acoustic pressure in each cavity is given by the superposition of waves moving in upstream and downstream directions

$$p_1 = Ae^{j(\omega t - kx)} + Be^{j(\omega t + kx)},$$

$$p_2 = Ce^{j(\omega t - kx)} + De^{j(\omega t + kx)},$$

(1)

where p, ω, k, x, and t represent acoustic pressure, angular frequency, wavenumber, axial coordinate, and time, respectively; j is the imaginary unit and subsripts 1 and 2 indicate the upstream and downstream cavities, respectively.

The complex constants A, B, C, and D are determined by boundary conditions. These are given first by the reflection coefficients at the junction and at the downstream end, and second, by consideration of the impedance at the mouth. The reflection factors R_{12} and R_{21} at the junction are given by

$$R_{12} = \frac{(D_1/D_2)^2 - 1}{(D_1/D_2)^2 + 1}, \qquad R_{21} = \frac{(D_2/D_1)^2 - 1}{(D_2/D_1)^2 + 1}$$

The reflection factor at the downstream end is equal to unity. Moreover, if the amplitude of acoustic velocity at the mouth is kept constant, i.e., $|u| = u_0$. the unknown complex constants A, B, C, and D are functions of u_0. When geometrical parameters are given, the acoustic impedance $Z \equiv p/u$ at the mouth is a function of frequency only. The eigenfrequencies are those frequencies for which the impedance vanishes. The eigenfrequencies calculated with this procedure are plotted in Fig. 4.

Particular values of eigenfrequencies are

$$f_1 = a/4(L_1 + L_2) \quad \text{if} \quad D_1 = D_2 \qquad \text{(1st mode)}$$

$$f_3 = 3 \left| a/4(L_1 + L_2) \right| \quad \text{if} \quad D_1 \neq D_2 \text{ and } L_2 = 2L_1 \qquad \text{(3rd mode)}$$

$$f_5 = 5 \left| a/4(L_1 + L_2) \right| \quad \text{if} \quad D_1 \neq D_2 \text{ and } L_2 = 4L_1 \qquad \text{(5th mode)}$$

When the frequencies are close to one of these particular frequencies, the oscillations are called 1st mode-, 3rd mode-, or 5th mode-oscillations, respectively.

3. NON LINEAR THEORY

The wave phenomena are computed with a numerical method (FLIC method) on a two-dimensional model of the tube. The basic equations used are the continuity and momentum equations

$$\frac{D\rho}{Dt} + \rho \nabla v = 0, \qquad \rho \frac{DV}{Dt} = -\nabla p$$

when ρ, V, p and t represent the density, velocity, pressure and time, respectively. In these equations, friction and heat conductivity are not taken into account, but artificial viscous pressure is introduced for the stability of the shock computation.

Wave diagrams obtained by this method are shown on Fig. 3. The diagramm for $L_2/L_1 = 5$ shows very clearly the head-on collision of shock-waves at the

step (Fig. 3a) and corresponds to the 5th mode. The computed frequencies are indicated on Fig. 4.

4. EXPERIMENTAL SET-UP

In Fig. 1, the H-S tube with constriction and the supersonic "needle noz-zle" are shown in schematic fashion. The length (L_1) of the upstream cavity has a fixed value (80 mm) whereas the length (L_2) of the downstream cavity can take several values ranging from 80-480 mm so that the length ratio L_2/L_1 can be varied from 1-6. The inner diameter D_1 of the upstream cavity is 18 mm and the diameter D_2 of the downstream cavity is 9, 6, or 3 mm, so that the dia-meter ratio D_1/D_2 takes the values 2, 3, or 6. The diameter D_N of the nozzle exit is identical to D_1. Since non-linear theory[5] applied to a sudden area change (step) shows that the flow near the constriction has a two-dimensional character, it can no longer be said that the step corresponds to a velocity node, as linear theory does. It therefore appears that if a sudden change in cross-section is replaced by a continuously changing section, the amplifica-tion of pressure amplitude and thermal effects could be further increased. Three different shapes of transition section, with length L_t, have been tes-ted (Fig. 2).

Pressure histories and time-average pressures are determined at various positions in axial direction of the tube. Instantaneous pressure is measured by piezoelectric transducers and mean pressure by a manometer. Three different shapes of the needle laid upon the nozzle axis were used in the test. They were giving correctly expanded supersonic jet for 3 Mach numbers : 1.2, 1.68 and 2.07.

5. EXPERIMENTAL RESULTS

4.1. Oscillation frequency

The oscillation frequency f in a constant area H-S tube is nearly equal to the 1st mode of the acoustic frequencies of a pipe closed at one end, i.e., $f \approx f_o = a_a/4L$, where a_a represents the ambient speed of sound and L the pipe length. The oscillation frequency is a slightly decreasing function of the jet Mach number. Whereas the ratio f/f_o is almost equal to unity for low values of M_j, it is about 0.88 for $M_j = 2.6$. The oscillation frequency of the constant area tube is not very sensitive to the length ratio L/D, except for small va-lues of this parameter where end effects become important. In contrast, the os-cillation frequency in a single-step H-S tube strongly depends on its geome-trical configuration, the main parameters being the length ratio L_2/L_1 and the diameter ratio D_1/D_2.

All the measurements reported in section 4.1. were made with the step con-figuration (sudden change).

4.1.1. Influence of length ratio

In Fig. 4, experimental results of oscillation frequency in a single-step H-S tube with $D_1/D_2 = 2$ are shown and compared with the values calculated by linear acoustic theory and by the FLIC method for two values of M_j. The measu-red frequencies are normalized with the acoustical frequency f_o of the total tube length, that is, $f_o = a_a/4(L_1+L_2)$.

It is seen that over a certain range, the experimental value of the oscil-lation frequency slightly increases with the length ratio until it reaches a domain of instability. In this domain, the frequency discontinuously changes from 1st-3rd mode. Then comes a range in which the frequency gradually increa-ses until it reaches another domain of instability in which the oscillation

discontinuously changes from 3rd to 5th mode. It is also observed that the frequencies given by the FLIC method are closer to experimental values than frequencies given by linear theory. The jump from one mode to the other, however, is not predicted accurately.

Fig. 5 shows the pressure histories for each mode at the middle position of the downstream cavity and at the closed end of the same cavity. Pressure fluctuations at the middle position are seen to be very different for each mode. In the 1st mode they are similar to those of a constant area tube and in the 5th mode, they are almost identical to the fluctuations at the closed end.

In the 3rd mode, however, the situation is quite different because the compression wave is not canceled by the rarefaction wave as happens in the acoustical case. This is because in nonlinear wave motions with traveling shock waves, pressure increases discontinuously across the shocks whereas it gradually decreases across the isentropic rarefaction wave bundle.

4.1.2. Influence of diameter ratio

In all the tests reported above, the diameter ratio D_1/D_2 had a value of 2. This ratio is also an important geometric parameter for the wave motion in a single-step H-S tube. If D_1/D_2 increases, the oscillation frequency generally decreases, the oscillation mode being unchanged. Also, the domain of length ratio for which the oscillations are unstable becomes wider. Moreover, the critical length ratio for mode change is a decreasing function of D_1/D_2. Figure 6 shows the effect of diameter ratio on frequency and on oscillation mode for a single-step H-S tube having a fixed length ratio ($L_2/L_1 = 2$). It can be observed that, for this length ratio, the 1st-mode frequency is an increasing function of D_1/D_2, whereas the 3rd-mode has a constant value corresponding to upstream cavity resonating at quarter-wavelength frequency and downstream cavity resonating at half-wave frequency. The critical diameter ratio for mode change at high jet Mach number lies in the region $2 < D_1/D_2 < 3$, whereas for $M=1.2$, it is smaller than 2. This is in agreement with the result reported in Ref.5, where the critical diameter ratio for mode change was found to be 1.3 for low jet Mach number ($M_j \simeq 1.34$).

4.2. Thermal effects

The temperature distribution of the tube wall depends very strongly on the oscillation mode.

4.2.1. 1st-mode

For this mode, the incident shock wave is amplified by the constriction so that maximum temperatures are observed at the end wall. The shape of the constriction has a strong effect on the temperature, especially for large diameter ratios (Fig. 7). In the 1st-mode, mixing of the driving and driven gas limits the temperature in the upstream part of the cavity (Fig. 8).

4.2.2. 3rd-mode

For this mode, the incident shock is reflected at the constriction. Mixing of the gas oscillating in the downstream cavity with the cold driving gas is much reduced, so that an almost uniform temperature is observed in this cavity. The shape of the constriction section has less effect on the temperature (Fig. 9).

5. CONCLUSION

The influence of various parameters on the oscillation mode of Hartmann-

Sprenger tubes presenting an area change has been studied both experimentally and theoretically. It has been shown that the oscillation mode has a strong effect on the maximum attainable temperature, as well as on the temperature distribution. These results are interesting for applications, such as the so called "fluidic" igniter.

REFERENCES

1. BROCHER, E.,"Amplification of non-linear standing waves in a cylindrical cavity with varying cross section", Proceedings of the 13 th International Symposium on Shock Waves and Shock Tubes, State University of New-York Press, Albany N.Y., 1981, p. 209
2. BROCHER, E., "Contribution à l'étude des générateurs acoustiques à jet d'air" ACUSTICA, Vol. 32, n° 4, 1975, p. 227
3. KAWAHASHI, M., BOBONE, R. and BROCHER, E., "Oscillations modes in single step Hartmann-Sprenger tubes", J. Acoust. Soc. Am. 75(3), March 1984, p. 780
4. MARCHESE, V.P., RAKOWSKY, E.L. and BEMENT, L.J., "A fluidic sounding rocket motor ignition system", J. Spacecraft, Vol. 10, n° 11, 1973, p. 731
5. KAWAHASHI, M., KURUTA, R. and SUZUKI, M., Trans. JSME 49, 1983, p. 1224 (in japanese)
6. BROCHER, E., MARESCA, M. and BOURNAY, M.H., "Fluid Mechanics of the Resonance Tube", J. Fluid Mech. 43, 1970, p. 369
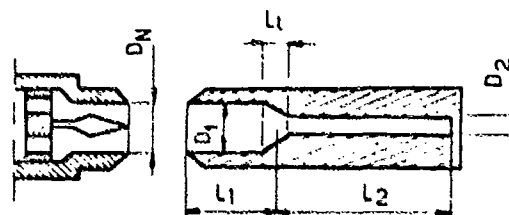
Fig. 1 : H.S. tube with area constriction
D_N = nozzle diameter ; L_1, D_1 = length and diameter of upstream cavity; L_2, D_2 = length and diameter of downstream cavity;
L_t = length of transition section.

Step ($\alpha = 0°$)   Conical ($\alpha \neq 0°$)   Sinusoidal
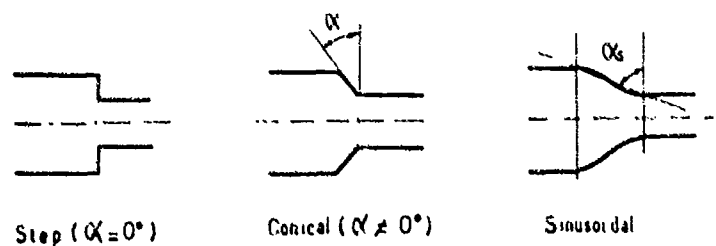
Fig. 2 : Different shapes of transition section tested.
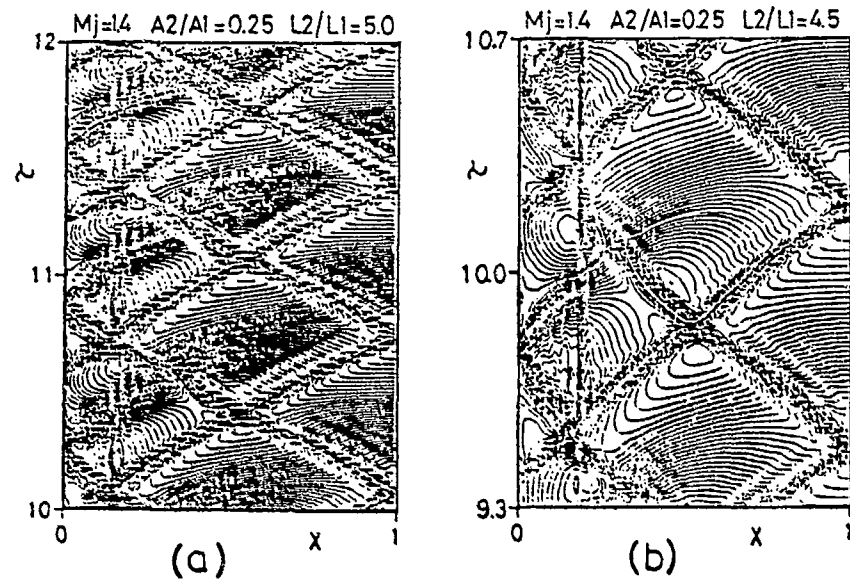
Fig. 3 : Wave diagrams for two different length ratios
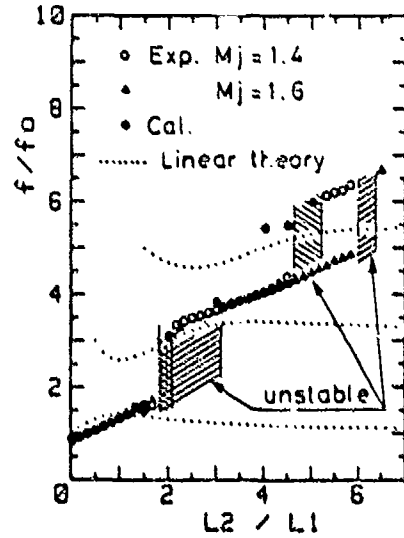
Fig. 4 : Frequency of oscillation
as a function of the length ratio
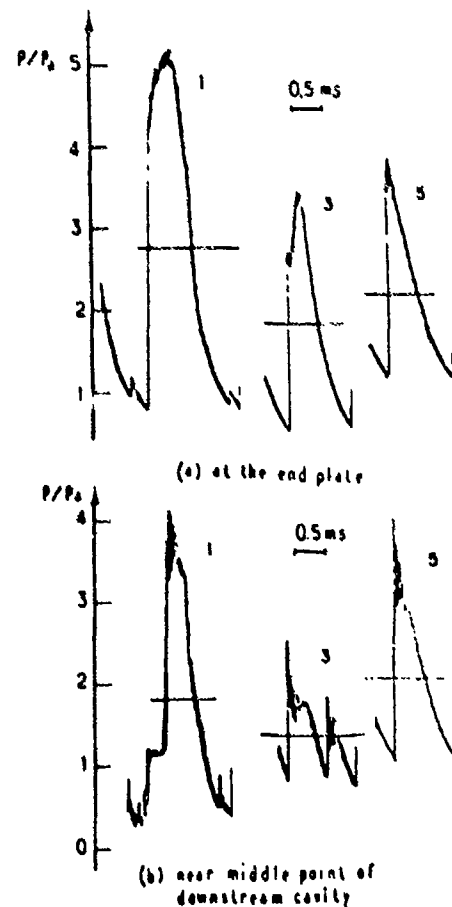
Fig. 5 : Pressure histories for
the 1st, 3rd and 5th modes

(a) at the end plate

(b) near middle point of
downstream cavity
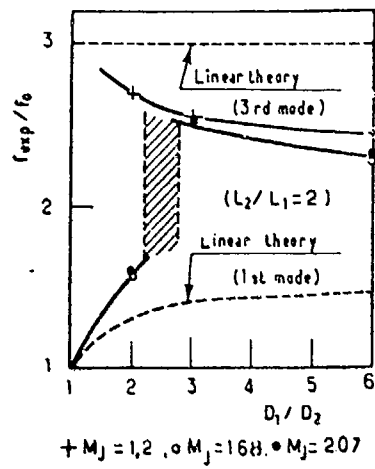
Fig. 6 : Effect of diameter ratio
on the oscillation mode
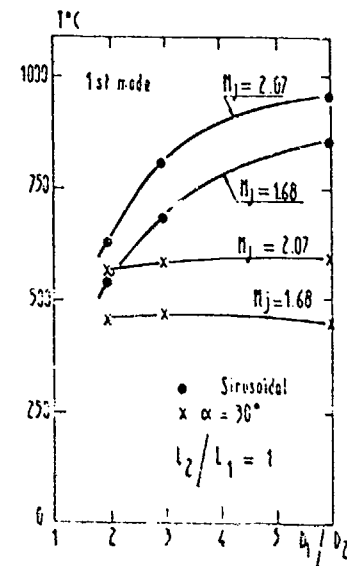
Fig. 7 : Effect of diameter
ratio on end wall
temperature
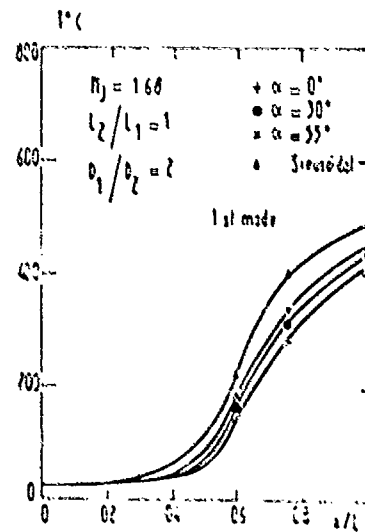
Fig. 8 : Temperature distribution along
the tube (1st mode)
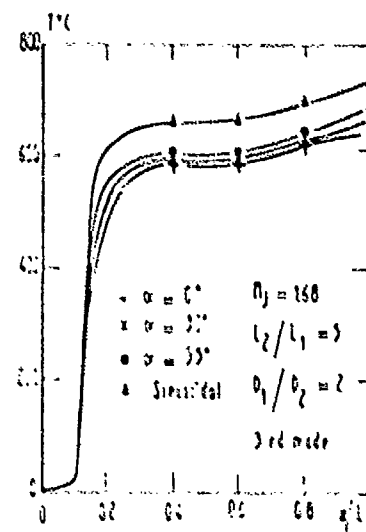
Fig. 9 : Temperature distribution
along the tube (3rd mode)

SHOCK WAVE INTERACTION WITH HIGH SOUND SPEED LAYERS

W. J. Glowacki, A. L. Kuhl[*], H. M. Glaz, R. E. Ferguson

Applied Mathematics Branch, Naval Surface Weapons Center,
Silver Spring, MD 20903

[*] R & D Associates, Marina del Rey, CA   90291

This paper presents results of computational studies of
planar shock wave (both square wave and decaying)
interactions with upstream high-sound-speed layers bounded
by a wall and ambient air. The computational approach taken
here solves the time-dependent hyperbolic conservation
equations of inviscid gas dynamics using the second-order
Eulerian Godunov scheme. Using the Godunov scheme, vector
programming, and a Cray I computer, it has been possible to
use computational grids fine enough to reveal the
development of very complex inviscid flowfield structures
subsequent to the shock wave/layer interaction.

The results presented here include density and pressure
fields for constant strength shock waves (square waves)
interacting with layers of constant and variable sound
speed, as well as a decaying shock wave interacting with a
constant sound speed layer. For the variable sound speed
layer cases, the sound speed varied only in the direction
normal to the initial shock direction (i.e., parallel to the
initial shock front). From these studies, we have found
that the scheme remains very stable despite the complicated
flowfields that develop, that the interface between the
layer and the ambient air rolls up into rotating vortices
that develop downstream of the shock, and that the overall
flowfield can contain both "random" and "coherent"
structures at several length scales.

1. INTRODUCTION

The study of interface dynamics has been advanced considerably in recent
years along several lines of development in many different fields. The
symposium volume[1] summarizes some of the analytical, numerical, and
experimental approaches taken as of 1983. The present paper is a
computational study of the interface dynamics occurring when planar shock
waves (square wave and decaying) interact with upstream high sound speed
layers bounded by a wall and ambient air. Our numerical methods predict the
development of very complex flowfield structures subsequent to these
interactions. For example, when a planar shock wave moves parallel to the
interface in a stratified two-temperature fluid, the portion moving in the
higher temperature (higher sound speed) region will move faster, causing an
oblique shock to develop in the region of the interface. This oblique shock
is necessary to tie together the portions of the shock as yet unaffected by
the ever-growing region of shock-interface interaction. A shear layer

develops along the interface and in time becomes unstable, leading to a roll-up of the interface, the formation of large vortices, and eventually to smaller scale structures and very complex flow patterns.

From a numerical point of view, the approach is to solve the equations of inviscid gas dynamics using the second-order Eulerian Godunov scheme. This is an upwind scheme for systems of hyperbolic conservation laws, especially the equations of gas dynamics. The scheme is specifically designed for problems involving complicated, non-linear wave interactions where high resolution calculations are important in determining small scale structures. The scheme is being applied for such problems[2-10] and assessments of its accuracy are appearing[5-9].

From a physical point of view, the interest is in the dynamics of the layer/ambient air interface after shock loading, the subsequent stable/unstable behavior of this interface, and interactions of the shock and interface with the disturbed flow. The second-order Eulerian Godunov scheme has been shown[2-10] to represent inviscid gas dynamics accurately and not introduce numerical diffusion away from discontinuity surfaces. However, the detailed viscous structures of the interfaces, the viscous-inviscid interactions, and the dissipation scales and their overall effect on the flowfield either are not modelled at all or may be perturbed, perhaps substantially, from their correct physical magnitudes.

2. APPROACH

To date, numerous computations have been made for an initially planar shock wave moving through air with various temperature/sound speed distributions normal to the initial shock direction. These gradients have been confined to relatively thin layers along or near the bottom wall of the computational grid (see figure 1). Typically the thickness (height) of the high sound speed layer is less than 10% of the height of the grid. The layer begins near the left boundary of the grid and extends to the right boundary. The planar shock wave starts just inside the left boundary and moves in time toward the right.

The initial air conditions above the layer are nominally atmospheric; specifically $p = 1.01325$ bars and $T = 293.16°K$. The air in the layer is at the same pressure but different temperatures. It is through the temperature that the sound speed in the layer is prescribed. For most of the computations, the layer temperature is constant at $2124°K$, but variations of these parameters have been included.

Parametric cases have been run to study the effect of mesh size, shock strength, layer temperature, and temperature distribution. Calculations have also been made to simulate blast waves in shock tubes where the top (roof) reflects waves rather than permitting them to pass out of the computational grid. Despite the high degree of vector optimization incorporated into the code, Cray 1 computer run times range from minutes for course grid, short shock travel computations to hours for the finer grid, longer travel computations needed to detect and follow the evolving flow structures. For each run, an extensive set of plots was obtained, showing snapshots of the flowfield properties at various times, as well as time histories at specified locations. The snapshots of the flowfield are presented in terms of contour plots with 30 contours equally spaced from minimum to maximum. For some of the more detailed (and interesting) calculations, movies have been made

showing the time evolution of the flow structures in terms of density contour patterns.

3. "TYPICAL" CONSTANT TEMPERATURE RESULTS

For relatively thin layers in contact with the bottom wall, the entire layer begins to wrap up into a vortex. This is shown in terms of the density field in figure 2a for a shock with pressure ratio of 3 moving across the constant temperature (=2124°K) layer. The ambient air originally above the layer is brought down and under the layer and rolls up with it into a vortex whose size grows with time as it moves along with the shock structure. Figure 2b shows the pressure field at the same times. The pressure wave moving through the layer ("precursor") appears to be a compression wave for this case, but becomes a shock for greater shock strengths. A triple point is formed where the main shock is intersected by the oblique shock to the precursor and a second turning shock which decays into a wave ending near a stagnation point on the wall behind the vortex. The precursor, the triple point, the downstream tip of the vortex, and the stagnation point all move at constant velocity except near the very start of the calculation. This motion would seem to support a view that the flowfield becomes self-similar. However, later and more detailed calculations show that although the motions of these points change very little so that the shock structure maintains a self-similar appearance, the flowfield itself becomes decidedly non-similar due to the growth of complex and "coherent" structures.

4. ACCURACY AND RESOLUTION TESTS

The results presented above were computed for a layer six zones high. Resolution runs were made to determine the number of zones needed to define the features of the flowfield. These tests indicated that five or six zones were an adequate compromise between resolution and computing time. Figure 3a shows a blow-up of the density field in the vortex region for runs made with two, six and ten zone high layers. The number of zones in the grid were scaled accordingly in order to keep the zones (cells) square. Figure 3b shows the corresponding pressure field results. Based upon these results, most runs were made using five or six zone thick layers. Although this was quite adequate for most of the parametric studies, it was found that zone size is a significant factor in resolving the small-scale structures which develop as shear layer instabilities grow during very long runs. For constant temperature layers, the precursor must travel distances equal to hundreds of layer thicknesses before these instabilities have a significant effect. However, temperature distributions in the layer can accelerate the process. For such long runs, it is costly to keep the cell size small and square. Instead nonsquare and moving grids must be used to obtain good resolution.

5. TEMPERATURE DISTRIBUTION RESULTS

Calculations were made to evaluate the effects of layer temperature distribution. Linear and double-linear temperature distributions (vertically through the layer) were used together with the constant temperature layer. These distributions are shown schematically in figure 4. For each temperature distribution, the maximum temperature in the layer was taken to be 2124°K. For the constant temperature layer, the temperature was 2124°K everywhere in the layer. For the linear distribution, the temperature varied linearly from 2124°K in the bottom zone to the ambient temperature of 293°K in zone 7, just above the layer. For the double-linear distribution, the maximum temperature

of 2124°K occurred in the middle of the layer and decreased linearly to 293°K in zones 1 and 7.

The results for the linear distribution were similar to the constant temperature case, resembling results for a thinner constant temperature case with about the same maximum temperature. The double-linear distribution produced very different results. As shown in figure 5a for a pressure ratio across the shock of about three, the flow is unstable and breaks up into many smaller scale structures. Unlike the constant temperature cases where the originally cool ambient air comes down and under the hot layer and then rolls up into a large vortex, the double-linear cases do not produce this single large vortex structure. Instead of moving under the hot layer, the heavier cool air begins to push itself through the lighter air from the layer. As it moves, this tongue of heavier air is deflected first upward by the layer of heavy air along the wall and then downward by the heavy air above the layer. As this pattern repeats sections of the lighter layer air are cut off alternatively along the top and bottom of the layer. These pockets of lighter air move more slowly than the main shock structure and so appear to be breaking loose. Figure 5b shows the corresponding pressure fields.

6. FLOATING LAYER RESULTS

To study this effect in more detail, runs were made with a 2124°K constant temperature layer located one layer height above the bottom wall. This geometry is apparent in figure 6 where the density and pressure fields are given for a five zone thick layer. The layer occupied zones 6-10, while the air in zones 1-5 matched that above the layer. Here again the shock pressure ratio is 3. Initially the flowfield is symmetric about the centerline of the high temperature layer, but it begins to become asymmetric when the lower triple point reaches the bottom wall. The reflections from the wall disturb the motion of the cool air tongue moving inside the layer air, causing the tongue to move upward and begin the oscillating motion which causes the formation of the light air structures. The formation of the lighter air structures is much more pronounced for this case. The results clearly show the structures detaching from the main shock pattern and drifting slowly downstream. This is in marked contrast to the constant and linear temperature distribution cases where the layer fluid is trapped within the large vortex and swept along with the main pattern.

Significant changes occur also in the shock structure during the shedding process. When one structure is finished forming and ready to begin falling behind, the rearmost turning shock which runs from this structure to the triple point moves forward along the upper surface of the structure and then jumps to the rear of the next one forming, where it remains until this one is finished forming. This oscillation in the motion of the lower portion of the shock relative to the upper portion causes a second triple point to form and with it a new oblique shock somewhat parallel to but under the original oblique precursor shock. This can be seen both in the density fields of and in the pressure fields. Because this new shock is moving in even higher temperature air than the precursor, the new shock begins to overtake the precursor. Near the end of this calculation, it appears that the precursor is weakening and the new shock is replacing it.

Another run was made specifically to capture in better detail the early time development of the floating layer case. In this second run, the layer and the region near it were enlarged by a factor of five, while the total number of grid points was left unchanged. Thus, for this run, there were 25

structures can be seen to form at the interface and grow as they flow downstream. Although better techniques are needed to follow the development of these structures as they proceed to flow through the roll-up, the results shown here shed some light on the flowfield development and show the ability of the second-order Godunov scheme to resolve small-scale inviscid flow structures.

ACKNOWLEDGEMENT

REFERENCES

1   Bishop, A. R., Campbell, L. J., Channell, P. J., eds., Fronts, Interfaces and Patterns, Proc. 3rd Ann. Intl Conf. Center for Nonlinear Studies, Los Alamos, May 1983, Elsevier, Amsterdam, 1984.

2   Colella, P., Ferguson, R., Glaz, H. M., and Kuhl, A., "Mach Reflection from an HE Explosion," 9th Intl. Coll. Gasdynamics of Explosions and Reactive Systems, 1985.

3   Colella, P. and Glaz, H. M., "Numerical Computation of Complex Shock Reflections in Gases," Proc. 9th Intl. Conf. on Numerical Methods in Fluid Dynamics, Saclay, 1984, ed. Soubbaramayer and J. P. Boujot, Springer-Verlag, Berlin.

4   Colella, P. and Glaz, H. M., "Efficient Solution Algorithms for the Riemann Problem for Real Gases," to appear J. Comp. Phys. (1985).

5   Colella, P. and Woodward, P. R., "The Piecewise-Parabolic Method (PPM) for Gas-Dynamical Simulations," J. Comp. Phys. 54, (1984), pp. 174-201.

6   Glaz, H. M., Colella, P., Glass, I. I., and Deschambault, R. L., "A Numerical Study of Oblique Shock-Wave Reflections with Experimental Comparisons," Proc. R. Soc. Lond. A398, (1985), pp. 117-140.

7   Glaz, H. M., Colella, P., Glass, I. I., and Deschambault, R. L., "A Detailed Numerical, Graphical, and Experimental Study of Oblique Shock Wave Reflections," University of Toronto, UTIAS Report No. 285 (1985).

8   Glaz, H. M., Glass, I. I., Li, J.-C., and Walter, P. A. "Interaction of Oblique Shock-wave Reflections in Air and CO_2 with Downstream Obstacles," 15th Intl. Symp. on Shock Waves and Shock Tubes, 1985.

9   Glaz, H. M., Glass, I. I., Hu, J. C. J., and Walter, P. "Oblique Shock Wave Reflections in SF_6: A Comparison of Calculation and Experiment," 9th Intl. Coll. Gasdynamics of Explosions and Reactive Systems, 1985.

10   Woodward, P. R., and Colella, P., "Numerical Simulation of Two-Dimensional Fluid Flow with Strong Shocks," J. Comp. Phys. 54 (1984), pp. 115-173.

zones in the layer and 25 zones below it. Because the only length scale in this problem is the layer thickness, this run is equivalent to a finer zone calculation of the previous run at early times.

The results of this fine zone calculation show the flow pattern beginning symmetrically with a negative vortex developing along the top edge of the layer and a positive vortex along the bottom edge. After the lower triple point reaches the bottom wall, the reflections begin to influence the lower vortex. The development of the asymmetry is shown in figure 7, beginning shortly after the lower shock structure reaches the bottom wall. The lower vortex is forced up and forward (relatively), while the upper vortex moves back and down and then is shed as the first element in a vortex street. As this vortex is shed, the rearmost shock is deformed, creating another vortex structure. Then the cycle begins again.

7. SHOCK TUBE RESULTS

Another interesting case calculated corresponds to a planar blast wave moving through a two-dimensional shock tube. The wave, whose strength decays in time, moves over a 2124°K constant temperature layer which is ten zones thick and located along the bottom wall. The top of the grid is now a reflecting wall (roof) thirty layers high. The length of the grid is equivalent to more than three hundred layer thicknesses which is over three times greater than that of any of the other cases presented.

Whereas the flowfields in previous constant temperature layer calculations seemed quite stable, the results for this calculation showed that at much longer times both the interface and the flowfield become unstable and structures begin to form. As can be seen in the density fields shown in figure 8a, these structures look considerably different than those of the floating layer case. As before, the air from the constant temperature layer rolls up with the ambient air stream and seems to remain "trapped" in the vicinity of the shock structure. However, even before the triple point reaches the roof and creates a reflected wave pattern, the flowfield begins to show signs of instability. The development of the instabilities, especially along the interface, can also be seen in the corresponding pressure fields shown in figure 9b.

The structures that develop form a somewhat periodic pattern, much less random in appearance than that of the floating layer case. This is better seen in the enlargement of the density field given as figure 9a. The instabilities grow along the interface as can be seen both here and in the corresponding pressure field shown in figure 9b. However, the entropy field plotted in figure 9c seems to show more clearly the main details of the flowfield especially in the shear layer which develops along the interface.

An attempt was made to determine the behavior of the interface after it passed through the precursor. Many points originally located along the front and top edges of the layer were tracked throughout the calculation. This was not completely successful even though ten points per cell were used and their positions were updated twice per time step. The early movement of each point was captured but at later times the motion became erratic. Figure 10a shows the rollup of the interface at early times before the flowfield becomes unstable. This clearly demonstrates that the air from the layer is being trapped in this region and carried along with the shock structure. Figure 10b shows the calculated behavior of the interface for the time corresponding to the density, pressure and entropy fields given in figures 9. "Coherent"
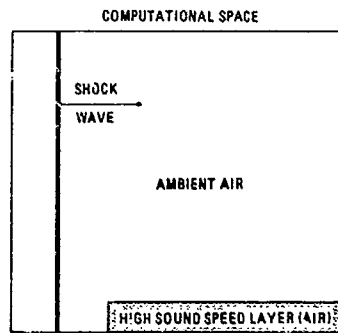
FIGURE 1. SCHEMATIC OF PROBLEM
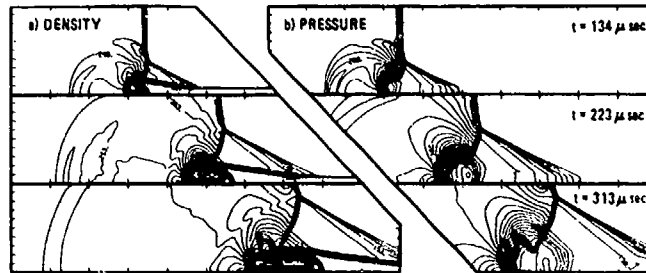
FIGURE 2. DENSITY & PRESSURE FIELDS FOR CONSTANT
TEMPERATURE LAYER
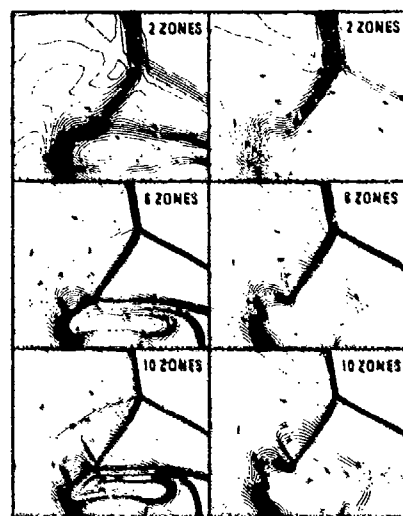
FIGURE 3. DENSITY & PRESSURE FIELDS FOR
2, 6, 10 ZONE THICK LAYERS
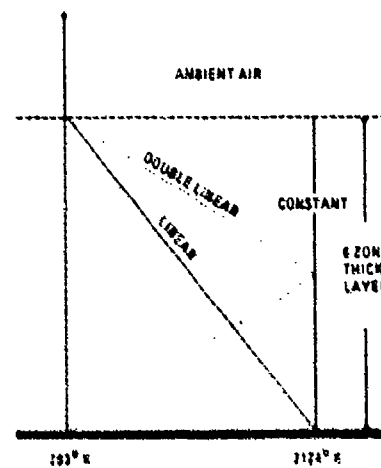
FIGURE 4. SCHEMATIC DIAGRAM OF TEMPERATURE
DISTRIBUTION USED IN 6 ZONE LAYER
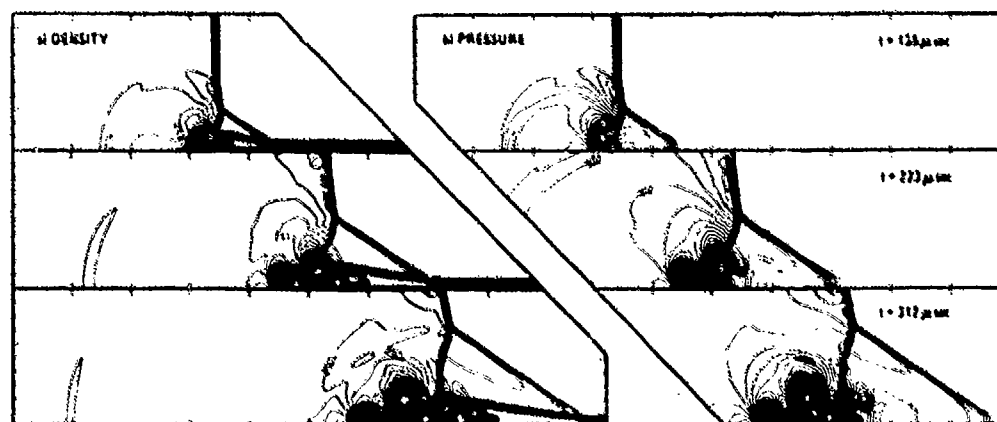
FIGURE 5. DENSITY & PRESSURE FIELDS FOR DOUBLE LINEAR TEMPERATURE DISTRIBUTION LAYER
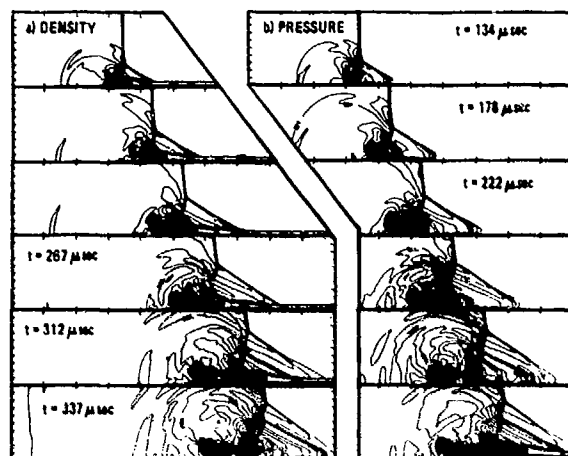
FIGURE 6.   DENSITY & PRESSURE FIELDS FOR FLOATING
LAYER CASE
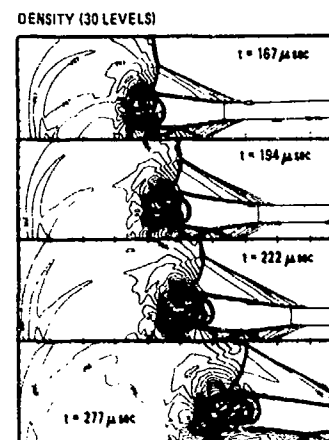
FIGURE 7.   EARLY DEVELOPMENT OF
DENSITY FIELD FOR 5X
FLOATING LAYER CASE
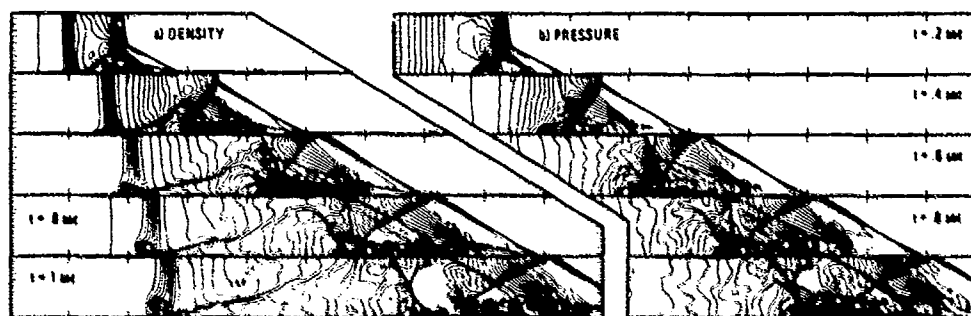
FIGURE 8.   DENSITY & PRESSURE FIELDS FOR SHOCK TUBE CASE
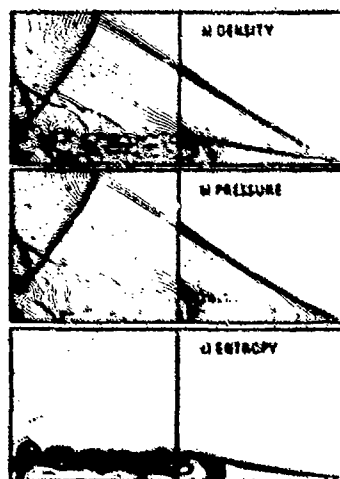
FIGURE 9.   FLOW FIELDS AT 0.5 sec FOR
SHOCK TUBE CASE
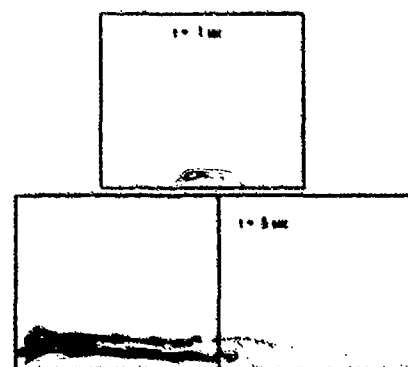
FIGURE 10.   POSITION OF ORIGINAL LAYER/
AMBIENT AIR INTERFACE AT
LATER TIMES

ON OBLIQUE SHOCK WAVES WITH A PHASE TRANSITION
IN RELATIVISTIC GASDYNAMICS

A. Granik

Mechanical Engineering Department
University of California, Berkeley, CA 94720

ABSTRACT

The theory of relativistic oblique shock waves with
a first order phase transition is studied. On the
basis of the general relations derived the shock
polar equations are obtained for an ideal gas
corresponding to the bag model of the quark matter.
The results suggest that a quark matter phase transi-
tion will significantly increase the flow angles in
high energy heavy ion collisions.

I. INTRODUCTION

It has been suggested that a strong compression of nuclear matter might
result in formation of a quark gas[1]. The transition from the nuclear matter
to the quark matter is quite possibly a first order phase transition[2]. There-
fore one faces a situation where a useful signature of the existence of the
quark matter can be defined within a framework of continuum mechanics. Because
the phase transition might occur at very high energies in the range
20-50 Ge V/nucleon, the appropriate description of the process of the quark
matter formation should be made using relativistic gasdynamics. The experi-
ments with the high energy ion collisions demonstrated that a strong oblique
shock wave is formed near the collision axis[3]. Therefore a plausible theo-
retical description of the expected phenomenon can be provided by a study of an
oblique relativistic shock wave accompanied by a first order phase transition.

This paper considers propagation of a strong relativistic oblique shock
wave. As a result of its propagation into the undisturbed gas two different
gases are formed. Considering their respective shock polars, it is possible
to find out that a significant increase in the maximum angle of deflection
occurs for one of these gases, namely the quark gas.

II. BASIC EQUATIONS

We study the problem in the fram of reference of the shock. Then the con-
servation laws across the oblique shock are[4]

$$(p_2+e_2)\gamma_2^2 \, \beta_{2n} = (e_1+p_1)\gamma_1^2 \, \beta_{1n} \qquad \text{(energy)} \tag{1}$$

$$p_2 + (p_2+e_2)\gamma_2^2 \, \beta_{2n}^2 = p_1 + (p_1+e_1)\gamma_1^2 \, \beta_{1n}^2 \qquad \text{(n-momentum)} \tag{2}$$

$$(p_2+e_2)\gamma_2^2 \, \beta_{2n} \, \beta_{2t} = (p_1+e_1)\gamma_1^2 \, \beta_{1n} \, \beta_{1t} \qquad \text{(t-momentum)} \tag{3}$$

where e is the energy per particle, p is the pressure, $\gamma = (1-\beta^2)^{-1/2}$ is the
Lorentz factor, β is the velocity normalized by the speed of light. As seen in

---

*Permanent address: Physics Department, University of the Pacific,
Stockton, CA 95211

Fig. 1, indices 1 and 2 denote the unshocked and shocked gases respectively, and subscripts n and t stand for the normal and tangential components of β. All the thermodynamic quantities are measured in the proper fram of the fluid element.

We derive the shock polar equation using Eqs. (1)-(3). Multiplying Eq. (1) by β_{2n} and substituting the result into Eq. (2) we obtain

$$\frac{\gamma_1^2}{\gamma_2^2} = 1 + \frac{p_2-p_1}{e_0+p_1} (1+x), \qquad x = \frac{\beta_{2n}}{\beta_{1n}} \tag{4}$$

where we use the identity

$$\frac{\gamma_1^2}{\gamma_2^2} = 1 + \gamma_1^2 \beta_{1n}^2 (1-x^2)$$

Note that the trivial root $x = 1$ is factored out. On the other hand, from Eq. (1) immediately follows

$$x = \frac{e_1+p_1}{e_2+p_2} \frac{\gamma_1^2}{\gamma_2^2} \tag{5}$$

Substituting (4) into (5) we obtain

$$x = \frac{\beta_{2n}}{\beta_{1n}} = \frac{e_1+p_2}{e_2+p_1} \tag{6}$$

Now we can derive expressions for $U_{1n}^2 \equiv \gamma_1^2 \beta_{1n}^2$ and $U_{2n}^2 = \gamma_2^2 \beta_{2n}^2$. Substituting Eqs. (5) and (6) into Eq. (1) we obtain

$$U_{1n}^2 = \frac{(e_2+p_1)(p_2-p_1)}{(e_1+p_1)(e_2+p_1-e_1-p_2)} \tag{7}$$

and

$$U_{2n}^2 = \frac{e_1+p_2}{e_2+p_1} \frac{p_2-p_1}{e_2+p_1-e_1-p_2} \tag{8}$$

To arrive at the shock polar equation one must specialize to specific equations of state. We consider the following equations of state

$$p_2 = (\Gamma-1)e_2 = \Gamma B \qquad \text{(shocked gas)} \tag{9}$$

$$p_1 = (\nu-1)(e_1-\rho_1) \tag{10}$$

where Γ, ν, and B are constants, and ρ is the particle density. Equation (9) describes the so-called MIT bag model, and Eq. (10) is a model equation for the baryon gas[5]. It is interesting to note that the structure of these two equations is identical to the equations used in the theory of a non-relativistic detonation[6].

To conclude the derivation of the shock polar we have to express x as a function of U_{1n}^2 and constants Γ, ν, and B. Using the expression for the sound speed[7]

$$\alpha_1^2 = \frac{\nu p_1}{\rho_1 + \frac{\nu}{\nu-1} p_1}$$

Eq. (6) and Eq. (9) we obtain from Eq. (7)

$$x^2 \frac{U_{1n}^2}{\alpha_1^2} - x \frac{\Gamma}{\nu} (\frac{\nu}{\alpha_1^2} U_{1n}^2 + Q_1) + (\Gamma-1) \frac{1+U_{1n}^2}{\alpha_1^2} = 0 \tag{11}$$

where $Q_1 = 1 + B/p_1$. Its solution is

$$x = \frac{1}{2M\alpha_1^2} (C \pm \sqrt{C^2 - 4M(1+U_{1n}^2)(\Gamma-1)}) \tag{12}$$

$$C = \frac{\Gamma}{\nu} (\frac{\nu}{\alpha_1^2} U_{1n}^2 + Q_1), \qquad M = \frac{U_{1n}^2}{\alpha_1^4}$$

In the following we specialize to the case of a very dense baryonic matter, $p = 0$. For this case from Eq. (10) we obtain $e_1 = {}_1$. To find out the physical meaning of two branches of Eq. (12) we consider a "phase" space $\in_2 - \in_1 (\in = e/B)$. From Eqs. (7) and (8) follows that the physical regions are dictated by the conditions U_{1n}^2, $U_{2n}^2 > 0$. This yields two regions

I) $$\in_2 > \Gamma/(\Gamma-1),$$

$$\Gamma - (\Gamma-1)\in_2 < \in_0 < (2-\Gamma)\in_2 + \Gamma \tag{13}$$

and

II) $$1 < \in_2 < \Gamma/(\Gamma-1) ,$$

$$\in_0 > (2-\Gamma)\in_2 + \Gamma \tag{14}$$

According to the causality condition constant Γ is less than 2. The Jouget curve is obtained from the Jouget condition $U_{2n}^2 = U_{s2}^2$ ($U_{s2}^2 = (\Gamma-1)/(2-\Gamma)$

$$\in_2 = \frac{b\Gamma}{2-\Gamma} (1 \pm 1 - \frac{2-\Gamma}{b(\Gamma-1)}),$$

$$b = \frac{\in_0}{\Gamma} - 1 \tag{15}$$

In Fig. (2) we present the possible regimes of flow. The shadowed areas represent physically allowed processes according to Eqs. (13) and (14). The dashed-dotted line is the Jouget curve. One of the allowed regions described by Eq. (14) correspond to a metastable regime with $D_2 < 0$. However, according to QCD in such a regime the dependence of p_2 on $\in_2$ does not obey the linear relation (9)[8]. Therefore we are left with only one physical region, namely given by Eq. (13). In this region the detonation, $U_{2n}^2 < U_{2s}^2$ can take place everywhere below the Jouget curve, and the deflagration, $U_{2n}^2 > U_{2s}^2$ can take place above the Jouget curve.

Because at the Jouget point U_{1n}^2 reaches its minimum, and because x is monotonically decreasing with U_{1n}^2, we find that the plus sign in Eq. (15) corresponds to the deflagration $(x > 1)$ and the minus sign corresponds to the detonation $(x < 1)$. In fact, the bag constant B for the quark k gas has such value that $\in_1 < \Gamma/(\Gamma-1)$. This means that a phase transition from the dense nuclear matter to the quark gas is described by Eq. (12) with the minus sign. Having this in mind we can write the shock polar equation

$$y^2 = -(1-r)\frac{(r-r_1)(r-r_2)}{1 + R - r} \tag{16}$$

where $y = \beta_{2y}/\beta_1$, $r = \beta_{2x}/\beta_1$ and $R = \dfrac{\Gamma}{\in_1 U_1^2}$. The intercepts of the strophoid (14) with the β_{2x} - axis are $r = 1$
and

$$r_{1,2} = \frac{1}{2}(\Gamma + R \pm \sqrt{(2-\Gamma-R)^2 + 4\frac{RU_1^2 - \Gamma+1}{U_1^2}}$$

As we mentioned earlier for a physically interesting case $\in_1 < \Gamma/(\Gamma-1)$. This leaves us with the only one point (apart from $r = 1$) of intercept, namely r_2. In the ultra-relativistic limit $U_1 \to \infty$ the shock polar (14) degenerates into a circle with a radius $(\Gamma-1)$.

Simultaneously with the formation of the quark gas the baryon matter is shock transformed into the baryon matter described by Eq. (10). The shock polar for this shock transition is easily obtained from the equation for x found in Ref. 4 if we take $\alpha_1^2 \to 0$ (equivalent to the assumption $e_1 \to \rho_1$).

$$x^3 + x^2(1-2\nu) + x(\nu^2-1)(\frac{1+U_{1n}^2}{U_{1n}^2}) - (\nu-1)^2\frac{1+U_{1n}^2}{U_{1n}^2} = 0 \tag{17}$$

The solution of Eq. (17) yields $x = x(\sin^2\phi)$ where ϕ is the angle of attack. Using two geometric identities

$$(1-r) = \sin^2\phi (1-x)$$

and   \hfill (18)

$$[(1-r)^2 + y^2]\sin^2\phi = (1-r)^2$$

we can construct the shock polar for the transition baryons-baryons. We performed the numerical solution of Eqs. (15), (16) for $\nu = 2.33$ and for a number of velocities in front of the shock, U_1. A typical shock polar for quark matter along with the corresponding shock polar for nuclear matter is shown in Fig. 3. The shadowed area indicates the region where one can expect quark matter.

III. CONCLUSIONS

A simple model of a shock transition within the framework of relativistic gasdynamics leads to a possible signature of the existence of quark matter. In view of ever-increasing energy capabilities of new supercollides it is quite conceivable that the predicted effect of a drastic increase in the deflection angle of quark matter will be detected.

REFERENCES

1. G. F. Chapline and A. K. Kerman, Lawrence Livermore Laboratory Report UCRL-80737 (Jan. 1978); R. Anishetly, P. Koehler, L. McLehran, Phys. Rev. D 22, 2293 (1980).

2. G. Baym and S. A. Chin, Phys. Zett. 62B, 241 (1976).

3. H. Stocker, J. Maruhn and W. Greiner, Phys. Rev. Zett. 44, 725 (1980).

4. A. Konigl, Phys. Fluids, 23, 1083 (1980).

5. H. Bethe and M. Johnson, Nucl. Phys. A230, 1 (1974).

6. L. Sedov, Similarity and Dimensional Methods in Mechanics, (New York, Academic Press), 1959.

7. A. Taub, Phys. Rev., 74, 328 (1948).
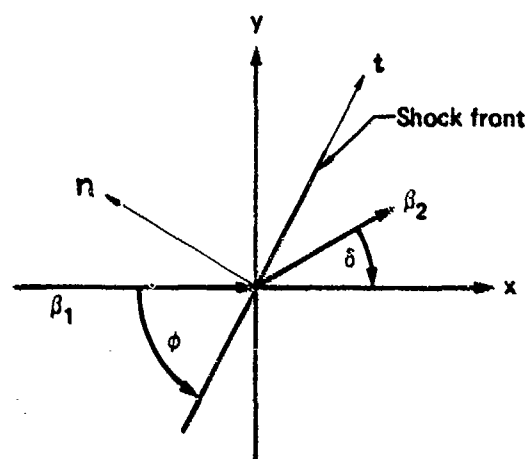
FIGURE 1.
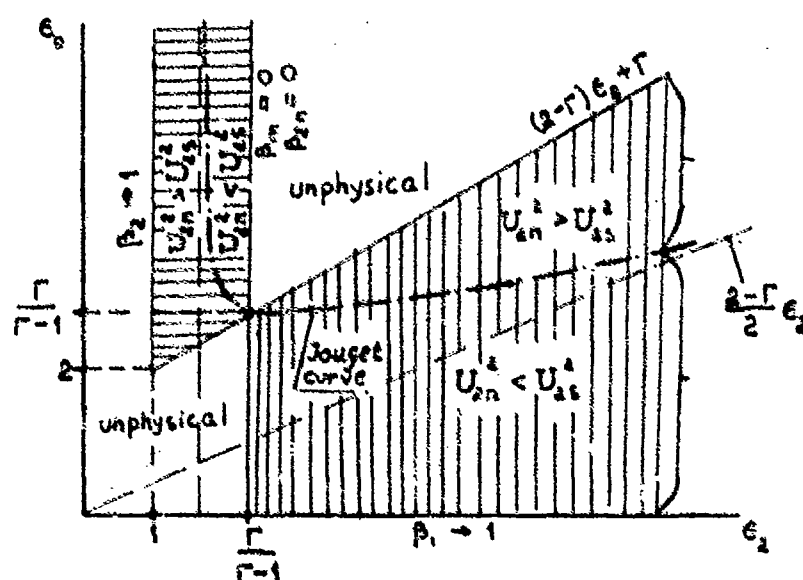
FIGURE 2.
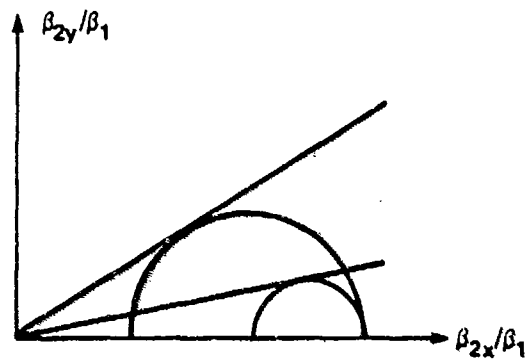
FIGURE 3.

THE REFLECTION OF A MACH REFLECTION OVER A SECONDARY RAMP

G. Ben-Dor[1], J.M. Dewey[2] and K. Takayama[3]

(1) Department of Mechanical Engineering, Ben-Gurion University of the
    Negev, Beer Sheva, Israel
(2) Department of Physics, University of Victoria, Victoria, BC, Canada
(3) Institute of High Speed Mechanics, Tohoku University, Sendai, Japan.

An analysis is presented of the various shock wave
configurations which will occur when a Mach reflection
propagating along a straight wedge encounters a sudden
increase or decrease in the slope of the wedge surface
which changes from θ_w^1 to θ_w^2. It is shown analytically
that four different reflection processes may be expected
depending on the incident shock wave Mach number (M_i) and
the two wedge angles (θ_w^1 and θ_w^2). The analytical predic-
tions have all been verified experimentally.

1. INTRODUCTION

Mach reflection is one of the two major types of reflection of a shock wave
over a solid surface[1]. In the case of an air burst explosion, for example, a
spherical blast wave is generated. During the early stages of its interaction
with the ground surface the reflection of the blast wave is regular
(figure 1a). As the blast wave propagates outwards the reflection changes to a
Mach reflection (figure 1b). Either reflection may encounter a sudden
compressive on expansive change in the slope of the reflecting surface. To
calculate the pressure distribution along such a surface an understanding of
the interaction of a regular or a Mach reflection with a secondary wedge is of
importance. The analysis to be presented aims at establishing both the
reflection processes and final shock configurations of a Mach reflection
encountering a sudden increase or decrease in the slope of the wedge surface.

2. ANALYSIS

A compressive and an expansive double wedge are illustrated in figure 2.
The slopes of the first and second wedges are θ_w^1 and θ_w^2, respectively, and the
slope of the second wedge with respect to the first is

$$\Delta\theta_w = \theta_w^2 - \theta_w^1 \qquad (1)$$

If $\Delta\theta_w > 0$ the double wedge is concave and if $\Delta\theta_w < 0$ the double wedge is
convex. The reflection over any double wedge depends on three parameters: the
incident shock wave Mach number, M_i, and the first and second wedge angles, θ_w^1
and θ_w^2, respectively. The phenomenon will be described in the (θ_w^1, θ_w^2) plane,
but, since the phenomenon also depends on the incident shock wave Mach number,
M_i, the (θ_w^1, θ_w^2) plane presentation is valid for a fixed value of M_i only.

The (θ_w^1, θ_w^2) plane is shown in figure 2. Equation 1 in this plane is
described by straight lines with 45° slopes along which $\Delta\theta_w$ is constant. In
the region above the line for which $\Delta\theta_w = 0$, $\Delta\theta_w > 0$ and the double wedge is
concave. Below this line $\Delta\theta_w < 0$ and the double wedge is convex. Since the
present paper is concerned with the reflection of a Mach reflection over a
secondary ramp only the region to the left of the line $\theta_w^1 = \theta_w^{det}$ will be
considered (θ_w^{det} is the "detachment" wedge angle for a given incident shock

wave Mach number, M_i, at which transition from regular to Mach reflection is expected to occur).

If $\theta_w^1 < \theta_w^{det}$ the incident shock wave reflects from the first wedge as a Mach reflection[2]. This Mach reflection propagates up the wedge until its Mach stem encounters the leading edge of the second wedge and reflects from it either as a regular or as a Mach reflection depending upon the size of the differential wedge angle, $\Delta\theta_w$, and the Mach number of the Mach stem, M_m.

Assuming that the Mach stem is straight and perpendicular to the first wedge surface we may write[3]:

$$M_m = M_i \frac{\cos \chi_1}{\cos (\theta_w^1 + \chi_1)} \tag{2}$$

where χ_1 is the first triple point trajectory angle. Equation (2) clearly indicates that $M_m > M_i$, but since the difference is not large and since for $M_i > 2$ θ_w^{det} is almost independent of the incident shock wave Mach number[4], it will be assumed that

$$\theta_w^{det}|_{M_m} \approx \theta_w^{det}|_{M_i} \tag{3}$$

For example for $M_i = 2.5$ and $\theta_w^1 = 20°$ the Mach reflection solution results in $\chi_1 = 12.88°$, thus $M_m = 2.902$. The corresponding detachment wedge angles for M_i and M_m are 50.77° and 50.72°, respectively. Using the assumption of equation 3, it may be concluded that the Mach stem of the first Mach reflection reflects from the second wedge as a Mach reflection if $\Delta\theta_w < \theta_w^{det}$. As the incident shock wave continues to propagate it will eventually encounter the second wedge. Thus the value of θ_w^2 defines the final reflection of the incident shock wave. If $\theta_w^2 < \theta_w^{det}$ the incident shock wave will finally establish a Mach reflection over the second wedge and, if $\theta_w^2 > \theta_w^{det}$ the final reflection of the incident shock wave over the second wedge will be regular.

Redrawing figure 2 with the addition of the lines $\theta_w^1 = \theta_w^{det}$, $\Delta\theta_w = \theta_w^{det}$ and $\theta_w^2 = \theta_w^{det}$ results in figure 3 in which four different regions representing four different reflection processes of a Mach reflection over a secondary wedge are obtained. In the following the reflection process in each of the four regions will be briefly described and illustrated with photography which were recorded on the 3" × 10" shock tube of the Department of Physics of the University of Victoria.

Region 1

Since $\Delta\theta_w < 0$ the double wedge is convex. The incident shock wave reflects over the first wedge as a Mach reflection ($\theta_w^1 < \theta_w^{det}$). Upon encountering the second expansive wedge the wave angles, change but the Mach reflection is maintained.

The reflection process in this region is shown in figure 4 for $\theta_w^1 = 35°$ and $\theta_w^2 = 15°$ ($\Delta\theta_w = -20°$). A shadowgraph of the Mach reflection over the first surface is shown in figure 4a. The unsteady wave system generated when the Mach stem encounters the sudden change in the slope of the surface is shown in figure 4b. A rarefaction wave travelling backwards is seen in the schlieren photograph. It carries with it the information about the sudden change in the model geometry. The final single Mach reflection over the second wedge is seen in figure 4c.

Region 2

Since $\Delta\theta_w > 0$ the double wedge is concave, and since $\Delta\theta_w > \theta_w^{det}$ the Mach stem over the first wedge reflects from the second wedge as a regular reflection. At a later time the triple point and the reflection point of the Mach and the regular reflections interact at point Q on the second wedge to finally form a regular reflection of the incident shock wave over the second wedge.

The reflection process in this region is shown in figure 5 for $\theta_w^1 = 20°$ and $\theta_w^2 = 75°$ ($\Delta\theta_w = 55°$). A shadowgraph of the Mach reflection over the first wedge is shown in figure 5a, where the Mach stem is just about to collide with the second wedge. The collision with the second wedge results in a regular reflection (figure 5b). The triple point of the Mach reflection over the first wedge and the reflection point of the regular reflection of the Mach stem along the second wedge interact on the second surface to produce the wave configuration shown in figure 5c. The incident shock wave reflects regularly from the second surface. The reflected shock wave of what used to be the Mach reflection (over the first wedge) also reflects regularly from the second wedge surface. Thus the major regular reflection is followed by a secondary regular reflection.

Region 3

Again $\Delta\theta_w > 0$ and therefore the double wedge in concave. Since $\Delta\theta_w < \theta_w^{det}$ the Mach stem over the first wedge also reflects from the second wedge as a Mach reflection. At a later time the triple points of these two Mach reflections interact to form a new Mach reflection. The triple point of this Mach reflection moves away from the wedge surface and therefore the final Mach reflection is maintained. The reflection process in this region is shown in figure 6 for $\theta_w^1 = 15°$ and $\theta_w^2 = 35°$ ($\Delta\theta_w = 20°$). The Mach reflection over the first wedge is shown in figure 6a. The Mach stem of this reflection reflects from the second wedge also as a Mach reflection (figure 6b). The two triple point interact at a later time (figure 6c) to result in a Mach reflection of the incident shock wave over the second wedge. A second triple point is formed along the reflected shock wave of this Mach reflection (figure 6d).

Region 4

The double wedge is concave ($\Delta\theta_w > 0$). Again the Mach stem over the first wedge reflects from the second wedge as a Mach reflection. At a later time the triple points interact to form a new Mach reflection. However, unlike the previous case, here $\theta_w^2 > \theta_w^{det}$. This means that the new Mach reflection cannot be maintained over the second wedge. The triple point of this reflection moves towards the wedge surface, i.e., the Mach reflection is an inverse Mach reflection[5]. Upon colliding with the wedge surface, the inverse-Mach reflection changes to a regular reflection of the incident shock wave over the second wedge.

The reflection process in this region is shown in figure 7 for $\theta_w^1 = 25°$ and $\theta_w^2 = 60°$ ($\Delta\theta_w = 35°$). The Mach reflection over the first wedge is shown in figure 7a. The Mach stem of this reflection reflects over the second wedge also as a Mach reflection (figure 7b). Similar to the previous case, the two triple points interact at a later time to form a new Mach reflection. However, unlike the reflection process in region 3 this Mach reflection is an inverse-Mach reflection[5], i.e., its triple point propagates towards the second wedge surface. Upon colliding with the second surface the inverse-Mach reflection terminates and changes to a regular reflection. The regular

reflection of the incident shock wave over the second wedge is shown in figure
7c. The reflection point is followed by a short shock wave emanating from the
reflection reflected shock wave (where it forms a triple point) and terminates
perpendicular to the second wedge surface.

4. CONCLUSION

The reflection process of a Mach reflection over a compressive on an
expansive corner has been analysed using the basic concepts of the reflection
of a planar shock wave over a single wedge.

The analysis suggests four different reflection processes which have all
been verified experimentally.

REFERENCES

1. Mach, E., "Uber Einige Mechanische Wirkungen des Electrischen Funkens",
    Akad. Wiss, Wien, Vol. 77, 1878, p. 819.

2. Neumann, J. von, Collected Works, Vol. 6, Pergamon Press, Oxford, 1963.

3. Ben-Dor, G., "A Reconsideration of the Shock Polar Solution of a
    Pseudo-Steady Single Mach Reflection", Canadian Aerospace and Space
    Journal, Vol. 26, No. 2, 1980, p. 98.

4. Ben-Dor, G. and Glass, I.I., "Domains and Boundaries of Non-Stationary
    Oblique Shock Wave Reflections. 1. Diatomic Gas"., Journal of Fluid
    Mechanics, Vol. 92, pt. 3, 1979, p. 459.

5. Takayama, K. and Ben-Dor, G., "The Inverse Mach Reflection", AIAA Journal,
    to be published 1985.
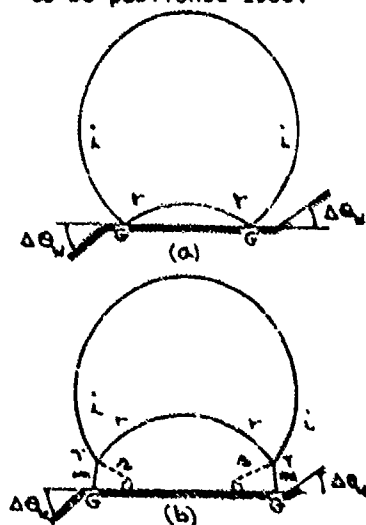
Fig. 1 Blast Wave Reflection
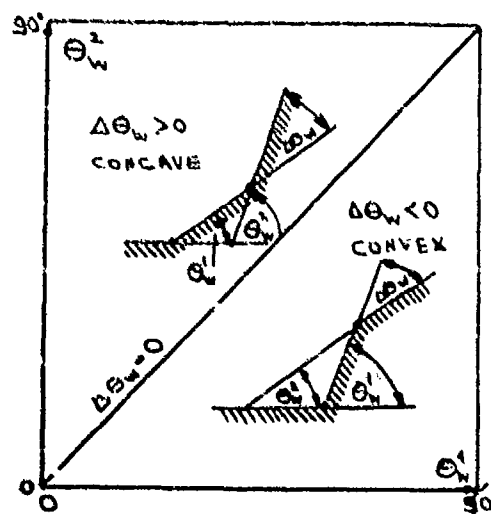
Fig. 2 Concave and Convex Double
Wedge Regions in the (θ_w^1, θ_w^2) Plane.
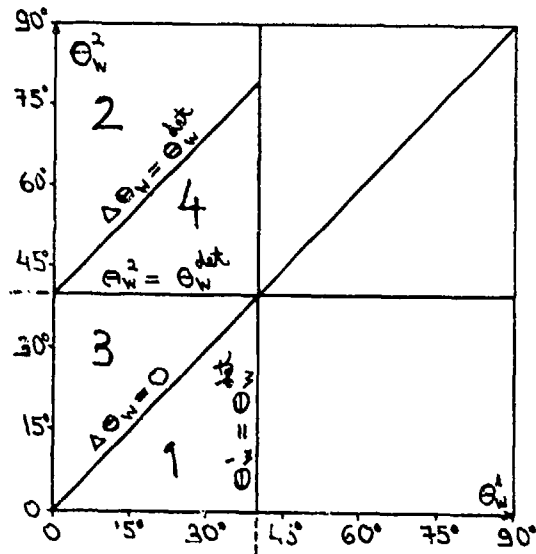
Fig. 3. Four regions of different reflection process of a Mach reflection over a secondary expansive or compressive ramp.
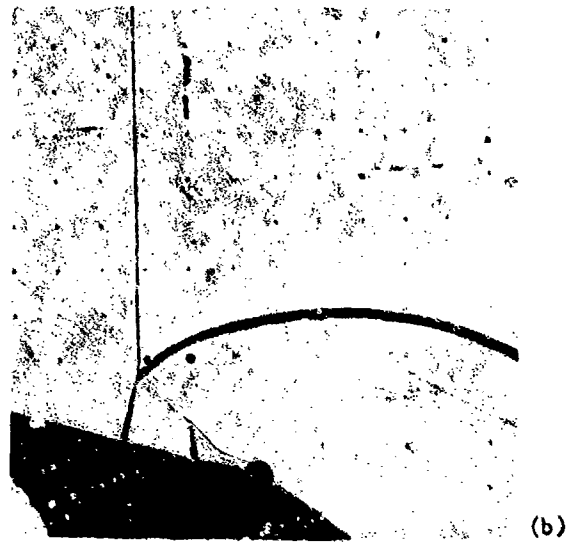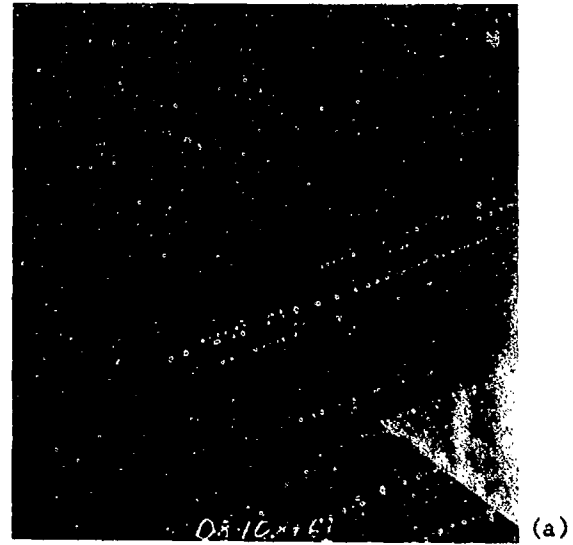
Fig. 4. Reflection process in Region 1

Fig. 5.   Reflection process in region 2.   Fig. 7.   Reflection process in region 4.

(a)

(b)

(c)

(d)
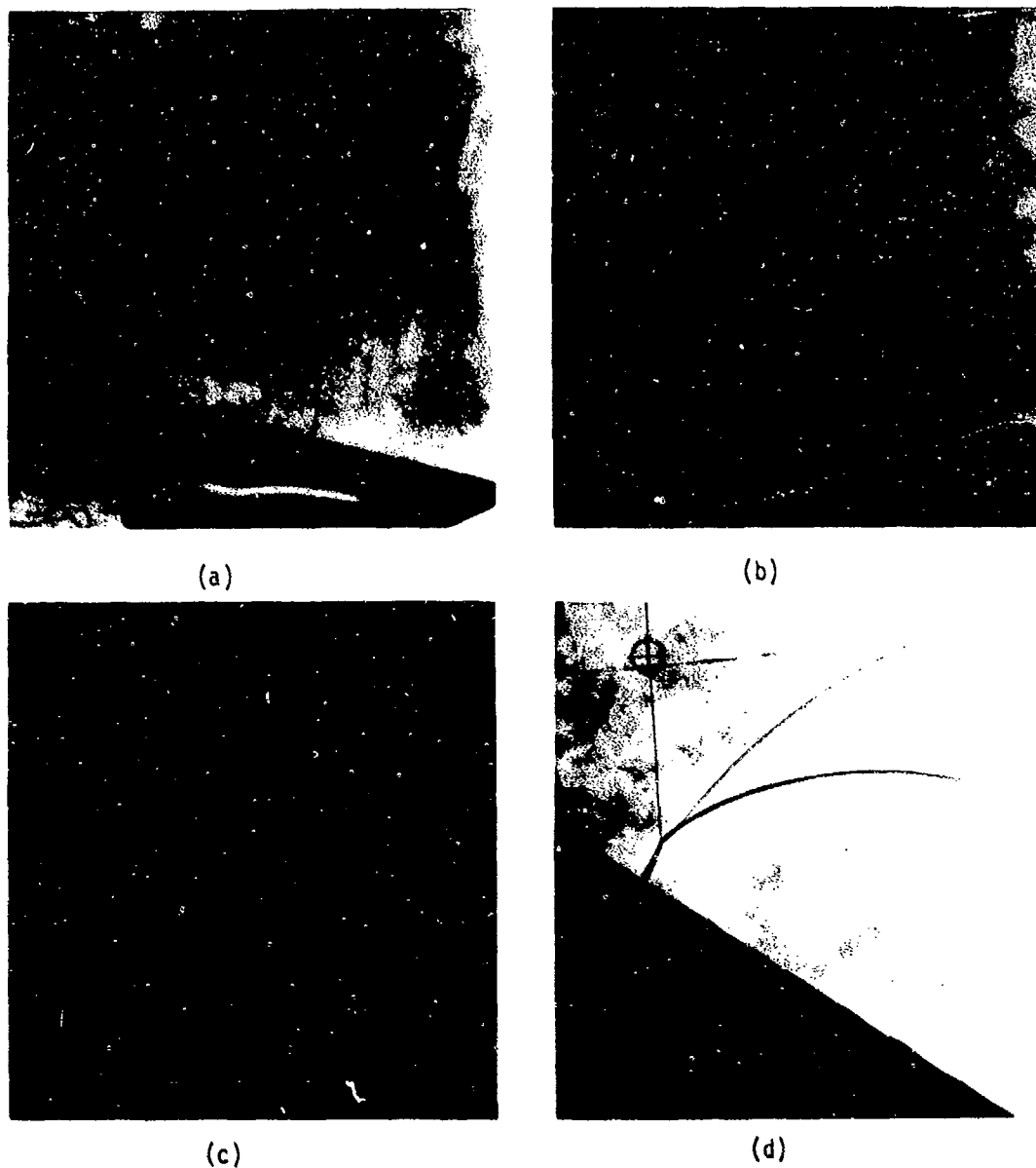
Fig. 6. Reflection process in region 3.

INTERACTION OF WEAK SHOCK WAVES REFLECTED

ON CONCAVE WALLS

M. Nishida, T. Nakagawa, T. Saito and M. Sommerfeld

Department of Aeronautical Engineering
Kyoto University, Kyoto 606, Japan

This paper describes computational and experimental
studies of the two-dimensional interactions of shock
waves reflected from a parabolically concave reflector.
The computations were carried out by solving the two-
dimensional Euler-type equations by means of the
piecewise-linear-method. In order to reveal the be-
havior of the interacting reflected-shock waves and the
flowfield behind them, two kinds of computer graphics
were developed: 1. three-dimensional graphics of pres-
sure fields, which were plotted at several time-steps
after the reflection, and 2. computer shadowgraphs based
on the principle of the optical shadowgraphs, whereby
the shapes of the shock waves were computer-visualized.
The numerical results show that the gasdynamic focus
exists between the geometric focus and reflector. For
the purpose of verifying the numerical results, density
histories of the incident and reflected shock waves were
measured in a shock tube with air as the test gas. The
density measurements were based on laser interferometry
using Wollaston prisms and PIN-photodiodes. The com-
parisons between the numerical and experimental results
show that numerical density histories are very similar
to the experimental ones, but that the numerical densi-
ties are slightly higher than the experimental ones.

1. INTRODUCTION

The focusing of curved shock waves can be observed not only in laser
fusion but also in the turn and acceleration of supersonic airplanes. Re-
cently, this phenomenon also has been applied to medical treatment of kidney
lithotripter.[1] For the purpose of understanding such a phenomenon, a basic
knowledge of shock focusing is necessary. Accordingly, the present study
describes the process whereby the interactions of weak shock waves, which are
reflected on concave walls, develop shock focusing.
For a recent, typical study concerning shock focusing, the work by
Sturtevant and Kulkarny[2] is referred to. They experimentally investigated the
behavior of focusing, weak shock waves in detail, by using a shock tube. In
their work, shocks are brought to a focus by reflecting plane and incident
shock waves from concave walls, and the behavior of the focusing shocks were
discussed based on shadowgraph pictures. Another experimental study of the
shock focusing was performed by Holl and Groenig.[3] In their work, a single
weak spherical blast wave generated by spark discharge was reflected from a
concave ellipsoidal wall. They derived patterns of focusing shock waves
similar to that of Sturtevant and Kulkarny in spite of the fact that the
patterns of incident waves differed.
The present work is concerned with computational and experimental studies

of the behavior of focusing shock waves once they have been reflected from concave walls. It is the aim of this paper to reveal the flowfields of focusing shock waves. The model of the shock focusing used here is such that in a duct with a rectangular cross section, a plane incident shock wave is reflected on the end wall of parabolic shape. Such reflection will form an oblique reflection, and then the reflected shock waves generated by this oblique reflection interact with each other. Consequently, the reflected shock waves converge and are focused. The shape of the reflector determines whether such an oblique reflection becomes a regular reflection or a Mach reflection. Therefore, in order to reveal the relationship, the behavior of the converging shock waves for two different shapes of the reflector was investigated.

2. NUMERICAL STUDIES

2.1 Numerical Calculations

Figure 1 shows a rectangular duct in which a shock wave propagates. The end of the duct is parabolic in shape which is given by $x = cy^2$. The shapes of the reflectors used in this study are such that $c = 0.575$(reflector R1) and $c = 0.325$(reflector R2). The distance in the x- and y-direction are non-dimensionalized by a half of an inner width in the y-direction, D. Initially, an incident shock wave is placed at $x = 1.8$. The initial conditions are such that stationary conditions are given to the gas left to the shock wave, and that conditions from shock relations are given to the gas right to the shock wave. The incident shock wave propagates towards the left. On the parabolic reflector, it is reflected, and then the reflected shock waves converge and are focused.

For the above model, a set of two-dimensional Euler-type flow equations has been solved by applying the operator-splitting-method, which results in three one-dimensional sweeps to obtain the solutions at the next time step. In each sweep, the piecewise-linear-method (PLM)[4] was employed.

The calculations were performed in the upper half region of Fig. 1, i.e., $0 \leq x \leq 1.8$ and $0 \leq y \leq 1$. The computational domain is divided into 90 x 50 square grid with $\Delta x = \Delta y = 0.02$, where Δx and Δy are spatial increments. The boundary conditions are (1) the reflection conditions on the reflector and side wall, and on the axis, (2) the inflow or outflow conditions at the right boundary.

2.2 Pressure Distributions

Figure 2 shows numerically calculated pressure distributions of the entire flowfields where the converging reflected-shock wave has an incident shock strength of $M_{s1} = 1.13$. In this case, the reflector R1 was employed. In the figure, the shock wave propagates to right, and the time shown in each figure is relative to the time when the incident plane shock wave reaches the edge of the reflector, i.e., $x = c$. In Fig. 2(a), the shock wave is completely reflected and propagates to right. As can be seen in the figure, the reflected shock wave is bow-shaped and two pressure peaks appear at the shock front. These two peaks travel towards the axis and meet each other in the center which results in a very high pressure as shown in Fig. 2(b). This may be recognized as shock focusing and referred to as gasdynamic focus. After the focusing, secondary reflected-shock waves are generated on the axis behind the original reflected-shock wave and then propagate towards the side walls. This is shown in Fig. 2(c) where the original reflected-shock waves are crossing. In the case of Fig. 2, the maximum on-axis pressure obtained at $x = 0.38$ reaches 2.8, which can be compared with the pressure of 1.31 for the normal reflection from a plane wall, where the pressure has been normalized by the pressure ahead of the incident shock wave. Similar crossed shock waves can be seen in the work in Refs. 2 and 3.

2.3 Computer Shadowgraphs

Computer shadowgraphs were developed in order to visualize converging shock waves. This was done based on the principle of optical shadowgraphs, namely the quantities $S = \Delta^2\rho/\Delta x^2 + \Delta^2\rho/\Delta y^2$ were calculated from the numerical data, and according to the magnitude of S, such figures as shown in Figs. 3 and 4 were drawn on the computer. Figure 3 is for the reflector R1 and Fig. 4 is for the reflector R2. The conditions in Fig. 3 are the same as in Fig. 2.

Figure 3(a) shows the pattern of the reflected shock waves before the focusing. This situation is the same as in Fig. 2(a). It is apparent that the shape of the shock wave is bow-shaped. The patterns of the shock wave at the focusing and after that are shown in Figs. 3(b) and 3(c), respectively. If the gasdynamic focus is defined as the position of a maximum on-axis pressure, then, as shown in the figure, the gasdynamic focus ($x = 0.38$) is between the geometric focus ($x = 0.43$) and the reflector. After the focusing, the shock waves cross which is very remarkable.

Figure 4(a) illustrates the pattern of a converging shock wave. This pattern also is bow-shaped but the bow is less deep than that in Fig. 3(a). Focusing is shown in Fig. 4(b) where the gasdynamic focus is at $x = 0.62$. However, the geometric focus stands at $x = 0.769$. Thus, the gasdynamic focus also falls between the geometric focus and reflector. Figure 4(c) is the shock pattern after the focusing, and the original reflected-shock waves are not crossed.

3. EXPERIMENTAL STUDIES

3.1 Experimental Setup and Procedure

In order to verify the numerically calculated results, experiments of the shock focusing were carried out by using a shock tube with air as the driver and driven gases. The driver section is 3.8 cm in a diameter and 50 cm in length. The driven section is 113.6 cm in length and its cross section is a 2.6 cm x 2.6 cm square. Two kinds of measurements were made: density histories and optical shadowgraphs. The density measurements were based on conventional laser interferometry using Wollaston prisms and PIN-photodiodes.[5] The optical setup of the laser interferometer is given in Fig. 5, in which the wave length of the laser beam is 632.8 nm, the focal distance of the lenses is 20 cm and the splitting angle of the Wollaston prisms is $3.9°$. The arrangement of the test and reference beams and the reflector is shown in Fig. 6. In all the experiments, the reflector R1 was used. By changing the position of the reflector relative to the beam, the data of the density history at several axial positions were obtained.

Analysis of the experimental data from the density measurements is easier when the test gas density is lower because the change in the optical path difference between the reference and test beams stays within only one fringe. Therefore, the initial pressure in the driven section was set at $p_1 = 52.1$ Torr, and the driver section pressure was set at $p_4 = 100$ Torr to realize weak shock waves. For such low driver and driven pressures, a very thin, stretched rubber was used as a diaphragm. By pricking it with a needle, the stretched rubber is instantaneously broken. Thus, weak shock waves can be easily obtained even in a low-density gas.

Incident shock strengths were determined by measuring time of flight between two laser beams (distance 1.36 cm) of the laser interferometer. For this measurement, the arrangement of the beams was changed in such a way that two beams pass through the viewing windows and cross the axis of the shock tube.

3.2 Experimental Results and Comparisons with Numerical Results

Figure 7 shows the comparisons between the experimental and computational

results of on-axis density histories at several axial locations. The strength of the incident shock wave was 1.13. As aforementioned, the gasdynamic focus is found at x = 0.38 so that Figs. 7(a) and 7(b) show the density histories at the positions which are between the gasdynamic focus and reflector, and Figs. 7(c) and 7(d) correspond to the density histories ahead of the gasdynamic focus. The arrival times of the incident shock wave for the the experiment and calculation are fixed at the same time. The first step of the density history results from the arrival of the incident shock wave, and the ensuing sharp peak is caused by the converging reflected-shock wave. Several small peaks can be observed behind the first sharp peak. These are due to the shock reflection between the axis and side wall. The numerical data always are slightly below the experimental density except for at the first peak. At the first peak, the comparison between the numerical and experimental densities is not clear but, in fact, the experimental density is lower than the numerical density. Never-theless, as for the arrival times of the reflected shock waves, the ensuing sharp peak and the second small peak, the numerical results agree with the experimental ones. In addition, the density decreasing rates behind the first peak are very similar in both results. The value of the density which would be realized for the normal reflection from a plane surface is shown in each figure. The density behind the first peak is near the value for the normal reflection.

Figure 8 shows the comparison between the experimental and computational maximum on-axis densities. At each time step, a maximum density is found on the axis, and then this density value is plotted which leads to Fig. 8. The numerical result shows that the maximum on-axis density ρ/ρ_1 = 2.13 can be found at x = 0.38, whereas the density for normal reflection is 1.47. However, in the experimental results the spatial extension of the shock focus is larger and the maximum density is lower. Ahead of the geometric focus, the maximum on-axis density decreases with increasing distance from the reflector. This situation is very similar to the computational result.

In Fig. 9, computer shadowgraphs are compared with experimental shadow-graphs. The time shown in each figure means the time from the arrival of the incident shock wave at the edge of the reflector. The experimental shadow-graphs similar to the shape of the numerical shock are selected. The patterns of the reflected shock wave predicted by computations can be also observed in the experimental shadowgraphs.

4. CONCLUDING REMARKS

According to the numerically calculated pressure distributions behind the reflected shock wave, two small pressure peaks are generated at both sides of the axis. These propagate towards the axis and then they are reflected by each other. This reflection produces a very high pressure peak. This may be men-tioned as the gasdynamic focus. For the initial shock strength M_{s1} = 1.13, the gas dynamic focus is, in general, different from the geometric focus. This is due to the nonlinearity of the shock waves. However, it is supposed that the gasdynamic focus will approach the geometric focus as the shock strength be-comes weaker.

The density measurements show that density histories are similar to those simulated by computations. Concerning the maximum on-axis density, the experi-mentally obtained values are lower than the computed ones. However, for weaker shock waves, this difference becomes smaller, which indicates that boundary layer effects may be responsible for this difference. Comparing the patterns of the reflected shock waves observed by the shadowgraph technique, with the computations by the PLM, good agreement was obtained.

REFERENCES

1. Schmiedt, E. and Bauer, H.-W., "Beruehrungsfreie Nierensteinzertruemmerung durch extrakorposal erzeugte, fokussierte Stosswellen", S. Karger AG. 1980.

2. Sturtevant, B. and Kulkarny, V.A., "The Focusing of Weak Shock Waves", Journal of Fluid Mechanics, Vol. 73, Pt.4, 1976, p.651.

3. Holl, R. and Groenig, H., "Focusing of Weak Blast Waves", Shock Tubes and Waves (Archer, R.D. and Milton, B.E. ed.), Sydney Shock Tube Symposium Publishers, 1983, p.563.

4. Collela, P. and Glaz, H.M., "Efficient Solution Algorithm for the Real Gases", Lawrence Lab. Univ. Calif. LBL-15776, 1983.

5. Smeets, G., "Laser Interferometer for High Sensitivity Measurements on Transient Phase Objects", IEEE Transactions on Aerospace and Electronic Systems, Vol. AES-8, 1977, p.82.
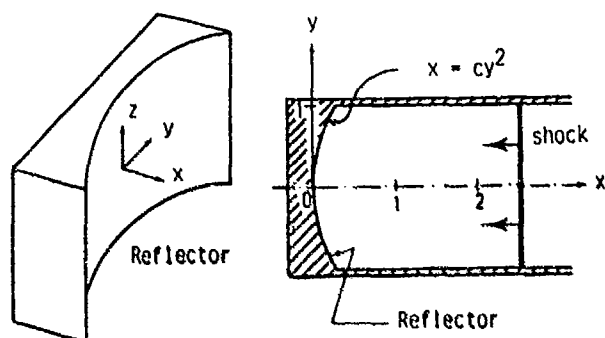
Fig. 1 Shock propagation in a duct with a parabolic reflector. x and y are normalized by a half of the height, D.
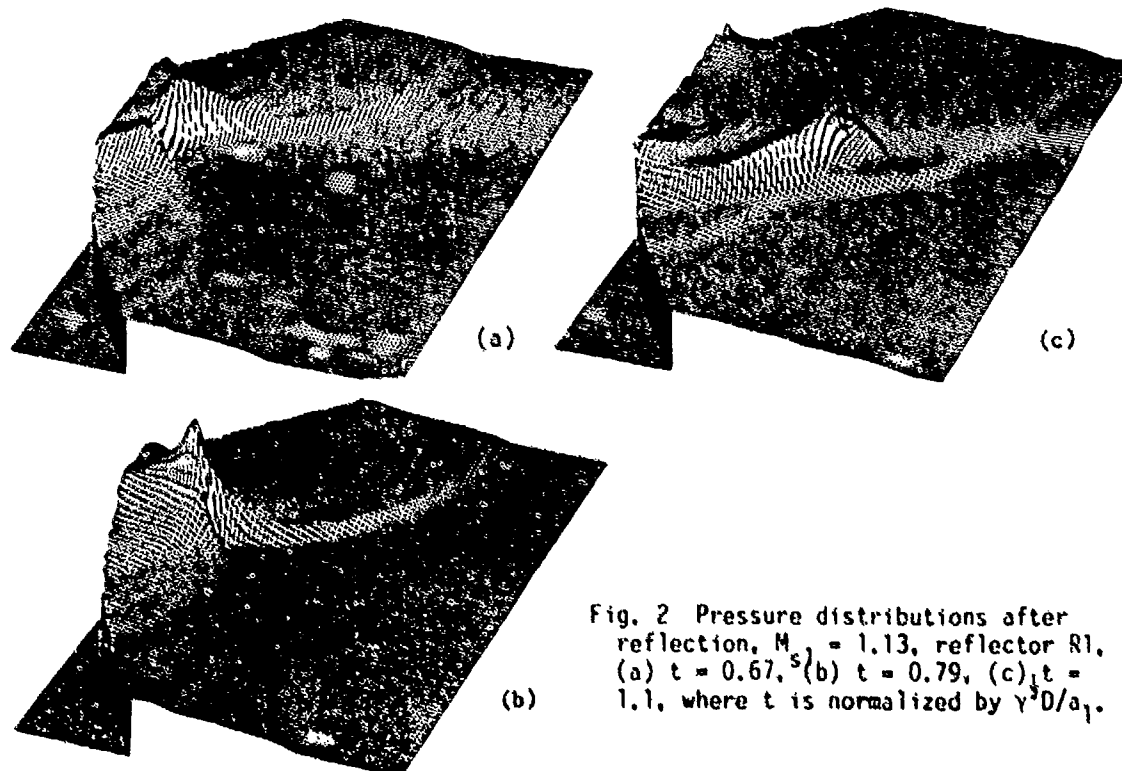
Fig. 2 Pressure distributions after reflection, $M_s = 1.13$, reflector R1, (a) $t = 0.67$, (b) $t = 0.79$, (c) $t = 1.1$, where t is normalized by $\gamma^{\frac{1}{2}} D/a_1$.

Gasdynamic focus ── ── Geometric focus

(a) t = 0.67　　　(b) t = 0.79　　　(c) t = 1.1

Fig. 3　Computer shadowgraphs, M_{s1} = 1.13, reflector R1.

Gasdynamic focus ── ── Geometric focus
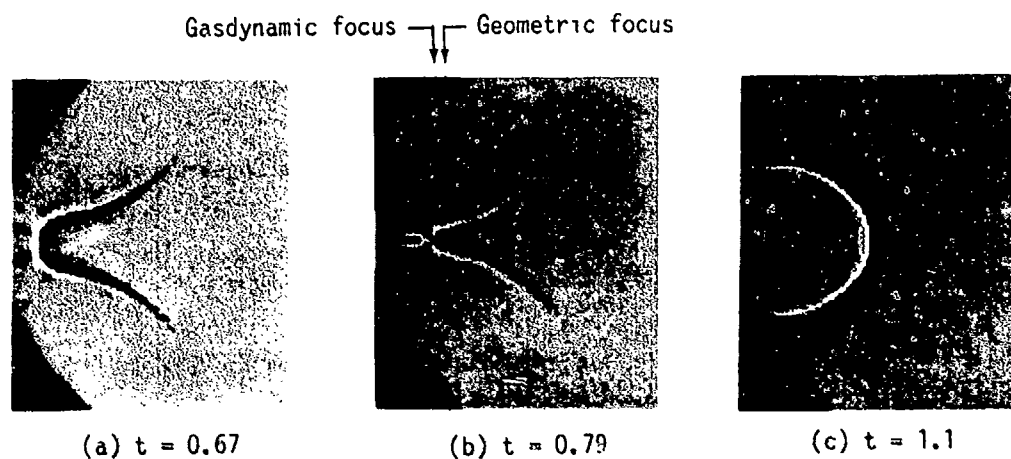
(a) t = 0.60　　　(b) t = 0.80　　　(c) t = 1.1

Fig. 4　Computer shadowgraphs, M_{s1} = 1.13, reflector R2.

Q : λ/4 plate
W : Wolloston prism
L : Lens
B : Babinet-Soleil compensator
P : PIN-photodiode
DC: Differential circuit
TM: Transient memory

MC: Micro-computer
MT: Magnetic tape
C : Computer
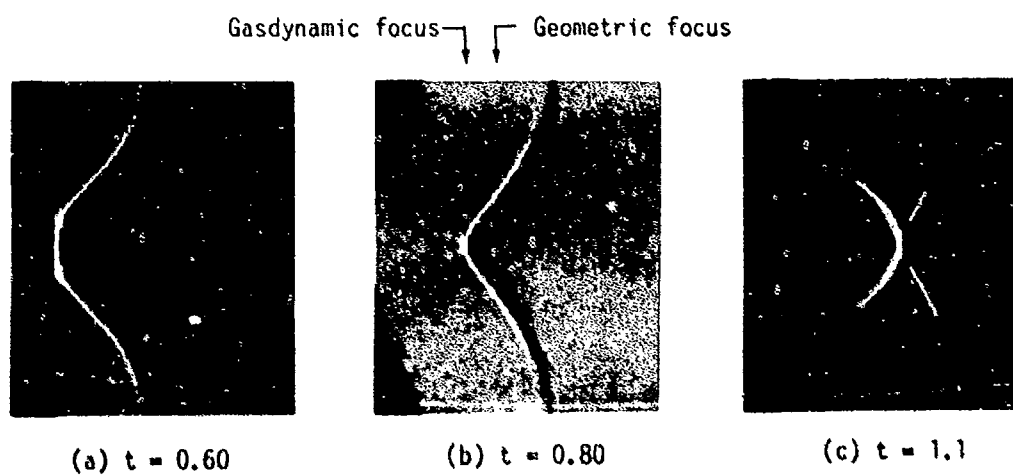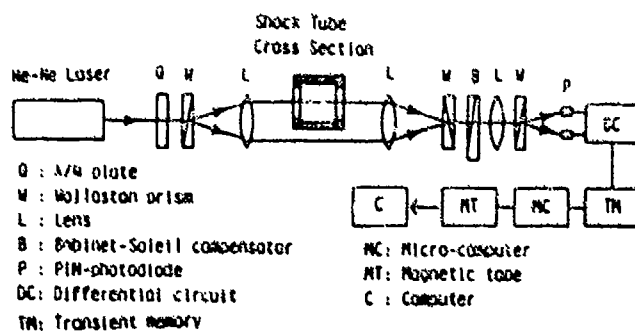
Fig. 5 Experimental setup of laser
interferometer.
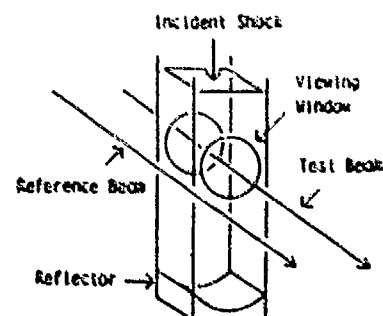
Fig. 6 Arrangement of reflector
and laser beams.
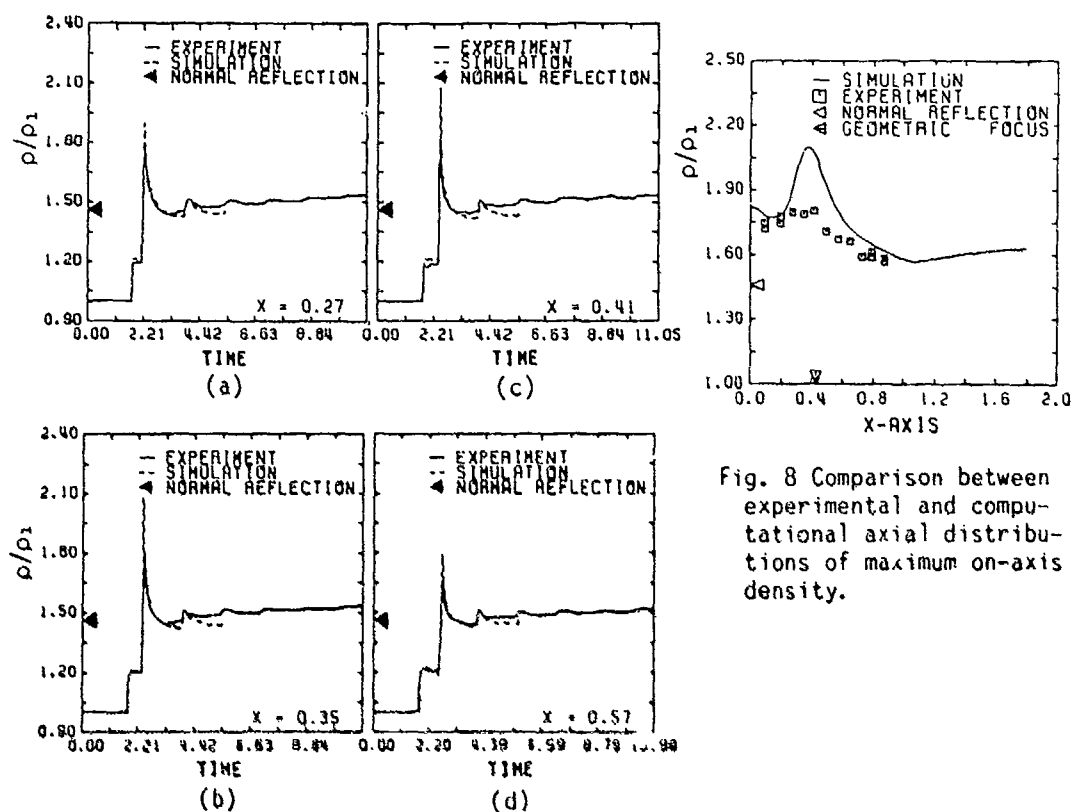
Fig. 8 Comparison between experimental and computational axial distributions of maximum on-axis density.

Fig. 7 Comparisons between experimental and computational density histories. Time is normalized by $\gamma^{1/2}D/a_1$.

t = 0.5   t = 0.6   t = 0.7   t = 1.0
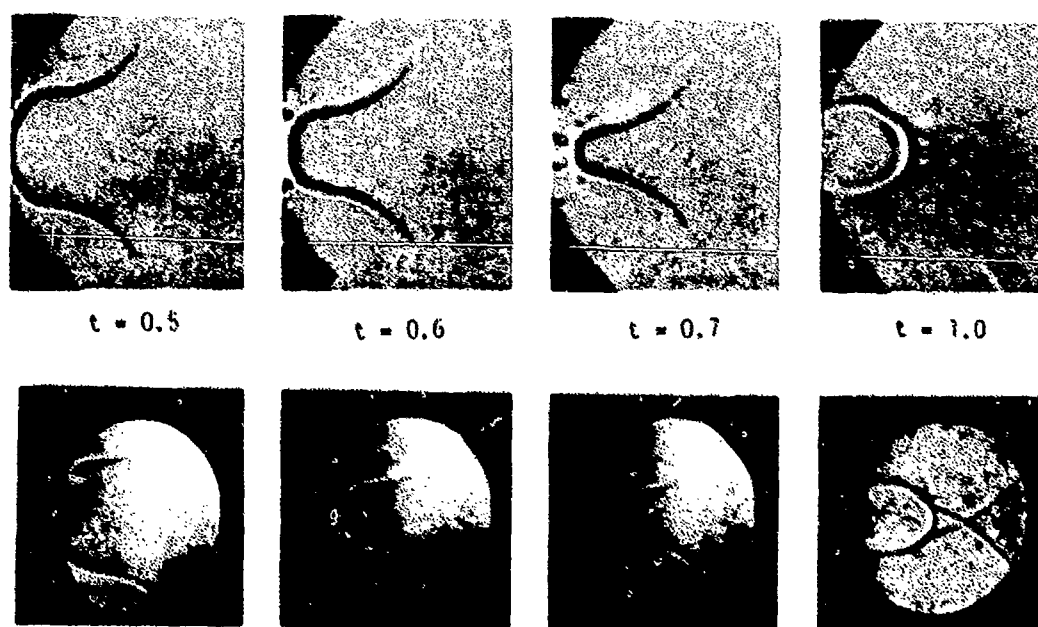
Fig. 9 Comparisons between computer shadowgraphs (upper) and experimental shadowgraphs (lower). M_{s1} = 1.13 and reflector R1.

INTERACTION OF OBLIQUE SHOCK-WAVE REFLECTIONS
IN AIR AND CO_2 WITH DOWNSTREAM OBSTACLES

H. M. Glaz, I. I. Glass[*], J.-C. Li[*], and P. A. Walter

Naval Surface Weapons Center, White Oak, Silver Spring, MD. 20903

[*]University of Toronto, Institute for Aerospace Studies
Toronto, Canada M3HT56

The problem of planar oblique shock-wave reflection
followed by the collision of the resulting Mach reflection
patterns with a downstream obstacle is considered here. A
direct comparison is made between interferograms obtained at
the University of Toronto Institute for Aerospace Studies
(UTIAS) 10 cm x 18 cm Hypervelocity Shock Tube and numerical
results obtained by using the second-order Godunov finite
difference scheme for solving the Euler equations of
unsteady compressible flow.

The main purpose of this study is to assess the
accuracy of the computational approach in resolving small-
scale flowfield structures for those problems involving
complex wave interactions. It is found that agreement
between the experimental and computational approaches is
extremely good in those flowfield regions for which nonideal
and viscous effects may be neglected in the experiment. In
particular, many details of these experimental flowfields,
e.g., multiple wave interactions, unstable slip surfaces,
and overexpansion shocks, are reproduced in the
computational results. Additionally, a quantitative
estimate of the effects of the shock wave-boundary layer
interaction on the overall flowfield pattern is possible by
comparing the inviscid numerics with the viscous experiment.

1. INTRODUCTION

The prediction of the pressure loading on obstacles or targets in the
path of a progressing blast wave is of obvious practical interest. Due to the
expense of full-scale field tests and recent advances in supercomputer
architectures, the development of numerical calculation methods for problems
of this type seem feasible and cost effective. A critical element in the
numerical code development process is the validation of the computer code
against results from controlled laboratory experiments. Especially useful are
experiments which provide whole flowfield data such as contour plots, since
this is generally not possible in field tests.

A spherical blast wave reflecting from the ground, especially in the
region near the leading Mach stem is analogous to a continuous sequence of
planar oblique shock wave reflections.[6,7] Therefore, an obstacle in the path
of such a Mach reflection flowfield in the laboratory would be a useful and
less expensive simulation of such an interaction in a blast wave field test.

Our purpose here is to present the results of a direct comparison of several cases of planar oblique shock-wave reflection followed by the interaction with downstream obstacles, between interferograms obtained at the University of Toronto Institute for Aerospace Studies (UTIAS) 10 cm x 18 cm Hypervelocity Shock Tube [1] and numerical results obtained by using the second-order Eulerian Godunov finite difference scheme[3] for solving inviscid gas dynamics. For the purpose of this paper, we take the point of view that the experimental results have been correctly obtained and address the following questions: (1) how well do the numerical computations reproduce the experimental interferograms, especially with reference to small-scale features?, (2) to what extent do localized viscous structures in the experiment, e.g., shock wave-boundary layer interactions affect the comparison?, and (3) do these local structures have more far-reaching influence on the flowfield dynamics? The question of nonequilibrium or other nonideal effects in the interferograms will not be taken up here.

In related work, results using the second-order Godunov scheme have been compared with interferogr. s of planar oblique shock-wave reflections.[6-8] The conclusions of this work were that the scheme is highly accurate for inviscid flow,[8] that local vis us boundary layer structures could be quite strong, and that these structures had a global influence on the quantitative results. This numerical method is being used on other shock-wave problems as well.[1-9]

2. EXPERIMENTAL TECHNIQUES AND NUMERICAL METHOD

All of the interferograms presented here are reproduced from work of Li and Glass[11]. A detailed discussion of the experimental facility and the data reduction techniques may be found there and in references therein. We simply remark here that the fringes in the interferograms represent lines of constant density and the confluence of several fringes indicates a flowfield discontinuity (i.e., a shock wave or a slip surface).

The numerical results have been calculated with a version of the Eulerian second-order Godunov scheme for nonstationary gas dynamics.[4,12] The scheme used here includes the modifications ne essa to handle a general equilibrium equation-of-state (EOS). The method is a finite-difference scheme in conservation form which achieves its second-order accuracy by combining monotonized intrazone profiles for the characteristic variables, a technique similar to the method of characterisitics, and Riemann problem solutions to obtain interzone fluxes with the final conservative differencing of these fluxes.[2-4] An accuracy and efficiency comparison study involving several schemes of this type has been carried out by Woodward and Colella.[12]

The cases presented here involve the use of two test gases, air and CO_2. In view of the very large pressures and temperatures obtained in the flowfields, especially after reflection from the obstacle, an accurate nonpolytropic EOS is necessary for both the interferogram data reduction and for the computation.[5-10] Since the experimental incident shock waves are run into relatively high pressure ambient conditions,[11] vibrational nonequilibrium effects may be assumed to be confined to the shock wave and the postshock flowfield to be in equilibrium.[5] It is possible, however, that subsequent shock-wave reflections may cause nonideal flowfield effects; such effects are precluded in the calculation by the assumption of an equilibrium EOS.

All computations were performed on a CRAY I at Los Alamos National Laboratory.

3. PROBLEM CONFIGURATION, INITIALIZATION, AND BOUNDARY CONDITIONS.

The four types of pseudo-stationary oblique shock-wave reflection are (a) regular reflection (RR), (b) single Mach reflection (SMR), (c) complex Mach reflection (CMR), and (d) double Mach reflection (DMR). We have illustrated the mach reflections, considered in this report in Figure 1 which defines the wedge angle θ_w, triple point trajectory angles χ,χ', various shock waves I, R, R', M, M', slip surfaces S, S', and the flow regions 1-5 produced by these reflections.[6-8]

If real gas and viscous effects can be ignored (as they are in the numerical calculations), the solution prior to collision with the obstacle is a function of the self-similar or pseudo-stationary variables $(\xi,\eta) = [(x-x_0)/(t\,t_0), (y-y_0)/(t-t_0)]$. Here (x_0,y_0) are the coordinates of the wedge corner (see Figure 2a) and t_0 is the time at which the incident shock reaches the corner. As a consequence of self-similarity, the wedge angle θ_w, the shock-wave Mach number M_s of the incident shock, and the EOS alone determine the solution for all times $t > t_0$, since these solutions are identical except for a scale factor.

Figures 2b,c illustrate the two possibilities at the time of collision with the downstream obstacle. If $\tan \chi < h/l$, then the triple point is beneath the top of the obstacle at this time, Figure 2b, and if $\tan \chi > h/l$, it is above the obstacle. Both cases are of practical interest. After the collision, an unsteady reflected bow shock-wave progresses outwards from the obstacle corner and ultimately interacts with the waves R,R'. The pattern is indicated schematically in Figure 2d. The flowfield in the region bounded by the reflected bow shock and the obstacle is no longer pseudostationary.[11]

The numerical computation proceeds in two stages. First, the pseudo-stationary Mach reflection pattern is computed as if the obstacle did not exist. Our techniques for initial and boundary conditions are the same as in our previous work.[6-8] At this point, the computation is restarted on a substantially refined computational grid which is confined to the region around the obstacle, represented by the dashed line in Figure 2a. The initial conditions for this computation are obtained by interpolation from the results of the first stage. The boundary conditions are outflow at the right-hand edge, reflection on the bottom[9] (with no special treatment at the corner), and Dirichlet at the top and left-hand edges, exploiting the flowfield self-similarity at these boundaries (in particular, they are chosen a priori so that the bow shock wave remains interior to the grid at the end of the calculation. To implement the Dirichlet boundary conditions, the solution of the first stage is saved in memory and is viewed in the (ξ,η) coordinate system. At later times, in the second stage calculation, linear interpolation on the (ξ,η) mesh is used to obtain boundary values. This procedure is exact up to errors in the first stage calculation and interpolation errors. We expect that the cumulative effects of this procedure on the computational error inside the bow shock wave to be quite small since the final time is not large and the initial flowfield of the second stage always contains the entire Mach stem region.

4. RESULTS

Table 1 lists the defining characteristics for 4 cases along with the size of the computational mesh. Each of SMR, CMR, and DMR are considered.

The results for Cases 1-4 are presented in Figures 3-6, respectively. For each case, interferograms were taken at several times, both before and after collision with the obstacle[11]. At each such time, the computational results were also sampled in the form of density contour plots, using the same isopycnic levels as obtained in the interferogram. A representative sample of these isopycnic comparisons is shown in the figures. For Case 4, an additional density contour plot using 30 equally spaced contours is also shown. This is necessary because the comparison using the experimental isopycnics is often inadequate in the region upstream of the obstacle and beneath its corner, e.g., for Case 4, the isopycnics in this region could not be determined in the experiment. The additional plot allows us to verify qualitative agreement, even if the results are in some error quantitatively or there is no quantitative comparison possible.

We are going to leave the case-by-case comparison to the reader, and instead make a few overall points. It should be noted that several of the interferograms exhibit strong bow shock wave-boundary layer interactions along the wedge surface; these wave patterns cannot be reproduced in the inviscid calculations. Around the expansion corner, the quantitative agreement between isopycnic levels in the expansion fan is quite good; in particular, the main characteristics of the recompression shock downstream of this corner are in good agreement. It may be observed that the portion of the contact surface beneath the expansion corner often exhibits unstable oscillations in both experiment and calculations. Close examination of the detailed shape of the reflected bow shock wave also reveals very good agreement. Finally, we take special note of Case 4, which is the only DMR case presented. The multiple wave interactions present in both experiment and calculations below the expansion corner are in remarkably good agreement, except near the wedge surface where the interferogram exhibits a marked lambda shock wave.

5. CONCLUSIONS

The main result of this work is that the numerical method has been further validated for the inviscid regions of flowfields of this type. However, there are substantial viscous effects after collision on the wedge surface boundary layer and in interactions of this boundary layer with the reflected bow shock wave. These effects do not seem to have more than a local influence on the flowfield structure, as evidenced by the results for Case 4.

It is possible that there are nonideal effects in the flowfield behind the bow shock wave, especially below the expansion corner. Our quantitative agreement is weakest in this portion of the results. Additionally, our numerical treatment of the singular corner could be improved and is a possible source of error. These areas will be the sources of future work on this problem. Finally, it would be of great interest to consider a DMR case for which the triple point trajectory lies above the corner of the obstacle.

REFERENCES

1.   Colella, P., Ferguson, R., Glaz, H. M., and Kuhl, A., "Mach Reflection from an HE Explosion," 9th Intl. Coll. Dynamics of Explosions and Reactive Systems, 1985.

2.   Colella, P. and Glaz, H. M., "Numerical Computation of Complex Shock Reflections in Gases," Proc. 9th Intl. Conf. on Numerical Methods in Fluid Dynamics, Saclay, 1984, ed. Soubbaramayer and J. P. Boujot, Springer-Verlag, Berlin.

3.   Colella, P. and Glaz, H. M., "Efficient Solution Algorithms for the Riemann Problem for Real Gases," to appear J. Comp. Phys. (1985).

4.   Colella, P. and Woodward, P. R., "The Piecewise-Parabolic Method (PPM) for Gas-Dynamical Simulations," J. Comp. Phys. 54, (1984), pp. 174-201.

5.   Deschambault, R. L., "Nonstationary Oblique-Shock-Wave Reflections in Air," Univ. of Toronto, UTIAS Report No. 270, 1984.

6.   Glaz, H. M., Colella, P., Glass, I. I., and Deschambault, R. L., "A Numerical Study of Oblique Shock-Wave Reflections with Experimental Comparisons," Proc. R. Soc. Lond. A398, (1985), pp. 117-140.

7.   Glaz, H. M., Colella, P., Glass, I. I., and Deschambault, R. L., "A Detailed Numerical, Graphical, and Experimental Study of Oblique Shock Wave Reflections," University of Toronto, UTIAS Report No. 285 (1985).

8.   Glaz, H. M., Glass, I. I., Hu, J. C. J., and Walter, P. "Oblique Shock Wave Reflections in SF$_6$: A Comparison of Calculation and Experiment," 9th Intl. Coll. Dynamics of Explosions and Reactive Systems, 1985.

9.   Glowacki, W. J., Kuhl, A. L., Glaz, H. M., and Ferguson, R. E., "Shock Wave Interaction with High Sound Speed Layers," 15th Intl. Symp. Shock Waves and Shock Tubes, 1985.

10. Hu, T.C.J., "Pseudo-Stationary Oblique-Shock-Wave Reflections in a Polyatomic Gas-Sulfur Hexafluroide," University of Toronto, UTIAS Report No. 253, 1985.

11. Li, J.-C. and Glass, I. I., "Collision of Mach Reflections with a 90-Degree Ramp in Air and CO$_2$," University of Toronto, UTIAS Report No. 290 (1985)

12. Woodward, P. R., and Colella, P., "Numerical Simulation of Two-Dimensional Fluid Flow with Strong Shocks," J. Comp. Phys. 54 (1984), pp. 115-173.

TABLE 1

CASE	TYPE	M_s	θ_w	GAS	l (cm)	h (cm)	P_0 kpa	ρ_0 (g/cm^3)	NX_1	NY_1	NX_2	NY_2
1	SMR	2.39	20	AIR	13.4	2.7	6.65	7.82×10^{-5}	494	228	432	305
2	SMR	2.37	20	AIR	13.4	1.35	6.65	7.87×10^{-5}	494	228	432	305
3	CMR	3.97	20	AIR	13.4	2.7	2.0	2.35×10^{-5}	520	240	432	305
4	DMR	5.73	20	CO_2	13.4	5.4	1.33	2.37×10^{-5}	520	240	432	305

(a) SINGLE MACH REFLECTION (SMR)   (b) COMPLEX MACH REFLECTION (CMR)   (c) DOUBLE MACH REFLECTION (DMR)
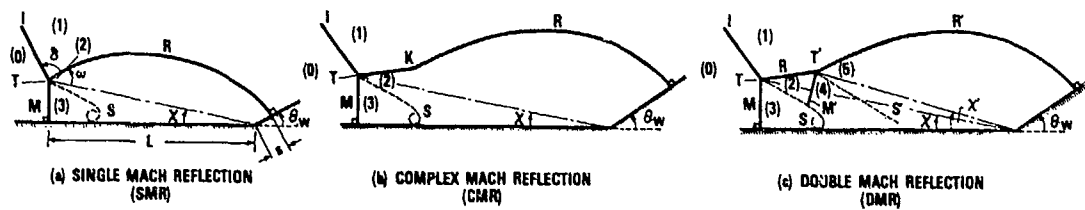
FIGURE 1   MACH REFLECTIONS

(a) INCIDENT SHOCK APPROACHES WEDGE CORNER

(b) MACH REFLECTION APPROACHES OBSTACLE CORNER $x < h/\ell$

(c) MACH REFLECTION APPROACHES OBSTACLE CORNER TAN $x > h/\ell$

(d) MACH REFLECTION PATTERN AFTER COLLISION
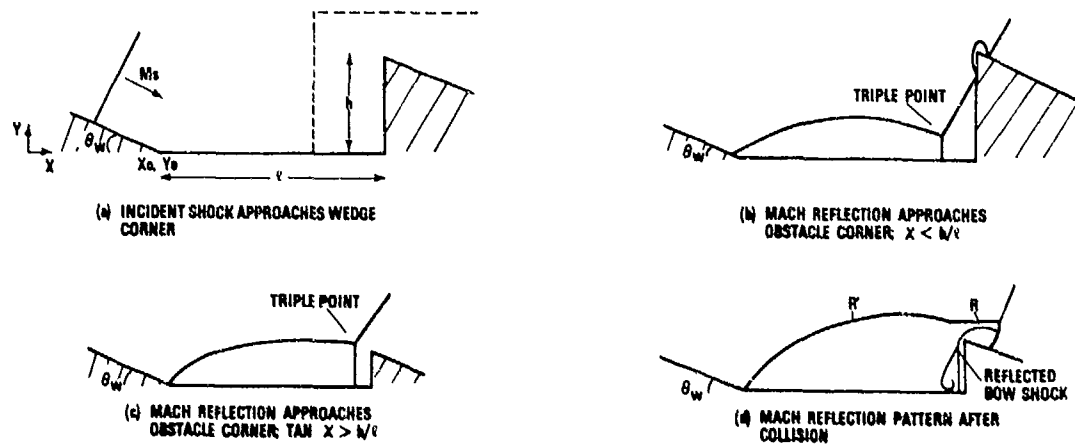
FIGURE 2   COLLISION PROBLEM GEOMETRY

CONTOUR
LEVELS:

(a) EXPERIMENTAL INTERFEROGRAM

(b) COMPUTED DENSITY CONTOURS

FIGURE 3, CASE 1, SMR, TAN x $>$ h/l

CONTOUR
LEVELS.

(a) EXPERIMENTAL INTERFEROGRAM

(b) COMPUTED DENSITY CONTOURS

FIGURE 4, CASE 2, SMR, TAN x $>$ h/l

CONTOUR
LEVELS:

(a) EXPERIMENTAL INTERFEROGRAM

(b) COMPUTED DENSITY CONTOURS

FIGURE 5, CASE 3, CMR, TAN x $>$ h/l

CONTOUR
LEVELS:

(a) EXPERIMENTAL INTERFEROGRAM

(b) COMPUTED DENSITY CONTOURS

FIGURE 6, CASE 4, DMR, TAN x $<$ h/l

AN INTERFEROMETRIC AND NUMERICAL STUDY OF PSEUDO-STATIONARY

OBLIQUE-SHOCK-WAVE REFLECTIONS IN SULFUR HEXAFLUORIDE (SF_6)*

T. C. J. Hu and I. I. Glass

Institute for Aerospace Studies, University of Toronto
Toronto, Canada

Pseudostationary oblique-shock-wave reflections in SF_6 were investigated experimentally and numerically. Experiments were conducted in the UTIAS 10 x 18 cm Hypervelocity Shock Tube in the range of incident shock wave Mach number $1.25 < M_s < 8.0$ and wedge angle $4° < \theta_w < 47°$ with initial pressure $4 < P_0 < 267$ torr (0.53 to 35.60 kPa) at temperatures T_0 near 300 K. Regular reflection (RR), single-Mach (SMR), complex-Mach (CMR) and double-Mach reflections (DMR), were observed. These were studied using infinite-fringe interferograms from a 23-cm dia field-of-view Mach-Zehnder interferometer. The analytical transition-boundary maps were established up to $M_s = 10.0$ for frozen and vibrational equilibrium SF_6. An examination of the relaxation length indicated that a vibrational-equilibrium analysis was required. Comparisons of experiment with analysis for transition-boundary maps, reflection angle δ and the first triple-point-trajectory angle χ verify that the reflections were in vibrational equilibrium. The behaviour of the angle between the two triple-point trajectories $(\chi' - \chi)$ is discussed and the unique pattern of DMR with $\chi' = 0$ was verified experimentally.

1. INTRODUCTION

Oblique-shock-wave reflections have been studied by many researchers for over a century.[1] A series of experimental, analytical and numerical investigations of this phenomenon began over a decade ago at the University of Toronto Institute for Aerospace Studies (UTIAS). To substantiate the claims made by the foregoing researchers[2-9] that real-gas effects do play an important role in nonstationary shock-wave systems, an investigation of a polyatomic gas such as SF_6, with many internal degrees of freedom, becomes an ideal candidate. Sulphur hexafluoride has 15 modes of vibrational degrees of freedom, a low specific heat ratio of 1.093 at 30°C. It is also non-toxic and has a high index of refraction, which is useful for optical studies. Therefore, it was the test gas used in this study.

2. EXPERIMENTAL PROCEDURES

Experiments were performed in the 10 cm × 18 cm UTIAS Hypervelocity Shock Tube in sulphur hexafluoride at initial pressures ranging from 4 to 267 torr and an initial temperature near 300 K in all cases. The incident shock wave Mach number range was $1.25 < M_s < 8$, over a series of sharp steel wedges

with θ_w ranging from 4° to 47°. Dual-wavelength laser-interferograms as well as shadowgrams were used to record the reflection process and were obtained with a 23-cm dia field-of-view Mach-Zehnder interferometer. The shock shapes and geometries, density field (isopycnics), and the density distribution along the wedge surface and through the bow shock wave in detached cases were determined from the corresponding interferograms. The experimental data were then compared with the numerical analyses.

The four basic types of pseudo-stationary oblique-shock-wave reflection observed in the experiment are illustrated schematically in Fig. 1. The definitions of wedge angle θ_w, triple-point-trajectory angles χ, χ', various shock waves I, R, R', M, M', slipstream S, S', and the flow regions (1) to (5) produced by the reflections are also shown in the diagrams. An infinite-fringe interferogram of each of the four basic types of reflection and the evaluation of the density field are presented in Fig. 2.

3.   VERIFICATION OF REAL-GAS EFFECTS AND TRANSITION BOUNDARIES

Several postulates were made regarding the transition criteria as noted below.

RR $\leftrightarrow$ MR	$\theta_1 + \theta_2 = 0$
SMR $\leftrightarrow$ CMR	$M_{2T} = 1$ and $\delta = 90°$
CMR $\leftrightarrow$ DMR	$M_{2k} = 1$

It becomes necessary to compare them with the experimental results and to justify their validity. The transition boundary lines in the (M_s, θ_w) and the (M_s, θ_w')-planes for the case of frozen and vibrational-equilibrium SF_6 were constructed according to the criteria proposed by von Neumann,[10] Ben-Dor and Glass,[3] and Shirouzu and Glass.[7] To verify the contribution of real-gas effects and the validity of the transition criteria, experiments were done along the transition lines as well as inside the transition regions.

Some physical phenomena of shock-wave reflection were compared. The polyatomic SF_6-molecule has 3 translational, 3 rotational and 15 vibrational degrees of freedom. The computations employ the equations of state for frozen SF_6 ($\gamma=4/3$) and vibrational-equilibrium SF_6. In the frozen-gas model, only translational and rotational degrees of freedom are excited to the new equilibrium state and the other degrees are frozen at their initial state. In the equilibrium-gas model, all translational, rotational and vibrational modes are excited to the new equilibrium state immediately behind the shock wave. The vibrational relaxation lengths behind a normal shock wave versus Mach number are plotted in Fig. 3 for the diatomic gases N_2 and O_2, triatomic gas CO_2 and polyatomic gas SF_6. These curves are for the initial conditions of $P_0=15$ torr and $T_0=300K$. They were obtained on the basis of the theoretical and empirical analyses given by Breshears and Bird[11] for N_2, Lutz and Kiefer[12] for O_2, Camac[13] for CO_2 and Breshears and Blair[14] for SF_6. The vibrational characteristic temperatures T_k and the degeneracy number n_k of these four gases are also listed in Fig. 3. In the problem of shock-wave reflection, a characteristic length of 1 mm was chosen by Shirouzu and Glass.[7] If the vibrational relaxation length is longer than the characteristic length, the flow can be treated as frozen, otherwise it can be assumed to be in vibrational equilibrium. The average T_k for SF_6 is lower than for the other four gases and it reaches vibrational equilibrium much faster than the others. Raising the pressure at a given temperature enhances particle collisions and vibrational equilibrium is reached more quickly. From Fig. 3, it is expected that vibrational relaxation in SF_6 at $M_s < 1.7$ with an initial pressure of 15 torr and a temperature of 300 K will take place in more than 1 mm. However, at such a low Mach number, a relatively higher initial pressure is

required for the experiment. Increasing the pressure will shift the vibrational relaxation length curve down, therefore no vibrational relaxation length will be observed. Since the vibrational relaxation length is less than 1 mm over the entire range of shock Mach number studied in this work, it can be safely assumed that SF$_6$ is in vibrational equilibrium.

3.1 TRANSITION BOUNDARIES

The experimental results are classified into the four possible types of reflection and are plotted in the transition maps for comparison. The reasons are twofold : first, to determine whether the experimental results agree with the frozen-gas or the equilibrium-gas analysis; second, to verify the validity of the transition criteria. The agreement between the frozen-gas analysis and experimental results is poor. However, there is definite agreement with the equilibrium SF$_6$ model as shown in Fig. 4.

The comparison of the RR ↔ MR boundary should be done in the (M_s, θ_w)-plane since there exists a multi-valued portion near this boundary in the (M_s, θ_w')-plane.[7] It is noted in Fig. 4(a) that several RR points lie in the domain corresponding to MR at $M_s < 2.11$ and $\theta_w = 45°$. On the other hand, three of the DMR points lie in the domain of RR, at $M_s = 3.45$ (3 runs) for $\theta_w = 42°$, and $M_s = 6.48$ (1 run) and 7.96 (2 runs) for $\theta_w = 37°$. Note that the RR ↔ MR boundary is predicted by the detachment criterion and is the limit for the two-shock theory[10] to have solutions. Therefore, any RR which exists beyond this boundary limited by the two-shock theory is a persistence of RR or it is known as the "von Neumann paradox". Furthermore, the mechanical equilibrium criterion[15] is the limit for the three-shock theory to have solutions. Thus any MR lying above the RR ↔ MR boundary into RR domain, on the contrary, is not a persistence of MR because it has not exceeded the limit of the three-shock theory for a MR to exist. It can be seen that the termination of the RR line, according to the detachment criterion, is in general very good for engineering applications. However, improvement is still necessary. This has been accomplished recently by Hornung and Taylor[16] and Wheeler and Glass,[17] who ascribe the cause to the boundary layer induced on the wedge wall by the shock-wave system.

In the (M_s, θ_w')-plane, the results for θ_w' do not require the measurement of χ. Transition boundaries in the MR region are more accurate in the (M_s, θ_w')-plane than in the (M_s, θ_w)-plane. In Fig. 4(b), there are two SMR points lying in the CMR according to the former criterion $M_{2T} = 1$. But according to the new SMR ↔ CMR criterion, there is only one CMR data point lying below the transition line, at $M_s = 3.47$ and $\theta_w' = 19.5°$. Therefore, the new criterion for SMR ↔ CMR transition agrees best with experiment. There are several DMR points lying beyond the CMR ↔ DMR transition line into the CMR region, and there is one CMR point just lying above the transition line in the DMR domain, at $M_s = 5.5$ and $\theta_w' = 17.8°$. Generally, except for low Mach numbers and high wedge angles, the CMR ↔ DMR transition criterion is reasonable, though not precise. Experimental results in air by Deschambault[8] showed that the CMR ↔ DMR transition line should meet the intersection point of the RR ↔ MR and SMR ↔ CMR transition lines. The dash-dot line in Figs. 4(a) and (b) indicates how the CMR ↔ DMR transition should meet at the point P on the RR ↔ MR transition line. Note the good agreement of the experimental results with this line.

3.2 COMPARISON OF ANALYTICAL AND EXPERIMENTAL RESULTS OF PHYSICAL QUANTITIES

Analytical results that are based on a frozen-gas model are distinct from an equilibrium-gas model. By comparing the experimental results with the

frozen or equilibrium-gas model for a given flow property, the validity of
each model can be justified.

Figure 5 shows the experimental results for δ plotted in the (M_s, δ)-
plane for fixed values of θ'_w. The number beside each experimental point
indicates the measured value of θ'_w. The analytical results for a vibrational-
equilibrium gas and for a frozen gas at several fixed θ'_w are drawn as solid
and dashed lines, respectively. They are used only as a guide to illustrate
the behaviour of δ in relation to M_S. The discrepancy of the experimental
value from the equilibrium-gas analysis is shown as straight lines extending
out of a data point. It can be seen that the maximum discrepancy found is
less than 2.5°. Thus, the agreement between the experimental results and the
equilibrium-gas calculations is excellent. However, the frozen-gas lines are
all shifted lower to the right from the vibrational-equilibrium case. Thus,
for a given Mach number and θ'_w, δ will have a smaller value with a frozen-gas
analysis than with a vibrational- equilibrium analysis. For example, at $M_s =$
5.0 and $\theta'_w = 40°$, $\delta = 150°$ with an equilibrium-gas analysis, whereas $\delta =$
126.7° using a frozen-gas analysis. The agreement between experiments and
frozen-gas analysis is poor.

3.3 FIRST TRIPLE-POINT-TRAJECTORY ANGLE χ

Law and Glass[18] proposed an empirical method for predicting the value of
χ based on experimental observations that the Mach stem, in many cases, is
straight and normal to the wedge surface, and introduced an additional
independent geometrical relation $\phi_3 = 90° - \chi$, where ϕ_3 is the incident flow
angle to the Mach stem. The plot of χ as a function of M_s, with the actual
wedge angle θ_w as a parameter for equilibrium and frozen SF_6 is shown in Fig.
6. The experimental points are also plotted in the figure. The agreement
between the analytical results and experiments is good in general, with
discrepancies of the same order of magnitude as the error in measurement
($\pm 1°$). The experimental points for $\theta_w = 10°$, 20° and 30° have the same
trend as the higher θ_w results in that they level off and become independent
of the Mach number M_s. The frozen-gas analytical lines are all shifted up
from the equilibrium values and χ becomes nearly independent of M_s at high
Mach numbers, even for low θ_w. In all cases, the frozen-gas analysis gives a
much larger value than obtained experimentally. Therefore, there is poor
agreement between the frozen-gas analysis and experiment.

The other angle that is worth discussing is the difference between χ' and
χ, since it indicates the position of the second triple point relative to the
first triple point. A $[M_s, (\chi' - \chi)]$-plot of the experimental results is
shown in Fig. 7 for five wedge angles $\theta_w = 42°$, 37° , 20°, 10° and 4°. A
dashed line is used to approximate the profile of $(\chi' - \chi)$ for each fixed
wedge angle. As SMR just terminates (e.g. at $\theta_w = 42°$ and $M_s = 1.55$), $(\chi' -
\chi) = 0$, and ω' is positive indicating that the two triple points merge as one
at the first triple point. When CMR and DMR begin to form, the value of $(\chi' -
\chi)$ increases with Mach number M_s. It then reaches a maximum and decreases
in value. In the positive region of $(\chi' - \chi)$, ω' is positive as shown in
Fig. 8(a). As M_s increases further, $(\chi' - \chi)$ crosses zero and becomes
negative. In the case of $(\chi' - \chi) = 0$, ω' is zero as shown in Fig. 8(b),
meaning that the second triple point lies at a finite distance away from the
first triple point and both have the same trajectory direction. It is seen in
Fig. 7 that the higher the wedge angle, the sooner $(\chi' - \chi)$ goes negative.
When $(\chi' - \chi)$ goes negative, ω' is also negative as shown in Fig. 8(c). At
higher wedge angle and Mach number, $\chi' = 0$, $(\chi' - \chi) = -\chi$ and ω' is negative
as shown in Fig. 8(d). Lee and Glass[5] studied this last case analytically for
a perfect gas with $\gamma = 1.093$ and reported that $\chi' = 0$ may only be

hypothetical. However they confirmed in their later paper[6] that this case does actually occur, based on the present experimental findings. This means that the second triple point T' attaches to the wedge surface and the reflected shock wave R strikes the wedge surface and is reflected like an RR. A shadowgram of a DMR with $\chi' = 0$ taken at $M_s = 7.96$ and $\theta_w = 37°$ is shown in Fig. 9. Note the small triangular region bounded by the Mach stem, the reflected shock wave and the wedge surface. The second reflected shock wave is lying low on the wedge surface and terminates at the corner as an attached straight bow shock wave showing that the state behind the second reflected shock wave is supersonic. A DMR with $\chi' = 0$ has two confluence points [one real (T) and one degenerate (T') triple point], two reflected shock waves, but only one Mach stem, one slipstream and the region behind the second reflected shock wave is supersonic instead of subsonic.

5. CONCLUSIONS

An experimental and numerical investigation was made of pseudostationary oblique-shock-wave reflections in SF$_6$. The domains and transition boundaries between the various types of reflection were established in the (M_s, θ_w) and (M_s, θ_w')-planes for both frozen and vibrational-equilibrium SF$_6$. The transition boundaries predicted on the basis of an equilibrium flow agreed well with the experimental results. The new criterion[7] $\delta > 90°$ was verified in the present work that it is an additional necessary condition for the transition from SMR to CMR. However, RR persists beyond the boundary line determined by the detachment criterion, as expected, owing to the boundary layer growth induced on the wedge surface by the moving shock-wave system.[16,17]

Comparisons of the fundamental angle δ in Mach reflection using θ_w' as the parameter, and the comparisons of the first triple-point trajectory angle χ using θ_w as the parameter, justified the validity of the equilibrium SF$_6$ analysis. The behaviour of the angle between the first and second-triple-point-trajectory angles ($\chi' - \chi$) was discussed and a DMR with $\chi' = 0$ was obtained experimentally as predicted by Lee and Glass.[6] (See Ref. 19 for complementary details.)

REFERENCES

1. Mach, E. and Sommer, J. 1877 Akad. Wiss. Wien abt.II 75, 101-130.
2. Ben-Dor, G. and Glass, I. I. 1978 AIAA J. 16, 1146-1153.
3. Ben-Dor, G. and Glass, I. I. 1979 J. Fluid Mech. 92, 459-496.
4. Ben-Dor, G. and Glass, I. I. 1980 J. Fluid Mech. 96, 735-756.
5. Lee, J. H. and Glass, I. I., "Domains and Boundaries of Pseudo-Stationary Oblique-Shock-Wave Reflections in Air", UTIAS Report No. 264, 1982.
6. Lee, J. H. and Glass, I. I. 1984 Prog. Aerospace Sci. 21, 33-80.
7. Shirouzu, M. and Glass, I. I., "An Assessment of Recent Results on Pseudo-Stationary Oblique-Shock-Wave Reflections", UTIAS Report No. 264, 1982.
8. Deschambault, R. L., "Nonstationary Oblique-Shock-Wave Reflections in Air", UTIAS Report No. 270, 1983.
9. Deschambault, R. L. and Glass, I. I. 1983 J. Fluid Mech. 131, 27-57.
10. von Neumann, J., "Oblique Reflection of Shocks", Explosives Research Report No. 12, Navy Dept. Bureau of Ordinance, Washington D.C., 1943.
11. Breshears, W. D. and Bird, P. F. 1968 J. Chem. Phys. 48, 4768-4773.
12. Lutz, R. W. and Kieffer, J. H. 1966 Phy. Fluid 9, 1638-1642.
13. Camac, M., "CO$_2$ Relaxation Processes in Shock Waves", Avco-Everett Research Lab. Research Report No. 194, 1964.
14. Breshears, W. D. and Blair, L. S. 1973 J. Chem. Phys. 59, 5824-5827.
15. Henderson, L. F., Lozzi, A. 1975 J. Fluid Mech. 68, 139-155.

16. Hornung, H. G. and Taylor, J. R. 1982 J. Fluid Mech. 123, 143-153.
17. Wheeler, J. M. and Glass I. I. 1985 (paper to be published).
18. Law, C. K. and Glass, I. I. 1971 CASI Trans., 4, No. 1, 2-12.
19. Glaz, H. M., Glass, I. I., Hu, T.C.J., Walter, P., "Oblique Shock Wave
    Reflections in SF_6: A Comparison of Calculation and Experiment", Proc.
    10th Int. Colloq. on Dynamics of Explosions and Reactive Systems,
    California, 1985.
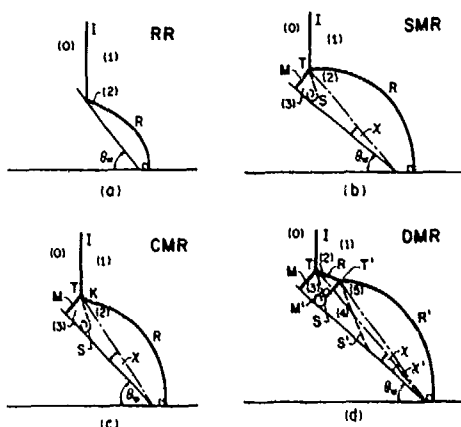
Fig. 1 Schematic diagrams of four
basic types of pseudo-stationary
oblique-shock-wave reflection patterns.
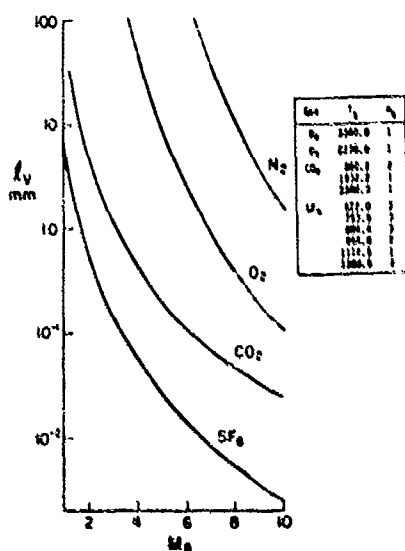
Fig. 3 Vibrational relaxation length ℓ_v
behind normal shock wave for various gases
at $P_0 = 15$ torr and $T_0 = 300K$. The charac-
teristic vibrational temperature T_k and
degeneracy number n_k for the various gases
are given in the table above.
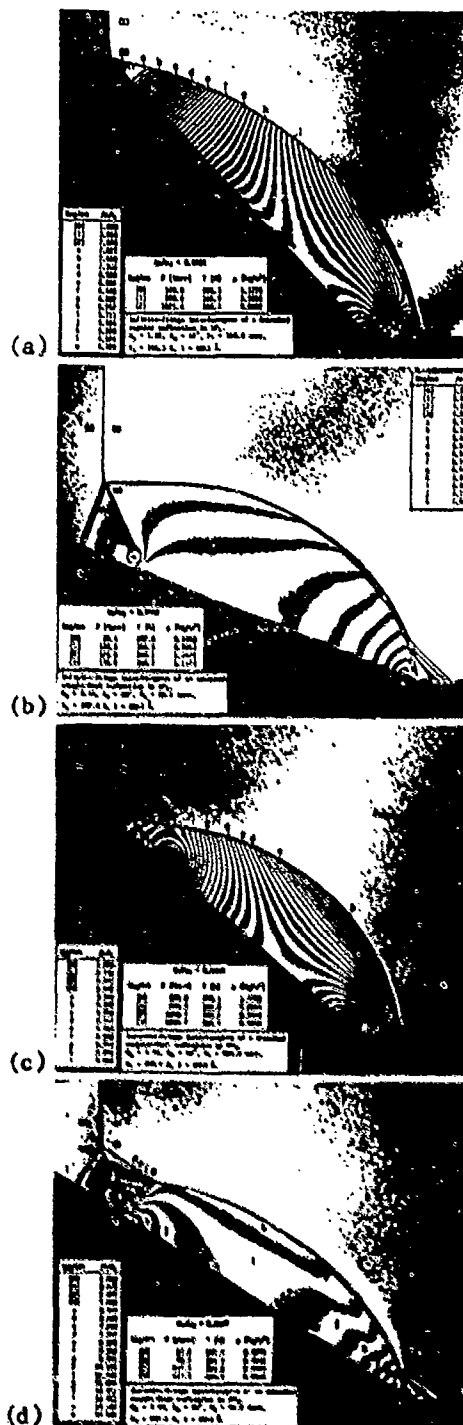
Fig. 2 Infinite-fringe interferograms of four possible pseudo-stationary
oblique-shock-wave reflections taken in SF_6.
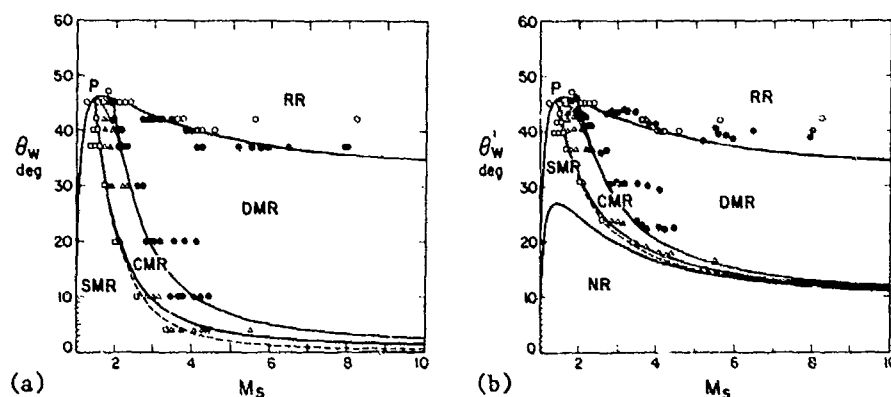
Fig. 4 Comparison of predicted domains of various types of reflection with experimental results for vibrational equilibrium SF_6: (a) in the (M_s, θ_w)-plane; (b) in the (M_s, θ_w')-plane. SMR ↔ CMR transition: solid line is $\delta = 90°$, dashed line is $M_{2T} = 1$. Types of reflection: O RR, □ SMR, △ CMR, ● DMR.
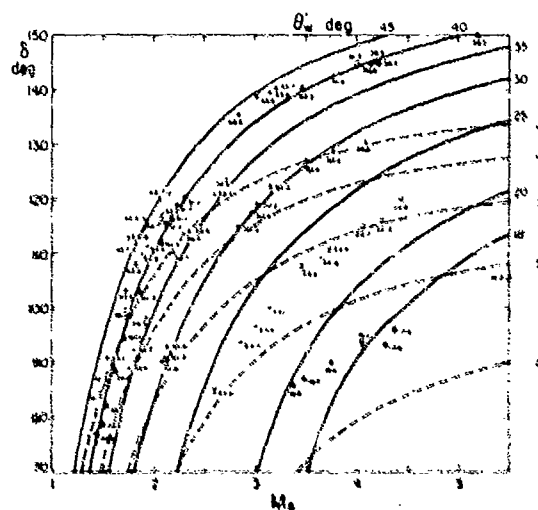
Fig. 5 Comparison of analytical and experimental values of δ in the (M_s, δ)-plane. Analytical lines calculated at $P_0 = 15$ torr and $T_0 = 300K$: ——— vibrational equilibrium SF_6, ------ frozen SF_6. Measured δ is indicated beside each datum point and discrepancy from vibrational equilibrium SF_6 is shown as a vertical line. Symbols for experiments at various θ_w: + 45°, × 42°, O 40°, ● 37°, △ 30°, ▲ 20°, □ 10°, ■ 4°.
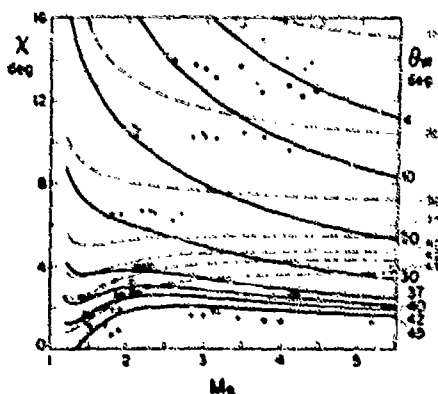
Fig. 6 Variation of χ versus M_s at fixed θ_w for SF_6. Analytical lines calculated at $P_0 = 15$ torr and $T_0 = 300K$: ——— vibrational equilibrium SF_6, ------ frozen SF_6. Symbols for experiments at various θ_w: ✶ 45°, × 42°, ■ 40°, □ 37°, ▲ 30°, △ 20°, ● 10°, O 4°.
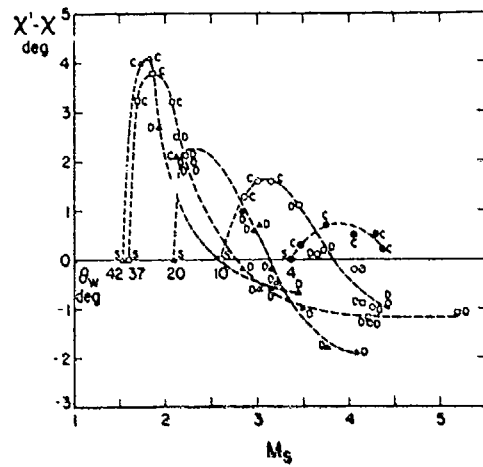
Fig. 7 Plot of the measured values of $(\chi'-\chi)$ versus M_S. Types of reflection: SMR S, CMR C, DMR D. Symbols for experiments at various θ_w: △ 42°, □ 37°, ▲ 20°, ○ 10°, ● 4°.
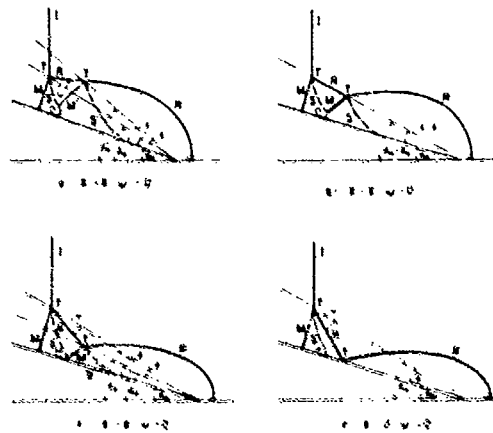
Fig. 8 Schematic diagrams of four patterns of double-Mach reflection.
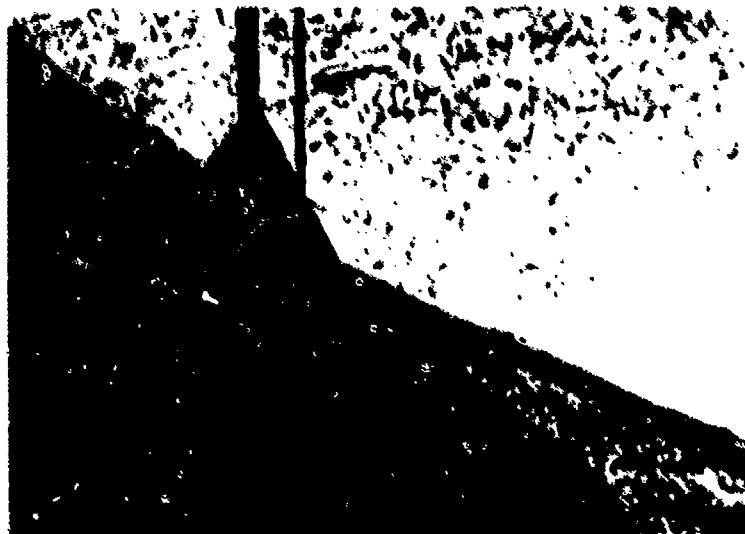
Fig. 9 Shadowgram showing a double-Mach reflection with $\omega' < 0$ and $\chi' = 0$. $M_S = 7.96$, $\theta_w = 37°$, $P_0 = 11$ torr, $T_0 = 296.6K$ in SF_6.

TRANSITION FROM MACH TO REGULAR REFLECTION
OF A SHOCK WAVE OVER A CONCAVE CORNER

K.Matsuo, T.Aoki, H.Hirahara and N.Kondoh

Graduate School of Engineering Sciences
Kyushu University, Kasuga, Fukuoka, 816, Japan

The problem considered in the present study is that of
transition from Mach to regular reflection of a shock wave
over a concave corner. For analytical purposes, it is
assumed that a circular cylindrical concave surface can be
represented by a sequence of infinitesimal wedges. The cal-
culated results show that the critical transition angle of
incidence of a shock wave increases with an increasing
initial angle of the concave surface and decreases with an
increasing strength of the incident shock wave. These
values are smaller than those predicted by the two shock
theory. To verify the validity of the present calculation,
an experimental investigation was performed using a concave
corner model which was composed of two straight walls, and
it was confirmed that the experimental results agreed well
with those of the present calculation.

1. INTRODUCTION

The transition between regular and Mach reflections of an oblique shock
wave has been extensively investigated theoretically and experimentally by
many researchers.[1-12] Unfortunately, however, the problem seems to be not
fully understood yet, especially in the case of a truly nonstationary reflec-
tion. For example, the critical transition angles of incidence ω_c of a shock
wave which strikes flat, convex and concave surfaces obtained in the previous
experiments[1-8] are shown in Fig.1 in terms of the reciprocal strength ξ (the
reciprocal of the pressure ratio across the shock) and the Mach number M_s of
incident shock waves. The critical angles of wall θ_c ($=90°-\omega_c$) are also shown
in the vertical axis. Curves 1 and 2 represent the values predicted by the
two and three shock theories, respectively. The experimental transition
angles for convex and concave surfaces are situated above and below the curve
1, respectively, and they seem to be independent of the radii of curvature of
the convex and concave surfaces r_0[5,8,11]. However, they seem to be located
on the plane rather scatteringly, and the dependence of the transition angle
on the initial angle of the convex or concave surface θ_i is not yet made clear.

The problem considered in the present study is that of transition from
Mach to regular reflection of a shock wave over a concave corner. The
critical transition angle of incidence of a shock wave which interacts with a
circular cylindrical concave surface was numerically obtained as a function of
the strength of the incident shock wave and the initial angle of the surface.
In order to examine the validity of the present calculation, an experimental
investigation was also performed using a concave corner model which was
composed of two straight walls.

2. NUMERICAL ANALYSIS

Consider the process of interaction of a plane shock wave of Mach number
M_s propagating from left to right with a concave circular cylindrical surface
OB with a radius of curvature r_0 and an initial angle θ_i shown in Fig.2. If
Mach reflection takes place at the point O, the initial angle of incidence of

the shock ω_0 and the initial angle of the triple point trajectory χ_0 at the point O can be predicted by the three shock theory for given M_S and θ_0. In order to determine the triple point trajectory shown by the dashed line and the critical transition point D, assume that the concave surface can be represented by a sequence of n pieces of straight line segments shown in Fig.3 and that the effects of the downstream pressure gradient can be neglected. If a shock wave strikes this concave corner model and Mach reflection occurs at the first wall OW_1, then the Mach shock T_0M_0 is reflected at the second wall W_1W_2', and Mach or regular reflection occurs, depending on the value of the increment of the wall angle $\Delta\theta=(\pi/2-\theta_0)/n$. If Mach reflection occurs, the two triple points T_0 and T' created by the first and the second Mach reflections approach to each other with time and come into collision at the point C_1. In this way, the triple point trajectory is bent, and the intersection of the trajectory with the solid surface gives the critical transition point D.

Fig.4 shows the flows before and after the collision of the two triple points T_{i-1} and T' at the wall W_iW_{i+1}. Let the flow properties and the angle of incidence ω_{i-1} near the triple point T_{i-1} in the state(1) be all known by the calculations up to the preceding wall $W_{i-1}W_i$. The properties around the triple point T' created at the point W_i, the angle of incidence ω_i' and the Mach number $(M_a')_i$ can be calculated in terms of the Mach number $(M_a)_{i-1}$ of the shock $T_{i-1}T'$ and the change of the angle of wall $\Delta\theta$. Then, the coodinate of the point of collision C_i is determined from the geometrical relation. At the moment of the collision, as shown in the state(2), two reflected shocks T_iR_{i-1} and T_iR' and two slip lines T_iS_{i-1} and T_iS' intersect the incident shock IT_i and the Mach shock T_iM_i at the point T_i, and these two reflected shocks and two slip lines coalesce into one reflected shock T_iR_i and one slip line T_iS_i, respectively, shown in the state(3), after the collision. The angle of incidence ω_i after the collision can be calculated by the following equation obtained from the geometrical relation, if the Mach number of the Mach shock after the collision $(M_a)_i$ is determined.

$$\omega_i = \frac{\pi}{2} - \theta_i - \tan^{-1}\left[\frac{\cos\theta_i - M_S/(M_a)_i}{\sin\theta_i}\right] \tag{1}$$

The value of $(M_a)_i$ may be estimated as follows. Since the pressures and flow directions of both sides of the slip line after the collision must be the same by the three shock theory, an unsteady wave of finite amplitude which adjusts the flow near the triple point will be generated, as shown in the state (2) in Fig.4. Considering this unsteady effect as a kind of Riemann's problem, the Mach number of this adjusting wave N_a will be given by the following equation;

$$\frac{P_t}{P_b} = \frac{2\kappa M_a^2 - (\kappa-1)}{\kappa + 1}\left[1 - \frac{\kappa - 1}{\kappa + 1}\frac{a_b}{a_t}\left(N_a - \frac{1}{N_a}\right)\right]^{-\frac{2\kappa}{\kappa-1}} \tag{2}$$

where p_b and a_b are the pressure and sound velocity behind the Mach shock $T'N_i$, and p_t and a_t are the pressure and sound velocity behind the Mach shock calculated by the three shock theory for the given N_i and θ_i. κ is the ratio of specific heats. The pressure behind the Mach shock after passing of the unsteady wave p_i is calculated in terms of N_a by the following equation.

$$\frac{p_i}{p_b} = \frac{2\kappa N_a^2 - (\kappa - 1)}{\kappa + 1} \tag{3}$$

If p_i is determined by Sq.(3), the Mach number $(M_a)_i$ of the Mach shock T_iM_i after the the collision of triple points is predicted by normal shock relations. Then the angle of incidence ω_i is calculated by Eq.(1), and the triple point trajectory is determined. In the present calculation, the pro-

pagation time of the unsteady adjusting wave is neglected and it is assumed that the Mach shock is strengthened instantaneously at the moment of collision of triple points.

3. EXPERIMENTS

In order to examine the validity of the present method of calculation, an experimental study was performed using a rectangular shock tube with a concave corner model shown in Fig.5 in its test section. The model is composed of two straight walls, and the first wall angle θ_0 is fixed at 20 degrees, and the second one is more inclined than the first one, so that the two walls form a concave corner. The inclined angle of the second wall θ_1 can be varied over the range of 20° to 60°. The process of shock reflections over this model was observed optically by shadowgraph method. Carbon dioxide and air were used as a test gas.

An example of the experimentally obtained trajectories of the triple points T_0 and T' created by the first and the second Mach reflections at the first and the second walls, respectively, and of the triple point T_1 which is formed by the collision of the two triple points T_0 and T' is shown in Fig.5 by triangles, squares, and circles, respectively, and the angles χ_0, χ', and χ_1 represent the angles of these triple point trajectories. Carbon dioxide is used in the experiment in Fig.5. In the case (a), the angle χ_1 is positive, so that the transition from Mach to regular reflection does not occur, because the triple point T_1 does not impinge on the wall, whereas χ_1 in the case (b) is negative and the triple point T_1 impinges on the second wall at the point D where the transition takes place.

Typical shadowgraphs in the cases (a) and (b) described above are shown in Figs.6(a) and (b), respectively. Three photographs in Fig.(a) show three reflected shock systems which are drawn in Fig.5(a), and it is observed in Fig.6(a-3) that the slip line from the triple point T_1 interacts with the slip lines from the triple points T_0 and T'. Figs.6(b-2) and (b-3) show the reflected shock systems just before and after the transition from Mach to regular reflection, respectively.

4. RESULTS AND DISCUSSIONS

The trajectory angle χ_1 of the triple point T_1 in Fig.5 was determined by optical observations for various values of θ_1 in the case of $\theta_0=20^\circ$ and $M_s=3.0$. The results are shown in Fig.7, where the curve 1 represents the calculated results by the present method described previously. By the way, the angle χ_1 can be predicted by the three shock theory for given M_s and θ_1. In this case, χ_1 is independent of θ_0 and it is equivalent to assume that the pressure p_1 behind the Mach shock after the collision of the two triple points is equal to the pressure p_t in Eq.(2), that is, the pressure behind the Mach shock predicted by the three shock theory. The curve 2 in Fig.7 shows the results in this case. On the other hand, if we assume that the pressure p_1 is equal to the pressure p_b in Eq.(2), that is, the pressure behind the Mach shock which is created at the second wall, by neglecting the effect of the unsteady adjusting wave described previously, another value of χ_1 can be calculated for given M_s, θ_0 and θ_1. The curve 3 in Fig.7 shows the results in this case. The experimental results agree with the curve 1 better than the curves 2 and 3, which seems to show that the present method of calculation may be reasonable.

An example ($M_s=5.0$, $\theta_0=20^\circ$, $\Delta\theta=3^\circ$, Air) of the triple point trajectory over a concave circular cylindrical surface calculated by the present method is shown in Fig.8, where the horizontal and vertical axes are nondimensionalized by the radius of curvature r_0, and the solid and dashed lines represent

the numerical results calculated by the same method as that employed in the curves 1 and 2 in Fig.7, respectively. The solid line agrees with the dashed line in the initial stage of reflection, whereas the transition point is much different. The open circle on each line denotes the point where $\chi=0$, that is, the point of stationary Mach reflection, and the left and right sides of this point correspond to the regions of direct Mach reflection and inverted Mach reflection, respectively.

Finally, the dependence of the critical transition angle of incidence ω_c on the initial angle θ_0 and on the incident shock Mach number M_s is summarized in Fig.9. This is the results for diatomic gases ($\kappa=1.4$). The four solid lines represent the results calculated by making choise of the minimum value of $\Delta\theta$ at which the present method of calculation can be performed up to the transition point($\Delta\theta=5.8°$, $4.2°$, $3.0°$, and $3.0°$ for $M_s=2.5$, 3.0, 4.0, and 5.0, respectively). The angle ω_c does not depend on the radius of curvature of the reflecting concave surface for a fixed angle θ_0 in the present method. The dashed line shows the results calculated by assuming $\Delta\theta=3°$ and that the pressure p_i behind the Mach shock after the collision of the two triple points in Fig.4 is equal to the pressure p_t in Eq.(2), that is, the pressure behind the Mach shock predicted by the three shock theory for given M_s and θ_i at each stage. This method of calculation is the same as that used in the curve 2 in Fig.7 and used in the dashed line in Fig.8, and this is shown for reference. The previous experimental values[5~9] in air and nitrogen in the case of concave surfaces are also plotted in Fig.9, together with the experimental points of the present concave corner model shown in Fig.5, and the figure attached to each experimental point designates the Mach number M_s of the incident shock wave. The theoretical transition angle predicted by the two or three shock theory is independent of θ_0 and depends only on M_s, and for $M_s=2\sim5$, for example, $\omega_c=39.4°\sim39.5°$ by the two shock theory, and $\omega_c=35.4°\sim24.4°$ by the three shock theory.

The calculated results in Fig.9 show that the transition angle increases with an increasing θ_0 and decreases with an increasing M_s, and they are smaller than the critical angles predicted by the two shock theory in the present range of calculation. The experimental results in Fig.9 show the similar dependency of the transition angle ω_c on the initial angle θ_0 and on the Mach number M_s, but they are rather different quantitatively according to different authors. This may be due to the accuracy of the experiment and the reflecting concave surfaces of different geometries (radius of curvature, roughness, etc.) in their experiments.

5. CONCLUSIONS

The critical transition angle of incidence of a shock wave which interracts with a circular cylindrical concave surface has been numerically obtained by assuming that the concave surface can be represented by a sequence of infinitesimal wedges. In the present method, the transition angle does not depend on the radius of curvature of the reflecting surface for a fixed initial angle θ_0 of the concave surface, and depends only on the angle θ_0 and the Mach number M_s of the incident shock wave.

The calculated results show that the transition angle increases with an increasing θ_0 and decreases with an increasing M_s, and the values obtained are smaller than those predicted by the detachment criterion according to the two shock theory. The previous experimental results show the similar dependency of the transition angle on the angle θ_0 and the Mach number M_s, but they are rather different quantitatively according to different authors.

In order to examine the validity of the present method, an experimental investigation has been performed using a concave corner model which is composed of two straight walls shown in Fig.5, and it has been confirmed that the present method of calculation may be reasonable.

REFERENCES

1. Bleakney, W. and Taub, A.H., "Interaction of Shock Waves", Rev. of Modern Physics, Vol.21, No.4, Oct.1949, p.584.
2. Henderson, L.F., "On the Whitham theory of shock wave diffraction at concave corners", J.Fluid Mech., Vol.99, Part 4, 1980, p.801.
3. Heilig, W.H., Diffraction of a Shock Wave by a Cylinder", Physics of Fluids, Suppl.I, Vol.12, 1969, p.I-154.
4. Lozzi, A. and Henderson, L.F., "Experiments of reflections of plane shock waves at cylindrical surfaces", Modern Developments in Shock Tube Research(Proc.10th Int. Shock Tube Symp.), 1975, p.363.
5. Gvozdeva, L.G., Lagutov, Yu.P., and Fokeev, V.P., "Transition from Mach reflection to regular reflection when strong shock waves interact with cylindrical surfaces", Fluid Dynamics, Vol.17, No.2, 1982, p.273.
6. Takayama, K. and Sasaki, M., "Effects of Radius of Curvature and Initial Angle on the Shock Transition over Concave or Convex Walls", Rep. Inst. High Speed Mech., Tohoku Univ., Vol.46, 1983, p.1.
7. Itoh, S. and Itaya, M., "On the transition between regular and Mach reflection", Shock Tubes and Waves(Proc. 12th Int. Shock Tube Symp.), 1979, p.314.
8. Gvozdeva, L.G., Bazhenova, T.V., Lagutov, Yu.P., and Fokeev, V.P., "Shock wave interaction with cylindrical surfaces", Arch. Mech., Vol.32, No.5, 1980, p.693.
9. Henderson, L.F. and Lozzi, A., "Further experiments on transition to Mach reflection", J.Fluid Mech., Vol.94, Part 3, 1979, p.541.
10. Henderson, L.F. and Lozzi, A., "Experiments on transition of Mach reflection", J.Fluid Mech., Vol.68, Part 1, 1975, p.139.
11. Ben-Dor, G., Takayama, K., and Kawauchi, T., "The transition from regular to Mach reflexion and from Mach to regular reflexion in truly non-stationary flows", J.Fluid Mech., Vol.100, Part 1, 1980, p.147.
12. Heilig, W.H., "A result concerning the transition from regular reflection to Mach reflection of strong shock waves", Shock Tube and Shock Wave Research(Proc.11th Int. Symp. on Shock Tubes and Waves), 1977, p.288.
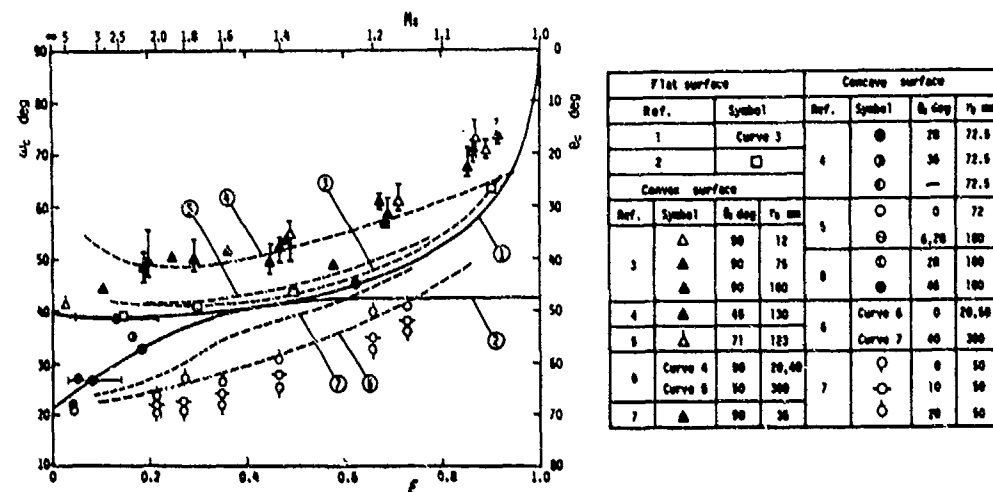
Fig.1 Theoretical and experimental transition angle of incidence between regular and Mach reflections ($\kappa=1.4$).
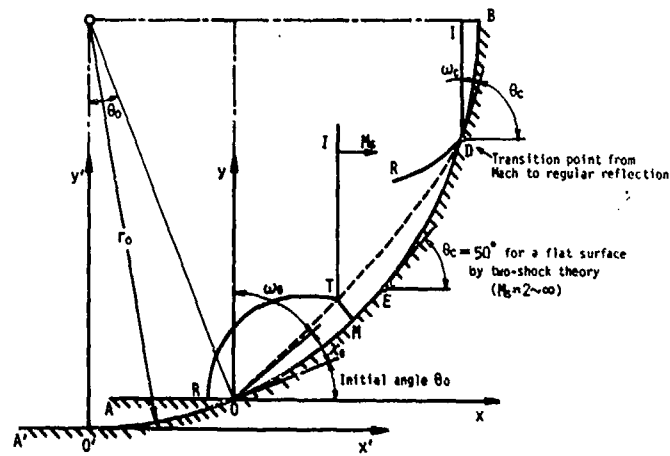
Fig.2   Reflection of a shock wave from a concave
circular cylindrical surface.
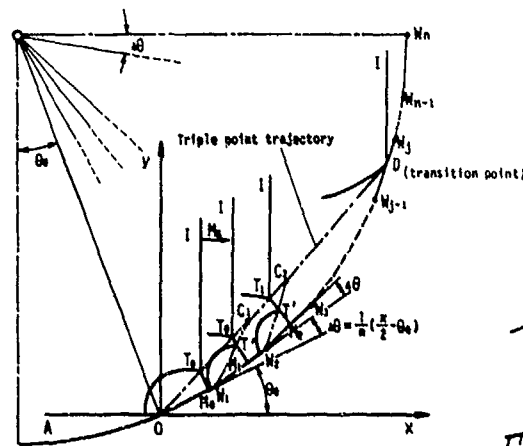
Fig.3   Concave circular cylindrical
surface represented by a sequence
of infinitesimal wedges.
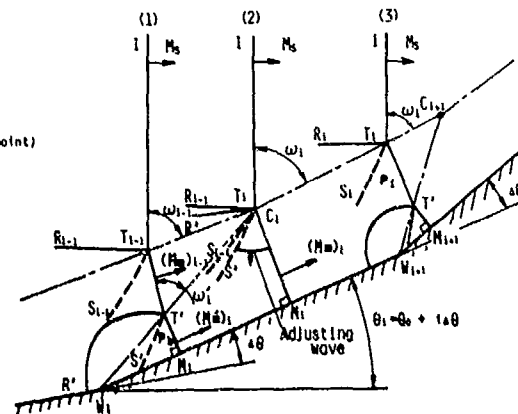
Fig.4   Collision of two triple points
in reflection process of shock at
wall W_iW_{i+1}.
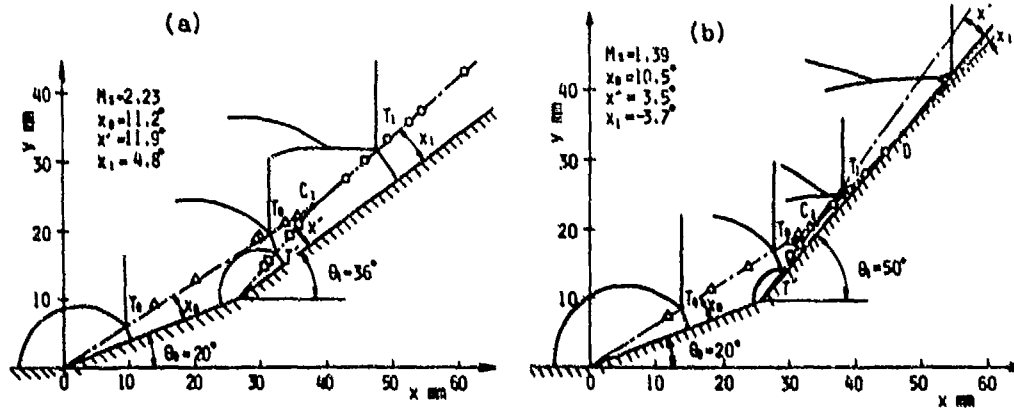
Fig.5   Sketch of shock reflection from concave corner model composed
of two straight walls (Carbon dioxide).

(a-1) (b-1)

(a-2) (b-2)

(a-3) (b-3)
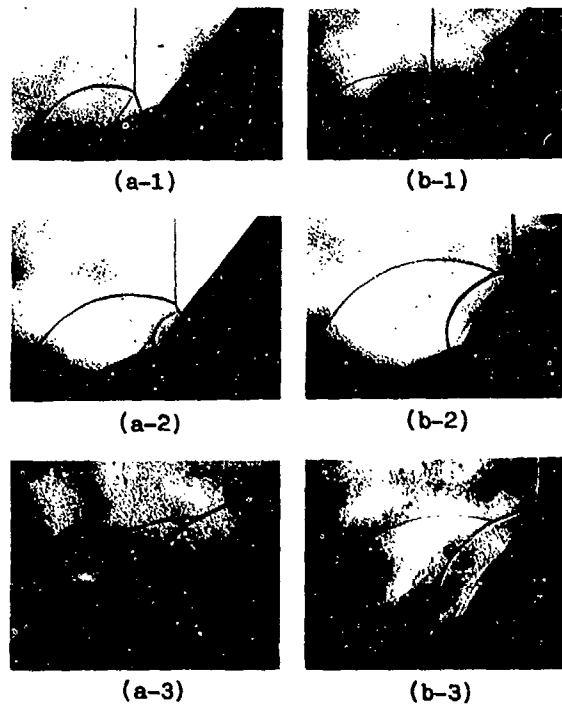
(a) $\theta_0 = 20°$, $\theta_1 = 48°$,   (b) $\theta_0 = 20°$, $\theta_1 = 54°$,
$M_s = 2.20$ $M_s = 1.80$

Fig.6 Shadowgraphs showing shock reflection from concave model of two straight walls.

Fig.7 Relation between triple point trajectory angle χ_1 and the second wall angle θ_1 (Carbon dioxide)

O	Ref.(9)
▲	Ref.(5)
△	Ref.(8)
□ ■	Ref.(6)
▽	Ref.(7)
☙	Present experiment

Fig.8 Triple point trajectory over concave circular cylindrical surface ($\kappa = 1.4$).
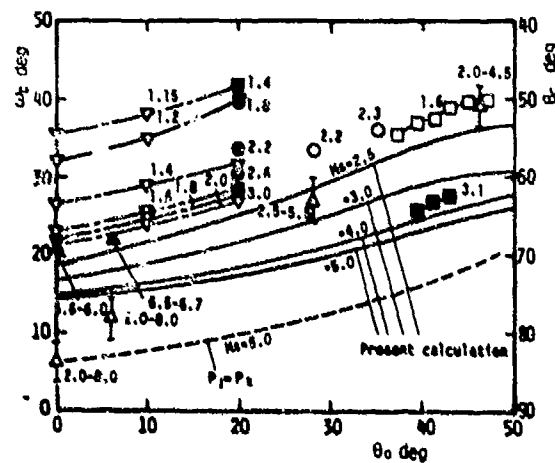
Fig.9 Critical transition angle over concave circular cylindrical surface ($\kappa = 1.4$).

Part III
Shock-Generated
Chemical Kinetics

MEASUREMENTS OF N ATOM CONCENTRATIONS IN

DISSOCIATION OF N_2 BY SHOCK WAVES

P. Roth, K. Thielen

Fachgebiet Verbrennung und Gasdynamik
Universität Duisburg, 4100 Duisburg, West Germany

The dissociation of N_2 has been measured behind
reflected shock waves in the temperature range
3390 K $\leqslant$ T $\leqslant$ 6435 K. By use of the atomic resonance
absorption spectroscopy (ARAS) the formation of
N atoms could directly be observed in the post
shock reaction zone. The experiments have been
performed in mixtures of N_2 and Ar at pressures
between 0.9 and 2.1 bar. The rate coefficient of
the reaction

$$N_2 + Ar \longrightarrow N + N + Ar$$

$$k_{N_2,Ar} = 1.71 \cdot 10^4 \ T^{-3.33} \ \exp(-113200 \ K/T) \ \frac{cm^3}{s} \pm 20\%$$

could directly be determined from the measured
N atom concentrations.

1. INTRODUCTION

The N_2 molecule is known to be very stable up to very high
temperatures. Nevertheless the dissociation of N_2 can be of con-
siderable interest in plasma reaction kinetics or in hypersonic
wind tunnels. Because of the very high activation energy of N_2
dissociation, experimental data are only available at temperatures
higher than 6000 K.

Essentially there are four experimental results of the N_2
dissociation which were evaluated by Baulch et al.[1]. These investi-
gations were performed in shock tubes using different detection
techniques. Cary[2] and Byron[3] observed the reaction in N_2/Ar mixtu-
res recording density profiles by interferometry. Hanson and
Boganoff[4] measured pressure profiles in the reaction zone of pure
N_2. A spectroscopic method was used by Appleton et al.[5] in mixtu-
res of N_2 and Ar. They monitored the rate of N_2 dissociation more
directly by the vacuum u.v. absorption of N_2 at 117.6 nm. Their
expression of the rate coefficient was recommended by Baulch
et al.[1] for use in the 6000-15000 K temperature range. The proposed
rate coefficients of Byron[3], Cary[2] and Hanson and Boganoff[4] were
found to be higher than the recommended value of Baulch et al.[1]

It is the aim of the present study to determine the rate co-
efficient of the N_2 dissociation in N_2/Ar mixtures by measuring
N atoms as reaction products, mainly in the temperature region
below the 6000 K limit.

2. EXPERIMENTAL

The experiments were conducted behind reflected shock waves in a stainless steel shock tube of 79 mm inner diameter. The tube is constructed as an ultra high vacuum apparatus and can be heated and evacuated down to pressures of about 10^{-8} mbar. Typical leak-plus-outgassing rates were $8 \cdot 10^{-7}$ mbar/min. A detailed description of the equipment is given elsewhere[6] . The test gases used in the experiments were supplied by Messer Griesheim, West Germany. They were certificated to be of the purities $N_2 \geqslant$ 99.9995% and Ar $\geqslant$ 99.9999%.

The atomic resonance absorption spectroscopy (ARAS) is the measurement technique applied in this investigation at the NI triplet at 119.9 nm. It is a very sensitive line emission-line absorption method for measuring N atom concentrations in the range of $5 \cdot 10^{11}$ to $3 \cdot 10^{13}$ atoms per cm^3. The spectral shape of the emitter line is not known in detail. It is supposed to be influenced by self reversal. Hence, calibration measurements were necessary to obtain the required relation between the measured resonance absorption and the corresponding N atom concentrations. The optical arrangement, the operating conditions of the resonance lamp, and the calibration procedure were described previously[7].

3. RESULTS

The dissociation of N_2 was studied in the temperature range 3390 K $\leqslant$ T $\leqslant$ 6435 K at pressures between 0.9 and 2.1 bar. In 34 shock tube experiments carried out, the relative initial concentrations of N_2 were between 87 ppm and 100%. In each experiment the measured incident shock speed served to calculate temperature and pressure behind the reflected shock. From the reacting gas mixture N atom resonance absorption signals were monitored. A representative absorption profile is shown in Fig.1. Using the calibration curve given in Ref.7, each absorption signal can easily be transformed to a N atom concentration profile. One example is shown in Fig.2. In all cases the N atom increase is nearly linear during the total experimental time. Only in some experiments, mainly at temperatures below 4000 K, an induction period of about 40 to 100µs after shock arrival was observed. This must be referred to vibrational relaxation or reaction incubation processes. Acceptable agreement with predicted values based on measurements of Millikan and White[8] and Appleton[9] was found.

A first reduction of the measured N atom concentration data were done by dividing the slope of the N atom increase $d[N]/dt$ by the product $2[N_2][M]$. As the maximum measurable value is about $3 \cdot 10^{13}$ N atoms per cm^3, the N atom concentrations in the experiments were very low with respect to the initial concentrations of N_2. Therefore the N_2 concentration can always assumed to be nearly constant over the experimental period of time. Concequently $[M] = [Ar] + [N_2]$ is the quasi total concentration of the reacting mixture. In Table I the experimental conditions and the reduced data of all experiments are summarized.

4. DISCUSSION

The first step in data interpretation is made by considering a reaction with unspecified collision partner

$$N_2 + M \xrightarrow{k_{N_2,M}} N + N + M \tag{1}$$
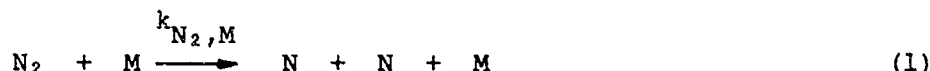
and evaluating the quantity

$$k_{N_2,M} = \frac{d[N]/dt}{2[N_2][M]} \tag{2}$$

as a function of the reciprocal temperature. Equation (2) represents the rate coefficient of the N_2 dissociation if Ar and N_2 are assumed to have the same collision efficiency. Results are given in Table I. If the values of $k_{N_2,M}$ were plotted in an Arrhenius diagram, a slight non Arrhenius behaviour could be found. For experiments with relative concentrations of $N_2 \le 5\%$, the data points scatter around a straight line, whereas for $N_2 \ge 5\%$, i.e. at the low temperature end of the Arrhenius plot, the experimental points appear to be systematically deviated from the straight line. This behaviour can be explained by the more effective collision partner N_2.

A more detailed kinetic interpretation of the dissociation experiments was done by considering the reactions

$$N_2 + Ar \xrightarrow{k_{N_2,Ar}} N + N + Ar \tag{3}$$

$$N_2 + N_2 \xrightarrow{k_{N_2,N_2}} N + N + N_2. \tag{4}$$
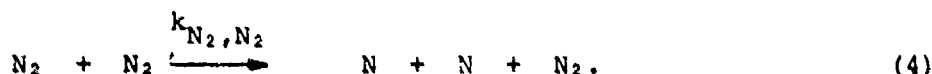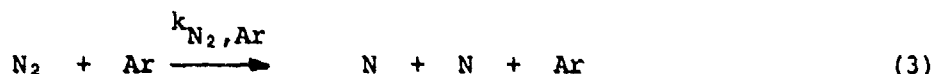
The rate coefficient of reaction (3) can therefore be described as

$$k_{N_2,Ar} = \frac{d[N]/dt}{2[N_2]([Ar] + \eta[N_2])} \tag{5}$$

where η is the dissociation efficiency of N_2 relative to Ar,

$$\eta = \frac{k_{N_2,N_2}}{k_{N_2,Ar}}. \tag{6}$$

Normally, the efficiency η can assumed to be independent of temperature. With the assumption of $\eta = 2.5$, the rate coefficient $k_{N_2,Ar}$ was determined as given in the last column of Table I.

It has been common practice to express dissociation rates in the form

$$k = A \cdot T^n \cdot \exp(-D/T) \tag{7}$$

with D as the dissociation tmeperature. A least square fit of the $k_{N_2,Ar}$ data, presented in Table I, leads to the expression

$$k_{N_2,Ar} = 1.71 \cdot 10^4 \ T^{-3.33} \ exp(-113200 \ K/T) \ \frac{cm^3}{s} \ \pm \ 20\% \quad (8)$$

$$3390 \ K \leqslant T \leqslant 6435 \ K$$

The given uncertainty is the percentage standard deviation. The absolute value of the temperature exponent seems to be too high from the theoretical point of view. It results from the approximation method used to fit the data points.

A comparison between equation (8) and the rate coefficients obtained by several other investigators[2,3,5] is shown in Fig. 3. It is obvious that an extrapolation of our expression up to more elevated temperatures crosses the rate coefficient proposed by Appleton et al.[5].

For the temperature range of this experimental study, the presented value of $k_{N_2,Ar}$ (eq.8) is in good agreement with estimates obtained from Troe's weak-collision unimolecular reaction rate theory[10]. The dissociation rate coefficient for the low pressure region can be expressed as

$$k_{N_2,Ar} = k_{N_2,Ar}^{sc} \cdot \beta_c \quad (9)$$

where $k_{N_2,Ar}^{sc}$ denotes the strong collision rate coefficient and β_c the weak collision factor. The strong collision rate coefficient depends on several molecular quantities and can be calculated according to Ref. 10. The weak collision factor includes all uncertainties of theory and experiments and will in general be fitted to the experimentally determined reaction coefficient. In the present case the strong collision rate coefficient $k_{N_2,Ar}^{sc}$ was computed based on the equations given by Troe[10]. The weak collision factor β_c can be determined using equation (9). Results are given in Table II. The values of β_c show the expected temperature behaviour and the absolute quantity seems to be in agreement with the unimolecular reaction theory of Troe[10].

5. CONCLUSION

Resonance absorption measurements of N atoms was shown to be a sensitive method to study N_2 dissociation kinetics in the temperature range $3390 \ K \leqslant T \leqslant 6435 \ K$ behind reflected shock waves. It seems to be the first time in N_2 dissociation that the reaction product could directly be observed. The rate coefficient for N_2 dissociation with Ar as collision partner was determined with acceptable uncertainties when the collision efficiency of the species N_2 relative to Ar is assumed to be $\eta = 2.5$. Comparison of the experimental data with theoretical data obtained using the weak collision unimolecular rate theory of Troe[10] leads to reasonable weak collision factors β_c.

6. ACKNOWLEDGEMENT

REFERENCES

1.   Baulch, D.L., Drysdale, D.D., and Horne, D.G., "Evaluated
      Kinetic Data for High Temperature Reactions",

      Homogeneous gas phase reactions of the H_2-N_2-O_2 system,
      1st ed., Vol.2, Butterworth, London, 1973, pp. 11-23.

2.   Cary, B., "Shock-Tube Study of the Thermal Dissociation of
      Nitrogen", Physics of Fluids, Vol. 8, Jan. 1965, pp. 26-35.

3.   Byron, S., "Shock-Tube Measurement of the Rate of Dissociation
      of Nitrogen", J. Chem. Physics, Vol. 44, Feb. 1966,
      pp.1378-1388.

4.   Hanson. R.K. and Boganoff, D., "Shock-Tube Study of Nitrogen
      Dissociation Rates Using Pressure Measurements",
      AIAA Journal, Vol. 10, Feb. 1972, pp.211-215.

5.   Appleton, J.P., Steinberg, M., and Liquornik, D.J.,
      "Shock-Tube Study of Nitrogen Dissociation using Vacuum-Ultra-
      violet Light Absorption", J. Chem. Physics, Vol. 48,
      Jan. 1968, pp.599-608.

6.   Roth, P., Barner U., and Löhr. R., "Messungen zum Hochtempera-
      turzerfall des Methyl-Radikals", Ber. Bunsenges. Phys. Chem.,
      Vol. 83, 1979, pp.929-932.

7.   Thielen. K. and Roth, P., "Resonance Absorption Measurements
      of N and O Atoms in High Temperature NO Dissociation and
      Formation Kinetics", Proceedings of the 20th Symposium (Int.)
      on Combustion, The Combustion Institute, Pittsburgh, 1985.

8.   Millikan, R.C. and White, D.R., "Vibrational Energy Exchange
      between N_2 and CO. The Vibrational Relaxation of Nitrogen",
      J. Chem. Physics, Vol. 39, Ju. 1963, pp 8-101.

9.   Appleton, J.P., "Shock Tube Study of the Vibrational
      Relaxation of Nitrogen Using Vacuum-Ultraviolet Light Absorp-
      tion", J. Chem. Physics, Vol. 47, Nov. 1967, pp.3231-3240.

10.   Troe, J. "Theory of thermal unimolecular reactions at low
      pressures. II. Strong collision rate constants. Applications",
      J. Chem. Physics, Vol. 66, Juni 1977, pp.4758-4775.

Table 1:   Experimental Conditions and Rate Coefficients.

T	ρ	N_2	N_2	Ar	$\dfrac{d[N]/dt}{2[N_2][N]}$	$k_{N_2,Ar}$
K	bar	%	cm^{-3}	cm^{-3}	$cm^3 \, s^{-1}$	$cm^3 \, s^{-1}$
3392	1,51	100	$3,24.10^{18}$	—	$2,45.10^{-22}$	—
3478	2,10		$4,38.10^{18}$	—	$5,99.10^{-22}$	—
3548	1,37		$2,76.10^{18}$	—	$1,10.10^{-21}$	—
3530	1,97	75	$3,03.10^{18}$	$1,01.10^{18}$	$7,35.10^{-22}$	$3,46.10^{-22}$
3421	2,16	50	$2,39.10^{18}$	$2,39.10^{18}$	$3,00.10^{-22}$	$1,71.10^{-22}$
3673	1,07		$1,05.10^{18}$	$1,05.10^{18}$	$1,42.10^{-21}$	$8,11.10^{-22}$
3675	2,12		$2,09.10^{18}$	$2,09.10^{18}$	$1,66.10^{-21}$	$9,48.10^{-22}$
3861	1,72		$1,60.10^{18}$	$1,60.10^{18}$	$5,30.10^{-21}$	$3,03.10^{-21}$
3953	1,99		$1,81.10^{18}$	$1,81.10^{18}$	$7,30.10^{-21}$	$4,34.10^{-21}$
3730	1,24	25	$6,03.10^{17}$	$1,81.10^{18}$	$2,85.10^{-21}$	$2,07.10^{-21}$
3805	1,13		$5,38.10^{17}$	$1,61.10^{18}$	$4,40.10^{-21}$	$3,21.10^{-21}$
4073	1,08		$4,80.10^{17}$	$1,44.10^{18}$	$1,63.10^{-20}$	$1,18.10^{-20}$
4142	1,07	5	$9,37.10^{16}$	$1,78.10^{18}$	$1,67.10^{-20}$	$1,48.10^{-20}$
4178	1,23		$1,07.10^{17}$	$2,02.10^{18}$	$2,20.10^{-20}$	$1,93.10^{-20}$
4240	1,20	2	$4,12.10^{16}$	$2,02.10^{18}$	$5,26.10^{-20}$	$5,00.10^{-20}$
4384	1,38		$4,56.10^{16}$	$2,23.10^{18}$	$8,11.10^{-20}$	$7,72.10^{-20}$
4510	1,17		$3,75.10^{16}$	$1,84.10^{18}$	$1,48.10^{-19}$	$1,41.10^{-19}$
4171	1,03	1	$1,20.10^{16}$	$1,76.10^{18}$	$2,99.10^{-20}$	$2,93.10^{-20}$
4238	1,17		$1,33.10^{16}$	$1,97.10^{18}$	$4,34.10^{-20}$	$4,23.10^{-20}$
4346	1,23		$2,05.10^{16}$	$2,03.10^{18}$	$7,57.10^{-20}$	$7,38.10^{-20}$
4526	1,16		$1,85.10^{16}$	$1,83.10^{18}$	$2,04.10^{-19}$	$1,99.10^{-19}$
4703	1,08		$1,65.10^{16}$	$1,64.10^{18}$	$3,60.10^{-19}$	$3,51.10^{-19}$
4894	1,04		$1,54.10^{16}$	$1,53.10^{18}$	$4,37.10^{-19}$	$6,21.10^{-19}$
4557	1,03	0,5	$8,18.10^{15}$	$1,63.10^{18}$	$1,99.10^{-19}$	$1,96.10^{-19}$
4806	0,95		$7,17.10^{15}$	$1,43.10^{18}$	$6,10.10^{-19}$	$6,02.10^{-19}$
5412	0,93		$6,23.10^{15}$	$1,24.10^{18}$	$6,05.10^{-18}$	$5,96.10^{-18}$
5243	1,06	0,25	$3,65.10^{15}$	$1,46.10^{18}$	$2,33.10^{-18}$	$2,31.10^{-18}$
5496	0,95		$3,13.10^{15}$	$1,25.10^{18}$	$6,02.10^{-18}$	$6,77.10^{-18}$
5385	0,91	0,20	$2,44.10^{15}$	$1,32.10^{18}$	$4,33.10^{-18}$	$4,31.10^{-18}$
5600	1,82	0,01	$2,42.10^{14}$	$2,42.10^{18}$	$1,31.10^{-17}$	$1,31.10^{-17}$
5835	1,91		$2,37.10^{14}$	$2,37.10^{18}$	$2,05.10^{-17}$	$2,05.10^{-17}$
6063	1,77		$2,12.10^{14}$	$2,12.10^{18}$	$3,67.10^{-17}$	$3,67.10^{-17}$
6634	1,70		$1,92.10^{14}$	$1,92.10^{18}$	$9,04.10^{-17}$	$9,04.10^{-17}$
5843	1,69	0,0087	$1,83.10^{14}$	$2,10.10^{18}$	$1,87.10^{-17}$	$1,87.10^{-17}$

Table II: Measured and Calculated Rate Coefficients
for the Unimolecular Low Pressure Dissociation
of N_2

$T\ [K]$	$k_{N_2,Ar}\ \left[\frac{cm^3}{s}\right]$	$k_{N_2,Ar}^{sc}\ \left[\frac{cm^3}{s}\right]$	B_c
3330	$5,49.10^{-23}$	$9,32.10^{-22}$	$5,89.10^{-2}$
4000	$8,86.10^{-21}$	$2,75.10^{-19}$	$3,22.10^{-2}$
5000	$1,21.10^{-18}$	$7,60.10^{-17}$	$1,59.10^{-2}$
7000	$2,54.10^{-16}$	$4,51.10^{-14}$	$5,64.10^{-3}$
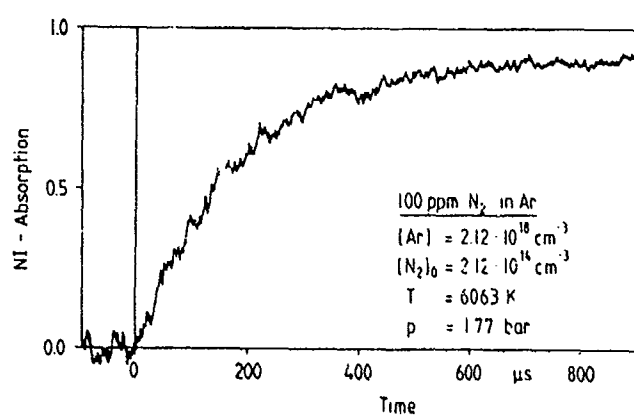
Figure 1. Example of a measured N atom absorption signal
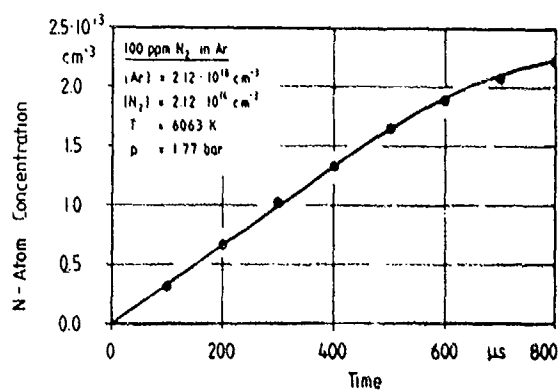
Figure 2. Measured N atom concentration profile
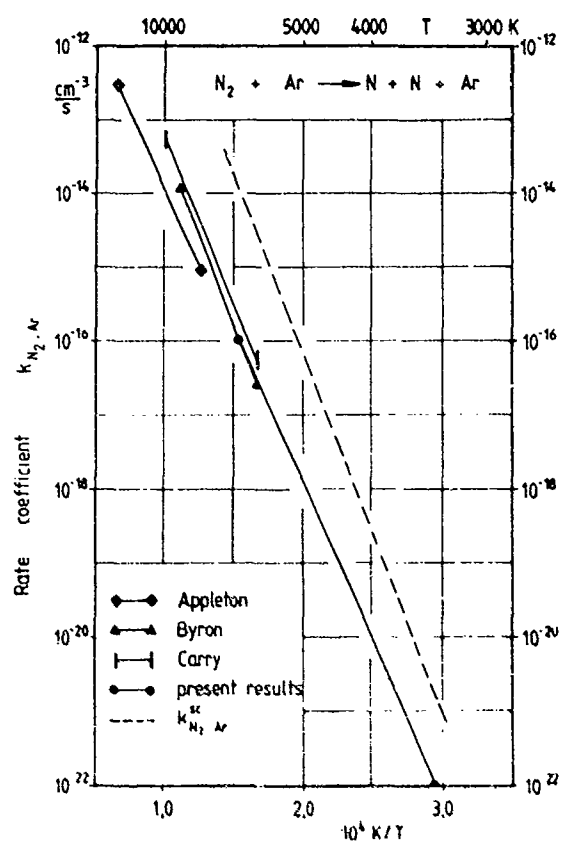
Figure 3. Comparison of rate coefficients for
$N_2 + Ar \longrightarrow N + N + Ar$

OXIDATION OF CYANOGEN. IV. THE MECHANISM OF
THE OXIDATION IN THE PRESENCE OF HYDROGEN

Assa Lifshitz and Menashe Bidani

Department of Physical Chemistry
The Hebrew University, Jerusalem 91904, Israel

A detailed investigation of the mechanism of cyanogen oxidation in the presence of hydrogen is presented. Recent induction time measurements of shock initiated ignition in mixtures containing cyanogen, oxygen and hydrogen, highly diluted in argon are computer modeled to verify the validity of a suggested reaction scheme. A 43-step mechanism is suggested. The reaction scheme is composed of 1. the cyanogen–oxygen–argon scheme (the "dry" system); 2. the hydrogen–oxygen–argon scheme, and 3. a set of elementary reactions that couple 1 and 2. The suggested scheme reproduces very well the experimental parameters E and γ_1–s in the relation: $\tau = A\exp(E/RT)\Pi C_i^{\gamma_1}$ in the presence of hydrogen (the "wet" system). It also reproduces the parameters of the "dry" system when $[H_2]_o$ is set equal to zero. The sensitivity analysis shows that the induction times in both systems are sensitive to the same elementary reactions. In addition, some sensitivity is observed towards steps in the H_2-O_2 and the coupling schemes. Part of the strong effect of the hydrogen on the induction times is the result of the heat released during its early burning.

INTRODUCTION

In the 12th International Symposium on Shock Tubes and Waves[1], we presented data, describing the ignition of cyanogen in mixtures containing cyanogen, hydrogen and oxygen, hightly diluted in argon. Mixtures of different compositions were subjected to reflected shock heating and induction times preceding the ignition of these mixtures were obtained from oscilloscope traces. A wide range of pressures, temperatures and mixture compositions were covered, running some 150 tests. This was done in order to examine the effect of each component and of the temperature on the induction times, and to compare the results to those obtained in the "dry" system. A least squares analysis of all the tests yielded the following relation[1]:

$$\tau = 2.27 \times 10^{-14}\exp(22.0 \times 10^3/RT)[C_2N_2]^{-0.67}[O_2]^{-0.59}[H_2]^{-0.41}[Ar]^{+1.52} \text{ sec.}$$

whereas the data of the "dry" system gave the relation[2]:

$$\tau = 1.07 \times 10^{-14}\exp(34.7 \times 10^3/RT)[C_2N_2]^{-1.01}[O_2]^{-0.21}[Ar]^{+0.22} \text{ sec.}$$

where concentrations are expressed in mole/cm³.

A computer modeling of the "dry" system was performed in the past and a qualitative agreement between the experiment and the calculation was achieved[3]. An explanation could be offered for the very strong dependence of the induction times on the cyanogen concentration and the very weak dependence on the oxygen concentration.

The parametric relation and the duration of the induction times obtained in the presence of hydrogen (the "wet" system) differs from the ones obtained in the

absence of hydrogen (the "dry" system) by the following features:

1. Much shorter induction times at the same temperatures.
2. A much weaker temperature dependence (22 compared to 35 kcal/mole).
3. A stronger dependence on the oxygen concentration and a weaker dependence on the cyanogen concentration as compared to the results without hydrogen.
4. A very strong dependence on the argon concentration.
5. A very strong dependence on the hydrogen concentration.

It is the purpose of this investigation to obtain a reaction scheme that will reproduce the ignition paramerters of the $C_2N_2-O_2-H_2-Ar$ system and will, by setting the initial hydrogen concentration equal to zero reproduce the parameters of the "dry" system. Once such a reaction scheme is constructed, a detailed sensitivity analysis can be performed in order to elucidate the elementary reactions that compose that scheme, utilizing the observed empirical relation.

DISCUSSION

1. General Comments on the Mode of Calculation

There are a number of "experimental conditions" under which a set of coupled differential equations representing an overall combustion reaction in a shock tube, can be numerically integrated. It can be integrated under constant density, constant pressure, or more precisely, coupled to the shock equations. The latter is very cumbersome and requires considerable and sometimes unaccessible computer time and memory. The second best is the use of constant density conditions, especially when the pressure rise upon ignition is measured at the end plate of the driven section. Here, the shock equations are solved without the chemistry to establish the initial conditions, and the kinetic scheme is then numerically integrated starting at these conditions. Since during the induction time temperature changes are not very big, the specific assumption of constant density or constant pressure affects the values of the concentrations only very slightly. However, the temperature increase during the induction time, small as it may be, is very important. It will be evaluated differently, whether constant density $(\Delta T_v = \Delta H/C_v)$ or constant pressure $(\Delta T_p = \Delta H/C_p)$ are assumed.

It has been found by numerous calculations[4] that whereas the actual value of τ might be somewhat affected by the method of clculation (shorter τ for constant v), its effect on E and γ_i's, which are always evaluated by ratios of τ's is very small. The calculations that will be referred to in this article were carried out under constant density.

The ignition in these calculations is detected by the sudden rise of the pressure (or temperature) from its semi plateau.   Its precise value is defined at the point where the derivative dT/dt passes through a maximum. An example of a calculated temperature and its time derivative in the $C_2N_2-H_2-O_2-Ar$ and $C_2N_2-O_2-Ar$ systems are shown in Fig. 1.

2. The Reaction Scheme – Results of the Calculations

The final reaction scheme suggested for the $C_2N_2-H_2-O_2-Ar$ system is shown in Table I. It is composed of 43 elementary reactions and is essentially divided into three sections. The first 16 reactions describe the oxidation of cyanogen in the absence of hydrogen, reactions 17–27 compose the hydrogen oxidation scheme and reactions 28–43 contain the reactions that couple these two systems. In addition to the rate parameters, the Table contains the results of a sensitivity analysis performed on one

of the mixtures. F gives the percent change in the induction times for a factor of 3 increase in the rate constant.

The reaction scheme was tested on mixture compositions, pressures and temperatures as shwon in Table II. These will be referred to as "calculated shocks". They represent typical tests performed in the laboratory.

The final results obtained using this scheme are shown in Table III. It contains three parts; the ignition parameters for the "wet" system, the "dry" system and an imaginary system represented by the $C_2N_2-O_2$ and H_2-O_2 subschemes.

In Fig. 2, a comparison is made between the calculated and the experimental induction times for the systems with and without hydrogen. The calculated induction times for the imaginary reaction scheme containing the first 27 reactions are also shown in this Figure. The implication of these results will be discussed later.

3. The Oxidation Mechanism

The kinetic scheme of the oxidation of cyanogen in the absence of hydrogen was described in detail in an earlier publication[3] and will not be discussed here The main features of the system were the very strong dependence of the induction time on the cyanogen concentration and the very weak dependence on the oxygen concentration. The suggested reaction scheme was able to qualitatively explain this behavior on the basis of the rate constant distribution in the thermal loop expressed by reactions 3 and 4. The same explanation was later offered for other systems with similar thermal loops, to account for the experimentally observed features[5,6].

When small quantities of hydrogen ($[C_2N_2]/[H_2] \sim 7-14$) are added to the reaction mixture, not only that the oxidation proceeds faster, but the entire picture changes[1]. The power dependencies and the temperature dependence of the induction times are entirely different. It is expected that the reaction scheme will be able to explain these changes.

In order to account for the effect of the hydrogen on the oxidation, two subschemes were added to the cyanogen oxygen scheme: the O_2-H_2 set of reactions and a scheme that couples the two systems. The question that arises is what is the relative importance of each subscheme and to what extent the addition of these two subschemes changes the relative importance of the elementary reactions in the "dry" cyanogen system.

In order to answer these questions and to learn the general characteristics of the "wet" system, the following three sets of computer experiments were performed.

1 The "dry" system — subscheme 1 which is composed of reactions 1–16.

2. The "wet" system — the entire 43 sets of elementary reactions.

3. Subschemes 1 and 2 which together contain the first 27 elementary reactions.

The two subschemes in calculation 3, are the independent cyanogen–oxygen and hydrogen–oxygen systems. Combining these two subschemes together to one reaction scheme is actually the coupling of the two systems with oxygen atoms only.

The induction times obtained in these three calculations are shown graphically in Fig. 2, as the solid circles. For the sets of calculations 1 and 2 the lines representing the best fit through the experimental data are shown on the figures as solid lines. The agreement is very good. It can be seen that the addition of 0.5% H_2 indeed shortens the induction times, in both the experiment and the calculation. Approximately, the same induction time is found in the "wet" system and in the "dry" system at 1400 and 1600 K respectively.

Hydrogen is much more reactive than cyanogen and is known to ignite (after the same induction time) at a much lower temperature. Figure 3 shows a calculated profile of the hydrogen concentration and the temperature during the induction time. It can be seen that after a very small fraction of the induction time the hydrogen is almost completely consumed from its initial value of 2×10^{-7} mol/cc. (It is being regenerated after the ignition owing to the thermochemistry.) The question that arises is to what extent the effect of the hydrogen is merely a temperature effect caused by its early burning and to what extent the richer chemistry associated with the burning of hydrogen is the main reason for the enhancement of the oxidation.

These questions can be clarified by examining the results obtained in calculation No. 3 (Fig. 2). As has already been indicated, this calculation consists of subschemes 1 and 2 (reactions 1−27). Here most of the chemistry that couples the hydrogen to the cyanogen is missing, and the O atoms together with the heat generated by the fast burning of the hydrogen are the only factors that play a role. By examining Fig. 2 it is clear that these factors are not enough to account for the observations in the "wet" system. Moreover, as can be seen in Table III, the ignition parameters are very different from the ones obtained in the "wet" system. The induction times become dependent on the hydrogen and the argon concentration and the main feature of the "dry" system, namely the very strong dependence on the cyanogen concentration and the very weak dependence on the oxygen concentration still remain. This is not the case in the "wet" system. The coupling reactions are very important.

The conclusion that one can draw from the calculations under these specific constraints (omission of the reactions 29−43) are those that the thermal effect and the coupling of the systems by O atoms alone, cannot account for the results obtained in the "wet" system.

To the oxidation of cyanogen (subscheme 1), which was previously described[5] a very important reaction has been added:

$$NCO+O_2 \rightarrow CO+NO+O \qquad\qquad .11$$

In the scheme previously suggested, only qualitative (although very significant) agreement between the experimental and calculated ignition parameters was obtained. Whereas this agreement was considered satisfactory in the "dry" system without reaction 11, we could not repdoduce the ignition parameters in the "wet" system unless this reaction was introduced into subscheme 1. It is somewhat surprising that a reaction that does not contain any hydrogeneous species will play such an important role in determining the ignition parameters of the oxidation in the presence of hydrogen, more than in its absence. In both systems this reaction has a strong enhancing influence on the oxidation.

We have assigned a rate constant:

$$k_{11} = 1.6 \times 10^{13} \exp(-19000/RT) \text{cc mole}^{-1} \text{sec}^{-1},$$

considering the 17 kcal/mole endothermicity of the reaction. The addition of this reaction to the scheme simply implies that the free radicals produced by reaction 3, namely CN and NCO both attack oxygen and participate in the propagation steps.

The behavior of the cyanogen system is determined to a large extent by the rate constant distribution in the thermal loop determined by reactions 3 and 4. This is true for both the "dry" and the "wet" systems. The strong effect of cyanogen and the very small effect of oxygen on the induction times in the "dry" system are due to the fact that $k_3 \gg k_4$. In our previous study of the "dry" system we used in our computer modeling the rate parameters suggested by Thrush and Boden[7]. At 1700 K where most of the calculations were carried out the ratio k_3/k_4 was approximately 25. This ratio was high enough to provide a qualitative agreement between the

experimental and the calculated power dependencies and to explain the calculated results. Hanson et al.[8] have reently suggested a different set of rate parameters for these two reactions both smaller than the ones suggested by Thrush and Boden. Again, whereas only some qualitative agreement betwen the experiment and the calculation in the "dry" system could be obtained by no means both the "dry" and the "wet" systems could be simulated by either set of rate parameters.

A good agreement for both systems in terms of the duration of the induction times, the power dependencies and the temperature dependence could be obtained only if a higher value for the ratio k_3/k_4 was taken.

We have used Thrush and Boden's[7] values but lowered k_4 by about a factor of four. Except for the effect of hydrogen which is somewhat overemphasized in the calculation, the agreement is very satisfactory.

The fact that a single reaction scheme can simulate two systems with two different experimental characteristics just by setting $[H_2]_o = 0$ is, we believe, a very strong support to our claim that indeed k_3/k_4 is higher than the values suggested by both Thrush and Boden[7], and Hanson et al[8].

4. Sensitivity Analysis

The sensitivity analysis shown in Table I (column 8) for the "wet" system, reveals a spectrum similar to the one previously obtained in the study of the "dry" system[3]. Both the "dry" and the "wet" systems are sensitive to the same reactions in subscheme 1 (reactions 1-16). However, since some sensitivity is observed towards steps in subscheme 3, the power dependencies, and the temperature dependence change. We find a weaker temperature dependence and a different distribution of dependencies between the oxygen and the cyanogen.

Table I contains also the rate constants of the individual reactions at 1300K (column 5), and their respective net rates at $\tau/2(=220\mu sec)$. As in the absence of hydrogen, the thermal loop of reactions 3 and 4 is still the fastest set of reactions. Although their respective rate constants differ by some 2.5 orders of magnitude, their rates are similar. In the absence of hydrogen the rates of reactions 3 and 4 are practically identical. In the "wet" system, the rate of reaction 3 is by some 70% higher, indicating that the main thermal loop is somewhat affected by the various coupling reactions.

As has been previously mentioned, reaction 11 :$NCO+O_2 \rightarrow CO+NO+O$ has been added to the scheme of the "dry" system, and enabled the attainment of a far better agreement between the calculation and the experiment. As can be seen in Table I, the system is highly sensitive to this reaction. It presents an additional very fast route to transfer the NCO radical to an oxygen atom, a transfer which directly affects the thermal loop and increases the oxidation rate.

ACKNOWLEDGEMENT

REFERENCES

1. LIFSHITZ, A. and BIDANI, M. *Shock Tubes and Waves*, Proceedings of the 12th Int. Symposium on Sock Tubes and Waves 1979, The Magnes Press, The Hebrew University, 1980,p.612.

2. LIFSHITZ A., SOHELLER, K. and BASS, D., J. Chem. Phys. ,1974,60,3678.

3. LIFSHITZ, A. and FRENKLACH, M., Int. J. Cem. Kinet., 1980,12,159.

4. LIFSHITZ, A., Unpublished results.

5. LIFSHITZ, A., FRENKLACH, M., SCHECHNER, P. and CARROLL, H. F., Int. J. Chem. Kinet., 1975,7,753.

6. LIFSHITZ, A., *Shock Tubes and Waves*, Proceedings of the 14th Int. Symposium on Shock Tubes and Waves, New South Wales University Press, 1984, p26.

7. BODEN, J. C. and THRUSH B. A., Proc. Royal Soc. London Ser., 1968,A305,107.

8. LOUGE, M. Y. and HANSON, R. K., Twentieth Symp. (Int.) on Combustion, 1984, in press.

Table I. The reaction scheme for cyanogen oxidation and its sensitivity analysis. Percent change in τ for a factor of 3 increase in k. Original τ is 440 μsec. Rates are given at $\tau/2(=220\mu sec)$

Reaction	Rate Constant			Rate Const.	Rate	τ μsec	%
	A	n	E	at 1300K			Chng.
The Cyanogen Oxygen Subscheme							
1. $C_2N_2+Ar\rightarrow CN+CN+Ar$	6.91E+20	0	128700	1.60E-01	-1.73E-08	436	-1
2. $O_2+Ar\rightarrow O+O+Ar$	3.60E+18	-1.0	118000	4.04E-05	-2.88E-08	441	0
3. $O_2+CN\rightarrow NCO+O$	6.00E+13	0	3300	1.67E+13	1.66E-03	436	-1
4. $C_2N_2+O\rightarrow NCO+CN$	2.40E+12	0	8840	7.84E+10	9.64E-04	180	-60
5. $CN+O\rightarrow CO+N$	2.04E+13	0	417	1.74E+13	2.16E-06	437	-1
6. $N+O_2\rightarrow NO+O$	6.00E+09	1.0	6300	6.81E+11	6.03E-05	452	3
7. $NO_2+Ar\rightarrow NO+O+Ar$	1.16E+16	0	66000	8.84E+04	-4.46E-05	473	6
8. $O+CO_2\rightarrow CO+O_2$	1.90E+13	0	54150	1.50E+04	6.33E-07	440	0
9. $NO_2+O\rightarrow O_2+NO$	1.00E+13	0	1000	6.79E+12	3.89E-05	442	0
10. $NO+N\rightarrow N_2+O$	1.60E+13	0	0	1.60E+13	2.15E-04	433	-2
11. $NCO+O_2\rightarrow NO+CO+O$[*]	1.60E+13	0	19000	1.02E+10	6.94E-04	295	-33
12. $NCO+CO\rightarrow CN+CO_2$[*]	3.00E+12	0	12000	2.85E+10	3.42E-04	311	-29
13. $NCO+O\rightarrow CO+NO$[*]	5.80E+13	0	0	5.80E+13	1.37E-03	600	36
14. $NCO+Ar\rightarrow CO+N+Ar$	6.81E+12	.5	40000	4.63E+07	2.72E-04	323	-26
15. $CN+NO\rightarrow NCO+N$	1.00E+14	0	42100	8.37E+06	1.48E-06	442	0
16. $CN+NO\rightarrow N_2+CO$	2.50E+10	0	0	2.50E+10	6.45E-07	440	0
The Hydrogen Oxygen Subscheme							
17. $H_2+Ar\rightarrow H+H+Ar$	2.34E+14	0	96000	1.70E-02	-5.70E-12	440	0
18. $O_2+H\rightarrow OH+O$	2.20E+14	0	16792	3.31E+11	5.09E-06	445	0
19. $O+H_2\rightarrow OH+H$	1.50E+14	0	13710	7.44E+11	2.45E-07	432	-3
20. $H+O_2+Ar\rightarrow HO_2+Ar$	1.50E+15	0	-1000	2.21E+15	-3.11E-07	440	0
21. $H+HO_2\rightarrow OH+OH$	2.50E+14	0	1888	1.20E+14	1.09E-07	441	0
22. $H+HO_2\rightarrow H_2+O_2$	2.50E+13	0	700	1.91E+13	1.56E-08	440	0
23. $O_2+H_2\rightarrow OH+OH$	2.50E+12	0	39010	6.92E+05	1.04E-09	439	-1
24. $OH+H_2\rightarrow H_2O+H$	2.20E+13	0	5147	3.00E+12	-1.42E-08	438	-1
25. $OH+H+Ar\rightarrow H_2O+Ar$	8.40E+21	-2.0	0	4.97E+15	1.17E-09	440	0
26. $OH+OH\rightarrow H_2O+O$	3.80E+12	0	1000	2.58E+12	-2.31E-05	427	-3
27. $H+O+Ar\rightarrow OH+Ar$	1.00E+15	0	0	1.00E+15	1.34E-09	440	0
The Coupling Subscheme							
28. $C_2N_2+H\rightarrow HCN+CN$	4.00E+13	0	6723	2.97E+12	1.60E-04	427	-3
29. $NCO+HCO\rightarrow HNCO+CO$[*]	1.00E+13	0	0	1.00E+13	8.17E-09	440	0
30. $NCO+H_2C\rightarrow HNCO+OH$[*]	5.00E+13	?	6000	4.90E+12	-5.14E-05	441	0

31. $NCO+HCN \rightarrow HNCO+CN^*$	5.00E+13	0	10000	1.04E+12	1.54E−04	439	−1
32. $HNCO+O_2 \rightarrow HO_2+NCO^*$	1.00E+13	0	70000	1.71E+01	−2.67E−07	441	0
33. $NCO+H_2 \rightarrow HNCO+H^*$	3.00E+13	0	5300	3.86E+12	−2.45E−07	431	−3
34. $HNCO+Ar \rightarrow NH+CO+Ar^*$	5.00E+13	.5	70000	3.08E+04	3.72E−06	442	0
35. $HNCO+O \rightarrow OH+NCO^*$	2.50E+13	0	15500	6.20E+10	1.18E−04	401	−8
36. $CN+H_2 \rightarrow HCN+H$	6.20E+12	0	5300	7.97E+11	−1.78E−09	440	0
37. $CO+OH \rightarrow CO_2+H$	1.50E+07	1.3	−760	2.25E+11	1.19E−04	375	−15
38. $HCN+O \rightarrow CN+OH$	4.22E+13	0	14825	1.36E+11	2.43E−05	422	−5
39. $HCN+O \rightarrow NCO+H$	7.23E+13	0	14825	2.33E+11	4.32E−05	395	−11
40. $HCN+O \rightarrow HCO+N$	4.00E+14	0	29767	3.96E+09	2.18E−06	433	−2
41. $HCN+OH \rightarrow CN+H_2O$	2.00E+11	.6	5000	2.13E+12	2.17E−05	440	0
42. $HCO+O_2 \rightarrow HO_2+CO$	3.16E+12	0	7000	2.10E+11	7.67E−09	440	0
43. $HCO+Ar \rightarrow CO+H+Ar$	3.00E+14	0	14830	9.64E+11	2.16E−06	440	0

Rate constants are expressed in units of mole,cm^3,sec.
Activation energies are expressed in cal/mole.
$k=AT^n exp(-E/RT)$.
*This investigation.

Table II. List of "Calculated Shocks"

1. The "wet" system

Shock	T,K	Composition			$C_5 \times 10^5$	Induction Times(μsec)	
		%C_2N_2	%O_2	%H_2	mole/cc	calc.	Exptl.
1	1300	7	7	0.5	4	440	400
2	1300	3.5	7	0.5	4	700	--
3	1300	7	3.5	0.5	4	655	700
4	1300	7	7	1.0	4	152	225
5	1300	3.5	3.5	0.5	8	415	650
6	1400	7	7	0.5	4	245	250

2. The "dry system"

Shock	T,K	Composition		$C_5 \times 10^5$	Induction Times(μsec)	
		%C_2N_2	%O_2	mole/cc	calc.	Exptl.
1	1700	9	9	4	136	140
2	1700	3	3	12	165	184
3	1700	9	3	4	177	180
4	1700	3	9	4	380	430
5	1900	9	9	4	45	47

Table III. A Comparison between the calculated and the experimental ignition parameters

1. The "wet" system

	γC_2N_2	γO_2	γH_2	γAr	E(kcal/mole)	τ(μsec)	
						1300K	1400K
Calc.	−0.67	−0.58	−1.53	+1.29	18.6−22.5	440	245
Exptl.	−0.67	−0.58	−0.81	+1.32	22.0	400	250

2. The "Dry" System

	γC_2N_2	γO_2	γH_2	γAr	E(kcal/mole)	$\tau(\mu sec)$ 1700K
Calc.	−0.94	−0.24	−	+0.16	35.7	136
Exptl.	−1.01	−0.21	−	+0.22	34.7	140

3. Coupling by O-atoms only (reactions 1–27)

	γC_2N_2	γO_2	γH_2	γAr	E(kcal/mole)	$\tau(\mu sec)$ 1400K
Calc.	−0.91	−0.17	−0.80	+0.88	30.7	560
Exptl.	−0.67	−0.58	−0.81	+1.32	22.0	250
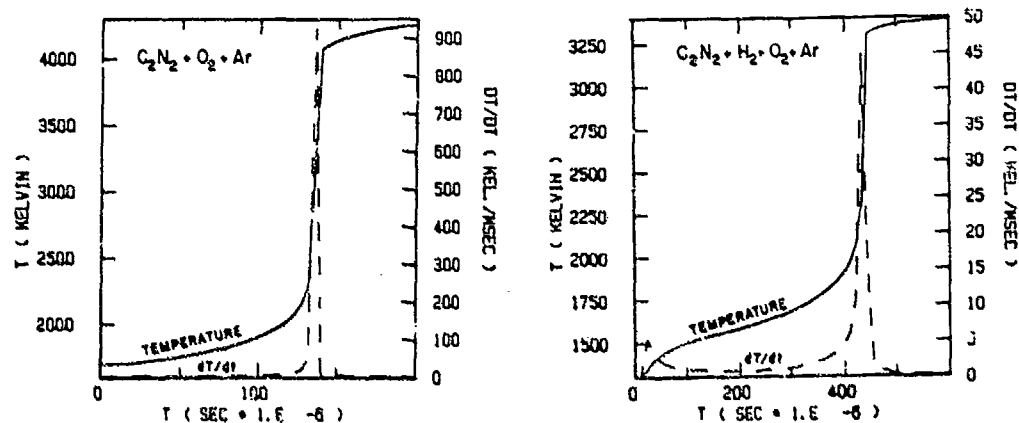
Figure 1. Temperature and dT/dt profiles with and without hydrogen. The ignition point is taken where dT/dt passes through a maximum.
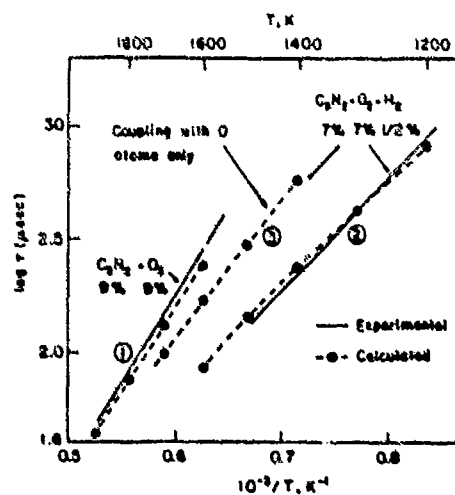
Figure 2. Calculated and experimental induction times for three different calculations.
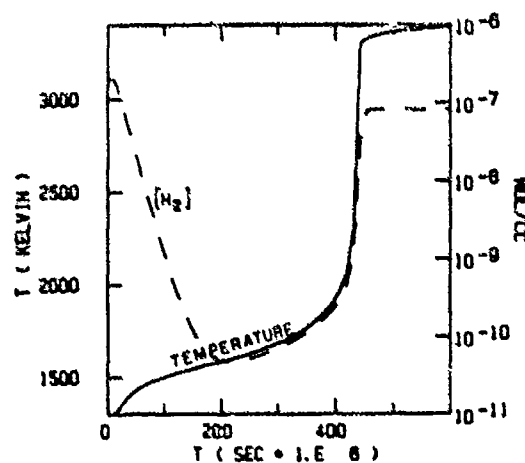
Figure 3. Temperature and hydrogen profiles. Hydrogen is consumed at the very early stages of the reaction.

DETERMINATION OF THE HIGH TEMPERATURE RATE CONSTANT OF THE REACTION,
$2NH \rightarrow 2H + N_2$, IN THE PYROLYSIS OF HYDRAZOIC ACID, HN_3

K. Hori, M. Oya*, H. Tanaka and T. Asaba

Department of Reaction Chemistry, University of Tokyo,
7-3-1 Hongo, Tokyo 113, Japan

* National Research Institute for Pollution and Resources,
Yatabe, Tsukuba, Ibaraki 305, Japan

The rate constant of the reaction, $2NH \rightarrow 2H + N_2 (k_{2-1})$,
has been determined in the temperature range between
1500 and 3200 K in incident shock waves ($P_1 = 6$ and/or
10 Torr) by use of atomic resonance absorption spectro-
photometry. HN_3 was diluted by argon to 0.005 mol %
and/or 0.01 mol %, which was pyrolyzed in shock waves
to produce NH radicals. The problem was that, since
HN_3 decomposed spontaneously on the stainless-steel
wall of the shock tube even in the room temperature, the
initial concentrations of HN_3 could not be estimated by
the conventional ways. In this study they were estima-
ted by the conventional ways. In this experiments they
were estimated by the indirect method as $(3 \sim 7) \times 10^{-11}$
mol/cm³. The rate constant of k_{2-1} is determined as
$$k_{2-1} = (1.4 \pm 0.2) \times 10^{14} \text{ cm}^3/\text{mol. sec.}$$
with little temperature dependence, here the rate cons-
tant of the reaction, $HN_3 + Ar \rightarrow NH(^3\Sigma) + N_2 + Ar$, was
estimated by RRKM calculation at the high temperatures
of the present experimental conditions.

1. INTRODUCTION

In the previous papers[1] several rate constants in the high temperature
reaction systems of nitrogen and hydrogen had been estimated by use of the
combination of shock tubes and atomic resonance absorption spectrophotometry.
In this study the similar technique was adopted to determine the rate constant
of the reaction,

$$2NH \rightarrow 2H + N_2, \qquad\qquad k_{2-1}$$

here NH radicals were produced by pyrolysis of HN_3 in shock waves.

There have been many studies carried out on the photolysis of HN_3 and the
related processes[2] in which the primary products were estimated as $NH(^1\Delta)$ and
N_2. On the other hand, thermal decomposition of HN_3 has been investigated by
several authors by use of shock tubes, i.e. Zaslonko et al[3] Kajimoto et al[4] and
Dupré et al[5] The rate constant of the reaction,

$$HN_3 + Ar \rightarrow NH + N_2 + Ar, \qquad\qquad k_1$$
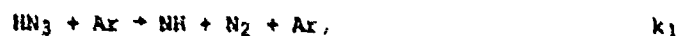
determined by Kajimoto et al and Dupré et al in the low pressure limit region
were in accord with each other, although their designation of the energy state
of NH radical produced were different. Besides, several studies on ignition
and combustion of HN_3 were carried out. Among them Avouris et al[6] recently

observed an explosion of HN_3 caused by a CO_2 laser and concluded the primary product of the reaction was $NH(^1\Delta)$.

The problem of the present study was that, since HN_3 was decomposed on the stainless-steel wall of the shock tube spontaneously even at the room temperature, it was difficult to estimate the initial concentration of HN_3 before shock generating by the ordinary methods, i.e. by pressure measurement or by some static methods. In this study by considering the reaction mechanism of this system the initial concentration of HN_3 in shock waves was estimated indirectly.

2. EXPERIMENTAL

The apparatus and the procedures were almost the same as those of the previous experiments [1, 7]. Experimental conditions are shown in Table I, here "mol fraction" means those of HN_3 and Ar in glass strage bulb in which HN_3 was not decomposed. HN_3 was prepared by the similar method as adopted by Kajimoto et al.

An example of the oscillograms of the Lyman α absorption by atomic hydrogen produced from the pyrolysis of HN_3 in shock waves is shown in Fig. 1. The time variation of the concentration of atomic hydrogen reduced from the oscillogram of Fig. 1 is shown in Fig. 2, here the correction of the boundary layer effect on the shock heating duration was carried out. As it can be seen from the figure, the concentration curves of atomic hydrogen were of sigmoid type and they reached steady states. The concentrations of atomic hydrogen at steady states seemed to be independent on temperature and so they were higher than those in equilibrium below 2400 K as shown in Fig. 3, here $(HN_3)_{app}$ means the initial concentration of HN_3 in the shocked gases on the assumption that no decomposition occurs before shock generating.

It was known that HN_3 had atendency to decompose spontaneously on the stainless-steel wall at the room temperature[5] and in this experiment there was an evidence which showed the existence of the decomposition of HN_3 in some extent before shock generating. Therefore, the initial concentration of HN_3 in shock waves could not be estimated directly. From Fig. 3 and the reaction mechanism of Table II it could be considered that the steady state concentrations of atomic hydrogen were close to the initial concentrations of HN_3 in shock waves, that is, the atomic hydrogen producing reactions, mainly k_1 and k_{2-1}, is much faster than the atomic hydrogen eliminating reactions, k_{3-1}, k_{3-2} and k_{3-3}, accordingly HN_3 is converted almost completely to atomic hydrogen regardless of the equilibrium under the experimental conditions. The initial concentrations of HN_3 in shock waves were estimated as $(3 \sim 7) \times 10^{11}$ mol/cm^3.

3. ESTIMATION OF THE RATE CONSTANT OF k_{2-1}

The mechanism of this reaction system is shown in Table II which was adopted by consideration of the previous studies and the experimental conditions.

3.1 The Initiation Reaction, k_1

There exists a discussion on the energy state of the primary product of HN_3, i.e. that of NH radical is whether $(^1\Delta)$ or $(^3\Sigma)$. Zaslonko et al and Dupré et al supported the former, while Kajimoto et al presumed the latter to be the case. In this paper, however, this problem would not consider furthermore, since the present experiment did not observe neither HN_3 nor NH radical. Instead, the rate constant of $NH(^3\Sigma)$ producing reaction at high temperatures of the present experiments, $1500 \sim 3200$ K, were estimated by RRKM calculation.

The rate constant which was fitted to the previous experimental data was adopted for further calculations. This is shown in Fig. 4 in which the curve of $E_a = 38$ kcal/mol seemed to be the competent one.

3.2 Atomic Hydrogen Producing Reactions, k_2

Two reactions should be considered for the atomic hydrogen producing reactions, i.e.

$$2NH(^3\Sigma) \rightarrow N_2 + 2H \qquad\qquad k_{2-1}$$

and

$$NH(^3\Sigma) + Ar \rightarrow H + N + Ar . \qquad\qquad k_{2-2}$$
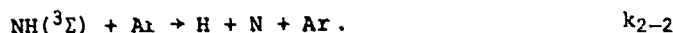
For the latter reaction the guessed value by Bahn[8] shown in Table II is considered to be too high. Even if this value was adopted, the latter reaction might be significant only above 3500 K, being compared with the former one. Therefore the latter could be neglected under the experimental conditions.

3.3 Atomic Hydrogen Eliminating reactions, k_3

Three reactions should be considered as the atomic hydrogen eliminating reactions, i.e.

$$2H + Ar \rightarrow H_2 + Ar, \qquad\qquad k_{3-1}$$

$$NH + H + Ar \rightarrow NH_2 + Ar \qquad\qquad k_{3-2}$$

and

$$NH + H \rightarrow N + H_2, \qquad\qquad k_{3-3}$$

The first reaction becomes fast as hydrogen atoms accumulate, while the latter two reactions have a maximum in the reaction rates in the course of the reaction, i.e. they decay as NH radical are consumed. The first and second reactions are influential at low temperatures, while the rate constant of the last reaction is almost constant in the temperature range of the experiment. Since the influences of these three reactions could be observed after 500 ∿ 800 μsec., they were not considered in this paper.

3.4 The Influences of the Products Decomposed before Shock Heating

HN_3 is decomposed spontaneously on the shock tube wall before shock waves are generated. The final stable products of decomposition in room temperature can be considered as H_2 and N_2. During shock heating H_2 may react with NH radical and produce atomic hydrogen as

$$H_2 + NH \rightarrow NH_2 + H. \qquad\qquad k_4$$

The condition under which this reaction had an influence for estimation of the rate constant of the reaction, k_{2-1}, was considered. The rate of the atomic hydrogen producing reaction of k_4 depended on both the extent of preshock decomposition and the temperatures of shock waves applied. According to the results of calculation the data in which the ratio of the steady state concentration of atomic hydrogen to the apparent initial concentration of HN_3 was less than 0.2 should have been omitted for derivation of k_{2-1}.

3.5 Determination of k_{2-1}

In addition to the above discussions the followings should be noted. First, the reaction,

$$NH + HN_3 \rightarrow NH_2 + N_3,$$

which is quoted in the paper of Kajimoto et al and others, is slow and negligible under the present experimental conditions.   Second, the several reactions of atomic nitrogen, i.e.

$$N + NH \rightarrow N + H,$$

$$N + H_2 \rightarrow NH + H$$

and

$$2N + Ar \rightarrow N_2 + Ar$$
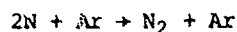
need not be considered, since the production of atomic nitrogen is negligible under the experimental conditions.

By adopting the rate constant obtained from RRKM calculation for the $NH(^3\Sigma)$ producing reaction, the rate constant of k_{2-1} was derived by simulative calculations.   Here, It was necessary to vary the initial concentration of HN_3, of which value should be a little less than the steady state concentration of atomic hydrogen.   In Fig. 2 an example of the simulative calculation is shown. In simulation of the experimental data it was noticed that the rate of the initiation reaction of HN_3 decomposition, k_1, seemed to be too high to simulate the experimental data precisely in the initial stage of the reaction.   Since the curve-fitting was performed after the inflection part of the curve of the concentration of atomic hydrogen, the error due to the incorrectness of k_1 was to be small, being compared with the experimental uncertainty.

The rate constant of k_{2-1} thus obtained are expressed as

$$k_{2-1} = (1.4 \pm 0.2) \times 10^{14} \quad cm^3 / \text{mol. sec.}$$

with little temperature dependence and is shown if Fig. 5.   Fig. 6 is the comparative figure of the present estimation with the previous ones.   The rate constant of k_{2-1} of the present study lies between those obtained by Meaburn et al[11] and by Kajimoto et al, which are contradictorily separated.

It should be noted that this estimation is consistent with an ab initio calculation performed by Fueno by use of 4-31 G**[12].

4.   CONCLUDING REMARKS

By pyrolysis of HN_3 to produce $NH(^3\Sigma)$ radical the rate constant of the reaction,

$$2NH(^3\Sigma) \rightarrow N_2 + 2H, \qquad\qquad k_{2-1}$$

was determined as

$$k_{2-1} = (1.4 \pm 0.2) \times 10^{14} \quad cm^3 / \text{mol. sec.}$$

with little temperature dependence in the temperature range between 1500 and 3200 K.

There left several problems: First, an ambiguity on the energy state of NH radical produced from HN_3 primarily exists.   This may cause an error in estimation of k_{2-1}, although it is considered not to be large.   Second, decay of the concentration of atomic hydrogen could be seen obviously in the latter period of shock heating.   The rate constant of the reaction, k_{3-1}, then, can be

estimated by a careful treatment of the non-ideality in particle time of flight, density and temperature in the shock heating zone which is far from the shock front.   Third, The rate constant of the reaction, k_4, may be estimated by picking up of the omitted data in the present study.   They will be done near future and the whole mechanism of the present system will be completed.

REFERENCES

1.   M. Yumura, T. Asaba, Y. Matsumoto and H. Matsui, International J. Chem. Kinetics, 12, 439 (1980). M. Yumura and T. Asaba, Proceedings of 18th Symposium (International) on Combustion, p. 863 (1981), The Combustion Institute.   M. Yumura and T. Asaba, Proceedings of the 14th International Symposium on Shock Tubes and Waves, p. 678 (1984).
2.   For Example, D. H. Stedman, J. Chem. Phys., 52, 3966 (1970).
3.   I. S. Zaslonko, S. M. Kogarko and E. V. Mozzukin, Kinetics and Catalysis, 13, 745 (1972).   A. I. Dremin, S. M. Kogarko, I. S. Zaslonko and E. V. Mozzukin, Kinetics and Catalysis, 14, 283 (1973).   I. S. Zaslonko, S. M. Kogarko and E. V. Mozzukin, Combustion, Explosion and Shock Waves, 12, 2 (1976).
4.   O. Kajimoto, T. Yamamoto and T. Fueno, J. Phys. Chem., 83, 429 (1979).
5.   G. Dupré, C. Paillard, J. Combourieu, N. A. Fomin and R. I. Soloukin, Proceedings of the 13th International Symposium on Shock Tubes and Waves, p. 626 (1982).
6.   Ph. Avouris, D. S. Bethune, J. R. Lankard, J. A. Ors and P. P. Sorokin, J. Chem. Phys., 74, 2304 (1981).
7.   H. Tanaka, A. Ishigaki and T. Asaba, Proceedings of 14th International Symposium on Shock Tubes and Waves, p. 672 (1984).
8.   G. S. Bahn, "Reaction Rate Compilation for the H-O-N System", Gordon and Research (1967).
9.   D. L. Baulch, L. D. Drysdale, D. G. Horne and A. C. Lloyd, "Evaluated Kinetic Data for High Temperature Reactions", Vol. 1, Butterworths, London (1972).
10.   T. R. Roose, R. K. Hanson and C. H. Kruger, Proceedings of the 12th International Symposium on Shock Tubes and Waves, p. 476 (1980).
11.   G. M. Meaburn and S. Gordon, J. Phys. Chem. , 72, 1592 (1968).
12.   T. Fueno, Private Communication.

Table I.   Experimental conditions

Composition	mol fraction *		Temperature (K)	P_1 (Torr)
	HN_3%	Ar%		
I	0.005	99.995	1530~3130	10
II	0.01	99.99	1550~3230	6 , 10

* see text

Table II. Reaction scheme and rate parameters, $k = A\,T^B\exp(-E/RT)$, cm^3 mol s unit

		log A	B	E	References
1-1	$HN_3 + Ar \rightarrow NH(^1\Delta) + N_2 + Ar$	16.54	0.0	51.0	(4)
1-2	$HN_3 + Ar \rightarrow NH(^3\Sigma) + N_2 + Ar$	13.77	0.0	30.6	(4)
2-1	$2NH(^3\Sigma) \rightarrow N_2 + 2H$	14.15	0.0	0.0	this work
2-2	$NH(^3\Sigma) + Ar \rightarrow N + H + Ar$	12.51	0.5	69.3	(8)
3-1	$H + H + Ar \rightarrow H_2 + Ar$	14.81	-1.0	0.0	(9)
-(3-2)	$NH_2 + Ar \rightarrow NH + H + Ar$	14.74	0.0	74.7	(1c)
3-3	$NH + H \rightarrow N + H_2$	13.0	0.0	6.37	(10)
4-1	$H_2 + NH \rightarrow NH_2 + H$	13.17	0.0	12.9	(10)
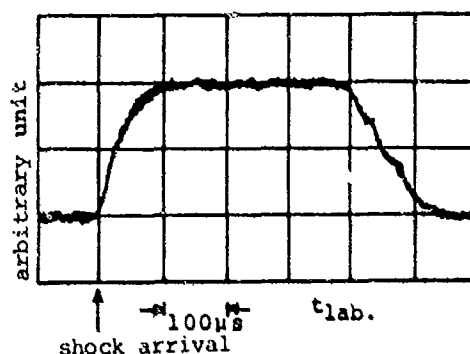
Fig. 1.   A typical oscillogram showing the absorption of Lyman α.

Sample gas : composition II
$T_2 = 1915$ K, $P_2 = 0.289$ atm.

Fig. 2.   The concentration of atomic hydrogen, (H), reduced from the oscillogram of Fig.1 and those obtained from the simulative calculation.

(H) in experiment is within the domain limitted by two curves. Circles : (H) of simulative calculations. vertical bars : the uncertainty of the simulation.

Fig. 3.   Comparison of (H) in equilibrium with (H) of the steady state. (* see text)
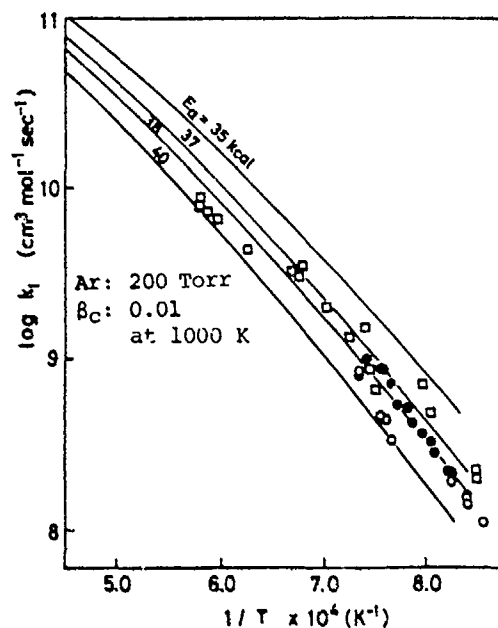
Fig. 4. The rate constants of k_1.

    Curves : calculated k_1 by RRKM theory.

    Experiments.

□ : Dupre et al, $-d(HN_3)/dt$ (0.5 mol % in Ar)

● : Kajimoto et al, $-d(HN_3)/dt$ (0.1 ∿ 0.3 mol % in Ar)

○ : Kajimoto et al, $d(NH(^3\Sigma)/dt$ (0.1 ∿ 0.3 mol % in Ar)
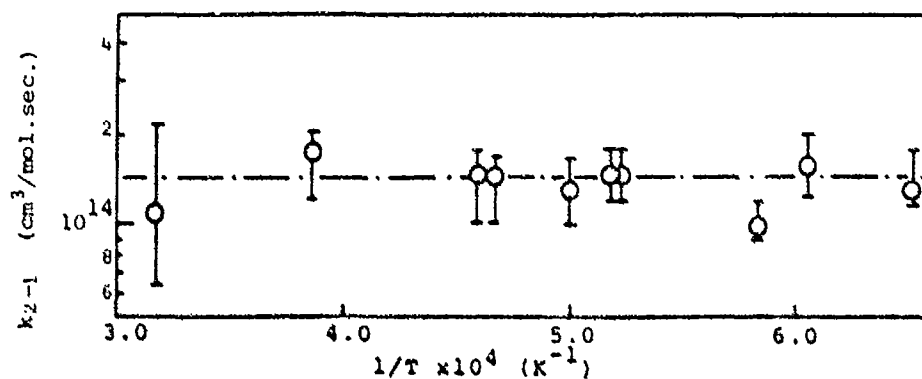
Fig. 5. Arrhenius plots of the rate constant, k_{2-1}.
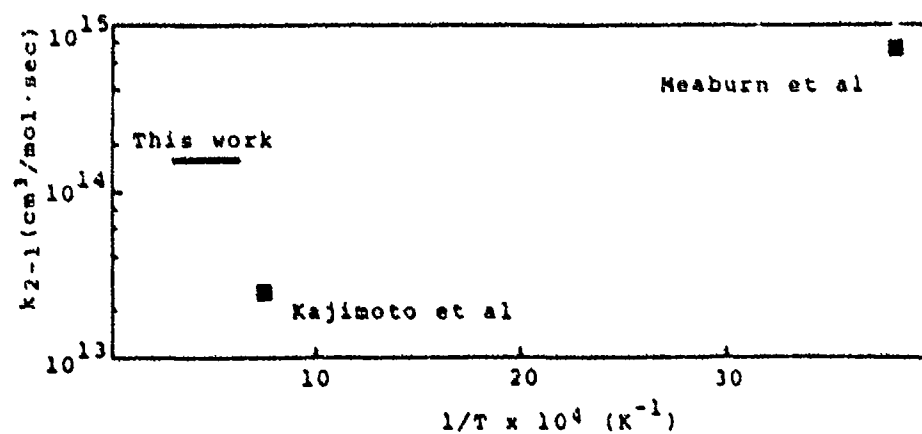
Fig. 6. Comparison of k_{2-1} of this work with the previous ones.

A SHOCK TUBE STUDY OF THE PYROLYSIS OF

PARTIALLY DEUTERATED PROPENES

V. Subba Rao and Gordon B. Skinner

Department of Chemistry
Wright State University, Dayton, Ohio   45435, U.S.A.

Very dilute mixtures of CD_2CHCH_3, CH_2CDCH_3,
and CH_2CHCD_3 were pyrolyzed at 1500-1800 K behind
incident shock waves at an average pressure of
0.42 atm, and behind reflected waves at 2.8 atm.
Analysis for H and D using resonance absorption
spectroscopy showed that propene dissociates partly
by formation of hydrogen atoms and allyl radicals,
and partly by formation of vinyl and methyl radi-
cals. Both of these unimolecular dissociation
reactions of propene are in the intermediate fall-
off region at our pressure and temperature range.

1.   INTRODUCTION

The goal of this study has been to learn about the unimo-
lecular initiating steps in propene pyrolysis. The two reac-
tions that have been most considered are

$$CH_2CHCH_3 \rightarrow CH_2CHCH_2 + H \qquad [1]$$

$$CH_2CHCH_3 \rightarrow CH_2CH + CH_3 \qquad [2]$$
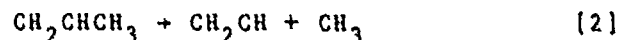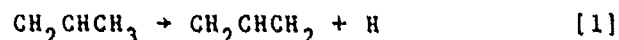
Other possibilities are loss of H_2 by reactions such as

$$CH_2CHCH_3 \rightarrow CHCCH_3 + H_2 \qquad [3]$$

$$CH_2CHCH_3 \rightarrow CH_2CCH_2 + H_2 \qquad [4]$$
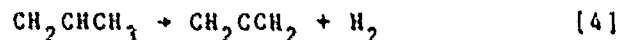
Earlier shock tube studies have not been able to distin-
guish among the possibilities, although reaction [2] has gene-
rally been said to be the main initiating step. The single-
pulse studies of Chappell and Shaw (1) and Burcat (2) in the
temperature range 1100-1700 K showed formation of approximately
equal concentrations of C_2H_4 and CH_4, which could be attributed
to reaction [2], and somewhat smaller concentrations of allene
and propyne (methyl acetylene), which could be produced by
reaction [1] or possibly by secondary reactions. The al-
lene/propyne ratio was greatest at low temperatures, suggesting
that allene is formed first, then rearranges to propyne.

In a study of propene pyrolysis in the presence of a large
excess of D_2, Yano (3) observed formation of CH_3D and C_2H_3D,
which could be formed via reaction [2], and also a substantial
amount of CH_2CHCH_2D, some of which, at least, could be formed
via reaction [1]. The fact that many different deuterated
compounds were formed in this study strongly suggests that the
overall reaction proceeds mainly by free radical process ini-

tiated by [1] and [2] rather than molecular processes initiated
by [3] and [4].

The laser-schlieren shock tube study of Kiefer, Al-Alami
and Budach (4) covered the temperature range 1650-2300 K, which
lies mainly above the range of the single-pulse studies. Their
results were interpreted using equation [2], but they pointed
out that the interpretation would be nearly as good if a sub-
stantial amount of initiation occurred via [1]. Basically, in
all of the experiments done so far, the concentrations of
propene were so large that product distributions and heat
effects are substantially affected by secondary reactions.

Our approach was to measure the formation of H and D atoms
in the pyrolysis of very dilute mixtures of partially deute-
rated propenes in argon. Because of the very low propene
concentrations, secondary reactions were of relatively minor
importance, so that the measurements of H and D concentrations
gave fairly straightforward evidence as to the initiating reac-
tions leading to their formation.

2. EXPERIMENTAL PROCEDURES

Our apparatus and techniques for measurements behind re-
flected shock waves have been described in an earlier paper (5).
We used a stainless steel shock tube with a test section 7.6 cm
in diameter and 4.5 m long. Concentrations of H and D atoms were
measured by resonance absorption behind the reflected shock wave,
2 cm from the end plate of the shock tube. For measurements
behind the incident wave, the measurement station was not
changed, but a 1.8 m extension was added to the tube to delay the
formation of the reflected wave beyond the desired test time.

Propene-1,1-d_2 (I) propene-2-d_1 (II) and propene-3,3-3-d_3
(III) were from Merck and Co., and were stated to be at least
98% of the stated compound. Argon was from Airco, Inc.,
Research Grade, with 2 ppm maximum total impurity, and less
than 0.5 ppm hydrocarbons reported as methane.

3. RESULTS

Because propene absorbs H and D Lyman-α radiation rather
strongly, all our mixtures were quite dilute. As mentioned
above, the low concentrations were also advantageous in minimi-
zing the effects of bimolecular reactions following the initial
unimolecular ones. We carried out experiments at two pressure
levels: 2.8 atm, with a standard deviation of 0.4 atm, and
0.42 atm, with a standard deviation of 0.07 atm. At the high
pressure, mixtures of 5 and 20 ppm of I, II and III in argon
were studied; while at the low pressure, mixtures of 10 ppm of
each of the propenes were used. All of these mixtures were
made by dilution of more concentrated mixtures. For each of
the above conditions, both H and D concentrations were measured
in separate experiments. A total of 153 experiments was car-
ried out.

Allowance for absorption of Lyman-α radiation by molecular propene (which had been measured in separate experiments at temperatures just below those at which H and D atoms could be observed) was made in all experiments, but the correction was significant only for experiments with 20 ppm propenes under reflected shock conditions. Typically, the Lyman-α intensity dropped suddenly when the reflected shock passed because of the molecular absorption, then subsequently more slowly due to H and D formation, so the two effects could be distinguished.

In general the concentrations of H and D atoms initially increased linearly, then subsequently fell below extrapolation of the linear relationship. There was no evidence of induction times for appearance of H or D in any of the experiments. In this paper we have carried out the data analysis by calculating the initial rate constants for formation of H and D, which will lead to values of the rate constants for initiating reactions. We plan to report on detailed modelling calculations which will simulate all the data over the experimental times in a subsequent paper.

Table I lists the initial rate constants for all our sets of experiments, in Arrhenius form, and also lists the rate constant at $10^4/T = 6.40$ (1562 K), a temperature that lies near the mid-point of our temperature range. We have combined the 20 ppm and 5 ppm data at high pressures, since the rate constant data overlapped. There seemed to be a slight tendency for the 5 ppm data to be higher, perhaps because at 20 ppm there was some loss of H or D by reaction with propene, even near the beginning of the experiment. The rate constants (in first-order form) were calculated by the equation

$$k_1 = mRT/Px$$

where m is the initial slope of a graph of [H] or [D] versus time, R the gas constant in cc atm mol^{-1} K^{-1}, P the pressure in atm, and x the mole fraction of propene in the mixture. The generally lower rate constants at 0.42 atm compared to 2.8 atm indicate some unimolecular fall-off in our experimental range.

4. DISCUSSION

Our data can be used to determine rate constants for the free radical reactions [1] and [2] given in the Introduction, but they cannot detect pyrolysis by the molecular channels [3] and [4]. These reactions could affect our results by causing less propene to be present than we would otherwise expect. Analogies with ethylene pyrolysis suggest that molecular channels may not be very important. Roth and Just (6) found that the reaction

$$C_2H_4 + Ar \rightarrow C_2H_2 + H_2 + Ar \qquad [2]$$
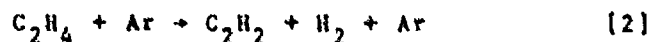
is second-order under conditions similar to ours. At 1562 K and 2.8 atm, the rate constant in first-order terms is 50 s^{-1}, while at 0.42 atm it is only 7 s^{-1}. If reactions [3] and [4]

Table I.   Initial Rate Constants for Propene Pyrolysis

Compound	Atom	A, s^{-1}	E,kcal	Std. Dev. in log k	k,s^{-1} at 1562 K	
					obs.	calc.
5ppm and 20 ppm propene at 2.8 atm						
I	H	4.3E10	57.9	0.14	350	490
	D	2.0E12	71.1	0.06	230	140
II	H	3.0E13	78.3	0.13	330	530
	D	5.4E13	81.1	0.19	250	150
III	H	1.0E15	91.7	0.17	150	260
	D	7.7E10	60.3	0.10	290	190
10 ppm propene at 0.42 atm						
I	H	3.8E12	72.9	0.09	240	300
	D	4.1E11	69.4	0.05	80	70
II	H	1.0E13	76.4	0.03	220	270
	D	1.1E10	57.6	0.09	90	90
III	H	4.4E13	81.9	0.06	150	140
	D	3.5E12	74.7	0.11	120	110

Table II.   Reactions Considered in Propene Pyrolysis

	Reaction	k at 1562 K cc, mol, s	Ref
1.	$CH_2CHCH_3 \rightarrow CH_2CHCH_2 + H$	310, 160	this work
1a.	$CH_2CHCH_3 \rightarrow CH_2CCH_2 + 2H$	210, 110	this work
1b.	$CH_2CHCH_3 \rightarrow CH_3CCH + 2H$	100, 50	this work
2.	$CH_2CHCH_3 \rightarrow CH_2CH + CH_3$	130, 50	this work
2a.	$CH_2CHCH_3 \rightarrow CHCH + H + CH_3$	130, 50	this work
3.	$H + CH_2CHCH_3 \rightarrow CH_3CHCH_3$	4.0×10^{12}	9
3a.	$H + CH_2CHCH_3 \rightarrow CH_3CHCH_2 + H$	4.0×10^{12}	9
4.	$H + CH_2CHCH_3 \rightarrow CH_2CH_2CH_3$	4.0×10^{12}	9
4a.	$H + CH_2CHCH_3 \rightarrow CH_2CH_2 + CH_3$	4.0×10^{12}	9
5.	$H + CH_2CHCH_3 \rightarrow CH_2CHCH_2 + H_2$	3.1×10^{12}	9
5a.	$H + CH_2CHCH_3 \rightarrow CH_2CCH_2 + H + H_2$	2.1×10^{12}	9
5b.	$H + CH_2CHCH_3 \rightarrow CH_3CCH + H + H_2$	1.0×10^{12}	9

Note: Units for reactions 1 and 2 are s^{-1}; for reactions
3,4 and 5 are $mol^{-1} cm^3 s^{-1}$. The two values for
reactions 1 and 2 are for 2.8 atm and 0.42 atm, respec-
tively. Rate constants were adjusted, as noted in the
text, when D atoms were present.

are this slow, they should cause the loss of no more than a few percent of the propene during the time needed to determine the initial rate of formation of H or D.

The way in which our studies can lead to an understanding of the reaction mechanism can be seen by writing equations for the free radical reactions of the partially deuterated propenes, as follows:

I. $CD_2CHCH_3 \rightarrow CD_2CHCH_2 + H$ [1]

                       $\hookrightarrow CD_2CCH_2 + H; \; CD_2HCCH + H; \; CDCCH_3 + D$

       $CD_2CHCH_3 \rightarrow CD_2CH + CH_3$ [2]

                       $\hookrightarrow CDCH + D$

II. $CH_2CDCH_3 \rightarrow CH_2CDCH_2 + H$ [1]

                       $\hookrightarrow CH_2CCH_2 + D; \; CH_2DCCH + H$

       $CH_2CDCH_3 \rightarrow CH_2CD + CH_3$ [2]

                       $\hookrightarrow CHCD + H$

III. $CH_2CHCD_3 \rightarrow CH_2CHCD_2 + D$ [1]

                       $\hookrightarrow CH_2CCD_2 + H; \; CHCCHD_2 + H; \; CH_3CCD + D$

       $CH_2CHCD_3 \rightarrow CH_2CH + CD_3$ [2]

                       $\hookrightarrow CHCH + H$
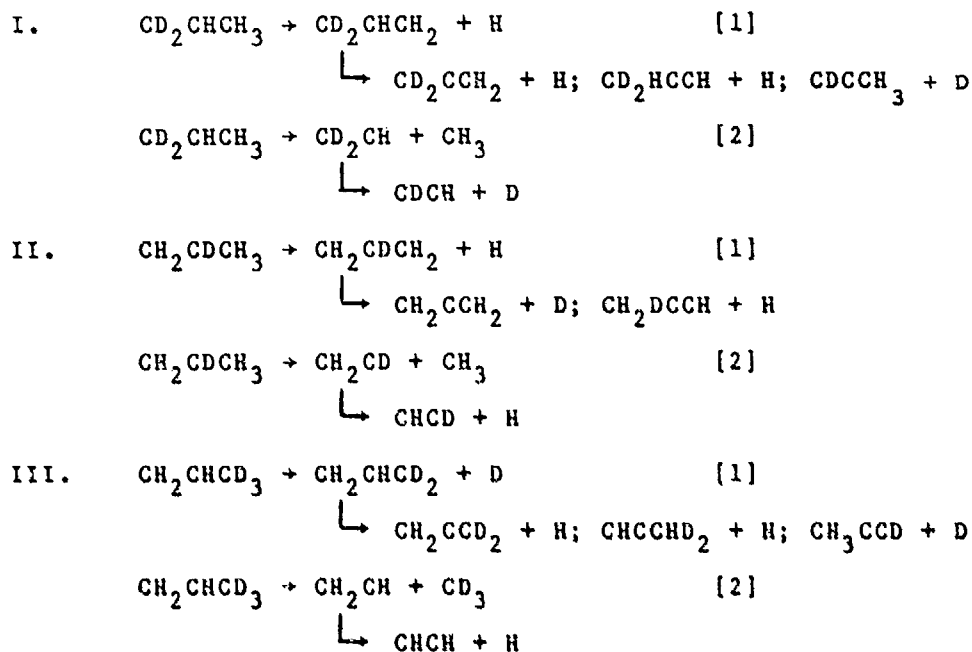
If these are the only reactions to be considered, then it is clear that reaction [2] produces only D from I and only H from II and III. The presence of both H and D in pyrolysis of all three compounds indicates that reaction [1] and [2] can be determined from the relative amounts of H and D in the various experiments.

Under our very low concentration conditions, it is expected that the allyl and vinyl radicals formed by reactions [1] and [2] will indeed dissociate by loss of hydrogen rather than react with other species. No bimolecular reactions will be very important, but reactions of H and D with propene (the most likely bimolecular reactions) should be considered. Methyl radicals will be relatively unreactive and will be assumed stable. We expect that the allyl radical will dissociate mainly to allene, but the possibility that some will form propyne should not be excluded. Dissociation of vinyl and allyl radicals is expected to occur within a few microseconds (comparable to our instrument response time of 5 microseconds) so formation of H and D will appear linear with time (at least at first), depending on the rate of dissociation of propene. Finally, we have assumed a kinetic isotope effect of 1.6 relating rate constants for reactions breaking a C-H bond

compared to a C-D bond. This value is based on experiments
and calculations we have made for CD_4 (7) and $CD_3CD_2CD_3$ (8).

All of the types of reactions we have considered are
given in Table II. For each elementary reaction we have writ-
ten one or more global reactions that show the more stable
products produced by dissociation of the radicals that are
formed first. These global reactions are the ones actually
used in the calculations. In testing for the distribution of
allene and propyne in dissociation of tne allyl radical, we
have maintained consistent ratios of k_{5a}/k_{5b} and k_{1a}/k_{1b}. As
shown in reference 9, isopropyl radicals formed by reaction 3
dissociate back almost entirely to isopropyl radicals, but
this process does produce a visible reaction with partially
deuterated propenes. However, normal propyl rad?cals produced
by reaction 4 dissociate primarily to ethylene and methyl,
thus effectively removing H or D. The general effect of
reactions 3, 4 and 5 in our mixtures is to lower the concentra-
tions of H and D, the loss of H being slightly faster. While
the number of reactions is quite small as written in Table II,
the total number increases to 42 when isotopic substitution is
considered.

Apart from allowing for isotope effects, we kept the rate
constants for reactions 3, 4 and 5 fixed at the values given in
reference 9. This left only three variable parameters: the
rate constants for [1a], [1b] and [2a]. These were adjusted
to give the best fits to the high pressure and low pressure
data sets, taken individually, since fall-off is expected for
reactions [1] and [2]. The criterion of best fit was to take
ratios of observed to calculated rate constants for formation
of H and D for each compound (see the last two columns of
Table I), and make the sum of the logarithms of these ratios
add to zero. The rate constants that gave the best fit are
given in Table II. The standard deviation in the logarithms
of the ratios was 0.15, corresponding to a factor of 1.4 in
the rate constant.

The calculation was not highly sensitive to the fraction
of allyl radical dissociating to allene or propyne. The best
fit occurred with about one-third of the allene going to
propyne, as noted in Table II, but the standard deviation
increased only to 0.20 as the ratio varied from zero to one-
half. Using a larger fraction of propyne led to a very bad
fit for propene-2-d_1, since this molecule depends on allene
formation to produce the observed D atoms.

We have made RRKM calculations for the dependence of the
rate constants of propene dissociation on pressure. Our mo-
dels are similar to those we used earlier for methane and
ethane (7,10). For reaction [1] we compared with loss of H
from methane, and consider the activated complex to have two
substantially lowered bending frequencies. For reaction [2]
we compared with dissociation of ethane, and considered the
complex to have four substantially lowered bending frequen-
cies. Use of the same lowered frequencies as we used for

methane and ethane, and the heats of formation of radicals
given by McMillen and Golden (11) led to first-order rate
constants close to those found experimentally. If the energy-
transfer model of Tardy and Rabinovitch (11) that we used
earlier is again applied, we obtain a collisional efficiency
of about 0.015 at 1562 K. This value is probably too low, but
when combined with RRKM calculations, which are themselves not
altogether realistic, this energy transfer model led to good
agreement with the extensively studied ethane dissociation
system. The calculations show a fall-off of a little less
than 2 for reaction [1] and a little more than a factor of 2
for reaction [2], between 2.8 and 0.42 atm of argon at 1562 K,
in agreement with experiment. At that temperature, k/k_∞ for
both reactions is about 0.5 at 2.8 atm.

Comparison of our rate constants with those of other
workers is difficult because conditions in the experiments
differ. To compare rate constants for propene dissociation,
we would note that our value would be the sum of k_1 and k_2,
440 s^{-1} at 2.8 atm and 210 s^{-1} at 0.42 atm, and 1562 K. In a
single-pulse experiment at 1570 K, 2.6 atm total pressure,
1.6% propene in argon, and 700 microseconds residence time,
Burcat (2) found 22% of the propene remained giving a first-
order rate constant of 2200 s^{-1}. While this is 5 times grea-
ter than our value, the difference could be due to secondary
reactions of H and CH_3 with propene, which would occur at this
much higher propene concentrations. Kiefer et al. (4)
worked at concentrations somewhat lower than our data at 0.42
atm. From their second-order equation we obtain $k = 1900 \ s^{-1}$
as a first-order value at 0.42 atm and 1562 K, which again is
substantially higher than our value, but the comparison is not
exact because of the intermediate order of the reaction
under our conditions and the lower temperature part of theirs.

In conclusion, we have shown that propene dissociates
substantially to allyl radicals and H atoms, as well as
to vinyl and methyl radicals. Both reactions are in the
transitional part of the unimolecular fall-off range at about
1600 K and 1 atm total pressure. The rate constants we find
are lower than those in the literature, which can be attri-
buted partly to the effects of secondary reactions in the
other experiments and the difficulty of extrapolating rate
constants when the order of the reaction is changing with both
temperature and pressure.

REFERENCES

1. Chappell, G.A. and Shaw, R.,Journal of Physical Chemistry,
   Vol. 72, 1968, p. 4672.

2. Burcat, A., Fuel, Vol. 54, 1975, p. 87.

3. Yano, T., International Journal of Chemical Kinetics,
   Vol. 9, 1977, p. 725.

4. Kiefer, J.H., Al-Alami, H.Z., and Budach, K.A., Journal of
   Physical Chemistry, Vol. 86, 1982, p. 808.

5. Chiang, C.-C., Lifshitz, A., Skinner, G.B., and Wood,
    D.R., Journal of Chemical Physics, Vol. 70, 1979, p. 5614.

6. Roth, P. and Just, T., Berichte Bunsen-gesellschaft
    Physikalische Chemie, Vol. 77, 1973, p. 114.

7. Chiang, C.-C., Baker, J.A. and Skinner, G.B., Journal of
    Physical Chemistry, Vol. 84, 1980, p. 939.

8. Chiang, C.-C. and Skinner, G.B., Symposium (International)
    on Combustion, 18, 1981, p. 915.

9. Westbrook, C.K. and Pitz, W.J., Combustion Science and
    Technology, Vol. 37, 1984, p. 117.

10. Rogers, D. and Skinner, G.B., International Journal of
    Chemical Kinetics, Vol. 13, 1981, p. 481.

11. McMillen, D.F. and Golden, D.M., Annual Reviews of
    Physical Chemistry, Vol. 33, 1982, p. 493.

12. Tardy, D.C. and Rabinovitch, B.S., Journal of Chemical
    Physics, Vol. 48, 1968, p. 1282.

ACKNOWLEDGEMENT
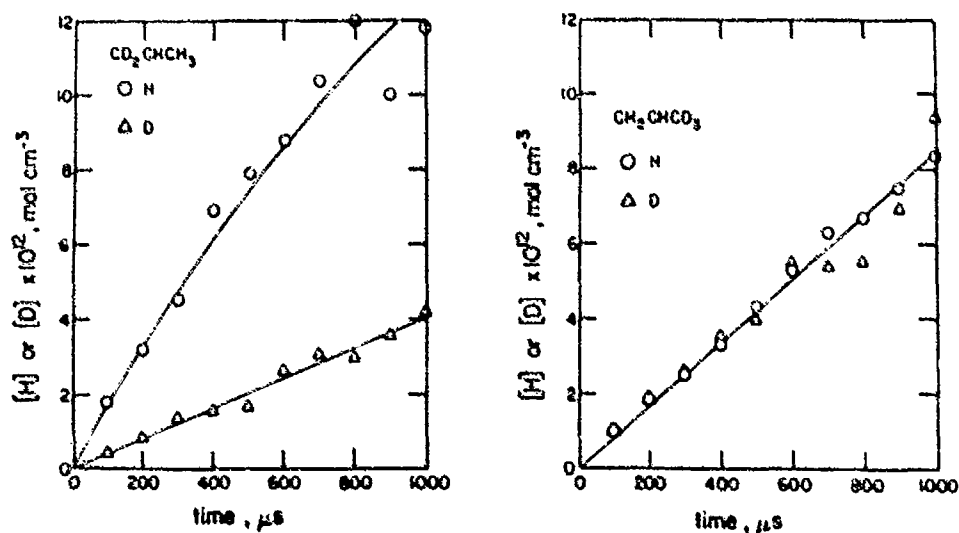
Figure 1. H atom profile for experiment with 10 ppm CD_2CHCH_3, 1597 K, total pressure 0.41 atm; and D atom profile for same gas mixture, 1605 K, 0.35 atm. Figure 2. H atom profile for experiment with 10 ppm CH_2CHCD_3, 1609 K, 0.41 atm; D atom profile (multiplied by 0.68 to compensate for difference in pressure) for same gas mixture, 1608 K, 0.60 atm.

Shock Tube Study of Acetaldehyde Oxidation

A. Koichi Hayıshi and Toshi Fujiwara

Department of Aeronautical Engineering
Nagoya University, Nagoya 464, Japan

The sensitivity analysis was applied to experimentally determine the rates of unknown reactions in an acetaldehyde oxidation system. The concentrations of O-atom and CO- and OH-molecules in this reaction system were measured behind a reflected shock wave using the ultraviolet and infrared emission spectroscopy. Two types of $CH_3CHO/O_2/Ar$ mixtures, the equivalence ratios 0.94 and 2.5, were used to investigate the concentrations of O,CO and OH species at the temperature 1470-1960 K and the pressure 0.46-0.67 MPa. The H_2/O_2 mixture was used to calibrate OH concentrations and CO/O_2 mixture O and CO concentrations. The previously proposed acetaldehyde oxidation mechanism was studied using the program which performs detailed chemical reaction simulation and sensitivity analysis. The extensive sensitivity analysis predicted the following four important reactions and their rates in $CH_3CHO/O_2/Ar$ reaction mechanism;
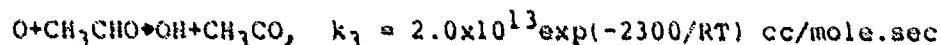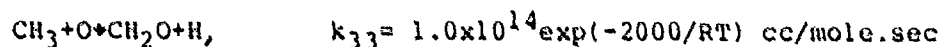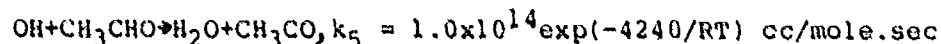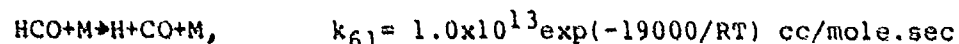
$HCO+M \rightarrow H+CO+M$, $k_{61} = 1.0 \times 10^{13} exp(-19000/RT)$ cc/mole.sec

$OH+CH_3CHO \rightarrow H_2O+CH_3CO$, $k_5 = 1.0 \times 10^{14} exp(-4240/RT)$ cc/mole.sec

$CH_3+O \rightarrow CH_2O+H$, $k_{33} = 1.0 \times 10^{14} exp(-2000/RT)$ cc/mole.sec

$O+CH_3CHO \rightarrow OH+CH_3CO$, $k_3 = 2.0 \times 10^{13} exp(-2300/RT)$ cc/mole.sec

1. INTRODUCTION

One of the consequential intermediates in hydrocarbon combustion is known to be acetaldehyde[1,2], which is a key component in the exhaust from internal combustion engines as a cause of photochemical smog. Numerous studies including a recent one by Benson[3] predicated since 1930's that aldehydes were important initiators of knocks in automobile engines. Acetaldehyde oxidation was studied at the low temperature 593 - 813 K by Baldwin et al.[4], and at the medium temperature 1030 - 1115 K by Colket[5]. However, the information on acetaldehyde oxidation at the temperature higher than 1200 K is very scarce despite its needs. Thus the acetaldehyde oxidation reaction mechanism has not completely been established at the high temperature 1200 - 2500 K, where combustion occurs. The purpose of the present study is to validate the previously developed acetaldehyde oxidation mechanism[6] and to experimentally determine some of the rates at the temperature 1470 - 1960 K and the pressure 0.46 -0.67 MPa and to analyze the data on the basis of sensitivity analysis.

2. EXPERIMENT

The experiment was conducted using a single-pulse shock tube of 50.8 mm i.d. and 5.86 m length. In order to produce a single-pulse shock wave, a 0.1 m^3 dump tank was installed 10 cm downstream of a plastic diaphragm, which separated the stainless steel driver section from the pyrex glass test one. The shock tube showed a leak rate of less than 1.0 Pa/min and was evacuated down to less than 0.1 Pa.

A ball valve was used to open the dump tank, pressurized up to the driven section pressure, just before rupturing the diaphragm by a needle. Acetaldehyde was Merck Grade 99.5 % pure with water as the most probable impurity. Argon, hydrogen, carbon monoxide and oxygen were Nihon Oxygen Grade 99.99 % pure. Prepared were the stoichiometric hydrogen/oxygen mixture diluted with argon, stoichiometric carbon monoxide/oxygen mixture diluted with argon and acetaldehyde/oxygen mixtures at the equivalence ratios of 0.94 and 2.5 diluted with argon. The shock speed was measured by a multichannel time counter signaled from a piezoelectric pressure transducer (Kistler 601H). The initial temperature and pressure immediately behind a reflected shock wave were calculated from shock relations taking account of the temperature dependency of enthalpies.

A schematic diagram of the experimental setup is shown in Fig.1.

The OH concentration was measured using the emission of the R_2 branches of $^2\Sigma - ^2\Pi$ (0,0) band system at 3064 A. The OH ultraviolet emission was focused on the entrance slit of a 10 cm monochromator (JASCO CT-10). Entrance and exit slits were set to 200 μm width to supply enough emission into a photomultiplier (Hamamatsu Photonics R106). A stoichiometric hydrogen/oxygen mixture was used to obtain a calibration curve for OH emission comparing experimental data with the computational results. A least square fit of the calibration results is shown in Fig.2 confirming that the observed emission intensity is proportional to the computed OH concentrations using nine well-known elementary reactions listed on Table 1.

The measurement of O-atom concentration was conducted using the same methodology as Bowman in 1975[7]. The chemiluminescent emission of the O+CO+CO$_2$+hν reaction at 3660 A passed through a quartz window and was focused on the entrance slit of a 10 cm monochromator. A photomultiplier (Hamamatsu Photonics R106) detected the ultraviolet light from the exit of the monochromator. In order to determine the O-atom concentration, the infrared emission from the fundamental band of CO molecules at 4.8 μm was measured simultaneously with the above ultraviolet emission. The infrared light passed through a CaF$_2$ window and focused on the entrance slit of a 25 cm infrared monochromator (JASCO CT-25). A cryogenically cooled infrared detector (Santa Barbara Research Center PbSe LTO Detector 4311) sensed the infrared emission from the exit slit. All the slit widths used in this experiment were 200 μm. The following relation between the intensity of chemiluminescent emission and the O-atom and

CO-molecule concentrations was used,

$$I = k [O][CO]$$

where k is a temperature and total pressure-dependent constant[8,9]. This $O+CO \rightarrow CO+h\nu$ reaction system was calibrated by a stoichiometric CO/O_2 mixture diluted with argon and compared with the computational results using three elementary reactions listed on Table 2. The least-square fits of the calibration data for the intensity of the chemiluminescent emission from the O+CO reaction and for the intensity of the CO infrared emission are shown in Figs.3 and 4, respectively.

When an Arrhenius type rate constant was applied, the activation energy of the O+CO reaction was 4570 cal/mole, which agreed with the result obtained by Bowman[7].

3. EXPERIMENTAL RESULTS

The concentrations of O-atom and CO- and OH-molecules were obtained behind the reflected shock waves using a near stoichiometric and rich acetaldehyde/oxygen/argon mixtures. The ranges of temperature, pressure and total species concentrations were 1470 - 1960 K, 0.46 - 0.67 MPa, and 2.89 - 6.19 x 10^{-5} mole/cc.

A typical experimental output of radiation intensities on an oscilloscope is shown in Fig.5. Fig.5-(a) shows a typical OH ultraviolet emission at 3064 A for the acetaldehyde/oxygen/argon mixture at the equivalence ratio 2.5, temperature 1760 K and pressure 0.503MPa. Fig.5-(b) is an example of the chemiluminescent light of the O+CO reaction at 3660 A and the infrared radiation of CO-molecule at 4.8 μ m for the acetaldehyde/oxygen/argon mixture at the equivalence ratio 0.94, temperature 1830 K and pressure 0.472 MPa. The transient spikes for the O+CO reaction and OH emissions are observed in the experiments at near-stoichiometric and rich mixtures. This transient spike of O-CO chemiluminescence contains unknown hydrocarbon emissions as Jachimowski pointed out[5] in the study of a methane oxidation system. Hence the maximum intensity of O-CO emission is extrapolated from its equilibrium value. The concentration of CO is obtained from the corresponding data to the maximum O-CO emission.

The maximum O-atom and OH-molecule and corresponding CO-molecule concentrations as well as the temperature, pressure and spike-time are tabulated for the near-stoichiometric and rich $CH_3CHO/O_2/Ar$ mixtures in Table 3. The uncertainties in the measurement of concentration are at most 20 % considering the optical systems, pressure and temperature calculations and the data calibration.
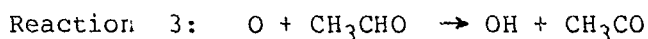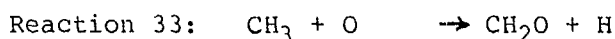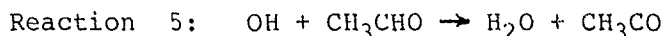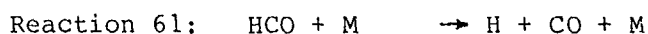
4. SENSITIVITY ANALYSIS

A sensitivity analysis (Green's Function Method[10,11]) for acetaldehyde oxidation was performed to the previously developed mechanism[6]. The purpose of using the sensitivity analysis in this study is to systematize the analysis of the present results;

in other words, to pinpoint the important reactions related with
O-atom and CO- and OH- molecules and to obtain the proper rate
constants for those reactions. The details of the concept and
method of our sensitivity analysis can be found out
elsewhere[11,12]. Table 4 tabulates several reactions having
sufficiently large sensitivity coefficients for near-
stoichiometric and rich mixtures of the $CH_3CHO/O_2/Ar$ system. The
hydrocarbon-related reactions such as;

Reaction 22: C_2H_5 $\rightarrow$ $H + C_2H_4$

Reaction 27: $CH_4 + M$ $\rightarrow$ $CH_3 + H + M$
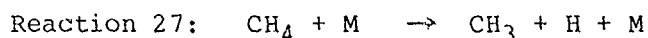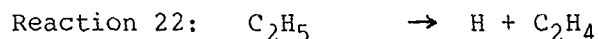
became more important for the reactions of rich mixtures than
near-stoichiometric mixtures.

The calculated time to the maximum concentrations of O-atom
and OH-molecule was found to agree with that of experimental
results without adjusting any rates except that of H_2O_2-related
reactions. The present acetaldehyde oxidation mechanism
contained 81 elementary reactions excluding ketene-related
reactions, as shown in Table 5. It was found out that H_2/O_2
reactions were important for the hydrocarbon combustion and the
same H_2/O_2 rate constants uld not be used for different
temperature ranges if those reactions were strongly temperature
dependent. The maximum concentrations of O-atom and OH-
molecule were calculated using the results of sensitivity
analysis. Basically, the following four elementary reactions
were adjusted to fit the maximum values of O-atom and CO- and OH-
molecules concentrations;

Reaction 61: $HCO + M$ $\rightarrow$ $H + CO + M$

Reaction 5: $OH + CH_3CHO$ $\rightarrow$ $H_2O + CH_3CO$

Reaction 33: $CH_3 + O$ $\rightarrow$ $CH_2O + H$

Reaction 3: $O + CH_3CHO$ $\rightarrow$ $OH + CH_3CO$

The rates of those reactions were obtained using typically
available experimental results on induction time,

$$k_{61} = 1 \times 10^{13} \exp(-19000/RT)   cc/mole.sec$$

$$k_5 = 1.0 \times 10^{14} \exp(-4240/RT)   cc/mole.sec$$

$$k_{33} = 1.0 \times 10^{14} \exp(-2000/RT)   cc/mole.sec$$

$$k_3 = 2.0 \times 10^{13} \exp(-2300/RT)   cc/mole.sec$$

where the published values on activation energy were used to
determine the rates. The above four reactions were chosen by
setting up the criterion that the well established reactions and
their rates were fixed. It should noted be that the important
reactions obtained using sensitivity analysis were essentially
valid only at the temperature where the sensitivity analysis was

applied. It should be necessary to check the sensitivity at different temperatures as well as for different mixtures in order to obtain the general reaction mechanism and associated reaction rates.

5. DISCUSSIONS

The sensitivity analysis is powerful to determine the rates of unknown reactions when the rates of well established reactions can be fixed, as is proved in the present paper.

Reaction 61 is one of the most important reactions in acetaldehyde chemistry. This one and the $CH_3CO \rightarrow CH_3 + CO$ reaction compete each other for CO production. As Warnatz describes that the further rate measurement is necessary for this reaction[13], it still has uncertainties. The presently obtained rates are rather close to that of Browne et al.[14] and Dean et al.[15] than that by Bowman.

Reaction 5 becomes more important for lean mixtures than for rich mixtures. The rates of this reaction for high temperatures are obtained only by Colket[5] with uncertainties. The normal sensitivity coefficient of Reaction 5 is one order smaller than the largest sensitivity coefficient in the same system. In other words, the obtained rates have a large uncertainty since a large frequency factor to adjust its rates does not affect the OH concentrations.

The importance of Reaction 33 is dramatic in contrast with the statement of Bowman that the $CH_3 + O_2 \rightarrow CH_2O + OH$ reaction is more important than Reaction 33. Instead, the sensitivity analysis for O-atom clearly discloses the higher importance of Reaction 33. The rates presently obtained are the same as obtained by other shock tube research.

Reaction 3 has also a large uncertainty in its rates, but the present result must be important since these data decrease the uncertainty at high temperatures. As seen in Table 4, this reaction becomes less important for richer mixtures, but still important for lean mixtures regarding both O-atom and OH-molecule.

The calculated values for O, CO, and OH concentrations using the newly obtained mechanism agree with the experimental data shown in Figs. 6, 7 and 8. The O-atom concentrations are explained well by the computed values. Fig. 6 shows an order of magnitude difference in O-atom concentrations between the stoichiometric and rich mixtures. The results for CO-molecules diverge a little, but the computational results agree with the experimental data.

Fig.8 shows the OH ultraviolet emission data. The computational results agree at high temperatures, but not at low temperatures since the pressure effects become large.

It is concluded that the proposed mechanism can predict the acetaldehyde/oxygen mixture combustion at high temperatures.

Acknowledgements

References

1. Westbrook, C. K. and Dryer, F. L., "Chemical Kinetic Modeling of Hydrocarbon Combustion," Prog. Energy Comb. Sci., Vol.10, 1984, pp.1-57.
2. Hayashi, A.K. and Dryer, F.L., to be published.
3. Benson, S.W., "Cool Flames and Oxidation : Mechanism, Thermochemistry and Kinetics," Oxidation Communications 2, 1982, p.169.
4. Baldwin, R.R., Matchan, M.J. and Walker, R.W., "The High-Temperature Oxidation of Acetaldehyde," Comb. and Flame, Vol.15, 1970, pp.109-123.
5. Colket, M. B., "High Temperature Pyrolysis and Oxidation of Acetaldehydes," Ph.D. Thesis, AMS Dept., Princeton Univ.,1975.
6. Ushimaru, S., Hayashi, A. K. and Fujiwara, T., "High Temperature Oxidation of Acetaldehyde Behind A Reflected Shock Wave, " Proceedings of the 14th Int. Symp. on Space Tech. and Sci., Tokyo, 1984.
7. Bowman, C.T.,"Non-Equilibrium Radical Concentrations in Shock Initiated Methane Oxidation," 15th Int. Symp. on Combustion, 1975, p.869-882.
8. Myers, B.F. and Bartle, E.R., "Shock-Tube Study of the Radiative Processes in Systems Containing Atomic Oxygen and Carbon Monoxide at High Temperature," J. of Chem. Phys., Vol. 47, 5, 1967, pp.1783-1792.
9. Jachimowski, C. J., "Kinetics of Oxygen Atom Formation During the Oxidation of Methane Behind Shock Waves,"Comb. and Flame, Vol.23, 1974, pp.233-248.
10. Hwang, J.T., Dougherty, E.P., Rabitz, S. and Rabitz, H., "The Green's Function Method of Sensitivity Analysis in Chemical Kinetics," J. Chem. Phys., Vol.69, 11, 1978, pp.5180-5191.
11. Hayashi, A. K., "Sensitivity Analysis for Chemical Reaction," Report for the Research Grant of Ministry of Education, No. 5835003, March 1985, p.101-108.
12. Hayashi, A.K. and Fujiwara, T., to appear.
13. Warnatz, J., "Rate Coefficients in the C/H/O System," Chap.5 of Combustion Chemistry edited by Gardiner, W.C., Springer Verlag, 1984.
14. Browne, W.G., Porter, R.P., Verlin, J. D. and Clark, A.H., "A Study of Acetylene-Oxygen Flames," 12th Int. Symp. on Combustion, 1969, p.1035.
15. Dean, A.M., Craig, B. L., Johnson, R. L., Schultz, M. C. and Wang, E. E., "Shock Tube Stdies of Formaldehyde Pyrolysis," 17th Int. Symp. on Combustion, 1974, p.577.

Table 1 H_2/O_2 reaction mechanism (Units:cc-mole-cal-K-sec)

Reaction			A	n	E
$H + O_2$	$=$	$O + OH$	$2.2x10^{14}$	0.0	16790.
$H_2 + O$	$=$	$H + OH$	$3.2x10^{14}$	1.0	104800.
$O + H_2O$	$=$	$OH + OH$	$5.4x10^{14}$	0.0	24239.
$H + H_2O$	$=$	$OH + H_2$	$1.26x10^{15}$	0.0	31932.
O_2	$=$	$O + O$	$7.9x10^{23}$	0.0	104800.
H_2	$=$	$H + H$	$2.2x10^{14}$	0.	96000.
H_2O	$=$	$H + OH$	$6.86x10^{26}$	-3..	122590.
HO_2	$=$	$H + O_2$	$2.3x10^{15}$	0.0	45900.
$H + HO_2$	$=$	$OH + OH$	$2.5x10^{14}$	0.0	1900.

Table 2 CO/O_2 reaction mechanism (Units:cc-mole-cal-K-sec)

Reaction			A	n	E
$CO + O_2$	$=$	$CO_2 + O$	$3.1x10^{11}$	0.0	37600.
$O_2 + M$	$=$	$O + O + M$	$1.7x10^{15}$	0.0	115000.
$CO + O + M$	$=$	$CO_2 + M$	$5.9x10^{15}$	0.0	4100.

TABLE 3   EXPERIMENTAL RESULTS

EQUIVALENCE RATIO	T_5 (K) ±30K	P_5 (ATM) ±1%	t.spike (mSEC)	TOTAL. CONCENTRATION $(10^{-3}$ MOLE/CC)	$[O]_{MAX}$ (10^{-8}) ±20%	[CO] (10^{-4}) ±20%	$[OH]_{MAX}$ (10^{-5}) ±15%
0.94	1275	5.88	2.21	5.625			0.097
0.94	1376	6.65	1.06	5.491			1.29
0.94	1470	5.60	0.49	4.647			9.13
0.94	1600	5.84	0.20	4.241			20.2
0.94	1683	4.73	0.14	3.638			23.2
0.94	1924	4.56	0.02	2.900			38.1
0.94	1385	7.03	1.14	6.186	0.261	1.93	
0.94	1523	6.29	0.41	5.031	0.765	1.12	
0.94	1546	5.46	0.29	4.249	1.15	0.67	
0.94	1595	5.69	0.23	4.346	0.88	0.35	
0.94	1709	5.40	0.13	3.852	4.16	0.22	
0.94	1727	5.54	0.14	3.911	1.76	0.60	
0.94	1833	4.66	0.04	3.100	1.81	0.22	
2.50	1334	6.28	1.43	5.739			0.265
2.50	1400	5.95	0.76	5.182			0.766
2.50	1569	6.11	0.29	4.747			7.01
2.50	1684	5.76	0.15	4.167			12.1
2.50	1762	4.97	0.09	3.441			15.1
2.50	1800	4.27	0.03	2.770			24.3
2.50	1962	4.63	0.03	2.886			30.3
2.50	1390	5.86	0.86	5.133	0.013	0.34	
2.50	1564	4.08	0.36	4.733	0.027	0.20	
2.50	1594	5.21	0.16	3.906	0.053	0.16	
2.50	1677	5.76	0.14	4.168	3.509	0.15	
2.50	1774	5.08	0.08	3.499	0.248	0.07	

TABLE 4   SENSITIVITY ANALYSIS

[O] ATOM ; T = 1700 K, P = 5 ATM

EQUIVALENCE RATIO ϕ = 0.94		ϕ = 2.5	
REACTION	SENSITIVITY COEF.	REACTION	SENSITIVITY COEF.
$CH_3CO + CH_3 + CO$	12.25	$CH_3CO + CH_3 + CO$	17.66
$CH_3CHO + CH_3 + CHO$	5.86	$HCO + M + H + CO + M$	12.42
$HCO + M + H + CO + M$	5.86	$CH_3CHO + CH_3 + CHO$	12.37
$CH_3 + CH_3 + C_2H_6$	-4.07	$CH_3 + CH_3 + C_2H_6$	-6.82
$H + CH_3CHO + H_2 + CH_3CO$	-0.38	$H + CH_3CHO + H_2 + CH_3CO$	-0.32
$H + O_2 + OH + O$	0.27	$C_2H_5 + H + C_2H_4$	0.23
$CH_3 + O + CH_2O + H$	-0.21	$H + O_2 + OH + O$	0.22
$O + CH_3CHO + OH + CH_3CO$	-0.11	$CH_3 + O + CH_2O + H$	-0.19
		$CH_4 + H + CH_3 + H + M$	-0.17

[OH] MOLECULE; T = 1700 K, P = 5 ATM

| EQUIVALENCE RATIO ϕ = 0.94		ϕ = 2.5	
REACTION	SENSITIVITY COEF.	REACTION	SENSITIVITY COEF.
$CH_3CO + CH_3 + CO$	8.44	$CH_3CO + CH_3 + CO$	25.80
$CH_3CHO + CH_3 + CHO$	4.57	$CH_3CHO + CH_3 + CHO$	18.29
$HCO + M + H + CO + M$	4.36	$HCO + M + H + CO + M$	18.25
$CH_3 + CH_3 + C_2H_6$	-2.53	$CH_3 + CH_3 + C_2H_6$	-10.00
$OH + CH_3CHO + H_2O + CH_3CO$	-1.46	$OH + CH_3CHO + H_2O + CH_3CO$	-0.57
$H + O_2 + OH + O$	0.80	$H + O_2 + OH + O$	0.38
$H + CH_3CHO + H_2 + CH_3CO$	-0.31	$C_2H_5 + H + C_2H_4$	0.32
$O + CH_3CHO + OH + CH_3CO$	0.21	$H + CH_3CHO + H_2 + CH_3CO$	-0.
$HO_2 + H + OH + OH$	0.14	$CH_4 + H + CH_3 + H + M$	-0.25
		$HCO + OH + CH_2O + O$	0.12
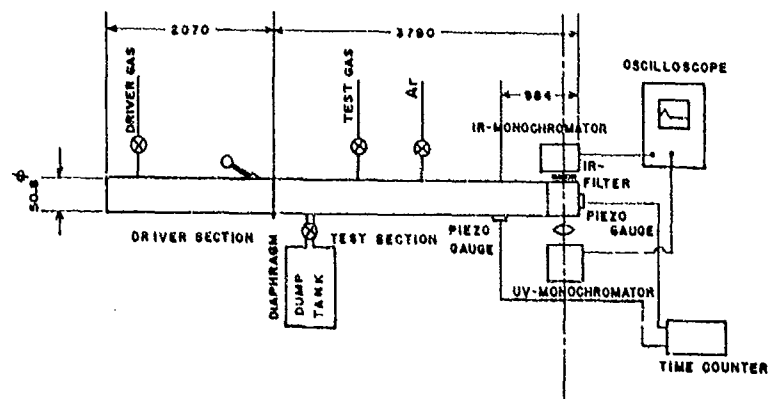
Fig.1 Schematic diagram of the experimental setup.

TABLE 5 Acetaldehyde oxidation mechanism (units:cc-mole-sec-kcal)

|	Reaction	log A	n	Ea	Reference
1	CH3CHO=CH3+HCO	16.15	0.0	85.80	Hayashi et al.(1985)
2	O2+CH3CHO=HO2+CH3CO	13.30	0.5	42.20	Colket (1977)
3	O+CH3CHO=OH+CH3CO	13.30	0.0	2.30	This study
4	HO2+CH3CHO=H2O2+CH3CO	12.08	0.0	10.70	Colket (1977)
5	OH+CH3CHO=H2O+CH3CO	14.00	0.0	4.24	This study
6	H+CH3CHO=H2+CH3CO	-4.23	5.6	1.36	Colket (1975)
7	CH3+CH3CHO=CH4+CH3CO	-7.22	6.1	1.72	Colket (1975)
8	CH3+CH3CHO=CH4+CH2CHO	-0.26	4.0	8.28	Colket (1975)
9	CH3CO=CH3+CO	13.51	0.0	17.24	Watkins & Word (1974)
10	CH3O+M=CH2O+H+M	13.70	0.0	21.00	Brabbs & Brokaw (1975)
11	CH3O+O2=CH2O+HO2	11.00	0.0	9.93	Engleman (1976)
12	CH3O=H+CH2O	13.95	0.0	30.00	Gray et al. (1967)
13	CH2O+M=HCO+H+M	14.00	0.0	36.74	Dean et al. (1980)
14	CH2O+CH3=HCO+CH4	10.00	0.5	19.00	Colket (1977)
15	CH2O+H=HCO+H2	14.52	0.0	10.50	Dean et al. (1980)
16	CH2O+OH=HCO+H2O	12.88	0.0	0.17	Atkinson & Pitts (1978)
17	C2H6+O=C2H5+OH	13.40	0.0	6.36	Herron & Huie (1973)
18	C2H6+OH=C2H5+H2O	13.04	0.0	2.45	Greiner (1973)
19	C2H6+H=H2+C2H5	2.73	3.5	5.20	Clark & Dove (1973)
20	C2H6+CH3=CH4+C2H5	-0.26	4.0	8.28	Clark & Dove (1973)
21	C2H5+O2=C2H4+HO2	12.00	0.0	5.00	Westbrook (1979)
22	C2H5=H+C2H4	15.30	0.0	30.00	Olson et al. (1979)
23	C2H4+M=C2H2+H2+M	17.41	0.0	79.28	Hartig et al. (1971)
24	C2H4+M=C2H3+H+M	17.58	0.0	98.16	Baldwin et al. (1970)
25	C2H3+M=C2H2+H+M	14.90	0.0	31.50	Herron (1969)
26	CH4+M=CH3+H+M	17.15	0.0	88.40	Zellner et al. (1976)
27	CH4+H=CH3+H2	14.11	0.0	11.90	Skinner et al. (1972)
28	CH4+O=CH3+OH	13.30	0.0	9.20	Brabbs & Brokaw (1975)
29	CH4+OH=CH3+H2O	3.54	3.1	2.00	Shepp (1956)
30	CH4+HO2=CH3+H2O2	13.30	0.0	18.00	Peeters & Mahnen (1973)
31	CH3+O2=CH3O+O	13.38	0.0	29.00	Fenimore (1969)
32	CH3+CH3=C2H6	13.34	0.0	0.00	Tunder et al. (1967)
33	CH3+O=CH2O+H	14.00	0.0	2.00	This study
34	CH3+OH=CH2O+H2	12.60	0.0	0.00	Just et al. (1977)
35	CH3+HCO=CH4+CO	11.48	0.5	0.00	Benson & Haugen (1967)
36	C2H4+H=C2H3+H2	7.18	2.0	6.00	Westbrook et al. (1976)
37	C2H4+O=CH3+HCO	12.52	0.0	1.13	Davis et al. (1972)
38	C2H4+O=CH2O+CH2	13.40	0.0	5.00	Westbrook et al. (1982)
39	C2H4+OH=CH3+CH2O	12.30	0.0	0.96	Westbrook et al. (1982)
40	C2H4+OH=C2H3+H2O	12.68	0.0	1.23	Westbrook et al. (1982)
41	C2H4+C2H4=C2H3+C2H5	14.70	0.0	64.70	Benson & Haugen (1967)
42	C2H2+O2=HCO+HCO	14.00	0.0	38.00	Gardiner & Walker (1968)
43	C2H2+H=C2H+H2	14.30	0.0	19.00	Browne et al. (1969)
44	C2H2+O=C2H+OH	15.51	-0.6	17.00	Browne et al. (1969)
45	C2H2+O=CH2+CO	13.83	0.0	4.00	Vandooren & Von Tiggelen (1977)
46	C2H2+OH=C2H+H2O	12.78	0.0	7.00	Vandooren & Von Tiggelen (1977)
47	C2H2+M=C2H+H+M	14.00	0.0	114.30	Jachimowski (1977)
48	C2H2+OH=CH3+CO	12.08	0.0	0.50	Smith & Zellner (1973)
49	C2H+O2=HCO+CO	13.00	0.0	7.00	Browne et al. (1969)
50	C2H+O=CH+CO	13.70	0.0	0.00	Browne et al. (1969)
51	CH2+O2=HCO+OH	14.00	0.0	3.70	Benson & Haugen (1967)
52	CH2+H=CH+H2	11.43	0.7	25.70	Mayer et al. (1967)
53	CH2+O=CH+OH	11.28	0.7	25.00	Mayer et al. (1967)
54	CH2+OH=CH+H2O	11.43	0.7	25.70	Peeters and Vicker (1975)
55	CH+O2=HCO+O	13.00	0.0	0.00	Jachimowski (1977)
56	CH+O2=CO+OH	11.11	0.7	25.70	Peeters & Vicker (1975)
57	CO+OH=CO2+H	7.11	1.3	-0.77	Baulch & Drysdale (1974)
58	CO+HO2=CO2+OH	14.00	0.0	23.00	Baldwin et al. (1970)
59	CO+O+M=CO2+M	15.48	0.0	4.10	Simonaitis & Heicklen (1974)
60	CO2+O=CO+O2	12.45	0.0	43.83	Gardiner et al. (1971)
61	HCO+M=H+CO+M	14.00	0.0	19.00	Westbrook et al. (1977)
62	HCO+O2=HO2+CO	12.52	0.0	7.00	Westbrook et al. (1977)
63	HCO+H=CO+H2	14.30	0.0	0.00	Niki et al. (1969)
64	HCO+O=CO+OH	14.00	0.0	0.00	Westenberg & de Haas (1972)
65	HCO+OH=CH2O+O	14.00	0.0	3.00	Baldwin & Walker (1973)
66	HCO+OH=CO+H2O	14.00	0.0	0.00	Bowman (1970)
67	H2+O=H+OH	10.26	0.0	8.90	Baulch et al. (1973)
68	O2+M=O+O+M	15.71	0.0	115.00	Jenkins et al. (1967)
69	H+O+M=OH+M	16.00	0.0	0.00	Moretti (1965)
70	H2+M=H+H+M	14.34	0.0	96.00	Baulch et al. (1973)
71	H+O2=OH+O	14.34	0.0	16.80	Baulch et al. (1973)
72	H+O2+M=HO2+M	15.51	0.0	-1.00	Baulch et al. (1973)
73	HO2+H=OH+OH	14.40	0.0	1.90	Baulch et al. (1973)
74	HO2+O=O2+OH	13.70	0.0	1.00	Lloyd (1974)
75	HO2+H=H2+O2	13.40	0.0	0.70	Baulch et al. (1973)
76	HO2+OH=H2O+O2	13.70	0.0	1.00	Lloyd (1974)
77	HO2+CH3=CH3O+OH	12.30	0.0	0.00	Colket (1975)
78	HO2+CH3=CH4+O2	12.30	0.0	0.00	Skinner et al. (1972)
79	H2O+M=H+OH+M	16.34	0.0	105.00	Baulch et al. (1973)
80	H2O+H=H2+OH	13.98	0.0	20.30	Baulch et al. (1973)
81	H2O+O=OH+OH	13.83	0.0	18.35	Baulch et al. (1973)
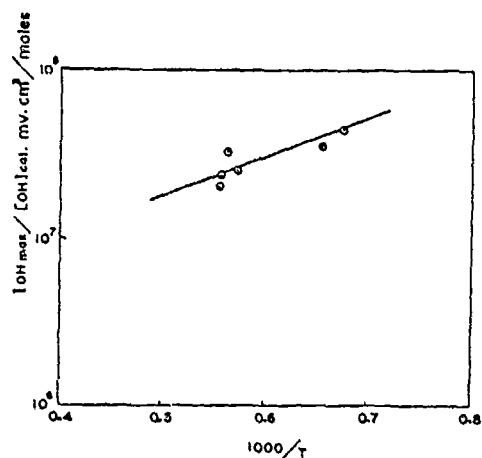
Fig.2 A least square fit of the calibration curve for the OH ultraviolet emission at 3064 Å and concentrations by a stoichiometric H_2/O_2 mixture diluted with argon.
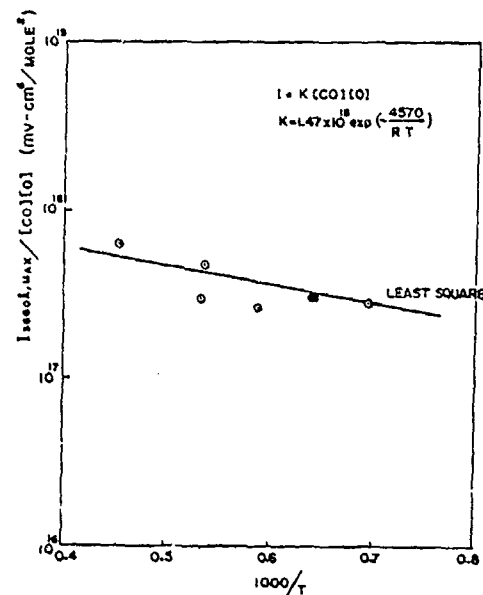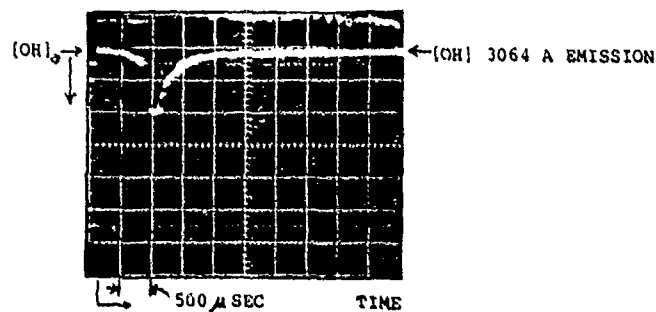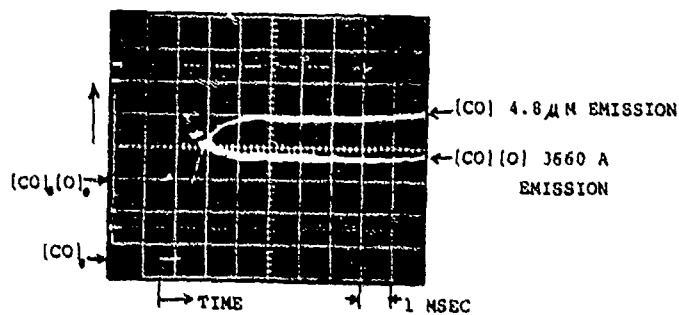
Fig.3 A least square fit of the calibration curve for the O+CO reaction at 3660 Å by a stoichiometric CO/O_2 mixture diluted with argon.

(a) $\phi = 2.5$, $CH_3CHO/O_2/Ar=1/1/98$, $T=1760$ K, $P=4.97$ ATM

(b) $\phi = 0.94$, $CH_3CHO/O_2/Ar=2/4.9/93.1$, $T=1830$ K, $P=4.66$ ATM

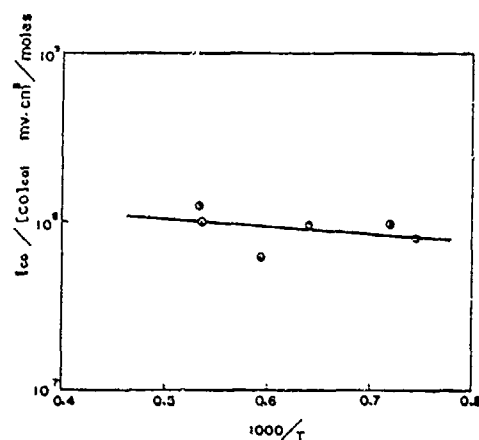Fig.5 A typical experimental output of radiation intensities on an oscilloscope.

Fig.4 A least square t.t of the calibration curve for
the CO infrared emission at 4.8 um by a stoichiometric
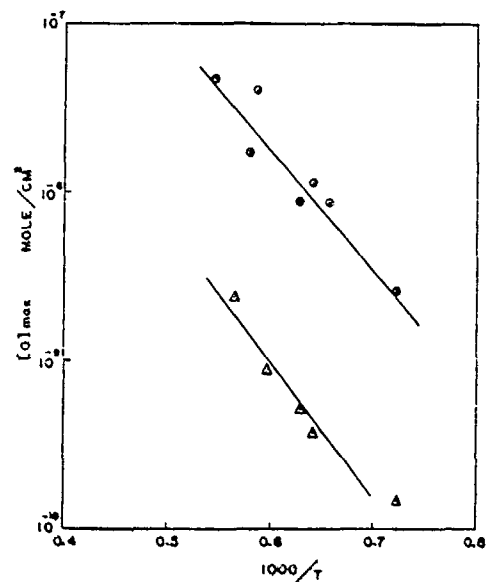CO/O₂ mixture diluted with argon.

Fig.6 Comparison of measured and calculated maximum
O-atom concentrations: ⊙ acetaldehyde/oxygen/argon
mixture at the equivalence ratio 0.94, △ at the
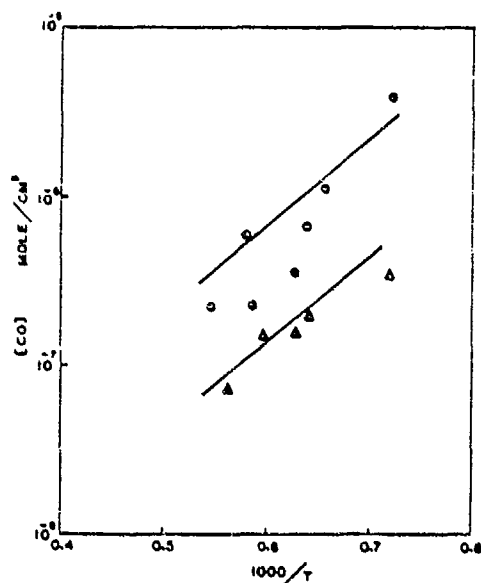equivalence ratio 2.5. Solid line is calculated maximum
O-atom concentrations.

Fig.7 Comparison of measured and calculated CO-molecule
concentrations: Ⓒ acetaldehyde/oxygen/argon mixture at
the equivalence ratio 0.94, △ .t the equivalence ratio
2.5. Solid line is calculated CO-molecule concentrations.

Fig.8 Comparison of measured and calculated OH-molecule
concentrations: ⊙ acetaldehyde/oxygen/argon mixture at
the equivalence ratio 0.94, △ at the equivalence ratio
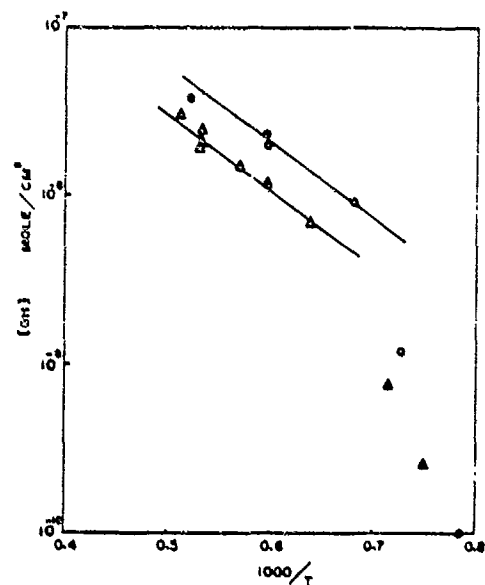2.5. Solid line is calculated OH-molecule concentrations.

CHEMICAL KINETICS MODELING OF THE INFLUENCE
OF MOLECULAR STRUCTURE ON SHOCK TUBE IGNITION DELAY

Charles K. Westbrook and William J. Pitz
Lawrence Livermore National Laboratory
Livermore, California   94550

Abstract

The current capabilities of kinetic modeling of hydrocarbon oxidation
in shock waves are discussed. The influence of molecular size and
structure on ignition delay times are stressed. The n-paraffin fuels from
CH_4 to $n-C_5H_{12}$ are examined under shock tube conditions, as well as
the branched chain fuel isobutane, and the computed results are compared
with available experimental data. The modeling results show that it is
important in the reaction mechanism to distinguish between abstraction of
primary, secondary and tertiary H atom sites from the fuel molecule. This
is due to the fact that both the rates and the product distributions of
the subsequent alkyl radical decomposition reactions depend on which H
atoms were abstracted. Applications of the reaction mechanisms to shock
tube problems and to other practical problems such as engine knock are
discussed.

INTRODUCTION

The analysis of shock tube experiments often involves the use of
detailed chemical kinetic reaction mechanisms. Shock tube ignition delay
time measurements and their variation with temperature, density, and
composition provide essential tests of reaction mechanisms for hydrocarbon
and other fuels. Numerical modeling studies are now using these reaction
mechanisms, tested against shock tube experiments, to examine the
structure and other properties of gaseous detonation waves, engine knock
in internal combustion engines, and other practical combustion systems.

In a particularly well formulated study, Burcat et al.[1] examined the
shock tube ignition delay of a series of n-alkanes from methane to
n-pentane, in oxygen-argon mixtures which were chosen to approximate
fuel-air mixtures. The general conclusions of this work were that methane
had a much longer ignition delay than the other fuels, ethane had a
slightly shorter delay period than the other fuels, and the other
n-alkanes all had very similar ignition delay times. The present
numerical modeling study was intended to simulate the experimental study
of Burcat et al. and interpret the results in terms of the elementary
chemical kinetic steps which control the overall rates of reaction.

NUMERICAL MODEL AND REACTION MECHANISM

The detailed reaction mechanism used in these computations was based
on the previous mechanism for n-butane[2], which has been tested
extensively against experimental results for a variety of conditions. The
mechanism was extended to include n-pentane, assuming that the rates of
primary and secondary H atom abstraction in n-pentane are the same as in
propane and n-butane. The decomposition reactions of the pentyl radicals
were assumed to follow the "one bond removed" rule of Dryer and
Glassman[3], leading immediately to C_3 and C_2 radicals and olefins.

Subsequent reactions of these C_2 and C_3 species have been tested extensively in the mechanism. An additional fuel, not considered in the experimental study of Burcat et al., is the branched chain species iso-butane (methyl propane), an isomeric form of butane. The interest in branched chain hydrocarbon fuels was motivated by the experimental fact that straight chain hydrocarbons tend to ignite more rapidly than branched chain fuels with the same overall composition. No shock tube ignition delay data were available to test the model predictions for iso-butane, but the mechanism for iso-butane oxidation has been tested against experimental data in the turbulent flow reactor[4] and should be reasonably accurate under shock tube conditions. It is also well known that branched chain hydrocarbon fuels tend to be more resistant to engine knock in internal combustion engines, so the applications of these reaction mechanisms to practical situations also tend to validate the model predictions.

The ignition delay calculations were carried out using the HCT program[5], assuming constant volume in the gaseous mixtures under reflected shock wave conditions. The variations in shock tube ignition delay times for methane, ethane, and propane have been examined in previous numerical studies[6,7], and the present mechanism reproduced the past results for these fuels. Results of modeling studies of the oxidation of n-butane[2] were incorporated into the present reaction mechanism, and further extensions to n-pentane and iso-butane were also included into the reaction mechanism[8].

RESULTS

The detailed chemical kinetic reaction mechanism was able to reproduce the observed ignition delay times for all of the fuels which were studied experimentally. The post-shock density was 3.54×10^{-3} gm/cm^3 for each mixture, and the initial temperatures were varied from 1150 K to 1700 K, except for methane, where the initial temperature ranged from 1500 K to about 1900 K. Computed results for methane and ethane (and for mixtures of methane and ethane) agree very well with experimental results[6]. Results for the methane mixtures are shown in Fig. 1, and results for ethane and mixtures of methane and ethane are reported in Reference 6. Computations presented previously[9] showed that the ignition of natural gas, which contains small but not negligible amounts of propane together with methane and ethane, could also be simulated well with the present reaction mechanism. Computed results for propane ignition were presented in earlier work[7], and the predictions are compared with experimental results of Burcat et al. in Fig. 1. Finally, comparisons between experimental and computed results for n-butane and n-pentane are summarized in Fig. 2. Also shown are the computed results for ignition of iso-butane, showing that the ignition of iso-butane is distinctly slower than the ignition of n-butane or n-pentane.

The overall conclusion of these comparisons between experimental and computed results is that the numerical model is accurately reproducing the experimental data for all of the fuels studied. Furthermore, the model is also indicating that iso-butane has a significantly longer ignition delay period than either n-butane or n-pentane. Although there are no comparable experimental data for comparison, the conclusion is that the numerical model and detailed reaction mechanism adequately reproduce the available experimental data.

For each fuel, the variation in ignition delay period can be traced directly to the details in the reaction mechanism. The case of methane has been studied extensively and can be summarized here very briefly. Every methane molecule eventually produces a methyl radical; these radicals are very difficult to oxidize further, particularly since recombination of methyl radicals to produce ethane

$$CH_3 + CH_3 = C_2H_6$$
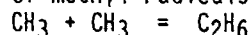
is very important. Because of this recombination, methane oxidation and ignition is not really typical of the ignition of most simple hydrocarbon fuels. In the case of ethane, all H atom abstraction reactions produce ethyl radicals, which subsequently decompose under shock tube conditions

$$C_2H_5 + M = C_2H_4 + H + M$$
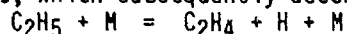
to produce H atoms. These H atoms then can react with molecular oxygen to provide chain branching through the reaction

$$H + O_2 = O + OH \qquad .$$
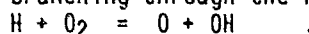
Therefore, all H abstractions from ethane lead to chain branching, explaining why ethane ignition is faster than all other n-alkanes.

For all of the higher hydrocarbon fuels, distinction must be made between different H atom sites in the fuel molecule. For propane, the two types of propyl radicals which can be produced are the n-propyl radical, which leads primarily to methyl radicals and ethene

$$n\text{-}C_3H_7 = CH_3 + C_2H_4$$
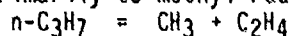
while isopropyl radicals lead to propene and H atoms

$$i\text{-}C_3H_7 = C_3H_6 + H \qquad .$$
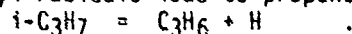
Since the methyl radicals lead to ethane formation through the reaction

$$CH_3 + CH_3 = C_2H_6$$
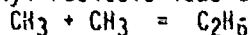
while H atoms lead to chain branching, it is clear that production of n-propyl radicals leads to retarding of the rate of ignition while production of iso-propyl radicals provides overall acceleration of the rate of ignition. Therefore, the key to describing propane ignition is the description of the relative rates of primary to secondary H atom abstraction reactions.

In similar terms, the ignition of n-butane and n-pentane can also be shown to depend on the relative rates of primary and secondary H atom abstractions. In the case of n-butane, abstraction of a primary H atom leads to the production of H atoms and chain branching through

$$p\text{-}C_4H_9 = C_2H_4 + C_2H_5$$
$$C_2H_5 = C_2H_4 + H$$
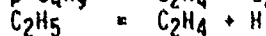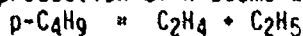
while the abstraction of a secondary H atom leads to chain termination

$$s\text{-}C_4H_9 = CH_3 + C_3H_6 \qquad .$$
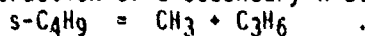
In the case of n-pentane, a new element appears. All of the secondary H atoms are not the same. The abstraction of a primary H atom leads to

$$p\text{-}C_5H_{11} = C_2H_4 + n\text{-}C_3H_7$$
$$n\text{-}C_3H_7 = C_2H_4 + CH_3$$
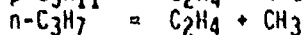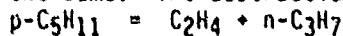
and chain termination. However, the abstraction of an H atom attached to a secondary C atom leads to

$$2\text{-}C_5H_{11} = C_3H_6 + C_2H_5$$
$$C_2H_5 = C_2H_4 + H$$
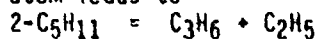
and chain branching, while the abstraction of a symmetric H atom leads to

$$3\text{-}C_5H_{11} = 1C_4H_8 + CH_3$$

and chain termination. Therefore, the rate of chain branching depends very sensitively on the relative rates of H atom abstraction from the parent fuel molecule at each H atom site.

The same trend applies in the case of iso-butane. There are nine identical primary H atoms in iso-butane. At the elevated temperatures of shock tube conditions, the dominant reaction is the abstraction of a primary H atom, although at lower temperatures the abstraction of a tertiary H atom is most important. After abstraction of a primary H atom, the alkyl radical decomposition is primarily

$$i-C_4H_9 = C_3H_6 + CH_3$$
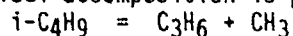
which results in chain termination. Only the t-butyl radical leads to chain branching through
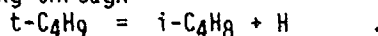
$$t-C_4H_9 = i-C_4H_8 + H \quad .$$

However, at the temperatures encountered in shock tubes, the production of isobutyl radicals is strongly preferred. The strong degree of chain termination which is the result of production of isobutyl radicals explains the slower rate of ignition for iso-butane.

Two practical combustion problems can be related to the rate of ignition of fuel-oxidizer mixtures under shock tube conditions. The first of these concerns the ignition of fuels in detonation waves. Previous modeling analysis[10] has shown how shock tube ignition delay times can be related to detonation properties including detonation limits, critical tube diameters, and minimum energy for initiation of detonation. Overall, these results indicate that branched chain hydrocarbon fuels should be less detonable than their straight chain counterparts. Specifically, methane is predicted to be much less detonable than the other fuel-oxidizer mixtures, which is certainly well established experimentally. In addition, the detonation parameters of the other n-alkane fuels are predicted to be very similar to each other, also in agreement with experimental observations. Although not available for comparison with experimental results, the model predicts that iso-butane mixtures should be less susceptible to detonation than the n-alkane mixtures.

The second application area in which ignition calculations are of particular interest is that of engine knock. In previous modeling studies of engine knock[11,12], it has been shown that the rate of ignition of fuel-air mixtures at elevated pressures can be related to the susceptibility of a mixture to engine knock. It is well known that straight chain fuels are more likely to knock than are branched chain fuels, and the present reaction mechanism indicates that these differences are due to differences in the product channels for the alkyl radicals which are produced. At the elevated pressures encountered in knocking engines, H atoms produced from ethyl radicals do not decompose into H atoms but rather react with O_2 molecules to produce HO_2 radicals. These radicals then react further with the fuel to produce H_2O_2 which then decomposes further to produce two OH radicals

$$H_2O_2 + M = OH + OH + M \quad .$$
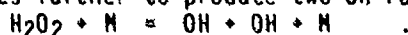
The result of this sequence is a net production of radical species and an increase in the rate of fuel oxidation. At the high pressures which are typical of engine knock, the production of HO_2 is preferred in comparison to the chain branching reaction producing O + OH, and the rate of fuel oxidation is more sensitive to variations in the abstraction of H atoms by HO_2 than the abstraction of H atoms by other radicals such as OH, H and O.

CONCLUSIONS

The reaction mechanism which has been developed in earlier modeling studies has been shown to be applicable to the shock tube ignition of a family or hydrocarbon-air mixtures. This mechanism correctly reproduces the observed shock tube ignition delay times reported by Burcat et al.[1] for a fairly wide range of hydrocarbon fuels. Since the mechanism has been so extensively tested for hydrocarbon ignition, it can be applied to other studies of shock tube ignition of fuel-air mixtures. Even more important, these reaction mechanisms, validated through comparisons with shock tube experiments, have been shown to be applicable to a variety of important and practical combustion environments. The shock tube data therefore provide an essential means of testing detailed reaction mechanisms under coditions that are impossible to achieve under other conditions. The relationships between shock tube conditions and detonation phenomena and engine knock problems make the study of shock tube phenomena of particular importance, and the present paper outlines the essential elements of these reaction mechanisms. Extension of the present formalism to more complex fuels should be very straightforward, given the fundamental basis provided by the reaction mechanisms for the more simple fuels discussed in this paper.

REFERENCES

1. Burcat, A., Scheller, K., and Scheller, K., Combustion and Flame 16, 29 (1971).

2. Pitz, W. J., Westbrook, C. K., Proscia, W. M., and Dryer, F. L., Twentieth Symposium (International) on Combustion, in press (1985).

3. Dryer, F. L., and Glassman, I., In Alternative Hydrocarbon Fuels, Combustion and Kinetics, C. T. Bowman and J. Birkeland, Eds., AIAA, New York (1979).

4. Westbrook, C. K., Pitz, W. J., and Dryer, F. L., manuscript in preparation (1985).

5. Lund, C. M., Lawrence Livermore Laboratory Report UCRL-52504 (1978).

6. Westbrook, C. K., Combust. Sci. Tech. 20, 5 (1979).

7. Westbrook, C. K., and Pitz, W. J., Combust. Sci. and Tech. 37, 117 (1984).

8. Westbrook, C. K., and Pitz, W. J., Proceedings of the National American Chemical Society meeting, April 1985.

9. Westbrook, C. K., and Pitz, W. J., Combust. Sci. Tech. 33, 315 (1983).

10. Westbrook, C. K., Combust. Flame 46, 191 (1982).

11. Smith, J. R., Green, R. M., Westbrook, C. K., and Pitz, W. J.,
Twentieth Symposium (International) on Combustion, in press (1985).

12. Pitz, W. J., and Westbrook, C. K., Combust. Flame, in press (1985).

FIGURE CAPTIONS

1. Comparison between computed (lines) and experimental (symbols)
ignition delay times for stoichiometric fuel-oxygen-argon mixtures at an
initial density of 3.54 x 10^{-3} gm/cm^3. Triangles indicate results for
methane, solid circles show propane, and squares show n-butane.

2. Comparison between computed (lines) and experimental (symbols)
ignition delay times for stoichiometric fuel-oxygen-argon mixtures at an
initial density of 3.54 x 10^{-3} gm/cm^3. Open squares indicate
experimental results for n-butane, solid squares for n-pentane. No
experimental results were available for iso-butane.
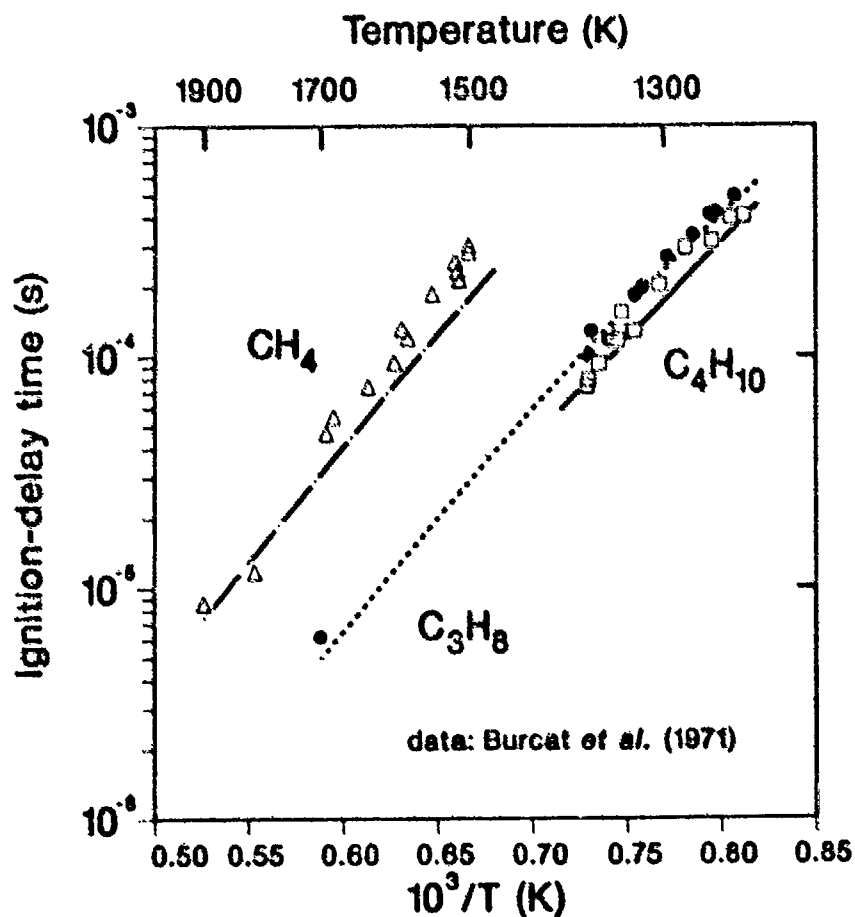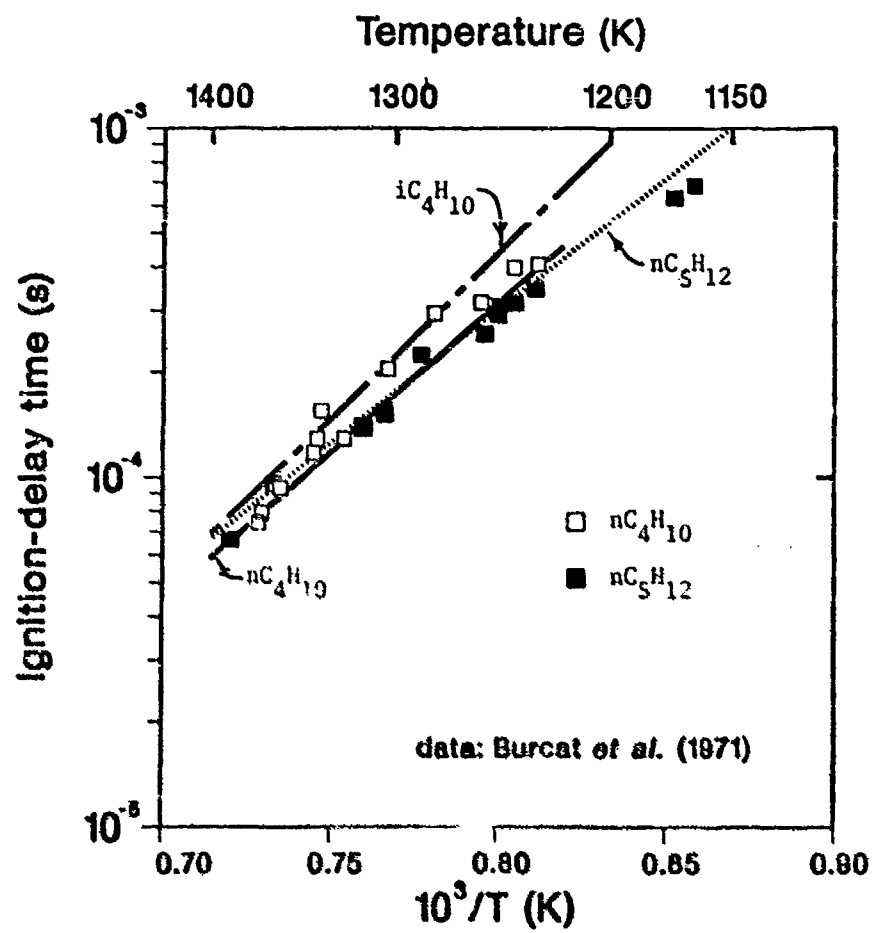
SHOCK-TUBE PYROLYSIS OF ACETYLENE: SENSITIVITY ANALYSIS

OF THE REACTION MECHANISM FOR SOOT FORMATION

M. Frenklach[*], D.W. Clary[#], W.C. Gardiner, Jr.[$] and S.E. Stein[+]

Department of Chemical Engineering
Louisiana State University
Baton Rouge, Louisiana 70803, USA

[*] Address correspondence to: M. Frenklach, Fuel Science Program,
Department of Materials Science and Engineering, Pennsylvania State
University, University Park, PA 16802, USA
[#] Currently at Ethyl Corporation, Baton Rouge, LA 70821
[$] Chemistry Department, University of Texas, Austin, TX 78712
[+] Chemical Kinetics Division, NBS, Washington, D.C.

The effects of variation in thermochemical data on
model prediction of soot yields in shock-tube
pyrolysis of acetylene and on the dominant reaction
pathway to soot identified in a previous study are
investigated. The computational results demonstrate
that the accuracy of thermodynamic data is as
important as that of rate coefficients in modeling of
high-temperature kinetics.

INTRODUCTION

Recently, we presented a detailed chemical kinetic mechanism of [1-3]
soot formation under the conditions of shock-tube pyrolysis of acetylene.
The model correctly accounts for the time and temperature dependences observed
experimentally[4] except for a mismatch in the temperature of the soot-yield
maximum. We suggested,[1] on basis of computational results demonstrating the
sensitivity of species concentrations to both rate coefficients and
thermodynamic parameters, that the mismatch is probably due to uncertainties
in thermochemical data. This suggestion is supported by the results of a
recent modeling study[5] which determined that inclusion of coagulation and
surface growth does not significantly affect computed soot yields at short
reaction times.

In the present work, the effect of thermodynamic parameters on the
model prediction for soot yield is systematically investigated. the influence
of changes in thermodynamic data on the dominant reaction pathway to soot is
analyzed, and the sensitivity analysis is expanded.

COMPUTER EXPERIMENTS

All computer experiments in this work were performed using the model
developed in the previous study.[1-3] Briefly, the reaction mechanism has three
logical components: initiation - a set of reactions describing the initial
stages of acetylene pyrolysis; cyclization - reactions describing the
formation of larger molecules and radicals and eventually small aromatic
molecules and radicals; and polymerization - a description of the further
growth of aromatic rings.

The initiation set is composed of 21 reactions and is based on the mechanism of Tanzawa and Gardiner.[6] One reaction of their mechanism, namely

$$C_2H_2 + C_2H_2 = C_4H_3 + H \quad , \qquad\qquad (R2')$$
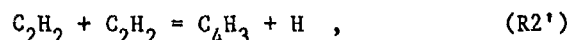
has been of particular concern. Originally, Tanzawa and Gardiner[7] introduced this reaction in an attempt to account for the rapid appearance of C_4H_3 in acetylene pyrolysis reported by Gay et al.[8] as well as to initiate chain reaction. We now recognize that the vinylacetylene radical, the structure assigned to the product of reaction (R2') in the previous work,[1] is so unfavored thermodynamically that no reactions could build up its concentration to a level that would have been observed in TOF mass spectrometric experiments; for example, no C_4H_3 or C_4H_4 was reported in a more recent TOF study.[9] Furthermore, computations performed during the course of this study at the experimental conditions of Tanzawa and Gardiner[7] indicated that replacing reaction (R2') by reaction

$$C_2H_2 + C_2H_2 = C_2H + C_2H_3 \qquad\qquad (R2)$$
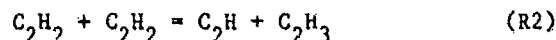
does not affect the computed laser-schlieren signals. Since reaction (R2') has never been identified by a direct experiment, it has been replaced for the rest of our study by a conceptually simpler, disproportionation reaction (R2), with a rate coefficient value for the reverse direction of 10^{13} cm^3 mol^{-1} s^{-1}.

The reactions of the cyclization and polymerization parts of the mechanism were grouped into classes.[1,3] The rate coefficient expression chosen for a prototype reaction within a class was assigned to the rest of the class. Thermodynamic properties were estimated using group additivity methods.[10,11] The computer experiments were performed at the same initial conditions as in the previous study,[1] that is, for a 1.09%C_2H_2-Ar mixture at ρ_5=3.8x10^{-5} mol/cm^3. The details of the calculations can be found in Refs. 1-3,10.

To test the effects of thermodynamic data, three basic and yet not well-established properties, namely C_2H-H and C_2H_3-H bond energies and the C_t-(C_t) group additivity value for ΔH°_{298}, were varied. Since in our work thermodynamic properties are estimated by group additivity methods, the variations in these basic values result in systematic, simultaneous variations in the properties of all the species. Six sets of thermodynamic data, S3 through S8, were constructed; they are shown in Table I. Also shown in Table I is set S2, which was used in our previous modeling of soot formation in acetylene systems.[12] Set S2 is the same as set S4 except for reaction (R2) being replaced by reaction (R2').

RESULTS AND DISCUSSION

Soot yields computed with the sets in Table I are shown in Fig. 1. As seen in this figure, replacement of reaction (R2') by reaction (R2) shifts the position of the soot-yield maximum by about 75 K to higher temperatures with a reduction in the maximum value of soot yield. Further examination of Fig. 1 reveals that: (a) a relatively small change in the C_2H-H bond energy strongly affects the temperature of the maximum and the absolute values of soot yield; (b) a change in the C_t-(C_t) group additivity value has a pronounced effect on the maximum value of the soot yield but not on its temperature location; and (c) variation in C_2H_3-H bond energy has no significant influence on the computed soot yields. Computer simulations performed at the conditions of the Tanzawa and Gardiner laser-schlieren experiments[7] resulted in longer induction

times and smaller maximum deflection values for sets S4, S5 and S7 compared to those for sets S3, S6 and S8. As mentioned earlier, no difference was obtained between cases S2 and S4.

It should be pointed out, however, that no decision can be made on which thermodynamic set is best based on the above analysis alone. The presented results identify computational trends. To determine the best-fit values, the entire acetylene pyrolysis mechanism must be reoptimized with respect to both thermodynamic and rate-coefficient data with all available experimental facts taken as constraints.

It is of interest, nevertheless, to analyze the effects of the changes in thermochemical data on the reaction mechanism. Inspection of the computational results revealed that for sets S2, S4, S5, S6, S7 and S8 the main reaction pathways to soot remain exactly as identified in our previous work. In the case of set S3, the dominant reactions leading to the formation of the first aromatic ring are
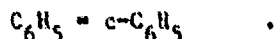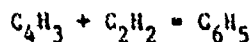
$$C_2H_3 + C_2H_2 = C_4H_5$$

$$C_4H_5 + C_2H_2 = C_6H_7$$

$$C_6H_7 = c\text{-}C_6H_7$$

$$c\text{-}C_6H_7 = c\text{-}C_6H_6 + H \qquad ,$$
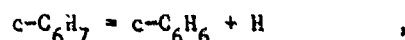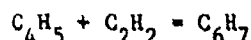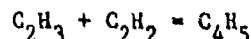
which are different from those in all other cases, namely

$$C_4H_5 = C_4H_4 + H$$

$$C_4H_4 + H = C_4H_3 + H_2$$

$$C_4H_3 + C_2H_2 = C_6H_5$$

$$C_6H_5 = c\text{-}C_6H_5 \qquad .$$

It should also be mentioned that the difference in the net rates of the dominant and minor routes of second-ring formation (see Fig. 1 in Ref. 1) is smaller for sets S3, S7 and S8 compared with that for the other sets. The ratio of the rates at 0.5 ms is a factor of 3 for set S3, 10 for S7 and 6 for S8; these ratios increase with reaction time.

Tables II and III present computed sensitivities. The sensitivities are defined as previously[1]

$$S_k^Y = \ln(Y_k/Y_0)/\ln(1/5) \quad \text{and} \quad S_k^Y = \ln(Y_k/Y_0)/\ln5,$$

where Y_0 is the soot yield computed for the 1.09% C_2H_2-Ar mixture at $\rho_5 = 3.80 \times 10^{-5}$ mol/cm^3, a reaction time of 0.5 ms, and at the temperature of the corresponding soot-yield maximum: 1675 K for set S2, 1975 K for set S3 and 1750 K for set S4. Y_k and Y_k are the soot yields computed at the same conditions but with the rate coefficient reduced by a factor of 5 and with the equilibrium constant increased by a factor of 5, respectively, for a given reaction (Table III) or reaction class (Table II). The reactions and reaction classes omitted have absolute sensitivity values less than 0.005. The pR values in Table III are defined in the usual manner.[13] Their values are given at two reaction times, 0.3 and 0.5 ms.

Table II presents the sensitivities computed with sets S2, S3 and S4. The results indicate that a change in thermodynamic data affects the sensitivity values. For some reaction classes the influence is significant; however, the relative ranking of the sensitivity values is not changed much. It should be pointed out that an analysis at fixed conditions can be incomplete. This is illustrated by Fig. 2, which depicts a sensitivity analysis performed for a single reaction class, class 30, but over the entire temperature range. As seen in the figure, a change in the equilibrium constant, K_{30}, not only increases the soot yields, but also shifts the temperature of the maximum.

The sensitivity information for the initiation reactions is given in Table III. There are only a few reactions with large sensitivity values, the largest being that of reaction (R6). The reason for this is that (R6) and (R7) constitute the fastest reaction chain, which controls the concentration of hydrogen atoms (and C_2H radical).[3] The rate of this chain is determined by the reverse reaction of (R6), because its rate coefficient is much smaller than that of the forward reaction of (R7).[13] Decreasing the rate coefficient of the latter does not affect the reaction rate but increases the concentration of C_2H, which explains the negative value of the sensitivity for reaction (R7). The surprisingly high sensitivity for reaction (R10) is due to the additional hydrogen atoms produced by the branching sequence (R10) and (R12); hydrogen atoms were identified as a dominant factor in polymerization kinetics of soot formation.[1,3,12] However, production of hydrogen atoms by reaction (R10) occurs only during the initial (induction) period of the pyrolysis, with the most significant contribution taking place during soot inception, after which the reaction proceeds in reverse, as follows from the pR values in Table III.

CONCLUSION

It is demonstrated that both the magnitude and the temperature location of the soot-bell maximum are affected by variations in thermochemical data. It is important to note that the chemical reaction pathway to soot remains basically unchanged with these variations. This observation supports the reaction mechanism for soot formation suggested by us recently.[1-3] A more general conclusion to be drawn from the results of this and previous work[1,3,12] is that the accuracy of thermodynamic data is as important as that of rate coefficients in modeling of high-temperature chemical kinetics. It would take more rigorous modeling and experimental efforts to determine the required basic parameters with sufficient precision to allow a closer comparison between theory and experiment.

REFERENCES

1.   Frenklach, M., Clary, D.W., Gardiner, W.C., Jr. and Stein, S.E., **Twentieth Symposium (International) on Combustion**, in press.

2.   Frenklach, M. and Gardiner, W.C., Jr., J. **Phys. Chem.**, 88, 6263 (1984).

3.   Frenklach, M., Clary, D.W. and Ramachandra, M.K., "Shock Tube Study of the Fuel Structure Effects on the Chemical Kinetics Mechanisms Responsible for Soot Formation. Part II," NASA Report No. CR-174880, 1985.

4.   Frenklach, M., Taki, S., Durgaprasad, M.B. and Matula, R.A., **Combust. Flame**, **54**, 81 (1983).

5.   Frenklach, M. and Harris, S.J., to be published.

6.   Tanzawa, T. and Gardiner, W.C., Jr., **J. Phys. Chem.**, **84**, 236 (1980).

7.   Tanzawa, T. and Gardiner, W.C., Jr., **Seventeenth Symposium (International) on Combustion**, The Combustion Institute, Pittsburgh, 1979, p. 563.

8.   Gay, I.D., Kistiakowsky, G.B., Michael, J.V. and Niki, H., **J. Chem. Phys.**, **43**, 1720 (1965).

9.   Kern, R.D., Singh, H.J., Esslinger, M.A. and Winkeler, P.W., **Nineteenth Symposium (International) on Combustion**, The Combustion Institute, Pittsburgh, 1982, p. 1351.

10. Stein, S.E. and Fahr, A., **J. Phys. Chem.**, to be published.

11. Benson, S.W., **Thermochemical Kinetics**, Wiley, New York, 1976.

12. Frenklach, M., Clary, D.W., Yuan, T., Gardiner, W.C., Jr. and Stein, S.E., to be published.

13. Frenklach, M., in **Combustion Chemistry** (W.C. Gardiner, Jr., Ed.), Springer-Verlag, New York, 1984, Chap. 7.

Table I.   Sets of Thermodynamic Data

Set No.	Bond Energy, kJ/mol		$C_t - (C_t)$ Group Value $\Delta H^\bullet_{298}$, kJ/mol	$C_2H_2 + C_2H_2$ Reaction Used
	$C_2H_3 - H$	$C_2H - H$		
S2	452	502	107	R2'
S3	452	552	107	R2
S4	452	502	107	R2
S5	452	502	125	R2
S6	452	552	125	R2
S7	427	502	107	R2
S8	427	552	107	R2

Table II.   Sensitivities of Soot Yield with Respect to Rate Coefficients
and Equilibrium Constants for Reaction Classes

Reaction Class	S_k^Y			S_K^Y		
	S2	S3	S4	S2	S3	S4
1	-0.09	-0.01	-0.07	0.09	0.01	0.07
2	0.00	0.04	0.00	0.00	0.00	0.00
3	0.05	0.30	0.04	-0.18	-0.32	-0.21
5	-0.01	0.07	-0.01	0.02	-0.08	0.02
8	-0.15	-0.37	-0.02	0.89	1.28	0.97
13	0.00	-0.27	-0.02	0.97	1.65	1.03
20	0.00	0.02	0.01	0.00	0.01	0.00
21	0.00	-0.01	-0.01	0.00	0.00	0.00
23	2.45	1.05	2.38	0.19	0.10	0.32
24	0.11	-0.01	-0.13	0.11	0.01	0.13
25	0.76	0.34	0.85	-1.16	-0.50	-1.35
27	1.34	1.18	1.66	0.29	1.03	0.34
29	-0.03	-0.05	-0.01	0.00	0.00	0.00
30	0.45	0.53	0.62	1.03	2.10	1.01

Table III.   Sensitivities of Soot Yield with Respect to Rate Coefficients and
Equilibrium Constants for Initiation Reactions with Set S4

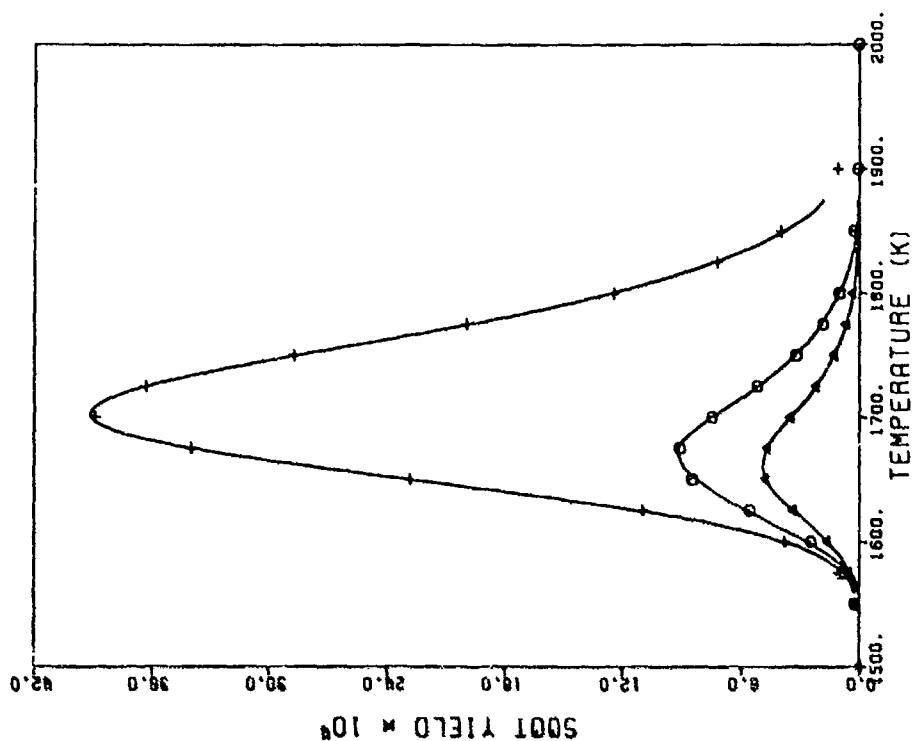| No.	Reaction	S_k^Y	S_K^Y	ρR_{300}	ρR_{500}
R1	$C_2H_2 + M = C_2H + H + M$	0.29	0.00	16.00	-15.23
R2	$C_2H_2 + C_2H_2 = C_2H_3 + C_2H$	0.03	0.00	15.27	-14.43
R3	$C_2H_2 + H = C_2H_3$	0.00	-0.01	18.10	17.68
R6	$C_2H + H_2 = C_2H_2 + H$	3.49	-3.49	-19.87	-19.86
R7	$C_2H_2 + C_2H = C_4H_2 + H$	-0.41	0.00	19.87	19.81
R10	$C_4H_2 + M = C_4H + H + M$	2.83	0.57	18.35	-17.03
R11	$C_4H_2 + C_2H = C_6H_2 + H$	-0.04	-0.05	18.02	18.81
R12	$C_4H + C_2H_2 = C_6H_2 + H$	0.17	0.13	18.36	18.62
R16	$C_6H_2 + M = C_6H + H + M$	0.00	0.01	16.06	-16.89

Figure 2. Soot yields versus temperature computed at a reaction time of 0.5 ms: middle curve - with set S2, upper - K_{30}x5, lower - k_{30}/5.
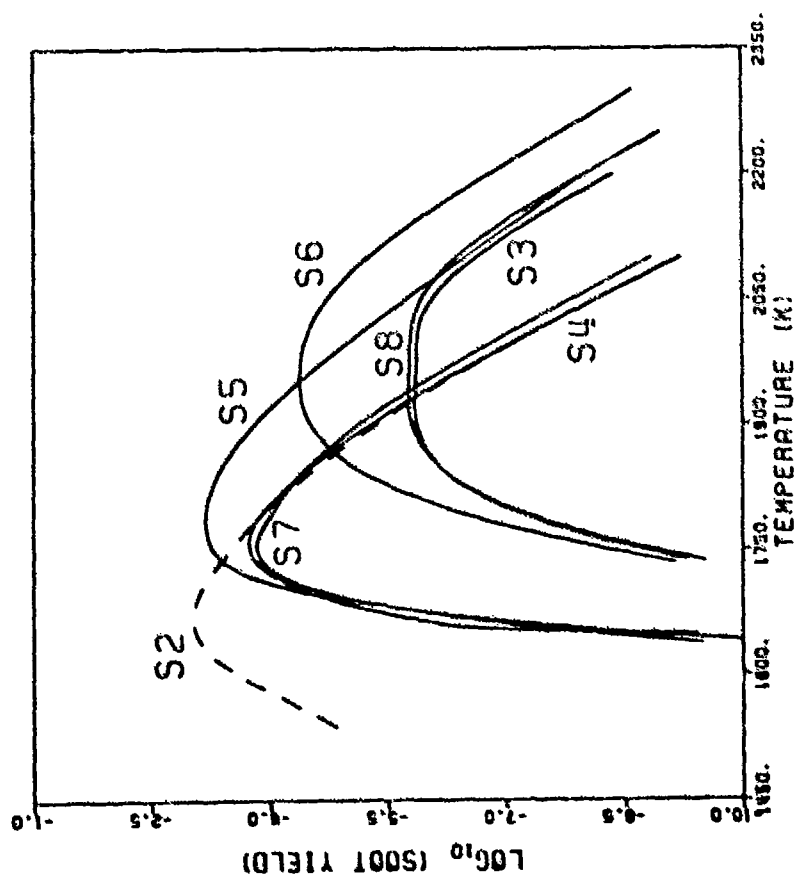

Figure 1. Soot yields versus temperature computed with thermodynamic data sets in Table I for a reaction time of 0.5 ms.

EMPIRICAL MODELING OF SOOT FORMATION
IN SHOCK-TUBE PYROLYSIS OF AROMATIC HYDROCARBONS

M. Frenklach, D. W. Clary and R. A Matula

Department of Chemical Engineering
Louisiana State University
Baton Rouge, Louisiana 70803

A method for empirical modeling of soot formation
during shock-tube pyrolysis of aromatic hydrocarbons is
developed. The method is demonstrated using data
obtained in pyrolysis of argon-diluted mixtures of
toluene behind reflected shock waves. The developed
model is in good agreement with experiment.

INTRODUCTION

The ability to predict the amount of soot formed under various experimental
conditions is one of the challenging problems for combustion science. Although
detailed modeling[1] will play an increasingly important role in the development
of this predictive ability, empirical models are still necessary. Empirical
models allow one to summarize the abundant experimental data on soot formation
in a systematic manner; to predict soot yield within the range of experimental
conditions for which the model was developed and, within this limitation, to be
used for design and optimization of practical combustion devices; and to serve
as constraints for the development of detailed models[2]. It is of interest to
consider the correlation of soot yields for transient rather than steady-state
conditions. A purely analytical approach to modeling of soot formation in
thermal decomposition of hydrocarbons was proposed by Gordiets et al.[3]; however,
they pointed out the presence of a "marked divergence between theory and experi-
ment".

In this paper, a quantitative approach to empirical modeling of soot forma-
tion is presented. The objective is to predict soot yield for a given reaction
time at various temperatures, pressures, initial reactant concentrations and
eventually various fuels. The approach is introduced by considering soot forma-
tion during shock-tube pyrolysis of toluene.

EXPERIMENTAL

Toluene - argon mixtures were pyrolyzed behind reflected shock waves in a
conventional shock-tube. The soot conversion was determined by measuring the
attenuation of a He-Ne laser beam at 632.8 nm. The details of the experimental
apparatus and procedures used in this study are described in previous works[4,5].
The results from five series of experiments were used for the development of the
empirical model. The experimental conditions are summarized in Table I.

DERIVATION

The empirical model is postulated as

$$A \xrightarrow{k_f} X_0 \qquad\qquad \text{fragmentation}$$

$$A + X_0 \xrightarrow{k_p} X_1$$

$$A + X_i \xrightarrow{k_p} X_{i+1} \quad , \quad i = 1, 2,\ldots, \qquad \text{polymerization} \qquad (1)$$
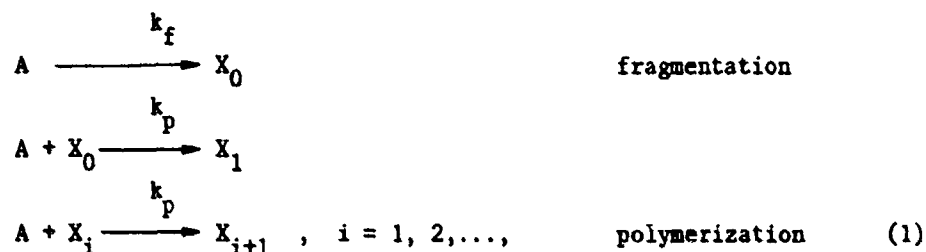
which is the mathematically simplest kinetic scheme that has all the features of
the conceptual model for soot formation in pyrolysis of aromatic hydrocarbons[5].
Reactant A in the mechanism denotes a species with an intact aromatic ring and
X_i denotes the i-th intermediate. The reactions are assumed to be irreversible;

this does not necessarily eliminate the thermodynamic resistance identified by
detailed modeling[1] - since the model is empirical by definition, this resistance
will be reflected in the parameter values. If the reversibility were included
explicitly, no analytical solution of the resulting differential equations would
be possible.

Species X_k, X_{k+1}, ... of the system constitute what we will call soot.

$$\text{The soot yield is defined as} \quad Y = \sum_{i=k}^{\infty} (i+1)\{[X_i]/[A]_0\} \qquad (2)$$

where: Y   is the soot yield;

   $[X_i]$ is the concentration of species X_i;

   $[A]_0$ is the initial concentration of A.

Defined in this manner, the soot yield is the fraction of fuel initially present
which is converted to soot. The (i+1) in Eq. (2) accounts for the number of
molecules of A "contained" in X_i.

The objective is to derive an expression for Y as a function of experi-
mental parameters. The differential equations for the reaction system (1) take
the form of

$$\frac{d[A]}{dt} = - k_f[A] - \sum_{j=0}^{\infty} k_p[A][X_j]$$

$$\frac{d[X_0]}{dt} = k_f[A] - k_p[A][X_0]$$ $$(3)$$

$$\frac{d[X_i]}{dt} = k_p[A][X_{i-1}] - k_p[A][X_i], \quad i = 1,2,\ldots,$$

with the initial conditions
$$[A]_{t=0} = [A]_0 \text{ and } [X_i]_{t=0} = 0, \quad i = 0,1,2,\ldots \ .$$

Introducing the "dimensionless concentrations"
$$a \equiv [A]/[A]_0 \quad \text{and} \quad x_i \equiv [X_i]/[A]_0, \quad i = 0,1,2,\ldots,$$

dividing both sides of each differential equation (3) by $k_f a$, and substituting,
as discussed by Holland and Anthony[6],
$$k_f a dt = d\tau \qquad (4)$$

we obtain
$$\frac{da}{d\tau} = -1 - \sum_{j=0}^{\infty} x_j/r \tag{5a}$$

$$\frac{dx_0}{d\tau} = 1 - x_0/r$$

$$\frac{dx_i}{d\tau} = x_{i-1}/r - x_i/r , \qquad i = 1,2,\ldots \tag{5b}$$

with the initial conditions
$$a\Big|_{\tau=0} = 1 \text{ and } x_i\Big|_{\tau=0} = 0, \qquad i = 0,1,2,\ldots, \tag{5c}$$

where: $\quad r = k_f/(k_p[A]_0)$. $\tag{6}$

The resultant system (5b) is composed of linear ordinary differential equations and it can be readily shown that the solution is:
$$x_i \equiv [X_i]/[A]_0 = r\, P(i+1,\, \tau/r), \qquad i = 0,1,2,\ldots, \tag{7}$$

where:
$$P(i+1,\, \tau/r) = \frac{1}{i!} \int_0^{\tau/r} e^{-u} u^i du$$

is the incomplete Gamma function[7]. It can be noted that $\sum_{i=0}^{\infty} x_i = \tau$ $\tag{8}$

as is demonstrated below:

$$\sum_{i=0}^{\infty} x_i = \sum_{i=0}^{\infty} r\, P(i+1,\, \tau/r) = r \sum_{i=0}^{\infty} \frac{1}{i!} \int_0^{\tau/r} e^{-u} u^i du$$

$$= r \sum_{i=0}^{\infty} \int_0^{\tau/r} \frac{e^{-u} u^i}{i!}\, du = r \int_0^{\tau/r} \Big(\sum_{i=0}^{\infty} \frac{e^{-u} u^i}{i!} \Big) du = r \int_0^{\tau/r} du = \tau,$$

since by definition of the Poisson distribution[9]

$$\sum_{i=0}^{\infty} \frac{e^{-u} u^i}{i!} = 1.$$

Substituting (8) into (5a), we obtain
$$\frac{da}{d\tau} = -1 - \tau/r,$$

the solution of which, taking into account the initial conditions (5c), is
$$a = 1 - \tau - \tau^2/2r . \tag{9}$$

Substituting (9) into (4), and integrating, we obtain

$$\tau = \frac{r(1 - e^{qk_f t})}{\frac{1}{\lambda_2} - \frac{1}{\lambda_1} e^{qk_f t}} , \tag{10}$$

where: $\quad \lambda_1 = -1 + q, \quad \lambda_2 = -1 - q; \quad$ and $\quad q = \sqrt{1 + 2/r};$

Expression (10) relates the "transformed time" τ, the physical meaning of which is disclosed through equality (8), with the real time t. Hence, substitution of (6) and (10) into (7) and (9) determines the kinetic behavior of reaction system (1).

Let us rewrite expression (2) as

$$Y = \sum_{i=\kappa}^{\infty} (i+1)x_i = \sum_{i=0}^{\infty} (i+1)x_i - \sum_{i=0}^{\kappa-1} (i+1)x_i \tag{11}$$

where the first sum on the right-hand side of this expression is:

$$\sum_{i=0}^{\infty} (i+1)x_i = \sum_{i=0}^{\infty} ix_i + \sum_{i=0}^{\infty} x_i. \tag{12}$$

As seen in (8), $\sum_{i=0}^{\infty} x_i$ equals τ. For the second term we obtain

$$\sum_{i=0}^{\infty} ix_i = \sum_{i=1}^{\infty} i \cdot r\, P(i+1, \tau/r) = r \sum_{i=1}^{\infty} i \cdot \frac{1}{i!} \int_0^{\tau/r} e^{-u} u^i du$$

$$= r \sum_{i=1}^{\infty} \int_0^{\tau/r} \frac{e^{-u} u^i}{(i-1)!} du = r \int_0^{\tau/r} \left(\sum_{i=1}^{\infty} \frac{e^{-u} u^i}{(i-1)!} \right) du$$

$$= r \int_0^{\tau/r} u \left(\sum_{j=0}^{\infty} \frac{e^{-u} u^j}{j!} \right) du = r \int_0^{\tau/r} u\, du = \tau^2/2r$$

where: $j = i-1$ and $\sum_{j=0}^{\infty} \frac{e^{-u} u^j}{j!} = 1.$

That is, $\sum_{i=0}^{\infty} (i+1)x_i = \tau + \tau^2/2r$. $\tag{13}$

In order to determine the second sum on the right-hand side of expression (11), let us recall one of the properties of the incomplete Gamma function[7],

i.e. $$P(i+1, \tau/r) = P(i, \tau/r) - \frac{e^{-\tau/r}(\tau/r)^i}{i!}$$

or $$P(i+1, \tau/r) = 1 - \sum_{j=0}^{i} \frac{e^{-\tau/r}(\tau/r)^j}{j!} \quad .$$

Therefore, using expression (7), $x_i = r \left[1 - \sum_{j=0}^{i} \frac{e^{-\tau/r}(\tau/r)^j}{j!} \right]$

and then $$\sum_{i=0}^{\kappa-1} (i+1)x_i = \sum_{i=0}^{\kappa-1} (i+1)r \left[1 - \sum_{j=0}^{i} \frac{e^{-\tau/r}(\tau/r)^j}{j!} \right]$$

$$= r \left[\sum_{i=0}^{\kappa-1} (i+1) - \sum_{i=0}^{\kappa-1} (i+1) \sum_{j=0}^{i} \frac{e^{-\tau/r}(\tau/r)^j}{j!} \right]$$

$$= r \left[\frac{\kappa(\kappa+1)}{2} - \sum_{i=0}^{\kappa-1} \frac{(i+1+\kappa)(\kappa-i)}{2} \frac{e^{-\tau/r}(\tau/r)^i}{i!} \right] \quad . \tag{14}$$

Thus, substituting (13) and (14) into (11), we obtain

$$Y = r \left[\tau/r + \tau^2/2r^2 - \frac{\kappa(\kappa+1)}{2} + \sum_{i=0}^{\kappa-1} \frac{(i+1+\kappa)(\kappa-i)}{2} \frac{e^{-\tau/r}(\tau/r)^i}{i!} \right] . \tag{15}$$

RESULTS AND DISCUSSION

Expression (15) together with relationships (6) and (10) constitute an empirical model for soot formation which contains 3 unknowns: κ, k_f, and k_p. A general approach for fitting the model would be to minimize

$$\sum_{i,t} (Y_{calc,i,t} - Y_{expt,i,t})^2, \tag{16}$$

where $Y_{expt,i,t}$ and $Y_{calc,i,t}$ are the experimentally observed and the calculated soot yields for the i-th experiment at observation time t. It was desirable that the modeling results not depend on the refractive index, the value of which is not well-established[5]. Therefore, instead of minimizing the objective function (16), we minimized $\sum_{i,t} (Y_{calc,i,t}/Y^*_{calc} - Y_{expt,i,t}/Y^*_{expt})^2$, (17) where Y^*_{expt} is the experimental soot yield at specified reference conditions and Y^*_{calc} is the soot yield calculated by Eq. (15) at these conditions. The reference conditions were chosen as the 0.311% C_7H_8-Ar mixture at T = 1977 K, ρ = 1.54 x 10^{-5} mol/cm^3 and time = 1.0 ms.

Since the present modeling is empirical in nature, meaning the goal is simply to fit experimental data, the objective function for minimization (17) can be rewritten as

$$\sum_{i,t} [(Y/Y^*)_{calc,i,t} - (Y/Y^*)_{expt,i,t}]^2. \tag{18}$$

The form of expression (18) implies that $(Y/Y^*)_{calc}$ should be considered as a single entity and no physical meaning should be attached to Y_{calc} or Y^*_{calc} alone. That is, the empirical model predicts relative values and in order to obtain the absolute value of soot yield at given conditions one must multiply the corresponding $(Y/Y^*)_{calc}$ by the actual soot yield at reference conditions, Y^*_{expt}. One way to estimate the value of Y^*_{expt} is to use the relationship $Y^*_{expt} \cdot E(m) = 10.11$; this method requires one to choose a value for the complex refractive index, m. The quantity E(m) is defined[9] as $E(m) = -Im[(m^2-1)/(m^2+2)]$ and the number 10.11 is an experimental result determined in this work.

After several trials, the following forms for the rate constants were assumed

$$k_f = A \exp(-\theta_f/T)\rho^\alpha \quad \text{and} \quad k_p = B \exp(-\theta_p/T)\rho^\beta[A]_0^\gamma$$

where: T   is the initial reaction temperature in K;
          ρ is the total density in mol/cm^3;
          $[A]_0$ is the initial concentration of toluene in mol/cm^3;
          the units of k_f and k_p are mole, cm^3 and s.

Thus there are 8 parameters to determine, namely A,B,θ_f,θ_p,α,β,γ and κ. Mini-

mizing expression (18) for all 5 toluene-argon series, the following results
were obtained:

$$A = 6.67 \times 10^{11} \qquad \theta_p = 6.47 \times 10^3$$
$$\theta_f = 2.38 \times 10^4 \qquad \beta^p = 0.139$$
$$\alpha^f = 0.858 \qquad \gamma = -0.413$$
$$B = 2.68 \times 10^{10} \qquad \kappa = 6 \quad \text{(assumed)}.$$

Although the quality of the fit was slightly better for $\kappa=3$, for physical
reasons[10] we assumed $\kappa=6$. Figures 1 and 2 compare the experimental and computed
values of Y/Y*. Figure 1 shows the time development and Fig. 2 the pressure
dependence of soot yields. A more complete discussion of the comparison of the
experimental and computed values can be found in Ref. 11.

It must be stressed that from the statement of the problem the model
developed here is _empirical_ in nature. Therefore, although the numerical values
of the obtained parameters can be rationalized conceptually (e.g., the differ-
ence of the temperature coefficients, $\theta_f - \theta_p$, is always a large positive number

regardless of the specific form assigned to the rate coefficients k_f and k_p;

this result is in accord with a recent conceptual model[5]), one should refrain
from assigning physical meaning to the parameter values of an empirical model[2,12].
The parameters would contain physical meaning only if reaction sequence (1) has
a strong physical basis.

ACKNOWLEDGEMENTS

REFERENCES

1.   Frenklach, M., Clary, D.W., Gardiner, W.C., Jr. and Stein, S.E. Detailed
     kinetic modeling of soot formation in shock-tube pyrolysis of acetylene.
     Twentieth Symposium (International) on Combustion, in press.
2.   Frenklach, M., in Combustion Chemistry (W.C. Gardiner, Jr., Ed.), Spring-
     Verlag, New York, 1984, Chap. 7.
3.   Gordiets, B. F., Shelepin, L. A. and Shmotkin, Yu. S. Combustion, Explosion,
     and Shock Waves 18, 189 (1982).
4.   Frenklach, M., Taki, S., Durgaprasad, M. B. and Matula, R. A. Combust.
     Flame 54, 81 (1983).
5.   Frenklach, M., Taki, S. and Matula, R. A. Combust. Flame 49, 275 (1983).
6.   Holland, C. D. and Anthony, R. G. Fundamentals of Chemical Reaction
     Engineering, Prentice-Hall, New Jersey, 1979, Chap. 10.
7.   Davis, P. J., in Handbook of Mathematical Functions (M. Abramowitz and I.A.
     Stegun, Eds.), Dover, New York, 1972, Chap. 5.
8.   Zelen, M. and Severo, N. C., in Handbook of Mathematical Functions (M.
     Abramowitz, and I.A. Stegun, Eds.), Dover, New York, 1972, Chap. 26.
9.   Graham, S. C., Homer, J. B. and Rosenfeld, J. L. J. Proc. Roy. Soc. Lond.
     A344, 259 (1975).
10. Bauer, S. H. and Zhang, L. M. 14th International Symposium on Shock Tubes
     and Waves, New South Wales University, Australia, 1983, p. 654.
11. Frenklach, M. Shock Tube Study of the Fuel Structure Effects on the
     Chemical Kinetic Mechanisms Responsible for Soot Formation. NASA Report
     CR-174661, 1984.
12. Côme, G.M., in Comprehensive Chemical Kinetics (C.H. Bamford and C.F.H.
     Tipper, Eds.), Elsevier, New York, 1983, Vol. 24, Chap. 3.

TABLE I.   Summary of Experimental Conditions

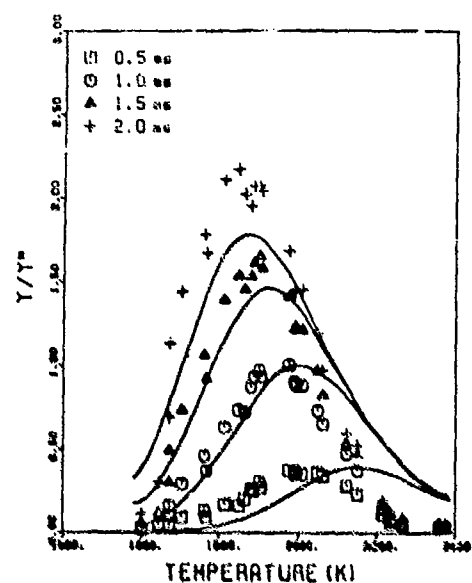| Series	Composition (Vol. % of Toluene in Argon)	T_5 (K)	P_5 (bar)	$[\text{Carbon}]_5 \times 10^{-17}$ (atoms/cm^3)
A	0.311	1600-2375	2.08-3.02	1.96-2.05
B	1.0	1529-2932	1.98-3.73	6.25-6.78
C	0.1	1647-2051	2.15-2.65	0.64-0.66
D	0.563	1463-2480	0.32-0.58	0.60-0.69
E	1.75	1668-2932	0.33-0.68	1.69-2.33

Fig. 1. Comparison of the model prediction with experimental observations for Series A. Time development. The symbols represent actual experimental points; the solid lines are the predicted values.
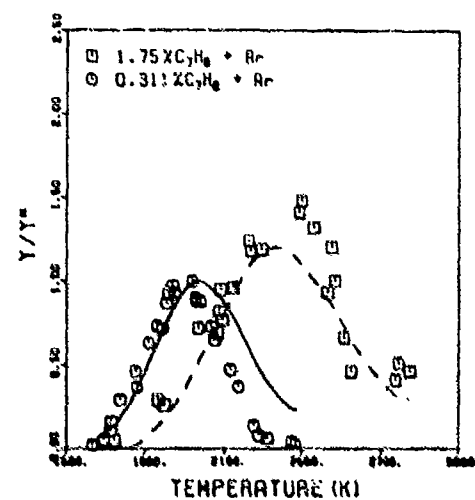
Fig. 2. Comparison of the model prediction with experimental observations for Series A and E. The effect of pressure. The symbols represent actual experimental points; the solid lines are the predicted values.

SINGLE-PULSE SHOCK TUBE EXAMINATION OF HYDROCARBON PYROLYSIS AND SOOT FORMATION

by

M. B. Colket, III
United Technologies Research Center
East Hartford, CT 06108

A single-pulse shock tube coupled to a capillary gas chromatograph has been used to observe the pyrolysis of a variety of hydrocarbons. Product species, mass balances, and H/C ratios of uncollected material have been determined. Relative "sooting" tendencies have been found to be toluene $\gtrsim$ benzene > allene > vinylacetylene $\gtrsim$ acetylene > 1,3-butadiene $\gtrsim$ cyclohexene for similar carbon-atom densities. A detailed chemical kinetic model has been constructed for the pyrolysis of acetylene and describes profiles of major species as well as the production of vinylacetylene, benzene and phenylacetylene.

Introduction

Shock tubes are frequently used for studying kinetics and mechanisms of both hydrocarbon pyrolysis and soot formation at conditions characteristic of diffusion flames. Single-pulse shock tubes (SPST) have been used perhaps most successfully for measuring rates of primary decomposition processes when fractional decomposition of the parent hydrocarbon is small[1]. Its applications to the study of soot may be limited by wall quenching and finite quenching in the rarefaction wave; but the potential for providing detailed species information with the aid of capillary gas chromatography has motivated the present research.

The ultimate goal of the experimental work is to provide data from which mechanisms of hydrocarbon pyrolysis and soot formation can be obtained. As part of that goal the relative tendency of different hydrocarbons to soot in a SPST is measured in this work. In addition, an objective of this paper is to extend a recent proposal[2] and present some results related to soot formation during the pyrolysis of acetylene. Specifically, experimental and modeling results on the production of vinylacetylene (VA), benzene, and phenylacetylene (PA) are shown.

Description of Facilities

The SPST used in this program is 258 cm long and has a diameter of 3.8 cm (i.d.). The driver is 88 cm in length and can be tuned by shortening its length in 3.8 cm increments; the driven section is 197 cm long. Pre-stressed aluminum diaphragms were used to control the rupture pressure. An 11.7 liter "dump tank" is located in the driver (lower pressure) section 30 cm downstream of the diaphragm. The pumping station is located at this tee. Pressure profiles were determined using Kistler pressure transducers located 15.25 and 2.50 cm from the end wall. Arrival times were determined to within one microsecond using

digitized pressure traces. Calculated quench rates are typically 10^5 K/sec in the rarefaction wave. Starting pressures prior to filling are 0.2μ and leak rates are less than 1μ/min. Post-shock temperatures were calculated based on the measured incident shock velocity and normal shock wave equations.

The procedures for performing an experiment are similar to those described by Tsang[1], except for an automated sampling system. The sample is collected at the endwall of the shock tube using 0.045 inch i.d. tubing heated to over 85 C. Approximately 30 milliseconds after the gas has been shock heated and cooled, a solenoid valve opens to the evacuated sample cell and then closes after 300 milliseconds. All valves and lines in this system have been degreased and rinsed in toluene to minimize condensation on the walls. The sample storage vessel is all stainless steel with an internal volume of 25 cc. Total internal volume of the remainder of the sampling system is less than 3 cc.

The sampling volume is directly coupled to a low volume, heated inlet system of a Hewlett Packard 5880 A gas chromatograph. Typical injection pressures are 0.5 atmospheres and are measured to within two percent using a calibrated pressure transducer. One gas sampling valve injects samples onto a 25 m x 0.33 mm i.d. CP Sil 5 CB (1 micron film thickness) fused silica capillary column (from Chrompack Inc.) followed by quantitative hydrocarbon analysis using a flame ionization detector. A second valve leads to a silica gel packed, stainless-steel column and a single-filament, modulated thermal conductivity detector for analysis of hydrogen. Valves, detectors and software integration routines enable this system to provide automatic quantitative detection of hydrogen and hydrocarbon species up to C_{10}-hydrocarbons. Based on repeated injections of calibrated samples, overall measurement accuracies are estimated to be approximately three percent. Calibration gases were stored in stainless steel cylinders with degreased valves and were heated to approximately 60C prior to injection.

Argon (99.999% pure) was obtained from Matheson and was the principal diluent. Other chemicals were at least 99.5% pure according to gas chromatographic analysis, except for vinylacetylene, allene, and acetylene. VA contained approximately 8000 ppm of an unidentified C_5-hydrocarbon. Allene was obtained from several different vendors yet was typically 87 to 93% pure with a variety of other C_3-hydrocarbons as impurities. Bulb-to-bulb distillation enhanced the purity level to approximately 97%. Similarly, the initial concentration of acetone in acetylene was reduced from approximately 2% of the initial acetylene to about 100 ppm.

Results

Toluene, benzene, cyclohexene, 1,3-butadiene, VA, allene, and acetylene have been pyrolyzed in a bath of argon. For each hydrocarbon, a series of shock tube runs were performed. Densities behind the reflected shock wave range were approximately 1.8×10^{18} carbon atoms/cc. Reflected shock temperatures and pressures ranged from approximately 1100 to 2500 K and 5 to 8 atmospheres, respectively. Dwell times were typically 550 to 800 microseconds although for the bulk

of runs, dwell times were close to 700 microseconds. Typical results
are shown in Figs. 1a and 1b for the pyrolysis of 1.17% benzene in
argon. Presented in these figures are the final product distribution
(for 18 separate shocks) after the test gas has been shock heated and
then quenched by the rarefaction wave. The general features, i.e.,
production of aromatics over the 1500 to 1900 K temperature range, and
the dominance of hydrogen and 'equilibrium' concentrations of the
acetylenes above 2200 K is apparent in virtually all fuels. For the
non-aromatic fuels, equilibrium concentrations are generally achieved
above 1900 to 2000 K. At temperatures below 1500 to 1600 K, the product
distribution is controlled by the kinetics of the decomposition of the
hydrocarbon parent.

Figure 1 exhibits a relatively large amount of hydrogen produced at
low temperatures. Modeling demonstrates that this 'low temperature'
hydrogen is principally formed via the sequence:

$$C_6H_6 \; ---> \; C_6H_5 + H$$
$$C_6H_5 + C_6H_6 \; ---> \; C_{12}H_{10} + H$$
$$H + C_6H_6 \; ---> \; C_6H_5 + H_2$$
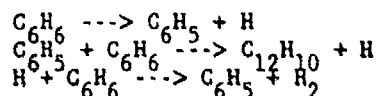
A comparable amount of biphenyl should be produced, yet is
unobserved due to its apparent loss during the sampling process or in
the inlet system to the gas chromatograph. The amount of carbon
converted to biphenyl at 1400 K would be approximately a few percent of
the total and is consistent with the measured mass balance. Total
hydrogen and carbon mass balances have been determined for the data in
Fig. 1 and are plotted in Fig. 2. Also shown are calculated H/C ratios
of the missing material. (Uncertainties in this calculation are
obviously large when either hydrogen or carbon are nearly fully
recovered.) At low temperatures, the ratio is in reasonable agreement
with the assumption that biphenyl (H/C = 0.825) or other small
multi-ringed compounds are produced. At higher temperatures, the H/C
ratio is very low, suggesting the formation of very large polynuclear
aromatics (PAH) or even soot. The low ratio of 0.1 observed in these
benzene experiments is atypical since for most other hydrocarbons, the
H/C ratio of the missing material ranges from 0.2 to 0.3 above 1700 K.
This difference between benzene and other hydrocarbons may not be
significant in light of the potential errors in calculating the H/C
ratios of the missing material.

The fractional mass recovered is a strong function of both the
concentration and the density of the parent hydrocarbon. The effect of
hydrocarbon type on mass balance is shown in Fig. 3. Assuming that the
mass loss is indicative of soot productions, the relative tendency to
soot is approximately toluene $\gtrsim$ benzene > allene > VA $\gtrsim$ acetylene >
1,3-butadiene $\gtrsim$ cyclohexene. The single-pulse shock tube data is in
excellent agreement with the relative tendencies to soot and with the
temperature dependence as determined using optical absorption[3]. The
detailed species profiles offer some insight to the relative sooting
tendencies. Production of aromatics, particularly PA, appears to be
critical. Allene, for example, produces large quantities of benzene and
PA. The conversion of allene to benzene is as high as 25% of the
initial carbon (and 4% to PA). If some benzene is converted to PAH and
possibly soot, then the actual production of benzene may be even larger.

Thus the "sooting" tendency of allene is quite similar to those of the aromatics. In comparison, only 9% of the initial butadiene carbon is converted to benzene and the production of PA is delayed (relative to its production during benzene or allene pyrolysis) by 100 to 150 K. The similarity in mass balance between acetylene and VA at elevated temperatures can be explained by the dominant overall chain process $C_4H_4 + H \rightarrow 2C_2H_2 + H$ apparent from the product distribution during VA pyrolysis. Also of interest are significant concentrations of PA, which are presumably formed via C_4H_3 addition to VA, followed by cyclization and H-atom loss. The production of PA near 1400-1700 K may lead to the significant mass deficit observed in this regime. The similarity between cyclohexene and butadiene is explained by the rapid unimolecular decay $c-C_6H_{10} \rightarrow 1,3-C_4H_6 + C_2H_4$ and the relatively low sooting tendency for C_2H_4 (ref. 3).

Detailed chemical kinetic modeling has been performed using Chemkin and a modified shock tube code originally developed at Sandia National Laboratories. The modified code includes the capability of modeling the quenching effect of the rarefaction wave in an SPST. The basic kinetic mechanism is similar to modifications[2,4] of a proposed mechanism[5] and as shown in Fig. 4 describes well the distribution of mono-, di-, and triacetylene. The production of VA, benzene and PA is indicated below:

	Log A	E(cal/mole)
$H + C_2H_2 \rightarrow C_2H_3$	12.74	2500.
$C_2H_3 + C_2H_2 \rightarrow NC_4H_5$	13.00	8000.
$NC_4H_5 \rightarrow C_4H_4 + H$	13.70	41400.
$NC_4H_5 + C_2H_2 \rightarrow C_6H_6 + H$	12.60	9000.
$NC_4H_3 + C_2H_2 \rightarrow C_6H_5$	12.48	5000.
$C_6H_5 + C_2H_2 \rightarrow C_8H_6 + H$	12.32	5600.

A in units of cc, moles, sec.

The selection of this reaction sequence and rate constants has been based on a combination of the SPST experimental results and pioneering work at other laboratories[2,6-8]. The experimental and modeling results compare well at low temperature, but suggest some revision may be required at temperatures above 1800 K.

References

1.   Tsang, W., Shock Waves in Chemistry, ed. by A. Lifshitz, Marcel
      Dekker, Inc., New York, pp. 59-129, 1981.
2.   Frenklach, M., Clary, D.W., Gardiner, W.C., Jr., and Stein, S.
      Twentieth Symposium (International) on Combustion, in press, The
      Combustion Institute, 1985.
3.   Frenklech, M. "Shock Tube Study of the Fuel Structure Effects on the
      Chemical Kinetic Mechanisms Responsible for Soot Formation", NASA
      CR-174661, Nov. 1983, also Frenklach, M., Clary, D.W. and
      Ramachandra, M.K., Part II, NASA CR-174880, May, 1985.
4.   Kiefer, J.H., Kapsalis, S.A., Al-Alami, M.Z., and Budach, K.A.,
      Combust. and Flame 51, 79 (1983).
5.   Tanzawa, T. and Gardiner, W.C., Jr., Combust. and Flame, 39, 241,
      (1980).
6.   Weissman, M. and Benson, S.W., Int'l. J. Chem. Kin. 16, 307 (1984.)
7.   Cole, J.A., Bittner, J.D., Longwell, J.P., and Howard, J.B., Comb.
      and Flame, 56, 51 (1984).
8.   Mallard, W.G., and Fahr, A., Stein, S.E., Chemical and Physical
      Processes in Combustion, 1984 Technical Meeting of Eastern Section of
      Combustion Institute, paper No. 92, Dec. 1984.
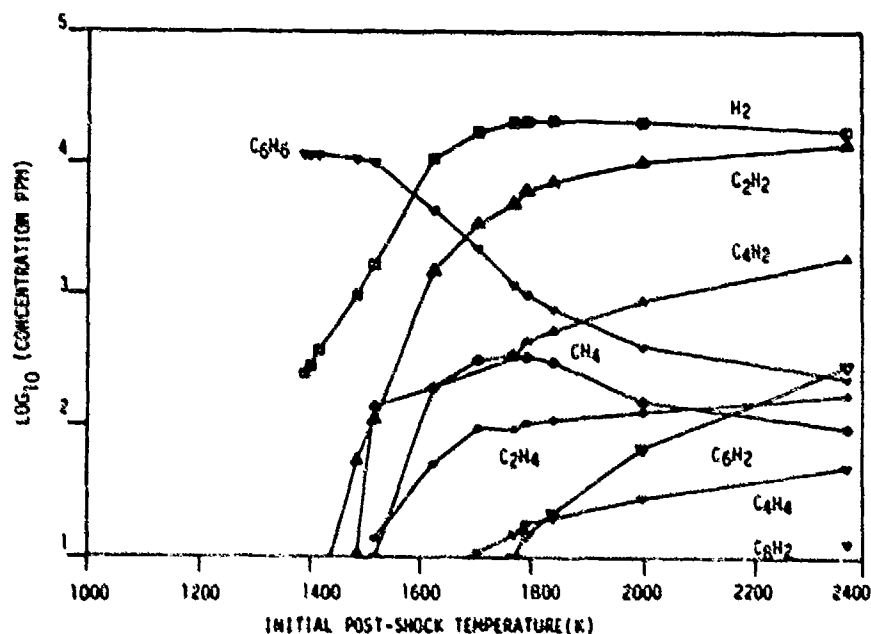

Fig. 1a SPST Pyrolysis of 1.17% Benzene at 6 atmospheres and for
         700 microseconds: distribution of aliphatic products.
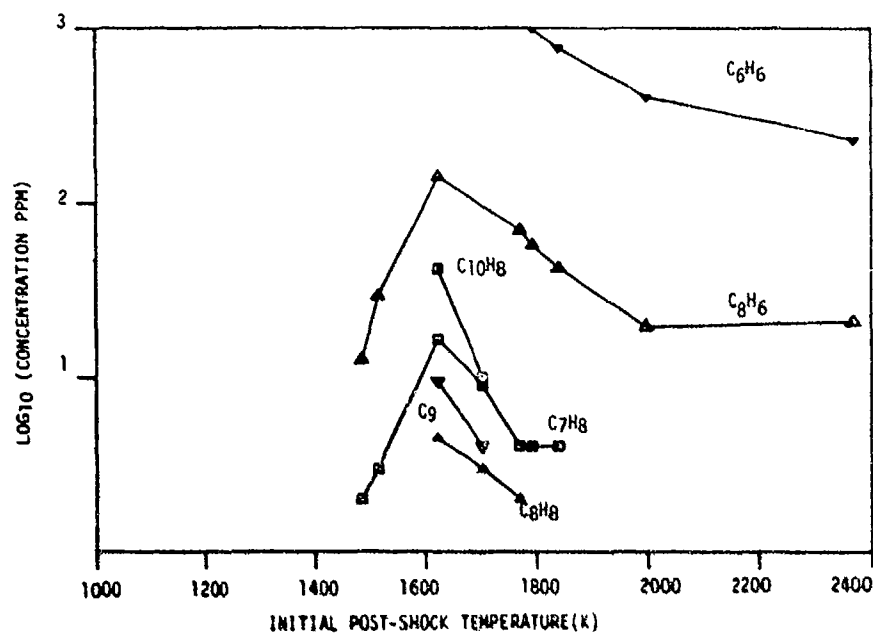
Fig. 1b   SPST Pyrolysis of 1.17% Benzene at 6 atmospheres and for
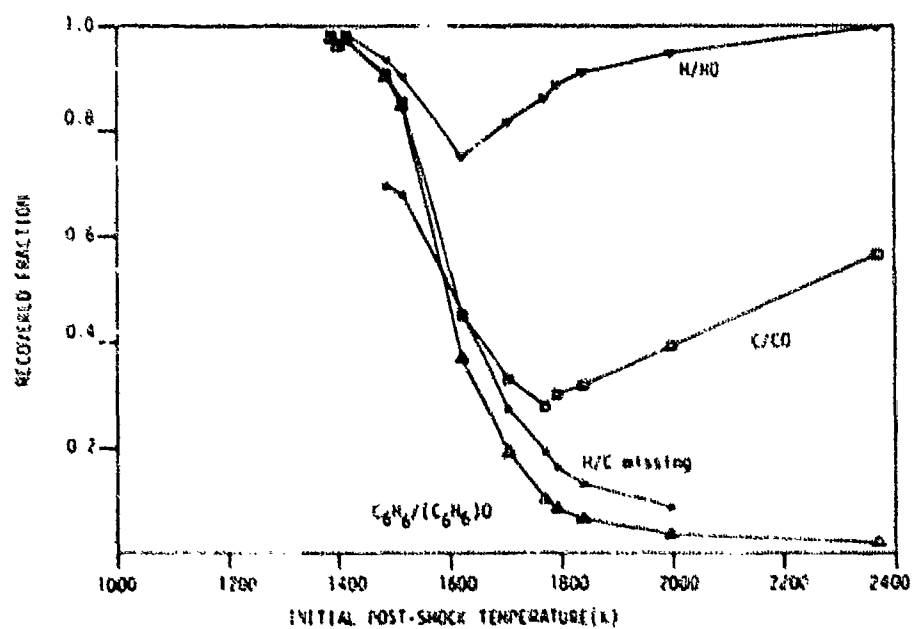700 microseconds: distribution of aromatic products.

Fig. 2   Fractional recovery of initial hydrogen, carbon, and benzene
during pyrolysis of 1.17% Benzene. Also shown is the calculated
hydrogen-to-carbon ratio of the uncollected mass.
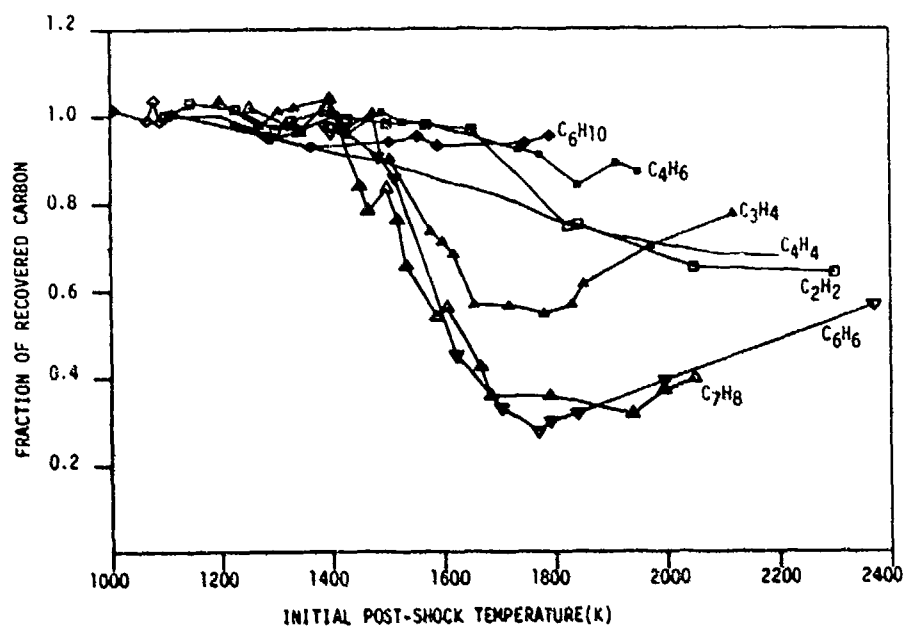
Fig. 3   Fractional carbon recovery for a variety of hydrocarbons at a
total pressure and carbon density of approximately 6 atmospheres
and 1.8×10^{18} carbon atoms/cc. $\triangle$-1.0% C_7H_8, ∇-1.2% C_6H_6
$\blacktriangle$-2.3% allene, —-1.75% C_4H_4, $\square$-3.7% C_2H_2, $\blacksquare$-1.75% 1,3-C_4H_6,
$\blacklozenge$-1% % C_6H_{10}. (C_4H_4 curve is an estimate based on runs at
dissimilar concentrations.)

Fig. 4   Experimental and model results for the pyrolysis of 3.7% acetylene.

SINGLE PULSE SHOCK TUBE STUDIES ON THE
STABILITY OF AROMATIC COMPOUNDS
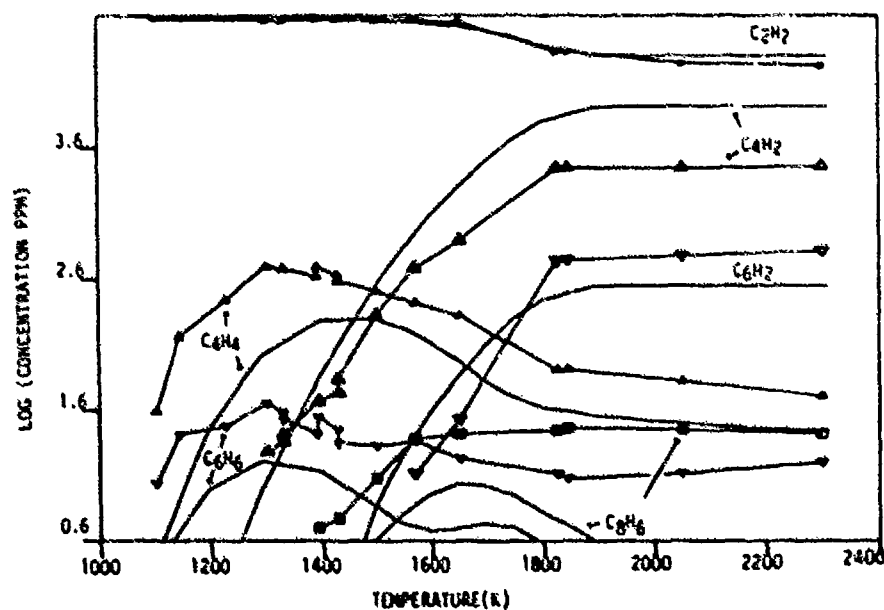
Wing Tsang and David Robaugh

Chemical Kinetics Division
National Bureau of Standards
Gaithersburg, MD 20899

ABSTRACT

Ethylbenzene, isopropylbenzene, phenyl iodide and nitrobenzene have been decomposed in single pulse shock tube experiments. Mechanisms and rates of the initial decomposition step have been determined. For the alkylbenzene compounds the initial reaction is in all cases the breaking of the benzylic C-C bond as opposed to the recent suggestion that benzylic C-H bond cleavage is the predominant process. In nitrobenzene decomposition the two important processes are C-NO$_2$ bond break and an isomerization process to form the nitrite followed by rapid cleavage of the O-NO bond. The branching ratio is approximately 2 to 1 in favor of C-NO$_2$ bond rupture at 1100K. The rate expressions for C-I and C-NO$_2$ bond cleavages are

$$k(C_6H_5I \Rightarrow C_6H_5{\cdot} + I{\cdot}) = 10^{14.9} \exp(-32800/T)/s$$

$$k(C_6H_5NO_2 \Rightarrow C_6H_5{\cdot} + NO_2) = 10^{15.3} \exp(-33020/T)/s$$

INTRODUCTION

This paper is concerned with the mechanisms and rates of decomposition of ethylbenzene, isopropylbenzene, phenyliodide and nitrobenzene. For these aromatic compounds, the initial consideration must be the mechanism of reaction. Indeed with our comparative rate method [1], the subsequent determination of the rate expression for unimolecular decomposition is straightforward and the only uncertainties are the proper interpretation of the rate expressions.

For many years it has been generally agreed that the mechanism for the decomposition of alkylbenzenes involve the initial cleavage of the benzylic C-C bond. However, Troe and coworkers [2] have recently reopened this issue by carrying out shock tube experiments on ethylbenzene and following in real time the formation of phenylethyl radical. They interpret their results in terms of a benzylic C-H bond split. This conclusion is of consequence not only for the ethylbenzene system but also have implications on how we go about estimating rates of decomposition of related systems. Indeed, the mechanism and rates of decomposition of ethylbenzene have been considered to be so well established that many workers have used it to establish the validity of their procedures [3].

In the case of the nitroaromatic compounds, there have not been any definitive studies with regard to the mechanism of decomposition. Obviously, the rate constants that have been reported for various postulated processes are extremely uncertain. In analogy to hydrocarbon systems, one would expect a rate expression for C-NO$_2$ bond cleavage in the range of $10^{16.5} \exp(-32500/T)/s$. Fields and Meyerson[4] have carried out extensive studies in flow systems. Their main emphasis was preparative in

nature in the sense of using these compounds as sources of aryl radicals.
Thus, although it is clear that $C-NO_2$ bond cleavage is important, the
possibility of other channels could not be ruled out. A particular
problem is the possibility of surface processes openings up new reaction
channels.

Single pulse shock tube studies represent an ideal means of determin-
ing the mechanism of unimolecular decomposition of complex organic
compounds under well defined conditions. Aside from the well known
attributes of rapid heating (thus preventing reactions during heat-up) and
the impossibility of surface processes making contributions, experiments
can be carried out under conditions that virtually guarantee that chain
reactions (the other major obscurant with regard to clear-cut conclusions
on initial processes) are suppressed. This means working with very dilute
mixtures and the use of chemical scavengers in large excesses. In
carrying out experiments in the single pulse mode, we give up real time
measurements, but gain the capability of detecting all stable products
with a sensitivity in the parts per billion level. This is necessary if
our reactant is present initially at very low concentrations. In studying
the decomposition of complex organics with the possibility of multiple
reaction pathways, it is obvious that the detection of more than one
species is absolutely necessary. It also means that we are able to carry
out a proper material balance, and thus assure ourselves that all reaction
channels have been accounted for. An important question is the fate of
the unstable species that are created during the course of the reaction.
Under our conditions where we are solely concerned with hydrocarbons,
radicals with available beta hydrogens or alkyl groupings will degrade
almost quantitatively to the appropriate olefins. Thermally stable, but
highly reactive radicals will when given the opportunity abstract a
hydrogen atom. The less reactive species will ultimately recombine. This
can occur either during or after the heating period. Given favorable
circumstances, they can also abstract hydrogens from compounds that will
lead to a resonance stabilized radical.

The validity of the procedure to be used here have been demonstrated
for the decomposition of scores of aliphatic organic compounds [1]. The
rate constants and expressions for unimolecular decomposition so deter-
mined are among the most accurately known kinetic parameters. They have
led to new values of alkane bond strengths [5] and form the basis for the
prediction of the thermal stability of related compounds. The present
investigation represents one of our first studies on aromatic systems.

EXPERIMENTAL

Our experiments are carried out in a standard single pulse shock
tube [1]. Due to the intention of using this instrument to study the
thermal stability characteristics of larger organic compounds, we have
developed a capability for heating the entire tube and the gas handling
system to temperatures in excess of 200C. For the tube itself, variation
in temperatures is held to better than one degree C. No problem was
encountered in carrying out our experiments under these conditions. The
thermal mass of the system is so large that the temperature is essentially
unchanged when the diaphragm is replaced or when the shock tube is
cleaned. At the operating temperature of 100.5C, we did not encounter any
problems in introducing or extracting from the shock tube compounds with
boiling points in the 200-250C range. Analysis was by gas chromatography
with a variety of columns and using a flame ionization detector.

The inhibitors used in these studies are propyne for the alkyl-benzenes and cyclopentane for nitrobenzene and phenyl iodide. All of these inhibitors are vastly more stable than the test compounds. For propyne, the final stable radical is propargyl radical. Presumably it will in time recombine and we have indeed detected benzene and other six carbon compounds in our reacting mixture. This is in conformity with evidence in the literature [6]. The sequence of reactions involving cyclopentane leads to allyl radical formation. At sufficiently high temperatures it can decompose to form allene and a H-atom. This will not cause severe problems in the present case as long as the extent of the H-atom induced decomposition of cyclopentane is small. This sets an upper limit to our reaction temperature. We have previously used it as an inhibitor in the decomposition of several halogenated organic compounds [7]. All of our inhibitors are present in 25 to 300 fold excess over the test gas. This is more than sufficient to ensure that chain reactions can only make minor contributions to the decomposition process. The internal standard used in these studies to define the reaction temperature is the reverse Diels-Alder reaction involving 1,2 dimethylcyclohexene with

$$k(1,2DMCH \Rightarrow C_6H_{10} + C_2H_4) = 10^{15.5}exp(-35250/T)/s.$$

The rate expression for this process has been determined in separate experiments using cyclohexene and methylcyclohexene decomposition as standards[1]. The use of the internal standard provides us with a direct means of estimating the average temperature and frees us from having to make extensive corrections for non-ideal shock tube behavior. The residence time of our experiments is of the order of 400 microseconds and is monitored by a pressure transducer at the end of the shock tube.

The experimental rate constant for decomposition is determined from the expression

$$k_n = (X_n/t) \ln(1-(product_n)_f/X_n(reactant)_i)$$

where t is the reaction time, and X_n is the mole fraction for the production of species n. The subscripts i and f pertain to initial and final concentrations.

RESULTS AND DISCUSSIONS

A) ALKYLBENZENE: Benzylic C-H bond cleavage in ethylbenzene will lead to the formation of phenylethyl benzene. On the other hand, benzyl C-C bond break will result in the formation of benzyl radicals. The latter is thermally stable until very high temperatures [8]. The former can decompose to form styrene. Note that if a hydrogen atom can be abstracted from the ethyl side chain, then styrene can also be formed. The exact rate of decomposition of phenylethyl radical has not been measured although it should be possible to estimate it fairly well. For the present purposes we will rely on direct experimental evidence. This involves generating phenylethyl radical from another source and demonstrating that within the same time scale as these experiments it is substantially decomposed into styrene. For this purpose isopropyl benzene is an idea precursor. C-C bond cleavage will yield phenylethyl radical. If it is sufficiently unstable it will now decompose to styrene. On the other hand, chain processes involving the abstraction of a secondary hydrogen atom or for what matter direct C-H bond cleavage will yield

methylstyrene. When a primary hydrogen is abstracted styrene will be formed from the 2-phenylpropyl radical. A key problem is then to distinguish between the two types of styrene. This is difficult to do when one carries out reactions in the absence of a scavenger. However, in its presence, chain processes are largely suppressed and most of the styrene must originate from the C-C bond cleavage process.

Experimental results that illustrate these considerations can be found in Table IA. These include data with and without inhibitor and from the styrene to methylstyrene concentrations one immediately perceives the role of inhibitor in reducing the concentration of the latter. As mentioned earlier, methylstyrene only arises from chain processes or benzyl C-H bond cleavage. Thus its virtual absence in the inhibited samples is indicative of the suppression of chain processes and that the latter does not occur unless the lifetime of the phenylpropyl radical is so long that it will be able to abstract an H-atom from the propyne inhibitor. This will be shown to be unlikely from the subsequent discussion. Most of the styrene must have originated from the phenylethyl radical. One notes the satisfactory mass balance. In addition, we were not able to detect any evidence for the presence of ethylbenzene. Thus phenylethyl radical does not abstract a hydrogen atom from propyne. Phenylpropyl radical will have an even smaller possibility of undergoing such a process.

With this information, the results of studies on ethylbenzene as summarized in Table IB are easy to interpret. Of key importance is the approximately 6 to 1 ratio of toluene to styrene. As pointed out in the earlier paragraph the latter can be formed from benzyl C-H bond cleavage or a chain process. Toluene, on the other hand can only originate from the benzyl radical, which in turn must be the result of benzyl C-C bond cleavage. We presume that in our system that a significant quantity of the benzyl radicals are able to abstract a hydrogen atom from the propyne inhibitor. The fact that some of the benzene is not recovered (note the mass balance problems in some of the runs) and that styrene can also be formed from chain processes that are not completely surpressed implies that the 6 to 1 ratio that we have observed represents a minimum value. Thus, our results are clearly in opposition to the observations of Troe and coworkers. As a final check, we compare in the last two columns of Table I calculated rate constants on the basis of styrene and toluene yields with results from VLPP experiments. Agreement is satisfactory [3].

B) NITROBENZENE and IODOBENZENE: We have mentioned the importance of C-NO2 bond cleavage in the decomposition of nitroaromatic compounds. Our first task is then to devise a method for trapping the phenyl type radicals that are formed during its decomposition. We selected cyclopentane as the inhibitor since as a saturated compound its only possible reaction with phenyl radical is abstraction. The important question is the amount of cyclopentane that will lead to quantitative conversion. For this purpose, we generate phenyl radicals from another source. Phenyl iodide is used. There can be little doubt that the initial reaction when it is pyrolysed is C-I bond break. Table II represent pertinent data. The important thing to notice is the very satisfactory mass balance in terms of recovered benzene and disappearance of the iodo compound except at the lowest concentrations of cyclopentane where deviations begin to occur. This then sets the range of cyclopentane concentrations that is appropriate for our studies.

Comparative rate results on iodobenzene decomposition can be found on Figure I. The rate relationship with 1,2 dimethylcyclohexene (1,2DMCH) decomposition as the internal standard is

$$\text{Log } k(C_6H_5I\rightarrow C_6H_5 + I) = (.930\pm.006)\text{Log } k(1,2DMCH) + (.46\pm.01)$$

This leads to

$$k(C_6H_5I\rightarrow C_6H_5 + I) = 10^{14.9} \exp(-32800/T)/s$$

It is in excellent agreement with the measurement of Kominar et al[9]

$$k(C_6H_5I\rightarrow C_6H_5{}^{\cdot} + I^{\cdot}) = 10^{15.0} \exp(-32500/T)/s$$

Table III contains data on the product distribution from nitrobenzene decomposition in the presence of various amounts of cyclopentane inhibitor. From the large quantitites of benzene that is formed, it is apparent that C-NO2 bond cleavage is the major reaction channel. On the other hand, we also detect the presence of significant quantities of phenol. Compared to the benzene, the phenol yields appear to be dependent on the amount of scavenger that is present but independent of the concentration of nitrobenzene. We conclude that while phenol itself must be formed from the reaction of a precursor with cyclopentane, the latter is in fact a primary product from nitrobenzene decomposition. The implication is then that the precurser must be phenoxy radical and that it can only be formed as a result of an initial isomerization process leading to the formation of a nitrite and followed by the rapid scission on the O-NO bond. From mass balance considerations, it would appear that these two processes represent the major channels for nitrobenzene decomposition. Our failure to achieve complete mass closure as against the situation with iodobenzene indicate that not all the phenoxy radical is scavenged even under the highest inhibitor concentrations. This is probably due to the fact that the phenoxy radical is resonance stabilized and the abstraction reaction is in fact 50 kjs endothermic. The branching ratio for $C-NO_2$ bond breaking as opposed to isomerization is 2 to 1.

Comparative rate results on $C-NO_2$ bond cleavage in nitrobenzene decomposition can be found in Figure II. Once again, 1,2-dimethylcyclohexene decomposition is the internal standard. The rate relationship linking the two decomposition process is

$$\text{Log } k(C_6H_5NO_2 \rightarrow C_6H_5 + NO_2) = (.937 \pm .005) \text{ Log } k(1,2DMCH) + (.756\pm .01)$$

This in turn leads to

$$k(C_6H_5NO_2 \rightarrow C_6H_5 + NO_2) = 10^{15.3} \exp (-33020/T)/s$$

The A-factor is substantially lower than what we would have expected on the basis of the results from alkane systems. This implies a considerably lower rate for the reverse combination process. The activation energy is however, very close to what we would predict on the basis of a 330 kJ/mol heat of formation [10] for phenyl radical.

Acknowledgement

REFERENCES

1. Tsang, W., "Comparative Rate Single Pulse Shock Tube Studies on the Thermal Stability of Polyatomic Molecules" in "Shock Waves in Chemistry" (A. Lifshitz, ed.) Marcel Dekker, New York, 1981, pg. 59.

2. Brauwer L., Muller-Margraf, W. and Troe, J., "Thermal Decomposition of Ethylbenzene in Shock Waves" Ber. Bunsenges. Phys. Chem. p. 7, 1031, 1983.

3. Robaugh, D. A. and Stein, S. E., "Very Low Pressure Pyrolysis of Ethylbenzene, Isopropylbenzene and tert-Butylbenzene" Int'l J. of Chemical Kinetics, 13, 1981, 445.

4. Fields, E. K. Meyerson S., "Formation and Reactions of Free Radicals from Pyrolysis of Nitro Compounds in Advancies in Free Radical Chemistry, Volume 5 (G. H. Williams, ed., 1971, Academic Press, NY, pg. 101.

5. Tsang, W., "The Stability of Alkyl Radicals" J. Amer. Chem. Soc., 107, 1985, 2872.

6. Brown, R. F. C., "Pyrolytic Methods in Organic Chemistry", Academic Press, New York, 1980.

7. Tsang, W., "Single Pulse Shock Tube Studies on the Decomposition of 1,2 Dibromoperfluoroethane and Allyl Bromide" 88, 2812, 1984.

8. Astholtz, D. C., Durant, J. and Troe, J., "Thermal Decomposition of Toluene in Shock Waves", 18th Symposium (International) on Combustion, 1981.

9. Kominar, R. J., Krech, M. J. and Price, S. J. W., "Pyrolysis of Iodobenzene by the Toluene Carrier Techniqu and the Determination of D(C6H5-I)", Can. J. of Chem., 54, 1976, 2981.

10. McMillen, D. F. and Golden, D. M., "Hydrocarbon Bond Dissociation Energies" in Annual Reviews of Phys. Chem., 33, 493, 1982

Table IA: Summary of Data on Isopropylbenzene (IspBz) Decomposition (3 atom pressure)

Experimental Configuration	Temp K	$\dfrac{\text{Styrene}}{(\text{IspBz})_i}$	$\dfrac{CH_3\text{-Styrene}}{(\text{IspBz})_i}$	$\dfrac{\Sigma \text{ Products}}{(\text{IspBz})_{i-f}}$	k(exp) /s	k(calc) /s
205 ppm IspBz	<1160	.077	.044	.88		
in argon	<1240	.53	.068	.81		
205 ppm IspBz	1220	.336		.97	768	1120
in 6% propyne	1350	.92	.012	.99	5460	18100
and argon						
142 ppm IspBz	1174	.05		.77	102	164
and 247 ppm	1191	.17		.93	375	502
1,2 DMCH in	1216	.25		.93	578	969
5.9% propyne	1243	.60		.97	1834	1840
and argon						

Table IB: Summary of Data on Ethylbenzene (EtBz)
Decomposition (2-4 atm pressure)

Experimental Configuration	Temp K	Toluene $\overline{(E+Bz)_i}$	Styrene $\overline{(EtBz)_i}$	Σ Products $\overline{(EtBz)_{i-f}}$	k(exp) /s	k(calc) /s
179 ppm EtBz	>1150	.005	.01	.80		
in argon	>1215	.043	.095	.76		
	>1283	.18	.18	.76		
179 ppm EtBz	1218	.05		.81	103	180
and 6.2% pro-	1276	.19	.035	1.00	480	707
pyne in argon	1298	.35	.063	.88	910	1149
203 ppm EtBz	1202	.037		1.0	75	121
and 197 ppm	1229	.070		.95	146	236
1,2 DMCH in	1256	.130		.90	278	448
6% propyne	1299	.394		.91	>1000	1170
and argon						

Table II Demonstration of Material Balance in Phenyl Iodide
Decomposition -1100K, 2-6 atm

Experimental Configuration	Benzene $\overline{(\phi I)_i}$	$\dfrac{(\phi I)_f}{(\phi I)_i}$
181 ppm ϕI in 5.1% cyclopentane and argon	.263	.730
35 ppm ϕI in 1% cyclopentane and argon	.262	.738
6.9 ppm ϕI in .2% cyclopentane and argon	.222	.761
3.4 ppm ϕI in .1% cyclopentane and argon	.183	.70

Table III. Aromatic Compounds from the Decomposition of
Nitrobenzene in Excess Cyclopentane, 3-8 atm Pressure

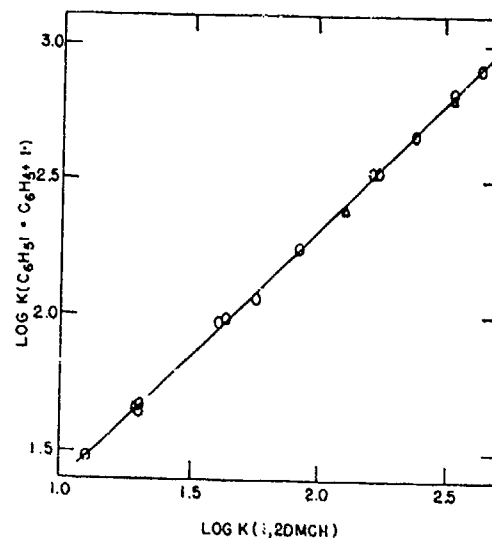| Experimental Configuration	$\dfrac{(C_6H_6)_f}{(C_6H_5NO_2)}$	$\dfrac{(C_6H_5OH)_f}{(C_6H_5NO_2)_i}$	$\dfrac{(C_6H_5NO_2)_f}{(C_6H_5NO_2)_i}$	T(K)
880 $C_6H_5NO_2$,	.052	.0087	.94	1089
804 ppm, 8.3%	.12	.022	.86	1122
C_5H_{10} in argon	.44	.068	.40	1190
132 ppm $C_6H_5NO_2$,	.023		.956	1060
1.4% C_5H_{10} in	.20	.011	.67	
argon	.43	.083	.39	1188
3572 ppm $C_6H_5NO_2$,	.17	.034	.74	1138
9.56% C_5H_{10} in	.32	.062	.49	1172
argon				

FIGURE I.   Comparative Rate Plot for the breaking of the C-I bond in
             Iodobenzene and 1,2 Dimethylcyclohexene (1,2 DMCH)
             decomposition.
             O 181 ppm iodobenzene and 230 ppm 1,2 DMCH in 5.1% cyclopentane
             Δ 35.2 ppm iodobenzene and 44.6 ppm 1,2 DMCH in 1% cyclopentane
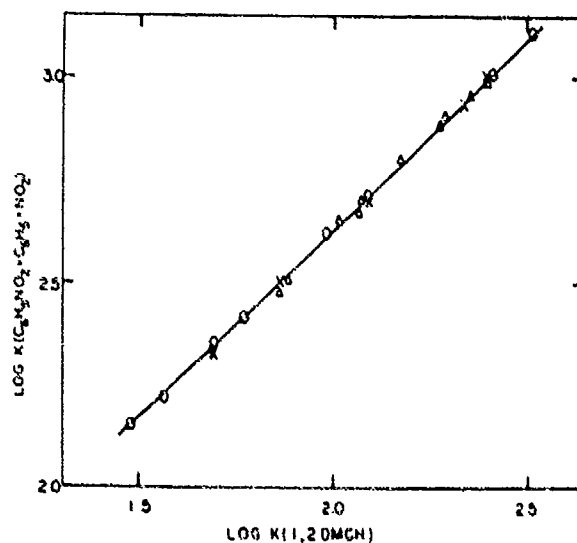   1050-1200K 3-8 atm.

FIGURE II   Comparative plot for the breaking of the $C-NO_2$ bond in
             Nitrobenzene and 1,2 Dimethylcyclohexene (1,2 DMCH)
             decomposition.
             O 444 ppm nitrobenzene and 879 ppm 1,2 DMCH in 5.1%
             cyclopentane and argon.
             X 111 ppm nitrobenzene and 220 ppm 1,2 DMCH in 1.3%
             cyclopentane and argon
             Δ 65 ppm nitrobenzene and 129 ppm 1,2 DMCH in 5.2% cyclopentane
             and argon
             1090-1180K 3-8 atm.

THEORETICAL AND EXPERIMENTAL STUDY OF VIBRATIONAL NON-EQUILIBRIUM

Dr.-Ing. F. Offenhäuser, Prof.Dr.rer.nat. A. Frohn

Institut für Thermodynamik der Luft- und Raumfahrt der Universität Stuttgart
Pfaffenwaldring 31, D-7000 Stuttgart 80, Germany

It is shown by theoretical investigations and shock tube experiments, that the vibrational relaxation time depends on the gas temperature and the vibrational state. Decrements of an order of magnitude have been observed for the relaxation time of CO_2 at the beginning of the relaxation zone. Further it was found, that for very strong shocks the assumption of local Boltzmann-distributions for the vibrational degrees of freedom ist not justified.

1. INTRODUCTION

Kinetic data for molecular collision processes are required for the modelling of molecular laser systems. In CO_2 laser systems, for example, strong deviations from local Boltzmann-distributions for all vibrational degrees of freedom may occur[1]. Therefore it is very important to know the relation between the vibrational relaxation time and the vibrational state of the molecules.

2. THEORETICAL INVESTIGATIONS

The vibrational transition probability for the harmonic oscillator in the presence of a time-dependent force $F(t)$ is given by Döring as

$$P_{m \to n} = \frac{m!}{n!} \cdot \exp(-/G/^2) \cdot \left| \sum_{j=0}^{1} \left[\binom{n}{j} \cdot \frac{G^{n-j} \cdot (-G^*)^{m-j}}{(m-j)!} \right] \right|^2 ,$$

where m and n are vibrational quantum numbers and 1 is the smaller one of
these two numbers[2]. The function G is defined by the Fourier transforms of
the force F(t). As an approximation the collisions are assumed to be elastical.
In this case the real part of G vanishes. The most probable transitions are
those between neighboring energy levels. For very small values of G one ob-
tains then as a first approximation for the mean transition probability

$$P_{1,n+1\to n} = (n+1)\cdot P_{1,1\to 0} \qquad ,$$

and for values /G/ < 0.4 one obtains as a second approximation

$$P_{2,n+1\to n} = (n+1)\cdot P_{1,1\to 0} - n\cdot(n+1)\cdot P_{1,1\to 0}\cdot\varphi + n^2\cdot(n+1)\cdot P_{1,1\to 0}\cdot\eta \quad .$$

The coefficients φ and η are functions of the gas temperature only. If mul-
ti-quantum transitions are neglected, the population density rates are given by

$$dx_n/dt = Z\cdot\{ P_{n+1\to n}\cdot x_{n+1} - (P_{n\to n+1}+P_{n\to n-1})\cdot x_n + P_{n-1\to n}\cdot x_{n-1} \} \quad .$$

It is assumed, that the population density distribution is an equilibrium-dis-
tribution. In this case the relaxation time is defined by

$$\tau_{vib} = \{ e_{vib,eq.}(t) - e_{vib}(t) \}/ de_{vib}/dt \quad , \quad (1)$$

and one obtains the vibrational relaxation time of the second approximation

$$\tau_{vib,2} = \tau_{vib,1}/\{ 1 - 2\varphi\cdot e_{vib}/R\theta + 2\eta\cdot(1+3e_{vib}/R\theta) \} \quad , \quad (2)$$

whereas the result of the first approximation is

$$\tau_{vib,1} = 1/\{ Z \cdot P_{1,1 \to 0} \cdot (1-\phi) \} \ .$$

The relaxation time at strong deviations from thermal equilibrium is therefore always less than the relaxation time for vanishing deviations. This effect has been observed indeed by Hurle for an expansive flow of N_2 in a supersonic nozzle[3]. The second approximation is valid for values $/G/ < 0.4$. This is connected with a limitation of the gas temperature. For the bending mode of CO_2 this limit is approximately 700K . For very high gas temperatures all mean transition probabilities are converging to the same value. The rate equation for the n-th vibrational level is then given by

$$dx_n/dt = Z \cdot P_{1 \to 0} \cdot \{ x_{n+1} - (1+\phi) \cdot x_n + \phi \cdot x_{n-1} \} \ .$$

In this case the local population density distributions do not remain Boltzmann-distributions during the change of state and it makes no sense to apply definition (1) to evaluate the relaxation time. The initial and the final states, however, have Boltzmann-distributions; for the initial state one obtains by application of definition (1) the relaxation time

$$\tau_{vib}(0) = 1/\{ Z \cdot P_{1 \to 0} \cdot (1-\phi) \cdot (1-\phi_0) \} \ ,$$

where $\phi = \exp(-\Theta/T)$, and for the final state one obtains

$$\tau_{vib}(\infty) = 1/\{ Z \cdot P_{1 \to 0} \cdot (1-\phi)^2 \} \ .$$

The present approximation is valid for gas temperatures $T > 3\Theta$; in the range of validity of these approximation the relaxation time for strong deviations from thermal equilibrium is not always less than the relaxation time for vanishing deviations. This is only the case for compressive changes of state. The experiments of Hurle refer to expansions at temperatures $T < 3\Theta$ and to N_2 [3]; in this case equation (2) is valid and agreement with the results of Hurle is obtained. Most measurements of vibrational relaxation times in the last decades

are based on sound propagation and shock tube methods. These two methods show one fundamental difference. In contrary to sound waves shocks may evoke strong deviations from thermal equilibrium; shock tube measurements should therefore show smaller vibrational relaxation times than sound propagation measurements, and the discrepancies should be more pronounced for low characteristic temperatures for vibration. This is in agreement with experimental results, available from literature.

3. EXPERIMENTAL RESULTS

In order to check these predictions, shock tube experiments with CO_2 have been performed. The low pressure section has an inner diameter of 72mm and a length of about 10m. The low pressure section was evacuated to less than 10^{-8}mbar before each run. The initial pressure was typically 0.3mbar and the initial temperature 300K. The profiles for the density rates were measured at four different positions in the shock tube with laser-differential-interferometers; the arrangement of these interferometers is shown in Fig. 1. For each run the shock Mach number, the tilt and the curvature of the shock front can be measured. According to previous theoretical and experimental results the shock front may be assumed to be of parabolic shape. In this case the measured mean density is

$$\rho_s(\mu) = 1/\{2(1-\sigma^2)^{1/2}\} \cdot \int_{\mu-1}^{\mu-\sigma^2} \rho(\psi)/(\mu-\psi-\sigma^2)^{1/2} \cdot d\psi \quad ,$$

where ρ_s is the measured mean density and ρ is the actual density on the axis of the shock tube. The variable μ defines the axial position of the laser beam and ψ defines the axial position of the apex of the parabola, which intersects the wall of the shock tube at the position μ ; both variables have been made dimensionless with the curvature parameter B . The variable σ defines the displacement of the laser beam from the axis of the shock tube divided by the radius of the shock tube. By an infinite sequence of partial integrations one obtains the linear differential equation of infinite order

$$\rho_s(\psi+1) = \sum_{n=0}^{\infty} \lambda^n \cdot (d^n \rho(\psi)/d\psi^n)\}/\{1\cdot3\cdot5\cdot\ldots\cdot(2n+1)\} \quad ,$$

where $\lambda = 2(1-\sigma^2)$. This differential equation is solved by a Fourier-expansion. The measured density can be expressed by the expansion

$$\rho_s(\Psi) = a_0' + \sum_{k=1}^{m} a_k' \cdot \cos(2\pi kB/1 \cdot \Psi) + \sum_{k=1}^{m-1} b_k' \cdot \sin(2\pi kB/1 \cdot \Psi) \quad ,$$

where 1 denotes the length of the interval, for which $L = 2m+1$ equidistant values for the mean density are known. The coefficients then are given by

$$a_0' = 1/(L-1) \cdot \sum_{i=1}^{L-1} \rho_{s,i} \quad ,$$

$$a_k' = 1/(L-1) \cdot \sum_{i=1}^{L-1} \rho_{s,i} \cdot \cos\{\pi k \cdot (i-1)/m\} \quad ,$$

$$b_k' = 1/(L-1) \cdot \sum_{i=1}^{L-1} \rho_{s,i} \cdot \sin\{\pi k \cdot (i-1)/m\} \quad .$$

From these coefficients a_k' and b_k' the coefficients a_k and b_k of the displaced density profile $\rho_s(\Psi+1)$ can be calculated. The actual density $\rho(\Psi)$ can be expressed by the same expansion using the coefficients c_k and d_k. By a comparison of the coefficients one obtains the equations

$$c_0 = a_0 \quad ,$$

$$c_k = (a_k \cdot \Gamma_1 - b_k \cdot \Gamma_2)/(\Gamma_1^2 + \Gamma_2^2) \quad k = 1,2,\ldots,m \quad ,$$

$$d_k = (a_k \cdot \Gamma_2 + b_k \cdot \Gamma_1)/(\Gamma_1^2 + \Gamma_2^2) \quad k = 1,2,\ldots,m \quad .$$

The variables Γ_1 and Γ_2 are given by the sums

$$\Gamma_1 = \sum_{n=1}^{\infty} \{(-1)^{n-1} \cdot \mathcal{A}_k^{2(n-1)}\}/\{1 \cdot 3 \cdot 5 \cdot \ldots \cdot /4n-3)\} \qquad ,$$

$$\Gamma_2 = \sum_{n=1}^{\infty} \{(-1)^{n-1} \cdot \mathcal{A}_k^{2n-1}\}/\{1 \cdot 3 \cdot 5 \cdot \ldots \cdot (4n-1)\}$$

with $\mathcal{A}_k = 4\pi \cdot (1-\sigma^2) \cdot B/\lambda \cdot k$. The profiles for the actual density were transformed to the shock fixed system and separated into the range of the gasdynamic shock and the zone of vibrational relaxation. The vibrational energy was determined by the conservation equations and the local vibrational relaxation time was evaluated by equation (1). The results of these experiments are shown in Fig.2; for each run one relaxation time profile is obtained. It can be seen, that the relaxation time at the beginning of relaxation is about one order of magnitude shorter than it was found by previous experiments. This cannot be explained by the decreasing gas temperature only. It is therefore assumed, that this is effected by the strong deviations from equilibrium at the beginning of relaxation.

REFERENCES

1. Offenhäuser, F.
   "Kinetisches Modell für den Schwingungsenergie-
   austausch in strömenden Molekülgasgemischen"
   Dissertation Universität Stuttgart, Februar 1985

2. Döring, W.
   "Einführung in die Quantenmechanik",
   Göttingen, Vandenhoeck & Ruprecht, 1962

3. Hurle, I.R.
   "Vibrational Relaxation Processes under
   Conditions of Extrem Non-Equilibrium"
   Chem.Soc.Spec.Publication No.20,
   The Chem.Soc., Burlington House, London,
   Academic Press, London - New York, 1966
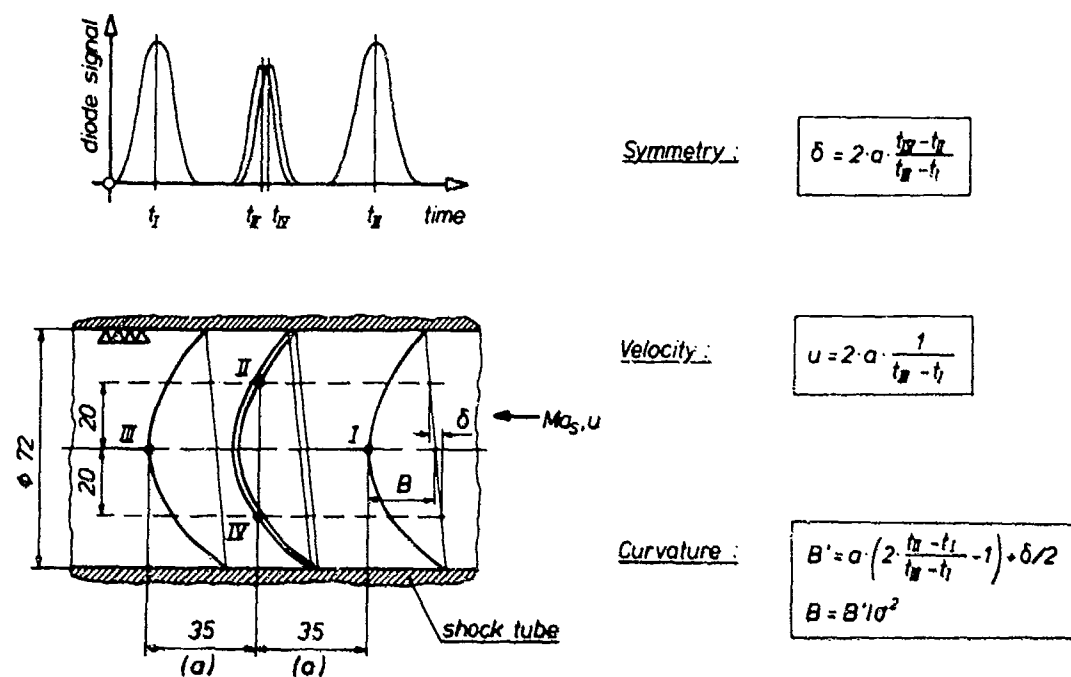
Fig. 1   Arrangement of the four laser differential interferometers.
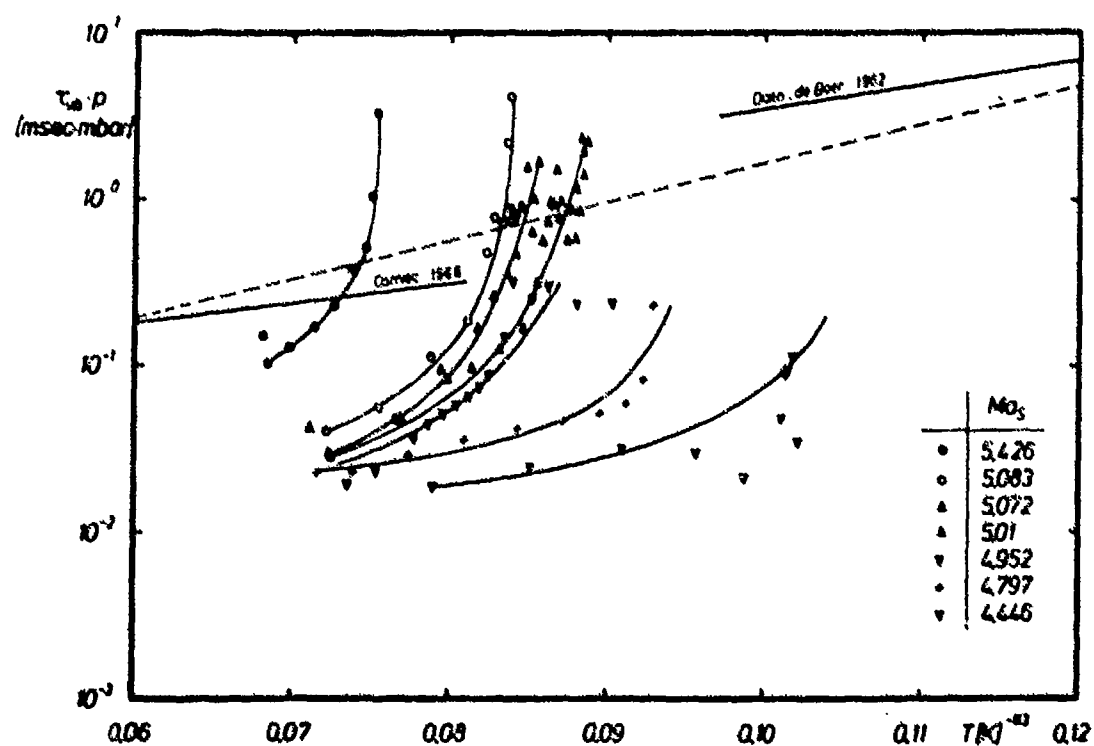

Fig. 2   Vibrational relaxation time profiles of CO_2 as a function
of the gas temperature and the local vibrational state.

IGNITION DELAY TIMES OF CYCLOPENTENE OXYGEN ARGON MIXTURES

Alexander Burcat Christopher Snyder* and Theodore Brabbs*

*Department of Aeronautical Engineering,
Technion – Israel Institute of Technology, Haifa 32000, Israel.*

NASA Lewis Research Center, Cleveland, Ohio, 44195.

The ignition delay times of cyclopentene with oxygen diluted in argon was investigated over a concentration range of 0.25 to 1% cyclopentene and 1.75 to 7% oxygen. The temperature range was 1323 – 1816K and the reflected shock pressures were 1.67 to 7.36 atmospheres.

Statistical evaluation of the experiments provide an over all equation with a 2σ confidence level as follows:

$$\tau = 5.86\times10^{-16}\exp(52770/RT)[C_5H_8]^{.59}[O_2]^{-1.51}[Ar]^{.55} \text{ sec.}$$

Detailed experimental information is provided.

1. INTRODUCTION

It was undertaken to study the oxidation of cyclopentene as a representing member of five carbon unsaturated ring compounds. The five membered ring compounds should be closely related to the kinetics of aromatic compounds.

Over two decades of investigation in the problems of soot formation and the role of aromatic compounds in this process, as well as the kinetics of oxidation of aromatic compounds have not yet been able to provide decisive answers to the above questions. A few mechanisms have been proposed but no crucial evidence has yet been supplied to favor any of them. One of the first oxidation proposals for benzene was given by Assaba[1]. Following this mechanism, phenyl radicals are formed from benzene which react to give biphenyl molecules, and these were supposed to be the precursors of soot. The oxidation steps that Assaba proposed were undecisive and he assumed the formation of a phenyl peroxy radical in the process of the ring opening.

Kern[2] who investigated the benzene pyrolysis with a mass spectrometer hooked to the shock tube, has shown that no phenyl and no biphenyl radicals and molecules are formed in the process. While the phenyl miss-appearance was blamed on the low sensitivity of Kern's system, the unavailability of biphenyl species seems real.

Glassman who investigated the oxidation of benzene in a flow reactor[3], proposed a mechanism by which the benzene is transformed to five membered ring intermediates, such as cyclopentadiene, which continue to decompose further. Thus it is clear that five membered ring compounds may have an important role in the oxidation kinetics of aromatic compounds. Since a direct investigation on this subject is complex, an investigation of the individual kinetics of five member ring compounds may clear the mechanism of the oxidation of aromatic compounds.

2. EXPERIMENTAL

A single pulse shock tube was used to perform the experiments. The shock tube was made of stainless steel pipe, flattened to a 3 by 3 inch square tube with rounded corners. The tube was honed and polished on all inside surfaces. The dump tank was located at the end of the driver section and separated from the driver section by an aluminum diaphragm. A second aluminum diaphragm was located between the driver and the driven section. The two diaphragms were burst by an auxilliary short shock tube. This short shock tube had a third diaphragm that was burst by a hand plunger.

The shock speed was measured over two separate intervals using three pressure transducers whose signals were fed to a dual channel Nicolete transient recorder. The shock speed was measured with an accuracy of ±0.1 μsec. A Kistler pressure transducer was located in the side wall, 3 mm away from the end plate. This pressure transducer was connected to a second Nicolete transient wave recorder, and was used to record and measure the ignition delay time from the pressure history of the gas (See fig. 1). The ignition delay time was measured to ±1 μsec.

The mixtures were prepared in stainless steel tanks at 50 PSI total pressure using a separate manifold. The gases and vapors were measured manometrically and let to expand into preevacuated stainless steel tanks. Pure 3H Argon was used to pressurize the tank to 50 PSI. The mixtures were allowed to mix for 24 hours before use. Different mixtures of pure grade Airco Helium and 3H Argon were used as driver gases. The cyclopentene was spectroscopical grade reagent.

The reflected shock temperatures were calculated using standard conservation equations and the ideal gas equation of state assuming frozen chemistry. All the thermodynamic data used were taken from new compilations[4]

3. RESULTS AND DISCUSSION

The experiments were performed with four different mixtures A–D. In total 76 shocks were run. The exact groups of experiments are given in Table I. The mixture were prepared so that delineation of power dependencies could be done from an empirical ignition delay equation:

$$\tau = 10^{-z}\exp(+E/RT)[Fuel]^a[O_2]^b[Ar]^c \ \text{sec.}$$

In each of the performed shocks, the mixture composition and initial properties are known. The post shock experimental properties were the reflected temperature T_5, the density ratio ρ_5/ρ_1 and the ignition delay time τ. The experiments were spread over a wide temperature range to permit maximum sensitivity to the determination of the so called "activation energy". An eyeball straight line fit was drawn through the experimental points to help visualizing the following explanation.

TABLE I. Experimental Conditions of Cyclopentene Mixtures.

Series	Compositions			P_1 torr	Number of experiments	Parameters determined
	%C_5H_8	%O_2	%Ar			
A	0.258	7.	92.74	50	22	a, b
B	0.25	1.75	98.0	50	13	b
C	0.333	2.33	97.33	150	25	c
D	1.0	7.0	92.00	50	16	a, c

Figure 2 presents series A and B in a log τ vs. $1/T_5$ plot for cyclopentene. Mixtures A and B have a fourfold difference in the oxygen concentration. The distance between the lines is 0.98 logarithmic units. Therefore

$$\log \tau_A = a \log(0.25\% [C_5H_8]) + b \log(4 \times 1.75\% [O_2]) + c \log [Ar]$$

$$\log \tau_B = a \log(0.25\% [C_5H_8]) + b \log(1.75\% [O_2]) + c \log [Ar]$$

subtracting log τ_B from log τ_A and disregarding the differences in Ar concentrations we get

$$-\Delta\log \tau_{(A-B)} = b \log 4$$

$$b = \Delta\log_{(A-B)}/ \log 4 = -0.98/0.6 = -1.63$$

Figure 3 consequently presents log τ vs. $1/T_5$ for series A and D to get the cyclopentene power dependence following the former calculation

$$a = \frac{\Delta\log \tau_{(D-A)}}{\log 4} = \frac{0.317}{0.6} = 0.53$$

Figure 4 presents log τ vs. $1/T_5$ for series C and D. In mixture C the concentration of the reactants is a third of that in mixture 4. But the pressure used was three times higher. Therefore the real concentrations of cyclopentene and oxygen are the same in both mixtures but the concentration of argon is three times higher in mixture C than in mixture D. The distance between the two lines in mixtures C and D is 0.216 log τ units and therefore

$$c = \frac{\Delta\log\tau_{(D-D)}}{\log 3} = 0.45$$

The former discussion was used to explain why the mixtures were chosen as they were, and how the experiments were performed. It was found however that a statistical approach to the determination of a, b, and c was more appropriate and more accurate since it could take into consideration such factors as ρ_5/ρ_1 and differences in concentration of argon between the gas mixtures. These parameters

were neglected in the graphical presentation on figures 2–4. The statistical results given below point out that the neglected parameters change the results obtained in the graphical form.

Figure 5 shows the overall plot of log β vs. $1/T_5$ for a maximum acceptable spread of 2σ. The correlation was found with a statistical "student–t" program using 67 experiments.

$$\tau = 10^{-15.53\pm.99}\exp(52770\pm1540/RT)[C_5H_8]^{0.60\pm0.07}[O_2]^{-1.61\pm0.07}[Ar]^{0.53\pm0.07} \text{ sec.}$$

The former reduced over all ignition delay equation is in good agreement with the graphical analysis shown above.

Table II contains a list of 5 representative shocks from each group performed in this study and their pre and post shock parameters.

The former value for cyclopentene should be compared with values found for benzene and toluene in a similar study[3].

Table II Reflected Parameters and Results of Representative Shocks

Series	Composition % C_5H_8	O_2	Shock No	P_1 torr	ρ_2/ρ_1	T_5 K	τ sec	P_5 atm
A	0.255	7.0	8	50	5.85	1343	1007	1.72
			12	50	6.00	1398	650	1.84
			13	50	6.50	1595	42	2.27
			15	50	6.19	1467	156	1.99
			21	50	6.06	1419	342	1.89
B	0.25	1.75	102	50	6.68	1565	454	2.11
			105	50	6.27	1676	170	2.30
			106	50	6.53	1816	40	2.60
			111	50	5.99	1543	622	2.03
			113	50	5.85	1482	1632	1.90
C	0.333	2.33	201	150	6.06	1533	236	6.13
			202	150	5.78	1400	1054	5.36
			206	150	6.19	1591	153	6.44
			209	150	6.45	1724	44	7.36
			214	150	5.89	1450	767	5.61
D	1.00	7.00	302	50	6.77	1431	580	2.12
			304	50	6.70	1410	876	2.07
			308	50	7.20	1574	96	2.49
			310	50	7.68	1748	20	2.94
			313	50	7.00	1505	223	2.31

For benzene using a 2σ maximum acceptable spread from 80 experiments the over all ignition delay time found was

$$\tau = 9.0 \times 10^{-16} \exp(41450/RT)[C_6H_6]^{0.44}[O_2]^{-1.77}[Ar]^{0.44} \text{ sec.}$$

For toluene using 54 experiments we get the over all value of

$$\tau = 5.28 \times 10^{-15} \exp(55100/RT)[C_7H_8]^{0.55}[O_2]^{-1.48}[Ar]^{0.85} \text{ sec.}$$

while for cyclopentene the value is

$$\tau = 5.85 \times 10^{-16} \exp(52800/RT)[C_5H_8]^{0.59}[O_2]^{-1.61}[Ar]^{0.88} \text{ sec.}$$

The comparison with benzene shows a similar oxygen power dependence, a lower power dependence of argon i.e. a small third body inhibiting effect.

The inhibiting effect of argon was not encountered in simple hydrocarbons i.e. methane[6], ethane[7], propane[8], propene[9], and propyne[10]. It was however encountered in long chain hydrocarbons like heptane[11], and pseudo ring compounds like ethylene-oxide[12].

It was shown in earlier studies[12] that the inhibiting effect of the diluent occurs, because it acts as a heat sink to the heat evolving from the reaction. This heat can be identified with the process of shattering the ring. To open the ring a large amount of energy is needed. But part of this energy is absorbed by the diluent thus causing an inhibition to the reaction.

Benzene is harder to shatter than toluene and toluene, than cyclopentene, thus it is clear that the inhibiting effect will be lowered when going from one to the other.

REFERENCES

1. Fujii, N., and Assaba, T., *14th Combustion Symposium*, 1973 p.433.

2. Kern, R.D., Singh, H. J., Eslinger, M.A., and Winkeler, P.W., *19th Combustion Symposium*, 1983, p.1351.

3. Venkat, C., Bresinsky, K. and Glassman, I., *19th Combustion Symposium*, 1983 p.143.

4. Burcat, A.,"Thermochemical Data for Combustion Calculations", Chapt. 8 *Combustion Chemistry*, Edited by W. C. Gardiner, Springer-Verlag, N.Y. 1984, 455–504

5. Burcat, A., Snyder, C., and Brabbs, T., "Ignition delay times of Benzene and Toluene with Oxygen, in Argon Mixtures". NASA Report, to be published.

6. Lifshitz, A., Scheller, K., Burcat, A., and Skinner, G. B., *Combustion and Flame, 16* (1971), 311

7. Burcat, A., Crossley, R. W., Scheller, K., and Skinner, G. B., *Combustion and Flame, 18* (1972), 115.

8. Burcat, A., Lifshitz, A., Scheller, K., and Skinner, G. B., *13th Combustion Symposium*, (1971), 745.

9. Burcat, A., and Radhakrishnan, K., "High Temperature Oxidation of Propene" *Combustion and Flame, 60* (1985), 157.

10. Radhakrishnan, K., and Burcat, A., "Kinetics of Ignition of Fuels in Artificial Air Mixtures. II The Oxidation of Propyne." to be published.

11. Burcat, A., Farmer, R. F., and Matula, R. A., *Shock Tubes and Waves, 13th International Shock Tube Symposium*, Niagara Falls, 1982, p.715.
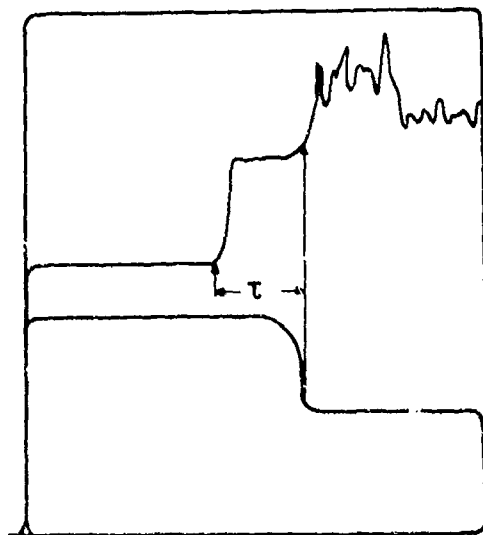
12. Burcat, A., *Comb. Sci. Technol., 21*, (1980), 169.

Figure 1. Pressure traces from which ignition delay times were determined.
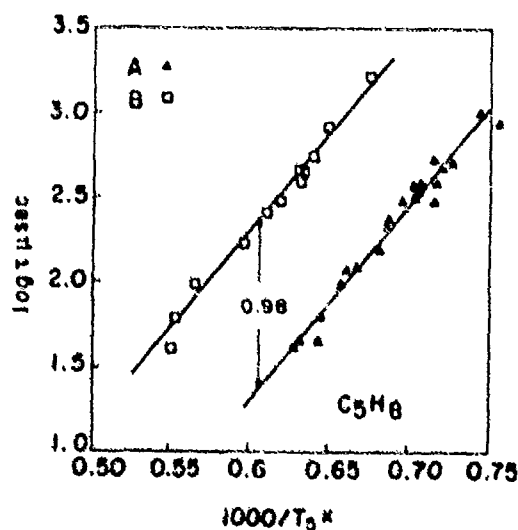
Figure 2. A plot of logτ vs. $1/T_5$ for mixtures A and B, representing the oxygen power dependence.
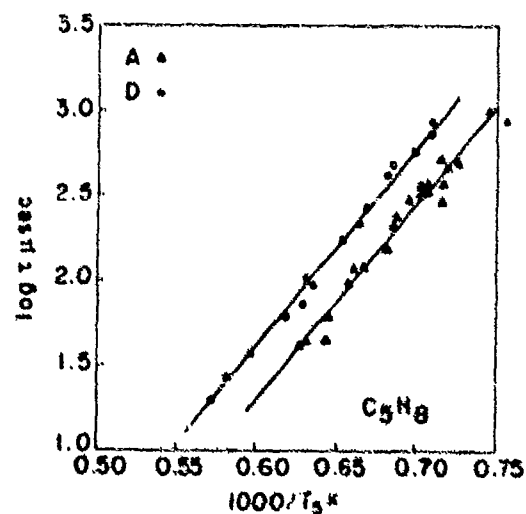
Figure 3. A plot of logτ vs. $1/T_5$ for mixtures A and D, representing the cyclopentene power dependence.
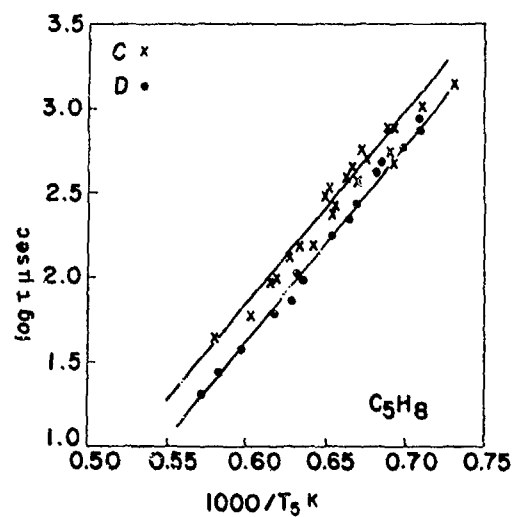
Figure 4. A plot of $\log \tau$ vs. $1/T_5$ for mixtures C and D, representing the argon dependence.
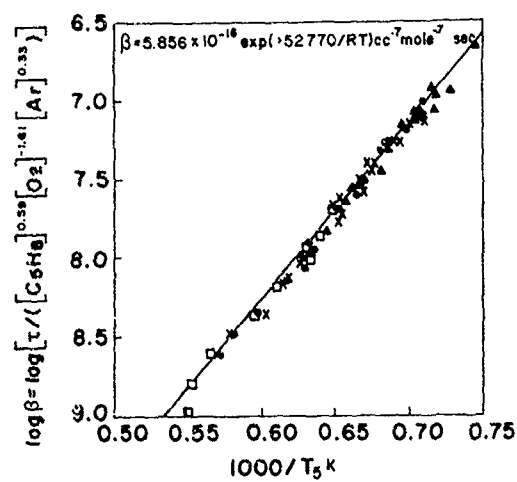
Figure 5. The plot of all experimental points as $\log \beta$ vs. $1/T_5$ for a maximum acceptable spread of 2σ.

ABSORPTION MEASUREMENT ON METHANE AND
HYDROXYL RADICALS IN A THERMAL NON-EQUILIBRIUM BOUNDARY LAYER

W. Sauer, J. H. Spurk

Institut für Technische Strömungslehre
Technische Hochschule Darmstadt
6100 Darmstadt, West Germany

Methane-air-mixture in argon heat bath is ignited
by shock reflected from the endwall. Simultaneous-
ly with the combustion a laminar, thermal boundary
layer develops near the cold endwall where chemical
reactions are substantially influenced by diffusion
and heat conduction. Time and space resolved measu-
rements of absorption on methane using a focused
helium neon laser beam at 3.391 microns, and measu-
rements of absorption on OH in the (0,0) vibration
band of the $A^2\Sigma^+$-$X^2\pi$ transition using a focused,
frequency doubled dye laser beam are reported. Ex-
perimental concentration profiles of methane and
OH show close agreement with numerical prediction.

1. Introduction

The prediction of the combustion process near a cold wall rests on a number of
assumptions, some concerning the transport coefficients in the multicomponent
gas mixture and others the chemical kinetics of the process. It is nearly im-
possible to establish how a specific assumption affects the predicted combust-
ion process, when the chemical reactions and the transport process are strong-
ly coupled. A measure of the overall consistency of the theoretical model may
be obtained from the comparison of measured and calculated variables. For shock
initiated methane combustion near the end wall of a shock tube such a compari-
son has been made for the density and the heat transfer to the end wall by
Keiper and Spurk[1,2]. The agreement between calculated and experimental density
histories at various distances from the end wall was very good, but density is
not very sensitive to gas composition and the agreement does not ascertain a
correct description of the chemical reaction and transport process.

In this paper we report on the absorption of laser beams by methane molecules
and by hydroxyl radicals. We show comparison between calculated and measured
beam intensity histories and concentration of these two constituents. The con-
centration of the hydroxyl radical exhibits a transient maximum and the con-
centration of methane a minimum in the boundary layer. This behaviour as well
as a transient maximum in the temperature and extrema in the other constituents
is predicted in Keiper's[3] calculation. Spurk[4] has shown that this effect can be
expected whenever chemical reactions and diffusion processes occur simultaneous-
ly.

2. Measurements

The shock tube used is described in ref. [1]. A lean mixture of methane, oxygen
and nitrogen diluted with argon, molfractions 0.0319, 0.161, 0.0984 and 0.7087
respectively, is heated by reflected shock waves to about 2000 °K. The experi-
mental set up for the absorption measurements on OH is shown in figure 1. The
beam from a tunable dye laser is focused on a KDP crystal. The frequency doub-
led beam passes the filter F_1 and is split into two beams, one traversing the
test section outside the end wall boundary layer at a fixed distance of 10 mm

from it; the other traverses the boundary layer at adjustable distances from the end wall. It is focused to a waist radius of 0.04 mm in the center of the test section giving a radius of 0.1 mm at the windows. A stop (S_3) of 0.1 mm width was placed immediately in front of the boundary layer detector in order to improve the spatial resolution and two other stops, slightly larger than the beam diameter, and a filter were used to suppress intensity due to spontaneous emission. The other beam passes through a monochromator, set in the third order, to a wavelength range of 0.8 Å and adjusted to the $R_1(9)$ line which forms the head of the (0,0) band of the $A^2\Sigma^+-X^2\pi$ transition in OH. The line width of the laser output is about $3*10^{-3}$ Å, substantially smaller than the width of the absorption line with Doppler broadening of about $2*10^{-2}$ Å and negligible pressure broadening. The width of the gain curve is 0.3 Å and the FSR 0.13 Å. To adjust the laser and monochromator, the emission of a laminar H_2-O_2 flame is viewed by the monochromator with a theoretical resolution of 0.3 Å. The monochromator is then adjusted to the band head. In this setting, the laser beam is passed through the flame and the dye laser is tuned, going from small to larger wavelength, until maximum absorption is obtained. This adjustment is made immediately before the test and checked immediately after the test. Figure 2 shows typical intensity traces for the boundary layer beam and the beam outside the boundary layer. Also shown is the difference between the intensities of the two beams. The set up for the absorption measurement for the methane component has been described previously[2], and typical intensity traces may be found in this reference. Because the beam of the He-Ne-laser at 3.39 μm is larger in the test section than the beam of the dye laser and the stop immediately in front of the detector is larger (0.2 mm) spatial resolution is smaller for the methane component.

3. Absorption coefficients

The ratio of transmitted to incident intensity I/I_0 of light at wavelength λ traversing the absorbing gas of length L (here L = 55 mm) is given by

$$I/I_0 = \exp(-k_\lambda L), \tag{1}$$

where effects of spontaneous emission have been omitted and the assumption has been made, that the absorption coefficient k_λ is constant along a beam parallel to the end wall. The absorption coefficient may be computed from[5]

$$k_{\lambda_0,OH} = \frac{\sqrt{\pi}e^2}{m_e c^2} \frac{\lambda_0^2}{\Delta\lambda_D} \frac{g_n \exp(-E_n/kT)}{Q_v Q_r} \frac{\rho}{M} X_{OH} N_A f_{mn} \tag{2}$$

using spectroscopic data and the data from the numerical solution of the combustion problems[3].

The index OH refers to the OH radical; λ_0 is the center wavelength of the $R_1(9)$ line in the (0,0) band of the $A^2\Sigma^+-X^2\pi$ transition (λ_0 = 3063.57 Å), $\Delta\lambda_D$ is the Doppler line width, which alone describes the line profile, since pressure broadening is negligible. N_A, k, e and m_e are respectively Avogadro's constant, Boltzmann's constant, electron charge and mass; c is the light velocity. M is the molecular weight of the gas mixture and ρ its density, while X is the mole fraction and g_n, E_n the degeneracy and the energy of the absorbing state respectively; T is the absolute temperature. The vibrational partition function is computed on the basis of an harmonic oscillator[7] and the rotational partition function by summing over all rotational states of the $^2\pi_{1/2}$ and $^2\pi_{3/2}$ series[8] using the spectroscopic data of ref. [6]. The transition probability is given by[9]

$$f_{mn} = \frac{f_{oo}}{4} \frac{S_{mn}}{g_n} T_{mn}, \tag{3}$$

where S_{mn} is the rotational transition probability (S_{mn} = 35.3)[6] and f_{00} the vibrational probability (f_{00} = 9*10-4)[10]. The vibration - rotation interaction factor T_{mn} is given by Learner[11] as T_{mn} = 0.922.

For the absorption measurements on methane we write (1) as

$$I = I_0 \exp(-\varepsilon_{CH_4} X_{CH_4} (\rho/M)L) , \tag{1a}$$

where the extinction coefficient ε_{CH_4} at room temperature is needed to determine the intensity change after filling the shock tube. We use

$$\varepsilon_{CH_4}(300) = 2.0*10^6 \text{ cm}^2/\text{mol}$$

from our own measurements which agrees with the value of Olson et al.[12] when extrapolated to room temperature. From the high temperature data published[12,13,14] we choose the polynomial temperature fit of ref. [12] for the extinction coefficient. Their data has been measured under experimental conditions similar to ours.

4. Results

In Figure 3 the experimental intensity histories of OH are compared with numerical computations. These are based on the condition given in figure 3 and result in an ignition delay time of 46 μs, while the experimental delay times vary, due to slight differences in shock velocities. The use of the dimensionless time t/τ_i nearly eliminates the dependence on ignition delay time.

The density behind a reflected shock is known to increase with time, even when gas is nonreacting. The increase is caused by small disturbances behind the incident shock wave (due to boundary layer growth on the sidewalls) into which the reflected shock moves. This density increase during ignition delay time can be written as[1,15]

$$\rho(t)/\rho(0) = 1 + Kt^{0.58} ; K = 99*10^{-4} ; t = [\mu s]. \tag{4}$$

This (slow) increase in density is not accounted for in the numerical computation, but since it causes a slow decrease of intensity during ignition delay time, we correct for it by dividing the logarithm of the measured intensity histories with the factor $\rho(t)/\rho(0)$. The correction is negligible for absorption by the OH component since the concentration of OH is very small during ignition delay; for the methane component it can amount to 8% in the concentration. The history at 10 mm is well outside the boundary layer during the observation time. The theoretical history for this station is determined from characteristic computation of the inviscid reacting flow using Bowman's[16] reaction mechanism for methane oxidation (with a different rate constant for thermal decomposition of methane[2]) and Nelson[21] for the nitric oxide formation. The intensity is seen to decrease rapidly after ignition delay, due to the combustion proper. Despite the large scatter in the experimental data, the agreement between it and the numerical prediction is quite good. The large scatter, especially after combustion, is due to the difficulty of accurately tuning the laser to the center frequency and to thermal drift of the laser. The other histories are all measured in the boundary layer. The boundary conditions for the boundary layer solution as x →∞ are found from the characteristic solution of the inviscid flow at x = 0. These are almost the same as those at x = 3 mm, which is the factual end of the boundary layer. In the numerical computation of the boundary layer flow, Sorret and Dufour effects have been neglected and the heat conduction coefficient and the multidiffusion coefficients are based on potential parameters of the Lennard-Jones potentials[17,18,19].

Figure 4 shows the difference of concentration of the OH component between the station at 10 mm and stations in the boundary layer. The concentration in the boundary layer is seen to be higher than the concentration at station x = 10mm for all or some time of the histories. This is caused by two effects: first, the gas at stations close to the wall is ignited earlier than the gas at station

$x = 10$ mm and second, apart from earlier ignition, the combustion proceeds faster in the boundary layer due to coupling of diffusion and chemical reaction. The solid line in figure 5 (and figure 4) is the predicted difference of concentration, i.e. the concentration in the boundary layer minus the concentration at station $x = 10$ mm. The latter, as mentioned before, is computed for the inviscid flow. The dashed line is the difference of concentration in the boundary layer minus the concentration prescribed as boundary condition for $x \to \infty$. The dashed line gives thus the advance of the combustion due to coupling, and the difference between the solid line and the dashed line, the advance due to earlier ignition and the dynamics of the inviscid flow. The concentration data in figure 6, $c'_{OH} = (\rho_{OH} M_0)/(\rho M_{OH})$, $M_0 = [\sum_i c_i(t=0)]^{-1}$, plotted as function of x with time as parameter, exhibit the transient maxima in the boundary layer, which is caused by the coupling between reaction and diffusion.

In figure 7, concentration histories of the methane component (referred to the initial methane concentration $c(0) = .87$ mol/kg) are compared to boundary layer computation. The solid curves and the dashed curves are curves computed for different initial shock speeds, resulting in different ignition delay times. As mentioned before, the use of the variable t/τ_i nearly eliminates the dependence on ignition delay time.

The same data plotted as functions of x, with time as parameter (figure 8), show transient minima in the methane concentration in the boundary layer.

Since Bowman's reaction scheme is applicable only in the high temperature region, we have included 9 higher hydrocarbon reactions from Warnatz[20]. Figure 9 shows results of this computation for station $x = 0.3$ mm, which is the station closest to the wall, for which measurements are possible with our set up. The experimental results for absorption are in better agreement with Bowman's scheme without the higher hydrocarbon reactions of Warnatz. However, it should be noted, that the temperature at this station is about 1900 $^{\circ}$K during the observation time.

5. Concluding remarks

The space and time resolved concentration measurements reported in this paper, and earlier density measurements[2] show, that the boundary layer development near a cold wall during methane combustion is in good agreement with numerical predictions, using Bowman's[16] reaction scheme and transport coefficient based on Lennard-Jones potentials. The transient extrema in concentration predicted by the theory[3,4] as a result of the coupling between chemical reaction and diffusion, are experimentally observed.

6. References

[1]   Keiper, R., Spurk, J.H., J. Fluid Mech. 113, 1981, p. 333

[2]   Keiper, R., Spurk, J.H., 13th Symp.(Int.) on Shock Tubes and Waves, New York 1982, p. 851

[3]   Keiper, R., Dissertation Darmstadt D 17, 1980

[4]   Spurk, J.H., Ing. Archiv 49, 1980, p. 269

[5]   Unsöld, A., Physik der Sternatmosphären, Springer Verlag Berlin 1938

[6]   Dieke, G.H., Crosswhite, H.M., J. Quant. Spectrosc. Radiat. Transfer 2, 1962, p. 97

[7]   Herzberg, G., Molecular Spectra and Molecular Structure, Van Nostrand Reinhold Co., New York 1950

[8]   Westenberg, A.A., J. Chem. Phys. 43, 1965, p. 1544

[9] Anketell, J., Pery-Thorne, A., Proc. Roy. Soc. A301, 1967, p. 343

[10] Rouse, P.E., Engleman, R., J. Quant. Spectrosc. Radiat. Transfer 13, 1973, p. 1503

[11] Learner, R.C.M., Proc. Roy. Soc. A269, 1962, p. 311

[12] Olson, D.B., Mallard, W.G., Gardiner, W.C., Appl. Spectroc. 32, No. 5, 1978, p. 489

[13] Olson, D.B., Gardiner, W.C., Comb. and Flame 32, 1978, p. 151

[14] Heffington, W.M. et al., J. Quant. Spectrosc. Radiat. Transfer 16, 1976, p. 389

[15] Dyner, H.B., Phys. of Fluids 9, 1966, p. 879

[16] Bowman, C.T., 15th Symp.(Int.) on Combustion, 1974, p. 869

[17] Hirschfelder, J.O., et al., Molecular Theory of Gases and Liquids, Wiley, New York 1967

[18] Morgan, J.E., Schiff, H.J., Canad. J. Chem. 42, 1964, p. 2300

[19] Khouw, B. et al., J. Chem. Phys. 50, 1969, p. 66

[20] Warnatz, J., 18th Symp. (Int.) on Combustion, Waterloo/Canada, 1980

[21] Nelson, H.F., AIAA 14, 1976, p. 1177
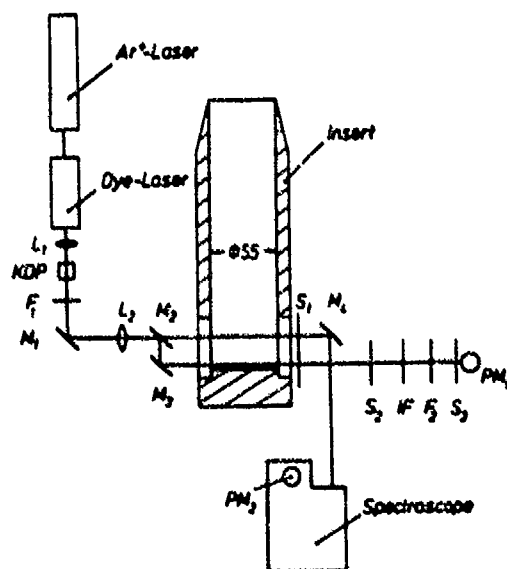
Figure 1:
Set up for absorption
measurement on OH
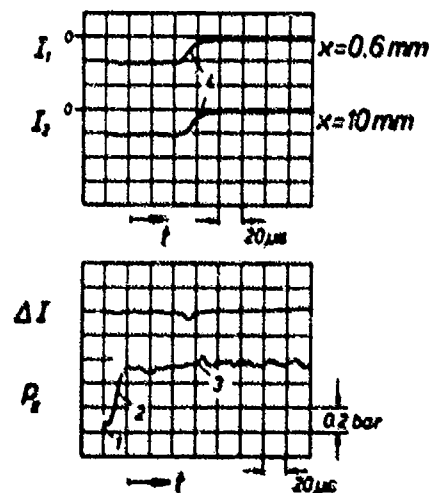
Figure 2:
Intensity and pressure traces
(p_{II} at x = 5 mm)

1 incident shock
2 reflected shock
3 combustion
4 OH radical formation
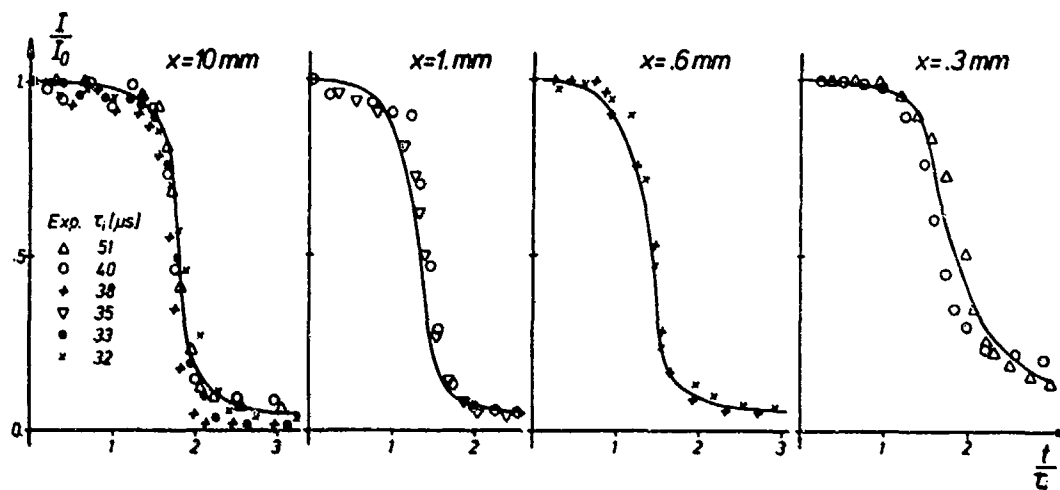
Figure 3: Transmitted to incident intensity for absorption by OH.
Theory: $T(t=0) = 2078$ K, $p(t=0) = 0.48$ bar, $\tau_i = 46$ μs.
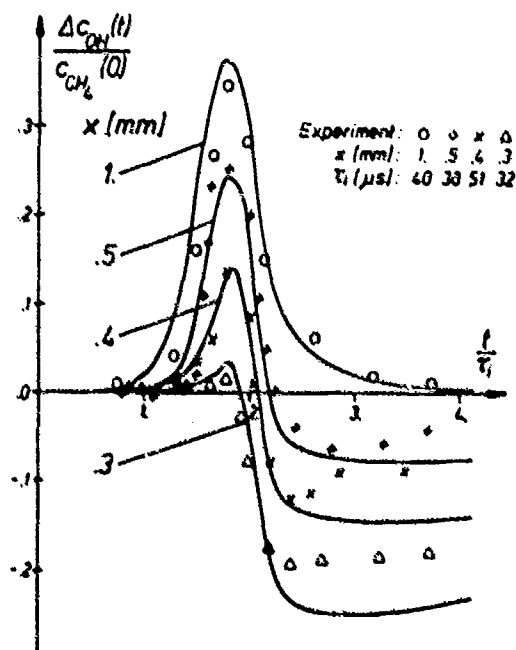
Figure 4:
Difference of OH concentration between
boundary layer and outer flow (x=10mm);
$c_{CH_4}(0) = .87$ mol/kg, same initial
conditions as in Fig. 3.
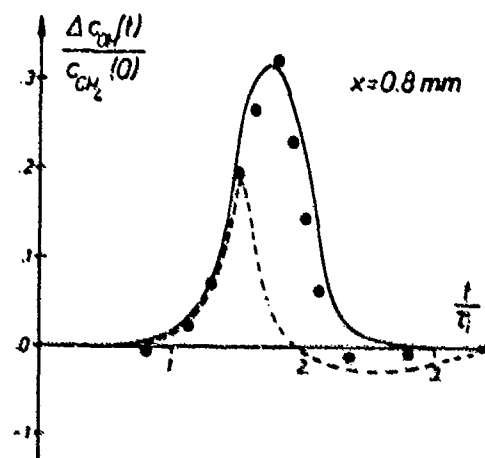
Figure 5:
Difference of OH concentration.
Exp.: $\tau_i = 33$ μs (same
conditions as in Fig. 4).
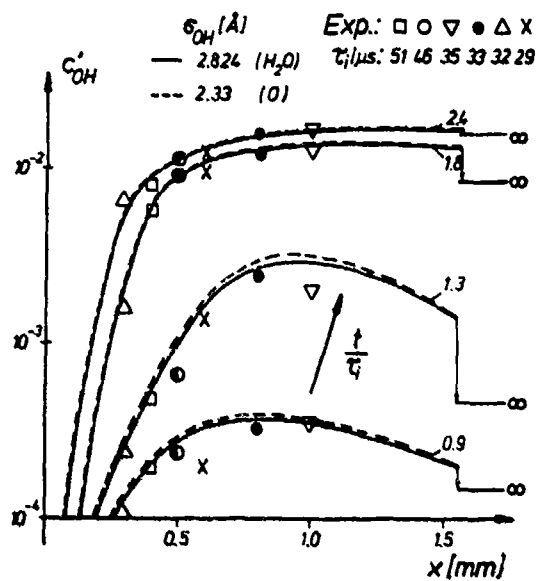
Figure 6: OH concentration profiles
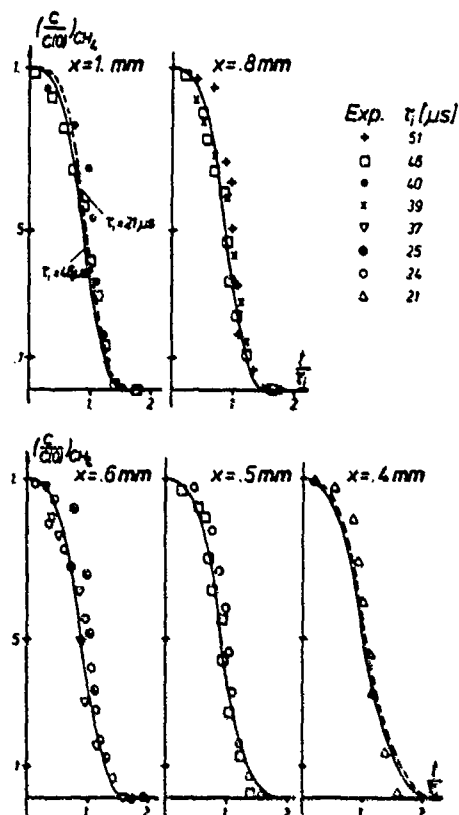
Figure 7: CH₄ concentration histories
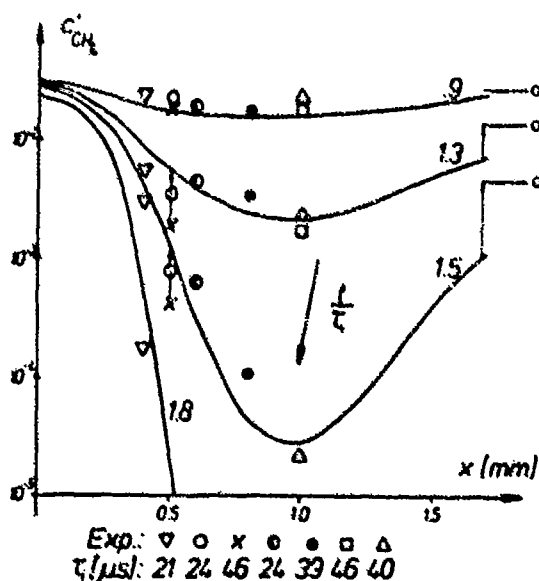
Figure 8:
Methane concentration profiles
(same conditions as in Fig. 3).
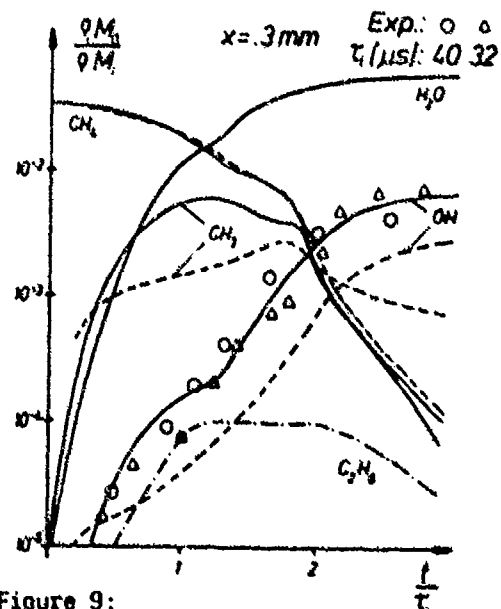
Figure 9:
Concentration histories near the wall
(solid line based on Bowman, broken
lines with inclusion of Warnatz'
reactions).

THE DISCHARGE FLOW / SHOCK TUBE AS A METHOD FOR STUDYING
CONTACT SURFACE MIXING

Patricia M.Borrell and Peter Borrell.
Department of Chemistry, Keele University,
Staffordshire, ST5 5BB, England.

Results are reported on the variation of the Lewis-Rayleigh and air afterglows with temperature between 293 K and 1000 K. These largely agree with earlier work, but differ in detail due to changes in emissivity with wavelength and spectral bandwidth.

At longer shock-flow times, an increase in emission is observed well in front of the contact surface. Experiments show that the disturbance is reproducible and travels at a speed intermediate between that of the shock front and the contact surface. The effect is attributed to changes in temperature and density as the driver and test gases mix. The possibility is raised of using our technique to study this mixing, provided that a satisfactory theoretical model can be found.

It may also be possible to use the technique to study boundary layer effects.

1. INTRODUCTION

Our current work is directed towards studying the kinetics and spectroscopy of reactive atoms at high temperature, and particularly the reactions of oxygen atoms, which are important in combustion but for which data is sparse and the extrapolations used in modelling may be unreliable. As preliminary work, we have studied the emission from nitrogen atoms and the air afterglow, some results of which are reported in this paper.

During the work a sudden increase in emission was noticed at much longer flows than we normally observe. It seemed worthwhile to report this and to suggest that, since the temperature and density dependence of the emission is known, it would be possible to use our technique to make a detailed study of this non-ideal behaviour on which there appears to be little information.

2. EXPERIMENTAL

The technique used is a combined discharge flow / shock tube, pioneered by Hartunian, Thompson and Hewitt[1] and Gross[2]. We have used it extensively in an improved form to study the reactions of singlet molecular oxygen[3,4,5].

A new apparatus similar in design to that described previously[4,5] was used for the experiments. Nitrogen atoms are generated by passing a flow of N_2 at 5 torr pressure through the cavity of a 2.45 GHz microwave generator (Microtron). The resulting flow is then passed into the 5 m test section of a 50 mm diameter glass shock tube, the direction of flow being opposite to that of the shock propagation.

The concentration, [N], is monitored with the yellow Lewis-Rayleigh afterglow:

(1)   N + N = N$_2$(B) = N$_2$(A) + hυ
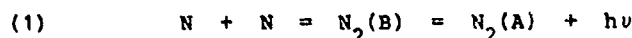
and the concentration gradient along the length of the tube in the pre-shock flow is observed with a mobile photomultiplier (EMI 9658B) and interference filters. The absolute concentration is measured by gas-phase titration with NO which reacts to give O atoms:

(2)   N + NO = N$_2$ + O

The addition of NO decreases the yellow glow, and at the dark equivalence point the flowrate of NO equals that of atomic N. Typically [N]/[N$_2$] = 0.4% in these experiments.

Addition of excess NO gives rise to the green air afterglow by reaction with the O atoms formed in (2):

(3)   O + NO = NO$_2$* = NO$_2$ + hυ
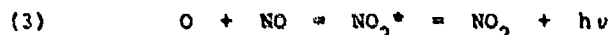
which again can be observed along the tube.

The shock part of the experiment is initiated after the initial flow conditions have been established and measured, by bursting naturally an aluminium diaphragm between the 0.9 m stainless steel driver section and the glass section, using N$_2$ or He as driver gas at ~1.5 bar pressure. The velocity is measured with laser light screens which trigger time interval meters; it is found that the velocity is constant in the 1 m measuring zone which is 3.5 m from the diaphragm.

The variation in emission with time is followed by fixed photomultipliers which view the tube either through an interference filter or a monochromator (Bentham). The outputs are recorded on transient recorders (Datalab) and passed for storage to a graphics terminal (HP2647A) and then on to the mainframe (GEC 4190) for processing by interactive graphics and non-linear least squares.

3. RESULTS

Normal Emission. Figure 1 shows a digitised trace of the change in emission for the Lewis-Rayleigh afterglow after shock heating. First can be seen the pre-shock emission from the N atoms in the flowing gas. At the shock front there is a jump due to the change in density, which is off-set by the lower emissivity found at higher temperatures. Then there is a fall in emission which simply reflects the pre-shock concentration gradient in the tube as the gas from up stream is swept past the observation station.

The trace can be described by the equation:

(4) $I(t) = K(T) (\rho_2/\rho_1)^2 I_{psg} \int_{t-\delta t}^{t} (1 + \alpha t)^{-1} dt / \delta t$

$I(t)$ and I_{psg} are the post- and pre-shock emissions at the observation station; δt is the integration time to allow for the finite slit width; the term in the integral describes the pre-shock decay along the tube in terms of second order kinetics; and $K(T)$ is the ratio of the emission observed, extrapolated to t=0, to that predicted from the pre-shock emission.

The constant, α, is measured from the post-shock trace, and can also be predicted from the pre-shock concentration gradient corrected for the shock compression and coordinate change; in a typical shock the pre- and post-shock values of α were found to be 2.35 and 2.32s, i.e. the same within experimental error.

In many previous studies with singlet oxygen[3,4,5], we found similar evidence that the ideal shock relations provide a good description of the post-shock flow in our apparatus. However with this work we notice that while the two values of α always agree, that predicted from the pre-shock measurements is always slightly higher than that from the post-shock trace. Thus the emission at any point is always slightly greater than expected, and the difference increases with time. Taking all the results into account therefore, we believe the difference to be significant and to show that we are observing directly the effect of the build-up of the boundary layer at longer times. The atoms in the cool region next to the wall would have a higher emissivity and lead to the effect observed.

For each run, equation (4) was fitted to the digitised points to optimise values of $K(T)$, δt and α. α and δt provide checks on the adequacy of each run; more than 100 runs were made and of these only 3 were rejected. The value of $K(T)$ gives the emissivity relative to its value at room temperature.

Variation of Emissivity with Temperature. For the air afterglow from $NO + O$, equation (3), the relative emissivity was found to vary in the following way:

(5) $\log K(T) = (-1.88 \pm 0.04) \log (T/293K)$

in agreement with that reported by Hartunian, Thompson and Hewitt[1] who were only able to study the jump at the shock front and were not able to analyse the subsequent flow. Thus the differences between the spectral properties of our detection systems and those of Hartuniun et. al. have no effect on the emissivity value, which is to be expected from the broad featureless spectrum of the emission[8].

In contrast, as figure 2 illustrates, much lower values for $K(T)$ were found for the Lewis-Rayleigh afterglow from atomic nitrogen (equation 2) than those which Gross[2] found with Hartunian's apparatus.

The relative emission was found to vary as:

(6) $\log K(T) = (-1.37 \pm 0.02) \log (T/293K)$

at 579 nm with a band width of 10 nm.

A variety of experiments were made to check the correctness of our lower values. We looked particularly at the values of I_{psq} obtained from the transient recorder traces and from the digital voltmeter which was normally used; the two were found to be the same within $\pm 3\%$. The spectrum for this emission is complicated[2,9] with much discrete vibrational structure. We are presently making a number of experiments[10] to study the variation of $K(T)$ with wavelength and spectral bandwidth; the first results indicate that there are marked differences from those in figure 2 which are appropriate to the prominent bands at 580 nm, and have the lowest $K(T)$ values. The higher values found by Gross[2] can only be reproduced with minor vibrational bands away from the main peaks in the spectrum[10].

The Anomalous Emission at Longer Times. Figure 3 shows an emission trace similar to figure 1, but displaying the behaviour at longer times which is not usually recorded or analysed. A prominent peak at ~1200 μs after the shock front is seen in a shock where the contact surface should arrive at 1700 μs. This was a surprise, but further experiments rapidly showed that the second peak appears on every trace, that the arrival time is quite reproducible, but that the peak height for a group of similar shocks is variable to $\pm 20\%$.

Figure 3 shows two traces from the same shock taken at observation stations 1 m apart. The time between shock front and peak is increasing with distance down the tube and shows clearly, as calculations do, that reflections from the end plate or the flow inlet are not responsible.

Shocks were tried with a He driver (M = 4), and a disturbance was observed but it was much less clear. However when the driver section was increased in length from 0.9 m to 1.25 m, clean peaks were again observed. Thus for faster shocks with the shorter driver, the rarefaction interferes with the second peak but is not responsible for its production.

The speed of the disturbance is intermediate between that of the shock front and that expected for the contact surface; for a M = 2.6 shock, for example, the speed of the front, peak and contact surface are 0.90, 0.77 and 0.71 km s^{-1} respectively. As figure 4 shows, there is an approximately linear dependence between time for arrival of the peak and shock speed.

As far as the emissivity measurements are concerned, the new peak has no effect since measurements are complete before its arrival. It is however interesting in its own right as an unexpected disturbance which shortens the expected hot flow time.

4. DISCUSSION

The variation of relative emissivity with temperature found for the air afterglow agrees well with that found previously[1], as is perhaps expected for a featureless spectrum. However, with the Lewis-Rayleigh afterglow from atomic nitrogen, the emissivity depends on the vibrational quantum number of the band being studied, and so varies markedly with wavelength and spectral resolution of the filter or monochromator being used. Thus, it is no wonder that our results do not agree in detail with those of Gross[2] although a linear dependence is found by both of us.

The good agreement found when comparing the experimental profile for the shock heated emission with that predicted from the pre-shock concentration measurements indicates that, in the first half of the flow regime, the fluid dynamic behaviour is near to ideal, as has been found in countless experiments with singlet molecular oxygen. However the small but consistent differences noted between pre- and post-shock concentration gradients does indicate that at longer times the boundary layer has an appreciable effect. Thus our method offers a more direct way of studying boundary layer effects than has hitherto been available.

At later flow times a peak in emission is observed which, it is fair to say, is not fully understood. The increase in emission indicates either a sudden increase in density of the shock heated gas, or a substantial fall in temperature. Rough calculations indicate that if the density and composition are constant, then the temperature falls to near room temperature from 600 K.

It seems likely that what is being observed is a mixing of the driver and driven gases. Since the effects are regular and reproducible, it appears the the discharge flow / shock tube might provide a simple method for studying non-ideal mixing effects which are still not well understood[1].

The beauty of the technique for this work is that the diagnostic emission is generated independently prior to the shock, and that the emission varies in a known way with density and temperature. The problem in interpreting the defined and regular profile is that ρ and T vary together, and that the emission will vary with the mixing. Thus a theoretical model is needed which will predict the development of ρ and T, and the extent of the mixing with time so that direct comparison with experiments can be made. Then the technique could offer one of the few ways of seeing the non-ideal effects at long times near the contact surface.

5. ACKNOWLEDGEMENTS

6. REFERENCES

1. R.A.Hartunian, W.P.Thompson and E.W.Hewitt, J.Chem.Phys., 1966, **44**, 1765
2. R.W.F.Gross, J.Chem.Phys., 1968, **48**, 1302
3. P.M.Borrell, P.Borrell and K.R.Grant, J.Chem.Phys., 1983, **78**, 748
4. P.Borrell, P.M.Borrell, D.S.Richards and R.Boodaghians, J.Photochem., 1984, **25**, 399
5. P.M.Borrell, M.D.Pedley, P.Borrell and K.R.Grant, Proc.Roy.Soc.Lond.A, 1979, **367**, 395
6. P.Borrell, Computers and Chemistry, 1980, **4**, 131
7. NAG Library Routine E04FCF, Numerical Algorithms Group, Oxford, 1982.
8. A. Fontijn, C.B.Meyer and H.I.Schiff, J.Chem.Phys., 1964, **40**, 64
9. R.W.B.Pearse and A.G.Gaydon, The Identification of Molecular Spectra, Chapman and Hall, London, 1963.
10. P.M.Borrell and P.Borrell, J.Chem.Soc.,Faraday Trans.2, (to be published.)
11. J.N.Bradley, Shock Waves in Chemistry and Physics,Methuen, London 1962.

Figure 1

The Lewis-Rayleigh Afterglow - a digitised shock trace

Figure 2

A log/log Plot of the Emission Efficiency
against Temperature
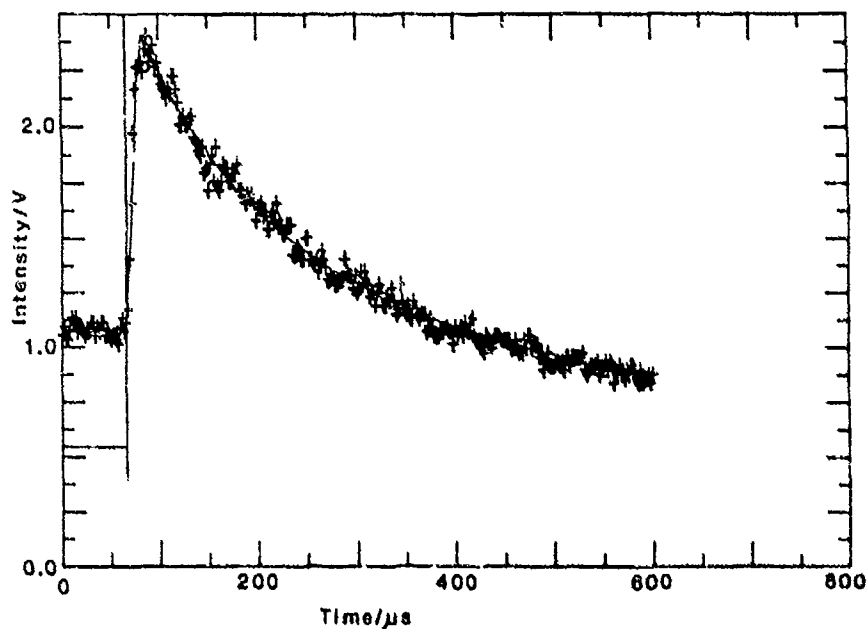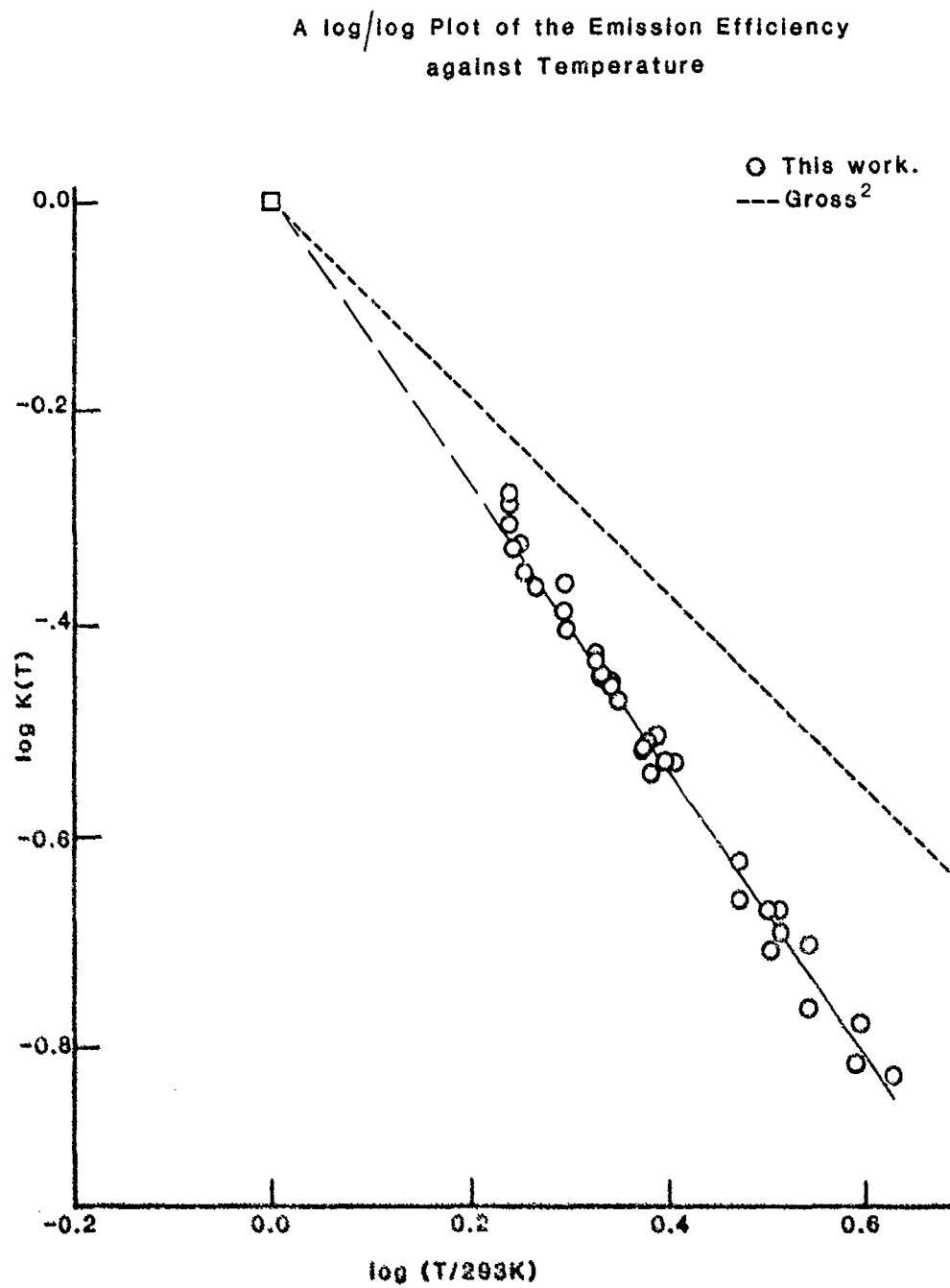
Figure 3

Emission Traces for the shock-heated Afterglow
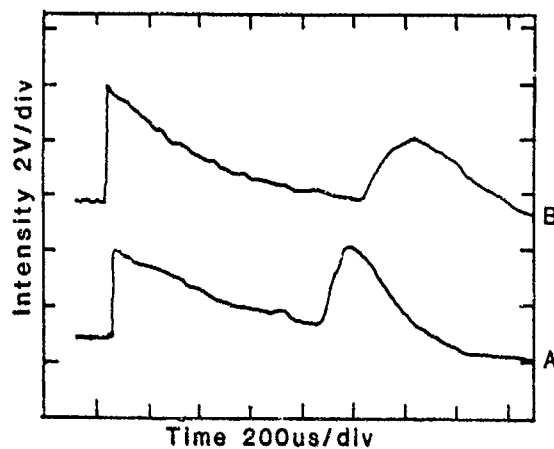
A – Detector 3m from diaphragm
B – Detector 4m from diaphragm

Figure 4

Variation of Time of Arrival
of Second Peak with Shock Speed.
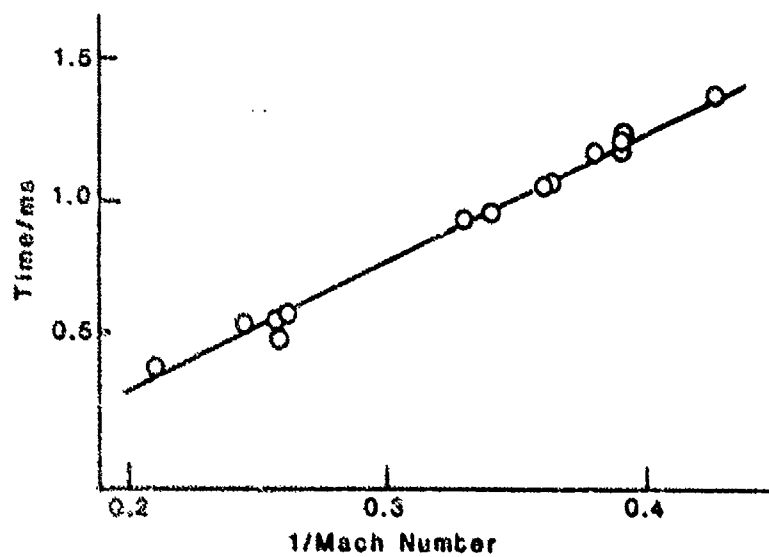
PERTURBATION ANALYSIS OF REACTIVE FLOWFIELDS IN SHOCK TUBES

Yasunari Takano

Department of Applied Mathematics and Physics
Tottori University, Tottori 680, Japan

This investigation considers effects of chemical reactions
on flowfields behind incident-shock waves in combustible gas
in shock tubes. The method of linearized characteristics is
applied to analyse gasdynamic disturbances due to chemical
reactions. The analysis treats cases where combustible gas
is sufficiently diluted in inert gas. The perturbed physi-
cal properties in the incident-shock region between shock
waves and contact surfaces are expressed mainly in terms of
a function representing amount of released chemical energy.
As numerical examples of the analysis, the formulations are
applied to calculate gasdynamic properties behind incident-
shock waves in H_2-O_2-Ar mixture. The analytical results are
compared with exact numerical solutions in order to examine
applicability of the analysis. It is shown that the formu-
lation can afford exact solutions in case chemical behaviors
are not affected essentially by gasdynamic behaviors. When
induction time of combustion process is reduced to some
extent due to gasdynamic disturbances, some discrepancies
appear between analytical results and exact solutions.

INTRODUCTION

The shock-tube techniques have been established for investigations of
reactive systems in gaseous medium.[1] When test gas is diluted in inert gas, its
chemical processes under an almost constant physical condition can be observed
behind a shock wave. However, the physical properties are not strictly constant
over the shocked region in reactive gas where gasdynamic disturbances are caused
by the release of chemical energy due to chemical reactions. Hence, in case the
gasdynamic disturbance can be estimated, rate coefficients of chemical reactions
are expected to be determined more precisely.

Chemical effects on shock-tube flowfields have been reliably predicted by
use of numerical procedures. Detailed modelings, which combine a finite differ-
ence method with a chemical kinetics simulation code, have been developed to
simulate phenomena of shocks and detonations in reactive gas.[2-4] As for analy-
tical treatments, Spence analysed the motion of a shock wave produced by impul-
sively started piston in relaxing gas by employing the method of linearized
characteristics and derived analytical forms for flowfields.[5] Also, Takano and
Akamatsu applied the method of linearized characteristics to consider gasdynamic
disturbances caused by chemical reactions in reflected-shock regions and ex-
pressed perturbations of the physical properties in terms of a function repre-
senting amount of chemical energy released to the flowfields.[6]

This investigation studies the gasdynamic behaviors behind incident shock
waves in combustible gas by employing the method developed in the previous
investigation.[6] It treats cases where combustible gas is so sufficiently
diluted in inert gas that chemical processes may not be affected by the gas-
dynamic disturbances. For numerical examples of the analysis, perturbed flow-
fields in hydrogen and oxygen diluted in argon mixture are calculated. The
applicability of the analysis to actual reacting shock waves is considered
by comparing the analytical results with exact numerical solutions obtained
by applying a detailed modeling reported in the previous symposium.[4]

ANALYSIS

In this analysis, we consider gasdynamic phenomena due to chemical reactions initiated by the heating of shock waves. The transport processes are negligible compared with wave motions. The basic equations for time-dependent, one-dimensional reactive flow can be written as follows (see Takano et al[6]),

$$\frac{\partial \rho}{\partial t} + u\frac{\partial \rho}{\partial x} + \rho\frac{\partial u}{\partial x} = 0, \qquad \frac{\partial u}{\partial t} + u\frac{\partial u}{\partial x} + \frac{1}{\rho}\frac{\partial p}{\partial x} = 0, \qquad (1,2)$$

$$\frac{\partial p}{\partial t} + u\frac{\partial p}{\partial x} + \gamma p\frac{\partial u}{\partial x} = q = (\gamma-1)\sum_{j=1}^{N}(M_w C_p T - M_j h_j)w_j, \qquad (3)$$

$$\frac{\partial}{\partial t}c_j + u\frac{\partial}{\partial x}c_j = \frac{1}{\rho}M_j w_j(c_1,\ldots,c_N;\rho,T), \qquad j = 1,\ldots,N, \qquad (4)$$

where ρ, u, p and T are the density, the velocity, the pressure and the temperature of mixture, respectively. c_j, M_j, w_j, h_j are the mass fraction, the molar weight, the molar production rate and the enthalpy for the jth species of the mixture with N components. C_p, M_w and γ are the specific heat, the molar weight and specific heat ratio. In addition, x and t are the distance from the diaphragm and the time after the diaphragm bursting, respectively.

In the present investigation, we consider a situation where combustible gas is diluted in inert ideal gas. Therefore, by taking the mass fraction for reactant as a parameter of expansions, ε, we introduce the following expansions:

$$\rho(x,t) = \rho_i\{1 + \varepsilon\tilde{\rho}(x',t') + O(\varepsilon^2)\}, \qquad (5)$$

$$u(x,t) = a_i\{\bar{u}_i + \varepsilon\tilde{u}(x',t') + O(\varepsilon^2)\}, \qquad (6)$$

$$p(x,t) = \rho_i a_i^2\{1/\gamma_i + \varepsilon\tilde{p}(x',t') + O(\varepsilon^2)\}, \qquad (7)$$

$$c_j(x,t) = \delta_{ij} + \varepsilon M_j\tilde{\sigma}_j(x',t') + O(\varepsilon^2), \qquad (8)$$

$$t = t_r(\varepsilon)t', \qquad x = a_i t_r(\varepsilon)x'. \qquad (9a,b)$$

Here, the subscript i denotes the physical properties of inert gas where no combustible gas is added in. The tilde is put to denote the dimensionless perturbed properties. a_i is the acoustic speed in the inert gas. δ_{ji} is the Kronecker's delta. $t_r(\varepsilon)$ is the characteristic time for chemical reactions.

Substituting the expansions (5)-(9) into gasdynamic equations (1)-(3) and rate equations (4), and equating terms in the order of ε, we obtain following linearized equations:

$$(\frac{\partial}{\partial t'} + (\bar{u}_i \pm 1)\frac{\partial}{\partial x'})(\tilde{p} \pm \tilde{u}) = \tilde{q}, \qquad (10,11)$$

$$(\frac{\partial}{\partial t'} + \bar{u}_i\frac{\partial}{\partial x'})(\tilde{p} - \tilde{\rho}) = \tilde{q}, \qquad \tilde{q} = M_i\sum_{j=1}^{N}\{1-\frac{h_j(T_i)M_j}{C_{pi}T_i M_i}\}\tilde{w}_j, \qquad (12,13)$$

$$(\frac{\partial}{\partial t'} + \bar{u}_i\frac{\partial}{\partial x'})\tilde{\sigma}_j = \tilde{w}_j(\tilde{\sigma}_1,\ldots,\tilde{\sigma}_N;T_i,\rho_i), \qquad (14)$$

where $\tilde{q}$ and $\tilde{w}_j$ are leading terms in expansions for production rates of chemical energy and moles of the jth species, respectively:

$$q = \rho_i a_i^2 t_r(\varepsilon)^{-1}\{\varepsilon\tilde{q} + O(\varepsilon^2)\}, \qquad (15)$$

$$w_j = \rho_i t_r(\varepsilon)^{-1}\{\varepsilon\tilde{w}_j + O(\varepsilon^2)\}. \tag{16}$$

As shown in Fig.1, the linearized equations (10)-(14) are integrated in the domain bounded by the shock front and the contact surface whose boundary conditions are written formally as follows,

$$\tilde{p} - \tilde{u} = R\ (\tilde{p} + \tilde{u}), \qquad \tilde{p} - \tilde{\rho} = L\ (\tilde{p} + \tilde{u}), \qquad \text{at } x' = \bar{u}_S t' \tag{17}$$

$$\tilde{p} + \tilde{u} = C\ (\tilde{p} - \tilde{u}), \qquad \text{at } x' = \bar{u}_i t' \tag{18}$$

where $\bar{u}_S$ is the normalized shock speed in the inert gas. In the present formulation, the boundary conditions at the shock front and at the contact surface are respectively applied on $x' = \bar{u}_S t'$ and on $x' = \bar{u}_i t'$ instead of real trajectories. These approximations cause errors of $O(\varepsilon^3)$ as long as the deviations of the real trajectories to the idealized ones remain $O(\varepsilon)$.

Substituting the expansions (5)-(9) into the Rankine-Hugoniot relations and equating terms in the order of ε, we obtain linearized relations, from which boundary conditions at shock fronts can be derived as follows,

$$R = (\bar{\rho}_1 \bar{a}_1 \frac{2M_S^3}{1+M_S^2} - 1)/(\bar{\rho}_1 \bar{a}_1 \frac{2M_S^3}{1+M_S^2} + 1), \tag{19a}$$

$$L = \frac{1+R}{2}\ [1 - \{\frac{1}{\bar{a}_1} \frac{\gamma_i + 1}{(\gamma_i-1)M_S^2+2}\}^2\ ]. \tag{19b}$$

where M_S is the Mach number of incident shock waves and $\bar{\rho}_1$ ($= \rho_1/a_i$) and $\bar{a}_1$ ($= a_1/a_i$) are respectively the normalized density and the acoustic speed in the region ahead of incident shock waves. Also, expanding similarly the relations for contact surfaces and assuming isentropic driver gas and no disturbing wave coming behind contact surfaces, we obtain boundary conditions at the contact surfaces:

$$C = (\bar{\rho}_3 \bar{a}_3 - 1)/(\bar{\rho}_3 \bar{a}_3 + 1) \tag{20}$$

where $\bar{\rho}_3$ ($= \rho_3/\rho_i$) and $\bar{a}_3$ ($= a_3/a_i$) are respectively the normalized density and the acoustic speed in the region behind contact surfaces. It should be mentioned that these conditions (19) and (20) are already given by Mirels who developed perturbation theory for the shock attenuation and nonuniform flows in in shock tubes due to side-wall boundary-layers.[7] Values of these coefficients and parameters of shock waves in monatomic gas are listed in Table 1.

As the upstream region ahead of incident shock waves is in chemically frozen state, $\tilde{\sigma}_j$ is constant over the upstream region. Hence, $\tilde{\sigma}_j$ remain constant along $x' = \bar{u}_S t'$. Therefore we obtain from (14),

$$\tilde{\sigma}_j(x',t') = S_j[(\bar{u}_S t'-x')/(\bar{u}_S-\bar{u}_i)], \tag{21a}$$

$$dS_j(t')/dt' = \tilde{w}_j(S_1,\ldots,S_N;T_i,\rho_i). \tag{21b}$$

Then, $\tilde{q}$ also becomes a function of the time elapsed after the shock heating:

$$\tilde{q}(x',t') = q_0[(\bar{u}_S t'-x')/(\bar{u}_S-\bar{u}_i)]. \tag{22}$$

By making use of this character of time-coherency for chemical process in mixture entering shock fronts, we integrate (10)-(14) along their characteristic lines and apply the boundary conditions. Then, $\tilde{p} + \tilde{u}$, $\tilde{p} - \tilde{u}$ and $\tilde{p} - \tilde{\rho}$ are expressed in terms of Q, an integral function of q_0, which is defined as,

$$Q(t') = M_i \sum_{j=1}^{N} \{1 - \frac{h_j(T_i)M_i}{C_{pi}T_iM_i}\}\{S_j(t') - S_j(0)\}, \tag{23}$$

Here, the function Q represents amount of chemical energy released to flow fields. After all, the variations of the perturbed physical properties are written as

$$\tilde{p}(x',t') = \frac{1}{2k}\{(-1+\frac{1}{\ell})Q(\frac{\bar{u}_S t'-x'}{\bar{u}_S-\bar{u}_i})+(1+\frac{C}{\ell})Q[(\bar{u}_i+1)t'-x']\} + O(R), \tag{24}$$

$$\tilde{u}(x',t') = \frac{1}{2k}\{-(1+\frac{1}{\ell})Q(\frac{\bar{u}_S t'-x'}{\bar{u}_S-\bar{u}_i})+(1+\frac{C}{\ell})Q[(\bar{u}_i+1)t'-x']\} + O(R), \tag{25}$$

$$\tilde{\rho}(x',t') = \frac{1}{2k}\{(-1+\frac{1}{\ell}-2k)Q(\frac{\bar{u}_S t'-x'}{\bar{u}_S-\bar{u}_i})+(1+\frac{C}{\ell})Q[(\bar{u}_i+1)t'-x']$$

$$-2(1+\frac{C}{\ell})LQ[k(x'-\bar{u}_i t')]\} + O(R), \tag{26}$$

where
$$k = \frac{1-\bar{u}_S+\bar{u}_i}{\bar{u}_S-\bar{u}_i}, \qquad \ell = \frac{1+\bar{u}_S-\bar{u}_i}{1-\bar{u}_S+\bar{u}_i}. \tag{27a,b}$$

In addition, the temperature variation is represented as

$$\tilde{T}(x',t') = \gamma_i\tilde{p}(x',t') - \tilde{\rho}(x',t') - M_i \sum_{j=1}^{N} S_j[(\bar{u}_S t'-x')/(\bar{u}_S-\bar{u}_i)] \tag{28}$$

NUMERICAL EXAMPLES

As numerical examples of the analysis, we calculate gasdynamic disturbances behind incident-shock waves in stoichiometric hydrogen and oxygen diluted in argon mixture by using the present formulation. A chemical kinetics model and thermochemical data used here are written in the previous papers. Parameters for calculations are listed in Table 2, where M_s is the shock Mach number and P_1 is the initial pressure of argon in the upstream region. As the parameter, ε, of the expansions, we use the mass fraction of oxygen molecules in the upstream region. Also, as the characteristic time $t_r(\varepsilon)$, we employ an induction time for the combustible gas added in the inert gas.

By numerically integrating rate equations (21), we obtain variations of concentrations for chemical species and determine a heat-release function from (23). Figure 2 shows S_j and Q for Case I. In the combustible mixture heated by a shock wave, intermediate species such as H, O and OH increase exponentially due to induction reactions which release almost no chemical heat. In the induction time, an ignition takes place; the formation of H_2O and the consumption of H_2 and O_2 occur rapidly and exothermic reactions dominate.

Distributions of the perturbed physical properties, $\tilde{\rho}$, $\tilde{u}$ and $\tilde{p}$, in the incident-shock region can be calculated from Q(t'), while the perturbed temperature is expressed in terms of Q(t') and $S_j(t')$. Figure 3 shows the perturbed physical properties in the incident-shock region as functions of the distance from the contact surface. The heat release begins in the gas adjacent to the contact surface in the induction time after shock heating. The pressure and the temperature rise in the region with the heat addition. A compression wave is generated and it propagates to the incident-shock front. The point where the pressure is the maxmum in the distribution refers to the start of ignition and it forms a reaction front in the flowfield. The parameter C = 0 of the contact surface means that acoustic impedances (ρa) are identical across it.

The parameter $C = 1$ refers to cases where the driven gas is pushed by the rigid piston, while $C = -1$ refers to cases where the driver gas is extremely light. It is observed that the heavier the driver gas is, the stronger compression wave is generated.

COMPARISONS WITH RIGOROUS SOLUTIONS

In order to examine a limit of the applicabily of the analysis, we compare the analytically obtained results with rigorous solutions which are numerically obtained by use of a finite difference method. Computations are conducted to simulate situations where an incident-shock wave, steadily propagating in pure argon gas, passes through stoichiometric hydrogen and oxygen diluted in argon mixture at the same pressure. Hence, the numerical results are comparable to the analytical ones for cases of $C = 0$. Figure 4 shows a comparisons of perturbed physical properties between analytical and numerical results for Case I, which is normalized according to (5)-(7) and (9) by using the parameter of the expansions, $\varepsilon = 0.013$. The comparisons are excellent except some discrepancy of the density distribution. It is shown that the present formulation can afford exact solutions of perturbed flowfields due to chemical reactions in the incident-shock region.

Another simulation is carried out for a situation where some coupling takes place between gasdynamics and chemical kinetics. Figure 5 shows comparisons for Case II between analytical and numerical results, which are normalized by using $\varepsilon = 0.02$. An induction distance from the shock front to the reaction front is reduced to some extent in the simulation, while it is invariable in the analysis because of the de-coupling of fluid motions and chemical processes. The reduction of the induction distance is caused by mainly the temperature rise in the induction region between the shock front and the reaction front. Unless the variation of the induction distance remains small, the analytical results become questionable.

CONCLUSIONS

The method of linearized characteristics has been applied to analyse gasdynamic disturbances due to chemical reactions in the incident-shock regions between incident-shock waves and contact surfaces in shock tubes. The analysis treats cases where combustible gas is diluted in inert gas so that chemical behaviors are not affected by the gasdynamic behaviors.

Perturbations of the physical properties in the incident-shock regions can be expressed in series terms of a heat-release function which represents amount of released chemical energy. As numerical examples of the analysis, gasdynamic disturbances behind incident-shock waves in H_2-O_2-Ar mixture are calculated by applying the formulation. The analytical results are compared with rigorous solutions numerically obtained by use of a finite difference method. It is shown that the analytical formulation can afford exact solutions in case chemical behaviors are not affected essentially by gasdynamic behaviors. However, it cannot give proper discriptions for fluid motions when the gasdynamic disturbances reduce the induction time (or distance).

ACKNOWLEGEMENTS

REFERENCES

1. Lifshitz, A., "Anatomy of complex reaction systems. Combustion reaction mechanisms from ignition delay times", Proc. 14th Intl. Symp. on Shock Tubes & Shock Waves. 1984, p.26.

2. Oran, E., Young, T. and Boris, J., "Application of time-dependent numerical methods to the description of reactive shocks", 17th Symp. (Intl.) on Combustion, 1978, p.43.

3. Oran, E., Young, T., Boris, J. and Cohen, A., "Weak and strong ignition", Comb. Flame 48, 1982, p.135.

4. Takano, Y., Kittaka, S. and Akamatsu, T., "Studies on gasdynamic behaviors on combustible gas in a shock tube", Proc. 14th Intl. Symp. on Shock Tubes & Shock Waves, 1984, p.730.

5. Spence, D., "Unsteady shock propagation in a relaxing gas", Proc. Roy. Soc. London A262, 1961, p.221.

6. Takano, Y. and Akamatsu, T., "Analysis of chemical effects on refected-shock flow fields in combustible gas", J. Fluid Mech. (in press) 1985.

7. Mirels, H. and Mullen, J., "Small perturbation theory for shock-tube attenuation and nonuniformity", Phys. Fluids 7, 1964, p.1208.
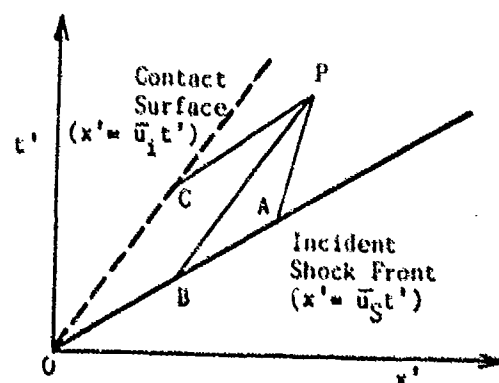
Fig. 1. Schematic (x,t)-diagram of Incident-Shock Region

Table 1. Coefficients for Boundary Conditions at Incident-Shock Fronts

M_S	$\bar{\rho}_1$	$\bar{a}_1$	R	L
1	1	1	0	0
2	0.437	0.694	-0.014	0.158
3	0.333	0.522	-0.030	0.287
4	0.297	0.413	-0.040	0.355

Table 2. Conditions for analytical and numerical results

Case	M_S	p_1 KPa	ρ_i Kg/m^3	a_i Km/s	T_i K	$\epsilon t_r(\epsilon)$ µs	ϵ
I	4	16	0.884	0.771	1718	0.304	0.013
II	3.4	16	0.833	0.674	1310	1.438	0.020
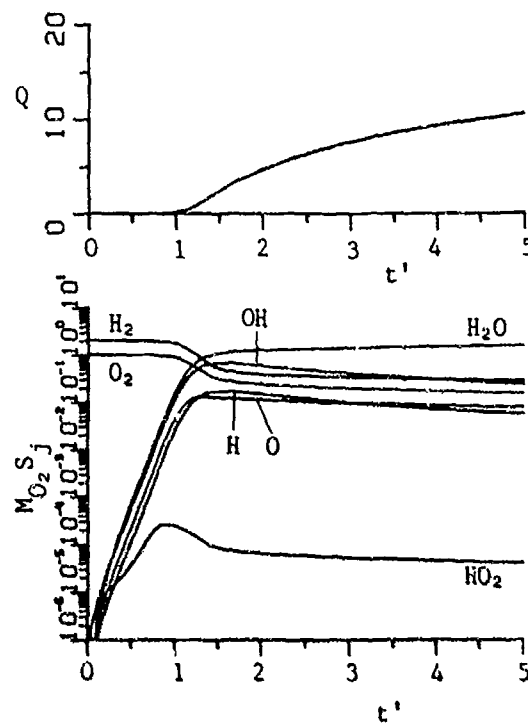
Fig. 2. Heat-release function and variations of concentrations for chemical species in shock-heated mixture. Simulations are conducted for Case I.

Fig. 3. Perturbed physical properties in incident-shock region at $t' = 2$ for Case I.

Fig. 4. Comparisons between analytical results (——) and numerical results (---) at $t' = 4$ for Case I with $C = 0$.
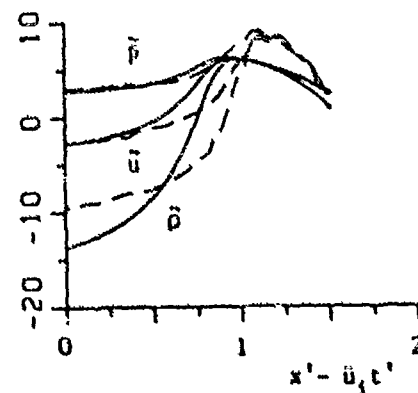
Fig. 5. Comparisons between analytical results (——) and numeircal results (---) at $t' = 3$ for Case II with $C = 0$.

NUMERICAL SIMULATIONS OF THE INITIATION OF
GASEOUS DETONATIONS IN SHOCK TUBES

K. Kailasanath, E.S. Oran and J.P. Boris

Laboratory for Computational Physics
Naval Research Laboratory
Washington, DC 20375.

In this paper we describe a time-dependent reactive shock
model and use it to simulate the initiation of gaseous
detonations in shock tubes. The results of the numerical
simulations are compared to the predictions of a theoretical
model developed earlier to study power-energy relations
for the initiation of detonations. The comparisons show
that the power-energy relation obtained from the detailed
simulations agrees with that predicted by the theoretical
model when the Mach number of the shock is high. However for
lower Mach numbers, the detailed simulations show initiation
with lower energies than those predicted by the theoretical
model. For the lower Mach numbers, the shock heated gas
mixture is shown to be in the weak-ignition regime and
therefore very sensitive to perturbations. We then study
the effects of velocity perturbations on ignition in a
hydrogen-air mixture. Finally we discuss the implications
of these results on the use of shock-tube simulations and
experiments for determining power-energy relations.

I. INTRODUCTION

In a previous paper[1], referred to below as Paper I, we developed a simple
theoretical model to determine the relation between the power and energy
required for the shock initiation of gaseous detonations. The model explained
the qualitative differences in the power-energy relations obtained from two
different experimental arrangements[1,2]. The model also gave qualitatively
good predictions of the power-energy relation for the initiation of cylindrical
detonations in an acetylene-oxygen-nitrogen mixture[1,2]. However, the minimum
power and the minimum energy predicted by the model were quantitatively
different from those obtained experimentally. In Paper I, we suggested that one
of the reasons for these differences is the uncertainty in one of the parameters
of the theoretical model, t_{cr}, the critical time in which energy must be
deposited to initiate a detonation. In this paper we address the problem of
uncertainty in t_{cr} by comparing the predictions of the theoretical model to
results obtained from detailed numerical simulations of the initiation of planar
detonations in shock tubes.

II. THE THEORETICAL MODEL

Since the theoretical model has already been discussed in detail in Paper I
and Ref. 2, we only give a brief outline here. The model considers the flow
generated by the motion of a constant velocity shock wave in planar, cylindrical
and spherical geometries. As this shock wave passes through a gas mixture, the
gas temperature and pressure increases. Due to this increase in temperature and
pressure, ignition can occur in the shock heated gas mixture after the elapse of
a certain time and this may lead to detonation.

A constant velocity shock wave can be formed in each of the three geometries by the motion of a constant velocity piston[2,4]. Furthermore it can be shown[5] that a pressure and velocity field identical to that ahead of a constant velocity piston can be generated by appropriate energy addition. For example, a flow field bounded by a constant velocity planar shock wave and a constant velocity planar piston can be generated by a planar energy source with a constant rate of energy deposition. An example of such an energy source is the high pressure driver in a uniform shock-tube. In Paper I, we have shown that the power and energy required for the initiation of a planar detonation is given by:

$$(P_{cr}) = p_p u_p \tag{1}$$

$$(E_{cr}) = p_p u_p t_{cr}, \tag{2}$$

where p_p and u_p are the pressure and velocity at the piston surface and t_{cr} is the minimum time in which energy must be deposited in order to initiate a detonation. In the planar case, the pressure and velocity at the piston surface are identical to those behind the shock wave and can be easily calculated using the equations given in Appendix C of Ref. 2. In order to determine the power-energy relation using Eqs. (1,2), we also need to know t_{cr}. As before we assume that this time is equal to the induction delay time corresponding to the conditions at the piston surface. We then critically examine this assumption by comparing the power-energy relation so obtained (from Eqs. (1,2)) to that from detailed numerical simulations. The numerical model used for these detailed simulations is briefly described below.

III. THE REACTIVE SHOCK NUMERICAL MODEL

The one-dimensional reactive shock model[6,7] solves the time-dependent conservation equations for mass, momentum and energy coupled to the equations describing the chemical kinetics. The model uses an explicit, Eulerian finite difference formulation with a sliding rezone capability to provide resolution around moving gradients. The solutions of the equations describing the fluid dynamics and the chemistry of the problem are coupled using time-step splitting techniques[7].

The convective transport terms in the conservation equations are solved using one variant of the Flux-Corrected Transport (FCT) method[8]. This is a conservative, monotonic algorithm with fourth-order phase accuracy and does not require artificial viscosity to stabilize shocks. The ordinary differential equations describing the chemical kinetics are solved using VSAIM, a vectorized version of the selected asymptotic integration method employed in CHEMEQ[9]. This algorithm identifies the stiff equations for treatment with a stiffly stable method. The remaining equations are solved with a standard classical method. The chemical kinetics rate scheme used consists of about fifty chemical rates relating the species H_2, O_2, H, O, OH, HO_2, H_2O and H_2O_2.

IV. POWER-ENERGY RELATION FOR THE INITIATION OF PLANAR DETONATIONS

We first used the theoretical model to determine the power-energy relation for the initiation of planar detonations in a hydrogen-oxygen-nitrogen (2:1:4) mixture. The Mach number of the shock wave was varied and for each Mach number the temperature, pressure and velocity of the shocked gas mixture were obtained using the modified shock relations given in Appendix C of Ref. 2. The time duration necessary for successful initiation was assumed to be equal to the chemical induction time of the mixture corresponding to the conditions at the piston surface. The induction time used was obtained by integrating the same chemical kinetics rate equations used in the numerical simulations. Knowing the

pressure, velocity and induction time of the shocked gas mixture, the power and energy are obtained from Eqs. (1,2). The power and energy deposited in the gas mixture are shown in Fig. 1 as a function of the shock Mach number.

V. INITIATION OF DETONATIONS IN SHOCK TUBES

We then set up the numerical model described in section III above to simulate shock tube experiments in which the driver was helium and the driven section was filled with a hydrogen-oxygen-nitrogen mixture (2:1:4) at 298 K and 0.5 atm. By varying the pressure ratio across the diaphragm of the shock tube we obtained constant velocity shocks of various strengths in the driven section. For each pressure ratio we noted the times at which ignition and detonation occurred as well as the pressure and velocity at the contact surface. For the problem at hand, we define the time at which ignition occurs as the first time at which a temperature increase of 10 % is observed anywhere in the shock heated gas mixture. The time at which detonation occurs is defined as the first time when the shock velocity attains the Chapman-Jouguet detonation velocity.

Some of the results from a typical simulation (corresponding to a pressure ratio of 200) are shown in Fig. 2. Here ignition is first observed at about 9.5 microseconds (after the bursting of the diaphragm) at the contact surface. The chemical energy released causes a rapid rise in the temperature and the pressure near the contact surface whose velocity then changes rapidly, as seen in Fig. 2b. The entire region between the contact surface and the shock front has ignited by 12 microseconds. The pressure behind the shock front (see Fig. 2c) has attained its peak value by this time. Both the "shock" velocity and the pressure history indicate that the shock transitions to a detonation by about 12 microseconds. For longer time both the shock/detonation velocity and the pressure gradually decrease towards the Chapman-Jouguet values.

Such calculations can be used to evaluate the power, which is the rate of energy input to the driven section. The power is equal to the rate of work performed by the contact surface which is the product of the pressure and velocity of the contact surface. The pressure at the contact surface is directly obtained from the simulations while the velocity of the contact surface is calculated from the history of the location of the contact surface. The energy is obtained as a time integral of the power.

The results from the simulations when the pressure ratio was 110 did not show any trace of detonation. The shock velocity, the contact surface velocity and the pressure behind the shock front are shown as functions of time for this case in Fig. 3. Here the contact surface velocity is constant until 0.6 ms, and it then decreases with time. This happens because the rarefaction waves have reached the contact surface (after being reflected from the driver end wall) before ignition could occur. The interaction between the rarefaction waves and the contact surface decreases the velocity of the contact surface. By 1.1 ms the rarefaction waves have caught up with the shock front and begun to reduce its velocity. The temperature behind the weakened shock front when the simulation was terminated after 1.6 ms was only 800 K. This case implies that for a shock tube of a given driver size there is a pressure ratio below which the rarefaction waves will interact so quickly with the shock front that they prevent a detonation from occurring. Therefore the minimum power determined using shock tube simulations or experiments would depend on the size of the driver used.

VI. COMPARISONS OF RESULTS

We then compared the results from the detailed simulations to those from the theoretical model. The power and energy from the theoretical model (from

Fig. 1) are shown in Fig. 4 along with the the data points from the numerical simulations. The predictions of the theoretical model agree with the results from the numerical simulations when the Mach number of the shock wave is high. However for low mach numbers, the numerical simulations show initiation with lower energies than those predicted by the theoretical model. One of the objectives of this work was to examine the assumption made in the theoretical model that the appropriate time to use is the induction time corresponding to the conditions at the contact surface. In Fig. 5, the induction time corresponding to the conditions behind the shock (and at the contact surface), the time at which ignition was observed, and the time at which the shock transitioned to detonation are shown as a function of shock Mach number. We observe that for high Mach numbers the assumption made in the theoretical model is quite good, but as we go towards lower Mach numbers the difference between the chemical induction time and the time at which ignition actually occurs increases. More surprisingly, ignition occcurs earlier in the detailed simulations. A closer look at the results show that the pressures and temperatures near the contact surface for the lower Mach number cases are in the weak-ignition regime and therefore very sensitive to perturbations[3].

VII. SENSITIVITY OF IGNITION TO PERTURBATIONS

The sensitivity of ignition to perturbations can be assessed by considering derivatives of the chemical induction time with respect to parameters of the system such as temperature, pressure or stoichiometry. One important quantity to consider is

$$S = - (T/\tau) \left(\partial\tau/\partial T|_{entr} \right) \qquad (3)$$

which shows the sensitivity of the induction time to acoustic perturbations. The value of S for the conditions behind the incident shock in some of the calculations described above is between 35 and 40, indicating a fairly strong susceptibility of ignition times to perturbations. This means that 2.5-3% change in temperature changes the induction time by 100%.

In order to evaluate the effect of perturbations on the power energy relation, we reconfigured the numerical model to simulate a closed tube containing the reactive mixture at a specific temperature and pressure. We then imposed velocity fluctuations of various amplitudes and frequencies and obspved the time at which ignition occured in the various cases. Consider the specific example of the shock tube simulation with a pressure ratio of 110. The temperture and pressure behind the incident shock in this case are 975 K and 800 kPa respectively. We then impose a velocity perturbation[3] on the system at each location x such that

$$V (x, t=0) = V_0 \, \sin (\pi x/L) \qquad (4)$$

where V_0 is the amplitude and L is the half wavelength of the velocity perturbation.

Figure 6 shows the time history of the temperature taken from one simulation in which there are roughly three periods of oscillation in an induction time. In this case, L is 90 cm (giving a frequency of 403 Hz) since the induction time is 7380 microseconds. The amplitude of the perturbation, V_0, is 100 m/s. With this perturbation, the system ignites first at the left wall at 4923 microseconds, then at the center and finally at the right wall at 5391 microseconds. Thus we observe that the time to ignition is reduced by 2457 microseconds due to the velocity perturbation.

A number of such calculations provided information on the change in the induction time as a function of amplitude and frequencies. Using this information in the power-energy relation (Eq. 1,2), the energy required for initiation of detonations has been calculated for the cases of the various disturbances. This is shown in Fig. 7. We observe that low frequency perturbations are more critical, since for these frequencies smaller amplitude perturbations are sufficient to substantially reduce the ignition times and the energy required for initiation of detonation. For example, to reduce the energy by a factor of three, we need low frequency perturbations (L = 270 cm) of amplitude 100 m/s or higher frequency perturbations (L = 2.7 cm) of amplitude 33 m/s. We also note that in the limit of no frequency (i.e. local hot spots) a small temperature perturbation could have an enormous effect on the ignition time and the energy required for initiation of a detonation.

VIII.   CONCLUSIONS

From the results presented in this paper, we observe that: (1) for the initiation of planar detonations, the appropriate time to use in the theoretical model is the induction time, provided the mixture under consideration is not in regime sensitive to perturbations;   (2) for mixtures which are sensitive to perturbations, the power-energy relation will also depend upon the actual perturbations present in the system;   (3) the minimum power determined using shock tube simulations or experiments will depend on the length of the driver used.

Acknowledgements

REFERENCES

1. Kailasanath, K. and Oran, F.S., "Power-Energy Relations for the Direct Initiation of Gaseous Detonations", Prog. in Astro.and Aero., Vol. 94, 1984, p. 38

2. Kailasanath, K. and Oran, E.S., "The Relation between Power and Energy in the Shock Initiation of Detonations-I. Basic Theoretical Considerations and the Effect of Geometry", NRL Memorandum Report 5179, Naval Research Laboratory, Washington, DC, 1983.

3. Oran, E.S. and Boris, J.P., Combust. Flame., Vol. 48, 1982, p. 149.

4. Taylor, G.I., Proc. Roy. Soc. (London), A 186, 1946, p. 273.

5. Chu, B.T., "Pressure Waves Generated by Addition of Heat in a Gaseous Medium NACA TN 3411, NACA, Washington, DC, 1955.

6. Oran, E.S., Young, T.R., and Boris, J.P., Seventeenth Symposium (International) on Combustion, The Combustion Institute, Pittsburgh, PA, 1979, p. 43.

7. Oran, E.S., and Boris, J.P., Prog. Energy. Combust. Sci. Vol. 7, 1981, p. 1.

8. Boris, J.P. and Book, D.L., Methods of Computational Physics, Academic Press New York, Vol. 16, 1976, p. 85.

9. Young, T.R., "CHEMEQ, A Subroutine for Solving Stiff Ordinary Differential Equations' NRL Memorandum Report 4091, Naval Research Laboratory, Washington DC, 1980.
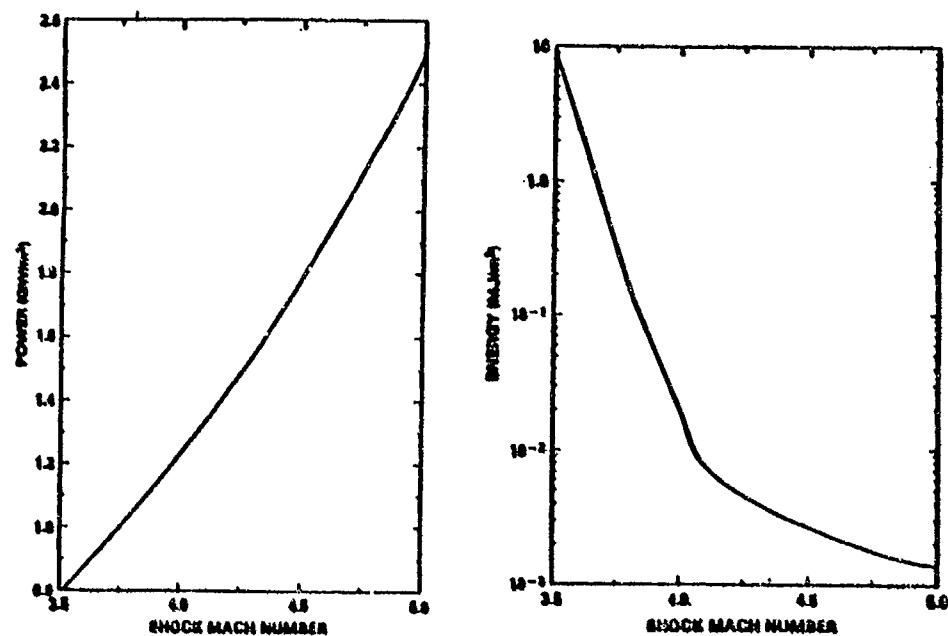
Fig. 1 The Power and Energy calculated using the theoretical model.
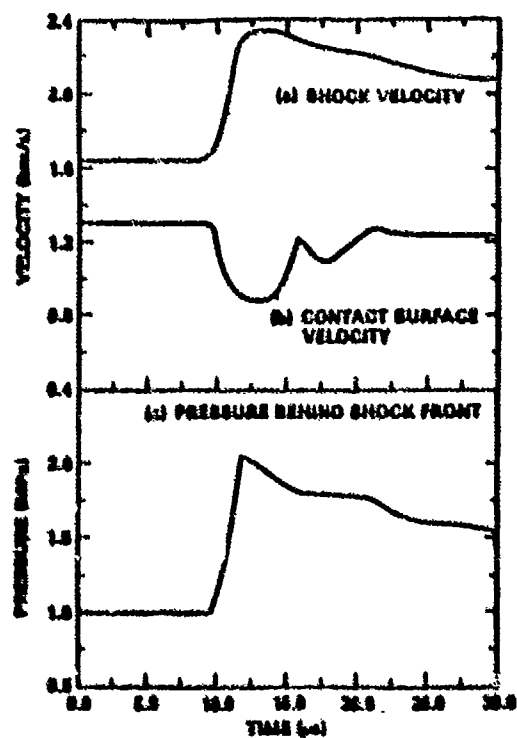
Fig. 2 Time history of (a) the shock velocity, (b) the contact surface velocity, (c) the pressure behind the shock front in the shock tube simulations for a pressure ratio of 200.
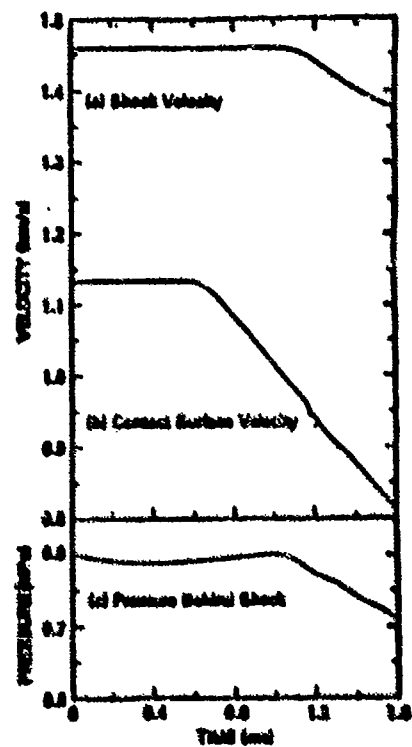
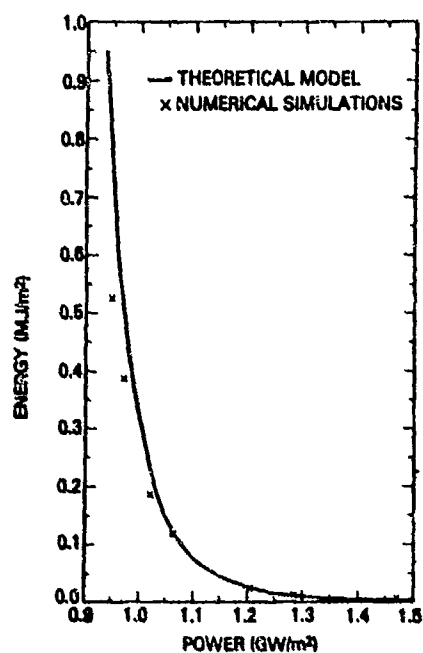Fig. 3 As in Fig. 2 but for a diaphragm pressure ratio of 110.

Fig. 4 Comparison of power and energy values obtained from the theoretical model and the shock tube simulations.
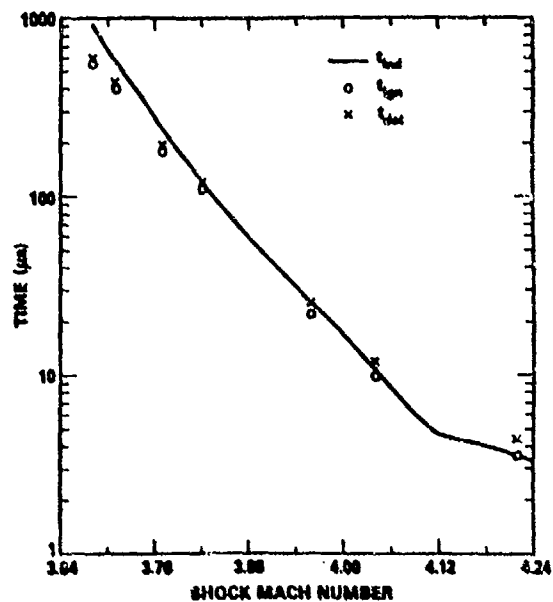

Fig. 5 The induction time (- t_{ind}), the time at which ignition is observed (o t_{ign}) and the time for detonation (x t_{det}) as a function of the shock Mach number.
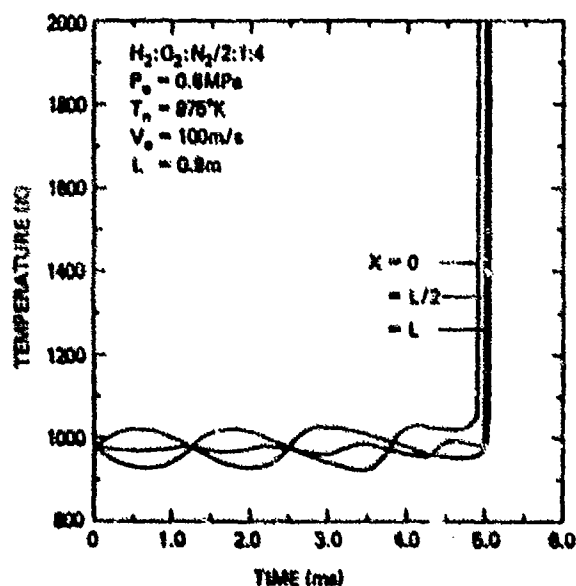
Fig. 6 Time history of the temperature at three positions in a 0.9 m long system when a velocity perturbation of amplitude 100 m/s is imposed.
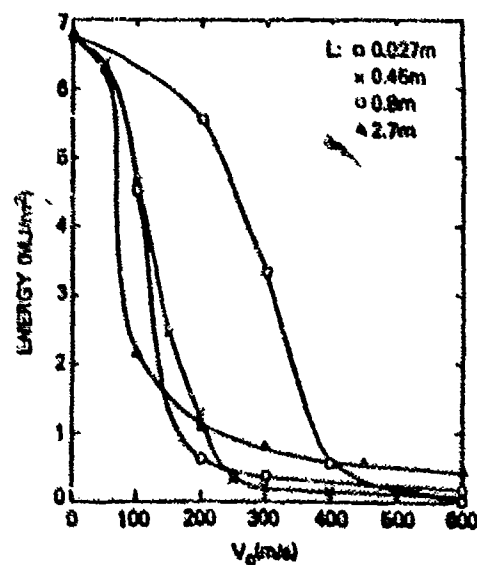
Fig. 7 The detonation initiation energy as a function of the amplitude and wavelength of the velocity perturbation.

SHOCK INITIATION AND DETONATION PROPAGATION

IN TUBES CONFINING AN EXPLOSIVE AIR FLOW

A. Persson and L. Jerberyd

Nitro Nobel AB, Detonic Laboratory
Vinterviken, S-117 48 Stockholm, Sweden

The front velocity and pressure time history of detonations in
an explosive air flow confined in tubes of polyethylene and steel
has been recorded in a lot of experiments. The results of the
experiment show that even coarse explosive grains (prilled ANFO)
can burn fast in a shock flow and thus support the propagation
of a detonation in the explosive air flow. The influence of the
confining material, concentration of explosive in the flow and the
tube diameter on the detonation parameters are illustrated in
diagrams. The hazard of initiating the mixture by static electric-
ity and detonation propagation into a column of the explosive at
bulk density is discussed.

1. INTRODUCTION

Prilled ANFO (ammonium nitrate mixed with fuel oil) is a common explosive
used in rock blasting. Rapid loading of the drillholes is accomplished by
mobile, pneumatic charging apparatus. In the ordinary loading operation,
the ANFO is transported from a vessel into the drillhole, fluidized in a
flow of compressed air confined partly in metallic tubes, partly in plastic
hoses. Although ANFO is a less hazardous explosive, a number of accidents
have happened in Swedish mines during loading operations with penumatic
apparatus. Accidental firing of the detonator put into the bottom of the
drillhole seemed to have caused these accidents and it was observed in some
of these cases that the plastic hose connected to the vessel had bursted
on a length of several meters outside the drillhole. The tube burst indicated
that a shock wave has propagated through the tube.

The aim of this investigation was to determine under what conditions
a shock wave sent through the explosive air flow could build up a detonation
wave in the tube which can propagate into the vessel of the loading apparatus.
A vehicle carried loading equipment can store up to 1 ton of explosive and
a detonation of such an amount in a mine will of course be disastrous. As
static electricity can be accumulated on a vehicle with rubber tyres it was
of great interest to determine if the energy of spark discharge from a
loading vehicle was large enough to generate a shock wave sufficiently
strong for initiating the explosive air flow.

Detonation in explosive air mixtures

Kaufman /1/ has reported characteristics of detonation of dust of RDX dis-
persed in air (1.3 g/dm^3) confined in steel tubes. Persson /2/ has investi-
gated the reaction in the NONEL tube. (NONEL is a nonelectric firing
system consisting of a thin plastic hose lined with a thin layer of fine
grain HMX). Both investigations show that a detonation wave can be initiated
by a shock wave sent into the tube and that the reaction propagates with a
velocity of 1500-2000 m/s. In NONEL the concentration of the explosive is
10 g/dm^3 and the particle size very small 10-50 um. The grain size of the
prilled ANFO is 0.5-2.0 mm. The explosive consists of porous grains of an
oxidizer soaked with fuel.

The concentration of explosive in a loading hose can vary from a full hose
850 g/dm^3 (about 61% by volume) down to a few per cent depending on the velo-
city of the air flow, the length of the hose and if the hose is bended.
In a series of experiments it was determined that the concentration of ANFO
grains in the air flow varied between 1-15% by volume or 14-210 g/dm^3.
The following parameters could be expected to affect the build-up and propa-
gation of the detonation and had to be investigated.

        1. The concentration of explosive in the flow

        2. The grain size of explosive

        3. The tube diameter

        4. The tube material

2. EXPERIMENTAL STUDIES OF REACTIONS IN ANFO AIR FLOW

The reaction of the ANFO air flow has been studied in several experiments
using both horizontal and vertical tubes. The tube material was either steel,
or polyethylene and the inner diameters of the tubes or hoses has been varied
from 27-52 mm. The explosive was fed into the horizontal tubes by connect-
ing these to an ordinary loading apparatus (fig. 1). In order to reach con-
centrations of ANFO higher than 3% by volume in the larger tube diameters
the explosive was fed into vertical tubes with a screwfeeder (fig. 2). By
calibrating the flow of the screwfeeder a better control of the concentration
of explosive was gained. The velocity and pressure of the reaction was
recorded by using piezoelectric or piezoresistive pressure gauges and simple
pressure sensitive switches. The pressure time history was recorded in
different positions of the tube making it possible to study the build-up
of the reaction wave. A photomultiplier and a light guide were used to record
the light from the flame zone of the reaction. A detonator containing 1 g
of explosive was fired in one end of the tube to generate the initiating
shock.

    In a series of experiments a slide valve was arranged in the bottom
end of a vertical tube making it possible to close the tube end and gather
the explosive in the bottom end before firing the detonator. The valve was
remote controlled and the flow out of the tube end could be watched in an
ITV-system.

Results of experiments

Fig. 3 shows the pressure time history at different positions along an ANFO
air detonation in a 50 mm diameter steel tube. Only 1% by volume of ANFO was
fed into the tube. The velocity of the reaction front was 1500 m/s and the
maximum front pressure 200 bar (20 MPa). The pressure recordings show the
typical behaviour of this type of detonation. The reaction zone is preceded
by an air shock behind which the explosive grains are heated. Pressure peaks
generated by local explosions or burning of grains in the flame zone catch
up the air shock front from behind and build up the pressure. The length of
the flame zone varied with the peak pressure of the reaction. At 1 kbar (100
MPa) the length of the zone was about 200 mm and at 500 bar (50 MPa) as long
as 600 mm. Increasing the amount of ANFO to 2% by volume increased the veloci-
ty to 1900 m/s and the peak pressure at the tube end to about 600 bars (60
MPa) bursting the 4 mm thick tube. In polyethylene tubes the appearance of
the pressure time history of the detonation wave was similar but the veloci-
ties and peak pressures were much lower. When the flow contained 5% explosive
or more the tubes were blown up.

In fig. 4 the detonation velocity of several experiments in both steel and
polyethylene tubes are plotted against the concentration of explosive. The
diagram shows the velocity of a Chapman-Jouget detonation calculated by using
the "Tiger" code /3/. It is obvious that the velocity of reactions confined
in plastic tubes were less than 1000 m/s (mean value 850 m/s) and did not
seem dependent of the concentration of explosive. The front velocity in steel
tubes were between 1500 and 2000 m/s and about 400 m/s lower than the calcu-
lated CJ velocity.

Fig. 5 shows peak pressure versus per cent by volume explosive. In
accordance with the low propagation velocity the peak pressure in the poly-
ethylene tubes was low and did never exceed 100 bar (10 MPa). It seemed to
be slightly dependent of the concentration of explosive too. The peak pressure
recorded in steel tubes was 1 kbar (100 MPa) at 5% by volume of explosive
in the flow. Compared to the calculated CJ-pressure which assumes a complete
reaction this level is about 60% of the ideal detonation pressure. All tubes
in the vertical experiments ended in a 1 m long steel tube with a sliding
valve in the bottom end. When this valve was closed a column of ANFO at bulk
density was gathered. The detonation waves in steel tubes which had a peak
pressure of 1 kbar were able to detonate the ANFO column. The reaction in
the polyethylene tubes compressed the ANFO column slightly but did not cause
any reaction in it.

The minimum charge size that could initiate a detonation in the ANFO
air flow was 0.25 g which corresponds to an explosion energy of 1600 Joule.
Maximum half of this energy is transferred to the shock wave in one direction
of the tube. Compared to the maximum energy released in a spark discharge
of static electricity on a mobile ANFO loader, the explosive energy is 1000
times larger. Therefore it seems impossible that static electricity can cause
initiation of an ANFO air flow.

3. CONCLUSIONS

An unstable detonation can propagate through plastic as well as steel tubes
at ANFO concentrations of the same magnitude as found in a common loading
apparatus. The large grain size however, caused incomplete reaction especially
when the confining tube was weak (plastic) the expansion losses behind the
reaction front resulted in a low propagation velocity and pressure. An in-
crease of the percentage of explosive could quench the reaction in plastic
tubes but not in steel tubes. An ANFO air detonation confined in a steel tube
could propagate detonation into a column of ANFO at bulk density. If the
plastic hose was connected to a steel tube the detonation velocity and pres-
sure was build up to the higher level.

As the air shock preceding the reaction zone does not increase the air
temperature enough to decompose the AN when the front velocity was
below 1000 m/s one can assume that the burning of the grains starts with
ignition of the vaporized fuel oil in the wake of the shock flow around the
grains. This burning increases the gas temperature and the grains start burn-
ing over the total surface, fig. 6.

4. ACKNOWLEDGEMENTS

REFERENCES

1. Kaufmann, C.W. "Detonation of dusts dispersed in air". Report UM 016968-2. Gas Dynamics Lab. The University of Michigan, Ann Arbor, Michigan, U.S.A.

2. Persson, A. "The reaction in the NONEL tube" Report DL 1981:18. Nitro Nobel AB, Detonic Laboratory, S-117 48 Stockholm, Sweden

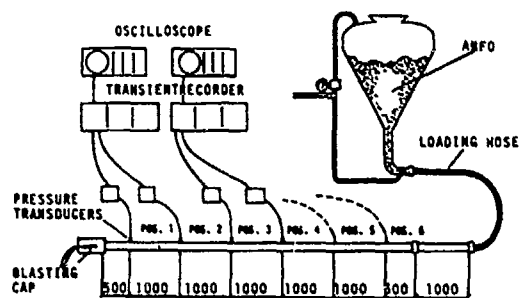3. Cowperthwaite, M. and Zwisler, W.H. "Tiger Computer program", Documentation, SRI, Pub. No. Z 106, 1973.
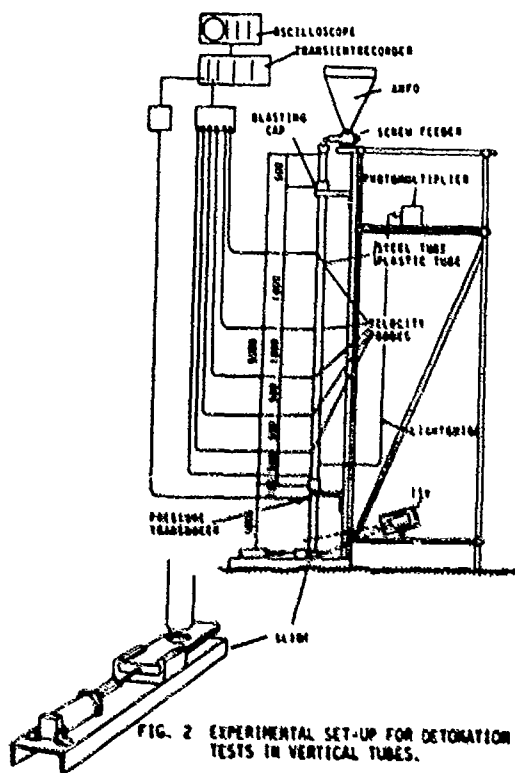
FIG. 1 EXPERIMENTAL SET-UP FOR DETONATION TESTS IN HORIZONTAL TUBES.

FIG. 2 EXPERIMENTAL SET-UP FOR DETONATION
TESTS IN VERTICAL TUBES.
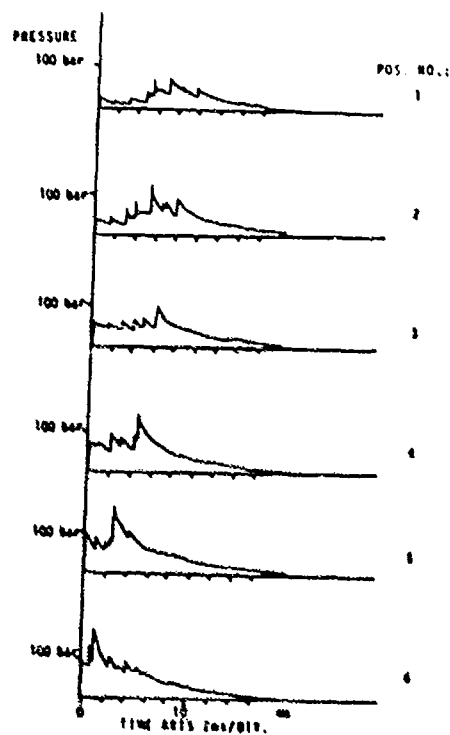
FIG. 3 PRESSURE-TIME RECORDINGS AT SIX DIFFERENT
POSITIONS WHEN THE ANFO/AIR MIXTURE IS
DETONATED IN A STEEL TUBE (b = 50mm).
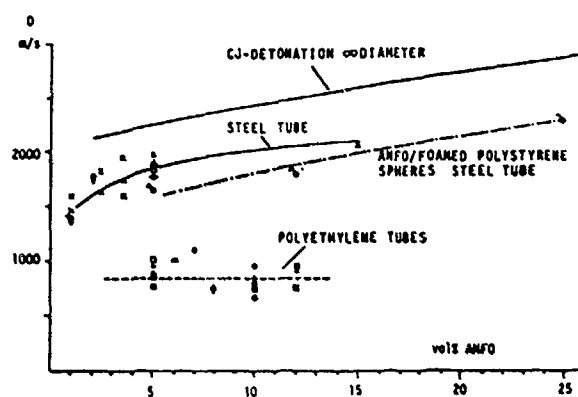
FIG. 4   EXPERIMENTAL- AND CALCULATED DETONATION VELOCITY VERSUS THE
CONCENTRATION OF EXPLOSIVE.
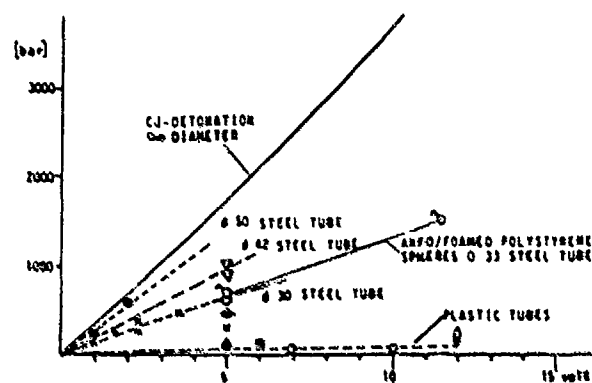
FIG. 5   EXPERIMENTAL PEAK PRESSURE AND CALCULATED CJ-PRESSURE VERSUS
THE CONCENTRATION OF THE EXPLOSIVE.
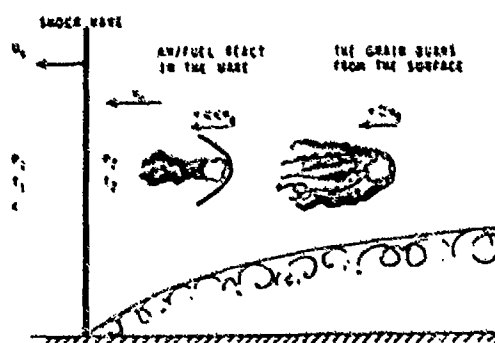
FIG. 6   PRINCIPAL FOR THE BURNING IN THE REACTION ZONE.

A SHOCK TUBE STUDY OF THE DECOMPOSITION OF CHLORINE DIOXIDE

C. Paillard, G. Dupré, S. Youssefi, R. Lisbet and N. Charpentier

Centre de Recherches sur la Chimie de la Combustion
et des Hautes Températures - C.N.R.S. et Université d'Orléans
45045 Orléans Cédex - France

The chlorine dioxide decomposition behind incident
shock waves has been investigated by measuring shock
velocities in function of shock strength in order to
determine the effect of reaction exothermicity on shock
propagation. Vibrational relaxation times have been
evaluated using a laser schlieren method. The reaction
is characterized by an induction period followed by a
rapid consumption of chlorine dioxide. The ignition
delay times τ_i of mixtures $\{x\ ClO_2 + (1 - x)\ Ar\}$ have
been measured behind reflected shock waves by the ab-
sorption technique at 360 nm. In a range of pressures P
and temperatures T of respectively 65 - 180 kPa and 1100
- 1450 Torr, a relationship has been established between
τ_i, P, T and ClO_2 molar fraction x :
$$\log \tau_i\ (s) = 4550/T(K) - 0.6 \log\{x\ P(Pa)/T(K)\} - 6.75$$
The temperature coefficient leads to an activation ener-
gy of 87 kJ/mol.

1. INTRODUCTION

Gaseous chlorine dioxide ClO_2 is known as to be a highly unstable compound
which is readily decomposable in an explosive manner. Laffitte[1] et al. have
determined the characteristics of ClO_2 decomposition flames from measurement of
burning velocities and quenching diameters. These authors found an overall
activation energy of about 8 kcal/mol, and an apparent overall reaction order
of 2.5 for non diluted ClO_2 and of 2 for mixtures diluted with inert gases.
Schumacher[2] et al. then Mc Hale[3] et al. have studied the thermal decomposition
of ClO_2 over the following pressure and temperature ranges : 0.2 - 40 Torr ; 40
- 134°C. The reaction is characterized by long induction periods which are a
function of temperature, pressure, vessel size, irradiation and dilution with
inert gases. Above 54°C, the decomposition of ClO_2 becomes explosive. The
explosion is of a degenerate chain-branching type where chlorine sesquioxide
Cl_2O_3 is the intermediate species responsible for the delayed reaction. The
photoinduced reaction of ClO_2 has been recently studied by Bethune[4] et al. With
a buffer gas present during photodissociation, they observed two intermediate
molecules : $ClOClO_3$ and probably Cl_2O_3 but they assumed that these molecules
would be too unstable to be present in any significant quantity during the
explosion. Moreover no actual data were obtained to confirm the detailed mecha-
nism the authors have proposed and no information is available on the ignition
delay times measured independently of wall effect.

In the present paper, the effect of the decomposition of ClO_2 in an argon
bath on shock wave velocities and on vibrational relaxation times have been
investigated in order to precise the kinetic mechanism of decomposition behind
shock waves.

2. EXPERIMENTAL

Two shock tubes have been used in this study. The first one, presented in figure 1, is coupled to a time of flight mass spectrometer in order to analyse reactant and reaction products behind reflected shock waves. The inside driven tube diameter is 22 mm and its length 2.15 m. This tube is also fit for the measurement of ignition delays by uv absorption or infrared emission behind reflected shock waves near the back wall.

The second shock tube, of inside diameter 50 mm and 6.44 m long for the driven section, is equipped with a series of plane windows made of CaF_2 in order to be coupled with infrared and uv-visible detectors and filters and with a laser schlieren technique.

This last technique, used to determine vibrational relaxation times, has been described and discussed by Kiefer[5]. A schematic diagram of the device is shown in figure 2. The beam was provided by a He - Ne laser operating at 632.8 nm. After crossing the shock tube it passed through a neutral density filter to prevent detector saturation and hit the apex of a reflecting prism. The separated halves were detected by two photomultipliers and the differential signal due to density variation and consequently laser beam deflection during the shock wave passage was recorded on a scope. The detectors were placed at about 4 m from the CaF_2 windows crossed by the laser beam. This device permits to determine vibrational relaxation time values greater than 1 µs with a reasonable accuracy (7 - 10 %).

The initiation of shock waves was produced in both shock tubes by the sudden rupture of the diaphragm made of Terphane, caused by a four bladed steel knife propelled by a pneumatic system. For a diaphragm of a given thickness, the conditions for the shock wave propagation in a fixed non reactive gas depend on the ratio of initial pressures P_4 / P_1 in driver and driven tubes respectively.

The ClO_2 generating apparatus and the storage vessel were made entirely from Pyrex glass and Teflon, so was the low pressure section of both shock tubes to avoid wall corrosion by chlorine dioxide.

Gaseous ClO_2 was generated from the reaction of concentrated sulfuric acid with potassium chlorate and stored at around 10°C in darkness. The purity of ClO_2 was checked by absorption spectrophotometry and mass spectrometry. An example of ClO_2 mass spectrum is illustrated in figure 3. It is noticed that the quantity of impurities is very small, consisting essentially of less than 1 mol. % Cl_2 and some traces of H_2O. However, despite of the great care to keep ClO_2 as pure as possible, a noticeable partial decomposition could be observed after a few days of storage.

3. RESULTS

a. Influence of reaction exothermicity on shock wave velocity

The ClO_2 decomposition is exothermic :

$$ClO_2 \longrightarrow 0.5\ Cl_2 + O_2 \qquad \Delta H^{\bullet}_{298} = - 105\ kJ/mol.$$

Various systems $\{x\ ClO_2 + (1 - x)\ Ar\}$ have been investigated in order to study the effect of reaction exothermicity on the incident shock wave propagation and to determine the conditions for which a coupling could be established between the reaction zone and the shock front. With this aim, we have plotted the shock wave velocity V_S as function of the logarithm of the shock strength P_4 / P_1. Results are illustrated in figure 4. For $x = 0.1$ and $P_1 = 25$ Torr, the explosive reaction is initiated for postshock pressures and temperatures greater than the critical values $P_c = 135$ Torr and $T_c = 820$ K. Above these values, the

shock velocity rapidly accelerates but never reaches the Chapman–Jouguet detonation velocity : a chemically enhanced shock wave is observed. For x = 0.02 the influence of exothermicity on shock wave velocity is not very sensitive. A kinetic study of ClO_2 decomposition becomes possible behind incident shock waves.

b. Vibrational relaxation times

Density gradient profiles behind incident shock waves have been determined in $\{ClO_2 - Ar\}$ mixtures containing 10, 25 and 50 mol. % ClO_2 in the temperature range 420 - 700 K. At higher temperatures a coupling was observed between the reaction zone and the shock fron and this last one could not be considered planar. In that case, the vibrational relaxation times deduced from laser beam deflection became unmeasurable. An example of a schlieren output signal for a non reactive mixture is illustrated in figure 5. We verified that the logarithm of the output voltage versus laboratory time was linear beyond the disturbance due to the shock front. None of our experiments gave any indication of multiple relaxation processes. A "laboratory" relaxation time τ_1 was deduced from the analysis of the exponential signal decreasing with time by using the method presented by Dove[6] et al. The vibrational relaxation time τ_v has been related to τ_1 with the Blackman[5] method by assuming the Bethe–Teller law with a single relaxation time. The Landau–Teller curves showing the dependence of standardized vibrational relaxation times $P\tau_v$ on temperature are plotted in figure 6. With the mixture containing 25 mol. % ClO_2 for which τ_v measurements have been done in the largest range of temperature, a numerical relation was found between $P\tau_v$ and $T^{-1/3}$:

$$\log P\tau_v = -1.4 + 10\ T^{-1/3}$$

The relaxation times in non diluted ClO_2 and in ClO_2 infinitely diluted in argon could be estimated from the mixture law in a small range of temperature. The corresponding values are reported in figure 6 (dashed lines).

c. Ignition delay times

The decomposition of pure or diluted ClO_2 is generally characterized by an induction period followed by a rapid consumption of the reactant. This mechanism of a degenerate chain–branching type was observed in a large range of pressures and temperatures behind the shock wave. In order to obtain values of induction periods behind reflected shock waves, we have followed the evolution of ClO_2 absorption at 360 nm and this one of ClO_2 emission at 8.89 μm, but the infrared signal is more complicated : at this 8.89 μm wavelength there is an interference with another non identified intermediate species.

Ignition delay times τ_i have been measured for several mixtures (x = 0.01, 0.02 and 0.10) in a range of pressures and temperatures of 65 –180 kPa and 1100 – 1450 K. The analysis of results has shown that a relationship can be established between τ_i, P, T and ClO_2 molar fraction x :

$$\log \tau_i\ (s) = 4530/T(K) - 0.60\ \log\left\{x \cdot P(Pa)/T(K)\right\} - 8.75 \qquad [1]$$

The validity of this relation is shown in figure 7 where the dependence of a function $Y = \log \tau_i + 0.6\ \log P/T$ on the inverse of temperature is reported. The curves corresponding to the expression $[1]$ fit with the experimental data.

The temperature coefficient leads to an activation energy of 87 kJ/mol. This value is almost twice as high as the one found by Mc Hale[8] et al. at low temperatures (363 - 407 K) by introducing ClO_2 mixtures into a preheated vessel. For P > 15 Torr the authors have shown that ignition delay times did not depend on pressure and that the reaction was initiated at the vessel wall. With the shock tube technique, the ignition delay times do not depend on wall

effect. Mc Hale's mechanism involves an intermediate species Cl_2O_3 responsible
for the delayed reaction. In our experiments with the shock tube coupled with
the time of flight mass spectrometer, we have not been able to identify Cl_2O_3.

From a ClO_2 flame study, Laffitte[1] et al. found that the apparent activa-
tion energy of the reaction of decomposition was about 39 kJ/mol. and a similar
value was given by Ben Caid[7] from a detonation study. In this late case photo-
lysis due to the radiation emitted from the reaction zone may contribute to the
thermal decomposition of ClO_2 which is a compound highly sensitive to light.
Moreover the mechanism of the explosive decomposition of ClO_2 is complex. A
simplified model of elementary processes cannot be given in a large range of
temperature and pressure.

For ClO_2 - Ar mixtures $(x \leqslant 0.1)$, ignition delay times τ_i can be compared
to vibrational relaxation times τ_v. At a pressure of 100 Torr and a temperature
of 2000 K, the ratio τ_i / τ_v is higher than 30 : the reactant is supposed to
be at thermal equilibrium when the reaction begins and the kinetic mechanism
can be studied at temperatures lower than 2000 K and pressures higher than 100
Torr. At $T > 2500$ K and $P \simeq 100$ Torr, the ratio τ_i/τ_v becomes very small,
equal or less than 4 from our estimations. In this case, we can assume that a
non equilibrium reaction would be observed.

ACKNOWLEDGEMENT

REFERENCES

1. Laffitte, P., Combourieu, J., Hajal, I., Ben Caid, M. and Moreau, R.,
    "Characteristics of Chlorine Dioxide Decomposition Flames at Reduced
    Pressures" , Eleventh Symposium (International) on Combustion, The Com-
    bustion Institute, Pittsburgh, Pennsylvania, 1967, p. 941.

2. Schumacher, H.J. and Stieger, G., "Thermal Decomposition of Chlorine
    Dioxide" , Zeitschrift des Physikalische Chemie, Vol 7B, 1930, p. 363.

3. Mc Hale, E.T. and von Elbe, G., "The Explosive Decomposition of Chlo-
    rine Dioxide" , Journal of Physical Chemistry, Vol. 72, Pt6, 1968, p.
    1849.

4. Bethune, D.S., Schell-Sorckin, A.J., Lankard, J.R., Loy, M.M.T. and
    Sorokin, P.P., "Advances in Laser Spectroscopy" , John Wiley and Sons,
    Inc., Vol. 2, 1983, p.1.

5. Kiefer, J.H., "Shock Waves in Chemistry" , Edited by Lifshitz A. ,
    Dekker M. Inc, 1981, p 219.

6. Bova, J.E. and Teitelbaum, H., "The Vibrational Relaxation of H_2" ,
    Chemical Physics, Vol. 6, 1974, p. 431.

7. Ben Caid, M., "Etude de la flamme de décomposition du bioxyde de chlore
    gazeux, limites d'inflammabilité, détonation, déflagration" , Thèse de
    Doctorat ès Sciences Physiques, Paris, 1966.
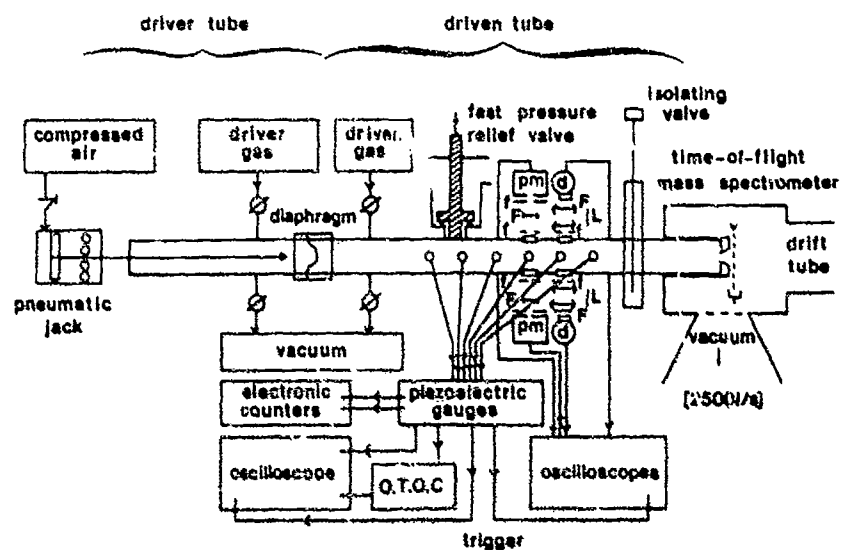
Figure 1 : Experimental set-up of the shock tube coupled to a time of flight
mass spectrometer.
pm : photomultiplier ; d : infrared detector
F : filter ; L : lens ; f : slit
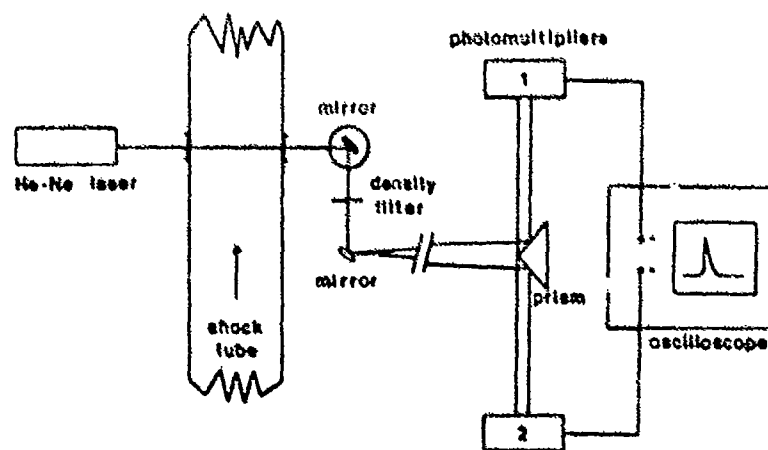O.T.O.C. : Oscilloscope Trace Offset Controller

Figure 2 : Schematic diagram of the Laser Schlieren Technique for the
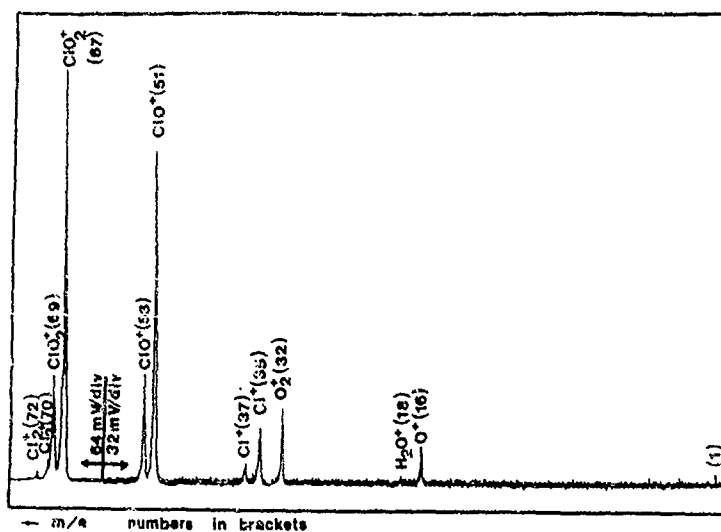measurement of vibrational relaxation times.

Figure 3 : Mass Spectrum of non diluted ClO_2.
Electron Energy : 70 eV
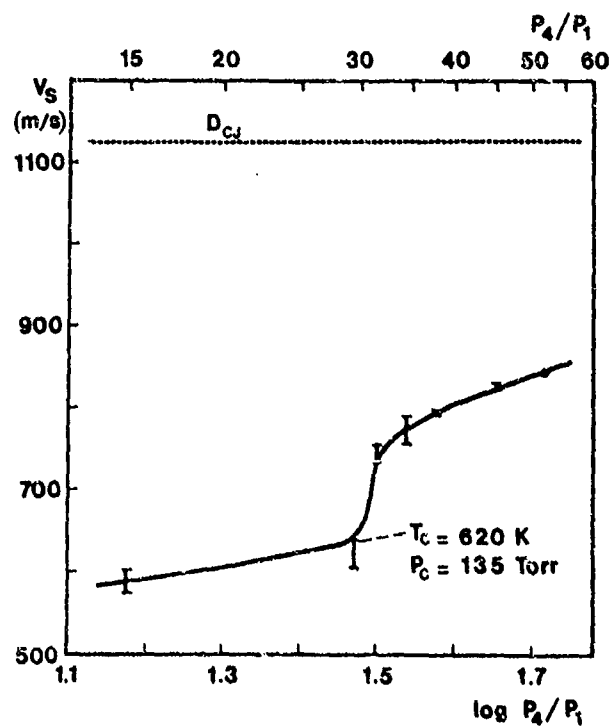Ion Source Temperature : 300 K
Mass increases from right to left.

Figure 4 : Effect of shock strength on shock velocity.
Mixture $\{0.10\ ClO_2 + 0.90\ Ar\}$
P_1 = 25 Torr ; $T_1 \simeq$ 293 K
T_C and P_C are the "coupling" temperature and pressure
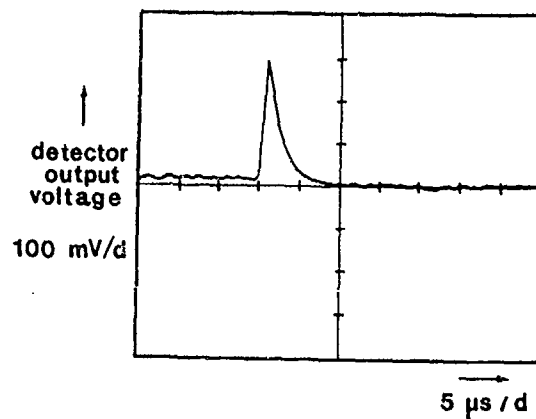
Detector output voltage correspon-
ding to the laser beam deviation
versus laboratory time.
Mixture $\{0.25\ ClO_2 + 0.75\ Ar\}$
$T_2 = 537\ K$; $P_2 = 125\ Torr$
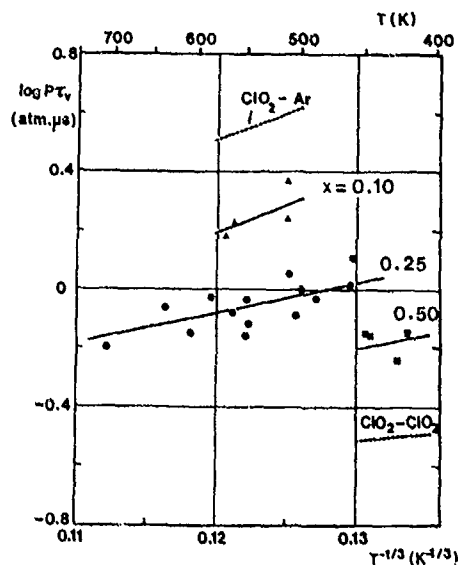
Landau–Teller plots for various
$\{x\ ClO_2 + (1-x)\ Ar\}$ mixtures
$(x = 0.10$; 0.25 ; $0.50)$.
The dashed lines correspond to vi-
brational relaxation times in non
diluted ClO_2 $(ClO_2 - ClO_2)$ and in
ClO_2 infinitely diluted in Argon
$(ClO_2 - Ar)$.
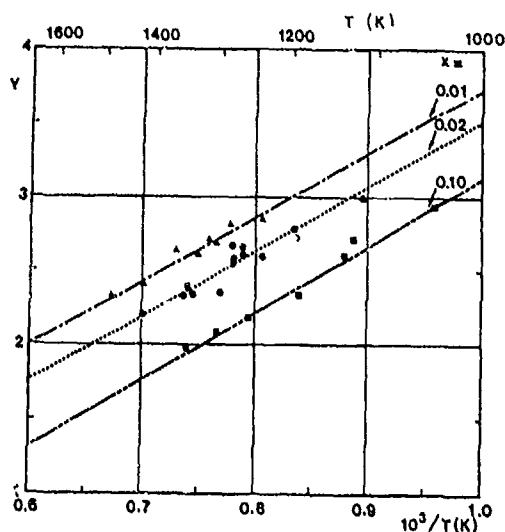
Influence of shock temperature on
the function:
$$Y = \log \tau_i\ (\mu s) + 0.6 \log \frac{P(Torr)}{T(K)}$$
for different $\{x\ ClO_2 + (1-x)\ Ar\}$
mixtures $(x = 0.01$; 0.02 ; $0.10)$.
The lines are obtained by using
the following expression:
$$Y = \frac{4550}{T(K)} - 2.02 - 0.6 \log x$$

Part IV
Shock Computation, Modeling, and Stability Problems

NUMERICAL PREDICTION OF SHOCK WAVE DIFFRACTION

R.Hillier and J.M.R.Graham,

Department of Aeronautics,
Imperial College, London S.W.7. U.K.

This paper presents a numerical study of shock wave diffraction
using an upwind Godunov-type method. The paper illustrates the
problems of obtaining accurate resolution of shock waves, contact
surfaces and vortex sheets by reference to various cases of shock
wave diffraction. These cover planar diffraction at isolated edges
which are examples of pseudo-stationary flows and also the truly
non-stationary problem of a shock wave emerging from the open end of
an axisymmetric tube.

1. INTRODUCTION

The diffraction of a shock wave is an important phenomenon in many
practical problems and has been the subject of extensive study, particularly
experimental (see,for example, Bazhenova, Gvozdeva and Nettleton, 1984; Lee
and Glass, 1984; Skews, 1967a,b). The objective of the present paper is to
present results from our current computational modelling of such flows, in
particular the blast field associated with a shock wave emerging from an
open-ended tube and the diffraction of a plane shock wave by an isolated edge.
There have been several experimental studies of the emergent flow from an
open-ended tube (see, for example, Schmidt, 1985; Phan and Stollery, 1983,
1984). At low shock wave Mach numbers the post-shock flow is subsonic and will
remain so despite further acceleration of the flow at the tube exit so that
the flow field is dominated by a primary shock wave S, a vortex sheet VS
separating from the tube lip and a contact surface C as shown in Figure 1a.
When the initial shock Mach number is high enough the flow leaving the tube
will either already be supersonic at exit or will accelerate sufficiently for
substantial portions of imbedded supersonic flow to form. This flow must be
decelerated eventually to match the conditions in the region behind the
primary propagating shock wave. This leads to a complicated internal wave
system (see Schmidt and Shear, 1974; Phan and Stollery, 1983, 1984) which is
sketched in simplified form in Figure 1b.

2. THE NUMERICAL METHOD

The method used here is based upon the one-dimensional second order
Godunov scheme developed by Ben-Artzi and Falcovitz (1983,1984) and it is
easiest here to describe the method first by its application to
one-dimensional flows. The flow field is divided into a sequence of
computational cells, the objective being to calculate the flux transfers (of
mass,momentum and energy) at the cell interfaces over each time step and hence
to update the appropriate values of cell variables by application of the
conservation equations to the control volume. Flow properties are assumed to
have a linear gradient across a computational cell immediately before the
commencement of a time step; at interfaces between cells there are then
discontinuities in both the variables and also their space derivatives as
shown in Figure 2. During the subsequent time step an estimate of the
variables at the interface, and hence the interface fluxes, is then made by
solving the resultant generalised Riemann problem at each interface. There is
no exact solution for this but to achieve second order accuracy in time it is
necessary only to evaluate interface variables (p_o say) and their time
derivatives ($\partial p/\partial t$ say) at the instant of commencement of the wave
interaction. Thus p (say) over a time step (see Figure 2b) is approximated
by

$$p(t) \simeq p_{\bullet} + \left(\frac{\partial p}{\partial t}\right)_{o} t$$

where t is the elapsed time. Here we have used the El approximation in the
terminology of Ben-Artzi and Falcovitz for the evaluation of the time
derivatives, which gives the simplest algebraic formula consistent with second
order accuracy. It should be noted incidentally that the generalised Riemann
problem takes account both of the initial spatial gradients and also the
"radial" nature of the flow for cylindrical and spherical problems.
Computationally, solving the basic Riemann problem for p is straightforward
but more expensive, and has been discussed in several other papers. Our
procedure here is firstly to solve it assuming that both left and right facing
waves are isentropic, which can be expressed economically. Only for those
cells where one or other of the isentropic waves is compressive do we have
conditions for shock formation and then the full (iterative) Riemann solver
is entered. In practice the isentropic solution will be the required one for
the major part of the flow field , since shock waves may occupy only a
restricted number of cells; in addition the isentropic solution provides a
sufficiently good initial guess that often one iteration only is required to
achieve adequate convergence.

    The method uses no artificial viscosity, although it is necessary to
apply a monotonicity constraint which limits spatial gradients within cells
and prevents the formation of new extrema at interfaces. Again the simplest
possible formulation is used here: the gradient across a cell is not permitted
to exceed the gradient between the cell centre and either of its neighbours
and if this generates an interface extremum the gradient is then set to zero.

    In two-dimensions we perform the computations on a mesh of rectangular
cells using an operator-splitting technique which regards the computation as a
sequence of "one-dimensional" Riemann problems in the axial and radial
directions respectively. The only modification required to the truly
one-dimensional Riemann solver is to ensure that proper account is taken of
the discontinuity in transverse velocityand its derivative at the cell
interface. It is commonly accepted that such splitting of a two-dimensional
wave problem cannot be justified mathematically - an obliquely travelling
plane shock wave cannot for example be regarded as a sum of two orthoganal
shock waves and it in fact generates both forward and backward travelling
components - but in the absence of an alternative formulation we have used it
here. Two-dimensional calculations will then be less than second order in
accuracy and as part of our study here we investigate its effect.

3.ONE-DIMENSIONAL TEST PROBLEMS
    Euler codes capture discontinuities most ..narply when they are
stationary relative to the mesh and/or aligned with it. Thus one-dimensional
test problems reveal the best resolution which can be expected of the codes as
well as providing essential validation checks on the accuracy of the
programming. Figure 3a shows a basic one-dimensional shock tube calculation
using the data specified by Sod(1978). The second order Godunov scheme shows
excellent resolution of shock waves and contact surface as well as the
derivative discontinuities at the leading and trailing edges of the
rarefaction wave. It should be noted t at the El approximation used for
calculating time-derivatives , and also the monotonicity constraint are both
the simplest formulation of this second order scheme so that improved
resolution may be possible. The figure also shows a computation using the
second order finite volume scheme of James ι and Caughey (1977). This shows
slightly more diffusion of the shock wave and contact surface and a more
severe rounding of the derivative discontinuities, but in compensation the
finite volume scheme is computationally fast.

It was remarked above that discontinuity resolution is enhanced when discontinuities are stationary relative to the computational mesh. This is particularly so for the Godunov schemes as illustrated by the shock tube problem in Figure 3b. In this case the governing equations were rewritten in the pseudo-stationary coordinates t and $\tilde{x}$ (= x/a t), and then time marched from the initial data to a steady state in which all waves are stationary in the coordinate frame $\tilde{x}$. All discontinuities are now captured within one transition value, which is the best which can be achieved. The calculations presented later for planar diffraction at an isolated edge were also performed in a pseudo-stationary reference frame to take advantage of this feature.

4. BLAST PROPAGATION FROM AN OPEN-ENDED TUBE

We present computations for two experimental test cases, by Schmidt (1985) and Phan and Stollery (1983, 1984a,b). Figure 4 compares measured pressure histories with computations for the experiments by Schmidt in which a shock wave emerges at a Mach number of 1.74 into air from an open-ended tube (corresponding to a post-shock Mach number of 0.73, which is sufficient to cause an extensive supersonic region in the exhaust flow). The relative dimensions of the tube and the location of the measurement stations are given in the figure together with the size of the computational domain. Figure 4a shows that along the centre line (θ =0°) the experimental data are represented well by the computations, bearing in mind the relative coarseness of the computational mesh employed here. In particular, both the primary shock wave and the secondary rearward facing shock are located accurately with good predictions of the pressure level except for the initial primary shock pressure overshoot which requires more computational cells for better resolution. The remaining comparisons in Figure 4 compare values at radii off the axis. In each case peak pressure levels are predicted well although the increasing diffusion of the shock wave is apparent. This reflects two effects. Firstly the maximum stable time step is established by the fastest wave speed on the mesh; the weaker parts of the blast wave propagate at reduced speeds so that they are computed at a reduced local Courant number which tends to increase the diffusion slightly.

More importantly the second contribution reflects the errors arising from using a splitting technique in two-dimensions as discussed earlier and the general difficulty experienced by all codes in propagating waves obliquely across a mesh. The best illustration of this is given by the data for θ =30°, where the secondary shock wave is still clearly apparent in the experimental data but has not been resolved very well by the numerical scheme.

In the second open-ended shock tube, for a shock Mach number of 1.5 (post-shock Mach number of 0.603, but again giving an extensive supersonic region in the exhaust) comparison is made with the data of Phan and Stollery (Figure 5). Curiously there is now a noticeable discrepancy in time scale between the two which we have not been able to resolve. This is illustrated well by the case θ = 0°, but nonetheless forward and rearward facing shock waves are clearly identified and pressure levels, including the extreme suction values as well as general trends, are predicted well.

5. PLANAR DIFFRACTION

Physically planar flows are easier to interpret than axisymmetric, and for our last computations we present results for diffraction of a plane shock wave at a 90° edge as illustrated schematically in Figure 6. For this class of problem the resulting flow field is pseudo-stationary. For this reason the computations were performed by recasting the finite difference equations in the frame of reference t, $\tilde{x}$ (= x/a t), $\tilde{y}$ (=y/a t) and time-marched from the initial state (with the shock wave just at the

separation edge) to a final steady state. The intention is to improve
discontinuity resolution compared with a purely unsteady scheme.

Computations have been performed for initial shock Mach numbers of
both 2.0 and 3.0. Figure 7 shows predictions of pressure, density and
v-component velocity on the diffraction surface for the case $M = 3.0$ (strictly
average values for the row of cells adjacent to the surface). The computations
were conducted on a mesh of 40 x 40 cells with $d\tilde{x} = d\tilde{y} = 0.1$ and $dT/T = 0.2$.
Computations were carried out for 500 time steps by which time data had
converged within 0.2% of their final values, probably an unnecessarily high
accuracy for most applications. The figure shows a rapid fall in pressure, and
increase in velocity near the edge which is a region of steady Prandtl-Meyer
expansion as the supersonic post-shock flow negotiates the corner. The fall in
velocity encountered at about four cells from the edge shows that the
computation has now crossed completely the vortex sheet separation from the
edge which divides the high velocity exhaust flow from the low energy gas
initially external to the tube. The shock is apparently captured with one
transition value; indeed the density value at $\tilde{r} = 1.55$ would indicate that the
shock wave is probably, in practice, located somewhat more than half the
distance across this cell (between $1.50 < \tilde{r} < 1.60$) and within the accuracy
of our computations we assume a value of 1.55 here. Skews (1967a,b) has
measured diffracted shock Mach numbers experimentally, and Figure 8 shows his
experimental data and our current predictions for both $M = 3.0$ and 2.0,
agreement being very good. Figure 9 finally shows a density contour plot for
the case $M = 3.0$, which is compared with the computation of Carafano (1984)
and the experimental data of Skews. An absolute comparison with Carafano is
difficult because his computations were implemented as fully unsteady, but on
a mesh of 28,500 cells compared with the 1600 used here. The present
computations reproduce many of the features well, bearing in mind that the
best accuracy in position must be of order 0.05 on our finite difference mesh.
The primary shock location is given well for both diffracted and transmitted
portions (indeed with our pseudo-steady formulation, a shock Mach number of
3.0 and $d\tilde{x} = d\tilde{y} = 0.1$, the transmitted shock is captured precisely at a cell
boundary), the limiting boundary for the reflected (acoustic) wave
propagating into the post-shock flow is identified accurately and the imbedded
rearward facing shock wave is located.

6. CONCLUDING REMARKS

We present computational results using a Godunov-type scheme for
two-dimensional axisymmetric and planar unsteady flows. The two-dimensional
formulation uses an operator-split implementation of the one-dimensional
second order algorithm of Ben-Artzi and Falcovitz (1983, 1984). Physically
such splitting is unjustifiable but, practically, computational predictions
are good particularly for the specialised planar diffraction cases which can
be reduced to a pseudo-stationary form. Our further practical efforts will
incluue computations with larger field sizes to check the effects of spatial
resolution, a more extensive study of diffracting flows and comparison with
experiment. More fundamentally we intend to study alternatives to the
operator-splitting approach.

7.ACKNOWLEDGEMENTS

8.REFERENCES

Bazhenova, T.V., Gvozdeva, L.G. and Nettleton, M.A. 1984. Prog. Aerospace Sci., Vol. 21, 249.

Ben-Artzi, M. and Falcovitz, J. 1983 Proc. of the Euler Workshop. F. Angrand and R. Glowinski (eds.), INRIA, SIAM Publ.

Ben-Artzi, M. and Falcovitz, J. 1984 J. Comp. Phys. Vol 55, 1-32.

Carafano, G.C. 1984. Benet Weapons Lab., Tech. Rep. ARLCB-TR-84029

Jameson, A. and Caughey, D.A. 1977. Proc. 3rd AIAA Conf. on Computational Fluid Dynamics, Albuquerque, 235.

Lee, J.H. and Glass, I.I. 1984. Prog. Aerospace Sci., Vol. 21, 3.

Phan, K.C. and Stollery, J.L. 1983. Proc. 14th Symp. Shock Tubes and Waves. 519-526.

Phan, K.C. and Stollery, J.L. 1984 (a)and (b). "Shock and Blast-Wave Phenomena", Cranfield, England.

Schmidt, E. 1985 Private communication to appear as a Ballistics Research Laboratory Report, USA.

Skews, B.W. 1967(a). J. Fluid Mech., Vol. 29, 297-304.

Skews, B.W. 1967(b). J. Fluid Mechs., Vol. 29, 705-720.

Sod, G.A. 1978. J. Comp. Phys., Vol. 49, 357-393.
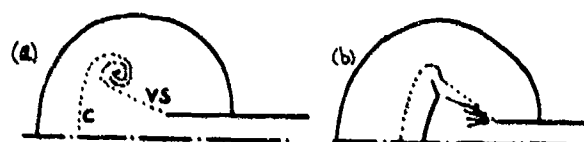
Figure 1. Schematic of flow from open ended tube.
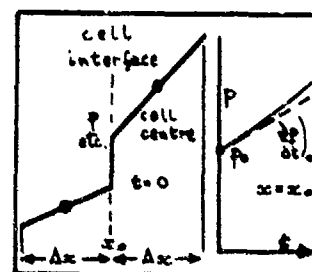
Figure 2.
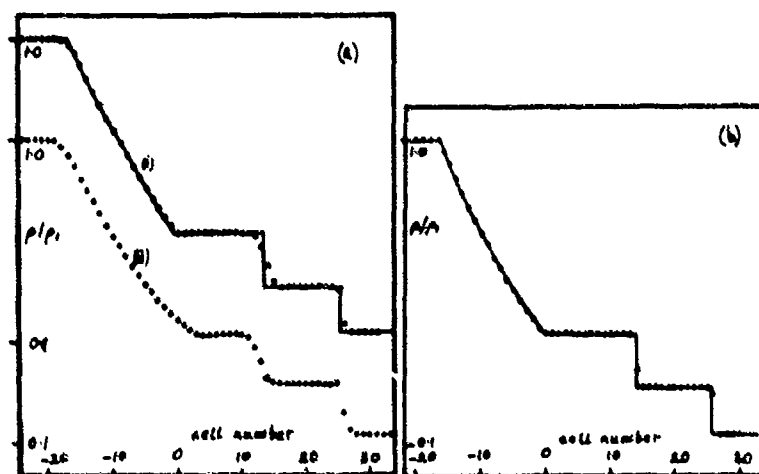
Figure 3a. Comparison with shock tube data of Sod (1978) ——, exact; (i), second order Godunov; (ii), finite volume scheme.

Figure 3b. ——, exact shock tube solution; ...., second order Godunov in pseudo-stationary form.
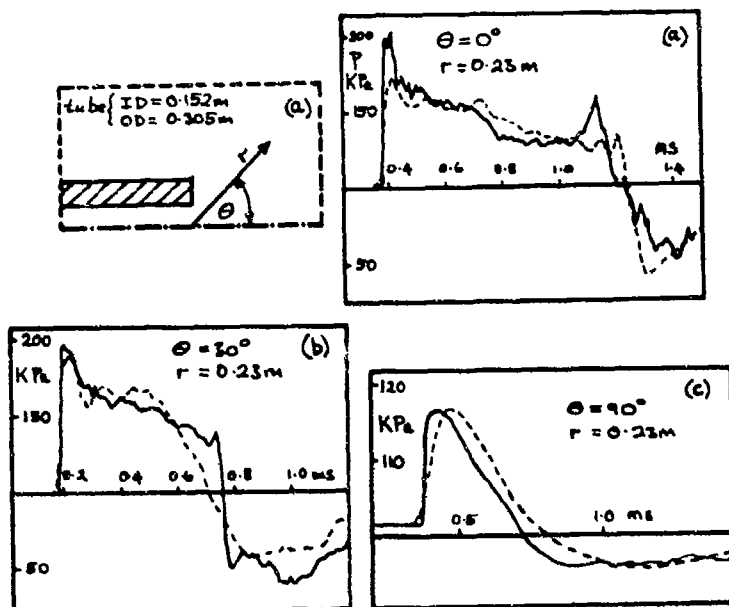
Figure 4. Open-ended tube. Comparison with data of Schmidt (1985).
——— expt.; ----- computation (dx = dy = 0.0127m, dT = 0.000015), 6
cells/internal radius.
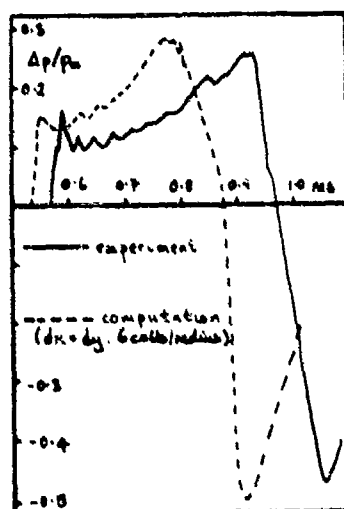
Figure 5. Open-ended tube. Comparison with data of Phan and Stollery
(1983) along axis ($\theta = 0°$)

Figure 6. Schematic of diffraction at
a $90°$ edge taken from Skews (1967).
Origin of coordinates at edge,
post-shock flow supersonic.
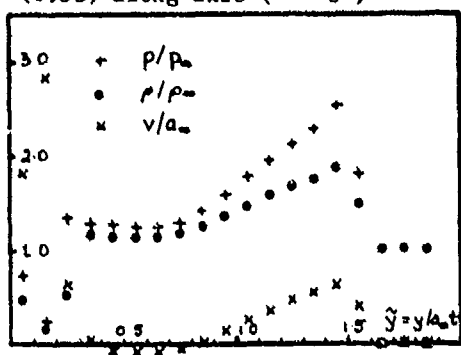
Figure 7. Computation of diffraction
of a plane shock wave by a $90°$ edge.
Data presented along diffraction
surface ($\theta = 90°$)
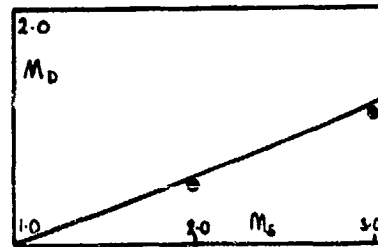
Figure 8. Prediction of diffracted shock Mach number along $\theta = 90°$ ———— , expt. of Skews (1967), ● ● , computations.
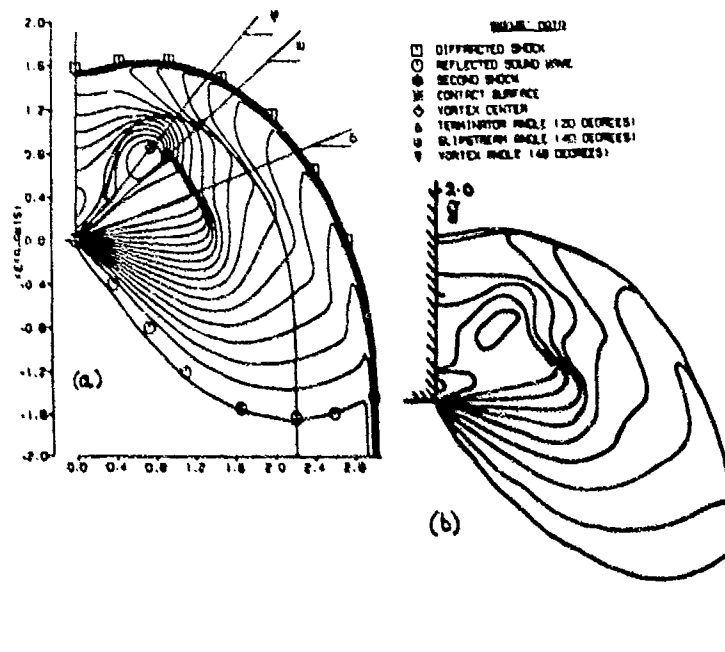
Figure 9. Density contours for diffraction case. (a) Carafano (1985), (b) present.

COMPUTATION OF NONSTATIONARY STRONG SHOCK DIFFRACTION BY CURVED SURFACES

J. Y. YANG

Computational Fluid Dynamics Branch
NASA Ames Research Center
Moffett Field, California, USA

C. K. LOMBARD

PEDA Corporation, Palo Alto. California, USA

D. BERSHADER

Department of Aeronautics and Astronautics
Stanford University, California, USA

SUMMARY

Strong shock wave diffraction generated by a blast wave with shock Mach number $M_* = 20$ impinging on a 15% circular arc model was simulated using a high resolution, shock-capturing numerical technique developed by the present authors. Detailed display of the complex shock diffraction process reveals interesting flow pattern including multiple Mach-shock, multiple slip surfaces, vortices, and backwards facing shock. A shock bifurcation study was also included by varying the specific heats ratio, γ, of the equation of state. Substantially different flow patterns were observed. Detached or attached bow shock may occur

INTRODUCTION

In recent years, due to the advance of numerical techniques for solving gasdynamic problems [1] and the advance of supercomputer such as CRAY, detailed numerical simulations of complex shock diffraction from obstacles have become feasible. A review of some of the application of numerical methods to gas dynamics with strong shock was given in [2].

In this study we apply a high resolution, shock-capturing algorithm for solving the Euler equations of gas dynamics developed by the present authors [3,4] to simulate the nonstationary strong shock diffraction by a 15% circular arc model in a 2-D shock tube, particularly for high incident shock Mach number ($M_* = 20$). Various flows can be easily generated with such a numerical experiment by choosing different geometries (models) and different initial starting conditions.

At high incident shock Mach number, complex flow patterns occurred and complicated shock wave/object interaction including multiple Mach shock, multiple slip lines, vortex, and backwards facing shock were observed, particularly after the incident shock past the trailing edge of the circular arc model.

The effect of different values of γ, the ratio of specific heats, on the shock diffraction process was also studied. Three values of γ, were calculated. They are 7/5, 6/5, and 5/3, respectively. Rather different flow patterns were observed.

THEORETICAL CONSIDERATIONS AND NUMERICAL ALGORITHM

The conservation equations of the two-dimensional unsteady gas dynamics in general curvilinear coordinate systems (ξ, η) can be written as follow:

$$\partial_\tau Q + \partial_\xi F + \partial_\eta G = 0 \tag{1}$$

where $Q = \dot{Q}/J$ and $F = (\xi_t \dot{Q} + \xi_x \dot{F} + \xi_y \dot{G})/J$, $G = (\eta_t \dot{Q} + \eta_x \dot{F} + \eta_y \dot{G})/J$, and $J = \xi_x \eta_y - \xi_y \eta_x$, the metric Jacobian $\dot{Q} = (\rho, \rho u, \rho v, e)^T$ is the conservative variables, $\dot{F} = (\rho u, \rho u^2 + p, \rho u v, u(e + p))^T$ and $\dot{G} = (\rho v, \rho v u, \rho v^2 + p, v(e + p))^T$ are the flux vectors in Cartesian coordinates. Here ρ is the gas density, u, v are the gas velocity components, e the internal energy and p the pressure and is given by $p = (\gamma - 1)[e - 0.5\rho(u^2 + v^2)]$. The speed of sound is defined by $c = \sqrt{\gamma p/\rho}$.

Due to the hyperbolicity of the system Eq.(1), the Jacobian coefficient matrix $A_\xi = \partial F/\partial Q$ of the transformed equations has real eigenvalues $a_1 = U$, $a_2 = U + c_\xi$, $a_3 = U$, and $a_4 = U - c_\xi$,

with $U = \xi_t + \xi_x u + \xi_y v$ and $c_\xi = c\sqrt{\xi_x^2 + \xi_y^2}$. (Similarly, the eigenvalues of $B_\eta = \partial G/\partial Q$ are $b_1 = V, b_2 = V, b_3 = V + c_\eta$, and $b_4 = V - c_\eta$, with $V = \eta_t + \eta_x u + \eta_y v$ and $c_\eta = c\sqrt{\eta_x^2 + \eta_y^2}$). One can find similarity transformation matrices T_ξ and T_η such that

$$T_\xi^{-1} A_\xi T_\xi = \Lambda_\xi = \text{diag}\{a_l\}, \quad T_\eta^{-1} B_\eta T_\eta = \Lambda_\eta = \text{diag}\{b_l\} \tag{2}$$

The eigenvalues and its signs of Eq.(1) provide the correct wave propagation information due to the theory of characteristic and the conservation form of the equations provides us the shock-capaturing property due to a theorem of Lax and Wendroff [6]. In the following, a numerical method of second-order accuracy in time and space which combines both characteristic and conservation features of Eq.(1) is briefly described. Define a uniform computational mesh system (ξ_j, η_k) with mesh sizes $\Delta\xi$, and $\Delta\eta$ and let $Q_{j,k}^n$ denote the value of Q at time level $n\Delta\tau$ and at position $(j\Delta\xi, k\Delta\eta)$. A conservative scheme for Eq.(1) can be expressed in terms of numerical fluxes F^N and G^N as follows:

$$\frac{Q_{j,k}^{n+1} - Q_{j,k}^n}{\Delta\tau} + \frac{F_{j+\frac{1}{2},k}^N - F_{j-\frac{1}{2},k}^N}{\Delta\xi} + \frac{G_{j,k+\frac{1}{2}}^N - G_{j,k-\frac{1}{2}}^N}{\Delta\eta} = 0 \tag{3}$$

Using dimensional splitting, the solution procedure becomes locally one-dimensional and can be represented as

$$Q_{j,k}^{n+2} = L_\xi(\Delta\tau) L_\eta(\Delta\tau) L_\eta(\Delta\tau) L_\xi(\Delta\tau) Q_{j,k}^n \tag{4}$$

In the following, only the L_ξ operator is given in detail. Similar expression can be given for the L_η operator.

For the L_ξ operator in the ξ-direction. we have

$$L_\xi Q_{j,k}^n = Q_{j,k}^* = Q_{j,k}^n - \lambda_\xi (F_{j+\frac{1}{2},k}^N - F_{j-\frac{1}{2},k}^N), \quad \lambda_\xi = \Delta\tau/\Delta\xi \tag{5}$$

In Eq.(5). $F_{j+\frac{1}{2},k}^N$ is the numerical flux, which for the present method [3,4]. is given by

$$F_{j+\frac{1}{2},k}^N = F_{j+1,k}^M - \dot{A}_{\xi_{j+\frac{1}{2},k}}^- \Delta_{j+\frac{1}{2},k} F^M = F_{j,k}^M + \dot{A}_{\xi_{j+\frac{1}{2},k}}^- \Delta_{j+\frac{1}{2},k} F^M \tag{6}$$

In Eq.(6). the split "normalized" Jacobian coefficient matrix $\dot{A}_\xi^\pm$ is closely related to A_ξ through the following definition:

$$T_\xi^{-1} \dot{A}_\xi^\pm T_\xi = \dot{\Lambda}_\xi^\pm = \text{diag}\{\dot{a}_l^\pm\}, \quad \dot{a}_l^\pm = \frac{1 \pm \text{sgn}(a_l)}{2} \tag{7}$$

The value of F^M at nodal point j, k is given by

$$F_{j,k}^M = F_{j,k} + E_{j,k}/\lambda_\xi \tag{8}$$

where F is the original flux vector and E is an additional column vector. The value of E at nodal point j, k is $E_{j,k} = (e_{1_{j,k}}, e_{2_{j,k}}, \dots, e_{4_{j,k}})^T$ and its l components is given by

$$e_{l,k} = s_{l_{j+\frac{1}{2},k}} \min(|\tilde{e}_{l_{j+\frac{1}{2},k}}|, |\tilde{e}_{l_{j-\frac{1}{2},k}}|), \quad \text{if} \quad \tilde{e}_{l_{j+\frac{1}{2},k}} \cdot \tilde{e}_{l_{j-\frac{1}{2},k}} \geq 0,$$

$$= 0, \quad \text{if} \quad \tilde{e}_{l_{j+\frac{1}{2},k}} \cdot \tilde{e}_{l_{j-\frac{1}{2},k}} \leq 0, \tag{9}$$

where $\tilde{e}_{l_{j+\frac{1}{2},k}} (l = 1, 2, \dots, 4)$ are components of the following column vector

$$\tilde{E}_{j+\frac{1}{2},k} = \lambda_\xi (\text{sgn} A_{\xi_{j+\frac{1}{2},k}} - \lambda_\xi A_{\xi_{j+\frac{1}{2},k}}) \Delta_{j+\frac{1}{2},k} F/2 \tag{10}$$

$$s_{i, -\frac{1}{2}, k} = \mathrm{sgn}(\hat{e}_{i, +\frac{1}{2}, k}) \tag{11}$$

The $\mathrm{sgn}A_\xi$ in Eq.(10) is given by

$$\mathrm{sgn}A_\xi = T_\xi \mathrm{diag}\{\mathrm{sgn}a_l\} T_\xi^{-1} \tag{12}$$

RESULTS AND DISCUSSION

The numerical experiment conducted in this study is the shock wave diffraction generated by a blast wave impinging on a 15% thick circular arc model placed in a 2-D shock tube.

The schematic outline of the problem is depicted in Fig. 1.

The conditions ahead of and behind a moving shock are related by

$$p_2/p_1 = [2\gamma M_s^2 - (\gamma - 1)]/(\gamma + 1)$$

$$\rho_2/\rho_1 = [\Gamma p_2/p_1 + 1]/[\Gamma + p_2/p_1]$$

$$u_2 = M_s[1 - \frac{(\gamma+1)M_s^2 + 2}{(\gamma+1)M_s^2}]c_1$$
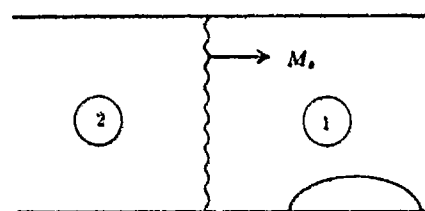
Fig. 1 Schematic diagram of a 2-D shock tube

with $\Gamma = (\gamma + 1)/(\gamma - 1)$ and $c_1 = (\gamma p_1/\rho_1)^{1/2}$ and 1 and 2 are the states ahead of and behind the moving shock, respectively. Initially, the conditions at state 2 are $p_2 = 1.$, $\rho_2 = 1.$, $u_2 = 0.$ and $v_2 = 0$.

Several values of γ are considered. They are 1.2, 1.4, and 5/3. A 201 by 101 computational grid was used. Explicit method with Courant number $CFL = 0.9$ was employed.

In Fig. 2, a sequence of isopycnics for $M_s = 20$ and $\gamma = 1.4$ are shown at different time. The incident shock (I), the development of the reflected bow shock (R) at the leading edge, the Mach shock (T_1), and the vortex (V) originated from the "roll-up" of the slip line of the first Mach shock are clearly shown. The vortex, departing from the surface due to the strong expansion over the bump and interacts with the slip line of the second Mach shock (T_2) and divides the slip stream of the second Mach shock into two branches. After the primary shock (I) past the trailing edge of the bump, a recompressed shock (S_b) formed which is similar to the backwards facing shock in a supersonic base flow.   Further downstream, the backwards facing shock interacts further with the Mach step, a complex flow starts evolving. The surface density distribution, pressure contours, and Mach number contours corresponding to Fig. 2(f) are shown in Fig. 2(h)-2(j). The density jump across the bow shock, the strong expansion over the bump and the second jump near the trailing edge due to recompression shock are clearly shown.

We also studied the effect of γ on the shock diffraction flow patterns. This is a shock bifurcation study similar to the one considered by Colella and Glaz [7].

In Fig. 3-4 the same profiles as in Fig. 2 are shown for comparison purposes for the cases of $\gamma = 1.2$ and $\gamma = 5/3$, respectively.

The flow patterns for these three cases show many similar features as well as some notable differences. First notable difference is the standoff distance for the reflected bow shock. For $\gamma = 1.2$, attached bow shock is observed. The other two cases show detached bow shocks. The standoff distance as well as the area enclosed by the reflected bow shock, the first Mach shock (T_1) and the bump (lower surface) seems to become larger as the value of γ increases. Also, the distances between the first and second Mach shocks display similar trend.

For the case of $\gamma = 1.2$, some shock bifucations are quite evident. Again, the primary incident shock I, and reflected shock R at the leading corner, two Mach shocks (T_1 and T_2), and a vortex V can be identified. Also at the trailing edge a backwards facing shock S_b forms at the wall. Contact surface type discontinuities originating from the second triple point T_2, interact with the vortex, which is departing alway from the wall. This feature creates a peculiar density structure around the second Mach shock. A new third Mach shock T_3 was formed right under the second Mach shock due to the interaction with the backwards facing shock which itself is curved.

In general, the present calculations reveal many details of the flow structures of shock diffraction process. The main structures such as bow shock, Mach shocks, slip lines, vortex and recompression shock are all well presented. Although no comparison with experimental works was attempted in this study, the validity of the present computer code has been verified in an earlier report [8], which compared with analytic results for 1-D shock tube problem and with experimental results from [9,10] for a 2-D pseudo-unsteady shock reflection by a 30° wedge. Good agreement was fond.

A comparison with analytic result by applying the Whitham's theory [11] in the same way as done by Bryson and Gross [12, for a circular cylinder and by Heilig [13] for a convex surface will be reported in the future.

CONCLUSIONS

The complex nonstationary shock wave diffraction by curved surfaces has been successfully simulated using a high resolution, shock-capturing numerical technique. Detailed flow patterns including multiple Mach shock, vortex, slip lines, and recompression shock were well represented. Detailed information such as the time-pressure history can be obtained. Shock bifurcations were also studied by varying the specific heats ratio. Rather different flow patterns were observed. Our calculations reveal details of the flowfields and provide useful information for better understanding of the complex shock diffraction flow process.

ACKNOWLEDGEMENT

REFERENCES

1.   Harten A., Lax, P. and Van Leer "Upstream Differencing and Godunov-Type Schemes for Hyperbolic Conservation Laws," SIAM Review, vol 25. 1983. pp. 35-61.

2   Woodward, P.R. and Colella, P., "The Numerical Simulation of Two-Dimensional Fluid Flow with Strong Shocks." J. Comp. Phys., vol. 54. 1984, pp 115-174

3   Yang, J.Y., Lombard, C. K. and Bershader. D . A Characteristic Flux Difference Splitting for the Hyperbolic Conservation Laws of Inviscid Gasdynamics," AIAA Paper 83-0040, 1983.

4   Yang, J Y.,"Second- and Third-Order Upwind Difference Schemes for Hyperbolic Conservation Laws," NASA TM-85959 J ., 1984, & AIAA Paper 85-0292, Jan 1985

5.   Harten, A.,"High Resolution Schemes for Hyperbolic Conservation Laws," J. Comp. Phys., vol. 49, p. 357-393, 1983.

6   Lax, P. D. and Wendroff, B.,"Systems of Conservation Laws," Comm. Pure and Appl. Math., 13, 1960. pp 217-237.

7.   Colella, P and Glaz,"Numerical Computation of Complex Reflections in Gases,"9th Int. Conf Numer Methods in Fluid Dynamics, Saclay, France, 1984.

8   Yang J Y , Lombard, C.K., Nagaraj, N, and Bershader, D." Numerical Simulation of Transient Inviscid Gas Flows in a Shock Tube." AIAA Paper 85-1679, 1985.

9.   Ben-Dor, G. and Glass, I.I.,"Domains and Boundaries of Nonstationary Oblique Shock-wave Reflexions 2. Monatomic Gas," J. Fluid Mech. (1980) vol 96, Part 4, pp 735-756.

10   Deschambault, R.L. and Glass, I.I."An Update on Non-stationary Oblique Shock-wave Reflections.Actual Isopycnics and Numerical Experiments," J. Fluid Mech (1983), vol 131, pp. 27-57

11. Whitham, G B .,"A New Approach to Problems of Shock Dynamics. Part I Two Dimensional Problem", J. Fluid Mech., (1957) vol. 2, pp. 145

12   Bryson, A.E. and Gross, R.W.F .,"Diffraction of Strong Shocks by Cones, Cylinders, and Spheres," J Fluid Mech , (1961) vol. 10, pp. 1

13 Heilig, W.H.,"A Result Concerning the Transition from Regular Reflection to Mach Reflection of Strong Shock Waves,"Shock Tube and Shock Wave Research, Proc. 11th Int. Shock Tube Symp., Seattle, 1977.
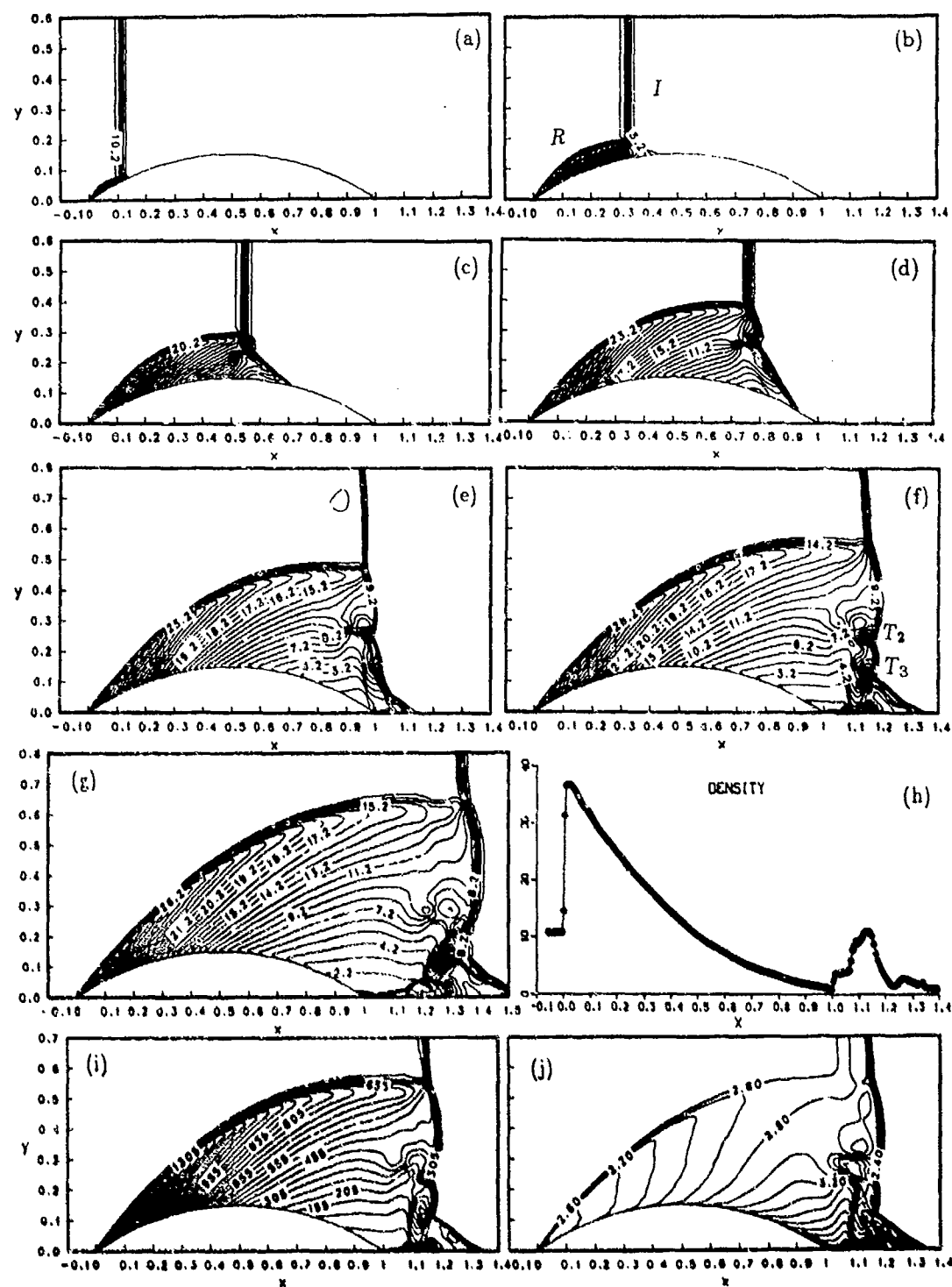
Fig. 2 Shock wave diffraction by a 15% circular arc $(M_s = 20, \gamma = 1.4)$ (a)-(g) Isopycnics; (h)-(j) Surface density profile, Pressure and Mach number contours corresponding to (f).
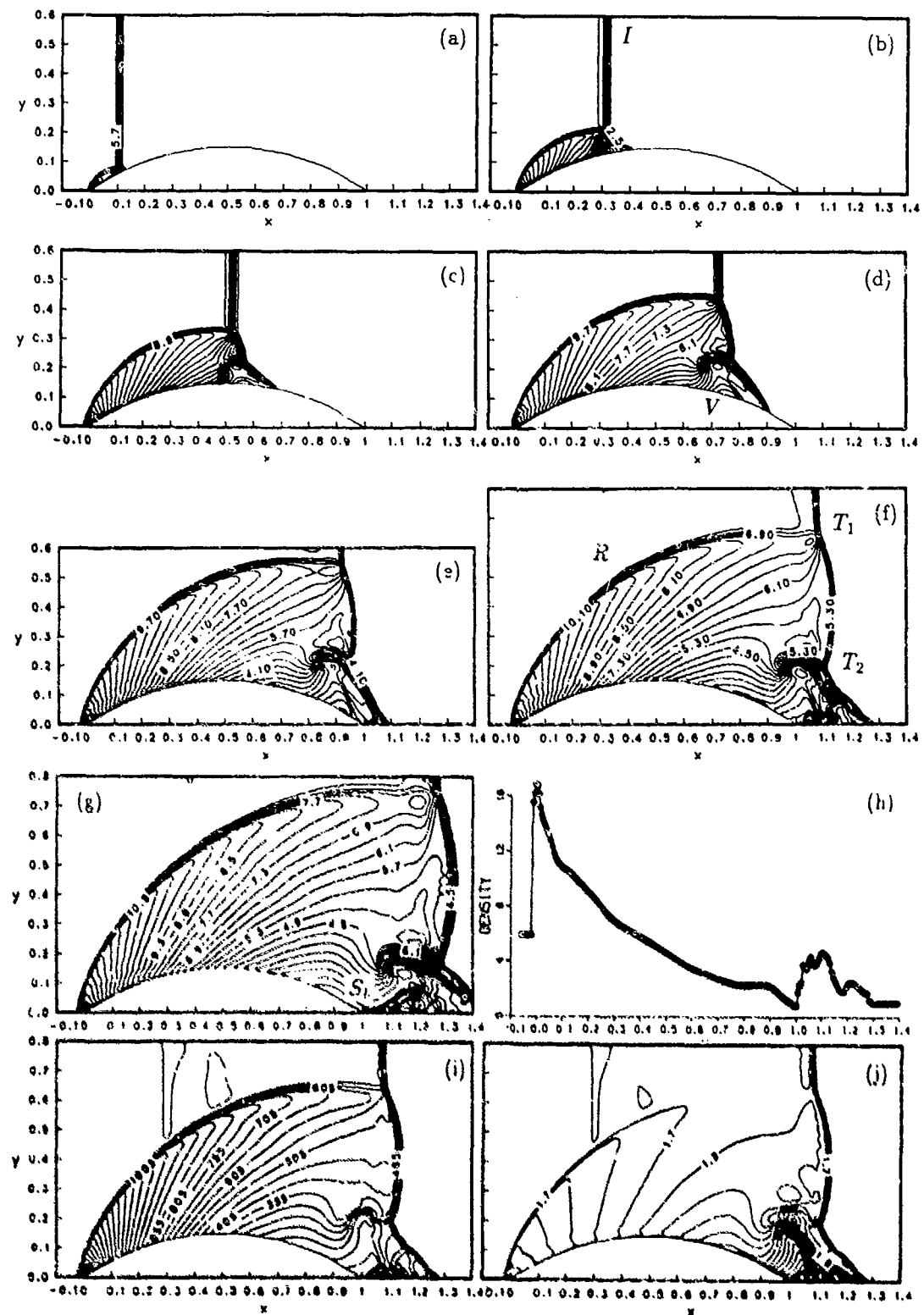
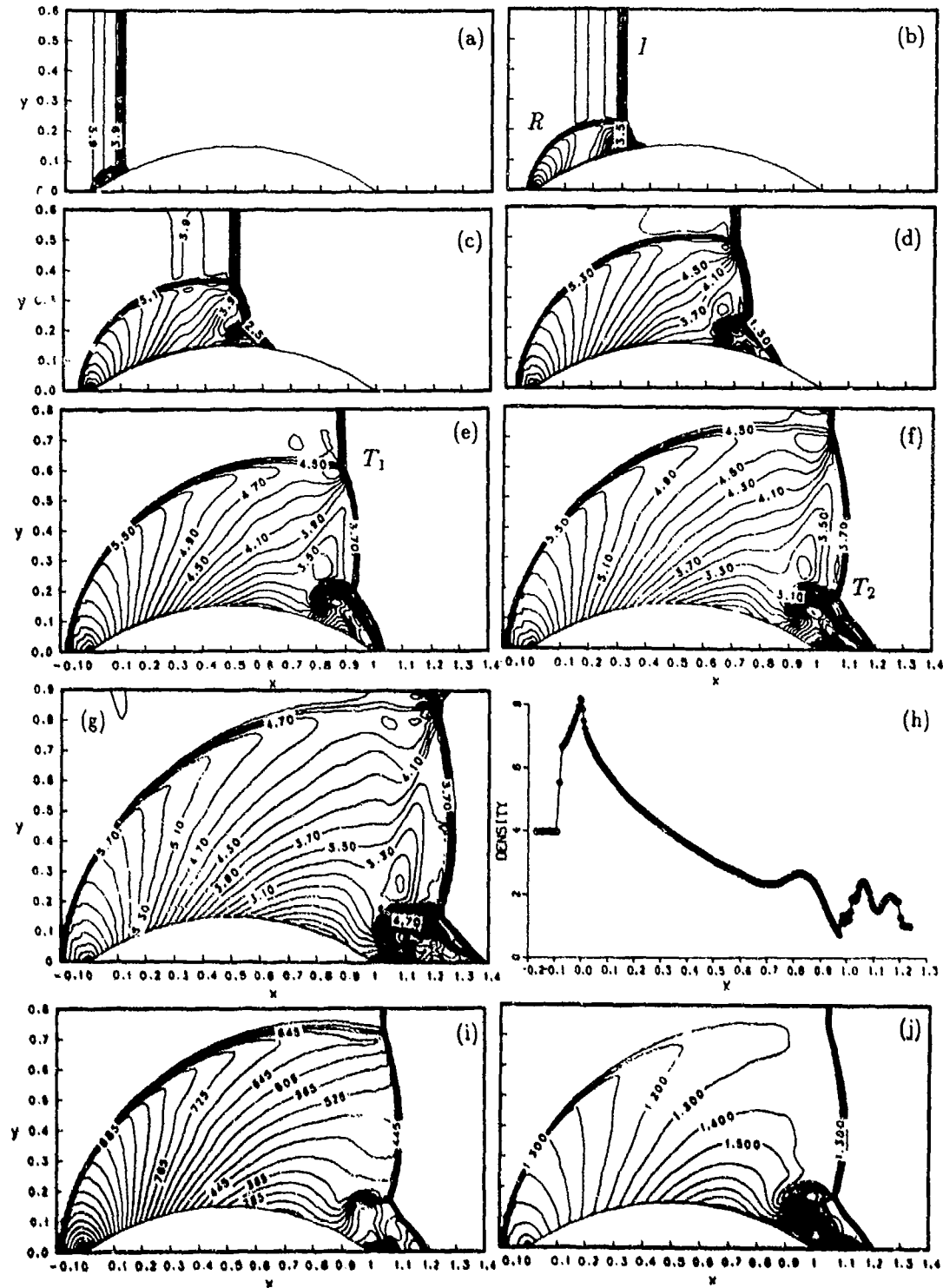Fig. 3 Shock wave diffraction by a 15% circular arc $(M_s = 20, \gamma = 1.2)$ (a)-(g) Isopycnics; (h)-(j) Surface density profile, Pressure and Mach number contours corresponding to (f)

Fig. 4 Shock wave diffraction by a 15% circular arc ($M_s = 20$, $\gamma = \frac{5}{3}$) (a)-(g) Isopycnics; (h)-(j) Surface density profile, Pressure and Mach number contours corresponding to (f)

THE EFFECTS OF WEDGE ROUGHNESS ON MACH FORMATION

Charles E. Needham, Henry J. Happ, and Dana F. Dawson

S-CUBED, A Division of Maxwell Laboratories, Inc.
5905 Marble Avenue, N.E.
Albuquerque, NM 87110

ABSTRACT

Theoretical calculations of shock reflections on wedges are presented.
Several calculations have been made, using the S-CUBED version of the
HULL hydrodynamic computer code, for the same incident shock strength
and wedge angle. The basic calculation, against which other results are
compared, used a perfectly smooth, perfectly reflecting wedge.

Roughness of the wedge was introduced by the inclusion of regular, two-
dimensional geometric protuberances on the wedges. The protuberances
varied in size from .02 to .2 cm. Shapes of the protuberances were
either square or triangular in cross section and the spacing varied from
one to four heights.

Comparisons of the calculations include: variation of the shock geometry,
effect of the roughness on near surface overpressure waveform and the
vertical extent of the flowfield modification induced by the roughness.
Full flowfield information is available from the hydrodynamic calculations.

Results are compared with experimental results of Ben-Dor and Takayama
(Tohoku University). Agreement between calculation and experiment is
good. The primary value of the calculations is their ability to provide
complete descriptions of all hydrodynamic variables as a function of space
and time. Calculations therefore serve as a supplementary source of
information for the description and understanding of complex flow
phenomena.

I. INTRODUCTION

Much work, both theoretical and numerical, has been done in the area of shock
diffraction over a wedge. Recently, Takayama, Gotoh, and Ben-Dor experimentally
investigated some effects of surface roughness on wedge flow, in particular looking at
the effect of surface irregularity on Mach transition.[1] Interest in surface roughness on
reflected flow from a height of burst was also shown in the DIPOLE WEST shots,[2]
where there was great interest in establishing some parametric fits for surface roughness
which can be included directly into computer codes. A purpose of the research pre-
sented here is to determine the feasibility of defining parametric fits, and, given the
feasibility, to find the best way to construct these fits. We ran one ideal surface
calculation, and then four calculations using similar 45° isosceles triangular protub-
erances, with heights of 0.02, 0.08, 0.2, and 0.8 cm, indicating increasing surface
roughness. We also ran a calculation using a square protuberance of height 0.02 cm,
with the protuberances spaced 0.02 cm apart to test the effect of roughness type, and
two calculations with square and triangular protuberances with larger spacing.

Increasing the height of the protuberances can be viewed as increasing the roughness.
Another view, which is correct for computations which assume an ideal gas, is that the
size increase represents an increase in resolution. In the ideal surface case, the flow is
self-similar. Computationally, this implies that parameters such as maximum pressure,

density, etc., will be asymptotic to the value obtainable with infinite resolution as a shock progresses up a ramp. As a function of time there will be no "new" effects beyond those obtained because there is increased resolution as the shock structure gets larger relative to zone size. Similarly, in this view actual protuberance size is not significant. If infinite resolution were achievable, the computational flow parameters should be the same after the shock traverses a constant number of protuberances, regardless of size. This implies that we can now determine just how much resolution is required for a particular degree of accuracy.

II. METHODOLOGY

The S-CUBED HULL hydrodynamic computer code was implemented for two-dimensional wedge calculations. This code has evolved from the HULL code developed at the Air Force Weapons Laboratory (AFWL)[3]. At S-CUBED, many enhancements and extended capabilities have been incorporated into the code. HULL is an efficient system for per-forming hydrodynamic calculations modeling compressible, inviscid, nonconducting fluid flow. The code solves the finite-difference analogues of the mass, momentum and energy conservation equations. The equation-of-state provides closure.

HULL accomplishes a time step in two phases. The first is a Lagrangian phase for momentum and energy, which is essentially a two-step Lax-Wendroff scheme.[4] This phase is second-order accurate in space and time. The second phase fluxes mass from the Lagrangian boundaries to the Eulerian mesh, conserving mass, momentum, and total energy. The mass transport phase uses a donor cell scheme, which introduces some stabilizing diffusion and kinetic energy dissipation.

Structures may be modeled in the fluid flow and are represented by totally-reflecting zones (islands) and half zones (shores). The shores follow the scheme developed by Chambers,[5] where two connecting edges of a zone are reflective and two are trans-missive, with a reflective surface along the diagonal.

INITIAL MESH CONFIGURATION

The initial mesh configurations for all the calculations were essentially the same. The only differences were the inclusion of differently sized, shaped and spaced structures along the wedge surface. The bottom boundary was reflective, representing the wedge surface. The top and left boundaries provided the constant square wave feed-in con-ditions for the incident shock with the incident shock moving along the top boundary. The right boundary was transmissive. Because the shock structure is essentially aligned along the wedge, letting the bottom boundary represent the wedge surface allows the number of active fluid zones in the grid to be maximized. That is, the number of totally reflecting zones was minimized and the ratio of ambient fluid zones to shocked fluid zones was kept small. Finally, the zones could remain square, which means the Courant condition would allow a maximal time step. The mesh extended horizontally from -1.156 cm to 9.2 cm and from 0.0 cm to 6.49 cm vertically. The base of the ramp was at $x = 1.2$ cm.

The ramp leading to the wedge surface was inserted into the grid as a triangular shaped package of island and shore zones. A cell which is an island zone is considered to be an obstacle of infinite strength, totally reflective of all four sides. Figure 1 displays the initial mesh configuration for the calculations. Also shown are the initial shock regions. The wedge surface structures are not shown. Stations, which are points in space at which hydrodynamic parameters are monitored as function of time, were included in the computational mesh.

All but one of the calculations involved surface roughness along the wedge surface. The wedge surface of the first calculation, case 1, was smooth. Roughness of the wedge surface, cases two to eight, was introduced by the inclusion of regular two-dimensional

geometric protuberances on the wedge surface at various spacings. The wedge surface extended along the horizontal axis from 1.2 cm to 9.2 cm. The geometric shape of the protuberances were 45° isoceles triangles and squares. Figure 2 displays the relationship between the height (k) and width of the structures along with the spacing between the structures. Table 1 gives the various values of k for each case.

INITIAL AND BOUNDARY CONDITIONS

The region in front of the ramp was filled with shocked nitrogen. The ambient pressure and temperature were 15 torr and 300°K, respectively, with Mach number 1.44, to match the Takayama conditions.[1] An ideal gas equation-of-state was used, with $\gamma = 1.4$. Rankine-Hugoniot relations were used to give the incident shock conditions.

The left boundary was provided with constant shock conditions. The shock front intersected the top boundary, so the boundary cells were updated with either ambient or incident shock conditions, depending upon the shock front location

III. ANALYSIS AND RESULTS

As mentioned in the introduction, pseudo-stationary (self-similar) calculations will yield different values for parameters such as maximum pressure solely because of the increase in resolution which results from the growing shock. Thus, looking at a variable such as maximum pressure versus Mach stem height, for case 1, can give one a good idea of how much resolution is "adequate." When the height of the Mach stem was 3, 7, 10, 20, 30, and 40 zones high the maximum pressure was 50.98, 51.36, 51.58, 51.66, 51.76, and 51.85 torr, respectively. For this parameter, a three-zone Mach stem might be adequate for some applications. Of course, more resolution would be required for a detailed look at something like a slip stream.

With protuberances (bumps), however, the amount of resolution required increases greatly. This can be seen by looking at a plot of the triple point path (Figure 3). Interpreting an increase in bump size as an increase in resolution, if there were infinite resolution the triple point would first appear after the shock traverses N bumps, regardless of bump size. Extrapolating the curves for $k = 0.02$ cm and $k = 0.08$ cm triangles to the range axis, we get "first appearance" range values of 1.70 and 2.3 cm for $k = 0.02$ cm and 0.08 cm, respectively. With the wedge starting at a range of 1.2 cm, this gives a value of N as 25 for $k = 0.02$ cm and 13.8 for $k = 0.08$ cm. We conclude that a bump height of one zone is probably insufficient for accurate details.

Another interesting feature of Figure 3 is that the effect of the triangular bump is greater than that of the square bump for the same bump height. Figure 2 shows that the actual bump area is the same for both geometries. We feel that this is due to the orientation of the geometries relative to the incident shock, i.e., the incident shock strikes the triangular geometry more "head-on" than the square geometry, and thus is presented a larger area for reflection.

Considering the increase in bump size as increasing surface roughness, Figures 4, 5, and 6 show full flow field contours of the pressure, density and energy 110 μsec after the shock strikes the wedge (the start time for the problem was 10 μsec). One can see the well-defined bow shock, Mach stem and slip stream. Figure 7 shows an expanded view of the energy contours in the region around the Mach stem. Figure 8 shows the same region for the $k = 0.02$ cm triangular bump calculation. An examination reveals that the triple point is lowered and that the Mach stem is "pulled in," i.e., no longer perpendicular to the wedge surface. The slip stream is perturbed--the point E in Figure 8 shows our best estimate of the extent of the perturbation. This point is 10 bump heights above the surface. Density and pressure contours (not shown) give similar results. Point E in Figure 9 shows the best estimate for the perturbation for a

rougher surface ($k = 0.08$) and it is 9 bump heights above the surface. Figure 10 shows the same result for density.

Although the essential waveform structure behind the Mach stem may be affected only 9-10 bump heights above the surface, the non-perpendicularity of the Mach stem to the wedge surface as a result of bumps (as shown clearly by Figures 8 and 10) indicates an effect on the entire waveform at least 30 bump heights above the surface. This calls into serious question a boundary layer approach to modeling surface roughness.

The triangular bumps also show that as the shock traverses the bump, on the back side of the bump the shock front aligns itself perpendicular to the wedge surface (Figure 15). The reason for this is that the back side of bump is at a -105° angle to the incident shock front and so here the shock is proceeding "down" a wedge surface. A surprising result appears in the calculations with a large spacing. Figures 11 through 14 show density contours for the $k = 0.02$ problems with k and 4k spacing. The intuitively "less rough" problems would be those with the larger spacing, but the plots show that the larger-spaced cases impede the progress of the Mach stem more. The reason is not apparent—further investigation will be required.

IV. CONCLUSIONS AND RECOMMENDATIONS

We have demonstrated the capability of the HULL code to model various rough wedge surfaces accurately. From these results, we conclude that a simple boundary layer approach to modeling surface roughness will probably be inadequate. The shock interactions from the bumps extend too far into the flow field. Some surprising results which deserve closer scrutiny show up in the calculations where the bumps are spaced further apart.

We recommend that further calculations be done for other types of Mach reflection, in particular CMR and DMR. The calculations done here show the fascinating insight may be gained from a thorough study of the effect of surface roughness on reflected shocks. We further recommend that a series of experiments be done to validate the computer models. These experiments should be done in an ordered fashion, changing the wedge angle, Mach number, bump size, bump shape, and bump spacing in a regular way so that parametric studies can be done. Using a monatomic or diatomic gas would also simplify the studies.

REFERENCES

1. Takayama, K., Gotoh, J., Ben-Dor, G., Shock Tubes and Waves, ed. by C. E. Treanor and J. C. Hall, S.U.N.Y. Press, Albany, NY (1981).

2. Keefer, J. H., Reisler, R. E., "Multiburst Environment—Simultaneous Detonations Project Dipole West," BRL R 1766, U. S. Army Ballistic Research Laboratories, Aberdeen Proving Ground, Maryland (1975.)

3. Fry, M., et al., "The HULL Hydrodynamics Computer Code," AFWL-TR-76-183, Air Force Weapons Laboratory, Kirtland AFB, NM (1976).

4. Lax, P., Wendroff, B., "Difference Schemes for Hyperbolic Equations with High Order of Accuracy," Comm. Pure Appl. Math., Vol. 17 (1964).

5. Chambers, B., Wortman, J., "Two-Dimensional Shore (Partial Island) Cells for BRL HULL," ARBRL CR-00497, U. S. Army Ballistic Research Laboratories, Aberdeen Proving Ground, Maryland (1982).

Table 1. Shape, Size, and Spacing of Surface Protuberances

Case	Surface Protuberance	Height, k (cm)	Distance Between Protuberance
1	Smooth	—	—
2	Triangle	.02	none
3	Triangle	.08	none
4	Triangle	.2	none
5	Triangle	.8	none
6	Triangle	.02	4K
7	Square	.02	1K
8	Square	.02	4K
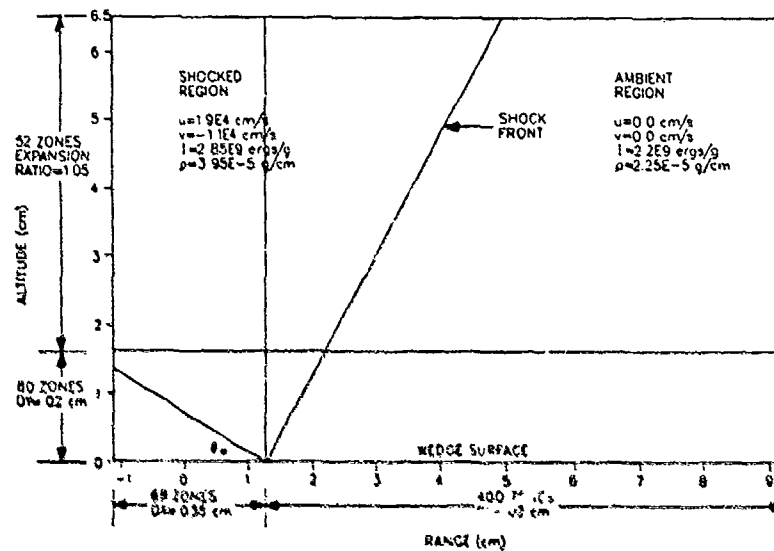
Figure 1.   Initial mesh configuration for all calculations.
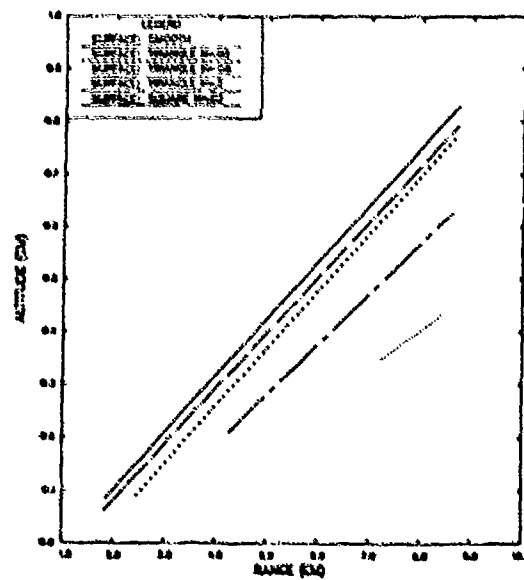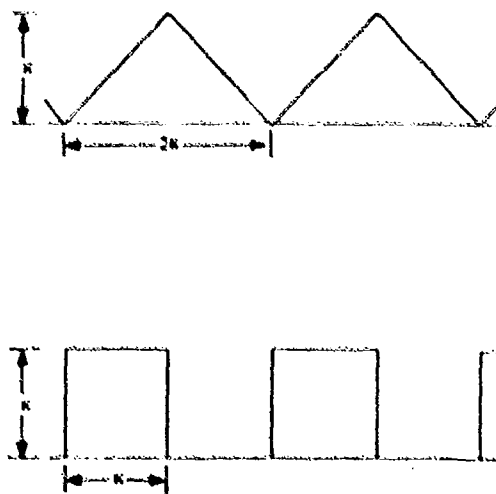
Figure 2. Shape and size of surface roughness.   Figure 3. Triple point path comparisons.
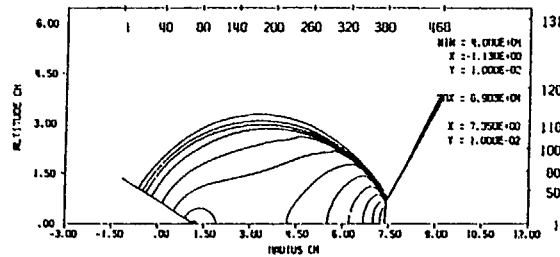
Figure 4.   Pressure contours at 110 μsec.
2.E3 dynes/sq cm contour increments
(surface: smooth).
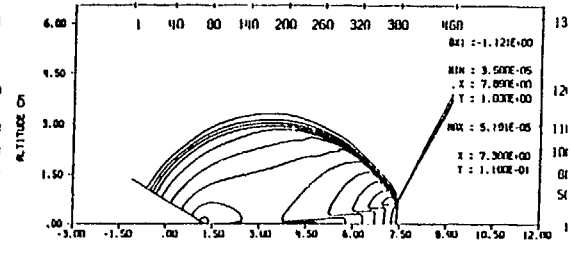
Figure 5.   Density contours at 110 μsec.
1.E-6 gm/cc contour increments
(surface: smooth).
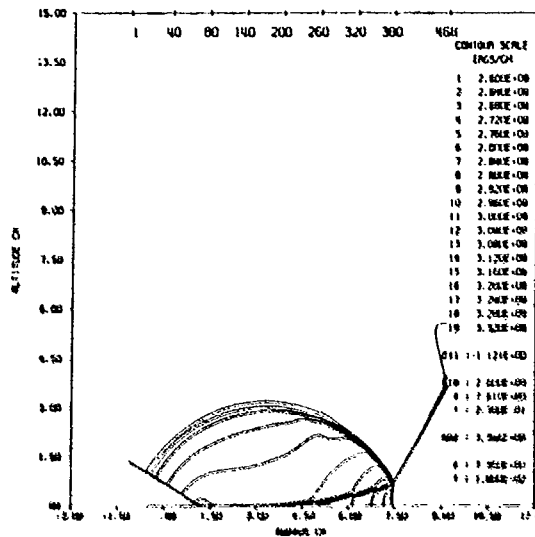
Figure 6.   Energy contours at 110 μsec
(surface: smooth).
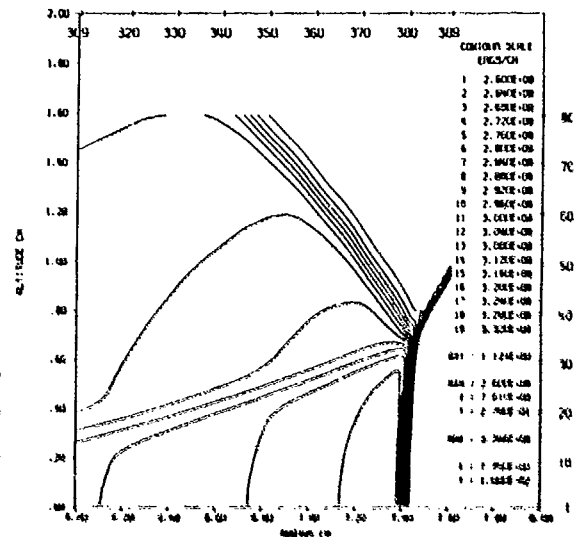
Figure 7.   Energy contours at 110 μsec,
triple point region
(surface: smooth).
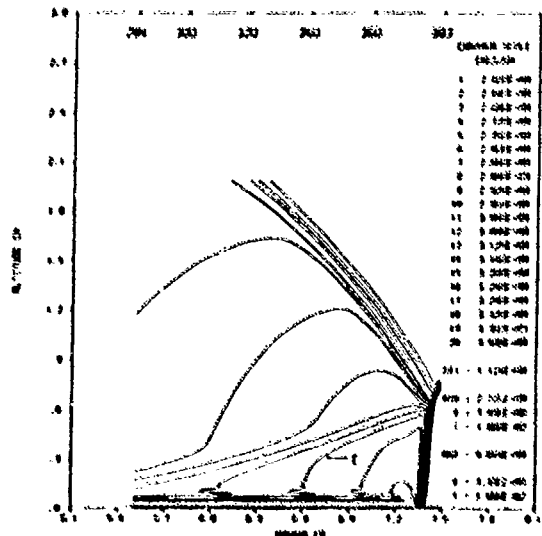
Figure 8.   Energy contours at 110 μsec.
triple point region (surface:
triangle, k=0.02, spacing=0).
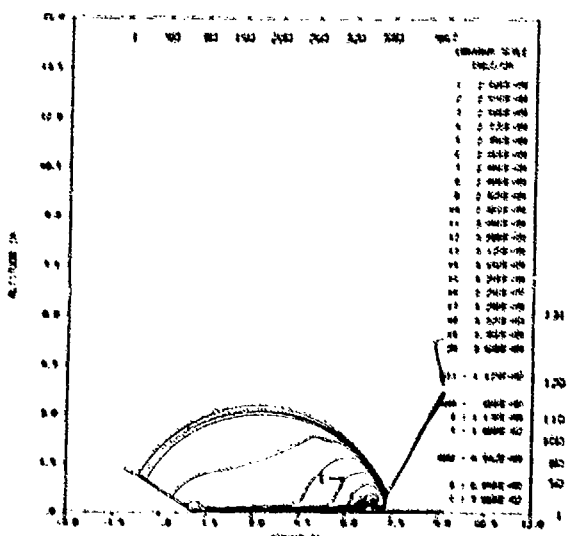
Figure 9.   Energy contours at 110 μsec
(surface: triangles, k=0.08,
spacing=0).
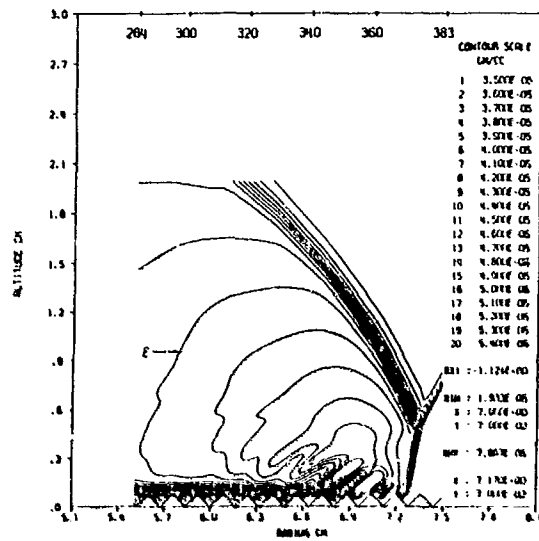
Figure 10. Density contours at 110 μsec, triple point region (surface: triangle, k=0.08, spacing=0).
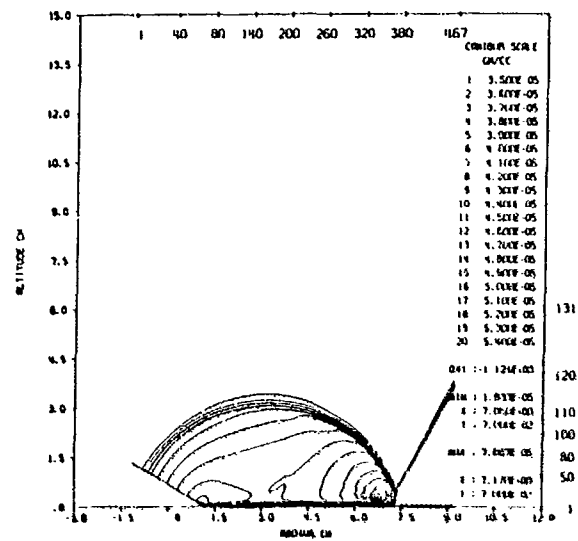
Figure 11. Density contours at 110 μsec (surface: triangle k=0.08, spacing=0).
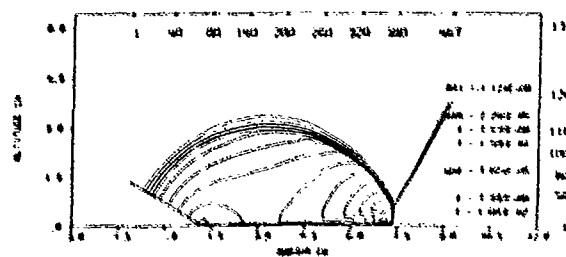
Figure 12. Density contours at 110 μsec, 1.E-6 gm/cc contour increments (surface: triangle, k=0.02, spacing=4K).
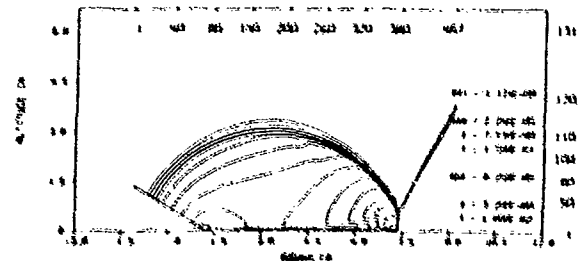
Figure 13. Density contours at 110 μsec, 1.E-6 gm/cc contour increments (surface: square, k=0.02, spacing=4K).
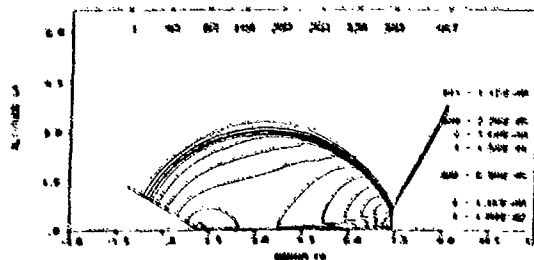
Figure 14. Density contours at 110 μsec, 1.E-6 gm/cc contour increments (surface: square, k=0.02, spacing=0).
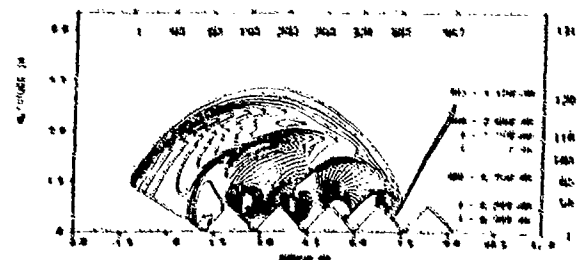
Figure 15. Density contours at 110 μsec, 1.E-6 gm/cc contour increments (surface: triangle, k=0.8, spacing=0).

INSTABILITY OF INTERFACES SUBMITTED TO SHOCK
ACCELERATION AND DECELERATION

L. Houas, R. Brun, M. Hanana

L.D.T.F. Université de Provence, Centre de St Jerôme
13397 MARSEILLE Cedex 13 . France

A. Froger, S. Gauthier, J.F. Haas, B. Sitt

C.E.A. Centre d'Etudes de Limeil/Valenton
B.P. 27 - 94190 VILLENEUVE St GEORGES. France

The behaviour of the contact zone between different gases
accelerated and decelerated by shock waves is the object of
an experimental and numerical study. The experiment uses a
three sections shock tube, where a carbon dioxyde - helium
or carbon dioxyde - argon interface is first accelerated by
a strong (Mach 4-6 in CO_2) incident shock and then decelera-
ted by the shock wave reflected from the shock tube end wall.
The time evolution of a characteristic average quantity of
CO_2 (product pressure - vibrational energy) in the mixing re-
gion is measured. Two types of behaviour are presented for
each gas pair. When the interface, materialized by a thin
membrane, is given an initial bulge, the thickness of the mi-
xing zone resulting from the interaction with the incident
shock is larger in the CO_2/He than in the CO_2/Ar case, thus
illustrating the growth of a single mode Richtmyer - Meshkov
instability. The reflected shock, however, leads to a larger
thickening rate of the CO_2/Ar mixing zone because of its stron-
ger deceleration by the shock as compared with the CO_2/He case.
When the separating membrane is kept as plane as possible, the
mixing zone appears to be equally thin after the acceleration
by the incident shock and approximatively equally thick after
deceleration by the reflected shock for the two gas combina-
tions. In the numerical part of this study, a one dimensional
model of the growth of the turbulent mixing zone is presented
and adjusted with the results of the classical shock tube expe-
riment of Andronov et al.

1. INTRODUCTION

In the context of inertial confinement fusion (ICF), the Rayleigh - Taylor
instability together with other types of instabilities induces some turbulent
mixing between the thermonuclear fuel and the outer shell material, thus redu-
cing the ignition probability and burn efficiency.

While the linear growth of small perturbations on the interfaces between
layers is relatively well understood, the non-linear growth and the subsequent
turbulent phase present some difficulties in their comprehension. Traditionally
simpler laboratory experiments are used to qualify numerical models which are
developed (Andronov et al./1,2,3/) for ICF target hydrodynamics. For example,
some shock tube experiments were performed by the same authors where a Mach
number 1.3 incident shock interacts with a Nitrogen/ Helium contact surface at
atmospheric pressure. The growth of the subsequent mixing zone was recorded
using flow visualization.

The purpose of our work is to study, in a shock tube operated at higher Mach numbers (4 - 6) and therefore lower initial pressures, the thickness and trajectory of a gas interface by measuring some quantity characteristic of one gas through its mixing region with the other.

A one-dimensional model of the shock-induced growth of the turbulent mixing zone (TMZ) is presented and its results, for the time being, are compared to the data from the earlier, low Mach number shock-tube experiment.

II. EXPERIMENTAL APPARATUS AND PROCEDURE

We study the behaviour of a shock acceleratd and decelerated carbon dioxyde/helium or argon contact surface in a two diaphragms shock tube with hydrog. in the driver section, carbon dioxyde in the first part of the test section an helium, or argon, in the second part. The gases are initially separated by a Mylar membrane (1.5 μm thick). The shock tube and a typical x - t diagram are schematically illustrated in figure 1.
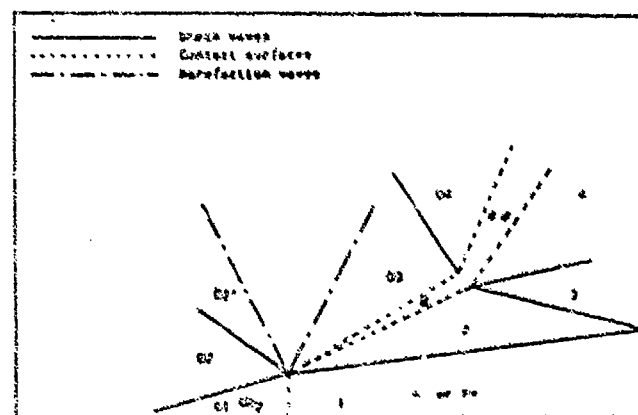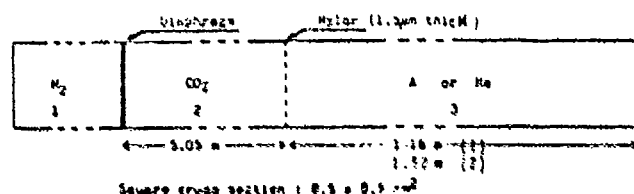
Fig. 1 : Shock tube and general x , t diagram

Because of the large difference in density between helium and argon which leads to different sound speed and Atwood number we expect a different behaviour of the interface under shock acceleration and deceleration. By recording the important I.R. radiation emitted by the shock heated carbon dioxyde, a characteristic average quantity of CO_2 can be determined through the mixing region CO_2/He or CO_2/A. It is the product $\rho . Ev_3$ or, assuming equilibrium (which is valid in our experimental conditions) $\rho . \overline{Ev_3}$ where ρ, p, Ev_3 and $\overline{Ev_3}$ represent, respectively, the density, pressure, energy per unit mass and energy at equilibrium of the third vibrational mode of carbon dioxyde. The oscilloscope records from the I.R. detectors as well as wall thermal probes are used to construct the experimental x - t diagrams shown in figures 2 and 3.

III. EXPERIMENTAL RESULTS AND DISCUSSION

1) Most experiments carried out so far were made with an initial curvature of the Mylar created by a small pressure difference between CO_2 on one side and He or Ar on the other.

The x-t diagrams in figure 2a show that the velocity of the contact surface after acceleration by the incident shock is constant (we are far downstream from the initial position where the effects of the mylar break-up may be felt). This velocity is approximately equal to the shock velocity (boundary - layer effect) and the thickness of the contact zone remains quasi constant after an initial growing.

The CO_2/He mixing zone is twice thicker than the CO_2/A mixing zone, which is consistent with predictions based on the linear Richtmyer-Meshkov instability formula :

$$\frac{d\eta}{dt} \simeq k\eta_o\, \mu U^* \left(1 - \frac{U^*}{U_{shock}}\right)$$ (1)

where η_o and k are respectively the amplitude and the wave number of the initial interface deformation, μ is the Atwood number, U^* is the average velocity of the mixing zone and $\frac{d\eta}{dt}$ is the rate of thickening of the mixing zone. The product μU^* is 2-3 times larger for CO_2/He than for CO_2/Ar. Small scale turbulent diffusion is superposed to the large single mode deformation and may be the cause of the more perturbed CO_2/He profiles. The x-t diagrams also show that, after interaction with the reflected shock, the mixing zone thickening rate is higher in the CO_2/Ar case than in the CO_2/He case. This may be interpreted as the effect of a stronger deceleration of the CO_2/Ar inteface. With a shock Mach number of about 3 in argon, the experimental condition is close to the tailored case for which, ideally, the contact surface is brought to rest. The deceleration of the CO_2/He mixing zone by the first reflected shock is less , but again, the profile seem to be more perturbed as shown in figure 2b.

2) In a more recent set of experiments, carried out at the same shock tube conditions (P_{CO_2} = 1520 Pa) but without the initial deformation of the mylar membrane, a different behaviour is observed. From the corresponding x-t diagrams (fig. 3) it appears that the mixing zone resulting from the acceleration by the incident shock is about 25-35 mm thick for both gas pairs and that the thickened (10-15 cm) mixing zone obtained after deceleration by the reflected shock is again similar for the two gas combinations*.The expected Atwood number dependence of the mixing layer thickening rate does not appear in the measurements and may probably be hidden by other effects such as boundary layer effects and the interaction of the reflected shock with the boundary layer. Note that in this case, where only small scale deformation and turbulent mixing should take place, the shock reflected from the contact zone remains imbedded in the contact zone which appears to be reaccelerated towards the end wall. Such behaviour is radically different from the gradual slowing down of the nitrogen/helium interface of the experiment mentioned in ref /1/.

IV. OUTLINE OF THE TURBULENT MIXING MODEL

We have built a two gas closure model for fully developped turbulence with one equation for the average turbulent kinetic energy k. In addition, we suppose that, in the plane normal to the shock propagation direction, the turbulence is statistically homogeneous and isotropic, therefore the motion is described by a one dimensional model. We use the classical conservation equations, and the following turbulent kinetic energy equation (the overbar and ~denote respectively the ensemble averaged and masse averaged value) :
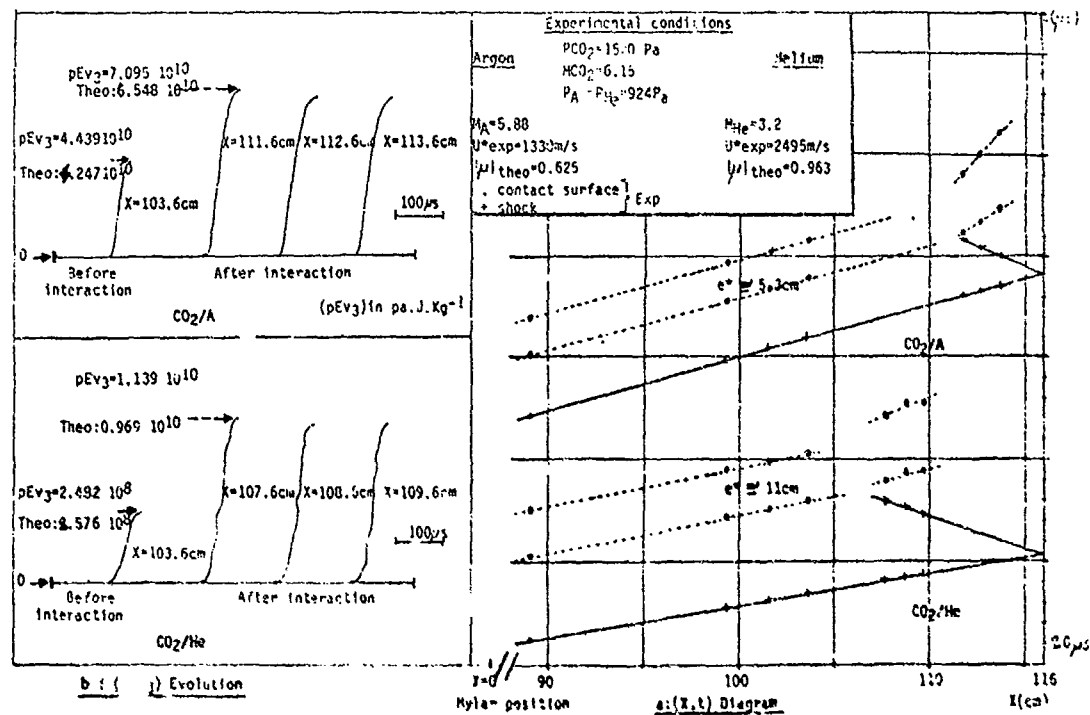
Fig. 2 : Comparison between CO_2/He and CO_2/A_r contact zones (Case 1).
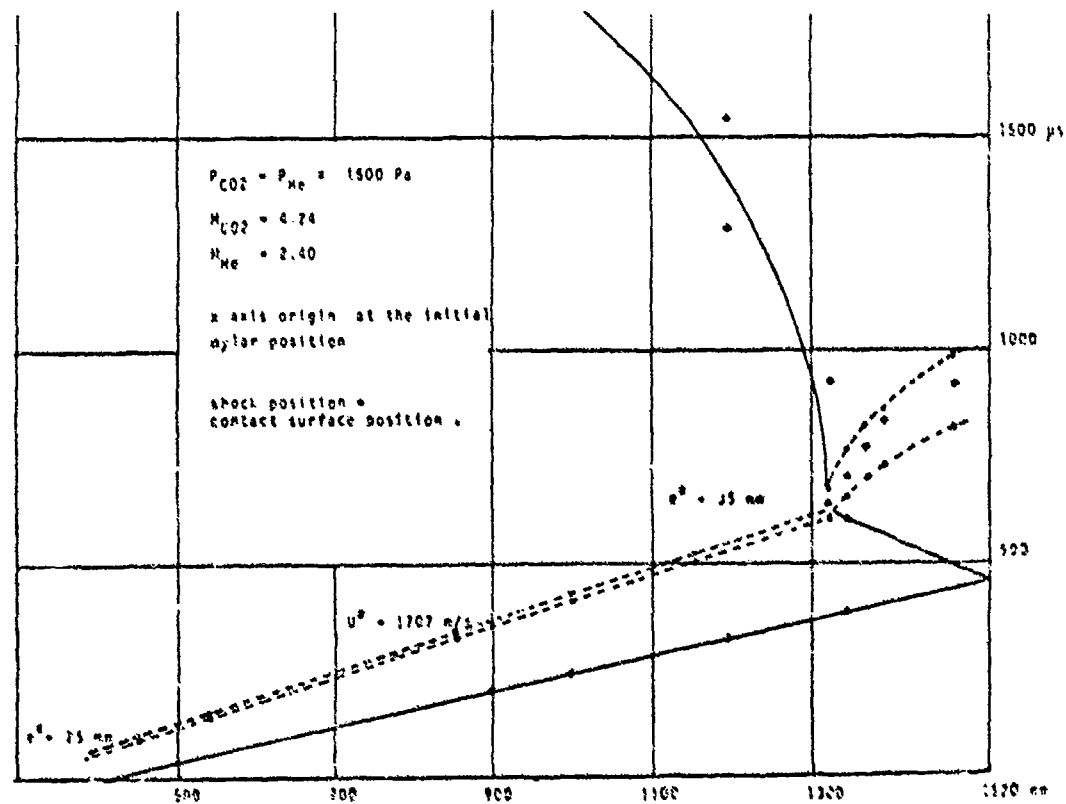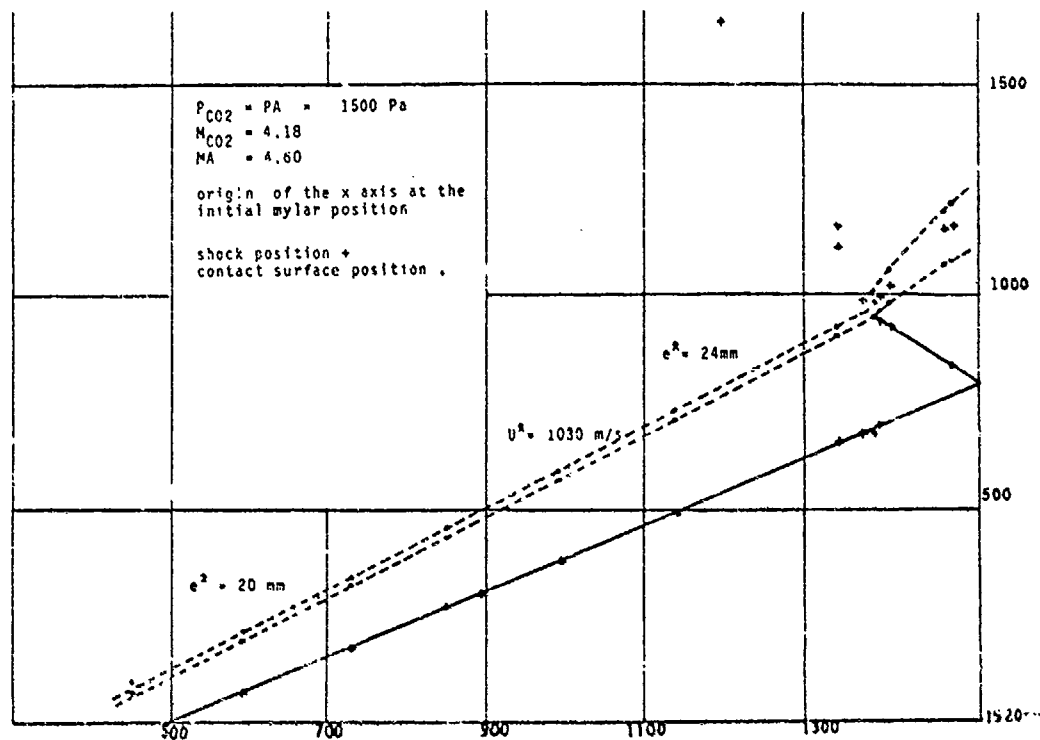

Fig. 3.a : CO_2/He contact zone (Case 2).

$P_{CO2} = PA = 1500$ Pa
$M_{CO2} = 4.18$
$MA = 4.60$

origin of the x axis at the initial mylar position

shock position +
contact surface position .

$e^R = 24$mm

$U^R = 1030$ m/s

$e^2 = 20$ mm

Fig. 3.b : CO_2/Ar contact zone (Case 2).

TIME (µs)

THZ

o Calculation

I Experimental results of Ref. 1

AIR   HELIUM
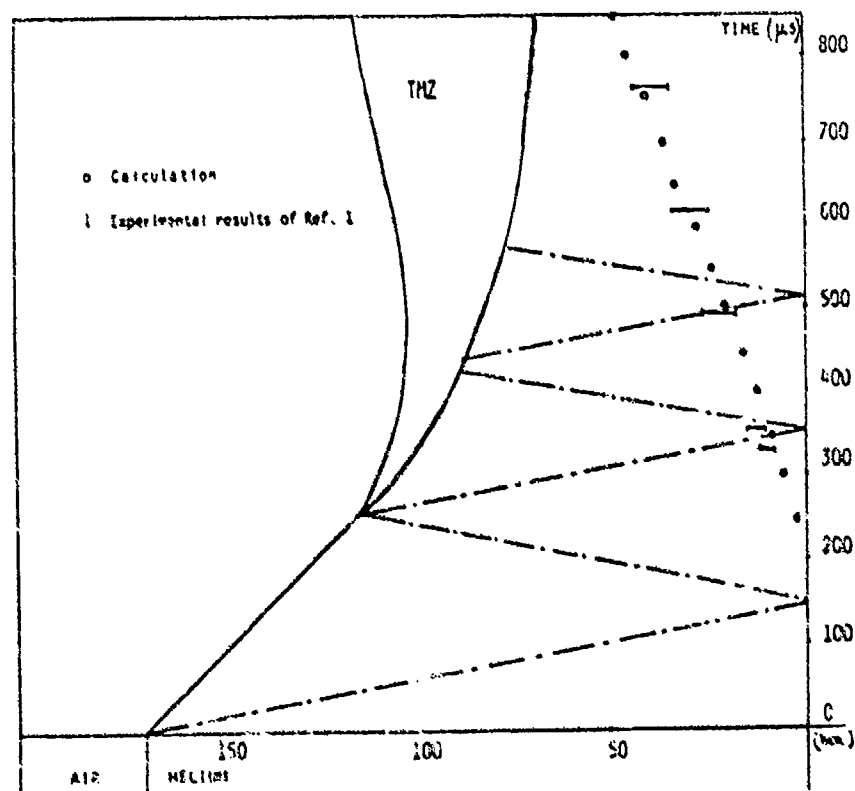
Fig. 4 : Thickening of a contact zone Air/He
o Present calculation . —·— Experiments /1/.

$$\bar{\rho}\,\frac{D\tilde{k}}{Dt} = -\overline{\rho\widetilde{u}'\widetilde{u}'} : \nabla\widetilde{\vec{u}} \;-\; \nabla\cdot\overline{\rho\widetilde{u}'\,k'} \;-\; \overline{\widetilde{u}'}\,\cdot\nabla\bar{p} \;-\; \alpha\,\bar{\rho}\,\frac{k^{3/2}}{L(t)} \tag{2}$$

where α is a dissipation coefficient, $L(t)$ is the width of the mixing zone, and all other quantities have their usual meaning. We have neglected the pressure - velocity correlation in equation (2).

The second order correlations are closed, as usual, for scalar quantities by first gradient laws of the type :

$$\overline{\rho\,\varphi'\,\vec{u}'} = -\,D\varphi\;\;\nabla\varphi \tag{3}$$

The Reynolds stress tensor $\overline{\rho\vec{u}'\vec{u}'}$ is closed by a similar law but limited in value on the shock wave. The diffusion coefficient $D\varphi$ is expressed, as usual, by

$$D\,\varphi = \alpha\varphi L(t)\;\widetilde{k}^{\frac{1}{2}}\,,$$

where $\alpha\varphi$ is a non-dimensional coefficient.

However, the first gradient laws hold only for small gradients. As it is not the case for shock waves, we must constrain the longitudinal stress component $\overline{\rho u'^{2}}$ between two extrema. The upper boundary limits the expression of $\overline{\rho u'^{2}}$ to a fraction of the total turbulent kinetic energy, while the lower boundary prevents the value of $\rho\overline{u'^{2}}$ from becoming too small a fraction of k.

We have kept, for simplicity, only one production term which describes best the shock - driven Rayleigh-Taylor instability. It appears in equation (2) as $\overline{\vec{u}'}\cdot\nabla\bar{\rho}$ where .

$$\overline{\vec{u}'} = -\,\frac{\overline{\rho'\vec{u}'}}{\bar{\rho}} = \frac{D\rho}{\bar{\rho}}\;\;\nabla\bar{\rho}\,.$$

As a first step we choose the value averaged over the mixing zone instead of the local value of the density gradient. When this production term is negative there is an excessively strong attenuation of the turbulence therefore we had to keep only its positive values.

This model has been tested so far on the Andronov et al's experiment/1/ (Air-Helium, Mach 1.3). This experiment was simulated using our one dimensional hydro-code and the results for the thickness of the TMZ appear in figure 4. While there is a relatively good agreement for the thickness, other calculated quantities display a seemingly unphysical behaviour (e.g. very high local temperatures). Therefore, further refinements of the model are needed.

V. CONCLUSION

The measurements of an integrated quantity characteristic of one gas through the mixing zone indicate that its apparent thickness can be decomposed into a large scale, single mode interpenetration of the two gases and a thinner, turbulent mixing zone. We have shown the Atwood number dependence of the large scale, single mode perturbation and the effect of a different deceleration by the reflected wave. The behaviour of an initially very plane gas contact surface indicates no measurable dependence of the turbulent mixing on the Atwood number. The turbulent mixing model presents a good agreement with the results of the low Mach number shock tube experiments and will be tested in the future in the more complex environment of our higher Mach number experiment.

* However, the thickness of the mixing zone CO_2/He remains slightly greater (30 %) than the CO_2/Ar one.

REFERENCES

/1/ ANDRONOV, V.A., BAKHRAKH, S.M., MESHKOV E.E., MOKHOV, V.N., NIKIFOROV,V.V., PEVNITSKII, A.V., and TOLSHMYAKOV A.I., Sov. Phys. JETP *44*, 424 (1976)

/2/ ANDRONOV, V.A., BAKHRAKH, S.M., MOKHOV, V.N., NIKIFOROV, V.V. and PEVNITSKII, A.V., JETP Lett. *29*, 56 (1979)

/3/ ANDRONOV, V.A., BAKHRAKH, S.M., MESHKOV, E.E., NIKIFOROV, V.V., PEVNITSKII, A.V. and TOLSHMYAKOV, A.I., Sov. Phys. Dokl. *27*, 393 (1982)

/4/ RICHTMYER, R.D., Comm. Pure. Appl. Math. *23*, 297 (1960)

STABILITY AND COLLAPSING MECHANISM OF STRONG AND WEAK CONVERGING CYLINDRICAL SHOCK WAVES SUBJECTED TO EXTERNAL PERTURBATION

R.A. Neemeh and Z. Ahmad

Department of Mechanical Engineering
Concordia University, Montreal, Canada

The stability of converging cylindrical shock waves is
studied both theoretically and experimentally by placing
cylindrical rods in their path and observing the behaviour
of the shocks as they progress. The theoretical analysis
is based on Whitham's Ray-Shock theory and the well known
Chester-Chisnell-Whitham's A-M relationship. Wave dia-
grams are constructed for various rod diameters to deter-
mine the growth or decay of perturbations, the shape of
the shock as it progresses, the trajectories of the inner
and outer triple points and the final shape of the shock
before it collapses. Experimentally, the cylindrical
shocks are produced in a 152 mm diameter shock tube using
a three-element area contraction for turning the annular
plane shock into a cylindrical one. For flow visualization,
a double headed spark shadowgraph system is employed.
For each cylindrical rod used, a series of photographs
are taken of the converging shock to determine its shape
and stability as it progresses. Theoretically, the collap-
sing mechanism of converging cylindrical shocks is found to
depend largely on the incoming shock Mach number, and on
the size of the rod used. For strong shocks the perturbed
shock collapses towards the rod side, whereas weak shocks
collapse beyond the geometric centre. An equation to deter-
mine the rate of growth of perturbation is developed as a
function of the rod diameter and its distance from the
centre. In the limit where the rod diameter is very small,
the perturbation parameter is found to agree with the
Butler's small perturbation analysis. Whereas, for large
diameters, a good agreement is obtained between theoretical
and experimental results.

1. INTRODUCTION

A great variety of physical and chemical processes can be studied in gases
at high temperature. These processes are of interest in the study of their
energy effects as well as, high velocity particle-collision which offers the
possibility of attaining plasma[1].

The production of such high temperatures in gases by means of symmetrical
collapse of converging shock waves has been under investigation for over three
decades. Guderley[2] proved theoretically that the strength of the shock
approaches infinity, as the radius of the converging shock tends to zero symme-
trically. Since then, it has been the interest of many investigators to prac-
tically achieve such conditions. Since stable converging shocks collapse
symmetrically at the center, it is of prime importance to analyse the stability
of converging shocks under various magnitudes of pertrubations.

Most of the work done so far is on the stability of plane shocks. It has
been shown by Freeman[3,4] that a perturbation of the plane shock wave, produced
by moving a corrugated piston impulsively from rest to a constant speed in the

stationary fluid, decays with time. Perturbations caused by non-uniformity of
walls was also investigated. A mathematical expression was derived, showing that
the perturbations die out in an oscillatory manner. These results were later
confirmed, both theoretically and experimentally, in the case of plane shocks
reflected from a wedge shaped concave walls[5].

The behaviour of slightly distorted strong converging cylindrical and
spherical shocks was studied by Whitham[6] and Butler[7]. The results show that the
amplitude of the perturbation increases as the shock converges. The analysis is
however approximate and is based on internally developed weak disturbances in
strong shocks only. Therefore, these results cannot be employed for externally
perturbed weak shock analysis. Perry and Kantrowitz[8] performed experiments to
produce symmetrical converging shock waves and showed that for initially weak
cylindrical shocks, the wave perturbations are damped out and the symmetry is
regained as the wave collapses. The stability of moderate strength converging
shocks was studied later by examining its behaviour following it interference
with a small circular aperture[9]. In this case, the perturbation is found to
first decrease, at large radii, then increases as the shock approaches the cen-
ter of collapse.

To date, no research work can confirm or deny the notion that converging
shocks are unstable. The opinion of various investigators are contradictory.
Lee and Knystautas[10] contend that cylindrical implosions are stable, while Wu et
al[11] and Butler[7] claim the opposite. Therefore a clear and decisive answer to
this problem is yet to be found.

The present work therefore, investigates the stability of converging cy-
lindrical shocks and their collapsing mechanism by perturbations of different
magnitude. The magnitude and rate of change of perturbation, the exact shape of
converging shock, and the trajectories of triple points are investigated
theoretically from wave diagrams constructed based on the Ray-Shock theory and
the use of Chester-Chisnell-Whitham's area-Mach number relationship. The final
shape of the collapsing shock, its strength, and the distance of the collapsing
region from the geometric centre are studied for weak shocks as well. The
theoretical results obtained from the wave diagrams are then compared with those
obtained experimentally to check the validity of the Ray-Shock theory in the
present investigation. The detailed description of the theory and its applica-
tion to the present problem is presented in the next section.

2. THEORETICAL ANALYSIS

The theoretical work is based on Whitham's Ray-Shock theory which was devel-
oped based on the assumption that the shock front and particle path are orthogon-
al at any one instant. A curvilinear coordinate system (α,β) was chosen, where
α represents the instantaneous shock shape and β represents the orthogonal tra-
jectories to the successive position of a curved shock wave, called " rays ", as
shown in Figure 1.

Based on the geometric representation, the following differential equa-
tions were developed.

$$\frac{\partial\phi}{\partial\alpha} = \frac{-1}{A}\frac{\partial M}{\partial\beta} , \qquad \frac{\partial\theta}{\partial\beta} = \frac{1}{M} \cdot \frac{\partial A}{\partial\alpha}$$

Solution to the above equations is obtained by the method of characteris-
tics. This method can be used to solve shock waves propagation problems, giving
the shock front shape and strength, provided that the Area-Mach number relation-
ship is given. Fortunately this relationship was derived by three investigators
and was named the Chester-Chisnell-Whitham's A-M relationship. More details
about the theory and its application are given in References (5, 9 and 11).

When a converging shock interacts with a cylindrical rod, regular reflec-
tion takes place followed by mach reflection when the incident angle reaches its
critical value. The trajectory of the tripple point of mach reflection is
called the shock-shock and its role in the wave diagram is exactly analogous to
that of a shock wave in more familiar case of unsteady-one dimensional gas flow.

In other words it can be said that the shock-shock represents the discontinuity not only to physical flow field but also to the characteristics.

The sketch illustrating the interaction of the imploding shock with a cylindrical rod is shown in Figure 2. As noted, two shock-shocks are present; one originating at the cylindrical rod surface at the critical angle ϕ_r and the other when the angle of the diffracted portion of the Mach stem reaches the critical value for transition from regular to Mach reflection. Any general point on the wave diagram can be obtained from the C^+ and the C^- characteristics passing by this point. At the shock-shock, however, the procedure is more complicated. One most first find the variables at point 15 say, by assuming the shock-shock angle χ, then check if the values obtained satisfy the C^+ characteristics passing by point 16 and the shock-shock relations applied between those two points.

In the case of weak incident shock waves, it should be pointed out that the Ray-Shock theory does not predict accurately χ and the characteristics angle m. Accordingly, these angles were not calculated from the theory. The results of Shirouzu and Glass[10], and Skews[13], were used to determine the shock-shock and the characteristic angles.

3. EXPERIMENTAL STUDY OF CONVERGING SHOCK-ROD INTERACTION

The stability of converging cylindrical shocks, perturbed externally, is studied by placing cylindrical rods in their path of convergence. Two sets of experiments were performed, one by placing a rod of diameter 5 mm and another by a rod of 1.75 mm, 25 mm from the geometric center. The spark shadowgraphs of this process of interaction, for the 5 mm rod case, is presented in Figure 3. As noted in the figure, two pairs of triple points are present on the shock front. The first pair, the outer triple points, is the result of Mach reflection taking place during the shock-rod interaction. The other, the inner triple points, form downstream of the rod. Both triple points are found to sweep around the shock front.

It is clear from the shadowgraphs presented in Figure 3 and others, that the shock front shape is largely affected by the change in the magnitude of the perturbations. The distortion of the shock front is found to increase with the increase in rod diameter. As a result of the disturbances introduced in the flow, the shock is seen to lag behind in the direction corresponding to the location of the cylindrical rod.

4. THEORETICAL RESULTS

The theoretical analysis of converging cylindrical shocks subjected to external perturbations is based on Whitham's Ray-Shock theory and the well known Chester-Chisnell-Whitham's A-M relationship. Wave diagrams were constructed to analyse the behaviour of initially strong and weak cylindrical shocks. External perturbations were generated by placing cylindrical rods of various diameters, 25 mm from the geometric center. The influence of these perturbations is discussed in details in the following sections.

4.1 The Behaviour of Initially Strong Shocks

The complete wave diagram for shock Mach number of 3, at a radius of 25 mm, perturbed by a cylindrical rod of diameter 5 mm, is given in Figure 4. Similar wave diagrams were also constructed for cylindrical rods of 1.75 mm, 0.8 mm and 0.25 mm in diameter.

From Figure 4, it is clear that Mach reflection starts when the incident angle of the converging shock, with the surface of the cylindrical rod, reaches the critical value. The trajectories of the triple of Mach reflection, shown in broken lines in Figure 4, are presented in Figure 5 together with those obtained for other rod diameters. Experimental values of outer triple points, measured from the shadowgraphs, are found in good agreement with those obtained theoretically. Surprisingly, smoothening of the shock front curvature was observed in

all cases of strong shocks and for the outer triple points only. The position where the disturbance dies out is found to depend upon the diameter of the cylindrical rod.

When the Mach stems that ride on the surface of the rod collide with each other behind the rod, their interaction may be considered as a reflection of a solid surface instead of the axis symmetry. Here again Mach reflection takes place at a distance of 0.6 to 0.7 times the diameter of the rod, as observed from the wave diagrams. The trajectories of the inner triple points are presented in Figure 5. As noted in the figure, the trajectories widen with the decrease in size of the rod. This is turn results in larger shock amplification, in the case of weak disturbances, since the amplification of Mach stem is proportional to the shock-shock angle. Therefore, the shock fronts perturbed by smaller rod diameters, travel faster than those perturbed by larger ones. Trajectories of inner triple points were also obtained from the shadowgraphs of Figure 3 and others. As noted, the experimentally obtained trajectories are close enough to those obtained theoretically. These results are, however, for initially strong cylindrical shocks. Those for weak shocks are discussed in the following section.

4.2 The Behaviour of Initially Weak Shock

A cylindrical shock of Mach number 1.5 at radius 25 mm from geometric centre is taken as initially weak shock. The external perturbations are generated on the shock front by placing a small rod of diameter 0.25 mm at a distance of 25 mm from geometric centre. The behaviour of such externally perturbed shock is analysed through the wave diagram, constructed by using the same technique described before. Two pairs of Mach reflections are generated during the interaction with the cylindrical rod, as explained in case of strong shocks. In the present case, the outer perturbations do not die out. The inner trajectories of triple points widen because of weak disturbances and meet with the outer trajectories of triple points close to the geometric centre as clear from Figure 6.

The inner triple points sweep along the disturbed part of the shock front causing bigger shock-shock angle as compared to the corresponding strong shock case. Therefore the disturbed part of the shock front travels faster than the undisturbed part. The change in flow deflection in this case is also higher as compared to the corresponding strong shock case, indicating that break down of the shock front takes place even at higher radius of cylindrical shock. This analysis indicates that weak shocks are more sensitive to external disturbances as compared to the strong shocks for the same magnitude of perturbation.

4.3 The Stability of Externally Perturbed Cylindrical Converging Shocks

The stability of cylindrical converging shocks is investigated theoretically from the wave diagrams, constructed for the various cases. The wave diagram, shown in Figure 4 corresponds to the case shown by the series of shadowgraphs in Figure 3. The successive positions of the shock wave are shown by thick lines and the avlues of displacement of perturbed part of shock front from its mean position are determined to check the stability. The perturbation factor 'ξ' is defined as,

$$\xi = \frac{\Delta R}{R_s}$$

where ΔR is the distance by which the perturbed part of shock front is displaced from its undisturbed position and R_s is the instantaneous radius of the cylindrical shock wave. The values of the perturbation factor are determined from the wave diagrams and are plotted in Figure 7.

From these results, a general mathematical expression is obtained

$$\xi = [F(\frac{d}{R_0})] (\frac{R_s}{R_0})^{-G(\frac{d}{R_0})}$$

where   d is the diameter of the cylindrical rod

R_0 is the radius at which the cylindrical rod is placed

$$F(\frac{d}{R_0}) = 0.182(\frac{d}{R_0}) - 24.59(\frac{d}{R_0})^2 + 349.19(\frac{d}{R_0})^3 - 118.6(\frac{d}{R_0})^4$$

$$G(\frac{d}{R_0}) = 0.67 + 3.22(\frac{d}{R_0}) - 38.7(\frac{d}{R_0})^2 + 121.4(\frac{d}{R_0})^3$$

This mathematical expression can be used to find the displacement of the shock front at any time perturbed by any size of the rod diameter. In case of very weak disturbances, the perturbation grows as follows:

$$\xi \alpha (\frac{R_s}{R_0})^{-0.67}$$

This result agrees fairly well with Butler's theoretical analysis for small perturbations, wherein he proved that the perturbation grows as

$$(\frac{R_s}{R_0})^{-0.64}$$

4.4 The Collapsing Mechanism of Cylindrical Shock Waves

Near the Center of Collapse, the wave diagrams were further enlarged and the shapes of the collapsing shock are obtained for the strong and weak cylindrical shocks. These diagrams are shown in Figure 8 for initially strong shocks with a cylindrical rod 5 mm in diameter. It is clear from the figure that the undisturbed portion of shock front reaches the geometric centre before the disturbed part because of higher rate of amplification. The magnitude by which disturbed part of shock front lags behind is found to increase with the increase in rod diameter. This difference causes the shock to collapse before it reaches the geometric center. It is worthwhile to note that the final state of collapse of the shock is not a single point but rather a region whose size depends upon the magnitude of the perturbations.

In the case of weak cylindrical shock an entirely different behaviour is observed. The amplification of the shock strength of disturbed section is observed to be higher than the undisturbed section of the shock front. Mach reflection in this case amplifies the disturbed shock front at a higher rate because of higher values of shock-shock angle and of relatively weak amplification of weak shocks. Therefore, the disturbed part of the cylindrical shock front accelerates and reaches the geometric center before the remaining part does, thus making the shock to collapse on the opposite side of perturbations as shown in Figure 9.

5. CONCLUSIONS

The stability of converging cylindrical shocks was studies both theoretically and experimentally. External perturbations were produced by means of cylindrical rods, placed in the path of converging shocks. Based on the various results obtained, the following conclusions are drawn:

1. The perturbed shock does not collapse to a single point, because the unaffected portion of the front seeks its true center of collapse whereas the perturbed part does not, either by lagging or acceleration. Further, the distance by which the collapsing region is shifted from the center is found to depend upon the initial Mach number of the shock and the magnitude of external perturbation.

2. For initially strong cylindrical shocks, perturbed by a cylindrical rod, the final state of collapse is shifted towards the rod side because the perturbed part lags behind the undisturbed part of the shock front. Whereas, for an initially weak cylindrical shock, the collapsing takes place beyond the geometric centre because the rate of amplification of the perturbed part is more than that of the unperturbed part.

3. A smoothening mechanism of the shock front was noted at the outer triple points for initially strong shocks only. Whereas, such a mechanism was not observed at the inner triple points.

4. In all cases considered, the perturbations grow as the shock progresses towards the geometric centre, indicating that the symmetry of the shock front cannot be regained before it collapses and that converging cylindrical shocks are unstable.

5. A mathematical expression was obtained to predict the magnitude and rate of growth of the perturbations of initially strong cylindrical shocks. In the limit where the rod diameter is very small, this expression reduces to that of Butler's small perturbation analysis.

6. High temperature resulting from converging shocks does not necessarily imply that such shocks are stable, since collapse of the unperturbed part of the shock may cause high temperature as well.

The theoretically obtained shapes of the shock front, the trajectories of triple points and the perturbation parameter were compared with those obtained experimentally. A good agreement is observed between them, which establishes the validity of the present theory in analysing the stability of converging shock waves.

REFERENCES

1.   Lau, J.H., Kekez, M.M., Laugheed, G.D. and Savic, P., "Spherically Converging Shock Waves in Dense Plasma Research", Proceedings of the 10th International Symposium on Shock Tube and Waves, 1979, p. 396.

2.   Guderley, G., "Powerful Spherical and Cylindrical Compression Shocks in the neighbourhood of the Centre of the Sphere and of the Cylindrical Axis", Luftfahrtforschung, Vol. 19, 1942, p. 302.

3.   Freeman, N.C., "A Thoery of the Stability of Plane Shock Waves", Proc. of The Royal Society, London, No. 2281, 1954, p. 341.

4.   Freeman, N.C., "On the Stability of Plane Shock Waves", Journal of Fluid Mechanics, No. 2, 1957, p. 397.

5.   Wu, J.H.T. et al., "Stability of Normal Shock Reflected from a Concave Wedge-Shaped Wall", Canadian Aeronautic Space Jrnl, May 1981, p. 376.

6.   Whitham, G.B., "A New Approach to Problems of Shock Wave Dynamics - Part I: Two Dimensional Problems", Jrnl of Fluid Mechanics, No. 2, 1957, p. 145.

7.   Butler, D.S., "The Stability of Converging Spherical and Cylindrical Shock Waves", AIAA Journal, Vol. 19, March 1981, p. 257.

8.   Perry, R.W. and Kantrowitz, A., "The Production and Stability of Converging Shock Waves", Journal of Applied Physics, Vol.22 No.7, July 1951, p. 878.

9.   Wu, J.H.T., Yu, T.S., Neemeh, R.A. and Ostrowski, P.P., "Stability of Cylindrical Converging Shock Perturbed by a Bleed Aperture", Proceedings of 12th Intern'tl Symposium on Shock Tubes and Waves, Jerusalem, 1979, p.324.

10.   Knystautas, R. and Lee, J.H., "Experiments on the Stability of Converging Cylindrical Detonation", Combustion and Flame Journal, Vol.16, 1971, p.61.

11.   Wu, J.H.T., Neemeh, R.A. and Ostrowski, P.P., "Experiments on the Stability of Converging Cylindrical Shock Waves", AIAA Jrnl, Vol.19, March 1981, p.257.

12.   Glass, I.I. and Shirouzu, M., "An Assessment of Recent Results on Pseudo-Stationary Oblique Shock Wave Reflections", UTIAS Report No. 264, 1982.

13.   Skews, B.W., "The Shape of a Diffracting Shock Wave", Journal of Fluid Mechanics, No. 29, 1967, p. 297.
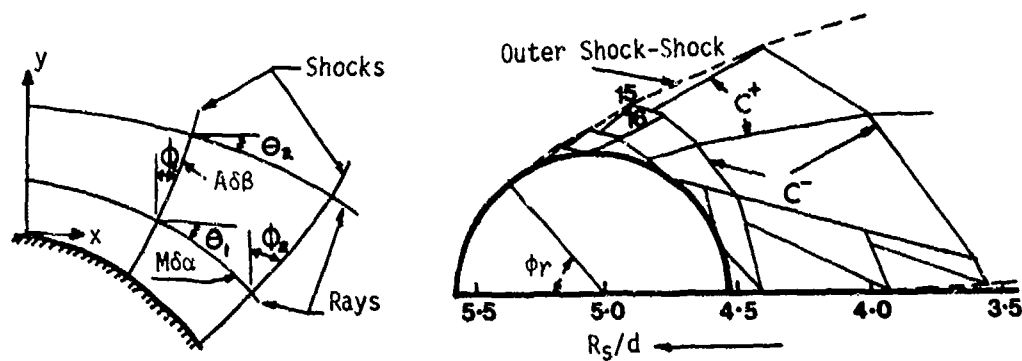
Fig. 1. Ray-Shock Coordinates

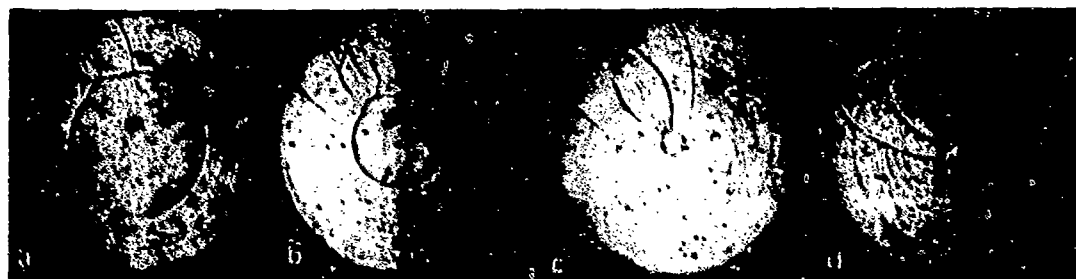Fig. 2. Initial Construction of Wave Diagram $M_i = 3$, $d = 5$ mm

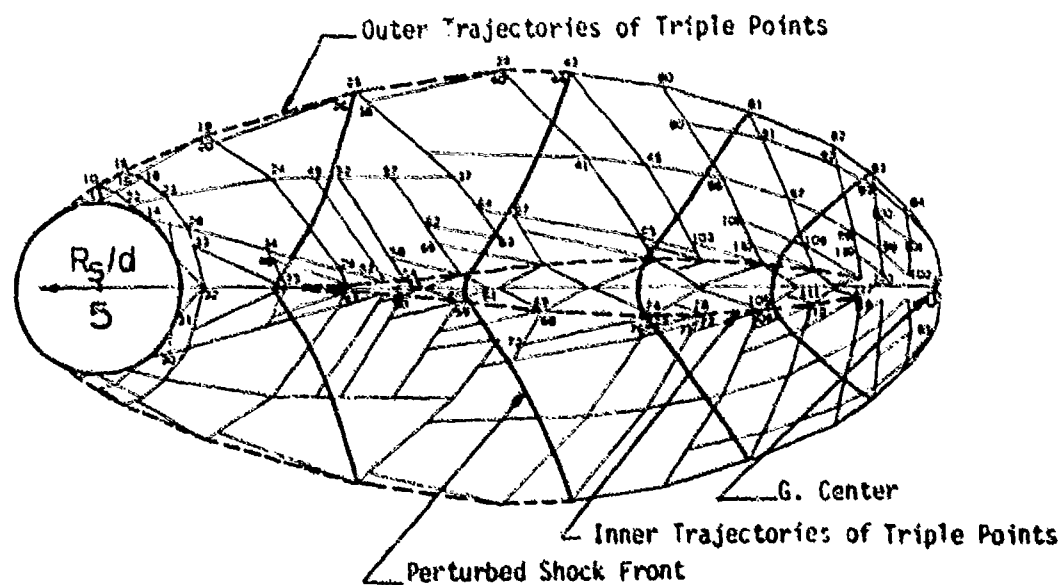Fig. 3. Spark Shadowgraphs of Perturbed Cylindrical Shock, $M_i = 3$, $d = 5$ mm

Fig. 4. The Wave Diagram Illustrating the Successive Positions of the Perturbed Shock Front, $M_i = 3$, $d = 5$ mm
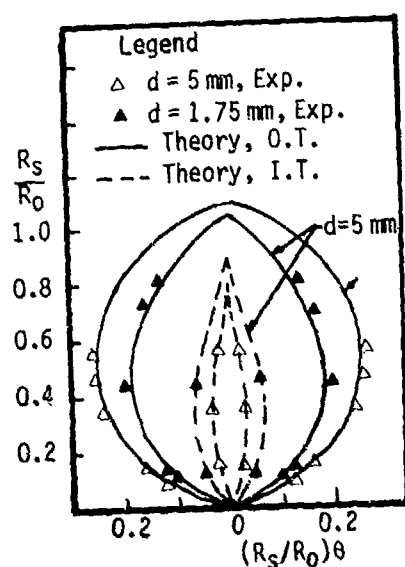
Fig. 5. Inner and Outer Trajec-
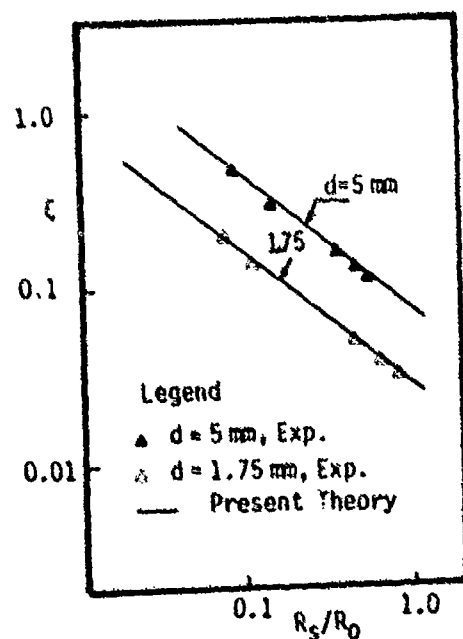tories of the Triple
Points, R_o = 25 mm

Fig. 6. Wave Diagram, M_i = 1.5,
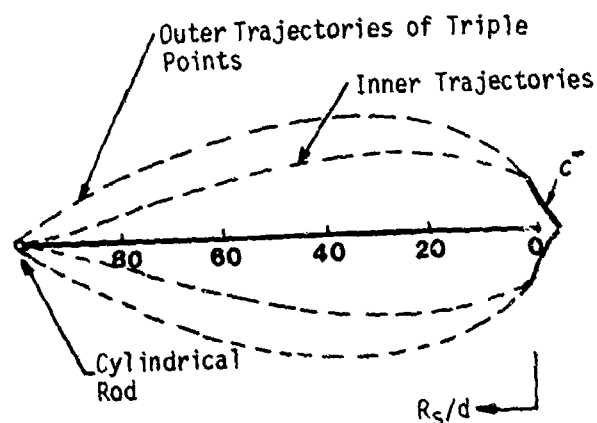d = 0.25 mm

Fig. 7. Perturbation Growth Rate
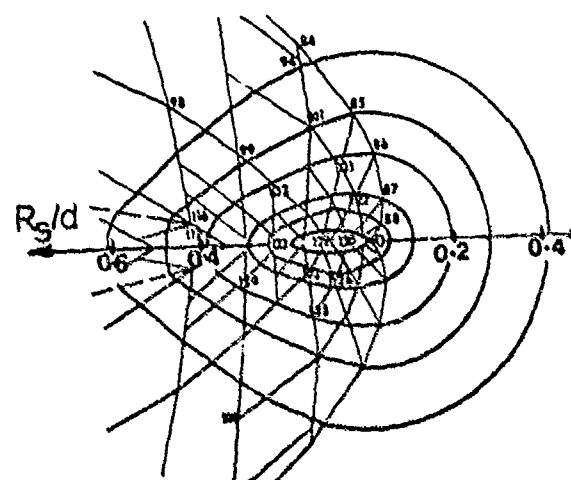
Fig. 8. The Collapsing of Initially Strong
Cylindrical Shock, d = 5 mm
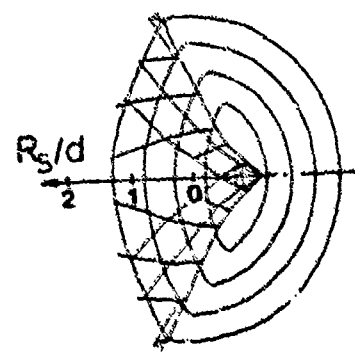
Fig. 9. The Collapsing of Initially Weak
Shock, d = 0.25 mm

ROLE OF THE BOUNDARY CONDITIONS IN THE PROBLEM OF
THE LINEAR STABILITY OF THE SEDOV POINT BLAST SOLUTION

David L. Book
Laboratory for Computational Physics
Naval Research Laboratory
Washington, DC   20375

The linear stability of those Sedov blast wave
similarity solutions for which the flow is homologous
behind the shock, of which the best-known example is the
Primakoff point blast model, along with that of their
two-dimensional counterparts, has previously been
demonstrated analytically by Bernstein and Book (1980).
Their conclusion that the eigenmodes are stable applies
to all perturbations in the three-dimensional case, and
to all flutelike ($k_z = 0$) modes in the two-dimensional
case. Gaffet (1984) has argued tht the treatment did
not allow for a jump in the entropy of the perturbations
at the shock front, and so must be incorrect. The anal-
ysis of Bernstein and Book, however, can easily be
extended to include anisentropic perturbations. The
additional terms, which have the same time dependence as
the basic state, and therefore cannot give rise to insta-
bility, in any case drop out of the treatment. The
resulting eigenvalue problem is identical with that
solved by Bernstein and Book, whose conclusion that the
Primakoff-Sedov blast waves are stable is therefore
restored.

1. Introduction

A highly localized release of energy in an unbounded pressureless ideal gas
medium gives rise to an expanding spherical blast wave. Because of the absence
of a characteristic length scale in the problem, the resulting flow is self-
similar. It consists of a shock followed by a rarefaction wave. If the density
ρ of the background medium satisfies a power-law distribution ($\rho \sim R^{-\omega}$, where R
is the distance from the blast center), then the solution of the problem can be
reduced to quadratures. This analysis was carried out by Sedov (1946, 1959) and
independently by Taylor (1950) and Von Neumann (1947). The analogous implosion
problem was treated by Guderley (1942).

Numerous workers have investigated the stability of the Sedov point blast
solutions. In its full generality the problem can be stated as follows: Given
a particular Sedov solution, specified by the values of Q and the adiabatic
index γ, for what wave numbers ℓ, m does the deviation in the shock amplitude
associated with an infinitesimal perturbation about this solution grow faster
than the shock radius S as $S \to \infty$? If no such wave numbers exist, the unper-
turbed point blast solution is stable. At present, a solution of this general
problem is lacking. As we shall note, very few results of any sort have been
established beyond dispute.

It is not trivial to demonstrate the stability even of planar shocks, a problem treated originally by D'yakov (1954) and later by Erpenbeck (1962). They found that for a wide class of differing fluids (characterized by different equations of state), planar shock waves propagating in a uniform medium are stable. The physical mechanism is easy to describe. A small ripple in the shock front gives rise to divergence (respectively, convergence) in the curved portions ahead of (behind) the main front. These regions become weaker (stronger) than the unperturbed shock, hence propagate slower (faster) than average, thus reducing the amplitude of the ripple. Evidently the longer the perturbation wavelength, the weaker the stabilizing effect of this mechanism, so by analogy we would expect $\ell = 0$ perturbations around the Sedov solutions to be the most unstable.

When variation of the density of the background medium is taken into account, however, this mechanism becomes obscure. For $\Omega > 3$, the unperturbed Sedov shocks accelerate with increasing radius. It is conceivable that the ripples ahead of the shock can run away, while those behind fall further behind, leading to instability. Lerche and Vasyliunas (1976) and Isenberg (1977), who treated the case $\gamma \neq 1$, have claimed that for some values of γ, Sedov shocks are unstable for all values of Ω. Their conclusions are remarkable in predicting instability at short wavelength ($\ell \gg 1$). Newman (1979) has disputed the results, on the ground that Lerche and Vasyliunas (1976) and Isenberg (1977) improperly treated the boundary conditions at the shock front.

Bernstein and Book (1980) studied the stability of a restricted class of the Sedov solutions, those in which the velocity behind the shock is proportional to the distance R from the origin (homologous or uniform expansion). This type of blast wave was apparently first considered by Primakoff (see Courant and Friedrichs 1948). He found that for $\bar{\rho}$ = const., the point blast similarity solution can be written explicitly in closed form when $\gamma = 7$. Keller (1956) generalized the results to nonuniform densities and found for each value of $\gamma > 1$ the value of Ω for which explicit solutions with homologous velocity distributions exist.

Bernstein and Book (1980) linearized the fluid equations about the Primakoff blast solution and applied the first-order Rankine-Hugoniot equations at the shock location. The resulting eigenvalue problem reduces to a quartic equation for the stability index Γ all of whose roots have negative real part. They therefore concluded that this class of Sedov solutions is stable, contradicting the conclusion of Isenberg (1977).

Subsequently Gaffet (1984) presented a refutation of the work of Bernstein and Book (1980). His criticism of the latter focused on the neglect of the entropy perturbations arising at the shock front. This, he claimed, resulted from an incorrect statement of the perturbed boundary conditions.

To clarify the matter, we rederive the results of Bernstein and Book (1980), taking into account both the corrected boundary conditions and the entropic perturbations. We find that the solution of the eigenvalue problem is the same as that found previously, and the conclusion that the modes are stable remains unchanged.

The plan of the paper is as follows. We begin by summarizing the approach followed by D'yakov (1954) in treating the planar shock problem, because his characterization of the acoustic and entropic modes is instructive in the present case. We then go through the revised treatment of the Primakoff blast wave stability problem, using essentially the notation of Bernstein and Book (1980). The paper concludes with a summary of the results and briefly explores their implications.

2. Stability of Planar Shock Waves

D'yakov (1954) analyzed the stability of a planar shock propagating in the positive x direction. He chose as his basic equations the adiabatic law expressed in terms of the entropy s, Euler's equation, and an equation for the pressure p. The latter, taken together with the adiabatic law, is equivalent to the continuity equation. The location of the shock front is perturbed by an amount

$$\zeta = \zeta_o \exp[i(kx - \omega t)]. \tag{1}$$

All other perturbed quantities then are taken to vary as $\exp[i(kx + \ell y)]$. In the frame of the unperturbed shock, the linearized equations assume the form

$$(\ell v - \omega)\, \delta s = 0 \; ; \tag{2}$$

$$(\ell v - \omega)\, \delta v_x + kV\delta p = 0; \tag{3}$$

$$(\ell v - \omega)\, \delta v_y + \ell V\delta p = 0; \tag{4}$$

$$(\ell v - \omega)\, \delta p + \rho c^2(k\delta v_x + \ell\delta v_y) = 0, \tag{5}$$

where $V = \rho^{-1}$ is the specific volume, $c = (\gamma p/\rho)^{1/2}$ is the speed of sound, and first-order fluid quantities are distinguished with a δ. From Eq. (2) it follows that two types of solutions are possible (indicated respectively by (1) and (2). For type (1) $\ell v - \omega = 0$, while $\delta s^{(1)} \neq 0$. It follows from Eqs. (3) and (4) that $\delta p^{(1)} = 0$, and from Eq. (5) that

$$k\delta v_x^{(1)} + \ell_1 \delta v_y^{(1)} = 0 \tag{6}$$

(the condition for incompressibility), and the perturbed specific volume $\delta V^{(1)} = (\partial V/\partial s)_p\, \delta s^{(1)}$ is nonzero. This is the "entropic" mode, which advects entropy and vorticity perturbations away from the perturbed shock.

The second type of solution of Eq. (2) satisfies $\ell_2 v - \omega \neq 0$, while $\delta s^{(2)} = 0$. Multiplying Eq. (3) by k, Eq. (4) by ℓ_2, adding and using Eq. (5) to eliminate $\delta v_x^{(2)}$ and $\delta v_y^{(2)}$, we obtain the acoustic dispersion relation:

$$(\omega - \ell_2 v)^2 = (k^2 + \ell_2^2)c^2. \tag{7}$$

The quantities $\delta v_x^{(2)}$, $\delta v_y^{(2)}$, and $\delta p^{(2)}$ are then related by any two of Eqs. (3)-(5), for example

$$(\ell_2 v - \omega)\, \delta v_x^{(2)} + kV\delta p^{(2)} = 0, \tag{8}$$

$$(\ell_2 v - \omega)\, \delta v_y^{(2)} + \ell_2 V\delta p^{(2)} = 0. \tag{9}$$

By virtue of the vanishing of the perturbed entropy $\delta s^{(2)}$, we have

$$\delta p^{(2)} = -(c^2/V^2)\delta V^{(2)}. \tag{10}$$

The general solution of the perturbed equation consists of a superposition of the entropic and acoustic modes.

By expanding the Rankine-Hugoniot relations through terms in first order, four boundary conditions can be obtained. These are the condition that the tangential component be continuous across the shock,

$$\delta v_x^{(1)} + \delta v_x^{(2)} = ik\zeta(\bar{v} - v), \tag{11}$$

two conditions obtained from the jump in the momentum normal to the shock and from the continuity equation, which D'yakov (1954) rewrites in the form

$$\delta v_y^{(1)} + \delta v_y^{(2)} = \frac{v - \bar{v}}{2} \left(\frac{\delta p^{(2)}}{p - \bar{p}} + \frac{\delta v^{(1)} + \delta v^{(2)}}{V - \bar{V}} \right) \tag{12}$$

and

$$\frac{2i\Omega\zeta}{\bar{v}} = \frac{\delta p^{(2)}}{p - \bar{p}} + \frac{\delta v^{(1)} + \delta v^{(2)}}{\bar{V} - V}, \tag{13}$$

and an equation derived from the energy jump condition. Since for given $\bar{V}$, V, and $\bar{p}$, p is a known function of V, D'yakov (1956) takes this last condition in the form

$$\delta p^{(2)} = (\partial p / \partial V)_H (\delta v^{(1)} + \delta v^{(2)}), \tag{14}$$

where the subscript H stands for "Hugoniot." We have consistently used an overbar to indicate quantities ahead of the shock.

Equations (6) and (8)–(14) constitute a set of eight algebraic relations in the eight coefficients $\delta v^{(1)}$, $\delta v^{(2)}$, $\delta v_x^{(1)}$, $\delta v_y^{(1)}$, $\delta v_x^{(2)}$, $\delta v_y^{(2)}$, $\delta p^{(2)}$, and ζ. Equation (7) is to be understood as a definition of ℓ_2 in terms of k and Ω. D'yakov (1954) goes on to analyze the dispersion relation

$$\frac{2\omega v}{\bar{v}} \left(k^2 + \frac{\omega^2}{v^2} \right) = \left(\frac{\omega^2}{v\bar{v}} + k^2 \right) (\omega - \ell_2 v) [1 + \frac{v^2}{V^2} \left(\frac{\partial V}{\partial p} \right)_H]$$

which follows, emphasizing the role of the Hugoniot curve in determining the stability of the perturbations. The interested reader is referred to that paper for the details.

3. Stability of the Primakoff Point Blast

For the sake of brevity we will not go through the whole derivation and solution of fluid equations linearized around the Primakoff-Sedov solutions. In this section we will refer to Bernstein and Book (1980) and to equations contained in it by using the abbreviation "BB." Except as noted, the notation here is that same as in BB.

The correct forms for the Lagrangian perturbed density ρ_1 and pressure p_1, expressed in terms of the infinitesimal displacement $\underline{\xi}(R,t)$ of an element of fluid whose unperturbed trajectory is $\underline{R}$, $(\underline{r},t)$, are

$$\rho_1 = \rho(-\nabla_R \cdot \underline{\xi} + \kappa) \tag{16}$$

and

$$p_1 = p(-\gamma \nabla_R \cdot \underline{\xi} + \lambda), \tag{17}$$

where κ and λ are time-independent quantities which were taken equal to zero in BB. Substituting (16) and (17) in the perturbed equation of motion then yields

$$\omega_0^{-2} r^{\nu(\gamma - 1)} + 2 \underline{\ddot{\xi}} + r\nabla \cdot \underline{\xi} - \frac{\gamma}{\nu} r^{2-\nu} \nabla(r^\nu \nabla \cdot \underline{\xi}) - (\nabla\zeta) \cdot r = r[\kappa \underline{r} - \frac{1}{\nu} r^{2-\nu} (r^\nu \lambda)], \tag{18}$$

where $\nu = 2$ for the cylindrical case and $\nu = 3$ for the spherical case. The solution of Eq. (18) may be written as the sum of a particular and a homogeneous solution:

$$\underline{\xi} = \underline{x}^{(P)}(r)f + \underline{x}^{(h)}(r) r^\beta = (\underline{x}^{(P)}f + \underline{x}^{(h)}r^\beta) H(\theta,\phi), \tag{19}$$

where the harmonic dependence of the solution is contained in $H(\phi) = \exp(im\,\phi)$ ($\nu=2$) or $H(\theta,\phi) = Y_{\ell m}(\theta,\phi)$ ($\nu=3$). Note that the definition of β here differs slightly from that in BB.

Since

$$\left(f^\beta\right)^{\cdot\cdot} = \beta f^{\beta-1}\,\ddot{F} + \beta\,(\beta-1)\,F^{\beta-2}\,\dot{f}^2, \tag{20}$$

we have by virtue of BB(2.23) and (2.24)

$$\omega^{-2}\,f^{\nu(\gamma-1)} + 2\,\left(f^\beta\right)^{\cdot\cdot} = -\mu f^\beta, \tag{21}$$

where

$$\mu = -\frac{\beta\,[2(\beta-1) - \nu(\gamma-1)]}{\nu(\gamma-1)}. \tag{22}$$

Writing

$$\chi_r^{(h)} = a r^\alpha\,H, \tag{23}$$

$$r\,\nabla \cdot \underset{\sim}{\chi}^{(h)} = b r^\alpha\,H, \tag{24}$$

we get Eq. BB(3.14)

$$(\mu + \alpha)\,a + \left[\tfrac{\gamma}{\nu}\,(\alpha + \nu - 1) - 1\right]\,b = 0 \tag{25}$$

from the r-component of (18), and an equation identical with BB(3.15) by taking the divergence of (18). Multiplying the first of these by $\alpha + \nu - 1$ and subtracting the second, we obtain the equivalent but simpler relation

$$\Lambda\,\left(\tfrac{\gamma}{\nu}\,b + a\right) + (\mu - 1)\,\left[(\alpha + \nu - 1)\,a - b\right] = 0, \tag{26}$$

where $\Lambda = m^2$ for $\nu = 2$ and $\Lambda = \ell(\ell+1)$ for $\nu = 3$.

The "particular" solutions of Eq. (18), which evidently correspond to D'yakov's entropic mode, depend on time as $f(t)$. Assuming

$$\kappa = K\,r^{\delta-1}H, \tag{27}$$

$$\lambda + L\,r^{\delta-1}H, \tag{28}$$

we can write

$$\xi_r^{(P)} = A\,r^\delta fH, \tag{29}$$

$$r\,\nabla \cdot \underset{\sim}{\xi}^{(P)} = Br^\delta fH, \tag{30}$$

where K, L, A and B are constants. Then substitution in the r-component and divergence of (18) yields two relations satisfied by the particular solution,

$$(\delta + 1)\,A - B + K = \tfrac{1}{\nu}\,(\delta + \nu - 1)\,(L - \gamma B) \tag{31}$$

and

$$(\delta + \nu - 1)\,\left[(\delta + 1)A - B + K\right] = \tfrac{1}{\nu}\,\left[(\delta + \nu - 1)^2 - \Lambda\right]\,(L - \alpha B) + \Lambda A. \tag{32}$$

Multiplying (31) by $\delta + \nu - 1$ and subtracting, we are left with

$$L = \nu A + \gamma B \tag{33}$$

if $A \neq 0$; substitution in (32) then yields

$$K = (\nu - 2)A + B. \tag{34}$$

Taking into account the additional terms arising from κ and λ in Eqs. (16) and (17), we can rewrite the first-order Rankine-Hugoniot relations [BB(3.34 – (3.36)] as

$$-r \, \sigma + (\nu{-}2) \, (\zeta - \xi_r) + \kappa s f^{\frac{\gamma+1}{2}} = q\zeta; \tag{35}$$

$$t\dot{\xi}_r + \frac{2(\zeta - \xi_r)}{\nu(\gamma-1) + 2} = \frac{2 \, t \, V_{1r}}{\gamma + 1}; \tag{36}$$

$$-\gamma r \sigma + \nu \, (\zeta - \xi_r) + \lambda s f^{\frac{\gamma+1}{2}} = \frac{4 \, \overline{\rho} \, S \, S \, V_{1r}}{(\gamma + 1) \, \rho} + q \, \zeta, \tag{37}$$

where $\sigma = \nabla \cdot \underset{\sim}{\xi}$, with all expressions evaluated at $r = s \, f^{\frac{\gamma-1}{2}}$, i.e., on the shock front. If we write

$$\zeta = z \, s^\alpha \, f^{\alpha \frac{\gamma-1}{2} + \beta} \, H, \tag{38}$$

$$tV_{1r} = c s^\alpha \, f^{\alpha \frac{\gamma-1}{2} + \beta} \, H, \tag{39}$$

and substitute $\underset{\sim}{\xi} = \underset{\sim}{\xi}^{(P)} + \underset{\sim}{\xi}^{(h)}$ in Eqs. (35) – (37), we find

$$[(\nu - 2)a + b+(q - \nu + 2)z]s^\alpha \, f^{\alpha \frac{\gamma-1}{2} + \beta} =$$
$$[K - (\nu - 2) A - B] \, s^\delta \, f^{\delta \frac{\gamma-1}{2} + 1}; \tag{40}$$

$$(\beta - 1) \, a + z + \frac{\nu(\gamma - 1) + 2}{\gamma + 1} c = 0; \tag{41}$$

$$\{\nu a + \gamma b + (q - \nu)z - \frac{2[\nu(\gamma-1)+2]}{\gamma + 1} c\} \, s^\alpha \, f^{\alpha \frac{\gamma-1}{2} + \beta} =$$
$$(L - \nu A - \gamma B) \, s^\delta \, f^{\delta \frac{\gamma-1}{2} + 1}. \tag{42}$$

But Eqs. (33) and (34) imply that the right hand sides of (40) and (42) vanish. Thus all the coefficients associated with the particular solution (i.e., the entropic mode) cancel out. We are left with three equations which, are identical with those found in BB. These yield the boundary condition

$$2\beta a + (\gamma - 1) \, b = 0. \tag{43}$$

Equations (25), (26), and (43) constitute three simultaneous expressions for a/b. Equating these, we can solve for α, β, and μ as before, obtaining the same quartic and hence the same values for the stability index

$$\Gamma = \frac{1}{2} \, [(\gamma - 1) \, \alpha - \gamma - 1] + \beta. \tag{44}$$

The arguments presented here must be modified slightly to treat the case $\Lambda = 0$, but the result is the same as that found by taking the limit $\Lambda \rightarrow 0$ in BB(4.8) and (4.13), which are analytic in Λ.

4. Discussion

We have seen that there are indeed terms in the corrected analysis which correspond to D'yakov's (1954) entropic mode, but they drop out of the problem and do not alter our earlier result. Gaffet (1984) was correct in pointing out the term corresponding to $\lambda \neq 0$ in Eq. (17) for the pressure, but he failed to note the analogous term in Eq. (16) for the density. The parallel with D'yakov's (1954) analysis of the planar-shock (section 2) is not complete; D'yakov found a

nonvanishing $\delta V^{(1)}$ (whence $\delta\rho^{(1)} \neq 0$), but $\delta\sim^{(1)} = 0$. We note that in our analysis the entropic mode has the same time dependence $\sim\tau(t)$ as the unperturbed shock. Hence the density contrast κ satisfies $d\kappa/dt = 0$, whereas in the planar case [by virtue of the incompressibility condition, Eq. (6)] it is the perturbed density of the entropic mode which satisfies $\frac{d}{dt}\rho^{(1)} = i(\omega - \ell_2 v)\rho^{(1)} = 0$.

Bernstein and Book (1980) made no use of the tangential velocity condition analogous to Eq. (11). In our notation this can be shown to take the form

$$\underset{\sim}{n} \times \underset{\sim}{\xi} + \underset{\sim}{v} \times \nabla\zeta = 0, \tag{45}$$

where $\underset{\sim}{n}$ is the normal to the unperturbed shock. Gaffet (1984) noted that the perturbation ξ found by Bernstein and Book (1980) does not vanish at the shock front, as it should. We readily see that Eq. (45), together with

$$\underset{\sim}{\xi} = 0 \tag{46}$$

at the shock front, just suffice to establish the connection between a, b and A, B, i.e., to determine the coefficients of the entropic part of the solution and the exponent δ, which turns out to satisfy

$$\delta = \alpha + 2\beta/(\gamma-1). \tag{47}$$

The analysis presented by Bernstein and Book (1980) and here is restricted to the discrete modes, another point which Gaffet (1984) criticized. Although it is conceivable that the continum modes (which are associated with the initial conditions) could give rise to instability, we believe this is unlikely. Certainly most conventional problems of the stability of ideal fluids in finite geometry can be treated in terms of the normal modes only.

References

1. Bernstein, I.B. and Book, D.L., 1980, Astrophys. J. 240, 223.
2. Book, D.L. and Bernstein, I.B., 1979, Phys. Fluids 22, 79.
3. Courant, R. and Friedrichs, K.O., 1948, Supersonic Flow and Shock Waves (Intescience Press, New York), p. 424.
4. D'yankov, S.P., 1954, Zhurnal Eksper. Teor. Fiz. 27, 288.
5. Erpenbeck, J.J., 1962, Phys. Fluids 5, 1181.
6. Gaffet, B., Astrophys. J. 279, 419 (1984).
7. Guderley, G., 1942, Luftfahrtforschung 19, 302.
8. Isenberg, P.A., 1977, Ap. J. 217, 597.
9. Keller, J.B., 1956, Q.J. Appl. Math. 14, 171.
10. Lerche, I. and Vasyliunas, V.M., 1976, Ap. J. 210, 85.
11. Newman, W.I., 1980 Astrophys. J. 236, 880.
12. Sedov, L.I., 1946, C.R. Acad, Sci. U.S.S.R 52, 17.
13. Sedov., L.I., 1959, Similarity and Dimensional Methods in Mechanics (Academic Press, New York), pp. 260 - 270.
14. Taylor, G.I., 1950, Proc. Roy. Soc. London Ser. A 201, 159.
15. Von Neumann, J., 1947, Ch. 2 of Blast Wave, Los Alamos Sci. Lab. Tech. Series, Vol. VII, Pt. II, Bethe, H., Ed., LA-200; reprinted in Collected Works, Taub, A.H., Ed., Vol. VI (Pergamon Press, New York, 1963), p. 219.

MODEL CALCULATIONS OF THE PRECURSOR

AHEAD OF THE SHOCK FRONT IN INERT GASES

D. Krauss-Varban

Institut für Plasmaphysik der Universität Hannover
Callinstr. 38, D-3000 Hannover 1, FRG

Calculations of particle density profiles ahead of
the shock front require a reactional kinetic model
in conjunction with a description of excitational
and ionizational radiative transfer processes. In-
vestigations are presented of krypton and xenon
precursors in the range of Mach numbers 11 to 21
with upstream gas densities of 1.5 to $6.5 \cdot 10^{23} m^{-3}$.
The work aims at clarifying effects of real shock
wave behaviour in shock tubes, realistic assumptions
about radiative transfer mechanisms and specific
reactional processes. The unsteadiness of the shock
wave and the boundary layers and radiative cooling
in the downstream flow are accounted for. The finite
region of emission, angle-dependent reflection on
tube walls as well as a non-Lorentzian line shape
and Stark broadening of the resonance line radia-
tion are included in the description. Good agree-
ment is found in comparison to experimental
excited state and electron density profiles ahead
of the shock front.

1. INTRODUCTION

It is well known that shock waves of medium and high Mach numbers lead to
a considerable amount of excitation and ionization ahead of the shock front,
creating the so-called precursor region[1-9]. The two main constituents of pre-
cursor calculations, resulting in particle density profiles ahead of the shock
front, are a reactional kinetic model and specific assumptions about the exci-
tional and ionizational radiative transfer processes[1-5].

Our aim is to clarify the effects of real shock wave behaviour in shock
tubes, realistic assumptions about radiative transfer mechanisms, and different
reactional processes. Since the downstream hot plasma serves as the source of
excitation for the precursor, exact computation of the physical condition of
this region is a prerequisite for precursor calculations.

To achieve this, we take into account the unsteadiness of the shock wave and
the effects of boundary layers as well as radiative cooling. We found that a two
step model of ionization relaxation usually gives sufficient accuracy. The non-
Maxwellian feature of the electron velocity distribution, predominant at lower
Mach numbers, can be accounted for.

Investigations are done in krypton and xenon in the range of Mach numbers
11 to 21, the preshock gas density being $1.5 \cdot 10^{23} m^{-3}$. Under these con-
ditions, the ionization relaxation and precursor calculations can be shown to
be uncoupled[9]. Details of the downstream calculation are given elsewhere[9-11].

2. REACTIONAL KINETICS

Precursor model levels have to be able to describe the most important reaction mechanisms and should include the levels being measured in experiments. Our collisional-radiative model consists of eight different states:

The first four levels are the four real metastable and resonant states in inert gases. Level (5) and (6) contain four and eight (five in Xe) resonant states, respectively, ensuring the total radiative excitation of all resonant states to be accounted for. Additionally, electrons and molecular ions are considered. The atomic ion density is then given by the difference of the aforementioned two particle densities.

Collisional and radiative processes lead to a specific redistribution of the total excitation into different states. An overview of the processes included in the model is given in table 1. In the presence of high electron densities, the model levels (5) and (6) also contain non-resonant states. This especially effects the spontaneous transitions' averaged branching ratios into lower levels and the effective statistical weights in respect to electron collisions.

In xenon, an additional excitation exchange between the 6s' states and the $6p[1/2]_1$ state has to be considered[12], resulting in one to two orders of magnitude lower concentrations of the $6s'[1/2]_1$ state. This is in excellent agreement to absorption measurements[8].

For the integration of the stiff rate equations describing the reactional processes, an explicit second order method by Steihaug and Wolfbrandt[13] is employed, utilizing a modified treatment of the non-autonomous terms[9] and an error estimate of Scraton[14] for a variable stepsize. The electron energy equation is solved by the secant method assuming a Maxwellian velocity distribution, since this assumption can be shown to be valid for thermal electrons[4,9], and we did not find a strong influence of high energy electrons.

Calculated electron temperatures range from 1000 to 2000 K (Kr) and 1000 to 4000 K (Xe) at lower Mach numbers, and up to 6000 K at high Mach numbers, slowly increasing towards the shock front. This is in good agreement with the results of ref. 4. In case of high rates of chemoionization, a slight temperature maximum can be found close to the shock front.

3. RADIATIVE TRANSFER

The equilibrium region in the downstream flow serves as an emitter of optically thin continuum radiation, which in turn gives rise to ionization of excited species in the precursor. The corresponding photoionization rates are calculated using recent values of the respective cross section profiles[15] and taking into account the temperature decrease in the radiative cooling region[9]. This improved treatment gives much lower rates of photoionization than prior investigations.

Thus, in contrast to the results of ref. 4 and 5, we always find (instead) associative ionization to be the dominant mechanism of electron production, even for coefficients of reflection from the shock tube walls as high as 0.5 to 0.95. This is in agreement with more recent interpretations of electron density measurements by T. V. Zhikhareva, D. G. Zavarin and G. K. Tumakaev[6].

In accordance with earlier investigations[4], the rates of ionization due to optically thick continuum radiation are always negligible.

In calculating the transfer of resonance line radiation, the usually applied black-body-emitter model[1-6] proved to be much too inaccurate (by a factor of up to 6 in the resulting particle densities). Consequently, the emitted radiation is calculated from the real source extensions, being enclosed by the shock tube wall and the contact surface. In taking into account the actual particle density

prcfiles behind the shock front, an approximative solution derived from model
assumptions was found to be in good agreement to the exact, but time consuming
numerical integration of the downstream values .

Since the main contribution to resonant excitation and deexcitation is
transmitted in the extreme far line wings, a non-Lorentzian line shape based on
the nearest neighbour approximation of the quasistatic theory[16] and measured mole-
cular potentials[17-19] is employed. Details are given in ref. 9. As an example,
the spectral resonant excitation rate in the krypton precursor is shown in fig. 1.
The considerable differences to the solution for a Lorentzian line shape can
easily be visualized. Frequency and angle integration are then conducted numeri-
ally. This generalized line shape results in about 50 % larger excited state
concentrations in the precursor.

Furthermore, even at low Mach numbers Stark broadening of the resonance
lines has to be included in the description of the radiative transfer through
the downstream plasma. At high Mach numbers, we then find that a large portion of
the effective emission originates from the relaxation zone as opposed to the
equilibrium region behind the shock front. Clearly, a black-body-emitter model
gives very inaccurate results in this situation, too.

A rough surface model[9] (mean surface roughness small compared to vacuum
ultraviolet wavelengths) accounts for angle-dependent reflection on the shock
tube walls, giving rise to much higher rates of excitation (than without reflec-
tion) far ahead of the shock front. Close to the shock front, the influence of
reflection becomes negligible.

The concept of a generalized line shape also has strong consequences on the
resonance line radiation escape in the precursor[9]. As an example, the ratio of
the calculated escape factor for the generalized line shape θ_G (n_0, R) to the
Lorentzian value θ_L (R) is plotted in fig. 2 against $n_0^2 \cdot R$ (n_0: ground state
density, R: (shock) tube radius), assuming a homogeneous excited state distribu-
tion. For the values of $n_0^2 \cdot R$ considered in this work, θ_G varies by a factor
of two in respect to the Lorentzian result.

There are important ramifications in cases, where the density dependence of
resonance state decay is interpreted as arising from specific collisional pro-
cesses. For example, from our results the coefficient of excitation exchange
between metastable and resonant states follows to be considerably lower than
previously assumed[20,21]. This is in accordance with measured[7] and calculated[9]
metastable concentrations in the precursor and with other investigations[22].

4. RESULTS AND DISCUSSION

Computations of particle density profiles are conducted for a given loca-
tion of measurement, thus allowing for direct comparison to experimental
results.

Our calculations show that all the effects and refinements discussed above
are of great importance in computing precursor particle densities, namely: the
unsteadiness of the shock wave, the boundary layers and radiative cooling in the
downstream flow, the finite extension of radiative emission, the angle-dependent
reflection of resonance line radiation, a non-Lorentzian line shape, Stark
broadening, and a detailed model of reaction kinetics.

The computed density profiles are in good agreement with absorption meas-
urements of the first four excited states by T. Hammer[7] (Mach number 11 to 13),
generally lying within the experimental error (i.e. 10 to 20 % for the resonance
states close to the shock front in Kr, see fig. 3). In xenon, there are some
indications of non-resonant line absorption. This effect has to be subject to
further study.

The calculations are also compared to absorption measurements of the first
two excited states in krypton at higher Mach numbers (17 to 21) done by W.

Bötticher and D. Kilpin[8]. The time constants of the excited state concentrations in front of the shock as well as the absolute values of the metastable densities are in excellent agreement, whereas the calculated resonance state profiles are about a factor of three higher than the measured values (fig. 4). No explanation has been found so far for this deviation, since ordinary reaction mechanisms cannot account for such a difference with respect to the metastables.

In xenon, measurements of electron density profiles in the precursor[5,6] are available for comparison (fig. 5). An excellent agreement results if the angle-dependent reflection of resonant line radiation is accounted for. Here chemo-ionization has been neglected, since no reliable rate coefficients for xenon are known to the author.

This work was supported by the Deutsche Forschungsgemeinschaft.

REFERENCES

1. L. M. Biberman, B. A. Veklenko, Radiative processes ahead of a shock-wave front, Soviet Physics JETP 37, 117-120, 1960.

2. R. A. Dobbins, Precursor photoexcitation and photoionization of argon in shock tubes, AIAA Journal 8, 407-414, 1970

3. M. Pinègre, P. Valentin, Precursor phenomena ahead of a shock wave in argon, in: Shock Tube and Shock Wave Research, Proc. 11th Int. Symposium on Shock Tubes and Waves, 186-192, Seattle, 1977.

4. M. G. Vasil'ev, T. V. Zhikhareva, G. K. Tumakaev, Elementary processes in front of a xenon shock, Sov. Phys. Tech. Phys. 24, 311-318, 1979.

5. M. G. Vasil'ev, T. V. Zhikhareva, G. K. Tumakaev, The relative contribution of associative ionization and photoionization in xenon precursors, Journal De Physique 40, C7 101-102, 1979.

6. T. V. Zhikhareva, D. G. Zavarin, G. K. Tumakaev, Experimental study of shock wave precursors in an inert gas plasma, Sov. Phys. Tech. Phys. 29, 284-289, 1984.

7. T. Hammer, Messung von Precursoreffekten bei Edelgasstoßwellen, Diplomarbeit Universität Hannover, 1984, and personal communication.

8. W. Bötticher, D. Kilpin, Excitation ahead of shock fronts in krypton measured by single line laser absorption, Experiments in Fluids 2, 177-181, 1984.

9. D. Krause-Varban, Strahlungstransport in Edelgasstoßwellen und die Modellbeschreibung von Anregung und Ionisation im Precursor, Dissertation Universität Hannover, 1985.

10. D. Krause-Varban, F. Demmig, Model calculations of the ionization relaxation and radiative cooling in unsteady krypton and xenon shock waves, J. Fluid Mech. 149, 375-383, 1984.

11. D. Krause-Varban, Ionisationsrelaxation in schwach instationären Kryptonstoßwellen unter Berücksichtigung von Strahlungskühlung, Diplomarbeit Universität Hannover, 1981.

12. N. Sadeghi, J. Sabbagh, Collisional transfer between the $6s'[1/2]_{0,1}$ and $6p[1/2]_1$ xenon levels, Phys. Rev. A 16, 2336-2345, 1977.

13. T. Steihaug, A. Wolfbrandt, An attempt to avoid exact Jacobian and non-linear equations in the numerical solution of stiff differential equations, Mathematics of Computation 33, 521-534, 1979.

14. R. E. Scraton, Some L-stable methods for stiff differential equations, Int. J. Computer Maths 9, 81-87, 1981.

15. D. Hofsäß, Photoionization cross sections calculated by the scaled Thomas-Fermi method ($h\nu \leq 50$ eV), Atomic Data and Nuclear Data Tables 24, 285-321, 1979, and personal communication.

16. W. Behmenburg, Line Shapes, Progress in Atomic Spectroscopy Part B, eds. W. Hanle, H. Kleinpoppen, Plenum Press, New York etc., 1978.

17. J. A. Barker, M. L. Klein, M. V. Bobetic, Lattice dynamics with three-body forces: Solid Xe and Kr, IBM J. Res. Develop. 20, 222-227, 1976.

18. P. Laporte, H. Damany, High density self-broadening of the first xenon and krypton resonance line, Journal De Physique 40, 9-22, 1979.

19. M. C. Castex, Experimental determination of the lowest excited Xe_2 molecular states from VUV absorption spectra, J. Chem. Phys. 74, 759-771, 1981.

20. R. Turner, Decay of excited species in a pulsed discharge in krypton, Phys. Rev. 158, 121-129, 1967.

21. W. Wieme, M. Vanmarcke, W. Bruynooghe, Radiative and collisional desexcitation of $^1P_1$ and $^3P_1$ resonance states in xenon, Journal de Physique 40, C7 3-4, 1979.

22. R. Brodman, G. Zimmerer, Vacuum-ultraviolet fluorescence under monochromatic excitation and collision processes in gaseous Kr and Xe, J. Phys. B 10, 3395-3408, 1977.

Table 1.

Collisional and radiative processes considered.

A_k: atoms in state (k), $(AA)^*$: excited molecules, $(AA)^+$: molecular ions, A^+: atomic ions, e: electrons, $h\nu$: photons.

No.	Reaction	Index-condition	Process
(1)	$A_0 + h\nu \rightleftharpoons A_i$	$i = 2,4,5,6$	resonant photoexcitation and deexcitation
(2)	$A_i \rightarrow A_k + h\nu$	$i = 5,6$ $k = 1...4$	non-resonant spontaneous emission
(3)	$A_0 + h\nu \rightarrow A^+ + e$	*	ground-state photoionization
(4)	$A_i + h\nu \rightarrow A^+ + e$	$i = 1...6$	excited-state photoionization
(5)	$A_i + A_0 \rightleftharpoons A_j + A_0$	$i = 1,3$ $j = i+1$	excitation exchange

Table 1. - continued

(6) $A_i + nA_o \rightarrow (AA)^* + (n-1)A_o$ $i = 1...4$ two and three-body excited mole-
       $(AA)^* \rightarrow 2A_o + h\nu$ $n = 1,2$ cule formation and spontaneous
                                                                                              decay

(7) $A_i + A_k \rightarrow A_o + A^+ + e$ $\begin{array}{l}i = 1...4\\k = 1...4\end{array}$ chemoionization

(8) $A_i + A_o \rightarrow A_k + A_o$ $\begin{array}{l}i = 5,6\\k = 1...4\end{array}$ collisional deexcitation by atoms

(9) $A_6 + A_o \rightarrow (AA)^+ + e$ %   associative ionization

(10) $(AA)^+ + e \rightarrow A_i + A_o$ $i = 1...5$ dissociative recombination

(11) $A^+ + 2A_o \rightarrow (AA)^+ + A_o$ %   ion conversion

(12) $A_i + e \leftrightarrow A_k + e$ $\begin{array}{l}i = 0...5\\i \leq k \leq 6\end{array}$ collisional excitation and deexcitation by electrons

(13) $A_i + e \leftrightarrow A^+ + 2e$ $i = 1...6$ collisional ionization and recombination by electrons
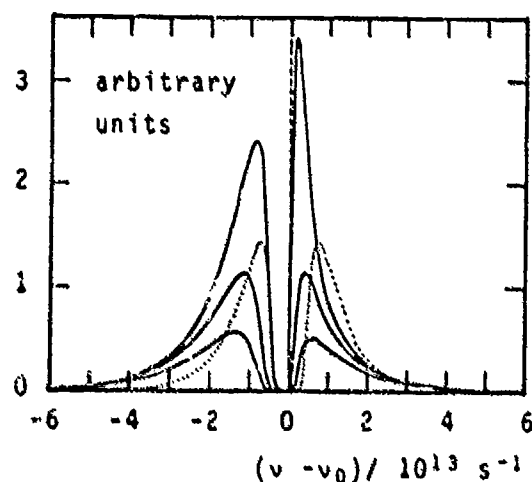
Fig. 1.

Spectral excitation per solid angle for rays along axis of shock tube. $5s[3/2]_1$ in krypton. Mach number 11.4 at $t = 0$, attenuation coefficient 2.4 % / m, preshock pressure 10 torr. Curves correspond to times $t = 0$, 500 and 1000 us (from top to bottom) before passage of shock front at a fixed location.
···· for Lorentzian case, $t = 0$ us.
ν_0: frequency at line center.
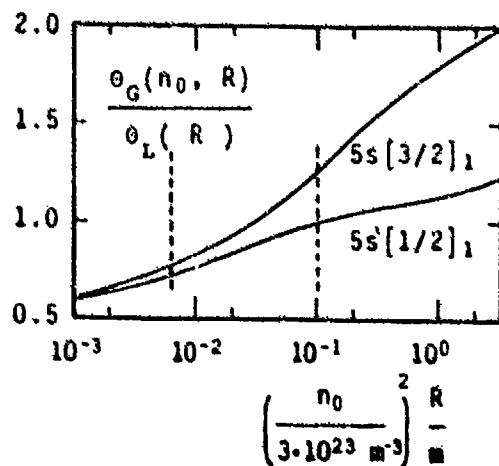
Fig. 2.

Ratio of escape factor for generalized line shape $\Theta_G (n_o, R)$ to Lorentzian values $\Theta_L (R)$ against function of ground-state density n_o and tube radius R.
First two resonance states in krypton at 300 K.
---- variation of $u_o^2 \cdot R$ considered in this work.

Fig. 3-5. Excited-state and electron density profiles in the precursor.

M : Mach number,
po : preshock pressure.

Fig. 3 krypton
M = 12.3 (t = 0)
p_0 = 5 torr

$\frac{n_i}{m^{-3}}$

$5s[3/2]_1$

$5s'[1/2]_1$

t/ μs

Fig. 4 krypton
M = 17.0
p_0 = 20 torr

$\frac{n_i}{m^{-3}}$

t/ μs

Fig. 5 xenon
p_0 = 5 torr
R = 5 cm

$\frac{n_e}{m^{-3}}$

M = 20.4

M = 19.5

x/ R
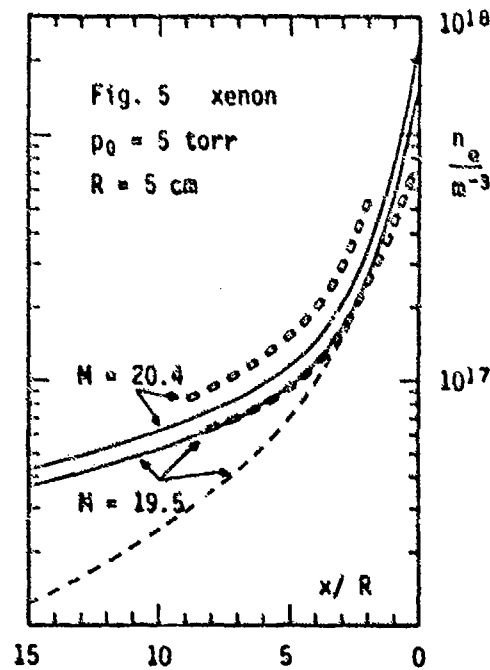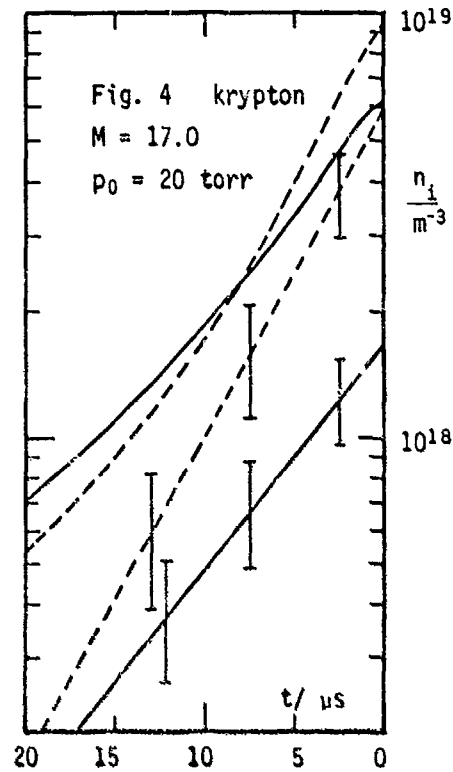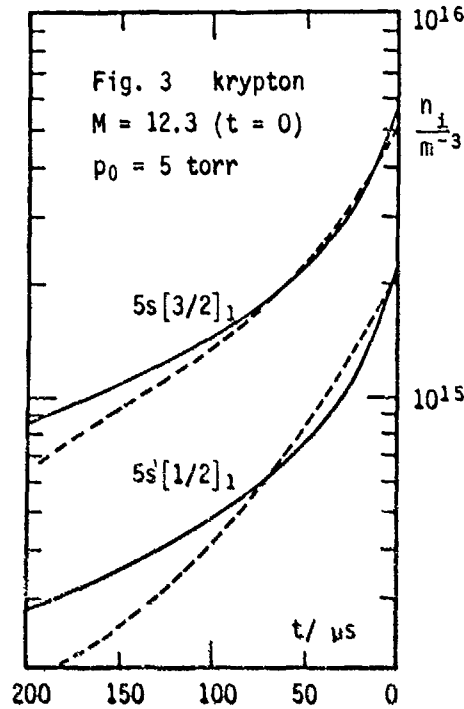
Fig. 3.

---- experiment, ——— calculated,
attenuation coefficient 2.1 % / m.
t : time until shock passes location
     of measurement.

Fig. 4.

lowest excited metastable (----)
and resonant (———) states in Kr.
Bars : error of measured profiles.
Without bars : calculated profiles.
t as in fig. 3.

Fig. 5.

electron density profile in Xe.
x : distance to shock front,
R : radius of shock tube.
==== experiment (taken from fig. 2
of ref. 5). ---- calculated,
---- without reflection of resonance
radiation.

APPLICATION OF THE GENERALIZED RIEMANN PROBLEM METHOD FOR 1-D COMPRESSIBLE FLOW WITH MATERIAL INTERFACES[1]

M. Ben-Artzi[*] and A. Birman[**]

[*]Department of Mathematics and Lawrence Berkeley Laboratory
University of California
Berkeley, California 94720

[**]Department of Physics
Technion — Israel Institute of Technology
Haifa 32000, Israel

The Generalized Riemann Problem (GRP) method has been
developed recently as a high resolution second order numerical
scheme for the solution of time-dependent one-dimensional inviscid
compressible flows (with variable cross section). The paper
presents a brief outline of the method and its extension to the
multi-material case, followed by two examples: (a) the resolution
of a discontinuity in a planar shock-tube; (b) the complex wave
pattern following the explosion of a pressurized Helium sphere into
air.

The quasi-conservation form of the Euler equations for time-dependent inviscid, compressible flow through a duct of variable cross-section are given by

$$A(r)\frac{\partial}{\partial t}U + \frac{\partial}{\partial r}[A(r)F(U)] + A(r)\frac{\partial}{\partial r}G(U) = 0,$$

$$U = \begin{pmatrix} \rho \\ \rho u \\ \rho E \end{pmatrix}, \quad F(U) = \begin{pmatrix} \rho u \\ \rho u^2 + p \\ (\rho E + p)u \end{pmatrix}, \quad G(U) = \begin{pmatrix} 0 \\ p \\ 0 \end{pmatrix}, \tag{1}$$

where $E = e + \frac{1}{2}u^2$ is the total energy and an equation of state $p = p(e,\rho)$ is assumed.

The purpose of this paper is two-fold.

1) To present a novel approach to the time integration of (1), based on an *analytic higher order extension of Godunov's scheme* [1].

2) To demonstrate how this method can be extended to deal with *material interfaces*, and to give an application to the case of an exploding Helium sphere.

To outline the numerical method assume, as is customary, that the flow field is divided up into cells (where "cell i" extends between $r_{i-\frac{1}{2}}$ and $r_{i+\frac{1}{2}}$) and the variables are evaluated at discrete time intervals $t_n = n\Delta t$. We designate (Fig. 1) by Q_i^n the average value of the variable Q over cell i at time t_n. Similarly, $Q_{i+\frac{1}{2}}^{n+\frac{1}{2}}$ denotes the value of Q at $r_{i+\frac{1}{2}}$ averaged over the time interval (t_n, t_{n+1}). Generally speaking, an "upwind" quasi-conservative scheme for (1) is given by

$$U_i^{n+1} = U_i^n - \frac{\Delta t}{\Delta V_i}\left[A(r_{i+\frac{1}{2}})F(U_{i+\frac{1}{2}}^{n+\frac{1}{2}}) - A(r_{i-\frac{1}{2}})F(U_{i-\frac{1}{2}}^{n+\frac{1}{2}})\right]$$
$$- \frac{\Delta t}{\Delta r_i}\left[G(U_{i+\frac{1}{2}}^{n+\frac{1}{2}}) - G(U_{i-\frac{1}{2}}^{n+\frac{1}{2}})\right]. \tag{2}$$

$$\Delta r_i = r_{i+\frac{1}{2}} - r_{i-\frac{1}{2}}, \Delta V_i = \int\limits_{r_{i-\frac{1}{2}}}^{r_{i+\frac{1}{2}}} A(r)\,dr\,.$$

The classical first-order Godunov scheme [3] is based on the following interpretation of (2).

(a)   Variables are uniformly distributed in cells (with jump discontinuities at the cell boundaries $r_{i+\frac{1}{2}}$).

(b) $U_{i+\frac{1}{2}}^{n+\frac{1}{2}} = U_{i+\frac{1}{2}}^{n}$ is the value along $r = r_{i+\frac{1}{2}}$ of the shock-tube problem with initial states U_i^n, U_{i+1}^n for $r < r_{i+\frac{1}{2}}$, $r > r_{i+\frac{1}{2}}$ respectively. Recall that the solution to this problem is "self-similar", namely, it is constant along straight lines emanating from the discontinuity.

The present scheme is indeed a second order modification of Godunov's scheme. The basic starting point here is the assumption that flow variables are *linearly* distributed in cells (again with possible jumps at $r_{i+\frac{1}{2}}$). The scheme (2) is supplemented by

$$U_{i+\frac{1}{2}}^{n+\frac{1}{2}} = U_{i+\frac{1}{2}}^{n} + \frac{\Delta t}{2} \cdot \left(\frac{\partial U}{\partial t}\right)_{i+\frac{1}{2}}^{n}. \tag{3}$$

As before, $U_{i+\frac{1}{2}}^{n}$ is obtained as a solution of a shock-tube problem involving the limiting values of flow variables at $r_{i+\frac{1}{2}}$. However, in order to evaluate $\left(\dfrac{\partial U}{\partial t}\right)_{i+\frac{1}{2}}^{n}$ one has to consider the initial gradients of these variables. This evaluation was done by an *analytic* method in [1] and constitutes the main building block of the GRP method. It is important to emphasize that the analytic solution provides the rate of change of variables along *any* direction emanating from the discontinuity. Thus, we were able to extend the scheme to multi-material flows. Most of the points in the numerical scheme are Eulerian (i.e., fixed with respect to laboratory coordinates), the only exceptions being the material interfaces themselves which are treated as Lagrangian points (i.e., moving with the fluid). We note that any adaptive mesh can be used with this scheme. In particular one could designate major shock trajectories as grid-lines etc. Furthermore, mesh distortion can be avoided by local cancellations and restorations of Eulerian points so that the case where a material interface is very close to an Eulerian point is excluded.

We give here the results of two numerical examples:

(a)   a shock-tube "test case" suggested by Sod [4]. The tube extends from $x = 0$ to $x = 100$ and is divided into 100 equal cells. The gas is initially at rest ($u = 0$) with $p = \rho = 1$ for $0 \le x < 50$ and $p = 0.1$, $\rho = 0.125$ for $50 < x \le 100$. Density and velocity profiles are given at $t = 15$, indicating the excellent resolution of both the contact discontinuity and the shock wave (Fig. 2).

(b)   Our second example involves the computation of flow profiles following the explosion of a pressurized Helium sphere into air. This case was taken from a paper by Glass and Saito [2], where calculations were done by the random choice method. Our results are similar to theirs, but much smoother in terms of the profiles in continuous regions of the flow. The exact initial conditions for the sphere are: Radius — 2.5 cm, Pressure — 18.25 atm, Density — 2.523 times that of the surrounding air.

At $t = 0.6$ (Fig. 3) one observes clearly the outgoing shock wave and the ingoing rarefaction wave. Note that due to the non-planar geometry the gas is "over-rarefied", the profiles are not monotonic, which leads to the formation of an inbound new shock. Indeed, this shock is clearly visible at $t = 1.8$ (Fig. 4), where it penetrates the inner zone of uniform low-density gas. In fact, the analytic solution for the GRP allows for reflections from the center of symmetry without difficulties.

REFERENCES

[1]   Ben-Artzi, M. and Falcovitz, J., "An Upwind Second-Order Scheme for Compressible Duct Flow", SIAM J. Sci. Stat. Comput. (in press).

[2]   Glass, I.I. and Saito, T., "Applications of Random Choice Method to Problems in Gas-dynamics", Progress in Aerospace Science, Vol. 21, 1984, p. 201.

[3]   Godunov, S.K., "A finite Difference Method for the Numerical Computation of Discontinuous Solutions of the Equations of Fluid Dynamics", Mat. Sbornik, Vol. 47, 1959, p. 271.

[4]   Sod, G.A., "A Survey of Several Finite Difference Methods for Systems of Non-Linear Hyperbolic Conservation Laws", J. Comp. Phys., Vol. 27, 1978, p. 1.
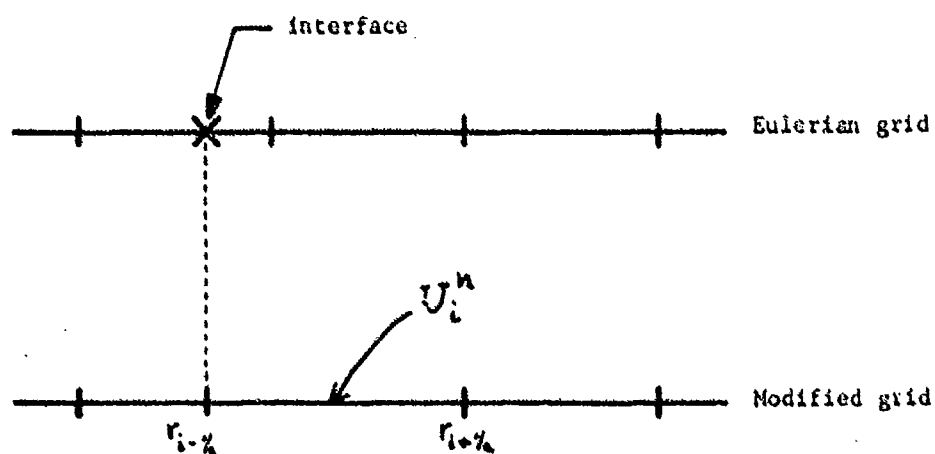
Fig. 1 Cell and grid scheme
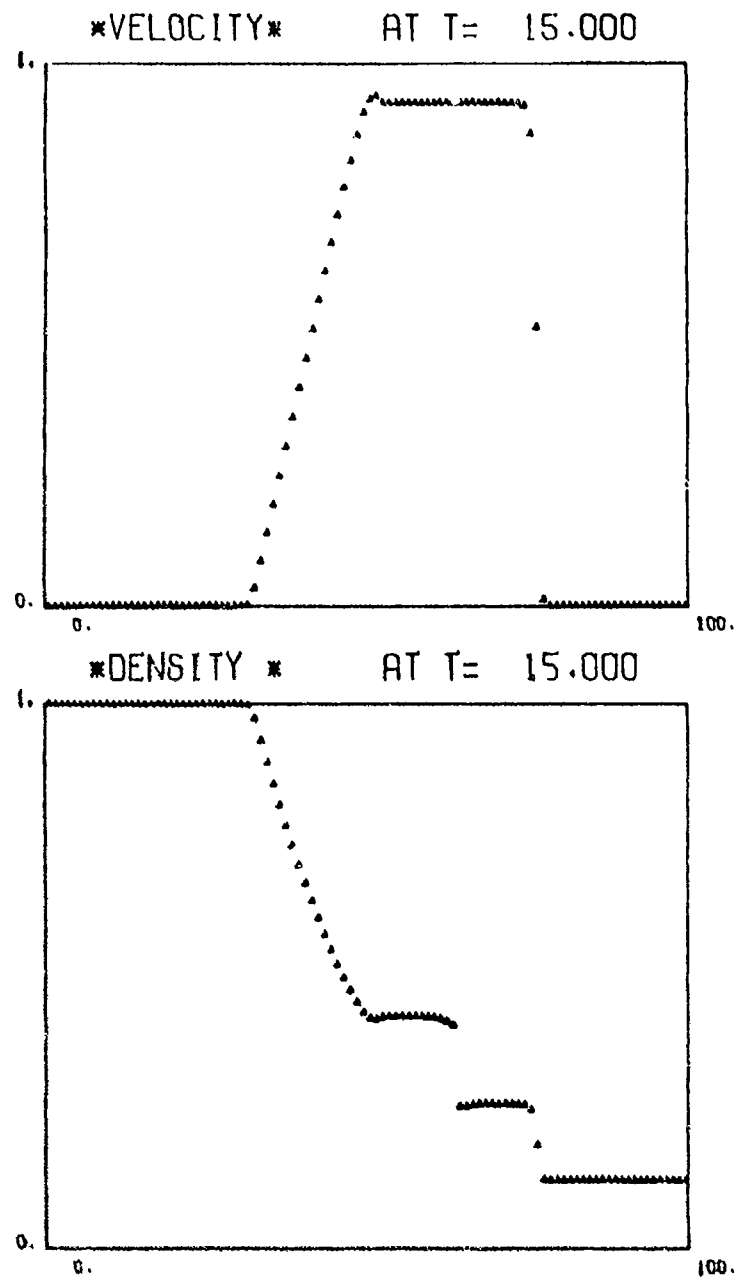
Fig. 2. Velocity and density profiles along the
shock tube at t = 15.000

VELOCITY AT T= .60000

DENSITY AT T= .60000
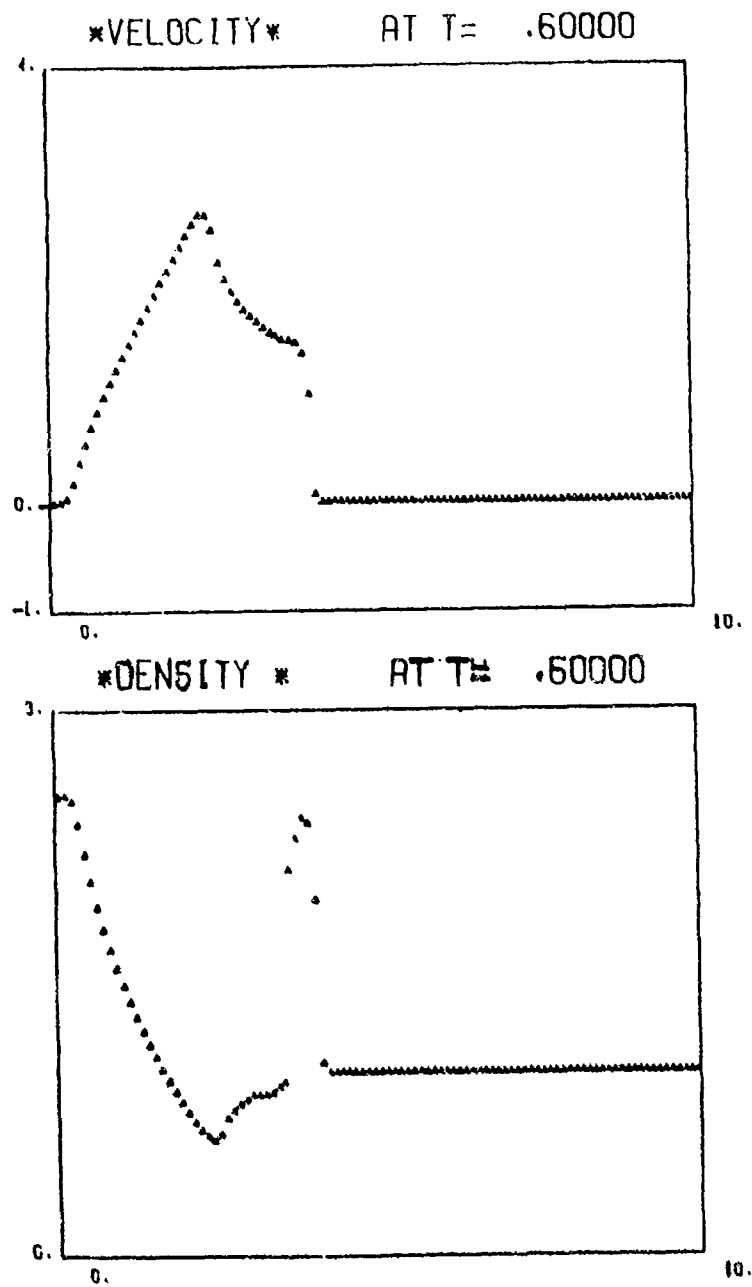
Fig. 3. Velocity and density profiles along the
shock tube at t = 0.600
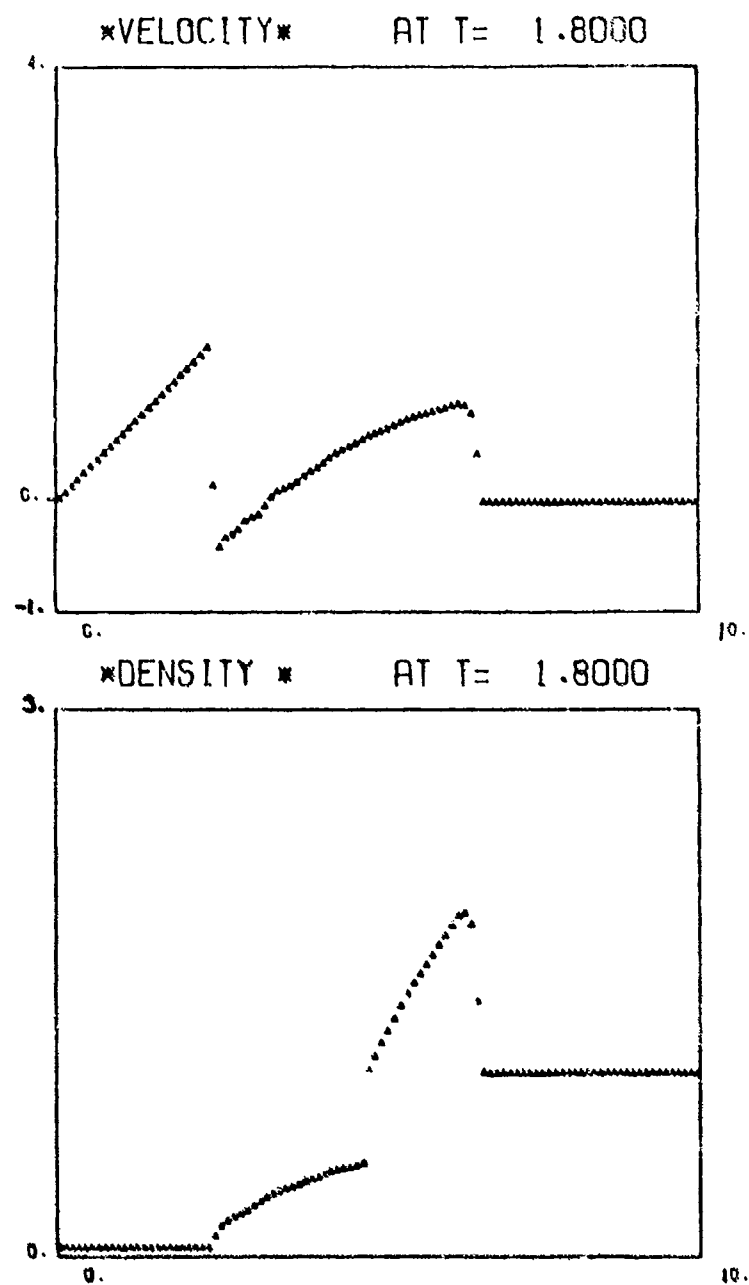
Fig. 4.   Velocity and density profiles along the
shock tube at   t = 1.800

TIME EVOLUTION OF THE RAREFACTION WAVE WITH ENTROPY INCREASE

MODIFIED TAUB-EQUATION FOR SHOCK EXPERIMENTS

R.W. Larenz and U. Steffens

Institute for Theoretical Physics
University of Duesseldorf, Duesseldorf, FRG

An exact analytical solution of the gasdynamic equations is
presented, which describes the time evolution of a gas expan-
sion process. This solution involves the well known homology
coordinate $z = x/t$ and furthermore an additional dependence on
the time t. The known rarefaction fan is obtained in a modi-
fied form and additionally a weak back running shock wave is
developed. This weak shock - delivering the entropy increase -
allows for fulfilment of all conservation laws and leads to the
disappearance of certain discrepancies which had to be noticed
hitherto. During the essential evolution time the analytic
solution is partly given by implicit relations; asymptotically,
however, one gets explicit expressions already given in 1977 at
the Seattle ISTS Conference. Application to the case of a shock
tube with a high pressure driving gas yields modified shock
Mach-numbers as compared to those of the Taub-equation.

1. INTRODUCTION

To start with a well known phenomenon, a so-called "N-wave" (Fig.1) shall
briefly be considered, this being a wave of finite amplitude which propagates
in a homogeneous gas, for instance generated as an idealized "sonic bang" Mach
wave of an aircraft flying at supersonic speed. As well known such a wave ex-
hibits a pressure bump at the front end, which propagates into the homogeneous
medium ahead of it with a velocity more or less markedly above the sound velo-
city depending on the strength of the bump, this bump forming a more or less
pronounced shock with a Mach number above 1. In reality there are two shocks
running one after the another in this one dimensional flow, so that the total
momentum of the wave is about zero, this being verified by the fact that the
medium will be at rest again after the passage of the N-wave. However, the sta-
te of the medium after the passage of the wave is not exactly the same as be-
fore: on account of the presence of shockfront: the temperature and the entropy
of the medium behind has increased, at least a little bit in principle, as com-
pared to the state before the passage.

Resuming these observations one has the following essential facts: A distur-
bance of finite amplitude propagates through a homogeneous medium with a velo-
city above the sound velocity beginning with a pressure rise as this is observed
with any acoustic signal, and the total momentum amounts to zero or maintains a
certain finite initial value if there is no further driving momentum source.

Now, if one goes down to vacuum density and zero pressure in the declining
after flow on dropping the second shock of the N-wave, evidently this resembles
nothing else than the expansion or rarefaction flow of a gaseous medium begin-
ning to expand from a homogeneous state in a half space at time $t = 0$. There
is a disturbance signal of finite amplitude running into the homogeneous medium,
because the rarefaction flow means naturally a quite strong disturbance of the

homogeneous state. However, it is clear that the pressure rise and the shock front running backwards into the homogeneous gas must develop or establish itself first within a certain time interval beginning at time t = 0, if before and at this time t = 0 the medium is assumed to be homogeneous throughout the whole half space.

2. FLOW EQUATIONS

From the foregoing reflections it will be evident, what has to be done, to describe the rarefaction flow in general as long as a gas dynamic concept shall be used. One has a flow pattern which is essentially given by a self similar or a so called homology solution of the gas dynamic equations as well known, but from the establishment time interval just mentioned, there has to be accounted for by an additional time dependence of the functions solving the rarefaction problem, often cited as "centered rarefaction". So introducing the two independent variables $z = x/t$ and t, the one dimensional flow equations are the following ones, if as dependent variables are chosen the flow velocty u, the local velocity of sound c (representing essentially the square root of the local gas temperature) and finally the entropy s per mole. Denoting by κ the polytropic coefficient and by R the gas constant one has with the usual notation of derivatives by a suffix t or z.

$$t \cdot c_t + (u-z)c_z + \frac{\kappa-1}{2} c u_z = 0 \qquad 1)$$

$$t \cdot u_t + (u-z)u_z + \frac{2}{\kappa-1} c c_z = \frac{c^2}{\kappa R} \cdot s_z \qquad 2)$$

$$t \cdot s_t + (u-z)s_z = 0 \qquad 3) \quad .$$

As well known these equations represent the mass, the momentum and the energy balance, if internal friction and heat conduction are neglected. In this case the local entropy s is given by that entropy gain the local mass unit under consideration has acquired at that earlier time when the back running shock front passed over it, or seen from the frame of the standing shock front, when the mass unit passed through the shock. The quantities pressure p and density ρ are related to the local velocity of sound c, the temperature T and the entropy s by

$$c^2 = \kappa p/\rho = \kappa RT, \qquad \frac{p}{p_0} = (\frac{\rho}{\rho_0})\exp(\frac{\kappa-1}{R}s) = (\frac{c}{c_0})^{\frac{2\kappa}{\kappa-1}}\exp(-s/R) \qquad 4) \quad ,$$

if the entropy in the homogeneous gas at rest is set to zero.

As border conditions one has the values c = 0, s = 0 resp. p = 0, ρ = 0 at the expansion head with the position $x_m = t \cdot z_m = t \cdot u_m$ on the one hand and the Rankine-Hugoniot equations at the instantaneous position of the back running shock front on the other hand, these equations being time dependent by means of a time dependent Mach number N(t) and the shock position being given by

$$x_M = t \cdot z_M = - c_0 \int_0^t N(\tau)d\tau \qquad 5).$$

3. ANALYTIC SOLUTION

Any entropy generation by internal friction is avoided if there is no curvature in the velocity of flow u(x)-pattern within the expansion fan, even in case one would allow for a friction term in the basic equations. This favorizes a linear u(x) or u(z) flow pattern for $z_M(t) < z < u_m = $ const.

$$u = u_m + \frac{2}{\kappa+1}(z-u_m), \qquad (u_t = 0) \qquad 6) \quad ,$$

which is adopted here in concordance with Burgers and Weizsäcker (see ref.[1]). Now, a relation among u, the local sound velocity c, the homology variable z and the entropy s shall be introduced by an "Ansatz":

$$c = (u-z) \cdot \sqrt{1 + \phi(s)} \qquad 7) \quad ,$$

where the function $\phi(s) \neq 0$ represents the modification which is effected by the entropy as compared to the well known characteristical equation

$$u-z = c \qquad (\text{or } (u-z)^2 = c^2 \text{ more generally})$$

in case of constant entropy. The two equations 6) and 7) then lead to the consequence, that the system of differential equations 1), 2), 3) has a uniform analytic solution, which can be written down in an implicit form if a intermediate variable y on solving eq. 3) is introduced by

$$y(z,t) = u_m + (z-u_m) \cdot (\frac{t}{t_o})^{\frac{\kappa-1}{\kappa+1}} \qquad 8)$$

leading to

$$1 + \phi(y) = \frac{2g(y)}{(u_m-y)^2} \int_y^{u_m} \frac{d\eta (u_m-\eta)}{g(\eta)} \qquad 9) \quad .$$

With equation 9) the system 1), 2), 3) is completely solved; the velocity of sound c can be expressed on using 6) and 7). The function $g(y)$ appearing in 9) is related to the time evolution of the shock Mach number M and it holds

$$s(z,t) = \frac{\kappa R}{\kappa-1} \ln g(y) \qquad 10)$$

Even in case there is no linear u(z)-pattern, the complete solution can be formulated in an implicit manner if the neglibility of entropy generation within the expansion fan is maintained. The essential point is, to make use of the Lagrangian formulation of flow equations instead of the Eulerian as given in 1), 2), 3), because under conditions of no entropy generation along the expansion fan, the Lagrangian formalism is very adequate to the conservation of entropy, fixed to that value a certain element of matter has gained when passing the time dependent shock front.

The time dependence of the shock Mach number M can be evaluated analytically by combination of one of the Rankine-Hugoniot equations

$$u(z_M) = u_M = -\frac{2}{\kappa+1} c_o (M-1/M) \qquad 11)$$

with eq. 6) at the instantaneous position z_M of the shock front given by eq. 5). This delivers a differential equation which easily can be integrated to

$$\frac{t(M)}{t_o} = M \cdot (\frac{M_\infty-1}{M_\infty-M})^{1+M_\infty^2} \cdot \exp(M_\infty(1-M)) \qquad 12) \quad ,$$

M_∞ being given by the maximum flow velocity u_m of the head of the expansion at $z_m = u_m$

$$M_\infty = \frac{2}{\kappa-1} \frac{c_o}{u_m} \qquad 13) \quad .$$

The Rankine-Hugoniot equation for the entropy gain

$$s(z_M) = s_M = \frac{\kappa \cdot R}{\kappa-1} \cdot \ln \left([1+\frac{2\kappa}{\kappa+1}(M^2-1)]^{1/\kappa} \cdot [\frac{(\kappa-1)M^2+2}{(\kappa+1)M^2}] \right) \qquad 14)$$

has to be equated to eq. 10) by inserting $z = z_M$ according eq. 5) and correspondingly $y = y_M$ according 8), z_M and y_M being pure time functions then. This defines the function g(y) and by generalization $y = y(z,t)$ again (eq.8) to any point in space and time within the expansion fan there is assigned the right entropy value. However, the evaluation of this implicit formalism should be handled by a computer. The Mach number M_∞ or the maximum flow velocity u_m (eq.13) is fixed by the total momentum balance or enthalpy balance (at any point of time).

The solution begins with $M = 1$ at a point of time t_o, which represents a first molecular collision time interval in a gas kinetic sense of course. This means that the evolution time of the shock is measured very plausibly in units of the gas kinetic collision time, which may have any prescribed value given by

the state of the homogeneous gas at time t = 0. (Mathematically the Mach number M may be considered as a transformed time scale itself for the problem as this can be seen from the foregoing derivation.)

With growing time the Mach number approaches the value $M_\infty = \sqrt{2}$ asymptotically, independent of the polytropic coefficient κ, the shock and the flow then becoming a stationary one, given by that homology solution which was presented already at the 1977 Seattle ISTS Conference[1]. The motivation of that latter solution was given by the postulate, that the global or integral balance equations should be fulfilled. This means in particular the conservation of the total enthalpy (including the kinetic flow energy). Furthermore the total momentum is conserved; there is no continous and unlimited production of total momentum as it seems to be with other treatments of the problem. (It can be shown that even the simple treatment of an collision-less expanding Knudsen gas offers two ways to evaluate the momentum mathematically by nonuniform convergence, one way delivering the known time increasing positive momentum share $I_+ = p_o \cdot t$, the other way delivering the total system momentum staying zero for all times as it is at t = 0 in conformity with known physical principles.)

A further essential point is the existence of a weak back running shock, which allows to meet two physical requirements, the first being that the acoustic signal propagating into the undisturbed medium begins with a pressure bump of finite amplitude as the disturbance itself is of finite intensity. The second requirement is that a gas expansion - particularly into a vacuum - constitutes an irreversible process, which must be accompanied by an entropy increase, this latter being delivered by the shock front.

The time evolution of the flow quantities is represented by Fig. 2 on choosing time points at 10^2, 10^4 and $10^6 \cdot t_o$, t_o being the molecular collision time as mentioned. The net result should yield the statement: "There is really no pure rarefaction wave in gas dynamics". However, meanwhile this sentence can be found in textbooks, often a few pages later on, a description of the rarefaction process can be found which seems to be in contradiction to the sentence. Only if there is a free stream velocity of the homogeneous gas with a particular velocity value directed towards the vacuum, an isentropic rarefaction can be obtained, as this is pointed out in[1].

4. APPLICATION

Naturally, as the back running shock with a Mach number of about 1.5 is a quite weak one, it might be difficult to observe it in real experiments, where often the pressure chamber is of little dimensions and where the reflection of the propagating disturbance takes place very soon at the rear wall of the chamber. But one consequence is the reduction of the peak velocities at the expansion head by a factor of the order $1/M_\infty$ as it was stated in[1] already. Such an reduction of the flow velocities should be expected at shock tube experiments too, where a low pressure test gas is driven by the expanding high pressure section. Assuming the establishment of the asymptotic stationary conditions one may arrange the description of this process now by writing down two sets of Rankine-Hugoniot equations, one for the forward progagating generally strong shock wave in the test gas and the other for the weak back running shock in the driver section. The situation is displayed by Fig. 3 and the balance equations then are delivering two coupled equations for both the Mach numbers involved and these two equations replace the well known Taub equation[2]. Designing by M_b the back running shock and by M_f the generally strong forward shock one gets

$$\frac{p_f}{p_b} \cdot \frac{\kappa_b+1}{\kappa_f+1} \cdot \frac{2\kappa_f M_f^2 - \kappa_f+1}{2\kappa_b M_b^2 - \kappa_b+1} = (\frac{\kappa_b+1}{(\kappa_b-1)M_b^2+2}(1 - \frac{c_f}{c_b} \cdot \frac{\kappa_b-1}{\kappa_f+1} M_b \cdot \frac{M_f^2-1}{M_f}))^{\frac{2\kappa_b}{\kappa_b-1}} \qquad 15)$$

and

$$\frac{2\kappa_f M_f^2 - \kappa_f + 1}{2\kappa_b M_b^2 - \kappa_b + 1} = \frac{2\kappa_f (M_f^2 - 1)}{(\kappa_b - 1)M_b^2 + 2} + \frac{p_b}{p_f} \cdot \frac{(\kappa_f + 1)\cdot(2 - M_b^2)}{(\kappa_b - 1)M_b^2 + 2} \qquad 16) \ ,$$

where the suffixes b and f denote the quantities referring to the high pressure (backward) and the low pressure (forward) side. The exact evaluation must be done numerically; examples of the evaluation are shown by Fig. 4. For strong forward shocks at large pressure ratios p_b/p_f a simple first approximation formula for the forward shock number M_f yields

$$M_f \simeq \frac{1}{\sqrt{2}} \cdot \frac{\kappa_f + 1}{\kappa_b - 1} \cdot \frac{c_b}{c_f} \qquad 17) \ ,$$

which holds particularly for large c_b/c_f ratios, the weak backward shock number M_b being near $\sqrt{2}$.

It may be that the reduction factors for the forward shock Mach number now result a little lower than observed by experiments, where one has generally values beneath the ideal Taub Mach number (the explanation for this mostly given by assuming wall friction and other losses). Accepting this new evaluation as a "lower limit Mach numbers" delivering one, a little bit higher observed values may be explained by the fact, that in real experiments the driver section is often very short - as stated in the beginning of this section already - , resulting in a driving amplification as soon as the back running shock is reflected from the rear wall of this section. A comparison with measurements taken from[3] is given in Fig. 5.

5. ADDITIONAL REMARK

As the back running shock is a weak one and therefore the entropy gain s as proportional to $(M-1)^3$ is not very important, one may try to integrate the basic equations analytically too even for s ≠ 0, but maintaining shock conditions at the back running disturbance of the rarefaction problem. This approximative integration indeed can be performed, using modified "Ansaetze" instead of eq. 8) and 9). An advantage might be seen in such a description, because there do not appear intrinsic implicit formulations to the same extent as with the exact integration.

RREFERENCES

1. Larenz, R.W. and Wenk, H., "Shock Phenomena Associated with Expansion Flows". Shock Tube and Shock Wave Research, Proc. of the 11th ISTS, Seattle 1977, Univ. of Wash. Press 1978, p. 179-185.
2. Taub, A.H. (1943), Quoted by Reynolds, G.T., in "A Preliminary Study of Plane Shock Waves formed by bursting Diaphragms in a Tube", OSRD Report 1519 (unpubl.) after Wright, J.K., "Shock Tubes", London, New York 1961, p. 39.
3. Greene, E.F. and Toennies, J.P., "Chemische Reaktionen in Stosswellen", Forschritte der Physikalischen Chemie, Vol. 3, Darmstadt 1959, Fig. 45 p. 86 and table 1 p. 89.

Fig. 1. a) "N-Wave" in a homogeneous medium.
b) Case of degeneration to a rarefaction flow.

u = flow velocity
c = local sound velocity

(c may stand qualitatively also for temperature, pressure or mass density)
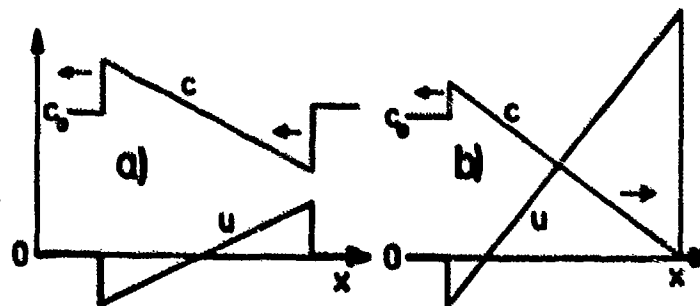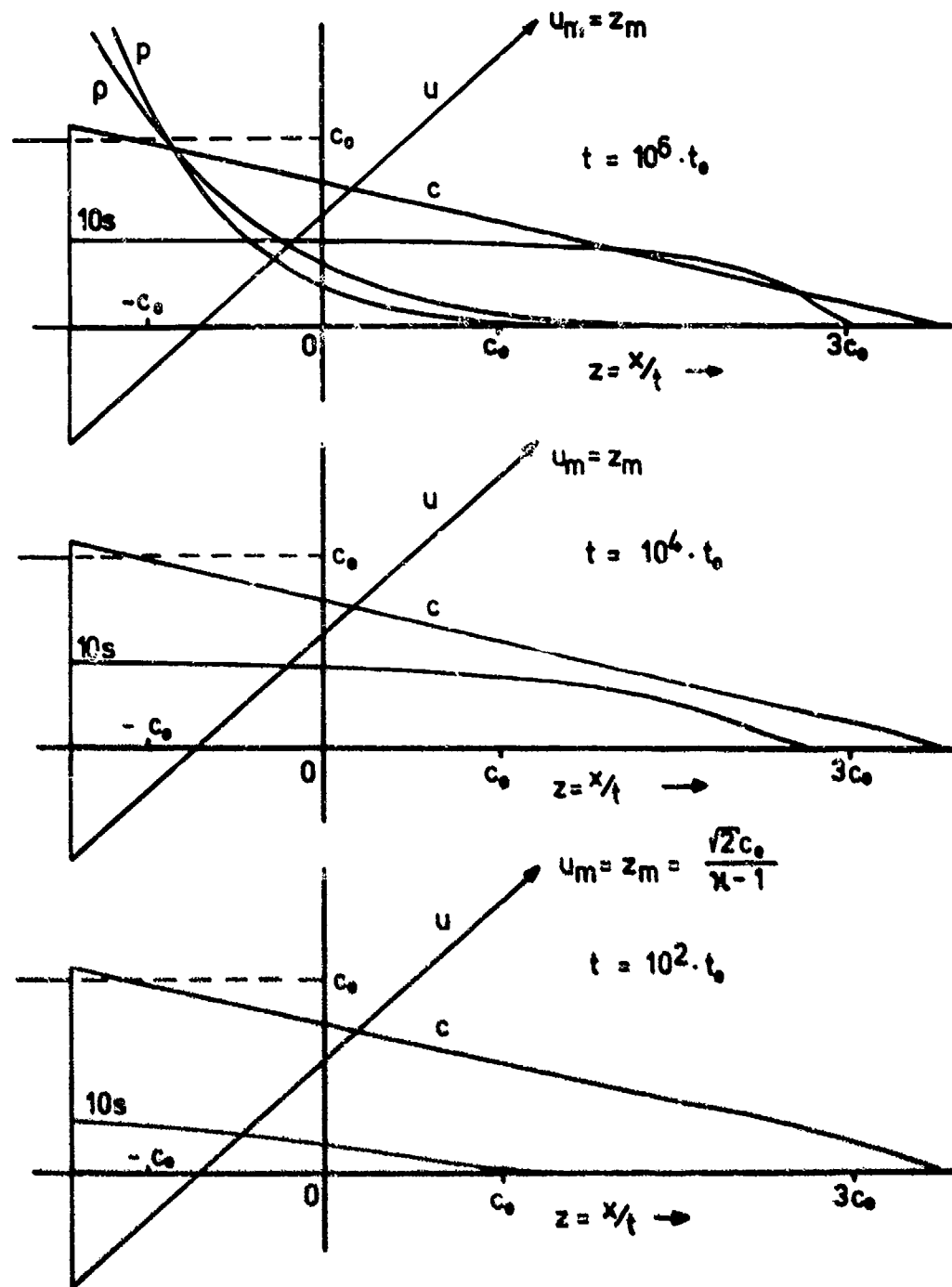
Fig. 2. Time evolution of the rarefaction displayed over the homology coordi-
nate $z = x/t$ for 3 points of time t at 10^2, 10^4 and $10^6 \cdot t_o$, t_o being the mean
molecular collision time interval. u = flow velocity, c = local sound velocity,
s = entropy, ρ = mass density, p = pressure (κ=7/5)
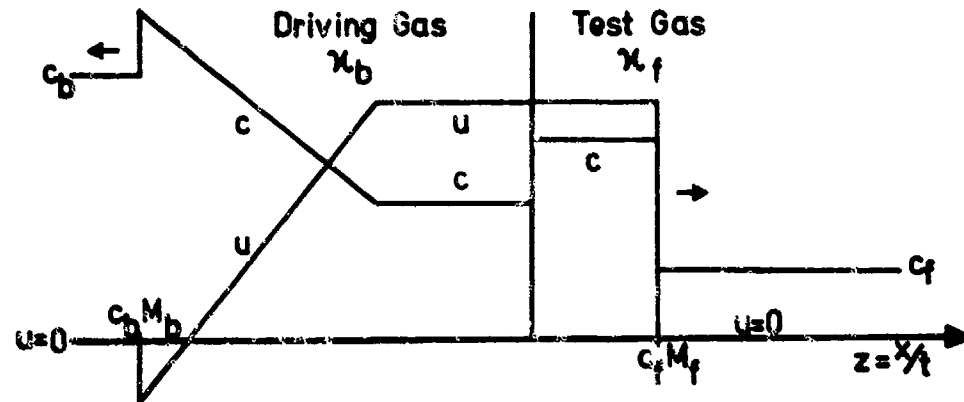
Fig. 3. Qualitative shock tube situation adapted to the presence of a weak back running shock according to this theory in the asymptotic case (time t large compared to the molecular collision time t_o) accounting for pressure equality at both sides of the contact surface in the usual manner.
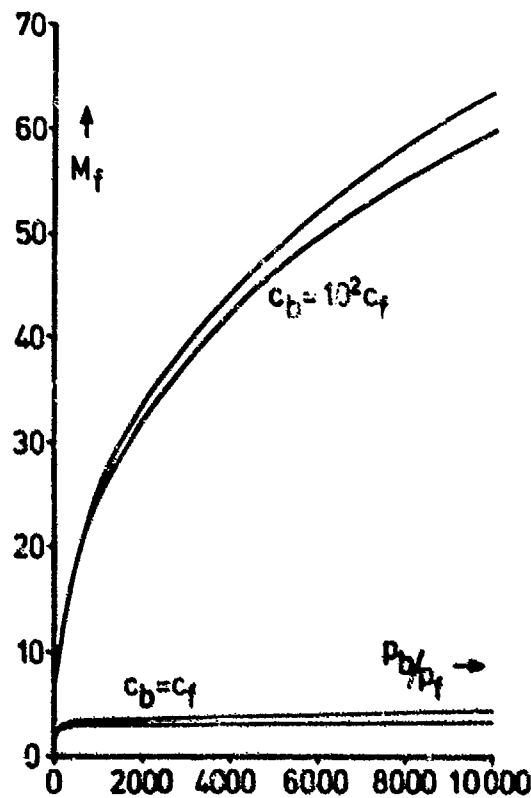
Fig. 4. Forward Mach number M_f from eq. 15), 16) for 2 cases: equal sound velocities of driving gas c_b and test gas c_f, resp. $c_b = 10^2 c_f$. Of the 2 pairs of curves the upper refers to the combination $\kappa_b = 7/5$, $\kappa_f = 5/3$, the lower to $\kappa_b = \kappa_f = 5/3$.
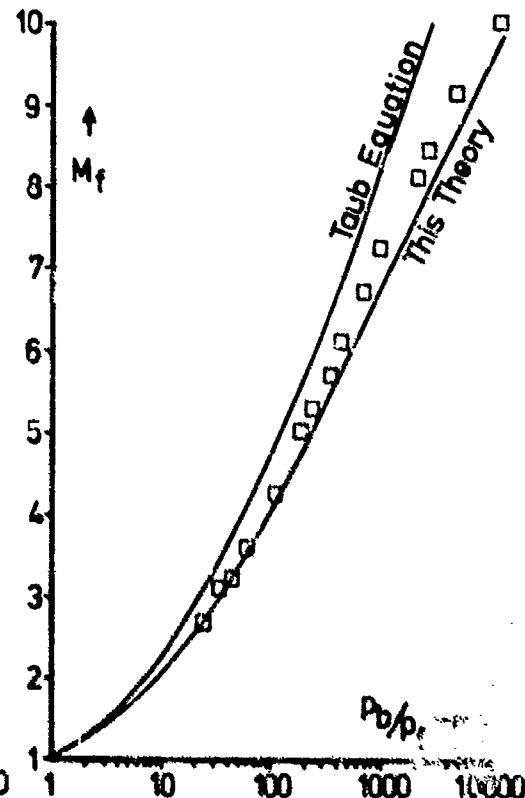
Fig. 5. Comparison with experimental results taken from[3] (quadrangels) and the theoretical Mach number M_f according to the Taub equation and the theory presented here referring to Argon as test gas ($\kappa_f = 5/3$) and hydrogen as driving gas ($\kappa_b = 7/5$).

TWO-DIMENSIONAL SHOCK FOCUSING AND DIFFRACTION IN AIR AND WATER

H. Olivier and H. Grönig
Stoßwellenlabor, RWTH Aachen, W. Germany

In the present paper the Random-Choice-Method is applied for
computing shock focusing and diffraction. This numerical me-
thod was developed by Glimm[1], Chorin[2] and Sod[3]. The two-
dimensional method is based on an operator splitting tech-
nique proposed by Chorin[2]. This method is used for the nu-
merical study of the shape of a diffracted shock wave in
air. The results which are compared with experiments by
Skews[4] are improved by an extension of the two-dimensional
method. This extension reduces the errors of the shock posi-
tion. A further application of the Random-Choice-Method is
the computation of shock focusing by concave reflectors.
First results of this problem were shown earlier[5]. A first
example shows the focusing of a plane shock wave in air by a
parabolic reflector. The agreement of experimentally and nu-
merically obtained pressure histories is quite satisfactory.
Underwater shock waves are computed by a simple transforma-
tion method, which allows to use all known equations for
shock waves in air. The validity of this transformation is
limited to pressures of less than 10 kbar. With this modi-
fied method for underwater shock waves the focusing of sphe-
rical shocks by elliptical reflectors is calculated. The re-
sults are compared with experimental ones.

1. INTRODUCTION

All numerical results which are shown in this paper are obtained by the
Random-Choice-Method (RCM). The RCM determines a new solution with the help of
an explicit wave solution. The explicit wave solution which is used in the RCM
is the well known Riemann problem. The final solution for a given grid point is
sampled by a random choice out of the solutions of the Riemann problem. Due to
this sampling in one space dimension no smoothing of discontinuities appears.
The advantages of the one-dimensional RCM in comparison with finite difference
methods are:
- Discontinuities as shock or contact surfaces are computed without numerical
  diffusion and dispersion.
- There are no numerical oscillations behind discontinuities.
- Boundary conditions are readily handled.

The disadvantages of the RCM in comparison with finite difference methods are:
- Due to the randomness the profile of a rarefaction wave is not computed
  smooth but on the average very close to the exact solution.
- The locations of discontinuities at any time are not exact, however, their
  average positions are.

An important building block in the RCM is the solution of the one-dimensional
Riemann problem. Since the analytical solution of the general two-dimensional
Riemann problem is unknown until now, the two-dimensional RCM is based on a
fractional step method proposed by Chorin[2]. This method works with the one-
dimensional RCM in alternating directions. Due to this splitting some advan-
tages of the one-dimensional method are lost. However, the results in this pa-
per show, that the two-dimensional method works well, if the Mach number of the
computed shock waves is not to high. Acceptable results for flows with high
Mach numbers can be obtained with the two-dimensional RCM, if a modified ver-

sion is used for the determination of the "passive velocities"[6]. This version works with averaging of the "passive velocities".

2. DIFFRACTION OF A PLANE WAVE AT A 90°-CORNER

The one-dimensional method is used in a fractional step method to compute the shock propagation in two space dimensions. This fractional step method was proposed by Chorin[2]. A detailed discussion of this method may be found in [6] and [7]. Figure 1a shows the pressure distribution in a channel with a 90°-branch. At the left end the pressure jump of the incident shock is seen. The incident shock runs from left to right. Figure 1b shows the pressure field after the shock has reached the branch. One sees the diffracted shock which propagates into the branch. In this example the Mach number of the incident shock is $M_o = 1.12$. In the next frame the diffracted shock has passed the opposite corner. A reflected shock propagates upstream. This reflected shock can be seen as a circular wave around the opposite corner. Because the area of the reflected shock increases continuously it is considerably attenuated.

(a)   (b)

(c)   (d)
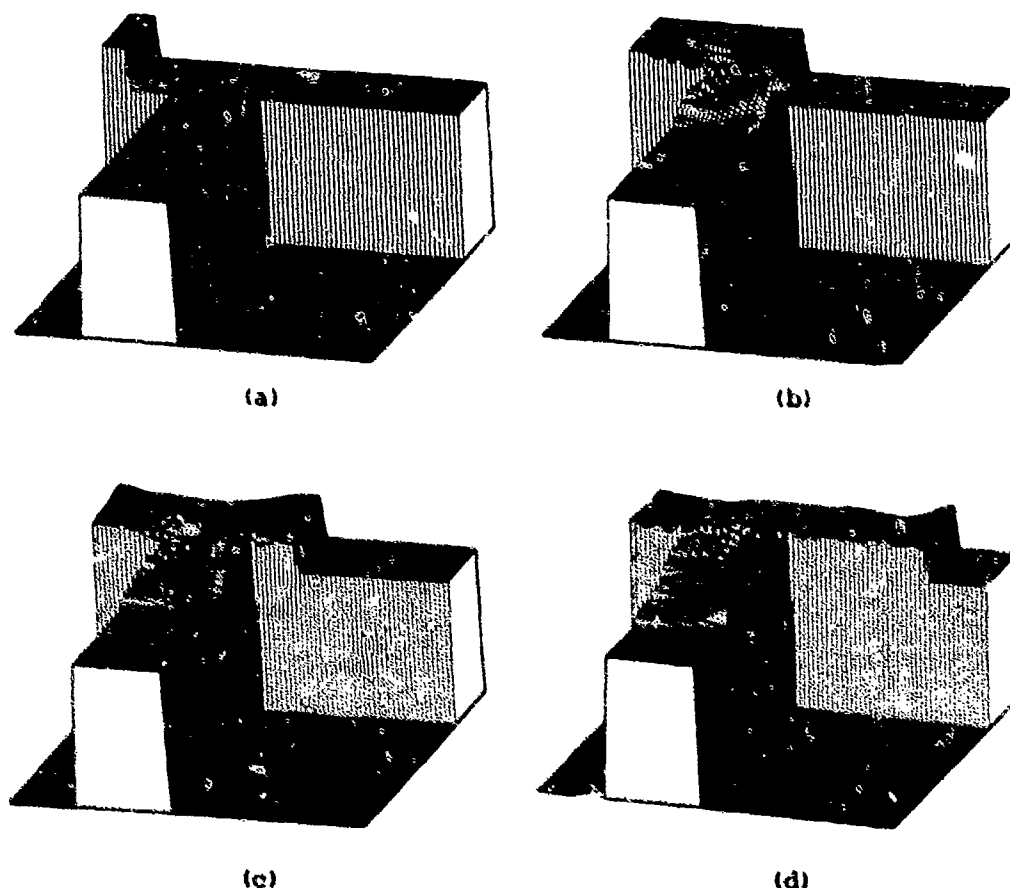
Fig. 1: Channel with a 90°-branch

In Fig. 1d one sees also that the diffracted shock is almost parallel to the cross section of the branch. In Fig. 2 for two different Mach numbers the diffracted pseudo-stationary shock wave position is compared with the experimental one found by Skews[4].

(a)   (b)
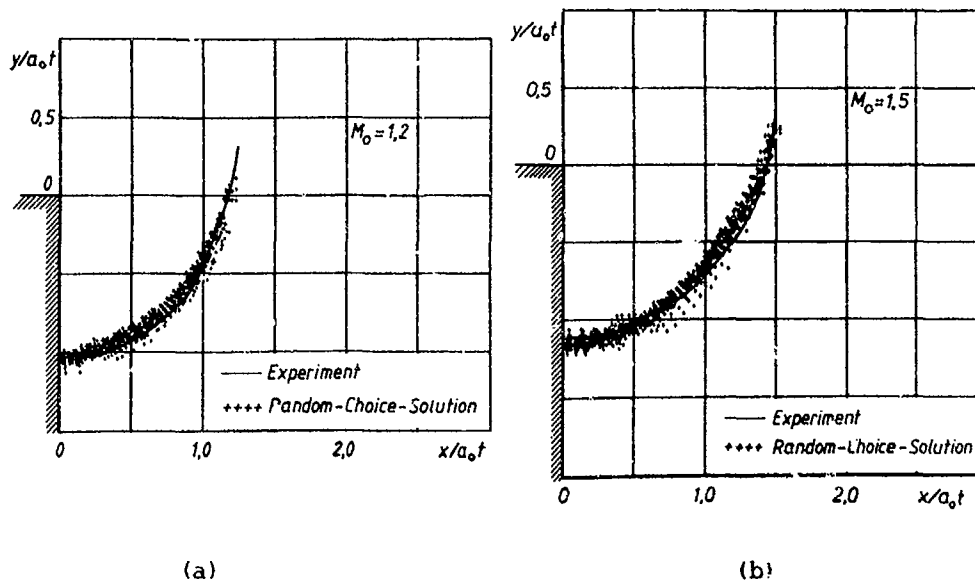
Fig. 2: Numerical and experimental pseudo-stationary shock wave position

The Figs. 2a and 2b show results obtained with the improved two-dimensional RCM. This method estimates the probabilities of the shock position after one time step and reduces the errors due to fluctuations of the shock position[6].

3. FOCUSING OF SHOCK WAVES IN AIR

In this chapter numerical and experimental results are compared, concerning the focusing of a plane wave by a parabolic reflector. The experiments have been carried out by Sturtevant and Kulkarny[8]. In order to compare the quality of the numerical results pressure histories are calculated for the same four locations close to the reflector as given in the paper of Sturtevant and Kulkarny [8] . For a detailed discussion concerning the influence of the number of grid points and the influence of the used random numbers on the solution see Olivier and Grönig[7]. Figure 3 shows one half pressure field of the reflected wave before, at the moment of and after focusing. The vertical line in Fig. 3 indicates the geometrical focus. The Mach number of the incident wave is $M_o = 1.1$.
One sees in the first picture of Fig. 3 , that the maximum pressure along the reflected shock is not reached at the axis of the reflector. The maximum pressure occurs outside the axis. During focusing this pressure mountain moves to the axis and reaches it at the moment of focusing. As seen in the second picture the gasdynamic focus is a short distance in front of the geometrical focus. This is predicted by the theory of nonlinear propagation of focusing shocks.

In Fig. 4 the calculated pressure histories are compared with the experimental ones of Sturtevant and Kulkarny[8]. One reason for the pressure fluctuations in the field behind the reflected shock is due to the stepwise approach of the reflector shape. Another reason is due to the errors arising from the operator splitting technique[6]. These fluctuations are also seen in the pressure histories as scattering. However, the average of the numerical results agrees very well with the experimental ones.
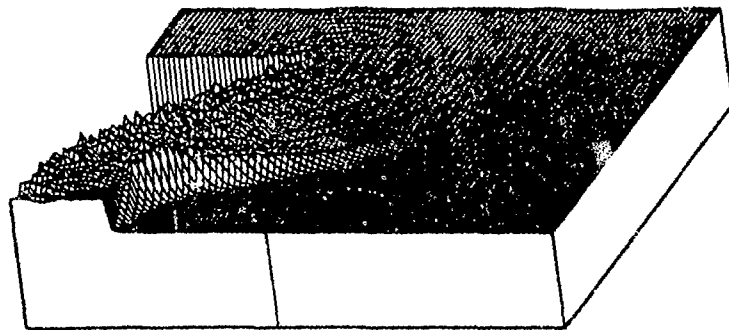
Fig. 3:
Pressure field before,
at and after focusing

Location 1

Location 2

Location 3   Location 4
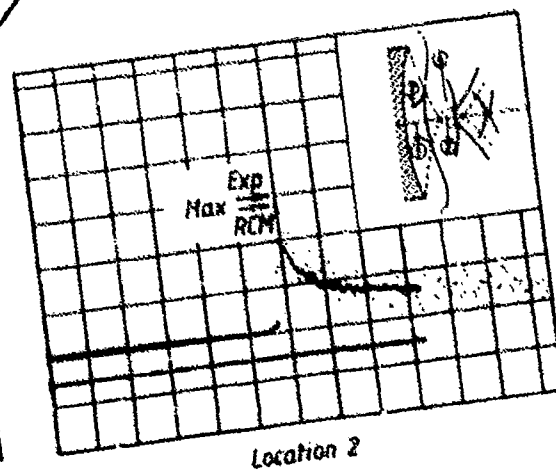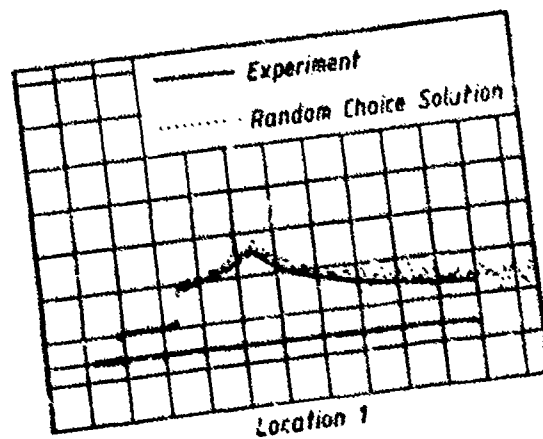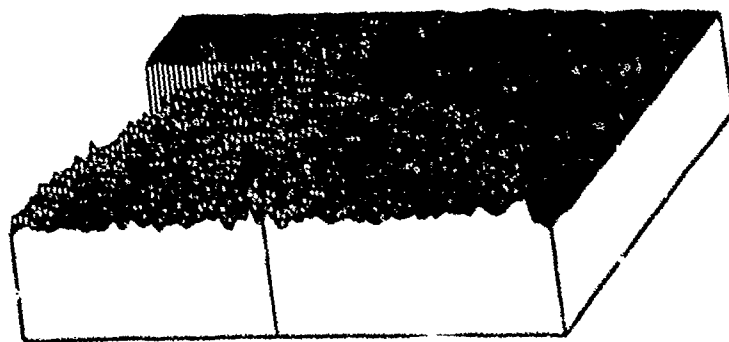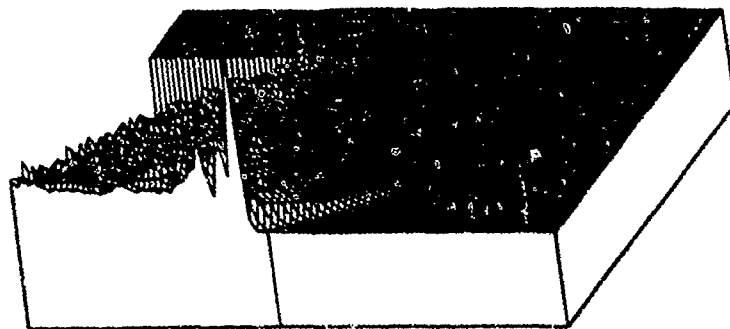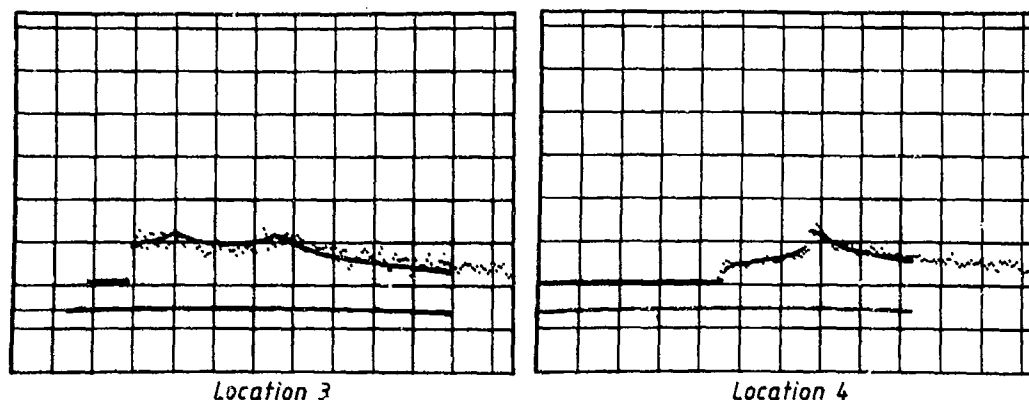
Fig. 4:   pressure histories, M_0 = 1.1
          Scales: 0.4 atm per div.; 0.05 ms per div.

4. FOCUSING OF SHOCK WAVES IN WATER

Holl[9] has shown, that shock waves in water can be computed with the same equations as shock waves in air, if the pressure p and the ratio of the specific heats are substituted by $p' = p + B$ and γ by n, where B ∿ 3000 bar and n ∿ 7.22. This simple transformation is valid up to pressures of 10 kbar. This transformation method was used to compute the focusing of spherical underwater shocks by elliptical reflectors. The extension of the two-dimensional RCM to two-dimensional rotationally symmetrical flow was made as proposed by Sod. Figs.5 and 7 show the principal arrangement. A spherical wave diverges from one focus point and reflects at the reflector. This reflected wave is focused at the other focus point . One sees that there are two main flow fields. For example in Fig. 5 the propagation of the spherical wave is symmetrical to the focus point F_1 , whereas the reflected wave is symmetrical to the axis of the reflector.

So throughout the computation a spherical and a cylindrical flow field has to be distinguished. This was done in the following way. The propagation of the spherical diverging shock was computed one-dimensionally along the axis. The obtained solution was turned around the focus point until the reflector shape was reached (see Fig. 5). At the left of this intersection point the solution is computed with cylindrical symmetry to the axis and at the right of this point as spherically symmetrical to the first focus point. Figure 6 shows the pressure field of one half of the symmetrical flow field for different moments of focusing.

The vertical line indicates the geometrical focus. The pressure jump of the incident wave is 200 bar. It was used an ellipsoidal reflector with a/b = 1.02. The maximum pressure is reached at the geometrical focus with p_{max} = 730 bar. Geometrical and gasdynamic focus coincide. That is expected, since the Mach number of the focusing shock is only M = 1.06.

In the next example the spherical wave diverges around the second focus point F_2 and reflects again at an ellipsoidal reflector (see Figs. 7 and 8).
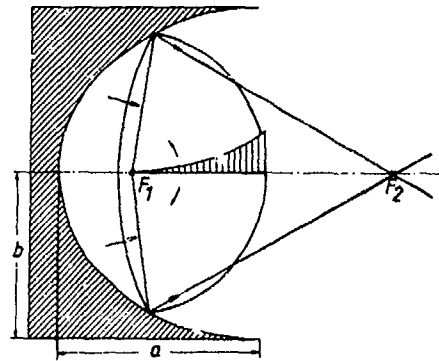
Fig. 5: Focusing of a spherical
wave at F_2
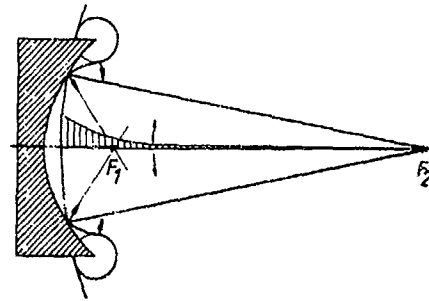
Fig. 7: Focusing of a spherical
wave at F_1
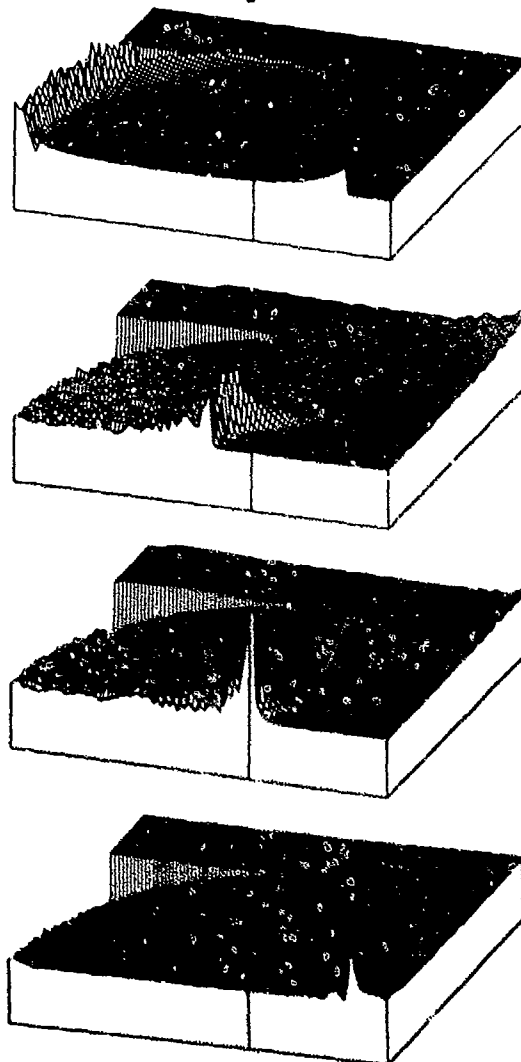
Fig. 6: Pressure field at several moments
of focusing at F_2
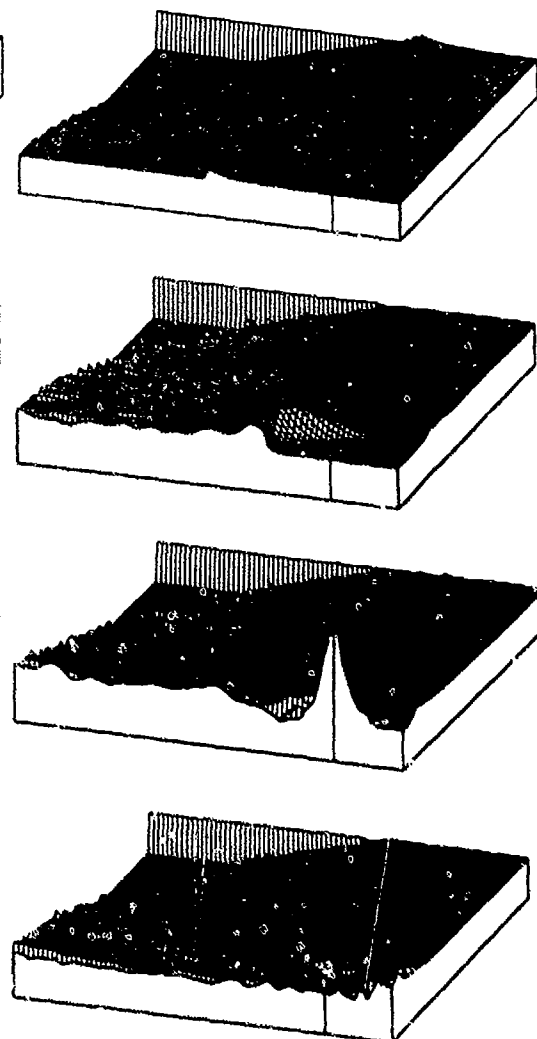
Fig. 8: Pressure field at several
moments of focusing at F_1

During reflection again a spherical and a cylindrical flow part must be distinguished. This is done in the same way as in the former example. Above the intersection between reflector shape and spherical wave the flow field is treated as cylindrically symmetrical. Below of this intersection point the flow field is spherically symmetrical. Figure 8 shows one half pressure field at several moments of focusing. The pressure jump of the incident wave is only 17. The reflector has a ratio of axis of a/b = 1.39. At the geometrical focus the maximum calculated pressure jump is 200. Figure 9 shows the comparison between measured and calculated pressure history at the geometrical focus. In the calculated pressure history after focusing a relative strong tensile stress occurs. In experiment the formation of this tensile stress is attenuated by the formation of gas bubbles. Computing focusing underwater shocks a large problem arises concerning the necessary grid size of the computing mesh. Since the sound speed of water is nearly 5 times larger than the sound speed of air all wave propagations in water are much faster than in air. Therefore one needs a much smaller grid size to resolve the wave propagation numerically. Due to the necessary small grid size and the limited central memory it was not possible to obtain quantitative agreement between experiment and numerical solution. However, the numerical solution shows a good qualitative agreement between computed underwater shock and experimental shock behaviour.

ACKNOWLEDGEMENTS

REFERENCES

1. Glimm, J., "Solution in the large for nonlinear hyperbolic systems of equations", Comm. Pure Appl. Math., Vol. 18, 1965, p. 697
2. Chorin, A.J., "Random choice solution of hyperbolic systems". J. Comp. Phys., Vol. 22, 1976, p. 517
3. Sod, G.A., "A numerical study of a converging cylindrical shock", J. Fluid Mech., Vol. 83, 1977, p. 795
4. Skews, B.W., "The shape of a diffracting shock wave ", J. Fluid Mech., Vol. 29, 1967, p. 297
5. Holl, R., Grönig, H., Olivier, H., "Focusing of weak blast waves", 14th International Symposium on Shock Tubes and Waves, 1983, p. 563
6. Olivier, H., "Zweidimensionale instationäre Stoßwellen. Anwendung der Random-Choice-Methode", Doctoral Thesis, RWTH Aachen 1985
7. Olivier, H., Grönig, H., "The Random Choice Method applied to two-dimensional shock focusing and diffraction", J. Comp. Phys., to be published
8. Sturtevant, B., Kulkarny, V.A., "Focusing of weak shock waves", J. Fluid Mech., Vol. 73, 1976, p. 7
9. Holl, R., "Wellenfokussierung in Fluiden", Doctoral Thesis, RWTH Aachen 1982.

Fig. 9: Experimental and numerical pressure history
Scales: hor. 5 µs/div
vert.(only valid for numerical pressure history) 20 bar/div

Part V
Shock Wave Aerodynamics

QUANTITATIVE STUDY OF SHOCK-GENERATED COMPRESSIBLE VORTEX FLOWS

M. Mandella, Y. J. Moon and D. Bershader*

Department of Aeronautics and Astronautics
Stanford University
Stanford, CA 94305

The method of pulsed holographic interferometry has
been applied to the study of the formation, transport
and interaction with a test surface of single two-
dimensional shock-generated vortices. Radial density
distributions have been determined, and preliminary
calculations of pressure and velocity distributions
have been obtained from the measured densities.
Strong density and pressure drops are found to occur
at the vortex center, verifying the serious transient
pressure loading which occurs when a vortex interacts
with an airfoil. There is also some indication that
these vortices have supersonic cores. Finite-difference
calculation of the density distribution shows a good
agreement with experiment. Preliminary studies of
interaction of vortices "hurled" at the leading edge
of a thin wedge show strong effects, featured by the
rapid growth of secondary vortices.

We report here some experimental and numerical results dealing with
the formation, transport and interaction with a test surface of two-
dimensional shock-generated vortices. The object is to determine in a
quantitative way the mutually interactive effects when a single well-defined
vortex interacts with a surface configuration - the effect on vortex
strength, trajectory, velocity, pressure and density distribution through
the vortex, and also the time history of the impulsive pressure loading
on an interacting surface. Motivation for this study stems from the need
to obtain a better understanding of the nature of blade-vortex interactions,
including sound generation, in the operation of rotary wing aircraft.[1]
The experimental studies were performed in the Stanford high-pressure shock
tube; related numerical calculations were performed by a finite difference
scheme applied to the Euler equation. The present work is part of an ongoing
study.

The first phase of the work deals with vortex formation by shock-wave
diffraction over obstacles or around corners, a well-known phenomenon which
has been observed in several laboratories and treated theoretically as
well.[2,3,4] In the present study a vortex trajectory control system was
developed, consisting of two sharp-edged vertically-positioned generating
wedges whose displacements from center line are independently variable
by micrometer adjustment. These are placed at the downstream end of the
constant-area low-pressure end of the tube. Vortices formed at the wedges
pass through into a larger 2-D section with acrylic windows, open to the
atmosphere (see Fig. 3). The control feature stems both from the adjustable

location of the edges and the degree of asymmetry in the positioning of the two wedges. For much of the present work, the edges were fully retracted to allow the production of symmetrical trailing edge vortices at the termination of the channel wall. More recently, the test section has been equipped with a center-plane splitter plate, on one side of which the desired interaction takes place. The other side then serves as a zero-interaction reference. Ability to describe the interaction in terms of variations with respect to the reference gives improved precision.

The principal experimental tool is double-pulsed laser holographic interferometry[5] with a Q-switched ruby laser as light source. A schematic of the optics is shown in Fig. 1, while Fig. 2 shows the timing arrangement. A signal from the shock wave sensor passes through an adjustable delay circuit which triggers the laser flashlamp as well as a second delay circuit for the Q-switch cell. The resulting "snapshot" interferogram represents a 10 nsec exposure, shorter than required to "freeze" the action. These image-plane holograms can be viewed in white light. Figure 3 shows typical pictures taken prior to insertion of the splitter plate. The timing notation T are in microseconds. As an example, Fig. 3(c) corresponds to 270 μsec after the estimated time of vortex formation. The diaphragm pressure ratio is controlled $\pm 3\%$ from shot to shot. The cross section of the shock tube exit is 5 cm. X 5 cm. The horizontal and vertical grid lines are spaced 1.00 cm so that the apparent vortex size is somewhat over 3 cm., a result of growth associated with convection and diffusion. The substantial radial density profile gives rise to about 15 fringes.

Analysis of fringe shifts has yielded density profiles as illustrated in Fig. 4. This is an axial distribution cutting through the vortex center. The Mach number of the generating shock was 1.36 while the flow Mach number was 0.47. The crosses represent the measurements while the continuous line is the output from a computer calculation described in later paragraphs. The scale is a normalized one, the horizontal portion of the profile on the far right representing atmospheric density. The jump starting at $X/R = 4.6$ represents the rightward moving generating shock which has been weakened by diffraction at the shock tube orifice. The strong density profile across the vortex is clear; the density drops by a factor of 3 at the vortex center. The asymmetry of the profile is due principally to the interaction of the vortex with its image across the flat end-face of the shock tube at $X/R = 0$. The 12% disagreement between experimental and computer results for the external flow has yet to be explained. Geometrical path of the vortex is indicated in Fig. 5. The trajectory makes an average angle of 40° with the x-axis.

Computation of comparable pressure and velocity profiles is, of course, less simple than in isentropic flow. However, it is possible to proceed from a point behind the incident shock which has suffered only small attenuation along the center line (note the uniformity of the density in that region) to a point just outside the vortex to obtain an estimate of "free stream" conditions. With this type of simplified modeling, radial pressure, velocity and Mach number profiles were determined. Also, the vortex strength in Fig. 3(c) was found to be 21.7 met^2/sec. The pressure decrease into the vortex is striking, reaching a value less than 30% of that at the outer edge. Velocity of gas flow relative to the trajectory of the vortex center reaches a value of nearly 500 met/sec. Coupled with the radial decrease in temperature toward vortex center, this means a significant increase in flow Mach number with decreasing radius, from an external value of about 0.6 to around 1.7 near the center. Mach 1.0 occurs at a radius of about

1.1 cm., leading to the concept of a sonic cylinder enclosing the supersonic region of the vortex. This hypothesis is intriguing but needs further experimental verification. In addition, we know that viscous effects become important very close to the vortex center, but such phenomena do not appear resolvable in the present study. In this connection, we note also that production of vorticity behind a curved shock is an inviscid phenomenon.

The compressible flow-field calculation already mentioned, including vortex formation and development, generated by the two-dimensional diffraction of a shock wave, has made use of a finite difference formulation. The Euler equation was solved by MacCormack's explicit scheme. The study treats the problem as inviscid and uses the perfect gas equation of state and constant specific heat. MacCormack's method is a second-order, noncentered predictor-corrector scheme. Two-dimensional Cartesian grids of constant size are used (61x61), which were varied to check the resolution. Initial conditions are given on both sides of the undiffracted shock while boundary conditions include those at the wall and at the plane of symmetry, the mirror image concept being used for the latter. These features are straightforward except for the boundary condition at the corner which is double-valued.

Experiments currently under way include extensions to vortex interactions with suitable aerodynamic surfaces appropriately positioned in the working section; and improved evaluation methods as required to account for the nonisentropic nature of the gas flow. In these studies, we make use of the "starting vortex", generated at, and then released from the trailing edge of an airfoil at about 30% angle of attack, following shock passage. Compared to vortices generated at the open end-face of the shock tube, discussed earlier, these are found to convect downstream at a faster rate, and they experience considerably smaller radial diffusion. These features make such vortices more suitable for interaction studies with downstream airfoil "targets".

Figure 6 includes a small sketch of the arrangement for studies of the interaction at the leading edge of a 4% half-wedge at a small angle of attack. The four pictures, taken at intervals of 50 µsec, show the incident vortex approaching the model, along with the growth of a relatively strong secondary vortex. The interaction slows down and weakens the incident vortex which mounts the upper side of the wedge while the secondary vortex lies below. Clearly, there are several parameters controlling the details of the behavior of these compressible vortices. Because of the large radial pressure gradients associated with these configurations as discussed earlier, the resultant transient pressure loading produces severe short-time fluctuations in lift coefficient. Present studies allow quantitative calculation of these important aerodynamic effects, and comparison with predictions of numerical computations. This work is continuing and further results will be presented in future publications.

REFERENCES

1. Johnson, W., Helicopter Theory, Princeton University Press, 1980, p. 962.

2. Howard, L.N. and Matthews, D.L., "On the Vortices Produced in Shock Diffraction", Journal Applied Physics, Vol. 27, No. 3, 1956, pp. 223-231.

3. Rott, N., "Diffractionof a Weak Shock with Vortex Generation", Journal

Fluid Mechanics, Vol. 1, Pt. 1, 1956, pp 111-128.

4. Evans, R.A. and Bloor, M.I.G., "The Starting Mechanism of Wave-Induced
    Flow Through a Sharp-Edged Orifice", Journal Fluid Mechanics, Vol. 82,
    Pt. 1, 1977, pp 115-128.

5. Vest, C.M., Holographic Interferometry, Wiley-Interscience, 1979, Chap. 5.
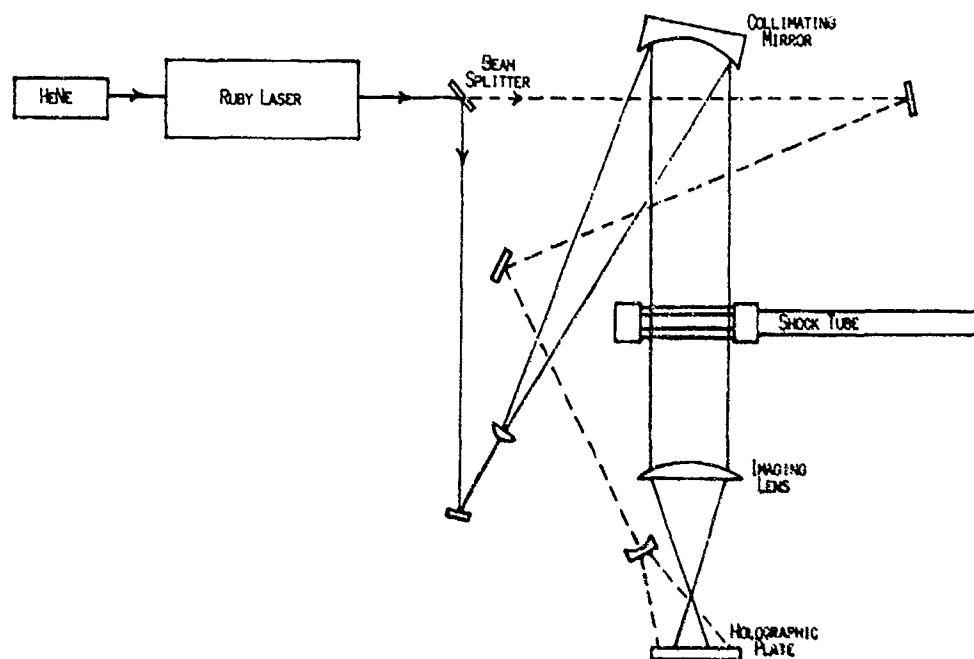
Fig. 1 Optical arrangement for pulsed laser interferometry of the vortex flows.
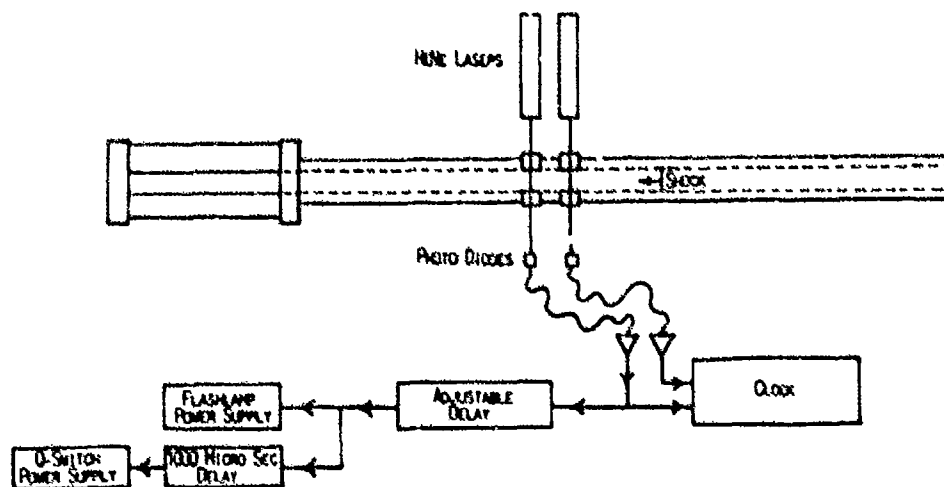
Fig. 2 Schematic flow diagram showing time synchronization for taking
holographic interferograms.

T=1600   P4/P1=6.3

T=1800   P4/P1=6.4

T=1700   P4/P1=6.5

T=1500   P4/P1=6.3
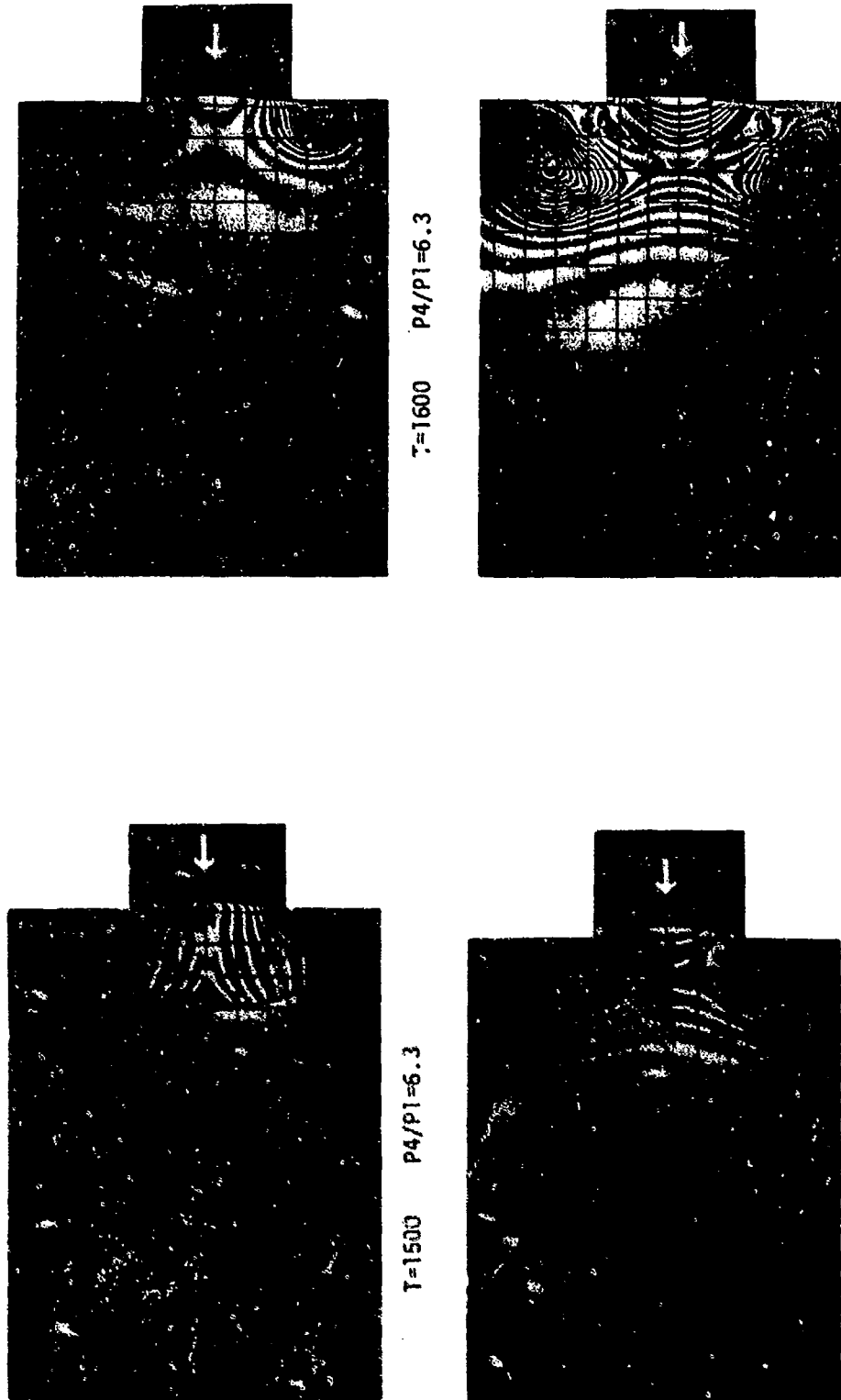
Fig. 3 Interferograms taken at 100 μsec intervals following shock diffraction at the open end of the tube. The grid spacing is 1.00 cm. Prior to diffraction, the shock strength used for these studies corresponds to a pressure ratio P_2/P_1=1.99, Mach number M_1=1.36 and stream velocity U=177 met/sec.

DENSITY PROFILE THROUGH THE CORE
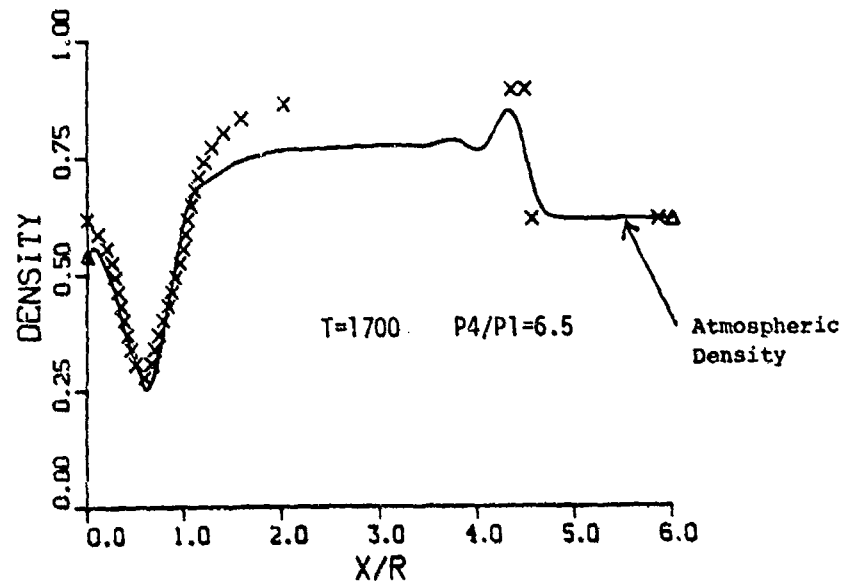
Fig 4. Axial density profile through center of vortex and across shock, corresponding to interferogram in Fig. 3(c). Density scale is non-dimensional.

VORTEX CORE TRAJECTORY
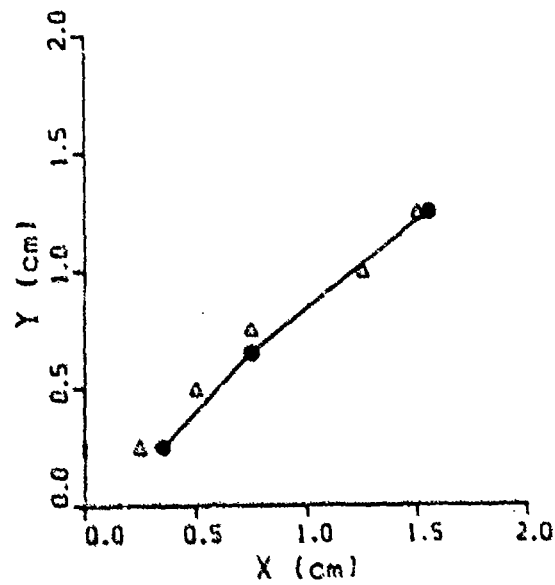
Fig. 5 Vortex core trajectory. Origin represents corner of downstream edge of shock tube.

P4/P1=38

T=1600

P4/P1=39

T=1700

θ=3.5°

φ=30°

L=6.7cm

Fig. 6

P4/P1=39

T=1550

P4/P1=39

T=1650
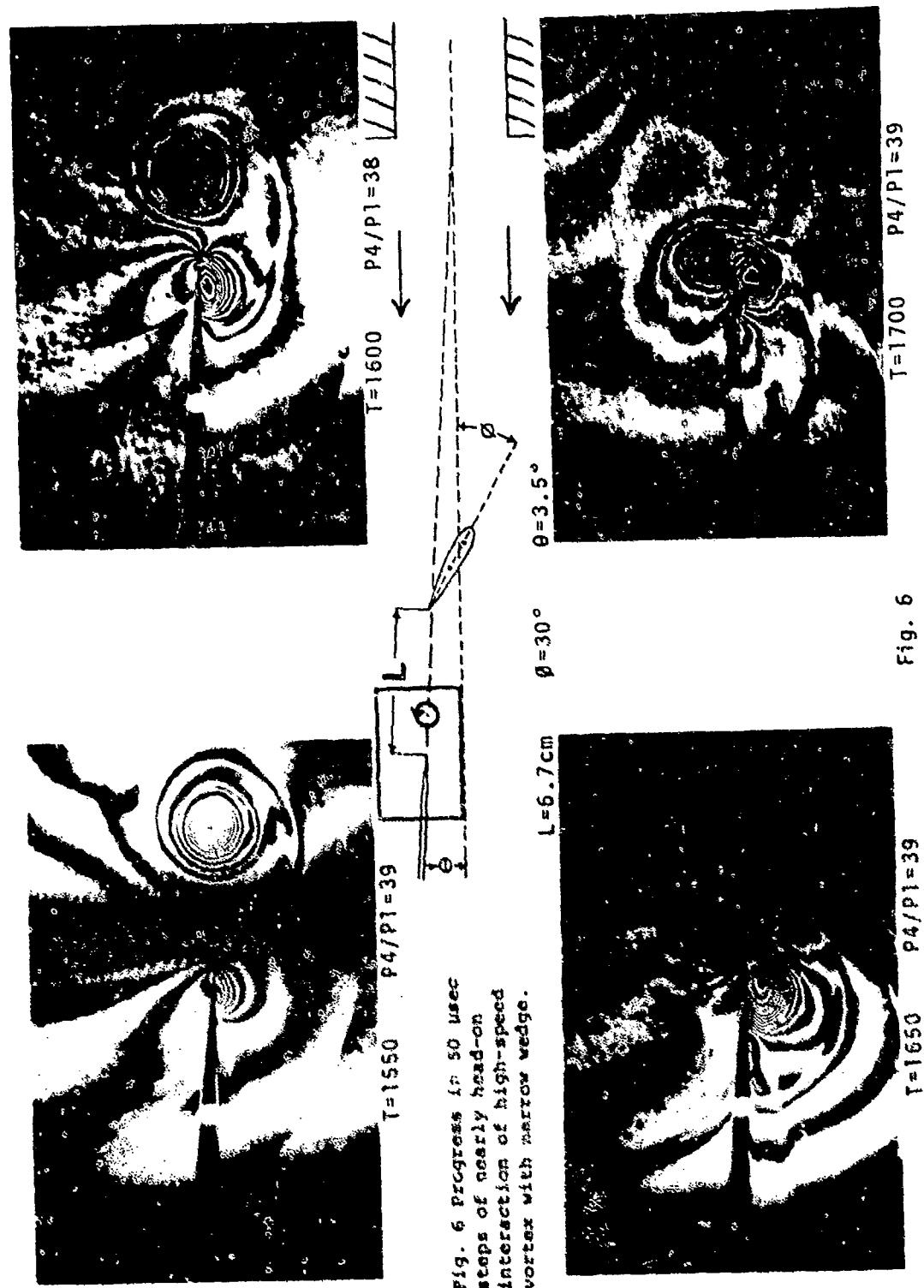
Fig. 6 Progress in 50 μsec
steps of nearly head-on
interaction of high-speed
vortex with narrow wedge.

UNSTEADY DRAG OVER CYLINDERS AND AEROFOILS

IN TRANSONIC SHOCK TUBE FLOWS

K. Takayama and K. Itoh

Institute of High Speed Mechanics
Tohoku University, Sendai, JAPAN

A shock tube can be used as an aerodynamic testing
facility. However, due to its short working
time the quantitative measurement such as pressure
distribution around a model installed in shock
tube is limited. The paper reports results of un-
steady drag measurement over a cylinder and an
NACA0012 aerofoil installed in a transonic shock
tube by using a pulsed laser holographic inter-
ferometry. The experimental results for the cylin-
der are compared with the PLM numerical simula-
tion, and a good agreement is obtained between
them.

1. INTRODUCTION

The purpose of this paper is to show an effectiveness of a shock tube
equipped with a double exposure holographic interferometry applied to a tran-
sonic wind tunnel.

In a shock tube, an uniform transonic flow exists behind the incident shock
wave [1]. Therefore, the shock tube has been used as a transonic wind tunnel
with variable Reynolds numbers, [2,3].

On the other hand, in the starting process of the transonic shock tube, the
interaction of planar shock wave passing over the obstacle placed in the shock
tube gives rise to the unsteady drag force to the obstacle. Heilig [4,5]
investigated the unsteady drag over a cylinder placed in the shock tube. He
measured the pressure distribution over the cylinder with pressure gauges.

Although the shock tube is a useful tool for transonic flow testing, its
short working time prevents from the quantitative flow measurement. Recently
in order to overcome this difficulty, a pulsed laser holographic interferometry
has been applied to the quantitative measurement of the transonic flow. The
interference fringes of holographic interferometry correspond to the isopycnics.
If the density distribution along the body was determined and the isentropic
flow was valid over the obstacle surface with the known stagnation condition,
the pressure distribution can be obtained within the accuracy of one fringe
shift distribution. Therefore, drag coefficient in terms of the uniform flow
condition is calculated. In this paper, the experimental results of unsteady
drag measurement around a cylinder or an NACA0012 aerofoil are described. For
the cylinder, the time variation of the drag coefficient was compared with the

PLM numerical simulation and a good agreement is obtained between them. The unsteady and steady aerofoil performances of an NACA0012 were examined and the result was compared with the previous wind tunnel testing.

2. EXPERIMENT

In Fig.1, the schematic diagram of the shock tube and the optical arrangement are shown. The transonic shock tube consists of a 1.5m long high pressure chamber and a 8.0m long low pressure channel of 60mm X 150mm cross section. The test gas was dried air at 1.03 - 101.3 kPa and the driver gas was helium at 0.1-2.0 MPa. Mylar films of 0.1 - 0.25mm thick were used as diaphragms. Shock speed was measured by two pressure transducers (Kistler 603A) placed 250mm apart ahead of the test section. Shock Mach number realized was 1.3 and 2.6 in the case of the 40mm diameter cylinder. For the aerofoil experiment the shock Mach number was from 1.7 to 2.3 which correspond to the uniform flow Mach number behind the shock wave was from 0.6 to 1.25 and to the Reynolds number to the airfoil chord length of 50mm was $0.7 - 1.6 \times 10^6$. These models were fitted into the grooves on the observation windows made of plastic glass.

The present optical system consists of a pair of schlieren parabolic mirrors of 300mm diameter and 3m focal length, the image lens system for the object beam, mirrors and lenses for the reference beam. As a light source, a pulsed ruby laser (Apollo Lasers Inc. 22HD) was used and for the reconstruction an Argon-Ion laser was used. The distortion of reconstructed images due to the difference between two wave lengths is negligible. In order to obtain an interferogram, two exposures are required. The first exposure is done before the event and the second exposure is triggered by the event. Consequently, the difference of the phase recorded on the hologram between these two exposures generate the interference fringes which correspond to the isopycnics in the two dimensional phenomena. Therefore, the interference fringe variation is defined in terms of the density variation as follows,

$$N = KL(\rho_1 - \rho_0)/\lambda \tag{1}$$

where N : the fringe number, K : Gladston-Dale constant, L : the width of the test section 60mm and λ : the wave length of the ruby laser 694.3nm.

3. RESULTS AND DISCUSSION

3.1 Cylinder

Figure 2(a),(b) show sequential infinite fringe interferograms of shock wave propagation over a cylinder for the incident shock Mach number Ms = 1.3 and 2.6, respectively. The corresponding Reynolds numbers are 0.7×10^6. The density distribution is determined from eq.(1). Assuming the isentropic flow condition over the cylinder surface with the given stagnation pressure which was determined from the reflected shock condition, the pressure distribution can be estimated. The whole processes were carried out by using a degitiser supported with a minicomputer.

In order to explain the experimental results, the PLM numerical simulation [6] of shock wave propagation over a cylinder was conducted for Ms = 1.3 and 2.6. The results are shown in Fig.3 (a),(b), respectively. The overall view of the isopycnics between the experiment and the numerical simulation agree fairly well especially for weaker shock wave case. For stronger shock wave case, it is found that the movement of the sliplines could not be described properly. In the present numerical simulation, the square mesh was used and the mesh numbers were 90 x 120.

The pressure distributions around the cylinder are shown in Fig.4 (a),(b) for Ms = 1.3 and 2.6, respectively. Due to the boundary layer effect observable in the experiment, discrepancies exist between the experiment and the numerical simulation. However, as a whole, the PLM numerical scheme provide a better agreement with the experiment.

As p(t,θ) is known, unsteady drag coefficient can be defined as

$$C_D(t) = \frac{\int p(t,\theta)\ \cos\theta\ d\theta}{\frac{1}{2}\ \rho\ U^2} \tag{2}$$

Figure 5 shows the time variations of the unsteady drag around the cylinder. The present results were compared with the numerical simulation and the Heilig's experimental curve [4,5]. Heilig distributed several pressure transducers over the circular cylinder surface and directly obtained the pressure distribution. It is remarkable that the both experimental and numerical unsteady drag coefficient agree well. When the shock wave arrives at the top of the cylinder, the drag force was maximum.

3.2 NACA0012 Aerofoil

The steady and unsteady drag and lift forces over an NACA0012 aerofoil observed in the similar manner. Figure 6 (a),(b) show shock wave propagation over the aerofoil for Ms = 1.7, i.e., uniform flow Mach number M = 0.80. The variation of unsteady drag around an aerofoil is also obtained by previous way and the result is shown in Fig.7. The wave interaction ceases after one millisecond from the arrival of the incident shock wave. The uniform transonic flow can exist and lasts for two milliseconds.

The typical steady transonic flow around an aerofoil at the later stage is shown in Fig.6 (c),(d). In these case the interaction between the shock wave on the aerofoil and the boundary layer can be seen clearly. It is noted that even in this complicated interaction region each fringe can be clearly recognised, therefore, the pressure distribution can be obtained by similar measurement. Fig.8 (a),(b) show the pressure coefficient distribution around the aerofoil for angle of attack α= 0 (a) and α= 2 (b), respectively. The drag coefficient C and the lift coefficient C against the angle of attack are shown in Fig.9. the present results for Re = 0.9 X 10^6 are compared with the transonic wind tunnel experiment for Re ≈ 4.5 X 10^6 done in the National Aerospace Laboratory, Mitaka, Tokyo. The present results agree fairly well with the NAL data, but the discrepancies seems to come from the difference of Reynolds numbers.

4. CONCLUSIONS

The results obtained are summarized as follows:

(1) A shock tube equipped with a double exposure holographic interferometry is found to be useful for the quantitative measurement of the transonic shock tube flow. The steady and unsteady performances of an NACA0012 aerofoil was quantitatively observed and the result agree well with the wind tunnel testing.

(2) The PLM numerical scheme is accurate enough to simulate the unsteady shock propagation over a circular cylinder. The interferometric results over the cylinder agree well with the numerical prediction.

5. ACKNOWLEDGMENTS

throughout the course of the present project. The authors are indebted to Messrs. O. Onodera, H. Ojima, S. Hayasaka, Y. Ohta and K. Takahashi for their assistance in conducting the present experiment. The authors acknowledge with thanks to Dr. M. Sommerfeld of Stosswellenlabor RWTH Aachen for the discussion about numerical simulation and thanks to Dr. K. Takashima of the National Aerospace Laboratory, Mitaka, Tokyo for providing us experimental data of wind tunnel.

REFERENCE

[1] R. Courant and K. O.Friedrichs, Supersonic Flow and Shock Waves, Willey (1948).
[2] W. J. Cook and M. I. Chaney, NACA Tech. Paper No. 1268 (1978).
[3] W. J. Cook, et al, Proc. 12th ISST & W (1980).
[4] W. Heilig, Proc. 15th International Congress on High Speed Photography and Photonics (1982).
[5] W. Heilig, Proc. 12th ISST & W (1980).
[6] P. Colella, LBL-17023, Univ. Calif. (1984).
[7] W. Koeckner, Pulsed Holography, laser Handbook (1979).
[8] K. Takayama, Proc. SPIE, vol.298 (1983).
[9] K. Takayama and W. Watanabe, Mem IHSM, vol.45 (1980).
[10] K. Takayama and M. Sasaki, RIMSM, vol. 48 (1983).
[11] M. Suzuki and M. Honda, Mem IHSM, vol. 48 (1983).
[12] M. Suzuki and M. Honda, ibid, vol. 48 (1983).
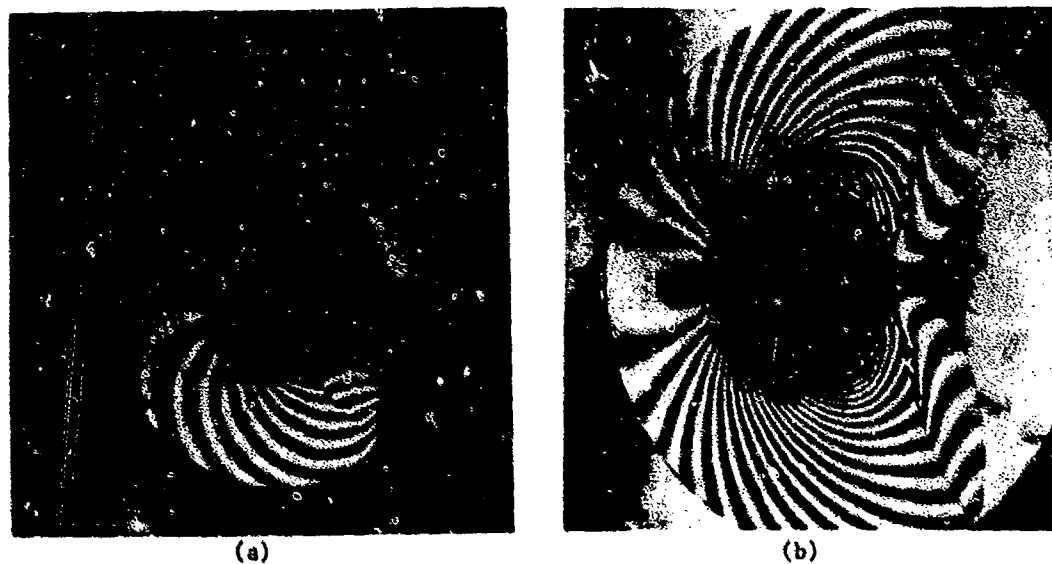
Fig.2 Shock wave propagation over a cylinder, (a) M_s = 1.3, (b) M_s = 2.6
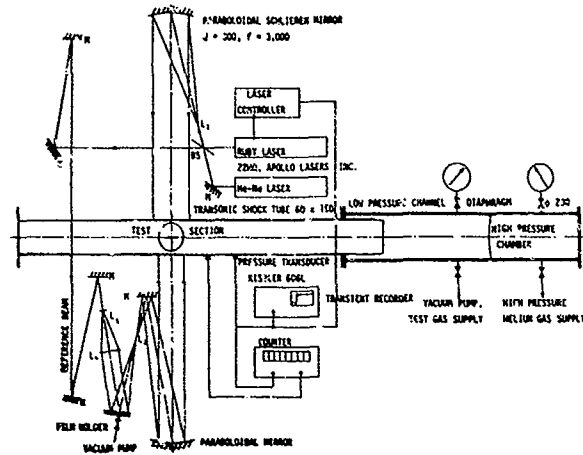
Fig.1 Schematic diagram of shock tube and optical arrangement

(a)   (b)
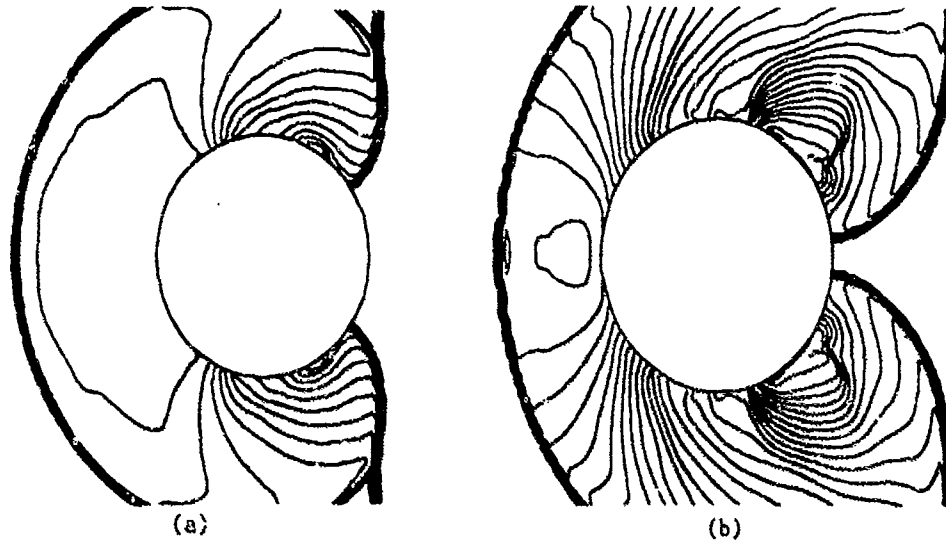
Fig.3 Numerical simulation of shock wave propagation over a cylinder.
(a)$M_S = 1.3$, (b)$M_S = 2.6$

(a)   (b)
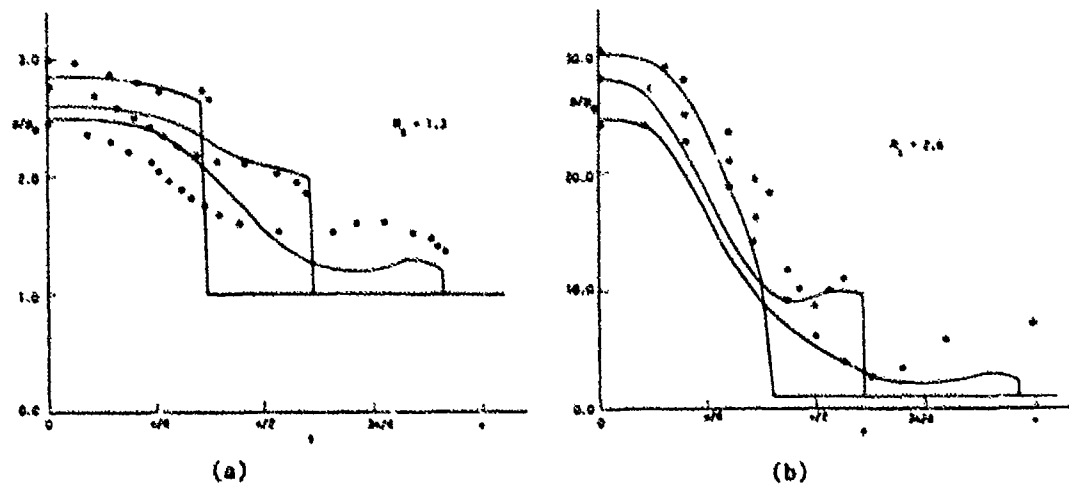
Fig.4 Pressure distribution around a cylinder,(a)$M_S = 1.3$,(b)$M_S = 2.6$
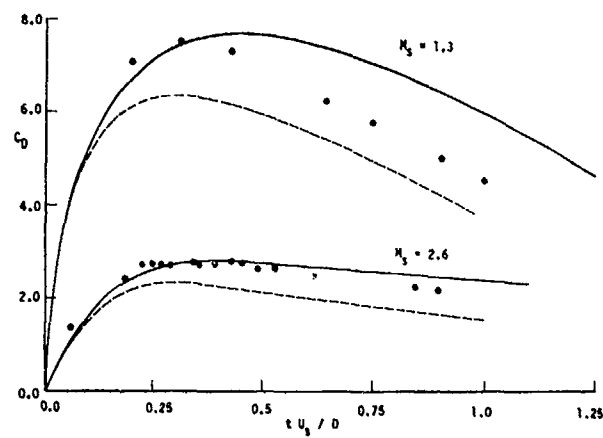
Fig.5 Time-dependent drag coefficient around a cylinder
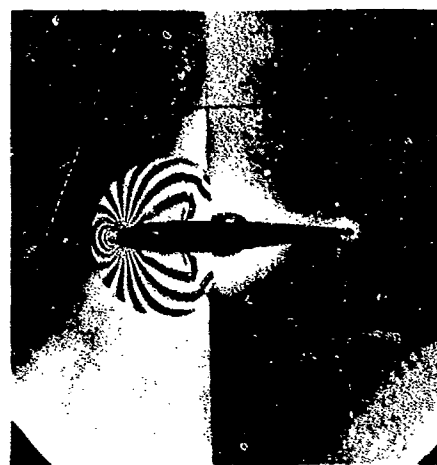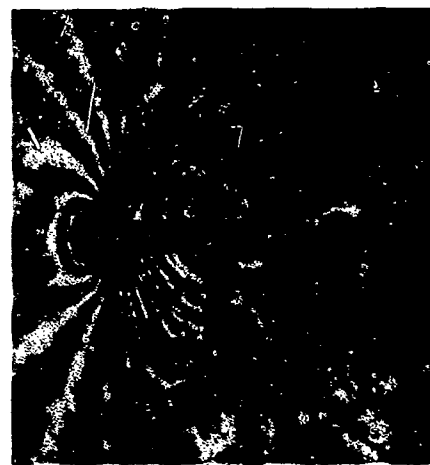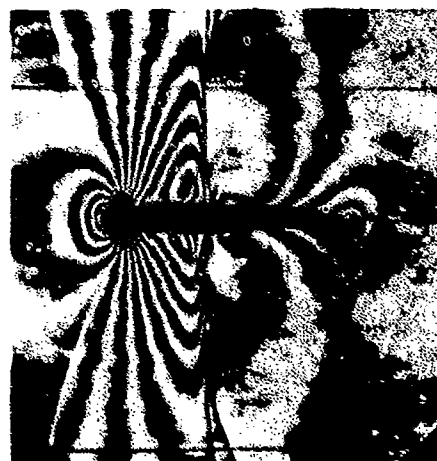
Fig.6 Shock wave propagation and steady transonic flow over an NACA0012 aerofoil

(a)   (b)
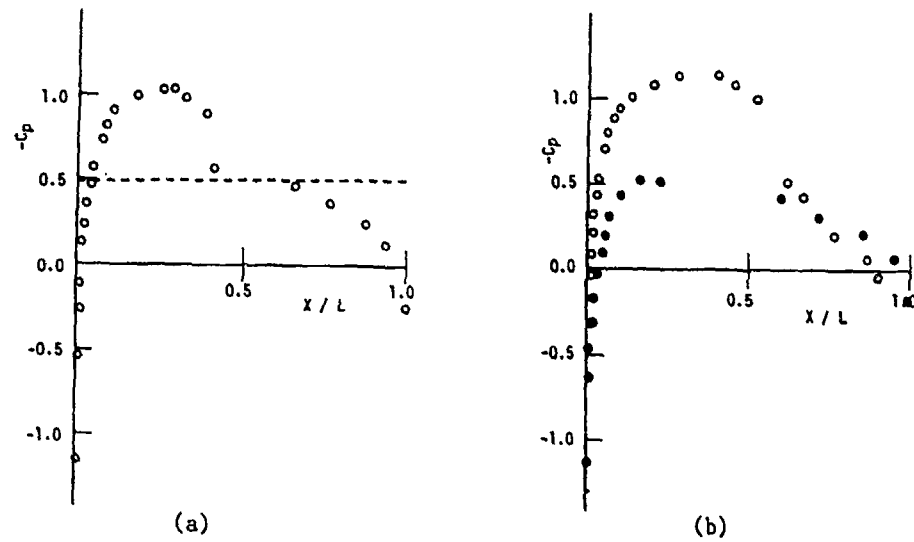
Fig.8 Pressure distribution around an NACA0012 aerofoil,(a) α= 0 deg, (b) α= 2 deg
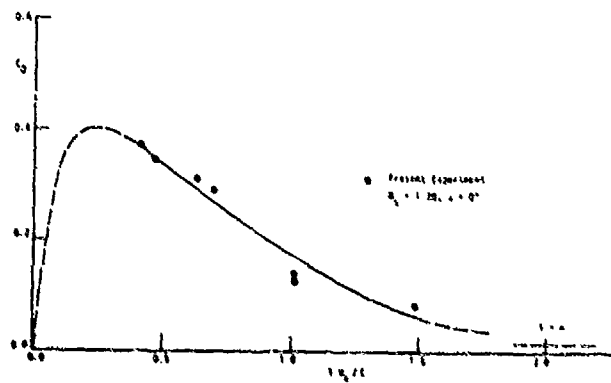
Fig.7 Time-dependent drag coefficient around an NACA 0012 aerofoil
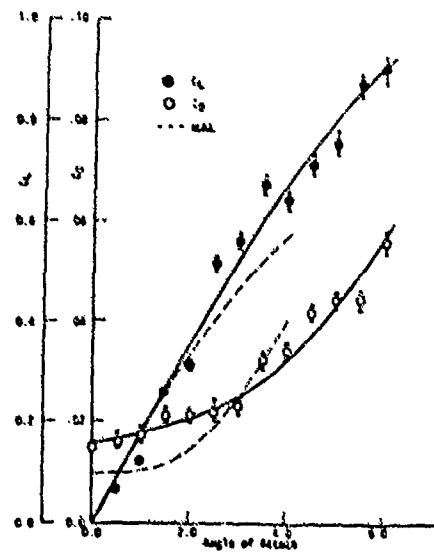
Fig.9 Variation of lift and drag coefficient to variation of angle of attack

NUMERICAL SIMULATION OF STEADY
AND UNSTEADY SHOCK BOUNDARY LAYER INTERACTION

E. Katzer, H. Oertel jr., H. Reister

Institute for Theoretical Fluid Mechanics
DFVLR-AVA Göttingen, FRG

The article deals with the numerical simulation of the
interaction of a steady oblique shock and of unsteady
pressure waves with a laminar boundary layer. The com-
pressible Navier-Stokes equations are solved by means
of a finite-volume method. Particular attention was
given to the influence of numerical dissipation and
grid choice on the interaction domain.

The trailing edge boundary-layer separation induces
upstream propagating pressure waves which form shock
waves in the transonic domain. The interaction of the
pressure waves with a flat plate boundary layer induces
an unsteady separation and is simulated numerically.
The differences in the flow structures of steady and
unsteady separation in a laminar compressible boundary
layer will also be shown.

1. Introduction

The growing interest in transonic laminar wings requires improvement of the
existing knowledge about the interaction of steady shocks and nonlinear pres-
sure waves with laminar compressible boundary layers. The supersonic domain on a
wing in general is terminated by a shock which interacts with the boundary layer
and may induce separation. The present design methods for modern transonic wings
seek optimum efficiency by a shock-free design. Were it possible, however, to
design a transonic laminar wing with a smaller leading edge curvature, then, the
drag could be reduced even with a weak shock on the wing. This idea has led us
to resume again the subject of steady laminar shock boundary layer interaction.
Thus, in the present article we deal with the model case of the interaction with
the flat plate boundary layer. The classical works of Ackeret[1], Liepmann[2], and
the numerical solutions of MacCormack[3], Beam and Warming[4], Haase et al.[5] are the
starting point of our studies. We intend to show to what extent it is possible
to resolve the details of the interaction region by means of numerical simu-
lation of the Navier-Stokes equations.

Heinemann et al.[6], Davis[7] and Oertel jr.[8] have already indicated that the
unsteady trailing edge separation is related to pressure waves moving upstream.
The unsteady separation and the shock boundary layer interaction domain are cou-
pled on a wing through these pressure waves. This can lead to resonance, which
eventually may result in shock buffeting. Here too, the flat plate boundary lay-
er serves as a model case for studying the details of the unsteady compressible
pressure waves boundary layer interaction neglecting the influence of a curva-
ture parameter.

2. Numerical method

Finite volume methods are used to calculate both the steady shock boundary layer interaction and the pressure wave boundary layer interaction. We start from the integral form of the two-dimensional compressible Navier-Stokes equations.

$$\frac{\partial}{\partial t} \int_V \vec{U} dV + \int \bar{\bar{H}} \vec{n} dO = 0 \tag{1}$$

$\vec{U}$ is the solution vector and $\bar{\bar{H}}$ describes the flux of the respective fundamental quantities through the surface O of the volume V under consideration.

$$\vec{U} = \begin{pmatrix} \rho \\ \rho u \\ \rho v \\ \rho e \end{pmatrix} \qquad \bar{\bar{H}} = \begin{pmatrix} \rho \vec{v} \\ \rho u \vec{v} + (p + \tau_{xx}) \vec{1}_x + \tau_{xy} \vec{1}_y \\ \rho v \vec{v} + \tau_{xy} \vec{1}_x + (p + \tau_{yy}) \vec{1}_y \\ (e+p) \vec{v} + (\tau_{xx} u + \tau_{xy} v) \vec{1}_x + (\tau_{xy} u + \tau_{yy} v) \vec{1}_y + \vec{q} \end{pmatrix} \tag{1a}$$

The principle of the finite volume method consists in the division of the entire flowfield into volume elements, for the two-dimensional case in surface elements, and the discretisation of the integral conservation laws for each volume element V .

$$\frac{d}{dt} U V + \sum_{k=1}^{4} (H^{(k)} O_k)_{ij} = 0 \tag{2}$$

Various approximations of the fluxes $\vec{H}^{(u)}$ through the element sides $\vec{O}_k$ as well as various methods for the integration of the resulting systems of ordinary differential equations in time direction result in a number of different finite volume methods.

For the steady shock boundary layer interaction we follow the predictor-corrector discretisation described by MacCormack[3] which is second-order accurate in space and time. In the case of the pressure wave boundary layer interaction it is the adequate numerical simulation of the flow's development in time that is of crucial importance. Therefore, we use the Runge-Kutta finite volume method introduced by JAMESON[4] which is fourth-order accurate in time.

3. Steady shock boundary layer interaction

When a steady oblique shock impinges on the laminar boundary layer on a flat plate, the increasing pressure in the interaction region causes the boundary layer to slow down and thicken as a consequence. This thickening of the boundary layer generates a compression zone in front of the interaction domain, followed by an expansion fan and a second compression zone leading to an again undisturbed boundary layer. A sufficiently strong shock will cause the boundary layer to separate. The expansion fan deflects the flow to the wall and closes the separation bubble. Fig. 1 shows the basic features of the interaction region, the wall shear stress and the wall pressure distribution. The boundary layer and the separation bubble are shown with the y-axis being stretched considerably. The forward influence of the shock in the interaction region reaches about 50 boundary layer thicknesses. A flat, long separation bubble is formed within the laminar boundary layer. The pressure at the wall increases within the compression zones at the beginning and the end of the interaction region while in the separation bubble a constant plateau develops. The wall shear stress at the beginning of the interaction region decreases as the boundary layer slows down and is negative in the separation region. A characteristic minimum of the shear stress distribution just before reattachment will be discussed below.

The isobars in fig. 2 of the numerical simulation show the oblique shock at a free-stream Mach number of 2. It is spread over several points of the computational grid, the same is valid for the two compression zones and the expansion fans in the outer field. Here δ_0^* is the displacement thickness of the undisturbed boundary layer without interaction and x_0 is the distance from the leading edge to the shock impingement.

The streamlines show the details in the interaction domain. The separation bubble is shown here some 10 times thicker that it actually is. In fact the bubble is very flat and thin. The asymmetric internal structure of the separation bubble is clearly recognizable reluting in a second minimum of the wall shear stress distribution just upstream of reattachment.

An accurate resolution of the structure of the separation bubble in the interaction region requires an analysis of the computational grid used and of the additional numerical dissipation needed to reach a stable numerical solution. The isobars calculated on a coarse and on a fine grid shown in fig. 2 make the differences quite clear. On the coarse grid, the impinging shock, the compression zones and the expansion fan are spread over large regions. An optimal resolution was found using a grid of 151 × 101 points with a dense distribution of grid points within the boundary layer and near the shock impingement. The boundary layer was resolved with up to 50 grid points. The large gradients within the shock domain lead to numerical instabilities. In order to smooth these instabilities an artificial numerical dissipation was added, which is of fourth-order in the spatial step. The amount of the numerical dissipation was optimized in order to suppress these instabilities sufficiently without changing the solution.

By plotting the bubble length l_B in an appropriate form, the similarity law shown in fig. 3 can be derived.

$$\frac{l_B}{\delta_0^*} \frac{M_1^3}{Re_{x_0}/C} = 4.4 \frac{p_3 - p_{inc}}{p_1} \tag{3}$$

The bubble length is normalized with the Mach number M_1^3 upstream of the shock and the Reynolds number based on x_0. C is the Chapman-Rubesin constant $C = \mu_w T_\infty / \mu_\infty T_w$. Fig. 3 shows that the length of the separation bubble increases linearly with the intensity of the shock. It is proportional to the difference between the pressure increase in the shock p_3/p_1 and the critical pressure increase p_{inc} which is necessary to induce separation. Further details can be found in the work of KATZER[18].

4. Pressure wave boundary layer interaction

Upstream moving pressure waves are the result of the periodic trailing edge separation and vortex shedding. The shock tube experiment of fig. 4 shows the vortex separation behind a plate and the pressure waves propagating with a relative velocity $U_\infty - a_\infty$. The amplitude of the pressure waves is only a small percentage of the free-stream level. The principle sketch of fig. 4 shows the model for the numerical simulation performed to investigate the viscous interaction of the periodic pressure waves with the laminar boundary layer on a flat plate. The pressure waves are imposed at the right-hand boundary of the integration domain. Depending on their amplitude, frequency and the free-stream Mach number M_∞ they can steepen to a sawtooth in the inviscid outer field. At the wall these waves are damped in the acoustic boundary layer. Due to the interaction with the viscous boundary layer a periodic unsteady separation may take place.

To test the numerical method the steepening of the waves in a free-stream without a plate was first investigated. By means of the second-order acoustic theory it is possible to determine where the wave steepens to a shock. The numerical simulation of the steepening process with the finite volume method agrees well with the second-order acoustic theory. Fig. 5 shows the steepening of a harmonic wave in the integration domain.

For the numerical simulation of the pressure wave boundary layer interaction the steady laminar flat plate boundary layer-solution of Chapman and Rubesin[11] was taken as an initial distribution. This solution was maintained at the inflow boundary and the calculation was finished once the waves had reached the inflow boundary. No numerical dissipation was added for this calculation. Fig. 6 shows the result of the viscous interaction with the boundary layer. The wall pressure distribution and the dimensionsless wall shear stress are plotted. The wall shear stress periodically becomes negative, a fact indicating the unsteady separation of the boundary layer. In order to visualize the structure of the unsteady separation region, we integrated the instantaneous streamlines in the interaction region for a free-stream Mach number of 0.5 and a pressure amplitude of 0.112 (fig. 7). We found that in the case of the unsteady interaction, a closed separation bubble does not have to form. Instead, the structure is determined by two nodes, a source and a sink, which show a back flow area on the wall, two saddle points and a focus. This unsteady separation structure remains unchanged with the distance from the trailing edge increasing.

Conclusions

The numerical simulation of steady and unsteady shock boundary layer interaction shows considerable differences in the structures of the separation. For the case of the interaction of a steady oblique shock with a laminar boundary layer we find an extremely long closed separation bubble. In the unsteady case, on the other hand, pressure waves generate separation regions with back-flow at the wall and a focus in the flowfield. This represents, however, only one possible unsteady separation structure. We expect further structures to be found in the unsteady interaction domain if free-stream Mach number, wave amplitude and frequency are varied.

We were able to show that by using the finite-volume method and by carefully optimizing the computational grid and the numerical dissipation it is possible to obtain stable solutions of the compressible Navier-Stokes equations. Moreover, the numerical simulation permits the resolution of the details in the interaction domain.

References

[1] J. Ackeret, F. Feldmann, N. Rott, "Untersuchungen an Verdichtungsstößen und Grenzschichten in schnell bewegten Gasen", Mitteilungen aus dem Institut für Aerodynamik an der Eidgenössischen Technischen Hochschule in Zürich, Nr.10, 1946, NACA TM 1113, 1947.

[2] H.W. Liepmann, "The Interaction between Boundary Layer and Shock Waves in Transonic Flow", J. Aeronautical Sciences, 13, 623-637, 1946.

[3] R.W. MacCormack, "Numerical Solution of the Interaction of a Shock Wave with a Laminar Boundary Layer", Lecture Notes in Physics 8, 151-163, Springer 1971.

[4] R.M. Beam, R.F. Warming, "An Implicit Factored Scheme for the Compressible Navier-Stokes Equations", AIAA J., 16, 393-402, 1978.

[5] W. Haase, B. Wagner, A. Jameson, "Development of a Navier-Stokes Method based on a Finite Volume Technique for the Unsteady Euler Equations", Notes on Numerical Fluid Mechanics, 7, 99-107, Vieweg 1984.

[6] H.J. Heinemann, O. Lawaczeck, A. Bütefisch, "V.Karman Vortices and their Frequency Determination in the Wakes of Profiles in the Sub- and Transonic Regimes", IUTAM Symposium Transonicum II, 75-82, Springer 1975.

[7] S.S. Davis, "Theory of Discrete Vortex Noise", AIAA Journal, 13, 3, 375-380, 1975.

[8] H. Oertel jr., "Vortices in Wakes induced by Shock Waves", Proceedings of the 14th International Symposium on Shock Tubes and Waves, 293-300, 1983.

[9] A. Jameson, W. Schmidt, E. Turkel, "Numerical Solutions of the Euler Equations by Finite Volume Methods Using Runge-Kutta Time-Stepping Schemes", AIAA-81-1259, 1981.

[10] E. Katzer, "Numerische Untersuchung der laminaren Stoß-Grenzschicht-Wechselwirkung", DFVLR-FB 85-34, 1985.

[11] D.R. Chapman, M.W. Rubesin, "Temperature and Velocity Profiles in the Compressible Laminar Boundary Layer with Arbitrary Distribution of Surface Temperature", Journal of the Aeronautical Sciences, 16, 547-565, 1949.
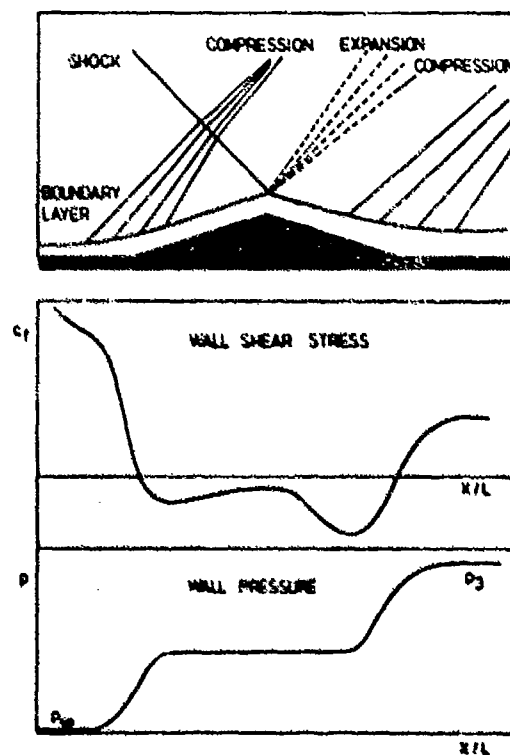
Fig.1 Principle Sketch of the Steady Shock Boundary Layer Interaction.
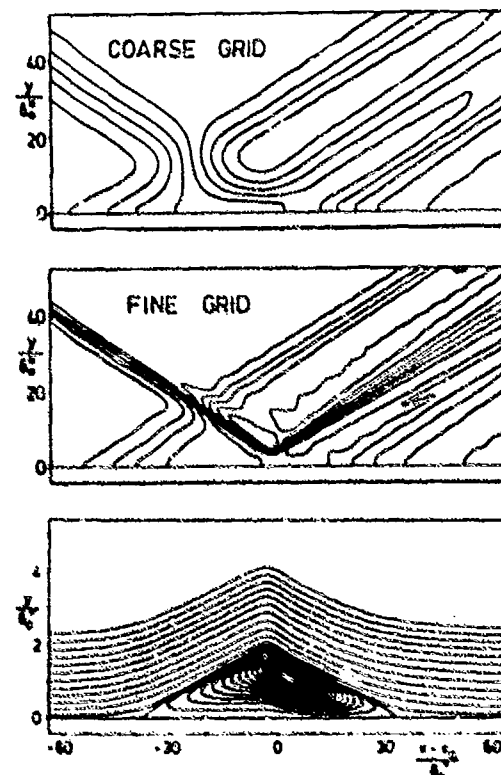
Fig.2 Numerical Simulation and Influence of the Grid Size.
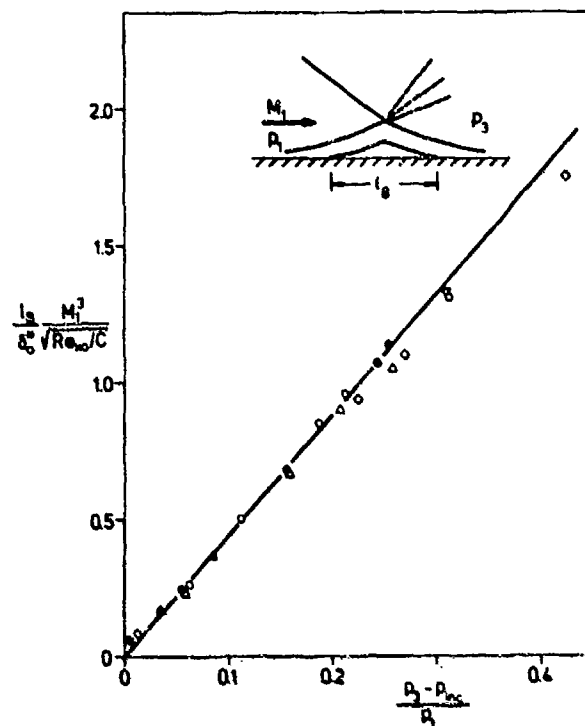
Fig.3 Similarity Law for the Length of the Separation Bubble l_B.
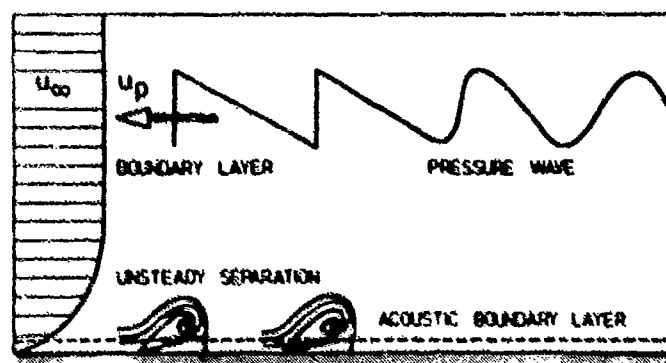
Principle Sketch
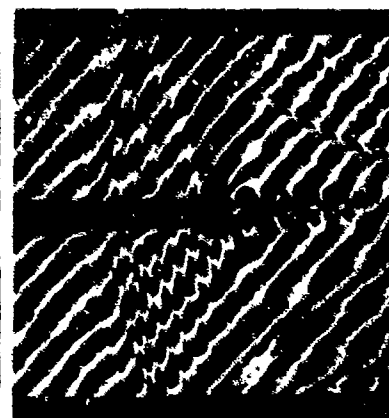
Shock Tube Experiment

Fig.4 Unsteady Pressure Wave Boundary Layer Interaction.

Fig.5 Nonlinear Steepening of a Periodical Pressure Wave in a Homogeneous Flow.
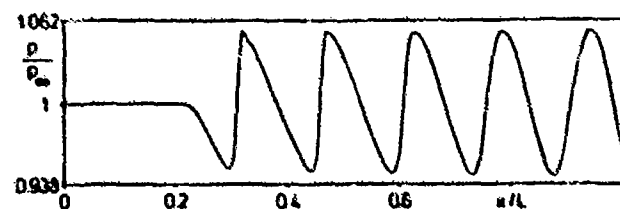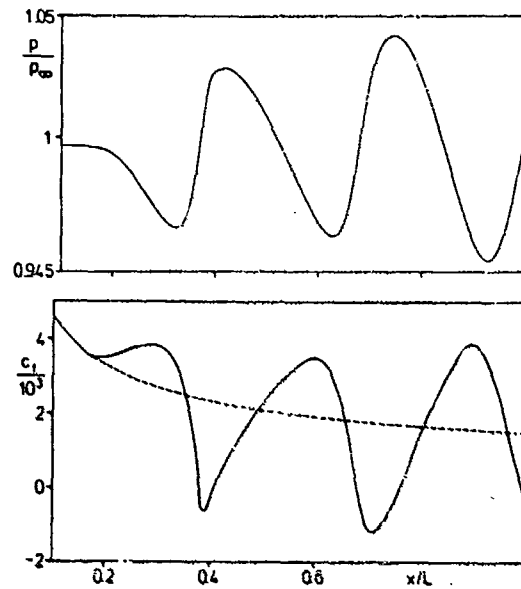
Fig.6 Unsteady Separation.
--- undisturbed flat plate so-
lution
$u_\infty = 0.5$, $Re = 2 \cdot 10^5$,
$(p_2 - p_\infty)/p_\infty = 0.112$
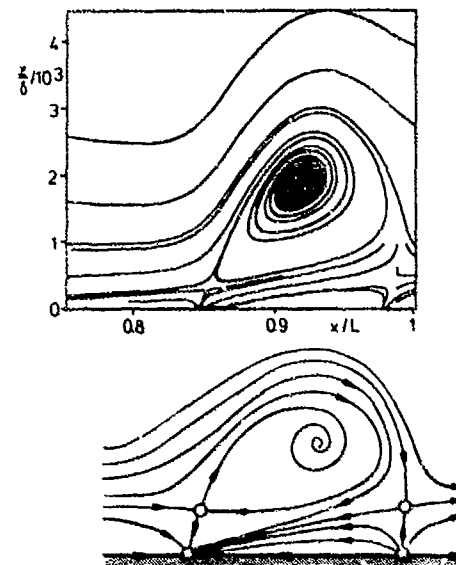
Fig.7 Streamlines and Topological
Structure.

LEADING EDGE EFFECTS ON BOUNDARY LAYERS BEHIND WEAK SHOCK WAVES

B.E.L. Deckker   D. Singh

Mechanical Engineering Department
University of Saskatchewan
Saskatoon, Canada   S7N 0W0

Experiments in which weak shock waves of strength $M_s = 1.22$
and $M_s = 1.29$ were made to impinge on a flat plate have
confirmed that the profile of the boundary layer is thicker
than that predicted theoretically although there are
several similarities between them.   Plates of three
different thicknesses with square leading edges were used.
There is some effect of plate thickness on the boundary
layer. With a semicircular leading edge, the quasi-steady
flow is separated but reattaches on the plate with the
unsteady boundary layer.   In the cases examined, the
unsteady boundary layer is laminar and self-similar.   The
steady boundary layer is apparently turbulent.

1.   INTRODUCTION

The abnormal thickness of laminar shock induced boundary layers behind
weak shock waves ($M_s = 1.11$, 1.19, 1.44) after they had impinged on the sharp
edge of a flat plate has been reported earlier[1].   The thickness of the
developing boundary layer was measured from schlieren photographs. Schlieren
photographs had also been used to measure the thickness of developing side-wall
boundary layers and where appropriate comparisons could be made with other
methods the results were found to be very satisfactory[2]. The same technique of
measurement has been adopted in the experiments reported in this paper. The
The present experiments differ from those reported earlier in that the plate on
which the boundary layer develops is supported in a way that prevents the
possibility of its responding dynamically to impingement of the shock. Also,
the leading edge of the plate is in the field of view so that the boundary
layer growing from the leading edge can also be observed.

2.   EXPERIMENTAL CONSIDERATIONS

The apparatus used was essentially the same as that described in ref. (1)
except for modification to the length of the plate which was increased from
0.75 m to 1.24 m, and to the method of supporting it in the expansion duct.

An inverted U-shaped steel channel of wall thickness 0.05 cm and with
square corners was used to divide equally the height of the expansion duct
(5.08 cm) across its span (7.62 cm) for a length of 1.24 m, and to provide a
flat smooth surface on which the boundary layer could grow. The leading edge
of the plate was located 1.5 cm from the upstream edges of the schlieren
windows, and, to minimize the disturbance in the plane of the leading edge, the
two vertical walls of the channel were extended upstream for a distance of
about 1 m.

The plate which was uniformly 0.05 cm thick had a surface roughness
smaller than 0.5 μm (5×10^{-7} m). To examine the effects of plate thickness and
of leading edge profile on the boundary layer, flat plates 0.05 cm, 0.368 cm
and 0.686 cm thick with square leading edges, and one with a semicircular
leading edge profile 0.686 cm diameter were used. The plate thickness was
increased by gluing to the underside of the steel channel, closely fitting
plastic strips of length equal to the plate.

The schlieren optical system has been described in ref.[1]. The time interval between successive photographs during passage of the shock wave could be made as small as 11.1 µs so that development of the boundary layer could be followed in some detail from the leading edge.

The two shock waves (M_s = 1.22, 1.29) used in this investigation were monitored over a distance of 1.0 m by their average speeds just before impinging on the leading edge. Several shock tube firings were made in the course of each set of experiments, and those in which the shock speed deviated by 1 percent or more from their respective theoretical values were rejected. In the course of the experiments the ambient pressure was 93 ± 3.0 kPa and the ambient temperature in the laboratory was held to 21 ± 0.6 C.

Multiple diaphragms of laminated cellophane were used and rupture initiated by means of a pulsed electrical discharge of 200 A at 900 V.

3. DISCUSSION AND RESULTS

There are several publications that deal theoretically and experimentally with the laminar boundary layer induced by the passage of a shock wave on a flat plate. In these publications, three regions have been identified in α, β space, where $\alpha = x/u_e t$ and $\beta = u/u_e$, that include: (a) the self-similar side wall boundary layer in shock fixed coordinates[3] which is bounded by $1 \leq \alpha \leq A$, $0 \leq \beta \leq 1$; (b) the steady bound layer at $\alpha = 0$; (c) the interaction region bounded by $0 \leq \alpha \leq 1$, $0 \leq$ 1. The strength of the shock wave is characterized by a $\cdot u_s/u_e$, where u_s is the speed of the shock wave and u_e the free stream velocity in shock fixed coordinates. Numerical solutions of the governing boundary layer equations satisfying (a), (b) and (c) have been obtained for the special case of a fluid obeying $\rho\mu$ = const.[4] as well as for the general case[5]. The laminar nature of the boundary layer has been verified by heat flux measurements[4,5,6]. An interferometric study of the boundary layer[7] has shown that the boundary layer is always laminar when the length Reynolds number Re_x was less than 7 x 10^5. When the Reynolds number exceeded 10^6, transition to turbulence occurred at some distance from the leading edge and caused the boundary layer to thicken. This thickened region between the two boundary layers was turbulent and led to the conclusion that there were two regions of transition, one associated with the unsteady boundary layer and the other with the boundary layer growing from the leading edge. This was the first publication in which internal features of the boundary layer flow were invoked in order to characterize its nature.

In the present experiments, development of the boundary layer between the leading edge and foot of the shock wave at different times is shown in Fig. 1(a). The strength of the shock wave is M_s = 1.29. According to the theoretical references cited earlier, the length bounded by $1 \leq \alpha \leq A$ conforms with Mirel's analysis[3]. For M_s = 1.29, A has the value u_s/u_e = 3.0.

Of particular interest in Fig. 1(a) is the profile at the earliest time of 22.2 µs. It is clear that the profile does not represent growth of a boundary layer in the usual sense. Rather, it would appear as if fluid has been carried on to the plate by the impinging shock wave as a result of the wave action associated with it, and then convected with the naturally developing boundary layer flow. While it is certain that some kind of wave action occurs at the leading edge, it is a matter for speculation as to how effective it is in transporting fluid, and for what duration. In Fig. 1(b), using an artificial datum of 0.34 mm, the theoretical laminar boundary layer profile in shock fixed coordinates[3] has been superimposed on the profile measured at the fixed position 8 or from the leading edge and it appears that the boundary layer is growing laminarly on a substrate flow that could have been entrained from the fluid accumulating near the leading edge. The difference of 0.34 mm between the theoretical and measured thickness is too large simply to constitute an error of measurement which, in any case, is constant.

Measured boudary layer thickness, δ, at a fixed distance from the leading edge, $x = 4.90$ cm, have been plotted in Fig. 2 using the non-dimensional quantity $\alpha = x/u_e t$ for the abscissa. The unsteady boundary layer is between $\alpha = 3.0$ and $\alpha = 1$ and in the interaction region the thickness δ approaches a steady value at about $\alpha = 0.2$. The variation of δ at a fixed time $t = 110.1$ μs, is also shown in that figure. The profiles of the experimental curves for fixed distance from the leading edge and for fixed time are similar to the corresponding theoretical ones[5] except for 'humping' of the experimental curves between $\alpha = 1$ and $\alpha = 0.2$. Theoretically, at a fixed distance from the leading edge, there is a gradual increase from $\alpha = 1$ to $\alpha = 0.2$. When the distance from the leading edge is fixed the theoretical dimensionless thickness is $\delta^* \sqrt{Re_x}/x$ (δ^* is the displacement thickness) and varies between 0 and 1.0. The term $\sqrt{Re_x}/x$ is numerically equal to one-fifth of the Blasius thickness at the position x so that δ^* cannot exceed two-tenths of the Blasius thickness. By comparison, at $\alpha = 0.2$ the measured thickness is 4.4 times the Blasius thickness. It should be borne in mind that the calculated values in ref. (4) are for very strong shocks and, therefore, for thinner boundary layers.

Superimposed on Fig. 2 are the measured values of δ for a shock of the same strength ($M_s = 1.29$) at a fixed distance of 8 cm from the leading edge. It may be noted that the variation of thickness of the unsteady boundary layer with α is essentially the same as for $x = 4.90$ cm. This agreement is a measure of the consistency of the measurements at the two stations and repeatability of conditions behind the shock wave in a large number of shock tube firings. More importantly, however, it confirms the validity of the assumption used in the theoretical analyses that the unsteady boundary layer is self-similar. In this case, the corresponding times are in the constant ratio 4.90/8.0.

It is interesting also to note that the experimental boundary layer thickness approaches a constant value at about $\alpha = 0.2$ as had been predicted theoretically[5] and later verified by heat flux measurements[6]. It is evident that between 4.90 cm and 8.0 cm changes are taking place that may eventually lead to the disappearance of the hump and to a gradual approach to the steady state thickness like that predicted theoretically.

The growth of the boundary layer from the leading edge is perhaps seen more clearly in Fig. 3(a) for the fixed times indicated in that figure. It may be noted that the thickness δ at $\alpha = 0.2$ increases, but more slowly as time is increased. At $t = 1200$ μs, it attains a thickness of about 1.12 mm, and the boundary layer is now steady between $\alpha = 0$ and $\alpha = 0.2$ corresponding to a distance of 3.6 cm from the leading edge. At later times the value of x at $\alpha = 0.2$ would also be greater. For example, when the time is a little greater than 2700 μs, the steady boundary layer would wholly occupy the plate. The thickness at this time is estimated to be 1.70 cm (Fig. 2). The shock front would then be 1.20 m from the leading edge, close to the farthest edge of the plate. That the steady boundary layer thickness is attained progressively from the leading edge is intuitively reasonable.

The measured steady boundary layer thickness at a fixed distance from the leading edge is thinner at $t = 1000$ μs than at $t = 200$ μs. This would appear to be contrary to Fig. 3(a) in which δ increases with time. However, the abscissa in the latter figure is α (not x) which for fixed time becomes a variable of x. In fact, Fig. 3(a) has been derived from measurements along the plate for the fixed times indicated in Fig. 3(b) in which δ is seen to decrease as time is increased.

Fig. 3(c) shows the steady part of the boundary layer growing from the leading edge at time $t = 1044.3$ μs and superimposed on it are the calculated values of thickness for a turbulent boundary layer given by $\delta = 0.37 \, x/Re_x^{0.2}$ measured from an artificial datum of 0.30 mm. It would appear from this figure that the steady boundary layer is growing in a turbulent manner and that, as in Fig. 2(b), it is superimposed on a substrate flow. The artificial datum in each case has been chosen so that the theoretical and experimental profiles are

matched as closely as possible and adjustment to a common datum of about 0.32 mm would not invalidate the inference regarding the nature of the growth. Although the position of the 'humped' region in the experimental profile does not correspond with that described in ref. (7), nevertheless, it conforms with the findings in that paper that the internal structure in the hump is turbulent. If, indeed, in the present experiments, the fluid in the hump is turbulent the juxtaposition of the unsteady boundary layer to it would require a process of re-laminarization. A suggestion on similiar lines was proposed tentatively ref. (1).

Increasing the plate thickness, and changing the profile of the leading edge from a square to a semicircular one, has some effect on the development of the unsteady boundary layer. This is to be expected on theoretical grounds since wave action at the leading edge could affect the transmitted shock wave and so bring about changes in the unsteady boundary layer. The measured boundary layer thickness for the shock wave $M_s = 1.29$ is shown in Fig. 4(a) for plates 0.05 cm and 0.686 cm thick with square leading edges as well as for the plate with a semicircular leading edge 0.686 cm diameter. The unsteady boundary layer is not affected by the change from the square to the semicircular leading edge but clearly there is an effect due to the change from a plate thickness of 0.05 cm to 0.686 cm which is substantial. For the shock wave $M_s = 1.22$, the unsteady boundary layers for same leading edge conditions are shown in Fig. 4(b). Also shown in that figure is a side-wall boundary layer[2] and a laminar boundary layer in shock-fixed coordinates[3] for a shock wave of the same strength ($M_s = 1.22$). The effect of shock wave impingement is quite marked compared with the side-wall boundary layer.

In the case of the plate with a semi-circular leading edge 0.686 cm diameter, flow in the wake of the unsteady boundary layer is separated at the leading edge for the two shock waves $M_s = 1.22$ and $M_s = 1.29$. However, the schlieren photographs show the same optical effect as in a boundary layer attached to a plate. In Fig. 4(a), the thickness of the separated boundary layer has been measured from the edge of the separation bubble and its distribution between $\alpha = 1$ and $\alpha = 0.4$ is similar to the attached boundary layers from square leading edges. In Fig. 4(c), the boundary layer growing from the leading edge of a plate 0.686 cm thick with a square leading edge is compared with that growing from a semicircular leading edge at a fixed time, $t = 377.7$ µs. Also shown in that figure is the profile of the separation bubble.

The separated flow is always reattached to the plate at the upstream extremity of the unsteady boundary layer at $\alpha = 1$ (Fig. 4(c)) where an oblique shock wave occurs. The length of the separation bubble increases with displacement of the interface ($\alpha = 1$) but cannot do so indefinitely. At about 700 µs after arrival of the shock wave at the leading edge, the separated flow tends to become reattached to the plate intermittently at points along it. After 900 µs reattachment is firmer and appears to propagate from the interface $\alpha = 1$ to the leading edge. The intermittency between 700 and 900 µs may signal the onset of transition although it is not until 1200 µs that there is some evidence that the free stream flow is weakly turbulent. However, the internal structure of a turbulent boundary layer as revealed by schlieren (2),(8) is not evident.

4. CONCLUSIONS

Schlieren photographs of the formation and development of the boundary layer on a plate after shock waves of strength $M_s = 1.22$ and $M_s = 1.29$ have impinged on its leading edge have confirmed the main results of an earlier publication[1]. The unsteady boundary layer and the boundary layer from the leading edge are both thicker than predicted theoretically. Measurements of thickness were made from schlieren photographs at a magnification X20 with a resolution better than 1/100 mm.

Qualitatively, the profile of the boundary layer developing between the leading edge and foot of the shock wave is similar to that predicted by numerical integration of the governing boundary layer equations except for a 'humped' region between $\alpha = 1$ and $\alpha = 0.2$ ($\alpha = x/u_e t$) in the experimental profile.

The presence of a 'humped' region which is turbulent and intermediate in position between the two boundary layers has been identified by an interferometric technique[1]. In contrast, schlieren photographs obtained earlier[1] and in the present experiments show a 'humped' region near the leading edge as in Fig. 1(a). The 'humped' region may also be thought of as being intermediate between the two boundary layers, although there is evidence that the unsteady boundary layer is growing laminarly while the steady boundary layer is growing in a turbulent fashion.

Increasing the thickness of the plate has some effect on the developing boundary layers. The effect appears to be more pronounced the weaker the incident shock wave. Changes in the unsteady boundary layer can only result from changes to the transmitted shock wave after the incident wave has impinged on the leading edge.

A semicircular leading edge causes the flow in the wake of the unsteady boundary layer to separate. The separated flow is always reattached to the plate at the upstream extremity of the unsteady boundary layer ($\alpha = 1$) and is associated with an oblique shock wave.

Schlieren photographs of the separated flow show the same optical effect near the edge of the separation bubble as in an attached boundary layer. Separation of the flow does not extend indefinitely and in the present experiments has shown a tendency to intermittent reattachment to the plate after 700 µs and firmer reattachment at about 900 µs. Reattachment appears to propagate from the interface $\alpha = 1$ to the leading edge. Intermittent reattachment may signal the onset of transition but no firm evidence of a turbulent boundary layer has been obtained.

5. ACKNOWLEDGEMENTS

REFERENCES

1. Deckker, B.E.L., Proceedings 13th Intl. Symp. Shock Tubes and Waves, 1981; p. 253.

2. Deckker, B.E.L., Weekes, M.E., Proc. I. Mech. E. (Lond.), 190, 11/76, 1976; p. 287.

3. Mirels, H., NACA TN 3712, 1956.

4. Lam, H., and Croooo, L., Jl. Aerospace Sci., 26, 1959; p. 54.

5. Cook, W.J., and Chapman, G.J., Phys. Fluids, 15, 1972; p. 2129.

6. Cook, W.J., Phys. Fluids, 7, 1974; p. 900.

7. Smeets, G., and George, A., Proceedings 9th Intl. Symp. Shock Tubes and Waves, 1973; p. 249.

8. Head, M.R. and Bandyopadhyay, P., Jl. Fluid Mech., 107, 1981; p. 297.
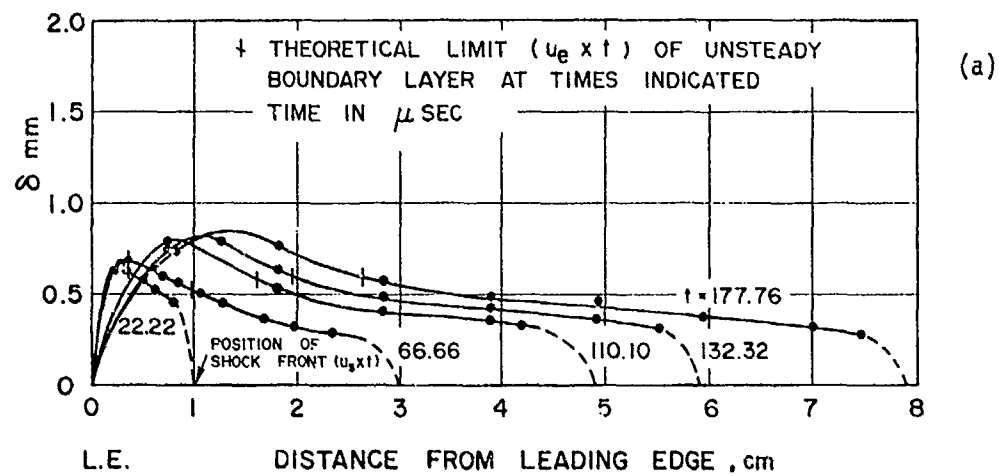
(a)   Profiles of developing boundary layer.

(b)   Comparison of measured and theoretical values of unsteady boundary layer thickness.

Fig. 1.   Growth of unsteady boundary layer.
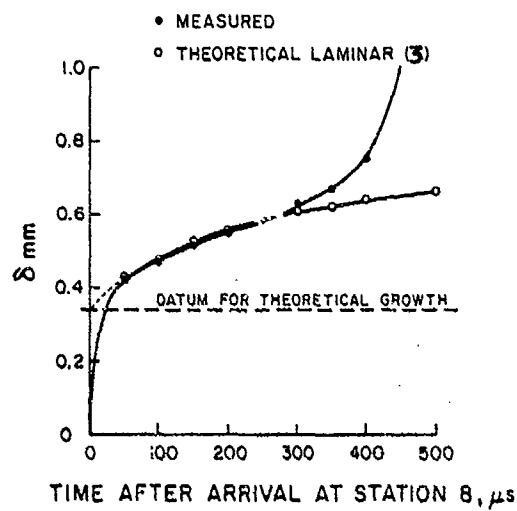
Fig. 2.   Variation of measured boundary layer thickness with α for fixed distances and fixed time.
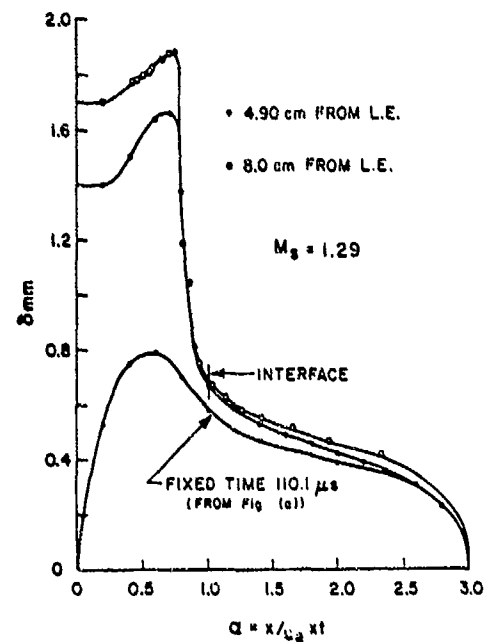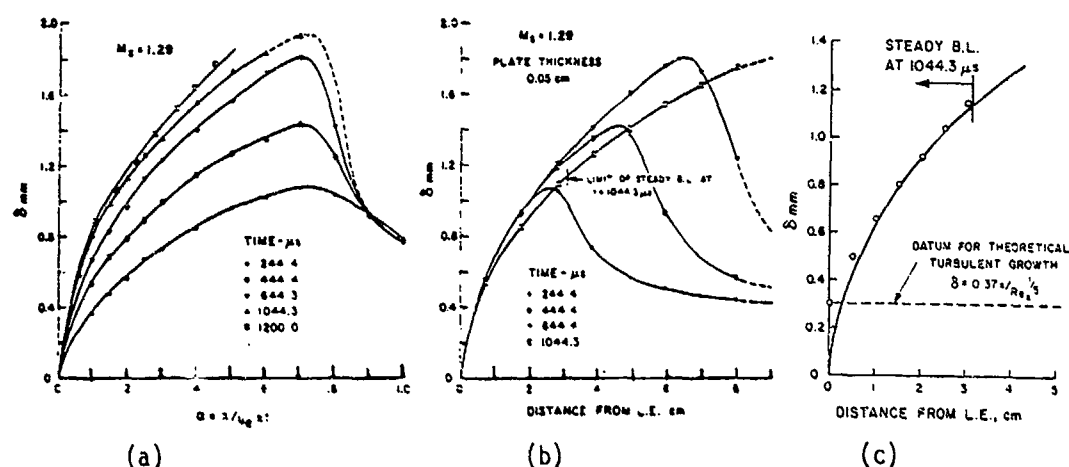
(a) Variation of boundary layer thickness at fixed distance, x = 8.0 cm.
(b) Variation of boundary layer thickness with distance from leading edge.
(c) Comparison of measured and theoretical (power law) values of steady boundary layer thickness.

Fig. 3. Growth of steady boundary layer.

(a) Variation of measured boundary layer thickness with α for fixed distance, x = 8.0 cm, due to plate thickness and leading edge profile.
(b) Effect of leading edge thickness or unsteady boundary layer.
(c) Effect of leading edge profile on boundary layer growing from leading edge.
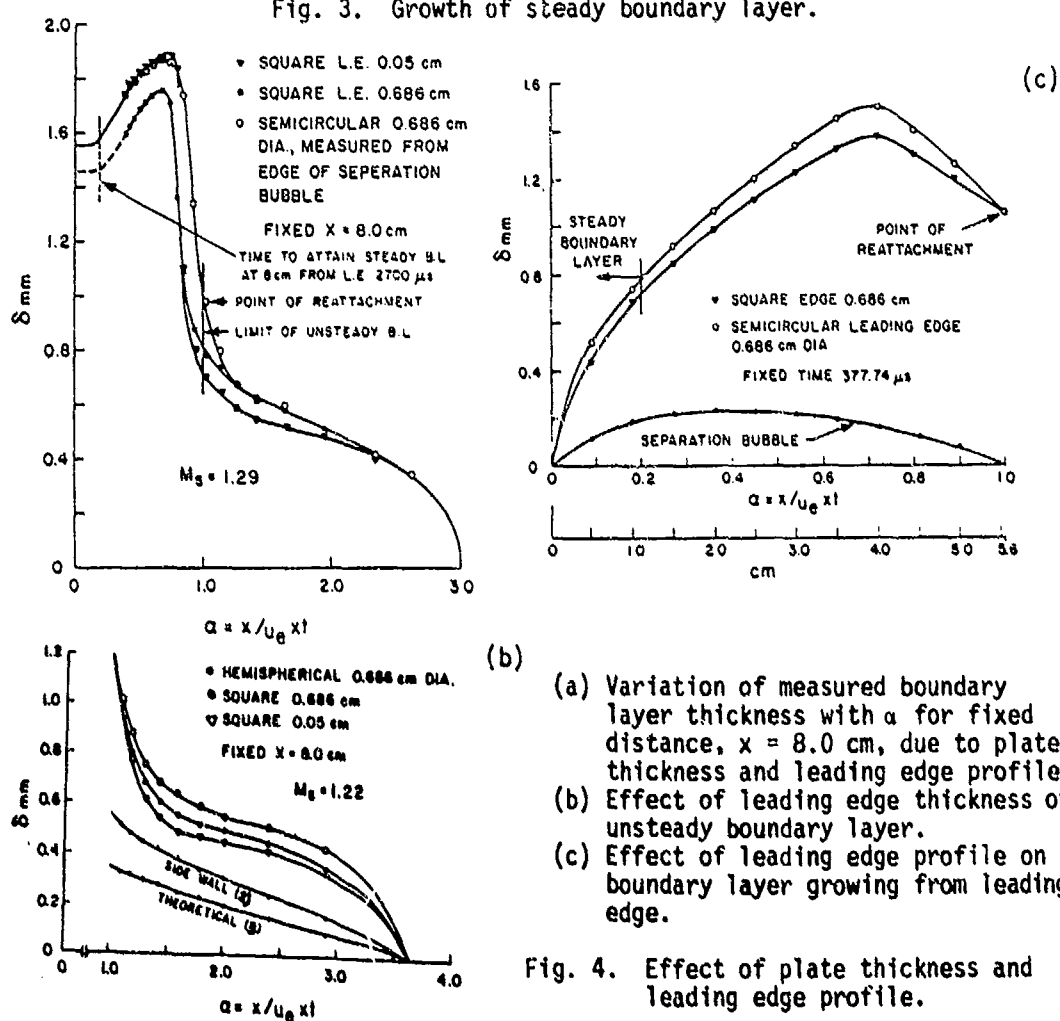
Fig. 4. Effect of plate thickness and leading edge profile.

SHOCK-TUNNEL STUDIES OF SEPARATION AVOIDANCE BY

BOUNDARY-LAYER BLEEDING IN HYPERSONIC FLOW OVER

FLARED BODIES

Lucien Z.Dumitrescu, Steliana Preda

Institute for Aeronautics - INCREST
79622 Bucharest, Romania

In hypersonic flow around flared axisymmetric
bodies or over concave 2D corners, the boundary-
layer separates, distorting the shock pattern
and inducing severe local heating. Providing a
bleed slit for the boundary-layer, at the corner,
stabilizes the flow and diminishes the heating
rate. In a shock-tunnel study, absorption was
produced by connecting the slit to the low-pres-
sure region behind the model base. The shock
became attached to the corner, taking a shape
in agreement with inviscid theory, while the
heat-transfer rate was reduced almost to the
flat-plate value.

INTRODUCTION

Flared bodies are often used in hypersonic vehicles; multi-
stage rockets and the Space Shuttle underside flap are two well-
known examples.
The present study originated some ten years ago in an attempt
to check experimentally a theory put forward by the late Professor
E.Carafoli[1,2],about the shape of the shock produced by axi-symmetric
flared bodies. It was soon found, however, that the boundary-layer
separates so severely under the adverse pressure gradient which
develops in the concave corner, that the shock pattern is complete-
ly distorted. To remove the separation, a boundary-layer bleed was
introduced at the root of the corner; the shock shape checked then
perfectly with theory.
Now, it is well known that, in the separated zone ahead of the
corner, high heat-transfer rates are developing, which could pose
severe insulation problems; the case of the Space Shuttle was dis-
cussed at a preceding Shock Tube Symposium[3]. Therefore, it was
thought interesting to pursue our study, to ascertain whether blee-
ding reduces also the thermal problem; in the following, we report
also on such a series of measurements.

THE EXPERIMENTAL SET-UP

Tests have been carried out in a shock-tunnel built by us and
described elsewhere[4]. It is 6 meters in length and 100 mm ID, and
the maximum charging pressure is 150 atm (air or hydrogen). The
test-section is fitted with reflected-type nozzles for M=4;7 and
10, contoured and conical. As our main purpose was just to validate
the concept, the testing conditions were chosen for easy shock-tun-
nel operation, and are listed in Table 1. In a separate round of

tests, the tunnel was operated as a Ludwieg tube, to increase the Reynolds number (see also Table 1). No significant differences were found, however, in the flow behaviour.

For the flow visualisations, axisymmetric models were used. In order to produce the pressure differential needed to ensure a good removal of the boundary-layer, the slit at the root of the body flare was connected to the low base pressure area, at the open rear end of the model. We note that, in practical applications, a convenient region of low pressures on the body surface has to be found, to which the bleed slit is to be connected, e.g. behind the expansion wave which develops around the outer, convex corner of the body flare.

The heat-transfer measurements were carried out on a 10 deg. wedge model, having its upper surface aligned with the flow; a simple 30 deg. flap was provided, which could leave a variable gap at its root. A thin-film platinum gage was fitted on the model surface, about 5 mm upstream of the corner.

The efficiency of the bleed system in reducing the heating may be judged by comparing directly the gage response recordings. Therefore, no attempt was made to compute the actual heat-transfer rates, which might introduce spurious errors

THE FLOW PATTERN

In figures 1,2,3,typical flow shadowgraphs for flared bodies are shown. At the lower Reynolds numbers and over steeper flares, the separated zone was so extensive that it reached the outer edge, distorting completely the shock (figure 2). A small amount of bleeding (figure 3) removes the separation and stabilizes the shock.

According to Carafoli's inviscid theory, in an axisymmetric configuration like that of figures 1,2,3, the shock should originate at the corner, starting with an angle corresponding to that of an oblique shock over a 2D wedge, and then would slope down gradually to the inclination predicted by conical flow theory. When the proper amount of bleeding is applied, the actual shock shape (e.g. in figure 3) coincides with the theoretical curve, within the resolution of the shadowgraphs.

A limiting case is obtained when the central body is missing altogether (figure 4), with a free passage provided through the model. Then, the shock develops undisturbed, following exactly the theoretical curve. Note that such a configuration might apply, for instance, to a ramjet inlet.

HEAT-TRANSFER RESULTS

In figure 5, oscilloscope recordings of the platinum-film gage response have been redrawn, superimposed, for three cases: A, flat plate (no flap); B, 30 deg. flap, no boundary-layer bleed; C, flap with 2 mm bleed slit.

Clearly, the improvement in heat loading is significant, curve C approaching that for the flat plate. Of course, over the flap itself, the heat-transfer rate is higher, depending on the deflection angle, but the upstream influence can be removed.

ACKNOWLEDGEMENTS

Carafoli (1901-1983), whose life and work have been an inspiration to all his pupils. Thanks are due the Director of our Institute, Dr.Constantin Teodorescu, for his support of our studies in the shock tube field.

REFERENCES

1.   Carafoli, E., Private communication.

2.   Berbente, C., "On a Quasi-Conical Motion in Supersonic-Hyper-sonic Flow, Considering the Entropy Effects", ZAMM, vol.55, 1975, p.589-594.

3.   Walter, S.A., "Shock-induced Flow Separation and the Orbiter Thermal Protection System", p.41-53 in: Treanor, C.E., Hall, J.G., eds: "Shock Tubes and Waves", State University of New York Press, 1982.

4.   Dumitrescu, L.Z., "Studies in Shock Tubes" (in Romanian), Editura Academiei, Bucharest, 1969, p.120.

TABLE 1. OPERATING CONDITIONS OF THE TUNNEL

Operating mode	Shock tunnel		Ludwieg tube
Mach number	4.0	7.0	4.0.
Stagnation pressure, atm abs	15.0	15.0	10.0
Stagnation temperature,degs K	1900.0	1900.0	293.0
Static pressure, torr	75.0	1.06	50.0
Test duration, msecs	4.0	2.0	30.0
Reynolds number/inch $X10^6$	0.4.	0.02	1.0

Figure 1. Flared axi-symmetric body, 40 degs.M=4.0 No bleeding.

Figure 2. Flared body, 90 degs. M=4.0 No bleeding.
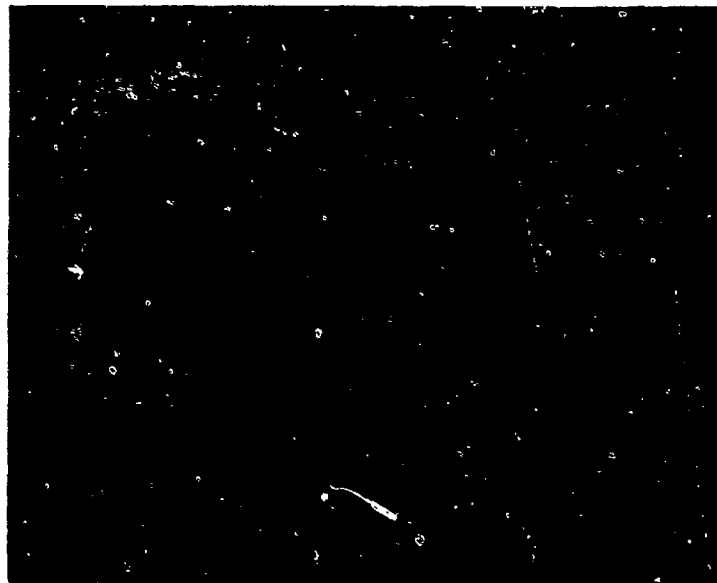
Figure 3. Flared body. 40 degs. N=4.0. Boundary-layer bleed active.
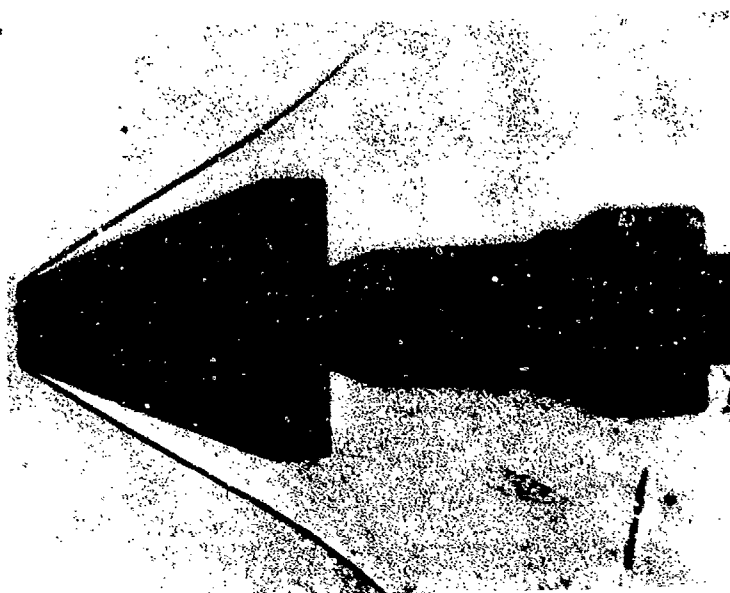
Figure 4. Hollow truncated cone, 40 degs. M=4.0.
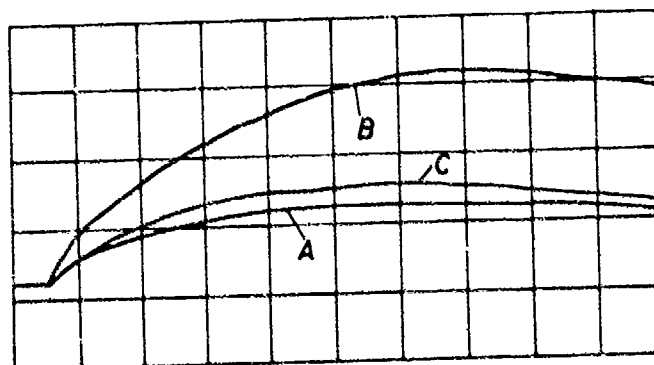
Figure 5. Superimposed heat-transfer gage recordings. Time base, 1 msec/sq. Amplification, 5 mV/div. M=4.0. Concave 2D corner 30 degs, gage position 5 mm upstream. A-flat plate (no flap); B - corner flap, no bleed; C - flap, 2 mm boundary-layer bleed slit.

SHOCK WAVE – LAMINAR BOUNDARY LAYER INTERACTION AT

FINITE SPAN COMPRESSION CORNERS

by R.J. Stalker

Dept. of Mech.Eng., University of Queensland, Brisbane, Australia

and

J. P. Rayner *

Physics Dept., Australian National University, Canberra, Australia

A shock tunnel study is made of the shock wave – laminar boundary
layer interaction occurring at a finite span compression corner.
The tests were conducted with a range of spans, at a corner angle
of 30°, and a test flow stagnation enthalpy of 16 MJ/kg. It
was found that the three dimensional development of the separated
region was not markedly different from that obtained in previous
studies at a test stagnation enthalpy of 1.1 MJ/kg. Also, for two
dimensional flows, a relation which has been developed for pre-
dicting the length of the separated region with adiabatic walls in
supersonic flow was found to remain effective for the high surface
heat transfer, hypervelocity, conditions of the present experiments.

1. INTRODUCTION

The shock-boundary layer interaction at a compression corner, such as that
formed by a flap or control surface on a wing at high speed, is an important
factor in determining the efficiency of such devices. When the corner angle is
large enough the boundary layer separates, and the surface pressure field due
to the corner then comes to depend strongly on the extent of the separated
region.

In very high speed flight situations, such as on the Space Shuttle Orbiter
during re-entry, shock induced laminar separation occurs in the presence of
strong surface cooling, and the extent to which the separated region is
influenced by this takes on special significance.

Of course, the importance of surface cooling effects in shock boundary
layer interaction have been appreciated for some time, and two dimensional
theories have been developed which attempt to account for them. Amongst these,
one due to Hakkinen et al[1] expresses the length of the separated region
for a corner on a flat plate in terms of the formula

$$\frac{\ell}{L}\left[1 - \frac{\ell}{L}\right]^{-.125} = 2.0 \; C_{ps}^{1.5} \; \frac{\rho_e}{\rho^*}\left[\frac{\bar{\mu}}{\mu^*}\right]\left[\frac{\rho_e}{\bar{\rho}}\right]^{.5} \; \frac{C_{pr}}{C_{ps}} + 0.1. \qquad (1)$$

where L is the distance from the plate leading edge to the corner ℓ is the
length of the separated region, measured from the corner, ρ_e, ρ, and ρ^* are
values of density in the freestream, in the separated region, and at the
boundary layer reference enthalpy (i.e. $h^* = 0.5 \; h_e + 0.5 \; h_w + 0.096 \; u_e^2$)
respectively, and μ and μ^* are values of viscosity in the separated region and
at the reference enthalpy. C_{ps} and C_{pr} are the pressure coefficients
corresponding to the pressure rise at separation and reattachment

---

* Now at Physics Dept. Canberra College of Advanced Education, Canberra.
    Australia

respectively, where the pressure coefficient is defined in terms of pressure rise Δp as $C_p = 2 \, \Delta_p / \rho_e u_e^2$. This relation has successfully predicted laminar separated lengths in blowdown supersonic tunnel experiments[1], where the wall temperature approximately equals the freestream stagnation temperature.

In equation (1), the μ and ρ terms both are strongly dependent on temperature in the separated region, showing that, even with fixed pressure coefficients, this temperature has a strong effect on the size of the separated region. Moreover, separating flow over finite span control surfaces and flaps is rarely two dimensional in nature, and there would be an a priori expectation that the separation region temperature would also play a role in the development of three dimensional separated flows.

Thus the shock tunnel study reported here centres on finite span compression corners, at a stagnation enthalpy of 16 MJ/kg. This yields a stagnation enthalpy to wall enthalpy ratio approaching 50, a value which, since it is somewhat in excess of possible expected flight values of 30, should allow any effects of this ratio on separation region temperature to be adequately displayed in the experiments. A corner angle of 30° is chosen, the span of the corner is varied in order to explore three dimensional effects, and the results are compared with previously published results obtained in a hypersonic blowdown facility. Maximum flap spans employed are sufficient to produce two dimensional flow, and so these tests also are used to check the validity of equation (1) for predicting the length of the separated region.

2. EXPERIMENTS

The experiments were conducted in the free piston shock tunnel T3 at the Australian National University[1]. A conical nozzle was used, with an exit diameter of 300 mm, an area ratio of 600, and an included divergence angle of 7.5^o. The model is shown schematically in fig.1. It was 300 mm. wide, in order to fully span the test section, and 165 mm. long, and was mounted at an angle of incidence of 18.5^o. This produced a flow over the plate with a Mach number of 4.0, (based upon a frozen speed of sound with a frozen ratio of specific heats of 1.43) a temperature of 2400 K, a static pressure of 7 kPa, and a unit Reynolds' number of 5.5×10^6 per metre.

Wedges of various spans were mounted on the plate, with the compression corner located at 110 mm. from the leading edge, except when separated region pressure measurements were made. In those cases, the position of the wedge was varied in order to allow complete distributions to be obtained. The face of the wedge ramps was 30 mm. long, which was sufficient to ensure that reattachment occurred on the ramp, rather than at its downstream corner.

Three dimensional flow visualization of the separated region was effected by using radiation from impurities in the test flow. These are predominantly Fe and Cr, corresponding to the material of the walls of the shock tube, and are introduced into the test gas by the vorticity associated with bifurcation of the reflected shock in the shock tube [3,4]. They are present in concentrations of roughly one part per thousand, and radiation measurements indicate that, although they are at their peak concentrations early during the test period, they persist for a millisecond or more afterwards. Time integrated photographs showed that radiation from the separated region was more intense than from the rest of the flow, probably because high impurity concentrations were established in these regions early in the flow process and, due to relatively poor mixing between the separated region and the mainstream, tended to persist whilst mainstream concentrations were decaying. Thus, if the plate was photographed in plan during a run, the outline of the luminous region upstream of the step could be used to indicate the extent of the separated zone.

In addition to the luminosity photographs, some pressure measurements were made in the separated region. Also, a Mach Zehnder interferogram was taken of

the case when a full span corner was used, and the flow was two dimensional. The light source duration and wavelength were 50 μ sec. and 540 mm. respectively, whilst the optical axis was, of course, then parallel to the corner.

3.   RESULTS AND DISCUSSION

(a) Interpreting the Luminosity Photographs

A typical luminosity photograph is shown in fig.2(a). The edge of the luminous region could normally be satisfactorily identified by eye and, where there was difficulty, this was resolved by a microdensitometer traverse, as shown in fig.2(b). However, because the luminosity persisted over a considerable period of time, the significance of the indication provided by the edge of the luminous region was not immediately clear.

As a first step in resolving this difficulty, the position of the luminous edge for a full span corner was compared with an interferogram, taken after steady flow had been established. This is presented in fig.3. It can be seen that the luminous edge occurs approximately 14 mm. downstream of where the boundary layer first shows signs of beginning to be affected by the interaction. Measurements of surface pressure distributions, and the assumption that, following the work of other investigators[4], separation occurs at approximately 60% of the overall separation pressure rise, indicated that the luminous edge occurs 2 to 3 mm. downstream of separation.

A second comparison was made with pressure distributions obtained with a corner of 38 mm. span, as shown in fig.4. In the figure, the same curve is used to fit data at two times after shock reflection, but the pressures obtained at 800 μsec. should be given greatest weight, since it is known that the test flow is contaminated by helium driver gas after approximately 1 millisecond[4]. Again, it can be seen that the luminous edge occurs some 2 or 3 mm. downstream of where separation is expected.

(b) Spanwise Correlation

Thus, having established that the edge of the luminous region correlates approximately with the separation line, the effect of span on the development of the separated region could be determined. This is shown in fig.5.

Fig.5(a) shows the variation of the separated length at midspan as the span is changed. Results are normalized with respect to δ_o, the undisturbed flat plate boundary layer thickness at the corner, which had a value of 2.7 mm. in those experiments. It can be seen that the length of the separated region approaches the two dimensional value as the corner semispan exceeds 10 boundary layer thicknesses. The results also are compared with results obtained by Ball[4] in a heated blowdown tunnel at a Mach number of 6.5, a corner angle of 20°, and a stagnation to wall enthalpy ratio of 2.8. The stagnation temperature was 1100 K. For these results, the distance to the initial pressure rise was measured, rather than the separation point, so only an approximate direct comparison can be made. Nevertheless, they demonstrate that the separated region length increases in roughly the same way as in the present experiments.

Fig.5(b) shows the spanwise development of the separated region. It can be seen that, when the distance upstream of the corner is normalized with respect to the midspan separated length, results for all corner spans collapse onto one curve. The same effect was recorded by Ball. He also correlated his results by fitting them to a cubic curve, and the same type of correlation is seen to be effective here. However, in developing his correlation to take account of Mach number and Reynolds' number changes, and corner angles down to 10°, Ball used an empirical expression for the constant in the cubic which is seen to fail completely in predicting the present results. In fact, the constant which satisfactorily correlates the results is the same as that used by Ball in correlating his results at a corner angle of 20°.

Whilst caution should be exercised in drawing conclusions from comparisons of only two sets of results, it seems possible that the concept of a "free interaction" may assist in explaining their similarity. This concept has arisen in two dimensional shock boundary layer interaction studies, where it has been found that as the length of the separated region increases, the flow near separation becomes independent of the agency provoking separation. With the relatively large corner angle of the present tests, and the 20° tests of Ball, it is plausible that a condition of "free separation" has been reached, and that the relation between three dimensional and two dimensional results is the same under both sets of test conditions.

(c) Length of Separated Region in Two Dimensional Flow

The experiments also provide an opportunity for checking the prediction of two dimensional separated length offered by equation (1). The pressure coefficient after separation, C_{ps}, may be checked from the interferogram in fig.3 by using the turning angle of the separated boundary layer, or the wave angle of the separation shock. Both methods give a value of $C_{ps} = 0.075$, from which, using the 30° angle of the corner, a Newtonian pressure calculation yields $C_{pr} = 0.42$. Returning to the interferogram, the mean fringe shift in the separated region can be measured and, knowing the pressure, used to deduce the temperature there. A value of 2800 K is obtained, which is the same as the boundary layer reference enthalpy temperature for these test conditions. Equation (1) then yields $l/L = 0.37$. This compares with $l/L = 0.23$, as measured from the luminosity indication, or 0.41 as measured to the point in the interferogram at which the boundary layer first shows signs of beginning to be affected by the interaction.

Equation (1) also was used to predict the two dimensional separated length obtained in Ball's experiment, once again taking the separated region temperature to be the boundary layer reference enthalpy temperature. A value of $l/L = 0.54$ was obtained, whereas the measured value, from the corner to the point at which the pressure first starts to rise, was 0.43.

Thus, it appears that equation (1) tends to slightly overestimate the length of the separated region, at least when the reference enthalpy value is used for the separated region temperature. However, the differences are small enough to be neglected as a first approximation.

4. WIND TUNNEL - FLIGHT COMPARISON

It is therefore of interest to use equation (1), with the separated region temperature calculated by the reference enthalpy method, to make a preliminary prediction of the relation between control forces exerted by a flap on a model in a conventional, heated, blowdown hypersonic tunnel, and on a vehicle in hypervelocity flight. To this end, a flat plate was considered, with a flap at its trailing edge deflected by 20°. The flow was considered to be two dimensional for the purposes of the comparison.

The flight flat plate was considered to be 30 m. long, with a surface temperature of 1200 K, flying at an ambient density of 6×10^4 kg. m^3 and a flight Mach number of 20, corresponding to a stagnation enthalpy of 16 MJ/kg. The blowdown tunnel was taken to be operating at $M=12$, with a stagnation temperature of 2000 K, and the test section density was chosen to match the flight Reynolds' number. The separation pressure rise was given by Chapman's relation[.]

$$C_{ps} = 2.1 \ C_{FL}^{0.5} \ (M_e^2 - 1)^{-0.25}$$

with

$$C_{FL} = 0.664 \ (\rho^* \mu^* / \rho_e \mu_e)^{0.5} \ R_{eL}^{-0.5}$$

where R_{eL} is the Reynolds' number based on shock layer conditions and the plate chord L. The reattachment pressure rise C_{pr} was obtained from a Newtonian approximation for $M_e > 4$, and from a linearized Prandtl–Meyer relation for $M_e < 4$. For the flight case, equilibrium real gas flow was assumed in the shock layer.

The control force due to the flap was taken to be proportional to the product of the separated region pressure and length, i.e. $\Delta p_s \ell$, and was normalized with respect to the product of shock layer pressure and chord, i.e. $P_e L$. The resultant variation of this ratio with plate angle of incidence is shown in fig.6, where it is seen that flight and wind tunnel follow curves which, given the approximate nature of the theory, are essentially indistinguishable. That is, the wind tunnel predicts the flight control forces.

5. CONCLUSION

Experimental studies of the shock induced laminar boundary layer separation at a finite span 30° compression corner, with a freestream stagnation enthalpy of 16 MJ/kg, have shown that the three dimensional development of the separated region is similar to that at lower enthalpies, when the two dimensional separated length is used as a reference. The two dimensional separated length itself is predicted approximately by equation (1).

Using equation (1), a comparison between estimated control forces in flight and in a blowdown hypersonic wind tunnel indicated that the wind tunnel would be expected to adequately predict flight control forces in the presence of shock induced laminar separation.

REFERENCES

1.   Hakkinen, R.J., Greber, I., Trilling, L., and Arbarbanel, S.S., Massachusetts Institute of Technology. Tech.Report 57-1, 1957.

2.   Stalker, R.J. "Development of a Hypervelocity Wind Tunnel", The Aeronautical Journal of the Royal Aeronautical Society, Vol.76. June 1972, p.374.

3.   Logan, P.F., "Radiating Argon Flows", Ph.D. Thesis, Australian National University, Canberra, Australia. 1972.

4.   Stalker, R.J., and Crane, K.C.A., "Driver Gas Contamination in a High-Enthalpy Reflected Shock Tunnel", AIAA Journal, Vol.16, March 1978, p.277.

5.   Needham, D.A., "A Heat-Transfer Criterion for the Detection of Incipient Separation in Hypersonic Flow" AIAA Journal, Vol.3, April 1965, p.781.

6   Ball, K.O.W., "Flap Span Effects on Boundary Layer Separation", AIAA Journal, Vol.9, Oct.1971, p.2080.

7.   Chapman, D.R., Kuehn, D.M., and Larson, H.K., "Investigation of Separated Flows in Supersonic and Subsonic Streams with Emphasis on the Effect of Transition", NACA TN 3869, 1957.
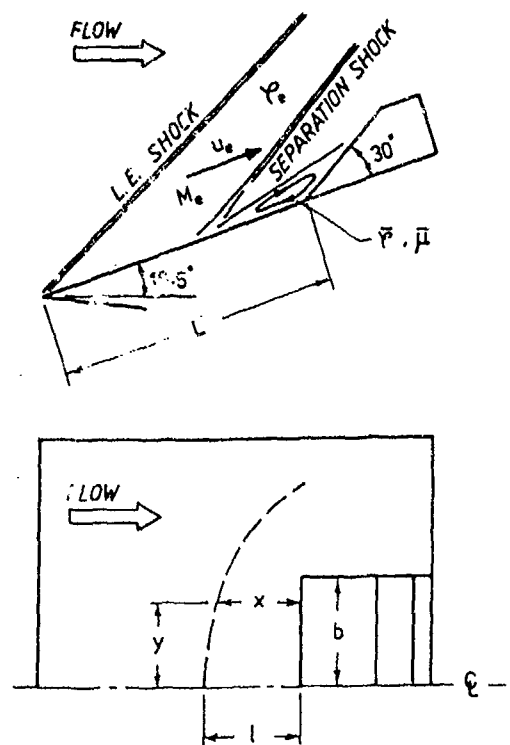
FIG. 1   MODEL DETAIL AND NOTATION

(a)   INTERFEROGRAM   *(900 μsec after shock reflection)*

A.   *Leading Edge Shock.*
B.   *Separation Shock.*
C.   *Separated Boundary Layer*
S.   *Edge of luminous zone in in luminosity photographs*

(b)   MAIN   FEATURES

FIG. 3   TWO DIMENSIONAL SEPARATION

(A)   PHOTOGRAPH OF 64 mm SPAN CORNER
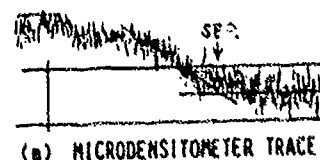
(B)   MICRODENSITOMETER TRACE

FIG. 2   LUMINOSITY MEASUREMENTS
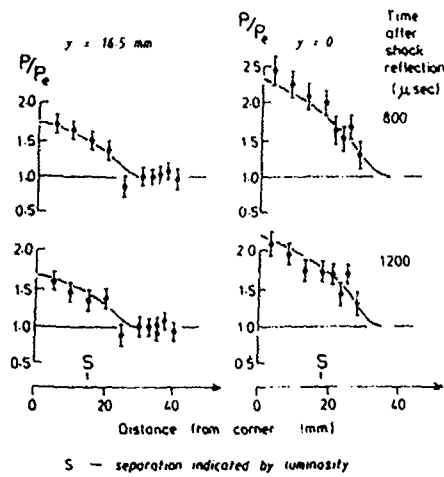
FIG. 4   SURFACE PRESSURE DISTRIBUTIONS
(CORNER 38 MM SPAN)

S — separation indicated by luminosity

(a)   CENTRELINE SEPARATED LENGTH.

$$\left(\frac{y}{b}\right)^3 = 5.5(1 - x/l)$$
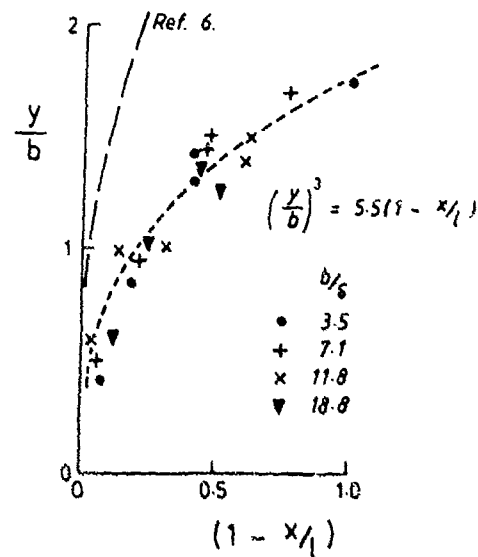
(b)   SPANWISE DISTRIBUTION

FIG. 5   BOUNDARIES OF SEPARATED REGION

FIG. 6   FORCE DUE TO SEPARATION

SHOCK DYNAMICS IN HEATED LAYERS

Mark A. Fry

Science Applications International Corporation
1710 Goodridge Drive
McLean, VA 22102
USA

David L. Book
Naval Research Laboratory
Washington, D.C. 20375
USA

Heated layers in shock tubes or along the surface
of the ground produce dramatic effects upon shock
structure. Besides changing the geometry, additional
triple points and contact discontinuities appear.
Numerical simulation in two and three-dimensions
have been performed to study the interaction of
shocks within heated layers. The heated layer has
been modelled with an underdense layer in pressure
equilibrium. Additionally, the effect of a rigid
structure has been studied.

I. INTRODUCTION

The modified shock geometry and additional gas dynamic
discontinuities that result from shock interaction with heated
layers have been experimentally modelled. In the laboratory,
helium gas can simulate the heated layer. We present numerical
simulations to study the interaction of the shock with this type
of "heated" layer. These results were performed using FAST2D[1].
Moreover, we further complicate the problem by inserting
obstacles such as ramps into the shock tube. This arrangement
produces a 3-D configuration which we have modelled with FAST3D,
a new 3-D numerical code.[1] FAST3D solves the 3-D hydrodynamic
equations for the conservation of mass, momentum and energy of
an ideal fluid using a new Flux Corrected Transport (FCT)
algorithm. The basic finite-difference technique is the fully
three-dimensional leapfrog scheme with no time splitting. The
FCT technique is used to minimize the dispersive errors found at
short wavelengths. The calculations reveal the development of a
weak shock running out ahead of the incident shock. A rollup
along the shock tube wall forms pushing cooler material
underneath the heated layer.

DESIGN AND IMPLEMENTATION OF FAST3D

We describe FAST3D, a code which solves the three-dimensional
hydrodynamic equations. The equations advancing the dependent
variables are

$$\frac{\partial \rho}{\partial t} + \nabla \cdot (\rho v) = 0; \tag{1}$$

$$\frac{\partial (\rho v)}{\partial t} + \nabla \cdot (\rho v v) = -\nabla (P - P_a) - (\rho - \rho_a) G(z); \tag{2}$$

$$\frac{\partial E}{\partial t} + \nabla \cdot (Ev) = \nabla \cdot (Pv) + S - L. \tag{3}$$

To calculate the pressure we employ an equation of state in the form

$$P - P(e, \rho), \tag{4}$$

where $e = E - \frac{1}{2} \rho v^2$. In Eq. (2), the ambient pressure P_a and density ρ_a are subtracted from corresponding time-dependent quantities in the source terms to avoid the "falling sky" problem; $G(z)$, the acceleration due to gravity, is generally taken to be constant at its nominal sea-level value. S and L denote energy sources and losses.

The solution is found by numerically advancing the equations in Cartesian geometry on a rectangular variable-spaced mesh. The basic finite-difference technique is the fully three-dimensional leapfrog scheme with no time splitting. This scheme has very low dissipation, with a linear amplification matrix of unity on a uniform grid, but is subject to a weak (grid separation) instability and large dispersive errors at short wavelengths. These difficulties are overcome by using the Flux-Corrected-Transport (FCT) technique, in which the final solution is made up of the weighted average of a high-order scheme (leapfrog) and a low-order scheme, in this upwind differencing, designed to maintain positivity (monotonicity) where it is required physically. The FCT algorithm is implemented in the code by adding to the leapfrog convective terms a diffusive flux proportional to the absolute velocity, plus a small velocity-independent diffusive term. If P represents any of the dependent fluid variables, the finite-difference scheme used to approximate the left-hand side of Eqs. (1)-(3) is given by

$$P^{td}_{ijk} = P_{ijk} + \frac{\Delta t}{\Delta x} [(Pu)_{i+1} - (Pu)_{i+1}] + \frac{\Delta t}{\Delta x} u_{i+1} (P_{i+1} - P_i)$$

$$\tag{5}$$

$$- \frac{\Delta t}{\Delta x} u_{i-1}(P_i - P_{i-1}) + C(P_{i+1} - 2P_i + P_{i-1}) + \text{other two directions}$$

for the half of the zones which are active at any given time step, and

$$P^{td}_{ijk} = P_{ijk} + (\frac{\Delta t}{\Delta x} u_i + C) (P_{i+1} - 2P_i + P_{i-1}) + \text{other two directions} \tag{6}$$

for the half which are inactive. Here C is a constant used to apply extra diffusion (beyond that needed to ensure positivity in strong-shock problems.

An antidiffusive step is added to the algorithm in timesplit fashion, removing most of the added diffusion. To do this we begin by using the transported diffused momenta and density to calculate an interim velocity in each direction:

$$\bar{u}_i = (\rho u)\,{}^{td}_i / \rho\,{}^{td}_i \ . \tag{7}$$

Then we calculate "raw" antidiffusive fluxes for the active zones,

$$\phi_{i+\frac{1}{2}} = (\ \frac{\Delta t}{\Delta x}\ \bar{u}_{i+1} + C)\ (F^{td}_{i+1} - F^{td}_i)\ \ , \tag{8a}$$

$$\phi_{i-\frac{1}{2}} = [\ \frac{\Delta t}{\Delta x}\ \bar{u}_{i-1} + C]\ (F^{td}_i - F^{td}_{i-1})\ \ , \tag{8b}$$

and the inactive zones,

$$\phi_{i+\frac{1}{2}} = (\ \frac{\Delta t}{\Delta x}\ u_i + C)\ (F^{td}_{i+1} - F^{td}_i\ )\ \ , \tag{9a}$$

$$\phi_{i-\frac{1}{2}} = (\ \frac{\Delta t}{\Delta x}\ \bar{u}_i\ + C)\ (F^{td}_i - F^{td}_{i-1})\ \ . \tag{9b}$$

Using the difference between neighboring values of the transported diffused quantities,

$$\Delta_{i+\frac{1}{2}} = F^{td}_{i+1} - F^{td}_i\ , \tag{10}$$

and the signs of the raw fluxes,

$$S_{i+\frac{1}{2}} = sign(\phi_{i+1/2})\ \ . \tag{11}$$

we calculate the "corrected" fluxes according to the Boris-Book[3] strong flux-limiting formula:

$$\phi^c_{i+\frac{1}{2}} = S_{i+\frac{1}{2}} max\{0, min[\ \phi_{i+\frac{1}{2}}\sigma,\ {}_{i+\frac{1}{2}}\Delta_{i+3/2}, \sigma_{i+\frac{1}{2}}\ {}_{i-\frac{1}{2}}\Delta]\}. \tag{12}$$

These fluxes are then used in the antidiffusion stage to get the new values of the dependent variable:

$$F^{new}_{ijk} = F^{td}_{ijk} + \phi^c_{i-1/2} - \phi^c_{i+1/2} + \text{two other directions.} \tag{13}$$

The flux-correction part of the solution leaves just enough of the low-order scheme to guarantee monotonicity of the solutions. The driving terms [right-hand sides of Eqs. (1)-(3)] can be added in at almost any point in the calculation. Currently this is done following the transport and diffusion in Eq. (5).

The main region of the calculation employs equally spaced zones to maintain high accuracy. The grid, which does not vary in time, may be stretched in regions of little activity or near the edges to reduce the influence of boundary approximations. Either reflecting or outflow boundaries may be applied in the transverse (y and z) directions and a choice of reflecting, outflow, or periodic boundary conditions is available in the longitudinal direction. A variable time step is used based on

the minimum CFL limit in each direction over the whole mesh, Δt < min[$\Delta x/(|v| + c)$, $\Delta y/(|v| + c)$, $\Delta z/(|v| + c)$]. The momentum equation contains a gravity term. A real-gas equation of state is also available for strong shock calculations in air.

For our applications, the shocks and other unsteady phenomena being simulated are initially localized near one end of the system, conventionally taken as the origin of the x axis. At early times it is unnecessary to update variables far from this region, so the number of active zones in this direction is (NX)' < (NX)'$_{max}$. At late time (NX)' increases until the entire mesh is active.

RESULTS

To simulate the shock tube we have used Cartesian geometry with the apropriate boundary conditions. The thermal layer has been modelled by use of a helium gas layer along the bottom of the tube. In Fig. 1 the initial configuration of a planar shock, Mach number 2, is shown. The helium layer is seen along the bottom and is modelled by rows of underdense air three zones high. A computational mesh of NX = 100, NY = 100 was chosen. When the shock waves encounters the helium layer it begins to propagate faster and creates an additional contact surface (discontinuity in density but not pressure). Furthermore, the shock is inclined, moving upward, as one moves away from the shock tube wall. Figure 2 shows the density and pressure contours somewhat later in time. Note the "toeing out" of the shock front into the heated layer. Also, a contact discontinuity begins at the leading edge of this precusor shock and extends back and up toward the triple point. A rollup in density is found behind the location of the incident shock. This is similar in appearance to the rollup produced by planar shocks encountering wedges.[4]

Figure 3 indicates the flow field for a spherical unsteady shock wave interacting with a heated layer ($\rho=\rho_a/6$). Numerous discontinuities result from this heated layer. The additional precursor shocks can be traced to the effective angle of interaction with the surface which is constantly changing. Notice the second triple point back and up from the first. The rollup behind the area where the incident shock would meet the surface is very similar to the planar case. The problem becomes three-dimensional when an obstacle is inserted into the flow. Three dimensional results are shown in Fig. 4. A series of four different density level contour plots, all at the same time, provide a look into the features of interest in the calculations. Starting from left to right, one first sees an outline of the density level $\rho = 5.0 \times 10^{-4}$ g/cm^3 which represents the helium layer. The intersection of the three axes is the origin for the Cartesian frame of reference. The shock wave is moving from the back to the front. The axis parallel to the horizontal is the z axis. Second from left is the density level, $\rho = 2.0 \times 10^{-2}$ g/cm^3, which shows the shock wave impinging on the rigid structure. The plot in the lower right with $\rho = 20$ g/cm^3 and the one in the upper right with $\rho = 1.0 \times 10^{-3}$ g/cm^3, show the structure and the diffraction of the shock over the structure, respectively.

REFERENCES

1. Pyfe, D., Gardner, J., Picone, M., and Fry, M., "Fast Three-dimensional Flux Corrected Transport Code for Highly Resolved Compressible Flow Calculations", 9th International Conference on Numerical Methods in Fluid Dynamics, Paris, June 1984.

2. Fry, M., and Book, D., "Adaptation of Flux Corrected Transport Algorithms for Modeling Dusty Flows", Shock Tubes and Waves, p. 463, New South Wales University Press, 1983.

3. Boris, J., and Book, D., "Solution of Continuity Equations by the Method of Flux Corrected Transport", in Methods in Computational Physics, Vol. 16, 85-129, Academic Press, New York, 1976.

4. Ben-Dor, G., and Glass, I., 1979, J. Fluid Mech. 92, 459-596.
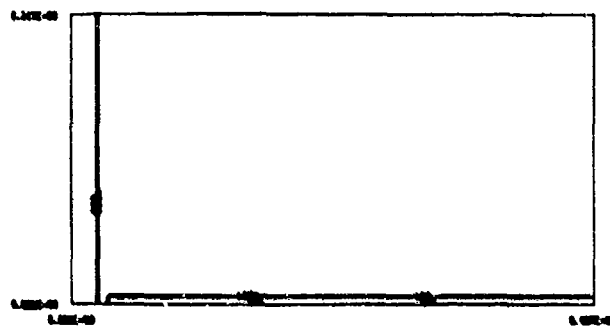
Fig. 1 Initial Conditions for Mach=2 Planar Shock into ambient air and heated layer.
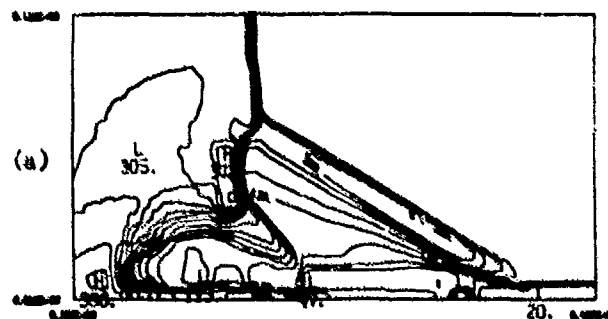
Fig. 2 (a) Density contour levels from 0.2 10^{-3} to 3.0 10^{-3} g/cm^3. (b) Pressure Contours from 0 to 5.1 10^6 $dynes/cm^2$. Enlargement of Mach=2 planar shock.
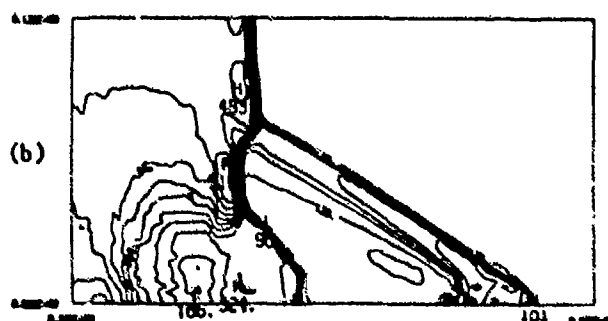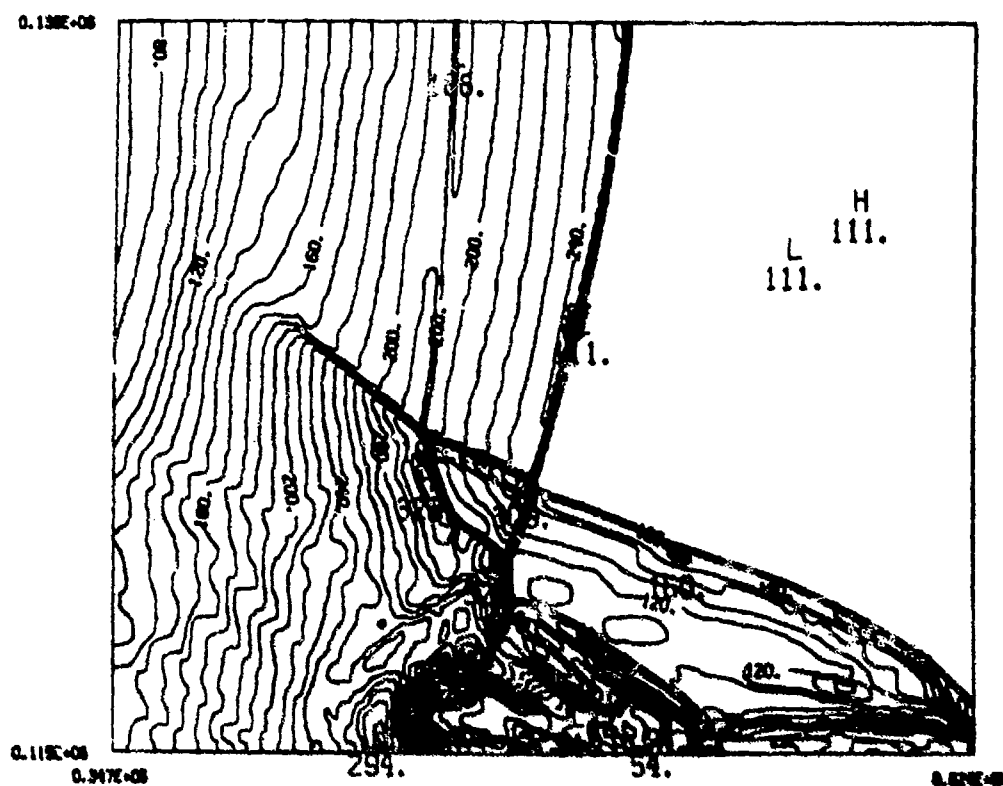
Fig. 3 Spherical blastwave interacting with heated layer. Levels from 0.2 10^{-3} to 3.0 10^{-3} g/cm^3.
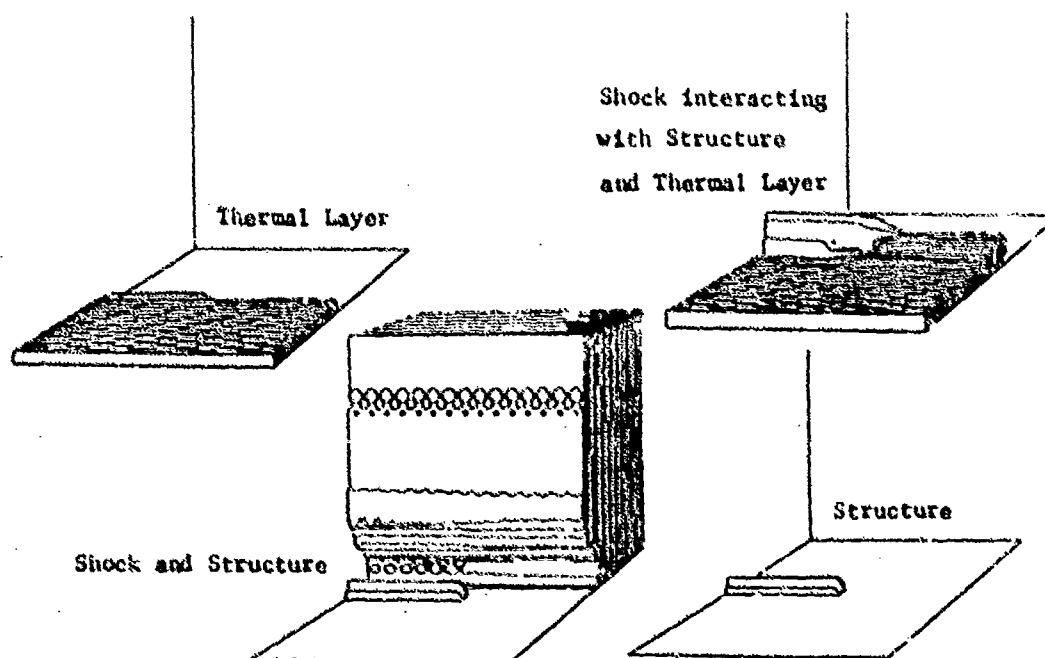
Fig. 4 THREE-DIMENSIONAL GRAPHICS
Shock on structure in heated layer

Rotational Motion Generated by Shock Propagation
Through a Nonuniform Gas

J. M. Picone, J. P. Boris, E. S. Oran, and R. Ahearne*

Laboratory for Computational Physics
U. S. Naval Research Laboratory, Washington, D. C. 20375

*Berkeley Research Associates, Springfield, Virginia

We use numerical solutions of the fluid equations for
conservation of mass, momentum, and energy to study the
interaction of a planar shock with a cylindrical or
spherical helium bubble. The Mach number of the shock
was ≈1.2 in both cases, the ambient gas was air, and the
pressure was 1 atmosphere. The passage of the shock
through a bubble generates vorticity at the boundary of
the bubble. This vorticity produces a jet of ambient gas
through the bubble and as a consequence the vorticity
rolls up into a vortex filament pair (cylindrical bubble)
or a vortex ring (spherical bubble). We discuss the
theoretical treatment of this nonlinear interaction of
the vorticity with itself and the relationship to
impulsive Rayleigh-Taylor instability theory. We relate
our results to recent experiments of Haas.

I. INTRODUCTION

The propagation of a shock through a nonuniform gas will result in
diffraction and reflection of the shock wave at the locations of the
inhomogeneities which are present. Such deviations from global symmetry will
certainly affect the transmission of energy through the gas. In addition, the
interactions of pressure waves with density fluctuations in a fluid are a major
source of vorticity and turbulent motion[1]. These rotational flows can have
important effects, for example, on the operation of ramjet engines[2], the
efficiency of inertial confinement fusion[3], and the rate at which lightning
channels cool[4].

Shock tube experiments have been the major source of data on the
generation of rotational motion by the interaction of shocks with inhomogeneous
gases. Particularly noteworthy are the studies of shock propagation
through flames by Markstein[2] and the recent work of Haas[5-7] on shock-bubble
interactions. The data of Haas are extensive and permit detailed comparison
with the numerical simulations which form the basis of this paper. The ambient
gas was air, and the bubble was filled with either helium or freon. Haas
studied geometrical factors by using bubbles which were cylindrical or spherical
in shape. Both of the authors noted the appearance of a vortex ring in the
axisymmetric geometry (spherical bubble), but the presence of vortex structures
was initially more difficult to discern in schlieren photographs of the
cylindrical bubble experiments[5]. In addition, Markstein[2] and Haas[5,6] used
linearized Rayleigh-Taylor instability theory to analyze the behavior of the
nonuniformity (the flame or bubble) after passage of the shock.

Recently Picone et al. have developed a nonlinear theory of shock-generated
vorticity[1,8] and applied the theory to the experiments of Markstein[8]. The
basis for the theory is the equation

$$\frac{d\,\underset{\sim}{\omega}}{dt} + \omega \, \Sigma \cdot \underset{\sim}{v} - \omega \cdot \Sigma \, \underset{\sim}{v} + (\Sigma\rho \times \Sigma P)/\rho^2 \qquad (1)$$

which governs the evolution of the vorticity $\underset{\sim}{\omega}$. Here the fluid velocity is $\underset{\sim}{v}$; the pressure is P; and the mass density is ρ. As shown by eq. (1), misalignment of the local pressure and density will lead to a nonzero source term

$$\underset{\sim}{S} \equiv (\Sigma\rho \times \Sigma P)/\rho^2 \qquad (2)$$

for the generation of vorticity. Numerical simulations[8] of Markstein's experiment on the interaction of a planar shock with a spherical flame assumed a smoothly varying radial density distribution for the flame rather than the steep gradients which we would expect at the edge of a flame or a bubble. Both the theory and the simulations showed that the evolution of the system is inherently nonlinear. The timescales of the simulations agreed closely with the experimental timescales.

In this paper, we present numerical simulations similar to the experiments of Haas on interactions of a shock with a cylindrical or spherical helium bubble. These calculations include the steep density gradients at the edge of the bubble; however, we have not accounted for the effects of surface tension. Section II discusses the computer model and procedures which we have used, and section III follows with our results. In the last section, we relate the shock-bubble interaction to the situation which is usually discussed in terms of linear, impulsive Rayleigh-Taylor theory.

II. NUMERICAL MODEL

We have used the FAST2D computer code[1,9] to simulate the experiments of Haas. The algorithm employs time-step splitting in conjunction with flux-corrected transport (FCT)[10] to solve the fluid equations for conservation of mass, momentum, and energy. The FCT algorithm is state-of-the-art in treating supersonic compressible flows involving discontinuities like shocks. In the region of a discontinuity, FCT uses a low order, diffusive scheme to integrate the conservation equations. The algorithm then transitions nonlinearly to a high-order scheme as the distance from the discontinuity increases. In this way, the numerical method remains stable in the vicinity of a discontinuity while maintaining high-order accuracy in cells which do not contain shocks and which constitute the vast majority of cells in the calculation. The FCT algorithm does suppress short wavelength (around two cells or less) variations and can offer a limited treatment of a fully developed turbulent field. In this paper, we will be concerned only with large scale rotational motion, which contains most of the energy and which FCT treats very accurately. The FAST2D code has produced excellent agreement with data from a variety of experiments, including studies of shock reflections from wedges in nonreactive fluids[9] and studies of detonation cell structure, in which the reactive chemistry was modeled[11].

We simulated a two-dimensional cross section of the cylindrical bubble case by using Cartesian coordinates. The x-axis was horizontal and the y-axis was vertical, as shown in Figs. 1 and 2. The calculation thus corresponded to a planar shock interacting with an infinitely long cylindrical bubble, the axis of which was perpendicular to the shock tube axis. The shock tube in the experiments was horizontal. Because the upper half of the system is a mirror image of the lower half, we simulated only the upper half by using reflecting conditions at the lower boundary of the computational grid. The lower boundary then coincided with the shock tube axis. We also used reflecting conditions at the upper boundary to simulate the shock tube wall. At the left boundary, from

which the shock propagated, we used uniform inflow boundary conditions with parameter values given by the Rankine-Hugoniot equations for a planar, uniform shock with the experimental Mach number (M = 1.23). At each time step we set the flow parameter values at the right boundary equal to those at the rightmost column of cells in the computational grid. This allowed us to model trans- mission of the shock out of the grid after the interaction with the bubble was complete.

We used cylindrical coordinates (r,z) to treat the case of the planar shock interacting with a spherical bubble. As shown in Figs. 3 and 4, the z- axis coincided with the axis of the shock tube, and the r-axis was vertical. We simulated only the upper half of the system, and because of the azimuthal symmetry about the z-axis, the semicircle in Fig. 3 represents a cross section (great circle) of a sphere. The boundary conditions were the same as those described in the previous paragraph for the cylindrical bubble case. Notice that, in the case of the cylindrical bubble, the simulation treats the shock tube as having an infinite slab geometry with the infinite dimension perpendicular to the computational grid. In the axisymmetric case (spherical bubble), the shock tube is a cylinder. Since Haas's test section had a square cross section, we do not model properly the effects of shock waves which reflect from the test section walls, producing secondary interactions with the bubble.

The representation of a bubble on the differencing grid required some care, since the bounding surface could not be as smooth as in the experiment. The simulated bubble had a jagged boundary characteristic of the rectangular cells of the grid. If the boundary were too irregular, the impulsive Rayleigh- Taylor[2] (or Richtmyer-Meshkov[12, 13]) instability could be induced by passage of the shock through the surface. However, this instability would not interfere quickly with the large scale flows in which we are interested. To reduce the irregularity of the bubble surface, we did the following:

(1) We imbedded a region of small grid cells in the computational grid at the location of the bubble. This fine grid moved with the bubble to maintain the necessary resolution of the bubble boundary. At the edges of the fine grid, the cell dimensions transitioned smoothly to those of the remaining coarse cells. This insured the numerical stability of the FCT algorithm throughout the grid.

(2) We interpolated carefully between the ambient density and the density of the gas in the bubble for the cells through which the bubble boundary passed. The interpolation depended on the fraction of boundary cell area which fell inside the bubble radius.

(3) A diffusive smoothing technique spread the boundary over approximately two cells.

The thicker boundary eliminated the Richtmyer-Meshkov instability from the simulations of the helium bubbles. When these techniques were not used, we observed slow linear growth of a small numerically induced ripple at the downstream edge of the bubble near the shock tube axis.

III. RESULTS OF NUMERICAL SIMULATIONS

Figures 1 and 2 show density and vorticity contour diagrams for the interaction of a planar shock of Mach number M = 1.23 with a cylindrical helium bubble of diameter D = 51 mm. The vertical dimension of the simulated shock tube is 8.9 cm while the dimension perpendicular to the figure is infinite. In the experiment of Haas, the test section had a square cross section which was

8.9 cm on a side. The density of the gas inside the bubble was 0.214 x 10^{-3} g/cm^3, which fell in the middle of the range of densities used by Haas. The density of the ambient gas was 1.29 x 10^{-3} g/cm^3 and the pressure was 1 atm. The Cartesian grid consisted of 150 x 50 cells, of which there were 50 coarse cells of dimensions $\Delta x = 0.422$ cm and $\Delta y = 0.089$ cm and 100 fine cells of dimension 0.089 cm on a side. We used a ratio of specific heats $\gamma = 1.4$.

We see from the vorticity contour diagrams that, in the upper half of the system, positive vorticity is produced along the edge of the bubble, excluding the portions near the axis of the shock tube (x-axis) where the pressure gradient of the shock and the density gradient at the edge of the bubble are aligned. By symmetry, we know that negative vorticity resides along the lower interface of the bubble with the ambient gas. The associated rotational motion pulls a jet of ambient gas through the center of the bubble. As the bubble deforms, the vorticity distribution rolls up with the fluid to form a vortex filament pair. This nonlinear self-interaction of the vorticity field causes the emergence of recognizable vortex structures in the fluid after the shock interacts with a local nonuniformity (e.g., a bubble). Notice that the presence of the vortex filament is readily discernable from the vorticity contour plot while the density contours do not clearly indicate the presence of the filament. Since the experiments of Haas show only features of the density distribution and because the filaments do not separate clearly from the bubble (Fig. 1), the evolution of the jet was not easily understood from the experimental data.[5-7]

The density contour diagrams show the features visible in experimental schlieren photographs.[6,7] (We remark that our figure represents a slice through the experimental device while experimental photos would show a two-dimensional projection of the three-dimensional density distribution.) The rarefaction wave produced by the acceleration of the shock through the bubble is visible, as is the similarity of the front of the jet to an arrow head. The curvature of the shock during passage through the bubble is as expected. Finally the timescales of the phenomena are in good agreement with the data of Haas. As anticipated, we do not see a cascade to small scale turbulence in our computer simulations. The characteristic velocities of the jet, the upstream edge of the bubble, and the vortex filaments are in good agreement with experiment.

Figures 3 and 4 show density and vorticity contour diagrams for the case of a planar shock (M = 1.25) passing through the upper half of a spherical bubble (D = 45mm) filled with helium. As predicted by Eq. (1), the shock again produces vorticity at the interface of the bubble with the ambient air. The associated rotational fluid motion causes a fluid jet through the bubble and rolls the vorticity into a vortex ring. This represents a nonlinear interaction of the vorticity with itself as mediated by the fluid. In contrast to the cylindrical bubble case, the roll-up is faster and tighter, producing higher velocities. Consequently, the vortex ring propagates more quickly from the remainder of the bubble, and appears prominently in the density contour diagrams. However, the vorticity dynamics that lead to the vortex ring formation and separation from the bubble were difficult to ascertain from the density contours alone. The characteristic velocities agreed well with the experimentally measured velocities.

IV. RELATIONSHIP TO RAYLEIGH-TAYLOR INSTABILITY

The conventional Rayleigh-Taylor instability theory begins with an infinitesimal spatial perturbation which exists for a long (infinite) period of time relative to the growth rate of the perturbation. In a previous paper [8], we pointed out that the source term of the vorticity evolution equation, Eq. (2),

provides the generalization of the usual notion of Rayleigh-Taylor instability to the entire conceivable range of space and time scales and geometry of a perturbation. In particular the problem which we consider in this paper consists of a finite "perturbation" (the bubble) and a finite time scale over which vorticity is produced (the time for shock passage through the bubble). The bubble introduces another difference from the usual picture, since the perturbation is not sinusoidal. This is a fundamental departure from the impulsive Rayleigh-Taylor or Richtmyer-Meshkov instability [12,13], in which a planar shock passes through a rippled interface or a perturbed shock passes through a planar interface. Such a system can initially show linear growth. In contrast, the shock-bubble interaction with the subsequent flow field evolution represents a nonlinear process from the beginning, as we have discussed above. We mention arguments that the linear theory can be made to fit this situation by having a sinusoidal "perturbation" of of wavelength $2\pi R$ (R = bubble radius) concide with the side of the bubble facing the shock. However, as shown by the simulation, the distortion of the upstream edge of the bubble has an apparent wavelength of about $(4/3)R$. Hence the choice of wavelength for the linear theory is ambiguous. Integrating over the impulsive, nonlinear source of vorticity and following the subsequent vorticity evolution has proved to be quantitatively correct.

V. ACKNOWLEDGEMENTS

REFERENCES

1. J. M. Picone and J. P. Boris, Phys. Fluids 26 (2), 365 (1983).
2. G. H. Markstein in Nonsteady Flame Propagation, AGARDograph No. 75, (Pergamon Press, Oxford, 1964), pp. 75-100.
3. M. H. Emery, J. H. Gardner, and J. P. Boris, Phys. Fluids 27 (5), 1338 (1984).
4. J. M. Picone, J. P. Boris, J. R. Greig, M. Raleigh, and R. F. Fernsler, J. Atmos. Sci. 38 (9), 2056 (1981).
5. J.-F. L. Haas, Bull. Am. Phys. Soc. 28 (9), 1359 (1983).
6. J.-F. L. Haas, Ph.D. Thesis (California Institute of Technology, (1984).
7. J.-F. L. Haas, J. Fluid Mech., to be published.
8. J. M. Picone, E. S. Oran, J. P. Boris, and T. R. Young, Jr., in Dynamics of Shock Waves, Explosions, and Detonations, (AIAA, New York, 1985), pp. 429-448.
9. D.L. Book, J.P. Boris, A.L. Kuhl, E.S. Oran, J.M. Picone, and S.T. Zalesak, in Proceedings of the Seventh International Conference on Numerical Methods in Fluid Dynamics (Springer-Verlag, New York, 1981), pp. 84 - 90.
10. J.P. Boris and D.L. Book, Methods in Computational Physics; Vol. 16 (Academic Press, New York, 1976), pp. 85 - 129.
11. E.S. Oran, T.R. Young, J.P. Boris, J.M. Picone, and D.H. Edwards, in Proceedings of the Nineteenth Symposium (International) on Combustion (The Combustion Institute, Pittsburgh, 1983), pp. 573 - 582.
12. R.D. Richtmyer, Commun. Pure Appl. Math. 13, 297 (1960).
13. Y.Y. Meshkov, NASA Tech. Trans. NASA TTF-13, 074 (1970).
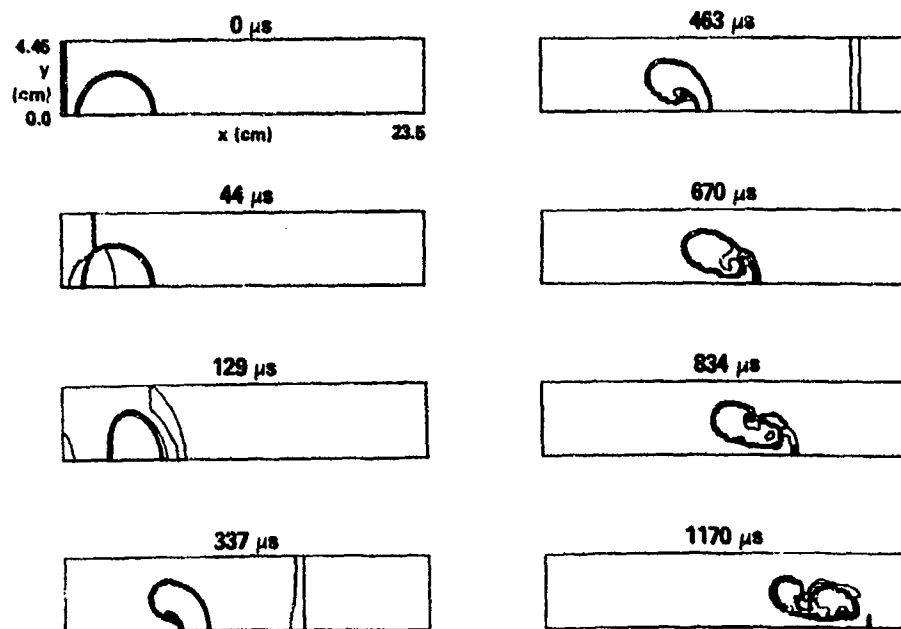
Fig. 1.   Density contours for a planar shock interacting with a cylindrical helium bubble.   The 6 contours are evenly spaced over the range from 2.2×10^{-4} to 1.62×10^{-3} g/cm^3.
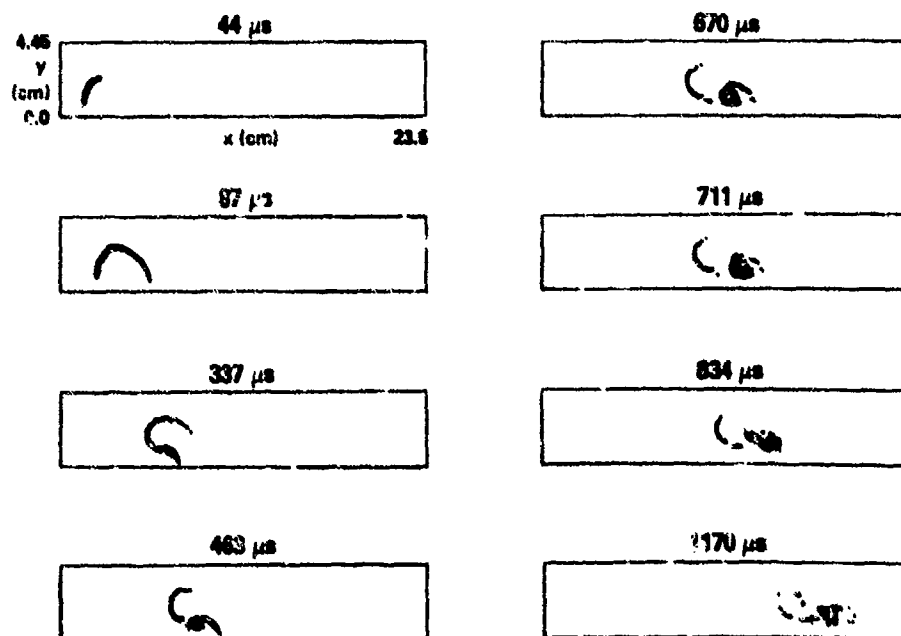
Fig. 2.   Vorticity contours for the cylindrical bubble case of Fig. 1.   Range: 6 contours from 2.0×10^4 to 8.0×10^4 s^{-1}.
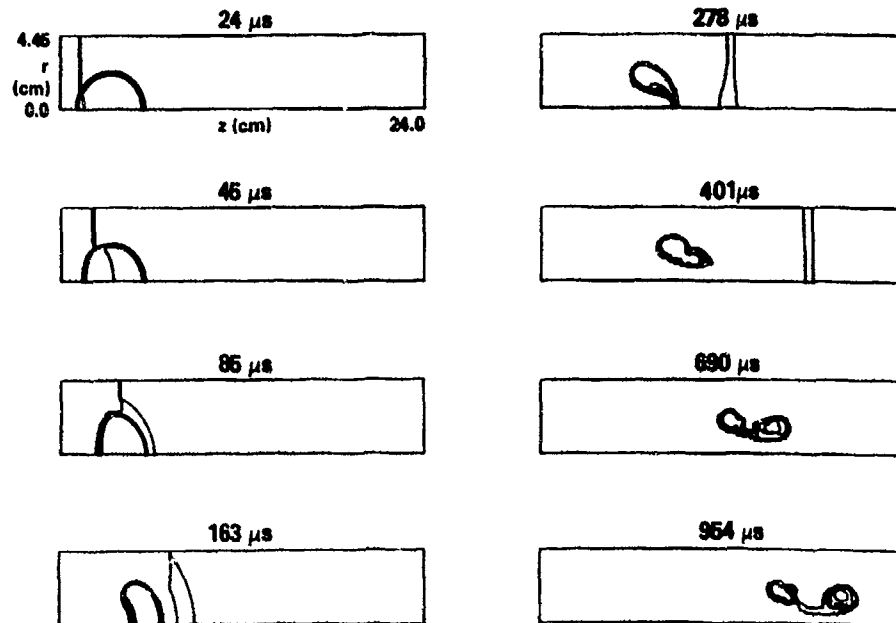
Fig. 3. Density contours for a planar shock interacting with a spherical helium bubble. Range: 6 contours from 2.2×10^{-4} to 1.62×10^{-3} g/cm^3.
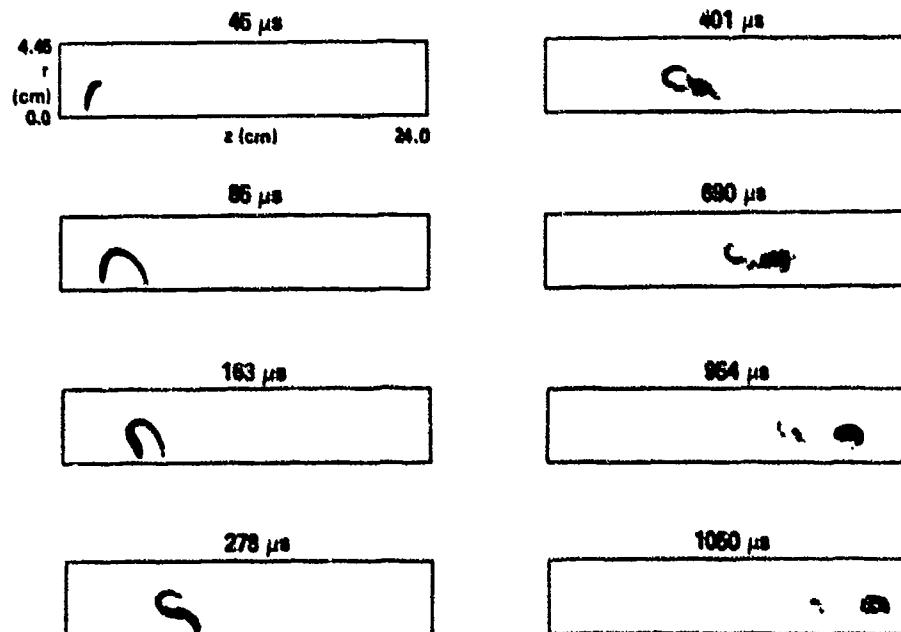
Fig. 4. Vorticity contours for the spherical bubble case of Fig. 3. Range: 6 contours from 2.0×10^4 to 8.0×10^4 s^{-1}.

Part VI
Experimental Methods

A METHOD FOR PERFORMING OBLIQUE SHOCK-BOW SHOCK INTERACTION IN DOUBLE DRIVER SHOCK TUBE(TUNNEL)

Z.Y.Han, Z.Q.Wang, X.Z.Yin, J.C.Yao, A.D.Du and K.Wang

Department of Modern Mechanics
University of Science & Technology of China
Hefei, Anhui
The People's Republic of China

Based on discussing and analysing the two types
of experiments for performing oblique shock-bow
shock interaction, a new method in a double driver
shock tube(tunnel) is presented. This method can
not only form a planar moving shock for making
oblique interaction, but also record the transient
pressure on the surface of a testing model and take
the photographs simultaneously. This method can
be used to study the transition between regular
and Mach reflection of a moving shock with a quasi-
stationary flow ahead of it on the surface of a
flat wedge or a cone. An improved method for measuring
moving shock Mach number is presented.

INTERACTION

Oblique shock- bow shock interaction is an important research task for gasdynamics and shockdynamics.

There are two types of experiments that can be used to perform oblique shock-bow shock interaction. One is so-called `moving model' experiments, the other is so-called `stationary(fixed) model' experiments. The experiments made by Merritt and Aronson(ref.1),Nicholson (ref.2)belong to the former and those made by Bingham(ref.3), Miller(ref.4) belong to the latter.

For the`moving model'experiments, a planar moving shock can be obtained, but it is difficult to directly measure the transient pressure on the surface of a moving testing model.

For the `stationary model'experiments, it is convenient to obtain the transient pressure on the surface of stationary(fixed) model by using pressure transducer, but it is difficult to generate a planar moving shock for making oblique interaction with a bow shock. It seems that if a shock tube inserts in the test section of a supersonic or hypersonic wind tunnel making at a desired angle with the axis of testing model, the oblique shock-bow shock interaction can be obtained. But the deformity of planar moving shock occurs when it moves out of the shock tube.

As a result, a rocket-propelled sled test, an oblique inter-action of a blast wave with a rocket-propelled sled travelling supersonic speeds, had been made by Ruetenik and Anon(ref.5) for recording the signal of transient pressure on the surface of the moving model, but it is too costly. In addition, it is hardly

to obtain the photographs of the oblique interaction.
Preceding two types of experiments are shown in Fig.1.

Our purpose is to find a new method for performing oblique
shock-bow shock interaction over a stationary model in a double
driver shock tube and shock tunnel.
This method can not only obtain a planar moving shock for
making oblique interaction with the bow shock attached to testing
model, but also record the transient pressure on the surface of
the model and take the photographs simultaneously.
In this paper, based on the experimental technique of electri-
cally controlled double driver shock tube(ref.6) and the oblique
interaction of a planar moving shock with the bow shock attached
to a stationary testing model in a double driver shock tube(ref.7),
an improved method for making interaction in a double driver shock
tunnel is presented.

EXPERIMENTAL METHOD AND FACILITY

The experiments were conducted in a conventional straight-
through shock tunnel. The driver section is 7.0m long with 140mm
i.d.. The driven section is 9.0m long with 106mm i.d.. The conical
nozzle is connected to the end of the driven section, its semi-
vertex angle is 7° and its exit diameter is 430mm. The testing
cross section is 500mm by 500mm.
In order to describe this method, the explanation of the double
driver shock tube and the oblique interaction in it is made.
1.   The Double Driver Shock Tube

In order to perform shock-shock interaction, it is necessary
to make some change in the shock tube, the tube can be divided
into three parts, the driver section, the intermediate section
and driven section. The driver section is 7.0m long, the inter-
mediate section is 5.2m long, the driven section is 4.0m long.An
aluminum diaphragm is between the driver section and the inter-
mediate section. The mylar diaphragm is between the intermediate
section and the driven section.
The diaphragms could be ruptured in two ways. One was sponta-
neous bursting for the aluminum diaphragm. The other was electrical
discharge bursting for the mylar diaphragm.
The wave patterns in the double driver shock tube are described
as follows(as shown in Fig.2):
As soon as the aluminum diaphragm is ruptured, a moving shock
will form (We call it second shock). When the moving shock just
arrives at the location where a piezo-electrical transducer is
mounted on, a voltage signal occurs on it. The signal is fed to
a delay circuit and then makes the high voltage capacitors discharge
through an explosion wire on the surface of the mylar diaphragm
and the diaphragm is ruptured. Thus, an another shock forms(We
call it first shock). At the same time, in opposite direction,
a rarefaction wave forms. The second shock firstly transmits the
region of the rarefaction wave and interacts with it, then inter-
acts with a contact surface and a transmitted shock forms. Thus,
the first shock is directly followed by the second shock.
The first shock is to establish the supersonic flow field
around the testing model in the test section of the shock tube
and makes the model form a bow shock. The second shock is used
as a planar moving shock for making head-on interaction with the

bow shock sttached to the model.

So-called head-on interaction is that the angle between the normal of moving shock front and the axis of testing model, β is equal to zero. This is a special case. In more general case, the angle β is not equal to zero, which corresponds to oblique interaction. The angle β is refered to as angle of interaction.

2.   Oblique Interaction in Double Driver Shock Tube

In order to perform an oblique interaction of a planar moving shock with bow shock attached to a stationary model in the double driver shock tube, a flat wedge can be used for deflecting the flow and planar moving shock. The wedge is placed and mounted in the test section instead of the original testing model.

Firstly, a head-on interaction of the planar moving shock with the bow shock attached to the wedge is made(as shown in Fig.3a) That is, a parallel supersonic flow behind the first shock passes through the wedge with a semi-vertex angle δ and makes the wedge form a planar oblique shock. Thus, the supersonic flow is deflected an angle δ through the oblique bow shock front. When a planar moving shock(i.e. the second shock) impings the wedge, the head-on interaction of the moving shock with the bow shock attached to the wedge occurs and a planar transmitted shock forms,which makes at an angle η with the original planar moving shock.

Secondly, an oblique interaction of the planar transmitted shock with the bow shock attached to a testing model is made(as shown in Fig.3b,3c). That is, the testing model is placed into the flow flied behind the oblique shock front and fixed on a sting mounted on the surface of the wedge to make the axis of the model parallel to the surface of the wedge towards the direction of the flow(i.e. the angle of attack is equal to zero.) and a bow shock forms at the stationary model.

If the planar transmitted shock is used as a new moving shock for making oblique interaction and the moving shock impings the testing model, the oblique interaction occurs.

The transmitted shock Mach number is denoted by Ms. The flow Mach number is denoted by M_∞. The following relations can be obtained:

$$Ms = (Ms_1 + M_1) \cdot \frac{\cos(\theta + \eta)}{\cos\theta} \cdot \frac{a_1}{a_4} - M_\infty \cos(\eta + \delta) \tag{1}$$

$$M_\infty = \frac{1}{\sin(\theta - \delta)} \cdot \left(\frac{1 + \frac{\gamma-1}{2}M_1^2 \sin^2\theta}{\gamma M_1^2 \sin^2\theta - \frac{\gamma-1}{2}} \right)^{\frac{1}{2}} \tag{2}$$

$$\beta = \eta + \delta \tag{3}$$

where a_1 and a_4 is the sonic speeds in region(1) and region(2); M_{s_1} and M_1 the moving shock Mach number and flow Mach number in region(1) respectively; θ is the angle of the bow shock attached to the wedge. η is the deflected angle of moving shock. δ is the semi-vertex angle of the wedge.

$$\eta = f(Ms , M_1 , \delta)$$

Here, neglecting the calculation of angle η .

3.   Oblique Interaction in Double Driver Shock Tunnel

Our purpose is to investigate the transition between regular

and Mach reflection of a moving shock over a wedge or a cone, it is necessary to change the angle ß under the condition keeping Ms and M_∞ unchanged (at least, approximately unchanged).

However, in above oblique experiments in the shock tube, it is impossible to change the angle ß under the preceding conditions, this is because to change the angle ß, it is necessary to change the wedge angle δ, which will make flow Mach number M_∞ change. to overcome this difficulty, an improved method is presented here. The basic idea explains as follows:

When the second shock moves out of the conical nozzle, the moving shock front becomes a curved surface(near a spherical surface with a large radius of curvature). If the curvature of the shock front can be used, the angle ß can be changed under the wedge angle given(that is, keeping Ms and M_∞ approximately unchanged) By means of moving the wedge along the direction parallel to the viewing window and perpendicular to the axis of the nozzle, the angle ß can be changed under the wedge angle given(as shown in Fig.4).

When the wedge moves up from its lowest position, the angle β_1 from $\beta_1 > 0$ to $\beta_1 < 0$. We have

$$\beta = \eta (Ms_1, M_1, \delta, \beta_1) + \delta \qquad (4)$$

It follows from relation(4) that the angle ß can be changed by means of changing the angle β_1 under Ms, M_1, δ given.

The shock Mach number Ms can be represented below:

$$Ms = (Ms_1 + M_1 \cos \beta_1) \cdot \frac{a_1}{a_2} \cdot \frac{\cos(\theta + \beta_1 + \eta)}{\cos(\theta + \beta_1)} - M_\infty \cos(\beta_1 + \eta + \delta) \qquad (5)$$

The flow Mach number M_∞ relation is the same as relation (2).

In order to avoid or weaken the influence of the non-uniform of the flow field between the bow shock and the surface of the wedge on the experimental results, a small testing model(only 50mm long) was used and placed in the plane perpendicular to the surface of wedge through its median.

An apparatus along which the wedge can be slided up and down is shown in Fig.5.

MEASUREMENT TECHNIQUE

The parameters to be measured in this experiment includes the moving shock Mach number Ms, the flow Mach number M_∞, the angle ß and the pressure ratio across incident shock and reflected shock on the surface of the testing model.

Measuring Ms is more difficult, this is because there is a flow ahead of the moving shock. Based on Miller's method(ref.4), an improved method is explained as follows:

A spark gap element was mounted somewhere over the surface of the wedge (as shown in Fig.6). When the moving shock to be measured arrives at the wedge and triggers the detector below the wedge, a voltage signal occurs on it. It makes the spark gap in the flow field inside the test section discharge. At the same time, the voltage signal is fed to a delay circuit and makes the double spark light source of a schlieren system outside the test section discharge, a schlieren photograph can be obtained. If the distance (L) between the centres of first and second circle, the distance(Ls) between successive two shocks and incident angle θ can be obtained, Ms can be calculated according to the following relation.

$$Ms=M_\infty(Ls/L -\sin\theta_i)$$

(6)

A Measurement system for recording the transient pressure and taking schlieren photographs is shown in Fig.7. The M_∞ and the angle ß can be measured on the schlieren photographs.

The transient pressure on the surface of the model can be measured using piezo-electrical transducer. Because the testing model is small and the time of the interaction is very short, a miniaturized and fast response pressure transducer is required. According to above requirements, a kind of miniaturized transducer with 4mm diameter and 5mm long was made by ourselves,its rise time is about 1.2 micro-seconds.

RESULTS AND DISCUSSION

The experiments were conducted in the following conditions:

case1: the pressures in region(1),(4),(5) of the shock tube
were 118 torr, 4.0 kg/cm², 16.0 kg/cm² respectively.
The intermediate section was filled with 30% N_2 -70% H_2
mixture. H_2 is driver gas, N_2 is driven gas.

case2: the pressures in region(1),(4),(5) of the shock tube
were 80 torr, 4.0 kg/cm², 16.0 kg/cm² respectively.
The intermediate section was filled with 50% N_2 -50% H_2
Mixture. H_2 is driver gas, N_2 is driven gas.

An 18°wedge was used.The angle ß from 24°to32°could be obtained.

The experiments of the transition between regular and Mach reflection of a moving shock with a flow ahead of it on the surface of a cone have been made in this facility. Fig.8 and Fig.9 show the regular and Mach reflection of a moving shock on the surface of a cone. Fig.10 shows the transient pressure measured on the surface of a cone. Fig.11 shows the reflection of a stronger shock on the surface of 18° wedge.

The experimental results show that

1. When moving shock Mach number Ms<1.4, the difference between region(4) and region(5) can be neglected and the contact surface in the triangle bounded by the transmitted shock S_r,reflected shock S_R, diffracted shock S_D disappears.Therefore, this method presented here is suitable for weak moving shock(as shown in Fig.3 and Fig.8).

2. When the moving shock moves out of the conical nozzle, there are two regions behind it. The region ahead of a contact surface is uniform, which can be used as test gas,but the region behind the contact surface is turbulent. As the moving shock strength increases, the turbulence in the region strengthens rapidly.

3. When the strength of the moving shock increases, a complex or double Mach reflection can occur.

CONCLUSION

1. Double driver shock tube(tunnel) is a useful tool for studying shock-shock interaction.

2. The method presented in this paper can be used to study the transition between regular and Mach reflection of a weak moving shock with a quasi-stationary flow ahead of it on the surface of a wedge or a cone.

3. It is important to investigate single, complex and double Mach reflection of a moving shock with a quasi-stationary flow ahead of it on the surface of a wedge.

REFERENCES

1. D.L.Merritt and P.M.Aronson,   Fifth Hypervelosity Techniques
   Symposium, pp. 325-346(1967).
2. J.E.Nicholson,   AIAA paper 67-180(1967).
3. G.J.Bingham,   AIAA J. Vol.3 No.3, pp.564-566(1965).
4. H.R.Miller,   AIAA paper 66-736(1966).
5. P.Kutler and L.Sakall,   AIAA paper 75-49(1975).
6. Z.Y.Han et al.   ACTA MECHANICA SINICA No.4 (1982).
7. Z.Y.Han et al.   ACTA AERODYNAMICA SINICA No.1 (1983).
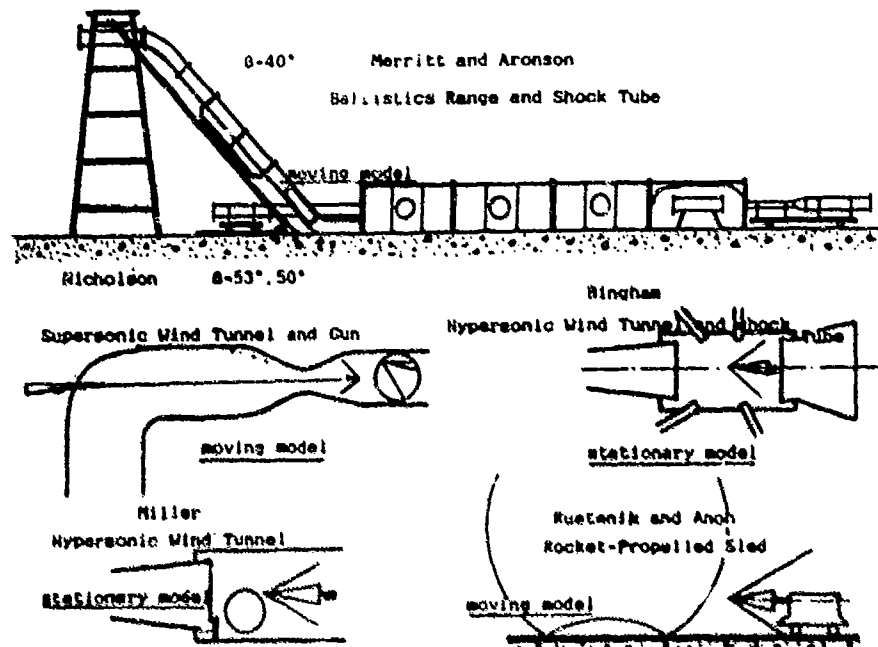
Fig.1   Two types of experiments on oblique interaction
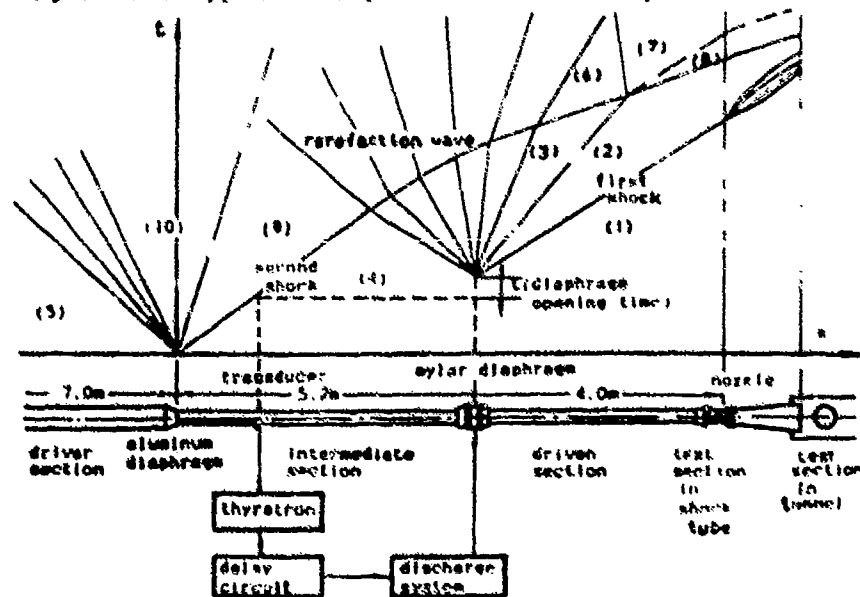
Fig.2 Double Driver Shock Tube (Tunnel)
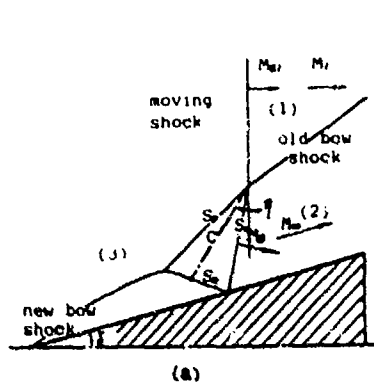
Fig.3 The wedge for deflecting
     the flow and planar
     moving shock.
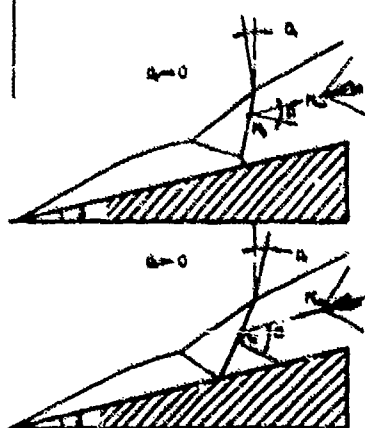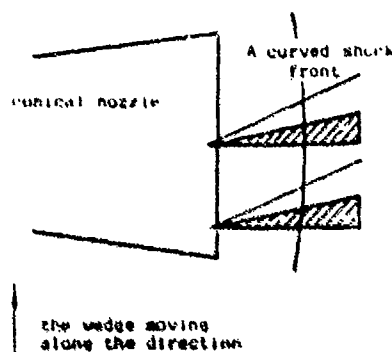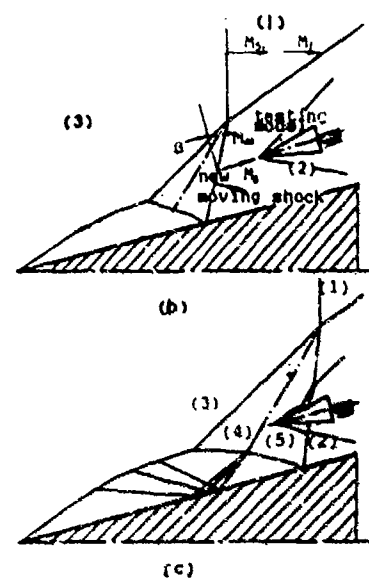
Fig.4   The wedge moves up
        from its lowest
        position.
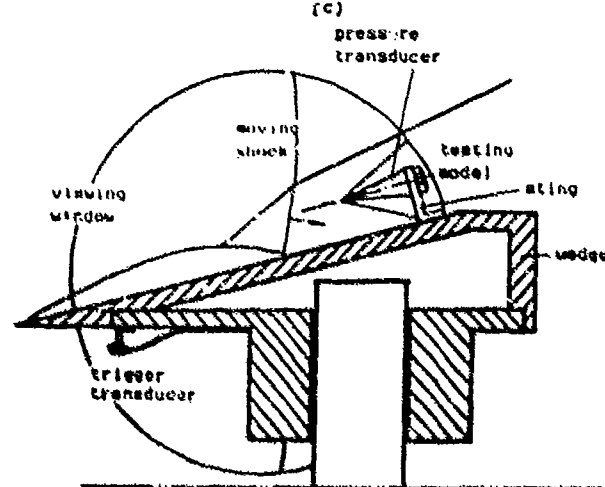
Fig.5   The apparatus for changing
        the angle of interaction ß
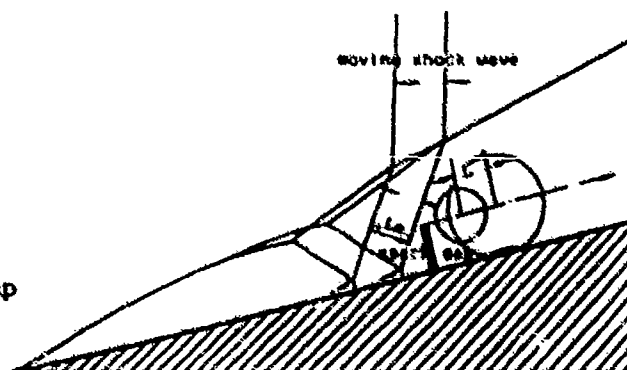
Fig.6 The measurement of the moving
     shock Mach number Ms
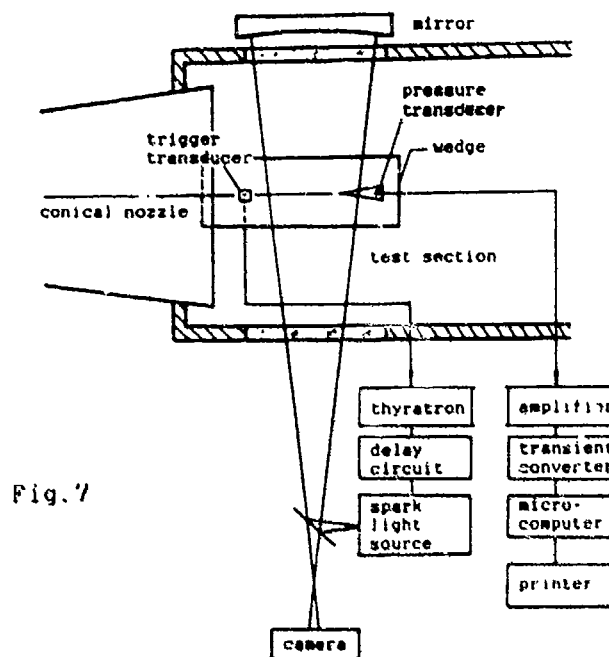
Fig. 7

The synchronization and measurement system

Fig.8 The regular reflection on the surface of a cone

Fig.9 The Mach reflection on the surface of a cone

Fig.10 The transient pressure measured on the surface of a cone (2μsec/div)

Fig.11 The reflection of a stronger shock on the surface of 18° wedge

FAST LOADING OF METALS USING A SHOCK

TUBE: APPLICATION TO ALUMINUM

Wesley R. Smith

Department of Physics #16
Lehigh University
Bethlehem, Pa. 18015

Air shock loading of a thin aluminum shock tube wall can
produce inelastic strain in the tube. If the shock velo-
city is much less than the minimum phase velocity of the
elastic real first vibrational mode of the metal tube,
the first complex vibrational mode controls the major
part of the elastic response. A simple "steady state"
displacement determined by the complex first mode propa-
gates with the shock. The rise time of the steady state
signal is of the order of 20μ sec. Shock loading of the
tube beyond the yield stress of the aluminum produces a
much larger inelastic wall displacement which also ex-
hibits a steady state character in that it too propa-
gates with the shock. The displacement signal begins
with a sudden rise, identical in appearance with a pure
elastic response, followed by an inelastic expansion.

I. INTRODUCTION

The modern study of dynamic inelastic behavior of metals began with plas-
tic wave propagations studies[1]. Demonstration of the real material behavior at
high strain rates, however, was achieved for compressional loading using split
Hopkinson bars and torsional loading using Kolsky bars[2]. The Kolsky bar techni-
que has been the most successful in demonstrating strain rate effects, and can
use single and double jump loadings, but it has not given information about the
early time details involved in yield. Because the strain in a thin walled tube
internally loaded by an axially moving shock wave can be monitored over the full
range of response times beginning with the earliest elastic signals, shock tube
loading studies can furnish unique information about yield and inelastic strain.

The conditions under which shock loading of a tube can produce simple inter-
pretable results can be described in terms of elastic theory. The elastic
strains in a thin walled tube produced by shock loading due to all possible
shock velocities have been discussed extensively in the literature[3,4]. For tube
vibration wave numbers, Γ, below the minimum of the first real elastic mode,
whose dispersion curve is shown in Fig. 2, both rotatory-inertia and transverse
shear effects are negligible. The normalized phase velocity is $C = V/C_1$, where
V is the mode phase velocity at the wave number Γ. The normalizing velocity $C_1 =$
$[E/\rho(1-\nu^2)]^{1/2}$ is the tube dilation velocity (E is Young's modulus, ρ is metal
density, ν is Poisson's ratio). A shock wave which propagates with a speed less
than the minimum first mode phase velocity produces an elastic response which
travels with the shock velocity and has a significant contribution only from the
complex roots of the first mode. Tang's[4] "steady state wave" solutions assumed
that in this case the longitudinal stress and integrated shear stress were neg-
ligible. The steady state solution accounts for greater than 90% of the total
elastic strain associated with the loading due to a shock traveling at $U^* = U/C_1 <$
0.2, where U is the shock velocity. The rest of the strain is the result of a
propagating wave of very small amplitude, whose leading edge moves with the fast-

est real first mode phase velocity. An example of the steady solution for an aluminum tube is shown in Fig. 3, for a shock velocity U=825 m/s (U/C$_1$=0.15),and thickness parameter h*=.1333 (h*=h/ϵ). The rise time for w* the normalized radial displacement (w*=w/a) is of the order of 20μsec.

When the loading produced by the shock wave exceeds the elastic limit, the tube material yields, and a much larger w* results as shown in Fig. 4. These experimental displacement-time strain gauge histories show steady state behavior in that displacement is identical in appearance at gauges located 10 cm apart. This tube behavior looks like an elastic transient followed by an inelastic approach to equilibrium. Preliminary data suggest that this behavior is affected by prior heat treatment of the tubes, so that the dynamical response may depend on the metallurgical state (grain size, geometry of grain boundaries, etc.) of the tube.

II. EXPERIMENT

The schematic of Fig. 5 shows the shock tube used in these studies. The tube is about 7.9m in length and consists of a driver section, DS, made of 3.8cm ID, .64 cm wall stainless steel pipe and a double-walled expansion section, ES, of similar stainless pipe on the outside and thin-walled aluminum tubing on the inside. The outer pipe supports the inner tubing. The expansion section is terminated by a large dump tank, DT, for pressure relief. The annealed test section, TS, is coupled to similar non-annealed tubes, ES1, and ES2, as shown in Fig. 6. The coupling section, CS1, is designed so that no metal-to-metal contact exists between CS1 and TS. When such contact occurs, large elastic vibrations sometimes obscure the strain signal associated with the shock wave.

The driver section has been operated at initial pressures up to 1.4×10^4 KPa and the expansion section up to $.4 \times 10^4$ KPa. When diaphragm, D1, bursts, an initial shock wave is formed which propagates down ES1, passing the pressure gauge, PG, just before entering the test section TS. The strain gauges, SG1, and SG2, monitor the strain in the walls of TS caused by the shock wave. When the shock wave reaches diaphragm, D2, it bursts and the compressed flow empties into the evacuated dump tank, DT. Proper opening of D2 prevents a reflected shock wave from propagating back through ES2. The test time duration for a constant pressure jump behind the initial shock wave with the present shock tube dimensions is approximately 10 ms for a Mach 1.5 shock.

The strain gauges SG consist of 12 turns of .0254 mm diameter Advance resistance wire wound under a tension of 10^3 dynes and secured with a very thin coat of polyurethane varnish. The winding tension is sufficient to insure that the gauges can follow contractions as well as expansions of the tube. The mass of the gauge and its hoop strength is negligible compared to the properties of the tube on which it is wound.

The static resistance of the gauges is measured using a pair of Keithley 5 1/2 digit voltmeters, one to measure the current through a precision series resistance and the other to measure the gauge voltage. Static measurements are made of the initial strain state before and final state after a run. These measurements show how much permanent displacement was produced by the shock wave. The same equipment is also used to measure the static stress-strain curve for the material. The dynamic displacement signal is measured as a change in voltage across a gauge and is recorded on a single sweep oscilloscope. For a gauge current of 50 ma, a typical dynamic elastic displacement voltage signal is about 5 mv. The dynamic inelastic displacement signal voltage can be of the order of tens of millivolts.

The pressure jump across the shock is measured using a Kistler piezo-electric pressure transducer, PG, and charge amplifier. The pressure record is recorded on a single sweep oscilloscope. This system can be calibrated statically and the pressure jump checked by measuring the shock speed and using the flow relation between pressure ratio and Mach number.

An example of a pressure and displacement record for a typical elastic response to low Mach number shock loading is shown in Fig. 7. Here the annealed 3003 Aluminum tube has $h^* = .073$. The vertical axis displays pressure P and normalized radial displacement w^*, and the horizontal axis oscilloscope sweep rate (different for the P and w^* records). The time at which the shock arrives at the gauge position is marked by S. The weak reflected shock produced by D2, before it broke, is marked by R. The maximum loading pressure P is behind the initial shock S, and the elastic response is that predicted by the steady state solutions.

In a given run, the final pressure behind the shock wave is controlled by the bursting pressure of D1 and the initial pressure in ES. The initial pressure may be adjusted so that only a modest jump in pressure caused by the shock wave will drive the wall material beyond the yield point. There is no dispersion in the stress applied by the shock to different parts of the test section TS, since the same strength shock loads all parts. The displacement-time records are observed to be identical at locations on TS separated by 10 cm., only differing in time of onset by the travel time of the shock through the air. An example of inelastic strain displacement records for gauges SG1 and SG2 is shown in Fig. 8. The tube displacement w^* begins with a rapid elastic response at S followed by an inelastic region. There appears to be a brief elastic plateau for a time T_d (delayed yield time) followed by a linear zone LZ (constant strain rate) and terminated by a relaxation zone RZ (strain hardening region). A strain hardening relaxation time T was determined from the two gauge records of Fig. 4 by plotting the log $(w^* - w_2^*)$ versus t. The equilibrium displacement is w_2^*, and the data for both gauges is shown in Fig. 9.

The dynamic displacement, even for inelastic behavior, shows the characteristics of a steady state response (i.e. a signal which propagates with the shock speed). It is because the dynamic strain shows a steady state behavior that there is hope for a relatively simple successful theoretical description of the complete time history of the material properties of the tube.

REFERENCES

1. Malvern, L. E., J. Appl. Mech. 18, 203 (1951).

2. Duffy, J., "Mechanical Properties at High Rates of Strain, 1979", ed. J. Harding (The Inst. of Physics, Bristol and London, Conf. Series No. 47) p.1.

3. Schiffner, K., and Steele, C. R., AIAA Journal, 9, 37 (1971).

4. Tang S., Proc. ASCE, J. Eng. Mech. Div., 91, 97 (1965).
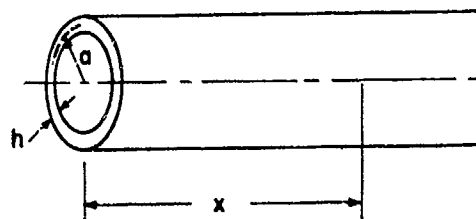
Fig. 1.   Tube Geometry. The axial
distance from the end is x.
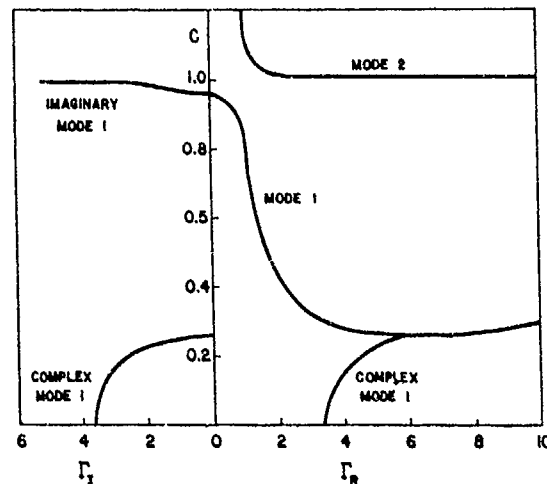
Fig. 2.   Elastic Modes of an Alum-
inum Tube, h*=1.33.   Speed C vs.
wave number Γ.
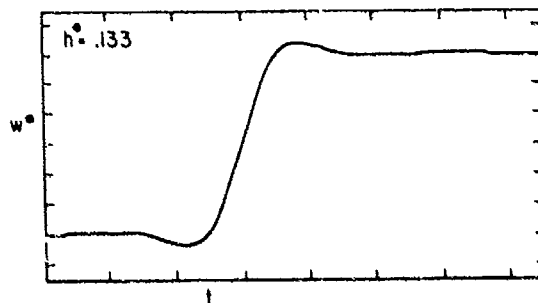
Fig. 3.   Steady State Elastic Solu-
tion.   Radial displacement w* vs.t
(10 µsec/div.).
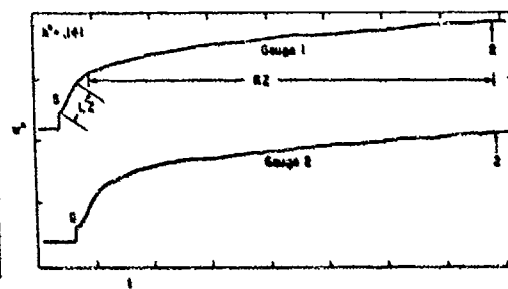
Fig. 4.   Inelastic Response.   Radial
displacement w* vs.t   (1 msec/div).

Fig. 5.   Shock Tube Schematic. Driv-
er Section, DS; Expansion Section,
ES; Test Section, TS; Dump Tank,DT;
Diaphragms, D1, D2; Converging
Section, CS.
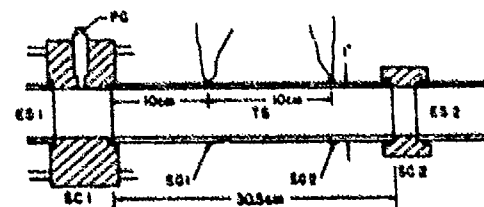
Fig. 6.   Test Section Schematic.
Test Section, TS; Couplers, SC1,
SC2; Pressure Gauge, PG; Wire Strain
Gauges, SG1, SG2.
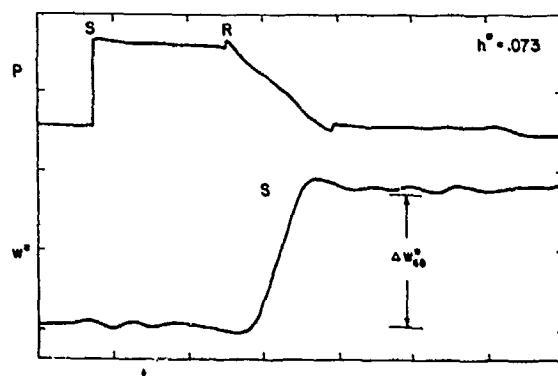
Fig. 7. Elastic Response. Upper Trace. Pressure vs.t (5 msec/div). Low Trace, w* vs.t (20 µsec/div).

Fig. 8. Inelastic Response. Upper Traces, w* vs. t (1 ms/div). Lower Trace, Region S, w* vs.t (20 µs/ div.).
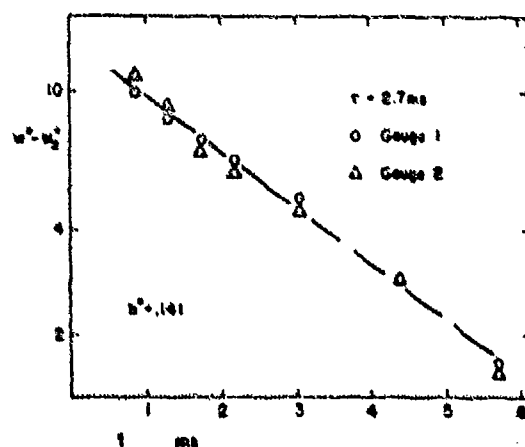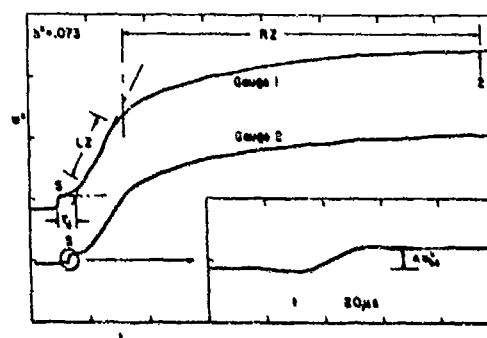
Fig. 9. Work Hardening Relaxation Time. w*-w*₂ vs.t (msec/ div); w*₂, equilibrium.

SPRAY DETONATION STUDIES USING

LASER DOPPLER TECHNIQUES

G. Smeets

Institut Franco-Allemand de Recherches de Saint-Louis,
12, rue de l'Industrie, 68301 Saint-Louis. France

Experimental spray detonation studies were performed in a
50 cm diameter vertical shock tube. The sprays were stoch-
iometric mixtures of different fuel droplets (methanol,
ethanol, propanol(1), hexanol, decanol and decane) with air.
The droplets had a defined diameter distribution (350 μm
mean diameter). The experiments showed that even in sprays
of low vapor pressure fuels like decane and hexanol, a
self-sustaining Chapman-Jouguet detonation can exist. How-
ever, a minimum vapor concentration is necessary. By
measuring several physical quantities within the reaction
zone on the basis of laser Doppler techniques, the pro-
cesses of liquid fuel fragmentation, evaporation, turbulent
mixing and combustion could be observed in detail. From the
data recorded it was concluded that for sprays of 350 μm
diameter fuel droplets, the controlling mechanism for the
reaction is turbulent mixing of the vapor originating from
the droplets.

1. INTRODUCTION

As is known from combustion engines, fuel sprays can form explosive mixt-
ures. The question arises under which circumstances these mixtures, normally
containing both fuel droplets and fuel vapor mixed with air, are capable of
detonating.

Of special interest here is the contribution and behavior of the droplets
and are the mechanisms allowing fuel in droplet form to be fast enough atomized,
evaporated and mixed with air such that the energy released by the chemical
reaction can still support the detonation wave.

Only a rather limited number of experimental investigations have been
reported so far in the literature dealing with two-phase detonations in air.
From these papers it can nevertheless be concluded that droplets of diameters
d > 100 μm can still contribute to detonation [1,2,3,4,5,6].

2. VERTICAL SHOCK TUBE

For experimental spray detonation studies under defined conditions, a
vertical shock tube as shown in Figure 1 was built. The tube is approximately
4 m long, has an inner diameter of 50 cm and is open at both ends (only closed
by thin plastic foils to avoid convection). The fuel spray is generated by
means of 12 fuel injectors located ringwise at the top of the tube. In falling
down inside the tube, the droplets agglomerate. Only at the bottom part of the
tube the spray becomes to a certain extent homogeneous. This spray has a volume
fraction of about 10^{-4}. A strong blast wave from a 1 kg explosive charge sus-
pended 35 cm above the upper tube end initiates the detonation.

7 pressure gages are mounted in the tube wall. They are mainly used for observing the shock transition. In addition, both a static pressure probe and an optical probe for Doppler measurements are placed in the vicinity of the tube axis close to the lower tube end. They allow different physical quantities to be recorded in the reaction zone.

3. SPRAY CALIBRATION

A photographic technique was used for determining the number density as well as the diameter distribution of the droplets in a test volume selected near the tube axis in its lower part. By means of an optical system (Figure 2) the spray was stroboscopically illuminated by an intense parallel laser light bundle with a rectangular cross section of 5 mm × 40 mm. Photographs – see Figure 3 – taken from a direction perpendicular to the light bundle exhibit traces of each particle in a well defined volume. Since the droplets are ideal spheres, there exists a rather accurate relation between their diameters and their sinking velocities. By analyzing 12 photographic records in measuring the distances separating the "dots" for each trace and in separately counting the traces for each species, the distribution of the liquid fuel as a function of the droplet diameters was determined (Figure 4). The total volume fraction of the liquid was found to be about $1.1 \cdot 10^{-4}$. This value, however, can only be regarded as an average one. The individual records show that at a scale of about 25 cm^3 – which is the size of the photographed volume – a considerable deviation up to about 50% is possible.

From the liquid volume fraction, the stochiometric equivalence ratio s_ℓ of the liquid fuel component can be calculated. s_ℓ is dependent on both the fuel and spray temperature. It was stochiometric or slightly understochiometric for all the fuels investigated.

In order to achieve a definite stochiometric equivalence ratio of the vaporized fuel component s_v, the vapor was always saturated by intermittently spraying several times prior to the experiment until an equilibrium temperature of the spray was reached. From this temperature, s_v was calculated.

4. LASER DOPPLER SYSTEMS

For non-intrusive measurements in the reaction zone of the detonation waves, an optical probe had to be built working in the environment of high pressures and temperatures (see Figure 5). A light fiber (monofiber, stepped index, 200 µm in diameter) transmits continuous monochromatic laser light from an Argon-ion laser (in monomode operation) into the probe. The light bundle is focussed at the measuring point. Light scattered from particles passing through this point is collected and transmitted by a second light fiber into a particular highly resolving spectrometer [7,8]. The Doppler shift of the light scattered is proportional to the particle velocity component along the axis of symmetry of the probe. The spectrometer generates an electrical signal following proportionally and in real time (with a time resolution better than 1 µs) the frequency variations of the Doppler shifted light. The optical components are shielded from the flow by solid rods and bear saphire windows heated to about 200 C in order to avoid vapor condensation.

In addition to the recording of particle velocities and life times, the same technique can also be used for measurements of the refractive index and mass density variations in the reaction zone. For this, the optical probe has only to be slightly modified in such a way that the laser light passes directly through the flow without scattering. The general relation for the Doppler shift is given by the formula:

$$\frac{d\nu}{\nu} = \frac{1}{c}\frac{\partial L}{\partial t} .$$ (1)

That is, the relative frequency shift is proportional to the time derivative of the optical path length L from the light source to the receiver divided by the vacuum speed of light. If ℓ denotes the length of the light path between the windows of the probe, L is related to ℓ by the refractive index n of the flow:

$$L = n \cdot \ell .$$ (2)

In this case, the Doppler shift is related to the time derivative of n by

$$\frac{d\nu}{\nu} = \frac{\ell}{c} \cdot \frac{\partial n}{\partial t} .$$ (3)

This Doppler shift is by two or three orders of magnitude smaller than the Doppler shift of the light scattered and can only be recorded with the highest resolving mode of operation of the spectrometer, which reaches the limit of about 10^{-10}.

5. TRANSIT TIME AND SPEED OF DETONATION WAVES

An indication of the overall amplification of the shock wave by the active medium is given by the transit time τ, defined as the time interval between ignition of the explosive charge and arrival of the detonation wave at the last pressure gage at the lower part of the tube. In Figure 6 the measured values of τ are plotted versus the equivalence ratio of the fuel vapor s_v. For each point, fuel liquid and equivalence ratio of the liquid fuel component s_ℓ (in percent) are indicated.

For all the liquids investigated (methanol, ethanol, propanol(1), hexanol, decanol and decane), the reaction energies of the stochiometric mixtures are nearly the same (627 cal/g for methanol and between 647 cal/g and 671 cal/g for the other mixtures). For this reason a plot in a common diagram is justified.

The dashed line connects the points of the experiments in the absence of droplets. In this case there is only an amplification for $s_v > 0.3$. Addition of droplets always leads to a reduction of τ except in the case of decanol when s_v was below 1% (not included in Figure 6). For $s_v < 0.3$, amplification is exclusively due to the liquid fuel component.

In Figure 7, shock speeds $\dot{x}_s$ measured in the lower part of the tube are plotted versus s_v. From all the experiments performed only those were retained for which a Chapman-Jouguet detonation characterized by a constant $\dot{x}_s$ was reached, that is, all events showing a decaying shock wave were excluded. Of greatest interest are here the three shots in decane and hexanol sprays. They clearly demonstrate that a real two-phase Chapman-Jouguet detonation does exist in sprays with mean droplet diameters of about 350 µm (and diameter distribution given in Figure 4) having vapor concentrations as low as $s_v = 0.06$. In contrast, in decanol sprays with $s_v < 0.01$ no detonation or even amplification of the shock wave was observed. A certain vapor concentration seems, therefore, to be indispensable for the spray detonation to occur.

6. INVESTIGATIONS OF THE REACTION ZONE

Prior to reacting with the oxygen, the fuel in liquid form has to be mixed with the air and distributed down to the molecule scale. The first step is the atomization of the droplets by stripping off the boundary layer in the flow behind the shock wave [9,10,11,12]. Thus, from each droplet a cloud of microparticles results. After rapid vaporization of the small liquid particles in the high temperature gas, the droplets lead to regions of high fuel vapor concentration in the flow behind the shock. A quick distribution of this gaseous

fuel is only possible by turbulent mixing because the diffusion is much too slow to be effective enough.

The optical investigations of the reaction zone give some insight into the different processes mentioned above. An example of simultaneous recordings of the scattered light level and the particle velocity is given in Figure 8. The period of light scattered (from the microparticles) is always limited to about 10 µs. The records taken show strong variations and are not reproducible. Some of them contain a large peak as examplified in Figure 8. The particle velocity determined from the Doppler shift of the scattered light rises within 2 µs and shows a spike which is probably due to the primary reaction of the relatively high fuel vapor component of the two-phase mixture. Whereas the spike does not always appear, a rise time as short as 2 µs is typical for all velocity records. From these measurements, the following informations can be drawn: atomization and evaporation of the liquid fuel occur very rapidly so that 10 µs after the shock has passed, the liquid is completely transformed into vapor. The diameter of the microparticles having a velocity relaxation time which does not exceed 2 µs cannot be greater than about 2 µm. The microparticles are rather unequally distributed before they evaporate. The vapor clouds from the droplets will therefore require considerable turbulent mixing before they can substantially contribute to the reaction.

Additional information is obtained by recording the optical path changes in the reaction zone. In Figure 9 the signals from both an ordinary shock wave in an inert medium and a detonation wave in an understochiometric mixture of air and ethanol vapor are compared. The light path was inclined by 15° with respect to the plane of the shock wave in order to avoid a singularity at the moment of shock passage. An ordinary shock wave leading to constant flow density ideally generates a rectangular signal during shock passage. In constrast a detonation wave, because of the sudden density decrease along with the beginning of the reaction, leads to a spike. It is followed by strong variations which can be due to fluctuations in pressure or temperature or both. Figure 10 shows two further records of detonation waves in stochiometric mixtures of air and ethanol vapor. In all these records, the fluctuations have vanished after about 100 µs. In contrast, corresponding signals from two-phase detonations in decane sprays (see Figure 11) contain high-frequency fluctuations (note the change of scale in Figure 11 !), which show no tendency to decay. They can only be interpreted as temperature (entropy) inhomogeneities passing through the light path, because pressure oscillations cannot persist after the end of the reaction. Entropy fluctuations are, however, an indication for the incomplete combustion of an unsufficiently premixed gas.

Integration of the records in Figure 11 leads to the density profiles given in Figure 12. In these profiles, the reaction zone can clearly be identified as the region of increased density corresponding to the von Neumann-spike in gas detonations. In the case of two-phase detonations, however, the reaction time is much longer. The plots in Figure 12 show the reaction to end only about 50 - 100 µs after shock transition. As vaporization is already completed after 10 µs it can be concluded that the reaction in two-phase detonation of the investigated sprays is mainly controlled by turbulent mixing.

The pressure records taken at both the wall and inner part of the tube also contain considerable fluctuations in the dynamic pressure during the first 100 µs after shock transition, which indicate a strong turbulence. At the same time during this period, the average pressure is higher than the equilibrium value. According to the theory of detonation this shows that part of the reaction energy (the kinetic energy of the turbulence) has not yet been transformed into thermal energy.

7. CONCLUDING REMARKS

The experiments clearly demonstrate that in sprays of low vapor pressure fuels like decane and hexanol having droplet diameters as indicated in Figure 4, a self-sustaining Chapman-Jouguet detonation can exist. The reaction of the liquid fuel with the available oxygen seems to be mainly controlled by turbulent mixing. As in sprays containing a fuel vapor concentration of less than 6% of the equivalence ratio, no detonation was attained, it is assumed that initial combustion of fuel vapor is vital for creating some turbulent mixing and for releasing the reaction of the fuel from the droplets. The efficiency of the liquid fuel to detonation was not 100% for the investigated sprays. The measured shock velocities for the stochiometric sprays do not attain 1800 m/s, found for stochiometric gas mixtures (see Figure 7). The measured data suggest that roughly half of the remaining oxygen is utilized by the liquid fuel.

REFERENCES

1. Dabora, E.K., Ragland, K.W., Nicholls, J.A., "Drop size effects in spray detonations", 12th Int. Symp. on Combustion (1969), pp.19-26

2. Pierce, T.H., Nicholls, J.A., "Two-phase detonations with bimodal drop distributions", Astron. Acta 17 (1972), pp.703-713

3. Fry, R.S., NICHOLLS, J.A., "Blast wave initiation of gaseous and heterogeneous cylindrical detonation waves", 15th Int. Symp. on Combustion (1974), pp.43-52

4. NICHOLLS, J.A., Sichel, M., Fry, R., Glass, D.R., "Theoretical and experimental study of cylindrical shock and heterogeneous detonation waves", Acta Astron. 1 (1974), pp.385-404

5. Lu, P.L., Slagg, N., Fishburn, B.D., "Relation of chemical and physical processes in two-phase detonations", Acta Astron. 6 (1979), pp.815-826

6. Nicholls, J.A., Bar-Or, R., Gabrijel, Z., Petkus, E., "Recent experiments on heterogeneous detonation waves", AIAA-Journal 28.5 (1980), pp.605-606

7. Smeets, G., "Michelson spectrometer for instantaneous Doppler velocity measurements", J.Phys. E: Sci.Instrum., Vol.14 (1981), pp.838-845

8. Smeets, G., Mathieu, G., "Optische Doppler-Messungen mit dem Michelson-Spektrometer", ISL - R 123/83 (1983)

9. Dabora, E.K., Fox, G.E., "The Break-up of liquid droplet columns by shock waves", Astron. Acta 17 (1972), pp.669-674

10. Ranger, A.A., "Shock wave propagation through a two-phase medium", Astron. Acta 17 (1972), pp.675-683

11. Fox, G.E., Dabora, E.K., "Break-up of liquid drops due to convective flow in shocked sprays", 14th Int. Symp. on Combustion (1973), pp.1363-1373

12. Pierce, T.H., Kauffmann, C.W., Nicholls, J.A., "Mechanisms of ignition in shock wave interactions with reactive liquid droplets", AIAA paper (1975), pp.75-163

Figure 1.
Vertical shock tube (sizes
given in mm)

1 LASER BEAM
2 ROTATING DISC WITH HOLES
3 LIGHT FIBER
4 CYL. LENSE
5 CYL. LENSE
6 LENSE

7 RECT. DIAPHRAGM
8 LENSE
9 LIGHT TRAP
10 SHOCK TUBE
11 OBJECTIVE LENSE
12 CAMERA

Figure 2.
Optical system for photographic recording of
the droplet traces

Figure 3.
Traces of sinking droplets

Figure 4.
Diameter distribution of spray
droplets

Figure 5.
Optical probe for laser Doppler
measurements
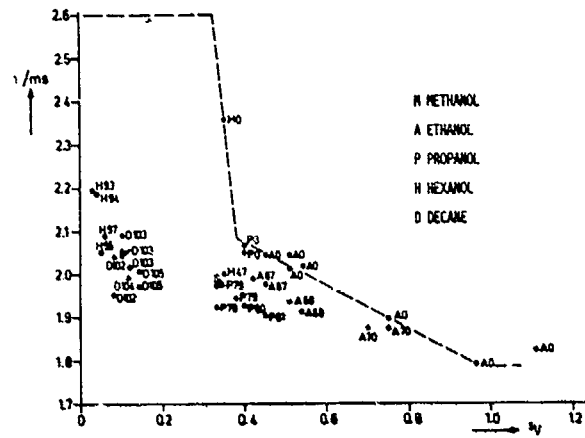
Figure 6.
Transit times of shock waves
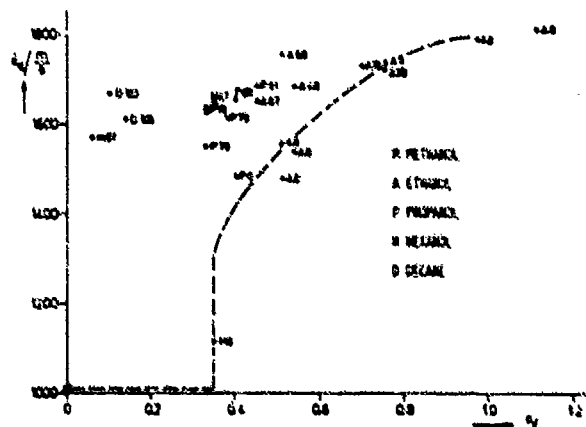
Figure 7.
Constant shock speeds in the lower part
of the tube
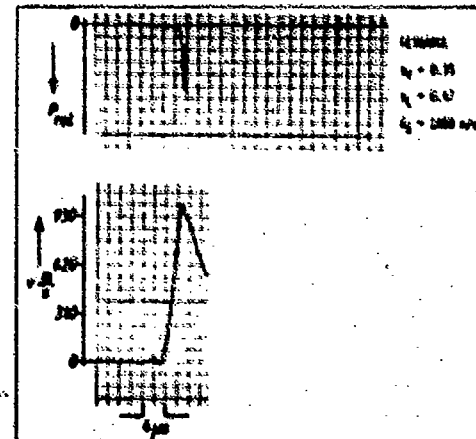
Figure 8.
Simultaneous records of light
level P and microparticle
velocity v
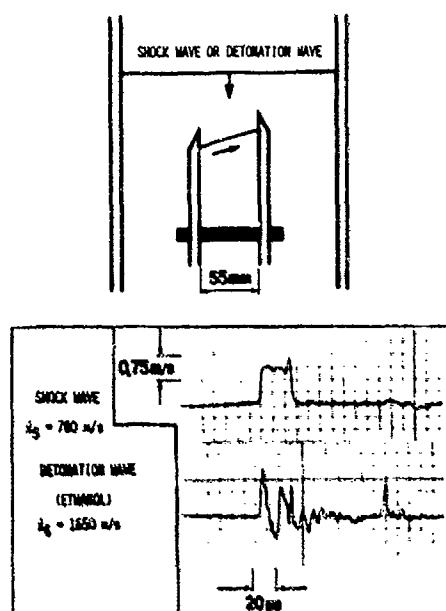
Figure 9.
Records of optical path changes in
a shock wave and in a detonation
wave
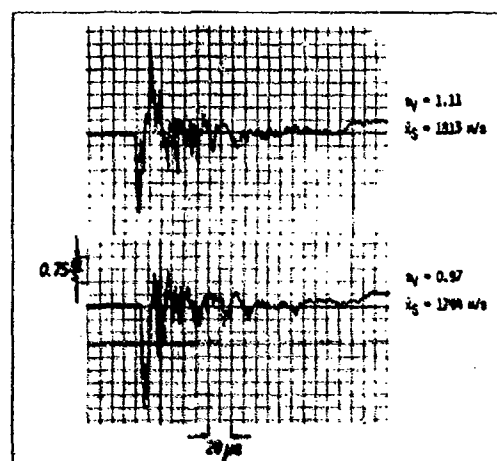
Figure 10.
Optical path changes in detonation waves
in ethanol vapours
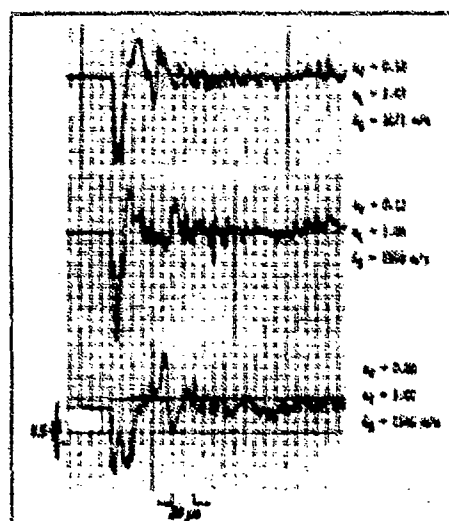
Figure 11.
Optical path changes in detonation
waves in decane sprays
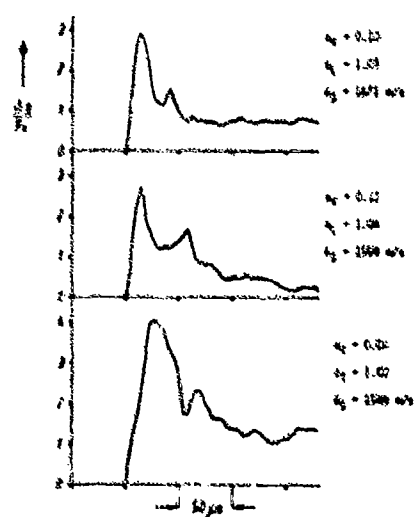
Figure 12.
Density profiles in detonation
waves in decane sprays

SELF-ACTING DOUBLE SHOCK TUBES AND APPLICATION

TO EXPERIMENT OF GASES MIXING PROCESS

H. Oguchi, H. Chue*, S. Sato and K. Funabiki

Institute of Space and Astronautical Science
Komaba, Meguro-ku, Tokyo, Japan

* Musashi Institute of Technology
Tamazutsumi, Setagaya-ku, Tokyo, Japan

Synchronized operation of double shock tubes is made in
nearly full automation. In utilizing the feasibility of the
operation, is studied a mixing process of two gases ejected
from the separate nozzles after the respective shock
compressions. The mass sampling probe developed for this
experiment is used to detect the mole fraction distributions
of gas species in the mixing region downstream from the
nozzle exit. The results are reasonable in comparison with
the previous measurement of the small signal gain in the
similar flow for CO_2/N_2 mixing gasdynamic laser.

1. INTRODUCTION

Previously the senior author (H.O.) and his colleagues reported the
mechanism and performance of a shock tube driven by the fast acting valves
using the free piston[1]. Specifically, the CO_2/N_2 mixing gasdynamic laser was
investigated by the synchronized operation of double shock tubes, in which case
the small signal gain of the laser media produced by the mixing was measured
while the mixing process itself was out of the study because of the lack of
appropriate method available[2].

In this paper, the double shock tubes of the same mechanism as the
previous one has been improved to be driven in nearly full automation with the
aid of the micro computer. This results in much feasibility in operation and
better reduction of the data. Secondly the instantaneous mixing of the two
gases in different stagnant conditions, which are produced by the separate
shock tubes, is experimentally studied by the mole-fraction measurement by
means of the mass-sampling-probe technique developed for this experiment. The
quadrapole mass filter is widely applied in the field of molecular
physics/chemistry. Recently there appear various applications for the study of
the shock tube flow. So far most of the mass filter measurements used to focus
on the molecular beam which is emanuated by introducing the sampled gases into
a high vacuum chamber separated from the shock tube. These are in category of
the molecular-beam sampling method. In the present experiment, however the
gases concerned in the flow are directly sampled through a small hole of the
probe which is connected to the mass filter. The output of the mass filter
provides an incoming rate of the gas species, which is proportional to the mole
fraction. This type of the mass sampling probe is employed for the measurement
of the mole fraction of gases mixture produced by the present facility.

II. EXPERIMEMTAL APPARATUS AND OPERATION

This experiment was conducted by a synchronized operation of double shock tubes, which produce separate stagnant conditions for each test gas. These double shock tubes are contrived to be driven by a fast acting valve consisting of a free piston and an auxiliary piston (Fig.1). The characteristic performance of this type of shock tube has already been reported[2]. Though the driving mechanism remains nothing changed from the previous one, the operation has been improved to achieve following the input of indications to c.p.u..

The operation of the present shock tubes and the related measurement were automated mostly following the input of the indications to the micro computer except the manual replacement of the separation diaphragm between two shock tubes. The indications to c.p.u. are as follows:

Input of driven pressures $\qquad$ $p_{1,N}$ (=75 torr), $\qquad$ $p_{1,C}$ (=200 torr)

Input of driver pressures $\qquad$ $p_{4,N}$ (=11 kg/cm^2), $\quad$ $p_{4,C}$ (=11 kg/cm^2)

Input of adjusted time $\qquad$ t_a $\quad$ (=3000 μsec)
for matching of C-tube shot
with N-tube shot

Input of voltages imposed $\qquad$ V_1, V_2 (V_1=450 mV for N_2, V_2=714 mV for CO_2)
on quadrapole of M.S.
and its pulse width $\qquad$ t_w $\quad$ (=1000 μsec)

where ( ) represents typical conditions and the subscripts N and C denote the quantities pertinent, respectively, to N_2 and CO_2. The resulting shock Mach numbers for the typical condition were

$$M_{S,N} = 3.88 \qquad\qquad M_{S,C} = 2.32$$

After input of all the indications, the shock tubes are run and then immediately followed by the charge-up of the driver sections and the evacuation of the driven sections for the next run. Apparently the experimental condition can be varied arbitrarily within an allowable range of pressures. In the present experiment, the test gases were N_2 for the primary tube and CO_2 for the secondary tube, and the driver gas was He.

As in the previous shock-tube experiment on mixing gasdynamic laser, two different gases, say CO_2 and N_2 are ejected through the multiple nozzles and the slit nozzle after the shock compression at each end. The nozzle geometry is shown in Fig.1. The mixing of gases is initiated just after the nozzle exit, connected with the test section of rectangular cross section, which has several ports for the mount of the mass filter probe.

The shock tubes are different from each other in dimension, the primary tube for gas (N_2) has a driven section of 50 mm in inner diam. and 5,500 mm in length with the following 20 x 80 mm cross section, and the secondary tube for the other gas (CO_2) is connected with the slit nozzle sandwitched between two rows of the multiple nozzles for the primary gas. In Fig.1 is shown the schematic of the nozzles. Two rows of 8 nozzles consist of the multiple nozzles for the primary gas and each nozzle is straight conical. Since the area ratio of the throat to the cross section was small, say 5%, no separation diaphragm was used between the primary tube and the test section. Before the shot of the tube, the primary tube is separated by a thin diaphragm from the secondary tube (see Fig.1).

As for the synchronization of the two shock-tube shots, the arrival of the shock wave at each tube end was monitored by the pressure record of the gauges mounted at the locations close to each tube end, and an adjusted time t_a was

selected from run to run . The typical pressure record is shown in Fig.3. For the input of the same operational condition, there was slight deviation in matching of the shock wave arrivals at two tube ends. Actually this deviation was within about ±200 micro sec in most of the runs, in which the present experimental data were acquired. The order of this deviation in matching may be allowable because it is enough less than that of the flow duration.

III. MOLE-FRACTION MEASUREMENT BY MASS SAMPLING PROBE

Principle of the method

The gas is sampled through a small circular hole (30 micro m) on the top side of the tube immersed in the flow (Fig.1). The sampled gas is introduced to a quadrapole mass filter (MS 105A ULVAC). Apart from the ordinary way of use of the mass filter we are concerned with the transient record of the mass filter, because the inflow of gases cannot reach the stationary state within comparatively short flow duration, which is of the order of several msec.

For a fixed hole with the area A, the incoming number flux N_i of gases species is

$$N_i = n_i v^* A$$

where v^* is the mass-averaged speed of gases and n_i the number density of i-th species. In the present set of the probe and mass filter, the total volume of the probe and mass filter itself acts as a sort of plenum chamber for the incoming gases, because of the small capacity of the vacuum system (turbo molecular pump and RP). The mass filter only records the increase in number of the concerned species; namely, the detected signal of the mass filter must be proportional to the number of the species. Therefore the time derivative $\dot{I}_i$ of the signal I_i must be proportional to the incoming rate N_i of the species number or the species number flux; that is,

$$\dot{I}_i \propto N_i \propto n_i \quad \rightarrow \quad \dot{I}_i / \dot{I}_j = n_i / n_j$$

From the records of the mass filter for different species, say I_C for CO_2 and I_N for N_2, we can obtain the ratio of species number density n_i/n_j, or the mole fraction of each species. It should be noted that from the principle of the method above described, the mole fraction thus detected does not depend on the flow direction to the sampling hole because the hole area A and the incoming velocity v^* are common for each species though they may vary in different flow direction to the hole.

Calibration of mass sampling probe

For the calibration an initially known condition must be settled. This can be done by using the flow which is produced by a single shock tube with gases of a given mixture ratio initially charged in the driven tube. For that case the initial mixture ratio remains unchanged in the whole flow region. For the gases mixture of CO_2 and N_2 concerned in the present experiment, the calibration was made by using the primary shock tube.

The sampling rate depends on the pulse width t_w of the electric potential imposed on the quadrapole of the mass filter (see Fig.2). In this experiment the pulse width t_w was chosen to be 1 m sec; namely, this provides one sampling / m sec alternatively for each species. One of the typical mass filter records for the calibration is shown in Fig.4, in which the imposed potential is also recorded. For the calibration the probe was set at the position ($x = 1.75$, $y = 0.5$, $z = 0.5$) in dimensionless scale referred to the distance (10 mm) between the upper and lower nozzle centers, where the x is measured from the center of the nozzle exit toward downstream, the y normal to the slit nozzle, the z parallel to the slit nozzle (Fig.1). For the present mass filter, the potentials imposed on the quadrapole were 450 mV for N_2 and 714 mV for CO_2. As

seen from Fig.4, the initial rise of the I's, say I_N and I_C can be obtained for the known mole fraction of either N_2 or CO_2. The ratio of $I_C/(I_N+I_C)$ is plotted in Fig.5 against the mole fraction of CO_2.

Measurements

The nozzle flow is initiated just after the arrival of shock waves at the end of the shock tubes. The flow duration is several m seconds, while the mass filter signals begin to rise with the delay of a few m seconds. This delayed response is likely to be mainly due to the volume of both tubing and mass filter compared with the incoming volume of gases or number of gases. In view of such delay of the mass filter signal, the driver gas (He) followed after the driven gases(N_2, CO_2) was traced by imposing the potentials for He (55 mV) and N_2 (450 mV) on the quadrapole. The record is shown in Fig.6. In this record the spikes pertinent to various impurities of molecular mass between He and N appear. The distinct signals pertinent to He and N_2 can be identified from the others. It follows from the comparison that the driver gas He reaches the probe with a delay of about 10 m sec from the driven gas N_2 does.

In this experiment we measured the mole fraction behavior in the mixing process of the gas (N_2) issued from a multiple nozzles with the other gas (CO_2) issued from a slit nozzle sandwitched between two rows of the N_2 nozzles. The observation by the mass filter probe was made for several cross sections from the near region of the nozzle exit toward downstream. One of the typical mass filter records for the mixing region is shown in Fig.7. The measured distributions of CO_2 mole fraction (%) are shown in Fig.8. The experimental data are preliminary because of crude coverage of the measured points. The results, however, show a qualitative picture of the mixing process from the nozzle exit to far downstream; for example, the mature mixing is established at the section downstream of the order of about 10 nozzle diameters. In comparison with the previous measurements of small signal gain in the similar mixing process of N_2 and CO_2, the location where the positive gain initiated to appear is identified with the location for the initiation of the mature mixing.

IV. CONCLUDING REMARKS

Fully automated operation of double shock tubes results in much feasibility in synchronization and better reproduction in data acquisition. Two different gases are ejected from the separate nozzles after shock compression by two shock tubes. The mixing process is studied by means of the mass sampling probe developed for this experiment. The sampling probe enabled us to detect the mole fraction of the concerned species in rather fast response. The measured distributions of the mole fraction over several sections provide a reasonable feature for the mixing process. Further applications of this type of the probe will be promising for a variety of the shock-tube flow studies.

REFERENCES

1. H. Oguchi, K. Funabiki, and S. Sato, "Modern Development in Shock Tube Research", Proc. 10th International Shock Tube Symposium (Kyoto Univ., Kyoto 1975) ed. by G. Kamimoto, p.95.

2. K. Maeno and H. Oguchi, "Study on N_2/CO_2 mixing gasdynamic laser by means of synchronized operation of two shock tubes", J. de Physique, Vol. 41, No. 11, Nov., 1980, p. C9-209.
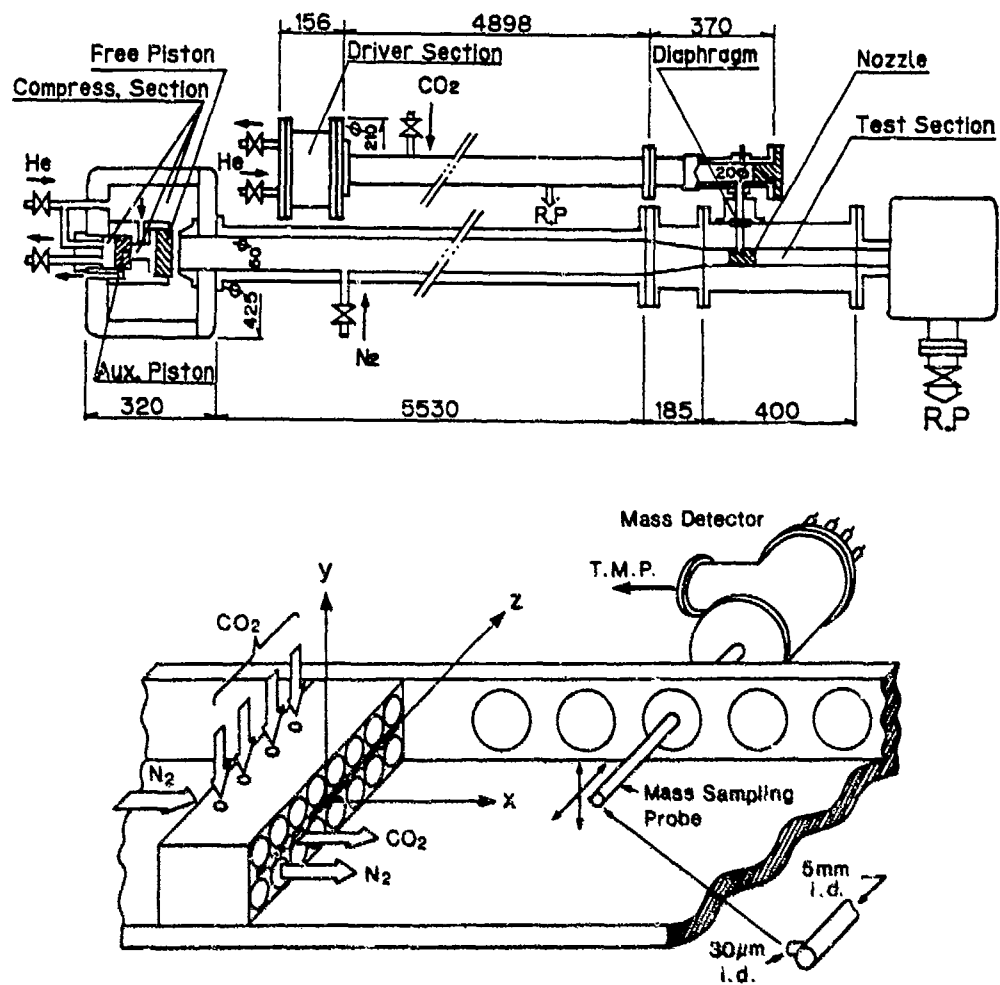
Fig.1. Schematic of shock tube and test section.
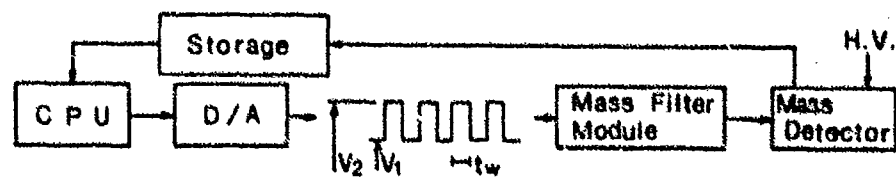
Fig.2. Measurement system of mass sampling probe.
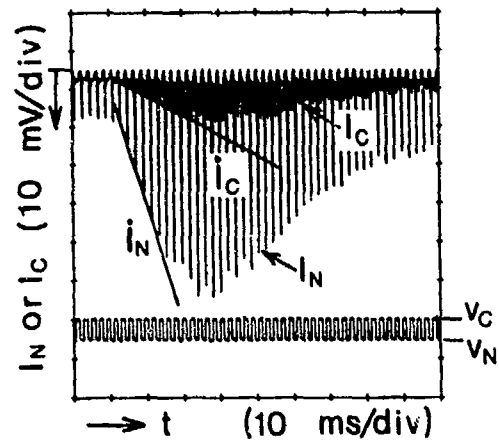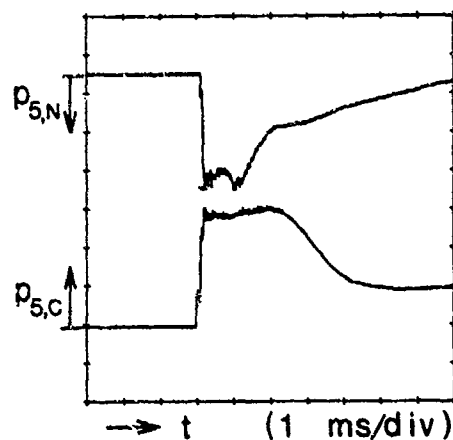
Fig.3. Pressure history at tube ends.   Fig.4. Sampling record for calibration.
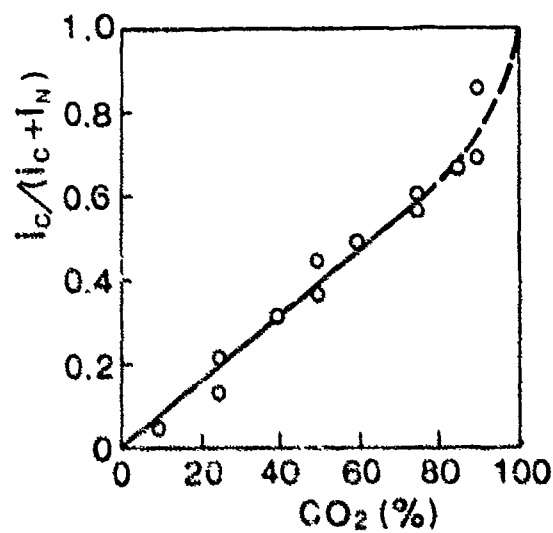
Fig.5. Calibration of
mass sampling record for
CO_2 mole fraction (%).
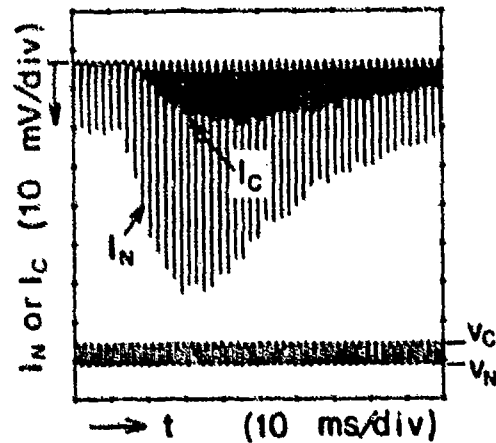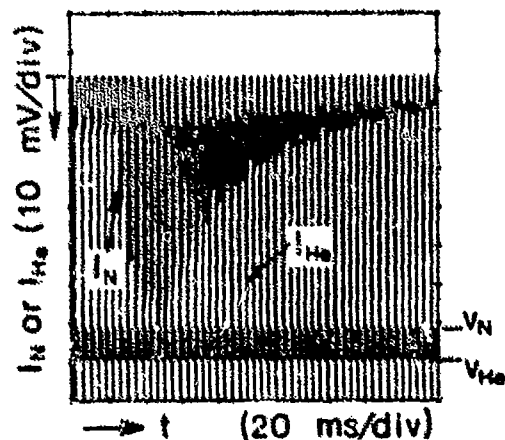
Fig.6. Sampling record for N_2 and He.   Fig.7. Sampling record for N_2 and CO_2.
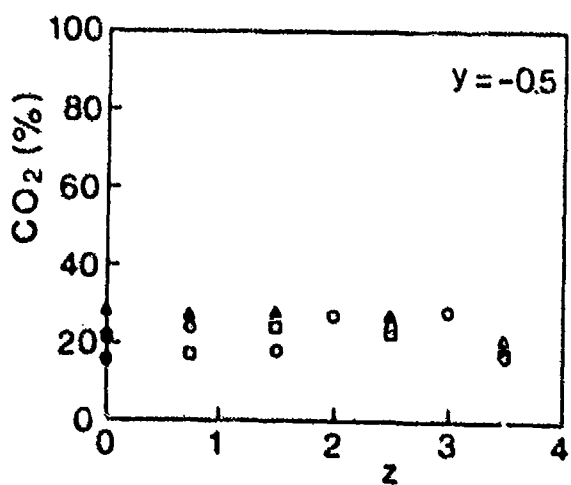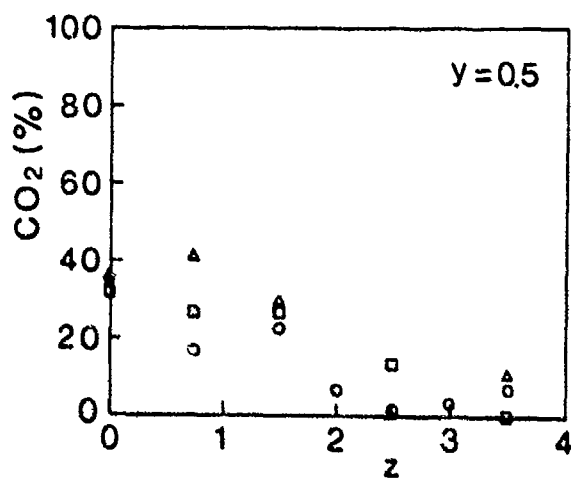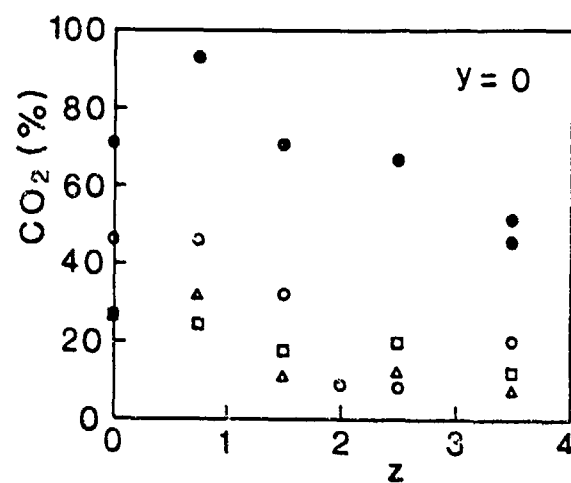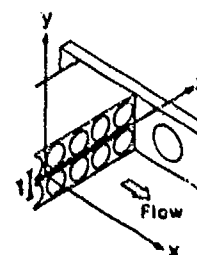
Fig.8. Distributions of CO_2 mole fraction (%).

STUDY ON SHOCK WAVES IN LOW TEMPERATURE GAS

BY MEANS OF A NON-DIAPHRAGM SHOCK TUBE

K.Maeno and S.Orikasa*

Department of Industrial Mechanical Engineering
Muroran Institute of Technology, Muroran 050, Japan

* Nissan Motor Co.,Ltd.

New apparatus for shock waves in low temperature gas is developed
by combining the non-diaphragm (snap-action) shock tube with
cooling by liquid nitrogen. With driver gas N_2 and He, experiments
are conducted for driven gases of N_2, O_2, and R-12. Along with
the measurements for initial pressure, temperature, velocities of
incident and reflected shock waves, and pressure changes with data
processing by microcomputer system, flow visualization by pulse
YAG laser and image converter (Imacon-790) are performed. Minimum
temperature of initial test gas ranges to about 150K (-123°C).
Among the results, shock waves in R-12 indicate real gas effect,
and shock condensation phenomena behind the waves in low temperature
conditions are observed.

1. INTRODUCTION

In proportion to the progress of cryogenic engineering in recent years,
the necessity of investigations for fluid dynamical phenomena has developed
extensively for such wide range of gases and liquids from room temperature to
cryogenic level as coolant recurrence, LNG transportation, liquid oxygen or
hydrogen feeding, and cryogenic superfluid technology. Although the multiphase
fluid dynamics or high speed gasdynamics in low temperature range have been
of great importance, practical data for this field are quite inadequate.

Shock tube is one of the prominent apparatuses for the experiments on
high speed gasdynamics. Owing to the atmospheric influx and freezing of water
vapor during the exchange of broken diaphragm, conventional shock tubes have
the severe limitation for the low temperature experiments, and only a few
investigations[1,2] have been reported by the conventional shock tube with com-
plicated contrivance for the diaphragm exchange.

Non-diaphragm shock tubes have high potentiality to these low temperature
experiments. In this paper a new apparatus[3] for shock wave experiments in low
temperature fluids is developed by consolidating the diaphragmless, snap-action
shock tube[4,5] with cooling by liquid nitrogen. Fundamental parameters of shock
waves in low temperature gases are studied. The condensation phenomena behind
the shock waves in low temperature R-12 (Freon 12; CCl_2F_2) are also investigated.

2. EXPERIMENTAL APPARATUS AND MEASUREMENTS

The schematic diagram of experimental setup for shock wave in low tempera-
ture gases is shown in Fig.1. The shock tube newly devised[3] has a main piston
made of nylon, which is substituted for conventional diaphragm, and also has
an auxiliary nylon piston controlled by an electromagnetic valve. The basic
mechanism of driver section is similar to those reported[4,5] . Some improvement
in such points as evacuation in valve chamber and feed-tubing between high

pressure chambers is achieved to prohibit from adverse air influx and to operate both pistons smoothly. This shock tube is free from pollution by broken diaphragm or freezing influx of water vapor in atmosphere, and many operations are possible by keeping the driver section in low temperature by liquid nitrogen.

The low pressure chamber is the stainless tube of 19.4mm inner diameter, whose horizontal length is 2.3 m. In order to maintain the saturation phase equilibrium or constant conditions in cold test section, low pressure tube has 90° bend portion of 150mm curvature, and 1.2m vertical portion including area adaptor and $20 \times 20 mm^2$ square test section. The diffraction and disturbances of shock wave through this bend portion are considered to become weak in downstream region of several times as long as tube diameter[6], because the ratio of curvature radius to tube inner radius is 15. Cooling section with liquid nitrogen and vacuum chamber for heat shield are equipped to vertical tube.

The pressure history of incident and reflected shock wave is monitored by piezoelectric transducer (PCB-111A24), and shock velocities are measured from duration between the trigger signal by a lead zirconate-titanic solid-solution piezoelectric pressure element (Tokin NPM-ND5Φ) and PCB transducer signal. Measured data are amplified to be recorded by storage oscilloscope, and processed by microcomputer. Initial gas temperature in test section is measured by CA thermocouple.

Flow visualization with shadowgraph is also conducted by motor-driven camera, high-speed image converter (Imacon-790), and by pulse YAG laser (second harmonics).

Nitrogen, O_2, and R-12 (CCl_2F_2, specific heat ratio; $\gamma = 1.14$, molecular weight; 120.9, atmospheric boiling point; 243.5K) are used as the test gas, with the driver gas of N_2 or He.

3. RESULTS AND DISCUSSION

Processed data by microcomputer are shown in Fig.2. Lower trace is pressure variation of PCB-111A transducer and upper trace is from NPM piezoelectric element. The velocities and Mach numbers of incident and reflected waves are also calculated from these data. Figure 3 presents measured and calculated incident Mach number M_1 to driver/driven pressure ratio p_{41} for test gas N_2. Idealized onedimensional shock tube calculation is employed. Owing to the difference between sound velocities, calculated Mach number in low temperature indicates higher distribution than normal range. Measured data for our non-diaphragm shock tube show lower distributions than the calculation curves, including some data scattering. Slightly higher trend can be seen for cold range than the data in room temperature. As regards the results for R-12 shown in Fig.4, however, measured data are too scattered to find a clear tendency. This is mainly attributable to initial pressure measurement by Hg manometer.

With respect to the incident shock strength, the ratio of pressure behind the wave to initial value is indicated in Fig.5 for test gas O_2. It can be seen that measured results are almost in accord with Rankine-Hugoniot relation in both room and low temperature conditions. Similar results are obtained for test gas of N_2. The data for R-12, however, show some discrepancy that originates from molecular relaxations.

As for the driven gas R-12, if the test section is cooled enough by liquid nitrogen below the equilibrium boiling point of R-12 under a given pressure P_1, condensed liquid phase accumulates at end section to achieve liquid-gas saturated phase equilibrium. The saturation curve of R-12 is presented in Fig.6. If the shock wave progresses into the gas in such phase equilibrium, flow parameters behind the shock jump up to the new conditions according to Rankine-hugoniot relations as indicated in Fig.6. The temperature of the gas adjacent to the wall, however, cannot follow the jump conditions, and condensation effect[7,8] may play a predominant role especially at cold solid wall or liquid surface[9].

As an example of low temper-

ature results, pressure variation for low temperature R-12 (about -39°C) is presented in Fig.7. Upper trace indicates the trigger signal from NPM pressure element. Rapid decay of pressure behind the incident shock wave is remarkable, and pressure decline behind the reflected shock is also observed. Dashed line represents the measured pressure behind the shock wave under the same initial pressure conditions for room temperature. This rapid decay is considered to originate from nonequilibrium condensation in the gas close to the wall behind the shock wave. In our preliminary experiments, strong scattering of He-Ne laser beam was also observed behind the waves, which also proves strong condensation effects and shock-boundary layer interaction at the reflected shock wave due to the real gas effects.

Owing to this real gas effects and condensation phenomenon, Mach number M_r of reflected shock(velocity U_r divided by sound velocity a_2 behind the incident shock wave) presents different features between the test gases as shown in Figs.8 and 9. Figure 8 is the result for test gas N_2, which indicates lower distribution than ideal and onedimentional calculation curve. The data for R-12 in Fig.9, however, represent higher and more scattered distributions than N_2, especially in low temperature range. These trends seem to be caused by strong bifurcation of reflected shock wave and interactive disturbances in reflected stagnation.

As regards the results from flow visualization, to our puzzled but pleasant surprise, a wide variety of flow features for R-12 shock reflection are obtained about saturated phase equilibrium, depending on initial parameters. Figure 10 shows the typical series of photographs obtained by Imacon-790 shadowgraph technique. On account of the curvature of cold R-12 liquid surface near the wall by surface tension, concentrated and counter-crossing shock waves in the reflected stagnant are observed. Condensation effect behind the incident wave darkens the visual field, and a compression wave into the liquid R-12 is visible in series number 4. As we have already obtained, experiments for the collapse of cavitation vapor bubbles are quite easy for cryogenic fluids utilizing this shock wave reflection.

The flow fields with condensation phenomena are shown from Fig.11-a to Fig.11-e by pulse YAG laser shadowgraph. Incident shock followed by liquefaction layer is observed in Fig.11-a, reflected shock and liquefied streaks behind the incident wave can be seen in Fig.11-b. The disturbances by boundary layer interaction and condensing instability or turbulence are clearly visible in Figs.11-c to 11-e. These observed phenomena should be analyzed by shock liquefaction[7,8] as well as wall condensation[9]

4. CONCLUSION

A new apparatus for shock wave experiments in low temperature gases is developed by consolidating the non-diaphragm shock tube with cooling by liquid nitrogen. Experiments are conducted for shock waves in N_2, O_2, and R-12 of temperature range from room conditions to the degree of 150K (-123°C), and fundamental shock parameters are measured, together with the flow visualization. The operations of our shock tube for such low temperature range are quite satisfactory. Complicated real gas effects on shock behavior of R-12 are observed, and condensation phenomena behind the incident and reflected shock waves in low temperature R-12 are measured.

REFERENCES

1. H.W. Liepmann, J.C. Cummings, and V.C. Rupert; "Cryogenic Shock Tube," The Phys. of Fluids, Vol.16, No.2 (1973), pp.332-333.

2. J.C. Cummings; "Experimental Investigation of Shock Waves in Liquid Helium I and II," J. Fluid Mech., Vol.75, Part 2 (1976), pp.373-383.

3. K. Maeno; "Non-Diaphragm Shock Tube and Shock Waves in Low Temperature Gases," Memoirs of the Muroran Institute of Technology (to be published, 1985).

4. H. Oguchi, K. Funabiki, and S. Sato;"An Experiment on Interaction of Shock Wave with Multiple-Orifice Plate by Means of Snap-Action Shock Tube," 10th International Shock Tube Symposium Proceedings (1975), p.386.

5. K. Maeno, K. Funabiki, and H. Oguchi; "Experimental and Analytical Study of CO_2/N_2 Mixing Gasdynamic Laser," ISAS Report (No.593), Vol.46, No.5 (1981), pp.175-197.

6. K. Takayama and O. Onodera; "Shock Wave Propagation Past Circular Cross Sectional 90° Bends," Shock Tubes and Waves, Proceedings of 14th Int. Symp. on Shock Tubes and Shock Waves (1983), pp.205-212.

7. G. Dettleff, P.A. Thompson, G.E.A. Meier, and H. Speckmann; "An Experimental Study of Liquefaction Shock Waves," J. Fluid Mech., Vol.95, Part 2 (1979), pp.279-304.

8. P.A. Thompson and D.A. Sullivan; "On The Possibility of Complete Condensation Shock Waves in Retrograde Fluids," J. Fluid Mech., Vol.70, Part 4 (1975), pp.639-649.

9. S. Fujikawa and T. Akamatsu; "Effects of The Non-Equilibrium Condensation of Vapour on The Pressure Wave Produced by The Collapse of A Bubble in A Liquid," J. Fluid Mech., Vol.97, Part 3 (1980), pp.481-512.
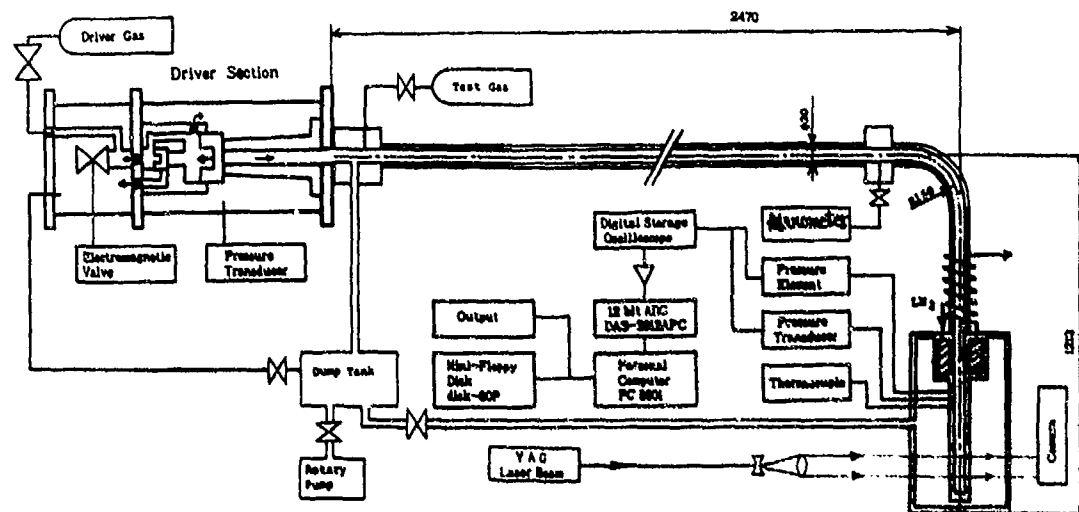
Fig.1　　**Experimental apparatus**
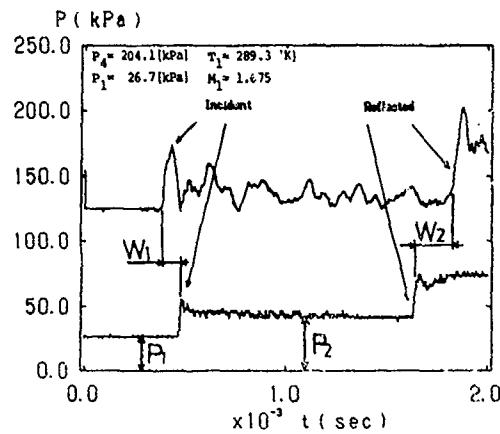
Fig.2   Processed prssure data by micro-computer
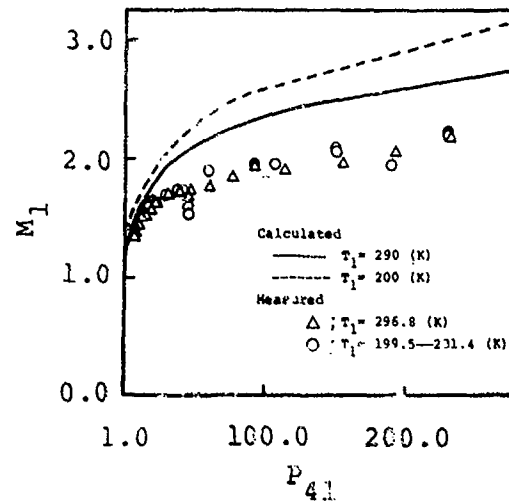
Fig.3   Relation between M_1 and p_{41}

(Driver gas ; N_2

     - Test gas ; N_2)
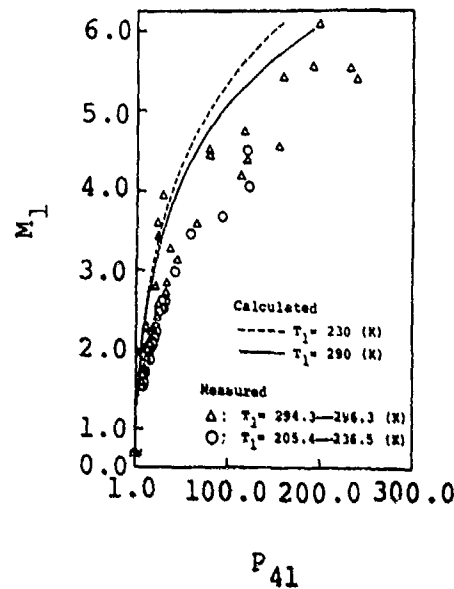
Fig.4

Relation between M_1 and p_{41}

(Driver gas ; He

     - Test gas ; R-12)
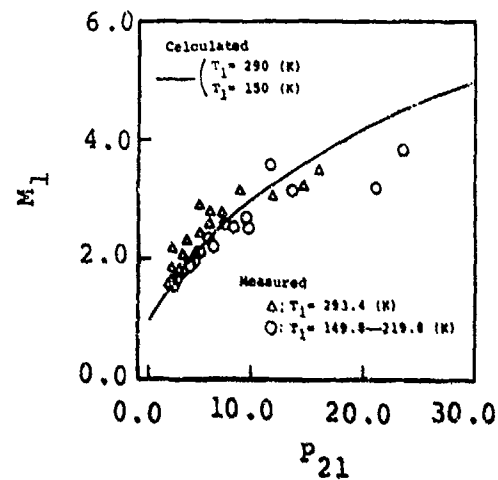
Fig.5   Relation between

M_1 and P_{21}

(Driver gas ; He

     - Test gas ; O_2)

Fig.6

Equilibrium saturation curve

of R-12
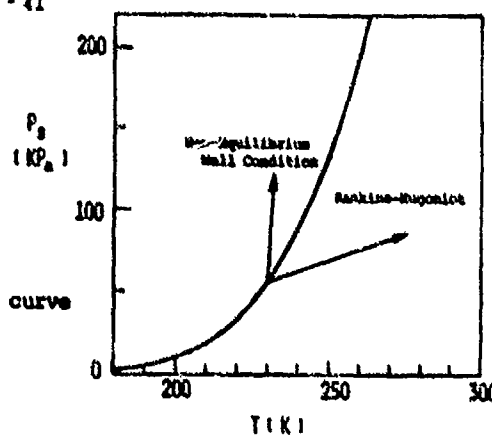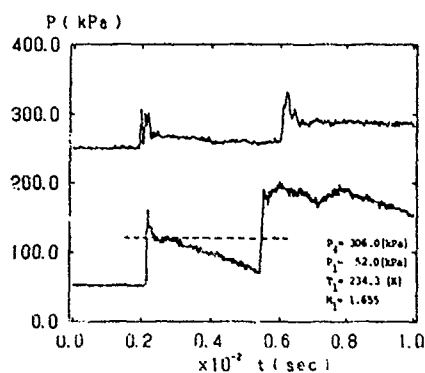
Fig.7 Pressure history of shock wave in low temperature R-12 (with condensation)
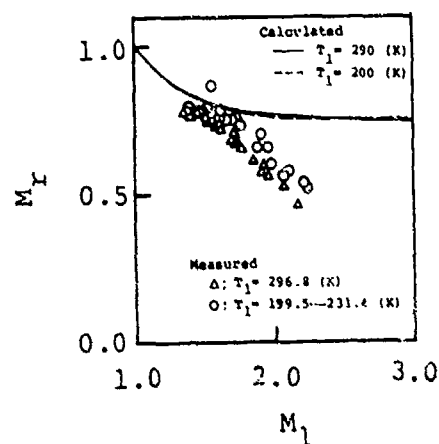
Fig.8 Relation between M_r and M_1 (Driver gas : N_2 -Test gas : N_2)
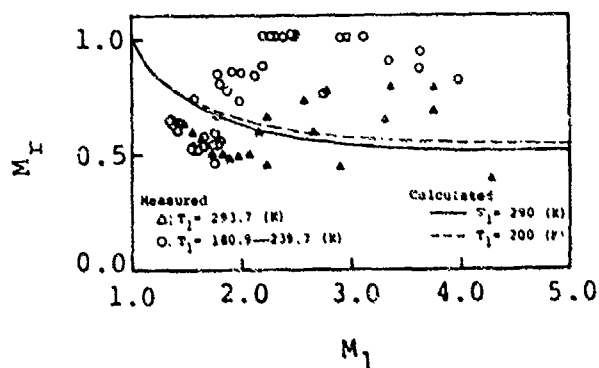
Fig.9

Relation between M_r and M_1 (Driver gas : N_2 - Test gas : R-12)

Fig.10 Flow Visualization by Imacon-790, Test gas;R-12,p_1=18.5kPa,T_1=210K Driver gas;N_2,p_4=452kPa

M_1= 1.97

1   3   5   7   9 10^5 frames/sec

reflected shock

R-12 liquid surface

2   4   6   8   10

(a)

(b)

(c)

reflected shock

condensation

liquid surface

(d)

(e)
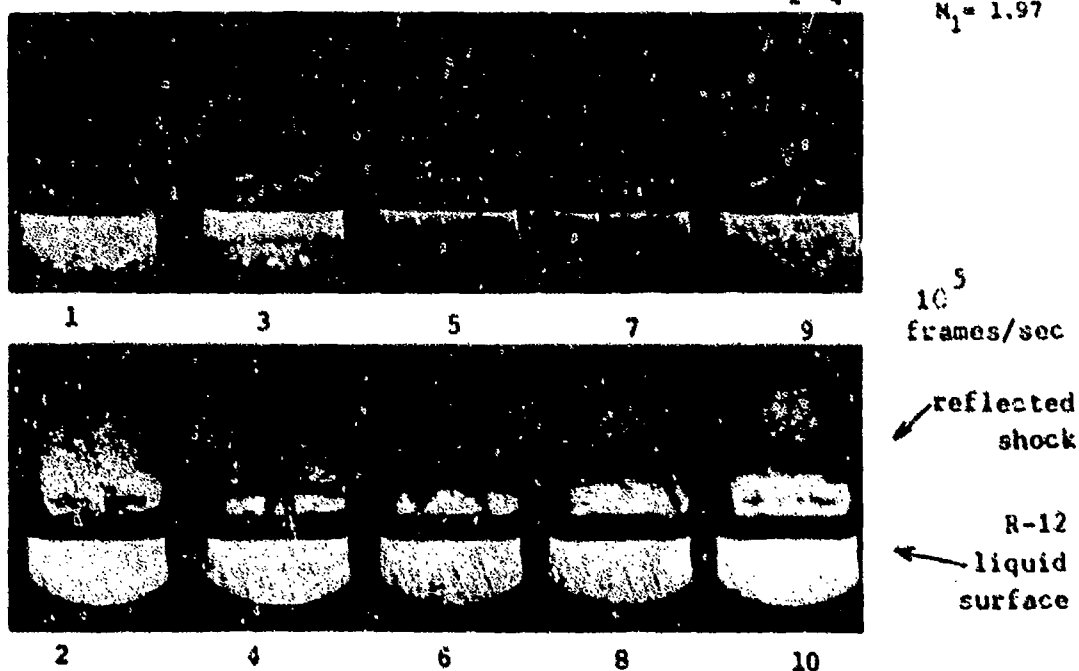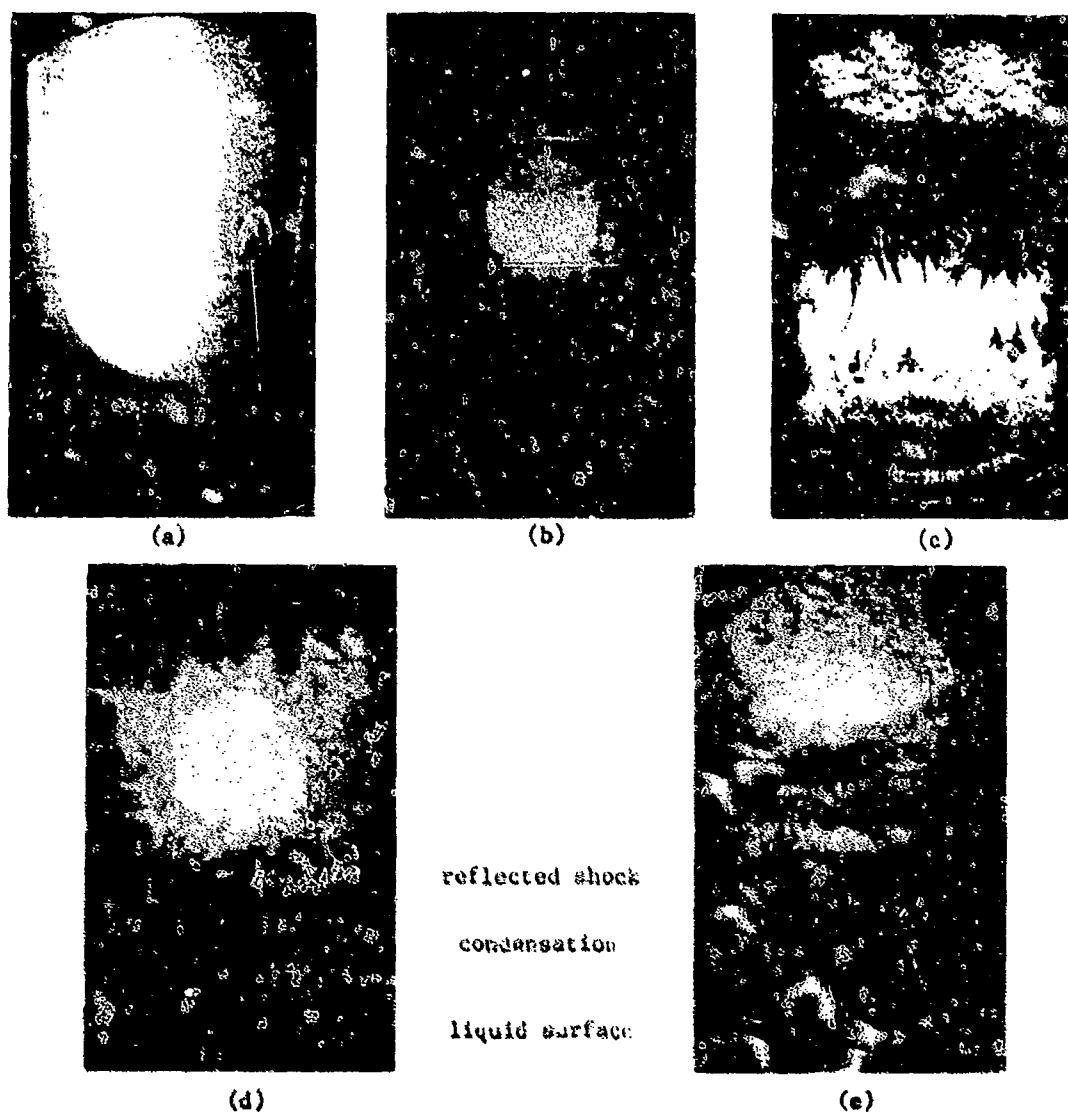
Fig.11 Flow visualization by pulse YAG laser for shock wave in R-12

(a) $M_1=1.6$

Test gas; R-12, $p_1=44$kPa, $T_1=232$K

Driver : N_2 , $p_4=514$kPa (Room Temp.)

(b) $M_1=1.6$

Test gas; R-12, $p_1=30$kPa, $T_1=227$K

Driver : N_2 , $p_4=425$kPa (Room Temp.)

(c) $M_1=2.1$

Test gas; R-12, $p_1=17$kPa, $T_1=211$K

Driver : N_2 , $p_4=516$kPa (Room Temp.)

(d) $M_1=2.5$

Test gas; R-12, $p_1=19$kPa, $T_1=218$K

Driver : He , $p_4=523$kPa (Room Temp.)

(e) $M_1=1.7$

Test gas; R-12, $p_1=40$kPa, $T_1=230$K

Driver : He , $p_4=425$kPa (Room Temp.)

IGNITION OF COMBUSTION REACTIONS BETWEEN DRIVER AND
DRIVEN GASES IN A DIAPHRAGMLESS FLEXIBLE SHOCK TUBE

Yong W. Kim

Department of Physics, B g. 16
Lehigh University, Bethlehem, PA 18015, U.S.A.

We have observed for the first time that a combustion reaction
between the driver and driven gas can be ignited in a dia-
phragmless flexible shock tube. This arises as a consequence
of the unique property of the shock tube that the multiply
reflected shock regime is up to two orders of magnitude longer
than in a conventional pressure-driven shock tube of comparable
length. The ignition threshold and percent completion of the
combustion reaction between hydrogen and oxygen as the driver
and driven gas, respectively, have been determined by time-
resolved spectroscopy and measurement of water molecules as a
reaction product. We have also established that the ignition
proceeds with atomic oxygen produced by thermal dissociation
of molecular oxygen.

INTRODUCTION

The concept of a pressure-driven shock tube with a fast-action valve in
place of a diaphragm and small-bore driven section(s) has been successfully im-
plemented in a number of configurations.[1,2] The combination of a valve and
small-bore tubing is instrumental in production of shock waves in that the rel-
atively slow throttling action of the valve is compensated by the strong con-
tribution of the boundary layer in the driven tube. The use of small-bore
tubing also introduces the feature of flexibleness to the driven section. In
the process, coupled with miniaturization possible with this design, the shock
tube can be built around diagnostic instrumentation rather than in the conven-
tional mode of adapting the diagnostics to a shock tube as a fixed hardware
facility.

The diaphragmless flexible shock tube is operated without exposure to the
atmosphere and permits significant recovery of the driver gas at high pressure
after each run. Also, it is simple to produce many shock waves simultaneously
in a large number of driven sections which are connected to one driver section.
These features provide new opportunities for application of the shock tube in
addition to those that have been the natural territory of the conventional
pressure-driven shock tubes.

We have been for some time pursuing the program of identifying and analy-
zing the unique characteristics of the diaphragmless flexible shock tube, pri-
marily in the luminous shock regime. One major such characteristic is that the
multiply-reflected shock flows persist for a duration which is at least an or-
der of magnitude longer than that in the conventional shock tubes. In a con-
ventional pressure-driven shock tube the duration is approximately equal to the
time of flight of the primary shock over the full length of the driven section.
A spectroscopic and calorimetric analysis has shown that the multiply-reflected
regime of the diaphragmless flexible shock tube indeed remains in a thermally
excited state for the entire duration.[2] This persistence of thermal excitation
is of considerable importance because one can now explore a broad range of re-
action phenomena which require long relaxation times, normally too long to be

studied by means of the conventional shock tubes.

One particularly striking example of such reactions, which bears on the diaphragmless flexible shock tube as an experimental tool, is the discovery that it is possible to trigger reactions between the driver gas and the driven gas in this shock tube. Here the reaction is combustion taking place between hydrogen, used as the driver, and oxygen in the driven gas of synthetic air or pure oxygen. In the conventional shock tubes the reaction between the driver and driven gases simply does not take place. The driven gas is heated by shock compression and comes into contact at the contact surface with the driver gas which is cooled by the rarefaction process. The duration of the contact between the two is not long enough for the precursor relaxation processes to evolve fully to the point of ignition in the conventional shock tubes. Our observation of the driver-driven gas reaction arises from the fact that the shock reflection takes place between the endwall of the shock tube and the contact surface repetitively for tens of times, allowing a sufficiently long period of relaxation between the two reactants. The reason for such an extraordinarily large number of shock reflections is in the fact that the driver gas pressure is continually steepened due to the throttling process of the valve opening and the large volume of the driver section.

In the present paper we report on the results of a new investigation into the energetics of the driver-driven gas reaction when the driver section of the diaphragmless flexible shock tube is filled with hydrogen and the driven section with pure oxygen. The threshold condition for ignition of self-sustaining combustion is determined in terms of the operating parameters of the shock tube. Also measured are the percent completion of the H_2-O_2 reaction in terms of total available oxygen at the start of each run. The percent completion as well as total thermal energy production is determined by measuring the total amount of water as a reaction product. In addition, time-resolved emission spectra have been obtained in order to establish the reaction pathway for the ignition of the driver-driven gas reaction. Namely, thermal dissociation of molecular oxygen into atomic oxygen leads to the ignition.

In the following sections, the experimental setup, the procedure for measurement of the percent completion of the reaction and the instrumentation for time-resolved spectroscopy as well as the analysis of the reaction pathway will be described.

EXPERIMENTAL SETUP

The shock tube used in this study has a 60 cm long, 2.22 cm diameter driver section, fitted with a spring loaded plug valve, and a 112 cm long driven section consisting of 7.9 mm diameter copper tubing terminated with a test section. The test section has an interchangeable cylindrical sidewall piece of either polished plexiglas or aluminum construction. The entire endwall consists of a fused quartz or germanium window. A piezoelectric pressure transducer is located 5 cm downstream from the valve and also 7 mm upstream from the endwall.

The emission spectra from the shock heated gas are examined primarily with a f.3.5 high-dispersion spectrograph of Littrow design. The image plane of the spectrograph is fitted with a 1024-element Reticon photodiode array detector whose output is directed to a Nicolet 3091 digital oscilloscope. The oscilloscope is interfaced with a microcomputer for digital control, data I/O and on-line analysis. Streak photographs are also taken on occasion by means of a rotating drum camera. The overall arrangement of the experimental setup is shown schematically in Fig. 1.

In order to determine the fraction of oxygen consumed in the combustion reaction with hydrogen, we have chosen to measure the total amount of water molecules produced by the reaction in each run. A lightweight cold trap was designed and constructed for this purpose. It is constructed of thin-walled stainless steel tubings and is fitted with two miniature vacuum valves, one each at the long inlet and outlet tubes connected to the main 15 cm long cylindrical vessel of 1.25 cm diameter. The vessel is filled with glass fibers to maximize the surface area of the cold trap. Fig. 2 gives the details of the cold trap. The total weight of the cold trap is 116.895 g when fully evacuated. It is cooled by liquid nitrogen and ethyl alcohol-ice mixture in different stages of the water vapor measurement as will be described later.

The typical range of shock tube operation is 30 to 70 atm in the driver gas pressure and 20 to 250 torr in the driven gas pressure. The turn-around time for each run is as short as two minutes. The most time consuming part of the operation is the evacuation of the driven section by an oil diffusion pump but this process can be speeded up by combining the pumping with flushings of the driven section with pure oxygen to rid of hydrogen from the preceding run.

MEASUREMENT OF THE PERCENT COMPLETION OF THE H_2-O_2 REACTION

In a full blown combustion reaction of the H_2-O_2 system, as in a diffusion flame, as many as 40 different reaction steps come into play. H, O, OH, HO_2 and H_2O_2 play prominent roles as transient intermediate reaction products. However, in a pulsed system, such as in the present case of the driver-driven gas reaction in the diaphragmless flexible shock tube, there is no ambiguity as to what the final reaction products are. They are unreacted molecular oxygen, molecular hydrogen and water molecules. The percent completion of the H_2-O_2 reaction in each run is then defined by the ratio of the total number of water molecules to twice the number of molecular oxygen available at the start of the reaction.

We have adapted the following procedure for measurement of the quantity of water molecules produced in each run. Before each run the cold trap is first baked out at $150^\circ C$ under high vacuum for twenty minutes and the valves are then closed and its total weight determined to a milligram resolution. The cold trap is then connected to the exhaust valve of the driven section on the inlet end and to the vacuum manifold on the outlet end. Both connections are made by means of Swagelok fittings with teflon ferrules in a completely greasefree manner to insure against any addition of extraneous weights to the cold trap in this process. The main cylindrical vessel of the trap is then fully immersed in liquid nitrogen. After the shock tube is fired, the plug valve is closed immediately, isolating all of residual oxygen and water molecules in the driven section. The dominant constituent gas species in the driven section is, of course, molecular hydrogen. In the next 10 to 30 minutes the driven section is slowly pumped out through the cold trap down to a few milli-torr pressure level. Both the inlet and outlet valves are closed and the cold trap is immersed in an ethyl alcohol-ice bath in order to boil off whatever oxygen that has been condensed in the trap while keeping the trapped water still frozen. The trap is then evacuated for 10 to 20 seconds to 0.2 torr or less in pressure and sealed off to be weighed. The increase in the total weight of the cold trap gives the total amount of water molecules produced in the run. The amount of water molecules collected in the trap were in the range of 4 to 26 mg.

We have also explored the threshold conditions for ignition of self-sustaining combustion. In view of the fact that the H_2O_2 combustion results in a strong emission around 5890 Å, the threshold pressure of the driver gas is sought for each given pressure of the driven gas such that a shock tube run would result in a detectable emission intensity in this wavelength region. Fig. 3 shows a summary of the results from representative runs. At each oxygen

pressure we show a range of the hydrogen pressure which is grouped into three categories: no ignition, intermittent ignition and ignition. The threshold value of the driver gas pressure lies somewhere in the intermittent ignition region.

Fig. 4 shows the measurement on the percent completion of the H_2-O_2 reaction as a function of the driven gas pressure for those runs whose driver gas pressure lies above the ignition threshold value. The results show that the percent completion is in the range of 53 to 95% with a weak dependence on the shock strength. This indicates not only that the self-sustained state of combustion is readily reached once ignition takes place, but also that the diaphragmless flexible shock tube is remarkably effective in igniting the driver-driven gas reaction which, in itself, is a most unusual phenomenon.

The total thermal energy produced by the reaction is quite substantial. For the runs shown in Fig. 4 it ranges from 56 to 350 Joules. In fact, the heating from such an intense release of a large amount of energy invariably causes a severe burn damage to the plexiglas part of the test section in each run. Attempts to prolong the lifetime of the plexiglas test section by adding a disposable, transparent plastic lining have not been successful because the lining becomes completely consumed in the combustion and the sidewall of the test section scorched as well. The multiply reflected flows persist for 10 to 100 msec and the energy release here represents a sustained heating at a multi-kW level.

ANALYSIS OF THE IGNITION PATHWAY

The H_2-O_2 reaction system has been investigated over a period of several decades. Interests are broadly ranged, from flames to explosions to propulsion. The system has been studied experimentally, analytically and by numerical simulation, resulting in a large body of literature.[18] The system is still being studied, however, because there are at least 40 recognized intermediate reaction steps, involving many transient molecular species,[8] and some rate constants and the majority of reaction collision cross-sections[9] remain only poorly understood.

The initiation of the H_2-O_2 reaction system can be classified into three categories: one starting with production of atomic hydrogen, a second beginning with atomic oxygen and a third with free radical OH. In steady state combustion systems, all three reaction pathways play a role in the combustion front. In view of the fact that the dissociation potential is lower for H_2 than for O_2, the atomic hydrogen pathway is expected to be the most prominent of the three in such systems.

The question of interest in the present investigation is whether the ignition of the driver-driven gas reaction in the diaphragmless flexible shock tube will take place along a particular reaction pathway. We anticipate here that the atomic oxygen pathway will be favored over the others because the primary and multiply reflected shocks exist in the driven gas of oxygen, raising its temperature sufficiently high for production of atomic oxygen by thermal dissociation. The oxygen atoms then react with cold hydrogen molecules at the contact surface to produce water molecules.

The measurable consequence of this scenario will be in the composition of the emission spectrum from the shock tube. Namely, the atomic oxygen spectrum should emerge from early on in the initiation stage of the driver-driven gas reaction. The method of time-resolved spectroscopy has been employed for close examination of such characteristics in the shock tube emission.

In view of the significantly long time interval (10 to 100 msec) over

which the multiply-reflected shock flows as well as the ensuing H_2-O_2 reaction persist, it has been possible to configure a single Reticon photodiode array detector and a digital oscilloscope in a special way to permit determination of both the spectral and temporal property of the emission simultaneously. The particular Reticon detector (model RL1024.S) contains 1024 PIN photodiodes in a linear array spanning 25.4 mm, each 2.5 mm in height. The photodiode elements are set up in an integrating mode whose time of integration is determined by the time between two successive read-outs of the integrated intensity from a given photodiode element. In the example shown in Fig. 5 the scan rate is set at 3.32 μsec per element and, together with an additional time delay of 600 μsec before the start of a next scan, it gives an integration time of 4 msec.

When the Reticon detector is placed on the image plane of the spectrograph and is set in a free-running scan mode, a given photodiode element provides the integrated intensity at a given wavelength once every 4 msec. An element next to it measures the integrated intensity at another wavelength in accordance with the dispersion of the spectrograph, again once every 4 msec but displaced in time by 3.32 μsec with respect to the previous element. If the full 1024 element scan is viewed repeatedly, one can follow the time evolution of the full spectrum of the shock tube emission. Fig. 5b shows ten such scans in succession. The history of the pressure over the same time span, as detected by the pressure transducer near the plug valve, is displayed in Fig. 5a.

Fig. 6 is a display of the data from Fig. 5b showing in greater detail the time-integrated emission intensity as a function of wavelength at 4 msec intervals starting some time after the shock tube firing. We note that the 1024 spectral intensities from each full scan of the Reticon detector are compressed into 340 10-bit addresses of the digital oscilloscope because there are only 4000 addresses available in the oscilloscope for the ten full scans. This means that one out of three photodiode elements is retained in this display. Remember also that each wavelength channel is displaced in time from its immediate neighbor by 3.32 μsec.

It is quite straightforward to obtain the spectral intensity as a continuous function of time from the time integrated segments of the spectrum of Fig.6. We can, however, adequately address the question we posed earlier with the results shown in Fig. 6. They show a prominent H_2 and H_2O emission around 5390Å, characteristic of the H_2-O_2 combustion. Atomic oxygen emission lines contribute also starting early in the shock tube emission at all known wavelengths between 5329.10 and 6653.83Å. But none of the atomic hydrogen lines are present with intensities approaching anywhere near those of the atomic oxygen lines. This observation is entirely consistent with the proposed scenario for the ignition of the driver-driven gas reaction. Hydrogen molecules remain cold until they interact with oxygen atoms which have been produced by thermal dissociation of molecular oxygen due to the heating in the multiply reflected shock flows.

REFERENCES

1. Y. W. Kim, "A New Luminous, Diaphragmless, Flexible Shock Tube", in the Proceedings of the 13th International Symposium on Shock Tubes and Waves, Niagara Falls, July 6-9, 1981, p. 09.

2. Y. W. Kim and T. R. Quinn, "Persistent Thermal Excitation in the Multiply-Reflected Regime of a Diaphragmless Flexible Shock Tube", in the Proceedings of the 14th International Symposium on Shock Tubes and Waves, Sydney, August 19-22, 1983, p. 610.

3. A. E. S. Green, P. F. Schippnick and D. E. Rio, Int'l. J. Quantum Chem., Quantum Chemistry Symposium 17, 127 (1983).

4. Y. Hidaka, S. Takahashi, H. Kawano, M. Suga and W. C. Gardiner, Jr.,
    J. Phys. Chem. 86, 1429 (1982).

5. J. A. Miller and R. J. Kee, J. Phys. Chem. 81, 2534 (1977).

6. W. T. Rawlins and W. C. Gardiner, Jr., J. Chem. Phys. 60, 4676 (1976).

7. C. J. Jackimowski and W. M. Houghton, Combustion and Flame 17, 25 (1971);
    15, 125 (1970).

8. D. L. Baulch, D. D. Drysdale, D. G. Horne and A. C. Lloyd, Evaluated
    Kinetic Data for High Temperature Reactions, Vol. 1, Homogeneous Gas
    phase reactions of the H_2-O_2 system (Chemical Rubber Company, Cleveland,
    1972).

FIGURES
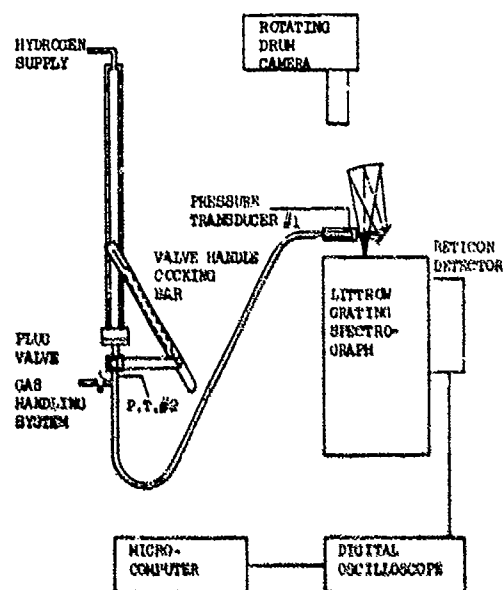
Fig. 1. A schematic diagram of the experimental setup, showing the diaphragmless flexible shock tube and associated diagnostic instruments.
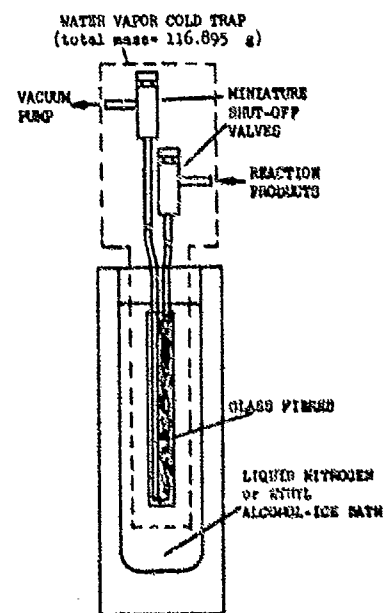
Fig. 2. The cold trap used for measurement of water molecules produced by the driver (H_2)-driven (O_2) gas reaction.
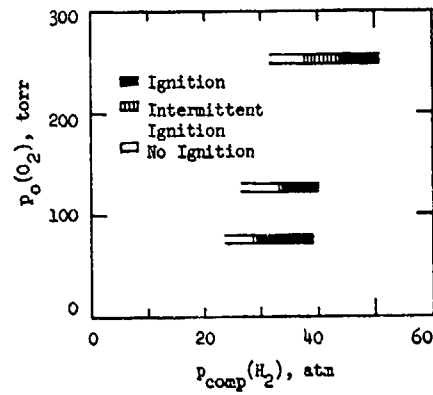
Fig. 3. A diagram showing the ignition threshold for the driver-driven gas reaction.
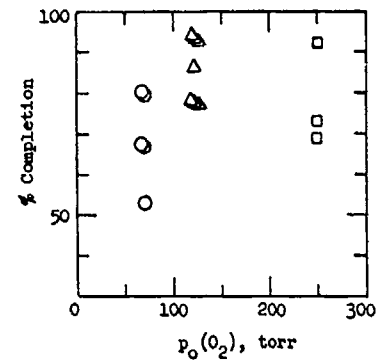
Fig. 4. Measured percent completion of the driver-driven gas reaction.
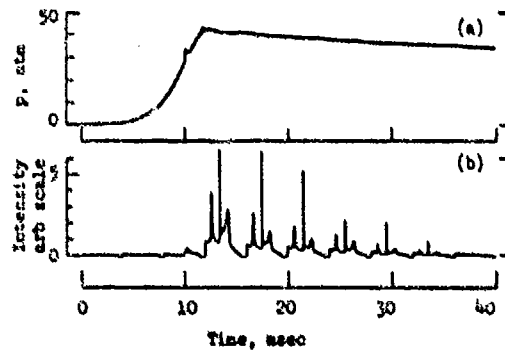
Fig. 5. a) The post-valve pressure transducer output and b) successive Reticon scans of the shock tube emission, as a function of time for a run in 30 torr oxygen at hydrogen driver pressure of 42.5 atm.
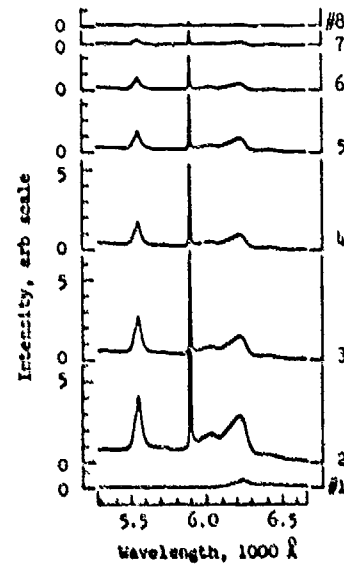
Fig. 6. Reconstructed emission spectra, integrated at 4 msec intervals, from Fig. 5b. The time increases from spectrum #1 to #8.

BLAST-WAVE DENSITY MEASUREMENTS

by

D. V. Ritzel

Defence Research Establishment Suffield
Ralston, Alberta, Canada

A density gauge has been developed at Defence Research
Establishment Suffield (DRES) for measurements of
density-time records at locations of interest in shock-
and blast-wave flows. The system employs the beta-
attenuation technique and resolves the total density of
gas and any other material passing between the beta
source and detector. Although this instrumentation has
been designed for deployment in blast field trials it
can also be used in laboratory shock-tube tests, and
the gauge has been successfully fielded in both kinds
of experiments. The value of this density gauge is
shown in its ability to resolve contact surfaces,
slipstreams and density effects of entrained dust or
debris previously unresolved by standard field instru-
mentation. These features have important implications
both in applied studies of blast loading of structures
and in basic research in shock-wave phenomenology. In
this paper, the density-gauge system is briefly
reviewed, and results from the large-scale height-of-
burst (HOB) blast test 'Direct Course' are presented
and compared with predictions from numerical computa-
tions. Current and future applications of the gauge in
various blast- wave research areas are also described.

1. INTRODUCTION

As more complex shock-wave problems are investigated, the requirement for
reliable and comprehensive experimental measurements of flowfield properties
using minimal assumptions about the flow will become more acute. Although
pressure gauges have been reasonably well developed through the past decades,
reliable types of instrumentation for the remaining flow conditions are still
in demand. This deficiency is most evident in large-scale shock-tube and blast
field trials in which there are severe design constraints on instrumentation
and few of the conveniences allowed laboratory techniques.

The present paper describes and discusses a few results from successful
applications of a density gauge, or densitometer, capable of resolving time
records of the total density at a particular location of interest in two-
dimensional shock- and blast-wave flows. Measurement of blast-wave density is
valuable due to its fundamental role in the stagnation and dynamic-pressure
loading of structures and its importance in defining blast-wave features such
as contact surfaces, slipstreams, and dust or other multi-phase flow, beyond
the scope of standard pressure instrumentation.

Blast-flow density can be determined in some cases using photographic methods such as interferometry or Dewey's particle-trajectory technique[1]. Although effective in some applications, particularly in the laboratory, there are disadvantages to such methods, especially their restriction to clear flows, the relatively low resolution of quantitative data obtained by tedious film-reading digitizing, and the fairly extensive set-up operations. Relatively few attempts have been made to develop a true density 'gauge' to provide a high-resolution analog record of the detailed density history at any location of interest. Such a gauge would be intended to be deployed as readily as a pressure transducer for shock-tube or field applications. A low-cost 'corona-microphone' technique was investigated in the early 1950s in Sweden and the United States[2] with apparently good results, but recent evaluations carried out by AWRE[3] have shown the method to be ineffective in field experiments with dust and fine debris in the flow. Futhermore, the sensor seems inappropriate for arbitrary two-dimensional flows. A light-attenuation method[4] has been attempted for dusty-blast flows, but problems appear to exist with total obscuration of the beam and correlating obscuration to actual density levels. The most promising generic type of blast densitometer for general applications is based on radiation attenuation, such as the present DRES system.

2. DENSITOMETER SYSTEM

The DRES density gauge and its development have been described in previous reports[5] [6] [7] [8]. The system consists of a beta-radiation source (Promethium-147 with an end-point energy of 0.224 MeV) which faces across a gap to a detector composed of a scintillator and photomultiplier tube (PMT); the measured intensity will be a function of the attenuation of the radiation beam due to the total density in the flow within this measuring volume. Although the equation governing the radiation attenuation is an exponential, signal conditioning and amplifying electronics are used to produce a convenient linearized output. In a recent paper[9] the most recent version of the densitometer is described as part of a new blast-gauge station, designed to combine several types of instrumentation (static and stagnation pressure, density and shock velocity) in a single convenient gauge head in order to define the complete gasdynamic flowfield at a location in a blast.

3. APPLICATIONS AND RESULTS

The original blast densitometer system was developed at DRES by Dr. Dewey in the 1960s for applications in large-scale blast field trials. The gauge structure is shown in Fig. 1, and basically consists of two vertical parallel panels secured to a base plate. Oriented towards the shock, the panels form a channel of prescribed width through which the blast wave passes undisturbed. The densitometer is configured across this channel near the centre of the panels at 46 cm elevation; one panel is used to mount the source, while the other contains the detector, amplifier and batteries. Each panel measures 165 cm long by 61 cm high by 8 cm thick and features sharp leading and trailing edges so as not to significantly disturb the blast flow. The detector side has a streamlined housing which protudes somewhat into the external flow in order to accomodate the PMT. This system was successfully fielded in large-scale surface blasts and shock-tube tests conducted at DRES, and very good records were reported[5] [6].

The system was virtually ignored until the large-scale blast test 'Direct Course' conducted by the Defense Nuclear Agency in October 1983. This test involved the detonation of 609 tons of ammonium-nitrate/fuel oil (ANFO) contained in a 10.7-m spherical fibreglass shell at a 50.6-m height of burst. Blast research studies were concerned with the evolution of the various forms

of Mach reflection but were concentrated on the dust-scouring phenomena in which fine surface material is entrained by HOB blast waves passing over realistic 'non-ideal' terrain. The dust entrainment and associated density increases had been observed to significantly alter the blast-wave characteristics.

The DRES densitometer system was hastily refurbished for this test; the instrumentation was upgraded[7] although configured as shown in Fig. 1. Three gauges were deployed in a 'natural blast' environment at peak overpressure levels of 245, 172 and 70 kPa, (183, 201, and 314 m from ground zero, GZ) at heights of 15, 46, and 46 cm, respectively. Two gauges were deployed over a surface which had been specially tilled, sifted and loosened to promote dust ingestion into the blast flow. These stations were located at the 550 and 245 kPa sites (122 and 183 m from GZ) at an elevation of 15 cm. Example results obtained from this test are shown in Fig. 2 in comparison to some computer-code predictions.

A dusty-blast density record is shown in Fig. 2a as obtained from the 550 kPa site. Features to note are the apparent second peak occurring about 40 msec after shock arrival and the abrupt density surge arriving about 100 msec after the blast front. As supported by other observations, measurements and computations, these are explained by dust-scouring mechanisms; the large density surge marks the arrival of the dust pedestal or toroid created by the ground vortex. A pre-shot computation from the DICE code of California Research and Technology[10] shows dust density alone. The amplitude has been reduced by a factor of four for the figure, but the waveform has some validation from the measurement. The discrepancy can be explained by the course gridding used (20-cm cells), simplified dust-ingestion modelling, and the fact that the numerical data station was lower (10 cm) than that of the experimental measurement. However, this and other density-history comparisons with DICE have shown fair qualitative agreement in describing dust sweep-up.

Figure 2b shows density histories at a distance of 183 m from GZ. Shown in the figure are traces from dusty, natural and clean blast environments; the clean-blast record is a HULL-code prediction and is further idealized by not including any dissipative effects. Although not included for brevity in this paper, the measured overpressure record at the 'natural' site is a classical smoothly decaying waveform of 235 kPa amplitude[8]. Comparing the HULL record and the natural-blast measurement, an abrupt density drop is observed in both cases, about 40 and 80 msec after blast arrival respectively, which corresponds to the passage of the slipstream roll-up in the ground vortex. Note that a density increase is expected upon passage through the Mach-reflection slipstream itself. It can be concluded that this density drop was due to the fact that the slipstream had rolled up and passed over the gauge site; therefore the site would experience the low-density jet drawn in behind and beneath the roll-up. The discrepancy regarding arrival and extent of the decay can be explained by dissipative effects, especially involved with the ground vortex, and the certain presence of some dust in the measured blast wave. The dusty-blast record shown as a dashed line reveals the effect of dust scouring: the density decay appears to be 'filled in' by the effects of entrained dust and/or enhanced dissipation of the ground vortex. The dust pedestal has evidently slowed and dispersed in comparison to the 122-m record; the sharp peak occuring about 300 msec after the blast front is the secondary shock, the effect of which is superposed on the density surge of the pedestal. These results illu-⟩ strate the importance of two-dimensional effects even at low overpressure sites which would not have been revealed by standard pressure instrumentation.

A final example of a density record is shown in Fig. 2c which compares the HULL prediction with the measurement from the 70 kPa natural-blast site. Here there is very good agreement since both dissipative effects and actual dust ingestion would be small.

4. APPLICATIONS AND DEVELOPMENTS OF THE DENSITOMETER

Since the Direct Course test the densitometer system continues to be applied and developed. Applications include blast field trials, and both small and intermediate-scale shock-tube tests. In small shock tubes the source and detector are configured across the test section. Very good results have been obtained for shock waves with durations as short as several milliseconds, and valuable data, particularly regarding contact surfaces, have been resolved.

Recently, the system has been configured in a smaller convenient gauge head for field applications which also includes other blast instrumentation as shown in Fig. 3. This new field blast-gauge station has been deployed in the large-scale blast test 'Minor Scale', although results are still being processed. In future developments it is intended to replace the pitot probe with a instrument to resolve local acoustic velocity in a direct fashion for arbitrary two-dimensional blast flows. Such a method may also allow discrimination of dust from gasdynamic densities in the densitometer measurement.

5. CONCLUSION

A densitometer system has been developed for resolving density-time records at locations of interest in two-dimensional shock-wave flows. Results have been presented here from its application in the blast field trial 'Direct Course', and important features of the blast flow have been revealed. In particular, effects of the HOB ground vortex and dust ingestion have been identified. It has been demonstated that such density measurements are useful in the analysis of shock-wave phenomena and the evaluation of hydrocode computations, beyond the scope of pressure gauges.

6. REFERENCES

1. Dewey, J. M., "The Air Velocity in Blast Waves from TNT Explosions", Proceedings of the Royal Society, London, A 279, 1964, pp. 366 - 385.

2. Weimer, D., "The Use of a Coronamicrophone in the Shock Tube", The Review of Scientific Instruments, Vol. 23, No. 7, July 1952, pp. 337 - 338.

3. Smith, A. V., private communication, Atomic Weapons Research Establishment, Foulness, United Kingdom, June 1985.

4. Wisotski, J., "Dust Measurements", from 'Pre-Direct Course Results Report, Vol. 1', POR 7116-1, Edited by R. Grayson, Test Directorate, Field Command Defense Nuclear Agency, Washington D. C., May 1983, pg. 26 & pp. 53 - 57.

5. Dewey, J. M., "The Air Velocity and Density in Blast Waves from TNT Explosions", Suffield Report No. 207, Defence Research Establishment Suffield, Ralston, Alberta, Canada, March 1964. UNCLASSIFIED.

6. Ross, J. R., "A System and Procedures for Measuring Blast Wave Density in a 500 ton TNT Surface Burst", Suffield Report No. 258, Defence Research Establishment Suffield, Ralston, Alberta, Canada, May 1971. UNCLASSIFIED.

7. Funk, J. F., and Saint, D. H., "A System for Measuring Total Density in Dusty Shock Waves Using the Beta Attenuation Technique", Proceedings of the 30th International Instrumentaion Symposium, Denver, CO, 7 - 10 May 1984, pp. 663 - 676.

8. Ritzel, D. V., "Measurements of Blast-Wave Density by a Special Beta-Ray Gage", presented at the Direct Course Results Symposium, Harry Diamond Laboratory, Adelphi, MD, April 1984 (proceedings to be published).

9. Ritzel, D. V., "The DRES Blast-Gauge Station", submission to the Ninth International Symposium on Military Applications of Blast Simulation, 23 - 27 September 1985, Oxford, England.

10. Rosenblatt, M., and Schlamp, R. J., "Dusty Airblast and Sweep-up Predictions for the Direct Course Experiment: Summary of Results", presented at the Direct Course Results Symposium, Harry Diamond Laboratory, Adelphi, MD, April 1984 (proceedings to be published).
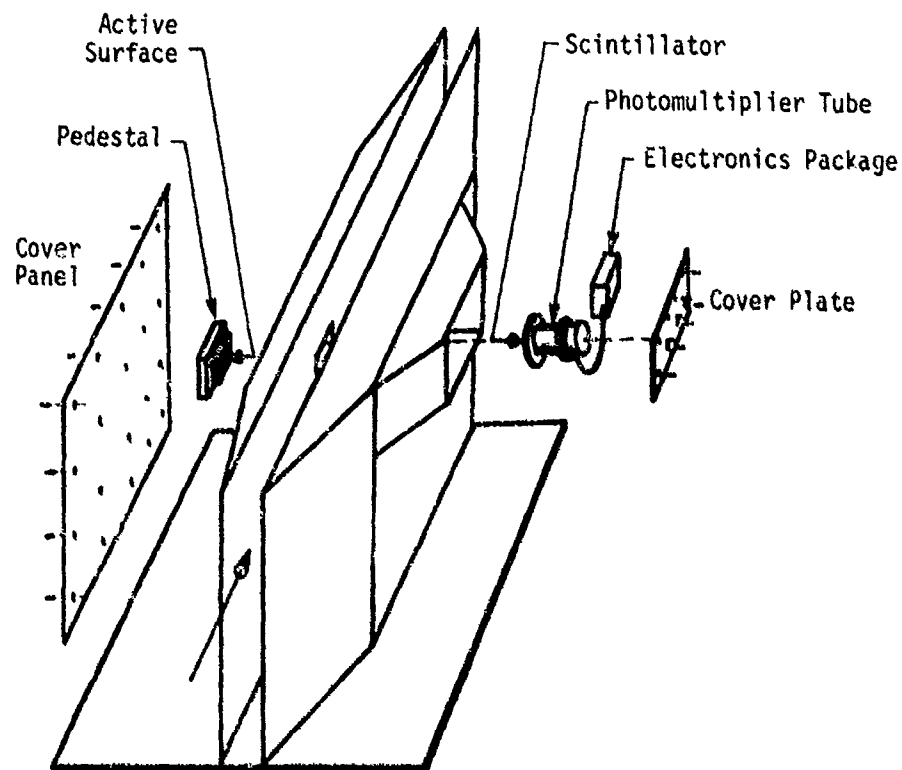
Figure 1. Exploded view of the original blast-gauge station showing the densitometer components.
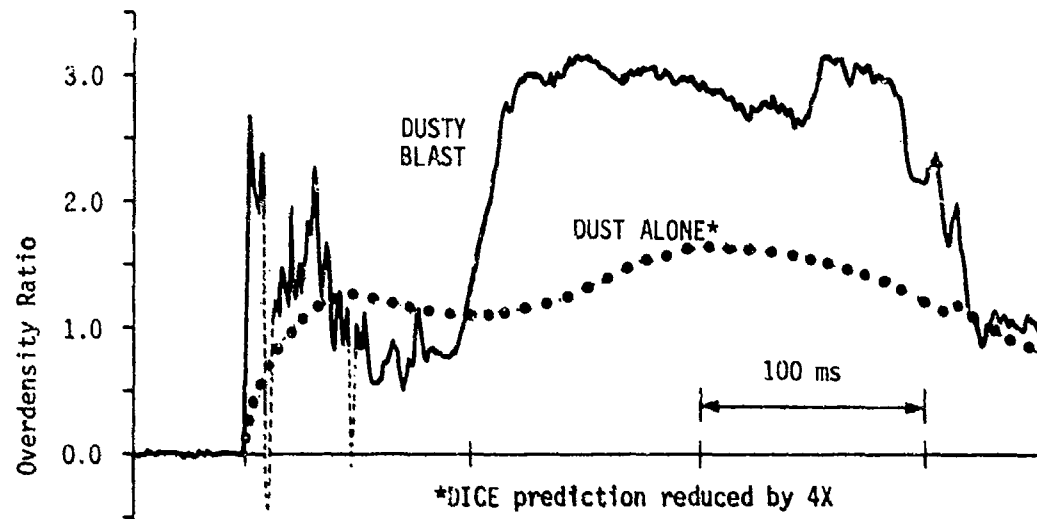
Figure 2a.   Measured total density history in the dusty blast (550 kPa site) in Direct Course; ambient density was 1.04 mg/cc.   The dotted trace represents a course-grid DICE-code prediction for dust density alone.
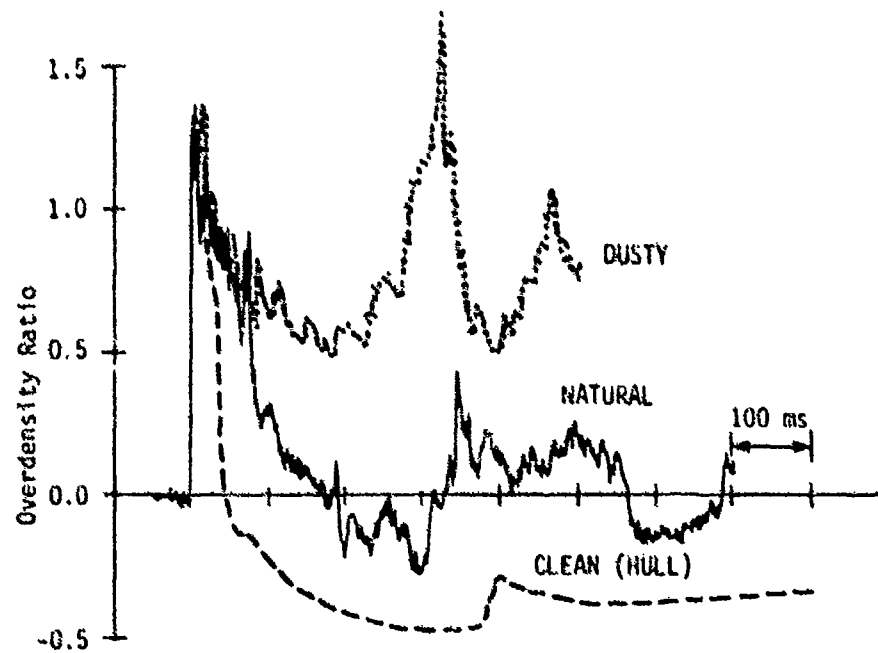
Figure 2b.   Measured and computed density histories at the 245 kPa sites, comparing dusty and natural blast measurements and the HULL-code prediction for an ideal blast.

Figure 2c. Measured and computed density histories at the 70 kPa site.
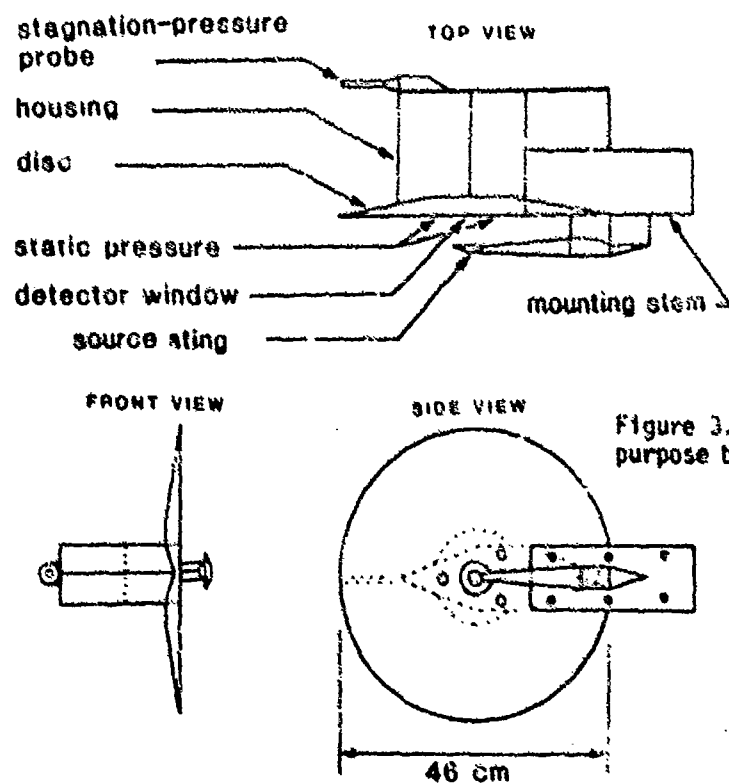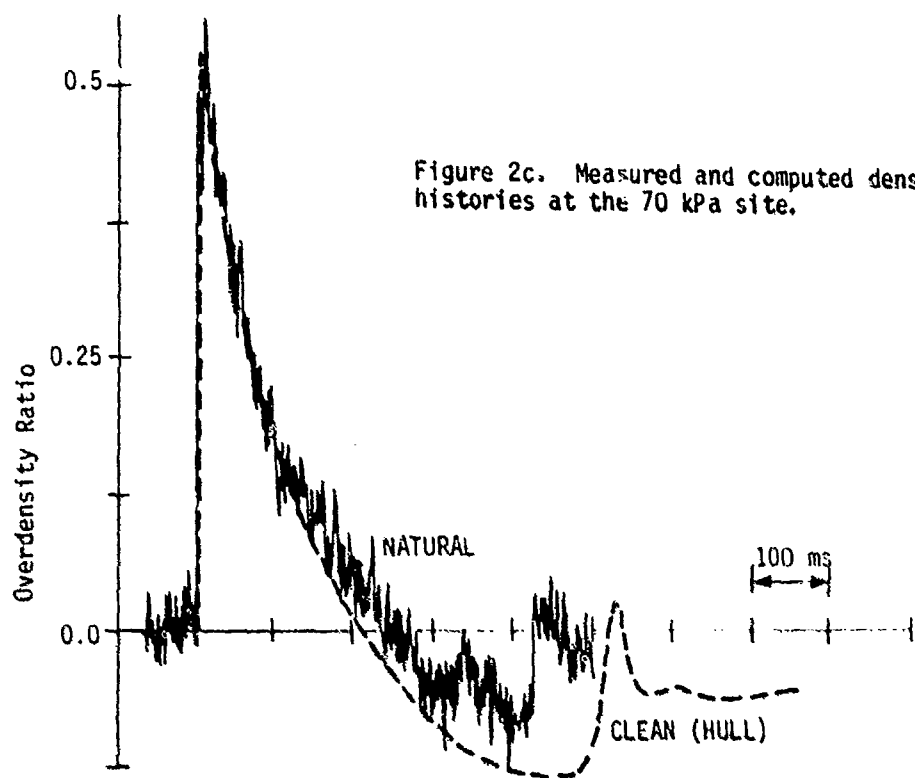
Figure 3. Sketch of new general-purpose blast-gauge head.

SIMULTANEOUS LASER MEASUREMENTS OF VELOCITIES AND

PARTICLE SIZES IN TWO-PHASE FLOWS

Y.M. Timnat and Y. Levy

Department of Aeronautical Engineering
Technion - Israel Institute of Technology
Haifa 32000, Israel

Measurements that allow to determine simultaneously
velocities and particle sizes in two-phase flow are of great
interest for the study of shock dynamics in dusty gases, for
fuel injection systems, sudden expansion combustors,
fluidized beds, pulverized coal combustion and filtration
processes. A technique based on the use of a modified Laser
Doppler Anemometer (LDA), allowing instantaneous measurement
of the sizes and velocities of individual transparent
spherical particles in a range from about 20 to 800
micrometers, with velocities up to 600 m/s was developed. It
is based on the linear relation existing between the particle
diameter and the pedestal amplitude, a characteristic of the
LDA signal. The technique developed in order to obtain the
parameters of this relation is described and preliminary
results are presented.

1. INTRODUCTION

Accurate measurements of particle sizes and velocities in two-phase flows
are important for studying the shock dynamics in dusty gases[1], fuel
injection in air breathing engines and liquid rockets, sudden expansion in
ramjets and ramrockets[2] as well as in other fields, such as fluidized beds,
pulverized fuel combustion and filtration processes. In addition, computer
codes for two-phase flow require preliminary information on the initial
conditions, which must be obtained experimentally.

There are a number of techniques, most of them based on a modified LDA
system, for local, instantaneous two-phase flow measurements. They can be
divided in three categories: a) the visibility technique[4,5], b) the pedestal
amplitude[2,6-8] and c) the phase Doppler anemometry[9,10].

In the first method one uses the visibility of the signal, V, given by

$$V = (I_{max} - I_{min})/(I_{max} + I_{min})$$

where I_{max} and I_{min} are defined in Fig. 1. The advantage of using
visibility values as a measure of the particle size is that it relates it to a
non-dimensional characteristic of the signal, independent of the absolute
signal intensity, and in some cases requires no calibration.

The pedestal amplitude is defined as the maximum amplitude of the low
frequency component of the signal detected by the photomultiplier, as shown in
Fig. 1. It was found to have a linear relationship to the particle diameter
over a wide size range. This technique is easier to implement, but requires a
calibration.

The phase Doppler anemometry utilizes the interference caused by particles crossing the control volume. A phase difference, linearly related to the particle diameter, is detected between signals obtained simultaneously by two photomultipliers at different location.

In all three categories the receiving optics must be aligned at some angle to the axis (off-axis detection), as shown in Fig. 2. In the present work the pedestal technique was chosen. Particles crossing the control volume scatter a burst of light with an oscillatory frequency related to the particle velocity (the Doppler frequency) and a pedestal amplitude linearly related to the particle size (see Fig. 1).

Since the light intensity in the control volume has a spatial distribution, it is possible to eliminate errors in the size measurements by reducing the sensitivity of the collecting optics to a predetermined section, chosen usually as the central part of the control volume (see Fig. 3). In this region the light intensity of the fringes is almost constant and can be considered to have the same reference level for all measured particles. Only signals of particles crossing the central part of the control volume are accepted.

2. THE EXPERIMENTAL SYSTEM

The measuring technique developed was tested by performing experiments with a system designed for collecting data on the two-phase flow in a sudden expansion combustor, also known as a dump combustor. The set-up, shown in Fig. 4 includes fuel injection, a sudden expansion from a 10 cm to a 16 cm dia. channel, equipped with pairs of optical windows, a 15 mW He-Ne laser, appropriate optics and a detecting and processing system.

The signal processing system consists of three parallel branches, that include the processing of the Doppler signal giving velocity information, of the pedestal amplitude, providing the droplet diameter and a validation pulse confirming the accuracy of the size measurements. A block diagram of the complete signal processing system is given in Fig. 5.

In the Doppler branch the signal from the photomultiplier is connected to a frequency processor through a high pass filter which acts as a buffer and an electronic mixer. The frequency processor (DISA model 55L90a) converts the Doppler frequency bursts to a linearly related analogue voltage. The purpose of the buffer is to prevent reverse influence of the mixer on the signal of the photomultiplier, to eliminate distortion of the amplitude information, required for the size measurements.

In the pedestal amplitude branch, the signal from the photomultiplier is connected in parallel (see again Fig. 4) to a system, which detects and stores the pedestal amplitude of individual signals. A diagram, which illustrates schematically the signal processing is given in Fig. 6. The signal is passed through a low-pass filter (self ouit, 1 MHz), which removes the Doppler frequency oscillations revealing the low frequency component of the signal; this is then directed to a specially built peak detector (described in detail in Ref. 8), which records the pedestal amplitude. The peak detector processes signals with an amplitude above a preselected trigger level. Lower amplitude signals, which usually come from gas tracking micron-size particles, are considered to have zero pedestal amplitude. The detector stores the signal until the arrival of a new one, which resets to zero the previous value. The peak detector records all signals from the photomultiplier, which have an amplitude above the trigger level.

The Doppler frequency processor performs an internal validation test, so that only part of the signals are accepted and converted to the analogue voltage. It follows that new signals come out of the peak detector at a higher rate than out of the Doppler processor; a synchronization procedure must therefore be introduced.

The validation signal, which indicates that a particle has crossed at the centre of the control volume, is generated by synchronizing signals obtained from two photodiodes aligned along the incident laser beam (see Fig. 3). The diodes record every particle, which crosses the beams. When a particle crosses exactly at the centre of the control volume, the two diodes will record signals instantaneously. The photodiode signals are processed to obtain a validation pulse generated when they overlap. The amount of overlapping specifies the dimensions of the region within the control volume, which the particles have to cross in order to be accepted.

For automatic data acquisition all three channels are recorded on a PDP 11/34 minicomputer. The signals are fed to an analogue to digital converter, sampled sequentially and stored continuously. Whenever sampling terminates, a data processing routine is called. It reveals the validated signals, which are to be considered for analysing the flow results.

In order to obtain from the pedestal amplitude, measured in voltage units, the particle size, a calibratic must be performed. This was done with droplets of known diameter as described in Ref. 2.

3. RESULTS AND DISCUSSION

The experiments were carried out in air with kerosene or water as the condensed phase. The information from the droplets is classified into sections, according to their size. The very small droplets serve as tracking particles, representing the gas flow. Local velocity histograms, means and r.m.s. values are obtained for each size.

A typical set of data is presented in Fig. 7; it shows the radial variation of velocity histograms and mean and r.m.s. values for the two phases across the combustor.

Figure 8 illustrates the gas flow along and across the combustor central plane. One can observe a slight attenuation in the velocity when proceeding downstream; on the other hand the figure displays clearly the recirculation zone formed near the sudden expansion, which stabilizes the flame and disappears downstream. Some asymmetry is evident, probably due to upstream distortion originating in the air supply.

Figure 9 presents the relative particle size distribution in the centre of the combustor, showing that over 40% of the droplets have a diameter smaller than one tenth of the maximum diameter.

The accuracy of the velocity measurements, which depends on the optical alignment, the signal to noise ratio and the settings of the frequency counter used, is estimated to give an error below ± 2%.

The particle size estimate depends strongly on the calibration curve, which shows repeatability limits better than 10%. This can be improved by refining the calibration technique.

REFERENCES

1. Marble, F.E., "Dynamics of Dusty Gases", Annual Rev. of Fluid Mech., Vol. 2, 1970, p. 397.

2. Levy, Y. and Timnat, Y.M., "Study of Sudden Expansion Combustion for Propulsion Applications", XXXIV IAF Congress, Budapest, 9-15 Oct. 1983, IAF 83-372.

3. Tambour, Y., "Vaporization of Polydisperse Fuel Spray in Laminar Boundary Layer Flow: A Sectional Approach", Comb. & Flame, Vol. 58, Nov. 1984, p. 103.

4. Bachalo, W.D., "Methods for Measuring the Size and Velocity of Spheres by Dual-Beam Light Scatter Interferometer", Appl. Optics, Vol. 19, March 1980, p. 383.

5. Farmer, W.M., "Measurements of Particle Size, Number Density and Velocity Using Laser Interferometer", Appl. Optics, Vol. 11, Nov. 1972, p. 2603.

6. Yule, A.J., Ereaut, P.R. and Ungut, A., "Droplet Sizes and Velocities in Vaporizing Sprays", Comb. & Flame, Vol. 54, Dec. 1983, p. 15.

7. Mituzani, Y., Kodama, H. and Miyasako, K., "Doppler Mie Combination Technique for Determination of Size Velocity Correlation of Spray Droplets", Comb. & Flame, Vol. 44, Jan. 1982, p. 85.

8. Levy, Y. and Timnat, Y.M., "Two Phase Flow Measurement Using a Modified Laser Doppler Anemometry System", in "Single and Multiple Flows in an Electromagnetic Field; Energy Metallurgical and Solar Applications", Progress in Astronautics and Aeronautics, AIAA, 1985.

9. Bauckhage, K. and Floegel, H.H., "Simultaneous Measurements of Droplet Size and Velocity in Nozzle Sprays", 2nd Int. Symp. on Application of Laser Anemometry to Fluid Mechanics, Lisbon, July 1984.

10. Bachalo, W.D. and Houser, M.J., "Development of the Phase/Doppler Spray Analyzer for Liquid Drop Size and Velocity Characterization", AIAA Paper 84-1199, 20th Joint Prop. Conf., Cincinnati, June 1984.
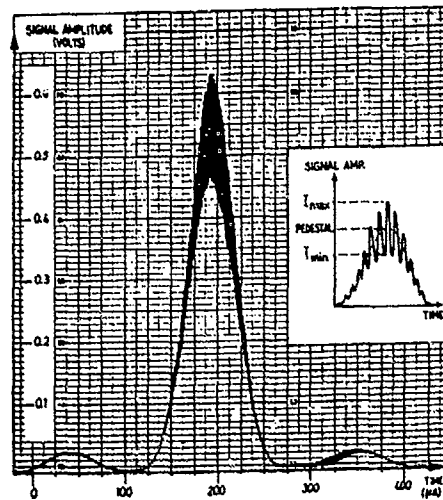
Figure 1. Typical plot of signal
          detected from large
          liquid drop.

Figure 2. General layout of
          LDA system.
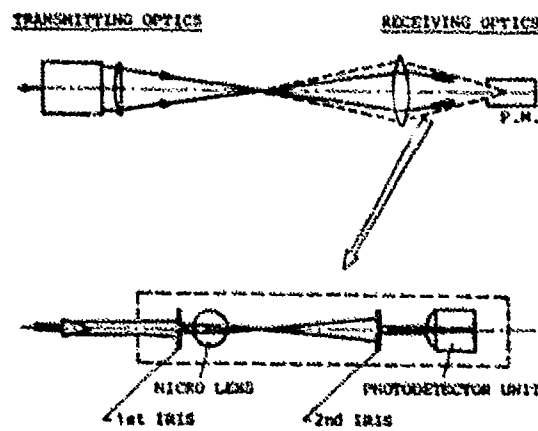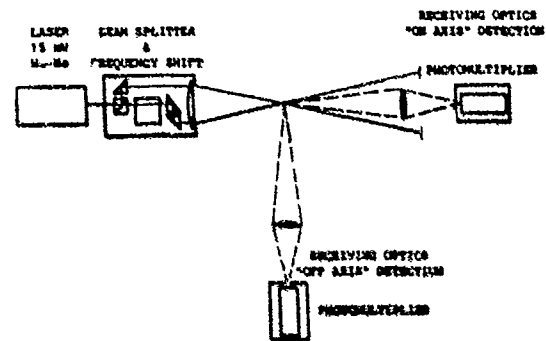
Figure 3. Modified receiving
          system.
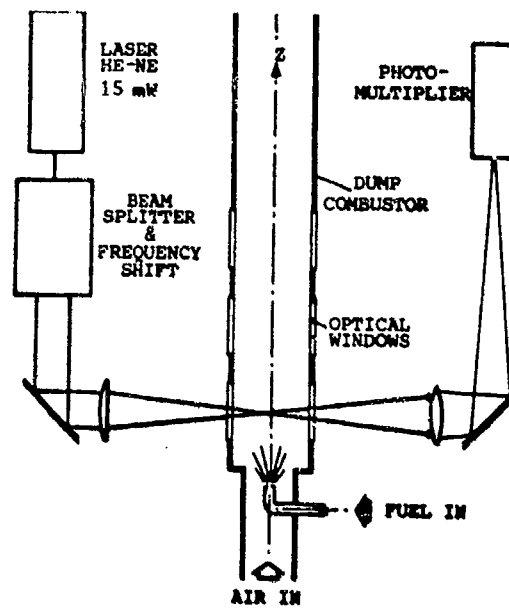
Figure 4. Dump combustor and optical system.
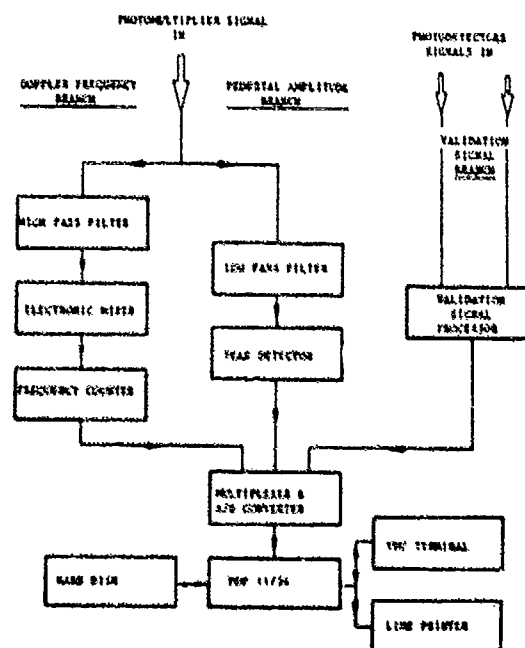
Figure 5. Signal processing system.
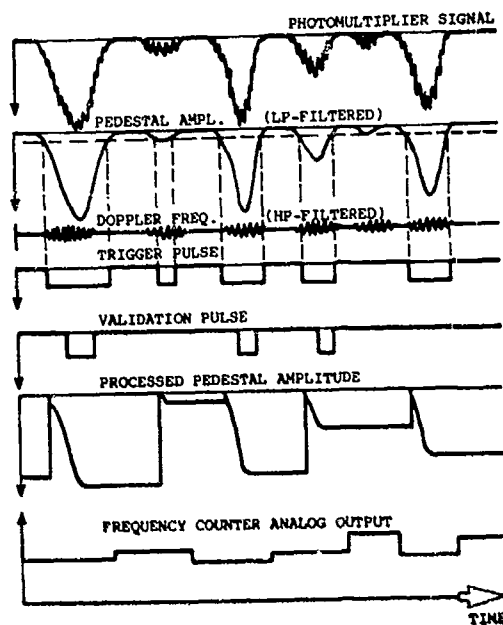
Figure 6. Schematic output.
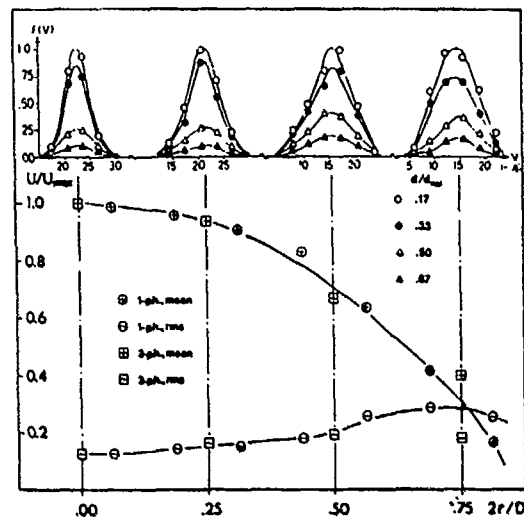
Figure 7. Radial distribution of velocity histograms and mean and rms values for different size sections in dump combustor.
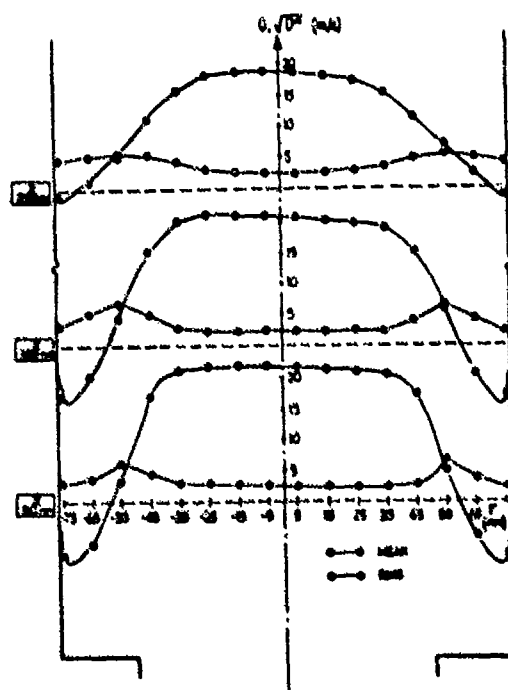
Figure 8. Gas flow variation inside combustor.
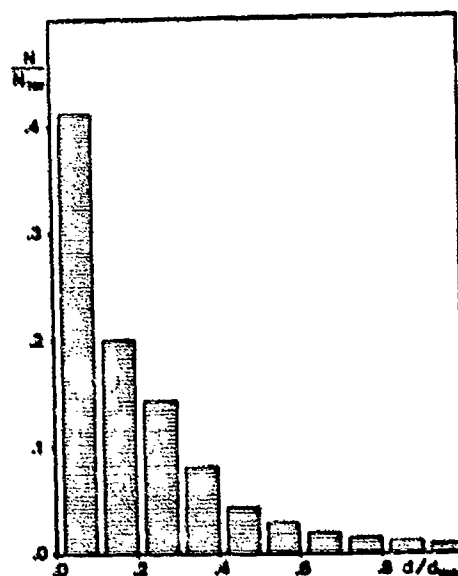
Figure 9. Relative droplet size distribution.

SHOCK WAVES IN A GAS FILLED FLEXIBLE TUBE

J. BROSSARD, J. RENARD, M. AMINALLAH

Laboratoire de Recherche Universitaire
63, Avenue de Lattre de Tassigny
18028 BOURGES CEDEX - France

After a brief review of the most signifiant results obtained
from the modelization describing the deformation of a long
tube loaded by a moving ideal pressure step, we report the
numerous data obtained from the experimental investigation on
a polyvinyl tube. The pressure step is a shock wave (M ~ 1.5
to 4.5) the strength of which is governed by the initial
pressure of the detonable mixture in the high pressure
chamber. A cellophan diaphragm isolates the low pressure
chamber which is a PVC tube 4 m long and 16 mm in dia. The
radial and longitudinal deformations are investigated by
strain gauges on the external wall. The amplitudes and the
frequencies of the deflections on both sides of the damped
shock front are in quite agreement with the predicted values,
in spite of the difficulty to evaluate the mechanical
properties of the material.

1 - INTRODUCTION

The damaging effect of shock waves on pressure vessel submitted to pressure
wave loading appears as a real problem with respect to safety[1]. In particular
the transient response can be catastrophic for the structure. In the case of
straight tubes, besides the geometry and the development of the boundary layer,
the mechanical stiffness obviously affects the velocity and the decrease of the
confined shock wave. Between the two extreme boundary conditions which are the
perfectly rigid mechanical confinement and the widely deformable or the brittle
fracture of the tube, there are many modes of interaction between the pressure
wave and the material. Specifically in the case of polymeric confinement and low
velocity pressure step, a procursor deformation is attached to the pressure front
; that means a fundamental interaction between the pressure wave propagation and
the expansion of the confining material.

After a brief review of the most significant results obtained from the
modelization applied to the long tubes confining an ideal pressure step we report
the numerous data obtained from the experimental investigation on a polyvinyl
tube. Then, from the comparison of the observed deformation with the predicted
values deduced from a more sophisticated numerical solution of the non-stationary
model, we conclude to the good agreement.

2 - MODELIZATION AND NUMERICAL SOLUTION

There have been several theoretical studies[2,3,4] of the deformation of a
flexible tube confining a propagating shock wave. The restrictive hypothesis
generally introduced are : the axially symmetry, the elastic behaviour of the
confining material, the thin walled tube and an ideal step pressure wave with a
constant velocity. In the most complete theory developped by Tang[3] are
introduced the shear deformations, the rotatory inertia and the bending moment.
For the steady state response the pressure is assumed to have acted for a long
time. The analysis of the partial differential equations leads to the
characteristic equation which defines four different critical velocities. The two

lowest values are dependent not only on the geometrical charateristics of the tube but also on the mechanical properties of the material. The two highest values are only dependent on the mechanical properties of the material. So, the four particular values of the velocity divide the spectrum velocity in five domains in which the analytical solutions are very different[3,5]. After the first approach given by Tang[3,6], more recently the non-steady state has been examined and the transient response of the confinement has been detailed[7,8] by means of numerical solutions. The most important problem is what happens when the confinement is loaded with a non-steady pressure step of which the velocity crosses over the critical values. We have investigated a large field of attenuating or accelerating shock waves in the case of a tube with finite length and simply hinged at the first extremity. One typical numerical solution is presented in Fig. 1. The radial deflection w is compared with the thickness h of the confining tube, and each line gives the relative radial deflection at different times. The four dotted lines correspond to the four characteristic velocities of the confinemment. The finite pressure step is applied at the origin of the tube and its decrease is correlated with the distance – time (x, t) function like $X = X_0 \, Ln \, (a + bt)$ which simulates the attenuation law experimentally observed. As the modelization necessitates the knowledge of the mechanical properties, we have introduced the values deduced from experiments with a polyvinyl tube (see the next part). The break in the line gives the shock front position at varied times. At the beginning of the tube, the shock velocity is nearly the first critical velocity and then as the shock velocity decreases, two precursor perturbations appear. A low frequency one which covers the tube along the part delimited by the highest velocity and a high frequency one, strongly damped, which is attached to the front. On the left side, at a distance from the front, we observe large amplitude oscillations and an evolutive wavelength which are the results of the decrease of the shock velocity. Generally speaking, the more decelarated is the shock wave, the more concentrated is the perturbated zone behind the front. On the contrary, the more accelerated is the shock wave, the more enlarged is the perturbated zone.

3 – EXPERIMENTAL TECHNIQUES AND RESULTS

The experiments[8] were conducted with a detonation – driven stainless – steel shock tube of 21 mm in. diameter and 3 m long. The strength of the shock wave generated by the detonation of propane – oxygen mixtures was governed by the initial pressure p_h of the detonable mixture in the high pressure chamber. A cellophane diaphragm separates the high pressure part from the low pressure chamber. The low pressure section was a polyvinyl chloride tube 16.1 mm in. diameter, 2.2 mm thick and 4 m long. The shock waves propagate in air at initial pressure $p_t = 1$ bar. The strength of the shock wave and the radial and longitudinal deformations of the confinement were investigated respectively by pressure gauges and strain – gauges on the external side of the tube. The decreasing behaviour of the shock was investigated by the velocity measurements at different positions on the wall. In spite of the difficulty of pressure measurements through the flexible wall, the values quite agree with those deduced from velocity measurements. With our experimental conditions, the decrease of the pressure p_2 just behind the shock front is well described by the exponential function $p_2 = p_{20} \exp (- 0.38 \, X)$ in which p_{20} (bar) $= p_2$ (X = 0) characterizes the shock when it penetrates the initial section of the flexible tube, and X (m) is the abscissa of the shock front. A similar function is deduced for the front velocity V (m/s) $= V_0 \exp (- 0.18 \, X)$. Table 1 lists the values of p_{20} and V_0 for the varied values of p_h. In fact the p_{20} value is dependent on the pressure p generated by the detonable mixture and consequently is dependent on the initial value of p_h, taking into account the mechanical effect of the diaphragm strength. In Fig. 2 are presented two typical records of the deformations obtained by means of very small strain – gauges. The first one (Fig. 2.A) shows the radial

deformation at two abscissae X = 1.07 and 1.57 m. From the difference $(t_2 - t_1)$ the mean velocity is deduced. The second one (Fig. 2.B) shows the radial (upper trace) and the longitudinal (lower trace) deformations at the same position (X = 3.00 m) on the tube. On both records we observed a precursor wave which is travelling with a characteristic velocity independent of the pressure wave loading. This precursor perturbation is the result of the impact of the pressure wave at the stainless - steel tube and polyvinyl tube interface. Its velocity is experimentally deduced (V$_p$ = 1700 m/s) and compared with the analytical value $\sqrt{E/\rho (1 - \nu^2)}$. By such a way and for a given material (the specific mass ρ = 1.414 x 10 kg/m³ is experimentally known) a first relation between E and ν (Young's modulus and Poisson's ratio, respectively) is obtained. Fig. 3 shows that the maximum amplitudes of the relative deformations $\epsilon_{\theta p}$ (radial), $\epsilon_{x p}$

(longitudinal) and the rate of increase $\dot{\epsilon}_{x p}$ which characterize the precursor are clearly related to the strength $\Delta p_2 = (p_{20} - p_0)$ of the shock wave at the origin (X = 0) of the polyvinyl tube. In Fig. 2 we note the splendid and strongly damped oscillations. From the analysis of the numerous records like those in Fig. 4, are deduced the apparent periods T_0' and T_0 of the oscillations before and behind the shock front, respectively, as function of the Mach number M = V/a$_0$. When M increases in the range 1.7 to 4.5, before the shock front, the period is decreasing from 20 - 25 to zero microseconds and that one behind the front increases from 20 - 25 to 40 microseconds. The apparent wavelength correlated with the period through the shock velocity V is lower than 60 mm. If we consider the strain - gauge measurements (Fig. 4) we observe the average relative deformations $\bar{\epsilon}_\theta$ and $\bar{\epsilon}_x$ on the external surface of the tube behind the shock front, a correction is required to determine the average values $\bar{\xi}_\theta$ and $\bar{\xi}_x$ at the mean radial position which is the radial abscissa considered in the modelization. The experimental data $\bar{\xi}_\theta$ are collected in Fig. 6 as function of the Mach number M.

4 - DISCUSSION

The validation of a model will be fruitful only if the dynamic properties of the material are known. In first approximation, the quality of the model is driven by the two coefficients E and ν. On one hand, we have mentionned above a first relation between them and deduced from the precursor wave propagation. On the other hand, many experimental results (for instance the periode and the amplitudes of the oscillations on both sides of the shock front perturbation) are available. Consequently, from the comparison of experiment and calculus it will be possible to make a choice of the more appropriate values of the numerical coefficients E and ν. If we consider that the quasi-stationary model is correct for a first approach, this comparison which put in evidence the two critical velocities (the first and the third ones) leads to the particular values E = 360 hbars and ν = 0.34.

5 - CONCLUSION

In fact we observe a non negligeable damping of the strength of the shock wave and the transient response of the tube is very complicated like the theoretical result presented in Fig. 1 in which the decrease is strongly imposed for a presentation reason. But we observe a very good similarity in the qualitative aspect of the deformation. As a conclusion, three important remarks must be done. The first one is the very rapid deformation of the confinement immediately on both the sides of the shock front. The dynamical deflection is observed during the first 10 μs and the interaction with the shock strength is not negligeable. The second one is the satisfactory good correlation between experiment and calculus in respect of both the qualitative and quantitative results. The last remark is about the maximum of the deflection which is not only a consequence of the critical velocities (the viscosity of the material

attenuates the effects of the mathematical discontinuity) but of the numerous interactions (Fig. 1) of the waves travelling along the tube. The next step is to correlate the deformation of the confinement with the characteristics of the shock wave.

REFERENCES

1.   Bartknecht, W., "Explosions, course prevention protection," Springer- Verlag, 1981, p.56.

2.   Niordson, F., "Transmission of shock waves in thin walled cylindrical tubes", Acta Polytechnica, Transactions of the Royal Institute of Technology, Stockholm, vol. 2, n° 57, Oct. 1952, 23 pp.

3.   Tang, S.C., "Dynamic response of a tube under moving pressure", Journal of the Engineering Mechanics Division, Proceedings of the American Society of Civil Engineers, EM5, Oct. 1965, p.97.

4.   Dawson, T.H., "Weak pressure wave in a gas filled elastic tube", Journal of Sound and Vibration, vol. 24, n°2, Sept. 1972, p. 241.

5.   Renard, J., Aminallah, M., Tronel, M. and Brossard, J. "Rhéologie d'un polymère à haute vitesse de déformation : tube parcouru par une onde de détonation", 17e Colloque G.F.R., 1982, Cahiers du Groupe de Rhéologie Français, tVI, n° 2, 1984, p. 99.

6.   Tang, S.C., "Response of a finite tube to moving pressure", Journal of the Engineering Mechanics Division, Proceedings of the American Society of Civil Engineers, 93, EM3, June 1967, p. 239.

7.   Fanelli, M., "On the dynamic response of pressure pipes having linearly variable velocity along their development", Energia Elettrica, n° 4, April 1972, p. 225.

8.   Renard, J., Tronel, M. and Brossard, J., "Shock waves in tubes : transient response to changing velocities and rheology of the confining material", Focusing of Mechanical waves in continuous media, Euromech 166, Aachen, March 1983.

9.   Aminallah, M., "Effets d'une onde de choc plane sur son confinement tubulaire souple, Thèse Doctorat 3e cycle, Université d'Orléans, Déc. 1982.

Table 1. Measured characteristics of the shock wave at the entrance of the flexible tube (X = 0)

p_0 (bar)	1.0	1.5	2.0	2.5	3.0
V_0 (m/s)	1300	1480	1650	1790	1900
p_{20} (bar)	17.2	22.8	28.0	33.0	37.2
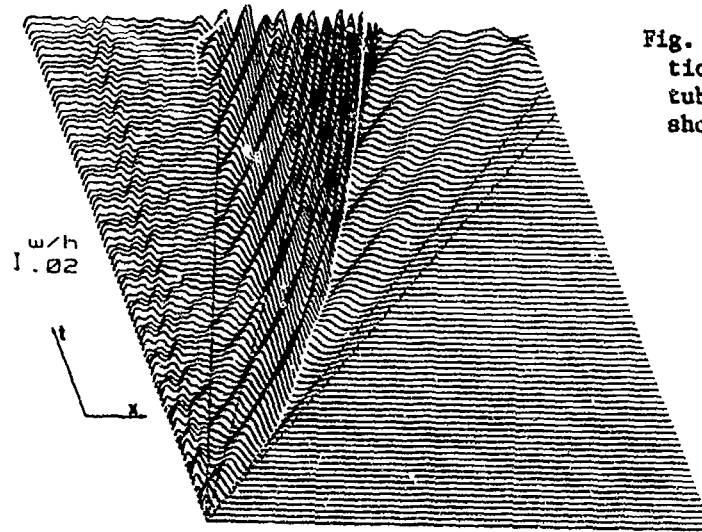
Fig. 1. Predicted radial deformation at different times. PVC tube loaded by a decelerated shock wave.

Fig. 2. Radial, longitudinal deformations and longitudinal deformation rate of the precursor wave as function of the initial shock strength.
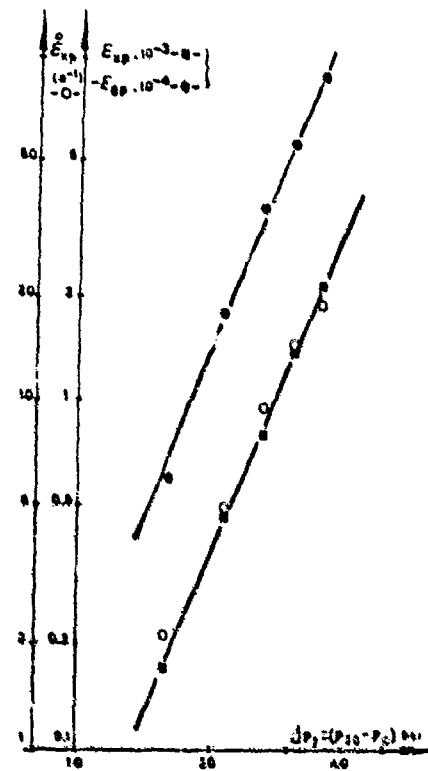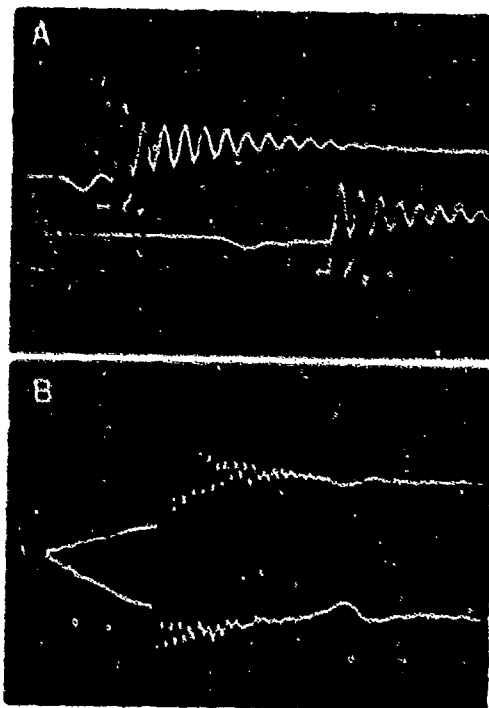
Fig. 3. Typical records : A - Radial deflections at two abscissae. B - Radial (upper trace) and longitudinal (lower trace) deflections at X = 3.0 m (M = 3.06).
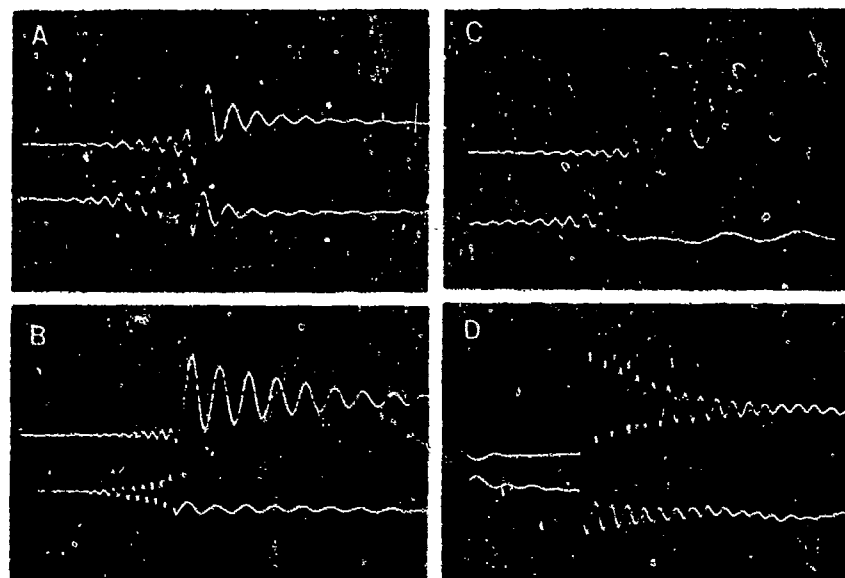
Fig. 4. Radial (u.t.) and longitudinal (l.t.) deflections. A, B and C X = 3.0 m
and M = 1.82, 2.14, 2.41 respectively. D, X = 1.07 m and M = 3.18.
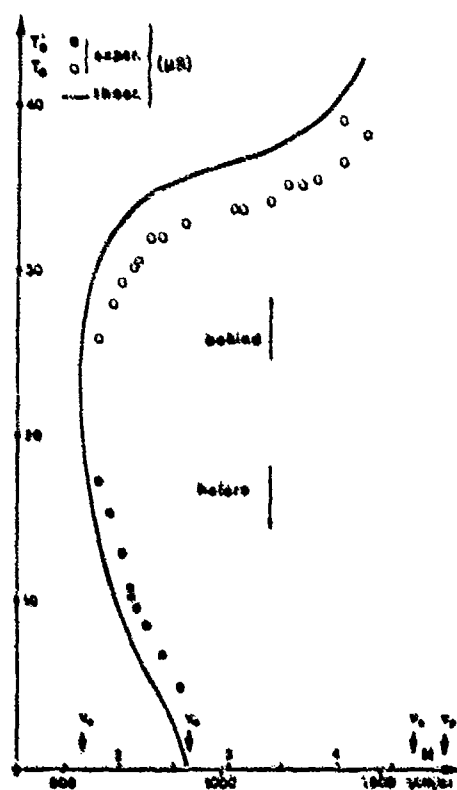
Fig. 5. Pseudo periods T'_0 and T_0
on the both sides of the shock
front as function of the Mach
number (X = 3.0 m).
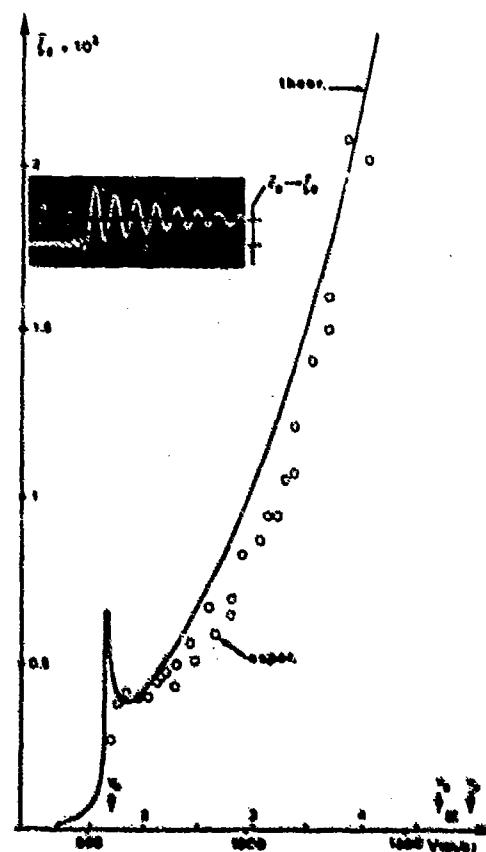
Fig. 6. Average amplitude of the
radial deflection behind the
shock front as function of the
Mach number.

FREE-FLIGHT OSCILLATORY EXPERIMENTS IN A HYPERSONIC GUN TUNNEL

by R.A. EAST and T.J. HILLIER

Department of Aeronautics and Astronautics

University of Southampton, Hants, U.K.

ABSTRACT

A new technique is presented for obtaining continuous records of
the trajectories of the free-flight motions of passive wind tunnel
models in short duration flow facilities. Reflected light from
selected externally illuminated points on the surface of the
model is focussed on to a position sensing photodetector and the
continuous analogue output signals recorded and digitised using a
high speed transient recorder. Application of the technique to
the measurement of the planar oscillatory motion of free-flight
cones in a hypersonic gun tunnel at Mach number of 8.4 and
Reynolds number of 2.2×10^5 is described. Methods of analysing
the trajectory data are presented and possible developments of
the technique are discussed.

1.0 INTRODUCTION

Both steady and non-steady aerodynamic forces acting on bodies in free-flight may
be deduced from accurate measurements of the trajectory of the centre of gravity (C.G.)
together with angular rotations about the C.G. made with respect to a fixed frame of
reference. Such techniques form the basis of methods used in aero-ballistic ranges and in
wind tunnel and air launched free flight experiments. The measurements obtained provide
aerodynamic data free from support interference effects but without the technical
complexity of magnetic suspension model support systems.

Free flight techniques applied to wind tunnel testing have been reviewed by
Dayman[1]. These test methods have been predominantly based on photographic techniques;
either high speed ciné-photography (see for example, Enkenhus et.al.[2]) or multiple
exposure spark shadow photography, as described by Penneleghon et.al.[3], to record details
of the model motion. Applications to continuous wind tunnels and short duration facilities
of shock/gun tunnel type (which have been reviewed by Bernstein[4]) are equally feasible;
the requirements for time resolution being a function of the ratio of the aerodynamic forces
and moments to the model mass and inertia. The present work is concerned with the
application of this technique in short duration flow facilities to the study of the dynamic
stability of re-entry vehicles at hypersonic Mach numbers and hypervelocity missile shapes,
for which models with small radii of gyration are required.

While the potential advantage associated with the interference free aspect of free
flight testing is considerable, aerodynamic forces are deduced from two differentiations of
the model distance - time trajectories; an inherently inaccurate procedure compared with
direct force measurements. High speed ciné-photographic methods (limited by framing
rate) and multiple spark shadow imaging (limited to about 10 superimposed images) are
capable of good spatial resolution and accuracy but analysis is time consuming and difficult
to automate.

A technique offering improved spatial resolution and greater numbers of data points
is the laser interferometer developed by Bernstein and Stott[5] to study the free flight
motion in a shock tunnel. Model positional data with a spatial resolution of the order of the
wavelength of light are obtained by utilising the interference between incident laser
illumination and the reflected radiation from retro reflectors embedded in the model
surface. However, the technique is limited in the extent of the model motion which is

allowable before the laser beam ceases to illuminate the retro-reflector and would be unsuitable for large amplitude motions.

More recent imaging techniques based on vidicon tubes or photo-diode arrays offer considerable potential advantages for automatic data recording and motion analysis. However, the scanning rates of readily available high speed television systems of approximately 240 pictures per second are inadequate to obtain more than 5 images during a typical model motion of about 15 ms in the field of view in an intermittent hypersonic wind tunnel, for example. Similarly, the positional accuracy of detection can be made extremely high by increasing the number of individual elements in a detector comprising a photo-diode array (say 100 x 100). However, the computer processing power and stor.. ge size to interrogate the array and to record and update images at framing rates of $O(100 \text{ kHz})$ are beyond those currently available in laboratory micro and mini-computers.

The present work aims to improve on the number of data points obtained from photographic techniques and to reduce the analysis time, but does not require the extremely large computing power required by photo-diode arrays. It is based on using a position sensitive photo detector onto which light reflected from bright spots on the model is focussed. Continuous analogue output signals are sampled at frequencies up to 1 MHz and processed using a microcomputer to obtain aerodynamic data.

2.0 THEORY

The detailed analysis of the free-flight motion of wind tunnel models has been described by Bernstein[4] together with the various procedures used to deduce aerodynamic data from such experiments. The free flight planar pitching motion of a rigid model released into the free stream flow of velocity V with respect to a frame of reference fixed with respect to the wind tunnel (see Fig.1) is given by the following set of coupled equations:

$$m\ddot{x}_G = C_D(\alpha) \tfrac{1}{2} \rho \left(V - \dot{x}_G \right)^2 S \tag{1}$$

$$m\ddot{y}_G = C_L(\alpha) \tfrac{1}{2} \rho \left(V - \dot{x}_G \right)^2 S - mg \tag{2}$$

$$mk^2\ddot{\theta} = M_{aero} = C_m \tfrac{1}{2}\rho \left(V - \dot{x}_G \right)^2 Sd \tag{3}$$

where $C_D(\alpha)$ and $C_L(\alpha)$ are both functions of the effective angle of attack α (= θ - γ)of the model, and the change in the angle of attack due to the model velocity relative to the free stream is given by $\gamma = \tan^{-1}(-\dot{y}_G/(V \cdot \dot{x}_G))$. For the hypersonic wind tunnel flow of the present work $V = 1500 \text{ ms}^{-1}$, $\dot{x}_G < 2.6 \text{ ms}^{-1}$ and $\dot{y}_G < 7 \text{ ms}^{-1}$. The value of γ is therefore less than -0.25 degrees and is considered to be negligible. Similarly $\dot{x}_G << V$ and is ignored in eqns(1) - (3). In eqns(1) - (3) x_G, y_G and θ are, respectively, the horizontal and vertical co-ordinates and the angular rotation about the centre of gravity, m the model mass, k the radius of gyration about the centre of gravity, and C_m is the aerodynamic pitching moment coefficient given by

$$C_m = C_{m_\theta} \theta + \left(C_{m_q} + C_{m_{\dot\alpha}} \right)\left(\frac{\dot\theta d}{2V} \right) \tag{4}$$

for an assumed linear aerodynamic model in which the aerodynamic stiffness C_{m_θ} and aerodynamic damping $(C_{m_q} + C_{m_{\dot\alpha}})$ are constants. For large amplitude motions at high Mach number Hutt and East[6] have shown that a linear aerodynamic model is no longer valid and the aerodynamic coefficients are functions of θ.

Measurements of x, y and θ as functions of time permit the estimation of $\dot{x}, \dot{y}$ and $\dot{\theta}$, from which the aerodynamic coefficients can be deduced although this direct method is inherently inaccurate due to the double differentiation involved. For a lightly damped motion the stiffness derivative C_{m_θ} is determined from the frequency of motion and the damping derivative $(C_{m_q} + C_{m_{\dot\alpha}})$ from the decay of the oscillation envelope. Alternatively, as for the present work the values of the aerodynamic coefficients may be found by computing the free flight trajectory by integrating eqns(1) – (3) using assumed values of the aerodynamic coefficients which are varied to give the best fit of the computed trajectory to the measured one. In practice, measurements of the x and y coordinates $(x_1, y_1$ and $x_2, y_2)$ of the two points on the model displaced distances s_1 and s_2 from the apex along the model axis (see Fig.1) permit the deduction of the trajectory of, and angular rotation about, the centre of gravity using

$$x_G = x_n + \left(s_G - s_n\right)\cos\theta \qquad n = 1,2 \tag{5}$$

$$y_G = y_n - \left(s_G - s_n\right)\sin\theta \qquad n = 1,2 \tag{6}$$

$$\tan\theta = (y_1 - y_2)/(x_1 - x_2) \tag{7}$$

Alternatively, if computed trajectories of th⸱⸱⸱ ⸱⸱⸱ are to be compared with measured trajectories of the illuminated points on the m⸱⸱⸱ ⸱⸱⸱, as for the parametric identification method of deducing the aerodynamic coefficients, eqns(1) – (3) are solved for x_G, y_G and θ and eqns(5) and (6) used to find x_n and y_n, which are then compared with experimental data for x_n and y_n directly. At the present stage of the current work the trajectory of only one point on the model may be measured on a single tunnel run. However, providing this point is well displaced from the centre of gravity, information can be deduced, as shown in Section 7.0, regarding certain of the aerodynamic coefficients.

An important consideration for free flight oscillatory experiments is the number of cycles executed while the model remains in the field of view of length x_F. By calculating the elapsed time t for the model to move a distance x_F in the x-direction due to a constant drag force, and the frequency f of the model oscillation calculated from the aerodynamic stiffness derivative C_{m_θ} the number of cycles N of the observed motion is given by

$$N = ft \propto \left(\frac{C_{m_\theta}}{C_D} \left(\frac{d}{k}\right)^2 \frac{x_F}{d} \right)^{\frac{1}{2}} \tag{8}$$

For a given aerodynamic shape, N is maximised by minimising both the radius of gyration and the ratio of body scale to field of view.

3.0 THE OPTICAL ARRANGEMENT

The principal features of the optical arrangement used to obtain an image of a region of the working section on the surface of a position sensing photodetector are shown in Fig.2. The working section and model are illuminated by light from a 750W quartz iodine projector lamp through an angled glass plate. Reflected light from the model is transmitted through the angled glass plate and focussed by a lens on to the surface of the detector. For the present work the optical system results in a field of view in the working section of 80mm x 80mm (permitting analysis of approximately 2 model lengths of motion).

The arrangement shown in Fig.2 incorporates two detectors illuminated through red and green filters respectively, onto which identical images of the model are focussed by means of a beam splitter. By this means the two detectors can respectively track the positions of two different coloured light spots on the model surface. Maximum reflected

illumination from the model was found to be obtained by using reflective tape which contains a layer of glass micro-spheres which internally reflect light along its entry path. For maximum reflected light it is therefore necessary to both illuminate the model and detect the reflected light along the same optical path. An important requirement of the optical system is to either eliminate, or to obtain a uniform, background illumination from an empty working section. Non uniform background illumination results in a non-linear detector response over its active area. Matt black screens were therefore used in the positions shown in Fig.2 to overcome this problem.

4.0 THE DETECTOR

Analogue outputs corresponding to the x and y co-ordinates of the illuminated spots on the model are obtained from a United Detector Technology SC10D photo-resistive position sensing detector. Separate electrical contacts are made at the four edges and the centre of the 10mm square surface. With the centre pin at -15V the device acts effectively as a resistor bridge with the contact point being the centroid of the illumination falling on the detector. Movement of the illumination from the centre of the detector therefore results in currents in the bridge which are dependent on both the position of the light spot and its intensity. These currents are converted to voltages using trans-impedance amplifiers and signal back-off is provided to remove the signal from the small unwanted background illumination which exists with no model in the field of view. For a given pair of contacts for a given axis, the pin voltages are summed and differenced to give outputs proportional to the intensity of illumination and the product of the intensity and position of the centroid of illumination, respectively, as shown in Fig.3. Division of the difference by the sum gives output signals proportional to the position of the centroid of the illumination only.

5.0 DATA RECORDING AND ANALYSIS

Data corresponding to x and y co-ordinates of the illuminated spots on the model are recorded using a 4 channel EMI Type SE2560 transient data store with 16K memory per channel and maximum 1 MHz sampling rate. After allowing for sequencing delays, approximately 7K data points per channel are obtained during a typical 15ms model motion. The data recording system is also used to record and store calibration data for spatial sensitivity and linearity for the detector. Data from the calibration map obtained from constant velocity model traverses across the field of view are used in the data analysis procedures to obtain x and y versus t records from the recorded voltages. Post-calibration data are compared with computed trajectories for models whose physical characteristics are known using the procedures described in Section 2.0. From this trajectory matching procedure the aerodynamic characteristics of the free flight model are obtained.

6.0 THE HYPERSONIC FLOW FACILITY AND THE FREE FLIGHT MODELS

The free flight experiments reported were performed in the open jet test section of a hypersonic gun tunnel having a run duration of approximately 20ms at Mach number of 8.4 and unit Reynolds number of 4.8×10^6 m^{-1}. A sequencing procedure ensured that the model, released into free-fall from a magnet above the tunnel working section, would be positioned at the centre of the flow at the instant of flow commencement.

Models of composite construction were used to obtain a statically stable configuration. The majority of the work has used a 10^0 semi-angle cone of 16mm base diameter manufactured from soft-iron (50% length from apex), balsa wood (next 45% length) and nylon (final 5% length). The nylon base enables the models to be re-used subsequent to capture (after a free-flight motion) in a wire mesh net positioned in the tunnel diffuser. The centre of gravity and radius of gyration of the models are calculated from the known densities of the constituent materials. Optically reflective stripes, of approximately 3mm width, are either painted or stuck (for reflective tape) onto the cone surface at the required axial positions.

7.0 RESULTS AND DISCUSSION

Free flight experiments have been performed at the conditions described in Section 6.0 using both an 8mm diameter reference sphere and a 10^0 semi angle cone of base diameter 16mm and centre of gravity at $x_G/\ell = 0.56$. For the sphere, the tracking point was its centre and for the cone, various tracking points along the cone axis have been explored. The cone models were dropped to free fall across the test section at nominally zero yaw and at various pre-set angles of attack.

Free-flight trajectory data from a single detector for a single point on the models were recorded using the instrumentation described in Section 5.0. It was found in early experiments that anomalous output signals were obtained from the detector even when no model was dropped into the tunnel flow. These signals which commenced when the flow established, and continued even after the flow ended, were eliminated by setting the open jet test section pressure prior to the run equal to the anticipated flow static pressure. An apparent explanation of this phenomenon is that the light falling on the detector from the background in the absence of the model is slightly affected by the refractive characteristics of the open jet flow and that it is necessary to have a correctly expanded nozzle flow in order to eliminate this.

Typical trajectory data for the 10^0 cone model are shown in Fig.4 for the case of the detection point situated at 97% of the cone length. This shows the constant x position and approximately linearly decreasing y position as the model free-falls at a fixed axial position in the test section prior to flow commencement. This is followed by an approximately parabolic variation of x with t due to aerodynamic drag. Oscillatory behaviour of the y signal associated with the expected motion of the rear of a statically stable model is observed, with the mean motion continuing in free-fall. Cessation of the signal occurs when the image of the illuminated point leaves the detector field of view after an observed free flight duration of 16ms.

Analysis of these data were effected using the technique of trial and error fitting of computed trajectories (see Section 2.0), to the experimental trajectories. For the case of the sphere, only eqn(1) is effective and analysis resulted in values of C_D approximately 15% in excess of the expected value of 0.95 at the flow conditions used. This was attributed to the surface roughness caused by the type of paint required to give adequate optical reflectivity.

For the analysis of cone trajectories, models for the variation of the aerodynamic coefficients must be assumed in the numerical integrations of eqns.(1), (2) and (3). For the cases considered, a linear variation of C_L with a, a parabolic variation of C_D with a and constant values of C_{m_a} and $C_{m_q} + C_{m_{\dot{a}}}$ have been considered. Results obtained for models with painted reflecting stripes gave values of C_D approximately 80% in excess of inviscid estimates based on Newtonian theory. The frequency of the oscillatory motion was best matched with a value of C_{m_a} of -0.15 and the damping with $C_{m_q} + C_{m_{\dot{a}}}$ of -0.4 which compare with values of -0.2 and -0.4 for small amplitude tests on sting supported models at higher Reynolds numbers. These differences are consistent with the observation of Hutt and East[6] that, for large amplitude oscillations ($\sim10^0$), transient effects associated with leeward surface separated flows, which are likely to be enhanced at the lower Reynolds numbers of the present experiments, can result in large effects on the aerodynamic derivatives.

In order to enhance the light reflected from the model for developments of the technique aimed towards a two point simultaneous detection system, light reflecting strips consisting of a layer of miniature glass spheres of thickness 0.5mm have been attached to the surface of the cone near the apex and near the base. Trajectory analyses for these tests have indicated drag coefficients some 100% in excess of Newtonian values of C_{m_a} of -0.33, and values of $(C_{m_q} + C_{m_{\dot{a}}})$ of +2.5. These results imply negative values of the aerodynamic damping associated with a diverging oscillation. This behaviour is not consistent with extensive data for pointed 10^0 smooth cones obtained in a wide variety of facilities and aeroballistic ranges. It is tentatively attributed to dominant dynamically destabilising

interactions occurring between the laminar boundary layer and the surface steps associated with the reflecting strips on the models in the present tests. These interactions are likely to be more severe at the low Reynolds numbers of the present tests. Further work is required to explain this anomaly.

The results reported have been obtained from trajectory analyses of a single point on the model surface. Future work will use two points tracked simultaneously as described in Section 3.0. Adaptation of the technique to three dimensional motions by using two orthogonal two-point systems appears feasible. Simultaneous analyses of the x and y trajectories of the two illuminated strips in two orthogonal planes will enable the x, y and z translations and pitch and yaw rotations of the model to be deduced.

8.0 CONCLUSIONS

A new optical tracking system has been developed which has been used to track the trajectory of spheres and oscillatory cones in free flight motion in the short duration hypersonic flow in a hypersonic gun tunnel. The techhnique has been developed in an attempt to overcome the limitations of photographically based methods from which limited numbers of data points are obtained and data reduction is time consuming. The features of the new method are:

1) a continuous analogue record of the translational co-ordinates of an illuminated point on a free-flight wind tunnel model may be obtained,

2) computed free flight trajectories using assumed values of aerodynamic coefficients may be compared with measured trajectories immediately after a tunnel run, and

3) successful demonstration of tracking the oscillatory motion of a 10° semi-angle cone in an intermittent hypersonic flow suggests that the technique will prove valuable for interference free dynamic stability studies.

9.0 ACKNOWLEDGEMENT

REFERENCES

1. Dayman, B. *'Free-flight testing in high speed wind tunnels'*, AGARDograph 113, (1966).

2. Enkenhus, K.R., Richards, B.E. and Culotta, S. *'Free-flight stability measurements in the Longshot Tunnel'*, Proc. 8th International Shock Tube Symposium, Chapman & Hall, London (1971).

3. Pennelegion, L., Cash, R.F. and Shilling, M.J. *'Free-flight tests in the NPL 6in (15cm) shock-tunnel of model HB-2 using multiple spark recording'*, ARC Current Paper, CP 934 (1967).

4. Bernstein, L. *'Force measurements in short-duration hypersonic facilities'*, AGARDograph 214, 1975.

5. Bernstein, L. and Stott, G.T. *'A laser-interferometric trajectory-following system for determining forces on freely flying models in a shock-tunnel'* in 'Shock Tubes and Waves' eds. Treanor, C.E. and Gordon Hall, J., State University of New York Press, (1982).

6. Hutt, G.R. and East, R.A. *"Effects of large oscillation amplitude on axi-symmetric vehicle longitudinal static and dynamic stability in hypersonic flow'*, AIAA-83-0215, (1983).
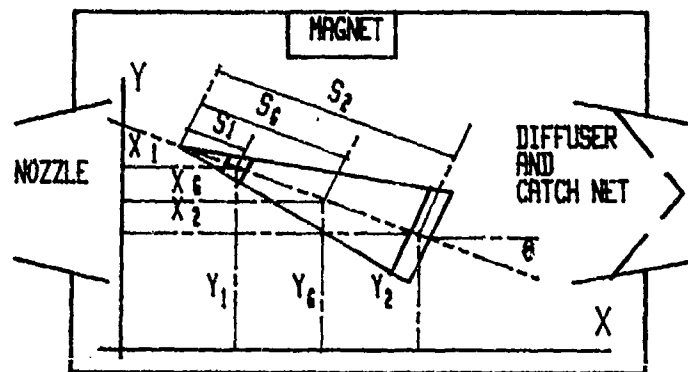
Fig.1 Diagram of Working Section and Model Dimensions (not to scale)
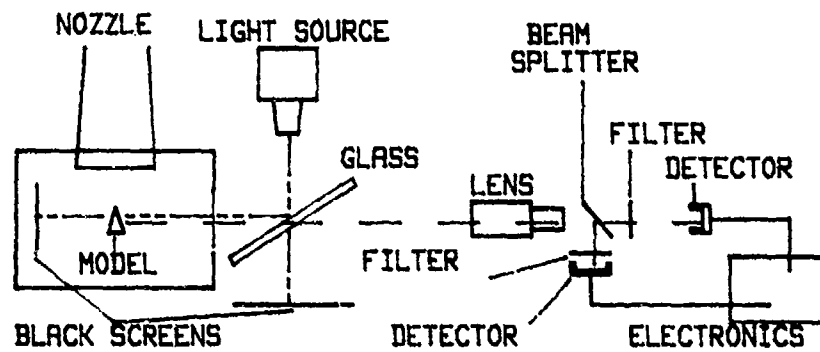
Fig.2 Overall View of Optical System
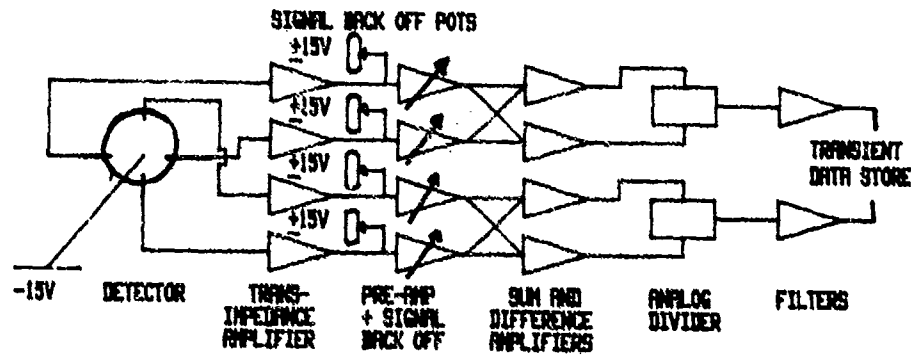
Fig.3 Schematic of Intensity Compensating Electronics
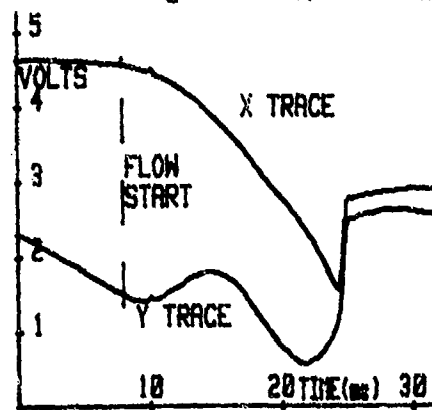
Fig.4 Photodetector Output
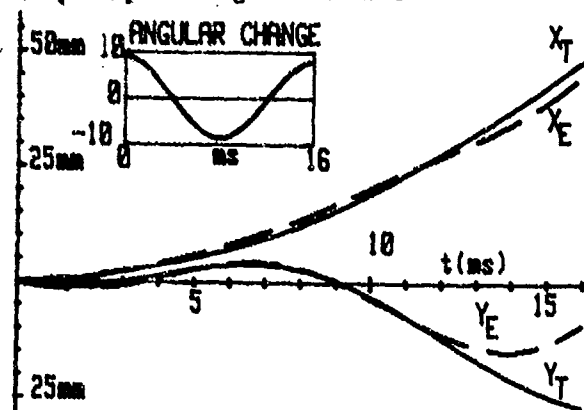
Fig.5 Free Flight Trajectories

TURBULENT MIXING MEASUREMENTS USING
SHORT-DURATION JETS

Corso Padova

Physical Sciences Department
Calspan Advanced Technology Center
Buffalo, New York 14225
USA

Measurements of mean flow properties in supersonic jets have been completed at Calspan which characterize the turbulent mixing phenomena in the range of interest for low-altitude rocket plumes. These measurements were obtained using jets of short duration (50-90 ms) and in an innovative apparatus developed from existing shock-tunnel technology. Using the short-duration testing technique, non-reacting plume flowfields were simulated in which compressible turbulent mixing of large-scale coflowing jets was observed over an axial extent of 0 to 60 nozzle diameters. A ratio of the jet diameters of 13:1 was obtained using a 3-inch exit diameter nozzle located in the large Calspan Ludwieg Tube. This paper concentrates on the development of the experimental technique and discusses its future applications to more complex mixing situations. A brief review of the results obtained to date is also given.

INTRODUCTION

Research on the problems associated with the use of high speed propulsive jets has been critically important for decades. In recent years in the area of exhaust plume technology for low-altitude rockets and for aircraft gas turbine engines a major objective has been the development of computer codes for the prediction of plume phenomena such as radiation scattering on IR signatures, induced fluctuations in the index of refraction and, for particulate laden cases, solid carbon oxidation and radiation. These codes model complex physical and chemically-reactive flow field and include phenomena which are not yet well defined.

A review of the several summaries and bibliographies on jets and related subjects indicates several areas in need of further theoretical and experimental research, especially for non-ideal jet mixing situations. In particular near term improvements in the computational simulation of exhaust plumes depend heavily on refined modeling of turbulent transport processes, three-dimensional exhaust plume flow field and radiance, the influence of jet entrainment/blockage on the afterbody drag, initial base/separated flow regions and nonequilibrium gas/particulate phases coupling. Work on these aspects is actively in progress.

In response to the projected need to corroborate the emerging codes, Calspan defined a new experimental approach[1]. The key concept of the approach is to use a unique short-duration technique that is flexible enough to sequentially investigate, in bootstrap fashion, several of the physical and chemical complexities of low altitude plumes. This paper describes the results of the experimental program conducted at Calspan to investigate the mixing phenomena in supersonic jets. The first part of the paper deals with the development of the experimental technique and discusses its future applications to non-ideal mixing situations; the second part deals with measurements of mean flow properties in ideal non-reacting jets which have

been completed to date. The short-duration approach was developed and applied
to obtain these results.

SHORT-DURATION TESTING APPROACH

To generate the data critical in the development of compressible mixing
models for non reacting supersonic jets a broad range of mixing conditions
were of interest. The testing approach formulated at Calspan is based on the
unique capabilities of the large-scale Calspan Ludwieg Tube (CLT) wind tunnel.
Using this facility, an experimental apparatus was configured as sketched in
Figure 1. A jet of controlled gas composition, three inches in diameter at
its origin, is exhausted into an essentially unconfined ambient which can
simulate a wide range of altitude conditions. The ambient surrounding the jet
is either still or moving at supersonic speed.

Severe configuration requirements for the jet nozzle/supply assembly
were met using a double expansion Ludwieg Tube for the jet supply. Thus both
the jet and the CLT operate on the same transient gasdynamic process and
provide short-duration flows with well defined, quasi-steady properties. In
addition, for studies of non-reacting mixing, the short-duration approach
provides an effective economical way to control gas species in both the jet
and the free stream flow. In the measurements already completed, combinations
of hydrogen and nitrogen gases were used to achieve a broad range of density
ratios. The molecular weight, and stagnation temperature of the jets were
varied to span values of the ambient-to-jet density ratio, ρ_∞ / ρ_j, from 0.6
to 10. This was achieved by using hydrogen-nitrogen mixtures heated as high
as 750°R. Variations in jet Mach numbers were obtained by using
interchangeable nozzles. In keeping with the objective of generating first a
fundamental data base for simple supersonic jets, complicating factors which
may charactrize "real" low altitude plumes, such as a repetitive shock
structure or significant base region flows, were avoided. In all cases, the
jet nozzles were contoured to provide a uniform, parallel flow at the exit.
The bluntness at the exit of the nozzles was minimal, with a difference
between inner and outer diameters of only 0.125 inch. The static pressures of
the freestream and jet at the exit plane were very closely matched. The
locations at which the mixing flowfield could be surveyed varied over a broad
range; and diagnostics were designed to cover radial locations from the jet
axis to fifteen times the exit jet radius in the outer region. The axial
location of the surveys could be chosen arbitrarily between zero and 100 jet
radii downstream of the exit plane.

An illustrative overview of the operation and performance of the jet
apparatus is presented in Figure 2 with the aid of typical measurement
histories . Pressure and temperature histories identify features of the
starting and terminating transients and the characteristics of the quasi-
steady flow used for testing. It is shown that, by using premixed gases, jets
were obtained which have uniform and repeatable properties. Both quiescent
and wind-on cases are discussed. The jet behavior is shown in Figure 2a. The
measurements of stagnation pressure, P_{oj}, in the nozzle plenum present the
expected characteristics of an initial sudden rise in pressure followed by a
constant plateau. The initial transient lasted no more than 25 ms. The
plateau corresponds to the steady supply conditions that existed in the charge
tube behind the expansion fan travelling upstream. In the case shown this is
of the order of 150 ms. Viscous effects in the long small diameter tube were
responsible for the slight steady decline in pressure. The jet duration
varies inversely with the speed of sound, hence it was shorter at the lower
molecular weight of the gas mixtures and at the higher charge temperatures.
Although the jet duration is independent of the nozzle used, the highest

charge tempertures with pure H_2 were used in M_j = 4 tests resulting in the shortest jet duration. The test plateau in this latter case lasted at least 50 ms. The recovery temperature trace, T_{oj}, in the nozzle plenum also shows the initial transient phenomena followed by the steady flow period. The apparent long duration of the transient resulted from the response lag of the probe. The initial overshoot in temperature is associated with the passage of the starting shock, soon followed by the cooler expanded gas from the charge tube. In Figure 2b pressure and temperature measurements in the supply tube upstream of the metering venturi are shown. Representative pressure conditions at the exit plane of the jet are shown in Figure 2c.

The test jets discharged in the M_∞ = 2 nitrogen stream in the wind-on mixing experiments. Measurements in these jets are shown in Figures 2d and e. Initially all chambers were filled with nitrogen at ambient temperature. The CLT driver pressure was set so that the static pressure at the exit of its supersonic nozzle matched the pressure of the jet and the ambient during the test. The CLT supersonic stream was initiated simultaneously with the jet by rupturing the mylar diaphragm that separated the high pressure driver from the low pressure tank. Initially there was speculation that synchronization of the jet and outer-stream may constitute a very critical aspect of the short-duration testing technique. The objective is to time the firing sequence so that the steady-state jet discharge optimally coincides with the steady flow available from each component of the apparatus. Figure 3 shows that firing the jet 3 ms after the outer stream achieved the objective. In this case, no adverse effects caused by mutual interference during the starting process were found. In fact, mutual interference effects were proven to be very modest over a range of sequences going from cases in which the jet was initiated 20 ms before the CLT stream to cases in which the jet was initiated 10 ms after the CLT.

Because of the innovative nature of the short-duration jet apparatus, several tests were dedicated to verify the performance of the apparatus and the validity of the technique. Generally, these initial tests involved (1) measurements to document the duration of the steady test time, the quick valve operation repeatability, the gas sampling system timing, and the jet/CLT synchronization, (2) measurements to establish the reproducibility of the data, the validity of assuming the jet alignment known, and the influence of the expansion waves from the lip of the CLT nozzles on turbulent mixing. Several tests were undertaken to measure the jet boundary layer near the exit plane of the jet nozzles. These tests used a boundary-layer probe rake installed at the jet exist plane. The results from these measurements were presented in Reference 2. In brief, the validity of the short-duration testing approach for obtaining accurate turbulent mixing data was analyzed by Calspan and, independently, in Reference 3. In these analyses it was shown that the technique is capable of producing high quality data.

Inclusion of "real" flowfield features in single phase non-reacting jets

Earlier it was noted that there are major advantages in making mixing measurements using the short-duration testing approach. Foremost among them is an apparatus that (a) is simple, flexible, and effective for experimenting over a wide range of test conditions with non-reacting jets, and (b) is substantially similar to that needed for mixing measurements in non-idealized jet situations. The results obtained to date in experiments with non-reacting jets are discussed in the last section of this paper. Here the future applications of the technique to experimenting with non-ideal mixing situations are discussed briefly in the order of implementation that is presently planned.

A relevant first step in investigating more complex supersonic mixing phenomena is to include "real" flowfield situations in which the effects of the vehicle base, three-dimensional geometry, non-ideal nozzle expansion, and non-parallel exit flow are included. The extension of the existing apparatus to treat these cases is easily accomplished. For example nozzle exansion ratios from 0.7 to 7.0 can be achieved by changing the driver pressure. Another example is the accommodation of vehicle base which requires only the fabrication of new interchangeable nozzles. It should be noted that the instrumentation which is needed for the above measurements is substantially the same as used in idealized jet flowfields.

Extension to particle-laden mixing

Experiments on particle dispersion in high speed turbulent jets are nearly non-existent. Literature reviews of low speed data may be found in the work of Melville et al.[4] Test data in high speed jets are urgently needed to achieve significant advances in the determination of radiative aspects of low altitude plumes generated by metallized rocket propellants. The facility at Calspan and a direct extension of the short-duration technique described above can provide mean flow data in jets of variable density for a broad range of particle sizes and mass loadings. To investigate the more complex problem of turbulent two-phase supersonic mixing, two major additions to the existing experimental apparatus are required: (a) a system for introducing monodisperse particles in the supersonic jets, and (b) a non-intrusive method to measure the particulate number density.

A particle introduction system especially designed for loading short-duration jets is shown schematically in Figure 4. It will be added to the existing apparatus to accurately control size and concentration of the suspended particles. The system is capable to generate jets with an accurately controlled loading that is spatially and temporally uniform. The jet charge tube and the surrounding plenum are initially connected (charge tube valves open), evacuated and then loaded with clean gas to the desired high pressure. During this phase valves A and C are closed. Once the jet supply pressure is established, particle-laden gas is admitted to the plenum at low flow rate by opening valves C and A simultaneously. Valve A is used to select the particulates feed rate and hence the concentration of the particles in the gas. To maintain the charge pressure, some of the particle-gas mixture is continuously removed at C and may be recycled post-test. After all the clean gas initially in the plenum has been flushed away, the plenum remains at the pressure and loading selected to generate a given jet. Valves B and C are quickly closed and the charge tube is isolated from the plenum (by closing all distributed openings along it). The jet is then initiated by releasing the quick opening valve.

Several candidate techniques were evaluated in terms of their application to the determination of particulate number density in the mixing jet. Recourse will be made to the use of extinction measurements, and in particular, to the multi-station, jet-sectioning method illustrated Figure 5. At each station of interest the system provides a cross-section scan of jet extinction, which can be deconvolved by the use of known extinction coefficients and assumed cylindrical symmetry. This scheme for measuring the particulate density distribution provides simultaneous surveys at multiple axial stations forward of the movable rake which supports the gas-phase diagnostics. The broad range of test conditions which is envisioned to study particle laden jets is indicated in Figure 5.

EXPERIMENTS IN IDEAL MIXING JETS

Mean velocity profiles were the primary data sought from the experiments completed in ideal jet mixing situations. To generate these profiles in the isobaric mixing of gases having different compositions, surveys of pitot pressure and of gas species concentrations were required. In addition, total temperature surveys were needed for the test cases in which the jet was heated. In Calspan's experiments, temperature measurements were also useful in obtaining accurate velocity profiles in the cold jet test cases. In the latter cases, deviations from strictly isothermal mixing occurred because the CLT and jet streams are accelerated differently by expanding from similar initial ambient conditions. In all experiments, isobaric mixing was obtained by controlling the initial pressure of the jets. However, small deviations from the isobaric conditions were expected, that could significantly affect the determination of local Mach number. Surveys of static pressure were thus used to obtain accurate velocity profiles. Besides surveying the mixing flow field, times of capture of gas samples from the mixing flow field were also recorded in each test. The instrumentation used in the mixing surveys consisted of four sets of single probes, three for the measurement of gasdynamic quantities, one for gas sampling, and two rakes for closely spaced pitot measurements. To survey the flow field at selected axial positions downstream of the jet nozzle exit, these instruments were mounted on a cruciform holder which was anchored to the walls of the receiver tank and optically aligned with the jet nozzle axis. Detailed design and operating characteristics of the gasdynamics diagnostics, the gas sampling probes and the gas analysis system were reported earlier[2].

Table 1 list the thirteen test conditions for the turbulent mixing experiments. The test cases covered a broad range of ambient-to-jet density and velocity ratios. Values of velocity ratio from 0.164 to 0.643 were obtained with the jets discharging into the Mach two outer stream (wind-on cases). These wind-on experiments simulated plumes from rockets at altitudes of about 50,000 ft flying at a speed of about 1600 fts^{-1}. Including the quiescent ambient cases the jet velocities ranged from 1740 to 9940 fts^{-1}.

The primary measurements were transformed into a detailed mapping of the mixing flow field by using the computer-based digital data acquisition system which is part of the CLT facility. The actual axis of symmetry of the jet was determined by reflection of diametrically opposed measurements. After this correction for jet misalignment, final radial profiles of the mixing quantities were obtained. Plots of the data in this format for all the test runs are available in Reference 5. In the next data reduction step the radial distributions of the mixing variables were fitted with cubic spline lines. From these the radial distribution of Mach number was derived. Finally, velocities were computed using the relationshp among velocity, Mach number, gas constant of the mix, and total temperature. Once the detailed mapping of the mixing flow field was completed, the results were correlated and interpreted to establish trends in global mixing characteristics based on density ratio and Mach number. In Reference 6 the results of the experiments are discussed from this point of view. Accordingly, the results have been divided into three major parts: (a) influence of density of the mixing of $M_j = 4$ jets into $M_\infty = 2$ ambient, (b) influence of density on the mixing $M_j = 3$ jets into still ambient, (c) influence of Mach number on the mixing of high and low density jets.

Influence of density on the mixing of $M_j = 4$ jets into $M_\infty = 2$ ambient

This case will be presented here to illustrate some of the results obtained. For the remaining cases the reader is referred to earlier publications.

The influence of density variations on radial velocity profiles is illustrated in Figure 6 where radial velocity distributions at axial location 40 R_j are compared for ambient-to-jet density ratios of 0.6, 1.0, 3.0 and 9. Best fit lines through the data points are used for clarity in the figure. The observations that follow, however, are firmly based on the actual data points. Starting with the higher jet density ($\rho_\infty/\rho_j = 0.6$), the velocity distribution retains all the characteristics of the uniform density case. In particular, the outer stream level was reached essentially at the same off-axis location and with a velocity defect present, although the velocity defect extended farther off-axis. The initial velocity of the jet was 26% lower than the uniform density case. Thus a more gradual shearing of the flow in the radial direction characterizes this mixing condition. The two jets with density lower than the outer stream ($\rho_\infty/\rho_j = 3$ and $= 9$) displayed characteristics which were different than those of the uniform density case. In both, a region of constant core velocity extending approximately a half jet radius was found. In the jet having $\rho_\infty/\rho_j = 3$, the velocity defect has been washed out completely. This may be attributed to the large difference in velocity between the jet axis and the outer stream. The inner stream reached the velocity of the ($M_\infty = 2$) stream at about three radii off-axis. The velocity defect was also absent in the case of the jet having $\rho_\infty/\rho_j = 9$. In addition, the inner stream reached the outer stream velocity farther off-axis, about 3.5 radii from the centerline.

Figure 7 presents core lengths of all the $M_j = 4$ jet cases. The somewhat surprising result that core length is nearly independent of density ratio is indicated. A core length markedly increasing with decreasing ambient-to-jet density ratio was expected based on the qualitative consideration that denser jets would be able to penetrate farther into the surrounding ambient. These expectations were quantitatively supported by pre-test calculations. Uncertainties have been estimated for each data point, but their magnitude does not alter the basic conclusion drawn from the results.

CONCLUSIONS

In support of low-altitude research an innovative short-duration testing technique was successfully developed and applied to the investigation of non-reacting jets. The jet apparatus is capable of varying gasdynamic parameters over a broad range, and validity of the fast response diagnostics has been proven. The short-duration technique offers a convenient basis for simulating "real" plume features, the presence of solid particulates, and reacting mixtures. It represents an effective and reliable tool for investigating fundamental plume phenomena.

The turbulent mixing of supersonic jets was investigated at jet Mach numbers of 4, 3 and 2, and with six values of the ambient-to-jet density ration in the range of 0.6 to 10. The analysis of the data indicates important trends in the mixing characteristics as jet density and Mach number are varied.

ACKNOWLEDGMENTS

REFERENCES

1. Wittliff, C.E., Wurster, W.H. and Marrone, P.V., "Non-Reacting Supersonic Mixing Experiments," Calspan Technical Memorandum submitted to AFRPL, May 1978.

2. Padova, C., "Non-Reacting Turbulent Mixing Experiments," Calspan Report No. 66320A0-3-Rev., March 1984.

3. Rhodes, R.P., "Analysis of Nonreactive Supersonic Turbulent Mixing Data," JANNAF 14th Plume Technology Mtg, CPIA publication 384, Vol II, Nov. 1983.

4. Melville, W.K. and Bray, K.N.C., "A Model of the Two-Phase Turbulent Jet," Int. J. Heat Mass Transfer, Vol. 22, 1979, pp. 647-655.

5. Padova, C. "Non-Reacting Turbulent Mixing Experiments - Phase II - Test Engineering Report and Supplement," August and September 1982.

6. Padova, C., Boyer, D.W. and Wurster, W.H., "Mach Number and Density Effects in the Mixing of Supersonic Jets," JANNAF 14th Plume Technology Mtg., CPIA publication 384, Vol. 1, Nov. 1983.

Table 1
MATRIX[a] OF TEST CASES

M	M_j	ρ_∞/ρ_j	MW_j	T_{oj} (°R)	GAS COMPOSITION (% H_2, BALANCE N_2)
0	3	0.6	16.12	528	49.6
		1.0	10.30		66.2
		2.0	6.367		87.0
		6.0	2.018	660	100.0
	2	0.6	26.60	528	8.19
	4		12.21		60.5
		1.0	6.047		84.5
2		0.6	22.01		23.1
		1.0	13.64		66.3
		3.0	4.542		99.9
		6.0	2.018	760	100.0
	2	10.0	3.212	528	66.4
	3		2.018		100.0

[a]CONDITIONS INTO WHICH THE JETS EXHAUST WERE:

$T_{o\infty}$ = 470°R, MW = 28, FOR WIND-ON CASES (M_∞ = 2)

$T_{o\infty}$ = 528°R, MW = 28, FOR NO-WIND CASES (M_∞ = 0)
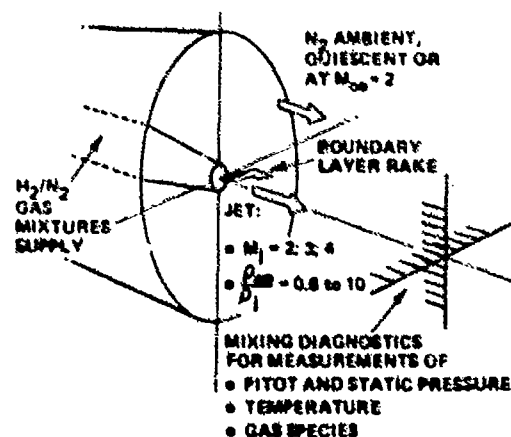
Figure 1 SCHEMATIC OF JET MIXING EXPERIMENT
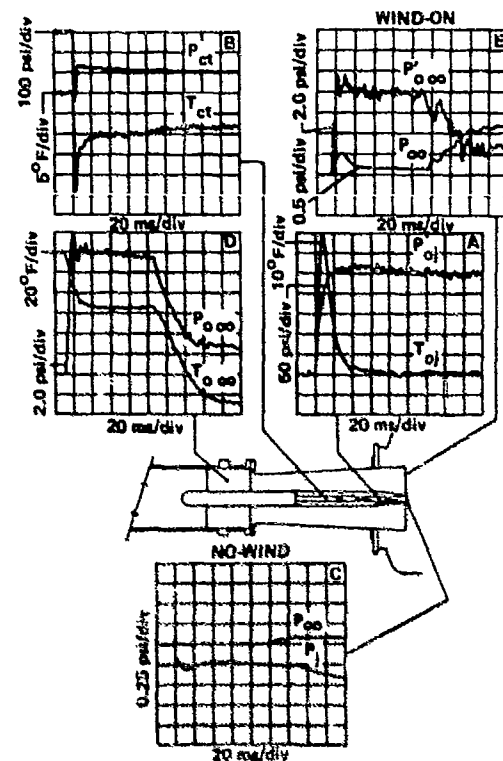
Figure 2   HISTORIES OF FLOW VARIABLES ILLUSTRATING THE JET/STREAM CHARACTERISTICS

TIME MILLISEC

(a) PRESSURES IN THE JET
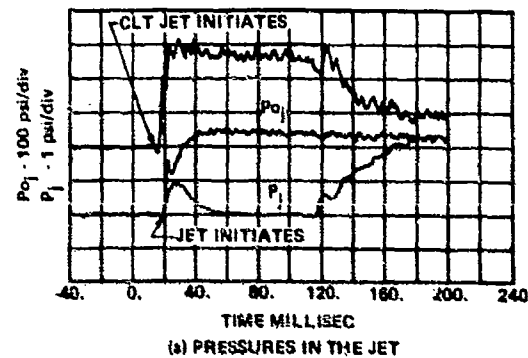
Figure 3   SYNCHRONIZATION OF THE CLT AND JET DISCHARGES
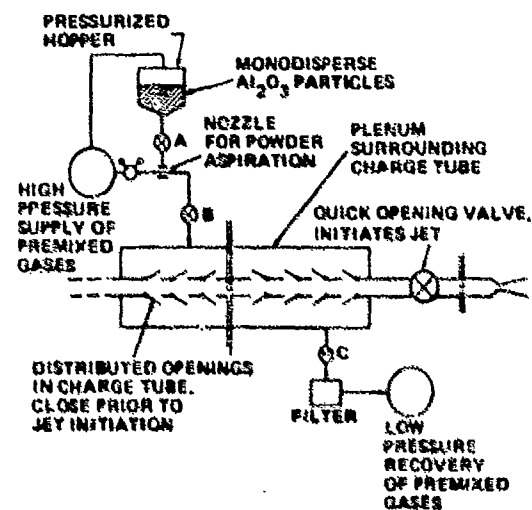
Figure 4   SCHEMATIC OF PARTICLE INTRODUCTION SYSTEM
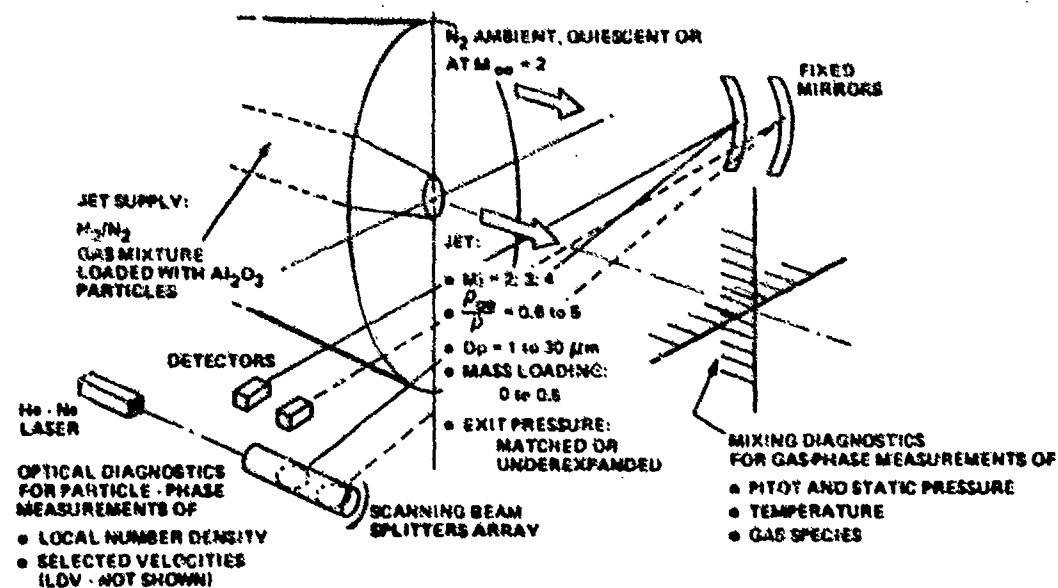
Figure 5   SCHEMATIC OF MIXING EXPERIMENT WITH PARTICLE LADEN JETS
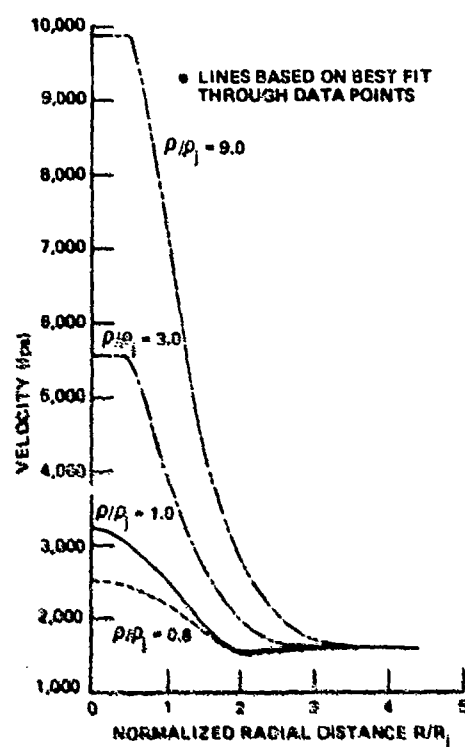
Figure 6 INFLUENCE OF DENSITY VARIATIONS ON VELOCITY SURVEYS AT 40 R_j, M_j = 4., M_∞ = 2
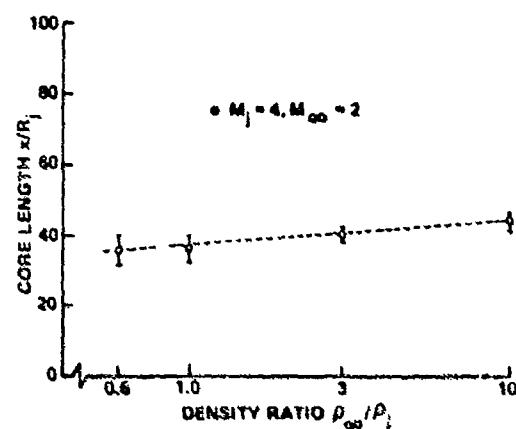
Figure 7 INFLUENCE OF DENSITY VARIATIONS ON CORE LENGTH

SHOCK TUBE MEASUREMENTS OF CONVECTIVE HEAT TRANSFER

FROM A HIGH REYNOLDS NUMBER, PARTICLE-LADEN, TURBULENT,

NON-STEADY BOUNDARY LAYER

G T Roberts*, D Kilpin[†], P Lyons[†], R J Sandeman[†],
R A East* and N H Pratt*.

* Department of Aeronautics & Astronautics, University of Southampton, Hants, U.K
[†] Department of Physics, Australian National University, Canberra, ACT Australia

Experiments were performed at high pressure, using the Australian National University (ANU) T3 shock tube facility, in which the effect of particle additives on the surface rate of heat transfer from a turbulent, non-steady boundary layer was investigated. These experiments were similar to and complemented those performed previously [1,2] at Southampton University (AASU) by extending the range of test conditions by nearly an order of magnitude to post incident shock pressures exceeding 100 bar. Heat transfer rates of order 10^8 W/m^2 were measured using robust miniature surface thermocouples. As found previously, the heat transfer to the shock tube surface decreased as the particle mass loading was increased; however, the measured heat transfer attenuation was greater than expected from extrapolation of the low pressure data. A possible explanation for the phenomenon is an enhanced interaction between the particles and the boundary layer turbulence.

INTRODUCTION

Presented here are the results of experiments, performed at high test pressures ($42 < p_2 < 119$ bar) in the ANU free-piston shock tube, T3, in which the surface rate of heat transfer from a two-phase, high Reynolds number, turbulent, non-steady boundary layer was measured. As in similar previous experiments [1,2], performed at comparatively low test pressures ($3 < p_2 < 15$ bar), whilst the primary objective was to advance the understanding of the mechanisms by which small (< 10 µm) particulate additives reduce the heat flux to, and hence erosion of, gun barrels, the results may also be of significance in many other turbulent two-phase flows [e.g. pumping of slurries, fluidised bed combustors, etc].

The experiments were arranged such that small particles (in the present case talc, mean diameter $\simeq 4.5$ µm) were entrained into the post-incident shock flow from a thin layer, of variable mass loading, deposited on the lower half of the shock tube sidewall prior to the run. The rates of heat transfer to both dusty and non-dusty ('clean') surfaces were measured simultaneously. Inert (argon) and reactive test gases [2] were employed but the data obtained exhibited little sensitivity to test gas composition at these conditions and only the inert gas data are presented here.

In particular, the purpose of the present experiments was to extend the range of post-shock conditions in order to investigate further the previously noted [2] correlation between the magnitude of heat transfer reduction and a non-dimensional particle mass loading parameter which, for a given mass loading of particles per unit surface area, is inversely proportional to the post-shock test gas density [3]. The latter was increased by an order of magnitude beyond those obtained previously (i.e. to $8.0 < \rho_2 < 20.0$ kg/m^3); as

a consequence of the very high rates of heat transfer experienced under such conditions ($\sim 10^8$ W/m^2) new, fast-response, heat transfer sensors were required as alternatives to conventional thin-film resistance thermometers.

EXPERIMENTAL TECHNIQUE

The ANU T3 shock tube

The operation and performance of the T3 free-piston shock tube facility have been described by Stalker [4]. The principle of operation is that energy is transferred from a large volume, compressed air reservoir to a small volume of driver gas (helium or argon in these experiments) via a heavy piston. The nearly isentropic compression of the driver gas ruptures a mild steel diaphragm and initiates the shock tube flow in the normal manner. The penalty paid for the consequently enhanced performance is that the test time available is small compared with conventional facilities due to the small volume of driver gas after compression. However, in the present application, the test time of $\sim$ 200 µs was similar to the duration of non-steady boundary layer flow in the experiments performed previously [1].

Usually, the facility is operated as a reflected shock tunnel at relatively lower test gas pressures but higher temperatures; the present use of the facility as a straight through shock tube at the required operating conditions was novel. The post-shock conditions (Table 1) were inferred, via the normal shock relations, from measurements of the incident shock velocity, monitored by piezo-electric pressure transducers positioned at known locations along the length of the shock tube.

Heat Transfer Instrumentation

The rate of heat transfer to a surface ($\dot{q}_w$) can, in principle, be inferred from the rise in surface temperature of a semi-infinite medium of known thermal properties by solving the equation for one-dimensional, unsteady heat conduction [5]. The device most commonly used in shock tubes to measure the surface temperature rise is, of course, the thin film resistance thermometer which offers advantages in terms of high frequency response (typically $0(10^6)$Hz) but is generally only suited to situations in which the heat transfer rate is relatively low, primarily because the low thermal conductivity of the (electrically insulating) substrate to which the film is bonded otherwise causes the gauge to overheat. For example, in the present experiments it was calculated that the surface temperature rise of a pyrex substrate subjected to a rate of heat transfer of $0(10^8)$ W/m^2 would be in excess of 900° C within the 200 µs run duration, well beyond its softening temperature ($\sim 650°$C). Alternative devices for measuring large rates of heat transfer have been developed, e.g. thick film gauges and calorimeter gauges [5], but their frequency response is generally much inferior to thin film gauges because of the increased time required for the thermal pulse to penetrate the relatively thick sensing element.

However, the recent success of Lawton [6] in measuring high rates of heat transfer in a gun prompted the use of miniature surface thermocouples, manufactured by ASEA (Sweden). Being of metallic construction (of relatively high thermal conductivity), the predicted maximum temperature of the thermocouple surface in these experiments was $\sim$ 200°C at the maximum post-shock pressure $\sim$ 120 bar. The device is sketched in Figure 1 and consists of two concentric thermocouple alloy (chromel/alumel) elements separated by a thin (2µm) dielectric across which the junction is formed by wiping the surface with an abrasive cloth. Because the junction is small, it has low thermal inertia, enabling the thermocouple to register very rapid variations in the surface temperature, from which heat transfer fluctuations at frequencies $0(10^6)$ Hz can be measured. The thermocouple assembly is enclosed in a stainless steel sheath which is tapered so that an interference fit with a suitable mount provides a gas-tight seal. It has the added advantage that the active surface may be machined to match the profile of the shock tube interior exactly.

Over a limited temperature range, such as experienced in these experiments, the emf generated by the thermocouple rises approximately linearly with hot/cold junction temperature difference. Since the run duration is short, changes in cold junction temperature can be neglected, in which case the voltage rise registered is directly proportional to the change in hot junction (surface) temperature. Therefore, as the instrument monitors the change in surface temperature and, despite its relatively large thermal conductivity, may be regarded as 'semi-infinite' (i.e. the thermal penetration distance during the shock tube run-time is small compared with its linear dimensions), it is possible to use an analogue network, similar in design to that employed for thin film gauges to convert the generated surface temperature signal into heat transfer rate. The analogue networks used here consisted of 12 arithmetically-lumped resistance capacitance stages [5], offering a wideband frequency response $10^2 < f < 10^6$ Hz. A characteristic of such networks is that they tend to amplify any noise present on the input signal; therefore, in these experiments, active 'notch' filters (centred on the thermocouple resonant frequency - see below) were employed to remove unwanted mechanically-generated noise on the temperature signal.

Both the temperature and heat transfer signals were, after suitable conditioning, captured by a transient recorder/digitiser (operating at a sample rate of 2×10^6 Hz) prior to transfer onto floppy discs for permanent storage and subsequent analysis.

EXPERIMENTAL RESULTS

As in previous experiments, the parameter by which the heat transfer reduction was quantified is the ratio of dusty to non-dusty ('clean') total heat transfer (i.e. the heat transfer rate integrated over the 200 μs run duration following shock transit $= Q$). In each run the ratio was obtained by comparing the heat transfer signals from two thermocouples sited across a vertical diameter of the shock tube, the particle layer being confined to the lower half of the tube [3].

Typical results obtained from both dusty and clean runs are shown in Figures 2 and 3. Figure 2 shows the surface temperature rise, with time after shock transit, as indicated by the unfiltered thermocouple output. For non-dusty flow, the rise was $\leq 200°C$ in the 200 μs run-time, which agrees well with initial predictions. It is clear, however, that the particles considerably reduce the peak temperature attained (by a factor of approximately two in the run conditions illustrated).

Superimposed upon the temperature signals are large amplitude fluctuations of frequency ~ 75 kHz. After investigation, these fluctuations were found not be be related to the fluid flow but mechanically induced. As described above, it was therefore necessary to employ a notch filter, centred on the apparent resonant frequency, to remove the unwanted noise on the temperature signals before input to the analogue network, the resultant heat transfer signals being shown in Figure 3. It appears the filtration was only partially successful: there is clear evidence of a relatively low frequency (~25 kHz) noise component and the amplitude of high frequency (~400 kHz) noise is considerably greater than had been recorded in the earlier low pressure tests using thin film gauges.

Nevertheless, the heat transfer rate indicated by the thermocouple/analogue combination agrees well with the theory of Mirels [7], for single-phase, turbulent, non-steady boundary layers. Although the accuracy of the semi-empirical theory has been firmly established in earlier experiments (e.g. Ref. 3), it is believed this is the first occasion that a comparison between theory and experimental data has been performed at such high Reynolds numbers $(10^{11} < $ Re/unit time $< 10^{12}$ $s^{-1})$. Here, the Reynolds number is defined as [8]

$$Re = \frac{u_e u_e (W-1)^2 (t-t_o)}{\nu_2}$$

where u_s is the incident shock speed, u_e is the (shock-fixed) post-shock freestream gas velocity, v_2 is the freestream kinematic viscosity, W is the density ratio across the shock and $(t\text{-}t_o)$ is the time elapsed since shock transit at the measuring station. With the Reynolds number defined in such a way, transition from laminar to turbulent boundary layer flow occurs at Re ~ 10^6, [3] (i.e. $(t - t_o)$<1µs in the present experiments). It is of interest to note that the magnitude of the heat transfer rate indicated by the thermocouple sensors (~ 10^8 W/m^2) is comparable to that measured by Lawton in his experimental 40 mm gun [6].

As in the previous experiments [1,2] it was found that the presence of particulate material in the boundary layer caused large reductions in the heat transfer rate, the magnitude of which depended on the initial mass loading per unit area of the particle layer. Figure 4 shows the variation of the ratio of dusty to clean total heat transfer with mass loading for the various run conditions listed in Table 1 and indicates that up to 80% reduction was achieved as the mass loading was increased to 28 g/m^2. However, in contrast to previous findings [2], in these experiments there appeared to be no test gas density dependent variation in heat transfer attenuation. Hence, at the present conditions, there is no clear correlation between the attenuation and the non-dimensional particle mass loading parameter, m_p/m_g (Figure 5). Here m_g is the average mass of gas in the non-steady boundary layer, which is also evaluated from Mirels' theory and is proportional to test gas density [3].

DISCUSSION

From Figure 5 it appears that the reductions in heat transfer observed in the current experiments, besides exhibiting no apparent test-gas density dependence, were somewhat greater than anticipated by extrapolation of the low pressure data. The inference is, therefore, that at least one of the possible mechanisms by which particles reduce convective heat transfer becomes stronger as the test gas density (hence Reynolds number) increases. In a previous paper [2], it was argued that the major contending mechanisms are (a) the insulating effect of a static layer of particles (b) the absorption of thermal energy by a motile layer of particles and (c) a particle-induced alteration of the boundary layer structure.

The first mechanism was demonstrated to be insignificant by performing experiments [2] with a short dust-free region upstream of the measuring station in which reductions in heat transfer were nevertheless observed. Laser beam extinction measurements confirmed the rapid entrainment of particles into the boundary layer. There appeared to be some supportive evidence that absorption of thermal energy might, in part, be responsible for the heat-transfer reduction, since the major parameter describing such a mechanism is the thermal mass ratio, which embodies the non-dimensional mass loading parameter (m_p/m_g) described above. However, the mechanism indicated a sensitivity to particle and test gas specific heat capacities that was not confirmed experimentally [2]. Moreover, such a mechanism remains active only so long as the particles are in thermal non-equilibration with the test gas. Even at comparatively low test pressures, equilibration with the mean gas flow occurred soon after shock transit (10-20 µs); at the conditions prevailing in the present experiments, equilibration was even more rapid (<5µs) [3]. Thus such a mechanism, if significant at all, is likely to become less so as the Reynolds number of the flow is increased.

The possibility remains that the particles alter the structure of the boundary layer, not because of lack of equilibration with the mean flow but with the turbulent fluctuations on a microscale. In the present experiments the mismatch between the comparatively large particle thermal/inertial response times and the smaller characteristic timescales of the turbulent fluctuations becomes even greater as the flow Reynolds number increases. Theoretical descriptions [9,10] of such a situation have shown that particles inhibit the production and enhance the dissipation of small (Kolmogoroff) scale turbulence, the consequence of which is to increase the laminar sub-layer thickness and thereby reduce both the wall shear stress and heat transfer.

In Lumley's model [10], the increase in sub-layer thickness (δ_s) with the addition of particles is described by a non-dimensional loading parameter (L) as well as the ratio of particle to turbulence characteristic times (Λ). Figure 6 shows the modelled increase in sub-layer thickness for the ranges of loadings and timescales pertinent to the current experiments. Since the wall shear stress is inversely proportional to the sub-layer thickness, it is clear that large shear stress and heat transfer reductions can be modelled. However, the values of Λ shown are far greater than those cited by Lumley for a 'strong' interaction and therefore the applicability of his model to the current experimental situation is at present somewhat speculative. It is anticipated that further investigations of this effect will appear in future publications.

CONCLUSIONS

Miniature surface thermocouples were used successfully to measure large rates of heat transfer ($\sim 10^8$ W/m^2) in shock tube boundary layer flows at high pressures ($42 < p_2 < 119$ bar), there being good agreement between experimental data and Mirels' theory for single-phase, non-steady, turbulent boundary layers. Even at high Reynolds numbers (Re/unit time $\sim 10^{12}$ s^{-1}) large reductions in heat transfer were observed when talc particles (mean diameter $\sim 4.5\mu$m) were entrained into the boundary layer from an initially static layer on the shock tube floor. The heat transfer attenuation increased (up to 80%) with increasing particle mass loading, and was greater than expected from extrapolation of data obtained previously [2] at lower pressures.

Since particle response times reduce with increasing pressure, it appears that heat transfer reduction mechanisms which rely on the particles remaining in non-equilibrium with the mean flowfield are not dominant. However, it is possible that the greater than expected reductions at high Reynolds numbers were a result of an enhanced interaction between the particles and boundary layer turbulence.

ACKNOWLEDGEMENTS

REFERENCES

1   Roberts, G.T, East, R.A., and Pratt, N.H. *'Heat transfer in flows with particulate additives - a shock tube study'*. Proc. 7th Int. Symposium on Ballistics, The Hague, (1983).

2   Roberts, G.T., East, R.A., and Pratt, N.H. *'Surface heat transfer measurements from a turbulent, dusty boundary layer'*. Proc. 14th Int. Symposium on Shock Tubes and Shock Waves, Sydney (1983), pp 455-462.

3   Roberts, G.T. *'Shock tube studies of convective heat transfer'*. University of Southampton, Ph.D Thesis (1985)

4   Stalker, R.J. *'Development of a hypervelocity wind tunnel'*. J. R. Ae. Soc., 76, (1972) pp 374-384.

5   Schultz, D.L. and Jones, T.V. *'Heat transfer measurements in short-duration hypersonic facilities'*. Agardograph No 165 (1973)

6   Lawton, B. *'Heat transfer and wear in gun barrels - 2nd year report'*. Royal Military College of Science Technical Note TN/108 (1982)

7   Mirels, H. *'Boundary layer behind a shock or thin expansion wave moving into stationary fluid'*, NACA TN 3712 (1956)

8   Mirels, H. *'Boundary layer growth effects in shock tubes'*. Proc. 8th Int. Symposium on Shock Tubes and Shock Waves, London (1971).

9   Landahl, M.T. *'Dynamics of boundary layer turbulence and the mechanisms of drag reduction.'* Physics of Fluids, 20, 10, Part II, (1977) pp S55-S63

10 Lumley, J.L. *'Two-phase and non-Newtonian flows'*. In 'Topics in Applied Physics 12: Turbulence', 2nd edition, Bradshaw, P. (ed), Springer-Verlag (1978).

Run condition	Initial Pressure (Torr)	Incident Shock Speed (m/s)	Post-shock Pressure (bar)	Post-shock Temperature (K)	Post-shock Density (kg/m³)	Re/unit time (s-1)
A	1016	1610	42	2570	8.0	3.83×10^{11}
B	2083	1740	102	2990	16.5	8.75×10^{11}
C	2286	1670	102	2760	18.0	1.09×10^{12}
D	2540	1710	119	2890	20.0	1.05×10^{12}

TABLE 1: Run conditions for experiments performed in the A.N.U. T3 Shock Tube. Argon Test Gas
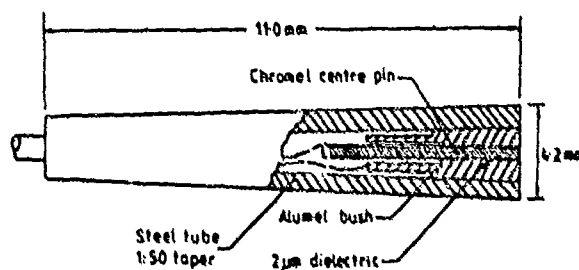
Fig.1   The ASEA miniature surface thermocouple
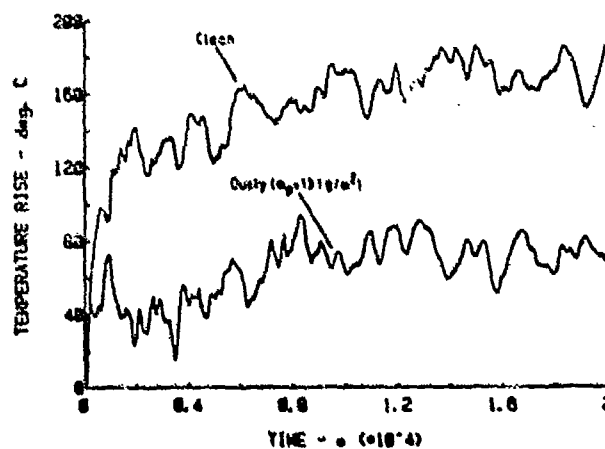
Fig. 2.   Surface temperature rise with time after shock transit
Run condition D
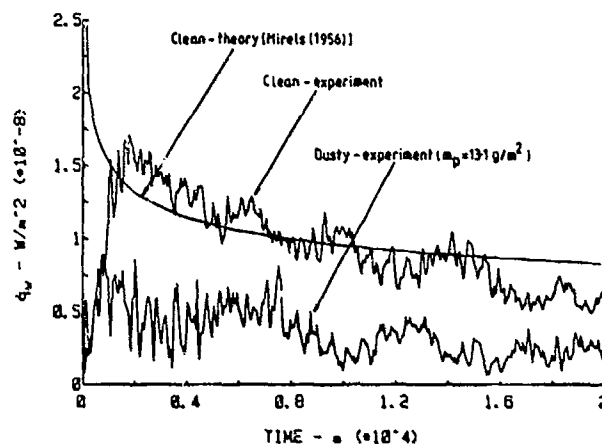
Fig. 3   Variation of surface heat transfer rate
with time after shock transit
Run condition D
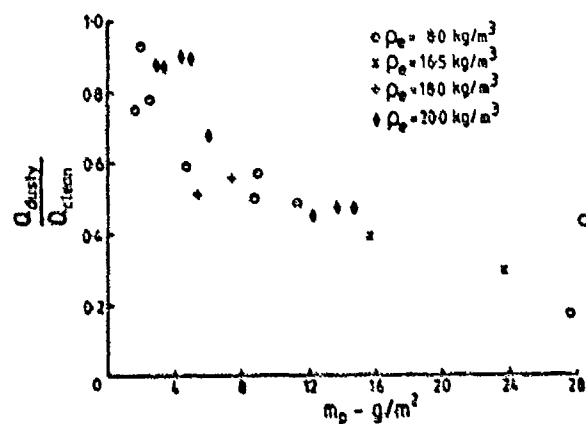
Fig. 4   Variation of heat transfer
reduction with particle mass
loading
Run conditions A - D
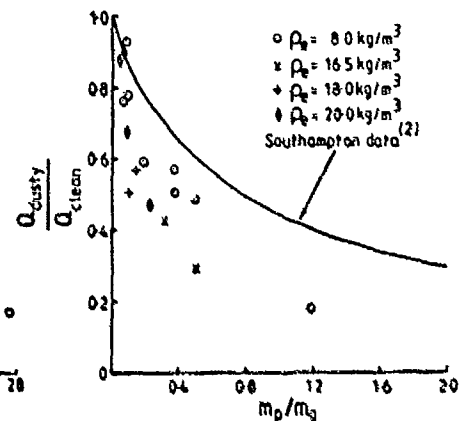
Fig. 5   Variation of heat
transfer reduction
with nondimensional
particle mass loading
Run conditions A - D
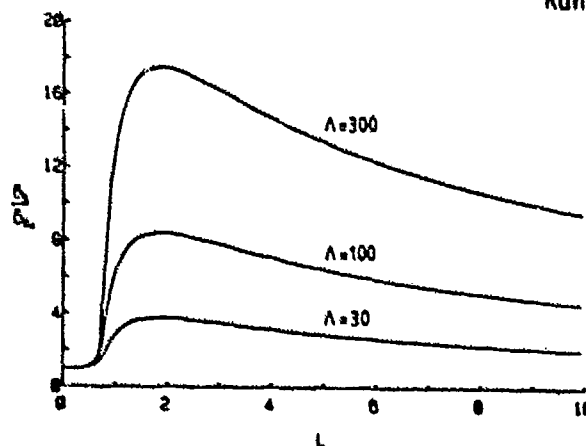
Fig. 6   Modelled[10] increase in sub-layer thickness with
particle mass loading L and particle/turbulence
timescale ratio Λ

EXPERIMENTAL STUDY OF PRESSURE AND HEAT FLUX DISTRIBUTION

ON INDENTED NOSETIP MODELS IN A SHOCK TUNNEL

H. T. Fan

Shanghai Jiao Tong University,Shanghai, China

G. X. Gou

China Aerodynamic Research and Development Center
Mianyang, Sichuan, China

The experimental study of the aerothermal environment on indented nosetip models in the 60-cm shock tunnel of CARDC is given. The models have two configurations:severely indented and mildly indented. The freestream conditions at which the models were studied are M_∞ =7.9-11, and $R_{a\infty}/m = 2.8 \times 10^6 - 4.25 \times 10^7$. The main feature of the flowfield over the models and the influence of indented shape on pressure and heat flux distributions were investigated.

1.INTRODUCTION

The investigation of the flow over the indented nosetip is of key importance to the design of the advanced reentry system employing slender high vehicles. On the one hand, the shape of the nosetip effects the drag and moment coefficients of the vehicle and may generate a large localized heating rate on it. On the other hand, the flow fields over such a indented shape involves many complex and interesting phenomena, such as shock wave-boundary layer interaction and shock-shock interaction. The large localized heating rate associated with such interactions causes the nose more concave. For such a sort of flow fields, analytical methods are not successful quite often and so the experimental investigation is necessary.

The purpose of the present study is observing the flow field over the indented nosetip and measuring the pressure and heat flux distribution on it. The influence of Mach number and Reynolds number of free stream and indented shape is also studied.

2.EXPERIMENTAL APPARATUS AND MODELS

The experiments were conducted in the 60 cm shock tunnel of CARDC. The shock tunnel consists of a shock tube, a nozzle, a test section and a vacuum tank. The driver gas is hydrogen diluted with nitrogen. The test gas is nitrogen of puring exceeding 99.9%. The conical nozzle with 60 cm exit diameter is connected to the end of the shock tube to provide a required steady flow. As the models are small in comparison with the exit dimension of the nozzle, the influence of conical flow stream is not significant. Owing to the relatively short test time, the temperature on the model wall remains essentially invariant with its initial value of $295°K$. The wall to stagnation temperature ratio was 0.36, 0.33 and 0.30 for M_∞ =7.92, 10.8 and 11, respectively.

Two kinds of models were used: severely indented and mildly indented.The structure of the mildly indented model is shown in Fig.1 and that of the severely indented model can be found in reference 1. The diameter of the base for both models is 18.5 cm. The models are made of aluminum. The surface roughness of the models is less than 2.5μm. The heat transfer gages and pressure transducers were flush-mounted on the surface of the model along the symmetrical rays. Some heat transfer gages were placed along the circumference of the model to check whether the measured quantities vary in circumferential direction. The heat transfer gages used in the present test are the thin film gages and the pressure transducers are the piezoelectric pressure gages. These gages were developed at CARDC for test in shock tunnel. The photographs of flow field were obtained by using a schlieren system.

3.RESULTS AND ANALYSIS

Fig.2 shows the schlieren photographs of the flow field over the models. The schlieren-photograph of the severely indented shape was taken at $M\infty=11$ and that of the mildly indented shape was at $M\infty=10.8$. These photographs illustrate that a three dimensional separated region is formed at the concavity, as the flow passes and expands through the spherical cap. From Fig.2 it is seen that the compression waves generated in the reattachment region converge to form a single shock- the re-compression shock. The bow shock interacts with the re-compression shock and generates a single shock and free shear layer.

The pressure and heat flux distributions on the severely indented model at $M\infty=11$ and 7.9 are shown in Fig.3. The q_s and p_s in the figure is stagnation heat flux and pressure, respectively. S is the surface distance measured from stagnation point, R_B is the radius of the model base (92.51 mm). As the pressure and heat flux increase suddenly after the separation, the separated point can be determined at about $S/R_B = 0.4$ from Fig.3. This is in agreement with the position shown in the schlieren photograph.The reattachment point should be located at the vicinity of a point at which the peak of the pressure and heat flux occurs. Consequently, from Fig.3, it is seen that the separated region is $S/R_B = 0.4 - 0.8$, the peak pressure and the peak heat flux are more than 0.8 times and 1.8 times of the stagnation value, respectively.

By comparing the data for $M\infty=11$ with the ones for $M\infty=7.9$, it can be seen that the pressure and heat flux distribution (normalized by the stagnation value) are not evidently different for both the Mach numbers (see Fig.3). This is consistent with the numerically obtained conclusion about the influence of Mach number on the pressure in Ref.2. Moreover, the heat flux distribution shown in Fig.3(b) clarify that the boundary-layer transition occurs in front of the separated point under the present test conditions. From Fig.3(a) and 3(b) along with the schlieren photographs, it can be concluded that the influence of Mach number on the characteristics of the separated flow over the indented nosetip is not substantial.

Fig.4 shows the comparison of the heating data of severely indented model for $M\infty=11$, $Re_\infty/m =4.3 \times 10^7$ with that for $M\infty=10.8$, $Re_\infty/m =2.9 \times 10^7$. The pressure distribution is similar to heat flux distribution and not shown. It can be seen from this figure that there is not remarkable difference under the present test conditions, even though the difference in Reynolds number is up to 49%. Based on our results along with the experimental data of AEDC-F tunnel (as shown in Fig.6), for turbulent separation the influence of the Reynolds number as well as Mach number on the main feature and properties of the separated flow field is not significant.

Fig.5 shows the pressure and heat flux distributions for the mildly indented model. It is evident that the separated region is about $S/R_B = 0.25 -$

0.51 and much less than the one for the severely indented model. The variation of the heat flux and pressure between the separated point and reattachment point is much less than that for the severely indented model.

The Fig.6 shows a comparison between the present experimental data and the ones of AEDC-F tunnel. The data shown in Fig.6 are all for the severely indented configuration. The experimental data of AEDC-F tunnel was given in references 1 and 3. It can be seen from Fig.6 that all the present data are in excellent agreement with the ones of AEDC. It lends great confidence to the two experimental data.

4.CONCLUSION

(1) For the two kinds of indented models used here, there exist interactions of shock – shock and shock – boundary layer, and a separated region at the concavity. The interactions and the separation are more severe for severely indented shape than for mildly indented one.
(2) The influence of Mach number and Reynolds number on the main feature and properties of separated flow field over indented nosetip model are not sub-stantial.
(3) By comparing the present data with that experimentally obtained in AEDC-F tunnel, a good agreement is obtained. It lends great confidence to the two experimental results.

REFERENCES

1. Rakich J.V. et al, "Navier – Stokes Calculations for Laminar and Tur-bulent Hypersonic Flow over Indented Nosetips" AIAA paper 78-260.

2. Hsien T.,"Calculations of Flow Field about Indented Nosetips" AD-A 125329.

3. Reeves B.L. et al,"Hypersonic Flow over Indented Nosetips" AIAA paper 77-91.
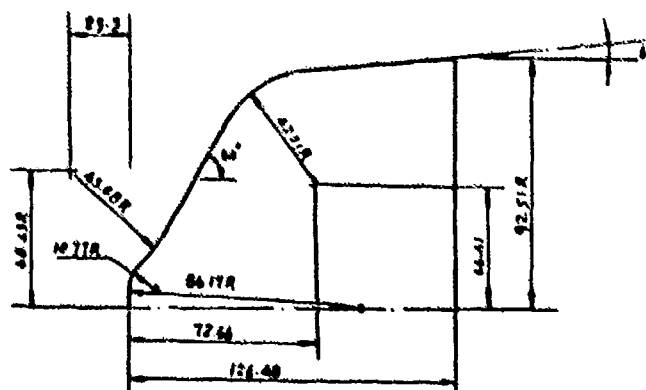
Figure 1 Mildly Indented Model Geometry (All Dimensions in Millimeter)
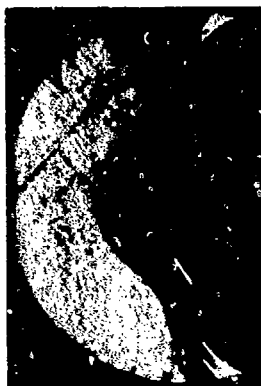
(a) Severely Indented
Configuration
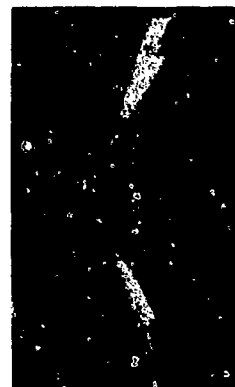
(b) Mildly Indented
Configuration

Figure 2   Schlieren Photographs of Flow
Over Indented Configurations

(a) Pressure
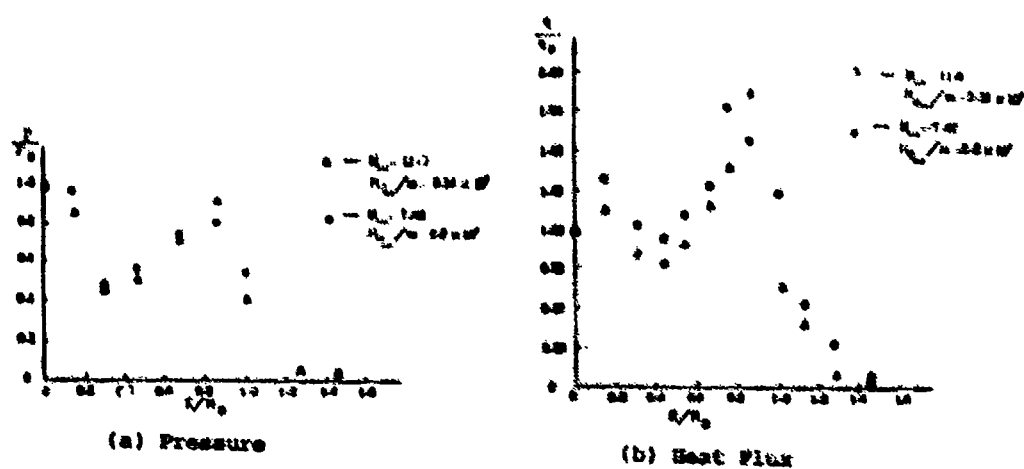
(b) Heat Flux

Figure 3   Pressure and Heat Flux Distribution
on the Severely Indented Configuration
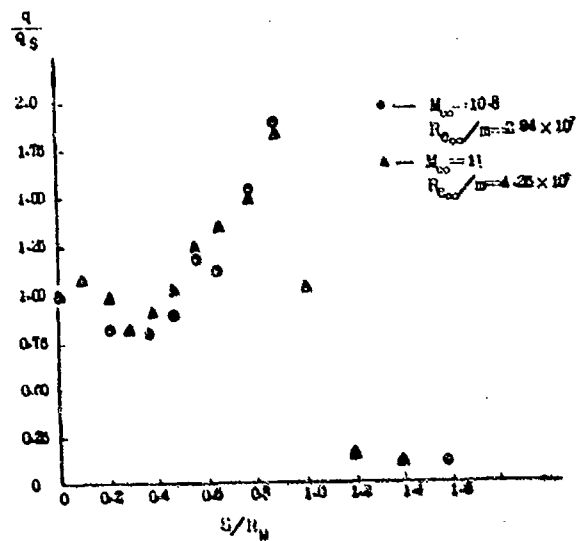
Figure 4   Heat Flux Distribution on the Severely Indented Configuration

(a) Pressure
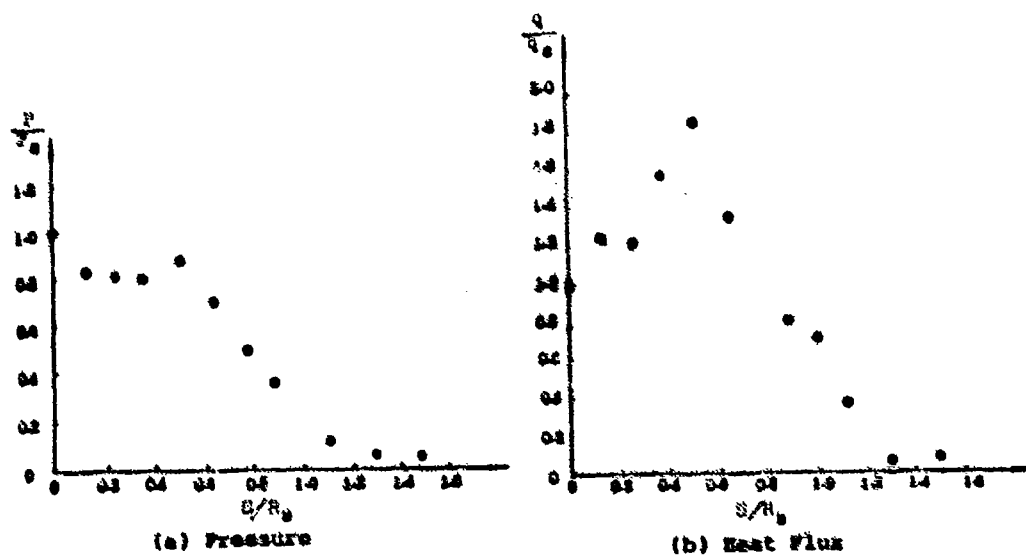
(b) Heat Flux

Figure 5   Pressure and Heat Flux Distribution on Mildly Indented Configuration
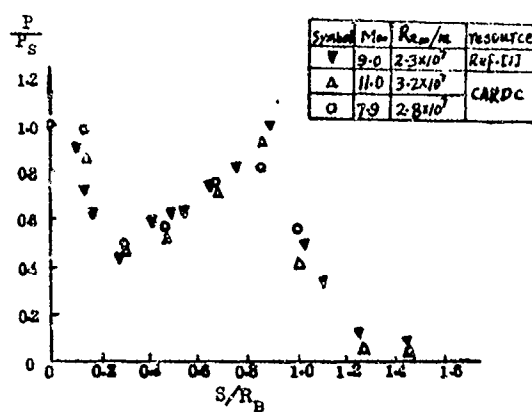
(a) Pressure
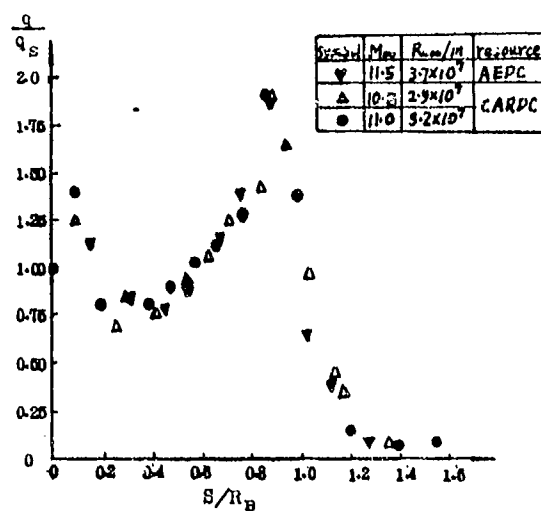
(b) Heat Flux

Figure 6   Comparison of Present Measured Data
            With Others

HOLOGRAPHIC INTERFEROMETRY OBSERVATION OF THE PROPAGATION OF CAVITATION INDUCED SHOCK WAVES IN AN ULTRASONIC VIBRATORY TYPE TESTING

N.SANADA*, K.TAKAYAMA**, O.ONODERA**, J.IKEUCHI*
* Government Industrial Research Institute of Tohoku, Sendai, Japan
** Institute of High Speed Mechanics, Tohoku University, Sendai, Japan

An investigation was made of the behavior of cavitation induced shock waves in an ultrasonic vibratory test, and was also made of the interaction of a small air bubble with the shock wave generated by a micro-explosion in water. In the vibratory test it was observed, by using a holographic interferometry, how the shock waves were transmitted through a solid test piece. The same method was applied to the small bubble collapsing test. It was also found by a pressure measurment that the intensity of impact pressure induced by the bubble collapse could be about 400 MPa.

1. INTRODUCTION

As a Japanese national project of developing geothermal energy, some studies have been conducted to develop the materials suitable to systems utilizing geothermal hot water and steam. One of the studies is directed to evaluating the resistance of materials to cavitation attack which simulated a severe erosive condition of the geothermal power plants, by using an ultrasonic vibratory test apparaus. This apparatus is widely used [1], but it has some ambiguity in determining the resistance of materials, because the mechanism of impact pressure produced in the cavitation field has not been made clear sufficiently.

The impact pressure can be induced when a cavitation bubble collapses near a solid wall. It is found that two factors are predominant in the generation of the impact pressure. One is a micro-liquid jet caused by the instability of collapsing bubble and the other is a shock wave induced when collapsing bubble re-expands [2]-[7]. However, more detailed study has to be done with bubble collapsing behavior and liquid field near the bubble in order to clarify the mechanism of generation of the impact pressure.

The present paper deals with an experimental investigation, by using a holographic interferometer and a PVDF pressure gage. Using the mehtod, the movement of the shock waves induced by cavitation in the ultrasonic vibratory test were studied, and the interaction of a small air bubble with the shock wave generated by a micro-explosion in water were also studied.

2. EXPERIMENTS

(1) Vibratory Test

In an ultrasonic vibratory test, a test piece was vibrated axially at a frequency "f" of 17.7 kHz and an amplitude "A" of 17.5 um in test water. A stainless steel test piece was 16 mm in diameter and 6.8 mm in thickness, and an acrylate test piece was 16 mm x 16 mm in rectangle and 6.8 mm in thickness. Stainless steels are generally used for geothermal power plants. The acrylate test piece was used to visualize the trajectory of the shock propagating in a solid material. The temperature of the test water ranged from 283 K to 293 K.

(2) Single Bubble Collapsing Test

Figure 1 shows the schematic diagram showing the bubble location in a single air bubble collapsing test. The 1.7 mm diameter bubble interacted with a primary shock wave. The primary shock wave was produced by igniting a 10 mg

lead azide pellet. The pellet could be detonated by a pulsed laser beam (100 mJ/pulse, pulse width: 20 nsec) which was transmitted through a glass fiber of 0.2 mm in diameter.

(3) Optical Observation System

Figure 2 shows the schematic diagram of a holographic interferometer. A ruby laser (Apollo Lasers Inc. 22HD: 2J/pulse, pulse width: 30 nsec) was used as a light source. The interferometer was used to construct holographic images of the bubble collapsing process. The magnification of the images was from 1/3 to 10. Details of the test apparatus and the optical observation system are shown in the previous papers [7][8].

3. RESULTS AND DISCUSSION

3.1 Propagation of a Shock Wave Induced in the Vibrating Test

(1) Generation of Shock Waves

If the test piece displacement "x" from the neutral point at any time "t" in water is given by eq.(1), the velocity "v" and acceleration "a" of the test piece can be written as follows:

$$x = A\sin(2\pi f t) \tag{1}$$

$$v = 2\pi f A\cos(2\pi f t) \tag{2}$$

$$a = -(2\pi f)^2 A\sin(2\pi f t) \tag{3}$$

where f=17.7 kHz and A=17.5 μm. The maximums of absolute "v" and "a" are 1.9 m/s and 2×10^4G, respectively. "G" means the gravity acceleration that is 9.8 m/s^2.

If the displacement "x" is set positive when the test piece moves toward the direction of the water surface, the enormous negative acceleration "a" occurs. Consequently enormous tensile stress acts on the water near the test piece surface in the process, and then cavitation bubbles are induced as shown in Fig.3(a). On the other hand, when the test piece moves down toward the other direction, enormous compressive stress acts on the water. In this process, the bubbles start collapsing, and shock waves can be induced as shown in Fig.3(b).

(2) Shock Propagation through a Vibrating Test Piece

In Fig.4, the shock wave which was induced by a bubble collapse on an acrylate test piece surface, was transmitted through the water (arrow 1) and the test piece (arrow 2). The relationship between the radius r_w of shock wave trajectories in water and radius r_a of shock wave trajectories in the test piece, of which the origin was common, was shown in Fig.5. The gradient of the solid line was very close to the value of ratio 1500/2700, which 1500 m/s and 2700m/s are sound velocities in water and acrylate at 293 K, respectively.

Figure 6 illustrates the propagations of shock waves shown with arrows in Fig.4. In Fig.6, the radius of a shock wave, which originated at the point "O" on the test piece surface, reachs to the r_w in the water and r_a in the acrylate test piece, respectively, after $t_{\theta o}$ sec from the origin. Therefore, if the average shock velocities in the water and acrylate, the length of $\overline{OB}$ and $\overline{OD}$ are shown as c_w, c_a, r_b and x_0, respectively, we obtain the radius r_θ of shock wave trajectory in the directions within an acute angle θo at which lines $\overline{OB}$ and $\overline{OC}$ cross as followes:

$$r_\theta = c_w t_{\theta o} + x_0(1-c_w/c_a)/\cos\theta$$

where $t_{\theta 0} = r_s/c_s$. r_s and x_o are obtained as 6.11 mm and 3.70 mm, respectively, from Fig.4. Therefore, the calculated radius r_θ of the shock front is drawn as $\overline{BC}'$ in Fig.6 if c_w=1500 m/s and c_s=2700 m/s. The calculated value of r_θ is smaller than the measured value of r_θ because of using the abovementioned values as c_w and c_s.

In Fig.6, a preceding shock wave in the water is illustrated with a dotted line. The preceding shock wave was induced by a shock wave propagating through the acrylate test piece. The gradient of the dotted line to the test piece surface was close to the value of ratio 1500/2700.

3.2 Interaction of an Underwater Shock Wave with a Small Air Bubble

(1) Collapse of a Bubble on a Solid Wall

Interferograms in Fig.7 show the interaction of a primary shock wave with the 1.7 mm diameter air bubble attached to a transparent resin wall in the test water. The sequential interferograms were taken at 13, 14, 20, 21.5 μsec after the primary shock wave was produced by detonating a 10 mg lead azide pellet which was placed 30 mm below from the air bubble.

When the underwater shock wave passed through the bubble, a wave was reflected from the bubble and the bubble began to shrink as shown in Figs.7(a) and (b). The reflected wave was an expansion wave due to the difference of acoustic impedances between air and water. After 20 μsec from the laser ignition, it is noted that with an increase of the ambient water pressure the bubble was shrinking significantly and the bubble top was moving toward its bottom and forming a micro-liquid jet which penetrated the bubble top toward the resin wall as shown in Fig.7(c).

Finally after 21.5 μsec from the ignition it became a flat spheroid in a minimum volume as shown in Fig.7(d). It is observable that the surrounding pressure around the bubble was increased as predicted by Fujikawa and Akamatsu [9], and different types of fringe patterns appeared in the transparent resin solid wall. One (arrow 1) seems to be produced by the micro-liquid jet crash against the solid wall, and the other (arrow 2) seems to be produced by a shock wave which was induced in the bubble collapsing process. In addition, a different fringe pattern (arrow 3) was observed at the bubble top. Its fringe pattern seems to be caused by another shock wave in the same process.

(2) Collapse of a Bubble at a Capillary Tip

Figure 8(a) shows a view after 25 μsec from the explosive ignition. The air bubble was attached to a capillary tip in order to minimize the effect of a solid wall on the bubble collapsing process. The explosion center was 30 mm apart from the bubble. It is observed that the bubble (arrow 1) was re-expanding, the ambient pressure around the bubble was increasing as shown by dense fringe pattern (arrow 2)[9], and a shock wave (arrow 3) was generated from the bubble. Figure 8(b) shows the field after 50 μsec from the ignition. The primary shock wave (arrow 1) produced by the explosion can be seen, and the expansion wave (arrow 2) and the other shock wave (arrow 3) induced by the bubble collapsing can be seen distinctly also.

(3) Impact Pressure Induced in a Bubble Collapsing Process

It is reported that the impact pressure induced in a bubble collapsing process was an order magnitude of 1 GPa [4][7][10]. It is found that the impact pressure magnitude depends upon initial volume of the bubble, the state inside the gas bubble and so on. But the impact pressure has not been made clear yet.

An interferogram in Fig.9 shows the view in the collapsing process of the 1.7 mm diameter air bubble attached to a PVDF pressure gauge. The interferogram was taken after 35 μsec from the explosive ignition at 30 mm below from the

bubble. It is shown that the expansion wave (arrow 2) and the shock wave (arrow 3) were generated from the collapsing bubble after the primary shock wave (arrow 1) passed through the bubble, even though a small disturbance was caused by the glass fiber and pressure gauge holder. If both the propagating velocities of the expansion wave and the shock wave from the collapsing bubble are assumed to be roughly equal to a sound velocity in water, it is calculated from Fig.9 that the expansion wave passed for 22 μsec and the shock wave passed for 11 μsec.

Figure 10(a) shows the variation of a peak pressure versus shock propagating time. The peak pressure was measured by using a pressure gauge which was 30 mm apart from the explosion. And it corresponded to the intensity of primary shock wave itself because there were no bubble on the gauge surface. The pressure gauge was made of a PVDF film of piezoelectric property, and it was not exactly calibrated yet, but it was superior to other known pressure gauges for its wide frequency response as shown by the rapid rise of the peak in Fig 10(a).

Figure 10(b) shows the variation of the peak pressure measured by the PVDF gauge with the 1.7 mm diameter bubble on its surface as shown in Fig.9. After 11 usec from the first peak occurrence owing to the micro-explosion, the second peak pressure appeared due to the different shock wave from the collapsing bubble on the gauge surface. This second peak was equivalant to the value of 2.0 V of the gauge output. It was determined experimentally that 2.0 V of the PVDF gauge output was roughly corresponding to 44 MPa, if we calibrate it by using the pressure transducer of Kistler 601 H.
The impact pressure did not act on all the sensitive surface of the gauge at the time instant of shock generation in the bubble collapsing process. At the time instant of this case, the impact pressure acted on the area in about half a diameter of the bubble before the interaction according to Fig.7(d), and the PVDF gauge could detect pressure on its gauge surface of 2.5 mm in diameter. Therefore the impact pressure "P" was evaluated as $44(2.5/0.85)^2$ MPa=381 MPa.

4. CONCLUSIONS

The results obtained are summarized as follows:
(1)The trajectory of the shock wave propagating through a transparent solid material could be observed by using the holographic interferometer. By this method it was observed that the micro-liquid jet crash against the solid material and the shock wave generation due to the bubble re-expansion occurred almost at the same time in the bubble collapsing process.
(2)The PVDF pressure gauge is found to be useful for the measurement of the impact pressure induced by shock wave because of its excellent frequency response. By using this gauge, the intensity of impact pressure induced in the 1.7 mm diameter bubble collapsing process could be estimated at least 400 MPa.

REFERENCES
[1]. Knapp,R.T., et al., Cavitation, MacGraw-Hill, New York, 1970, p.375.
[2]. Naudé,O.F., and Ellis,A.T., J. Basic Eng., Trans. ASME, Ser.D, Vol.83,1961, p.648.
[3]. Plesset,M.S., and Chapman,R.B., J. Fluid Mech., Vol.47, 1971, p.283.
[4]. Fujikawa,S., and Akamatsu,T., Bull. JSME, Vol.21, No.152, 1978, p.223.
[5]. Shima,A., et al., Acustica, Vol.21, 1983, p.293.

[6]. Shima,A., et al., AIAA Journal, Vol.21, 1983, p.55.

[7]. Sanada,N., et al., Shock Tubes and Waves, R.D.Archer, and B.E.Milton, Editors, New South Wales University Press, Sydney, 1983, p.405.

[8]. Takayama,K., and Watanabe,W., Memoirs Inst. High Speed Mech., Tohoku Univ., Vol.45, 1980, p.1.

[9]. Fujikawa,S., and Akamatsu,T., Trans. JSME, Ser.B, Vol.50-454, 1984, p.1467.

[10]Jones I.R., and Edwards,D.H., J. Fluid Mech., Vol.7, 1960, p.596.
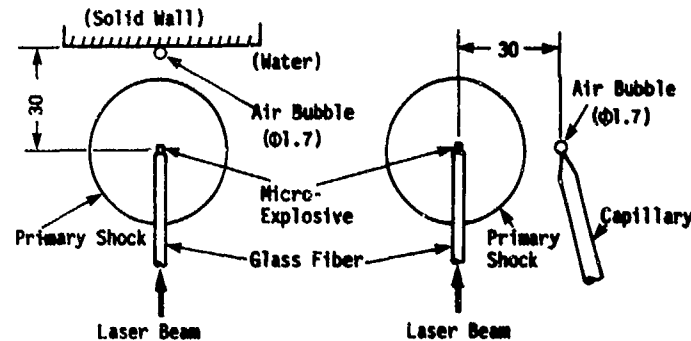
Figure 1.   Schematic diagram showing the bubble location in the single bubble collapsing test.
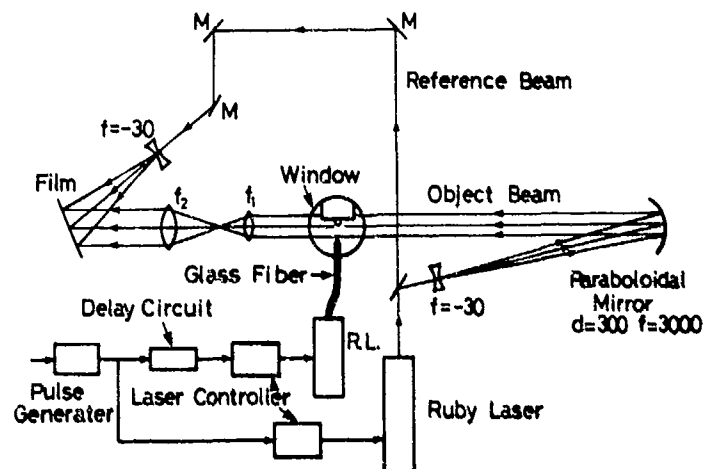
Figure 2.   Schematic diagram of the optical arrangement of holographic interferometer.

Figure 3.   Holograms of the field below a vibrating test piece surface.
(a)Distribution of bubbles, (b)Distribution of spherical shock waves.

Fig.5

5mm
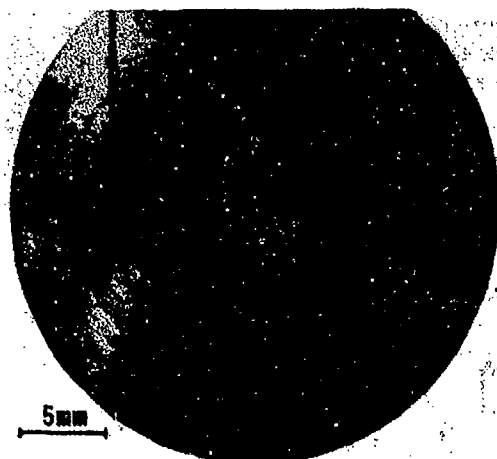
Figure 4. Shock waves propagating through
a vibrating acrylate test piece.

Figure 5. Relationships between shock
wave trajectories r_w and r_s.

Figure 6. Illustration of the shock wave
propagating through a vibrating
test piece.
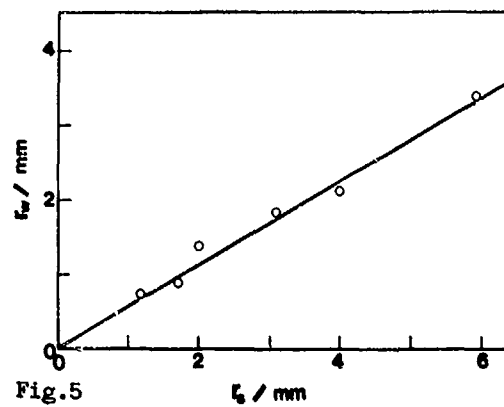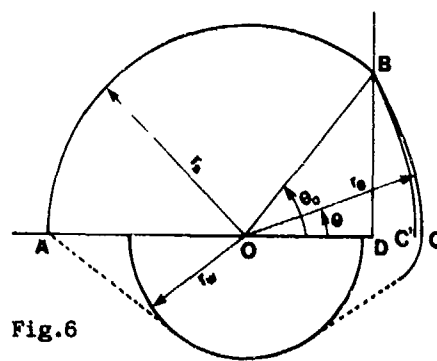
Fig.6
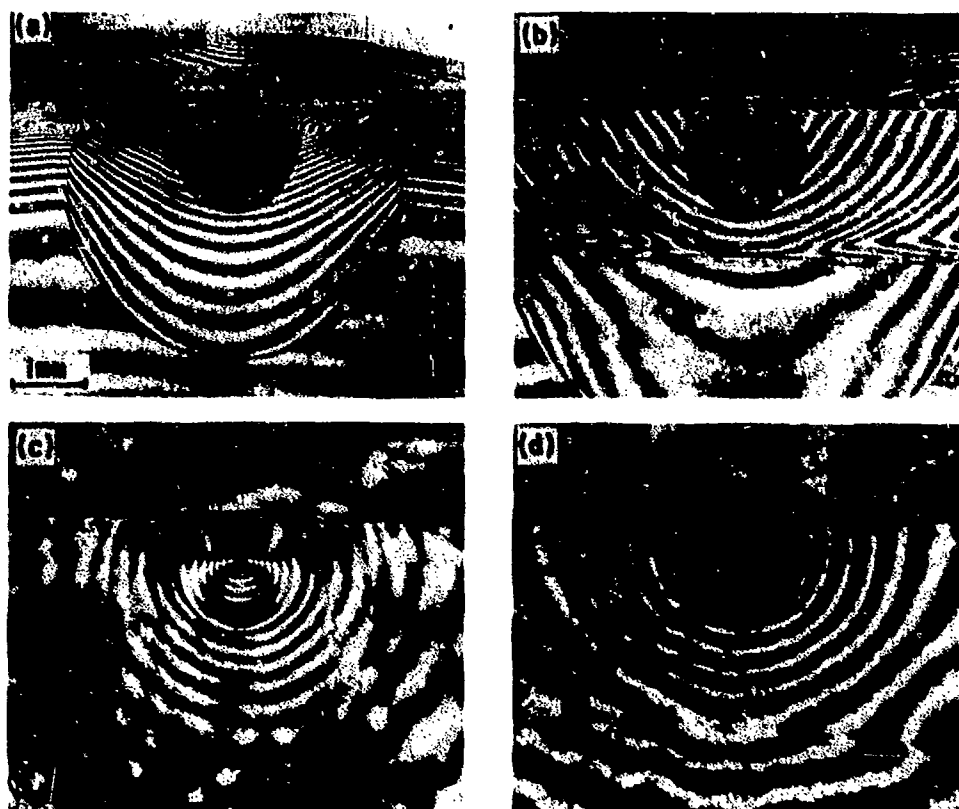
Figure 7. Interaction of the primary shock wave with the air bubble
on a solid wall. (a)13 μs, (b)14 μs, (c)20 μs, (d) 21.5 μs.
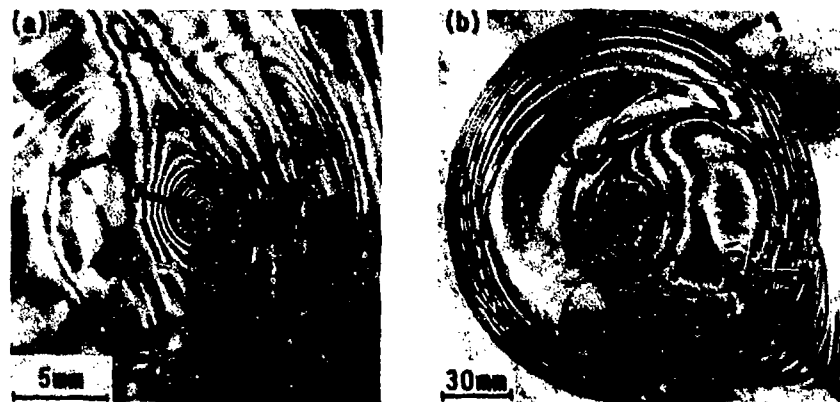
Figure 8. Interaction of the primary shock wave with the small bubble
at a capillary. (a) 25 μsec, (b) 50 μsec.

Figure 9. Propagation of the shock
wave induced by a collapsing
bubble on the PVDF pressure
gauge.
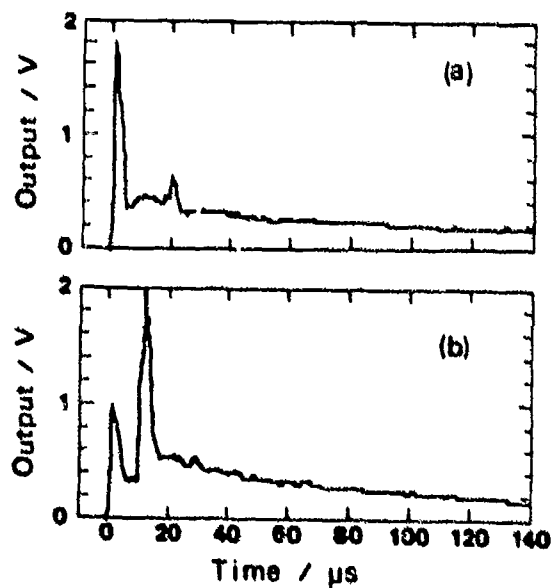
Figure 10. Variation of the peak pressure measured by the PVDF gauge versus
propagating time in a bubble collapsing process.
(a)with no bubble on the gauge surface, (b)with a bubble on the gauge surface.

UNDERWATER SHOCK WAVE FOCUSING

AN APPLICATION TO EXTRACOPOREAL LITHOTRIPSY

K. Kambe, M. Kuwahara and S. Kurosu
School of Medicine, Tohoku University
Sendai 980, JAPAN

K. Takayama, O. Onodera and K. Itoh
Institute of High Speed Mechanics
Tohoku University, Sendai 980, JAPAN

This paper reports a successful application of underwater shock wave focusing to the disintegration of the urinary stones. Lead azide pellet was used as an energy source, and focusing process was precisely studied. The results were applied to clinical treatment of disintegrating upper urinary tract stones with satisfactory consequence.

1. Introduction

In 1950 in USSR, Yutkin proposed an idea of disintegrating urinary tract stones by an electrohydraulic shock wave. He invented an apparatus named "YPAT-1" [1] which was composed of a condenser bank and a flexible thin tube with coaxial bipolar electrodes at the tip. Approaching the electrodes to the urinary bladder stone and discharging the condenser bank, the discharge induced shock wave could break the stone into fragments. This technique was employed by many urologists and successful results were reported from 1969 to early 1970s.

In 1973, by introducing the electrodes to the ureter through cystoscope, Reuter and Kern were the first to remove the upper urinary tract stones by diminishing their size by using shock waves [2]. Since 1976, many attempts have been made to remove kidney stones via percutaneous nephrostomy. Though small stones being easily extracted by forceps, the larger stones can not be removed through the nephrostomy channel. For this purpose, an ultrasonic stone disintegrator was used and found to be very effective. However, this method was applicable to the stones to be reached directly through the nephrostomy channel. For the stones located behind renal calyces, again the electric discharge method must be used coupled with the flexible endoscope [3].

In 1977 in Japan, Watanabe et al. started breaking the urinary bladder stones by an underwater microexplosion of lead azide pellet [4]. They cooperated with the experts of explosives of the National Chemical Laboratory in Tsukuba Japan. They used a specially designed catheter with an explosive pellet at the tip. In 1981 the first clinical treatment was carried out successfully [5].

In 1975, Heusler was the first to propose an epoch making idea of disintegrating the kidney stone by using focused underwater shock waves [6]. Chaussy et al. followed his idea and developed a prototype of a kidney stone disintegrator. A half ellipsoidal reflector with the electrodes installed at its first focus was set in the water bath. This reflector was directed toward the stone which was located at the second focus of a reflector. The spark generated shock wave was reflected and focused at the second focus with a very sharp pressure spike strong and short enough to disintegrate the stone into the

fragments.

The first clinical application was successfully conducted in February 1980 [7]. This technique was named extracoporeal shock wave lithotripsy (ESWL),and it is reported that more than 20,000 cases have been treated successfully.

It was a dream of the not only the urologists but also the people who suffer the kidney stone diseases to have the urinary calculi removed without any surgical procedure. This comes true.

No doubt, this is a unique application of shock waves to peaceful purposes. Shock waves are responsible for the creation of the life on this earth [8] and at the same time are recognized for their catastrophic power once they are misused for the dreadful purpose. It is worth emphasizing here that the shock wave can cure human, and this research will open a new important application of the shock wave research.

2 Basic Research

2.1. Shock Propagation

A 10 mg lead azide pellet was used as an energy source. To detonate the pellet, a Q-switched ruby laser beam was used for the laboratory experiment. For the clinical application, a Pt-bridge heated by a 9 V dry cell was used. Fig.1 shows the pressure-distance curve of the 10 mg lead azide pellet. The pressure measured by a pressure transducer (Kistler model 601 H) was compared with the Random Choice numerical simulation. A good agreement can be seen.

2.2 Shock Focusing

The spherical underwater shock wave, generated at the first focus of the ellipsoidal cavity and reflected by its wall, was making focus near the second focus point. The configuration of the ellipsoid is one of the important factors to have a sharp and strong pressure rise at the second focus. The preparatory experiment was conducted with 8 different ellipsoidal reflectors whose aspect ratios were ranging from 1.2 to 2.0 .

In order to observe the peak pressure trace from the ellipsoidal cavities, a sheet of the pressure sensitive paper was used. This paper named Prescale (Fuji Film Inc.), changes its colour from white to pink depending on the pressure level. The colour intensity is roughly linear to the pressure level if the pressure rise is slower. However for the very rapid rise of the pressure as is the case here, it merely indicates the time integral of the pressure which exceeds the certain level. Fig.2 shows the pressure print. By treating with computer analysis it can be seen that the peak pressure zone is elongated toward the direction of motion of shock wave and narrow in width. This indicates the integration of the reflected shock forms the caustic. It is found that there is an optimal configuration. When the non-linearlity of the underwater shock propagation was taken into consideration to realize a better focusing process, a modification to the ellipsoidal configuration can be done. However, this amount of modification is very small so far as using a 10mg lead azide pellet as an energy source.

2.3 Pressure Measurement

The pressure measurement along the center line of the ellipsoid (90 mm X 127.3 mm) was carried out by pressure transducers (Kistler model 601 H and PVDF Piezofilm gauges). Fig.3 shows peak pressure distributions. Filled circle, open circle and filled triangle correspond to the measured data along the axis,

those along the line 10 mm and 20 mm from the axis, respectively. The origin corresponds to the geometrical focus point and the exit of the ellipsoidal cavity is at x = -130 mm. High peak pressure nearly 2-3 Kbar exists at the region of 5 mm in diameter. This region can last for a few microseconds and is shifted about 5 mm toward the exit. This is due to the non-linearlity of the wave interaction and the shape of the exit of the ellipsoid. As was shown in [9], it is remarkable that the peak pressure distribution drastically decreases from the focal point to the radial direction.

2.4 High Speed Cinematography

In order to observe the crushing process by the focused shock wave, the extracted human kidney stone was suspended with a thin thread in the test chamber and a high speed movie was taken . Figs.4 a-c show an example of a high speed movie (12,000 FPS) of a Magnesium-Ammonium-Phosphate stone (MAP 25 mm X 35 mm, 25 g). The crack propagation over the stone and its disintegration started about 1 msec from the arrival of focused shock wave at the stone. In a few   micro sec, the highest peak pressure suddenly decreased to the level of few bar resulting in the inception of the cavitation cloud. This cavitation cloud being composed of water vapour bubbles of 0.02 to 0.2 mm in diameter, were expected to be responsible in part for crushing the stone and may be for giving damage to the human tissue. This cavitation bubbles disappeared in several hundred micro sec. This phenomena were not fully investigated yet.

In order to simulate the real stone disintegration, kidney stones were put into the Japanese gelatine whose acoustic impedance was similar to that of the human soft tissues. It took ten shots for a 15 mm diameter extracted kidney stones to be coarsely crushed but additional 40 shots were necessary for further fragmentation whose size distribution is shown in Fig.5.

3. In vivo Experiment

3.1 Materials and Method

After above preliminary experiments, we attempted to destroy kidney stones of the experimental dogs. Fig.6 is the brief illustration of the equipment; a half ellipsoid reflector is installed vertically on the wall of the bath, a dog is placed on the table suspended from the bar of the lifter and stone position- ing was assisted by use of a C-arm X-ray TV.

Human kidney stone of about 10 mm in diameter was put in the canine renal pelvis by open surgery about 3-6 months prior to the experiment.

Under intravenous anesthesia, the dog was fixed on the table and placed in the bath. The position was adjusted so as to the stone was correctly located at the second focus of the reflector. After 10 to 100 shots of the microexplosion, the dogs were sacrificed to examine the kidneys and other organs.

3.2 Results

Though the effect was unclear on the X-ray TV, the stone was found broken into fragments in the extracted kidney. Any serious change was not observed macroscopically in the kidneys or other neighbouring organs but the slight hemorrhage was seen in the lower part of the experimental side of the lung . By the microscopic observation, slight bleeding was seen in the renal tubuli and the parenchyme of the lung. These pathological changes are not considered to be of major problems, but further investigation is necessary including long term observation after treatment.

4. Clinical application

4.1 Equipment

The prototype of the clinical equipment was designed by scale-up the experimental apparatus (Fig. 7). Movable chair is located at the bottom of the bath and positioning is controlled by three electric motors along the x,y and z axes. Specially designed catheter with lead azide pellet at its tip is inserted to the first focus of the reflector and 9 volt dry cell is used for ignition. As water lessens the x-ray permeability, two air bags are furnished on both lateral sides of the bath to get the good visibility. Temperature of the water is kept about 33 C .

4.2 Treatment

Patients were carefully examined over general conditions, heart, lung and kidney functions, hemorrhagic tendency etc. During two days before treatment they received low residual meals and some kind of drugs so as to decrease the intestinal gas content. After epidural anesthesia, the patient was fixed to the chair by seat belts. As we used weak anesthetizing drugs to preserve the motor activities, patients could keep their sitting postures easily. Rough adjustment was made about the position of the stones, then the bath was filled with warm water and re-adjustment was made. As kidneys move up and down about 5 cm with respiration, we usually made an explosion at the timing of deep expiration which is the condition that lungs are deflated and located rather upwards.

At the instant of microexplosion, patients felt no pain but some kind of pressure sensation such as being patted by a palm. After about 10 to 20 shots, the stones were found rather larger of their size because of the initial cracking. Further 100 to 200 shots were necessary to diminish the size of each fragments. At this period, the shadow of the stones became more faint and finally they were demonstrated as clouds of dust.

After treatment, patients could stand and get out from the bath on their feet. Usually no changes were seen on their skin, but in few cases faint errythema were observed. There was no abnormal findings on electrocardiogram during and after the treatment.

4.3 Results

Since March 1985, 17 cases were treated in our clinic. Size of stones were 10 to 30 mm in diameter. Numbers of shots of microexplosion were 100 to 200 per one session, and treatment time was within two hours. 10 cases could be treated by one session but for rather larger stones additional sessions were necessary for sufficient fragmentation. Stone delivery began at the next day and usually within 2 to 3 weeks all stones passed naturally. In two cases, stone fragments were trapped in the lower part of the ureter and they were extracted by transurethral ureteroscopic manipulation. Any serious complications were not found except one case of a high fever which required percutaneus nephrodrainage to control the fever.

Figs. 8 -10 are the X-ray photographs of the typical case. Before treatment, the stone of 20 mm in diameter was seen in the right kidney (Fig.8). On the next day, fragments began to fall down and we can see the sand stream at the lower part of the ureter (Fig.9). Fig.10 is the photograph of the fourteenth day. No residual stone is existing.

5.Discussion

Heusler's idea to destroy kidney stones by means of focused underwater shock waves was really epoch making. According to this idea, Chaussy et al. developed the prototype of the extracorporeal stone disintegrator and now commercial equipment is produced from the Dornier System Inc., West Germany. More than 20,000 cases have been treated successfully by these systems and both effective-

ness and safetiness are generally recognized.   Their energy source to generate shock wave is an electric spark.   Therefore complicated system is necessary to avoid the electrical influence to the body.

We have been studying on the possibility to use the microexplosion as an energy source, and as described above, it was revealed that accurate focusing can also be obtained by use of the underwater microexplosion.   Accuracy of the focusing was studied by use of the Prescale paper and there was an optimal configulation of the reflector.   The advantages to use the microexplosion as the energy source are as followings;
  1. Accurate and strong power concentration can be obtained.
  2. Low cost and space saving machine can be expected without sophysticated electrical equipment.

Thus, shock wave has become one of the most attractive medical tools for stone treatment.   But as to the biological effect of the shock wave, there are many unknowns.   Further investigations will find new biological or medical application of the shock wave in the near future.

References

1. Apparat "YPAT-1" V/O Medexport, USSR, Moscow
2. Reuter, H.J. and Kern, E. : J.Urol.,110:181,1973
3. Raney,A.M. and Handler, J.: Urology,6:439,1975
4. Watanabe, H. and Oinuma,S.: Jap.J.Urol.,68:243,1977
5. Watanabe, H., Watanabe,K.,Shiino,K. and Oinuma,S.:J.Urol.,129,183
6. Heusler, E.:2nd European Congress on Ultrasonics in Medicine, Munich,1975
7. Chaussy,C.,Brendel.W. and Schmiedt,E. : Lancet.1265,1980
8. Glass,I.I. "Shock Waves and Man", Univ. of Toronto Press,1974
9. Takayama,K.,Esashi,H. and Sanada,N. :Proc. 14th Intern. Symp. Shock Tubes and Waves, pp 553 - 562.
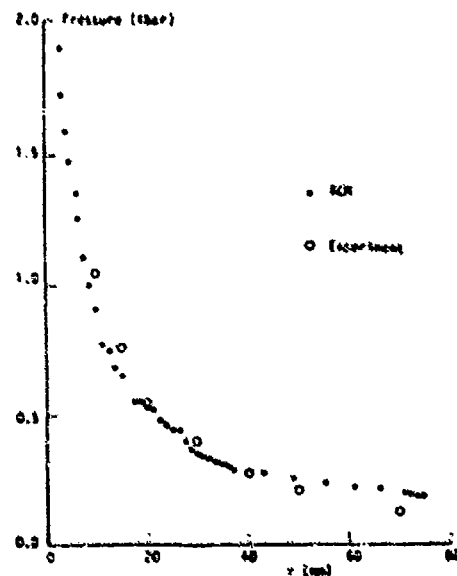
Fig.1 Pressure around the spherical shock wave
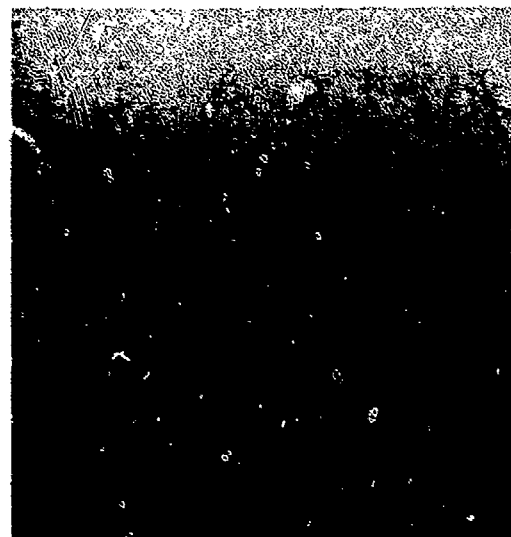
Fig.2 Pressure print by the *Prescale* paper
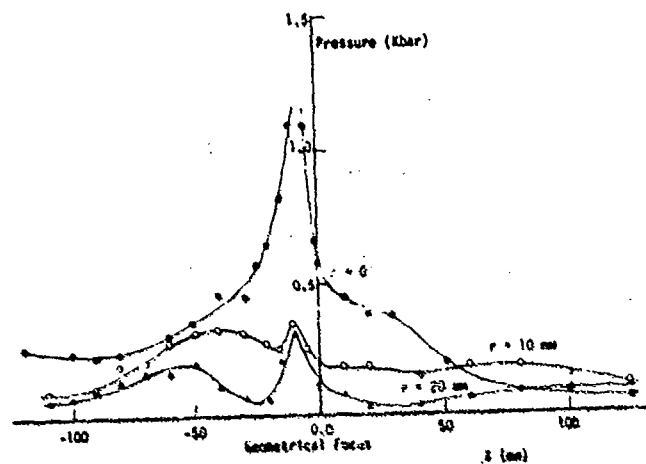
Fig.3 Pressure distribution around the focus
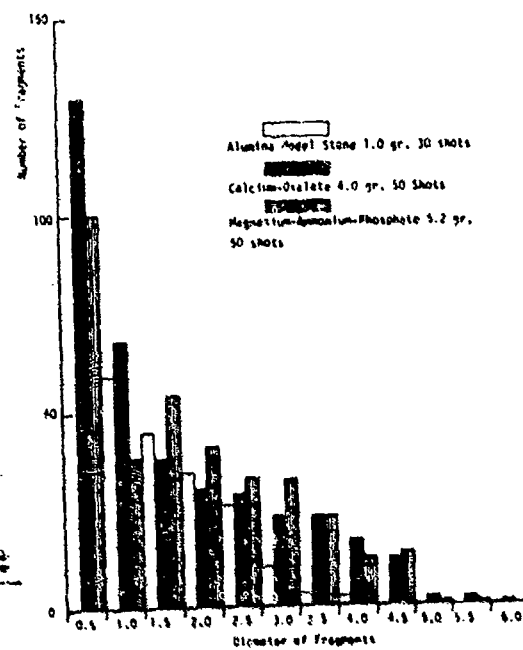
Fig.5 Size distribution of the stone fragments
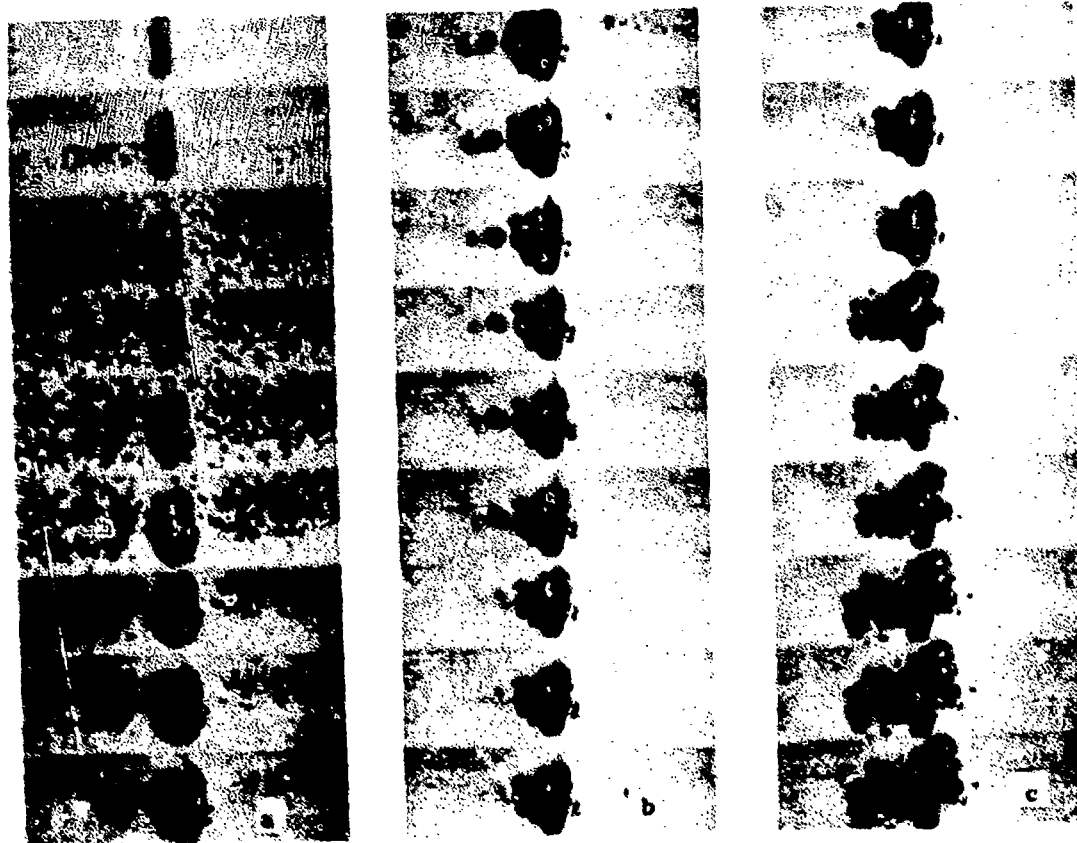
Fig.6 High speed film (12,000FPS) of the collapsing process
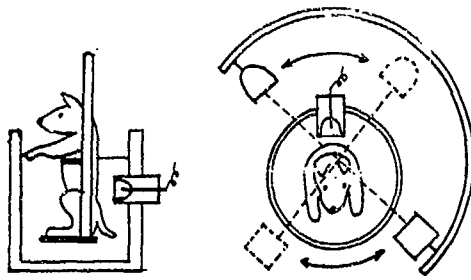
Fig.6 Experimental equipment
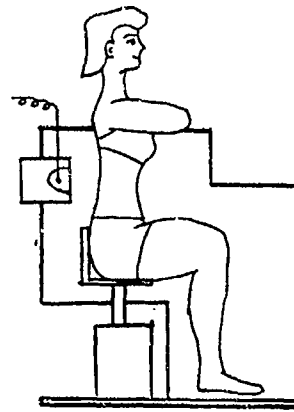
Fig.7 Prototype of the stone disintegrator

Fig.8 X-ray photo before treatment
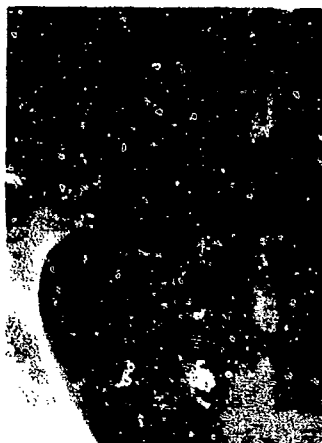
Fig.9 the day after treatment

Fig.10 3 weeks after treatment

SOME HEAT TRANSFER MEASUREMENTS OVER A SPHERE-CONE IN

HIGH ENTHALPY NON-EQUILIBRIUM FLOW

S.L. Gai*, P.R.A. Lyons#, J.P. Baird*, and R.J. Sandeman#

*Department of Mechanical Engineering,
University of New South Wales, Duntroon, A.C.T. 2600 Australia

#Department of Physics and Theoretical Physics,
Faculty of Science, The Australian National University
Canberra, A.C.T. 2601, Australia.

Heat transfer measurements in the stagnation region of a spherically blunted cone are described. These experiments were conducted at a range of enthalpies relevant to re-entry speeds using the Australian National University free piston driven Shock Tunnel T3. The test gas was nitrogen. The results show that flow non-equilibrium in the shock layer in the stagnation region of the body strongly affects the heat transfer rates both at zero and non-zero incidence. The results are consistent with earlier theoretical calculations and similar measurements.

1. INTRODUCTION

There has been a resurgence of interest in the study of aerothermo-dynamic problems of hypervelocity flight with the proposed plans for building aero-assisted orbital transfer vehicles. These new generation of space vehicles will be subject to prolonged radiative and convective heating during their trajectory through low density upper atmosphere at speeds ranging typically between 10 km s^{-1} to 5 km s^{-1}. It is important therefore, to understand the physical and chemical gas dynamic processes in the flow over such vehicle configurations. One such is the 'biconic' configuration.

A comprehensive data-base on spherically blunted biconics, both on-axis and bent nose, in real gases, has been built up by the NASA in recent years[1],[2],[3],[4]. This includes aerodynamic coefficients, pressure distributions, shock shapes and heat transfer measurements. The experiments have mainly been performed in conventional hypersonic wind tunnels and the NASA Langley expansion tube[5].

Although the heat transfer data obtained by NASA Langley[4] do extend to hypervelocity real gas flows, the results, especially for air and nitrogen, still do not cover higher enthalpy ranges and stagnation temperatures. In the present study, we place emphasis on the nose region of a spherically blunted fore-cone of a biconic model and present some stagnation point and sphere-cone junction heat transfer measurements.

2. EXPERIMENTAL TECHNIQUES

2.1 Facility

The experiments were conducted at the Australian National University free piston shock tunnel T3[6] with nitrogen as test gas and helium as a driver gas. The flow was generated by a conical nozzle whose exit and throat diameters were 203 mm and 12.7 mm respectively. The freestream speeds ranged from 5 km s^{-1} to 7 km s^{-1} and the corresponding reservoir enthalpies from 15 MJ kg^{-1} to 40 MJ kg^{-1}.

2.2 Models and Instrumentation

The basic model used for the tests was a 26°-total-angle spherically blunted fore-cone portion of a bent biconic. It was 105 mm long with a base radius of 27.8 mm and nose radius of 5.8 mm. The heat transfer measuring surface thermocouples were located at the geometric stagnation point and the junction of the spherical cap and the cone. The model is shown in figure 1 where the thermocouple locations are also shown.

Miller et al[4] have noted in their stagnation point measurements that the survival rate of their film gauges was not good and that due to sand blasting during the post-run period and annealing of the gauge, there was a loss of accuracy and repeatability. Similar problems have been encountered before by other workers[7]. This is also a problem with the present facility wherein, following diaphragm rupture, erosive particles tend to impact the model after a period of steady flow.

These constraints, therefore, dictated the need for a robust temperature sensor. Following the success of Roberts[8] in the present facility in the use of surface thermocouples for measuring high heat transfer rates in dusty and non-dusty gases, the miniature surface thermocouples type YL641015 by ASEA Corporation of Sweden were chosen for the present measurements. These thermocouples are specially designed to operate in hostile environments of very high temperatures and pressures.

The device as mounted in the nose of the model is shown in figure 2. It consists of a type K (Chromel-Alumel) thermocouple of coaxial symmetry sheathed in a stainless steel casing. A rise time of ~1 μs is claimed owing to the very thin (~ 2 μm) dielectric separating the two thermocouple elements, thus resulting in a very low active mass at the junction. The sensors are enclosed in Delrin sleeves (for electrical isolation) and then each assembly is mounted in its own aluminium nose cone which could be screwed into the body of the model.

3. DATA ACQUISITION METHOD AND ACCURACY.

Since the thermocouples monitor surface temperatures, they may be regarded as semi-infinite in mass so that it is possible to calculate the heat transfer rate $\dot{q}$ in real time using an RC analog network which simulates the flow of heat into a substrate. The 'semi-infinite' assumption is valid for these run-times (~200μs) since the thermal penetration depth is very small compared with the thermocouple dimensions (Shultz and Jones[3]). The output of the electrical analog is then proportional to $\dot{q}$. The design was based on that of Schultz and Jones[9] with a bandwidth of 10^2-10^5 Hz and a response time of the order of 6 μs. The filtered and unfiltered temperature and heat transfer signals were recorded using a LeCroy 2264 waveform digitizer. The schematic of the data acquisition and processing is shown in figure 3(a) and a typical data record in figure 3(b).

The present experiments in this facility have all been carried out within the enthalpy range for which extensive data base has been established over a period of time[10]. The calculated and measured accuracies of free stream stagnation enthalpy and pitot pressure are of the order of ±10 per cent and ±8 per cent respectively. Based on this, it is estimated that heat transfer measurements are accurate to ±15 per cent.

4. RESULTS AND DISCUSSION

4.1 Stagnation Point Heat Transfer Measurements.

Figure 4(a) shows the stagnation point heat transfer rate $\dot{q}_s$ at various enthalpies for a range of incidences with nitrogen as test gas. It is seen that for all the enthalpies the heat transfer rate decreases with increasing incidence. Also heat transfer rates increase with increase in enthalpy for the range of enthalpies considered. Because of the relatively high stagnation temperatures, the flow within the shock layer departs from equilibrium and the degree of non-equilibrium increases with enthalpy. A number of investigations in this facility[10],[11], have established that for air, nitrogen and CO_2, in the enthalpy range considered, a non-equilibrium shock layer prevails around blunt bodies so that measured stagnation region heating rates are influenced by non-equilibrium flow conditions.

In their work, Miller et al[4] find that stagnation point heat transfer measurements were about 20 percent higher for air and nitrogen but about 16 percent lower for CO_2 when compared to theoretical equilibrium values calculated on the basis of Ref.12. Ref. 12 predicts values which are about 8 to 10 per-cent lower than the well known Fay and Riddell theory. Miller et al[4] inferred that while their air and nitrogen results were not affected by flow non-equilibrium, CO_2 results were. The higher than equilibrium value heating rates for air and nitrogen were attributed to rarefaction effects.

Figure 4(b) shows a comparison between present measurements and theoretical predictions based on Ref.12. Referring to the upper curve, the measured values vary from about 1.5 to 2.5 times the theoretical values. Also, the differences are less as the enthalpy is increased.

While it is not clear as to the large discrepancy between the theoretical and experimental values as seen in the upper curve of Fig. 4(b), a likely explanation could be along the lines put forward by Richards et al[13]. Ref. 13 postulates that roughness elements can cause, through mixing processes, a high energy transfer from the outer part of a laminar boundary layer to the layers immediately adjacent to the surface thus rendering higher heat transfer rates without actually causing turbulent flow. Such a phenomenon is not altogether unlikely in the present instance because firstly, the boundary layer is likely to be laminar as the Reynolds number is low $[O(10^3)]$ based on nose radius. Secondly, due to the sand-blasting effect on the nose at each shot, the surface erodes, inducing micro-roughness elements. This would then cause the high heat transfer rates and also the considerable scatter of the data observed in the tests.

In order, therefore, to further test the conjecture that nose surface roughness was contributing to the higher heat transfer rates, a model with a thin coat of lacquer (Incralac) sprayed on to it was tested. It was ensured that the coat was thin enough so as to not affect the measurements of the heat transfer rate. Examination of the traces of temperature and heat transfer showed that the response of the gauge was not affected by the coating. The model was coated before each shot. It may also be pointed out that all tests by Miller et al[4] were conducted with the model coated with Krylon.

The results with lacquered nose all showed reduced heat transfer rates as seen by the lower curve in Fig. 4(b). They also show that measured values are less than the theoretical predictions. Some previous calculations such as in Ref. 14 show that non-equilibrium flow in the shock layer results in a lesser convective heating than the corresponding equilibrium value.

4.2 Sphere-Cone Junction Measurements

In order to assess the effect of angle of attack on the nose region, measurements were made of the heat transfer at the sphere-cone junction. The results are shown in figures 5 and 6.

From figure 5 we note that with increase in angle of attack, at a given enthalpy, the windward ($\phi = 180°$) heating increases and this trend is the same for all the enthalpies.

However, the effect of incidence on leeward ($\phi = 0°$) heat transfer is different as seen from figure 6. Note that initially heat transfer decreases with increase in incidence but at the higher enthalpies, the 21° results show an increase. Such an inconsistency in leeward heat transfer rates has also been observed by Miller et al[4]. The discrepancy in Leeward heating rates, as pointed out in Ref. 4 is due to the likely flow separation resulting in the formation of streamwise vortices emanating from the fore-cone region.

5. CONCLUDING REMARKS

Heat transfer measurements have been made in the nose region of a sphere-cone in hypersonic high enthalpy nitrogen flows generated in a free piston shock tunnel. The range of stagnation enthalpies and temperatures was higher than that reported previously by Miller et al[4]. The results show that flow non-equilibrium results in reduced convective heat transfer rates.

REFERENCES

1. Miller, C.G. and Gnoffo, P.A., "Pressure distributions and shock shapes for 12.84°/7° on-axis and bent-nose biconics in air at Mach 6", NASA TM83222, December 1981.

2. Miller, C.G., "Measured pressure distributions, aerodynamic coefficients, and shock shapes on blunt bodies at incidence in hypersonic air and CF_4 flows", NASA TM84489, August 1982.

3. Miller, C.G., Blackstock, T.A., Helms, V.T. and Midden, R.E., "An experimental investigation of control surface effectiveness and real-gas simulation for biconics", AIAA paper 83-0213, January 1983.

4. Miller, C.G., Nicol, J.R. and Gnoffo, P.A., "Laminar Heat Transfer Distributions on Biconics at Incidence in Hypersonic Hypervelocity Flows", NASA Tech. Paper 2213, Jan. 1985.

5. Miller, C.G., "Operational experience in the Langley Expansion Tube with various test gases", NASA TM78637, December 1977.

6. Stalker, R.J., "Development of a hypervelocity wind tunnel", The Aeronautical Journal, Roy. Aero. Soc., Gt. Britain, Vol. 76, p.374, 1972.

7. Richards, B.E. and Enkenhus, K.R., "Hypersonic Testing in the VKI Long Shot
    Free Piston Tunnel", AIAA Journal, Vol.8, No.6, p.1020, 1970.

8. Roberts, G.T., "Heat transfer from a turbulent, two-phase, non-steady bound-
    ary layer: measurements at high pressure using the Australian National
    University T3 free piston shock tube", University of Southampton (UK) Dept.
    of Aeronautics and Astronautics Memorandum No. 84/7, 1984.

9. Schultz, D.L. and Jones, T.V., "Heat transfer measurements in short duration
    facilities", AGARD Report 165, February 1973.

10. Stalker, R.J., Personal communication, 1982.

11. Gai, S.L., Sandeman, R.J., Lyons, P.R.A. and Kilpin, D., "Shock shape over
    a sphere-cone in hypersonic high enthalpy flow", AIAA Journal, Vol.22, No.7,
    p.1007, 1984.

12. Sutton, K. and Graves, R.A., "A general stagnation point convective heating
    equation for arbitrary gas mixtures", NASA ;R R-376, November 1972.

13. Richards, B.E., Dicristina, V. and Minges, M.L., "Heat transfer and
    pressure distribution on sharp and finite bluntness biconic and hemispher-
    ical geometries at various angles of attack in a Mach 15-20 flow",
    VKI Rept. 71-4, September 1971.

14. Zoby, E.V. and Moss, J.N., "Preliminary Aero-Thermal Analysis for Saturn
    Entry", Prog. Aeronautics and Astronautics, Ed. A.L. Crosbie, Vol.77,
    p.374, 1980.

Figure 1. *Schematic of sphere-cone. All dimensions in mm.*
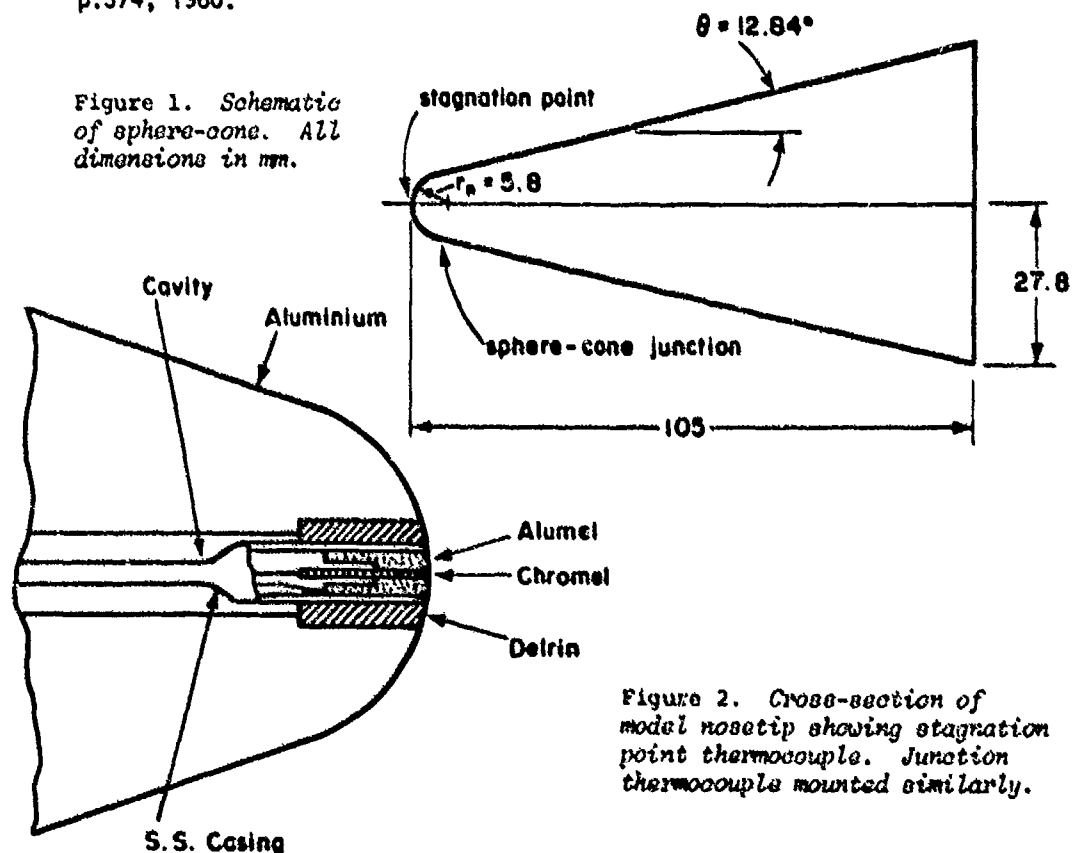
Figure 2. *Cross-section of model nosetip showing stagnation point thermocouple. Junction thermocouple mounted similarly.*
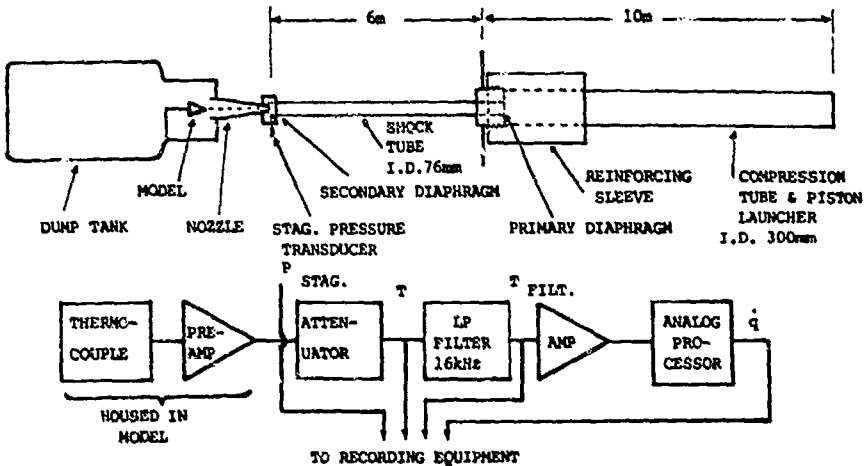
Figure 3(a). *Schematic of T3 shock tunnel and experimental instrumentation.*

Figure 3(b). *Typical data trace for nitrogen. 100 μs/div.*

TOP: *tunnel stagnation pressure   180 bar*
CENTRE: *temperature ΔT (21 K)*
BOTTOM: *heat transfer $\dot{q}_s$ (1.2 kW cm^{-2})*
      at $U_\infty = 3.9$ km s^{-1}
      $h_0 = 9.6$ MJ kg^{-1}
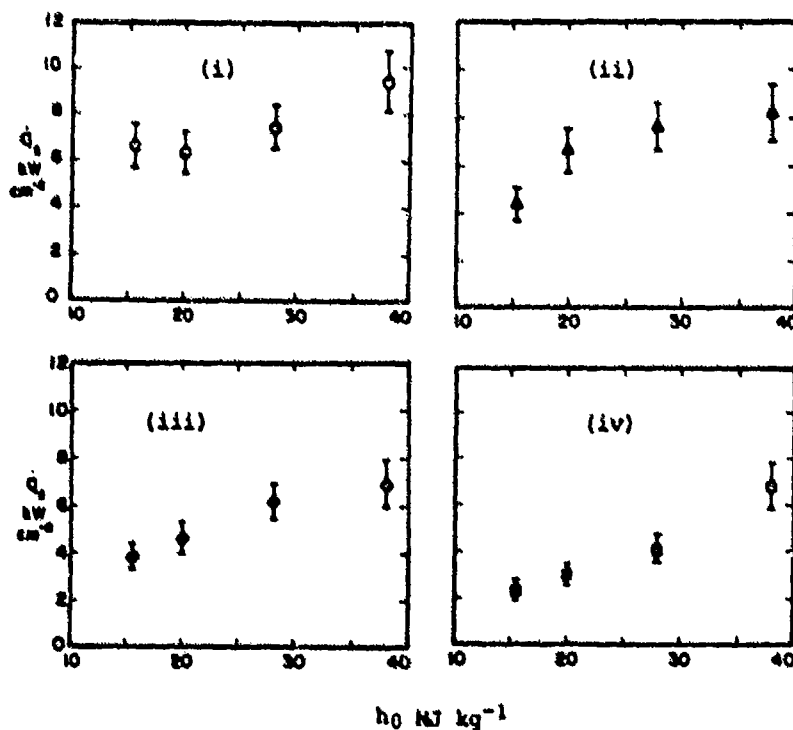
Figure 4(a).
Stagnation point heat transfer in nitrogen.

(i)   α = 0°
(ii)   α = 7.5°
(iii)   α = 15°
(iv)   α = 21°

h_0 MJ kg^{-1}
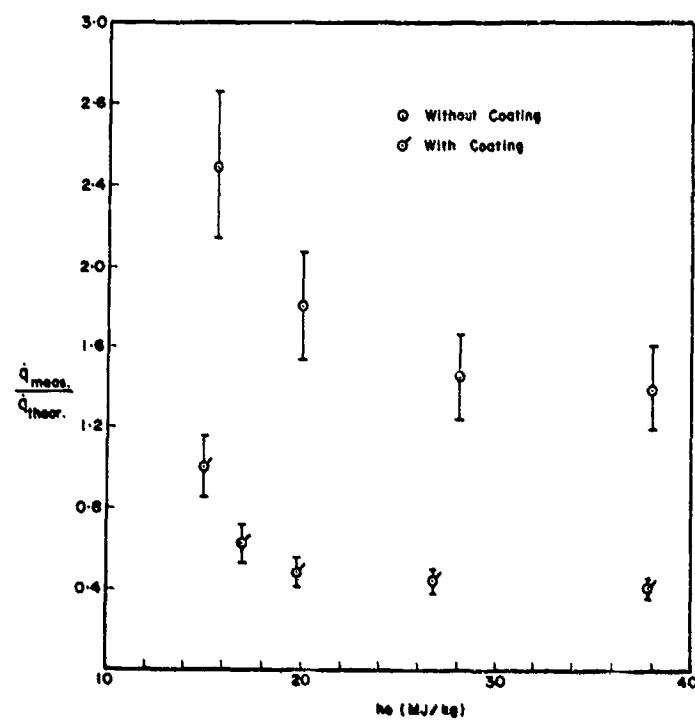
Figure 4(b).

$\dfrac{\dot{q}_s \; (measured)}{\dot{q}_s \; (theory)}$

for the stagnation point
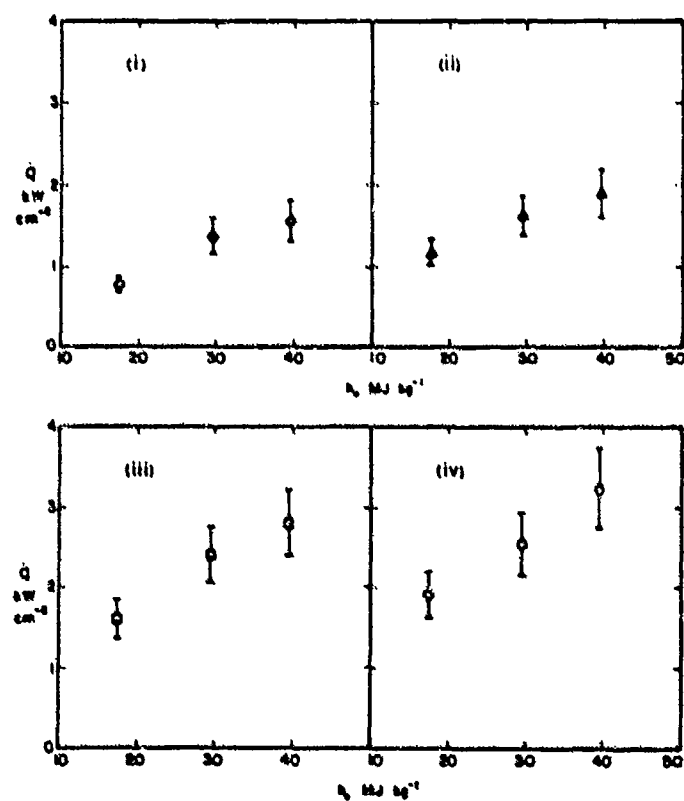
Figure 5.
Sphere-cone-juntion heat transfer in N_2, windward ray ($\phi = 180°$)

(i) $\alpha = 0°$

(ii) $\alpha = 7.5°$

(iii) $\alpha = 15°$

(iv) $\alpha = 21°$
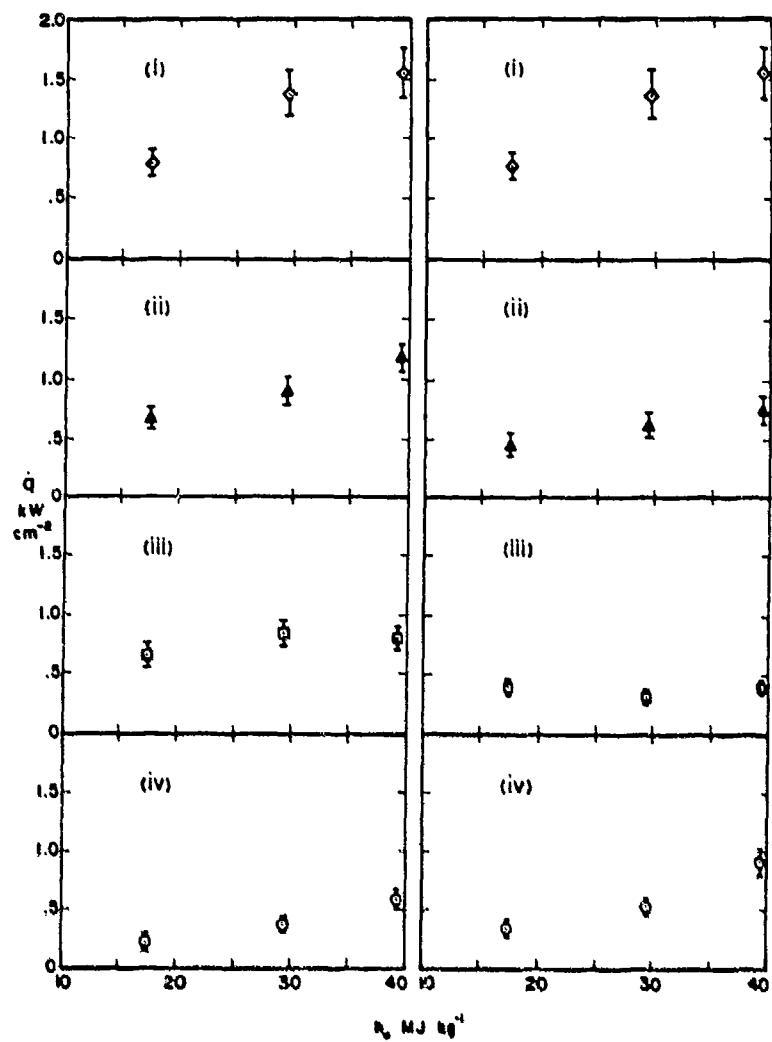
Figure 6.   *Sphere-cone-junction heat transfer in N_2.*
       Left: side ray ($\phi = 90°$)
       Right: leeward ray ($\phi = 0°$)
               (i) $\alpha = 0°$ (ii) $\alpha = 7.5°$
               (iii) $\alpha = 15°$ (iv) $\alpha = 21°$

A HIGH REPETITION RATE, LOW TEMPERATURE SHOCK TUBE

E. L. Resler, Jr., Mechanical and Aerospace Engineering

and S. H. Bauer, Department of Chemistry

Cornell University, Ithaca, New York 14853-1301

The gas dynamics of the flow in a tube positioned coaxi-
ally with a pulsed high pressure nozzle is analyzed. The
tube, situated in an evacuated plenum, is fed by a pulsed
jet at a repetition rate (10-200) pulses per second. A
reflected shock develops in the tube when the injected
supersonic flow arrives at the closed (or partially closed)
end. A sample of gas, initially in the source at ambient
temperature and density $(T_0; \rho_0)$, is cooled by expansion to
$(T_j; \rho_j)$ while being accelerated. Upon reaching the
closed end of the tube, it is brought to rest by means of
a reflected shock, which processes the inrushing gas,
raising its temperature to $T_s > T_0$, with $\rho_s \approx 4\rho_j$.
The magnitude of the jump conditions can be roughly con-
trolled by selecting a carrier gas with the desired molec-
ular weight (μ) and heat capacity ratio (γ). The jump
conditions can then be fine tuned by varying the ratio of
the open area in the end wall to that of the tube. Poten-
tial applications are indicated.

1. INTRODUCTION

Investigations of "fast" reactions provide significant insights into the
dynamics of intra as well as inter-molecular energy transfers. The principal
parameters are the ratio of the activation energy to the thermal energy, and the
effective molecular collision cross section for state-to-state population
changes. Since the dominant factor is the dependence of rates on $\exp(-E_a/RT)$,
the design of experiments to measure accurately the magnitude of the pre-expo-
nential factor involves selection of conditions under which (E_a/RT) is rela-
tively small (< 25), and this requires either that the temperature be high or
that the activation energy be low.

More than three decades ago chemical kineticists began to exploit vigor-
ously the use of shock tubes for generating controlled high temperatures for
such studies.[1-3] In contrast to other techniques, gas dynamic heating provides:
(a) controlled high temperatures over a wide range of gas densities --- but is
limited at the low density end; (b) very rapid heating, such that the operating
translational temperatures are attained in an interval measured in terms of
molecular collisions (about 5); (c) heating is homogeneous across any tube
diameter --- except for small perturbations at the walls due to boundary layers;
(d) the reactant to be studied can be present at very low concentrations, now-
adays in the range of few parts per million,[4] in the presence of an inert gas
carrier; (e) due to the rapid heating one can separate in time successive steps
in a sequence of reactions --- samples taken along the tube axis have experi-
enced different thermal histories; (f) heterogeneous contributions to gas phase
reactions are negligible because the diffusion time through the boundary layers
is much shorter than the experimental observation time. Of course, there are
limitations: (i) the absolute temperature is difficult to establish;[5] (ii) one
must use a rapid analytical device with a response time of the order of micro-
seconds, or (iii) induce a rapid gas-dynamic quench, with cooling rates of the
order of 10^6 K per second, and then analyze the final products; (iv) it is
difficult to reproduce successive runs precisely, and turn-around-times are of

the order of an hour or more per run. While the major preoccupation of chemical dynamicists has shifted during the past fifteen years from shock tubes (as a tool) to the use of lasers, there are continued developments in the introduction of sophisticated diagnostic techniques[6] so that shock tubes still provide an important laboratory device for studying reactions at high temperatures.

Shock tubes as conventionally used are devices for initiating reactions which have high activation energies at high temperatures but are very difficult to set up for investigating fast reactions with low activation energies at low temperatures. Attempts have been made to cool the driver section, and to use modest driving pressures; however, such experiments are difficult to conduct. There are unavoidable problems associated with cooling. One has to contend with fogging of windows and the condensation in critical locations of reactants which have inadequate vapor pressures at low temperatures. Another technique which was tested is admixing reactants with the driver gas, in the high pressure section of the shock tube, and thus subject the test material to rapid cooling when the diaphragm is burst.[7] However, this generates an unsteady expansion fan which is difficult to control, and it is questionable whether one can determine accurately the effective temperature as a function of time.

2.   PROPOSED EXPERIMENT

Here we propose the design for a miniature shock tube which has the following attractive features. Besides providing very fast, homogeneous, gas dynamic heating, it is (i) small and easily constructed [certainly within the current state-of-the-art]; (ii) one can operate it at high repetition rates (up to 200 pps), and thereby use lock-in detection to increase the sensitivity of the diagnostics devices used to follow the conversions; (iii) the test fluid can be brought to controlled low temperatures while all the equipment is maintained at room temperature so that the reactants which are investigated are not restricted to materials which have high vapor pressures at low temperatures. The operating ranges are: ρ_0=ambient; T_s (500$\rightarrow$250°K); reactant gas temperatures are briefly reduced to T_j(100$\rightarrow$30°K); gas densities (ρ_0) can vary initially from $10^{-3}\rightarrow10^{-5}$ gm/cm^3 while post shock-wave densities are typically approximately 10^{-2} of the original reactant gas mixture.

The principle of this device is illustrated schematically in Fig. 1. Item #1 designates a pulsed nozzle source[8] for jetting the source fluid into an evacuated vessel. Generally, the nozzle source is at ambient temperature and density $(T_0; \rho_0)$; however, because it is a small structure, both $(\rho_0; T_0)$ can be controled by heating or cooling coils. Typical compositions are several Torr of the reactant species dispersed in a carrier gas, Ar(γ=1.67); N_2 or CO (γ=1.40); or any other nonreactive carrier. Numerous analyses of the density and temperature distributions in such jets have been published;[9,10] Fig 2 displays typical sets of contours. Note that in the supersonic stream, with laboratory velocity u_j, both the temperature and density drop dramatically. They are functions of the dimensionless parameters (x/D) and (R/D); the calculations apply only when D is much larger than the mean free path in the source. Supersonic streams can also be generated with small Laval nozzles.[11]

Consider what happens after the supersonic stream enters the coaxial evacuated tube (#7), of the same diameter as the skimmer aperture, and of length L; the lip of the skimmer is cut back to attach a shock externally (#6). The leading portion of the pulse of gas reaches the back plate at t_1=L/u_j. The inrushing gas is compressed, and the back reflected pressure wave reduces the forward velocity to zero if there is no exit orifice. A shock wave develops in the tube moving out to the left with the speed U_s. Ultimately the tube fills, the gas in the tube which has been processed by the shock remains essentially stationary, and rapidly attains the temperature T_s when there is no processes which requires a finite time for relaxation. There is a concurrent density jump across the shock front of ~4. At t_2 = L(1/u_j +

$1/U_s$) the shock wave reaches the leading edge of the skimmer and the tube is completely filled to a density ρ_s. Ultimately a standing shock develops a little in front of the skimmer edge, as though the tube were replaced by a rod of the same dimensions. [The gas which passes through this stationary shock rises only to the stagnation temperature $T_0(<T_s)$, because the flow is not contained, but expands when the gas passes over the sides of the "blunt" body.] For a fluid which requires a finite time for relaxation, as in a dilute mixture of H_2O in Ar, the temperature of the inrushing stream is affected ($T_h>T_j$), due to the heat released during condensation. Then, immediately past the shock front an overshoot in temperature occurs, $T_v>T_s$, but eventually the fluid in the tube which has been processed by the shock attains its equilibrium temperature T_s.

It is important to adjust the repetition rate of the nozzle valve so that there is sufficient time between successive pulses for all of the injected gas (including that in the tube) to be completely exhausted before the next pulse initiates the same scenario. Thus, for a repetition rate ≈ 200/s, we estimate that an interval of 10^4 μs is more than long enough compared to $t_2≈2×10^2$ μs.

The basic relations needed to develop a design for any specific experiment are summarized below. Since these are based on well established gas dynamic principles,[1,12] no detailed derivations are included. The ideal gas law and constant γ are assumed. These equations may be readily extended to real gases via computer codes. For any specified source fluid, ρ_0, T_0, with mean molecular weight (μ) and heat capacity ratio (γ), $a_0=(\gamma RT/\mu)^{1/2}$. Let the tube entrance be placed at a selected contour, $\alpha_j \equiv (\rho_j/\rho_0)$. Define, $\phi_j \equiv (\rho_j/\rho_0)^{(1-\gamma)}$

Then, $\phi_j = (1 + \frac{\gamma-1}{2} M^2)$ determines the Mach number in the jet, at that contour. The other parameters are:

$$(T_j/T_0) = \phi_j^{-1}; \quad (u_j/a_0) = M_j \phi_j^{-1/2}; \quad (a_j/a_0) = (T_j/T_0)^{1/2} \qquad [1]$$

Since the tube walls prevent further expansion the state of the confined fluid remains unchanged until it impinges on the closed end. For the reflected shock (subscript s) the Mach number is determined by M_j:

$$(M_s - 1/M_s) = (\frac{\gamma+1}{2}) M_j \qquad [2]$$

$$(\rho_s/\rho_j) = \frac{(\gamma+1) M_s^2}{(\gamma-1) M_s^2 + 2}; \quad (T_s/T_j) = 2\phi_s \frac{[2 M_s^2-(\gamma-1)]}{[\gamma+1]^2 M_s^2} \qquad [3]$$

and $\quad U_s = [a_j M_s - u_j]; \quad (a_s/a_j) = (T_s/T_j)^{1/2}; \quad u_s = 0 \qquad [4]$

The shock wave leaves the channel at a time t_2, where t_2 is given by $(t_2-t_1) = L/U_s$.

Standard boundary layer theory for the growth of the displacement thickness in the tube developed by the inrushing gas shows that careful attention will have to be given to the selection of the geometric parameters. For a monatomic gas (Ar), with the tube entrance located at a density contour $\alpha = 10^{-2} = \rho_j/\rho_0$, the boundary layer thickness 5 cm downstream would be (for $\rho_0=1$ atm); $\delta_1 = 0.27$ mm.

$$\delta_1/x = \frac{1.721}{(Re_x)^{1/2}}; \quad Re_x = 1.618 \frac{u_j}{a_j} \frac{x}{\lambda} = 1.01 \times 10^5.$$

Comparison with boundary layers calculated for conventional shock tubes indicates a value $\delta_1 = 0.51$ mm at $x = 5$ cm. In our case flow divergence will tend to reduce this thickness. We concluded that for a tube diameter ≈7 mm, length 4 cm, the boundary layer perturbation will be small enough to permit use of

small correction factors.

The relaxation time for the shock processed fluid is determined primarily by the magnitude of T_s, and to a lesser degree by ρ_s. These are all determined by the initial values ρ_0, T_0, μ, γ and α, which permit relatively coarse control since their magnitudes must be selected for the gas of interest and be compatible with the sensitivities of the available diagnostic devices. However, T_s can be fine-tuned by modifying the strength of the reflected shock, as indicated in Fig. 3. Instead of terminating the tube with a reflecting surface, insert a contoured steady flow nozzle with exit area A*. The sub=j quantities remain unchanged. The following relations give the design parameters (A_f/A^*) for any desired reflected shock temperature (designate T_{sx}). Select an M_{sx} compatible with:

$$(T_{sx}/T_j) = 2\phi_{sx}\frac{[2\gamma M_{sx}^2 - (\gamma-1)]}{[\gamma+1]^2 M_{sx}^2} \; ; \qquad [3']$$

As previously,

$$U_{sx} = [a_j M_{sx} - u_j] \; ; \; \rho_{sx}/\rho_j = \frac{(\gamma+1)M_{sx}^2}{2\phi_{sx}} \; ; (a_{sx}/a_j) = (T_{sx}/T_j)^{1/2} \qquad [4']$$

Introduce: $M_r^2 = \dfrac{2\phi_{sx}}{2\gamma M_{sx}^2 - (\gamma-1)}$ and $M_f = M_r - (\dfrac{a_j}{a_{sx}})(M_{sx}-M_j)$ [5]

Then: $A_f/A^* = \phi_f^\beta/M_f^f(\dfrac{\gamma-1}{2})^\beta$,   where $\beta = \dfrac{\gamma+1}{2(\gamma+1)}$.   [6]

3.   DIAGNOSTICS AND TYPICAL MAGNITUDES

Two sets of measurements should be made. First, it is essential to fully characterize the composition of the jet, via LIF and/or REMPI. It seems more convenient for the laser beam line (#3) and the electrode system (#4) of the TOF mass discriminator to remain fixed, so as to minimize alignment difficulties. Hence the pulsed nozzle should be mounted through a gland for lateral displacement. One can measure the rotational temperature (assumed equal to the local T_j) of the carrier gas, by recording the VUV laser induced fluorescence[13] of admixed CO. If there are chemical transformations or condensations (for example, in a CO/H_2O mixture) the n^{mer} distributions can be determined for several nozzle positions to establish the magnitudes of $N_n(\rho_0;T_0)$ along the principal axis, beyond the "freezing distance", $(x/D)_{fr}>3$. Composition changes can be estimated by multiphoton ionization using "soft" radiation to minimize fragmentation, and the ions mass-analyzed according to their time-of-flight to the channeltron (#5).

For the second set of measurements, the nozzle assembly should be moved to the right, so that the leading edge of the shock tube is within the "zone of silence"[14] in the overexpanded region of the free jet, at the selected contour (α). Values for u_j can be calculated using the Ashkenas-Sherman equations,[9] and checked by direct measurements. The thermodynamic states of the fluid in the tube are most readily determined with the integrated-schlieren device developed by Resler and Scheibe.[15] At sharply defined apertures located at one or more positions along the tube (#8a;8b), the magnitude of u_j thus can be measured for the inrushing stream, and later U_s for the reflected shockwave. More important, the density distribution behind the shock wave can be recorded and the relaxation time induced by the temperature jump $(T_j \to T_s)$ derived. Knowing U_s the density gradient provides a direct measure of the time dependent endo-exo thermic balance behind the shock front.

Estimates of the quantities expressed in the above (ideal) gas dynamic

relations are listed in Table I for several interesting cases, to provide the reader with typical operating ranges of the proposed configuration. The source compositions are:

(a) Ar at 1 atm, 294°K.
(b) as (a), but with the imposed condition that $M_{sx}=9.0$, achieved by opening the rear end of the tube (as in Fig. 3).
(c) $CO(98\%) + H_2O(2\%)$, at 1 atm, 294°K. We assumed that no condensation occurs in the jet.
(d) as (c), but kinetically limited condensation was postulated. Typical experimentally observed n^{mer} distributions are of the form $\log_{10} N_n = \theta - \psi n$. On imposing the conditions

$N_{20}/N_1 = 10^{-3}$ and $\sum_{1}^{20} nN_n = N_1^0$, one finds $\theta = 16.83_1$ and

$\psi = 0.158$. The estimated rise in temperature due to the heat of condensation is 11.4°K. The effective $\langle \gamma \rangle = 1.38$.

The following expression for the enthalpy applies to a relaxing system without recourse to identifying a specific temperature:

$$(H_z - H_j) = \frac{(u_j + U_s)^2}{2} \frac{(\rho_z/\rho_j - 1)(\rho_z/\rho_j + 1)}{(\rho_z/\rho_j)}$$

where the z subscripts refer to the post shock front condition of the fluid, displaced $\bar{z}$ from the the front, and j to the corresponding quantities for the incoming jet; again the complete solution for a real system can be solved via a computer code.

4. CONCLUSIONS

The proposed experimental configuration has numerous potential applications. As indicated, the dynamics of evaporation of molecular clusters could be explored. The n-dependent heats of vaporization of $(H_2O)_n$ could be estimated, analogous to the method used by Freund and Bauer[16] for deriving the heats of condensation of $(Fe)_n$. There are numerous association-dissociation reaction, such as $2HCOOH \rightleftharpoons (HCOOH)_2$ and $(CH_3)_2O + BF_3 \rightleftharpoons (CH_3)_2O:BF_3$, for which no rate constants are available[17] because such systems are characterized by very short relaxation times, even at room temperature. Similarly, rates of

rotation about single bonds $(HC\begin{smallmatrix}O\\O\end{smallmatrix} H \rightleftharpoons HC\begin{smallmatrix}O\\O\end{smallmatrix} H)$, inversions and fluxional

transformations have yet to be measured. Of course, the proposed technique is applicable only to conversions between states which differ in their enthalpy content; it cannot be applied to cases such as bond inversions at nitrogen atoms in amines.[18]

5. REFERENCES

1. E. F. Greene and J. P. Toennies, *Chemical Reactions in Shock Waves*, Arnold Publishing Co., London, 1964.
2. S. H. Bauer, *Chemical Kinetics in Shock Tubes*, Science, 141, 867 (1963); Ann. Rev. Phys. Chem. 16, 245 (1965).
3. E. L. Resler, Jr., *Fluid Dynamics and Applied Mathematics*, Ed. J. B. Diaz and S-I. Pai, Gordon and Breach, New York (1962), p. 125.
4. P. Frank and Th. Just, *Shock Tubes and Waves*, Proc. 14th Int. Symp., New South Wales Press (1983), p.705, Ed. R. D. Archer and B. E. Milton.
5. This difficulty is obviated by measurements of relative rates, a technique developed by W. Tsang [J. Chem. Phys. 40, 1171 (1964)]. A compound with a known reaction rate is mixed with the unknown, and the ratio of their conversions determined analytically [for example: Int. J. Chem. Kin. 16,

1543 (1984)].
6. a. R. K. Hanson et al., Proc. 14th Int. Symp. on Shock Tubes & Waves, p.594 (1983).
   b. J. H. Kiefer and J. C. Hajduk, Proc. 12th Int. Symp. on Shock Tubes and Waves, Magnes Press, Jersalem (1980), p.97, Ed. A. Lifshitz and J. Ronn.
   c. J. V. Michael, et al., Int. J. Chem. Kin. **17**, 315 (1985).
7. R. A. Zahoransky, J. Chem. Phys. **82**, 2783 (1985).
8. W. R. Gentry and C. F. Giese, Rev. Sci. Inst. **49**, 595 (1978).
9. H. Ashkenas and F. S. Sherman, Rarefied Gas Dynamics, Vol. 2, Ed. J. H. de Leeuv, Academic Press, New York (1966).
10. K. L. Gallcher and S. H. Bauer, J. Phys. Chem. **78**, 2380 (1974).
11. O. Abraham, et al., Phys. Fluids **24**, 1017 (1981).
12. E. L. Resler, Jr., S-C. Lin and A. R. Kantrowitz, J. Appl. Phys. **23**, 1390 (1952).
13. J. W. Hepburn, N. Sivakumar and P. L. Houston, AIP Conf. Proc. **119**, 126 (1984).
14. R. Campargne, J. Phys. Chem. **88**, 4466 (1984).
15. E. L. Resler, Jr. and M. Scheibe, J. Acous. Soc. Am. **27**, 932 (1955).
16. H. J. Freund and S. H. Bauer, J. Phys. Chem. **81**, 994 (1977).
17. K. I. Lazaar and S. H. Bauer, J. Am. Chem. Soc. **107**, 3769 (1985).
18. S. H. Bauer, Int. J. Chem. Kin. **17**, 367 (1985).
19. Professor J. Fenn, Private communication.

TABLE I: All Sources at $T_0 = 294°K$; $\rho_0 = 1$ atm

	Ar(a)	Ar(b)	$CO+H_2O$(c)	$CO+H_2O$(d)
ρ_0(gm cm^{-3})	1.65×10^{-3}	as (a)	1.15×10^{-3}	as (c)
μ(at.units)	40	"	27.8	"
γ	5/3	"	1.399	"
a_0(cm s^{-1})	2.9×10^4	"	3.5×10^4	"
α(specify)	0.01	as (a)	0.01	as (c)
M_j	7.85	"	5.14	4.62
T_j (°K)	13.5	"	46.8	58.2
u_j(cm s^{-1})	5.01×10^4	"	7.20×10^4	as (c)
a_j(cm s^{-1})	6.38×10^3	"	1.40×10^4	1.56×10^4
M_s	10.58	(specify) 9.0	6.32	5.68 ($\gamma = 1.38$)
T_s/T_j	35.71	26.18	8.69	6.92
T_s(°K)	482	352	407	403
ρ_s/ρ_j	3.89	3.84	5.34	5.38
U_s(cm s^{-1})	1.73×10^4	7.32×10^3	1.65×10^4	as (c)
M_r		0.456		
M_f		0.231		
a_f(cm s^{-1})		3.26×10^4		
U_f(cm s^{-1})		7.53×10^3		
A_f/A^*		2.52		

Figure 1: (See next page)
#1.   Pulsed nozzle: operates 10-200 pps
                        open time ≈ 100 μs; initial "settling time" ≈10 μs
                        aperture D; flow field calculated as function of (x/D)
#2.   "zone of silence" in overexpanded region of the free jet
#3.   probing (ionizing) laser beam -- pulsed in synchronism with the nozzle,
       but delayed about 50 μs after opening of the valve
#4.   electrodes, to extract the n[mer] ions for TOF mass discrimination
#5.   channeltron for ion collection
#6.   indicates the shock attached to the lip of the skimmer
#7.   tube: length L ; area A_f. Calculations show that the boundary layer
       will attain negligible thickness during the operational period
#8a,b slotted windows for observation of the density profiles;
#9.   removable plug --- may be replaced by a contoured orifice

$(s_0 \to s_1)$ incorporates the first 10 μs of flow; this segment is perturbed
by the opening of the nozzle[19]

s_1, s_2...etc. indicate successive segments of the gas pulse which arrive
in sequence, as shown in the diagram

$(t_\alpha; t_\beta)$ indicate two sets of observation times

The shock wave is generated upon impact of the rapidly moving gas upon
the closed end of the tube, at $t_1 = L/u_g \approx 50$ μs, where u_g is the
terminal velocity in the jet

$T_h > T_j$, due to the heat of condensation($2\%H_2O$ in CO)

$T_v > T_s$. The overshoot is due to the finite rate of evaporation of
water n[mers].
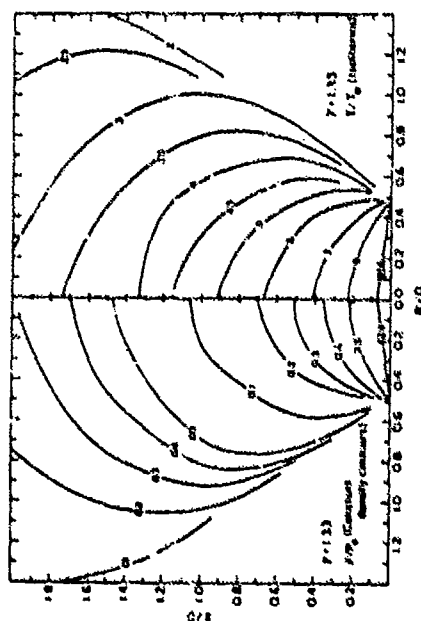
Figure 2. Typical; ρ_j/ρ_0 and
T_j/T_0 contours for γ≈1.33.[10]
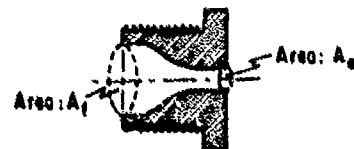
Figure 3. Gas dynamic parameters for an open
rear plug.
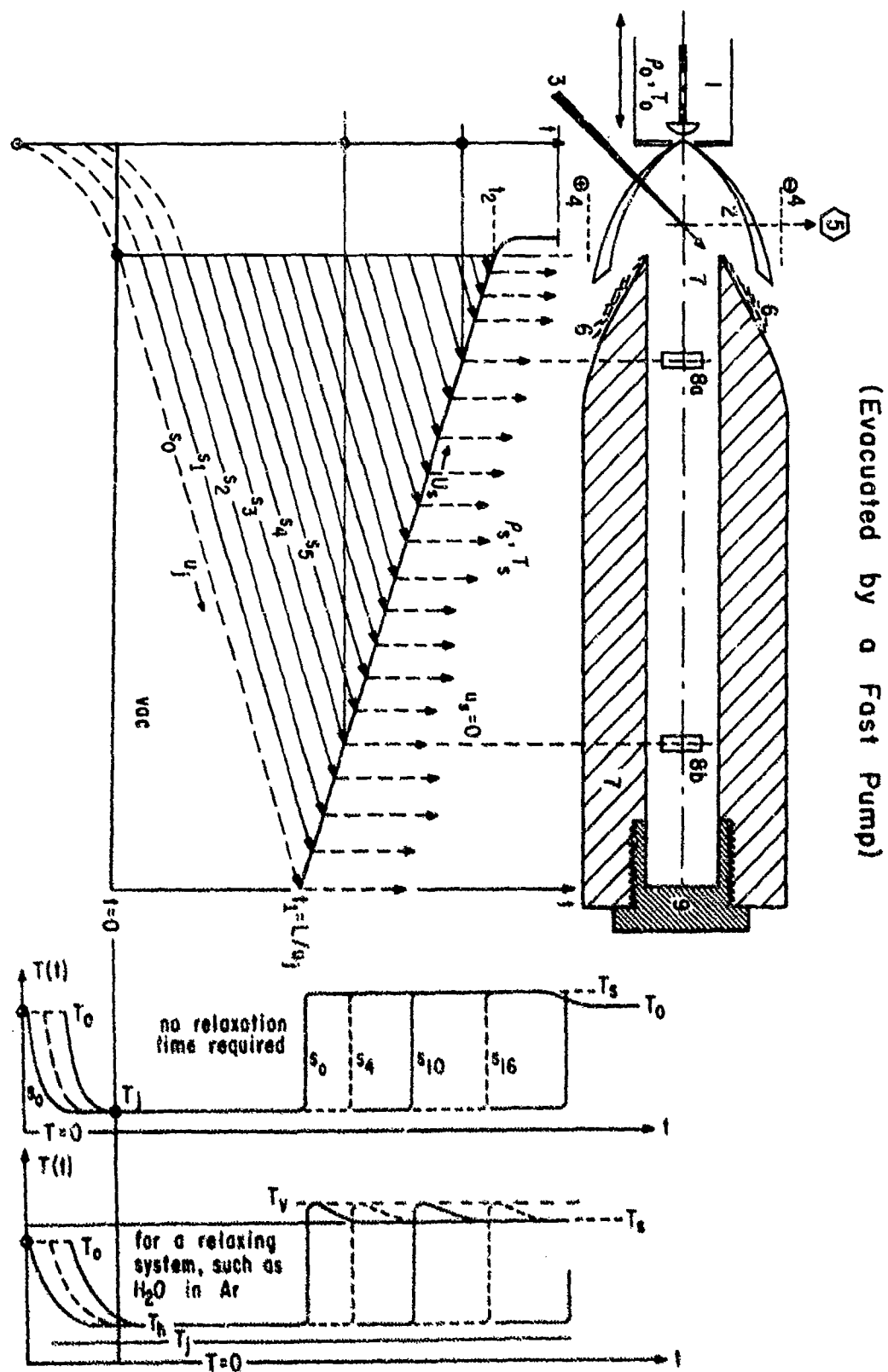
Fig. 1

Part VII
Shocks in Multiphase and Heterogeneous Media

AN EXPERIMENTAL STUDY ON SHOCK WAVES
PROPAGATING THROUGH A DUSTY GAS
IN A HORIZONTAL CHANNEL

H. Sugiyama, H. Hatanaka*,
A. Takimoto and T. Shirota

Department of Mechanical Engineering
Muroran Institute of Technology, Muroran 050, Japan

*Toshiba Com. Ltd, Japan

An experimental study was performed on shock waves
propagating through a dusty gas in a horizontal channel
using a horizontal dusty-gas shock tube. For dusty gas
air containing fly ash (mean diameter 3.3 μm) was used.
Pressure and particle concentration behind the shock
fronts were simultaneously measured by means of pressure
transducers and a laser beam attenuation method. The
effect of suspended particles and initially deposited
particles on the variation of particle concentrations
behind the shock fronts and the effect of the particle
loading ratio on frozen shock Mach numbers are
discussed, and schlieren photographs of the shock waves
taken with an Imacon 790 camera are shown. The
experiment was done for shock Mach numbers below Mf=1.6
and the loading ratio of the particles in the gas below
$\eta_0=0.1$.

1. INTRODUCTION

High-speed dusty-gas flows have been studied by a number of authors in the
last two decades in view of their engineering applications relating to rocket-
nozzle flow, dust explosion and supersonic flight[1,2,3,4]. Studies of shock waves
in dusty gases are important as one of the bases to understand these flows.

So far there have been a number of theoretical and experimental studies
relating to unsteady shock waves in a gas and large particle (diameter 10 to 450
μm) mixture. For instance, Selberg and Nicholls[5], Rudinger[6] and Outa et al.[7]
investigated experimentally a drag coefficent of spherical particles. Using the
random-choice method Miura and Glass[8] clearly showed the numerical results about
the decay of a discontinuous frozen shock wave, the formation of a stationary
shock structure and an effective contact front of finite thickness. Recently
Sommerfeld and Grönig[9] studied experimentally and numerically the decay of shock
waves in a vertical dusty-gas shock tube.

On the other hand there are few studies on the properties of shock waves in
a gas and small particle (diameter 1 to 10 μm) mixture. For instance, König and
Frohn[10] investigated shock wave structure in a dusty gas (particle diameter 0.6
and 1.5 μm) at low Mach number. Roberts et al.[11] investigated the effect of
entrained, small particles (diameter 1 to 10 μm) on the boundary layer structure
behind shock waves.

In this paper we report an experimental study on a horizontal dusty-gas
shock tube. An air and fly ash (mean diameter 3.3 μm) mixture was used. The
purpose of the experiment is to know (1)how suspended particles and deposited
particles affect the variation of particle concentration behind shock fronts,
(2)how the particles behave at contact regions, and to observe (3)how the shock
waves propagate through a dusty gas in a horizontal channel when vertical
particle concentration gradients exist.

2. EXPERIMENTAL APPARATUS AND METHOD

The schematic diagram of the horizontal dusty-gas shock tube apparatus used in this experiment is shown in Fig.1. The high pressure chamber is a circular tube of 50mm diameter and 1m long. The low pressure chamber has a rectangular cross section of 40mm x 30mm (height x width) and 3.7m long. Figure 2 shows the dusty-gas generator using a fluidized bed. Particles are supplied into the fluidized bed from a hopper by a screw feeder, and gas-particle mixtures are generated in an agitated mixing chamber. The dusty gas generator was mounted just downstream of the shock tube diaphragm. Particle concentration was changed by changing the revolution speed of the screw feeder and the suction speed of the gas-particle mixture.

Particle concentration was measured by a laser beam attenuation method. Figure 3 shows the optical measuring system of vertical particle concentration profiles. A laser beam was expanded by a beam expander and split into two beams which pass through appertures (diameter 5mm) to enter the test section. Transmitted laser beam strength I was detected by a photodiode and attenuated light rate α was determined by the following equation

$$\alpha(dB) = -10 \log(I/I_0) \qquad (1)$$

where I_0 is the laser beam intensity when no particles are included in the test section. Particle concentration ρ_p was determined using empirical calibration data. The initial loading ratio of gas-particle mixture η_0 is calculated by the following equation

$$\eta_0 = \rho_p/\rho_0 \qquad (2)$$

where ρ_0 is an initial gas density.

The particles used were fly ash (nominal mean particle diameter 5 μm) having material density $\rho_m = 2.5$ g/cm³. Nitrogen was used as the driver gas and the air-fly ash mixture as the driven dusty gas. Initial pressures in high and low pressure chambers were from 400 to 1000 kPa and atomospheric pressure respectively.

The pressure and particle concentration signals were recorded by a digital memory and the digital data was subsequently transferred to a microcomputer for permanent storage and analysis.

3. EXPERIMENTAL RESULTS AND DISCUSSION

Particle size distribution of the suspended particles in a horizonal channel before arrival of a shock wave is shown in Fig.4. The abscissa is particle diameter d(μm) and the ordinate is cumulative weight $W_t(\%)$. Figures 5(a),(b) and (c) show the micrographs of the suspended particles which were sampled at the upper,center and lower parts of the test section. Agglomerations of particles are seen in Fig. 5(c). From Figs.4 and 5 it is seen that the mean and largest diameters of the suspended particles are 3.3 μm and 10 μm respectively.

Figure 6 shows the particle concentrations in a horizontal channel before and after the arrival of a shock front at center (y=20mm) and upper (y=35.5mm) positions , where y is the height above the channel floor. In this horizontal channel vertical particle concentration gradients always exist.

In a horizontal dusty-gas shock tube some dust particles settle on the channel floor , so it is necessary first to investigate how these deposited particles affect the variation of particle concentrations behind shock fronts. Figures 7(a),(b) and (c) show the variations of particle concentration behind shock fronts as a function of time when dust particles exist only on the channel floor before arrival of a shock wave. The data was measured at y=20mm(center), X/D=66.2, where X is distance from the diaphragm and the

hydraulic diameter of the shock tube D=34.3mm. It is clearly seen that the deposited particles rise up faster as shock Mach numbers Mf increase and the risen particles disappear when the contact region arrives at the measuring point. In Fig.7 pressures behind shock fronts are also shown. It is seen that the rarefaction waves from the high pressure chamber side appear almost at the same time for different diaphragm pressure ratios $P_{30}=4.5$, 6.8 and 10.7.

Figures 8(a),(b) and (c) show the variations of particle concentration behind frozen shock fronts propagating through a dusty gas in a horizontal channel for initial loading ratio $\eta_0= 0.03$ and frozen shock Mach numbers Mf= 1.38, 1.48, 1.61 respectively. The particle concentrations increase abruptly behind the frozen shock front, keep constant for a while, then increase gradually as initially deposited particles are lifted up and finally decrease with the arrival of the contact region. We can see that a contact region has a finite thickness, which is the same as the prediction of Miura and Glass'numerical results[8]. The thickness of the contact region decreases as the frozen shock Mach number Mf increases.

Figure 9 shows the effect of the initial loading ratio η_0 on frozen shock Mach number Mf at X/D=66.2. An initial diaphragm pressure ratio P_{30} was taken as a parameter. Mf decreases with increasing η_0, because the particles remove momemtum and energy from the gas behind the frozen shock front. From Fig.9 it may be said that the mass of the particles can be found from the propagation velocity of the frozen shock wave.

The schlieren phtographs of shock waves in a dusty gas in a horizontal channel taken with an Imacon 790 camera are shown in Figs.10 (a),(b) and (c). The experiment was done for an initial diaphragm pressure ratio $P_{30}=6.8$ and initial loading ratios $\eta_0= 0$, 0.07 and 0.09 respectively. Framing speed was 1 x 10^5 frames/sec (10 µsec/frame), and exposure time was 2 µsec. In the case of pure gas ($\eta_0= 0$) the shock shapes are normal to flow direction, while in dusty gas ($\eta_0 = 0.09$) the shock shapes are inclined towards the flow direction because of the vertical particle concentration gradient. In the case of $\eta_0= 0.07$ the shock shape is normal near the upper wall, where there are no particles, and is inclined at the lower part of the test section.

4. CONCLUSIONS

An experimental study on shock waves propagating through a gas-small particle mixture in a horizontal channel was performed for frozen shock Mach numbers below Mf=1.6 and the initial loading ratio below $\eta_0=0.1$. As a gas-particle mixture air containing fly ash (mean diameter 3.3 µm) was used. The results are summarized as follows:(1) The variation of particle concentrations behind the frozen shock front is affected by both suspended particles and particles which have settled on the channel floor. (2) At a contact region particles disappear gradually, that is, the contact region has a finite thickness. (3) In the horizontal dusty gas channel with a vertical particle concentration gradient, the shock shapes are inclined towards the flow direction. In the future it is planned to compare the experimental results with a random-choice method solution.

REFERENCES

1. Soo, S.L., "Fluid Dynamics of Multiphase Systems", Blaisdell, 1967, p.277.
2. Marble, F.E., "Dynamics of Dusty Gases", Annual Reviews of Fluid Mechanics, Vol. 2, 1970, p.397, Annual Reviews.
3. Rudinger, G., "Fundamentals of Gas Particle Flow", Elsevier, 1980, p.53.
4. Sugiyama, H., "A Numerical Study of Gas-Particle Supersonic Flow Past Blunt Bodies (The Case of Axisymmetric Flow)", Bull. JSME, Vol. 27, No.231, 1984, p.1913.
5. Selberg, B.P. and Nicholls, J.A., "Drag Coefficient of Small Spherical Particles", AIAA Journal, Vol. 6, No.3, 1968, p.401.

6. Rudinger, G., "Effective Drag Coefficient for Gas–Particle Flow in Shock Tubes", Trans. ASME, Journal of Basic Eng., Vol. 92, 1970, p.165.

7. Outa, E., Tajima, K. and Suzuki, S., "Cross-Sectional Concentration of Particles During Shock Process Propagating Through a Gas–Particle Mixture in a Shock Tube", Proc. of 13th Int. Symp. on Shock Tubes and Waves, State Univ. of New York Press, 1981, p.655.

8. Miura, H. and Glass, I.I., "On a Dusty–Gas Shock Tube", Proc. R. Soc. Lond. A382, 1982, p.373.

9. Sommerfeld, M. and Grönig, H., "Decay of Shock Waves in a Dusty–Gas Shock Tube with Different Configurations", Proc. of 14th Int. Symp. on Shock Tubes and Waves, New South Wales Univ. Press, 1983, p.470.

10. König, G. and Frohn, A., "Shock Wave Structure in Gas–Particle Mixtures at Low Mach Numbers", Proc. 13th Int. Symp. on Shock Tubes and Waves, State Univ. of New York Press, 1981, p.646.

11. Roberts, G.T., East, R.A. and Pratt, N.H., "Surface Heat Transfer Measurements from a Turbulent, Dusty Boundary Layer", Proc. 14th Int. Symp. on Shock Tubes and Waves, New South Wales Univ. Press, 1983, p.455.

1 High pressure chamber   10 Digital volt meter
2 Low pressure chamber   11 Dusty gas generator
3 Dump tank   12 Pressure transducer
4 Diaphragm   13 Universal counter
5 Rupturing device   14 Digital memory
6 Optical window   15 Micro computer
7 Optical window   16 X-Y plotter
8 Driver gas bottle   17 Filter
9 D.C. amplifier   18 Vacuum pump
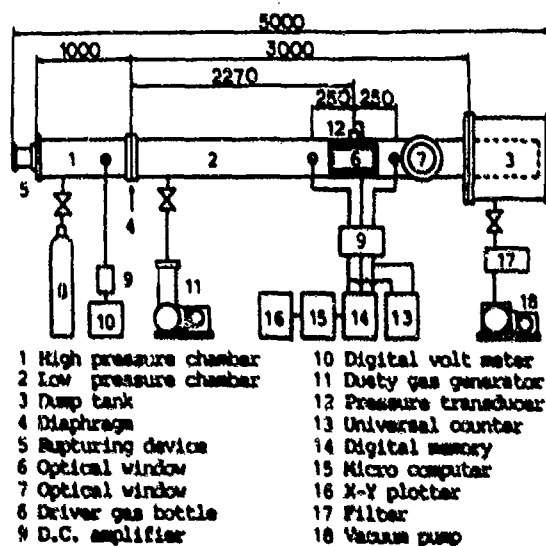
Fig.1 Schematic diagram of horizontal dusty-gas shock tube apparatus.

1 Hopper
2 Screw feeder
3 Agitated mixing chamber
4 Fluidised bed
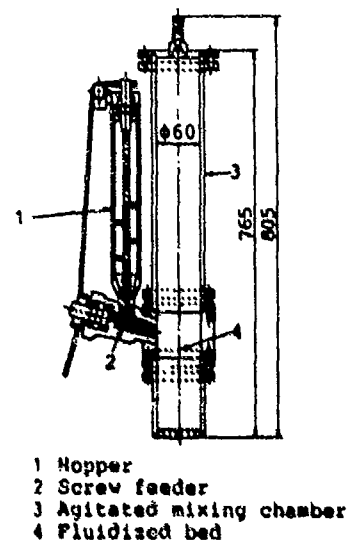
Fig.2 Dusty-gas generator using fluidised bed.

1 He-Ne laser light   5 Mirror
2 Beam expander   6 Photo detector
3 Aperture   7 D.C. amplifier
4 Shock tube   8 Pen recorder
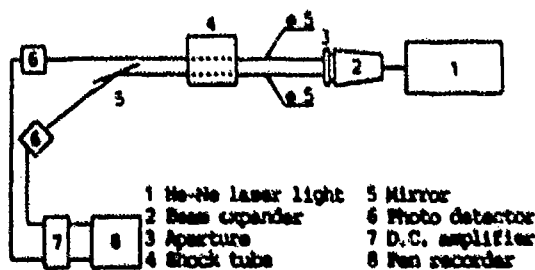
Fig.3 Optical measuring system of particle concentration.
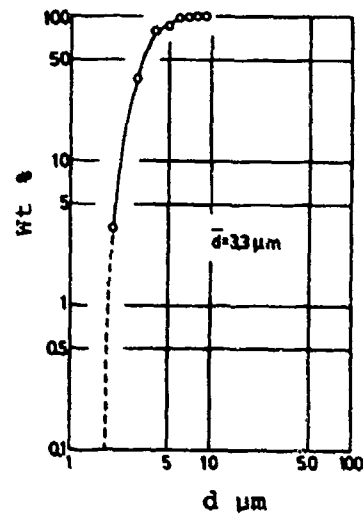
Fig.4
Particle size
distribution of
suspended particles
in a horizontal
channel.

$\bar{d}$=3.3 μm

(a)
Upper

(b)
Center

(c)
Lower

|←——→| 18 μm
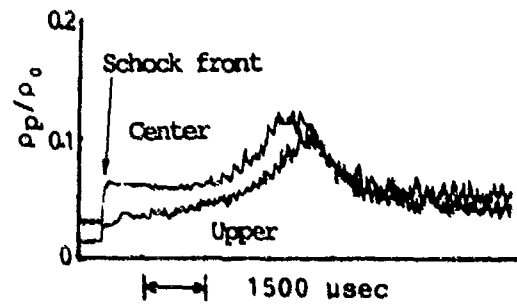
Fig.6 Variations of particle
concentrations at center (y=20mm)
and upper (y=35.5mm) positions in
a horizontal channel, where y is
the height above the channel
floor.

Schock front

Center

Upper

|←——→| 1500 μsec

ρ_p/ρ_0

Fig.5 Micrographs of suspended
particles in a horizontal
channel sampled at upper,
center and lower parts of
the test section.

M_f

P$_{18}$
○ 4.4
● 6.8

η×10^{-2}

Fig.9 Effect of initial loading
ratios η_0 on frozen shock
Mach numbers Mf.(X/D=66.2)

(a) $P_{30}=4.4$, Mf$=1.39$

(a) $P_{30}=4.43$, Mf$=1.38$

(b) $P_{30}=6.84$, Mf$=1.50$

(b) $P_{30}=6.89$, Mf$=1.48$

(c) $P_{30}=10.7$, Mf$=1.63$

(c) $P_{30}=10.8$, Mf$=1.61$
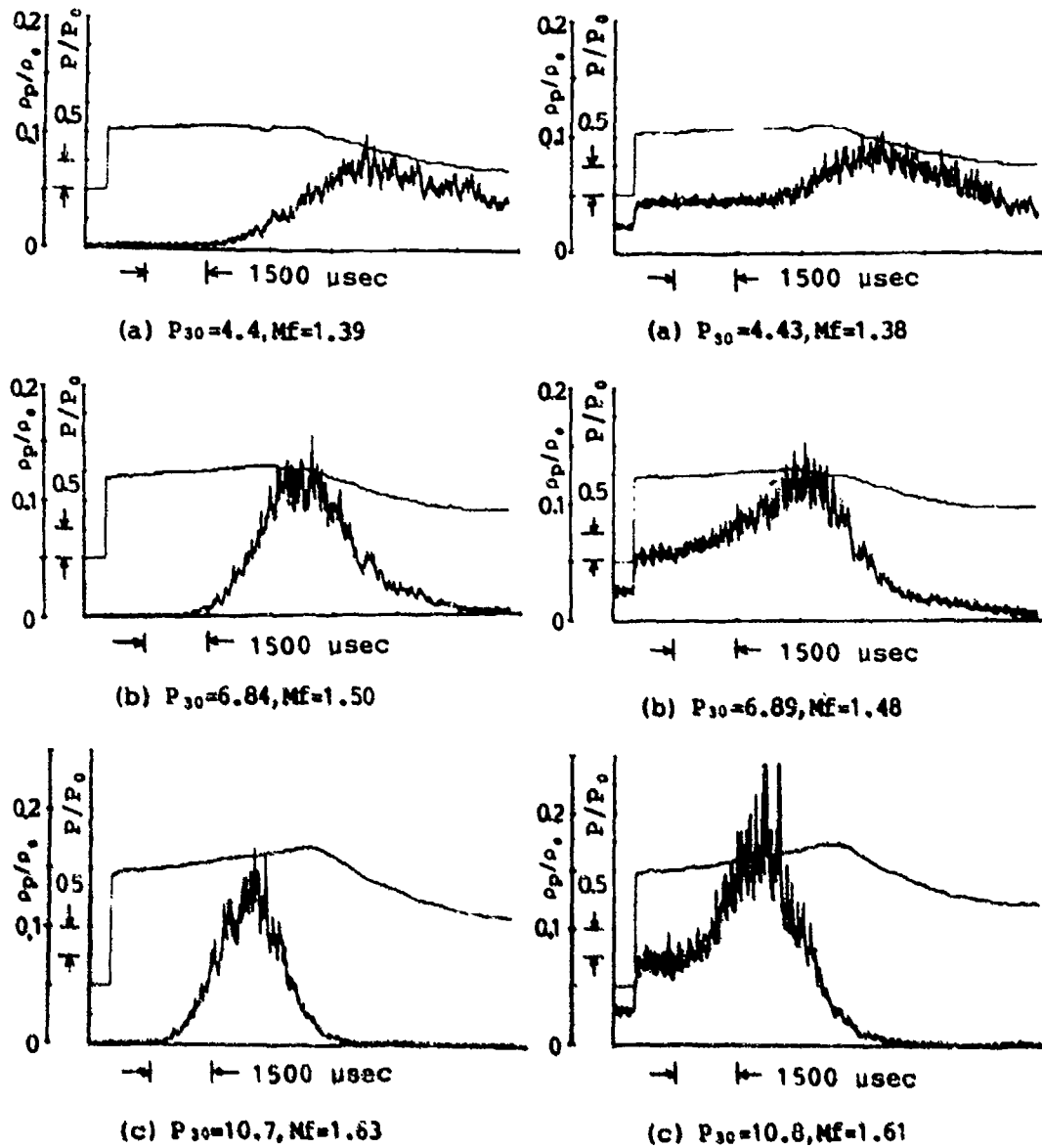
Fig.7 Variation of particle concentration and pressure behind shock waves when particles existed only on the channel floor before shock arrivals, measured at y=20mm, X/D=66.2.

Fig.8 Variation of particle concentration and pressure behind shock waves in a dusty gas in a horizontal channel, measured at y=20mm, X/D=66.2. ($\eta_0=0.03$)

(a) $\eta_0 = 0$ (pure gas), $Mf = 1.49$

(b) $\eta_0 = 0.07$, $Mf = 1.45$
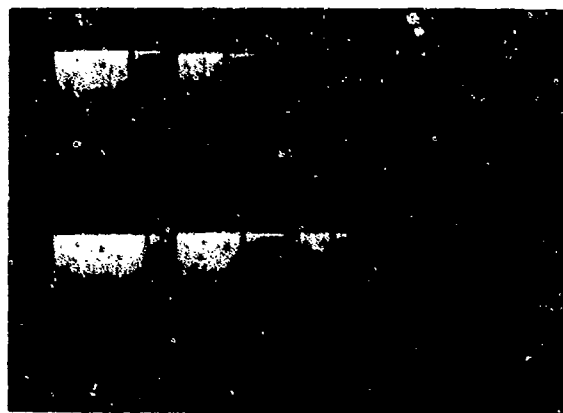
(c) $\eta_0 = 0.09$, $Mf = 1.44$

Fig.10 Schlieren photographs of shock waves in a dusty gas
in a horizontal channel for an initial diaphragm
pressure ratio $P_{30} = 6.8$.
Framing speed : 10 μsec/frame
Exposure time : 2 μsec

STRUCTURE OF SHOCK WAVES IN DUSTY GASES

R.S. Srivastava

Defence Science Centre, Metcalfe House,
Delhi-110054, India.

SUMMARY:

The structure of shock wave has been analysed in a mixture of solid particles and gas. Srivastava and Sharma[5] (1980) have obtained the structure of normal shock waves by including the particle volume effect. The present work is an extension of this work. In the present paper structure of normal shock waves in a dusty gas has been investigated by including the particle volume effect and simultaneously incorporating the effect of drag coefficient and heat transfer coefficient. The two phase flow equations with the relevant boundary conditions have been solved numerically.

Introduction: The structure of normal shock waves in a mixture of solid particles and gas has been investigated by several people, ie., Carrier[1] (1958), Rudinger[2] (1964) etc. The structure provided in these papers ignores particle volume. The assumption of neglecting particle volume is well justified but if either the mass fraction of the particles or the gas density is sufficiently high, the particle volume fraction becomes significant. Rudinger[3] (1965) determined the frozen and equilibrium conditions by taking particle volume into account. Srivastava and Sharma[5] (1982) computed the relaxation zone by taking into account particle volume effect.

The dependence of relaxation zone on the choice of drag coefficient and heat transfer coefficient is well known. Keeping this fact into account Rudinger[2] (1964) obtained the effect of drag coefficient and heat transfer coefficient on the structure of shock waves. The dependence of drag coefficient and heat transfer coefficient were obtained by Rudinger without taking into account particle volume effect.

In the present paper structure of normal shock waves in a mixture of solid particles and gas has been investigated by including the particle volume effect and simultaneously incorporating the effect of drag and heat transfer coefficients.

Nomenclature

a	= Speed of sound in the gas phase.
c	= Specific heat of particle material.
C_D	= Drag coefficient.
D	= Particle diameter
ρ_p	= Density of the particle material.
k	= Coefficient of thermal conductivity of gas
M_s	= Shock Mach number
m	= Mass flow rate of the gas
N_u	= Nusselt number.

```
n     = Mass flow rate of the particle
Pr    = Prandtl number.
p     = Gas pressure
R     = Gas constant
Re    = Reynolds number
T     = Temperature of the gas
x     = Distance behind the shock
u     = Velocity of the gas
up    = Particle velocity
α     = Equilibrium speed of sound in the mixture.
Γ     = Ratio of specific heats of mixture
γ     = Ratio of specific heats of the gas
δ     = Relative specific heat
ε     = Particle volume fraction
η     = Particle loading ratio
μ     = Coefficient of viscosity of the gas
ρ     = Density of the gas
Tp    = Particle temperature
Cp    = Specific heat of gas at constant pressure
```

<div style="text-align:center"><u>Subscripts</u></div>

```
o     = Conditions up stream of shock wave;
f     = Frozen conditions behind the shock wave;
e     = Equilibrium conditions behind the shock wave.
```

<div style="text-align:center"><u>Mathematical Formulation</u></div>

<u>Assumptions:</u> For the computation of flow variables in the relaxation zone, some assumptions have to be made, namely,

1) The gas is treated as a perfect gas with constant specific heats;
2) The particles are treated as incompressible, their density and specific heat are assumed constant;
3) There is no mass transfer between two phases, i.e., condensation, evaporation or combustion is excluded from the analysis;
4) The particles do not contribute to the pressure.

<u>Basic Equations:</u> Consider a shock wave that is propagating in a gas filled with a suspension of uniformly distributed small particles. Ahead of the shock wave the particles are assumed to be in temperature and velocity equilibrium with the gas. The flow is steady in the shock-fixed coordinate system. The equation of the continuity for the gas is

$$(1-\epsilon)\rho u = (1-\epsilon_o)\rho_e u_o = m \tag{1}$$

$$\epsilon \rho_p u_p = \epsilon_o \rho_p u_o = \eta \tag{2}$$

The momentum equation for gas-particle mixture is given by

$$mu + \eta u_p + p = (m+\eta)u_o + p_o \tag{3}$$

The energy equation for gas particle mixture is given by

$$m\left(\frac{u^2}{2} + C_p T\right) + n\left(\frac{u_p^2}{2} + C\, T_p\right) + \frac{np}{\rho_p} = \frac{1}{2}(m+n)u_0^2 + (mC_p + nc)T_0 + \frac{n\,p_0}{\rho_p} \quad (4)$$

The equation of state for the gas is

$$p = \rho R T \quad (5)$$

We introduce non-dimensional variables

$$U = \frac{u}{a_0}, \quad V = \frac{u_p}{a_0}, \quad \Theta = \frac{T}{T_0}, \quad \Phi = \frac{T_p}{T_0} \quad (6)$$

Equations (1) - (4) after transformation give

$$(1-\epsilon)\rho\, U = (1-\epsilon_0)\rho_0\, U_0 \quad (7)$$

$$\epsilon\, \rho_p V = \epsilon_0\, \rho_p U_0 \quad (8)$$

$$U + \eta V + \frac{\Theta V}{\gamma(V - \epsilon_0 U_0)U} = (1+\eta)U_0 + \frac{1}{\gamma(1-\epsilon_0)U_0} \quad (9)$$

$$U^2 + \eta V^2 + \frac{2}{(\gamma-1)}(\Theta + \eta\,\delta\Phi) + \frac{2\epsilon_0 U_0 V\Theta}{\gamma(V - \epsilon_0 U_0)U}$$
$$= (1+\eta)U_0^2 + \frac{2}{(\gamma-1)}(1+\eta\delta) + \frac{2\epsilon_0}{\gamma(1-\epsilon_0)} \quad (10)$$

where $\eta = \frac{n}{m} =$ Particle loading ratio.

Equation (5) can be written as

$$\frac{p}{p_0} = \frac{(1-\epsilon_0)}{(V - \epsilon_0 U_0)}\frac{U_0 V}{U}\Theta \quad (11)$$

The equations of momentum and heat balance for the particle are given by

$$(1-\epsilon)u_p\frac{du_p}{dx} = -\frac{3\rho}{4D}\frac{C_D}{\rho_p}(u_p - u)|u_p - u| \quad (12)$$

$$u_p\frac{dT_p}{dx} = \frac{6 k N_u}{c\, D^2 \rho_p}(T - T_p) \quad (13)$$

We have

$$\frac{p}{p_0} = \frac{\rho}{\rho_0}\frac{T}{T_0} = \frac{\rho}{\rho_0}\Theta \quad (14)$$

Therefore, from (11) we would obtain

$$\rho = \rho_0 \frac{(1-\epsilon_0) \mathcal{U}_0 V}{(V - \epsilon_0 \mathcal{U}_0) \mathcal{U}} \tag{15}$$

Using (6), (15), equation (12) becomes

$$(1-\epsilon) V \frac{dV}{dx} = - \frac{3}{4} \frac{\rho_0 \mathcal{U}_0 V}{D \rho_P} \frac{(1-\epsilon_0)}{(V - \epsilon_0 \mathcal{U}_0) \mathcal{U}} C_D |V-\mathcal{U}|(V-\mathcal{U}) \tag{16}$$

If we substitute

$$x = \frac{4}{3} \frac{\rho_P}{\rho_0} \frac{D}{\mathcal{U}_0} X \tag{17}$$

equation (16) becomes

$$(1-\epsilon) V \frac{dV}{dX} = - C_D \left[\frac{V(1-\epsilon_0)}{(V - \epsilon_0 \mathcal{U}_0) \mathcal{U}} \right] (V-\mathcal{U})|V-\mathcal{U}| \tag{18}$$

We have R_e (Reynolds number) $= \frac{\rho |\mathcal{U}_P - V| D}{\mu}$

$$= \frac{a_0 \rho_0 \mathcal{U}_0 (1-\epsilon_0) D |V-\mathcal{U}| V}{\mu \quad (V - \epsilon_0 \mathcal{U}_0) \mathcal{U}} \tag{19}$$

Using equations (8), (18) and (19) we finally obtain

$$\frac{dV}{dX} = - C_D \frac{(V-\mathcal{U})}{(V - \epsilon_0 \mathcal{U}_0)} \frac{\mu}{a_0 \rho_0 \mathcal{U}_0} \frac{R_e}{D} \tag{20}$$

Using equation (6), (13), (17), (19), we would obtain

$$\frac{d\Phi}{dY} = \frac{8 N_u}{8 P_r} \frac{(V-\mathcal{U})(\Theta - \Phi)}{(V - \epsilon_0 \mathcal{U}_0) \mathcal{U} R_e} (1-\epsilon_0) \tag{21}$$

Boundary conditions: The boundary conditions for the particles are

    i) $T_f = T_0$ or $\Phi_f = 1$ (22)

    ii) $V_f = \mathcal{U}_0 - \frac{2}{(\gamma-1)} \epsilon_0 \frac{(\mathcal{U}_0^2-1)}{(1-\epsilon_0)\eta \mathcal{U}_0}$ (23)

    iii) $\epsilon_f = \epsilon_0$ (24)

The boundary conditions for the gas are

    i) $\mathcal{U}_f = \frac{1}{(\gamma+1) \mathcal{U}_0} \left[2 + (\gamma-1) \mathcal{U}_0^2 \right]$ (25)

    ii) $\theta_f = \frac{1}{(\gamma+1)^2 \mathcal{U}_0^2} \left[2\gamma \mathcal{U}_0^2 - (\gamma-1) \right] \left[(\gamma-1) \mathcal{U}_0^2 + 2 \right]$ (26)

    iii) $p_f = \frac{p_0}{(\gamma+1)} \left[2\gamma \mathcal{U}_0^2 - (\gamma-1) \right]$ (27)

Equilibrium conditions: The equilibrium value of velocity $\mathcal{U}_e$, temperature Θ_e density ρ_e and pressure p_e are given by Rudinger[3] (1965)

$$\frac{u_e}{u_o} = \frac{(\Gamma-1)M_S^2 + 2 + 2\epsilon_o(M_S^2-1)}{(\Gamma+1)M_S^2} \quad , \quad \epsilon_e = \epsilon_o \frac{u_o}{u_e}$$

$$\frac{\rho_e}{\rho_o} = \frac{(1-\epsilon_o)}{(1-\epsilon_e)} \cdot \frac{u_o}{u_e}$$

$$\frac{p_e}{p_o} = 1 + (1-\epsilon_o)\gamma(1+\eta)(u_o-u_e)u_o , \quad \theta_2 = \frac{p_e}{p_o}\frac{\rho_o}{\rho_e}$$

(28)

In (28), $\Gamma = \frac{\gamma(1+\eta\delta)}{(1+\gamma\eta\delta)}$ and $M_S = \frac{u_o}{\alpha_o}$ where $\alpha_o = \frac{a_o}{(1-\epsilon_o)}\left[\frac{\Gamma}{\gamma(1+\eta)}\right]^{1/2}$

<u>Numerical calculations and Results</u>: The computations have been carried out for $\epsilon = 0$ and $\epsilon = 0.05$ and for the following combinations of drag coefficient and heat transfer coefficient.

	C_D (Drag Coefficient)	N_u(Nusselt Number) $= 2 + 0.533\,Re^{0.5}$	$N_u = 2$
Steady Flow	$0.48 + 28\,Re^{-0.35}$	A	B
Ingebo	$27\,Re^{-0.84}$	C	D
Stockes	$24/Re$	E	F

Curve F denotes the computation for $C_D = 24/Re$ and $N_u = 2$. The computations for the curves A, B, C, D, E are to be inter- preted in the same manner. The loading ratio has been assumed to be one and Mach number of the shock wave has been taken to be 1.5 for all the six cases. The equations (20), (21), (9) and (10) have been solved numerically using the boundary condi- tions (22) to (27).

In Fig. 1, the effect of C_D, N_u on the velocity distribution for $\epsilon = 0$ has been shown. The curves are similar to those obtained by Rudinger[2](1964) for different initial conditions. As Rudinger[2](1964)observed, here also the drag coefficient has a marked effect, while the influence of heat transfer coefficient is quite small.

In Fig. 2, the velocity distribution has been shown for $\epsilon = 0.05$. In this case the velocity distribution for curve B is lower than A (as distinguished from the case $\epsilon = 0$ when the curve A is lower than B). The behaviour of the velocity distri- bution for other cases is similar to those of $\epsilon = 0$. The particle velocity for the cases A, B, C, D attain equilibrium at almost the same distance behind the shock wave but for E and F cases the equilibrium is attained at a slightly greater distance. Same situation develops for $\epsilon = 0$. Drag coefficient has a marked effect while the influence of heat transfer coefficient is small.

Both for $\epsilon = 0$, $\epsilon = 0.05$ (Figs. 3 and 4), the temperature distribution is similar to those obtained by Rudinger[4] (1969) except that some of the curves overlap. The temperature distribution both for $\epsilon = 0$ and $\epsilon = 0.05$ attain equilibrium at almost the same distance behind the shock wave.

Acknowledgements:

REFERENCES

1. Carrier, G.F., "Shock waves in a dusty gas", Journal of Fluid Mech., Vol. 4, 1958, p. 376-382.

2. Rudinger, G., " Some properties of shock relaxation in gas flows carrying small particles", Physics Fluids, Vol. 7, 1964, p. 658-663.

3. Rudinger, G., "Some effects of finite particle volume on the dynamics of gas-particle mixture", AIAA Jour., Vol. 3, 1965, p. 1217-1222.

4. Rudinger, G., "Relaxation in gas-particle flow, non-equilibrium flows", (P.P. Wegner, ed.) Marcel Dekker, New York, Vol. 1, Part 1, 1969.

5. Srivastava, R.S. & Sharma, J.P., "Structure of normal shock waves in gas-particle mixture", ZAMP, Vol. 23, November 1982.

FIG.1 DISTANCE BEHIND SHOCK WAVE, X

PARTICLE VELOCITY, v

$\eta = 1$
$\varepsilon_e = 0.0$

FIG.2 DISTANCE BEHIND SHOCK WAVE, X

PARTICLE VELOCITY, v

$\eta = 1$
$\varepsilon_e = 0.05$
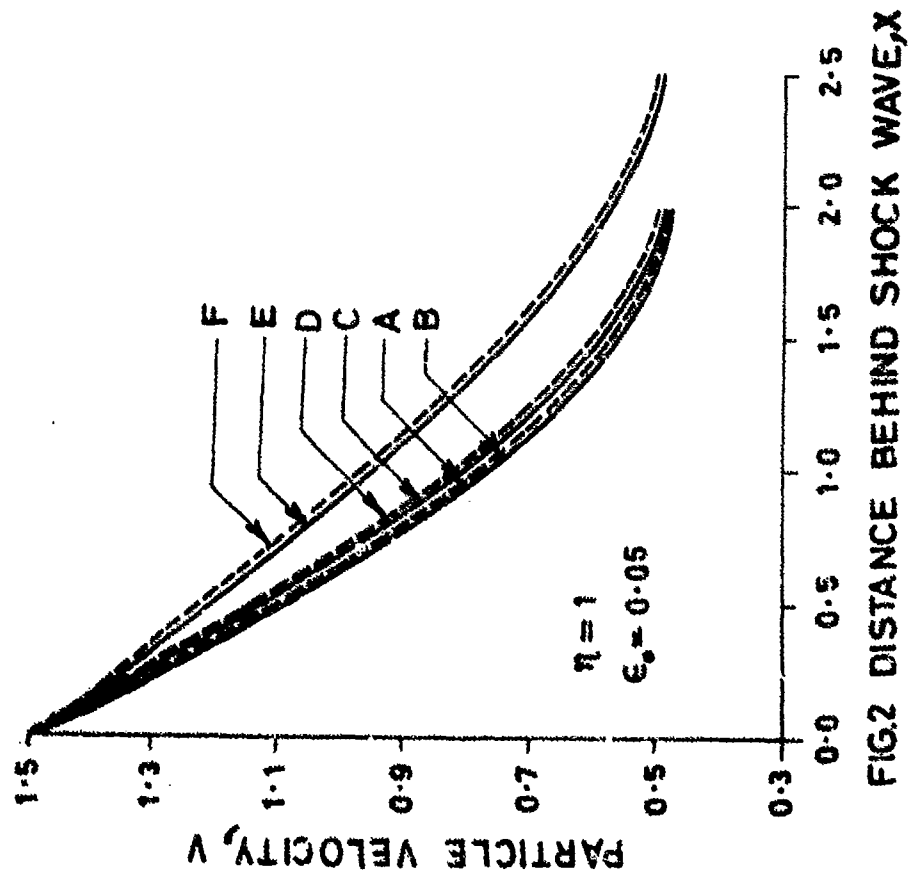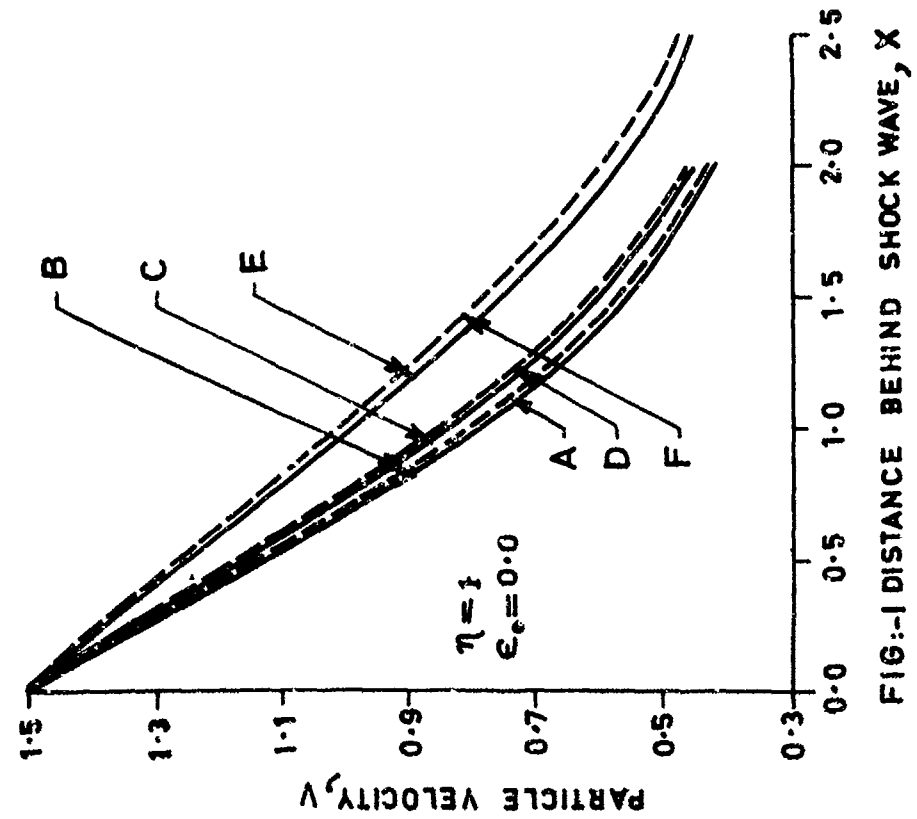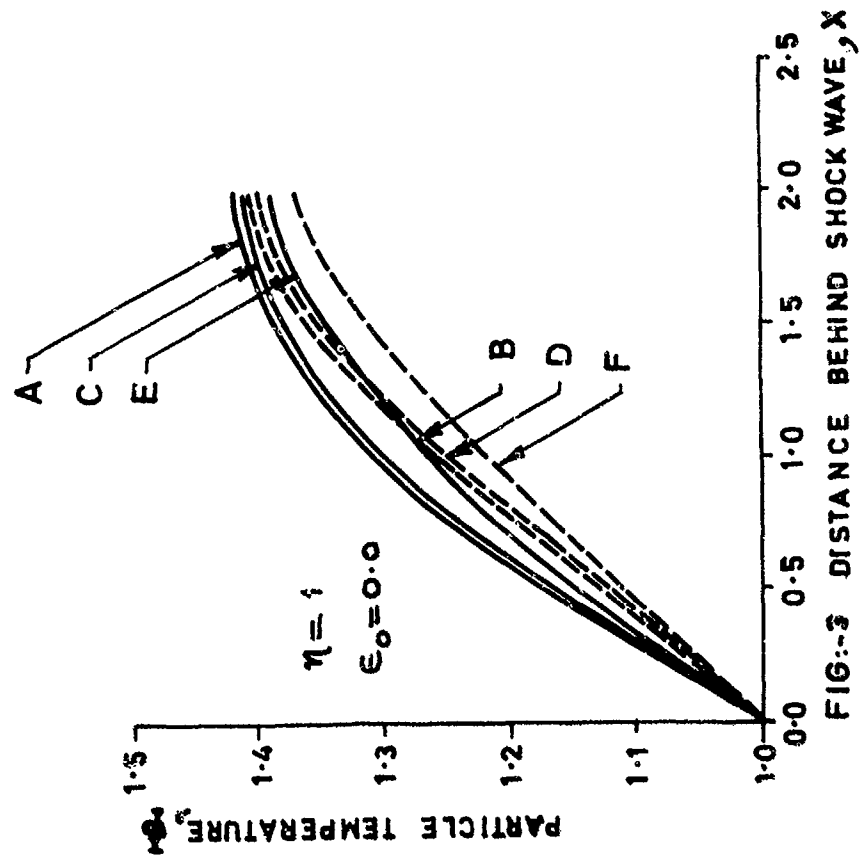
FIG:-3 DISTANCE BEHIND SHOCK WAVE, X
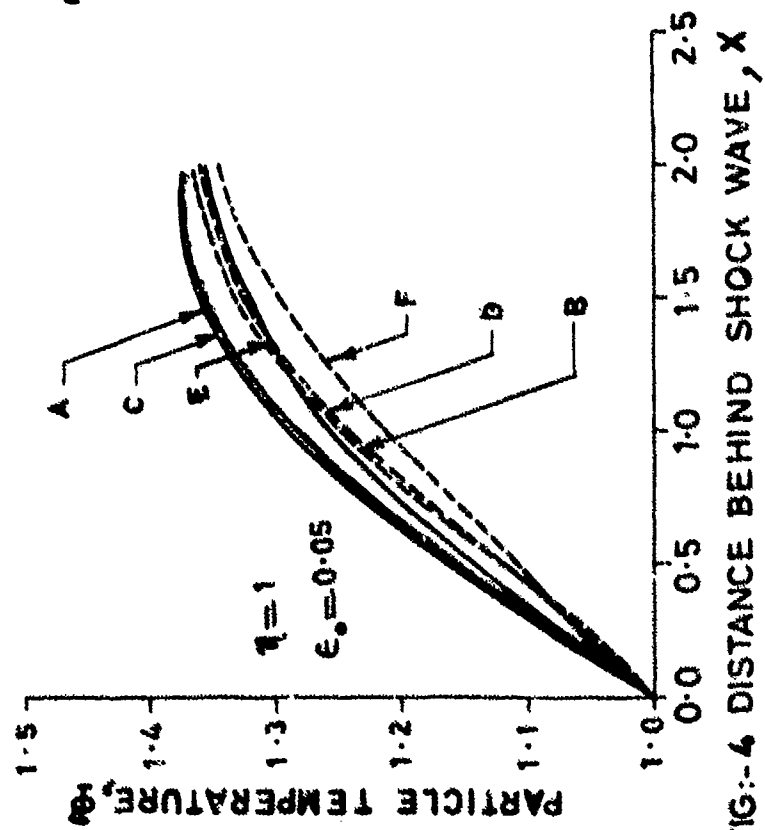
FIG:-4 DISTANCE BEHIND SHOCK WAVE, X

SHOCK WAVE REFLECTIONS IN DUSTY GAS

M. Sommerfeld, M. Selzer and H. Grönig

Stosswellenlabor der RWTH Aachen, West Germany

Shock wave reflections in a dusty gas are studied
by means of a vertical shock tube, where two cases are
considered. In the first case the reflection of a dusty
gas shock wave at the closed end of a shock tube is
investigated and the effects of the relaxation phenomena
on the pressure history and the shock wave propagation
are shown. In the second case the pressure history of
transmitted and reflected shock wave is measured in a
sudden area constriction. In both cases the influence of
Mach number and loading ratio is investigated. Numerical
calculations are mainly made using the piecewise-linear-
method which is applied to one- and two-dimensional
shock wave propagation in a dusty gas.

INTRODUCTION

Shock waves propagating through a mixture of gas and micron-sized
particles are of scientific interest since many years. The phenomena associated
with a shock wave which is initiated within or incident onto a dusty gas are
already quite well understood and examined experimentally and theoretically[1-4].
The effects occuring in connection with the reflection of a shock wave in a
dusty gas also are of great interest.

One close application are dust explosions, which are a severe problem in
pneumatic conveying and in coal mine galleries and always are accompanied by
shock waves and reflections at bends or area constrictions. The first step, to
give some insight into this problem is to study the reflection of dusty gas
shock waves excluding chemical reaction.

Concerning the reflection of a dusty gas shock wave at the closed end of
a shock tube some numerical results are presented by Marconi et al.[5] using the
method of characteristics, and also the random-choice-method was applied to
this problem[6,7]. Besides this one-dimensional problem we are also interested in
two-dimensional effects which become important for example in the case of an
area constriction.

Experimental results are obtained by using a vertical shock tube[3].
Numerical calculations for the one- and two-dimensional case are made by
applying the piecewise-linear-method(PLM)[8] to dusty gas flows.

EXPERIMENTAL EQUIPMENT

The experiments have been performed using a vertical shock tube (inner
diameter 50 mm) with the appropriate dust supplying system described earlier[4].
The glass particles used in the experiment have an average diameter of 27 um
and a material density of 2500 kg/m^3. Since we produce a continuous gas
particle flow in the low pressure section in order to get a homogeneous
mixture, we use a fast acting slide valve to produce the shock tube end wall.
To keep the mixture near the end wall rather homogeneous this valve must be
closed only after the shock wave is initiated. In order to perform this
requirement we developed a slide valve, which has shutting times of less than
10 ms. The valve is triggered after the shock wave passes a pressure gauge

about 4m ahead of the valve.

Using a slide with a hole we also examined partially reflected shock waves. The pressure history and the velocity of the incident and reflected shock waves is measured by means of several Kistler pressure gauges(Type 603B).

CHARACTERISTICS OF SHOCK REFLECTIONS IN A DUSTY GAS AND NUMERICAL COMPUTATION

Recently the PLM has been applied to dusty gas flows[9]. This method has been already successfully applied to two-dimensional flow fields with shock waves[8]. The main feature connected with the shock wave reflection in a dusty gas are shown with the aid of some computational results for the one- and two-dimensional case, where the drag coefficient is taken to be $c_D = 112\ Re^{-0.98}$.

First we consider the one-dimensional shock tube problem, where a shock wave (s0) propagates from a pure gas section into a dusty gas. Throughout the dusty gas the shock wave decays until equilibrium is attained and then it is reflected at the closed end of the shock tube. Due to the typical relaxation profiles of dusty gas shock waves, the reflected shock wave propagates into a region of increasing gas velocity, whereby it is decelerated until the gas velocity is constant (Fig.1). In the case of the shock tube problem a dusty gas layer develops near the end wall, therefore the shock wave is again accelerated, when propagating out of the mixture and an expansion wave is reflected.

Since the particles are decelerated and heated behind the reflected shock front, this momentum and heat exchange causes an increase in pressure, gas density and temperature. The equilibrium pressure at the end wall is considerably higher as in the pure gas case (Fig.1). For the lower range of incident shock strenths the equilibrium temperature slightly increases with the loading ratio.

The equilibrium values are calculated by applying the equivalent gas model analysis using the equations for the reflected shock wave. In Fig.2 the equilibrium pressure, temperature and velocity of the reflected shock wave are shown for different shock Mach numbers of the incident shock wave and loading ratios.

If the incident shock strength approaches infinity, the pressure and temperature ratio of the reflected shock wave remains finite. The values of the limiting pressure and temperature ratio are shown in Table I for different particle loadings.

Table I

n	p_{52}	T_{52}
0.0	8.0	2.286
0.5	10.7	2.206
1.0	13.53	2.160
2,0	18,38	2.115

Behind the reflected shock wave the particles will continue to flow towards the end wall and collide with it. Because we consider solid particles, they will be reflected elastically from the rigid wall and interact with the particles still flowing in the opposite direction. This process will cause an increase of the particle density near the end wall. Since the reflection of the particles in our computation would imply a multivalued solution in the particle velocity , we assumed the particles to be suddenly decelerated to zero velocity, whereby they stick to the wall. This boundary condition describes the above mentioned mechanism very close and also results in an increase of the particle density near the wall (Fig.1).

If we consider a dusty gas shock wave interacting with an area reduction we will have a certain flow pattern depending on the strength of the incident shock wave. In the considered range we will have a reflected shock wave propagating upstream. With increasing loading ratio the reflected shock front will be shifted towards the area constriction, because the equilibrium gas velocity behind the incident shock wave also increases. The initially transmitted and reflected shock fronts will be overtaken by several disturbances and multiple reflections until they attain equilibrium.

In Fig.3 the time history of this process is shown by means of computed shadowgraphs, comparing pure and dusty gas case. The two-dimensional shock wave structure will only be considerably effected, if the particle relaxation length is in the order of the dimension of the flow field. Otherwise the initial interaction of the shock wave with the area reduction can be considered as nearly frozen (unaffected by the presence of the particles) and the disturbances caused by the area change already decayed before the relaxation effects become important (Fig.4).

Due to the particle deceleration and heating the pressure is increased behind the reflected shock front and the equilibrium pressure ahead of the area reduction attains much higher values than in the comparable pure gas case for the same incident shock strength (Fig.4).

Another effect, which was also observed in the experiments, is that the disturbances propagating behind the initially transmitted and reflected shocks decay much faster in the dusty gas case (Fig.3). In the case of very small particles the concave shape of the reflected shock front will be flattened since the outer parts of the wave front propagate in a region of higher gas velocity than the inner parts.

EXPERIMENTAL RESULTS AND COMPARISONS WITH THE THEORY

Shock wave reflections at the shock tube end wall

The pressure history of the incident and the reflected shock wave near the shock tube end wall is shown in Fig. 5. Propagating through the relaxation zone of the incident shock wave, the reflected shock wave is decelerated until equilibrium is attained.

From these results and from time measurements between two gauges the time history of the incident and reflected shock waves is obtained and shown in Fig.6. Furthermore, numerical results for different loading ratios are included, indicating the increasing deceleration of the reflected shock with increasing loading ratio. In the experiment the reflected shock wave is decelerated at a lower rate, but finally approaches nearly the same velocity. This is quite evident, since the relaxation length predicted by the numerical calculations is slightly shorter than in the experiment, using the above relation for the drag coefficient[7].

The equilibrium pressure ratio and the equilibrium velocity of the reflected shock, obtained from several experiments with different Mach numbers and loading ratios, are compared in Fig.7 with the results of the equivalent gas model analysis. The experimentally obtained equilibrium pressure ratio is in general slightly lower than the theoretical one. The causes for this may be found in the influence of the boundary layer. For the equilibrium velocity of the reflected shock wave the agreement between theory and experiment is quite good.

Interaction of a dusty gas shock wave with an area constriction

The interaction of a shock wave with an aperture-like area constriction is studied for an area ratio of 0.25. A typical experimental result is shown in Fig.8 by using 5 pressure gauges in front and 3 pressure gauges behind the constriction. The incident shock wave is partially reflected, whereby the transmitted shock wave is reduced in strenth.

The experimental equilibrium pressure ratio of the reflected shock wave for the above area constriction ratio shows its dependence on the shock wave Mach number and the loading ratio (Fig.9). The pressure ratio is of course lower than theoretical equilibrium value for the total reflection.

The time history of incident, reflected and transmitted shock waves is shown in Fig.10 indicating the effects of the loading ratio on the velocity of the reflected shock wave, which is shifted towards the constriction with increasing loading ratio. In the considered range of loading ratios the

velocity of the transmitted shock wave is almost independend of it.

CONCLUSION

The features of shock wave reflections in a dusty gas for one- and two-
dimensional cases have been shown with the aid of numerical calculations. The
effects of dust loading and particle size on the pressure history and the shock
wave patterns have been investigated.

In the case of the reflection of a dusty gas shock wave at the shock tube
end wall, the experimentally obtained equilibrium pressure ratio at the end
wall and the equilibrium velocity of the reflected shock wave agree quite well
with the theory.

In the case of the area constriction a comparison of the experiments with
the numerical calculations could not yet be made. Since the particles used in
the experiments are rather large, this would require a large computational
domain to simulate the whole transition from the incidence to the equilibrium,
whereby we would have an unreasonable increase in computer time. Therefore,
experiments have to be done using smaller dust particles.

ACKNOWLEDGEMENT

REFERENCES

1. Rudinger, G., "Some properties of shock relaxation in gas flows carrying
    small particles", Phys. Fluids, 7, 1964, p.658-663.

2. Outa, E., Tajima, K. and Morii, H., "Experiments and analysis on shock wave
    propagation through a gas-particle-mixture", Bull. JSME, 19, 1976, p. 384-
    394.

3. Sommerfeld, M., "The unsteadyness of shock waves propagating through gas-
    particle mixtures", Exper. in Fluids, 1985, (in print).

4. Sommerfeld, M. and Grönig, H., "Decay of shock waves in a dusty-gas shock
    tube with different configurations", Shock Tubes and Waves, Proceedings of
    the 14th Int. Symp. on Shock Tubes and Waves, 1983, p.470-477.

5. Marconi, F., Rudman, S. and Calia, V., " Numerical study of one-dimensional
    unsteady particle-laden flows with shocks", AIAA J., 19, 1981, p.1294-1301.

6. Miura, H., Saito, T. and Glass, I.I., "Normal reflection of a shock wave at
    a rigid wall in a dusty gas", UTIAS Report No. 274, 1984.

7. Sommerfeld, M., "Instationare Stosswellenausbreitung in Gas-Teilchen-
    Gemischen", Dr. Thesis, RWTH Aachen, 1984.

8. Colella, P. and Glaz, H.M., " Efficient solution algorithms for the Riemann
    problem for real gases", LBL Report No. 15776, 1983.

9. Sommerfeld, M. and Nishida, M., "Dusty gas flows with shock waves", to be
    presented at Int. Symp. Comp. Fluid Dynamics, Tokyo, Sept. 1985, (preprint).
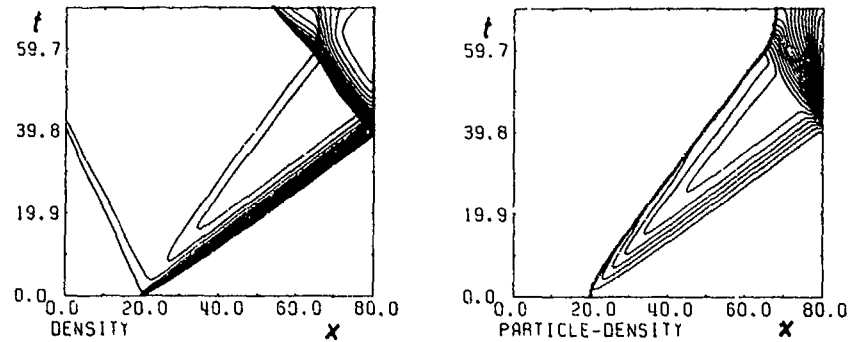
Fig.1 Contour lines in the x-t-
plane and pressure history
of a shock wave propagating
through a dusty gas and
reflecting at the shock tube
end wall ($M_{s0} = 1.55$,
$\eta = 0.66$, $\rho_p^{s0} = 2500$ kg/m³,
$D_p = 27$ μm)
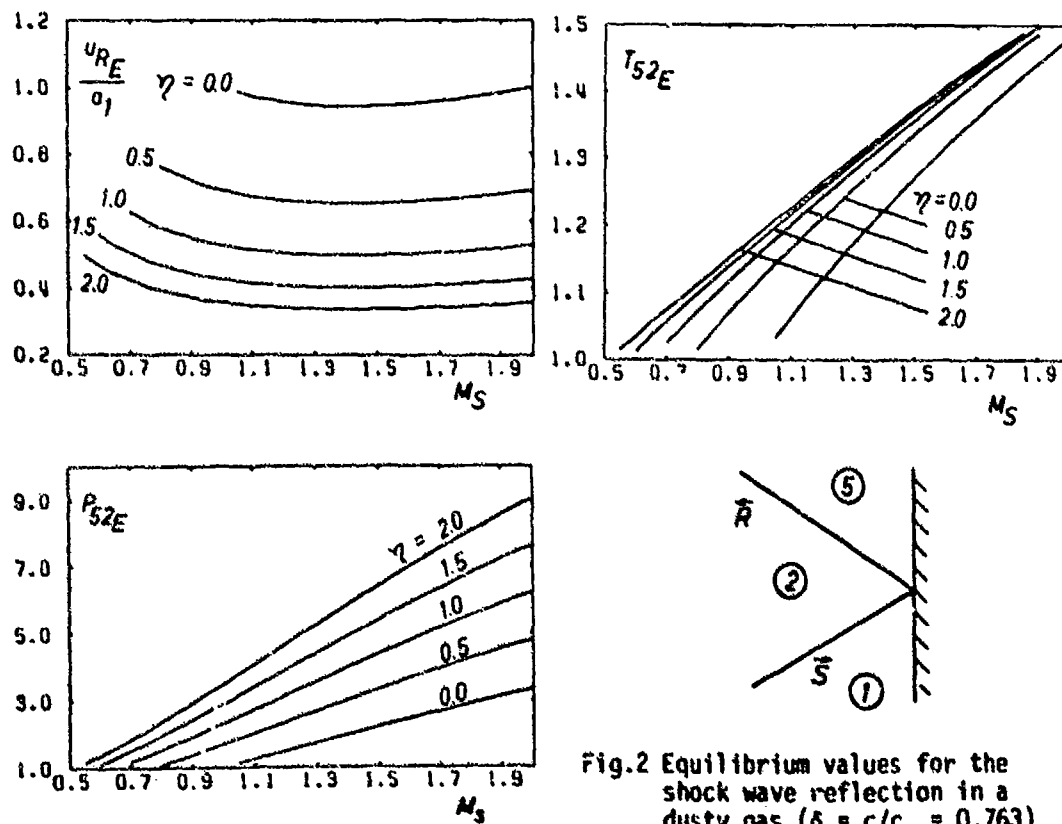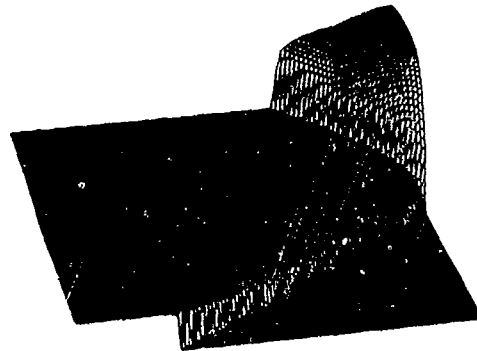
Fig.2 Equilibrium values for the
shock wave reflection in a
dusty gas ($\delta = c/c_p = 0.763$)
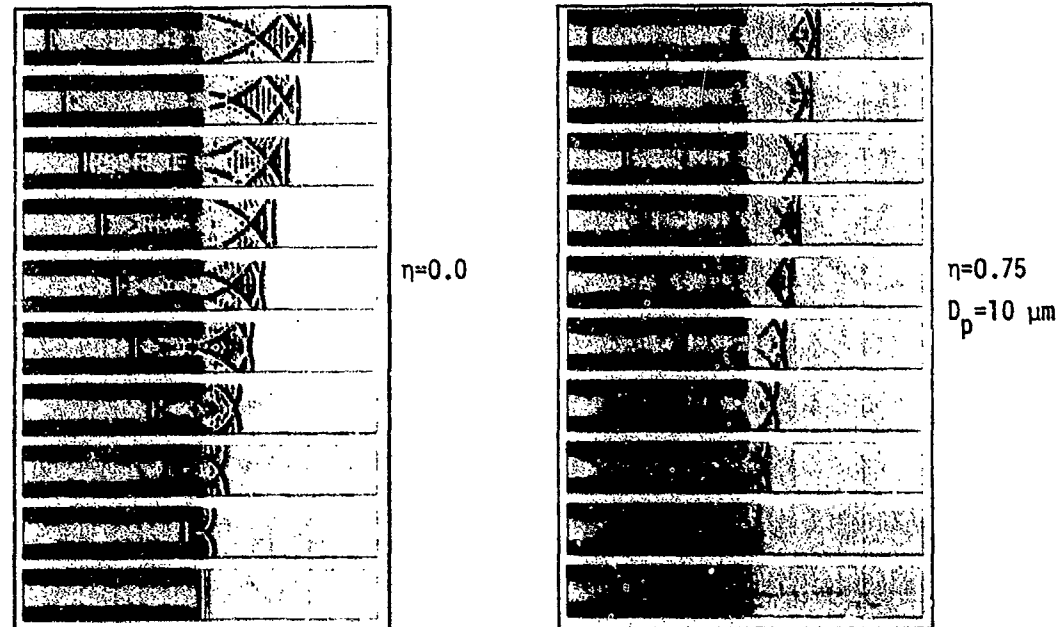
Fig.3 Computed shadowgraphs showing the interaction of a shock wave with an area reduction (M_{si} = 1.2, ρ_p =2500 kg/m^3, area ratio: 0.25, Δt = 0.5)
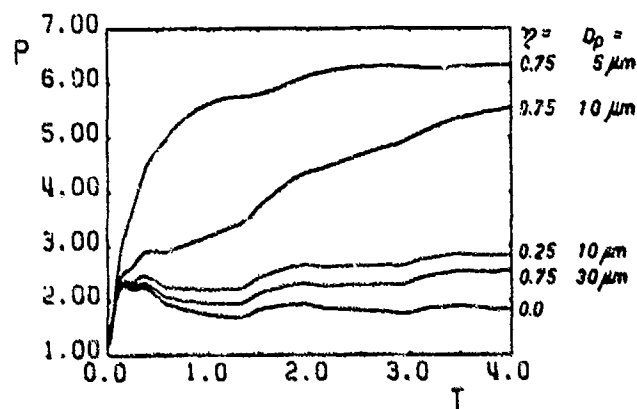
Fig.4 Pressure history at the area reduction
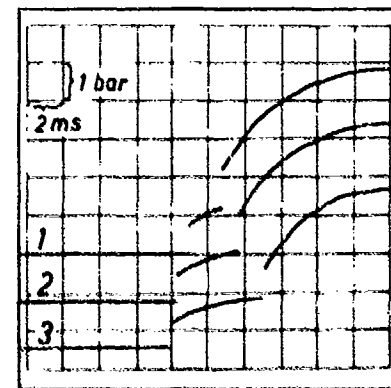
Fig.5 Pressure history ahead of the end wall (x_1=0.31, x_2=0.58, x_3=0.83 m, M_{si}=1.25, η=0.6)
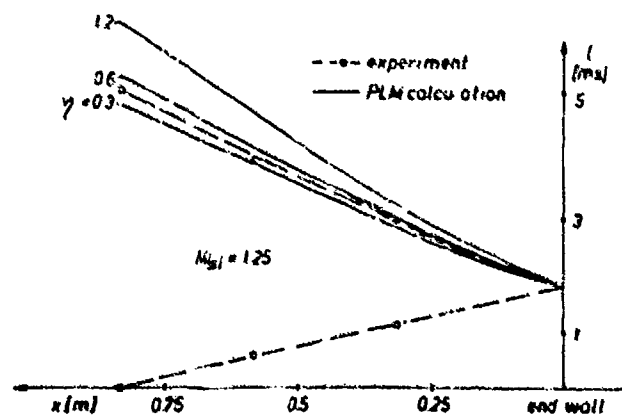
Fig.6 x-t-diagram of the shock wave reflection at a rigid wall
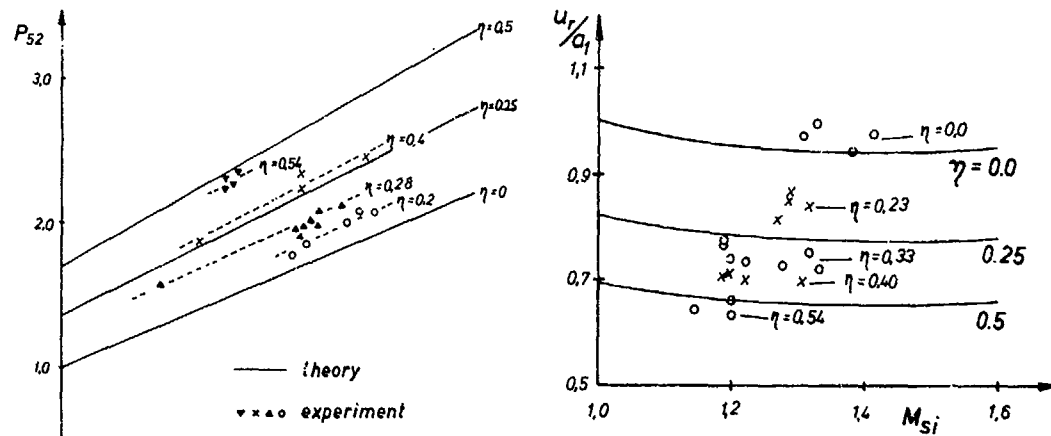
Fig.7 Equilibrium values, comparison
between experiment and theory
for total reflection (δ = 0.763)
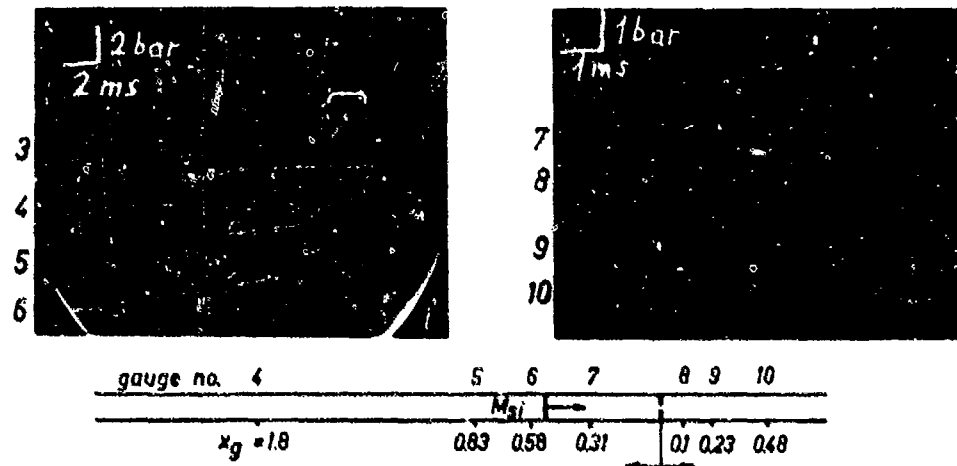
Fig.8 Pressure traces of a dusty gas shock wave impinging on a aperture-like
area constiction (M_{si} = 1.2, η = 0.6)
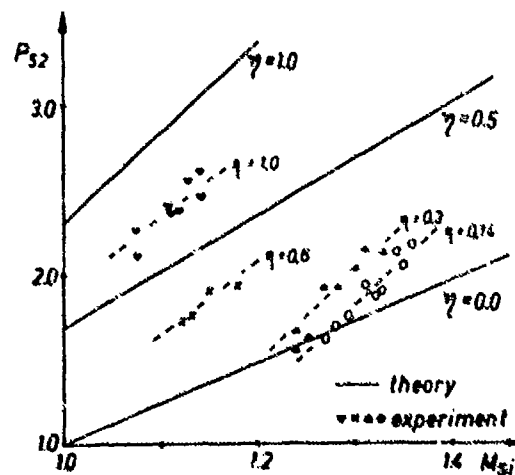
Fig.9 Equilibrium pressure at the
area constriction
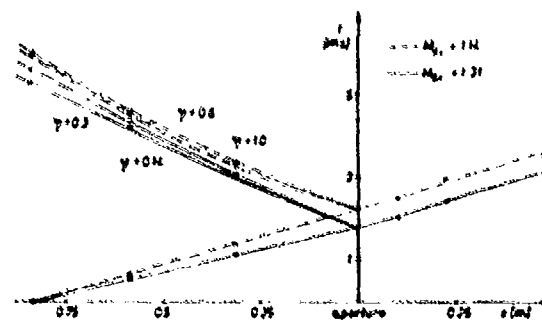
Fig.10 x-t-diagram for different Mach
numbers and loading ratios
(area constriction)

MEASUREMENT OF LARGE MASS FRACTIONS IN
DUSTY GASES WITH WEAK SHOCK WAVES

J. Ming and A. Frohn

Universität Stuttgart
Institut für Thermodynamik der Luft- und
Raumfahrt
Pfaffenwaldring 31
7000 Stuttgart 80

A method for measuring large mass fractions in gas particle mixtures is dis-
cussed. By measuring the velocity and the pressure difference of weak shock
waves the mass fraction can be determined with good accuracy.

1. INTRODUCTION

The mass fraction is cne of the most important parameters for describing the
behaviour of dusty gases. Most measurements of the mass fraction are based on
sampling techniques.[1-8] .
For the investigation of transient phenomena it is often necessary to measure
the mass fraction instantaneously without sampling. Such in situ-measurements
are of course ve.y interesting for many practical applications. In situ-measure-
ments of the mass fraction can be made for example by using the extinction of
light [9] . The disadvantage of this method is that it is difficult to use for
high mass fractions. The present paper deals with in situ-measurements of high
mass fractions in dusty gases using the equilibrium properties in front of and
behind weak shock waves. With this method mass fractions up to $\mu = 0.96$ have
been measured. The experiments have been performed in a shock tube. Pressure
transducers have been used to measure the velocity of the shock wave and the
equilibrium pressure behind the shock wave.

2. BASIC EQUATIONS

The pressure ratio across shock waves in dusty gases can be written as

$$\frac{p_1 + \Delta p}{p_1} = \frac{2\overline{\kappa}}{\overline{\kappa} + 1} \overline{M}_1^2 - \frac{\overline{\kappa} - 1}{\overline{\kappa} + 1} \quad , \tag{1}$$

where p_1 is the pressure in front of the shock wave, Δp the pressure difference across the shock wave, $\overline{\kappa}$ the specific heat ratio for the mixture and $\overline{M}_1$ the Mach number of the mixture [10]. The specific heat ratio for the mixture is given by the relation

$$\overline{\kappa} = \frac{1 + (c/c_{pG}) \cdot \mu/(1-\mu)}{1 + (c/c_{vG}) \cdot \mu/(1-\mu)} \cdot \kappa_G \quad . \tag{2}$$

Here c_{pG} and c_{vG} are the specific heat of the gas at constant pressure and constant volume, c is the specific heat of the particle material and κ_G the specific heat ratio of the pure gas. The Mach number of the mixture is

$$\overline{M}_1 = u_s/\overline{a}_1 \quad \cdot \tag{3}$$

where the quantity u_s is the velocity of the shock wave and $\overline{a}_1$ the equilibrium sound speed of the mixture in front of the shock wave.

The sound speed $\overline{a}_1$ can be expressed as

$$\overline{a}_1 = ((1-\mu) \cdot \overline{\kappa}/\kappa_G)^{1/2} \cdot a_{G1} \tag{4}$$

where a_{G1} is the sound speed of the pure gas. It is assumed that the quantities p_1, c, c_{pG}, c_{vG}, κ_G, a_{G1} are known. In this case it is possible to determine the mass fraction μ with the equations just given, when Δp and u_s are measured.

3. EXPERIMENTS

The experiments have been performed in a vertically mounted shock tube which is shown schematically in Fig. 1. The high pressure section is located above the low pressure section, so that the shock waves are running downwards. Paper

diaphragms have been used in order to get weak shock waves. By a feeding device (Retsch Typ DRL 10) the particles are transferred to a high output rotating table dust feeder, which has been developed in our laboratories. The rotating table dust feeder consists essentially of a chambered disc. The chambers are filled continuously with dust on the upper side of the disc. The excess dust is removed with a knife edge, in order to ensure a steady dust output. The dust is released by flaps in the bottom of the chambers and loaded into a hopper. From the hopper the dust is fed into an air injector which ends in the shock tube. With this method a constant mass flux is obtained in the shock tube. The mass flux of air through the injector is determined by a variable area flowmeter (Fischer und Porter Typ FP-1/4 - 25 à 5 /81). The pressure transducers, used to determine the pressure jump Δp and the wave velocity, are mounted 2.2 m below the injector inlet. A balance (type 1401 MM 7-2, Satorius) below the open end of the driven section is used to measure the outcomming mass flux continuously;the results are transmitted to a plotter. From the mass flux of the air and the mass flux of the particles the mass fraction μ in the tube is calculated. The mass fraction determined with the known mass fluxes of gas and particles is compared with the mass fraction derived from the pressure and velocity measurement. Air was used as low pressure gas in the mixture and lycopodium spores as particles. These particles are nearly spherical with an approximate diameter of 30 μm. They were chosen, since they are light and they don't tend to agglomerate. The specific heat was assumed to be c = 1500 J/kg K. It should be mentioned that the mass fraction depends only weakly on this quantity. Increasing the value of the specific heat for example by a factor of two would result in a variation of the mass fraction μ of less than o.2 %. Frigen 13 (C Cl F$_3$) was chosen as driver gas. On account of the low sound speed of 167 m/s the arrival of the expansion wave is delayed and thereby long test times of morethan 12 ms were achieved. Under these conditions a well defined equilibrium region behind the shock wave is obtained for the evaluation of the mass fraction. In Fig. 2 some measured pressure profiles are shown for different values of μ.

It is often assumed that shock waves in gas particle mixtures may be separated in a discontinuous gas dynamic shock and a relaxation zone [11]. It can be seen from Fig. 2 that the strength of the gasdynamic shock decreases with increasing mass fractions. Finally one has a fully dispersed wave. Some experimental results for μ are shown in Fig. 3. The mass fraction μ_1 which has been derived from the measured values of pressure and velocity is chosen as abscissa. The ordinate represents the mass fraction μ_2 determined directly by weighting. For

perfect experiments the measured values must lie on the straight line $\mu_1 = \mu_2$.
It can be seen in Fig. 3 that the deviations for most of the experimental
results are less than $\pm$ 0.02.

4. SUMMARY

It has been shown, that it is possible to determine the mass fraction in gas
particle mixtures from the pressure difference and the velocity of weak shock
waves. The measurements can be performed with two pressure transducers. The
average error in these measurements for $\mu > 0.5$ is less than 2 % for $\mu < 0.5$
the average error is approximatly 6 %. It has been demonstrated that it is
possible to determine large mass fractions with the proposed method. In the
future the method should be improved by using a microcomputer for on line
data evaluation. In that case fast in situ-measurements would become possible.
By producing weak shock waves in short intervals it would be possible to
measure the mass fraction even when it is varying with time.

REFERENCES

1. Dresia, H.; Fischötter, R.; Felden, G.:
    "Kontinuierliches Messen des Staubgehaltes in Luft und Abgasen mit Beta-
    Strahlen", VDI-Zeitung, 106, Nr. 24, p. 1191, 1964.

2. Husar, R.8 :
    "Atmospheric Particulate Mass Monitoring With a β-Radiation Detector"
    Atmospheric Environment, Vol. 8, p. 183, 1974.

3. Nottrodt, K.H.; Georg, H.W.:
    "Absolute Element Concentrations in Aerosols Analysed by Atomic-Absorbtion-
    Spectroscopy and by Proton-Induced X-Ray Emission, a Comparison", Journal
    of Aerosol Science, Vol. 9, p. 169, 1978.

4. Sauerbrey, G.:
   "Verwendung von Schwingquarzen zur Wägung dünner Schichten und zur Mikro-
   wägung", Zeitschrift für Physik, 155, p. 206, 1959.

5. Olin, J.G.; Sem, G.J.:
   "Piezoelectric Microbalance for Monitoring the Mass Concentration of
   Suspended Particles", Atmospheric Environment, Vol. 5, p. 653, 1971.

6. Clarke, A.G.; Moghadassi, M.A.; Williams, A.:
   "A Comparison of Techniques for Automatic Aerosol Mass Concentration
   Measurement", Journal of Aerosol Science, Vol. 8, p. 73, 1977.

7. Muschelknautz, E.:
   "Auslegung von Zyklonenabscheidern in der technischen Praxis", Staub-Rein-
   haltung der Luft, 30, Nr. 5, p. 187, 1970.

8. Oeseburg, F.; Roos, R.:
   "Properties of the Stöber Centrifugal Aerosol Spectrometer at a High
   Sampling Flow Rate: Calibration Factors for Particle Losses", Journal
   of Aerosol Science, Vol. 10, p. 539, 1979.

9. König, G.; Frohn, A.:
   "Relaxation of Small Solid Particles in Shock Tube", International
   Symposium on Flow Visualization, 1980.

10. Frohn, A.; König, G.; Ming, J.:
    "Untersuchungen von Aerosolen im Stoßwellenrohr", VDI-Verlag GmbH,
    ISBN 3-18-419075-1.

11. Rudinger, G.:
    "Relaxation in Gas-Particle Flow", SQUID Technical Report Nr. Cal-96-PU.
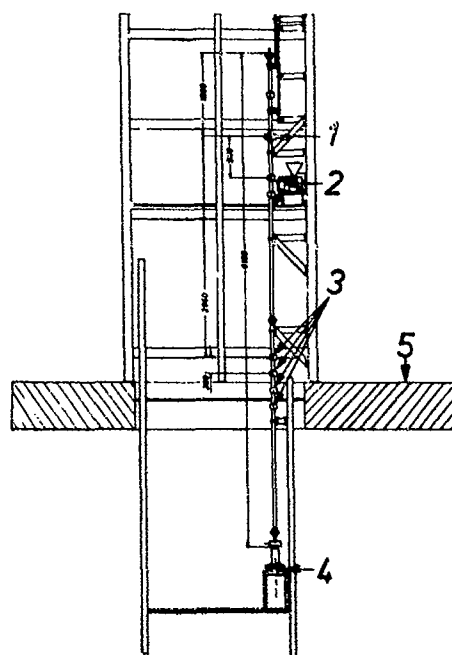
Figure 1.   Schematic diagram of shock tube:

1) diaphragm,
2) feeding device, rotating table dust feeder and injector,
3) pressure transducers,
4) balance,
5) floor.
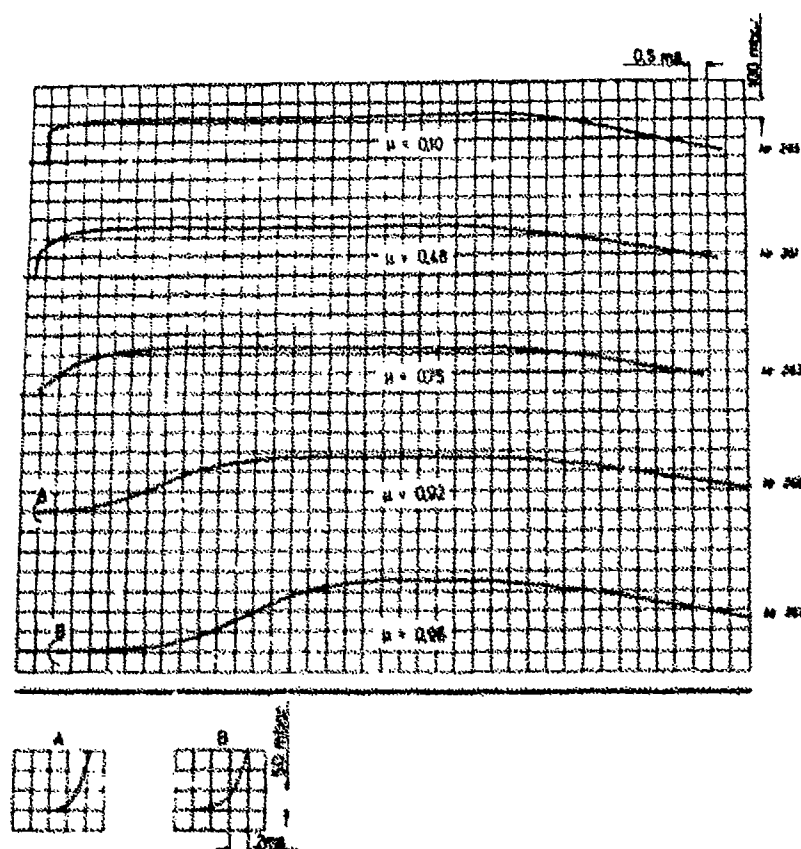
Figure 2.

Pressure profiles for different mass fractions.

Nr. 265: $\bar{M} = 1.1$,

Nr. 261: $\bar{M} = 1.12$,

Nr. 263: $\bar{M} = 1.11$,

Nr. 266: $\bar{M} = 1.13$,

Nr. 267: $\bar{M} = 1.18$.

$\bar{M}$ is the Mach number of the mixture.
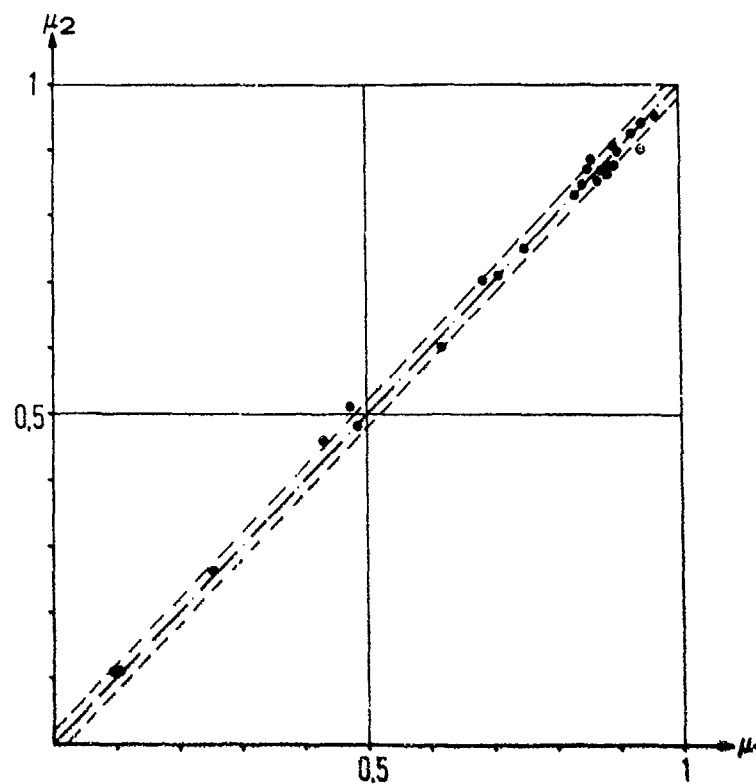
Figure 3.

Comparision of the mass fraction μ_1 determined with weak shock waves with the mass fraction μ_2 obtained directly by weighing. The dashed lines indicate deviation of ± 0.02.

EXPERIMENTAL OBSERVATION OF THE STRUCTURE

OF SHOCK WAVES IN DUSTY GAS

Yu Hongru   Lin Jiangmin
Yuan Shengxue   Li Zhongfa

Institute of Mechanics, Academia Sinica
Zhong-Guan-Cun, Beijing, China

ABSTRACT

The structure of shock waves in dusty gas are studied by
shock tube experiments. Pressure, shock wave propagation
velocity and particle concentration are measured under the
condition that the particle loading ratio is less than 0.4
and the shock Mach number is less than 1.5. The frozen and
equilibrium pressures behind the shock wave are well de-
scribed by the Rankine-Hugoniot relation. But the rela-
xation length is significantly shorter than that calculated
from drag of sphere at steady motion. And the disperse shock
wave in dusty gas are observed. It is found that the pre-
sence of dust decreases the pressure fluctuation in the wall.
The propagation velocity of shock wave in shock tube agrees
with the result of the model analysis on a "effective gas".

INTRODUCTION

An analysis of shock wave in dusty gas was first performed by Carrier[1] and
a number of analyses were published subsequently[2-7]. In all these papers publi-
shed it has been based on the following assumptions: The particle cloud is treat-
ed as a continuous medium; The particles do not collide with each other; The
shock wave is separated into gasdynamic shock wave followed by relaxation zone
due to acceleration and heating of the particles; Both the viscous drag coeffi-
cient and the rate of heat trnsfer for a single sphere in steady motion are used
for the system.

Only few experimental vertification for the analytical results of shock wave
in dusty gas have been published[8,9]. Outa, Tajima and Morii measured the pres-
sure profiles of relaxation zone behind the leading front. In real flows most
of fine particles of whitecarbon used coalesce into agglomerations. The experi-
mental results can not be compared with the theory because of the difficulty in
knowing the reasonable values of effective diameter. Konig and frohn have in-
vestigated the structure of weak shock wave under the condition that fine parti-
cles and low loading ratio($\gamma < 10^{-2}$) are used. In present experiments larger
sphere particles and larger inner diameter of shock tube are used for weakening
the effect of agglomeration and effect of boundary layer respectively.

THEORETICAL BACKGROUND

If the plane shock wave propagates with constant velocity through the stat-
ic dusty gas, the dusty flow is steady in coordinate system fixed in the shock
wave. In case the particle volume can be neglected, the continuity equations
for the gas and for the particle cloud, the momentum and energy equations for

dusty gas are

$$\dot{m} = \rho u = \rho_0 u_0 \tag{1}$$

$$\dot{m}_p = \eta \dot{m} = \sigma u_p = \sigma_0 u_{p_0} \tag{2}$$

$$\dot{m}u + \eta \dot{m}u_p + P = (1 + \eta)\dot{m}u_0 + P_0 \tag{3}$$

$$\frac{1}{2}u^2 + C_p T + \eta\left(\frac{1}{2}u_p^2 + C_p \delta T_p\right) = \frac{1}{2}u_0^2(1 + \eta) + C_p(1 + \eta\delta)T_0 \tag{4}$$

where ρ and σ represent mass of gas and particles per unit volume of the system; $\dot{m}$ and $\dot{m}_p$ represent mass flow of gas and particles respectively; $\eta = \dot{m}_p/\dot{m}$ is loading ratio; δ is relative specific heat.
The state equation of gas

$$P = \rho RT \tag{5}$$

The foregoing set of equations is short of two equations to solve for seven unknown variables u, ρ, T, p, u_p, δ and T_p provided the condition ahead of the shock wave are determined.

According to Rudinger the shock transition can be separated into three regions.

In frozen region closed immediatly the shock front it may be assumed that the velocity and temperature of particles is frozen.(i.e. $u_{pf}=u_0$; $T_{pf}=T_0$) due to the width of gasdynamic shock is extremely thin and density of particle is larger over 1000 time than density of gas usual. Therefore the terms concerned about particle can be omitted from the conservation equations. The foregoing set of equations is turned out the set of equation for a particle free gas. The condition in frozen region can be completely determined.

In equilibrium region the difference of velocity and of temperature between gas and particles vanish finally.(i.e. $u_{pe}=u_e$; $T_{pe}=T_e$) The overally shock transition can be computed in the same manner as for a gas from the Ranking-Hugoniot relation but using the spectifitic heat $\Gamma = (1 + \eta\delta)\gamma/(1 + \gamma_s\delta)$ and the equilibrium shock Mach number $M_{se} = u_s/\alpha_e$.

There are following relations for the pressure and the velocity of gas in frozen and equilibrium regions.

$$\frac{P_f}{P_0} = \frac{2\gamma}{\gamma+1}\left(\frac{u_s}{\alpha_0}\right)^2 - \frac{\gamma-1}{\gamma+1} \tag{6}$$

$$\frac{P_s}{P_0} = \frac{2\Gamma}{\Gamma+1}\left(\frac{u_s}{\alpha_e}\right)^2 - \frac{\Gamma-1}{\Gamma+1} \tag{7}$$

$$u_s u_0 = \frac{2\gamma R}{\gamma+1}T_0 + \frac{\gamma-1}{\gamma+1}u_0^2 \tag{8}$$

$$u_s u_0 = \frac{2\Gamma \bar{R}}{\Gamma+1}T_0 + \frac{\gamma-1}{\gamma+1}u_0^2 \tag{9}$$

In relaxation region between the frozen and equilibrium region it is necessary to add the equations of motion and heat transfer for a particle to the set of equations.

$$\frac{du_p}{dt} = \frac{3}{4}\frac{C_L}{D}\frac{\rho}{\rho_p}(u - u_p)|u - u_p| \tag{10}$$

$$\frac{dT_p}{dt} = \frac{6KNu}{CD^2\rho_p}(T - T_p) \tag{11}$$

Because of the uncertainly of the drag coefficient and Nusselt number it is im-

portment to check the numerical results in relaxation region by experiments.

EXPERIMENTS

It is well known that shock tube are the most convenient tools to obtain basic knowledges about the structure of shock wave. But it is experimental techniques that must be treated carefully for reliability of experimental results. For suspending particles in the gas, to date a quantites of gas inject into shock tube. Therefore, there is initial flow in driven section before running. The boundary layer induced by initial flow must destroy the uniformity of particle dispersal due to the velocity shear in it and interact with the incident shock wave. In present experiments it is used particle settling to disperse particle.

The shock tube used is schematically shown in fig.1. It is vertically mounted with the driver section in the upper part. The inner diameter of driven section of 5m long is 185mm. The reservior connected to the bottom end of the driven section. Air is used for the driver and driven gases and the driven gas is initially atmosphric.

Velocity of the incident front is determined by the trevelling times between parts of piezoeletric transducers mounted 0.5m apart. The data measured show that the decay of incident shock velocity is very weak due to large inner diameter of driven section.

Shape of the particles of polyethylene used is sphere perfectly. The particle diameters range from 55μm to 80μm. The particles are injected into driven section at position near the diaphragm and are settled by gravity. The particle concentration has been measured by the extinction of a light beam. Using Bouguer's law

$$\frac{1}{I_0} = \exp-(n_p A_p l E) \tag{12}$$

where I/I_0 is the transmittance; A_p is the projected area of particle; n_p is number density; E is the extinction coefficient; 1 is path length of the light beam in the dusty gas.

Transmission light is received by photocell. Output of the photocell is in direct proportion to the transmission. The average concentration of particles

$$\sigma(t) = k \ln \frac{V_0 - V_d}{V(t) - V_d} \tag{13}$$

where V_0, V_d, V(t) represent output under condition in dust free, dark and running respectively. k depend on shape and size of particle, its value is calibrated on the spot. All of output are recorded by transient recorder.

RESULTS

The foregoing analyses shown that the frozen pressures do not depend on the loading ratio, size and shape of the particles. The present data of frozen pressure are summarized in fig.2. The figure demonstrates that all data fall about the theoretical curve. The curve in fig.2 plotted according to following relation

$$\frac{(P_f - P_0)}{P_0} = \frac{2\gamma}{\gamma + 1} [M_{sf}^2 - 1] \tag{14}$$

The equilibrium pressures depend on the loading ratio of the particles. Experimented results of the equilibrium pressure are shown in table together with theoretical values which computed by following equation

$$\frac{(P_e - P_0)}{P_0} = \frac{2\Gamma}{\Gamma + 1} [M_{se}^2 - 1] \tag{15}$$

No	$M_{sf} = \dfrac{u_o}{a_o}$	η	Γ	α_e/a_o	$(p_e - p_o)/p_o$		meas/theor
					theor	meas	
197	1.35	0.13	1.365	.929	1.28	1.31	1.02
201	1.30	0.17	1.356	.910	1.20	1.21	1.01
202	1.24	0.40	1.309	.817	1.48	1.35	.912

The experiments shown in fig.2 and in table have verified the theoretical predictions on the frozen and equilibrium pressures.

As for the parameters of relaxation region it must be computed by solveing the foregoing set of equations(1)-(5), (10),(11) Numerically. The numerical values are significant dependence on the drag coefficient. Fig.3 shown the measured pressure profile and numerical curves which are based on a Nusseltnumber of 2. The comparison between the measured curve and numerical curves shows similar in their variation tendence. But Measured width of relaxation zone is shorter than both of two computed. When the shock wave propagate with sound velocity. For which shock transition is posible in dusty gas, but a discontinuous front is not. This is the disperse shock wave in which the entire transition is continuous. It is difficult to observe such transition experimentally due to weakness of shock wave and absent of discontinuous. Fig.4 shown the pressure profile of the disperse shock wave. The experimental condition list as following: The driver and driven pressures are 0.54 and 0.1 MPa respectively; initial concentration of particles is $0.3mg/cm^3$;the combient temperature is 27°C; measured shock velocity is 355m/s.

It is known that the addion of solid particles to a gas flow can lead to reduction of friction factor for turbulent. Various mechanisms had been proposed to exploain the phenomenon. Kene and pfeffer[10] concluded that thickening of the laminar sublyer is the predominant effect. The pressure profiles measured at the wall of shock tube for the dust free gas and for the dusty gas are shown in fig.5. The comparison between two profile curves in fig.5 denotes that the presence of particles descrease obviously the pressure fluctuation at the wall. It may be help for foregoing conclusion.

If the length of driven section is evidently longer than the width of relaxation zone, the shock strength can be computed in same manner for a dust free gas from shock tube theory but using the parameters of "effective gas". The fig. 6 shown that the prediction of shock Mach number in dusty gas on a "effective gas" is satisfactory.

CONCLUSIONS

1. The predictions of the frozen pressure and equilibrium pressure were verified by experiments.

2. The variable tendency for the pressure profiles in the relaxation zone were similar between the measured and computed. But the measured width of relaxation zone is shorter than the computed based on the drag coefficient of a single sphere in steady motion.

3. The disperse shock wave was observed.

4. The presence of particles in gas flow can decrease obviously the pressure fluctuation at the wall.

ACKNOWLEDGMENT

REFERENCES

1. Carrier, G.F., Jour. of Fluid Mechanics, 4(1958), 376.
2. Kliegel, J.R., IAS paper, 60-5(1960).
3. Kriebel, A.R., Trans. ASME, Jour. of Basic Eng., 86(1964) 655.
4. Rudinger, G., Physics of Fluids, 7(1964), 658
5. Varma, T.D., Chopra, N.K., ZAMM 18(1967), 650
6. Marble, F.F., Ann. Rev. Fluid Mecha. 2(1970), 397
7. Schmitt-Von Schuber, B., Zamm 50(1970), 1008.
8. Outa, E., Tajima, K., Morii, H., Bull. JSME 19(1976), 384.
9. Koenig, G., Frohn, A., Proceedings of 13th Symp. on Shock Tubes & Waves, (1981), 646.
10. Kane, R.S., Pfeffer, R., NASA CR 2267(1973).
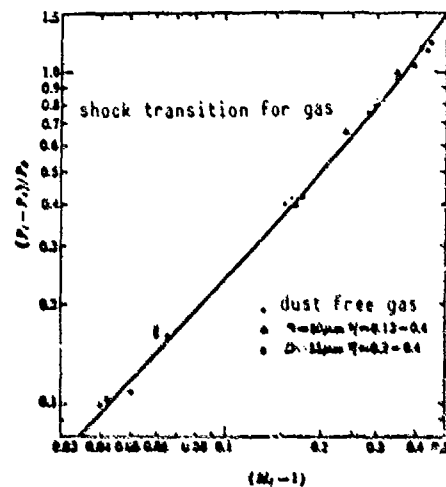
Fig.2 measured frozen pressures
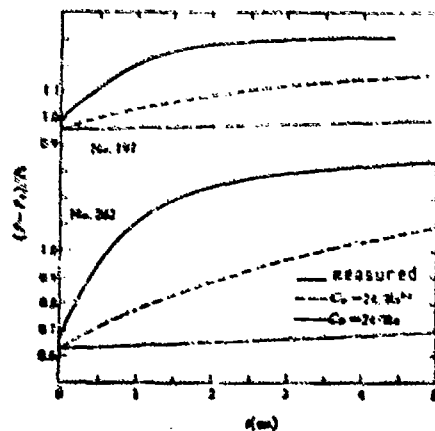
Fig.3 measured & computed pressures traces in relaxation zone
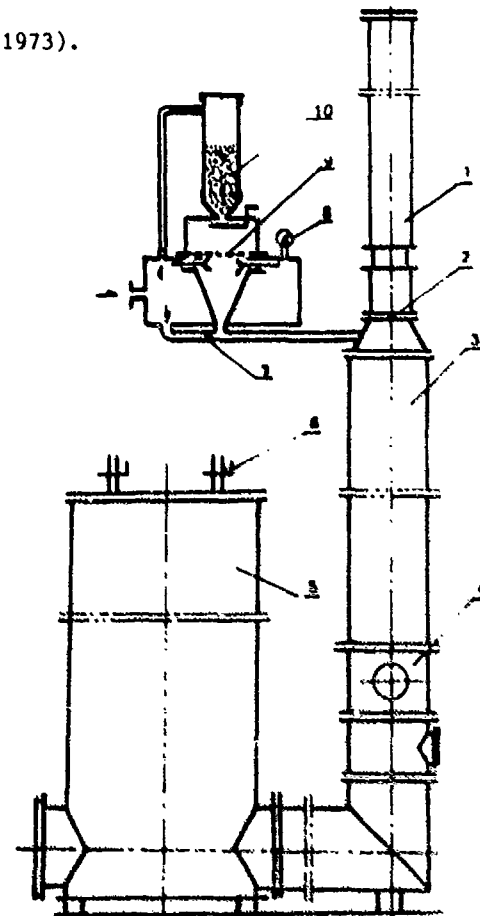
Fig.1 schematic of shock tube with particle injector

1 driver section
2 diaphragm
3 driven section
4 testing section
5 tank
6 exhaust valve
7 injection nozzle
8 pressure gauge
9 screen
10 particle reservior
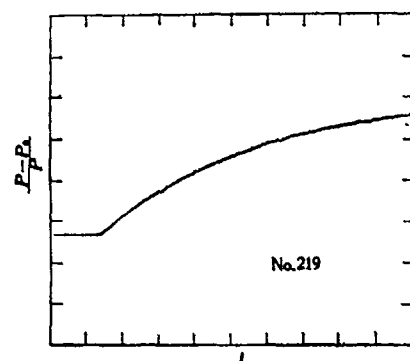
25 kpa, 0.5ms/div.

Fig.4   pressure trace of disperse
        shock wave
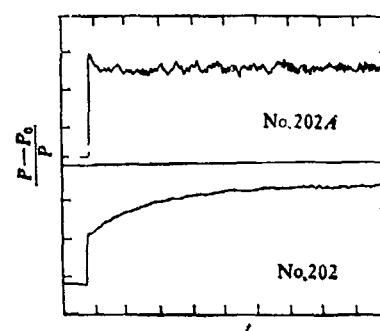
50kpa, 0.5ms/div.

Fig.5   typical wall pressure historied

upper line: dust free gas, M_s = 1.44

Lower line: = 0.17, D=80um. m_{sf} = 1.24
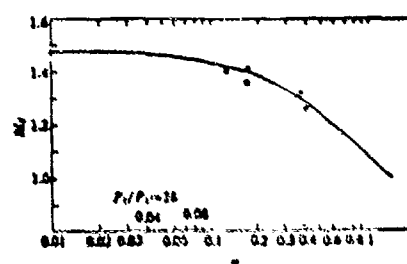
Fig.6   comparison of measured and
        computed shock Mach number

TWO-PHASE OXYGEN-CARBON DUST FLOW

THROUGH A NORMAL SHOCK WAVE

I. Elperin, O. Igra and G. Ben-Dor

The Pearlstone Center for Aeronautical Engineering Studies
Department of Mechanical Engineering
Ben-Gurion University of the Negev, Beer Sheva, Israel

The propagation of a normal shock wave into a quiescent oxygen gas
seeded with carbon particles is studied. Due to the elevated post-
shock temperature the carbon particles ignite and burn until they
disappear. For evaluating the effect of the burning carbon
particles on the post-shock wave flow field, i.e., the relaxation
zone, the conservation equations for a steady one-dimensional
reactive suspension flow are formulated and solved numerically.
The solution was repeated for a similar inert suspension flow.
Comparing the two solutions revealed that the carbon burning has a
major effect on the suspension properties in the relaxation zone
and on the eventually reached post-shock equilibrium state.

1. INTRODUCTION

The propagation of a normal shock wave into a dusty gas has drawn a great
deal of attention during the past three decades. The first investigators to
treat dusty shock waves were Carrier[1], Kriebel[2] and Rudinger[3]. They treated
the gaseous phase of the suspension as an ideal gas and the solid phase (dust)
was assumed to be inert. Their solutions were extended to cover monatomic
(argon) reacting gases by Ben-Dor and Igra[4] and diatomic reacting gases
(nitrogen) by Igra and Ben-Dor[5]. However, in both cases the solid phase (dust)
was considered to be inert in spite of the fairly high post-shock temperature.
The main reason for treating the dust as an inert phase is the difficulty in
formulating the dust chemical behavior at high temperatures. In order to
overcome this difficulty several "simple-dust-models" have been proposed and
solved. For example, Rakib, Igra and Ben-Dor[6] overcome the difficulties in
formulating the dust chemistry by its replacement with water droplets whose
behavior at high temperatures is well known. In their solution both the argon
and the water droplets were treated as reactive phases. Krier and Mozaffarian[7]
treated a case of normal shock wave propagation into a suspension composed of
air and reactive dust. In order to simulate the dust chemistry at relatively
high temperatures they defined the dust to be a black powder. This definition
enabled them to describe the response of the dust to the relatively high post-
shock temperatures (dust-burning) by a simple pressure controlled burning rate.
In essence, Krier and Mozaffarian[7] overcome the difficulty of describing the
dust chemical reactions by a prescribed fast burning in which a significant
amount of energy is released. This formulation simplified the inclusion of the
dust chemistry in the conservation equations and their subsequent solution.

The purpose of the present paper is to study the effect of a reacting dust
on the post-shock flow field. Unlike previous attempts a realistic burning-
model will be used for a specified dust. In order to present a physically
meaningful model the suspension to be treated is composed of oxygen gas seeded
with carbon dust. The shock wave Mach number will be limited to $M = 5$ for

which the real gas effects in the gaseous phase of the suspension can be ignored. However, the post-shock temperature is high enough to initiate burning of the carbon particles. As will be shown, this burning has a major effect on the relaxation zone.

2. THEORETICAL BACKGROUND

The steady flow field to be solved is shown schematically in figure 1. While crossing the shock front the gaseous phase of the suspension experiences a sudden increase in its pressure, density and temperature and a sudden decrease in its velocity. The magnitude of these changes can be evaluated using the well known Rankine-Hugoniot shock relations.

Unlike the gaseous phase, the solid phase of the suspension crosses shock front unaffected because the diameter of the carbon particles (used in the present solution) is 100 μm while the width of the shock front is of the order of the mean free path (for the present study about 0.1 μm) and the characteristic response time of the solid phase is much longer than that of the gaseous phase. As a result, immediately behind the shock front the two phases of the suspension are no longer in a state of equilibrium. The gaseous phase is relatively hot and is moving relatively slowly while the carbon particles are relatively cold (they are at the pre-shock temperature, $T = 300$ K) and are moving relatively quickly. This difference in temperature and velocity between the two phases of the suspension will stimulate an intense heat and momentum transfer between the two phases. Once the carbon particle temperature reaches the ignition point a combustion process starts. It continues until the carbon diameter is reduced to zero. The flow region where these processes take place is called the relaxation zone. It starts immediately behind the shock front and ends with the carbon disappearance via burning. At the end of the relaxation zone the gas mixture, composed of oxygen and the combustion products, is in a new state of equilibrium.

In the following, the conservation equations describing the flow field in the relaxation zone are listed. Their detailed derivation is given in Ref. 8. The assumptions upon which their derivation was based are:

1. The flow is steady and one-dimensional.
2. The gas mixture (resulting from the carbon burning) can be treated as a mixture of ideal gases.
3. Heat transfer and viscous effects within the gaseous phase can be neglected. (These mechanisms are important in the interaction between the two phases.)
4. All the components of the gaseous phase have the same velocity.
5. The carbon particles are small, rigid spheres of equal diameter, uniformly distributed in the gaseous phase.
6. The volume occupied by the carbon particles is negligibly small in comparison with the suspension volume.
7. There is no temperature distribution within the carbon particle. (This is a reasonable assumption considering the small size of the carbon particles and their relatively high heat conductivity.)
8. Interactions between carbon particles can be ignored.
9. The carbon particle weight and the buoyancy force it experiences are negligibly small in comparison with the drag force.
10. Heat transfer between the two phases is via heat convection only.
11. The thermal motion (Brownian motion) of the carbon particles can be ignored.
12. Ahead of the shock wave the suspension is in a state of complete equilibrium.

13. The carbon burning can be described by the following reaction only,

$$C(s) + O_2(g) \rightarrow CO_2(g) + h_b$$
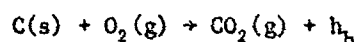
where h_b, the CO_2 heat of formation, is 3.937×10^5 KJ/Kgmole. A justification for this assumption is given subsequently.

14. The heat released by the burning carbon particles is independent of the suspension temperature and/or pressure.

15. The CO_2 gas generated in the combustion process is instantly mixed with the oxygen.

16. During the chemical reaction the CO_2 heat of formation releases into the surrounding gas only.

The conservation equations are:

CONTINUITY - carbon particles

$$\frac{d}{dx}(\rho_c v) = -\frac{M_c \rho_c r_c}{m_c} \tag{1}$$

CONTINUITY - oxygen gas

$$\frac{d}{dx}(\rho_{O_2} u) = -\frac{M_{O_2} \rho_c r_c}{m_c} \tag{2}$$

CONTINUITY - CO_2 gas

$$\frac{d}{dx}(\rho_{CO_2} u) = \frac{M_{CO_2} \rho_c r_c}{m_c} \tag{3}$$

MOMENTUM - carbon particles

$$\frac{d}{dx}(\rho_c v^2) = -\frac{\rho_c}{m_c}(F + M_c r_c v) \tag{4}$$

MOMENTUM - gaseous phase

$$\frac{d}{dx}[(\rho_{O_2} + \rho_{CO_2})u^2] + \frac{dP}{dx} = \frac{\rho_c}{m_c}(F + M_c r_c v) \tag{4}$$

ENERGY - carbon particles

$$\frac{d}{dx}[\rho_c v(C_T + v^2/2)] = \frac{\rho_c}{m_c}[Q - Fv - M_c r_c(C_T + v^2/2)] \tag{6}$$

ENERGY - gaseous phase

$$\frac{d}{dx}[\rho_{O_2} u(C_{p,O_2} T + u^2/2) + \rho_{CO_2}(C_{p,CO_2} T + u^2/2)]$$

$$= -\frac{\rho_c}{m_c}[Q - Fv - M_c r_c(C_T + v^2/2 + h_b)] \tag{7}$$

EQUATION OF STATE

$$P = (\rho_{O_2} R_{O_2} + \rho_{CO_2} R_{CO_2})T \qquad (8)$$

CHANGES IN THE CARBON PARTICLE DIAMETER

$$\frac{dD}{dx} = -\frac{2}{\pi} \frac{M_c r_c}{\sigma_c D^2 v} \qquad (9)$$

Equations (1) - (9) contain nine variables: the carbon dust spacial density ρ_c, oxygen density ρ_{O_2}, carbon dioxide density ρ_{CO_2}, carbon velocity v, gas velocity u, carbon temperature τ, gas temperature T, particle diameter D and the suspension pressure P. For solving equations (1) - (9) the parameters F, r_c and Q (the drag force on the carbon particle, the carbon burning rate and the amount of heat transferred from the gas to the carbon particles, respectively) must be expressed in terms of the above mentioned nine variables. Detailed derivation of these expressions is available in Ref. 8. Due to space limitation it is not given here.

Computational Procedure

The numerical solution of equations (1) - (9) was conducted in two steps. First, the derivatives of the flow variables (du/dx, dv/dx, dT/dx, dτ/dx, dρ_c/dx, dρ_{O_2}/dx, dρ_{CO_2}/dx, dD/dx and dP/dx were evaluated. Thereafter, the flow variable (u, v, T, τ, ρ_c, ρ_{O_2}, ρ_{CO_2}, D and P) were calculated by numerical integration. As a starting value for this integration the appropriate frozen value (as predicted by the Rankine-Hugoniot shock relations) were used. The integration was terminated at the end of the relaxation zone which was defined as the distance at which $D \leq 1$ μm (the carbon particle disappeared). Details regarding the numerical solution of equations (1) - (9) as well as a print-out of the computer program can be found in Ref. 8.

3. RESULTS AND DISCUSSION

In order to demonstrate the effect of the burning carbon particles on the flow properties in the relaxation zone, equations (1) - (9) were solved numerically for the following conditions: shock wave Mach number M = 5, pre-shock pressure P_0 = 50 torr, pre-shock temperature T_0 = 300 K, initial carbon particle diameter D_0 = 100 μm and carbon loading (mass ratio carbon-oxygen) η = 0.05. The solution was repeated for a similar inert particle (no burning) and the results obtained for both cases are shown in Figs. 2 to 6.

The variations in the gas (T) and dust (τ) temperatures in the relaxation zone are shown in Fig. 2. The results are normalized by the pre-shock suspension temperature (T_0 = 300 K). Immediately behind the shock front the gas temperature experiences a sudden raise (according to the Rankine-Hugoniot shock relations) while the carbon particles pass through the shock front unaffected. Because of this large temperature difference, between the two phases, an intense heat transfer from the gas to the carbon particles takes place and as a result the carbon particles are heated and the gas is cooled; see Fig. 2 for $0 < x < 8$ m. As could be expected, until the carbon ignition identical temperature variations are obtained for the two cases (active and inert particles). This is no longer the case after the start of carbon burning ($x \approx 8$ m). From that point on, the gas and dust temperatures in the suspension containing the burning carbon particles are higher than those obtained for a similar inert case. The reason for this is quite simple; during the carbon oxidation the

heat of formation is absorbed by the gaseous and solid phases of the suspension to result in higher values for T and τ in comparison with a similar inert suspension. Since larger amounts of heat have to be transferred between the two phases in the reactive case, the extent of the relaxation zone is longer than that obtained for a similar inert suspension (see Fig. 2). In the reactive case the post-shock equilibrium suspension temperature is 60% higher than the temperature of the inert case.

The kinematic 1 behavior of the suspensions (reactive and inert) is shown in Fig. 3. The gas (u) and carbon (v) velocities are normalized by the pre-shock speed of sound (a_0 = 330 m/s). The carbon particles enter the relaxation zone with the pre-shock suspension velocity (in the present case it is five times the pre-shock wave speed of sound), while the gaseous phase experiences a sudden decrease in its velocity when it crosses the shock front. The relative velocity between the two phases which is initially quite high, is reduced rapidly due to momentum change between the carbon particles and the gas. As in the temperature variations, here, too, until the carbon ignition both suspensions (reactive and inert) follow identical patterns; see Fig. 3 for 0 < x < 8 m. After the carbon ignition the velocity profiles differ significantly. In the reactive suspension, part of the released thermal energy is converted to kinetic energy resulting in an increase in both the gas and the carbon velocities; see Fig. 3. In the reactive case the post-shock equilibrium velocity is 100% higher than that obtained in the similar inert suspension. Furthermore, while the inert suspension reaches uniform and constant velocity fairly quickly (at x ≈20m) it takes about 80 m for the reactive suspension to reach an equilibrium velocity.

In the inert suspension the only mechanism through which equilibrium suspension velocity is reached is the viscous interaction between the two phases manifested as a drag force which acts on the carbon particles. This force is strongly dependent upon the relative velocity v-u. As a result, for the inert suspension the gas and dust velocities approach each other asymptotically and each behaves monotonically; see Fig. 3. In the reactive suspension two forces are acting on the carbon particles -- the drag force F, and a force generated by momentum disappearance due to burning. As the two velocities, u and v, approach each other, the drag force becomes of secondary importance and the "burning force" becomes the dominant one. The latter causes the carbon particles to be decelerated to velocities lower than the gas velocity, v < u. Now the drag force changes its direction (since v < u) and it causes the dust to be accelerated to the gas velocity (see Fig. 3).

Variations in the gas density, ρ_g, the oxygen gas density, ρ_{O_2}, and the carbon dioxide gas density, ρ_{CO_2}, in the relaxation zone are shown[2] in Fig. 4. All values are normalized by the pre-shock gas density, ρ_0 = 0.085 kg/m³. As could be expected, until the start of carbon ignition identical variations are observed in ρ_g for the two suspensions (reactive and inert). Furthermore ρ_g is equal to ρ_{O_2} and ρ_{CO_2} = 0 until the carbon burning starts. Up to this point ρ_g increases monotonically with distance. This increase is expected because of the monotonic decrease in the gas velocity, u (see Fig. 3). For a steady, inert one-dimensional flow the continuity equation is $\rho_g u$ = const. Obviously when u decreases ρ_g must increase. Once the burning starts the variations in ρ_g differ from that observed for the inert suspension. Now, due to the carbon oxidation a new species is generated -- CO_2. Its production depletes the amount of O_2 molecules in the suspension. It is therefore expected that after ignition ρ_{CO_2} will increase while ρ_{O_2} will decrease and this pattern should persist as long as the carbon burning continues. This, indeed, is the case as is evident from Fig. 4. It is also apparent from Fig. 4 that in the reactive suspension ρ_g decreases with increasing distance, as long as the carbon particles burn. This

behavior should be expected from observing the continuity equation for the suspension which is $\rho_g u + \rho_c v$ = const. Excluding the early part of the relaxation zone $u \simeq v$, see for $x \geq 10$ in Fig. 3. Therefore, the above-mentioned continuity equation can be approximated by $(\rho_g + \rho_c) u$ = const. It was shown in Fig. 3 that due to the carbon burning, the gas velocity, u, increases in the relaxation zone in comparison with a similar inert suspension case. Therefore $(\rho_g + \rho_c)$ must decrease. In the present solution the mass ratio, carbon to oxygen gas η, is equal to 0.05; therefore $\rho_g \gg \rho_c$ throughout the relaxation zone. As a result, in spite of the fact that ρ_c decreases in the relaxation zone (see Fig. 5), the reduction in ρ_c is too small to ensure a decrease in $(\rho_g + \rho_c)$ without having a meaningful reduction in ρ_g, as is shown in Fig. 4.

The behavior of the carbon spacial density, ρ_c, in the relaxation zone, is shown in Fig. 5. In the inert suspension case ρ_c reaches a plateau; when the carbon particles burn a maximum in ρ_c is reached at the ignition point, thereafter ρ_c decreases monotonically until the carbon particles disappear via burning. Like the changes in the other suspension properties, identical variations in ρ_c are observed for both suspensions (reactive and inert) up to the carbon ignition.

Variations in the suspension pressure are shown in Fig. 6. The results are normalized by the pre-shock suspension pressure, P_o = 50 torr. As expected, up to the carbon ignition point both suspensions show the same behavior -- an increase in the static pressure with increasing distance measured downstream of the shock front. This behavior can easily be explained. For a steady, inert one-dimensional suspension flow the momentum equation is: $P + \rho_g u^2 + \rho_c v^2 = C_1$. Furthermore, from continuity $\rho_g u = C_2$ (for the gaseous phase) and $\rho_c v = C_1$ (for the solid phase) where C_1, C_2 and C_3 are constants. The momentum equation can be written alternatively as: $P + C_2 u + C_3 v = C_1$. It was shown before that u and v decrease in the pre-ignition part of the relaxation zone (Fig. 3). Therefore, based on the last expression for the momentum equation it is apparent that P must increase up to the carbon ignition point, as is shown in Fig. 6. Once the carbon ignition starts, the pressure variations for the burning suspension differs from that of the inert case. While the inert suspension is reaching a pressure plateau, in the reactive one the pressure reduces monotonically after the carbon ignition. This, of course, is expected since during burning both u and v increase, in comparison with the values obtained for the inert case. For the considered case, the post-shock equilibrium pressure is about 20% lower than the value of the inert suspension. The extent of the relaxation zone for the burning carbon particles case is significantly longer than that obtained in a similar inert case. It takes about 80 m until an equilibrium pressure is reached for the burning carbon particles case while an equilibrium pressure is reached after about 20 m only for the inert case (see Fig. 6).

4.   SUMMARY AND CONCLUSIONS

The conservation equations for a suspension composed of oxygen gas and solid carbon particles through which a normal shock wave is passing with a constant velocity were formulated and solved numerically. It was shown that the carbon particle burning caused by the relatively high post-shock wave gas temperature has a major effect on the suspension properties in the relaxation zone and the eventually reached post-shock equilibrium state. For example, it was shown that higher temperatures and velocities are obtained in the relaxation zone of the burning suspension as compared with a similar inert case. On the other hand, the static pressure and gas density of the burning suspension are lower than the values obtained for a similar inert case. In the considered

case (M = 5, P_0 = 50 torr, D_0 = 100 μm and η = 0.05) the post-shock equilibrium
suspension temperature is 60% higher than that obtained in a similar inert
case, the equilibrium velocity is almost double that of the inert case and the
post-shock equilibrium suspension pressure is 20% below the inert suspension
value. In addition to its effect on the suspension properties, burning of the
carbon particles significantly extends the relaxation zone. The ratio between
the lengths of the kinematic relaxation zones for active and inert suspensions
is about four.

REFERENCES

1. Carrier, G.F., "Shock Waves in a Dusty Gas," Journal of Fluid Mechanics,
   Vol. 4, 1958, pp. 376-382.

2. Kriebel, A.R., "Analysis of Normal Shock Waves in a Particle-Laden Gas,"
   ASME Journal of Basic Engineering, Vol. 86, 1964, pp. 655-665.

3. Rudinger, G., "Some Properties of Shock Relaxation in Gas Flows Carrying
   Small Particles," Physics of Fluids, Vol. 7, 1964, pp. 658-663.

4. Ben-Dor, G. and Igra, O., "The Relaxation Zone behind Normal Shock Waves
   in a Reacting Dusty Gas. Part 1, Monatomic Gases," Journal of Plasma
   Physics, Vol. 27, 1982, pp. 377-395.

5. Igra, O. and Ben-Dor, G., "The Relaxation Zone behind Normal Shock Waves
   in a Dusty Reacting Gas. Part 2, Diatomic Gases," Journal of Plasma
   Physics, Vol. 31, 1984, pp. 115-140.

6. Rakib, Z., Igra, O. and Ben-Dor, G., "The Effect of Water Droplets on the
   Relaxation Zone Developed behind Strong Normal Shock Waves," ASME Journal
   of Fluids Engineering, Vol. 106, 1984, pp. 154-159.

7. Krier, M. and Mozaffarian, A., "Two-Phase Reactive Particle Flow through
   Normal Shock Waves," International Journal of Multiphase Flow, Vol. 4,
   1977, pp. 65-79.

8. Elperin, I., "The Effect of Carbon Particles on the Flow Field Developed
   behind a Normal Shock Wave in Oxygen," M.Sc. Thesis, Department of
   Mechanical Engineering, Ben-Gurion University of the Negev, 1984.
   (in Hebrew)
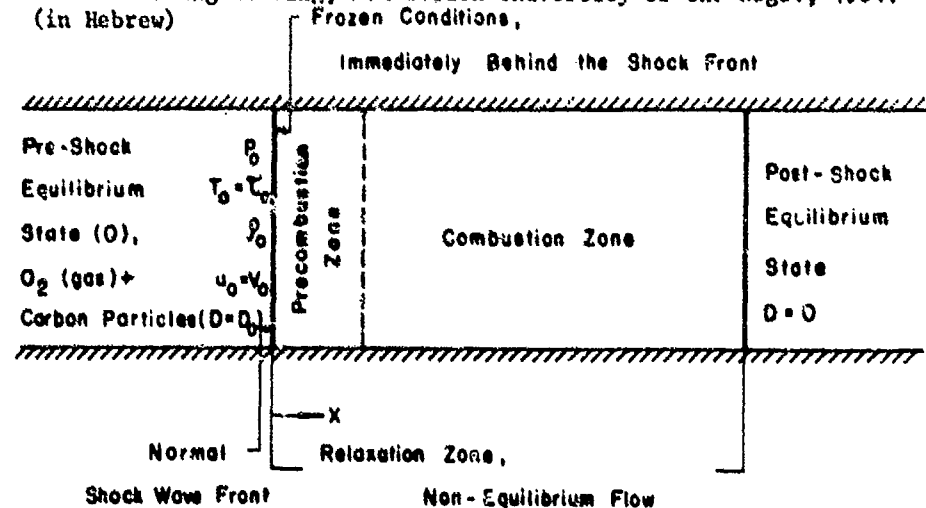
Fig. 1 Schematic description of the considered flow field.

Fig. 3 Variations in the gas (u) and the carbon (v) velocities in the relaxation zone. ——— Reactive suspension, - - - inert suspension.
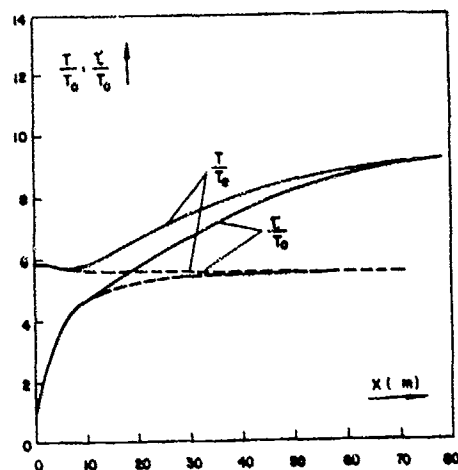
Fig. 2 Variations in the gas (T) and the carbon particles (τ) temperatures in the relaxation zone. ——— Reactive suspension, - - - inert suspension.
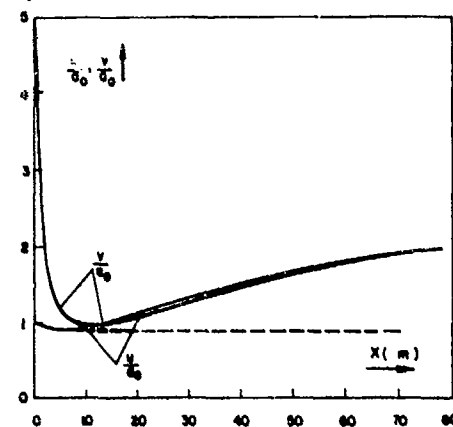
Fig. 5 Variations in the carbon space density in the relaxation zone. ——— Reactive suspension, - - - inert suspension.

Fig. 4 Density variations in the relaxation zone. ——— Reactive suspension. - - - inert suspension.

Fig. 6 Pressure variations in the relaxation zone. ——— Reactive suspension, - - - inert suspension.
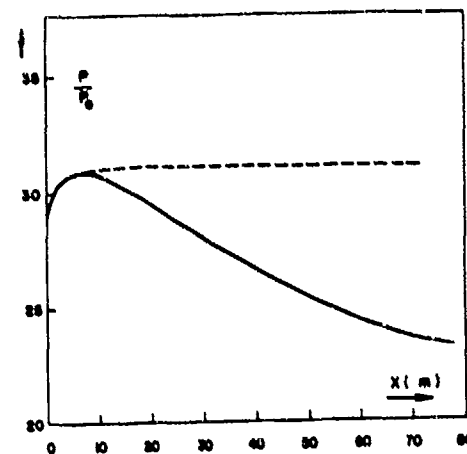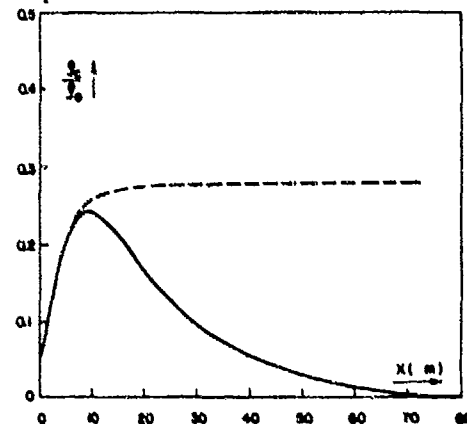
SHOCK WAVES IN BINARY GAS MIXTURES

R. Herczynski, M. Tarczynski and Z. Walenta

Department of Fluid Mechanics, Institute of Fundamental
Technological Research, Polish Academy of Sciences
Swietokrzyska 21, 00-049 Warsaw, Poland

Experimental and theoretical research on shock
wave structures in binary mixtures of very
heavy and very light gases are presented. The
experiments were performed in a shock tube
(with simultaneous use of an electron gun
and laser differential interferometer) and in
a low density wind tunnel (using electron
beam luminescence method). The theory is based
on a new kind of variational technique. The
results indicated very strong separation of
the component gases inside the shock wave.
Mach number and temperature influence on the
shock structure were also considered.

1. INTRODUCTION

Preliminary results from the shock tube experiments in helium
and xenon mixtures (the lightest and the heaviest of the noble
gases) indicate that a shock wave structure is, in this case,
strongly deformed and differs from the classic shock structure. On
the oscillograms one can see the additional inflection point and
a sort of a "hump". This hump occurred under different experimental
conditions and, contrary to our expectations, was found not to be
an artifact.

We introduced a new method of measurement which enables us
to determine, in the shock tube, the density distribution of each
component separately. The technique used simultaneous measurement
by both electron beam attenuation and and laser differential
interferometry. Because these methods are based on different
physical principles, the first exploiting the scattering effect,
the second sensitive to the change of the index of refraction, we
were able to obtain experimentally the density distributions of
each component of the mixtures separately.

The density distributions of helium and xenon inside the shock
wave zone indicated a strong separation of the mixture species.

The assumption that this strong separation of species is the
cause for the "humped" shock wave structure appears to be valid.

The investigation of shock wave structure in gas mixtures was performed for years. The nonequilibrium effects, among others, manifest themselves by separation of the component gases within the shock wave, which leads to pronounced broadening of the shock wave thickness. This effect was calculated and measured by a number of authors [1-4]. They found that species separation inside the shock zone depends on the molecular mass ratio of mixture components and on the composition of the mixture. The most pronounced effect of separation should be visible in a mixture with disparate molecular masses and comparable weights of components. The mixture of helium and xenon with 3 per cent (by volume) seems to be the case with the strongest separational effects among mixtures of noble gases.

Further investigation should give answers to the following questions:

1. What is the influence of gas parameters on the separation phenomena and the shock wave structure?
2. How to explain the humped shock wave theoretically?

2. THE INFLUENCE OF MACH NUMBER ON SHOCK WAVE STRUCTURE

Measurements made in a shock tube offer an answer to the part of the first question. The experiments were performed in two series: for Mach numbers ranging from 3.5 to 5.0 and for lower Mach numbers ranging from 1.6 to 1.8. Each series was used on two different percentage mixtures, since we were looking for strong separation effects, we used only mixtures with a small amount of xenon - less than 9 per cent by volume. Some of these measurements have already been presented at XI RGD Symposium in Cannes [5].

In each series the temperature in front of the shock was equal to room conditions, i.e., about 300K.

Conditions for each shock tube experiment are summarized in Table I.

Table I
Conditions of the experiments in the shock tube.

A	B	C	D	E
4.38	300	3.0	86.0	1.24
5.00	300	6.0	90.2	1.06
1.54	300	3.0	224.8	0.47
1.66	300	6.0	225.8	0.42

A - Mach number
B - Temperature T^- in front of the shock (K)
C - Concentration of xenon (%)
D - Initial pressure of mixture (μm Hg)
E - Mean free path of the mixture in front of the shock (mm)

The results are shown in Figs. 1 through 4. Each Figure is the result of one test run. In each Figure two curves are presented:

one representing helium density distribution, and the other, xenon density distribution.

In both cases of the first series, performed with high Mach numbers, the humped structure is clearly visible. The details of the strong shock measurements and preliminary description of the mechanism of the hump formation were given in previous paper [ ].

The structures of shock waves for low Mach numbers, those in the second series of measurements, are similar to the classic hyperbolic tangent shape structure.

The separation of the mixture components relative to the shock wave thickness is, in the first case, much more pronounced than in the second case. But the shock wave thickness in both cases is much higher than in pure gases and this is in agreement with current theories and experiments.

3. THE THEORETICAL FINDINGS

Because of very strong nonequilibrium effects produced by shock waves in mixtures of gases with disparate molecular masses, the theoretical description is based on kinetic theory of gases.

It is not possible to solve the full Boltzmann equation even for the case of the plain shock wave, and the problem of describing the shock wave structure in mixtures of gases with disparate molecular masses is much more complex. An attractive variational method of approximate solution of the Boltzmann equation was proposed by Tamm. The method used initially for hard spheres molecules was extended to more realistic potentials (i.e., Lennard Jones potential) and also for gas mixtures [ ]. This theory predicted the existence of the "hump" in the shock wave structures in mixtures of gases with disparate molecular masses.

The sample of theoretically calculated results for 6.0 per cent mixture are shown in Figs 5 and 6. The first Figure shows density distribution of helium and xenon, the second, shows temperature distribution.

The physical picture offered by this theory in the case of shock waves one-component gas is the following: the shock wave structure depends on two non-dimensional parameters, beside the Mach number, on the Fi number (to honour Professor Wladyslaw Fiszdon) defined as $Fi = \mathcal{E}/kT^-$, where $\mathcal{E}$ - the depth of the potential well, ι - the temperature in front of the shock, k - the Boltzmann constant. The Fi number is therefore a ratio of two energies, the first associated with the atomic structure, the second with the mean energy of the medium in front of the shock wave.

This theory predicted the influence of temperature on the shock thickness and structure, both in the case of pure gas and gas mixtures. The effect of T^- seems to be related to the fact that for molecular collisions with lower energy the potential well influences the process of collision to a greater extent than for collisions with greater energy, the "efficiency" of impulse exchange for low energy is lower. This is also the physical reason behind the theoretical prediction of very high temperature overshoot of the heavy component. The Fi number affects the shock wave in a way similar to the Mach number, the rise of Fi leads to the thickening of the shock wave. The theory fails however to give accurate quantitative characteristics of the shock wave, the separation effect found in the experiment is larger than that given by theory.

4. TUNNEL EXPERIMENTS

The theoretically predicted temperature T^- influence on the shock wave structure and temperature overshoot of heavy component needed an experimental confirmation. Both of these problems, because of experimental difficulties, were impossible in shock tube experiments.

Experiments to confirm temperature influence and overshoot are possible only in stationary conditions, were the time for measurement is appropriately long. For this reason further research on shock wave structure in a mixture was performed in a specially designed and build small scale low density wind tunnel. This setup produced a supersonic jet of rarefied gas. The time of measurements was practically unlimited. The diameter of the jet was about 4 cm, preasure in the flowing gas was about 10^{-1} milimeters of mercury, the Mach number was about 2, and the gas temperature, T^-, about 100K. The model was placed in the jet and in front of it the shock wave was formed.

The electron beam induced luminescence method was used to investigate the shock wave characteristics. This method enables us to obtain the density profile of each component of the mixture separately, by measuring the intensity of the spectral lines characteristic for each gas. Using this method, it is also possible, in principle, to obtain the temperature profile of each species, by measuring the Doppler broadening of spectral lines.

Unfortunately, since the signals were very low, temperature measurements could not be made, and research on the theoretically predicted overshoot of the temperature of the heavy component within the shock wave is still to be done.

The influence of the temperature T^- on the shock wave structure in He-Xe mixtures was investigated. As it is impossible in shock tube to create the temperature differences (in front of the shock) necessary to make a meaningful measurement of the affect of temperature on the shock wave, an experiment using wind tunnel was used for comparision. In the supersonic jet a temperature of 100K could be obtained, while in the shock tube 300K could be achieved with the same Mach number. The comparision of results coming from the jet and shock tube enable us to confirm the second prediction of the theory, about the influence of kinetic temperature in front of the shock wave.

The jet experiments were performed for mixtures of 3.08, 6.23 and 9.53 per cent of xenon. The density profiles of helium and xenonfor each mixture (in the case of 3.08 per cent xenon mixture, since the amount of xenon in the mixture is very small, the signals from xenonlines were so low that was impossible to measure the xenon density profiles) are shown in Figs. 7 - 9.

Conditions for each tunnel experiment are summarized in Table II.

The humped structures appear in the case of mixtures of 3.08 and 6.23 per cent of xenon. The hight of the first step, similar to the shock tube experiments, decreases with the rise of xenon concentration. This suggests that the front part of the signal is mainly due to the compression of the light component. For the 9.53 per cent mixture, the front part of the signal is so small that the humped structure nearly disappears. For detailes see reference 7.

At this point, it is important to point out the differences between conditions in the case of shock tube and jet experiments. In the shock tube, the gas in front of the shock can be assumed to

be uniform, while the supersonic jet, downstream from the nozzle, is slightly divergent, thus the density of gas in the jet decreases along the axis. The shock wave structures presented in the Figures are a result of a procedure which consists of subtracting the density distribution in the case when there is no model in the jet from the profiles with the model in the jet.

Table II
Conditions of experiments in the wind tunnel

A	B	C	D	E
2.0	100	3.08	200	2.6
2.0	100	6.23	200	1.8
2.0	100	9.53	200	1.6

For symbol meaning see Table I.

5. CONCLUSIONS

The experimental findings can be summarized in the following way:

In the mixtures of helium and xenon containing no more than about 6 per cent of heavy component by volume

- strong shock waves (Mach number about 4) generated in the shock tube, i.e., at the initial temperature about 300K, have a definite "humped" structure,

- much weaker shock waves generated in the low density wind tunnel (Mach number about 2), i.e., at the initial temperature about 100K, have the same kind of "humped" structure, perhaps more pronounced,

- shock waves in the same range of Mach number as in the wind tunnel, generated in the shock tube, i.e., for initial temperature 300K, do not exhibit the "humped" structure.

In all reported experiments a very pronounced broadening of the shock wave was observed. However due to the shape of the shock wave the commonly used shock wave thickness characteristic, the Prandtl shock thickness is of no more use.

These results are in qualitative agreement with the theoretical predictions of a shock structure dependence on temperature T. The Fi number in the case of jet experiments is much higher than in the case of shock tube measurements.

Although the theory provides a fair qualitative description, including both the broadening of the shock wave as well as its humped structure, it fails to give quantitatively correct value of the separation of species.

Work in the open field of temperature overshoot measurements is now in progress.

6. REFERENCES

1. L.N. Harnett, E.P. Muntz, Phys. Fluids, 15, 4, 1972
2. E. Goldman, L. Sirovich, J. Fluid Mech., 35, 3, 1969
3. R.E. Center, Phys. Fluids, 10, 1777, 1967
4. B.B. Hamel, X RGD Symposium, 1976
5. A. Gmurczyk, M. Tarczynski, Z. Walenta, XI RGD Symposium, 1979
6. M. Bratos, R. Herczynski, Arch. Mech., 35, 2, 1983
7. M. Tarczynski, Ph.D. Dissertation, IFTR Warsaw, 1985
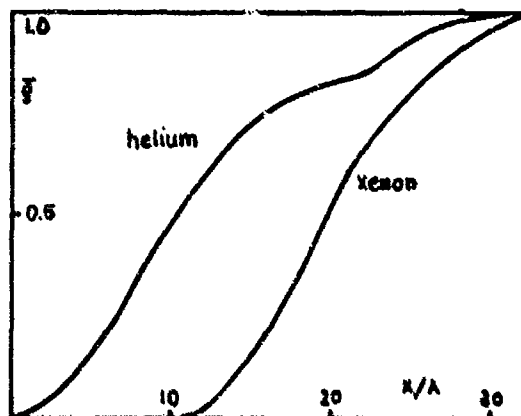
Fig. 1. Shock tube experiments 3.0% mixture, M_s = 4.38, T^* = 300K.
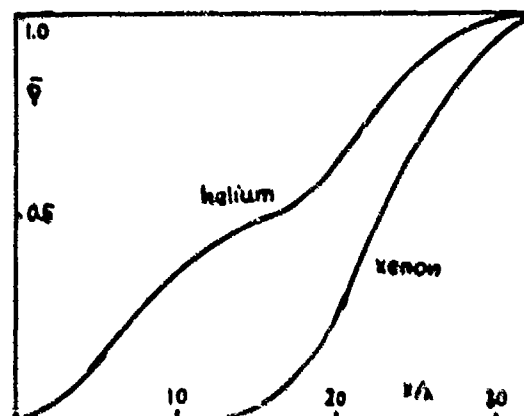
Fig. 2. Shock tube experiments 6.0% mixture, M_s = 5.00, T^* = 300K.
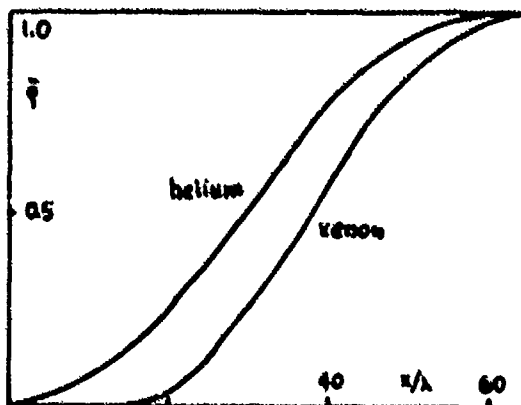
Fig. 3. Shock tube experiments 3.0% mixture, M_s = 1.54, T^* = 300K.
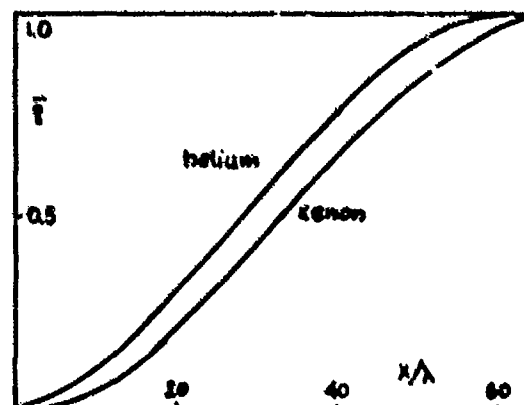
Fig. 4. Shock tube experiments 6.0% mixture, M_s = 1.66, T^* = 300K.
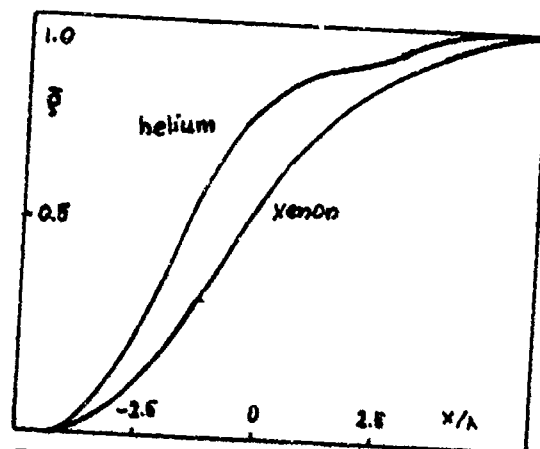
Fig. 5. Theoretical calculation
6.0% mixture, M = 2.5,
density profiles.
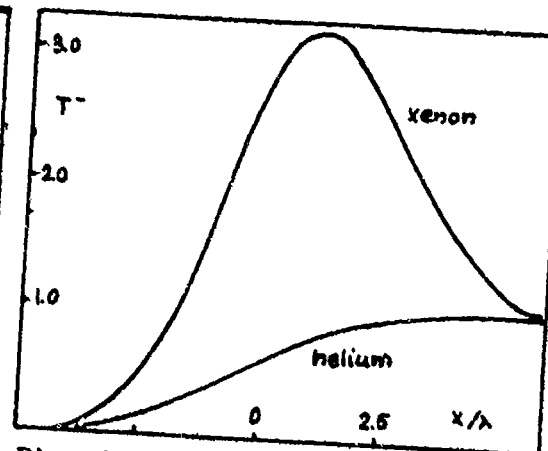
Fig. 6. Theoretical calculation
6.0% mixture, M = 2.5,
temperature profiles.
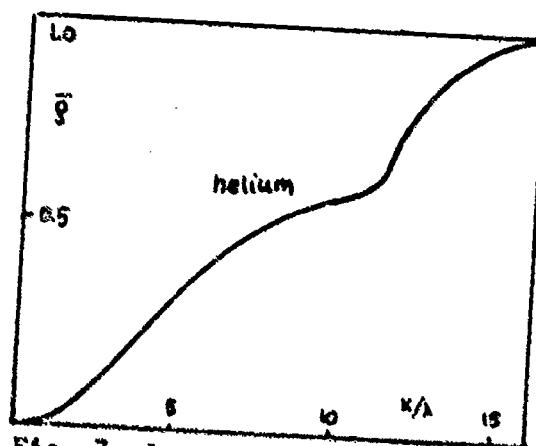
Fig. 7. Jet experiments
3.08% mixture, M = 2.0,
T = 100K.
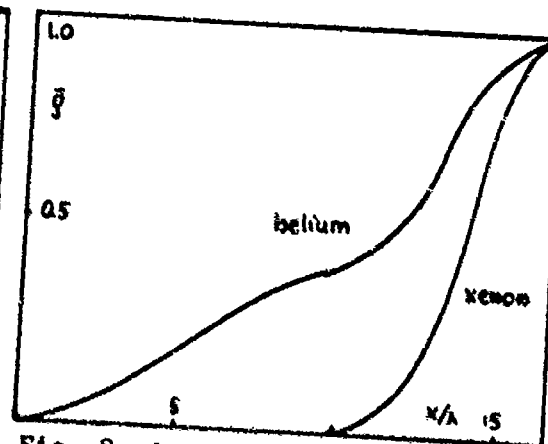
Fig. 8. Jet experiments
6.23% mixture, M = 2.0,
T = 100K.
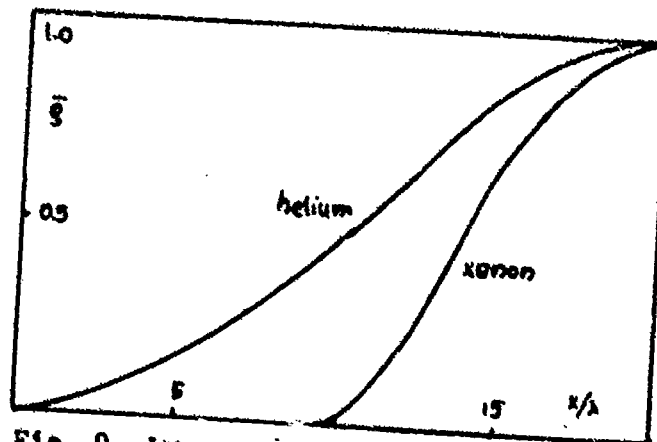
Fig. 9. Jet experiments
9.53% mixture, M = 2.0,
T = 100K.

where
x - distance
λ - mean free path
$\bar{\rho}$ - normalized
    density
$\bar{T}$ - normalized
    temperature

EXPERIMENTAL INVESTIGATION OF WEAK SHOCK WAVES, PROPAGATING IN A FOG

H.W.J. Goossens, M.J.C.M. Berkelmans and M.E.H. van Dongen

Eindhoven University of Technology
Department of Physics, Eindhoven, The Netherlands

Shock wave propagation in a fog is investigated
experimentally. The fog is produced by means of
an adiabatic expansion of a mixture of nitrogen
and water vapour in the test section of a shock
tube. Measurements of pressure, density and light
transmission are made to observe shock structure
and relaxation processes. The frozen and equilibrium
values of pressure and density are in good agreement
with theory. Preliminary results are shown of the
structure of the relaxation region where the droplets
evaporate. A comparison is made with a simple
theoretical model, the agreement being satisfactory.

1. INTRODUCTION.

Phase transition has a noticeable effect on the thermodynamic state of a
mixture of water droplets, vapour and carrier gas. The propagation and the
structure of weak shock waves in such a medium is quite strongly affected by
the presence of the droplets even at low values of the droplet mass fraction.

Shock wave propagation through gas-particle mixtures has been a subject of
numerous investigations, partly concerning the calculation and measurement of
the shock structure in dusty gases[1-9]. In many practical situations however,
gas-particle mixtures consist of suspensions of liquid droplets in a carrier
gas. In addition to heat and momentum transfer, mass transfer becomes an
important factor in these systems.

In the present paper, attention is focussed on shock wave propagation and
subsequent relaxation processes in an aqueous fog which is produced by a fast
adiabatic expansion of humid nitrogen. A related theoretical study was reported
by Marble[10] and experimental investigations on shock induced droplet evaporation
were carried out by Hastings and Hodgson[11] and Roth and Fischer[12].

2. THEORY

2.1. FROZEN AND EQUILIBRIUM POST SHOCK STATE

We will assume that the gas and vapour behave as calorically perfect gases
with equal velocity and temperature and that the droplets do not contribute to
the pressure, whilst the water mass fraction expressed in terms of the densities
as $K_w = (\rho_v + \rho_d)/\rho$, is a constant. Denoting the different constituents by means
of the subscripts g, v, d we have the following expressions for the density ρ,
the velocity u and the enthalpy h:

$$\rho = \sum_i \rho_i, \quad \rho u = \sum_i \rho_i u_i, \quad \rho h = \sum_i \rho_i h_i, \quad i = g, v, d \tag{1}$$

$$h_g = C_g T, \quad h_v = C_v T + L_r, \quad h_d = C_d T_d, \quad L = L_r + (C_v - C_d) T_d \tag{2}$$

where L is the latent heat per unit mass, L_r is the value of L at 0 K and c_i is
the heat capacity at constant pressure. For the pressure we have:

$$P = P_g + P_v = \rho_g R_g T + \rho_v R_v T \tag{3}$$

In equilibrium P_v and ρ_v are related to T by the Clausius-Clapeyron expression, with P_v^* and T^* as reference values:

$$P_v = P_{vs}(T) = \rho_{vs} R_v T = P_v^* (\frac{T}{T^*})^{(C_v - C_d)/R_v} . \exp\{\frac{L_r}{R_v}(\frac{1}{T^*} - \frac{1}{T})\} \tag{4}$$

In a reference frame in which the shock is stationary the initial mixture is moving with a constant velocity u_0. A good approximation of both the frozen post-shock state (f), in which the droplets are not yet affected, and the final equilibrium state (e) satisfies the following basic conservation laws:

$$[\rho u]_{f,e} = \rho_0 u_0 \tag{5}$$

$$[P + \rho u^2]_{f,e} = P_0 + \rho_0 u_0^2 \tag{6}$$

$$[\tfrac{1}{2}u^2 + h]_{f,e} = \tfrac{1}{2}u_0^2 + h_0 \tag{7}$$

The frozen state is a solution of eqs. (5)-(7), subject to the additional conditions:

$$f: \; T_d = T_0, \quad u_d = u_0, \quad \rho_d = \rho_0 \tag{8}$$

while the equilibrium state is a solution of the same eqs., but subject to:

$$e: \; \rho_d = 0 \; \text{ or to: } \; T_d = T, \quad u_d = u, \quad P_v = P_{vs}(T) \tag{9}$$

2.2. THE RELAXATION REGION

The transport equations describing the structure of the relaxation zone are based on those discussed extensively by Marble[10]. We will use them in the following form:

$$\frac{d}{dx} (\rho_g u_g) \qquad = 0 \tag{10}$$

$$\frac{d}{dx} (\rho_v u_v) \qquad = - \frac{d}{dx} (\rho_d u_d) = \mu_v \tag{11}$$

$$\frac{d}{dx} ((\rho_v + \rho_g) u_g^2 + P) \qquad = -F_d + \mu_v u_m \tag{12}$$

$$\frac{d}{dx} (\rho_d u_d^2) \qquad = F_d - \mu_v u_m \tag{13}$$

$$\frac{d}{dx} \sum_{g,v} (\rho_i u_i (\tfrac{1}{2}u_i^2 + h_i)) = -F_d u_d + \mu_v (h_d + L + \tfrac{1}{2}u_m^2) \tag{14}$$

$$\frac{d}{dx} (\rho_d u_d (\tfrac{1}{2}u_d^2 + h_d)) \qquad = F_d u_d - \mu_v (h_d + L + \tfrac{1}{2}u_m^2) + Q \tag{15}$$

where $u_m = u_d$ for condensation, and $u_m = u_g$ for evaporation. For the source terms of mass, momentum and energy, the following expressions were used in the calculations:

$$\mu_v = \frac{6\rho_d D}{d^2 \rho_\ell} \{\rho_{vs}(T_d) - \rho_v\}\{2 + 0.6Sc^{1/3}.Re^{1/2}\} \tag{16}$$

$$F_d = \frac{18\rho_d \eta}{d^2 \rho_\ell} \{u_g - u_d\}\{1 + \frac{1}{6}Re^{2/3}\} \tag{17}$$

$$Q = \frac{6\rho_d \lambda}{d^2 \rho_\ell} \{T_d - T_g\}\{2 + 0.6 Pr^{1/3}.Re^{1/2}\} \tag{18}$$

In these expressions, D is the binary diffusion coefficient, η is the viscosity, λ is the thermal conductivity, ρ_ℓ is the liquid density, and d is the droplet diameter. The Schmidt, Reynolds and Prandtl numbers are defined as:

$$Sc = \frac{\eta}{(\rho_v + \rho_d)D} \quad ; \qquad Re = \frac{d(\rho_v + \rho_g)(u_g - u_d)}{\eta} \quad ; \qquad Pr = \frac{\eta C_{v,g}}{\lambda} \tag{19}$$

The expressions (16)-(18) are valid in the continuum regime, for Reynolds numbers in the range 1-500. The droplets are spherical and have no mutual interaction and the contribution of the overall pressure gradient to the interaction force is neglected.

3. EXPERIMENTS

3.1. EXPERIMENTAL SET UP

The experiments have been performed in a shock tube which is shown schematically in figure 1. The test section consists of a Ni-coated steel tube with an internal square cross section of side 0.1 m and a length of 7.76 m. The tube is by-passed by a recirculation system which is used to mix the gas and the vapour. The high pressure section has a length of 2.52 m. The low pressure part consists of a 0.4 m³ steel vacuum vessel. The test section is separated from the other sections by polyester membranes of 24 μm thickness. These membranes are supported on metal wires and can be bursted by heating the wires electrically.

Prior to the experiment, all parts of the shock tube are evacuated. The test section is supplied with vapour until the desired pressure is reached. The tube is filled to atmospheric pressure with pure nitrogen and the gas and vapour are mixed. Correcting for the absorption of vapour by the shock tube walls is done. After bursting the righthand membrane, an expansion wave travels into the test section and reflects at the second membrane. The pressure and temperature of the mixture decrease adiabatically. With a square orifice mounted between the test section and the vacuum vessel, the expansion is controlled in such a manner that the onset of the homogeneous condensation occurs in the reflected wave. Subsequent reflections at the low pressure section can be suppressed by adjusting the initial pressure in the vessel. A more or less static and homogeneous mixture of droplets, vapour and gas is obtained using this method. Bursting the second membrane causes a shock wave to propagate through the fog.

3.2. EXPERIMENTAL RESULTS AND COMPARISON WITH THEORY

Transient pressure measurements are recorded with Kistler transducers, type 603B, at various places in the shock tube. At three locations, light transmission measurements are made using a 0.5 mW He-Ne laser, Spectra Physics type 155. The optical sensor has a 1 mm diameter aperture, a focussing lens

and a photodiode. Density measurements are carried out with a Mach-Zehnder interferometer based on a design of Smeets[13]. Using the interferometer in the phase quadrature mode, an accurate and unambiguous determination of density changes is possible even if some of the light from the object beam is scattered by the droplets.

The results of measurements of pressure, density and light transmission at 1.55 m from the orifice are shown in fig. 2A-2C. Calculation of the entropy showed that the decrease of pressure, density and temperature by the expansion wave and its reflection was adiabatic until the moment of condensation which could be determined by the increase of the light extinction (fig. 2C). After the onset of condensation a period of about 60 ms occured in which the state of the fog was fairly constant. The droplet mass fraction has been determined by measuring the temperature rise due to the condensation. The droplet diameter was calculated on the basis of the droplet mass fraction and the experimentally determined value of the extinction coefficient. As to the nonhomogeneity of the pre-shock state, it was found from transmission and pressure recordings that the axial variation of the extinction coefficient was + 15% while the velocity variations were in the range + 10 ms^{-1}. Typical conditions of this pre-shock state were: Temperature 273+5 K, pressure 0.5 bar droplet diameter 2-5 μm, droplet mass fraction $(3+1)*10^{-3}$ to $(6+2)*10^{-3}$.

The shock wave passage was recorded simultaneously with a much higher sample frequency. Results are shown in fig. 2D-2F. In fig. 2D it can be seen that the shock wave consisted of a gas-dynamic shock followed by a relaxation zone. The discontinuity in the density across the shock front which was measured with the Mach-Zehnder interferometer occured over a few microseconds due to the oblique position of the object beam with respect to the wave front. The extinction signal (fig. 2F) shows that the droplets had a rapid velocity relaxation causing the light extinction to increase followed by a much slower relaxation due to evaporation.

The values of the pressure and density behind the shock discontinuity P_f and ρ_f are measured in three series of experiments: 1) pure nitrogen and normal shock tube operation, 2) expanded pure nitrogen followed by shock compression, and 3) a shock wave in a fog. The results of the measurements are presented in fig. 3A, together with the theoretical values predicted by the Rankine-Hugoniot relations for pure nitrogen. All the results coincide and are in good agreement with the theoretical values. It is shown that the gas-dynamic part of the shock in a fog does indeed have a "frozen" character. The equilibrium values of the pressure and density are corrected for the contribution of the side wall boundary layers. For these corrections, the results of the second series of experiments have been used. Corrected values for the equilibrium pressure and density P_e and ρ_e, for two values of the droplet mass fraction, $K_d = \rho_d/\rho$, are shown in fig. 3B together with the results of the theoretical calculations. The calculations show that the P-ρ curve for the equilibrium state of the gas-droplet mixture deviates from the pure gas curve as long as droplets are present in the post-shock state. If the shock wave is strong enough to vaporize all droplets, the curves show a discontinuous slope and become more or less parallel to the pure gas curve. The experiments show the expected tendency although the experimental accuracy is not yet sufficient for a detailed comparison. A numerical solution of the relaxation model of section 2.2. for the conditions of the experiment of fig. 2 has also been plotted in fig. 2F. The agreement is quite satisfactory, regarding the simplicity of the applied model and the uncertainty in the parameters defining the fog.

In conclusion, the experiments show a good qualitative picture of the shock structure, including the various relaxation processes. The measuring procedures showed to be reliable.

REFERENCES

1. Carrier, G.F., "Shock Waves in a dusty Gas", J. Fluid Mech. 4, p. 376, 1958.

2. Rudinger, G., "Relaxation in Gas-Particle Flow", Nonequilibrium Flows,
   part 1, Edited by Wegener, P.P., Marcel Dekker, Inc., New York, 1969.

3. Marble,F.E., "Dynamics of Dusty Gases", Ann. Rev. Fluid Mech. 2, p. 397,
   1970.

4. Miura,H. and Glass, I.I., "On the Passage of a Shock Wave through a Dusty
   Gas Layer", UTIAS Report No. 252, 1982.

5. Rudinger, G., "Flow of solid Particles in Gases", AGARDograph No. 222,
   1976.

6. Outa, E., Tajima, K. and Morii, H., "Experiments and Analyses on Shock
   Waves Propagating through a Gas-Particle Mixture", Bull. JSME 19, p. 384,
   1976.

7. Konig, G. and Frohn, A., "Shock Wave Structure in Gas-Particle Mixtures",
   Proc. 13th Int. Symp. Shock Tubes and Waves, State University of New York
   Press, Albany N.Y., 1981.

8. Sommerfeld, M. and Gronig, H., "Decay of Shock Waves in a Dusty-Gas Shock
   Tube with different Configurations", Proc. 14th Int. Symp. Shock Tubes and
   Waves, New South Wales University Press, Kensington, N.S.W. Australia, 1983.

9. Sommerfeld, M., "Instationare stosswellenausbreitung in Gas-Teilchen
   Gemischen", Dissertation RWTH Aachen, 1984.

10. Marble, F.E., "Some Gasdynamic Problems in the Flow of Condensing Vapours",
    Astronaut. Acta 14, p. 585, 1969.

11. Hastings, D.L. and Hodgson, J.P., "The Formation of an Aqueous Fog in a
    Shock Tube", J. Phys. D. Appl. Phys. 12, p. 2111, 1979.

12. Roth, P. and Fischer, R., "Shock Tube Measurements of Submicron Droplet
    Evaporation", Proc. 14th Int. Symp. Shock Tubes and Waves. New South Wales
    University Press, Kensington, N.W.S. Australia, 1983.

13. Smeets, G., "Laser Interference Microphone for Ultrasonics and Nonlinear
    Acoustics", J. Acoust. Soc. Am. 61, p. 872, 1977.
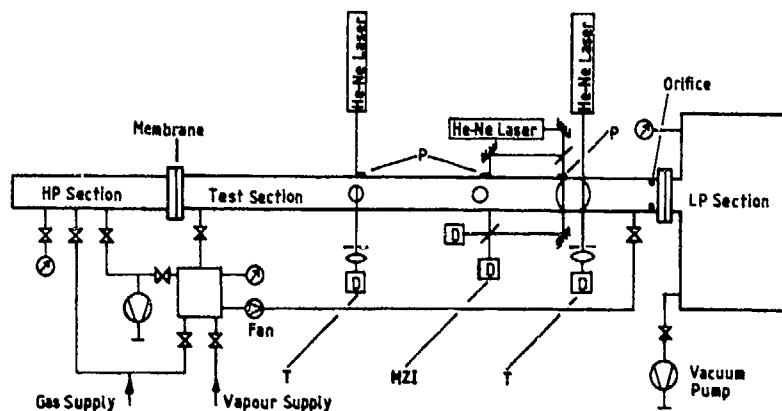
Fig. 1   Experimental setup. T: transmission measurement; P: pressure
transducer; MZI: density measurement.
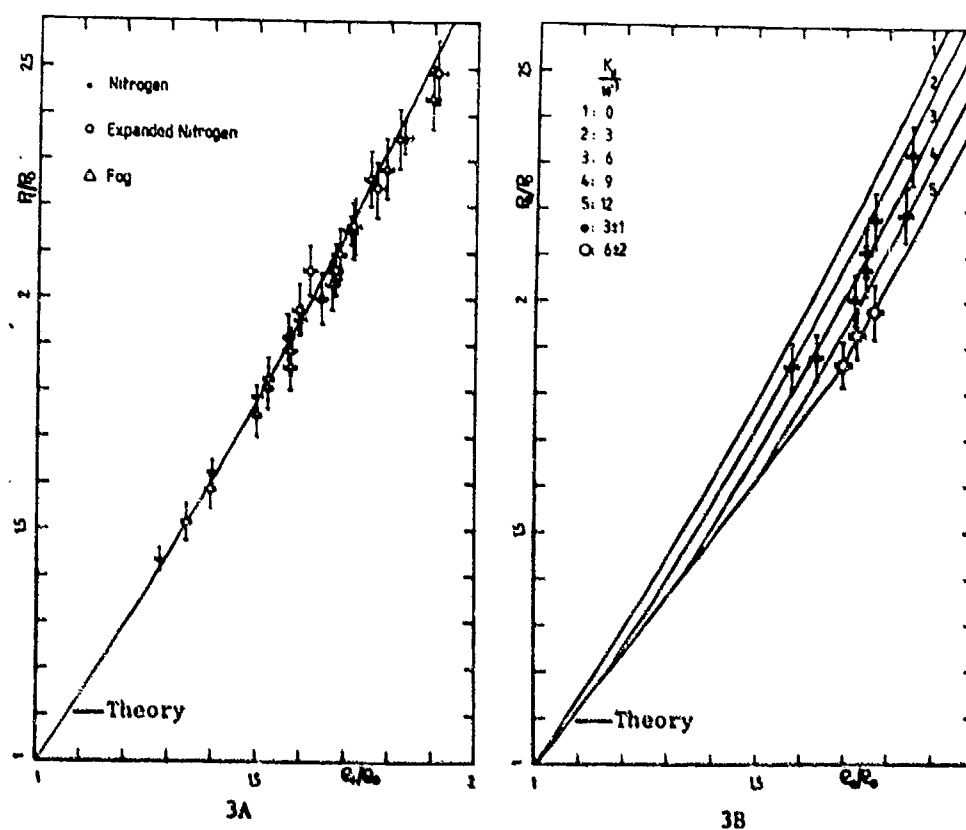
Fig. 3   Pressure- and density values after shock wave passage in different
media. A: Frozen values for 3 different media; B: Equilibrium values
for fogs with various values of the droplet mass fraction.

See next page for figure 2.
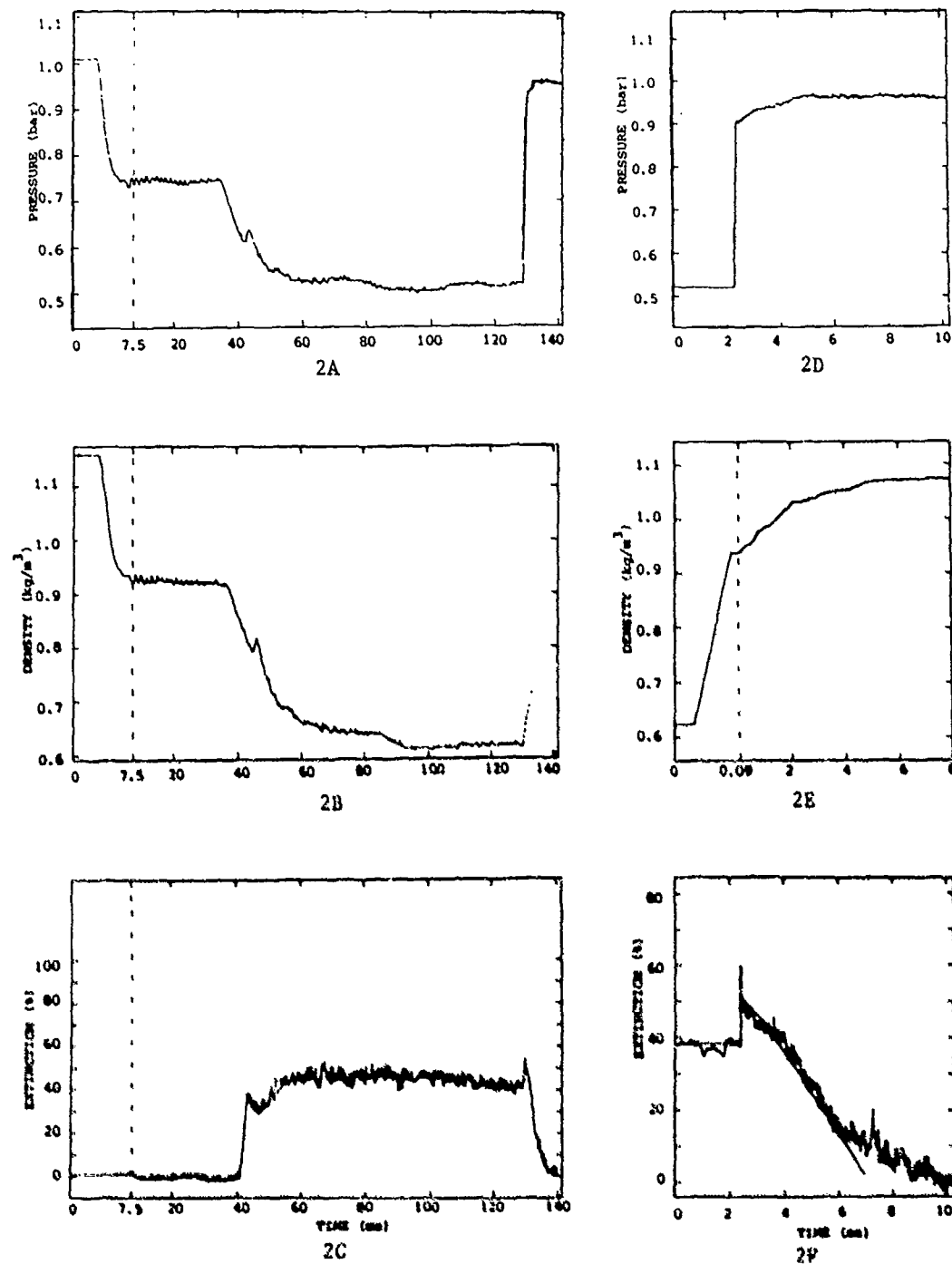
Fig. 2 Experimental recordings of pressure (A and D), density (B and E) and light extinction (C and F) at 1.55 m from the orifice. The pre-shock conditions were: Pressure 0.503 bar; Temperature 273 K; Droplet mass fraction 6×10^{-3}; Droplet diameter 2.1 μm. Calculations of the extinction are plotted in fig. 2F.

PRESSURE INCREASE IN TWO-PHASE MEDIA BEHIND AIR SHOCK WAVES AND

BY SHOCK WAVE ACCELERATED PISTONS

Dr. G. PATZ, Dr. G. SMEETS

Franco-German Research Institute Saint-Louis (ISL)
68301 Saint-Louis, France

In two-phase media we have extremely small sound veloc-
ities in comparison to other materials, therefore when
they are compressed, we find a nearly isothermal behav-
iour because of their special structure. For this reason
we expect very interesting results at compression of two-
phase media. We have compressed different two-phase media
– foams and rubber foam – in a shock tube by air shock
waves of shock mach numbers between $1,5 < M_s < 2$ and by
shock accelerated pistons. Pressure developments and
peak pressures have been recorded. They can also be cal-
culated theoretically with the gasdynamic equations and
are in good agreement with the experimental results. We
have seen that extremely high peak pressures in two-
phase media occur. These peak pressures may be to one
order of magnitude higher than those we will get by com-
pression gases under the same conditions.

1. INTRODUCTION

A two-phase media is defined as the homogeneous mixture of a gas with a
liquid or solid state material. These are for instance foams, lather, powdery
snow or others. These two-phase media have some special properties very differ-
rent of those of their initial components. A special property of these two-
phase media is their very small sound velocity of some 10 m/s. In gases or con-
densed material we have sound velocities of some 100 to 1000 m/s. The density
of such a two-phase medium lies in the order of magnitude of that of a liquid,
but it is compressible and its thermodynamic behaviour is similar to a gas with
high number of degree of freedom of molecules f and with high molecular mass μ.
Consequently the adiabatic exponent $\kappa = \frac{f+2}{f} \approx 1$. This means, that the compres-
sion of a two-phase media takes place at nearly constant temperature. We can
explain this in a simple way by imagining, that the compression heat of the gas
is stored in the structure of the foam which behaves like a heat sink.

In Fig. 1 we can see as an example of a two-phase media the microscopic
picture of the bubble structure of lather. This material was used most often in
our experiments.

The sound velocity of a two-phase media as a function of the volume ratio
$V = V_g/V_k$, where V_g is the portion of the volume of the gas and V_k is the por-
tion of the volume of the condensed part and of the adiabatic exponent κ.

Our analysis was made up of two parts:
1) the direct action of a shock wave on a two-phase medium,
2) the compression of a two-phase medium by a piston which has been accelerated
   by the pressure behind a reflected shock.

2. THE DIRECT INTERACTION OF A SHOCK WAVE ON A TWO-PHASE MEDIUM

2.1 Theory

The upper part of Fig. 2 shows the main operation. The shock tube is filled with the two-phase medium at its closed end. When the shock arrives at the foam surface at x_1, it will be first reflected as had it hit a solid wall. In the lower part of Fig. 2 we see the distance time diagram of what happens in the shock tube. Behind the reflected shock there is the pressure p_R acting on the contact layer between gas and two-phase medium. A shock into the two-phase medium which is reflected at the endwall of the shock tube is now generated, increasing the pressure to p_R'. Since the sound velocity inside the two-phase medium is very slow, the shock will need a long time to reach the end wall. During this time the pressure p_R is acting on the two-phase medium.

The momentum is transmitted to the endwall during the short time, where the pressure p_R' is acting on the endwall (when the contact layer and the reflected shock are coming together). So it is obvious, that p_R' must be higher than p_R.

By means of the one-dimensional conservation laws it is possible to calculate the conditions in the two-phase medium in a similar way as we calculate the gas condition behind a shock front.

Fig. 3 shows the calculated pressure ratio p_R'/p_1 as a function of the pressure ratio p_2/p_1 of the primary shock for different volume ratios V and the two limiting values for the adiabatic exponent κ. It can be clearly seen, that p_R' is higher than the pressure p_R for the completely reflected shock in a two-atomic gas (lower curve).

2.2 Experiments

The experiments have been performed with one of the two high-pressure shock tubes at the ISL (Franco-German Research Institute, Saint-Louis). In Fig. 4 we see the experimental set-up. At the end of the shock tube we placed the test chamber, which was filled with the two-phase medium, lather or foam rubber. The pressure gage for measuring the reflected pressure p_R' was placed on the end wall of the test chamber. To suppress the critical vibrations of the pressure gage, the signals were filtered by a low pass filter with 150 kHz.

In Fig. 5 we can see a few recordings of pressure behind foam rubber of different thickness using the same shock mach number of the primary shock. With a thickness of more than 20 mm we can see the strong pressure increase on the foam rubber in comparison to the pressure p_R behind the directly reflected shock which is reached after a short time.

Fig. 6 shows 3 pressure recordings behind lather at different shock mach numbers M_s. It is clearly seen, that the peak pressure increases with increasing shock mach number and for $M_s = 2$ we get a peak pressure of about 90 bar in comparison to p_R of about 12 bar. All the pressure records show a somewhat flat pressure increase which means that the shock is dispersing in the two-phase medium.

Fig. 7 shows a comparison of the experimental data of p_R' with the theoretical data for $\kappa = 1$ and $\kappa = 1.4$. The experimental values are somewhat smaller than the theoretical values for $\kappa = 1$. The following reasons may account for this:

- The cross section of the test chamber was somewhat bigger than that of the shock tube.

- The foam may not have filled homogeneously the entire volume of the test chamber.

- The porous structure of the foam rubber was not closed.

- The shock was disperged in the foam.

However, if we take into account the logarithmic scale of the diagram we can see the enormous pressure increase in comparison to the direct shock reflection at a stationary solid wall.

3. COMPRESSION OF A TWO-PHASE MEDIUM BY A SHOCK ACCELERATED PISTON

3.1 Theory

If we put a free moving piston in front of the foam in the shock tube (Fig. 8), the primary shock will be reflected at the surface of the piston. The reflected pressure p_R will accelerate the piston into the two-phase medium which will be compressed to a peak pressure $\hat{p}$, when the piston has reached the final position where it changes its direction.

By means of the conservation equation for the momentum we are able to derive the differential equation for the path of the piston (Fig. 9, equ. 3). There we suppose, that a certain time the density in the two-phase medium is equal and that the velocity $\dot{x}$ in the two-phase medium increases linearly from the end wall of the test chamber to $\dot{x}_k$ (velocity of the piston). This means that the velocity of the piston is always slow compared with the sound velocity in the two-phase medium and therefore there are no shocks or any inhomogeneous pressure distribution in the foam.

After introduction of the isentropic equation (equ. 4) of the volume ratio V and of the normalized parameters τ and y we will find the solution for the path of the piston (equ. 6). With this we can also derive the pressure time function. For $\frac{dy}{d\tau} = 0$ we get the peak pressure $\hat{p}$, this means that the expression under the root is equal to zero (equ. 8).

Here we can see the very interesting fact, that the peak pressure depends only on p_R if we suppose, that $\kappa = 1$ for all two-phase media.

On Fig. 12 we see the calculated pressure time function $p/p_1 = f(\tau)$ for $\kappa = 1$ and $\kappa = 1.4$ for a special condition. Compression at const. temperature ($\kappa = 1$) gives a pressure increase which begins later and then increases much steeper until a peak pressure has been reached, which is 10 times higher than at compression where $\kappa = 1.4$.

3.2 Experiments

For the experiments we have placed in front of the foam inside the test chamber solid plates of different masses (Fig. 4). The other part of the experiment was similar to the direct shock interaction experiments.

Fig. 10 shows 3 pressure records with lather at 3 different shock mach numbers. The peak pressure increases very strongly with the shock mach number. At a shock mach number of $M_s = 1.9$ ($p_R = 10.7$ bar) we get a peak pressure of about 800 bar. At these high pressures the test chamber was not stable enough and therefore we can observe oszillations on our records.

Fig. 11 shows 3 pressure records with lather at the same shock mach number but with different piston masses. The peak pressure remains constant. This is in agreement with our theoretical assumption.

On Fig. 12 we compare a pressure record with the theoretical curves. The experimental curve agrees approximately with the calculated curve for $\kappa = 1$; the experimental peak pressure reaches only half the theoretical value. This can be explained by the somewhat larger cross section of the test chamber as compared with that of the shock tube and by the fact that at these high pressures the test chamber was not really rigid. There was also the possibility that the test chamber was not homogeneously filled with foam.

On the last picture, Fig. 13, we compare the experimental peak pressures in different foams with different pistons and the calculated values as a function of the reflected pressure p_R. The experimental values are not as high as the theoretical values for $\kappa = 1$, but if we consider the logarithmic scale, we can see that they are much higher than the values for $\kappa = 1.4$. It is also ob-

vious that the influence of κ increases very strongly with increasing pressure p_R.

3.3 Final Remarks

Essentially our experiments have confirmed the theoretically predicted behaviour of two-phase media in direct interaction with a shock wave and compressed by a shock wave accelerated piston.

The differences between the experimental and the theoretical values of the peak pressures can be explained by the mechanical behaviour and the geometry of the test chamber and by an eventually inhomogeneous foam filling.

The principal effect, the enormous pressure increase in a two-phase medium by shock interaction and by compression has been confirmed basically and there are only some quantitative differences.

We cannot clearly explain why we did not find any shocks in the two-phase medium although we did expect them in the direct shock interaction and in the piston compression cases. A possible explanation for the moment is the dispersion of shock waves in these two-phase media which we have used in our experiments.
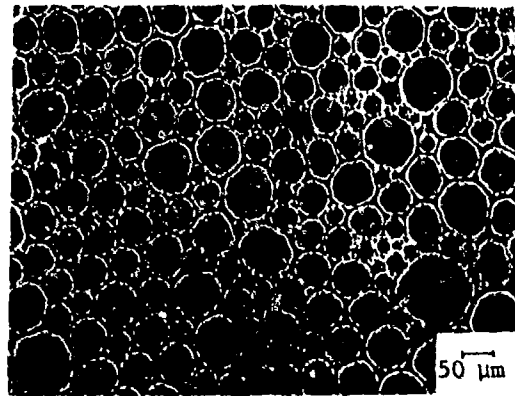
Fig.1
Bubblestructure
of Lather

50 μm
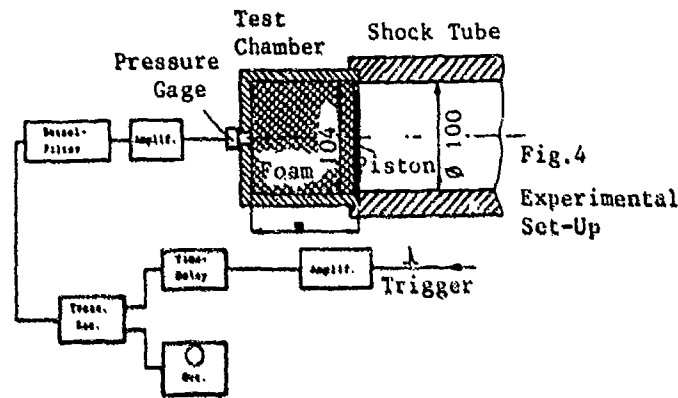
Fig.4
Experimental
Set-Up
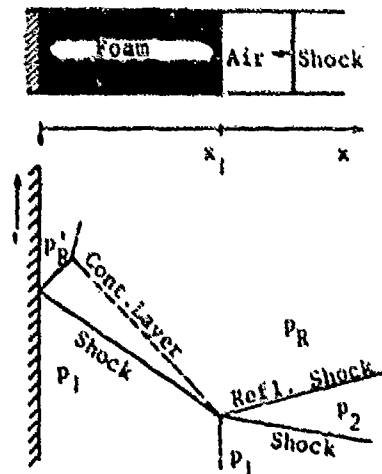
Fig.2 Operating Diagram
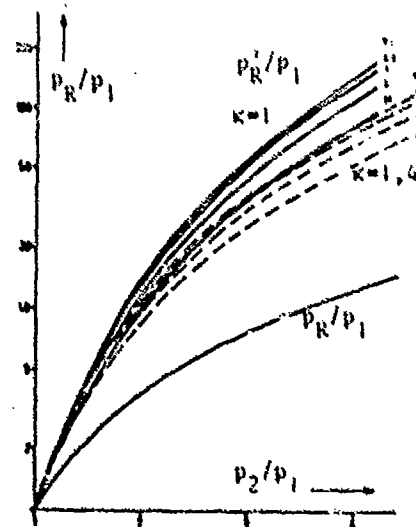
Fig.3 Pressures behind a refl. Shock

$p_2=2,5$ bar

P_R

2 bar
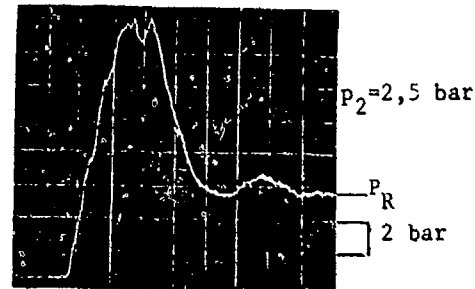
Thickness $d=100$ mm

$\rho=0,078$ g/cm^3

$p_2=3,4$ bar

10 bar

P_R

$p_2=4,5$ bar

20 bar

P_R
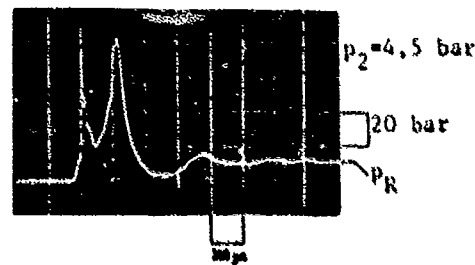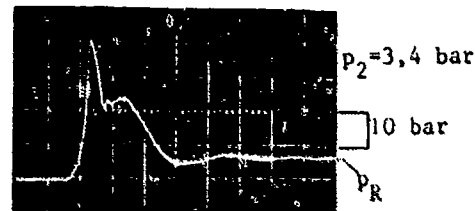
Fig.6 Pressure Records
behind Lather

$d=5$ mm

$p_2=3,8$ bar

$\rho=0,05$ g/cm^3

$d=20$ mm

$d=100$ mm

5 bar

P_R
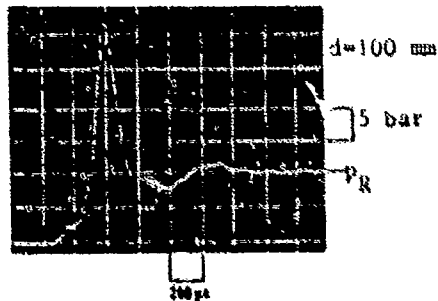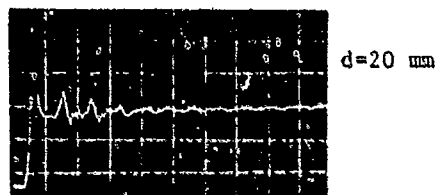
Fig.5 Pressure Records
behind Foam Rubber
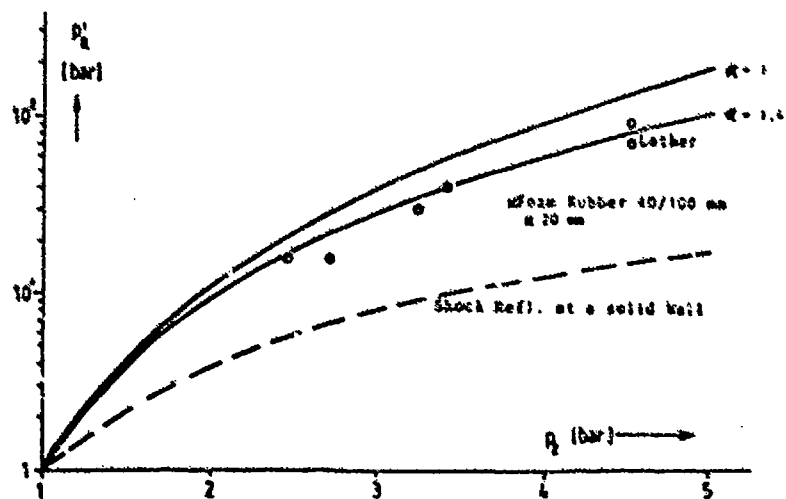
Fig.7 Theor. and exp. Pressures at the End Wall
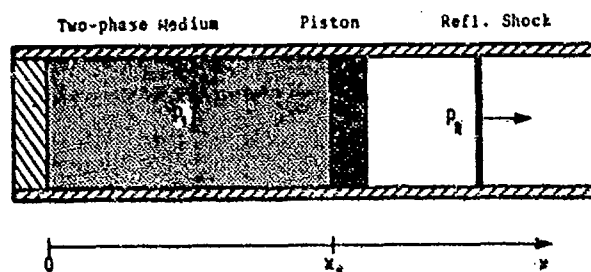
Fig.8 Compression of a Two-phase Medium by a Piston
driven by a reflected Shock Wave

1) $\dfrac{dJ}{dt} = -\Gamma(p_R - p)$

2) $\dot{x} = f(x) = -\dot{x}_R \dfrac{X}{X_R}$

3) $J = m_R \dot{x}_R + \Gamma \rho \int_0^{X_R} \dfrac{X}{X_R} \dot{x}_R \cdot dx$

4) $\begin{cases} \dfrac{p}{p_1} = \left(\dfrac{\rho_1}{\rho_{21}}\right)^{*} \\[2mm] V = \dfrac{\rho_R - \rho}{\rho - \rho_2} \end{cases}$

5) $\begin{cases} \Gamma = \dfrac{t}{t_0} \quad t_0 = \sqrt{\dfrac{x_1(m_R - m(z))}{2\Gamma p_1} \cdot \dfrac{V}{1+V}} \\[3mm] y = \dfrac{(1+V)\frac{X_R}{X_1} - 1}{V} \qquad \Gamma = 0 \begin{cases} y=1 \\ \dfrac{dy}{dt}=0 \end{cases} \end{cases}$

6) $\Gamma = \int^y \dfrac{dy}{\sqrt{\dfrac{p_1}{p_R}(1+V) + \dfrac{t}{1-x}(y^{1-x}-1)}}$

7) $\dfrac{p}{p_1} = y^{*}$

8) $\hat{p} \to \dfrac{p_1}{p_R}\left[1 - \left(\dfrac{p_1}{\hat{p}}\right)^{*}\right] + \dfrac{1}{1-x}\left[\left(\dfrac{\hat{p}}{p_1}\right)^{\frac{x-1}{x}} - 1\right] = 0$

Fig.9 Formulas for Calculation of Piston-path
and Peak-pressure

104 bar

p_R=5,7 bar

Lather:
ρ=0,078 g/cm^3 100 μs

104 bar

m_k=30,6 g

p_R=6,7 bar
ρ=0,078 g/cm^3

104 bar

p_R=6,7 bar

m_k=30,6 g   50 μs

208 bar

m_k=99 g

50 μs

208 bar

p_R=10,7 bar

50 μs
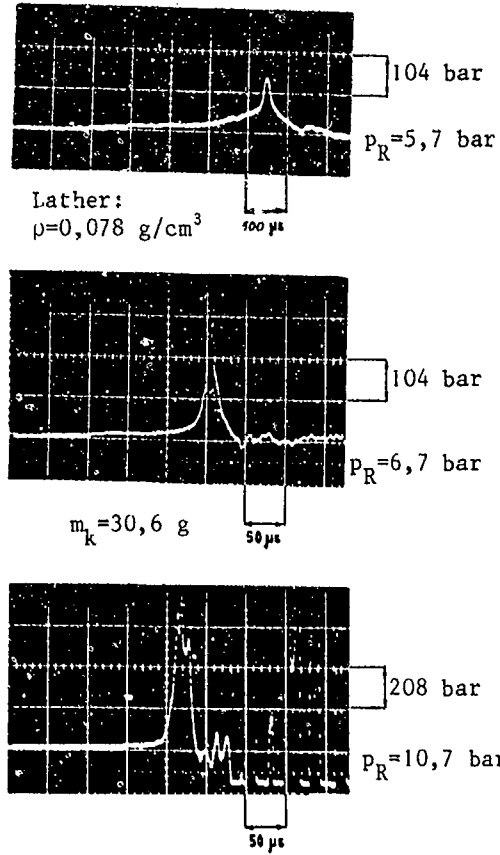
Fig.10 Pressure Records at
         different Pressures p_R

104 bar

m_k=259 g

50 μs
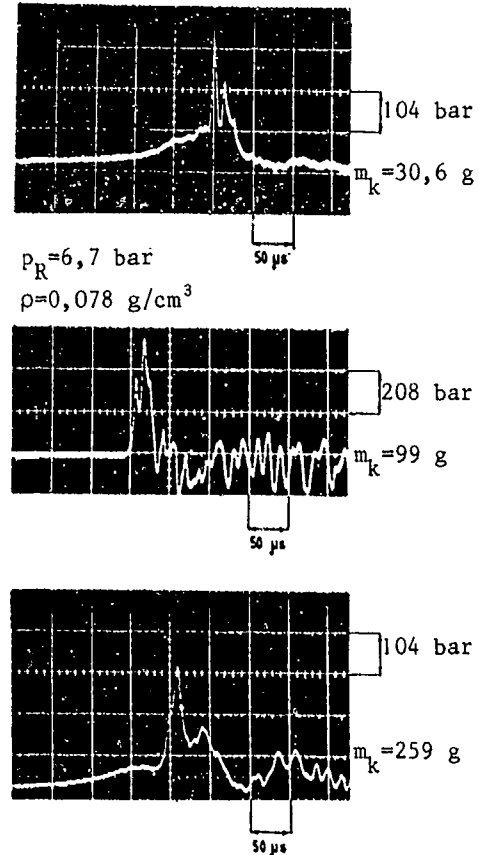
Fig.11 Pressure Records at different
         Masses of the Piston m_k

Lather
m_k=30,6 g
p_R=6,7 bar

p/p_1

Experiment

K=1

K=1,4

τ
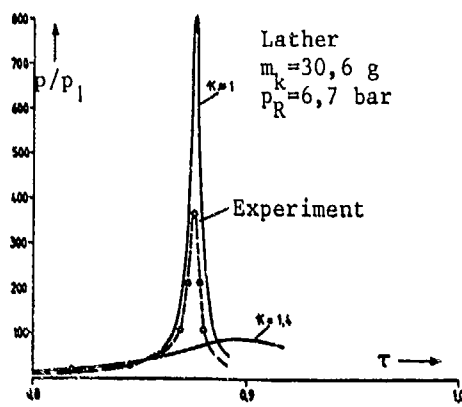
Fig.12 Pressure Time Functions

p/p_1

p_R/p_1
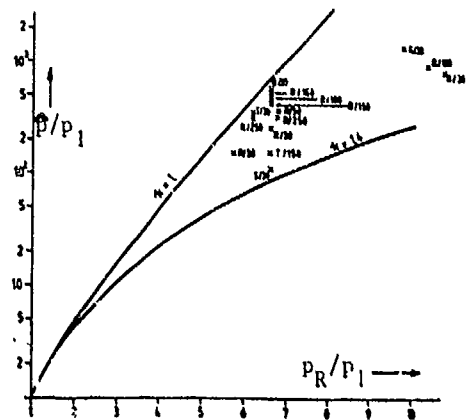
Fig.13 Peak Pressures

UNDERWATER EXPLOSION OF TWO SPHERICAL OR NONSPHERICAL BUBBLES AND THEIR INTERACTION WITH RADIATED PRESSURE WAVES

S. Fujikawa, H. Takahira & T. Akamatsu
Department of Mechanical Engineering, Kyoto University,
Kyoto 606, Japan

Mutual interaction between two spherical or nonspherical bubbles in a liquid and pressure waves radiated from them is treated on the basis of a linear acoustic theory. It is shown that there exist some special combinations of initial radii of two bubbles and initial gas pressures of bubble interior which lead to the generation of particularly high pressures in the liquid from the smaller spherical bubble. The generated pressure may attain to a value of more than 6 times in comparison with that of a single bubble. Due to the mutual interaction between bubbles and pressure waves the instability takes place on the bubble walls.

1. INTRODUCTION

Mutual interaction among bubbles in liquids is an important subject which deals with basic aspects of fluid mechanics on gas-liquid two phase media: underwater explosions, shock structures in gas-liquid two phase media, bubble detonations in liquid explosives, and mechanisms of cavitation erosion.

Until now, a very few theoretical investigations have been made on the interaction among bubbles [1-4], although innumerable works on the dynamics of a single bubble have been performed. Recently, Chahine[4] investigated the effects of interaction among bubbles on the pressure developed during their collective collapse in an incompressible liquid. However, the analysis has not been made about the bubbles with different sizes and for the condition where the compressibility of liquid may become essentially important. As to the experiments, on the other hand, there are a few papers by Lauterborn[5], Smith & Mesler[6], Fujikawa & Akamatsu[7], Sanada et al.[8] and Tomita et al.[9]. Sanada et al. observed a number of strong shock waves higher than 1 GPa on the surface of an ultrasonic vibrator in water and pointed out that the interaction between bubbles and shock waves radiated from them may induce further violent collapses of these bubbles and the formation of a number of stronger shock waves. They called this chain-reaction like phenomenon an avalanche effect for the formation of shock waves. Tomita et al. made experiments on the collapse of a single gas bubble attached to a solid wall by a spark-generated shock wave. They showed, depending on the initial size of the bubble, the strength of the shock wave and the distance from the center of the shock wave to the bubble, the gas bubble acts as either the energy absorber from the shock wave or the source of more intensive pressure than that by the original shock wave. However, details of the interaction between bubbles and radiated shock waves have not been fully clarified. It seems therefore that the theoretical understanding on the interaction of bubbles with radiated shock waves is more and more necessary.

In this paper, as the first step of the analysis on the interaction among a number of bubbles, the interaction between two spherical or nonspherical bubbles and pressure waves radiated from them is theoretically treated. We will deal here with, not shock waves but pressure waves. In case where one bubble is situated in the far-field from another bubble, the nonlinearity of liquid compressibility is very small, so that a linear approximation may be adequate for our problem. The dynamical equations of the bubble walls which are valid to the first order corrections concerning the mutual interaction of two spherical or nonspherical bubbles and the compressibility of liquid are presented and numerically solved.

2. THEORY

Details of the mathematical formulation are presented in the previous paper by the first author[10]. Only the minimum results necessary for the understanding of the theoretical background will be presented here. A spherical coordinate system with the fixed origins O_1 and O_2 at the initial centers of two bubbles is shown in Fig. 1. The radial motion and the deformation of two bubbles are expressed by a set of differential equations as follows.

$$R_{i0}(t)\,\ddot{R}_{i0}(t)\left\{1-\frac{2\dot{R}_{i0}(t)}{C}\right\} + \frac{3}{2}\dot{R}_{i0}^2(t)\left\{1-\frac{4\dot{R}_{i0}(t)}{3C}\right\}$$

$$+\frac{1}{\varrho}\left\{P_\infty + \varrho\epsilon_{j0}(t-\lambda_j)\left[R_{j0}(t-\lambda_j)\,\ddot{R}_{j0}(t-\lambda_j)\right.\right. \tag{1}$$

$$\left.\left. + 2\,\dot{R}_{j0}^2(t-\lambda_j)\right] - p_{i0}(R_{i0},t) - \frac{R_{i0}(t)}{C}\,\dot{p}_{i0}(R_{i0},t)\right\} = 0$$

(for bubble 1 $i = 1$, $j = 2$;   for bubble 2 $i = 2$, $j = 1$)

$$p_{i0} = P_v + P_{ig0}\left(\frac{R_{i00}}{R_{i0}}\right)^{3\gamma} - \frac{2\sigma}{R_{i0}}$$

$$\epsilon_{j0} = \frac{R_{j0}}{L}$$

$$\ddot{R}_{in} + A_{i1}\,\dot{R}_{in} + A_{i2}\,R_{in} + A_{i3} = 0 \qquad (n = 1,2,3,\ldots) \tag{2}$$

$$A_{i1} = \frac{3\dot{R}_{i0}}{R_{i0}} - \frac{(n+1)\epsilon_{i0}}{2R_{i0}}\left(\frac{\partial\phi_{i0}}{\partial x_j}\right)_{x_j=L}$$

$$A_{i2} = -\frac{(n-1)\ddot{R}_{i0}}{R_{i0}} + \frac{\sigma(n^2-1)(n+2)}{\varrho\,R_{i0}^3} + \frac{(n+1)}{R_{i0}}\left[\frac{\dot{R}_{i0}}{C}\left(\ddot{R}_{i0} + \frac{2\dot{R}_{i0}^2}{R_{i0}}\right)\right.$$

$$+\left\{\left(\frac{\partial^2\phi_{i0}}{\partial t\partial x_j}\right)_{x_j=L} - \left(\frac{\partial\phi_{i0}}{\partial x_j}\right)_{x_j=L}\left[\frac{2\dot{R}_{i0}}{R_{i0}} - \left(\frac{\partial^2\phi_{i0}}{\partial x_j^2}\right)_{x_j=L}\right]\right\}\cos(\theta+\omega)$$

$$-\dot{R}_{i0}\left\{\frac{\epsilon_{i0}}{R_{i0}}\left(\frac{\partial\phi_{i0}}{\partial x_j}\right)_{x_j=L} + \left(\frac{1}{x_j}\frac{\partial\phi_{i0}}{\partial x_j}\right)_{x_j=L}\sin^2(\theta+\omega)\right.$$

$$\left.\left. + \left(\frac{\partial^2\phi_{i0}}{\partial x_j^2}\right)_{x_j=L}\cos^2(\theta+\omega)\right\}\right]$$

$$A_{i3} = \frac{n\epsilon_{i0}^{n-1}}{R_{i0}}\left\{n\,\dot{R}_{i0}\left(\frac{\partial\phi_{i0}}{\partial x_j}\right)_{x_j=L} + R_{i0}\left(\frac{\partial^2\phi_{i0}}{\partial t\partial x_j}\right)_{x_j=L}\right.$$

$$\left. - \frac{(n+1)\epsilon_{i0}}{2}\left(\frac{\partial\phi_{i0}}{\partial x_j}\right)_{x_j=L}^2\right\}$$

$$\phi_{j0} = -\frac{R_{j0}^2(\xi_j)}{x_j}\left[\dot{R}_{j0}(\xi_j) - \frac{1}{C}\left\{R_{j0}(\xi_j)\,\ddot{R}_{j0}(\xi_j)\right.\right.$$

$$\left.\left. + 2\,\dot{R}_{j0}^2(\xi_j)\right\}\right] \qquad (x_1 = r,\quad x_2 = s) \qquad (3)$$

$$\xi_j = t - \frac{x_j - R_{j0}(\xi_j)}{C} \qquad\qquad (4)$$

$$R_i = R_{i0}(t) + \sum_{n=1}^{\infty} R_{in}(t)\,P_n(\cos\psi_i) \qquad (\psi_1 = \theta,\; \psi_2 = \omega) \qquad (5)$$

where C is sound speed in liquid, L distance between two bubbles, p_{ig0} initial gas pressure inside bubble, p_v vapour pressure inside bubble (= constant), p_∞ pressure at infinity, p_n Legendre polynominal of order n, R_i radius of bubble (R_{i00} initial radius, R_{i0} zeroth mode radius, R_{in} nth ($n \geq 1$) mode radius), t time, γ ratio of specific heats of gas, ρ density of liquid, σ surface tension coefficient, symbols $(\cdot)$, $(\cdot\cdot)$ = d/dt, d^2/dt^2. The equation (1) is the general expr ..sion on the spherical (i.e. , zeroth mode) motion of two bubbles and is valid to the first order corrections concerning the compressibility of liquid and the mutual interaction between two bubbles. The ϕ_j is a delay time of the influence from another bubble and can be determined from Eq.(4). Suppose that time t just elapsed after the start of the simultaneous collapse of two bubbles and that pressure wave which were radiated some time before from the bubble 1 arrived at the center of the bubble 2 (Fig. 2). The times ξ, when the pressure waves were just generated can be found as to satisfy Eq. (4) at $x_j = L$. All physical quantities necessary for evaluating the interaction term in Eq.(1) can be thus obtained. For the bubble 1, the same is the numerical procedure. The equation (2) describes the deformation of the walls of bubbles. The pressure throughout the liquid is given by the Bernoulli's equation.

3. NUMERICAL RESULTS AND DISCUSSION

Numerical calculations are performed for water under the following condition: temperature 20 $^\circ$C, p_∞ = 101.3 kPa, ρ = 998.2 kg/m^3 , C = 1483 m/s, σ = 7.061 x 10^{-2}N/m , γ = 1.4 (air).

3.1 Interaction between two spherical bubbles

Figure 3 shows the time histories of (a) bubble radius, (b) pressure at the bubble wall and (c) pressure in the liquid at the initial radius and ω = 180°. Initial conditions for bubbles a.. R_{100} = 1 mm, R_{200} = 0.175 mm, L = 3 mm, p_{1g0} = p_{2g0} = 1.013 kPa (= 0.01 p_∞). The interaction becomes strongest for this initial radius ratio. Dashed lines are for the bubble 1 (the initially larger bubble) and the solid lines for the bubble 2 (the initially smaller bubble). The time is normalized by τ = 99.30 μs, the radius by R_{100} for the bubble 1 and R_{200} for the bubble 2, the pressure by p_∞ and the velocity by V_1 = 10.07 m/s for the bubble 1 and V_2 = 1.762 m/s for the bubble 2. The motion of the bubble 1 is not influenced by the existence of the bubble 2, it collapses and rebounds as if it were like a single bubble in an infinite liquid. The motion of bubble 2, on the other hand, is drastically influenced by the bubble 1 to consequently produce a particularly high pressure of about 6.7 x 10^3 MPa on its fourth collapse. This value is about 4.5 times of the pressure generated by a single bubble under the same condition. The oscillating motion of bubble 2 is largely damped due to the effect of compressibility of liquid. The attained maximum Mach number of the wall of bubble 2 in collapsing phases is about 0.3. The linear model is found to be still valid[11].The mechanism of the generation of high pressure from the bubble 2 may be explained as follows. The bubble 2 reaches

its minimum radius at about 3 μs after the bubble 1 collapsed and rebounded and then radiated pressure waves. The pressure waves from the bubble 1 arrive at the center of the bubble 2 "in collapsing phases" at about 2 μs after they were radiated. Therefore, the collapsing motion of bubble 2 is to be further accelerated during about 1 μs under the high pressure due to the passage of pressure waves. In consequence, the bubble 2 collapses very violently and produces a high pressure. The time history of liquid pressure is composed of the pressure waves radiated from bubbles 1 and 2 (Fig. (c)). The first small pulselike pressure is principally due to the bubble 1 and the second one principally due to the bubble 2. The maximum value of the pressure is about 27 MPa. From a number of calculations, it is clarified that the bubble 2 produces a particularly high pressure only for some special values of the initial radius ratio.

Figure 4 shows the time histories of (a) bubble radius and (b) pressure at the bubble wall in case of R_{100} = 1 mm, R_{200} = 0.253 mm, L = 3 mm, p_{1g0} = p_{2g0} = 101.3 Pa (= 0.001 p_{w}). The time is normalized by τ = 99.30 μs, the radius by R_{100} for the bubble 1 and R_{200} for the bubble 2 and the pressure by p_{w}. The motion of bubble 2 is violently excited on the fourth collapse under the influence of the bubble 1, but the generated pressure is then never higher than that of bubble 1 on its first collapse. This behaviour of bubble 2 is very different from that in Fig. 3. The difference comes from the fact that the motion of bubble 2 is remarkably damped owing to the compressibility of liquid. That is, the lower is the initial gas pressure within the bubble 2, the more violently collapses it, the higher becomes the pressure generated on its first collapse, but then the larger becomes also the damping effect due to the compressibility of liquid. Then, the subsequent motion of bubble 2 is not greatly excited even under the strong influence of pressure waves radiated from the bubble 1, so that the bubble 2 may never produce a pressure higher than that of the bubble 1.

Figure 5 shows the time histories of (a) bubble radius and (b) pressure at the bubble wall in case of two bubbles with different initial gas pressures and radii: R_{100} = 1 mm, R_{200} = 0.088 mm, L = 3 mm, p_{1g0} = 101.3 Pa (= 0.001 P_{w}), p_{2g0} = 1.013 kPa (0.01 p_{w}). The time is normalized by τ = 99.30 μs, the radius by R_{100} for the bubble 1 and R_{200} for the bubble 2 and the pressure by p_{w}. It is noteworthy that the bubble 2 generates a high pressure higher than 9×10^{4} MPa, more than 6 times in comparison with that of a single bubble under the same condition.

3.2   Interaction between two nonspherical bubbles

Figure 6 shows the dynamical behaviour of two nonspherical bubbles. It is assumed that the initial shape of bubbles is spherical. Initial conditions are: p_{w} = 101.3 kPa, p_{1g0} = p_{2g0} = 5.065 kPa (0.05 p_{w}), R_{100}= 1 mm, R_{200} = 0.8 mm, L = 3 mm. The time elapses below. Two bubbles are fairly stable in the sense that the shape change of bubbles is very small, however, the center of the bubble 2 (the smaller bubble) approaches to the bubble 1 (the larger bubble) due to the flow induced by the collapsing motion of bubble 1 and the instability occurs on the wall of bubble 2 far from the bubble 1 but it soon disappears after the rebound. The center of bubble 1 does not almost move except the very late stages of its collapse. When the bubble 1 is in a rebounding process, the bubble 2 already rebounded and radiated pressure waves. By the passage of pressure waves from the bubble 2, the flow field around the bubble 1 deviates from the spherical symmetry and, in consequence, the shape change of bubble 1 takes place. After some time, the shape becomes nearly spherical. The same is it for the bubble 2. However, in the second contracting process of bubble 2, the deformation of it quickly becomes large. This seems to suggest that an initially nonspherical bubble easily becomes unstable and deforms in its contracting process.

In this analysis, the fixed coordinate system is used to describe a set of equations for bubble motions. However, when the bubble largely deforms, the

present equations may become invalid because the part of the bubble surface farthest from another bubble reaches the origin in the late stages of collapse. For subsequent times, the origin is outside the bubble. The use of the moving coodinate system may overcome the difficulty encountered here.

4. CONCLUSION

The mutual interaction between two spherical or nonspherical bubbles in a liquid and radiated pressure waves has been theoretically investigated. It has been shown that a very high pressure may be produced in the liquid due to the bubble-pressure wave interaction and it may attain to a value of more than 6 times in comparison with that of a single bubble under the same condition. The interaction causes instability on the walls of bubbles and makes bubbles deform.This paper was prepared in the Stoßwellenlabor of the Technische Hochschule Aachen, West Germany. The authors wish to thank Prof. H. Grönig and Mrs. von Hoegen for their kind help.

REFERENCES

1. Shima, A., "The Natural Frequencies of Two Spherical Bubbles Oscillating in Water", ASME Journal of Basic Engineering, Vol.93,1971, p.426.
2. Shima, A., "The Natural Frequencies of Three Spherical Bubbles Oscillating in Water", Report of Institute of High Speed Mechanics(Japan),Vol.31,1972,p.81.
3. Morioka, M., "Theory of Natural Frequencies of Two Pulsating Bubbles in Infinite Liquid", Journal of Nuclear Science and Technology (Japan), Vol. 11, 1974, p.554.
4. Chahine, G.L., "Collective Collapse of Cavitation Bubbles", Proceedings of IAHR Symposium,1982, p.1.
5. Lauterborn, W.,"Kavitation durch Laserlicht", Acustica, Vol.31,1974,p.51.
6. Smith, R.H. and Mesler, R.B., "A Photographic Study of the Effect of an Air Bubble on the Growth and Collapse of a Vapor Bubble near a Surface", ASME Journal of Basic Engineering, Vol.94,1972, p.933.
7. Fujikawa, S. and Akamatsu, T., "Experimental Investigations of Cavitation Bubble Collapse by a Water Shock Tube", Bulletin of JSME, Vol.21,1978, p.223.
8. Sanada, N., Ikeuchi, J., Takayama, K. and Onodera, O., "Observation of Cavitation Induced Shock Waves in an Ultrasonic Vibrating Test", Transactions of JSME, Vol. 50, 1984, p. 2275.
9. Tomita, Y., Shima, A. and Takahashi, K., "The Collapse of a Gas Bubble Attached to a Solid Wall by a Shock Wave and the Induced Impact Pressure", ASME Journal of Fluid Engineering, Vol. 105, 1983, p. 341.
10. Fujikawa, S., "Interactions between Two Slightly Nonspherical Bubbles in a Compressible Liquid (Part I), Proceedings of ASME International Cavitation Symposium, 1985, p. 167.
11. Knapp, R.T., Daily, J.W. and Hammitt, F.G., Cavitation, 1970, McGraw-Hill.
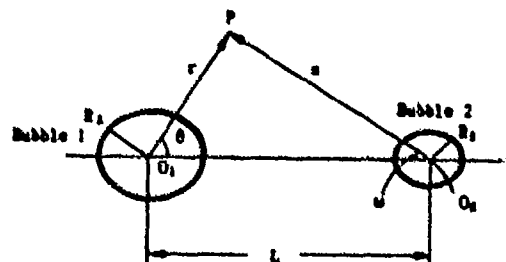
Fig. 1: Spherical coordinate system.
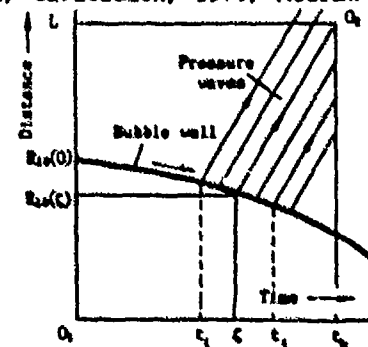
Fig. 2: Interaction between one bubble and pressure waves radiated from another bubble.
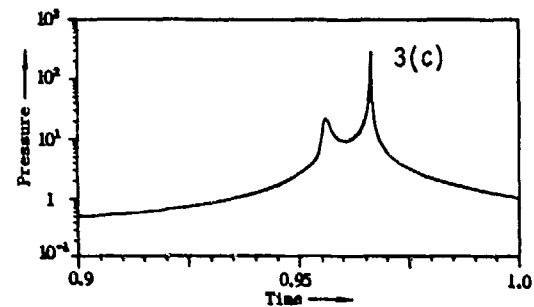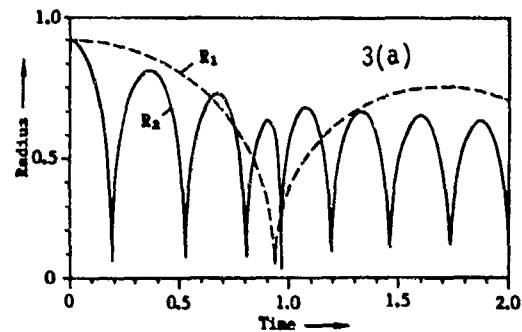
Fig. 3: Time histories of (a) bubble radius, (b) pressure at the bubble wall and (c) pressure in the liquid at the initial radius of bubble 2 and $\omega = 180^{\circ}$ ($p_{1g0} = p_{2g0} = 0.01\ p_{\infty}$).
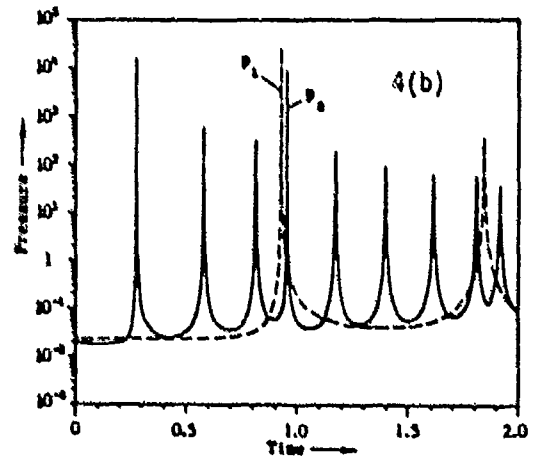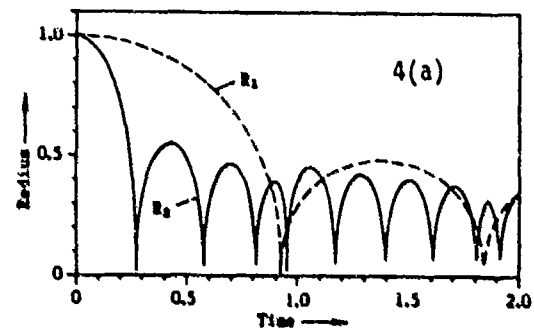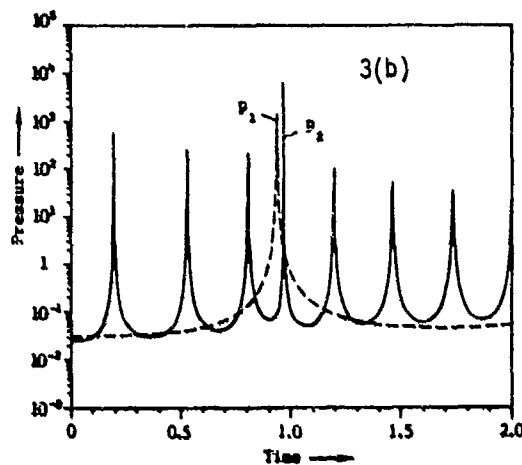
Fig. 4: Time histories of (a) bubble radius and (b) pressure at the bubble wall ($p_{1g0} = p_{2g0} = 0.001\ p_{\infty}$).
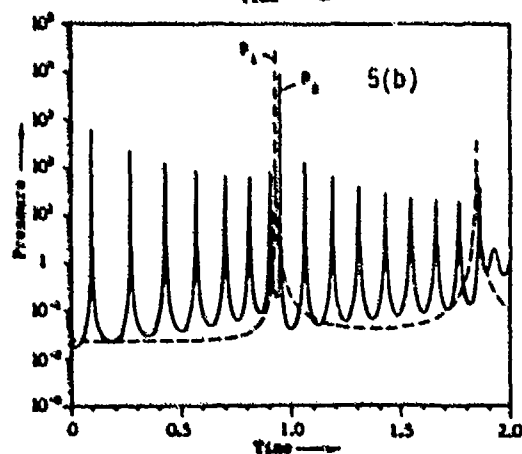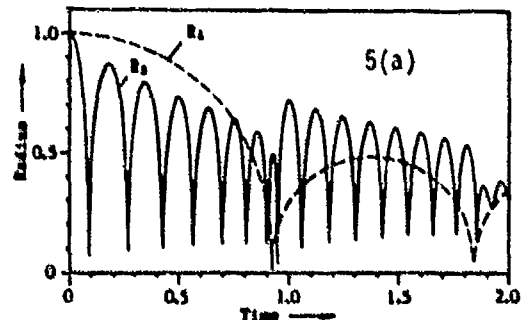
Fig. 5: Time histories of (a) bubble radius and (b) pressure at the bubble wall ($p_{1g0} = 0.001\ p_{\infty}$, $p_{2g0} = 0.01\ p_{\infty}$).
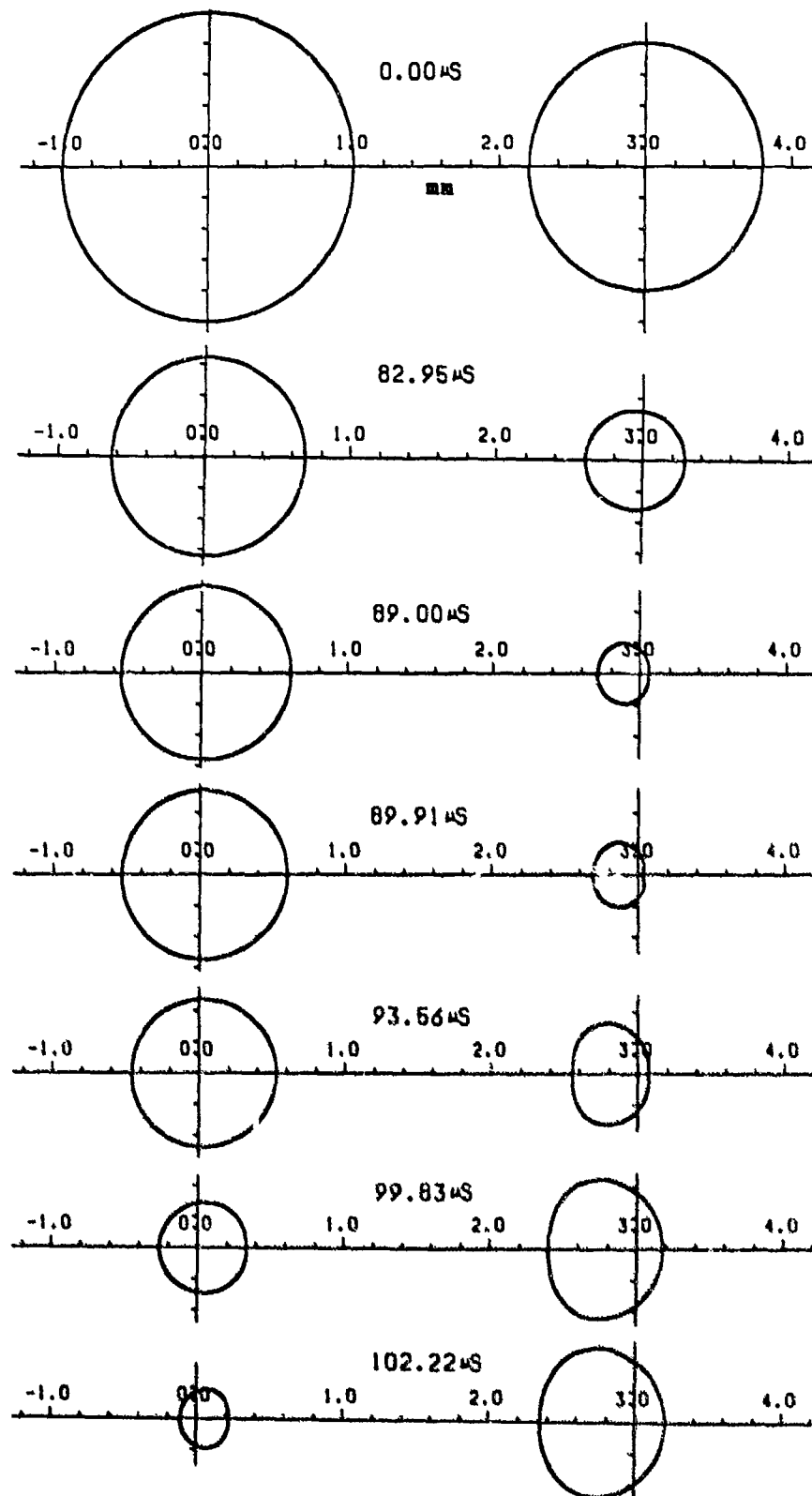
Fig. 6: Dynamics of two nonspherical bubbles ($p_{1g0} = p_{2g0} = 0.05\ p_\infty$).
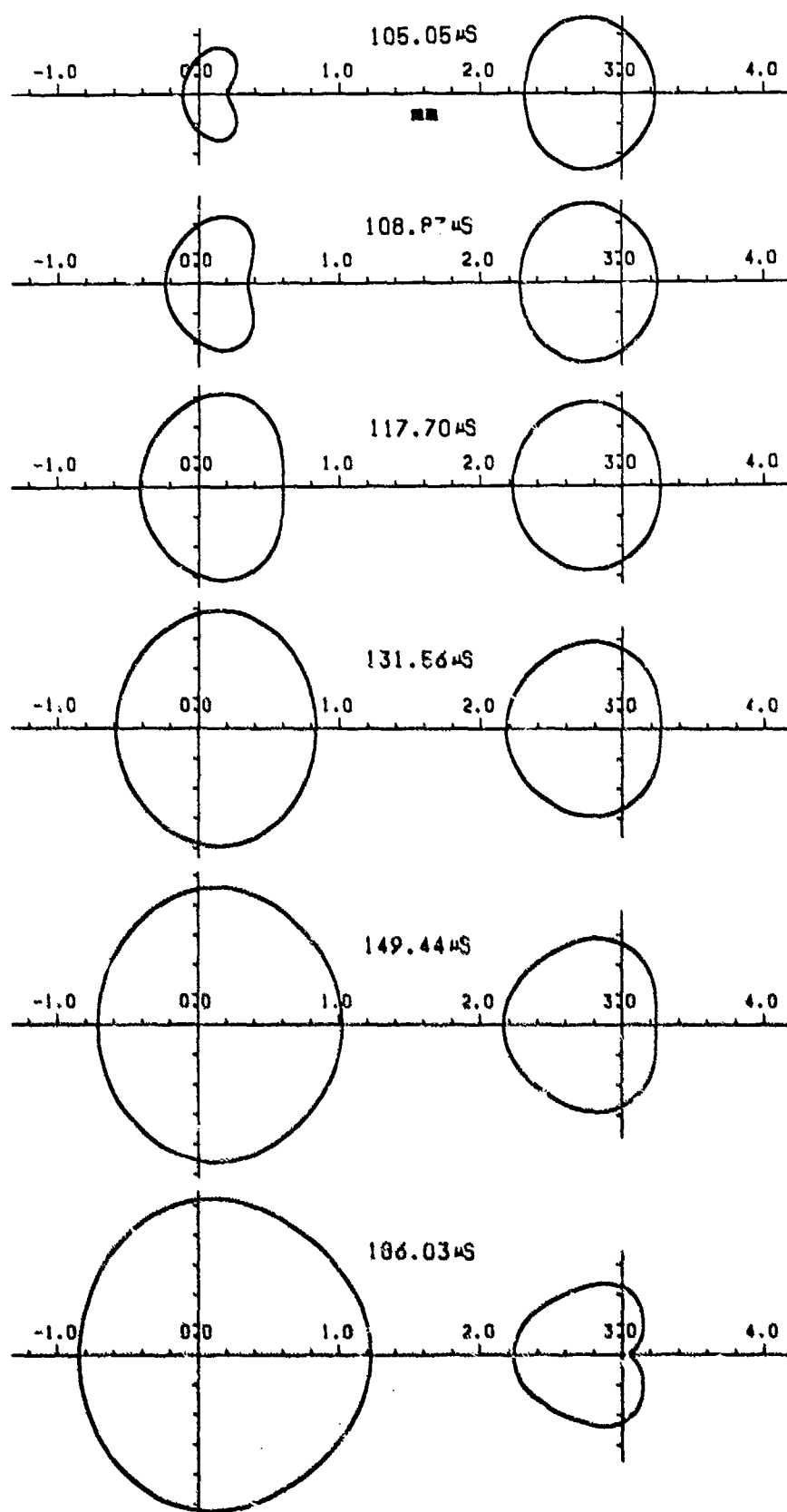
RADIAL FLOW OF A METASTABLE LIQUID

Raymond J. Emrich

Physics Bldg. 16, Lehigh University
Bethlehem, PA 18015 USA

The expansion of a rapidly moving liquid through a ra-
dial flow configuration reveals transition to a vapor or a
2-phase mixture of vapor and liquid taking place over a short
distance and in a short time experimentally indistinguishable
from a discontinuous shock front. Photography of the discon-
tinuous surface with 1 ns flash illumination from a nitrogen
laser reveals no bubble formation within the 2 micrometer de-
finition of the microscope lens. The flow of liquid CO_2 is
studied in a confined layer, of the order of 10 μm thick, be-
tween the end of a metal cylinder and a quartz window. Vis-
cous effects play a significant role in controlling the
pressure drop in the radial direction, and the transition
from the metastable liquid state to the vapor or 2-phase state
can be triggered by roughness elements on the confining walls.
Pressure taps in the face of the metal cylinder reveal that
the liquid pressure is lower than the supply pressure near
the center, rises as shear forces reduce the liquid speed, and
then falls logarithmically until the explosive transition.
Mechanisms involved in the explosive transition are discussed.

INTRODUCTION

The flow of a rapidly moving liquid from an orifice into a gas filled re-
gion leads to separation and formation of a free surface. When liquid emerges
into a region where the pressure is below its saturation vapor pressure, the
liquid boils and a 2-phase mixture continues into the low pressure region; this
process is termed "flashing" by chemical engineers. The reported work is an
attempt to study the mechanisms by which the liquid changes to a 2-phase
mixture.

A study of the explosive evaporation of a superheated liquid by short ex-
posure photographs and fast response pressure gages has been carried out by
Shepherd and Sturtevant[1]. Their results suggest that conventional nucleation
and bubble growth theories do not predict sufficiently rapid transition to va-
por to account for the observed rate of evaporation.

In the nuclear reactor power industry, considerable interest exists in the
choking or critical conditions with unsteady outflow of a boiling liquid after
a pipeline break. Rassokhin et al.[2] and Mayinger[3] have reviewed the informa-
tion acquired since the summary prepared by Smith[4].

Experiments in a shock tube-like device have been performed by Edwards and
O'Brien[5], Alamgir et al.[6], Alamgir and Lienhard[7] and Isaev and Pavlov[8]. In
these experiments high pressure water, or carbon dioxide, is depressurized at
one end by removing a stopper or by breaking a diaphragm and the pressure ex-
cursions at positions within the tube are recorded with fast response (order of
10 microsecond response time) piezoelectric or diaphragm gages in the tube
walls. The observed pressures fall rapidly (in a few microseconds) at the head
of the relief wave propagating into the tube, falling below the saturation
pressure at the initial liquid temperature, then rising to a nearly constant

pressure still below saturation in about a millisecond. The lower-than-saturation pressures are interpreted as associated with reaching metastable states of the liquid with delayed rates of nucleation of bubbles. The steady pressure reached after 1 ms can be interpreted as a lower saturation pressure and temperature in a two-phase equilibrium state.

It was observed by Stuart and Yarnell[9], and Kinderman and Wales[10] that hot water under high pressure can flow through an orifice into a chamber where a pressure considerably below the initial saturation pressure prevails. An irreversible transition to 2-phase equilibrium occurs within the intermediate chamber. The saturated liquid resulting, possibly mixed with vapor, then flows through a second orifice, again emerging as a metastable liquid in which delayed vaporization (flashing) occurs some distance beyond the orifice exit. Photographs of a metastable hot water jet emerging into the atmosphere are shown by Stuart and Yarnell[9] in which the delay in vaporization can be seen to depend on the degree of superheating in the emerging liquid.

An extensive study of flow rates of saturated liquid, saturated vapor, and two-phase liquid-vapor carbon dioxide was carried out by Hesson and Peck[11]. Their observations are consistent with the hypothesis that saturated liquid and saturated vapor both emerged from an orifice without any phase change occurring in the flow through the orifice. These authors report no observations of the events occurring in the carbon dioxide after it emerges in the metastable state.

Skripov[12] describes time characteristics of the processes when a new phase is separated from a liquid in terms of a homogeneous nucleation of bubbles and an explosive growth of the vapor phase. He mentions that the time delay of bubble formation is about 10^{-9}s, but notes that Zel'dovich and Todes concluded that sufficiently rapid decompression leads to the decomposition of the liquid without formation of bubble nuclei. Exponential increase in the number of spontaneous nuclei and the higher growth rate of the bubbles hinder approach to the spinodal states where the decomposition envisioned by Zel'dovich and Todes would occur.

Pavlov[13,14] has considered a number of situations in which superheating of liquids occurs very rapidly. He analyzes each of the cases employing the exponential growth of viable boiling centers presented by Skripov. He proposes tentatively that the exponent in the growth rate formula is proportional to (p-p*), where p* is the saturation pressure at the temperature of the metastable liquid and p is the metastable liquid pressure.

Fuchs and Legge[15] studied water at room temperature and pressure emerging from a nozzle into a vacuum. They observed that under certain test conditions, the water jet left the exit in homogeneous form but burst into droplets and ice particles after traveling many nozzle diameters downstream. They related the delay in the phase transition to the absence of dissolved gases in the water.

When high pressure liquid flowing in a transparent converging-diverging nozzle to a region of lower pressure is viewed, a sharp discontinuity is seen exactly at the cross section of the throat; a 2-phase mixture continues in the diverging section[16].

The study method described here consists of visual observation and photography of a thin layer of liquid moving radially between parallel, or nearly-parallel, plates[17]. Liquid CO_2 supplied commercially at saturation pressure of about 5.5 MPa (55 bar) at room temperature is studied as it expands from this or other supply pressures to atmospheric pressure. As seen in Figure 1, high pressure liquid from a supply chamber moves slowly in the 1 mm diameter central

core of the nozzle and enters the thin radial flow region between the face of the nozzle and the glass plate. The outer diameter of the nozzle is 12.7 mm. There is a large pressure drop as the liquid enters the thin region and the liquid is accelerated to a high speed and may undergo a transition to a 2-phase mixture. Wall friction reduces the fluid speed, the pressure rises with increasing radius, and vapor which may have formed condenses. With continued outward motion, liquid acceleration gradually ceases to play a role and the wall friction is essentially balanced by a pressure gradient. When the pressure has fallen sufficiently far below the saturation pressure, the metastable liquid is subject to explosive boiling. This is the process of interest in this study.

Viscous-inertial radial flow of liquid between parallel plates.

An asymptotic solution to the 2-dimensional flow of a viscous incompressible liquid with no slip at the parallel surfaces gives, in dimensionless form, for the pressure as a function of radius[18]

$$\overline{\Delta p} = -12\varepsilon \ \ln \overline{r} - \frac{27}{35} \ \frac{1}{\overline{r}^2} + \ldots \text{terms in higher powers of } \frac{1}{\overline{r}} . \quad (1)$$

The pressure $\overline{\Delta p}$ is determined only within an arbitrary additive constant and the value of radius $\overline{r}$ at which the logarithmic term dominates is a function of the Reynolds number

$$1/\varepsilon = 2 \ \pi h \nu / m, \quad (2)$$

where h is the separation of the parallel surfaces, ν is the kinematic viscosity of the liquid, and m is the volume flow rate:

$$m = 2\pi r \ h \ \langle u \rangle . \quad (3)$$

$\langle u \rangle$ is the average radial component of fluid velocity. The dimensional forms of r and of Δp are:

$$r = h\overline{r} \qquad ; \qquad \Delta p = \frac{\rho m^2}{4\pi^2 h^4} \ \overline{\Delta p} \quad (4)$$

where ρ is mass density (960 kg m^{-3} for CO_2 at $0^{0}C$). Figure 2 shows the variation of pressure with radius predicted by the inertial-viscous solution Equation (1). The additive constant in Δp was chosen to give p = 100 kPa at r = 6.5 mm. The asymptotic solution[18] shows the radial velocity component of the fluid u to have an essentially parabolic profile at large r if plotted against the distance y from one of the parallel surfaces. The maximum value of u, u_{max}, varies as 1/r. At r = 2 mm for the set of parameters for curve 1, u_{max} = 167 m s^{-1}; for the set of parameters for curve 2, u_{max} = 239 m s^{-1}.

p is predicted to go to large negative values. Attaining negative values of pressure experimentally requires avoiding vapor formation at the internal edge of the radial flow section. The lowest pressure attained with liquid CO_2 has been +1400 kPa in a tap at r = 3 mm. The supply pressure in this case was 5500 kPa. The central supply hole in the nozzle extends to r = 0.5 mm; if the edge is machined to a sharp corner, a vaporization cloud is seen in the radial flow region with relatively small flow rates. If this edge is rounded off to a bell shape out to r = 1 mm, vapor formation is avoided for significantly larger flow rates.

Flow patterns.

Six characteristic flow patterns are produced in experiments with nozzle and window, depending on liquid supply temperature and pressure, nozzle-to-window spacing h, and the contour of the nozzle.

1. Cloudy 2-phase mixture throughout the field. With h greater than 100 μm, no part of the field is liquid. The transition occurs within the center supply tube.

2. Liquid center with radius r = 0.5 mm, remainder of field cloudy. This occurs when the inner edge of the nozzle is sharp and the nozzle face is not beveled; h must be of the order of 10 μm.

3. Liquid center surrounded by cloudy ring surrounded in turn by liquid ring bordered with sharp "petals" outside, remainder of field cloudy.

4. Entire center clear liquid, bordered with "petals" outside, remainder of field cloudy. This is seen in place of categories 2 and 3 when the inner edge is rounded off to a bell shape.

5. Clear liquid to rim. With the nozzle to plate spacing h at its minimum and effectively zero, clear liquid is seen over the whole face out to the rim. Liquid leaking out at the rim is seen to convert to a vapor-solid mixture across a sharp, finely scalloped interface in the region in which the outer rim is not perfectly sharp but rounded off.

6. Vapor bubbles at small radii, surrounded by a liquid region with decreasing size and density of bubbles. Scalloped interface at rim similar to category 5. This is characteristic of liquid supply pressure near to saturation pressure, and values of h less than 5 μm.

Information on liquid to vapor transition.

Observations of flow patterns with the microscope and 1 ns flash illumination permit some conclusions and provide some grounds for speculation on mechanisms. The appearance of bubbles in category 6 patterns is strikingly different from the cloudy patterns in categories 1 to 4. I have some confidence that the cloudy regions are vapor with particulates too small to identify at the 2 μm resolution of the photographs.

Without the bell mouth at the entry to the radial flow section, it is possible to see clear liquid at the center out to about 0.5 mm and small "spikes" of liquid extending into a cloudy ring. An example of this flow is presented in Figure 3. Since this transition occurs in a region where the layer thickness is changing rapidly--machining a sharp edge at the hole boundary inevitably leaves small burrs or depressions--details of the liquid-vapor boundary vary with azimuthal position. Some "spikes" appear to have shock-like boundaries, while others appear more diffuse, perhaps because they are 3-dimensional. I speculate that some of the "spikes" are metastable liquid transforming to a vapor-particulate mixture in the same process discussed next.

Of greater interest are the oblique transition boundaries in the radial flow region with parallel boundaries termed "petals". An example is shown in Figure 4. Since details of this photograph may be difficult to see in reproduction, Figure 5 is presented to show the nature of the pattern in a similar photograph with the camera centered on the nozzle. The "petals" are seen near the center hole in Figure 4; a decrease in nozzle-to-window spacing has the effect of moving the petals nearer to the rim.

If a piece of solid material fastens itself to the surface of the polished nozzle, it serves to anchor the root between two petals. This suggests that small irregularities in the nozzle surface may deflect the liquid, creating local pressure fluctuations which trigger the phase transition at the roots of all the petals. On the other hand, visual study of the flow patterns as h is varied shows that some visible imperfections occasionally serve to anchor the base of petals, but most of the imperfections are ignored and petal bases may form nearby, ahead of or behind the imperfections. Petal patterns remain steady indefinitely, or at least for up to several minutes, and appear visually much like the photographs. The flow with petal structure may therefore be considered a steady flow.

Regardless of the initiating mechanism for the petal structure, the existence of the sharp, mostly straight, oblique fronts separating the homogeneous liquid and inhomogeneous vapor and particulate states bears on the question of the non-equilibrium process of phase transformation. As in the case of the unsteady bubble wall growth into the metastable liquid observed by Shepherd and Sturtevant[1], the liquid appears to transform at a steady rate. This rate is considerably faster than that predicted by the theory of Prosperetti and Plesset[19], based on the rate of heat flow in the thermal boundary layer in the liquid.

A mechanism providing for release of enthalpy stored in the metastable liquid, analogous to the mechanism considered to prevail in a chemical detonation, would seem to be worthy of consideration. The initiation of a vaporization front is considered to result from the exponential growth of the density of viable boiling centers by Skripov[12] and Pavlov[13]. In our experiments it is not likely that the same pressure exists in the metastable liquid from the petal root out to the petal point; a pressure variation with radius as given by Equation (1) and illustrated in Figure 2 is more likely.

I propose that a transition surface, once formed, propagates like a Chapman-Jouguet front with a speed in the metastable liquid which depends on the enthalpy release per unit mass of fluid and the normal velocity, density and pressure of the two states of the fluid on the vapor and liquid sides of the discontinuity surface. Thus one considers each facet of the petal boundary as a bubble wall, growing into the advancing metastable liquid. If it advances faster than the oncoming liquid, it finds itself moving in less metastable liquid and slows down. This accounts for the stability of the pattern and its steady nature. A viable bubble needs to be born only once and what we see is its wall growing into the advancing liquid.

REFERENCES

1. Shepherd, J. E., and Sturtevant, B. 1982:, "Rapid evaporation at the super-heat limit," J. Fluid Mech., Vol. 121, 1982, pp. 379-402.

2. Rassokhin, N. G., Kuzevanov, V. S., Tsiklauri, G. V., Marinchek, Z. and Sella, J. 1977:, "Critical conditions with unsteady-state outflow of a two-phase medium with a pipeline break," Teplofizika Vysokikh Temperatur, Vol. 15, No. 3, 1977, pp. 589-597.

3. Mayinger, F. 1982:, "The state of knowledge of thermohydraulic pressure release phenomena," Ger. Chem. Eng., Vol. 5, 1982, pp. 297-305.

4. Smith, R. V. 1963:, "Choking two-phase flow literature summary and idealized design solutions for hydrogen, nitrogen, oxygen, and refrigerants 12 and 11," Technical Note 179, US National Bureau of Standards, 1963.

5. Edwards, A. R. and O'Brien, T. P. 1970:, "Studies of phenomena connected with the de ssurization of water reactors," J. British Nuclear Energy Soc., Vol. 9, 1970, pp. 125-135.

6. Alamgir, Md., Kan, C. Y. and Lienhard, J. H. 1980:, "An experimental study of the rapid depressurization of hot water," ASME Journal of Heat Transfer, Vo . 102, 1980, pp. 433-438.

7. Alamgir, Md. and Lienhard, J. H. 1981:, "Correlation of pressure undershoot during hot water depressurization," ASME J. Heat Trans., Vol. 103, 1981, pp. 52-55.

8. Isaev, O. A. and Pavlov, P. A. 1980:, "Ebullition of a liquid in a large volume following rapid depressurization," Teplofizika Vysokikh Temperatur, Vol. 18, 1980, pp. 812-818; in High Temperature, translation by Plenum Publ., New York, pp 631-636.

9. Stuart, Milton C. and Yarnell, D. Robert 1944:, "Fluid flow through two orifices in series-II," Trans. ASME, Vol. 66, 1944, pp. 387-397.

10. Kinderman, W. J. and Wales, E. W. 1957:, "Fluid flow through two orifices in series-III: The parameters of metastable and stable flow in hot water," Transactions of ASME, Vol. 79, 1957, pp. 183-190.

11. Hesson, J. C. and Peck, R. E. 1958:, "Flow of two-phase carbon dioxide through orifices," AIChE J. Vol. 4, 1958, pp. 207-210.

12. Skripov, Vladimir Pavlovich:, Metastable Liquids, John Wiley & Sons, New York, 1974.

13. Pavlov, P. A. "Explosive boiling of liquids," Thermophysical properties of liquids in the metastable state, Skripov, V. P., Sinitsin, E. N., Pavlov, P. A., ed., Atomizdat, Moscow, 1980, pp. 162-195, Teplofizicheskie svoistva zhidkostei b metastabil'nom sostoyanii.

14. Pavlov, P. A., "Shock regime of boiling," in Phase transformations in metastable systems, Akademia Nauk SSSR Ural'skii Nauchny Tsentr, Sverdlovsk, 1983, pp. 3-10.

15. Fuchs, H., and Legge, H., "Flow of a water jet into a vacuum.," Acta Astronautica, Vol. 6, 1979, pp. 1213-1226.

16. Fomin, N. A., Labuda, S. A., Lysenko, O. G., Soloukhin, R. I. and Emrich, R. J. 1980:, "Transition of liquid carbon dioxide to a gas-solid mixture," <u>Internacional Sympos..um on Flow Visualization</u>, Merzkirch, W., ed., Ruhr-Universitat Bochum, Germany, 1980, pp. 358-362.

17. Emrich, R. J., "Nonequilibrium expansion of liquid upon rapid pressure reduction," in <u>Shock Tubes and Waves</u>, Archer, R. D. and Milton, B. E., ed., Sydney Shock Tube Symposium Publishers, Sydney, 1983, pp. 391-396.

18. Blythe, P. A., "Private communication."

19. Prosperetti, A. and Plesset, M. S., "The stability of an evaporating liquid surface.," <u>Phys. Fluids</u>, Vol. 27, No. 7, July 1984, pp. 1590-1602.
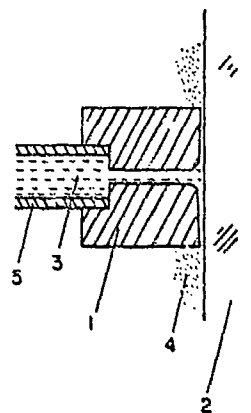
Figure 1. Arrangement for study of phase transition. 1 - metal nozzle; 2 - glass plate; 3 - liquid CO_2; 4 - 2-phase CO_2 after expansion; 5 - tube supplying liquid CO_2.

Figure 2. p vs. r relation of Eq. 1 for two sets of parameters. Curve 1 - $h_s = 5$ μm, $m = 0.7 \times 10^{-5}$ m³ s⁻¹. Curve 2 - $h_s = 5.5$ μm, $m = 1 \times 10^{-5}$ m³ s⁻¹. Symbols are pressures read at four taps for three different spacings h, when liquid CO_2 was at 0°C and when the supply pressure was 6200 kPa.
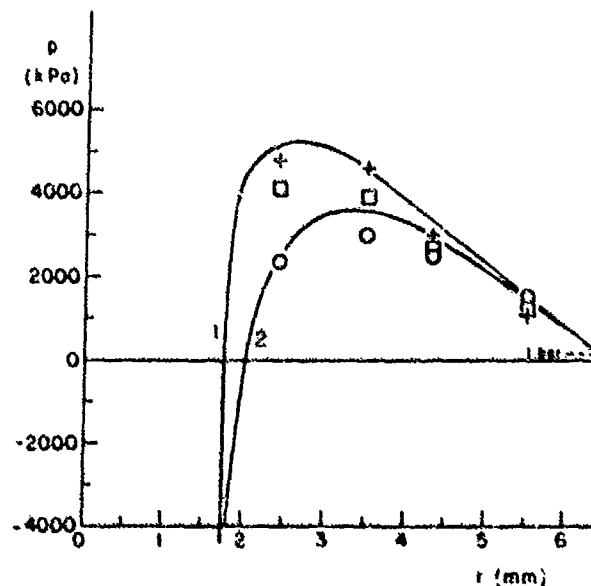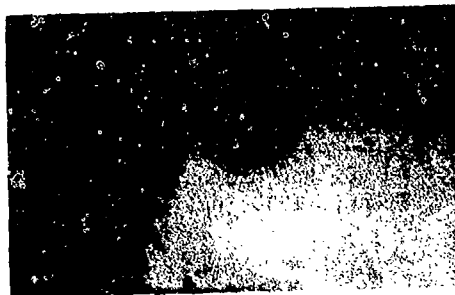
Figure 3. Liquid to
2-phase transition at
sharp-edged entry to
radial flow section.
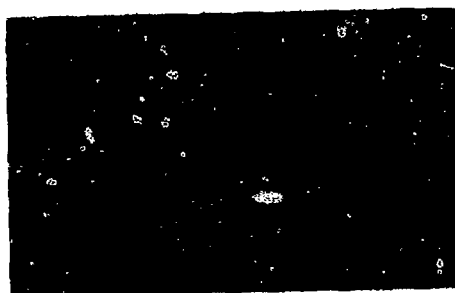
Figure 4. Liquid to 2-phase
transition within the radial
flow section. Light reflec-
tion from polished edge of
center hole is bright feature
at left. "Petals" are seen be-
low and to right of hole.
Cloudy 2-phase fluid in middle,
and outer rim of nozzle at
right are also seen.
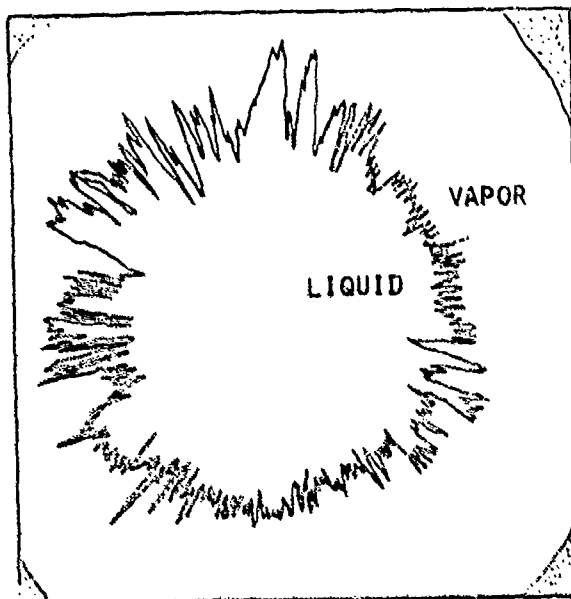
Figure 5. Tracing of
petal configuration.

SPATIAL DISTRIBUTIONS OF DUST PARTICLES

DISPERSED BY A SHOCK WAVE OVER A DUST LAYER

Takashi ADACHI   and   Tateyuki SUZUKI

Department of Mechanical Engineering
Saitama Institute of Technology
Okabe, Saitama 369-02. Japan

In the present paper the problem of dust dispersion by a
shock wave propagating over a dust layer on a horizontal
rigid floor was studied experimentally. Amberlite was
used as a model dust because it promised good reproduci-
bility of experiment. The spatial density distributions
and the velocity components of the dispersed dust parti-
cles from the dust layer were obtained from visualized
photographs. It was found that the density near the dust
layer is much larger than usually expected one and that
the profiles for different propagating shock Mach number
are reduced to a single curve when nondimensionlized
distance is taken in place of y.   The height of dust
cloud and the integrated density $\int \rho_p(x,y)dy$ were obtained,
showing that the dispersion rate is constant spatially
and with time. The comparison of velocity components for
various floor conditions revealed that the surface rough-
ness is the important factor for the mechanism of dust
dispersion by a shock wave.

1. INTRODUCTION

The interaction of a high speed flow with a dust deposited surface, and
the subsequent lofting of dust particles, is of special interest. With an
increase in uniform air speed, the dust particles enter suspension. This
process is of interest in the generation of dust clouds in coal mine explosions
and other areas. Relatively few experimental studies have been made of dust
ingestion into a high speed air flow (see Fig.1). Dawes[1], Garrard[2], Fletcher[3],
and Merzkirch and Bracht[4] have been studied the mechanism of dust dispersion
during the first hundred microseconds after the passage of a shock wave in air
over a dust deposit on a horizontal surface. Mirels[5] has investigated the dust
ingestion into high speed turbulent boundary layers on a flat plate and behind
a moving shock wave. We have also discussed in our previous papers[6,7] the effect
of a shock wave on a dispersion of dust, leaving the problem of the detailed
mechanism of dust raising.

In spite of these studies determinate theory has not been reported yet on
the mechanism of dust removal from a plane surface of dust deposit by a shock
wave. Since the dust density near the surface is so large that no conventional
technique of photographs nor optical extinction technique were available. Hence
we used a model floor which has a gutter in streamwise direction in order to
obtain the particle density and velocity near the initial dust surface. The
purpose of the present paper is to obtain the data for its precise analysis.

We used so called "Amber'ite" for a model dust, which promise a good re-
producibility. Two methods are adopted for the visualization of particles

in the neighbourhood of the shock front. They are : (1)taking direct shadows
of particles dispersed in air after the passage of a shock front in order to
see the spatial and time distributions of dust particles, and (2) taking
double-flashed color photographs of lofted particles in order to see the fine
structure of initial stage of dust cloud formation and dust particles'
velocities.

2. EXPERIMENTAL APPARATUS AND METHOD

Experiments have been performed in a horizontally placed shock tube in
order to measure the development of the dust clouds, using air as a working
gas. The tube is a 50 mm square cross section. The driver section is 1.4 m
long, and the driven section is 3.8 m. The last segment is a 2.6 m test
section, whose upper wall is removable in order to lay dust easily. It has
optical viewing windows of 45x200 mm, whose center is 3.4 m apart from the
diaphragm between the driver and driven section. Three types of floor of the
tube were used for experiments. The #1 floor has a gutter of 2 mm in depth,
2 mm in width and 1.5 m in length, in the test section, to take photographs of
the dust particles rising up from dust layer. The #2 floor has a roughness;
the #240 sand paper, whose roughness is nearly the same as that of the surface
of the dust layer, was pasted on a rigid shock tube floor. The #3 floor has
a smooth rigid surface. We placed dust particles in a line on the #2 and #3
floors to see the velocities of lifted particles. The lifting of particles on
#2 and #3 floors were investigated as the reference to the lifting on #1 floor.

Model dust used were "Amberlite CG-50 I", and "IRC-50" (hereafter we call
them Dust A and B respectively), obtained from Tokyo Organic Chemistry Ltd.,
Tokyo. Table 1 shows the properties of the dusts.

The experiments were performed with smaller shock strength, $M=1.4$ and 1.7.

Before every experiment on the #1 floor the dust surface is spread to be
smooth and flush with the rest of the tube floor surface. Optical arrangement
is the same as in our earlier report. The photographs of dispersed dust parti-
cles in the air flow behind the shock wave is taken with a $0.7\mu s$ Xenon flash.
Repeating the experiments and triggering the spark with certain delay with
respect to the shock passage deliver a cinematographic recording of the rising
up of the dust bed. The velocities of dust particles are obtained by the
photographs taken with two flash light sources, one of them has a color filter.
The photographs from these experiments can be used to measure the dust density
and the velocities of the particles as a function of time and space location.

3. EXPERIMENTAL RESULTS AND DISCUSSIONS

3.1 The Dust Cloud Developments

Direct shadows of the early stages of dust dispersion behind the shock
front are shown in Fig.2 for the purpose of better understanding of the rising
up of dust particles. The appearance of the top of the dispersed dust cloud
is not sharp. The edge of dust cloud is defined here as the point where the
number density of dust particles is about 1000 per cubic centimeter whereas
Gerrard and Fletcher identified it by the plate negatives (using a travelling
microscope) and also by projected image; Mirels did it by the commencement of
optical extinction at the specified vertical positions. They did not define
the quantitative edge condition, leaving rather ambiguity.

Figure 3 shows dust cloud profile that was produced by the passage of a
shock wave over a dust layer. It is seen:
(1) The height of a dust cloud exceeds that of the boundary layer produced by

a shock wave on a smooth surface.

(2) The delay in dispersion after the passage of the shock wave is observed for both of Dust A and B when the propagating Mach number is 1.44, as reported by Gerrard. It is about 20 μs for Dust A when the Mach number is 1.70. It seems that the delay becomes smaller as the Mach number becomes larger.

(3) The dependence of the dust cloud formation on the particle size is evident. The height to which the dust rises depenas on the particle size. Smaller particles lift up higher than the larger particles. The delay between the passage of the shock front and rasing of dust becomes smaller as the particle size becomes smaller.

The development of the structure of the dust cloud or the spatial distribution of the number density of particles in a dust cloud is shown in Figs. 4 which is obtained from Figs. 2 etc. by counting particles that appear in the air. The density distribution of dust particles are strictly obtained. The solid line indicates the data of Mirels at 29.7 cm behind a shock front at M=1.7. The dashed line indicates the extrapolation by Mirels. Figure 4 shows that the dust density immediately next to the initial dust surface increases rapidly. Mirels' extrapolation gives much less estimation than our experimental data, because optical extinction method is not suitable for such higher density region. Figure 5 shows that the density profiles for different Mach numbers can be reduced to a single curve, when $\bar{y}$ is used instead of y where

$$\bar{y} = y/(\sqrt{\rho_g/\rho_{p,m}}\ u_g x/U_s).$$

This indicates that momentum of a free stream has an important role in lifting up dust particles and the development of dust clouds.

Figure 6 shows the mass of particles above a unit area at the station x, which is obtained by integrating the density of particles along y-coordinate, that is, $\int \rho_p(x,y)dy$, where ρ_p is the density of the dust particles, and y is the distance from the initial dust surface. This figure explains the delay in dispersion of dust particles after the passage of a shock wave from another point of view. The result that the integrated mass is a linear function of the distance from the shock front shows that the dispersion rate of dust particles is uniform with respect to the distance from shock front and the time from shock passage.

3.2 The Velocity of Dust Particles Dispersed in Air

Figure 7 shows the vertical and horizontal velocity components of dust particles lifted in air from the dust beds on three kinds of model floor, that is, model floor #1, #2, and #3. The #1 floor has a gutter in which dust was laid. The #2 floor has a roughness on which dust was laid in a line. The #3 floor has a smooth surface on which the dust was laid in a line. These figures show : (1) as the particles go up higher, the horizontal and vertical components of velocity increases for all cases; (2) vertical speed seems zero when the particles leave dust bed, and then they are accelerated; (3) the data for the #3 floor are different from other data for #1 and #2 floors. On #3 floor horizontal velocity components are larger, especially near the surface, and the vertical components are smaller, whereas the data on #1 and #2 floors have nearly the same value. Therefore that the surface roughness has a significant effect on the mechanism of dust cloud formation.

4. CONCLUSION

A study was made on the problem of dust cloud formation by a shock wave over a dust layer on a horizontal rigid floor. Especially the structure of

the dust cloud of dispersed particles was investigated experimentally. From direct shadows of the dispersed particles, the density profiles and the height of the dust cloud were obtained as a function of distance from a shock front.

It was found that the density in the neighborhood of the dust layer is larger than the usually expected one and that the density profiles for different shock Mach numbers are reduced to a single profile when appropriate dimensionless height was used. It was also found that the delay between the passage of the shock front and raising of dust becomes smaller as the particle size composing the dust layer becomes smaller, and as the propagating Mach number becomes larger. Obtained integrated mass of dust particles increases linearly with the distance x from the shock front, showing that the dispersion rate is constant spatially and with time. The velocity components of the distpersed particles were obtained. It showed that the surface roughness has a significant effect on the mechanism of dust dispersion by a shock wave.

References

1. Dawes, J. G., "Dispersion of Dust Deposits by Blasts of Air, Part 1", Safety in Mines Res. Establ. Res. Rept., No.36, May, 1952, pp.1-69.
2. Gerrard, J. H., "An Experimental Investigation of the Initial Stage of the Dispersion of Dust by Shock Waves", Brit. J. Apply. Phys., Vol.14, 1963, pp.186-192.
3. Fletcher, B., "The Interaction of a Shock with a Dust Deposit", J. Phys. D: Apply. Phys., Vol.9, 1976, pp.197-202.
4. Merzkirch, W. and Bracht, K., "The Erosion of Dust by a Shock Wave in Air: Initial Stages with Laminar Flow", Int. J. Multiphase Flow, Vol.4, 1978, pp.89-95.
5. Mirels, H., "Blowing Model for Turbulent Boundary-Layer Dust Ingestion", AIAA J., Vol.22, No.11, 1984, pp.1582-1589.
6. Suzuki, T. and Adachi, T., "The Effects of Particle Size on Shock Wave-Dust Deposit Interaction", Proc. 14th Int. Symp. on Space Tech. & Sci., 1984, pp.483-490.
7. Adachi, T. and Suzuki, T., "The Singular Pressure Wave in a Dust Layer over which a Shock Wave is Propagating", Proc. 14th Int. Symp. on Shock Tubes & Waves, 1983, pp.497-504.

Table 1.   Dust properties.

Particle's dimension	Dust A (CG-50 Type I)	Dust B (IRC-50)
Mean diameter, d_p	100 μm	335 μm
Mean mass, m_p	5.1×10^{-4} mg	1.95×10^{-2} mg
Material density, $\rho_{p,m}$	0.98 g/cm^3	0.98 g/cm^3
Particle shape	nearly spherical	spherical
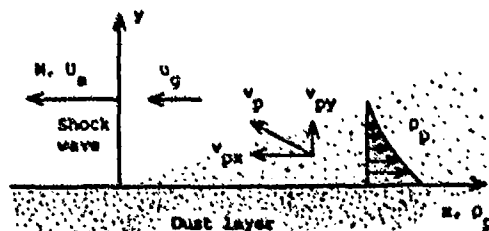
Fig. 1.   Flowfield and coordinate system.

(a)   (b)
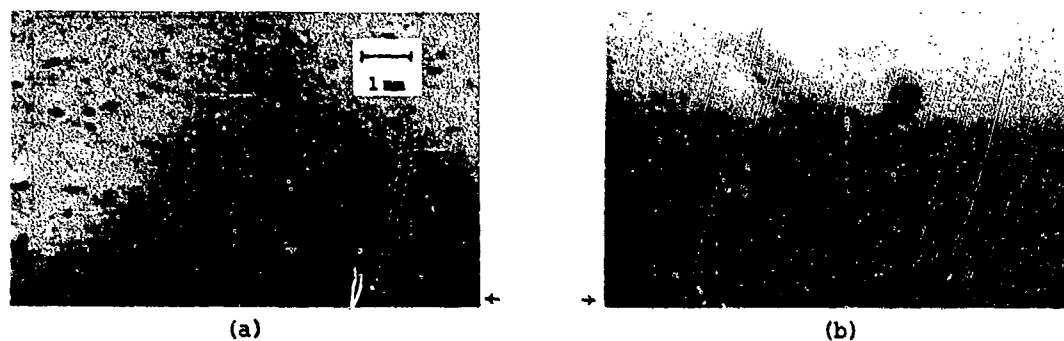
Fig. 2.   Direct shadows of dispersed particles at 20 cm downstream from shock front.   Symbols, ← and → denote the initial surface of dust layer.   a) Dust A and M=1.70.   b) Dust B and M=1.70.
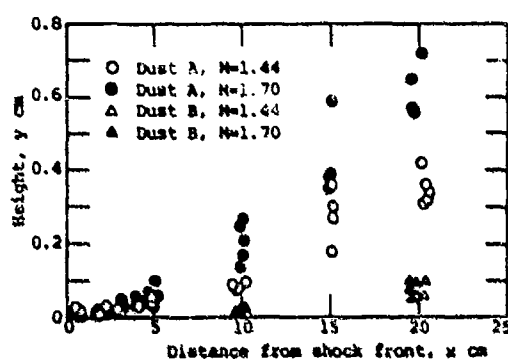
Fig. 3.   Dust cloud height vs distance from the shock front.
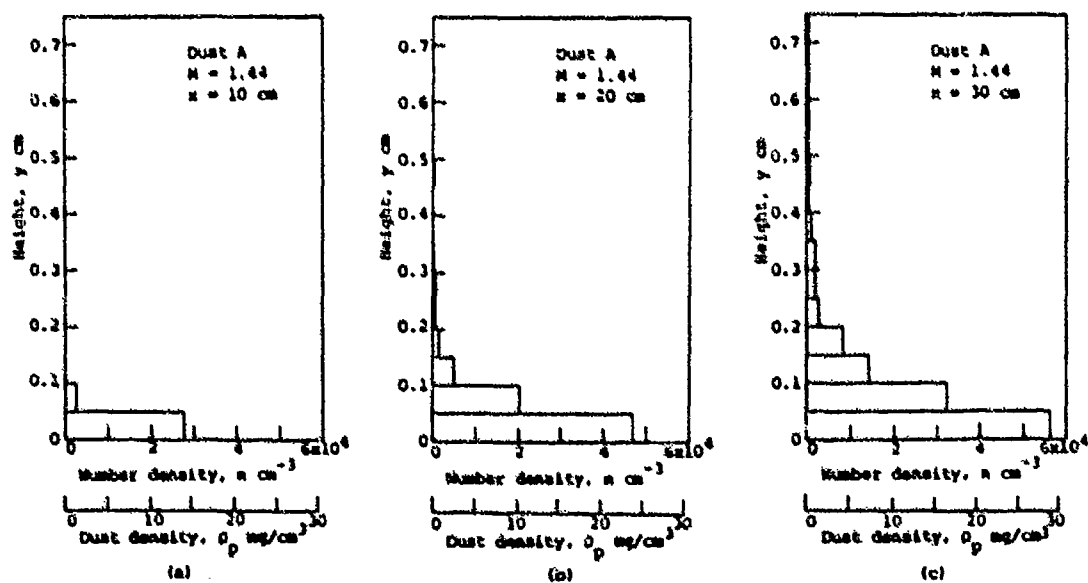
Fig. 4.   Dust density profiles.
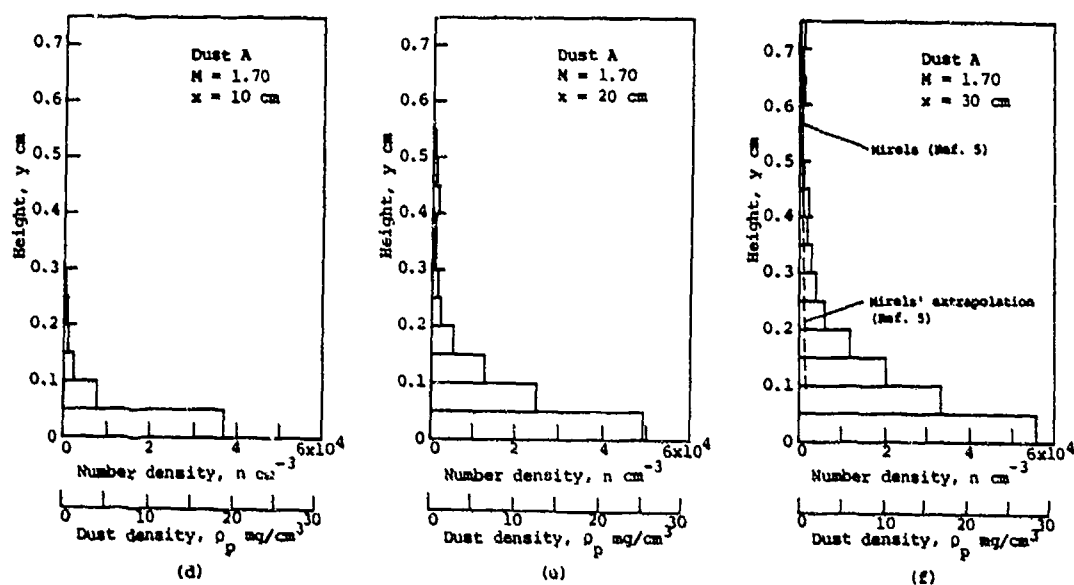
Fig. 4(Continued). Dust density profiles.
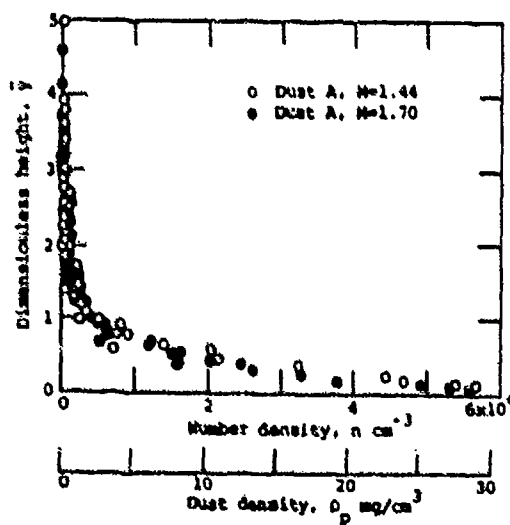
Fig. 5. Dust density vs dimensionless height $\bar{y}$.
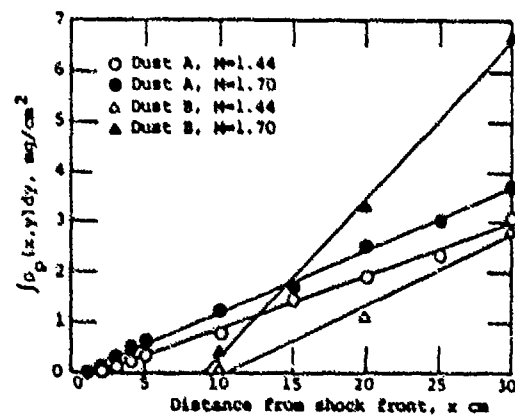
Fig. 6. Mass of dust cloud above unit area at the station x. Solid lines are determined by the least squares method.

(a)

(b)

(c)
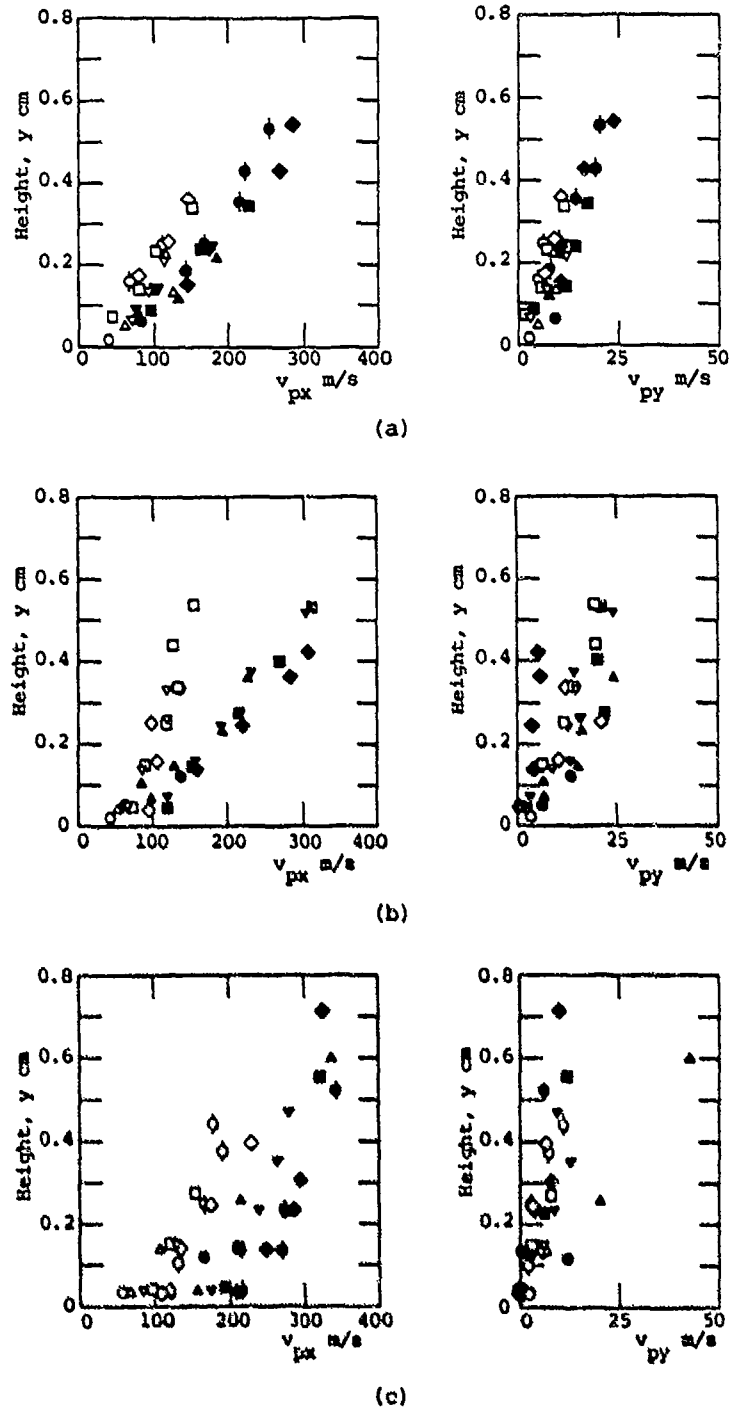
Fig. 7. Velocity components of dust particles (Dust A): a) #1 floor with a gutter, b) #2 floor with #240 sand paper, c) #3 floor with smooth surface. Symbol ○ is the data at x=5 cm with M=1.44; △,x=10 cm, M=1.44; ▽,x=15 cm, M=1.44; □,x=20 cm, M=1.44; ◇,x=25 cm, M=1.44; ◊,x=30 cm, M=1.44; ●,x=5 cm, M=1.75; ▲,x=10 cm, M=1.75; ▼,x=15 cm, M=1.75; ■,x=20 cm, M=1.75; ◆,x=25 cm, M=1.75; ◆,x=30 cm, M=1.75;

LIMITING GAS-PARTICLE FLOWS - A NEW APPROACH

C.K. Baruah and N.M. Reddy
Department of Aerospace Engineering
Indian Institute of Science
Bangalore-560012, India.

The equilibrium and frozen flow limiting cases in gas-particle flows are re-examined. With a view to obtain physically possible limiting cases, a new definition which is related to the dimension of the particle is proposed. With this definition new equilibrium and frozen flow limits for the gas-particle mixtures are deduced using the existing general governing equations. By using the available experimental results, it is argued that the limits for the equilibrium and frozen flows obtained from the present analysis tend to physically meaningful limits. Also it is shown that all the nonequilibrium solutions would be within these two limits.

1. INTRODUCTION

The presence of particles in flowing gases can cause significant flow changes in rocket and wind tunnel nozzle flows leading to performance deterioration. The fundamental thermodynamic behavior of these gas-particle mixtures has been extensively investigated and published in the literature[1,2]. The gas particle flow analysis becomes very complex due to the presence of non-equilibrium effects between gas and particles[1]. Hence, following the ideas as in the case of real gas flows, limiting flows called "equilibrium and frozen" flows are often defined and used as simple bench mark solutions to this complex problem[1,2]. In the present study these limiting flows and their implications are re-examined with a view to obtain an understanding regarding the conditions to be satisfied in order to attain these limiting flows in practical flow applications like in one-dimensional nozzle flows.

In the present investigation an attempt has been made to redefine the limiting flows so that they are physically possible solutions. It is argued that in order to obtain equilibrium flows, the particle size should become nearly equal to gas molecular size and consequently it can be assumed that the particle becomes indistinguishable from the gas molecule. This requirement is necessary to ensure velocities and temperatures equilibrium everywhere. It should be noted here that there exists considerable velocity slips even in the case of the flow of mixture of two gases with disparate molecular sizes[3]. Hence the indistinguishability creteria is invoked. From this basic assumption, the governing equations for equilibrium flow are formally derived from the general governing equations given in Ref.1. These equations turn out to be the same as that of pure gas case with mixture thermodynamic properties including mixture speed of sound identically equal to that of pure gas. The "frozen limit" is defined as the limit in which the changes in particle velocity and temperature tend to zero every where. It is shown that to ensure this limit, the particle size should tend to infinity. Then, from the general governing equations, the pure solid properties are inferred and this also implies that there is no gas flow in this limit. The mixture speed of sound and mixture pressure in this limit also tend to zero.

The physical validity of equilibrium flows as defined in the present analysis is justified with the help of existing experimental measurements made in one dimensional nozzle flows[4]. The present analysis gives unique values for mixture speed of sound

in both the limits which are independent of loading ratio. This is in contrast to the case of equilibrium flow as defined in Ref.1 where the equilibrium mixture speed of sound varies from pure gas value to almost zero as the mass concentration ratio $\phi \to 1$ before it shoots up to infinity for $\phi = 1.0$. It may also be noted that the "equilibrium" limit as defined in Ref.1 may not be realizable in actual flow situations.

2. DEFINITION OF A NEW EQUILIBRIUM LIMIT

The drag force and heat transfer rate can be written as[2] ;

$$F_p = (\beta (u_p - u)) / (\tau_v) , Q_p = (\beta C(T_p - T)) / (\tau_T) \tag{1}$$

where $\tau_v = (m_p/3\pi d_p \mu) = (\rho_p d_p^2 / 18\mu)$ and $\tau_T = 3/2 \delta P_r \tau_v$

F_p and Q_p can also be expressed as;

$$F_p = 18\beta\mu (u_p - u) / \rho_p d_p^2 \text{ and } Q_p = 12\beta k(T_p - T)/ \rho_p d_p^2 \tag{2}$$

We postulate that when the particle size reduce to the molecular size, instantaneous equilibration of velocities (ie, $u = u_p$) and temperatures (ie. $T_p = T$) is possible. This means that in the actual flow situations the equilibrium limit occurs even when τ_v is not zero but finite, although very small. Then $F_p = 0$ and $Q_p = 0$. In this limit we will assume that particles loose their seperate identity and behave as the gas phase does. Hence the bulk specific heat of the particles is assumed to tend to the same value as that of the specific heat of gas phase. Since the particles are of molecular size, the volume fraction $\epsilon \to 0$ in this limit and pressure due to random motion of the particle becomes as significant as gas phase.

3. DEFINITION OF FROZEN LIMIT

In this limit we postulate that the size of the particles tend to infinity ($d_p \to \infty$) so that there would not be any change in the velocity or temperature of the particle. The volume fraction $\epsilon \to 1$ in this limit since the size of the particle $d_p \to \infty$.

4. GOVERNING EQUATIONS FOR THE GAS-PARTICLE MIXTURE

Conservation of mass

$$[(1 - \epsilon) \rho u + \beta u_p]A = (1 + \eta)\dot{M} \tag{3}$$

Conservation of momentum

$$(1 - \epsilon) \rho u (du/dx) + \beta u_p (du_p/dx) + (dP_m/dx) = 0 \tag{4}$$

Conservation of energy

$$[(udu/dx) + C_p (dT/dx)] + \eta [u_p (du_p/dx) + c (dT_p/dx) + (1/\rho_p) (dP_m/dx)] = 0 \tag{5}$$

Note:

The total mixture pressure P_m should be used in Eq.(4) and (5) since the particle pressure due to random motion is as significant as that of gas in the equilibrium limit.

Equation of state,

$$P_m = \rho_m R_m T \tag{6}$$

In the above equations, $\eta = \beta u_p/(1 - \epsilon) \rho u$, $\beta = \epsilon \rho_p$

The partial pressures of gas phase and particle phase are given as $p = (1 - \epsilon) \rho RT$ and $p_p = \beta R_p T$

Here we will not consider the rate equations for particle velocity and temperature since they are not required for the present consideration of limiting flows. Besides, it is felt that due to the new definition of limiting flows as done here, the existing rate equations[2] may have to be suitably modified in order to obtain consistent meaningful results.

4. MIXTURE EQUATION OF STATE

$$P_m = \rho_m R_m T = (P + P_p)$$

$$\rho = (1 - \epsilon)\rho RT, \quad P_p = \beta R_p T, \quad \rho_m = [(1 - \epsilon) + \beta/\rho]\rho$$

$$P_m = \rho RT[(1 - \epsilon) + (\beta/\rho)m_r]$$

$$R_m = R[((1 - \epsilon) + (\beta/\rho)m_r) / ((1 - \epsilon) + (\beta/\rho))]$$

(7)

where $m_r = (MW/MW_p)$.

For equilibrium flow, $m_r = 1$ and $(\beta/\rho) = n$

Then, $P_m = (1 + n)\rho RT = (1 + n)P$

$$\rho_m = (1 + n)\rho$$

$$P = \rho RT \text{ is true for the mixture also}$$

(8)

$$C_{p_m} = C_p, \quad \gamma_m = \gamma \text{ for pure gas}$$

$$(a_m)_e^2 = \gamma_m R_m T = \gamma RT$$

5. EQUATIONS FOR EQUILIBRIUM LIMIT

In this limit the particle size is assumed to reduce to molecular size so that the "particle-molecule" and "gas molecule" become indistinguishable. Then the following assumptions are assumed to hold good.

$$u_p = u, \quad T_p = T, \quad C = C_p, \quad \epsilon = 0, \quad (\beta/\rho) = n$$

Then the governing equations for equilibrium flow can be reduced and written in terms of mixture quantities as:

$$\rho_m uA = \dot{M}_m$$

$$\rho_m (u\,du/dx) \cdot (dP_m/dx) = 0$$

$$u(du/dx) \cdot C_{p_m}(dT/dx) = 0$$

(9)

$$P_m = \rho_m R_m T$$

$$(a_m)_e^2 = \gamma_m R_m T$$

where $\dot{M}_m = (1 + n)\dot{M}$

Thus the mixture behaves as a single perfect gas. By using the equilibrium relations between the mixture and pure gas quantities (Eq.8), this system of equations can be shown to reduce to the case of single pure gas. Thus the mixture behaves as a single pure gas.

6. EQUATIONS FOR FROZEN FLOW LIMIT

By definition, $d_p \to \infty$, τ_v and $\tau_T \to \infty$, $m_r = 0, \epsilon \to 1.0$, and T_p and u_p are constant. Then, from the governing equations the following can be inferred.

mixture mass $\to \infty$; mixture momentum $\to 0$; mixture energy $\to 0$

$$p_m = P = 0 ; a_m \to 0 ; \gamma_m \to 1.0 \qquad (10)$$

Above limits indicate that there is no flow and the whole volume is filled with particles of very large dimensions and these particles behave very similar to "Newtonian" gas in hypersonic flows.

Here, the two limits namely equilibrium and frozen flows as defined in Ref.1 needs some examination. In Ref.1, the equilibirum limit is defined as the one which would have $u=u_p$ and $T=T_p$ instantaneously (meaning zero relaxation times). Then the gas properties and bulk properties of particles contribute to the thermodynamic properties of the mixture, with almost infinite heat transfer rate irrespective of particle size. This limit is derived from the ideas presented in the relaxation of gases at high temperatures. We feel that this definition for equilibrium limit does not seem to occur in any physical situations until one reduces the particle size to molecular size. Then, the present analysis shows that the new equilibrium limit as defined in this note gives values for mixture properties different from those given in Ref.1 and this new limit appears physically meaningful as shown in the present analysis.

In Ref.1, the frozen limit also defined as the one at which there would be no change in the properties of either particles or the gas; and this limit is attained as the relaxation time tends to infinity. Then invoking $u_p = 0$ and $(dT_p/dx) = 0$ in the governing equations derived for $\epsilon = 0$, a set of equations have been derived which are the same as that of pure gas case. This seems to lead to non-physical situations for the following reasons. For relaxation times to tend to ∞, the diameter of the particle has to assume very large values. Then, the flow certainly gets affected with large particles existing in the stream.

In the present analysis, we have also used the same definition for this limit but we get different limits which seem to be reasonable from the physical grounds. This is mainly due to use of exact governing equations including volume fraction effects and in taking limits we have assumed $\epsilon \to 1.0$. Then in this limit the whole volume is filled with particles alone and no gas flow is possible. The limiting values derived from the present analysis also show that the whole volume should contain loosely packed large size particles and these particles would behave very similar to "Newtonian fluid" in hypersonic flows as Mach number $\to \infty$.

7. COMPARISON OF THEORY WITH AVAILABLE EXPERIMENTS

Hultberg and Soo[6] have carefully measured the pressure distribution as well as the gas and particle velocity variations along a supersonic nozzle. Also they have computed the flow quantities by using the existing system of nonequilibrium equations[1]. The experimental results as well as the computed values are shown in Fig.1. The conditions for their analysis were $P_o = 29.895$ in.Hg, $T_o = 24.4°C$, $\delta = 0.83$, $\rho_p = 2230$ Kg/m^3, $n = 1.39$, glass particles of $d_p = 230\mu$ m and $\tau_v = 0.366$ sec. The optical density of a negative of a view of the system of particles in the test section was determined with a Weston densitometer. Since the optical density is directly proportional to the particle density β , and since the loading ratio n and the velocity of the gas are known, then the velocity of the particles are determined.

From Fig.1 it may be observed that their computed gas pressure and gas velocities exactly agree with their measured values. However, the computed particle velocities deviate considerably from the measured ones. More significantly, the measured particle velocity follows very closely the measured gas velocity even after the nozzle throat section, eventhough the particle size used is very large (230 μ m). This appears surprizing at the out set considering the fact that the computed particle velocity shows rather large slip from the computed gas velocity. They[4] have not offered any serious reason for this rather large discrepency.

In Ref.1, assuming instantaneous equilibration of particle velocity and temperatures with corresponding gas values, the thermodynamic properties of gas-particle mixture have been derived, where-in the ratio of specific heats of equilibrium mixture is given as

$$(\gamma_m)_e = (\gamma[1 + \eta \ \delta \ ]) / [1 + \eta \ \delta \ \gamma \ ] \qquad (11)$$

where γ corresponds to the pure gas value (1.4 for air). For the Hultberg's experimental conditions $(\gamma_m)_e = 1.14$. By using this value, the pressure and the velocity variation along the nozzle used by Hultberg was computed and these variations are also shown in Fig.1. As can be seen from the Fig.1, the equilibrium values[1] are much lower than the measured values. The pressure corresponding to $(\gamma_m)_e = 1.14$ is also higher than the measured values.

In the earlier sections we have proposed a new equilibrium limit where-in we have shown that the mixture $(\gamma_m)_e = \gamma$ of pure gas. By using this value for air, the equilibrium pressure and velocity distributions were computed and these are also shown in Fig.1. These are exactly equal to the ones computed by Hultberg using nonequilibrium theory. The measured pressures and velocities also agree with this theory. Hence, it may be stated that the new equilibrium limit proposed in the present paper has physical validity and can be used as an upper and ideal limit for the gas-particle flows.

Another significant point to note here is that although the particle size is rather large (230 μ m) the particles seem to follow the gas velocity very closely even in the supersonic section of the nozzle where as the computed particle velocities are much smaller. We have no reasons not to believe the particle velocity measurements. But we have some doubts about the rate equation for the particle that has been used in the nonequilibrium computations. An order of magnitude estimate shows that if the drag term $(\beta \ D/m_p)$ is reduced, the particle velocity decreases; on physical grounds this is contradictory since, if the drag force is reduced, the particle should move faster. Another situation that we have come across in the literature is that, all the nonequilibrium nozzle flow computations show large slips (in effect low particle velocities). But most of the available experiments in rocket nozzles[4,5] show velocity and temperature slips of a few percent (5 to 10%) even at very high temperatures[5]. This implies that the gas particle flows in nozzles with particle diameter up to a few hundreds of μ m may always be in near equilibrium.

LIST OF SYMBOLS

ρ -   mass density of gas phase
u   -   velocity of gas phase
A   -   nozzle area
M   -   mass flow of gas phase
β -   mass density of particle phase
u_p -   velocity of particle phase
M_p -   mass flow of particle phase
η - $(M_p/M) = (u_p \epsilon)/[\rho u(1 - \epsilon) \ ]$

P_m —   mixture pressure

P —   pressure of gas phase

P_p —   pressure of particle phase

F_p —   force per unit volume exerted by particles on fluid

Q_p —   heat transfer rate per unit volume from particles to gas

T —   temperature of gas phase

C_p —   specific heat of gas at constant pressure

x —   linear distance along the nozzle

C —   bulk specific heat of particles

T_p —   bulk temperature of particles

R —   gas constant for gas phase

a —   speed of sound

τ_v —   characteristic time associated with velocity equilibrium of the particle

μ —   viscosity of gas

R_e —   Reynolds number $(Re = \rho(u-u_p)d_p/\mu$

R_p —   gas constant of particle phase

ε —   volume fraction

m_p —   mass of each particle

P_r —   Prandtl number

ϕ —   mass concentration ratio

ρ_p —   bulk density of particles

MW —   molecular weight of gas

MW_p —   molecular weight of particle gas

Y_m —   mixture ratio of specific heats

δ — C/C_p

REFERENCES

1. Rudinger, G., "Fundamentals of Gas-Particle Flow", Elsevier Publishing Company, 1980, p.40.

2. Marble, F.E., "Combustion and Propulsion", 5th AGARDO-graph Colloqium, Pergamon", 1963, p.175.

3. Mitra, N.K., & Fiebig, M., "Flow in a Nozzle with Gas Mixtures of Disparate Molecular Masses", Proceedings of the 15th Rarefied Gas Symposium held in Japan, 1984, p.655.

4. Hultberg, J.A., & Soo, S.L., "Astronautica Acta", Vol.11, No.3, 1965, p.207.

5. Carlson, D.J., "Experimental Determination of Thermal Lag in Gas-Particle Nozzle Flows, ARS Journal, Vol.32, No.7 or 8, 1962, p.1107.
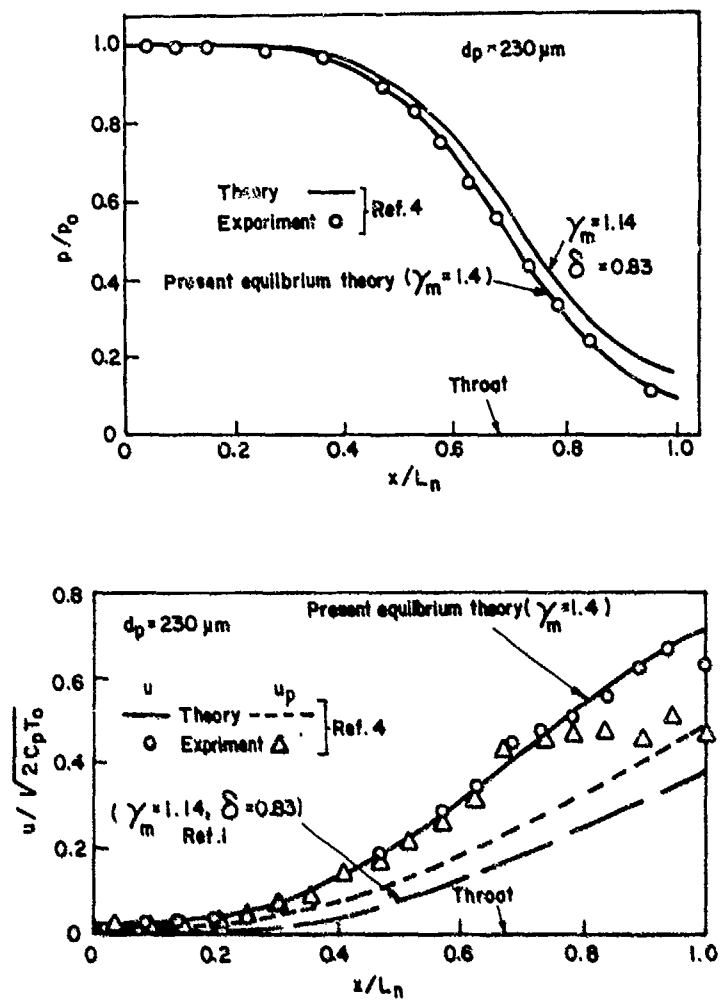
FIG.I COMPARISON OF PRESENT THEORY WITH
EXPERIMENTS

THE STRUCTURE OF SHOCK WAVES IN A BOILING LIQUID

V.Ye.Nakoryakov, B.G.Pokusaev, I.R.Shreiber

Institute of Thermophysics, Siberian Branch
of the USSR Academy of Sciences, 1 Lavrentyev Avenue
Novosibirsk 630090, USSR

Wave propagation in a liquid with vapour bubbles
is under study. The structure and dynamics of
linear waves are investigated. The calculated
results are compared with the results of experiments
on vapour-water and vapour-freon mixtures. The
dynamics of non-linear waves is also under study.
A model is offered and numerical and experimental
investigations have been performed which concern
the structure and dynamics of nonlinear waves.
The problem about the existence of shock waves
is also considered.

The structure and dynamics of shock waves in a liquid with
gas bubbles have been studied sufficiently well[1,2]. To model
the propagation of waves in a boiling liquid, we consider the
system "liquid - gas bubbles" which is on the saturation line.
Assuming that the basic nonlinearity of the system (as with a
liquid with gas bubbles) is conditioned by the high compressibi-
lity of the medium, we will write the basic equations for a
bubble suspension with phase transitions:

$$\frac{\partial^2 \rho}{\partial t^2} = \frac{\partial^2 \rho}{\partial x^2} \; ; \qquad \rho = \frac{\rho_1}{1 + \frac{4}{3}\pi(R^3 - R_o^3)n} \qquad (1)$$

$$R\frac{d^2 R}{dt^2} + \frac{3}{2}\left(\frac{dR}{dt}\right)^2 = \frac{P(R)-\rho}{\rho_1}$$

$$\frac{\partial P(R)}{\partial t} + \frac{3\gamma P(R)}{R}\frac{dR}{dt} = \frac{3(\gamma-1)}{R}\left(-q_\text{l} - (c_p T - L)(q_v - q_\text{l})\right)$$

where ρ_1 = liquid density; ρ = mixture density; ρ = mixture
pressure; $P(R)$ = vapour pressure in a bubble; R = bubble
radius; q_l = heat flux directed into the liquid; q_v = heat
flux directed into the vapour on the "bubble - liquid" boundary;
c_p = heat capacity of the liquid; L = latent heat of evaporation.
In terms of the weak-nonlinearity approximation, the initial
system can be reduced to one equation for pressure waves:

$$\frac{\partial^2 \rho}{\partial t^2} - c_o^2\frac{\partial^2 \rho}{\partial x^2} - \frac{2\gamma}{\gamma+1}c_o^2\frac{\partial}{\partial x^2}\left(\frac{\Delta \rho^2}{P_o}\right) - 2\beta\frac{\partial^4 \rho}{\partial t^2 \partial x^2} = \frac{3\gamma\rho}{R_o \rho_2 L}\frac{\partial q_\text{l}}{\partial t} \qquad (2)$$

ρ_2 = vapour density; $c_o = \frac{\gamma P_o}{\rho_o \varphi_o}$ = frozen sound velocity of

bubble suspensions, $2\beta = R_o^2/3\varphi_o$, where φ_o is the initial void
fraction of the mixture.

To determine q_μ, we consider the temperature field in the vicinity of a bubble with a constant radius, the temperature of whose boundary, T_S, corresponds to the instantaneous pressure value in the system, and the temperature T_∞ at an infinite distance from the bubble is equal to T_0, i.e. the initial temperature of the liquid.

The solution of this problem can have two asymptotics:
- If the length of the heat waves is much smaller than the distance between the bubbles, then

$$q_\mu(t) = -\lambda_{\varkappa c}\left(\frac{\Delta T_S}{R} + \int_0^t \frac{\partial T_S}{\partial \tau}\frac{1}{\sqrt{t-\tau}}\,d\tau\right) \tag{3}$$

where T_S and P are related by the Clapeyron – Clausius equation, $dT/dP = T_S/\rho_2 L$.
- In case when the lengths of the heat waves are on the order of the distance between the bubbles, then, within the framework of the bubble-medium cellular model, the asymptotic of the heat flux

$$q_\mu(t) = \frac{c_\rho \rho_1 T_S}{\rho_2 L}\frac{R}{3\varphi_0 a}\frac{\partial P}{\partial t} \tag{4}$$

After the substitution into (2), the heat flux (4) reduces this equation to the wave equation with the characteristic velocity

$c_1 = \dfrac{L\,P_0}{c_\rho \rho_1^2 \beta^2 T_0}$, where c_1 is the equilibrium sound velocity in a medium with phase transitions.

In real experiments (see refs. 2,3) carried out in shock tubes, case (4) is practically never realized, therefore equation (2), together with (3), was considered as underlying the analysis of the structure and dynamics of shock waves:

$$\frac{\partial^2 \rho}{\partial t^2} - c_0^2\frac{\partial^2 \rho}{\partial x^2} - c_0^2\frac{\partial}{\partial x^2}\left(\frac{\Delta\rho^2}{\rho_0}\right) - \varepsilon\beta\frac{\partial^4 \rho}{\partial x^2\partial t^2} = \alpha\frac{\partial}{\partial t}\int_0^t\frac{\partial \rho}{\partial \tau}\frac{1}{\sqrt{t-\tau}}\,d\tau \tag{5}$$

$$\alpha = \frac{3\gamma P_0\lambda_{\varkappa c}T_S}{R(\rho_2 L)^2\sqrt{\pi a}}$$

In case when the interphase heat transfer is not dominating, we can pass from (5) to the equation for waves propagating in one direction:

$$\rho_t + c_0\rho_x + \frac{\gamma+1}{\gamma}c_0\frac{\Delta\rho}{\rho_0}\rho_x + \beta c_0\rho_{xxx} = \frac{\alpha}{2}\int_0^t\frac{\partial \rho}{\partial \tau}\frac{d\tau}{\sqrt{t-\tau}} \tag{6}$$

The linearized equation (6) has an analytical solution in case when the initial pulse is defined as a "step":

$$\rho = \rho_0 \cdot erfc\left(\frac{\alpha\sqrt{\pi}\,x}{c_0\sqrt{t-x/c_0}}\right) \tag{7}$$

The legitimacy of the transition to the evolutional equation was investigated specially. The structure and dynamics of the waves were also studied in experiment. The experiments were carried out on a shock tube which was specially thermostatted.

The liquid under study was in the saturation state along the entire length of the tube ($L \approx 1.5$-2 m). The vapour was bubbled through special calibrated capillaries at the bottom of the tube. In such a way we could achieve homogeneity of the bubbles along their diameters. Experimental pressure profiles were registered by piezoelectric ceramic pressure probes mounted into the tube wall.

In studying small-amplitude linear waves, we compared the results obtained by the fast Fourier transform (FFT) and with those obtained by using formula (7). In case when the waves in a vapour-freon mixture are considered ($\alpha_2 = 0.002$), the calculations by the FFT technique and formula (7) coincide with experimental profiles. In the case of a vapour-water mixture ($\alpha_1 = 0.02$), the calculations by the FFT technique are in good agreement with experimental profiles and differ almost two fold from the calculations by formula (7). Figs. 1,2 compare the calculated results (solid lines) with experimental profiles (dots in fig. 1). The reason for such a discrepancy is quite obvious from analyzing the solutions of equation (2) for the initial "bell-like" distribution at $\alpha_1 = 0.02$ and $\alpha = 0.002$.

Figs. 3,4 show the results of such calculations. One can see that in the case $\alpha_2 = 0.002$ the initial pulse is divided into two diverging waves. In this case formula (6) gives good results. In the case $\alpha = 0.02$ the initial pulse is not split into two waves and evolves as a whole formation. Due to the fact that the case α corresponds to more intensive phase transitions, the heat conductivity processes (parabolic problem) dominate over the wave propagation processes (hyperbolic problem) and therefore the transition from (2) to (6) is not correct. Owing to this, one can observe discrepancy between the calculations by formula (6) and experiment.

Model (1) has enabled us to understand the problem of the existence of shock waves in a liquid with vapour bubbles.

In our experiments on vapour-water mixtures (2,3) we could observe waves of various structure. If the initial pressure was 1 atm., we could not observe shock waves, i.e. with increasing the intensity of a wave its velocity did not increase and only its profile became diffused (fig. 1). In a vapour-water mixture with the high initial pressure of 0.8 MPa we could observe shock waves of oscillating structure which were reminiscent of the jumps in a liquid with gas bubbles. If we assume that the shock waves exist during the time t^*, then expression (3) will take the form

$$q_L \approx -\lambda_{\mathcal{K}} \int_0^{t^*} \frac{\partial T_S}{\partial \tau} \frac{d\tau}{\sqrt{t - \tau}} \tag{8}$$

If we assume that a shock wave has the form of a "step", then from (8) and (6) follows the shock-wave existence condition

$$t^* < \frac{4 \pi R_0^2}{m^2} \left(\frac{\Delta P}{P_0} \right)^2 ,$$

where $m^2 = \dfrac{3 \chi P_0 \rho_1 c_{p_1}}{\rho_2 L} \left(\dfrac{dT}{dP} \right) a_1$; a_1 is the temperature

conductivity of the liquid. The distances x^* at which the shock waves exist can be estimated assuming $x^* = c_0 \cdot t^*$. Let us give some estimates for x^*.

water: 1) P_o =0.1 MPa, T_o =100°C X^* =0.012 m;
         2) P_o =8.5 MPa, T_o =300°C X^* =13.6 m

freon12: P_o =0.66 MPa, T_o =25.4°C X^* =1. m

Therefore in the experiments which correspond to the first case
we could not observe shock waves, and in case (2) we observed
the picture of oscillating shock waves shown in fig. 5 by the
dotted line. The results of the calculations using equation (6)
are also given there.

REFERENCES

1. Kuznetsov, V.V., Nakoryakov, V.E. and Pokusaev, B.G.
   "Experimental investigation of wave processes in gas-liquid
   mixture", J. Fluid Mech., 1978, Vol. 35, pt 1, p. 85-96.

2. Nakoryakov, V.E., Pokusaev, B.G. and Shreiber, I.R. "Wave
   propagation in gas- and vapour-liquid media". Institute of
   Thermophysics, Siberian Branch of the USSR Academy of Sciences,
   Novosibirsk, 1983.

3. Nakoryakov, V.E., Pokusaev, B.G., Pribaturin, N.A. and
   Shreiber, I.R. "Shock waves in boiling liquids". Intern. Comm.
   Heat Mass Transfer 1984, Vol. 11, n. 1, p. 55-62.
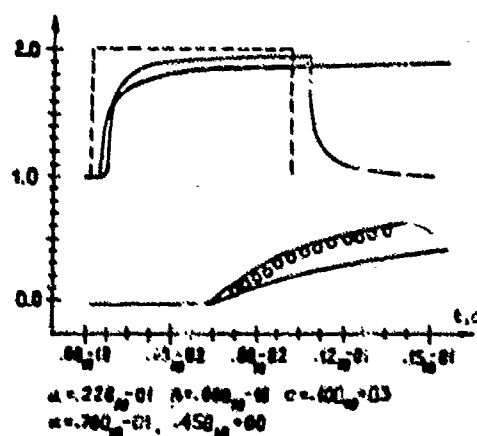
Fig. 1.
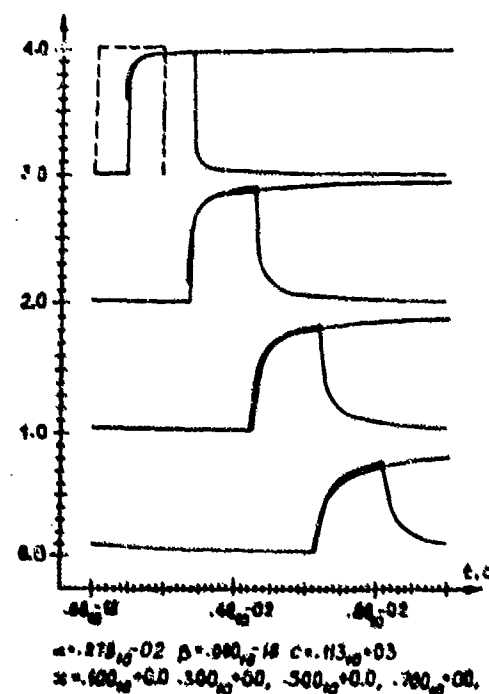
Fig. 2.
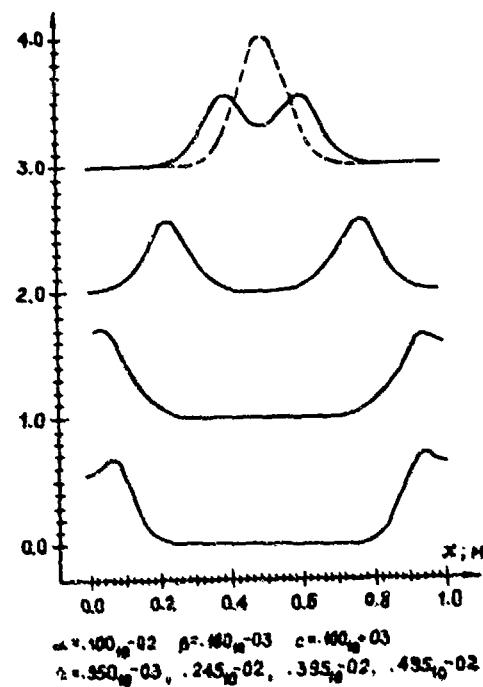
Fig. 3. Evolution of a finite signal with weak interphase interaction.
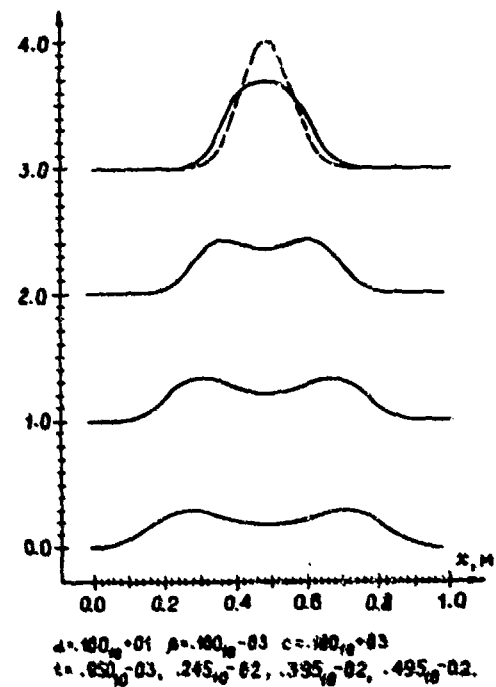
Fig. 4. Evolution of a finite signal with intensive interphase interaction.
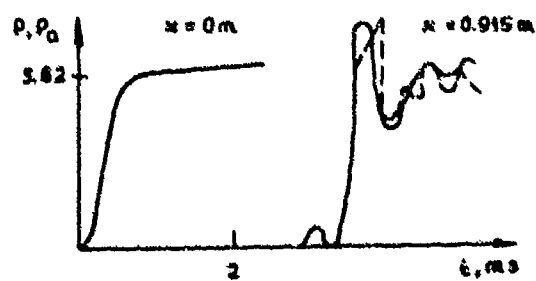
Fig. 5.

HOMOGENEOUS AND HETEROGENEOUS CONDENSATION OF NON-IDEAL BINARY

VAPOUR MIXTURES IN SHOCK TUBE EXPANSION FLOW

G.H. Spiegel, R.A. Zahoransky and S.L.K. Wittig

Institut für Thermische Strömungsmaschinen,
Universität Karlsruhe (T.H.), Kaiserstr. 12,
D-7500 Karlsruhe, W. Germany

The present experimental and theoretical study is concerned with the homogeneous nucleation and the subsequent process of heterogeneous droplet growth in supersaturated binary water/n-propanol vapours. The phase change of this strongly non-ideal system was observed in the expansion fan of a heated shock tube in the whole mixing range under variation of the stagnation properties. The pressure traces were recorded simultaneously with the condensation onset, which was detected by means of light extinction at several measurement planes thus providing conclusions on the influence of the cooling rate. The experimental results i.e. onset conditions and time resolved traces of droplet diameter and number density, are compared with classical nucleation theory and a recently developed binary droplet growth model. By using the dynamic surface tension for small binary droplets, good agreement between theory and experiment was found over the whole mixing range. The droplet growth was obtained by the optical dispersion quotient technique, which is extended to the UV-range.

INTRODUCTION

As previously discussed [1,2,3], condensation phenomena are of primary importance in a variety of technical and atmospheric processes. Due to the fact, that not only one pure component is involved in most of the real applications, the homogeneous nucleation and the subsequent heterogeneous condensation in the subcooled vapour phase of multicomponent mixtures have predominantly to be taken into consideration. Especially, the utilization of binary vapours as working fluids in low temperature cycles, the analysis cf gas separation in fast expansion flows, applications in chemical engineering and the study of meteorological phenomena have to be mentioned.

In this work, the spontaneous phase change of strongly non-ideal water/n-propanol vapour mixtures was investigated in a shock tube. The experimental results are compared with the extension of the classical nucleation theory to binary vapours [4,5,6] and a binary droplet growth model described in previous papers [3,7,8]. The strong influence of surface enrichment effects on the surface tension of small microclusters, which is of primary importance at water-rich vapour compositions, is accounted for [9].

EXPERIMENTAL

The high pressure section of the previously described heated shock tube was used in producing the fast subcooling of the vapour mixtures, leading to the homogeneous nucleation and subsequent condensation [1,2,3,10]. The optical

diagnostics and the data acquisition of the tube have been modified. Figure 1 illustrates the schematic of the setup, the measurement arrangement and the nearly fully automatic data acquisition.

The water/n-propanol mixture, which has an azeotropic composition closer to equal component concentrations than the previously discussed water/ethanol mixture was vapourized and mixed with the inert gas as discussed in preceding papers [1,2,3].

Specifically, care was taken to maintain constant temperatures along the tube's axis within ±1 °C. Three measurement stations at 25, 111 and 197 cm from the diaphragm served for recording the isentropic expansion process after the membrane's rupture. The pressure traces and light extinctions were recorded, which allowed the definition of the condensation onset and its time characteristics. In the majority of the experiments, the extinction of a HeNe-laser beam only was followed in plane 1 and 3, whereas the droplet growth and the number concentrations were obtained in plane 2 using the earlier described dispersion quotient technique [11]. The extension of the measurement range to lower droplet sizes down to $r \leq 0.05$ μm was achieved by selecting one wavelength in the UV-range ($\lambda = 250$ nm). A high pressure UV-arc lamp was combined with a monochromator, the other light source was an argon-ion laser ($\lambda = 488$ nm). The well known simple gasdynamic relations were applied in determining the parameters of interest, i.e. pressure, temperature and cooling rate during the expansion in the measurement planes as well as along the particle paths, up to the onset of condensation. Threedimensional effects due to the opening of the diaphragm require a correction of the location of the expansion fan [13].

THEORY

Two major steps are taking place during the spontaneous phase change of supersaturated vapours. The first one - the homogeneous nucleation - determines the size and number concentration of the clusters in the subcooled metastable binary vapour, which are capable of growing and thus provide the initial conditions for the subsequent heterogeneous droplet growth. Only classical theory can be utilized in describing the nucleation process for real binary systems with their complex molecules as found in the mixture analysed in the present work [5,6]. Indeed, as found in several experimental studies this approach confirms the observations [2,3,4,9,13,14].

Formally, the basic expression, which allows the calculation of the nucleation rate corresponds to the classical equation:

$$I = C \cdot \exp(-\Delta G/kT) \qquad (1)$$

Here, ΔG is the Gibbs free energy expended in producing the cluster from the vapour phase, k is the Boltzmann-constant and T is the temperature. The pre-exponential factor C for binary mixtures, which has been derived by Reiss [6], is primarily determinded by the kinetics of the process. If the definition of the total and the partial supersaturations $S = S_1^{x_1} \cdot S_2^{x_2}$ and $S_i = p_i/p_{si}^0 \cdot \gamma_i \cdot x_i$ (i = 1,2) are utilized, the critical values for ΔG^* and the critical radius r^* can be expressed as follows:

$$\Delta G^* = -n_1 kT \ln S_1 - n_2 kT \ln S_2 + 4\pi r^2 \cdot \sigma(n_1, n_2, T) \qquad (2)$$

$$r^* = 2\sigma(n_1, n_2, T) \, v/kT \ln S \qquad (3)$$

Here, x_i are the mole fractions of the components in the liquid phase, n_i the numbers of molecules in the nucleii, p_i the partial pressures, p_{si}^0 the saturation pressures of the pure components, γ_i the activity coefficients and

v the specific molecular volume. The important role of the binary surface tension is immediately apparent when equation 3 is combined with equation 2. Metastable equilibrium between the vapour phase and the nucleii of critical size and composition is attained on the saddle point of the energy surface indicated by an asterix. It separates two regions with the vapourization process dominating one and stable growth of the nucleii the other. A binary model which has been previously introduced by us for the description of the subsequent heterogeneous droplet growth leading to the thermodynamic equilibrium [3,7,8], has been modified in the context of the present work for water/n-propanol mixtures. Thus, the mass increase of the droplets can be described as a function of the partial supersaturations, the droplet size, the thermodynamic state and the physical properties of the components and the mixture.

$$\dot{m}_i = f(S_i, r^*/r, \text{thermodynamic state, physical properties})\qquad (4)$$

RESULTS AND DISCUSSION

The condensation temperature range for the experiments was chosen to be within 275 K to 295 K. As the results with water/n-propanol solutions cannot be presented for the whole range of concentration in the p-T-diagram in a readily accessible way due to the additional degree of freedom, the activities were used for the representation of the data. The activities a_1 and a_2 are here defined as the ratio of the partial pressures to the saturation pressures of the pure components of water and n-propanol, respectively.

The results of the present study are compared in Figure 2 with cloud chamber experiments by Flageollet et al.[14] with considerably lower cooling rates. Calculations of the droplet growth, which will be discussed later (see Figure 4) reveal, that nucleation rates of approximately 10^{17} m^{-3}s^{-1} are achieved at condensation onset in our experimental setup, whereas typical rates for cloud chamber experiments are in the order of $2-3 \cdot 10^6$ m^{-3}s^{-1}. This may be responsible for the differences in Figure 2. The effects of the temperature variation between 295 K and 275 K at constant nucleation rates are indicated by the theoretical predictions of the activities. As found in our earlier studies for similar mixtures, the use of the macroscopic surface tension will lead only for alcohol-rich compositions to an acceptable agreement of theory and experiment.

This is especially true for relatively small clusters as shown in Figure 3. In order to account for the changing enrichment of alcohol molecules on the micro-cluster's surface, the semi-empirical model of Flageollet-Daniel et al. was applied [9]. This has been derived from the monolayer model introduced by Defay et al. [15]. Figure 3 illustrates the effects of the various approximations, the monolayer model and the pure dynamic surface tension, in comparison with macroscopic surface tension. It is evident, that with decreasing number of molecules N_t especially in water-rich mixtures, the increase of the surface tension with respect to the bulk value must be taken into consideration. This is supported by the comparison of experiment and theory as shown in Figure 2. It should be noted, though, that the model developed by Flageollet et al. is not quite consistent thermodynamically. This can be shown in comparing the purely dynamic surface tension with those calculated following the proposed model for very small clusters, where the former yield smaller values. Because of the fact, that the pure dynamic surface tension is the limiting case of no alcohol enrichment, this behaviour is physically not realistic. In the present study, therefore, the dynamic surface tension was used for further calculations.

With respect to the influence of the cooling rate, no remarkable effect was noticed during the course of the present experimental campaign. This is

probably due to the small cooling rates ($-dT/dt \leq 50\,^{\circ}C/ms$), which is in agreement with the observations by Wegener et al.[16]. On the other hand the relatively small differences in the cooling rates in our measurement planes can be held responsible.

A comparison between the calculated and the experimentally observed droplet size and number density along with the nucleation rate is shown in Figure 4. Specifically, a water-rich mixture ($x_2'' = 0.1$) has been selected to demonstrate the accuracy of the predictions and especially of the influence of the surface tension. It can be seen, that the application of the macroscopic surface tension in the calculations leads to a considerable underprediction of the critical supersaturation, whereas the introduction of the dynamic surface tension, which is essential a limiting value, will lead to a surprisingly good agreement between experiment and theory. The results are supported by a large number of other comparisons with different mole fractions. In consulting Figure 4, it can be seen, that the calculations have been extended beyond the time of condensation onset under assumption of critical heat addition with corresponding pressure and temperature increase [17,18]. Again, despite approaching that limiting assumption, the experimental results are in excellent agreement with the predictions.

Frequently, the question arises as to the droplet size distribution during the progress of the condensation process. Figure 5 in combination with Figure 4 demonstrates the history of the size distribution. In considering approximately 50 droplet classes it can be seen, that in the early stages of nucleation (t_1 and t_2) the distribution broadens and will approach almost monodisperse character after the nucleation rate becomes small (t_3 to t_5), i.e. a broader distribution during the nucleation phase is found and relatively narrow banded distributions are formed during the subsequent condensation. This is in good agreement with physical reasoning and supports the applicability of the dispersion quotient technique in measuring the droplet size.

In summary, by using real binary/n-propanol mixtures, the present study illustrates good agreement between theory and experiment even in water-rich mixtures as long as appropriate values for the surface tension of micro-clusters are introduced. The onset of condensation as well as the droplet growth and number density can be predicted with sufficient accuracy even beyond the initial phases of condensation. Furthermore, the calculations confirm the applicability of the optical droplet diagnostics, which has been extended to lower particle sizes. The assumption of monodisperse size distributions especially in the latter stages of condensation has been shown to be no major restriction.

ACKNOWLEDGEMENTS

REFERENCES

1 S.L.K. Wittig, R.A. Zahoransky, S.S. Kim and D.E. Wurz: Shock Tubes and Waves, Eds. A. Lifshitz and J. Rom, Hebrew Univ. Jerusalem, 437 (1979)

2 R.A. Zahoransky and S.L.K. Wittig: Shock Tubes and Waves, Eds. C.E. Treanor and J.G. Hall, State Univ. of New York, 682 (1981)

3 W. Studzinski, R.A. Zahoransky and S.L.K. Wittig: Shock Tubes and Waves, Eds. R.D.Archer and B.E.Milton, Univ. of New South Wales, 421 (1983)

4 H. Flood: Z. Phys. Chemie A 170, 286 (1934)

5 K. Neumann and W. Döring: Z. Phys. Chemie A 186, 203 (1940)

6 H. Reiss: J. Chem. Phys. 18, 840 (1950)

7 W. Studzinski, R.A. Zahoransky and S.L.K. Wittig: Wärme- und Stoffübertragung 17, 241 (1983)

8   W. Studziński, R.A. Zahoransky, S.L.K. Wittig and D. Barschdorff:
    Int. J. Heat Mass Trans. 27, 451 (1984)

9   C. Flageollet-Daniel, J.P. Garnier and P. Mirabel:
    J. Chem. Phys. 78, 2600 (1983)

10 W. Studiński, R.A. Zahoransky, S.L.K. Wittig and G.H. Spiegel:
    Heat and Mass Transfer in Rotating Machinery, Eds. D.E. Metzger and
    N.H. Afgan, Hemisphere Publ. Corp. (1984)

11 S. Wittig, R. Zahoransky and Kh. Sakbani: Aerosols in Science,
    Medicine and Technology, Eds. W. Stoeber and D. Hochrainer,
    Ges. f. Aerosolforschung 8, 145 (1980)

12 D. Barschdorff, Phys. Fluids 18, 529 (1975)

13 P. Mirabel and J.L. Katz: J. Chem. Phys. 67, 1697 (1977)

14 C. Flageollet, M. Dinh Cao and P. Mirabel: J. Chem. Phys. 72,
    544 (1980)

15 R. Defay and I. Prigogine: Surface Tension and Adsorption,
    Longmans, London (1966)

16 P.P. Wegener und K.R. Sreenivasan: Appl. Scientific Res. 37, (1981)

17 J. Zierep: Theoretische Gasdynamik, Verlag G. Braun Karlsruhe, 1972

18 F. Bartlmä: Z. Flugwiss. 11(4), 160 (1963)

19 Teitelbaum, Gortalova and Sidorova (1951), cited in: J. Timmermans,
    Physico-Chemical Constants of Binary Systems, Interscience New York,
    Vol.4 (1960)
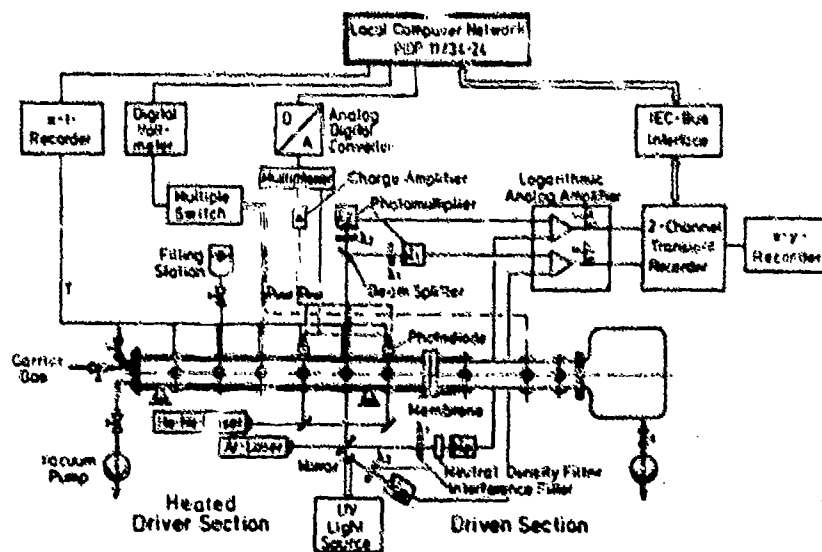
Fig. 1: Schematic of the experimental setup
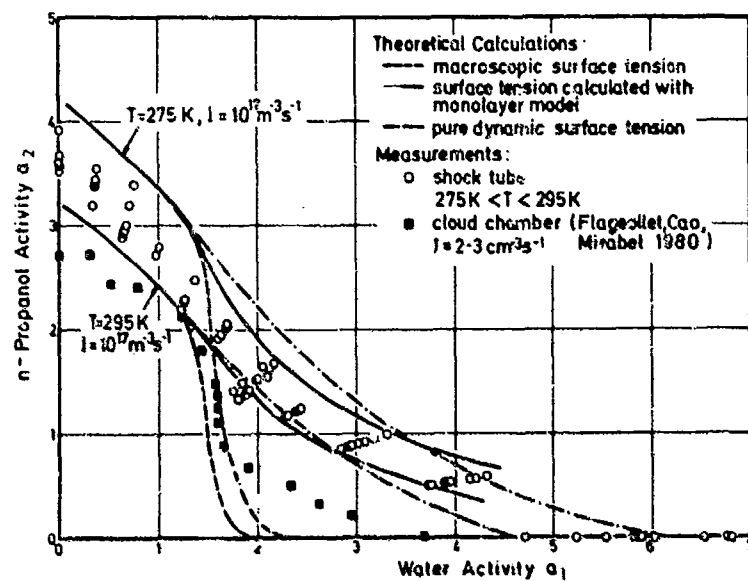
Fig. 2: Homogeneous binary nucleation system water/n-propanol:
Comparison of theory and experiment
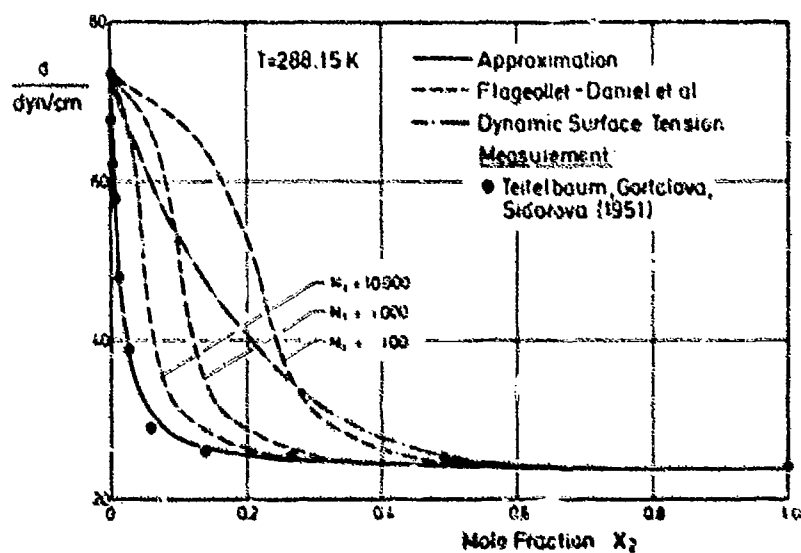
Fig. 3: Binary surface tension system water/n-propanol
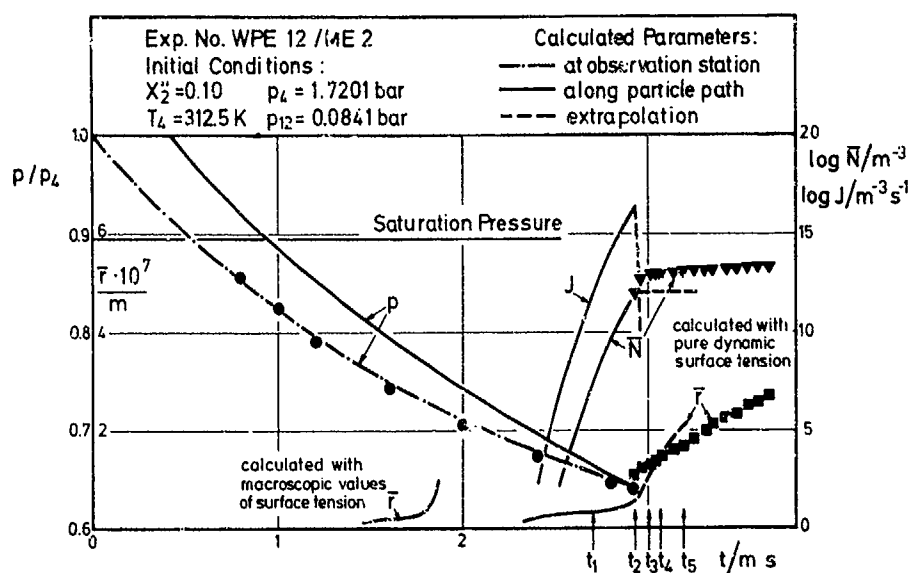
Fig. 4: Droplet growth and number densities in the expansion-wave for a water-rich mixture of water/n-propanol
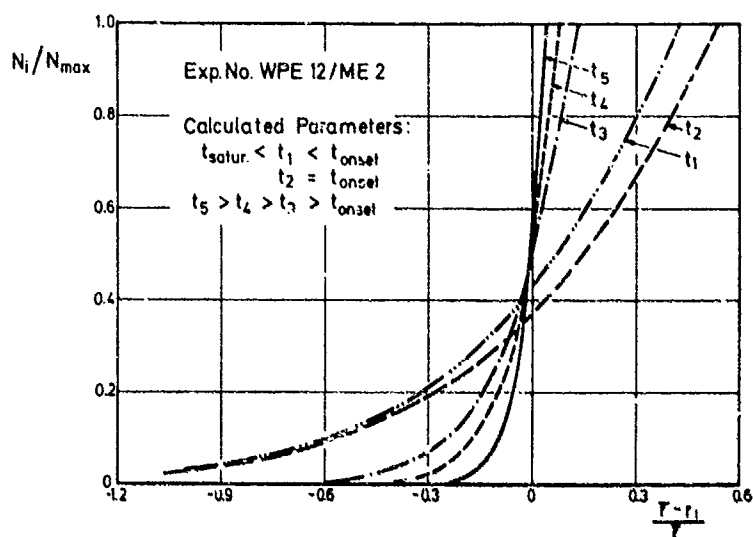
Fig. 5: Calculated history of size distribution for the specific experiment shown in Figure 4

STOCHASTIC SIMULATION OF CONDENSATION IN SUPERSONIC EXPANSIONS (Ar)

C. F. Wilcox, Jr. and S. H. Bauer

Department of Chemistry, Cornell University, Ithaca, New York 14853

Analysis of the simplest kinetic model for nucleation/
condensation of argon clusters in an overexpanded jet
shows that along the central streamline: (i) the cluster
size distribution declines logarithmically, as observed;
(ii) within a distance somewhat less than twice the aper-
ture diameter the distribution is given essentially by
the equilibrium conditions; for larger distance the dis-
tribution is kinetically limited; (iii) at about (2.3-
2.4) diameters downstream "freezing-in" occurs, where the
collision rate declines so rapidly that no significant
additional conversions take place; (iv) to achieve con-
cordance between experimental observations and deductions
from this model one must assume that the clusters are
hotter than the ambient medium.

1. INTRODUCTION

As a consequence of the current preoccupation of many physical scien-
tists with studies of clusters, imaginative programs have been initiated to
measure their spectroscopic, electrical and chemical properties. However, only
theoretical estimates are available for their energetics and of the molecular
dynamics which leads to their formation. Clearly the significant parameter
which characterizes such an ensemble is the size distribution (N_n). The
development of pulsed nozzles for generating molecular beams evoked a barrage
of investigations wherein their approximate mass distributions was determined
mass spectrometrically, either with quadrupole or time-of-flight mass filters,
exemplified by the Ar and Kr mass spectra recorded by Ding and Hesslich[1] and by
Broyer, et al.[2] for I_2. Generally these distributions show relative population
levels which decline logarithmically with n^{mer} number, but there are reports
of the production of bimodal distributions, and the appearance of some n^{mers}
which have higher stabilities than the species adjacent to them (designated
magic numbers). In some cases these can be rationalized in terms of greater
stabilities of "regular" geometric configurations on the basis of Lennard-Jones
or ionic-interaction potentials.

Here we describe our attempt to reproduce via a stochastic calculation the
distribution of micro-cluster sizes produced by supersonic expansion from a
high pressure reservoir into an evacuated chamber through a small orifice
(D>mfp). Our calculations follow the pattern we developed for stochastic simu-
lation of condensations in a fixed volume[3]. It is based on algorithms initial-
ly developed by Gillespie[4] and modified by Hanusse[5]. We anticipate answers to
the following questions:

(i)   Does a reasonable kinetics model lead to a logarithmic decline?

(ii)   At what stages in the expansion does the distribution switch from one
determined by the equilibrium for a supersaturated system to one determined by
kinetics? Is there a "freezing-in" beyond some specified distance along the
central streamline?

(iii) What are the effects of the heat of condensation on the kinetics and
ultimately on the computed distribution?

(iv)   Do the clusters have a temperature distribution which differs from the
carrier gas?

2.   THERMOCHEMISTRY AND THE KINETIC MODEL

Prior to discussing the flow field for an overexpanded jet we summarize the underlying thermochemical relations which control the association equilibrium, and develop a kinetic model which accounts for cluster formation. Let ΔH^0_n and ΔS^0_n denoted the enthalpy and entropy increments for the reaction: $nA_1 = A_n$. Then, $\Delta G^0_n = \Delta H^0_n - T\Delta S^0_n$ is the corresponding free energy increment, and

$$N^{eq}_n/(N^{eq}_1)^n = (R\,T)^{n-1} \exp(-\Delta G^0_n/RT) \equiv K_n ,$$ [1]

N_n is measured in (moles cm^{-3}), $R = 82.06\ cm^3$ atm $mole^{-1}$ deg^{-1}, ΔG^0_n is measured in (cal $mole^{-1}$ of n^{mer}), $R=1.982$ cal $mole^{-1}deg^{-1}$. When a monomeric gas is brought to supersaturation by rapid cooling, it first passes through a condition of "constrained" equilibrium (i.e. obeys eq. [1]), prior to onset of catastrophic condensation to the bulk liquid. This is attained in a sequence of steps:

$$A_{n-1} + A_1 \underset{k_{n-1,n}}{\overset{k_{n,n-1}}{\rightleftharpoons}} A_n$$ [2]

The ratio of rate constants obeys the relation

$$\frac{k_{n-1,n}}{k_{n,n-1}} = R\,T\,\exp\left[-\frac{\Delta G^0_n - \Delta G^0_{n-1}}{RT} \right] \equiv K_{n-1,n}$$ [3]

and for the __equilibrium__ distribution: $(N_1)_{initial} = \sum_{n=1}^{\infty} n(N^{eq}_1)^n K_n ;$ [4]

Although numerous theoretical calculations of the thermodynamic quantities $(\Delta H^0_n;\ \Delta S^0_n)$[6,7] have been reported, to our knowledge only a single experiment has been performed[8] for estimating the dependence of the heat condensation on cluster size. That, when combined with the theoretical values led to a remarkably simple correlation, expressed in dimensionless terms:

$$\frac{\Delta H^0_n}{n \cdot Q} = -(1 - n^{-.25})$$ [5]

Less secure are the parameters for the entropy and the heat capacity:

$$\frac{\Delta S^0_n}{n \cdot \Sigma} = \frac{-n^2}{n^2 + (20 - \Sigma/R)}$$ [6]

$$\frac{c^{(v)}_n}{n \cdot C^v_{liq}} = (0.60 - \frac{0.40n}{10+n})$$ [7]

where Q, Σ and C^v_{liq} are the bulk (liquid) heat of vaporization, entropy of vaporization, and molar heat capacity, respectively. The values so derived are in acceptable agreement with the ΔG^0_n's calculated by McGinty[9] for argon clusters, assuming a Lennard-Jones (12-6) potential between spherical atoms. Our smoothed representations are first approximations to a more sophisticated evaluation of the total potential energy for argon clusters derived by Birge[10] which shows alternating values for even/odd n^{mers}, with a small maximum $n=13$. The empirical relations [5, 6 and 7] should be treated as estimates which are useful for analyzing n^{mer} dependent trends. There is no claim that local departures from these smooth functions do not appear at specific n-values. (For argon, $Q = 1560$ cal $mole^{-1}$; $\Sigma = 17.9$ e.u. at its b.p.(87.3°K);

and $C^V_{liq} = 4.78$ cal mole^{-1}.]

To estimate the temperature dependent magnitudes of $k_{n-1,n}$ we used the two step energy transfer model which satisfactorily accounts for atom pair recombinations.[11]

$$A_{n-1} + A_1 \underset{\kappa_n}{\overset{\kappa_{-n}}{\rightleftharpoons}} C_n \qquad [8a]$$

$$C_n + A_1 \underset{\kappa_{ns}}{\overset{\kappa_{-ns}}{\rightleftharpoons}} A_n + A_1 \qquad [8b]$$
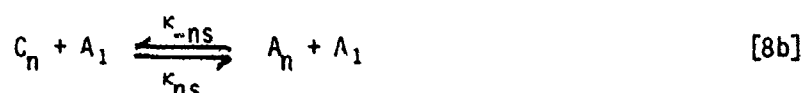
Upon imposing a steady state condition on C_n,

$$\frac{dA_n}{dt} = \kappa_{ns} \left[\left(\frac{\kappa_n}{\kappa_{-n}}\right) A_{n-1} + \left(\frac{\kappa_{-ns}}{\kappa_{-n}}\right) A_n \right] \frac{A_1^2}{1+(\kappa_{ns}/\kappa_{-n})A_1} - \{\kappa_{-ns} A_n A_1\} \qquad [9]$$

Since κ_{ns} in [8b] represents stablizing the cluster by removal (in part or in entirety) of the heat of condensation, at low temperatures the reverse term $\{\kappa_{-ns} A_n A_1\}$ is negligible compared with the major term of the right member. The same applies to $(\kappa_{-ns}/\kappa_{-n})A_n$ and $(\kappa_{ns}/\kappa_{-n})A_1 < 1$ at low pressures, when n is not too large. [Note: Our calculations were based on this assumption, however, a general kinetics program can incorporate this term in the denominator and thus allow for a switch-over from third to second order rate equations for large n.] The final rate equation reduces to

$$\frac{dA_n}{dt} = \kappa_{ns} \left(\frac{\kappa_{+n}}{\kappa_n}\right) A_{n-1} A_1^2 \qquad [9']$$

The ratio (κ_{+n}/κ_n) is an equilibrium constant for particles interacting pairwise (i.e. n^{mer} plus 1) in a Lennard-Jones potential:

$$\left(\frac{\kappa_{+n}}{\kappa_n}\right) = \frac{8\pi\hbar\sigma^2_{LJn}}{(2\pi\mu_n k_b T)^{1/2}} \left(\frac{\epsilon_{LJn}}{k_b T}\right)^{1/3} \Gamma(2/3) \qquad [10]$$

The effective radius is $\sigma_{LJn} = \left[\frac{3n}{4\pi} \frac{1}{\rho_n}\right]^{1/3}$ with $\rho_n = 2.14 \times 10^{22} \left[\frac{n^{2/3}}{4+n^{2/3}}\right]$ Ar atoms per cm^3; μ_n is the reduced mass of the interacting pair and ϵ_{LJn} is the well-depth. We set

$$\epsilon_{LJn} = \left(\frac{n+5}{n+10}\right)(E_{n+1} - E_n), \text{ with } E_n/n = [4.7\log_{10}n - 0.80] \times 10^{-14} \text{ ergs atom}^{-1} \qquad [11]$$

This dependence of ϵ_{LJn} on cluster size was obtained from an empirical fit to values for the potential energy of argon n^{mers} by combining calculations of McGinty[9] and Hoare and Pal[12]. The stabilization rate constant κ_{ns} is the binary collision rate between the transient C_n and the dominant species A_1 under a (hard-sphere + r^{-6}) attractive potential

$$\kappa_{ns} = \frac{\pi\sigma^2_{sn}}{2} \left(\frac{8k_b T}{\pi\mu_n'}\right)^{1/2} \left[\frac{2\epsilon_{sn}}{k_b T}\right]^{1/3} \Gamma(2/3) \qquad [12]$$

where $\sigma_{sn} = (\sigma_{LJn} + 1.71 \times 10^{-8})$ cm ; $\mu_n' = \frac{(n+1)M_{Ar}}{2+n}$; $\epsilon_{sn} = 4\epsilon_{LJn}$. The identification of $k_{n-1,n} \Longrightarrow \kappa_{ns} \left(\frac{\kappa_{+n}}{\kappa_n}\right)$ indicates that the net rate constant for monomeric

accretion to a cluster has a $T^{-2/3}$ dependent.

We call attention to critical features of the above idealized model.

(a) Steps [8a] are assumed to attain equilibrium very rapidly. These represent the development of enhanced densities of monomers in the immediate vicinity of n<u>mers</u>, due to their L-J attractive potential, which grows with n. [8b] are the rate determining steps, i.e. the removal of sufficient energy from the complexes C_n to trap the added monomers.

(b) The amount of energy removed from C_n per collision is not explicitly stated but the model implies that steps [8b] directly bring the A_n's to local temperature equilibrium. Furthermore unit collision efficiency is assumed. This crucial question will be discussed below.

(c) Equations [10] and [12] lead to a T^{-m} with m=2/3 temperature dependence for the net rate constant. However, m may be considerably larger (≈ 2) if these accretions are analogous to the association of free radicals[13].

3.   THE FLOW FIELD

In the jet, the dependence of the Mach number (M) on (x/D), well as the temperature ratio (T/T_0), the density ratio (ρ/ρ_0), the stream velocity ratio (u/u_∞) and the time spent per unit length (τ_u) along the central streamline, were evaluated by "fairing-in" two calculations: for $(x/D) > 1$, the well known parameterized relations developed by Ashkenas and Sherman[14] were used. However these are invalid for distances $(x/D) < 1$. That field was mapped in detail by the method of characteristics for various γ's[15]. From these smoothed plots, specific sets of values were tabulated for argon with p_0 = 10 atm; D = 30 μm (exhausting into a vacuum) to match the conditions in (ref. 1). A one-dimensional grid along the central streamline was selected, with increments equal to 0.1(x/D). In these calculations, the ideal gas law, with constant heat capacity ratio (γ) was incorporated. In our first model we assumed that this flow field remains unperturbed by the condensation process.

The effects of nozzle geometry on the kinetics of jet expansion recently have been analyzed by Murphy and Miller[16] and Wu, <u>et al.</u>[17]. The temperature and density distributions in a nitrogen free-jet expansion was explored by Beylich[18] with an electron beam and found them to be in general agreement with one-dimensional stream calculations. The most recent analysis of over-expanded supersonic jets and of skimmed molecular beams was presented by Comparge.[19]

For (x/D)>1, the following relations apply: Given a source fluid at T_0, with density ρ_0, mean molecular weight μ, and constant heat capacity ratio γ, the characteristic sound velocity is $a_0 = (\gamma RT/\mu)^{1/2}$. Then at any selected isodensity contour in the jet, $\alpha_j \equiv (\rho_j/\rho_0)$, define the quantity $\phi_j = (\rho_j/\rho_0)^{(1-\gamma)}$.

At that contour the Mach number is given by $\phi_j = (1 + \frac{\gamma-1}{2} M_j^2)$. The other parameters are:

$$(T_j/T_0) = \phi_j^{-1} \; ; \; (u_j/a_0) = M_j \phi_j^{-1/2} \; ; \; (a_j/a_0) = (T_j/T_0)^{1/2} \qquad [13]$$

4.   EQUILIBRIUM AND KINETIC ANALYSES

Consider a sample of 3×10^4 Ar atoms which issues from a reservoir at 10 atmospheres, 300°K. At the instant it crosses the exit plane of the aperture, it occupies a volume equal 1.22×10^{-16} cm^3. At M=1 the sample is streaming at $a_0 = 3.47 \times 10^4$ cm s^{-1}. Hence the time required to cross a distance along the central streamline equal to 0.1(x/D) is 8.63×10^{-9} s. During that interval there will be approximately 2.7×10^7 binary collisions in this little volume. In the stochastic simulation we follow this sample as it moves along the central streamline. Downstream, as the density decreases the volume allocated to it is increased by allowing the square root of the radius of the pill-shaped

enclosure to increase in proportion to m(0.1 x/D): $V_m = \dfrac{\rho_0}{\rho(0.1\ mx/D)}$, where $\underline{m}$ specifics the ordinal number of the slice. Also as the sample moves downstream the time spent in each slice decreases with the increasing Mach number, which reaches a little over 6 at $(x/D)=2.6$. The equilibrium n^{mer} populations in the 20 cells into which the axial distance $0 < (x/D) < 2$ was divided were calculated _via_ eq. [4]. In each case (slice m) the local temperature and density were assumed to be those given in the flow field, and the initial state that computed for the equilibrium composition of slice (m-1). In this approximation we neglected the heat injected into the stream due to condensation and the associated lowering of $\gamma (< 1.667)$. The upper n^{mer} bound was set at 25, and mass conservation was imposed. The opposing effects of simultaneously lowering the density and temperature appear clearly at low (x/D) values. The number of dimers initially decreases but then begins to increase at $(x/D) > 0.6$. On a scale of $\approx 7 \times 10^{-9}$ s (approximate passage time per slice) the flow reaches condensation equilibrium for all distances up to $(x/D) \approx 1.6$; then a relatively abrupt transition occurs, when the equilibrium calculation indicates that 25-mers appear at $T=44°K$. Thereafter the composition of the flow is kinetically controlled.

Solution of the coupled set of differential equations [9'] can be affected by one of several numerical integration codes [e.g. CHEMKIN by Kee, Miller and Jefferson[20]], which computes time dependent species concentrations and temperature changes due to enthalpy increments. At this stage of our analysis we chose to use the stochastic procedure because it provides a transparent simulation of the randomness inherent in molecular dynamics; it is easily programmed and can be performed with a CompuPro 8085/88 microcomputer.

In the alogorithms developed by Gillespie[4] and Hanusse,[5] unconventional rate constants were introduced. These are related to the constants which appear in [2]:

$$\beta_{n,n-1}[\text{molecule}^{-1}\text{s}^{-1}] \approx \frac{k_{n,n-1}[\text{mole}^{-1}\text{cm}^3\text{s}^{-1}]}{A \cdot V_m[\text{cm}^3]} \tag{14}$$

where A is Avagadro's number and V_m is the volume available to the sample tested.

$$\beta_{n-1,n} = \frac{k_{n-1,n}[\text{mole}^{-2}\text{cm}^{-6}\text{s}^{-1}]}{A^2\ V_m^2} \ \Bigg| \ \hat{K}_{n-1,n} \equiv \frac{\beta_{n-1,n}}{\beta_{n,n-1}} = K_{n-1,n}/A\ V_m \tag{15}$$

In this notation $\tilde{N}_n \beta_{n,n-1} \delta t$ measures the probability that a dissociation will occur somewhere in V_m during the next time interval δt, when $\tilde{N}_n$ is the total number of n-mers in V_m.

5.   CLUSTER SIZE DISTRIBUTIONS

The results of several stochastic games are best summarized in a series of graphs. The reference case (I) is that described above. Figure 1 shows the dependence of N_n for n=1,2,3... on x/D. The solid lines are equilibrium values; these were also given by the converged kinetic solution for m(0.1x/D), with m<15, calculated for the time slices allocated to each 0.1x/D interval. However, due to the rapidly decreasing local temperatures and densities significant departures from [1] take place for m>15. While the equilibrium equation indicates precipitous declines in all N_n for n<25 and a sharp rise in N_{25}, the kinetic limitation shows that the populations of all n^{mers} continue to increase for larger x/D values. Finally these calculations demonstrate the eventual appearance of a "freezing condition" for m>22, and a rise in (the limiting) N_{25}. In Figure 2 these values were replotted as a function of n for

selected values of x/D. The logarithmic dependence of N_n on n is apparent; by the time the sample attains the freezing condition this relation applies up to n≈12, beyond which statistical noise dominates. The breakthrough to the limiting N_{25} appears at $2.0<(x/D)<2.2$. Beyond x/D=2.4 the statistical fluctuations in N_n smooth out due to the code limit imposed at n=25.

Case II: To ascertain the sensitivity of these general features on sample size and upper n^{mer} limit, the stochastic program was repeated for a sample consisting of 3×10^5 Ar atom with n(max)≈50. The results are shown in Fig. 3. The dependence of N_n on x/D is essentially the same as in Fig. 1. In Fig. 4 the break-through appears at $1.9 < (x/D) < 2.0$, and the statistical fluctuations become quite small for x/D=2.3.

There is another measure of cluster evolution rate. The basic model allocates a finite interval for passage of the sample through any specified $\overline{m}$ slice. Typical intervals are about 7 ns at x/D ≈ 2. The stochastic process permits one to determine the production rate of the limiting $n^{\underline{mer}}$. In Table I the rates of production of N_{25} (case I) and N_{50} (case II) are compared for a sequence of x/D values. Local temperatures are those given by the initial flow field calculations. The ratio $\Delta N_{50}/\Delta N_{25}$ declines from 6.0 at x/D=2, to 2.6 at x/D=2.4. We conclude that the initial sample size (3×10^4) and upper cluster limit (N_{25}) were adequate to demonstrate the essential features of the condensation process.

Cases III and IV illustrate the effect of changing all the association rate constants ($k_{n-1,n}$) by a factor of 1/5, and of reducing the driving pressure (p_0) by a factor of $1/\sqrt{5}$ (but increasing the aperture so as to allow 30,000 monomers to escape). The rates of production of 25 mers are compared in Table II. It appears that direct scaling does not apply because of the complex coupling of the association kinetics with the rapid changes in density and temperature in the flow field.

6.   EFFECTS OF THE HEAT OF CONDENSATION

The heat developed within any (m+1) slice due to changes in the cluster distribution from that of the preceeding slice (m) is given by

$$h_{(m+1)} = -\sum_{n=2} \frac{\Delta H_n^0}{A} [N_n^{(m+1)} - N_n^{(m)}] \qquad [16]$$

If one assumes that this increase in enthalpy is immediately equilibrated over the material contained within all the species present in that slice, then the rise in temperature of the stream during its sojourn in (m+1) is $\delta T_{(m+1)} = h_{(m+1)}/C_{(m+1)}^{eff}$,

$$C_{(m+1)}^{eff} = \frac{3}{2} \frac{RN^{(m+1)}}{A} + \sum_{n=2} \frac{C^n}{A} N_n^{(m+1)} \qquad [17]$$

In Fig. 5 the lower curve is the axial temperature along x/D, assuming no energy transfer, while the upper curve would be the temperature developed were condensation to take place as in case I with its heat uniformly distributed. Interestingly, the calculation of these elevated temperatures were numerically unstable at large x/D. When clustering occurs, the sample temperature of that cell rises; in the next cell, which has a temperature based on the previous value, the clusters degrade and the temperature declines. Whether, the resulting oscillations would persist for limitingly small cell volumes is unclear; however, the mean temperature increments would allow very little clustering, contrary to reported observations.[1] This problem has been previously encountered in the analysis of homogeneous nucleation rates; the latest report was that by P. E. Wagner and coworkers[21]. This is a particularly significant factor in an analysis of condensation under protoplanetary conditions (cf. the

work of Salpeter and Draine[22]).

Two factors are involved. As indicated above, we assumed that except for the incremental temperature the flow field remained unperturbed. This can be corrected by recalculating the flow field, including a specified distributed heat source. It is difficult to predict how this coupling would affect the condensation kinetics along the central streamline. However at this stage we are of the opinion that the effort is not justified in view of the second factor. It is unlikely that the stabilizing collisions [8b] remove all the heat of condensation in single steps. Indeed, in view of the rapidly decreasing density there may not be sufficient numbers of collisions for $x/D>1.8$ to bring the cluster temperature down to the ambient gas temperature. The dashed curve in Fig. 5 shows the anticipated temperature profile were only 0.1 of the heat generated within any slice so distributed. Under this assumption condensation would occur but with diminished N_n populations, while the temperature of the clusters remained higher than that of the surrounding gas. The analogy with the de-excitation sequence following free radical recombination favors this argument[23].

Both Kung[24] and Freund[8] have demonstrated that during the initial stages of homogeneous condensation of Fe_n from its supersaturated vapor the temperatures of the clusters are indeed 50-150°K above that of the ambient Ar. To calculate the cluster temperatures one would have to insert several additional collisional stabilizations associated with each condensation step, and to postulate the fractions of energy removed by each collision type. For such an analysis solution of the coupled differential equations rather than the use of stochastic simulation appears more suitable. At this stage the heat of condensation problem remains unresolved.

REFERENCES

1. Ding, A. and Hesslich, J., "Abundance of Ar and Kr Microclusters Generated by Supersonic Expansion", Chem. Phys. Lett., Vol. 94, 1983, p.54.

2. Broyer, M. et al., "Photodissociation of an I_2 Supersonic Beam in the Nozzle Expansion Region...", Chem. Phys. Lett., Vol. 107, 1984, p.307.

3. Bauer, S. H. and Wilcox, C.F., Jr., "Stochastic Simulation of Homogeneous Condensation", J. Phys. Chem., Vol. 82, 1978, p.59.

4. Gillespie, D.T., "A Stochastic Analysis of the Homogeneous Nucleation of Vapor Condensation", J. Chem. Phys., Vol. 74, 1981, p.661 and p.5295.

5. Hanusse, P. and Blanche, A., "A Monte Carlo Method for Large Reaction-Diffusion Systems", J. Chem. Phys., Vol. 74, 1981, p.6148.

6. Abraham, F.F., Homogeneous Nucleation Theory, Academic Press, Inc., 1974.

7. Freeman, D.L. and Doll, J.C., "Quantum Monte Carlo Study of the Thermodynamic Properties of Argon Clusters...", J. Chem. Phys., Vol. 82, 1985, p.462.

8. Freund, H. and Bauer, S.H., "Dependence of the Heat of Condensation on Cluster Size", J. Phys. Chem., Vol. 81, 1977, p.994.

9. McGinty, D.J., "Vapor Phase Homogeneous Nucleation and the Thermodynamic Properties of Small Clusters of Argon Atoms", J. Chem. Phys., Vol. 55, 1971, p.580.

10. Birge, R.R., Private communication --- an extension of J. Chem. Phys., Vol. 72, 1980, p.5312.

11. Smith, I.W.M., Kinetics and Dynamics of Elementary Gas Reactions, Butterworths, London, 1980, p.72 and 230.

12. Hoare, M.R. and Pal, P., "Physical Cluster Mechanics: Statics and Energy Surfaces for Monatomic System", Adv. Phys., Vol. 20, 1971, p.161; also, J. Cryst. Growth, Vol. 17, 1972, p.77.

13. Viggiano, A.A. and Paulson, J.F., "Three-body Association Rate Coefficients as a Function of Temperature and Cluster Size", Pre-publication abstract from AFGL at Int. Conf. on Chem. Kin., June 1985.

14. Ashkenas, H. and Sherman, F.S. in Rarefied Gas Dynamics, Vol. 2, Ed. deLeeuw, J. H., Academic Press, New York, 1966, p.84.

15. Gallaher, K.L. and Bauer, S.H., "On the Thermochemical State of Gaseous Electron Diffraction Samples", J. Phys. Chem., Vol. 78, 1974, p.2389. See also: Hagena, O. F., "Nucleation and Growth of Clusters in Expanding Nozzle Flow", Surface Science, Vol. 106, 1981, p.101.

16. Murphy, H.R. and Miller, D.R., "Effect of Nozzle Geometry on Kinetics in Free Jet Expansions", J. Phys. Chem., Vol. 88, 1984, p.4474. See also, Abraham, O., et al., "Gas Dynamics of Very Small Laval Nozzles", Phys. Fluids, Vol. 24, 1981, p.1017.

17. Wu, B.J., Wegener, P.P. and Stein, G.D., "Condensation of SF_6 in Steady State Supersonic Flow", J. Chem. Phys., Vol. 68, 1978, p.308.

18. Beylich, A.E., Report at Euromech. Kolloquim 88, from Technische Hochschule, Aachen.

19. Campargne, R., "Progress in Overexpanded Supersonic Jets...", J. Phys. Chem., Vol. 80, 1984, p.4466.

20. Kee, R.J., Miller, J.A. and Jefferson, T.H., CHEMKIN, Sandia Report #SAND 80-8003.

21. Wagner, P.E., et al., "Strong Reduction of Homogeneous Nucleation Rates in Associating Vapors...", Abstract #23, 5th Int. Conf. on Surface and Colloid Science, Clarkson University, Potsdam, New York, 1985.

22. Draine, B.T. and Salpeter, E.E., "Time-dependent Nucleation Theory", J. Chem. Phys., Vol. 67, 1977, p.2230.

23. Hippler, H., "Direct Observation of Energy Transfer of Vibrationally Highly Excited ... Molecules", Ber. Bunsenges. Phys. Chem., Vol. 89, 1985, p.303.

24. Kung, R. T. V. and Bauer, S. H., "Nucleation Studies of Fe Vapor in Shock Tube Flow", 8th Int. Shock Tube Symp., Ed. J. L. Stollery, Chapman and Hall, 1971, paper #61.

TABLE I: RATES OF CLUSTER PRODUCTION

Y/D	T(°K)	R(30,000)[a]	R(300,000)[c]
1.0	37.96	—	—
2.0	35.44	—	160[b]
2.1	33.20	250[b]	200[b]
2.2	31.18	8.2	47
2.3	29.36	4.5	19
2.4	27.71	1.9	6

(a) defined as 25-mers produced per ns.
(b) show an initial delay followed by a linear rise.
(c) defined as 50-mers produced per ns.

TABLE II: N_{25} VALUES FOR THE 30,000 SAMPLE AT ---

Y/D	Case I	Case III	Case IV
1.9	0	0	0
2.0	0	0	0
2.1	109	13	13
2.2	169	25	61
2.3	198	30	81
2.4	208	34	93
2.5	212	34	100
2.6	212	34	101

Figure 1

Figure 3

300,000 atoms
Nmax = 50

EFFECTS OF HEAT OF CONDENSATION

Figure 5

Figure 2

Figure 4
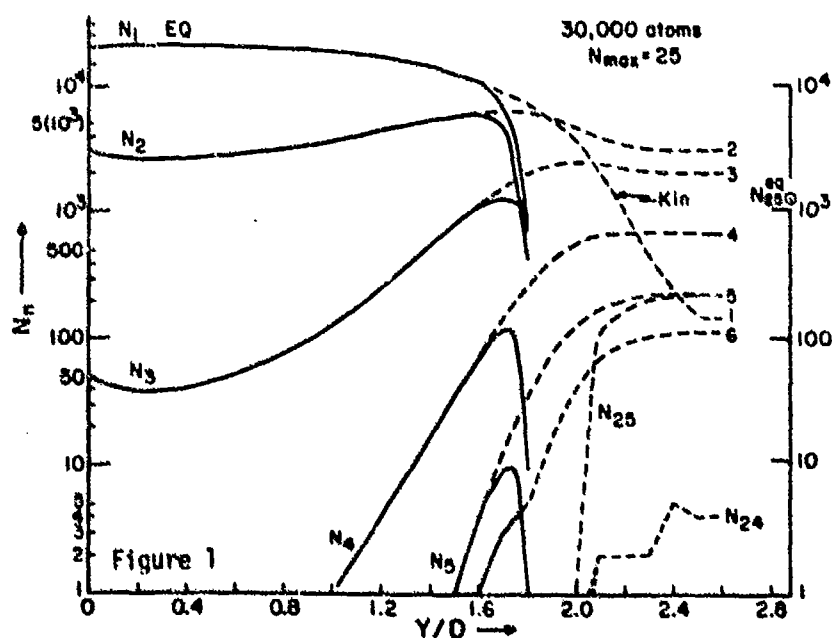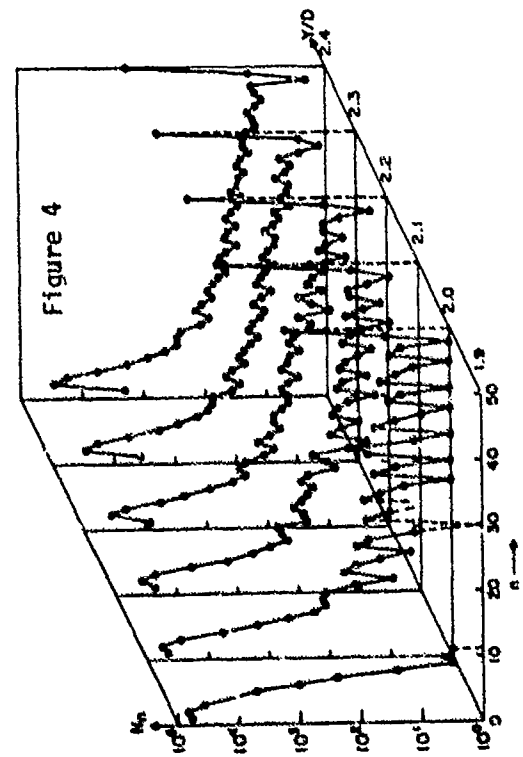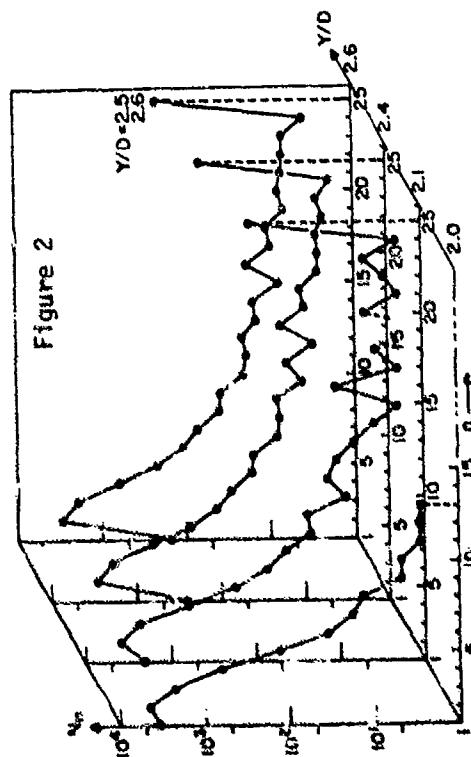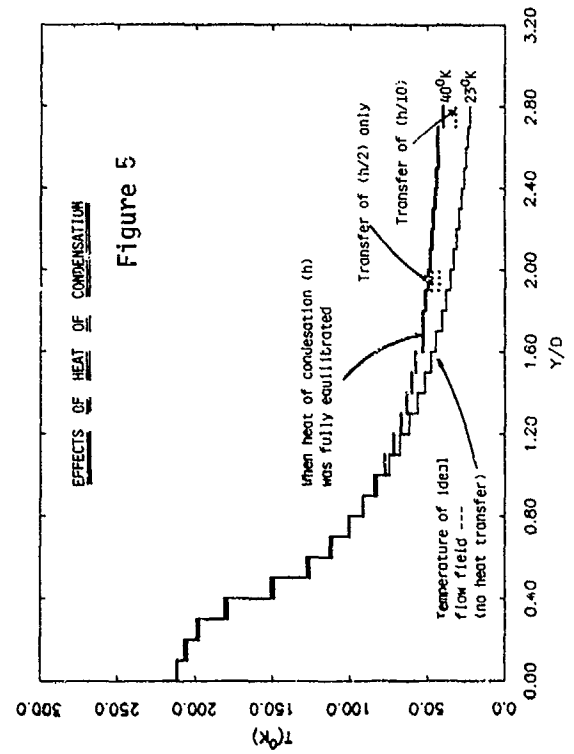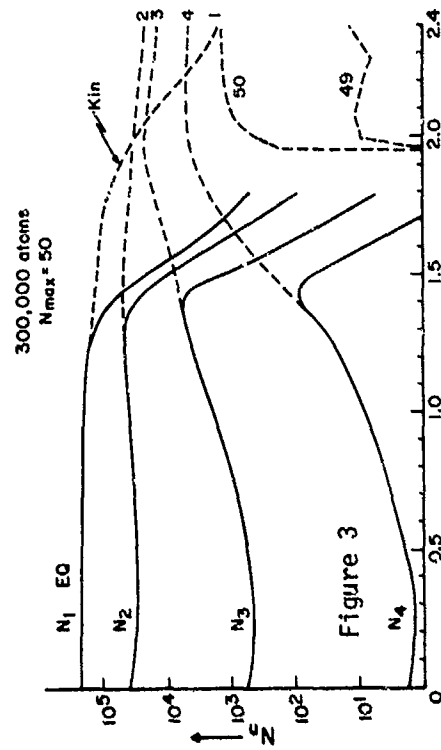
Part VIII
High Energy Gas Excitation and Wave Phenomena

HIGH-ENERGY AIR SHOCK STUDY IN A GROUT PIPE

H. D. Glenn, D. D. Keough,* H.R. Kratz,**
D. A. Duganne, D. J. Ruffner, and D. Baum[+]

Lawrence Livermore National Laboratory, Livermore, CA 94550
*SRI International, Menlo Park, CA 94025
**Systems, Science and Software, LaJolla, CA 92037
[+]Artec Associates, Hayward, CA 94545

A modified Voitenko compressor generated a 43 mm/µs
air shock in a 20-mm-i.d. 3.0 m. long pipe containing
ambient atmospheric air. The first 0.15 m of outlet pipe
was constructed of steel and the last 2.85 m of DR-1 grout.
Between 0.10- and 2.5-m from the diaphragm the velocity of
the shock front attenuated from 43- to 4.5-mm/µs and peak
pressure from 2.28- to 0.024 GPa. The rate of wall expan-
sion uniformly decreases and asymptotically approaches an
apparent final radius between 60-100 µs behind the shock
front. Plasma flow measurements indicated a flow velocity
of 27.4 mm/µs and a magnetic Reynolds number >60. Wall
expansion was <1 mm at the end of the pipe indicating
significant attenuation of the shock front between 2.5 m
and 3.0 m.

INTRODUCTION

For nearly two decades the Voitenko generator[1] has been used to study
high-energy air-shock and gas-jet propagation. Early Voitenko studies[1,2]
used outlet pipes with walls of transparent material. High gas pressures
resulted in massive venting and limited optical studies to conditions in or
just behind the air shock or gas jet front. The use of steel walls[3] for the
outlet pipe virtually eliminated venting and fiber optic ports significantly
extended the period for optical measurements (e.g. brightness temperature[4]).
The steel walls also provided the rigid mechanical support for installation of
other diagnostic sensors[3] (e.g., sigma pins, pressure gages).

This paper describes an experiment that used a modified Voitenko
compressor[2,3] to study air-shock propagation in a 3 m long outlet pipe.
Some of the hardware and diagnostics coverage are common to an earlier
experiment using a steel outlet pipe.[5] For example, the high-explosive (HE)
assembly, compressor section, and the first 0.15 m of the outlet pipe are
identical within tight machine tolerances. The last 2.85 m of outlet pipe,
with its walls of DR-1 grout, allowed use of diagnostics (flat-pack, wall
motion, and plasma flow gages) for the first time since their use would not
have been feasible in earlier experiments with outlet pipes of glass or
steel. Optical and pressure measurements along the first 0.15 m of outlet
pipe provided assurance that the initial air shock and plasma flow conditions
were similar to previous experiments.

Figure 1 and Table 1 summarize the physical features and diagnostics for
the compressor outlet pipe. The detonated HE drives the stainless-steel plate
into the chamber, compressing the 1.066-MPa air (initially in the chamber) to
high pressures (>100 GPa), densities (>1.0 Mg/m³), and temperatures (>10 eV)
before the diaphragm breaks.[6,7] Expansion of this compressed air down the
exit pipe generates a high velocity (Mach 130) air shock. Fiber-optic
ports provided optical records are then reduced to give time-of-arrival (TOA)
information about air-shock propagation down the outlet pipe. Ser[8] and
flat-pack[9] gages provided pressure profiles at numerous locations and the

radial wall motion induced by the high pressures was monitored with mutual inductance particle-velocity gages.[10] Finally plasma flow velocity and conductivity measurements[11] were obtained in the grouted segment of the outlet pipe.

2.0 GROUT SHOCK-TUBE ASSEMBLY

Problems and complexity of the grout shock tube construction added considerably to the effort and expense. Accommodation of the extensive diagnostics required the grout shock tube to be assembled in stages. A cylindrical steel frame was built and four DR-1 grout disks 19 mm thick, 152 mm o.d., with a 20 mm hole in the center, were installed in the center of the frame at specific locations. The grout disks eliminated any effect of the steel frame on wall motion induced by pressures in the plasma flow during the experimental times of interest. A 3-m-long, 19-mm o.d., 0.9-mm-thick copper tube covered with a 0.5 mm-thick heat-shrink plastic tube was inserted through the four disks. This 20-mm-o.d. copper and plastic tube, or bore tube, provided the form for the the 20 mm bore through the grout section of the shock tube.

The plasma flow velocity sensors, conductivity sensors, and the flat-pack gages were attached to the steel frame. The steel frame was then inserted into a 0.508-m-o.d. steel pipe. Fiber optics, bar and wall motion gages were inserted through ports in the steel pipe until contact was made with the bore tube. End plates were mounted and all ports (sensor, alignment, and cable exit) were sealed with epoxy. To remove air entrained in the grout the grout was mixed at reduced pressure in a large tank and added to the steel pipe after it had been evacuated with a roughing pump. Preliminary tests indicated that entrained air tended to migrate to the nearest surface and collect as small air pockets of up to 1 mm in diameter. A large number of air pockets along the bore wall would have a significant but indeterminate effect on the plasma flow. A week prior to the shot date a 0.33 N solution of nitric acid was circulated for 16 h through the bore tube to dissolve the copper tubing. The heat-shrink tubing was left in place to prevent drying of the surface of the 20 mm grout bore and removed shortly before the shot. Visual inspection of the 20 mm bore indicated a smooth wall along its entire length.

3.0 OPTICAL AND ELECTRONIC DIAGNOSTIC COVERAGE

Two framing cameras were focused on the first 0.20 m of the steel-grout outlet pipe to detect the location and duration of possible venting. Of particular interest were the bar gage at 0.10 m and the junction between the steel pipe and grout pipe at 0.15 m. Four of the light pipes were located in the 0.15 m section of steel outlet pipe and the other 11 light pipes were located in the grout section (Table 1). The other end of the light pipes were terminated in an optics display board for scanning by streaking cameras.

The input ends of the first eight bar gages were machined to a 10-mm radius to conform to the curvature of the bore radius. The end of the stagnation bar gage at 3.0 m was flush with the end wall. The seven flat-pack gages were installed in the grout section with the center of the piezoresistance elements at the same axial location as the bar gages. The flat-pack gages were initially developed[9] to monitor high-energy gas flows comparable to those in the present experiment. Radial wall motion was monitored using a mutual-inductance particle velocity gage[10] at seven different axial locations. Each gage consisted of a closely wound primary and secondary conducting wires forming two rectangle loops with lengths large compared to the lateral dimensions. Radial motion of the walls results in alteration of mutual inductance between loops and can be related to wall motion. Plasma

flow velocity, plasma resistance, and plasma electrical conductivity measurements were made at 367, 427, and 735 ;;m from the diaphragm. Reference 11 gives details of the theory, diagnostics sensors, calibration procedures and previous experimental results.

4.0 EXPERIMENTAL RESULTS

The optical and electronic measurements were correlated in time by reference to the electronic signal used to initiate detonation of the plane-wave lens. The time interval between detonation of the plane-wave lens and diaphragm breakage was 57.6 μs. This time was determined with a light pipe oriented to view the center of the diaphragm and the streaking camera focused on the display board. The diaphragm breaking time is taken as the new zero time reference for all experimental results in this test.

4.1 Optical and TOA Results

The framing camera provided photographic evidence that a small amount of venting around the bar gages at 0.10 m began at 25 μs after the diaphragm broke. Venting continued until high-explosive gases from the driver section obscured the field of view approximately 20 μs later. Venting after 25 μs should have negligible influence on propagation of the shock front.

Table 1 summarizes TOA results for the shock front. The TOA values for the fiber optics are the times that the first luminosity peak was recorded at each location. The TOA values for the bar and flat-pack gages are the times when the rate of pressure increase was the greatest for the first pressure peak. This time was chosen instead of the peak pressure since the peak pressure was delayed by dispersion for the bar gage and time for the shock to travel the length of the piezoresistant grid for the flat-pack gages. A similar criterion was applied to the TOA values for the wall motion gages. Figures 2 and 3 show TOA and velocity plots, respectively, for propagation of the shock front in the exit pipe. After a short period of acceleration the shock attains a maximum velocity of 43 mm/μs at a distance of 0.10 m from the diaphragm. The velocity of the shock front attenuated from 43 to 4.5 mm/μs between 0.10 and 2.5 m. The only other documented study in the open literature using a grout type wall material was the Marvel experiment.[12] That study identified the delayed entrainment of wall material as the principal mechanism for attenuation of the shock front.

4.2 Pressure Profiles

Figures 4-11 give pressure profiles obtained for this experiment. Peak pressures in the shock front decayed from 2.28 GPa at 0.10 m to 0.024 GPa at 2.5 m from the diaphragm. For locations where bar and flat-pack gages can be compared there appears to be agreement in timing and amplitudes of the first two peaks. Generally the pressure oscillations of the flat-packs are larger and probably more indicative of the pressures exerted at the walls. Dispersion in the input bar of the bar gage tends to broaden the pressure pulse and lower the peak pressure arriving at the quartz crystal. The observed pressure oscillations result from axial and radial oscillations of the flow induced by early diaphragm break[13] and radial convergence of driver gas in the compressor chamber.[7] The fact that the oscillations persist over a substantial distance supports the argument of delayed entrainment of wall material.

4.3 Radial Wall Motion

Figure 12 gives radial displacements vs time where the time axis for each radial displacement shown has been shifted so that zero time corresponds to TOA of the shock front (Table 1) at the respective wall motion gage. The initial rapid wall expansion is consistent with the high pressures immediately behind the shock front. Most of the radial expansion appears complete by 60 μs when pressures behind the shock front are greatly reduced. Postshot the grout section beyond 0.8 m was recovered intact. The final bore diameter at 0.8 m measured 60 mm, corresponding to a radial expansion of 20 mm. Wall motion measurements of radial expansion at 100 μs behind the shock front at 0.50 and 1.00 m were 19 and 4.6 mm, respectively. If these values are reasonably accurate, then appreciable radial wall motion occurred after 100 μs. Post-shot measurement of the bore diameter at 3.0 m indicated <1 mm radial expansion. Consequently, significant attenuation occurred between 2.5 and 3.0 m since measurements at 2.5 m indicated a shock propagating at 4.5 mm/μs.

4.4 Plasma Flow Velocity and Conductivity Measurements

Figure 13(a) illustrates the time history for the plasma flow velocity from an analysis of the velocity gage record at 367 mm from the diaphragm. Figure 13(b) shows the plasma effective conductivity vs time results from the load voltage and load current measurements. The conductivity measurements resulted in a magnetic Reynolds number >60 requiring correction to the velocity and plasma-resistance results. Corrections based on the eddy current effects are shown as the dashed line in Fig. 13(a) and have already been incorporated in the conductivity history of Fig. 13(b). At 367 m the shock velocity (U) was measured at ~ 32 mm/μs (Fig. 3). The plasma flow velocity (u) can be obtained from the measured shock speed using the relation $u = 2 U/(\gamma+1)$, where γ is the gas equation of state parameter. Using $\gamma = 1.208$ for air gives $u = 29.0$ mm/μs, which is in good agreement with the corrected measured initial flow velocity of 27.4 mm/μs. For a more detailed discussion of the diagnostics and experimental results than is presented in this paper the reader is referred to reference 13.

REFERENCES

1. Voitenko, A.E., "Generation of High Speed Jets," Sov. Phys. Dokl. Vol. 9, 1966, p. 860.
2. Sawle, D., "Characteristics of the Voitenko High Explosive Driven Gas Compressor," First Intern. Colloq. of Gas Dynamics of Explosions, Brussels (18-21 Sept. 1967).
3. Glenn, H.D.,and Crowley, B.K., "Optical Technique for Monitoring High Energy (Mach 34-130) Shocks in Steel Pipes Containing Ambient Atmospheric Air," LLNL Report UCRL-71007 April 1968.

4. Glenn, H.D., "High Energy Oxygen Jet Propagation," J. Appl. Phys. Vol. 44, June 1973, p. 2585.
5. Glenn, H.D., Kratz, H.R., Keough, D.D., and Swift, R.P., "High-Energy Air Shock Study in Steel Pipe," Proc. 13th Intern. Symp. Shock Tubes and Waves, Niagara Falls, NY, 6-9 July 1981, p. 191.
6. Crowley, B.K., and Glenn, H.D., "Numerical Simulation of a High Energy (Mach 120 to 40) Air Shock Experiment," Proc. 7th Intern. Shock Tube Symp., Toronto, Canada, 23-25 June 1969, p. 314.
7. Brown, P.S., and Lohmann, M.L., "Computer Modeling of the Voitenko Tube Generator," in Proc. Sixth Intern. Symp. on Military Applications of Blast Simulations, Cahors, France, 25-29 June 1979.
8. Hartenbaum, B., "A Piezoelectric Transducer for Measuring Sub-Millisecond Pressure Pulses with Amplitudes up to 30 Kilobars," Gulf General Atomic Report GAMD-8474, 1968.
9. Glenn, H.D., "Diagnostics Techniques Improvement Program," Defense Nuclear Agency Report, Systems, Science and Software, DNA 2978T, 1972.
10. Danek, W.L., Shooley, D.J., and Jerogal, F.A., "Particle Velocimeter for Use Close in to Underground Explosions," Engineering Physics Co., Report, DASA-1431-3, 1967.
11. Gill, S.P., Mukherjee, D., and Baum, D.W., "MHD Velocity Gage Study," Artec Associates Inc., Final Report 128, 1979.
12. Crowley, B.K., Glenn, H.D., and Marks, R.E., "An Analysis of Marvel - A Nuclear Shock Tube Experiment," J. Geophys. Res. Vol. 76, May 1971, p. 3351.
13. Glenn, H.D., Kratz, H.R., Keough, D.D., Duganne, D.A., Ruffner, D.J., Swift, R.P., and Baum, D., "High-Energy Air Shock Study in Steel and Grout Pipes," LLNL Report, UCRL-52826, 1979.

Table 1. Diagnostics used and air shock time-of-arrival (TOA) data.

Axial Distance (m)	Diagnostics[a]	Fiber Optics TOA (µs)	Bar Gage TOA (µs)	Flat Pack TOA (µs)	Wall Motion Gage TOA (µs)
0	F	0.0			
0.02	F	1.3			
0.05	F	2.13			
0.10	F, B	3.45	3.9		
0.20	F, B, PM, W	5.74	6.6	6.5	5.6
0.30	F, B, PM, W	8.6	9.6	9.8	9.4
0.40	F	11.4			
0.50	F, B, PY, W	14.6	13.3	14.2	13.4
0.75	F	22.9			
1.00	F, B, PY, W	31.8	32.5	32.8	32.6
1.25	F	43.0			
1.50	F, B, PY, W	57.4	57.4	57.5	56.8
1.75	F	76.9			
2.00	F, B, PY, W	107.7	108.6	108.4	107.4
2.50	F, B, PY, W	208.0	209.3	193.4	
3.00	B				

[a]F = fiber optics; B = bar gage (SSS); PM = pressure - Manganin (SRI); PY = pressure - ytterbium (SRI); W = wall-motion sensor (particle velocity loop) (SRI).
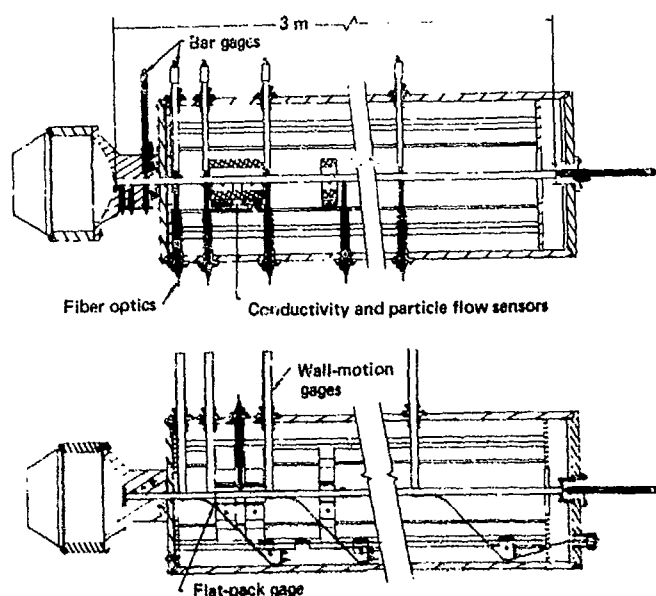
Fig. 1. Compressor, grout pipe and diagnostics.
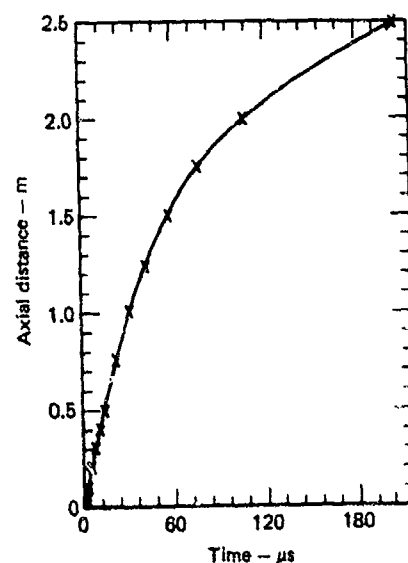
Fig. 2. Air shock TOA.
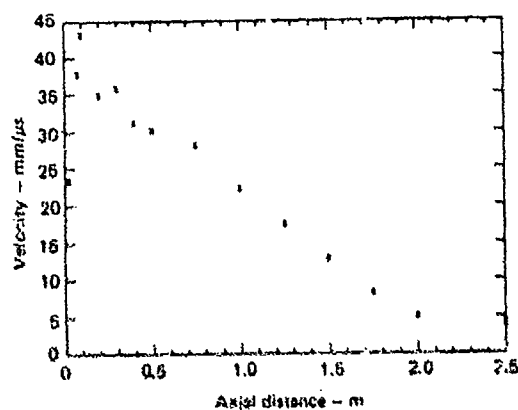
Fig. 3. Shock velocity vs axial distance.
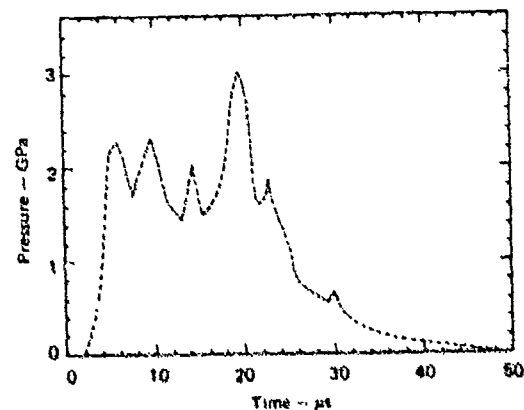
Fig. 4. Pressure history at 0.10 m.
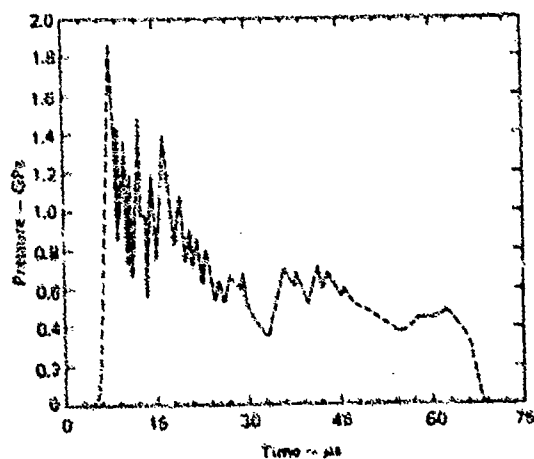
Fig. 5. Pressure history at 0.20 m.
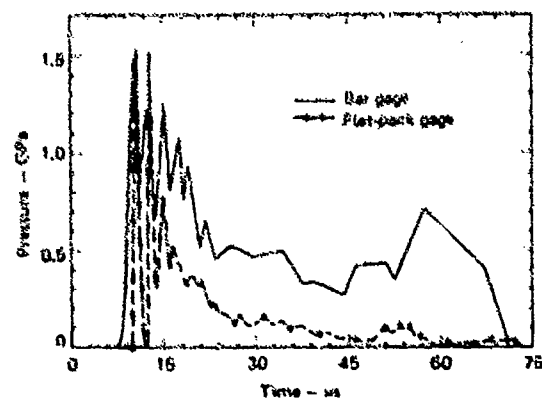
Fig. 6. Pressure history at 0.30 m.
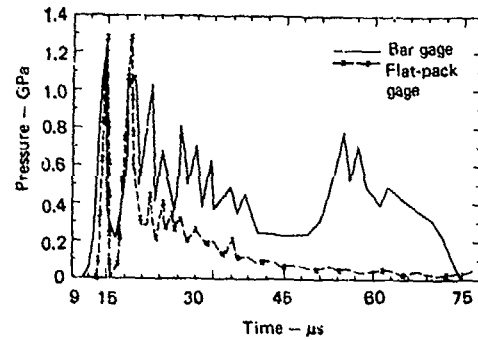
Fig. 7. Pressure history at 0.50 m.
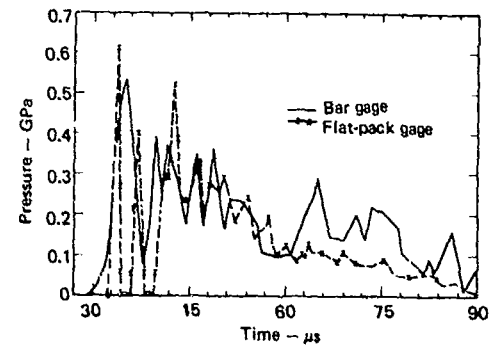
Fig. 8. Pressure history at 1.0 m.
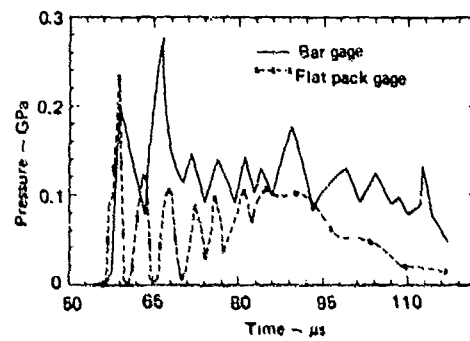
Fig. 9. Pressure history at 1.5 m.
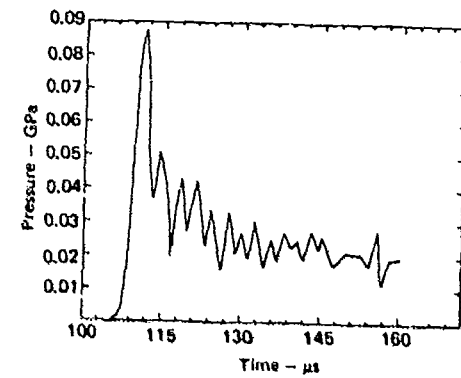
Fig. 10. Pressure history at 2.0 m.
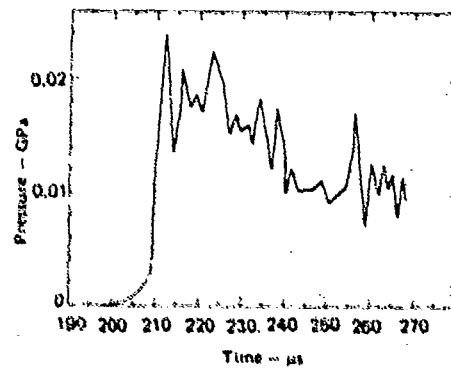
Fig. 11. Pressure history at 2.5 m.
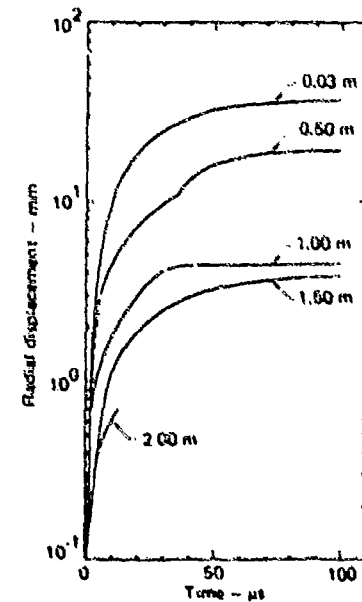
Fig. 12. Wall motion at 0.03, 0.50, 1.00, 1.50 and 2.00 m
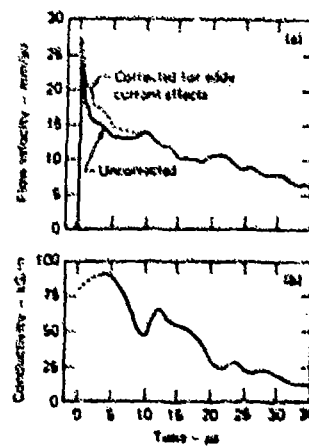
Fig. 13. (a) Plasma flow velocity vs time at 367 mm; (b) plasma effective conductivity vs. time at 427 mm.

SHOCK TUNNEL MEASUREMENTS
OF AOTV BOW SHOCK LOCATION

Dick Desautel

Department of Mechanical Engineering

San Jose State University, San Jose, California

Hypersonic bow shock geometry and standoff distance
are of central importance to aerothermodynamic
design of the NASA proposed aeroassisted orbital
transfer vehicle (AOTV). This paper reports shock-
tunnel measurements of bow shock standoff distance
for the NASA aerobrake AOTV configuration (70
blunted cone) at zero and nonzero angles of
attack. The shock tunnel operates with compressed
helium driver gas and NaCl seeded argon test
(driven) gas, and produces test flows of $M = 3.8$
to 7.9. Flow visualization is by self-luminosity
of the NaCl seed in the shock layer, and shock
position is determined by densitometric analysis
of the luminosity imagery. Over the indicated range
of angle of attack, the results are that the AOTV
equivalent-sphere radius is about 35% greater than
the actual AOTV base radius, somewhat less (thinner
shock layer) than that implied in previously reported
experiments.

1. INTRODUCTION

Currently, there is renewed interest in blunt-body aerothermodynamics
in high-altitude hypersonic flight; that interest derives from NASA's
proposed aeroassisted orbital transfer vehicle (AOTV). The drag-brake
AOTV perigee regime is characterized by significant nonequilibrium flow and
radiative heat transfer. The bow shock standoff distance largely controls
shock-layer aerothermodynamics, but the standoff distance is difficult to
predict accurately for AOTV configurations. The research reported here
deals with determination of hypersonic bow shock standoff distances for the
70 blunted-cone AOTV at zero and nonzero angles of attack. Bow shock
standoff distance in these experiments was measured by self-luminosity of
the seeded test gas in the shock layer as interpreted through the use of
photodensitometry.

Recent tests of several drag-brake AOTV configurations have been
reported that were primarily aimed at determining heat-transfer rates.
Included in the discussion were wind-tunnel schlieren photographs of bow
shock formation for a 70 blunted-cone configuration similar to that
studied in the present research. In addition, photographs have been taken
from earlier free-flight range facility tests of the same AOTV
configuration that were performed at Ames Research Center. It is found
that the previous wind-tunnel results for radius-normalized standoff
distance, /R , are approximately 35% greater than the current results.
The range facility data suffer from ambiguity in the shadowgraph visualization.

The experimental result desired is the radius-normalized AOTV standoff distance, or what is just as useful, the equivalent-sphere radius of the AOTV. From basic principles (conservation of mass), the shock standoff distance is controlled by the mean density ratio k =   /   across the normal shock on the stagnation streamline. In the hypersonic limit for nonreacting equilibrium flow, k depends only on the effective ratio of specific heats   . In the drag-brake AOTV perigee regime (altitude about 60 to 80 km), the atmosphere   = 1.3 to 1.4 , corresponding to k = 0.13 to 0.17. In the experiments reported here, sphere shock standoff distance   , measured under the same hypersonic flow conditions as those for the AOTV, is used to determine the test-flow k from published correlations.

2. EXPERIMENTAL PROCEDURE

The shock tunnel operates with NaCl - seeded argon gas driven by compressed helium, both initially at room temperature. Seeding of the argon by NaCl lowers the effective ratio of specific heats considerably. Incident shocks typically have M = 4, and upon reflection from the secondary diaphragm, produce nozzle reservoir conditions T   = 4,000 to 6,000 K and p = 150 to 250 psi. Shock-tunnel response in terms of extended time for constant p has been studied in overdriven, underdriven, and "tailored" conditions. The latter produces maximum test-flow durations of about 1 msec before viscous attenuation sets. Various nozzles are used to produce test section flow conditions with estimated M = 3.8 to 7.9 and unit Re = 950,000 to 55,000 per meter. Sphere and the AOTV (70 blunted cone, base radius - nose radius) models are alternately used in the tests. Tunnel instrumentation is simple: thin-film shock-arrival sensors (incident shock speed), piezoelectric pressure sensors (p and p) and test-section photodiode luminosity sensor, all supported by various amplifiers, circuitry, and oscilloscopes. Still photographs of imagery data are taken using 4- by 5-in. B/W negatives in a Graflex camera. An external, electronically driven Uniblitz shutter is used to control exposure initiation and duration.

Figure 1 shows the overall SJSU shock-tunnel facility, Fig. 2 illustrates the tunnel diagnostic and data-acquisition instrumentation, and Fig. 3 shows a photograph and drawing of the AOTV model. Typical luminosity images are shown in Fig. 4 for the sphere, and in Fig. 5 for the AOTV.

3. DATA REDUCTION AND ANALYSIS

Figure 6 characterizes the data-reduction and analysis procedure. Densitometric analysis is performed on the luminosity imagery to determine either film-transmission profiles using a Jarrell-Ash densitometer or film-density profiles using a Joyce-Loebel densitometer along the stagnation and adjacent streamlines. Examples of sphere and AOTV film-density profiles are shown in Figs. 7 and 8, respectively. These profiles are then converted by means of film-characteristic curves to normalized luminous-intensity profiles. The intensity profiles are then curve-fitted (least-squares) with polynomials of various orders, and the fit with the lowest residuals provides the best determination of the bow-shock location. Care

must be taken to recognize shock-precursor luminosity data in the profiles
in order to exclude such data from the curve fit. In nearly all cases, the
fourth-order polynomial fit provides the best results (lowest residuals).

The radius-normalized sphere shock location /R thus measured is used
to determine k, the mean density ratio across the normal shock from
published correlations. It is also used together with the measured AOTV
radius-normalized standoff distance   /R to determine the ratio of
equivalent sphere radius to actual AOTV radius R /R .

Estimates of the effective free-stream ratio of specific heats   and
Mach number M are determined from the known nozzle area ratio and mean-
density ratio across the shock, by inverting the equations for isentropic
nozzle flow and normal shock Rankine-Hugoniot relations.

A Zenith Z-100 microcomputer is used to 1) store film-characteristic
curve data; 2) convert film-transmission (or density) readings to
normalized intensity, using the film-characteristic curves; 3) least-
squares curve-fit-the resultant intensity profiles and calculate ; and 4)
determine estimates of   and M by the process described. Also, both types
of densitometers mentioned have been used on the same imagery in certain
cases. Under equal sensitivity and spatial scale settings, , , M results
derived from the two instruments show close agreement.

4.   RESULTS AND DISCUSSION

Table 1 lists the estimated flow conditions and measured shock
locations for the four Mach numbers tested. Figure 9 shows the main
results for the current experiments . These results are measured values of
 /R and R   /R as functions of k, shock mean-density ratio. For
comparison, the figure includes data values estimated from reports of
previous tests. Also shown in the figure are the sphere and disk /R
functions. Figure 10 shows examples of measured bow shock geometry in the
nose region at angle of attack. Figure 11 presents estimates of the
variation of /R for angle-of-attack from 0 to 20; also shown for
comparison are the sphere and disk /R, the latter for the disk normal to
the flow.

The basic results (Fig. 9) indicate that within the range of k shown,
the AOTV 70 blunted-cone configuration has the same bow shock standoff
distance as would a sphere with a radius about 35% larger than the AOTV
radius. This is also the amount by which the AOTV standoff distance would
exceed that of a sphere of equal radius.

The angle-of-attack results shown in Figs. 10 and 11 are less
comprehensive than the Fig. 9 results, but it is clearly evident the
standoff distance increases with angle-of-attack. This is expected since
the apparent model bluntness as seen by the flow increases with angle-of-
attack up to the normal-surface limit.

5. CONCLUSIONS

Experimental measurements were made of the radius-normalized bow shock
standoff distance   /R as a function of shock mean-density ratio for the

drag-brake, 70 blunted-cone AOTV configuration. The experimental range of density ratios overlaps that of the AOTV perigee flight regime. The results indicate a thinner shock layer (smaller /R) than previously expected; the equivalent sphere radius is about 35% greater than the radius of the actual AOTV base (or nose). This has important implications for radiative heat transfer, suggesting that previous predictions based on larger bow shock standoff distances may be excessive.

6. ACKNOWLEDGMENTS

REFERENCES

1. Walberg, G. D., "A Survey of Aeroassisted Orbit Transfer, "Journal of Spacecraft and Rockets, Vol. 22, No. 1, 1985.

2. Rowe, J. T., "Introductory Aerothermodynamics of Advanced Space Transportation Systems, "Journal of Spacecraft and Rockets, Vol. 22, No. 1, 1985.

3. Desautel, D., "Analytical Characterization of AOTV Perigee Aerothermodynamic Regime," Progress in Aeronautics and Astronautics, Vol. 96, 1985.

4. Shih, P. K. and Gay, A., "Low L/D Aerobrake Heat Transfer Test at Mach 10," AIAA Paper 8-0309, Reno, Nev., 1984.

5. Lombard, C. K., Vankatapathy, E., and Barding, J., "Forebody and Base Flow of a Dragbrake OTV by an Extremely Fast Single Level Implicit Algorithm," AIAA Paper 844-1699, Snowmass, Colo., 1984.

6. Park, C., "On Convergence of Computation of Chemically Reacting Flows," AIAA Paper 85-0247, Reno, Nev. 1985.

7. Park, C., "Calculation of Radiation from Argon Shock Layers," Journal of Quantitative Spectroscopy & Radiative Transfer, Vol. 29, No. 1, 1982.

Table 1   AOTV bow-shock experimental results

Sphere		AOTV		Estimated		
δ_s/R_s	$k = \rho_1/\bar{\rho}_2$	δ_A/R_A	R_{eq}/R_A	γ_e	N	Re_D
0.181	0.219	0.230	1.27	1.39	3.8	60,000
0.157	0.191	0.217	1.38	1.36	4.8	28,000
0.140	0.171	0.190	1.36	1.37	7.8	8,000
0.126	0.154	0.170	1.35	1.32	7.9	3,500

Fig. 1 Gas Dynamics Laboratory
Shock Tunnel Facility.
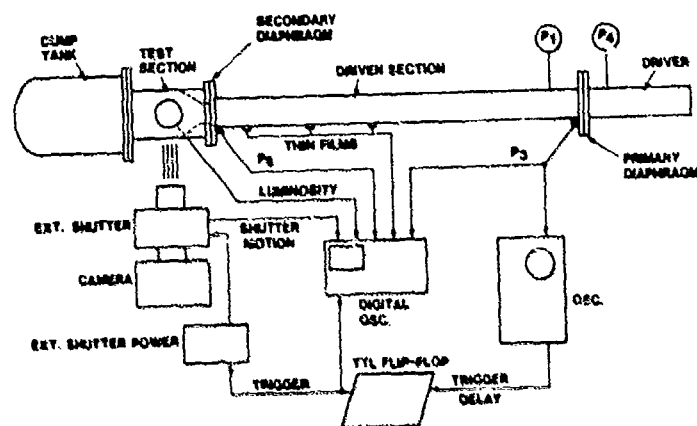
Fig. 2 Shock Tunnel Instrumentation
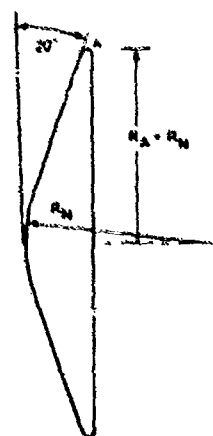
Fig. 3 Drag brake AOTV model.
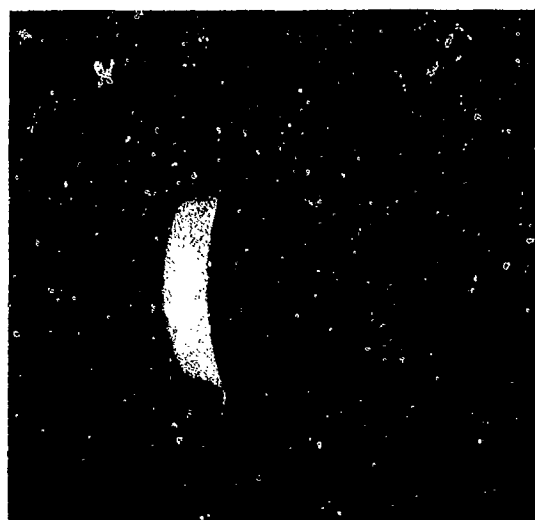
Fig. 4 Sphere luminosity photograph
(M = 7.8).
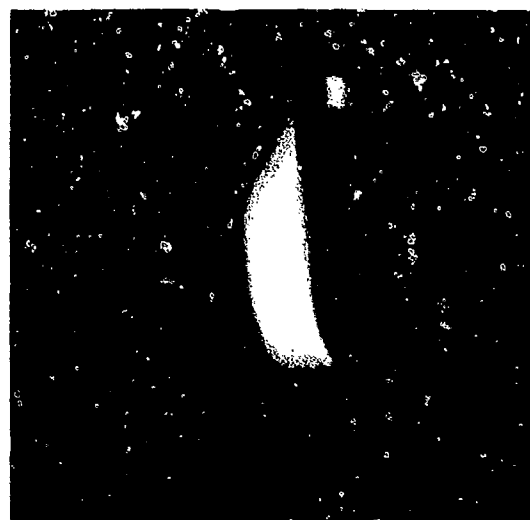
Fig. 5 AOTV luminosity photograph
(M = 7.8, a = 20°).
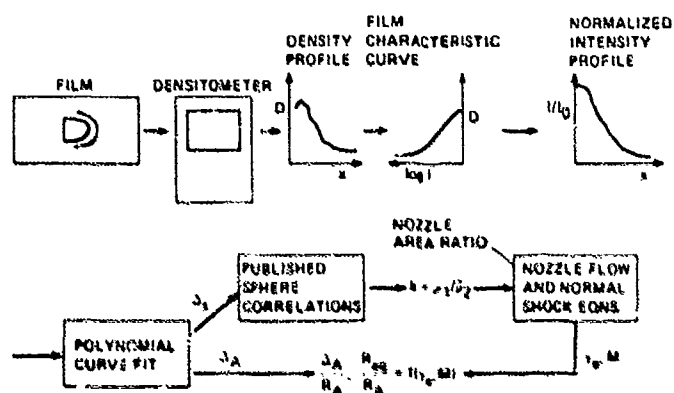
Fig. 6 Luminosity data reduction
and analysis procedure.
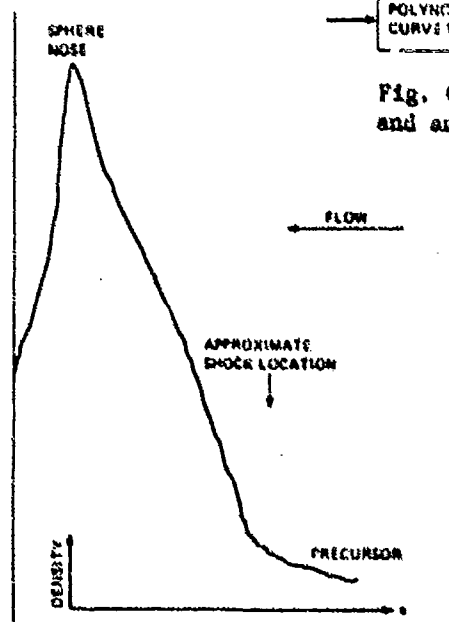
Fig. 7 Sphere film density profile
along stagnation streamline.

Fig. 8 AOTV film density profile along
stagnation streamline.

△ AOTV (SHIH AND GAY[4])
○ AOTV (LOMBARD et al.[5])
□ AOTV (PRESENT RESULTS)
- - - DISK }
     SPHERE } (PARK[6])
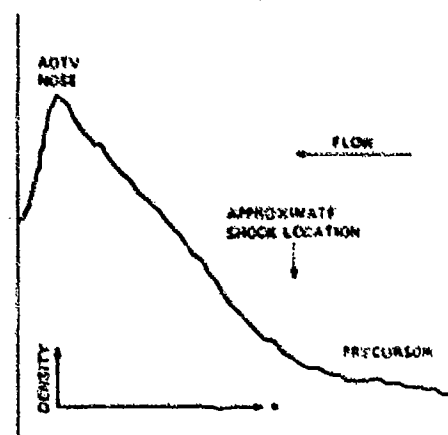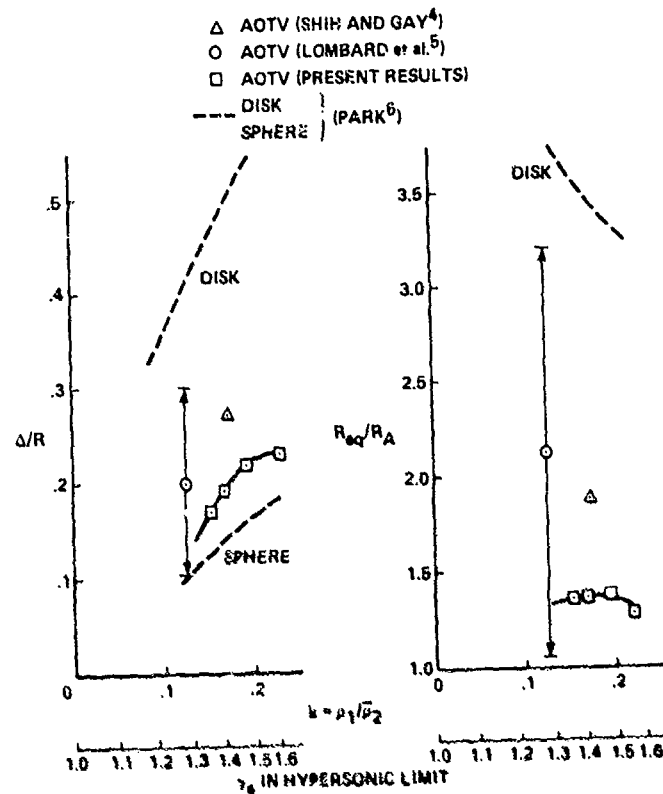
Fig. 9 AOTV bow shock standoff distance
variation with mean shock density ratio.
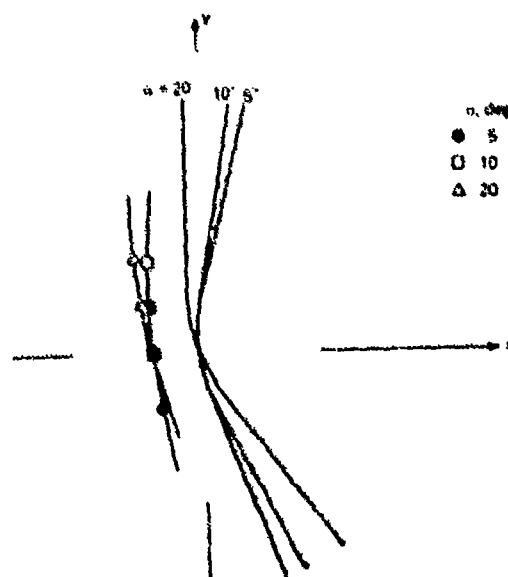
Fig. 10 Variation of AOTV bow shock
geometry with angle of attack.
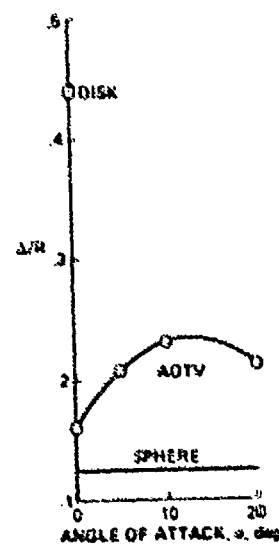
Fig. 11 Variation of AOTV
bow shock standoff distance
with angle of attack.

LINEAR AND NONLINEAR ABSORPTION OF HOT

SF_6, AND NH_3 AT 10.6 μm

R.H. Krech, L.M. Cowles, G.E. Caledonia and D.I. Rosen
Physical Sciences Inc., Research Park, Andover, MA 01810

A series of shock tube measurements to determine the laser
absorption coefficients of hot SF_6 and NH_3 were conducted on the
10.6 μm P(20) CO_2 laser transition. Measurements were made behind
both incident and reflected shocks from 500-3000K at pressures from
10 to 70 atm. Simultaneous high intensity (100 kW/cm^2) and low
intensity (1 mW/cm^2) measurements were made in NH_3 to determine if
saturation would occur under the temperature and pressure conditions
to be encountered in a laser-heated rocket thruster. No indication
of saturation was observed and the results can be described by a
simple two-level model verified by room temperature saturation
measurements with SF_6.

1. INTRODUCTION

The concept of using energy, beamed from a remotely stationed laser, to
power a rocket thruster is attractive since it provides high specific impulse at
high thrust levels.[1-4] When a high power CW laser is used to heat the propel-
lant, the physical processes involved are simply described by a direct, high
pressure gas-phase absorption of the beam in a stagnation chamber followed by a
supersonic expansion of the hot gas through a nozzle. Stagnation conditions
yielding a specific impulse of 1000s can be obtained if the equivalent of nine
10.6 μm photons per molecule are absorbed into a propellant mixture where
hydrogen is the primary constituent.

The original CW laser propulsion concept required a laser induced breakdown
in a pure hydrogen propellant followed by the formation of a stable laser
supported combustion (LSC) wave. Absorption occurs via inverse electron
bremsstrahlung which requires that a significant fraction of the hydrogen be
ionized. In pure hydrogen ionization becomes significant above 10,000K, with a
stable LSC wave forming at approximately 30,000K. Such high temperature would
create a severe thermal environment in the stagnation chamber of the thruster and
thus motivated a study of seeding the propellant with alkali metals to produce
electrons at lower temperatures. The addition of cesium, which thermally ionizes
above 3000K, would allow the formation of an LSC wave at temperatures below
10,000K, and thus provide a less severe environment, however it is not yet clear
that the LSC wave would stabilize at such low temperatures.

Alternatively, molecules having optical transitions at the laser wavelength
can absorb energy, and by collisional energy transfer, heat the hydrogen propel-
lant.[5] The primary advantage is that formation of a stable LSC wave is not
required to process the hydrogen since the heating is continuous from the inital
injection temperature to the final stagnation temperature. Furthermore, if mole-
cular absorption can heat the gas to 3000-5000K, then specific impulses of 1000-
2000s can be obtained with ionization (and cesium seeding).

The high resolution absorption properties of most potential absorbers are
not well known at temperatures over 1000K, especially at the pressure conditions
that are required for thruster operation (10 to 100 atm). Important absorption
paths due to hot bands cannot be adequately probed at low temperatures, and

indeed most molecules dissociate in the temperature range of interest. Finally, it is not known to what extent saturation will limit absorption at high irradiance levels, i.e., 1-1000 kW/cm^2. The propellant heating rate in a CW laser heated thruster is determined by the absorbed incident laser intensity. Above the optical saturation intensity, further energy cannot be absorbed due to depletion of the population of the absorbing states. Since saturation is a primarily a function of the collisional relaxation time of the absorbing species, the saturation intensity of the propellant mixture will vary with composition, temperature and pressure. The lack of adequate data in the temperature and pressure range of interest for thruster operation has motivated a series of laser absorption studies in shock heated gas mixtures Potential molecular seed species studied thus far included H_2O, CO_2, NH_3, SF_6 and NF_3.

The high temperature absorption properties of $H_2O/H_2/Ar$ mixtures at 10.6µm have been reported previously.[6,7] These measurements indicated that an additional absorber species would be required below 2000K for thruster operation. This paper presents the results of recent measurements of the 10.6 µm P(20) CO_2 laser absorption coefficients of SF_6 and NH_3 from room temperature to approximately 3000K. In the NH_3 experiments, simultaneous measurements were conducted at low intensity (1 mW/cm^2), and high intensity (100 KW/cm^2) to directly ascertain whether saturation might occur at high incident intensity.

2. EXPERIMENTAL

The laser absorption coefficient measurements were performed behind both incident and reflected shocks in a 1.5 inch diameter double diaphragm shock tube with a 5 foot long driver and a 12 foot long driven section. Optical measurements were made through anti-reflection coated zinc sulfide windows located 1 inch from the end wall in a 5 foot long test section with a 1.31 inch square cross section. Shock pressure was measured by four piezoelectric pressure transducers located at one foot intervals along the test section. Shock velocity is measured from the time of arrival of the incident shock wave at successive stations. The last transducer is located at the optical port to allow a direct correlation of the absorption with total pressure.

The optical configuration used for the low intensity CW laser absorption coefficient measurements is shown in Figure 1. A line-tuned, waveguide CO_2 laser (California Laser Corp. Model 81-5500-TG-T) is the CW radiation source. The main beam traverses the shock tube and a reference beam is split off near the laser source to provide a continous measurement of the laser output. Both beams are detected by HgCdTe detectors which have linear responses at the operating intensities. The detector outputs are amplified, and digitized by a Camac data acquisition system at a 1 MHz rate, and stored in a computer for analysis. A monochromator (PTI Optics Mini-Chrom-1) is mounted in front of the transmission detector to eliminate any background emission that may exist outside the narrow bandwidth of the laser line being studied. Transmitted light is collected and focussed on the entrance slit of the monochromator with an AR coated Ge lens. CaF_2 attenuators are mounted in beam path to limit the intensity through the shock tube and on the detectors. Typically the incident intensity was restricted to 1 mW/cm^2 and the power incident on the detector below 500 µW.

The high intensity measurements required that a pulsed CO_2 be coupled into the optical path, together with a dual beam pulsed detection system. This configuration is shown in Figure 2.

The pulsed laser (Lumonics TEA K-203) was operated line-tuned on a single mode without N_2 to obtain a triangular pulse with a width of 0.2 µs. The pulsed

beam was directed by two gold mirrors to a germanium beam splitter situated 10
degrees off axis. The reflected beam was directed to a Laser Precision RJP-735
pyroelectric probe to monitor the laser energy. The transmitted beam is next
directed to a NaCl beam splitter at Brewster's angle where it is mixed with the
CW beam. From this point onward the beams are coincident. A third turning
mirror directs the beams to the shock tube, where a 30 cm focal length BaF2 lens
located 15 cm from the center of the test section is used to concentrate the
beams. The incident intensity can be adjusted by CaF_2 attenuators and/or by
repositioning the lens. After passage through the test section the beams are
separated by a second NaCl beam splitter at Brewster's angle. The pulsed beam is
transmitted and detected by a second RJP-735 probe. The pulsed detectors are
connected to a Laser Precision 7200 Ratiometer where the energy incident on both
detectors is recorded on a digital readout.

The wavelength of both the CW and pulsed CO_2 laser was determined by an
Optical Engineering Spectrum Analyzer before each test.

Gas mixtures were prepared in a 31.4 liter stainless steel mixing tank. The
partial pressure was monitored by a Validyne DP-15 pressure gauge. The gases
were taken directly from the cylinders without further purification. Stated
purities were: Ar-99.999%; SF_6-99.8%; NH_3-99.998%; H_2-99.999%.

The temperatures behind the incident and reflected shocks were calculated
from the measured incident shock velocity for both frozen and equilibrium
equilibrium cases using the standard Rankine-Hugoniot real gas relationships.
When different post shock conditions were obtained from the calculations: i.e.,
where dissociation of the absorber occurs, a kinetics code was used to determine
the gas temperature and density history after shock passage.

The absorption coefficient α is determined by measured optical transmission,
I/I_0, total pressure P, temperature T, path length ℓ, the initial mole fraction
of absorber Xi, by the following equation:

$$\alpha_{(cm^{-1}-ama^{-1})} = \frac{\ln (I_0/I)}{X_i \, P_{(atm)} \, \ell_{(cm)} \, \left(\frac{273}{T(K)}\right)}$$

3. RESULTS AND DISCUSSIONS

The first set of measurements were conducted with 0.0006 SF_6/0.9994 Ar mix-
tures on the 10.6 μm P(20) CO_2 laser transition from 500 to 2500K at pressures
from 10 to 70 atm. SF_6 was chosen since it is one of the most efficient
absorbers of CO_2 laser radiation, and is a known saturable absorber.

A typical absorption signal obtained during the SF_6/Ar tests is shown in
Figure 3. The peak of the band is located at 948 cm^{-1} at room temperature and
due to the anharmonicity in SF_6 shifts to lower frequencies as the temperature is
increased.[8] Therefore the absorption coefficient decreases with increasing
temperature, and the room temperature absorption is higher than that of the shock
heated gas even though the density is higher after shock passage. The results of
our measurements are shown plotted in Figure 4, together with fits obtained from
the experimental measurements of Nowak and Lyman.[8] The measured absorption
coefficients are in reasonable accord with the previous values, although a slight
divergence is noted at the lower temperatures.

At the pressures of interest to laser propulsion, the absorption is due to many overlapped transitions in the SF_6 and the entire vibrational manifold is involved in the absorption process. Therefore a simple two level saturation model is sufficient to describe the absorption:

$$x + hv \ (10.6 \ \mu m) \rightarrow x^*$$

$$x^* + M \rightarrow X + M \ .$$
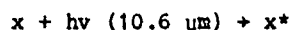
It can be shown that the CO_2 laser absorption coefficient α at any intensity I is related to the low intensity absorption coefficient α_o, as a function of the quench rate, kq and total quencher density M, by

$$\alpha = \alpha_o \ \frac{kq \ M}{(kq \ M + 2 \ \alpha_o \ (ama^{-1}cm^{-1}) \ I \ (W/cm^2))} \ .$$

To verify the model, a series of room temperature saturation measurements were conducted in SF_6/Ar mixtures at atmospheric pressure. The results are shown in Figure 5. On the P(20) laser transition, the low intensity room temperature SF_6 absorption coefficient is $\sim 300 \ cm^{-1}$-ama^{-1}. At atmospheric density ($M = 2.6 \times 10^{19} \ cm^{-3}$), and a quench rate of $3 \times 10^{-13} \ cm^3/s$, the predicted absorption coefficient is reduced by half at an intensity of 14 KW/cm^2. This is in reasonable accord with the data.

The third series of measurements were conducted in 0.094 NH_3/0.906 Ar and 0.05 NH_3/0.45 H_2/0.50 Ar mixtures on the P(20) CO_2 laser transition from 900 to 2900K at pressures from 10 to 40 atm. A typical absorption signal in the NH_3/Ar series is shown in Figure 6 for a reflected shock temperature of 2315K. A fairly rapid decay of the signal is observed after the reflected shock. Simultaneous measurements were made of the low and high intensity absorption coefficients behind the reflected shock, and the spike in the trace is a result of the pulsed laser. No difference in absorption was noted between absorption coefficients obtained from the pulsed measurements at intensities slightly in excess of 100 KW/cm^2 and those obtained with 1 mW/cm^2, indicating that ammonia is not saturating under the conditions behind the reflected shock.

The dissociation of the absorber species below the stagnation temperature is not desirable. In the absence of significant concentrations of H_2, the disappearance of NH_3 is rapid. Equilibrium calculations predict that even with H_2 added to the mixture to shift the equilibrium towards NH_3, the concentration of NH_3 behind the reflected shock above 1500K will be too low to give significant absorption if equilibrium is attained. The kinetics of ammonia decomposition are reasonably well known and indicates that below 2500K little decomposition occurs if a substantial fraction of the propellant is H_2. The $H_2 + NH_2 \rightarrow H + NH_3$ reaction plays a major role in regenerating NH_3 and slowing the overall decay rate. Figure 7 shows that the NH_3 absorption signal does not decay in the several hundred μs of available test time at 2290K with 45% H_2 in gas mixture. The results of our measurements are shown in Figure 8. Under all test conditions the absorption coefficients obtained from the pulsed laser matched those obtained at low intensity with CW laser.

From the two level saturation model presented above, the intensity required to obtain significant saturation is shown to be inversely proportional to the low intensity absorption coefficient. As the absorption coefficient of NH_3 is between 1 and 2 cm^{-1}-ama^{-1} above 1000K, saturation should not occur at the intensities encountered in our pulsed measurements, and indeed none was observed.

4. CONCLUSIONS

The absorption coefficients for potential laser heated thruster propellant additives are shown in Figure 9. At temperature below 1500K, SF$_6$ is by far the best absorber on a weight basis, but since SF$_6$ will react with H$_2$ it is not the most desirable low temperature absorber. NH$_3$ is a strong absorber which does not rapidly decompose in the presence of H$_2$ from room temperature to 3000K. Above 3000K, H$_2$O is the best absorber. A significant absorption advantage is gained by chemical nonequilibrium during the short flow times (hundreds of μs) involved in these experiments and appropriate to a CW laser heated thruster. This study suggests that a propellant mixture containing NH$_3$, H$_2$O, and H$_2$ is suitable for a high performance laser heated rocket thruster powered by a CW CO$_2$ laser.

ACKNOWLEDGEMENTS

REFERENCES

1. Caledonia, G.E., Wu, P.K. and Pirri, A.N., "Radiant Energy Absorption Studies for Laser Propulsion," Physical Sciences Inc., PSI TR-20 (NASA CR-134809), 1975.

2. Kemp, N.H., Root, R.G., Wu, P.K., Caledonia, G.E. and Pirri, A.N., "Laser-Heated Rocket Studies," Physical Sciences Inc., PSI TR-53, (NASA DR-1315127), 1976.

3. Fowler, S.C., Newman, L.A. and Smith, D.C., "Beamed Energy Coupling Studies," Final Technical Report for Contract No. F04611-77-C-0039, AFRPL-TR-79-51, September, 1979.

4. Nebolsine, P.E., Pirri, A.N., Goela, J.S., Simons, G.A. and Rosen, D.I., "Pulsed Laser Propulsion," Paper VI-2, AIAA Conference on Fluid Dynamics of High Power Lasers, Cambridge, MA 1978 (also PSI TR-142).

5. Caledonia, G.E., "Conversion of Laser Energy to Gas Kinetic Energy," J. of Energy, 1, 1977, p.121-134.

6. Krech, R.H., Pugh, E., "Determination of Absorption Coefficients in Shock Heated Propellant Mixtures for Laser-Heated Rocket Thrusters," 13th Int. Symp. on Shock Tubes & Waves, Niagara, NY, 1981, p.462-469.

7. Pugh, E. and Krech, R.H., "Absorptivity of Water Vapor for 10.6 μm Radiation, AIAA J., 20, 1982.

8. Nowak, A.V. and Lyman, J. "The Temperature-Dependant Absorption Spectrum of the ν$_3$ Band of SF$_6$ at 10.6 μm," J. Quant. Spectrosc. Radiat. Transf. 15, (1975), p.945.

9. Baulch, D.L., Buxbury, J., Grant, S.J. and Montague, D.C., "Evaluated Kinetic Data for High Temperature Reactions," Vol. 2, Butterworth, London-Boston, 1976.
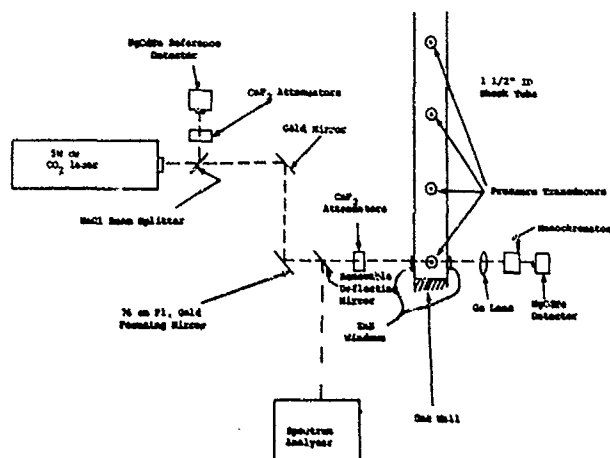
Figure 1. Optical Setup for Low Intensity Absorptions Measurements.
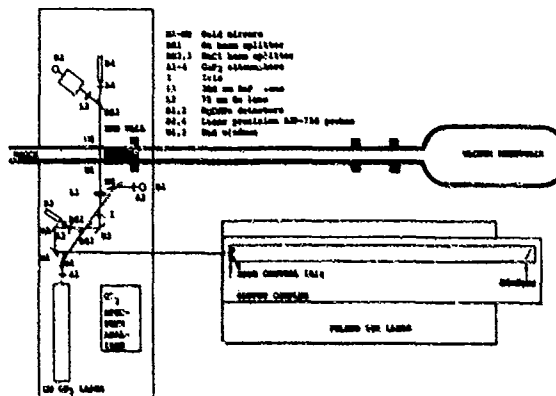
Figure 2. Optical Setup for Simultaneous Low and High Intensity Absorption Measurements.
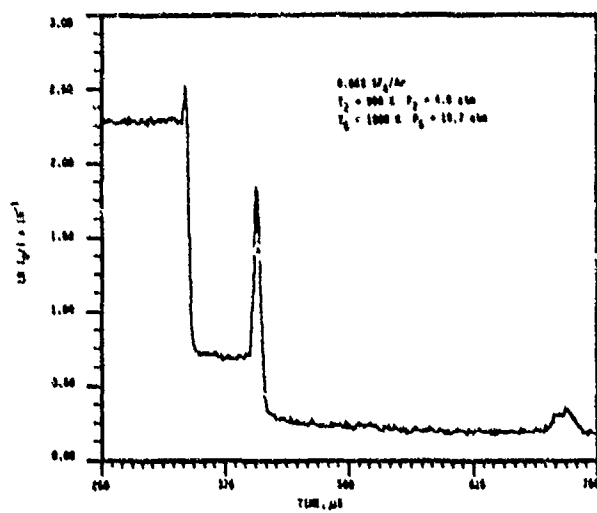
Figure 3. Typical SF_6 Absorption Trace.
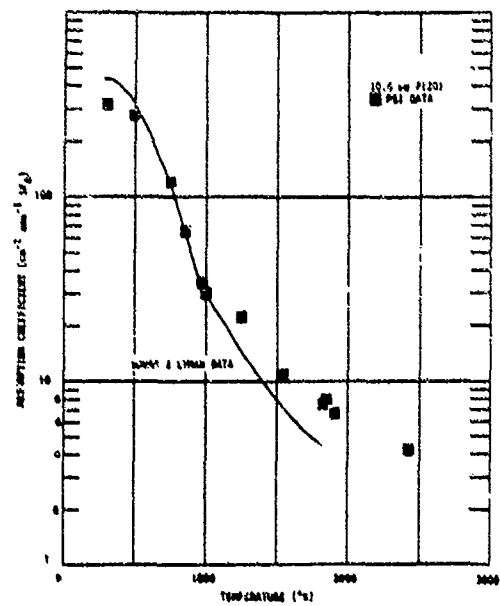
Figure 4. SF_6 CO_2 Laser Absorption Versus Temperature.
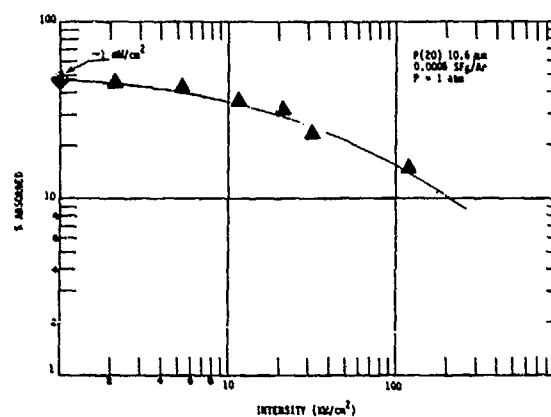
Figure 5. SF₆ Laser Absorption Versus Intensity.
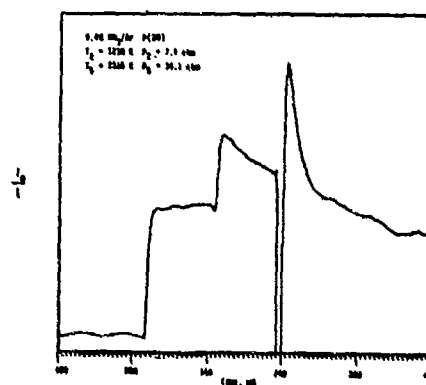
Figure 6. Absorption Signal From NH₃/Ar Mixture Without N₂.
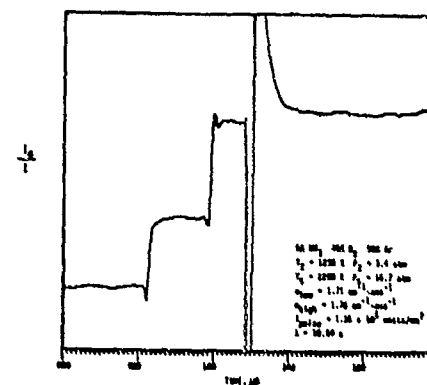
Figure 7. Absorptions Signal From NH₃/N₂/Ar Mixture.
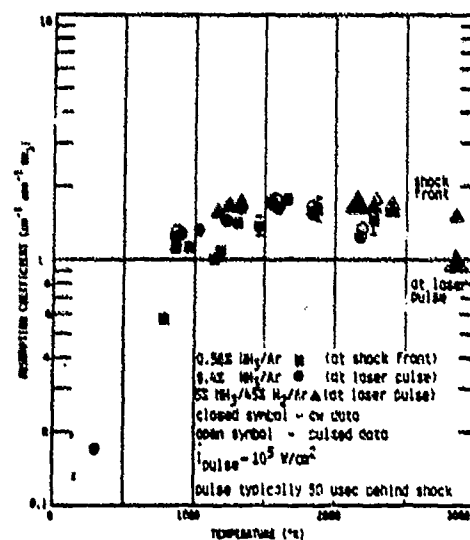
Figure 8. NH₃ Absorption Versus Temperature.
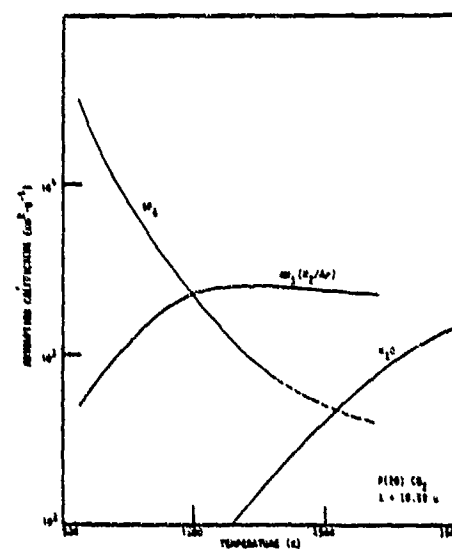
Figure 9. Absorption Coefficients Versus Temperature of Potential Seed Absorbers.

TIME RESOLVED ABSORPTION TECHNIQUE FOR

SHOCK-TUBE KINETICS USING PULSED LASER SOURCES

J.H. Kiefer, J.S. Sitasz, A.C. Manson, and H.C. Wei

Department of Chemical Engineering
University of Illinois at Chicago
Chicago, Il 60680

The "Pulsed Laser Flash Absorption" (PLFA) technique for
kinetic absorption measurements in shock waves is briefly
described. This method essentially uses a very short laser
pulse to take a stop-action snapshot of absorption in the
shock flow. The method provides an extremely high resolution,
<0.1μs, a very good S/N, and may be used with any short pulse
laser source. Examples showing dissociation in 1, 3-butadiene
and ethylbenzene are presented.

Measurement of the variation of specific species absorption with time
has been a principal method in shock-tube kinetics since its inception!
Infrared absorption being weak and often nonspecific, and visible absorption
sparse, the uv region has received the greatest attention. In fact, time-
resolved absorption measurements in the uv are responsible for a major part
of the kinetic data which has been obtained from shock-tube studies.

Till recently, optical measurements in shock waves have employed con-
ventional (discharge) sources, observing the time variation of absorption,
for example, at a fixed location. Such sources are usually quite limited
in intensity, are poorly collimated, and have a large spectral bandwidth. For
one thing, these limitations severely restrict the achievable space/time
resolution, usually to something no better than 10μs. They also limit
the possible detection S/N, can lead to serious deviations from Beer's law,
and cause difficulties in the calibration of species absorptivity.

All the above problems can evidently be avoided by the use of laser
sources, but lasers operating cw are still restricted to the near uv, often
with limited intensity. However, pulsed lasers have now been successfully
operated well into the vacuum uv. In this paper we present a fully devel-
oped and operating technique using pulsed lasers for kinetic absorption
measurements in shock waves. We will identify this method hereinafter as
"Pulsed Laser Flash Absorption" (PLFA). As will be seen below, this method
provides absorption profiles with extremely high resolution and an excellent
S/N.

In essence the PLFA method is quite simple: we use an expanded, par-
rallel beam from any very short pulse laser to take a stop-action "snap-
shot" of absorption in the shock flow. The transmitted beam is observed by
a linear CCD (charge coupled device) which has 1728 independent silicon
photodetector elements (pixils) in a length of 22.5 mm, and acts here as a
quantitative "film" with a very fast shutter.

Fig. 1. Schematic of the PLFA
Apparatus.
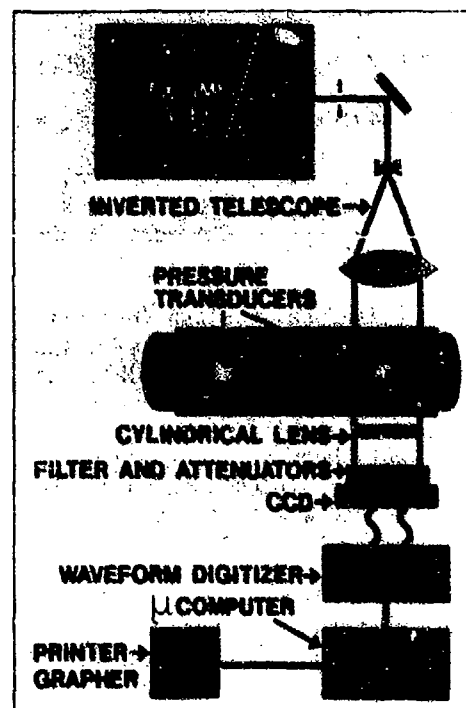
A schematic of our current apparatus is shown in Fig. 1. Here the short pulse (~10 ns) provided by an excimer laser is expanded by a factor ten to a broad and highly parallel beam. After traversing the shock tube[2] this beam is then focused onto the CCD through a wavelength (interference) filter and other gray attenuators as needed.
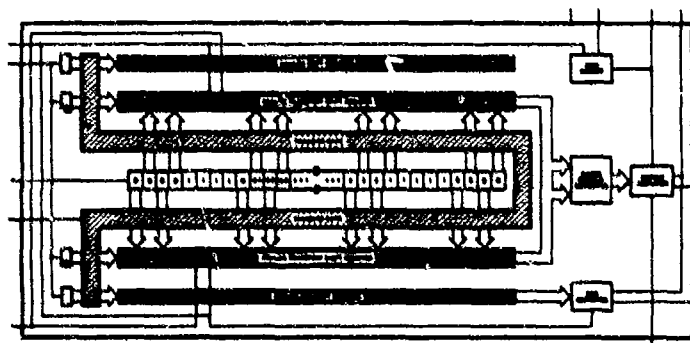
Fig. 2. Schematic of Fairchild 122 CCD. (Reproduced with the permission of Fairchild Camera and Semiconductor)

The CCD presently in use is a Fairchild 122 whose essential elements are shown in Fig. 2. The pixils (clear rectangles) accumulate charge proportional to incident energy, $E = It$, which can be transferred en masse to

the shift register arrays by setting the transfer voltage ($\emptyset_x$) high. The charge packets are then transported along these registers to a charge detector amplifier providing a serial read of the accumulated charge at a frequency set by the reset voltage ($\emptyset_R$) waveform. The important control waveforms used in the present application are shown in Fig. 3. On manual reset, the transfer voltage ($\emptyset_x$) is held high with continuous read, which keeps all arrays clear of dark charge. On signal from a piezoelectric shock pressure transducer centrally located along the CCD axis, $\emptyset_x$ goes low, separating pixils and shift registers; the laser then fires, $\emptyset_x$ goes high, transfering charge, and it finally stays low, blocking any further reading of pixil charge/radiation.
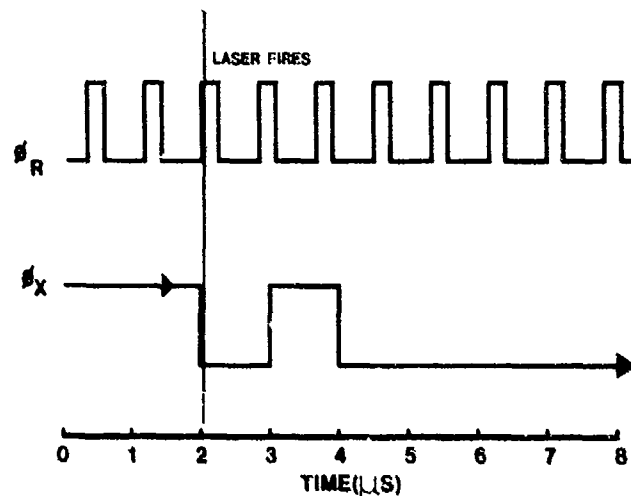
Fig. 3. CCD control
      waveforms.

As shown, the serial read proceeds at 1MHz into a Lecroy 8210 10 bit waveform digitizer interfaced to an Intertec microcomputer. A detailed specification of the apparatus will be presented elsewhere.
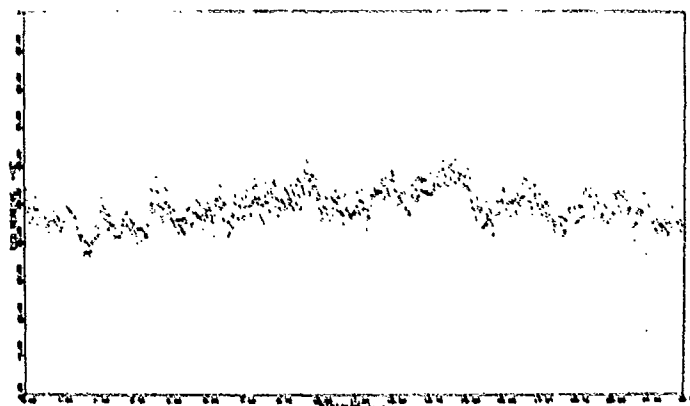
Fig. 4. Single-shot
      blank record-
      ing of excimer
      laser pulse.
      The vertical
      axis is in
      arbitrary units.

In a shock experiment, a preshock "blank" recording (Io) is first made, and the shock signal (I) divided by this, element by element, to form I/Io. An example Io is shown in Fig. 4. The "noise" seen here is clearly not noise in the usual sense, but a "graininess" of the laser beam from various sources of diffraction/interference which is quite reproducible. The ratio of two such blank recordings is shown in Fig. 5., where we see a signal to RMS noise ratio better than 100/1. Unfortunately, we have found it difficult to achieve this S/N routinely.

Fig. 5. Blank-to-blank ratio of excimer laser pulses at 222 nm.
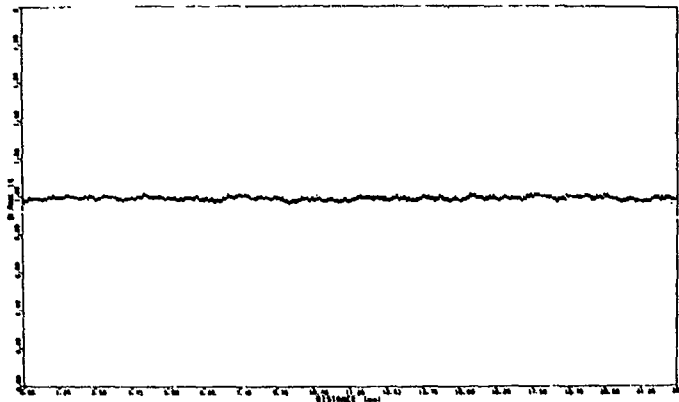
The signal recorded for a rare-gas shock is shown in Fig. 6. The rapid intensity variations between 4 and 5 mm are the shock-front "shadow", here composed of a very rapidly varying initial Fresnel diffraction preceding an essentially refractive displacement of radiation by the curved front. The resolution of the measurement is diffraction limited to $\Delta x \sim \sqrt{\lambda D}/4$ where D is roughly the distance of the CCD from tube center. For the KrCℓ excimer line used in this experiment, λ = 222nm, and with $D \sim 20$ cm, $\Delta x \sim 0.05$ mm is about the resolution. The effective time resolution is then $\Delta x/U_1$, or near $0.03\mu s$ in Fig. 6. Note that the post-shock observation time in this example is about 18.4 mm/U_1 = 10.6 μs.
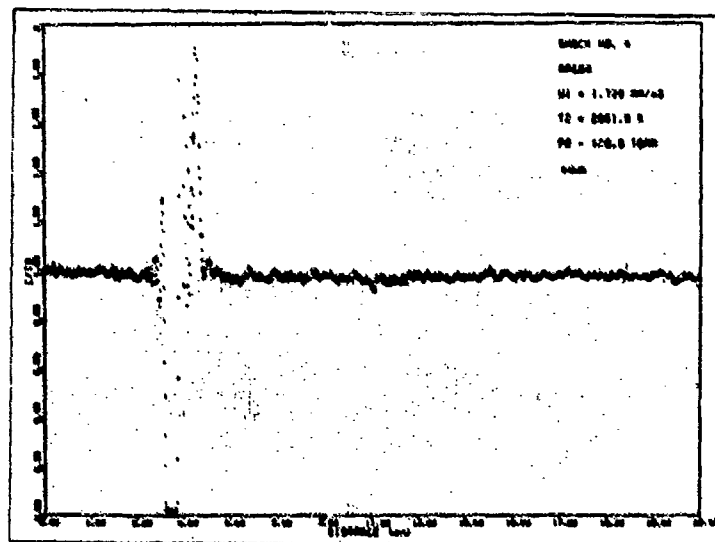
Fig. 6. PLFA record of an incident shock in a rare gas.

Application of the PLFA method to pyrolysis kinetics is illustrated in the examples of Figs. 7-10. Figs. 7-9 show the results of experiments on 1,3-butadiene pyrolysis at 222 nm where the butadiene absorbs quite strongly permitting the use of a very dilute mixture. In the example of Fig. 7, the butadiene is almost completely dissociated in 5μs and I/Io nicely returns to unity, showing minimal interference by product absorption. If this dissociation is a simple first-order process, as would be expected for these conditions[3], lnln (Io/I) should be linear with slope = -k for this reaction.

Fig. 7. PLFA record of a
shock in 0.2%
1,3 butadiene-
argon
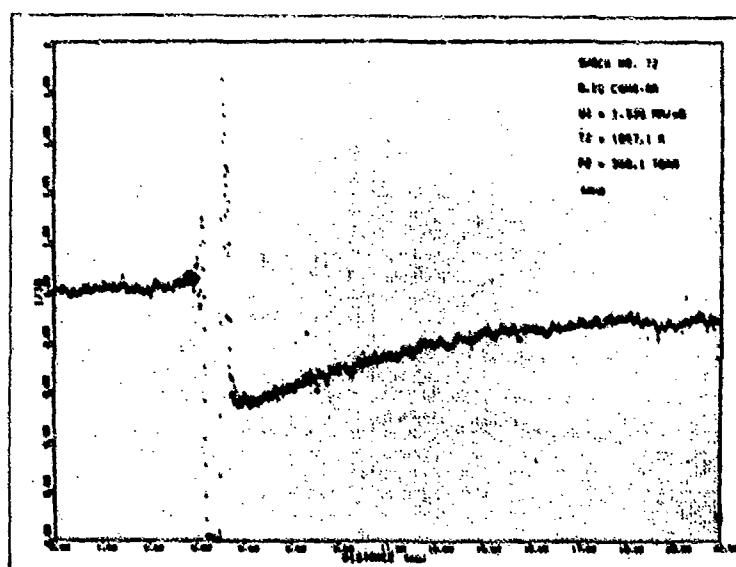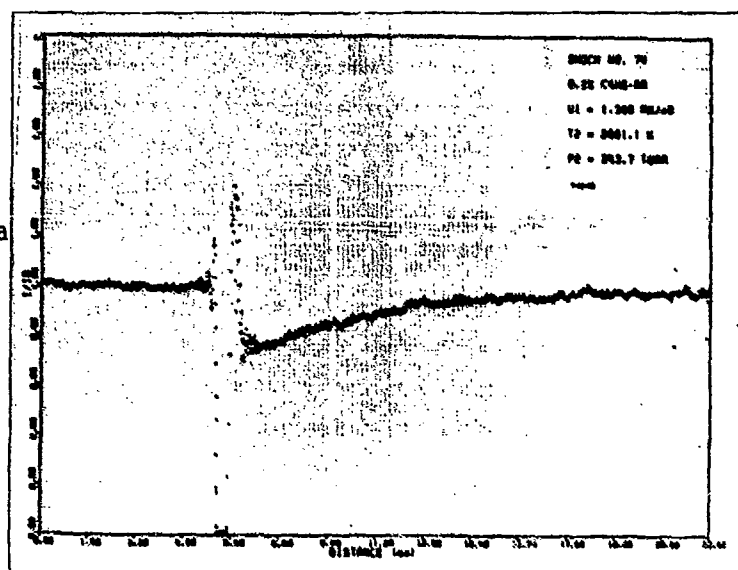
Fig. 8. PLFA record of
a shock in 0.2%
1,3 butadiene-
argon

This is confirmed in Fig. 9 where the data of Fig. 8 are replotted this way.
Fig. 10 shows ethylbenzene pyrolysis recorded at 308 nm (XeCl lines),
where the result requires some interpretation. The absorption is presumed .o
be from benzyl radical[4],[5] rapidly formed by ethylbenzene dissociation at this
temperature. The subsequent rise in transmission then shows decomposition of
the benzyl radicals. For some unknown reason we never achieve as good a S/N
at 308 nm.

Fig. 9. log-log plot
        of the data of
        Fig. 8.
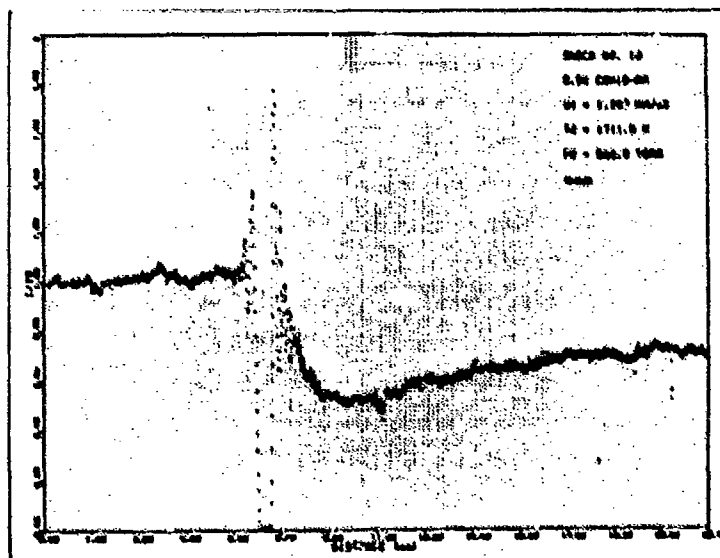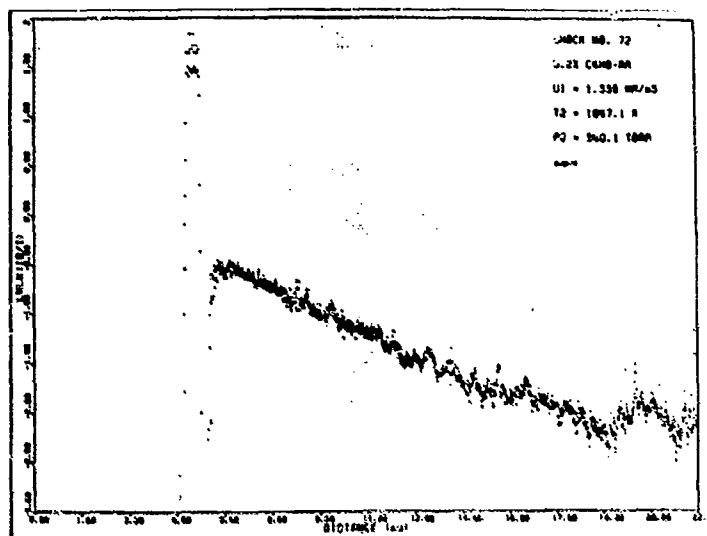
Fig. 10. PLFA record of
        a shock experi-
        ment in 0.5%
        ethylbenzene-
        argon.

The method generally provides a very good S/N, has a truly exceptional resolution (near a 300-fold improvement over conventional methods), a complete indifference to shock emission, and can employ laser sources with very narrow line width. Using phosphor-coated CCD's[6], the method may be extended well into the vacuum uv, making its many advantages available for atomic resonance absorption experiments.

ACKNOWLEDGEMENTS

REFERENCES

1) J.N. Bradley, Shock Waves in Chemistry and Physics, Wiley, N.Y. 1962.
2) J.H. Kiefer and A. C. Manson, Rev. Sci. Instrum. 52, 1392 (1981).
3) J.H. Kiefer, H.C. Wei, R.D. Kern, and C.H. Wu, Int. J. Chem. Kinet. 17, 225 (1985).
4) D.C. Astholz, J. Durant, and J. Troe, Eighteenth Symposium (International) on Combustion, The Combustion Institute, Pittsburgh (1981), pg. 885; D.C. Astholz and J. Troe, J. Chem. Soc. Faraday Trans. 2, 78, 1413 (1982); N. Ikeda, N. Nakashima, and K. Yoshihara, J. Phys. Chem. 88, 5803 (1984).
5) L.J. Mizerka and J.H. Kiefer, submitted to Int. J. Chem. Kinet.
6) M.M. Blouke, M.W. Cowens, J.E. Hall, J.A. Westphal, and A.B. Christensen, Appl. Optics 19, 3318 (1980).

SHOCK TUBE STUDY OF HIGH TEMPERATURE ABSORPTION

SPECTROSCOPY OF CH AT 431 nm

Michel Y. Louge[*] and Ronald K. Hanson

High Temperature Gasdynamics Laboratory
Department of Mechanical Engineering
Stanford University
Stanford, California 94305 USA

An experimental survey of CH absorption near the $Q_{2d}(7)$ and $Q_{1c}(7)$ lines of the $\{A^2\Delta \ (v=0) \leftarrow X^2\Pi \ (v=0)\}$ band was obtained at 2840°K, 0.2 atm using a remotely located cw ring dye laser source and a shock tube. Mixtures of methane and argon were shock heated to provide reproducible peak concentrations of CH, and narrow-line absorption was measured in repeated experiments with the laser set at different wavelengths. The spectral absorption data were interpreted with a theoretical model in order to verify the measurements and establish the sensitivity of this technique as an in situ absorption diagnostic for CH at 431.132 nm (vac.).

INTRODUCTION

The species CH is of interest in combustion. Its characteristic blue emission spectrum can be observed in the reaction zone of most premixed flames [1]. The spectral characteristics of CH have been studied in detail [2], and absolute absorption measurements of its concentration in combustion environments were made possible by the publication of reliable data on its oscillator strength [3,4]. Relative measurements of CH in flames using laser-induced-fluorescence have also been reported [5]. Useful studies of spectral line assignments were reported by Fagerholm, who studied the $^2\Sigma^- \leftarrow \, ^2\Pi$ and the $^2\Delta \leftarrow \, ^2\Pi$ systems of CH and CD [6], and by Gero [7]. In addition, Kiess and Broida provide a useful overview of spectroscopic data on CH [8].

In this study, a laser absorption technique previously demonstrated in this laboratory for the quantitative measurement of NCO [9] was applied as a diagnostic of CH behind incident shock waves. Mixtures of methane dilute in argon were shock heated to generate reproducible levels of CH under specified conditions of pressure (0.2 atm) and temperature (2840°K) in the shock tube. The narrow-linewidth absorption spectrum in the vicinity of the $Q_{1c}(7)$ and $Q_{2d}(7)$ lines of the $(A^2\Delta(v=0) \leftarrow X^2\Pi(v=0))$ band of CH was mapped out by conducting a series of nearly identical experiments, each at a different laser wavelength. Using the known spectroscopic parameters of CH, detection limits were inferred from the present experimental conditions and extrapolated to other temperatures.

Experimental spectra reported by Fagerholm [6] and Gero [7] indicate the accidental coincidence of the $Q_{2d}(7)$ and $Q_{1c}(7)$ lines, which belong to different branches of the $\{A^2\Delta(v=0) \leftarrow X^2\Pi(v=0)\}$ band. The present diagnostic takes

advantage of this coincidence and is therefore characterized by higher absorption levels than would be obtained on a single line. In this paper, the experimental facility and optical techniques will first be described, then the spectroscopic models and results will be presented.

EXPERIMENT

The experiments were conducted behind incident shock waves in a 15.24 cm internal diameter pressure-driven shock tube. Shock speeds varied between 1.79 and 1.84 mm/µsec, with attenuation of 0.5%/m or less. Typical leak plus out-gassing rates were 10^{-4} torr/min. Methane was obtained from a commercial cylinder (Liquid Carbonic) with 99% purity. The absorption from the $Q_{1c}(7)$ and $Q_{2d}(7)$ lines of CH around 431.13 nm (vac.) was observed using the optical setup shown in Fig. 1. This system was described in detail elsewhere [10,11]. It consisted of an Ar^+-pumped ring dye laser with an output power of 40 mW. The performance of the stilbene S3 dye degraded rapidly at this wavelength and required the use of fresh dye each day of laser operation. Amplitude stabilization was necessary for this ring laser operating near threshold to prevent excessive amplification of Ar^+ laser power fluctuations. Verification of the single mode operation of the visible dye laser beam was obtained using a confocal interferometer (Spectra-Physics Model 470, free spectral range 2 GHz), but proved difficult at this wavelength as a result of finesse degradation. The component of the laser power rejected by the amplitude stabilizer was sufficient to drive the wavemeter (Burleigh model WA-10) used for setting the laser wavelength. It was necessary to correct the displayed wavelength for the change in the index of refraction of air between the helium-neon reference wavelength at 632.991 nm and the blue wavelengths around 431.13 nm (correction = actual - displayed wavelength = +0.0019 nm).

The visible output of the laser system was transported 65 m via a 200 µm optical fiber to the shock tube facility where it was double-passed through the shock tube test section. The incident and return beams were filtered (FWHM: 40 nm, center at 450 nm) and monitored on separate detectors. The signals were electronically balanced prior to each experiment using small dc offset and gain adjustments on one of the differential amplifiers. The difference $(i_0 - i)$ and reference (i_0) signals were recorded on two separate channels of a digital storage oscilloscope (Nicolet Explorer III, dc coupled through a 100 kHz upper frequency cut-off filter). The data were subsequently transferred to a computer for analysis. Six runs were conducted with the following mixtures and conditions: CH_4 = 4.95 ± 0.15% dilute in argon, T_2 = 2840 ± 45°K, p_2 = 0.22 atm, ρ_{21} = 4.25 ± 0.02 (ρ_{21} is the density ratio across the shock and also the ratio of particle time to laboratory time), and wavelengths in the range 431.129 < λ < 431.134 nm (vac.). A test was conducted with the laser blocked to monitor possible spontaneous emission interferences from the test gas, but these emission levels were found to be insignificant.

RESULTS AND INTERPRETATION

The fractional transmission of the laser system is related to the mole fraction of CH through the Lambert-Beer law,

$$i/i_o = \exp\left[- \beta(\lambda)p\ x_{CH}L\right] ,$$

where i/i_o is the fractional transmission, $\beta(\lambda)$ the absorption coefficient at wavelength λ, x_{CH} the mole fraction of CH, p the total pressure and L the optical path length (30.5 cm). Under the present experimental conditions, it

was assumed that the dilute mixtures of CH_4 could provide reproducible levels of CH. By running nearly identical experiments and recording the absorption of CH at the peak concentration, relative absorption coefficients of CH as a function of wavelength were measured. A typical absorption trace obtained in these experiments is shown in Fig. 2. Note that the present methane mixtures produced small amounts of soot, causing a small level of extinction from light scattering, at late times in the experiments.

The peak absorption levels recorded in the six shock tube experiments were corrected for slight variations in the initial conditions and plotted as a function of wavelength in Fig. 3. The solid line is a theoretical profile assuming Doppler broadening (FWHM = 0.246 cm^{-1} at 2840°K), which can be expected under these high temperature shock tube conditions. Good agreement is found between the Doppler model and the experimental points. In addition, the inferred line peak lies at 23194.76 cm^{-1}, in reasonable agreement with Fagerholm, who reported the $Q_{1c}(7) + Q_{2d}(7)$ lines at 23194.81 cm^{-1}.

In order to assess the sensitivity of the present laser diagnostic, the relative absorption coefficient of the individual CH lines can be calculated using [11]

$$\frac{\beta}{f_{oo}} = \left(\frac{\Pi e^2}{m_e c^2}\right) \times \frac{(2J'' + 1)\ \exp\left[-\frac{hc}{kT} F(J'')\right]}{Q_{rot}\ Q_{vib}\ Q_{el}} \times \frac{N}{RT} \times \frac{S}{(2J'' + 1)} \times \phi \ ,$$

where β is the absorption coefficient (cm^{-1} atm^{-1}) at line center; f_{oo} is the oscillator strength of the $[A^2\Delta\ (v=0) + X^2\Pi(v=0)]$ band; $F(J'')$ is the rotation energy of the lower state (cm^{-1}); R is the universal gas constant (82.1 atm cm^3/mole/°K); N is Avogadro's number; Q_{rot}, Q_{vib} and Q_{el} are the rotational, vibrational and electronic partition functions, respectively; S is the rotational line strength; and ϕ is the Doppler line shape factor (cm) evaluated at line center,

$$\phi = 2\left(\ln 2/\Pi\right)^{1/2}/\Delta\omega_D \ ,$$

where $\Delta\omega_D = 0.246$ cm^{-1} is the Doppler width. The quantities $(\Pi e^2/m_e c^2)$ and hc/k are equal to 8.826 10^{-13} cm and 1.4388°K cm, respectively.

The partition functions are evaluated using the approximate expressions

$$Q_{rot} \simeq \frac{kT}{hcB_0''} \ , \qquad Q_{vib} \simeq \left[1 - \exp\left(-\frac{hc}{kT} \omega_e\right)\right]^{-1} \ ,$$

and $Q_{el} \simeq 4$. (There are two levels arising from electronic spin, and two levels arising from the possible orientations of the electronic orbital angular momentum.) By convention, the lower energy level of a given rotational transition is defined such that its degeneracy is equal to $(2J'' + 1)$. As a consequence, the normalization rule for the rotational line strengths must read for a given J''

$$S\left(Q_{1c}\right) + S\left(R_{1dc}\right) + S\left(P_{1dc}\right) = S\left(Q_{2d}\right) + S\left(R_{2cd}\right) + S\left(P_{2cd}\right) = 2J'' + 1 \ .$$

The corresponding rotational line strengths were taken from Kovacs [12].

The rotational energy of the ground state was evaluated using the Hill and Van Vleck formulae [2]

$$F'' = B''_o \left[(J''+1/2)^2 - \Lambda^2\right] \pm B''_o \left[(J''+1/2)^2 + \frac{1}{4} Y'' (Y''-4) \Lambda^2\right]^{1/2}$$

$$- D''_o K''^2 (K''+1)^2 , \qquad (cm^{-1})$$

where $\Lambda = 1$; in the present case, the $+$ sign corresponds to Q_{2d} and the $-$ sign to Q_{1c}. An additional correction was introduced to account for Λ-doubling of the ground state, namely -0.85 cm^{-1} for $Q_{2d}(7)$ and $+0.54$ cm^{-1} for $Q_{1c}(7)$. Using $B'' = 14.1961$ cm^{-1}, $D''_o = 1.48 \cdot 10^{-3}$ cm^{-1} [6] and $Y''(Y''-4)\approx-4$, $\omega_e = 2868.5$ cm^{-1} [8], it follows that: $F'' = 774.27$ cm^{-1} and $S = 6.56$ for $Q_{2d}(7)$; and $F'' = 777.58$ cm^{-1} and $S = 7.56$ for $Q_{1c}(7)$. Finally, the relative absorption coefficient at the center of the superposed $Q_{1c}(7)$ and $Q_{2d}(7)$ lines can be written as a function of temperature, assuming a Doppler width $\Delta\omega_D = 0.0046 \ T^{1/2}$ (cm^{-1}),

$$\frac{\beta}{f_{oo}} = \frac{\beta(Q_{2d}) + \beta(Q_{1c})}{f_{oo}} \approx 9.52 \cdot 10^{13} \times \frac{1-e^{-4130/T}}{T^{5/2}} \times e^{-1120/T} \ (cm^{-1} atm^{-1}) .$$

A plot of β/f_{oo} vs. temperature is given in Fig. 4. At the present experimental temperature (2840°K), $\beta/f_{oo} \approx 114000$ cm^{-1}atm^{-1}. Using the oscillator strength of Sawada and Kamada [3] and the Franck-Condon factor of Liszt and Smith [4], $f_{oo} \approx 0.0065$ and β (2840°K) ≈ 740 cm^{-1} atm^{-1}. From Fig. 3, the measured line-center absorption at 431.132 nm is $(1 - I/I_o) \approx 4.9\%$. This value corresponds to a CH mole fraction of about 20 ppm.

From the experimental record of Fig. 2, the minimum detected absorption level is seen to be quite low, a few tenths of a percent, and this is attributed primarily to scattering interferences from soot particles. Without any correction for scattering, the inferred value of CH is about ± 2 ppm, suggesting this as a "detection limit" for present conditions. It is clear that a proper account of soot scattering could further reduce the minimum detectable level of CH. Such account could be taken by simultaneously monitoring non-resonant scattering of laser light, and subtracting the scattering extinction trace from the resonant absorption signal. The resulting detection limit of CH should be below 1 ppm at 3000°K.

In conclusion, we believe that the present diagnostic has significant potential for high temperature studies of CH kinetics and spectroscopy in a shock tube.

ACKNOWLEDGMENTS

REFERENCES

1.   Gaydon, A.G.: "The spectroscopy of flames", Wiley, NY (1974).

2.   Herzberg, G.: "Molecular spectra and molecular structure – II. Spectra of diatomic molecules", Van Nostrand, NY (1950).

3. Sawada, T. and Kamada, H.: Bull. Chem. Soc. Japan, 43, 325 (1970).

4. Liszt, H.S. and Smith, W.H.: J. Quant. Spectrosc. Radiat. Transfer, 12, 947 (1972).

5. Bonczyk, P.A. and Shirley, J.A.: Comb. and Flame, 34, 253 (1979).

6. Fagerholm, E.: Ark. Mat. Astr. Fys., 27A, 1 (1940).

7. Gerö, L.: Z. Physik, 118, 27 (1941).

8. Klass, N.H. and Broida, H.P.: Astrophys. J., 123, 166 (1956).

9. Louge, M.Y., Hanson, R.K., Rea, E.C. and Booman, R.A.: J. Quant. Spectrosc. Radiat. Transfer, 32, 353 (1984).

10. Louge, M.Y. and Hanson, R.K.: 20th Symposium (International) on Combustion, The Combustion Institute, Pittsburgh, PA, in press.

11. Louge, M.Y.: Ph.D. Thesis, Stanford University, Stanford, CA (1984).

12. Kovacs, I.: "Rotational structure in the spectra of diatomic molecules", Elsevier, NY (1969).
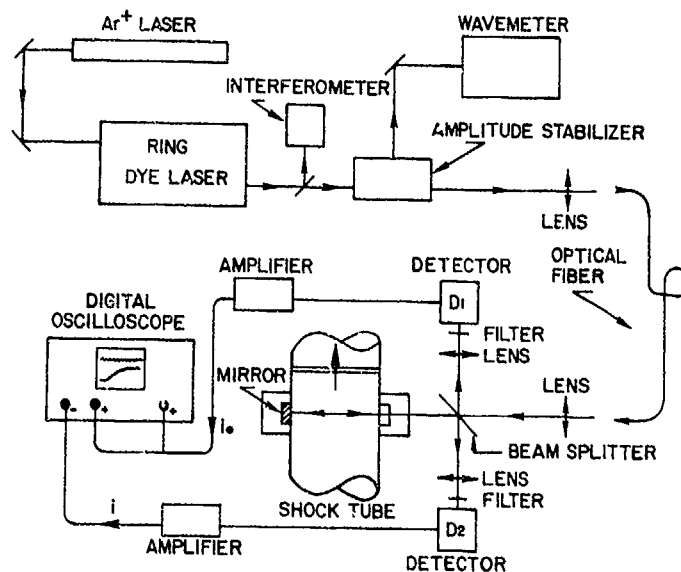
Fig. 1   Shock tube laser absorption diagnostic
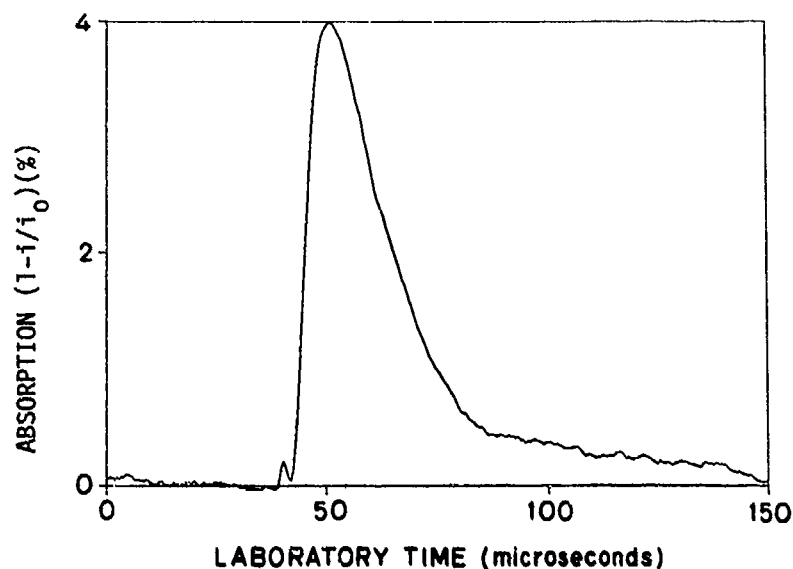
Fig. 2   A typical laser absorption $(1 - i/i_0)$ record at 431.133 nm, with the conditions T_2 = 2830°K, p_2 = 0.22 atm, ρ_{21} = 4.28, CH_4 = 4.95% dilute in argon. The initial spike results from a Schlieren effect, useful in defining the shock arrival time. The absorption level at late times is attributed to a small amount of soot formation.
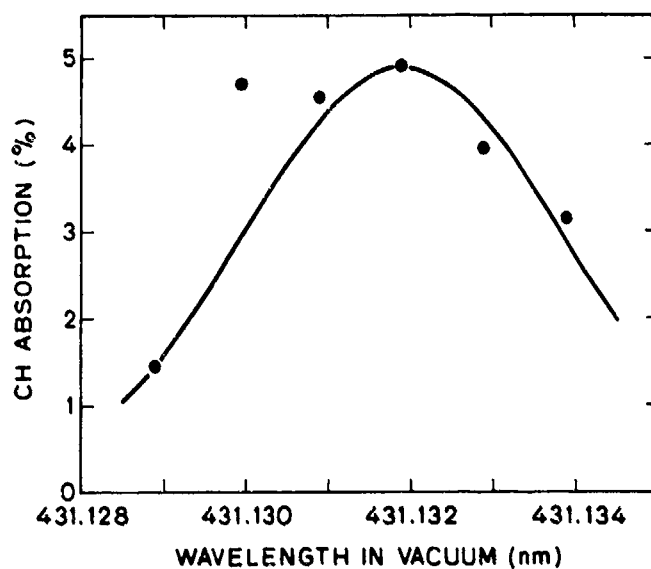
Fig. 3. CH absorption levels around 431.131 nm (vac.). The conditions are $T_2 = 2840 \pm 45°K$, $p_2 \simeq 0.22$ atm, $CH_4 = 4.95 \pm 0.15\%$ dilute in argon, path length L = 30.5 cm. The inconsistency of the experimental point at 431.130 nm may be attributed to a mode hop of the ring laser.
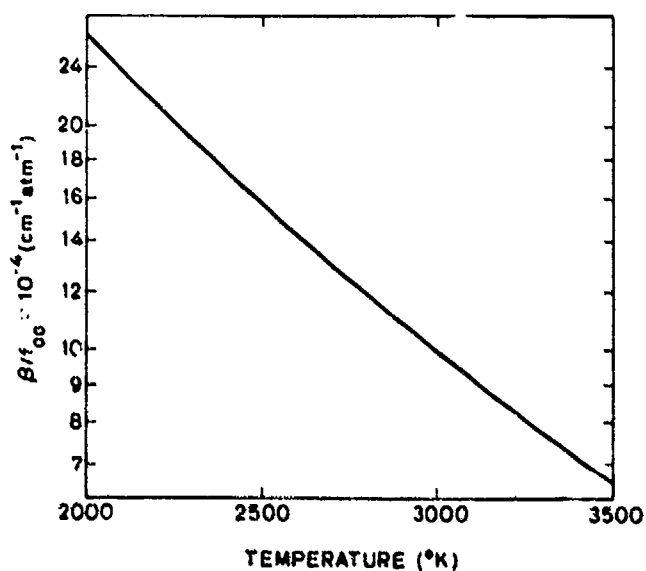
Fig. 4. Theoretical temperature dependence of the relative absorption coefficient of CH. The calculation is performed at the center of the superposed $Q_{1c}(7) + Q_{2d}(7)$ lines and assumes a Doppler-broadened line shape function.

STUDIES OF COLLISION-INDUCED EMISSION IN THE
FUNDAMENTAL VIBRATION-ROTATION BAND OF H_2[*]

G.E. Caledonia and R.H. Krech
Physical Sciences Inc., Andover, MA 01810

and

T. Wilkerson
Institute of Physical Science and Technology
University of Maryland, College Park, MD 20742

and

R.L. Taylor
CVD Inc., Woburn, MA 01810

and

G. Birnbaum
National Bureau of Standards, Washington, D.C. 20234

We present measurements of the collision induced
emission (CIE) from the fundamental vibration-rotation
band of H_2 taken over the temperature range of 900-
3000 K. The spectral shape and strength of this
infrared band centered about 2.4 μm has been measured
behind reflected shocks in mixtures of H_2/Ar. The
observed radiation at elevated temperatures is found
to be dominantly in the Q branch. The results have
been compared with theory. These comparisons show
that radiation at elevated temperatures is primarily
the result of an induced dipole moment in H_2 induced
by the overlap between the H_2 and Ar electron clouds
during collision. The strength of this interaction
has been evaluated by an analysis of the measured
temperature dependence of the absolute bandstrengths.

1. INTRODUCTION

This paper describes measurements and interpretation of collision induced
emission (CIE) in the fundamental vibration-rotation band of H_2 at elevated
temperatures and pressures using a high density, medium temperature shock tube
as the controlled lightsource. Although collision induction has been well
characterized in absorption at low temperatures,[1] <400 K, it has only
recently[2] been studied in emission. Collision induced processes give rise to
optical spectra for molecules which because of their symmetry do not have an
electric dipole moment in the electronic ground state. The collisions induce
a transient dipole resulting from interactions due both to permanent quadru-
pole moments and to the overlap of the molecular electron clouds. The induced
dipole moment gives rise to vibrational, rotational and translational transi-
tions.

The present study investigates the spectral shape and bandstrength of the
H_2 fundamental vibration-rotation band centered at 2.4 μm. We have studied
the band emission behind reflected shocks over the temperature range of

900-3000 K in H_2/Ar mixtures. Since the emission is collision induced, its intensity scales as the square of the density; measurements have been made over the density range of 10-50 amagats.

As described in the next two sections both the absolute intensity and the spectral band shape have been measured. The data have been interpreted in terms of a theory for CIE developed by Van Kranendonk and co-workers.[3,4] The measured and theoretical spectral shapes are compared in Section 4. The data have been used in conjunction with the theory to evaluate parameters describing the dipole induced in collisions between H_2 and Ar. These results are also presented in Section 4.

2. EXPERIMENTAL

The measurements have been performed in the Physical Sciences Inc. shock tube facility. This 6" diameter system has been described previously[2,5]. In brief, the stainless steel tube has a 6m long test section. Pressure was measured directly with a piezo-electric pressure transducer located at the optical port. Temperature was calculated from the shock velocity which was deduced from a temporal analysis of the responses from pressure transducers spaced at 50 cm intervals along the test section. The gases used were UHP grade, (99.999% purity) and the test section was evacuated down to 10^{-8} atm between runs to minimize impurities.

Spectrally resolved measurements were performed with an 0.5m Ebert, synchronized high speed scanning spectrometer[6] focussed into the center of the shock tube through sapphire windows located 5 cm from the end wall. This grating instrument utilized an InSb detector and was operated to scan 1.5 μm in <1 ms (a typical test time) with a resolution of 0.1 μm. The spectrometer was calibrated with a standard blackbody. The absolute calibration was cross-checked by measuring the radiation from the CO first overtone band which occurs in the same spectral region.[5] The test gas was also monitored with an absolutely calibrated narrow band radiometer consisting of an InSb detector and a 2.1-2.7 μm bandpass filter. This diagnostic provided both a monitor of uniformity during the test time, and a separate measurement of absolute in-band radiance.

Since the analysis hinges upon absolute spectral emission measurements the CO calibration provides a critical check on the data and its analysis. A typical measured CO overtone spectrum is shown in Figure 1, compared with a theoretical prediction. Since the theory for CO is well established the excellent agreement between data and theory demonstrates the systems ability to record spectral band shapes with high fidelity. The measured CO overtone bandstrengths were also in good agreement with expectations.[5]

Uniform test times (as defined by the pressure trace) of greater than 1 ms behind the reflected shock were routinely achieved. Measured shock pressures were always within a few percent of the ideal pressures, as determined from the Rankine-Hugoniot conservation equations using the measured incident shock velocity.[7] This velocity is typically measured to within an accuracy of 1%; the corresponding temperature is ±50 K.

Typically radiometer traces exhibited a reflected shock jump, followed by a slow increase, which levels off within 0.5 ms. This increase in radiation level was correlated with radiation that was emitted downstream of the observation window and reflected by the shock tube walls.[5] The spectrometer data

were corrected for this spurious additional signal arising from scattered light. The correction factor varied between 1.0 and 1.45, the value of 1.35 being typical.

3. DATA

Measurements were performed for reflected shock temperatures between 900 – 3000 K, typically in 20% H_2/80% Ar mixtures. The calibrated signal given in W/cm^2-sr-μm is converted into spectral emissivity by ratioing the signals to the blackbody function. A typical result is shown in Figure 2. As discussed in Section 4 the observed emission is primarily from Q branch transitions. Also shown is a measurement performed in pure argon under similar density/temperature conditions. Continuous background radiation was always observed in the clean argon shots. We corrected the CIE emission observation for this radiation although its origin was not identified.

In the absence of background radiation the reduced bandstrength can be deduced directly from the emissivity observations through the relationship

$$\alpha = (\bar{\nu} \ L \ \rho^2)^{-1} \int \epsilon_\nu \ d\nu \ , \tag{1}$$

where $\bar{\nu}$ is the band center frequency, 4160 cm^{-1}, L is the path length, 16.2 cm, and ρ is the gas density in amagats. Note that both H_2 and Ar are collision partners for vibrationally excited H_2. The definition of Equation (1) is specific to the gas mixture studied and would have to be corrected by the H_2 mole fraction to be compared with a pure gas reduced bandstrength, i.e., for an H_2/Ar mixture

$$\alpha = [H_2] \left(\alpha_{H_2,Ar}[Ar] + \alpha_{H_2,H_2}[H_2] \right) \tag{2}$$

where the brackets represent mole fraction and $\alpha_{H_2,Ar}$, α_{H_2,H_2} are pure gas reduced bandstrengths.

The emission data has been analyzed by means of Equation (1) to provide values of the reduced bandstrength, although the presence of the background radiation precludes a precise evaluation. Upper and lower limits of α have been deduced by either (1) assuming that all the emissivity within the band limits is due to CIE, or (2) that only that radiation above the average value on either side of the peaked region is due to CIE. The resulting evaluation is shown versus temperature in Figure 3 where the bars represent the upper and lower limits corresponding to the two assumptions described above, and the symbol represents our best estimate of the correct value.

The filled symbol corresponds to a measurement performed in a 10% H_2/90% Ar mixture which has been scaled by a factor of two. Measurements performed in 50% H_2/50% Ar mixtures exhibited higher background than the 20% H_2/80% Ar data and lower scaled reduced bandstrengths. This implies that H_2 is a less efficient collision partner than Ar, an observation borne out by the analysis provided in the next section.

The data point at T=300 K shown in Figure 3 has been evaluated from Equation (2) using earlier measurements of the pure gas reduced bandstrengths.[1] Note that the data exhibit an order of magnitude increase in the H_2 CIE bandstrength as temperature is increased from 300 to 3000 K. The implications of this variation are discussed below.

4. ANALYSIS

Van Kranendonk has developed a model to predict the bandstrength and shape of the H_2 CIE spectrum.[3,4] This model describes the transient dipole induced by the collision in terms of a long range induced component due to quadrupolar induction and a short range component resulting from charge deformation caused by the electron cloud overlap forces. The four parameters in this model are ξ and ρ which are respectively, the strength and range of the overlap portion of the induced moment, and η_1 and η_2 which are measures of the strength of the quadrupole interactions of the collision pair, namely η_1 is proportional to the product of the quadrupole transition matrix element of particle 1 and polarizability of particle 2.

The resulting expression for the reduced bandstrength of the H_2 CIE 0-1 band is

$$\alpha \approx \lambda^2 I \, \bar{\gamma} + (\mu_1^2 + \mu_2^2) J \, \bar{\gamma} \quad ; \quad cm^{-1}\text{-amagat}^{-2} \tag{3}$$

The quantities I and J are radial integrals for overlap and quadrupolar forces respectively.

$$I = 4\pi \int_0^\infty e^{-2(x-1)\sigma/\rho} g_0(x) x^2 dx \tag{4}$$

$$J = 12\pi \int_0^\infty x^{-8} g_0(x) x^2 dx \ , \tag{5}$$

where g_0 is the classical pair-distribution function

$$g_0 = \exp(-V^*(x)/T^*) \tag{6}$$

The potential V, intermolecular separation R, and temperature T are normalized, i.e.,

$V^* = V/\varepsilon$, $x = R/\sigma$ and $T^* = kT/\varepsilon$, where σ and ε are respectively range and energy parameters, we use here the Lennard-Jones potential

$$V(R) = 4\varepsilon \left[(\sigma/R)^{12} - (\sigma/R)^6 \right] \tag{7}$$

where $\varepsilon/k = 66.6$ K and $\sigma = 3.17$Å.[3]

The remaining quantities in Expression (3), λ, μ, and $\bar{\gamma}$ are defined in terms of the above parameters, as described in Reference 3.

In general information is available on the quadrupolar interaction. Thus this spherical theory can be used in conjunction with measured bandstrengths to evaluate the parameters describing the overlap interaction. For the case of H_2-Ar, we have used a recent evaluation of the H_2 quadrupole moment function[8] to determine that at room temperature ≈43% of the measured H_2-Ar[1] bandstrength of 9.2×10^{-7} amagat^{-2}-cm^{-1} is due to the quadrupole interaction. The quadrupolar contribution produces Q, O, and S branch transitions whereas

the overlap induced moment provides only Q branch transitions and thus the relative contributions of the two can be discerned by analyzing the band shape.

The quantity $\lambda^2 I \bar{\gamma}$ for H$_2$-Ar is evaluated to be 5.3×10^{-7} amagat^{-2} cm^{-1} at T=300 K. In the past a value for the parameter ρ/σ has been assumed to obtain λ. For example, in Reference 3 the quantity ρ/σ for H$_2$/Ar collisions was assumed to be 0.145 in analogy with the case for H$_2$-H$_2$ collisions. Since the integral I is a function of temperature, the present data can be used to evaluate these two quantities independently.

Predicted values for reduced bandstrengths, assuming Ar to be the collision partner, are shown in Figure 3 for several choices of the parameter ρ/σ. These values have been scaled to the room temperature value of the 20% H$_2$/80% Ar mix. As can be seen the choice of ρ/σ = 0.145 provides for a much weaker temperature dependence than observed. A value ρ/σ = 0.08 appears to be most appropriate. This would correspond to a value of λ^2 = 9.5×10^{-5} for α_{H_2-Ar}. This analysis is approximate inasmuch as the observed radiation is due in part to the H$_2$ collision partner. Nonetheless $\alpha_{H_2-H_2}$ is less than α_{H_2-Ar} at room temperature and is predicted to exhibit a weaker temperature dependence. Thus the observed radiation is deduced to be due predominantly to collisions between hydrogen and argon. Note further that the quadrupole induced moment is predicted to vary only weakly with temperature. Thus the increase in bandstrength with temperature is primarily the result of overlap induction. This is in accord with the observation of dominantly Q branch emission.

This analysis represents the first evaluation of the reduced range of the overlap induced moment, ρ/σ, from measurements at elevated temperatures. McTaggart and Welsh[9] performed a detailed analysis of the spectral shape of H$_2$-Ar fundamental absorption band over the temperature range of 77-300 K. From an analysis of the intercollisional interference dip, a phenomenon not studied in the present work, they estimated that ρ/σ~0.08 in good agreement with our results.

We have used these parameters to predict the spectral shape of the band at elevated temperatures. The synthetic spectrum was evaluated on a line-by-line, including all branches and hot band transitions (V>1). A realistic line shape function was incorporated[10] and the result convoluted over the instrument slit function. Such a prediction is shown in Figure 2 and can be seen to be in good agreement with the data, providing further confidence in our analysis.

REFERENCES

1. Welsh, H.L., "International Reviews of Science, Physical Chemistry, Vol. 3: Spectroscopy," Butterworths, London 1972, Chap. 2, pp. 33-17.

2. Krech, R., Caledonia, G. Schertzer, S., Ritter, K, Wilkerson, T., Cotnoir, L., Taylor, R. and Birnbaum, G., Phys. Rev. Lett. 49, 1913(1982).

3. Van Kranendonk, J., Physica (Utrecht) 23, 825(1957) and 24, 347(1958), and Can. J. Phys. 46, 1173 (1968).

4. Van Kranendonk, J. and Kiss, J.Z., Can. J. Phys. 37, 1187 (1959).

5. Caledonia, G.E., Krech, R.H. and Wilkerson, T., "Measurements of the CO First Overtone bandstrength at Elevated Temperatures," accepted for publication, J. Quant. Spectrosc. Rad. Transfer, 1985.

6. Camm, J.C., Taylor, R.L. and Lynch, R. Appl. Opt. 6, 885 (1967).

7. Green, E.F. and Toennies, J.P., "Chemical Reaction in Shock Waves," Arnold, London, 1964.

8. Poll, J.D. and Wolniewicz, L.J. Chem. Phys. 68, 3053 (1977).

9. MacTaggart, J.W. and Welsh, H.L., Can. J. Phys. 51, 158 (1973).

10. Levine, H. B. and Birnbaum, G., Phys. Rev. 154, 86 (1976).
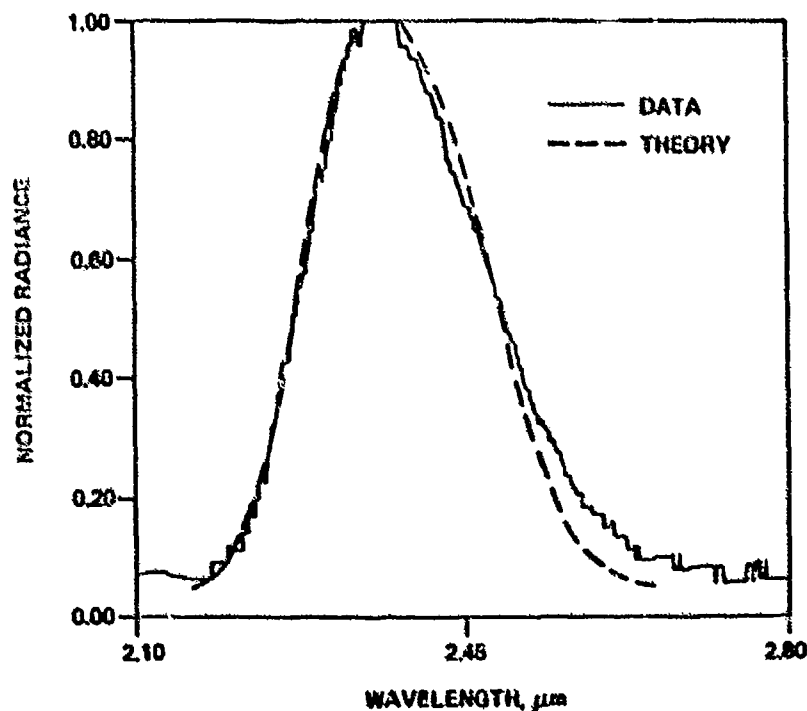
Figure 1. Observed CO First Overtone Compared with Synthetic Spectra.
T = 2650K, ρ = 7.4 Amagat.
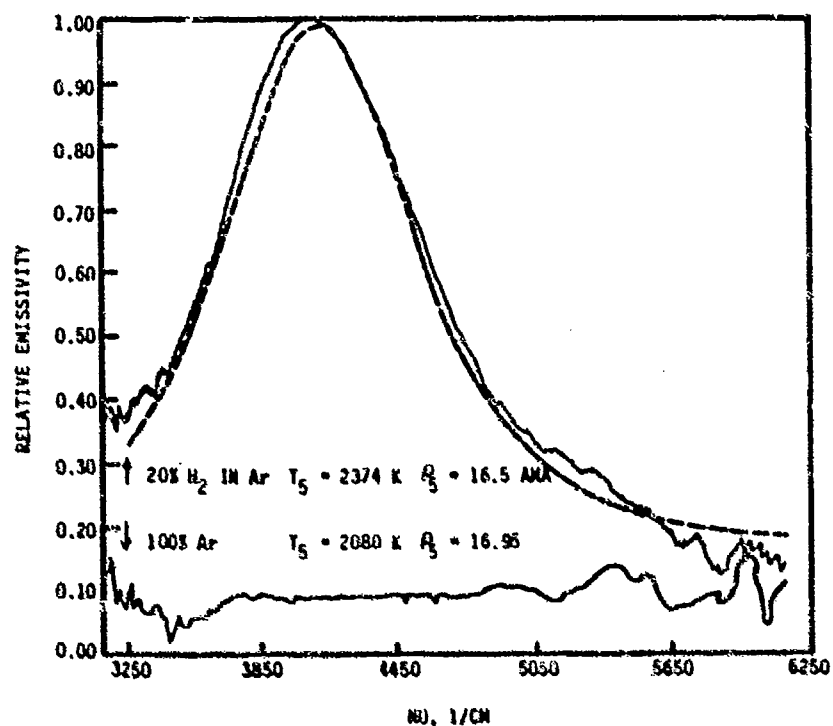
Figure 2. Relative Emissivity of the Fundamental CIE Vibration-Rotation Band of H₂ Contrasted to Typical Background Measurement in Pure Argon. Conditions as shown. --- Synthetic Spectrum of H₂ CIE Band.
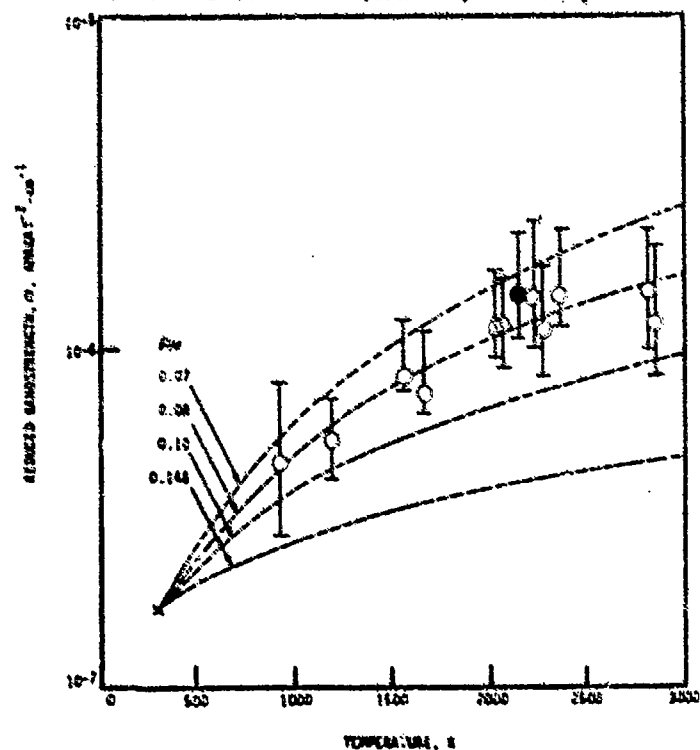
Figure 3. Measured H₂ CIE Fundamental Vibration-Rotation Band Bandstrength Versus Temperature. Specific to 20% H₂/80% Ar Mixture. --- Predicted Bandstrength for Various Values of the Reduced Range.

DEVELOPMENT AND CONTROL OF LASER SUSTAINED ABSORPTION WAVES

M. Onorato, D. Tordella, M. Cantello*, L. Garifo**, F. Pandarese**

Dipartimento Ingegneria Aeronautica e Spaziale Politecnico di Torino
C. Duca degli Abruzzi, 24 - 10129 Torino - Italia

* R.T.M. - Vico Canavese - Torino
** C.I.S.E. - Segrate - Milano

The energy coupling between a laser beam and a metal target
is strongly influenced by the presence of plasma above the
target, that may propagate toward the incident beam as an
absorption wave. This paper deals with the control of this
plasma and its aim is to show how the absorption waves
development and propagation are affected by gas jets and by
the pressure of the external ambient and to show how the
energy transmitted to the target is influenced by the plasma
behaviour.
Results from high speed photography and from measurements of
energy absorbed by the target and of backscatterd 10.6 μ m
radiation are presented.

1. INTRODUCTION

Since the early 1970, with the development of multikilowatt CO_2 lasers, the
potential of using laser beams for material processing was clearly recognized and
actively pursued. In view of this application, the interaction of CO_2 high power
laser beams with a target material has been a subject of intensive studies during
the past few years (References 1÷24).

As a consequence of the material heating by the laser radiation, the surface
starts to emit vapor that expands away from the target. The properties of the
developing flow depend on the initial conditions of the emitted vapor, that in
turn depend, for a given material, on laser intensity and ambient pressure. Due
to the presence of free electrons, the emitted vapor starts to absorb the
incident radiation by inverse bremsstrahlung and, if the heating rate by this
process exceeds the rate of cooling by gasdynamic expansions and by other possi-
ble cooling mechanisms, the flow temperature will rise and a plasma will develop
in the vapor above the metal and next in the surrounding ambient. The plasma
ignition threshold radiation intensity, Io, is about 10^4 W/cm^2, at atmospheric
external air pressure. Once ignited, this plasma propagates at subsonic velocity
(if Io $< 10^7$ W/cm^2) along the laser beam, as an absorbing wave, until some mainte-
nance conditions are reached at a distance from the target where losses of energy
by radiation, thermal conductivity and convection are offset by the power absorb-
ed from the incident laser beam. This wave, after remaining for a certain time at
its maximum distance of propagation from the interaction point, becomes extin-
guished and a new one originates from the target and develps. The frequency of

this repetitive phenomenon, the dimension of the waves, the maximum propagation length from the target depend on many causes. These are the target material and its motion, the intensity of the incident laser beam, its spatial distribution and temporal dependence, the focussing system and the conditions of the external environment.

For an incident radiation power of about 10kW, the electron number density (n_e/cm^3) may range from 10^{16} in the external boundaries of the wave to $2\ 10^{17}$ in its core, the corresponding electron temperature ranges from 10,000 K to 17,000 K and the corresponding plasma absorption coefficient ranges from 0.1 cm^{-1} to 0.7 cm^{-1} (Ref. 5).

The energy coupling between the laser beam and the target material is clearly strongly dominated by the presence of these absorption waves and by their behaviour; mainly four effects must be expected:
- the incident laser beam is strongly absorbed and backscattered by the plasma;
- the incident laser intensity at the focus is lowered by blooming, due to the fact the beam propagates through a field where a very large electron density gradient is present;
- the plasma reradiates in the direction of the target energy at much shorter wavelengths, that is more efficiently absorbed by a metal target;
- the plasma transmits energy to the target by direct conduction.

As a consequence of these effects the development of laser supported absorption waves can be at the same time detrimental and beneficial for the energy coupling between the laser beam and the metal. The efficiency of this coupling depends strongly on the frequence of the wave emissions, on the plasma dimension and on the maximum propagation distance from the target. Therefore, a suitable control of the plasma above the target is of a great importance in order to increase the efficiency of the energy transfer to the material.

Moreover, in some applications, as in deep welding, where highly focused high power laser beams are needed, it is required that the laser energy were transmitted into the metal in a very narrow region down below the beam-target interaction point. This requirement makes even more important the plasma control operation.

This paper deals with plasma control and its aim is to show how the plasma development and propagation are affected by gas jets, and by the physical properties and pressure of the external ambient and to show how consequently the energy transmitted to the target is influenced by the plasma behaviour.

2. EXPERIMENTS AND RESULTS

In order to study the plasma behaviour and the consequent energy coupling between the radiation and the metal, the following measurements were carried out:
- plasma motion by high-speed photography,
- 10.6 μm radiation backscattered by the target and by the volume above the interaction point,
- energy absorbed by the target.

Details of the measurement techniques are reported in References 15÷18.

Two lasers were used for the experiments, a 15 kW AVCO HPL continuous wave CO_2 laser equipped with a f/7 focussing telescope and a 2.5 kW Spectra-Physics continuous wave CO_2 laser equipped with a f/4 focussing lens. The spot diameters

of the two laser beams at the focus are respectively 0.7 mm and 0.5 mm.

The results that will be here shown refer to stainless steel AISI 304 targets, kept in motion at speed of few meters per minute, as during the process of welding.

The influence of a lateral jet stream of different gases, at different dynamical pressures, on the laser induced plasma will be first analyzed.

In figures 1÷5 pictures selected from the high speed films are reported. These pictures show absorption waves at the maximum propagation distance, D, from the target surface, for an incident radiation power of $P = 10$ kW. In the figures the flowing gas and its dynamical pressure, q, are indicated. Fig. 1 refers to the case in absence of lateral jet stream. The averaged plasma life time is estimated to be, in this case, about 5 ms and the maximum propagation lenght, D, is about 30 mm. The distance D is measured from the leading edge of the wave. The influence of the air stream on the interaction region is evident from figures 2, 3 and 4. The luminous vapor emitted by the metal is entrained by the flowing gas, on the contrary the absorption wave continues to propagate in the direction of the incident beam. Both the maximum propagation lenght and the wave averaged life time, become shorter in comparison to the case of Fig. 1. This effect is more pronunced at increasing values of the dynamical pressure of the air jet.
For $q>80$ N/m^2 no propagation of the plasma from the metal is observed.

The main influence of the transverse air flow on the evolution of the absorption wave is probably due to the fact that the wave propagates initially more easily into the vapor emitted from the metal than in surrounding air. This is true at least for the experimental conditions of the present results. As a consequence, the removal of the metal vapor by the flowing air inhibits the absorption wave to propagate away far the target. Besides this influence, the wave motion and life time are affected by transverse flows because of two other causes: removal of heat by convection and introduction of disturbances that may influence the stability of the plasma.

For the case of gas Helium, two more additional causes must be taken into account to explain its strong influence on the generation and evolution of absorption waves: the very high value of the ionization potential and the very high value of the thermal conductivity in comparison with those of the Air. As a result of these properties, even at the lower value of the dynamical pressure, 8 N/m^2, no waves propagation is observed (Fig. 5), as in the case of air flow at high velocity.

In Table I some results of the measurements of the total energy absorbed by the target are reported; α is the ratio between absorbed and incident power.

TABLE I

Beam-power kW	gas	q N/m^2	α
10	Air	0	0.15
10	Air	8	0.65
10	Air	80	0.81
10	Helium	8	0.95
10	Helium	80	0.74

In absence of lateral jet stream the laser-matter energy coupling is very poor. For low values of the dynamical pressure, the Helium permits a more efficient energy coupling. This result well correlates with Fig. 5, where it is shown that the absorption wave does not propagate away from the target surface in presence of Helium. For the high value of q, on the contrary, a better energy coupling is obtained with a lateral jet flow of Air. This is due to the fact that the Helium, even if it keeps the plasma on the metal surface, produces an excessive cooling effect on the interaction region.

Observing the shapes of the melted bead cross sections, same results are obtained. As an example, in Fig. 6 bead cross sections for the case in absence of transverse flow and for the case of Helium flowing at $q = 8$ N/m^2 are compared. Clearly, keeping the plasma on the target surface, a narrow and deeper penetration is obtained.

The efficiency of the energy coupling between the laser beam and the target may be also verified observing the 10.6 µm radiation backscattered from the interaction region. In figures 7 and 8 time averaged spatial distributions of power per unit solid angle, PΩ, are reported for $q = 0$ and for the case of Helium flowing at $q = 8$ N/m^2. Assuming cilyndrical symmetry respect to the laser beam axis, the total backscattered 10.6 µm power may be easily calculated by integration. The result is that for the case of Fig. 7 the total power backscattered is about five times higher than for the case of Fig. 8.

Now some preliminary results, obtained controlling the plasma by lowering the ambient pressure, p, above the target, will be shown. Experiments have been performed in the low range of the incident power, keeping the target in a vacuum chamber and using the Spectra-Physics laser opereted at $P = 2$ kW. The target speed is about 1.5 m/min. The pictures in figures 9a and 9b refer to the case of interaction in ambient pressure of 760 Torr, with the chamber filled respectively of Air (Fig. 9a) and Helium (Fig. 9b). Due to the low power of the incident radiation the plasma does not propagate away from the target. In the case of Fig. 9a a luminous plume is visible above the plasma. This plume appears, from the film, to be very unstable and probably it is produced by the combustion of emitted material from the metal. Looking at the melted bead cross sections, it seams that this plume does not influence appreciably the energy transmitted to the target. In both cases the melted bead shows the same configuration characterized by the cup shape (Fig. 10), due to the presence of the plasma. The effect of lowering the external pressure is shown in Fig. 9c, where no plasma is present above the metal; only a luminous spot is visible in correspondence of the hole. The picture refers to the case of an external pressure equal to 76 Torr. Probably, in this case, as a consequence of the low external pressure, the vapor emitted by the metal expands very rapidly, reaching low temperature and density, such that it becomes transparent to the radiation. From Fig. 11 it appears that, in this case, the melted bead cross section shows a very narrow shape and a very deep penetration.

3. COMMENTS AND CONCLUSIONS

Results have been given showing how the efficiency of the energy coupling between the laser radiation and a metal is influenced by the development and propagation of laser sustained absorption waves.

It has been shown how the wave dimension and evolution is controlled by lateral jet streams at different dynamical pressure, and the distinct behaviour of Air and He, as flowing gases, has been pointed out.

For the test at 10 kW incident power the highest energy coupling has been obtained for the case of Helium flowing at $q = 8$ N/m^2, when the plasma does not propagate away from the target.

Preliminary results have been reported showing the effect of the external pressure on the interaction phenomena. In the low power range (P = 2 kW) of the incident laser beam and at an external pressure of one tenth of an atmosphere, plasma development has not been observed above the target. It seems that in this conditions the plasma is confined into the key-hole. In this case the penetration shape is very narrow and deep.

Due to the high refractivity of metals to the 10.6 μm radiation, certainly the production of plasma during the interaction is useful to enhance the energy coupling. Moreover, when the plasma propagates away far from the metal its shelding character dominates and the energy coupling becomes poor.

REFERENCES

1. Y.P. Raizer, "Subsonic Propagation of a Light Spark and Threshold Condition for the Maintenance of a Plasma by Radiation" - Soviet Physics JEPT, vol.31, n. 6 (1970)

2. E.L. Klostermann, "Measurements of Subsonic Laser Absorption Wave Propagation Characteristics at 10.6 μm - J. Appl. Phys., vol. 45, n. 11 (1974)

3. E.L. Klosterman, "Experimental Investigation of Subsonic Laser Absorption Wave Initiation from Metal Targets at 5 and 10.6 μm" - MSNW-75-123-2, Math. Sci. Northwest Rept., Seattle (Washington) (1975)

4. A.N. Pirri, "Analytic Solutions for Laser-Supported Combustion Wave Ignition above Surface" - AIAA J., vol. 15, n. 1 (1977)

5. M.C. Fowler & D.C. Smith, "Ignition and Maintenance of Subsonic Plasma Waves in Atmospheric Pressure Air by CWCO$_2$ Laser Radiation and Their Effects on Laser Beam Propagation" - J. Appl. Phys., vol. 46, n. 1 (1975)

6. P.D. Thomas, "Laser Absorption Wave Formation" - AIAA J., vol. 18, n. 10 (1975)

7. C.J. Knight, "Theoretical Modeling of Rapid Surface Vaporization with Back Pressure" - AIAA J., vol. 17, n. 5 (1979)

8. R.G. Root, "Laser Interaction: Thermal and Mechanical Coupling to Targets" - 3rd Int. Symp. on Gas Flow and Chem. Lasers, Marseille (1980)

9. M. Germano & M.S. Oggiano, "Gasdinamica dei prodotti di vaporizzazione super- ficiale dovuta ad intensa radiazione termica" - IV Congresso Naz. AIDAA, Roma (1981)

10. G. Herziger, "Laser Material Processing" - 4th G.C.L. Int. Symp. on Gas Flow and Chem. Lasers, Stresa (1982)

11. N. Cantello, R. Nenin, V. Donati, L. Garifo, A.V. LaRocca, M. Onorato, "Flu-

id-Dynamical Aspects of Laser-Metal Interaction" - 13th Int. Symp. on Shock Tubes and Waves, Niagara Falls (1981)

12. J.A. Woodroffe, "Pulsed Laser-Material Interactions" - 4th G.C.L. Int. Symp. on Gas Flow and Chem. Lasers, Stresa (1982)

13. J.F. Ready, "Material Processing - An Overview" - Proc. IEEE, Vol. 70, n. 6 (1982)

14. A. Matsunanawa, S. Katayama, T. Tokumuta, T. Ariyasu, "Characteristics of Plume Induced by Pulsed Nd:YAG Laser Irradiation and their Effects on Material Processing" - 3rd Int. Coll. on Welding and Melting by Electrons and Laser Beam", Lyon (1983)

15. M. Cantello, V. Donati, L. Garifo, R. Menin, F. Pandarese, A.V. LaRocca, M. Onorato, P. Savorelli, "On the Interaction of High-Power Laser Beam with Metal Targets" - 4th G.C.L. Int. Symp. on Gas Flow and Chemical Lasers, Stresa (1982)

16. V. Donati, L. Garifo, R. Menin, F. Pandarese, M. Onorato, P. Savorelli, "Analysis of High Power CO_2 Laser-Material Interaction Results with High Speed Photography and 10.6 μm Absorption Measurements" - 2nd Int. Cong. on Applications of Lasers in Material Processing, Los Angeles (1983)

17. V. Donati, L. Garifo, F. Pandarese, A.V. LaRocca, M. Cantello, M. Onorato, P. Savorelli, "Effects of Lateral Wind on the Development of Absorption Waves During Laser-Matter Interaction" - 14th Int. Symp. on Shock Tubes and Waves, Sydney (1983)

18. V. Donati, L. Garifo, R. Menin, F. Pandarese, M. Onorato, P. Savorelli, M. Cantello, A.V. LaRocca, "On the Development of Absorption Waves During the Laser-Metal Interaction" - 3rd Int. Coll. on Welding and Melting by Electrons and Laser Beam, Lyon (1983)

19. Y. Arata, N. Abe, T. Oda, "Beam Hole Behaviour During Laser Beam Welding" - L.I.A., Vol. 38, ICALEO (1983)

20. G.L. Petrov, V.V. Bashenko, E.A. Mitkevich, V.A. Lopote, "Peculiarities of Heat and Mass Transfer in Welding Using High Energy Density Power Sources" - 3rd Int. Coll. an Welding and Melting by Electrons and Laser Beam, Lyon (1983)

21. R.S. Arnot, C.E. Albeight, "Plasma Plume Effects in Pulsed Carbon Dioxide Laser Spot Welding" - L.I.A., Vol. 38, ICALEO (1983)

22. R.D. Dixon, G.K. Lewis, "The Influence of a Plasma During Laser Welding" - L.I.A., Vol. 38, ICALEO (1983)

23. V. Donati, L. Garifo, F. Pandarese, M. Onorato, P. Savorelli, A.V. LaRocca, M. Cantello, "On the Ignition of Laser Supported Waves from Solid Targets by $CWCO_2$ Laser Radiation" - AIAA paper n. 84-1573, (1984)

24. Y. Arata, N. Abe, T. Oda, "Fundamental Phenomena in Laser Welding" - 5th G.C.L. Int. Symp. on Gas Flow and Chemical Lasers, Oxford (1984)

Figures 1—5. Laser supported absorption waves. P = 10 kW; 1. Air q = 0;
2. Air q = 8 N/m^2; 3. Air q = 40 N/m^2; 4. Air q = 80 N/m^2; 5. He q = 8 N/m^2
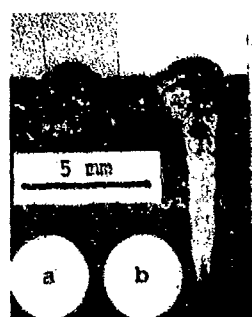
Figure 6. Bead
cross sections.
P = 10 kW;
a. Air q = 0;
b. He q = 8 N/m^2
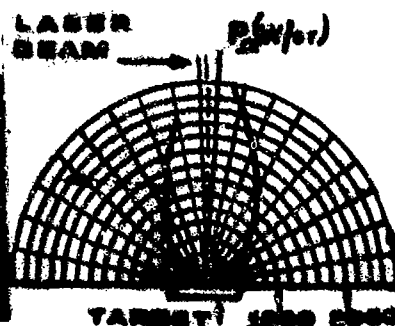
Figure 7. Backscattered
10.6 μm power.
P = 10 kW
Air q = 0
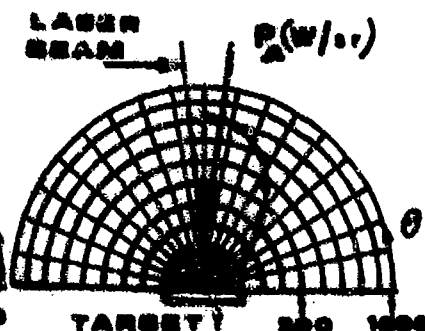
Figure 8. Backscattered
10.6 μm power.
P = 10 kW
He q = 8 N/m^2
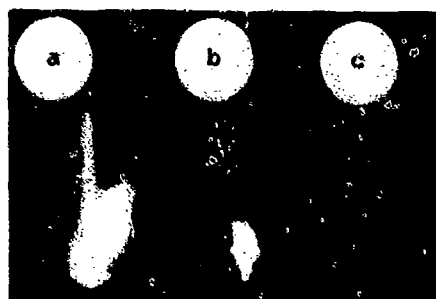
Figure 9. Plasma behaviour in
controlled external ambient.
P = 2 kW
a. Air p = 760 Torr;
b. He p = 760 Torr;
c. Air p = 76 Torr.
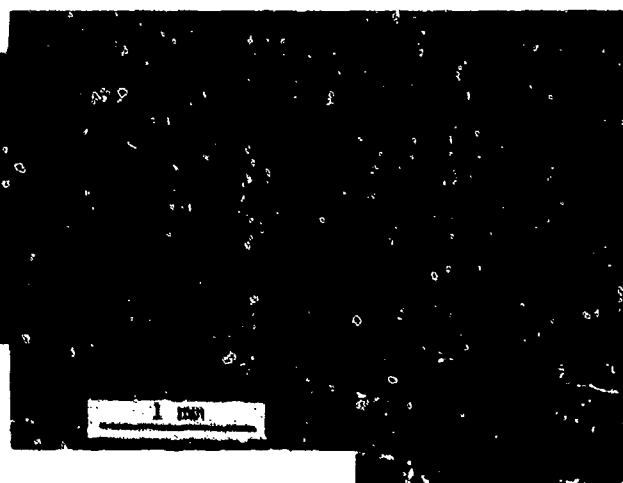
Figure 10. Bead cross section.
P = 2 kW;
Air p = 760 Torr.

Figure 11. Bead cross
section.
P = 2 kW;
Air p = 76 Torr.

WAVE BEHAVIOUR IN A HIGH AVERAGE POWER

EXCIMER LASER[*]

M.L. Sentis, B.L. Fontaine and B.M. Forestier

Institut de Mécanique des Fluides de Marseille, UA 03 CNRS
1, rue Honnorat, 13003 MARSEILLE (France)

An E-beam or X-rays preionised high purity construction low
turbulence level closed cycle flow rare gas halide laser
called LUX has been developed to study laser characteristics
at high pulse repetition frequency. Experimental results
obtained on laser energy, discharge stability and acoustic
waves behaviour with this test-bed are presented. With
X-rays preionisation an average laser power of 150 Watts in
60 ns pulses (FWHM) at 1 KHz has been achieved in burst mode
(50 pulses) with LUX at λ = 308 nm from a 70 cm^3 active volume,
2,3 atmospheres pressure Ne/Xe/HCl mixture for a flow
speed of 50 m/s . The laser efficiency was greater than 1 %.
It is shown that excimer laser average power at high PRF
($\geqslant$1Khz) is much more strongly dependent of gas mixture, elec-
trical excitation parameters and flow characteristics than energy
per pulse at low PRF. This dependence is attributed to
variation of stable discharge time duration with modifica-
tion of these parameters.

1. INTRODUCTION

Potential applications such as semi-conductor processing, isotope
separation and long range communications have recently stimulated considerable
interest in the scaling up of UV and visible wavelength excimer discharge
lasers to high output energy pulse rate frequency (PRF), and average power
($\bar{P}_L \simeq$ 0,1 - 1 Kw)[1]. However, for further development of these systems,
numerous problems remain to be solved. Among the most important of these pro-
blems related to fluid mechanics and acoustic are :

- laser discharge stability, noticeably when long pulse large volume and high
PRF are considered,

- schemes well fitted to efficiently deposit, very rapidly and at very high
PRF the needed high specific excitation power and energy,

- laser medium homogeneity ; the time necessary to recover flow homogeneity
has for consequence a strong lowering of laser beam quality and energy per
pulse at high PRF.

Low density electron beam and X-rays preionisation schemes proposed and
recently demonstrated (2) (3) represent a very promising alternative to
the well developed UV preionisation scheme for many applications requiring
high energy per pulse and high PRF. Advantages of these new preionisation
schemes mainly consist in the possibility to preionise homogeneously a large
volume of high pressure laser mixture at high PRF and to maintain a stable
discharge during several hundred of nanoseconds for long pulse laser operation[1]

Little experimental work has however been fulfilled up to now on the flow and
acoustic behaviour of such high PRF excimer laser systems and in particular
for the case of the very promising XeCl system[4][5]. Moreover, it has been
shown that average laser power saturates and then decreases at PRF as low as a
few hundred hertz at constant pulsed input electrical excitation[5][6][7][8].

A programme has been undertaken at IMFM on the study of high repetition rate
($\geq$1 KHz), long pulse (50-100 ns) avalanche discharge excimer laser preionised
by either a low density E-beam or low density X-rays. A test-bed called LUX
has been constructed. The laser system which is most studied is the XeCl system
(λ= 308 nm) with Ne as diluant gas. The IMFM programme includes an experimental
investigation with the LUX test-bed of base-line cavity flow[9], strong
disturbances induced in the active medium, optimum excitation and flow con-
ditions of LUX[10][11]. This programme also comprises numerical modelling of
the laser plasma time behaviour and flow behaviour[12] for various condi-
tions.

In the present paper, most recent experimental results obtained at IMFM related
to flow and acoustic waves effects on laser characteristics in a fast flow
closed loop high pulse rate frequency X-rays preionised discharge XeCl laser
with Ne diluant are presented and discussed.

2. LUX TEST-BED

The LUX test-bed mainly comprises a fast flow subsonic closed cycle wind tunnel
and a high average power electrical excitation system.

The 170 liters volume stainless steel loop already described elsewhere[9][10] has
 been designed to achieve long "life time" of the working mixture, very low
base-line flow turbulence level and low pressure drop. Provision has been made
for fast damping of acoustic waves. A centrifugal compressor powered by a 4 KW
continuous current motor allows an average flow velocity up to 80 m/s in the
laser discharge head (2.5 x 30 cm^2 cross section).

An experimental study of LUX system base-flow characteristics (without electri-
cal excitation) has shown that the flow velocity field is constant within $\pm$ 1%
outside boundary layers and that the turbulence intensity (RMS) is equal to
10^{-3}. Density variations outside boundary layers for U = 80 ms^{-1} as measured
by Michelson interferometry are inferior to the $\Delta\delta /\delta = \pm 2,5.10^{-4}$ measurement
uncertainty (air, 1 atmosphere).

The electrical excitation system consists in a 100 KW average power pulser
allowing active medium preionisation by either E-beam or X-rays and excitation
by the main discharge both with 1.5 KHz PRF in burst mode (50 pulses)[9][10].
The preionisation is produced by a cold cathode gun with 3 x23 cm^2 surface win-
dow controlled by a lead mask. The gun is driven by a 200 KV fast pulse
transformer type pulser energised by use of a 50 KJ - 15 KV storage capacitor
bank [9]. In the X-rays mode the system allows to evenly deposit into active
medium, through a 0.6 mm thick aluminium window, an X-rays dose up to 50 mrad by
shot in a 300 ns duration pulse at a PRF up to 1500 Hz with good reproducti-
bility and a low jitter. The X-rays beam is very uniform and the window has a
long life time.

The main discharge circuit is energised by a 50 KJ - 16 KV storage bank which
charges a main capacitor Cp through a resonant circuit and a diode (resonant
charging). The discharge of the C-L-C type [10] is controlled by either a

triggered hydrogen filled spark gap or an hollow anode high power ceramic thyratron (E.E.V. CX 1572).Typically, the main discharge delivers 2-20 joules of electrical energy to the active medium at a voltage up to 30 KV. The fig. 1 shows a scheme of the $C - L - C$ transfer type circuit which has been used.

The dielectric laser head of low inductance ($L \simeq 15$ nh) allows a useful volume up to 150 cm3. The very low inductance of the laser head is reached by use of two rows of 6 current returns set symmetrically backward and forward of the electrodes and separated by 10 cm. The present volume controlled by electrodes width and lead mask on gun window is 23 x 1,5 x 2,2 cm3 for Ne/Xe/HCl mixture. The main discharge system permits a PRF of 1.5 KHz with very good reproductibility of electric characteristics and very low jitter for discharge self triggering. The discharge current is $I_D \simeq$ 30 000 A in 50 ns FWHM pulse for V_p = 26 KV.

The laser cavity is of the stable type with long radius mirrors (R_{cc} = 2 m).

The multicoated electric quartz mirrors are set directly in the laser head side walls. Laser energy is extracted through a 50 % transmission mirror.

3. EXPERIMENTAL RESULTS ON LUX HIGH AVERAGE POWER AND HIGH PRF XeCl LASER

The following experimental studies related to high average power and high PRF XeCl laser have been fulfilled with LUX test-bed :

- laser energy per pulse at low repetition rate
- discharge electrical parameters time variation during a pulse and comparison with numerical results from IMFM circuit modelling programme
- time integrated energy input spatial variations by use of side photographs of discharge
- density field time behaviour in laser cavity by use of Michelson interfero-metry
- second pulse laser power and energy v.s. delay after first pulse in double pulse experiments for various flow speeds
- effect of working mixture composition, PRF and flow speed repetition rate on laser energy per pulse and average laser power in bursts of 50 pulses.

For all the experiments reported here, working mixture is Ne/XeHCl at a pressure of 1 or 2,3 atmospheres and the electrical parameters are those reported on fig. 1.

Laser energy dependence with main capacitor voltage Vp for a given set of conditions and two typical gas mixtures (P = 2,3 atm) in the case of low PRF is shown on fig. 2. It has been possible to obtain a laser energy per pulse Wl = 290 mJ for a useful volume of 70 cm3. For these conditions of excitation comparison between experimental and calculated values of electrical and laser pulse time history is given on fig. 3 for Vp = 27,5 KV. The model developed at I.M. F.M. takes into account the various components of electrical circuit and time variations of load impedance due to laser plasma kinetics. Numerical simulation shows that only 60 % of the electrical input is useful for lasing (i.e. is added before end of lasing), indicating that present excitation system is not very well fitted to reduce extra-energy addition to the flow at high PRF ; this extra energy strongly increases active medium disturbance for a given extracted laser energy during the first shot and then limits laser average power

Typical snapshot interferograms at various time delays after excitation for single pulse conditions are presented on fig. 4. Ne/Xe/HCl 5300/190/10 mixture at P = 1 atm is used and flow speed is 50 m/s. Calculated absorbed energy is Wel = 38 J/l. Various phases of density modifications and flow clearing are clearly visible on the interferograms. Noticeably, on photograph taken at

$\Delta t = 37$ µs, shock and expansion waves induced by energy deposition are clearly visible. These waves are progressively blown down and at $\Delta t = 1$ ms, density homogeneity inside laser cavity is sufficient to allow a new laser excitation. The density time histories at cavity center for flow and no flow conditions are shown on fig.5 for pure neon. A comparison of measured density profiles with those deduced from a numerical model developed at IMFM[12] shows that experimental density profiles are smoother than numerical ones. This difference is attributed to dissipative processes across entropy surfaces which are not taken into account in the model.

Laser energy of a second pulse v.s. repetition rate is shown on fig. 6 for different values of flow speed in laser cavity for typical conditions. These results confirm those of the interferometric study and numerical modelling in the simple case of a double excitation (no resonance). For 1 KHz PRF and $U = 44$ ms^{-1}, flow speed is not the limitation of the laser energy per pulse.

Pulse to pulse laser energy variation during a burst for Ne/Xe/HCℓ 5300/50/10, $P = 2,3$ atm, $V_p = 26$ KV, is presented on fig. 7a. This record is obtained by means of laser power signal time integration. Time integrated discharge luminescence recorded for the same conditions is shown on fig. 7b. This photograph is obtained by use of a camera focused on laser head side through the lucite mirror holder with an off axis angle of $\simeq 25$ degres. The records of fig. 7 correspond to the highest laser average power achieved with LUX : $\overline{P}_\ell = 150$ watts for 47 successive shots at 1000 Hz PRF. Variation of laser energy from pulse to pulse is very low and much lower than variations reported in literature for quite similar conditions of flow speed, active volume and excitation[7][8][13]. The missing shots at the burst end allow to evaluate loss of energy per pulse induced by the high PRF. Decrease of pulse to pulse laser energy variation and increase of laser average power obtained in present experiments compared to others can be attributed to an increase of discharge stability produced by use of preionisation with higher intensity and duration, mixture with much lower Xe percentage and laser head design. Photograph of fig. 7b shows an homogeneous bulk discharge luminosity and hot spots on electrodes which are aligned in flow direction on well defined lines. These hot spots are attributed to the presence of transversal waves induced by interaction of flow and current returns in laser head which may be detrimental. It is to be noted, on the other side, that these current returns allow a turbulent mixing of heated and not heated gas leading to a strong attenuation of waves reflected on previous heated plasma slug.

Laser energy variations from pulse to pulse in burst mode for various conditions of flow speed and PRF are presented on fig. 8, while fig. 9 shows a comparison of these laser energy variations. For 500 Hz PRF (fig. 8a and fig. 9) decrease of energy is very low and that whatever the mixture and excitation conditions. Average laser power is there typically $P_\ell \simeq 80 - 100$ Watts. For 1000 Hz PRF good shoot to shoot reproductibility has been obtained with LUX (fig.7a and 9a) but is much more difficult to reach. Fig. 8b and 8c represent extreme results achieved with LUX. It appears that mixture composition is very critical for stable laser output and high average power for a PRF higher than 750 Hz.

4. CONCLUSION

Experimental results obtained with LUX and presented here allow the following conclusions :

- flow clearing processes have been diagnosed for high speed Ne/Xe/HCℓ mixture; density disturbances time history has been characterized for one pulse, double pulse and multipulses conditions ; bidimentional phenomena and hot spots near

electrodes have been observed
- an average laser power of 150 Watts has been obtained at λ = 308 nm with X-rays preionisation in long pulses (60 ns) at 1000 Hz PRF from a 70 cm^3 Ne/Xe/HCℓ active medium at P = 2,3 atm and U = 50 ms^{-1}. The decrease of energy per pulse relative to low PRF conditions is particularly low ($\approx$20%), for optimised conditions
- average laser power is much more dependent of gas mixture, electrical excitation parameters, flow homogeneity in laser cavity and laser head design than laser energy per pulse at low PRF. Decrease and pulse to pulse fluctuations of laser energy after the first shot in a burst at high PRF are attributed to fluctuations in discharge stability time duration. Discharge stability appears to be strongly coupled to flow homogeneity and nature of mixture, noticeably percentage of Xe and HCℓ in Ne/Xe/HCℓ mixtures.

These results are very encouraging, however much work remain to be done on high PRF high average power XeCℓ laser mainly in flow and acoustic control, discharge stability at high PRF and system efficiency for future development of an excimer laser system in the class of one kilowatt laser average power.

REFERENCES

1. Fontaine,B.L.,"Lasers à excimeres" in "Réactivité dans les Plasmas",Les Ed.de Phys.1984.

2. Levatter, J.I. et al, "X-ray preionization for electric discharge lasers", Appl.Phys.Lett. 34, April 1979, p. 297.

3. Forestier, B.M. et al, "XeCl laser pumped by an E-beam and X-ray assisted discharge",J.Phys.(Paris)Letters 42, 1981, p.211.

4. Wang, C.P. and Gibb, O.L. "2 KHz repetition rate XeF laser", IEEE J. Quant. Electr., QUE15, 1979, p. 318.

5. Cassady, Ph., "Advanced laser development for isotope separation", NSNU Bellevue (USA), Final report DOE/EI/33067 T1, June 1983.

6. Miller, J.L. et al "Operating characteristics of a closed cycle flow rare gas halide laser", Appl. Phys. Lett. 35, 15 December 1979, p. 912.

7. Baranov Vyn. et al, "Characteristics of the pulse periodic regime of excimer lasers", Sov. J. Quant.Electronic, 13, March 1983, p.318.

8. Natera, M. et al, "Diagnostic measurements on a high repetition rate XeCl discharge laser", Conference on Lasers and electrooptics, CLEO 85, Baltimore,paper ThW3 , May 1985.

9. Sentis, M.L., "Description d'un systeme laser à exciplexes à vocation de grande puissance moyenne", Entropie 115, 1984, p.3.

10. Sentis, M.L. et al, "High PRF electron beam or X-rays preionised discharge XeCl laser", 5th International Symposium on Gas Flow and Chemical Lasers, Oxford, August 1984.

11. Forestier, B.M. et al, "Flow and acoustics in a closed loop high pulse rate frequency XeCl laser", 5th International Symposium on Gas Flow and Chemical Lasers, Oxford , August 1984.

12. Sentis, M.L. et al, "Waves on the flowing active medium of a high energy high repetition rate excimer laser", 14th International Symposium on Shock Tubes and Waves, Sydney, August 1983, Proceedings 1984, p.573.

13. Borisov, V.M. et al, "Establishement of a steady-state power level in a pulse periodic excimer laser", Sov. J. Quantum Electron. 14, October 1984, p. 1363.
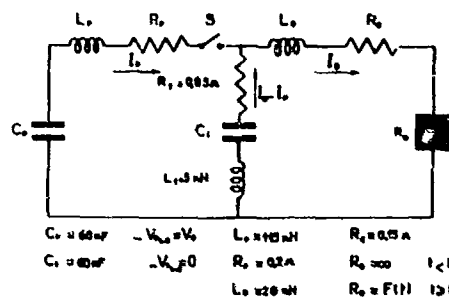
Fig.1 Scheme of main discharge circuit used for reported LUX experiments
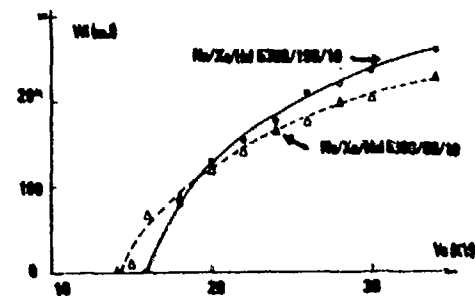
Fig. 2 Laser energy per pulse v.s. charging voltage for two typical gas mixtures (low repetition rate)
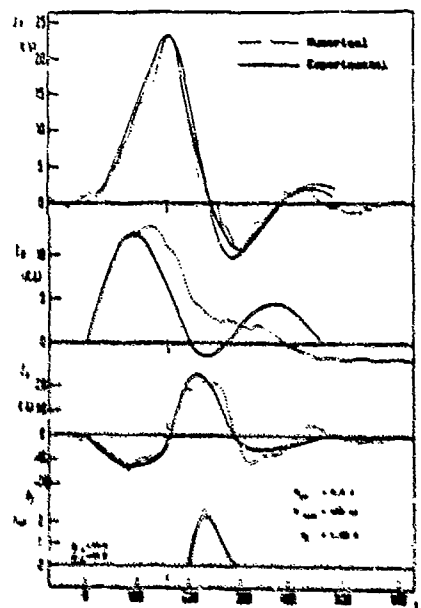
Fig. 3 Comparison between experimental & numerical values of electrical and laser parameters. for typical laser conditions

reference

Δt =7 μs

Δt = 37 μs

Δt = 357 μs

Δt = 1000 μs
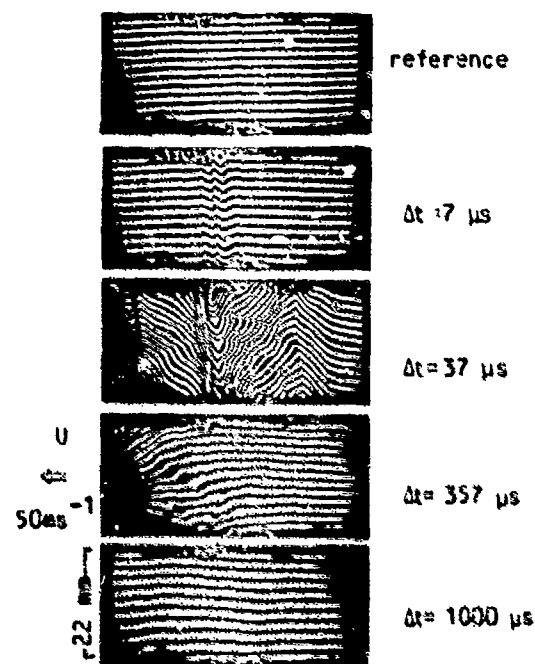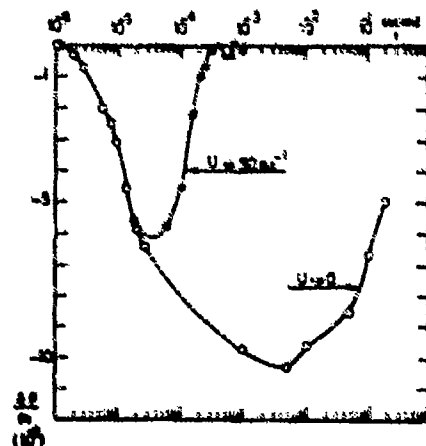
Fig. 4 Typical snapshots interferograms at various delays after excitation Ne/Xe/HCl 5300/190/10, P = 1 atm, W_{in} = 38 J/l

Fig. 5 Density disturbance v.s. time after excitation at cavity center for flow and no flow conditions. Neon, 1 atm, W_{el} = 21 J/l
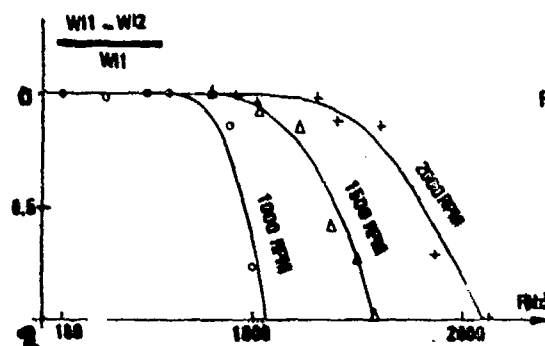
Fig. 6 Comparison between second and first pulse laser energy v.s. PRF and compressor speed.
He/Xe/HCl 5300/50/10 ;
$p = 2,3$ atm ; $U = 44$ ms^{-1} ;
$V_p = 22$ KV ; $W_l = 72$ mJ for first pulse
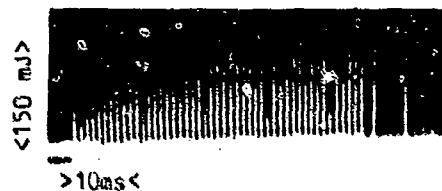
Fig. 7a Laser energy by shot versus time F = 1 KHz, Ne/Xe/HCl 5300/50/10 $p = 2,3$ atm ; $V_p = 26$ KV, optimal conditions

Fig. 7b Time integrated discharge luminescence corresponding to conditions of Fig. 7a

(a) F=500 Hz; U = 44 ms^{-1} (b) F= 1000 Hz ; U = 44 ms^{-1} (c) F=1500 Hz ;U =63 ms^{-1}
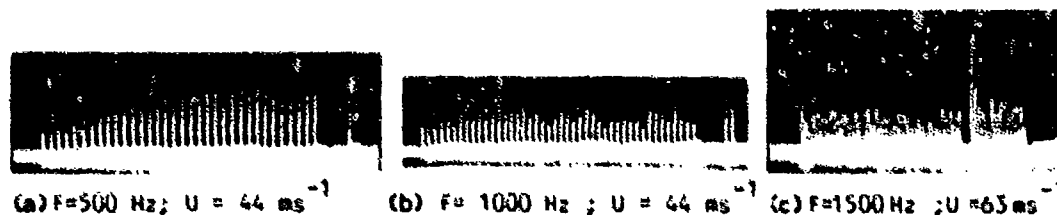
Fig. 8
Laser energy per pulse versus time for various conditions
Ne/Xe/HCl 5300/50/10 ; $p = 2,3$ atm ; $V_p = 26$ KV

Fig. 9 Variation of the ratio : laser energy of nth pulse/laser energy of first pulse. Ne/Xe/HCl 5300/50/10 ; $p = 2,3$ atm ; $V_p = 26$ KV. (a) best results , (b) unoptimized conditions
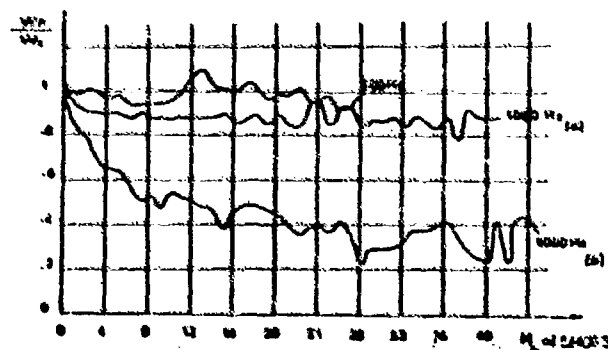
THE EFFECTS OF FLOW BLOCKAGE IN A BLAST
SIMULATOR AND THE MITIGATION OF THESE EFFECTS
WITH FLARED AND VENTED TEST CHAMBERS

Lynn W. Kennedy and Russell E. Duff

S-CUBED, A Division of Maxwell Laboratories, Inc.
P.O. Box 8243
Albuquerque, NM   87198

In order to investigate the effects of flow blockage on the blast environ-
ment experienced by an object in a shock tube and to determine whether
blockage effects could be mitigated by some simple test chamber modifi-
cations, such as flaring or venting of the chamber wall, a series of two-
dimensional, hydrodynamic, finite difference code calculational experiments
was undertaken.   These calculations utilized S-CUBED's version of the
Eulerian hydrocode HULL. Flow characteristics for flared and vented test
chambers were compared with those from straight tubes. Simple generic
test model shapes were used. All calculations were performed with a
non-decaying square wave input.

A series of more than 20 calculations indicates that, for the conditions
studied, the flared test section degrades blast simulator performance in
the diffraction phase but improves it during the drag phase of blast
loading. It appears that the influence of flow blockage is less severe
than might have been expected for strong shock waves, in that flow
choking in the transient hydrodynamic processes does not lead to dra-
matic modifications of the flow field during a time equivalent to
13 shock-wave transits across the test object. Some attractive results
were also obtained with perforations in the test chamber to allow a
portion of the gases to escape.

I. INTRODUCTION AND BACKGROUND

Large high-explosive experiments are conducted periodically in order to investigate the air
blast effects of detonations. Equipment and facilities are often exposed in these experi-
ments to assess their survivability to air blast. To supplement the free-field testing,
additional experiments are conducted with full size and scaled-down models of the test
items in shock tubes. A problem may arise, however, if the test model is so large that
it significantly blocks the flow of gases in the tube. For test model/shock tube cross
sectional area ratios of more than 10 or 20 percent, flow blockage may perturb the flow
around the model to the extent that test results are invalidated or at least rendered
questionable.

It has long been recognized that any object placed in a shock tube will obstruct the
cross sectional area of the tube and hence modify the late-time flow field developed
around the object. The problem can be alternatively understood in terms of waves
reflected from the object, which travel to the walls of the tube, reflect there and return
to the object, thus generating a flow field which is different from that which would be
experienced in a free field environment.

A number of calculations of the quantitative influence of blockage in a particular con-
figuration have been made, primarily by Ethridge, et.al.[1,2], Lottero, et.al.[3], and Wortman
and Lottero[4]. Experimental investigations have been made by Amann[5]. Calculations by
Duff, Northrop and Pierce[6], have looked at the possibility of flaring the test section of

the tube so as to preserve the flow area and thereby minimize choking, which would otherwise occur at the constricted, or blocked, section. The calculations which comprise the present study extend this earlier work and investigate several of the relevant variables.

The fundamental idea in the flared concept is the following. In a quasi-one-dimensional, steady flow, the hydrodynamic variables are functions of area. It is well known that subsonic flow conditions approach sonic values as the flow contracts. If a flare is installed such that the cross-sectional area at the test chamber (with the test object in place) is the same as the area upstream from the test chamber, to first approximation blockage effects would be eliminated. The calculations investigate the influence of flare shape on the forces developed on a test object in a flared or unflared chamber. Additional calculations considered the effects of wave strength and obstacle shape, but space limitations have prevented the inclusion of any of these latter results here.

II. CALCULATIONAL CONFIGURATION

The HULL hydrodynamic code was used for all of the calculations in this series. HULL is a pure-Eulerian finite difference code which is fully second-order accurate except in the mass-transport phase. HULL, originally developed at the Air Force Weapons Laboratory, has been extensively validated and is used in a production mode for calculations of this type. This series of calculations was run in two-dimensional cylindrical geometry with the axis of symmetry running lengthwise in the tube. The configuration is illustrated in Figure 1, which is a pressure contour plot from one of the calculations. The left vertical axis is the axis of symmetry and the incident shock is moving upward. The test sample and the flared tube wall are shown.

A total of 21 calculations were completed, but only five of these are discussed here. Zoning for all calculations was identical, with 5-cm zones in the radial direction and 20-cm zones in the longitudinal (vertical) direction. Variations in shock-tube radius, flare configuration and test object shape were incorporated for the different calculations. Long duration, non-decaying shock waves at 30 psi. were introduced in the lower (upstream) part of the tube and allowed to flow upward into the flared region and over the test object. Shock conditions were fed in at the lower boundary to maintain the flat-topped wave. The ends of the tube, as defined by the calculational grid, were sufficiently remote that reflections from the ends could not perturb the flow field during the time of interest.

The test object shape is shown in Figure 2. It should be kept in mind that this shape becomes a cylindrical disk when rotated about the axis of symmetry. Dimensions of the object are given in the figure, and the lettered points indicate positions at which pressure-time histories, to be presented later, are given.

The five shock tube configurations discussed here include the reference case (2 percent blockage), the "standard" flare, the square flare, the straight tube, and the vented straight tube. The last four, at 30 percent blockage ratio, are shown in Figure 3. The 30 percent blockage figure actually applies only to the straight tube. For the flared configurations, the radius of the flare was adjusted so that cross-sectional tube area at the flare, with the test object in place, was equal to cross-sectional area upstream and downstream from the test object. For the 10 percent (for lack of space, results from the 10 percent blockage calculations have not been included) and 2 percent (reference configuration) blockage ratios, the tube and flare radii were increased, but the above rules about cross-sectional areas were retained. Obviously, the 10 percent and 2 percent blockage ratio cases had much shallower flares than the one shown in Figure 3. The vented straight tube was the same as the straight tube, except that it incorporated a one-zone (20-cm) hole in the tube wall at the sample center.

The calculations in each case were run from a time set arbitrarily to 1 msec until 50 msec. At 1 msec, the shock was just upstream from the beginning of the flared section. The 30 psi shock struck the test object at about 5 msec in each case. The total calculation time, 49 msec, represents about 13 shock transit times across the object for the 30 psi shock. The time is sufficiently long that we are well into the "drag" phase of the test object response.

III. RESULTS

The comparisons presented will be for the 30 psi, 30 percent blockage ratio results, using the rectangular test sample. This high pressure, high blockage ratio regime exaggerates the effects of blockage and is the one in which the most interest has been shown. For this series the 2 percent blockage ratio case is used as a reference. It comes very close to the free-field, or unblocked, configuration. Results from the straight tube, the vented straight tube, the standard flare, and the square flare are compared with the reference configuration.

Results are presented in terms of "net force" and "top force" versus time on the test object. For this analysis, the rectangular test object is considered to be a half cylinder resting on a flat floor in a semi-cylindrical shock tube. The net force at a given time is just the difference in forces on the front (shock-facing) and back faces in the axial direction. The forces are computed by integrating pressure levels at a given time over the test object surfaces. The top force is the vertical force tending to hold the object to the floor of the tube. This is derived from the radially inward force calculated in the axisymmetric representation by trigonometric resolution of this force over the cylindrical surface, keeping only the vertical component. The expressions used to calculate net and top forces are:

$$F_{net}(t) = \sum_i P_i(t)\, dA_i - \sum_j P_j(t)\, dA_j$$

The i index indicates summation over stations on the front of the sample and the j index is for stations on the back. P is the recorded pressure for the station.

$$dA_i = dA_j = \frac{\pi}{2}\left[r_i^2 - r_{i-1}^2\right]$$

where r_i and r_{i-1} are the outer and inner radii of the ring element in which the ith or j[th] station is located. Note that the area element is only half of the ring.

$$F_{top}(t) = \sum_\ell P_\ell(t)\, dA_\ell$$

where the ℓ index is for those stations at the top of the sample.

$$dA_\ell = 2R_s\left(h_\ell - h_{\ell-1}\right)$$

h_ℓ and $h_{\ell-1}$ are the axial coordinates of the edges of the cylindrical element on which the station is located. This area element is that parallel to the floor plane. R_s is the sample radius. For this series of calculations, a station for monitoring pressure time histories was located in each zone adjacent to the test object.

The net force and top force results for the four tube configurations are compared against the reference configuration in Figures 4 and 5. As can be seen, the net forces in the two straight tube configurations (vented and unvented) are identical to those from the reference up until about 18 msec, when they rise to a higher value because of the blockage. The flared tube configurations depart from the reference record earlier.

but oscillate about a value which is closer to the reference at late times. The effects of blockage are also apparent in the top force records. Flared tube walls do not seem to help much here. In fact, the vent configuration seems best for ensuring correspondence of reference and blocked top force records.

Some individual station records, at points on the test object indicated in Figure 2, are given in Figure 6. Records from each station are compared for the five calculations. Flares provide some improvement in records from the front surface (Stations A and C) but back (Stations B and D) and top (Stations E and F) records do not compare as well with the reference case as does the straight tube result. The top surface correlation is somewhat improved by the vented configuration.

The calculations provided an enormous amount of information and specific results for the cases studied. Space limitations do not allow the inclusion of more of them here, but a more extensive set is provided in Reference 7.

IV. CONCLUSIONS

A number of conclusions were reached as a result of this study, not all of which are obvious from the limited results presented here. It is worthwhile, however, to present in statement form those conclusions which the authors consider to be most important to blast simulator designers and experiment planners.

First, calculations of the sort presented here provide a great deal of insight into the nature of the flows to be expected in a blast simulator. They can be performed quickly and are relatively inexpensive. Insofar as they adequately represent reality and insofar as a credible two-dimensional approximation can be defined for a case of interest, such calculations can be very valuable in data interpretation from shock tube tests which, by their very nature, must deviate from free-field conditions. The calculations can also be very valuable in designing the simulation experiments so as to maximize the anticipated data return.

Flow blockage in a simulator is an important perturbation to a flow field. However, even in the case of a 30 psi blast and a 30 percent blockage for a steady non-decaying wave, blockage is no more than a perturbation. It is not the dramatic modification which is suggested by the concept of a choked flow. The qualitative features of the late-time loadings seem independent of whether or not sonic conditions are predicted in steady state theory.

A test section flare appears useful, particularly for drag sensitive targets, but it does not solve all blockage problems. Additional geometric configurations might be profitably investigated. Perforations in the vicinity of the test chamber also appear beneficial to simulator performance, particularly if interest centers on forces at the top or back of the test object.

The calculations performed have illustrated the influence on simulator performance of blockage, and have shown how the basic flare concept and several variants of flare geometry and test section venting can be used to mitigate these effects. It appears that, to match particular sets of requirements, a combination of test section geometric factors might be chosen. It is the opinion of the authors that a large blast simulator could be designed with blockage ratios of up to 30 percent anticipated for the largest test objects, if provisions are included to permit geometric options such as adjustable flares and vents in the test chamber.

REFERENCES

1. N.H. Ethridge, R.E. Lottero, J.D. Wortman, and B.P. Bertrand, "Flow Blockage and Its Effect on Minimum Incident Overpressure for Overturning Vehicles in a Large Blast Simulator," Proceedings of the Seventh International Symposium on Military Applications of Blast Simulation, Vol. II, Medicine Hat, Alberta, Canada, 13-17 July 1981.

2. N.H. Ethridge, R.E. Lottero, J.D. Wortman, and B.P. Bertrand, "Blockage Effects in a Large Blast Simulator," Proceedings of the Eighth International Symposium on Military Applications of Blast Simulation, Vol. I, Spiez, Switzerland, 20-24 June 1983.

3. R.E. Lottero, B.P. Bertrand, N.H. Ethridge, and J.D. Wortman, "Predictions of the Effect of Blockage on Late-Time Steady Flow Conditions Near a Target in a Shock Tube," Proceedings of the 14th International Symposium on Shock Tubes and Waves, Sydney, Australia, 19-22 August 1983.

4. J.D. Wortman and R.E. Lottero, "Comparison of HULL Hydrocode Computations of Shock Tube Blockage Effects on Target Loading for Step Shocks and Rapidly-Decaying Shocks," ARBRL-MR-03232, U.S. Army Ballistic Research Laboratory, Aberdeen Proving Ground, MD, December 1982.

5. H.-O. Amann, "Flow Blockage and Its Effects on the Loading of a Model in the Test Section of a Shock Tube," Proceedings of the 14th International Symposium on Shock Tubes and Waves, Sydney, Australia, 19-22 August 1983.

6. R.E. Duff, J. Northrop, and T. Pierce, "Blast/Thermal Simulator Facility Review," DNA-TR-81-156, Defense Nuclear Agency, Washington D.C., June 1982.

7. R.E. Duff, L. Kennedy, and K. Lie, "Airblast Simulator Studies," SSS-R-84-6495, S-CUBED, La Jolla, CA, February 1984.
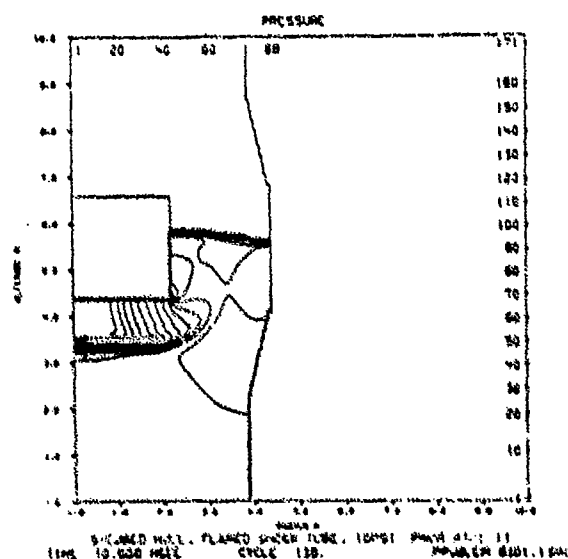
Figure 1. Pressure Contour Plot Showing Configuration for Calculations
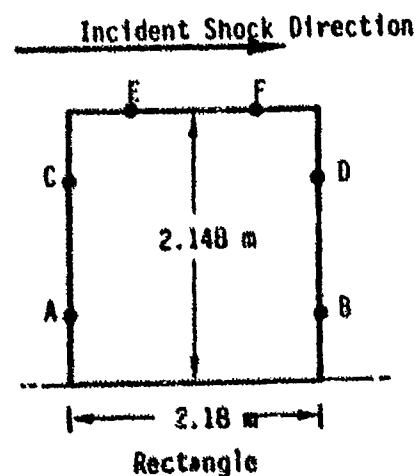
Figure 2. Test Object Shape for Calculations in This Study
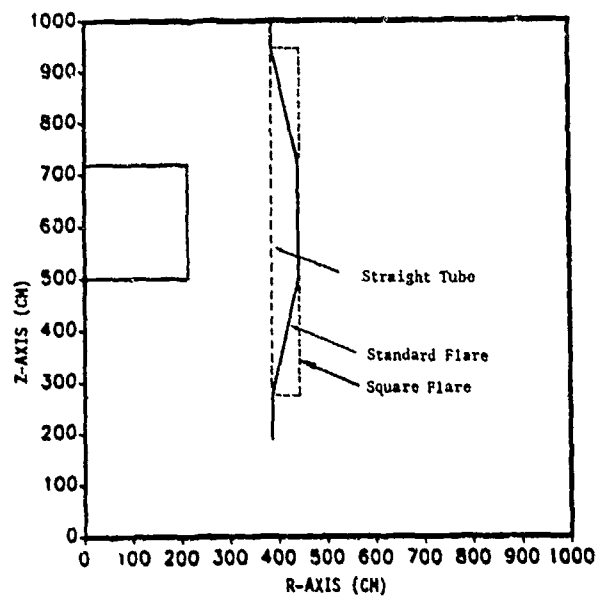
Figure 3. Shock Tube Configuration for 30% Blockage Ratio Cases

Rectangular Sample, 30 psi, Straight tube vs. reference.

Rectangular sample, 30 psi Std. flare vs. reference.

Rectangular sample, 30 psi, Vent vs. reference.

Rectangular sample, 30 psi, Square flare vs. reference.
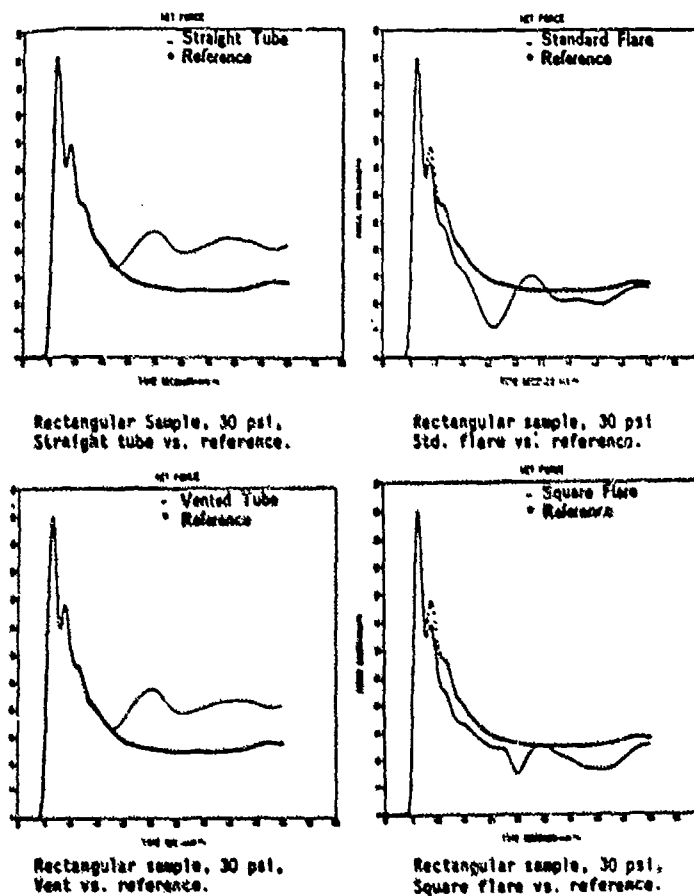
Figure 4. Net Force Records for Several Tube Configurations Compared to the Reference Case, for a 30 psi Shock Incident on the Rectangular Test Object

Rectangular sample, 30 psi,
Straight tube vs. reference.

Rectangular sample, 30 psi
Std. flare vs. reference.
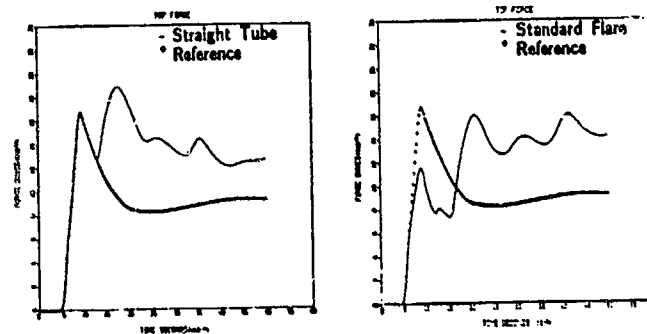
Rectangular sample, 30 psi,
Vent vs. reference.

Rectangular sample, 30 psi,
Square flare vs. reference.

Figure 5. Top Force Records for Several Tube Configurations Compared to the Reference Case, for a 30 psi Shock Incident on the Rectangular Test Object
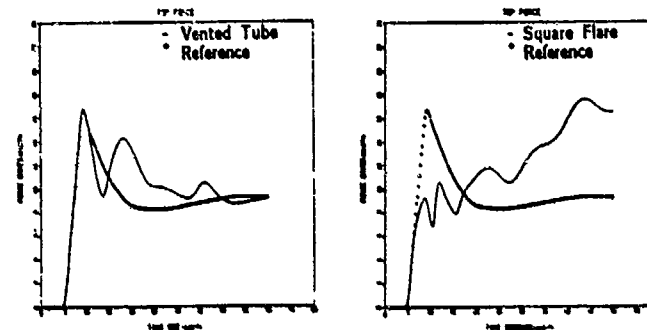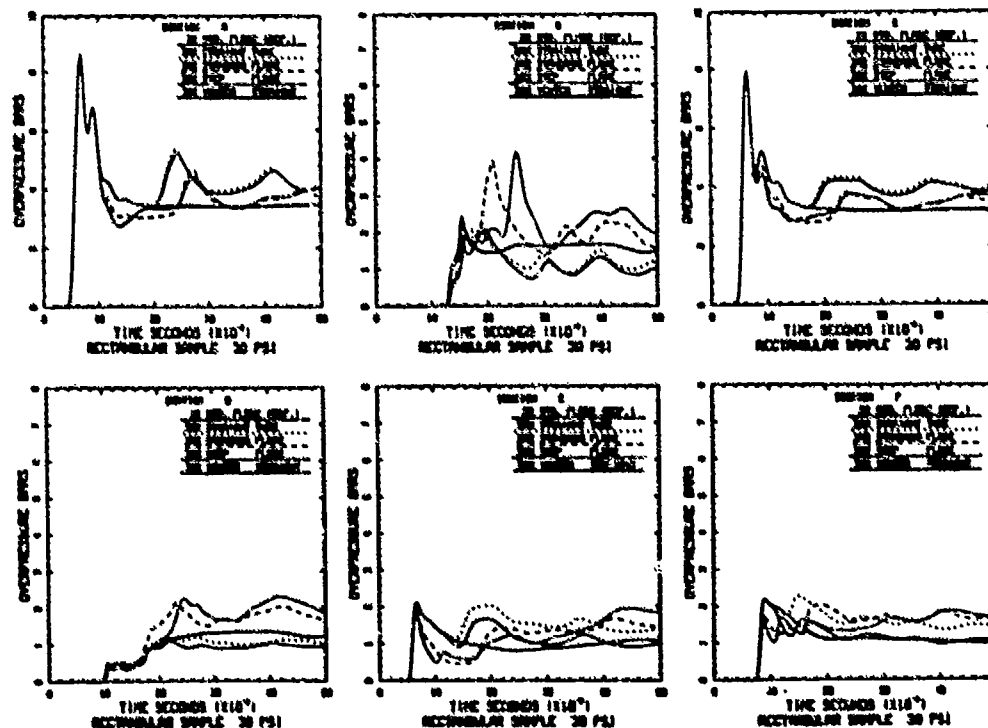
Figure 6. Pressure-Time Records from Individual Stations (Indicated in Figure 2) for the 30% Blockage, 30 psi, Rectangular Sample Configurations

Part IX
Technical Applications and Shocks in Condensed Matter

STUDY OF MACH REFLECTION IN PMMA PLATES

A. Henckels; K. Takayama and H. Grönig
Stoßwellenlabor, RWTH Aachen, W. Germany

The intention of the present work has been to study the generation of Mach reflection in solids, using PMMA plates loaded by detonation waves created by small pellets of explosives. Two pellets were located within a short distance inside the plate and fired simultaneously. Thus two circular wave fronts were generated showing an oblique shock reflection on the symmetry axis between the explosives. A ruby laser stroboscope together with a rotating mirror camera allowed the observation of this reflection process. Picture series with frequencies up to 250 kHz were taken. Mach reflection phenomena could be recognized on the shadowgraphs. In addition to this the pressure profile of a wave could be measured by using PVDF foils. To confirm the possibility of Mach reflection in the experiments a shock polar analysis for PMMA had been performed. The transition curve from regular to Mach reflection could be calculated with the detachment criterion and was compared with foil gauge measurements of the wave pressure.

1. INTRODUCTION

At higher pressure loading a solid tends to behave like a fluid. It is therefore interesting to compare the wave propagation process in solids with that in fluids. One question in connection with this problem is the appearance of nonlinear wave propagation effects. Recently Holl et al.[1] studied shock wave propagation in water and observed the Mach reflection in their experiments. It is the main goal of the present paper to prove the occurrence of the Mach effect in a solid like PMMA similar to that in a fluid.

To generate a Mach stem in PMMA wave pressure amplitudes must be much higher than those in a fluid. So the first question is how to produce longitudinal stress waves of high intensity. In the past years there has been a number of experiments done at the Stoßwellenlabor of the RWTH Aachen to produce stress waves of high amplitudes in PMMA plates by wave focusing[2]. Figure 1 shows an interferogram of a semi-circular plate loaded by the plane reflected shock wave generated in a shock tube. One can recognize a focusing spot of a longitudinal pressure pulse after the reflection of the wave at the plate boundary. It was found that the energy loss of the travelling pulse due to the reflections at the plate side walls prevents the wave amplitude from reaching values sufficient to produce observable Mach effects in the focus area.

The loading of PMMA plates by detonation waves created by small pellets of explosives presents an interesting method for the generation of stronger pressure waves. Figure 2 shows an interferogram taken 12 μs after ignition of the explosive. The simultaneous detonation of two pellets is used in this paper to confirm the appearance of Mach reflection as seen in Fig. 3. The propagation of two circular wave fronts shows an oblique shock reflection over a wedge of the variable angle θ_w depending on the shock front radius r due to the symmetric arrangement. Similar to experiments in gases a transition from regular to Mach reflection may be observed in the PMMA plate.

2. EXPERIMENTAL FACILITIES

The thickness of the used PMMA plates was 10 mm to obtain sufficient sensitivity and good transparency for optical visualization of the wave propaga-

tion process. One or two pellets of about 30 mg PETN were placed inside a hole drilled in the plate, and fixed by a two-component adhesive. The ignition of the pellets was achieved by an exploding wire connected to a high voltage capacitor of 2.5 kV. After the explosion of the detonator a primary longitudinal pressure pulse of circular symmetry was travelling through the plate and reflected several times at both plate surfaces.

Due to the high longitudinal wave speed of 2770 m/sec in PMMA it was necessary to use gauges of very high time resolution to measure the normal stress of this primary pulse. Therefore, pressure gauges consisting of PVDF foils (24 μm thickness) were applied. These foils, coated with aluminum on both sides, were also cemented into the plates. Their output signals could directly be measured by an oscilloscope (Fig. 4). Knowing the capacity of the gauge and its connecting wires quantitative pressure measurements were possible with a time resolution up to about 100 MHz.

In addition to the foil gauge measurements the sketched optical arrangement (Fig. 5) was used for observing the wave propagation process. The light source consists of a ruby laser stroboscope switched by a high speed Pockels cell. Series of 1 to 2.5 x 10^5 frames per second – shadowgraphs as well as interferometric pictures – were taken using a rotating mirror camera. To avoid damages to the optical system the PMMA plates with the explosives were located in a steel tank with specially protected observation windows.

3. GAUGE MEASUREMENTS RESULTS

To determine the strength of the primary longitudinal wave pulse, foil gauge measurements were accomplished at different distances from the center of explosion. One example of a stress record is shown in Fig. 6. In the lower part of the figure a sectional drawing of the plate is presented. Some of the characteristic points found by geometrical construction of several reflections at the plate side walls coincide with peaks of the stress record shown in the upper part of this figure. Behind the primary longitudinal pulse a second steep wave amplitude is generated due to transversal wave reflection indicated by the dashed line. The decay of the primary stress amplitude depending on the radius r of the circular wave front is given in Fig. 7. Because of small differences of the pellet mass there is a range of scattering around the approximation line.

4. SHOCK POLAR ANALYSIS

To confirm the possibility of Mach reflection in the experiments a shock polar analysis for PMMA has been performed. Therefore, the oblique shock wave relations were solved by using an equation of state instead of the energy equation. The equation of state was obtained from available data[3] and found to have a similar form in the low pressure region as the Tait equation for liquids. The best fit curve for the experimental values of PMMA is given by

$$\frac{p + B}{B} = \left(\frac{\varrho}{\varrho_0} \right)^{4.08} \tag{1}$$

where B = 2.23 GPa.

Figure 8 shows a shock polar for a very weak shock of Mach number M_0 = 1.001. The polar of the incident shock is drawn as well as three polars of the reflected shock for different wedge angles. For determination of the transition from regular to Mach reflection the detachment criterion can be used. In the given example of Fig. 8 the transition from regular to Mach reflection occurs at a

wedge angle of $0_w = 2.3^\circ$.

By the help of a number of such shock polars the transition curve in Fig.9 can be found as a function of the incident shock strength, i.e. the pressure p, and the wedge angle θ_w .

The wedge angle θ_w obtained in the experimental setup as shown in Fig. 2 is given by the geometrical relation

$$\theta_w = \text{arc sin} \frac{r_o}{r} \quad . \qquad (2)$$

The normal stress 0_{11} of the incident shock is then found from Fig. 7 as a function of the shock front radius. Reducing this normal stress of the longitudinal wave to a hydrostatic pressure p_H and combining it with the geometrical relation above, the measured pressure strength can also be drawn in Fig. 9 (shown as dashed line). The range of scattering of the wave strength is dotted. The diagram verifies measured pressure amplitudes to be in the Mach reflection region below the transition curve for small wedge angles θ_w. At a wedge angle of about $\theta_w = 6^\circ$ the average strength of the explosive is sufficient to generate a Mach stem. If the detonators are placed in a distance of $r_o = 4$ mm from the axis of symmetry one will find the transition point in a distance of about 40 mm from the explosive centers.

5. OBSERVATION OF MACH REFLECTION

To verify the idea given in the section above, shadowgraphs of the described experiment were taken. Figures 10a and 10b confirm the development of a Mach stem. Both photos show the region of 40 to 60 mm distance from the explosives, which can not be seen in the pictures, but are located below in the extension of the two vertical marks. On the left hand shadowgraph the two primary longitudinal wave pulses penetrate each other nearly as ideal circles. 10 µs later a dark straight line indicating the Mach stem is recognized on the axis of symmetry as shown on the right hand side shadowgraph. The development of Mach reflection in this experiment was found to be in good agreement with the transition calculated above.

The Mach stem can be found also in the pressure foil gauge record by a sudden initial pressure rise. Figure 11a shows a wave pressure record of a single explosive. The pressure recordin Fig. 11b shows the pressure history caused by the Mach stem for comparison. It points out a remarkable first pressure rise due to the Mach stem and a higher maximal amplitude of the whole wave train.

6. CONCLUSION

For describing nonlinear wave propagation phenomena in solids it seems possible to use similar equations to those known from gas dynamics. The predictions made by using a shock polar for PMMA for instance was helpful to confirm the Mach reflection experiment described in this paper. The appearance of a Mach stem in the shadowgraph shows the similarity between shock waves in fluids and waves in high pressure loaded solids.

7. ACKNOWLEDGEMENT

8. REFERENCES

1.   Holl, R.; Takayama, K.; Higashino, F.; "Generation, Propagation and Reflection of Underwater Shock Waves", Proc. of the 14th National Shock Tube Symp., Editor: H. Oguchi, Tokyo, 1983, p. 44.
2.   Henckels, A.; Grönig, H.; "Experimental Studies of Stress Waves in Elastic Plates with Curved Boundary", Optical Methods in Dynamics of Fluids and Solids, Editor: M. Pichal, Springer Verlag, Berlin, Heidelberg, 1985, p. 143.
3.   Marsh, S.P., "LASL Shock Hugoniot Data", University of California Press Berkeley, 1980, p. 446.

Fig. 1: Interferogram of the focusing process in a PMMA plate.

Fig. 2: Interferogram of the wave pattern generated by a PETN pellet in a PMMA plate.
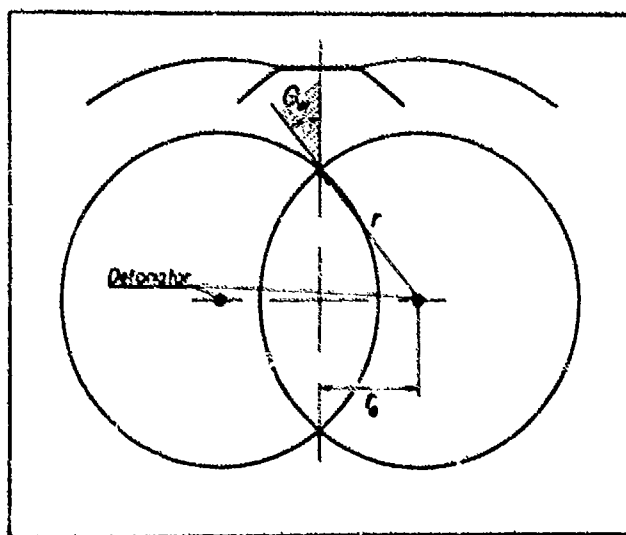
Fig. 3: Detonator arrangement for the generation of Mach reflection as seen in the upper part of the figure.
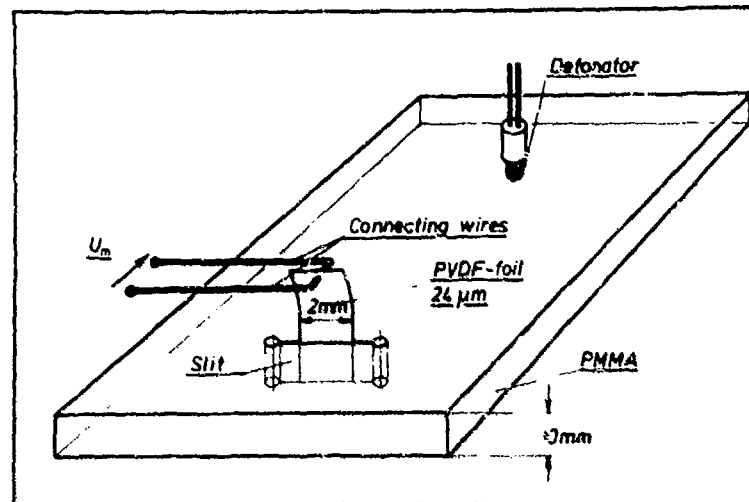
Fig. 4: Arrangement of a foil gauge and the pellet of explosive in the PMMA plate.
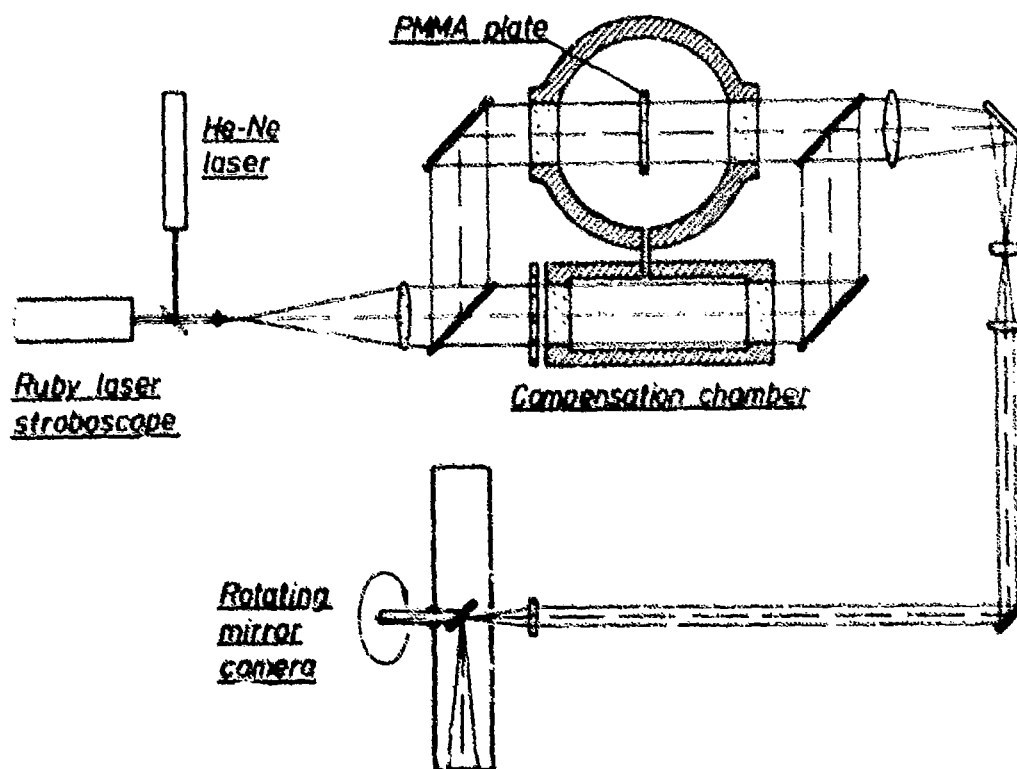
Fig. 5: Optical arrangement for observing the wave propagation process by shadowgraphs or interferograms.
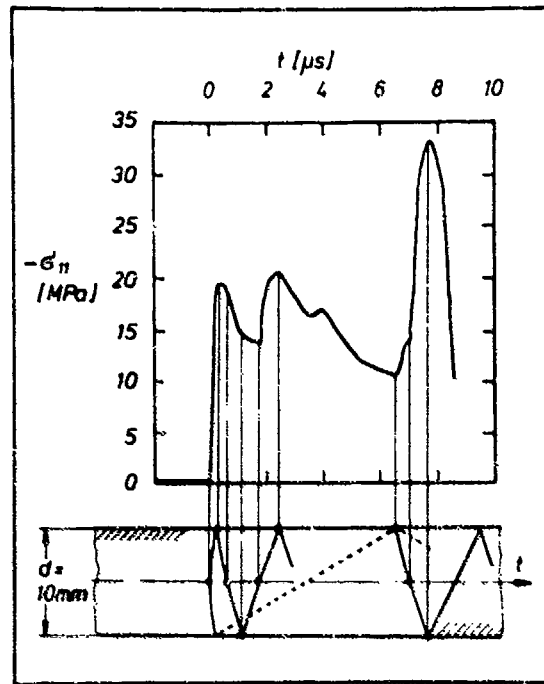
Fig. 6: Above: Stress profile of a wave in a distance of 40 mm from the explosive center. Below: Sectional drawing through the plate with additional geometrical construction of several wave reflections.
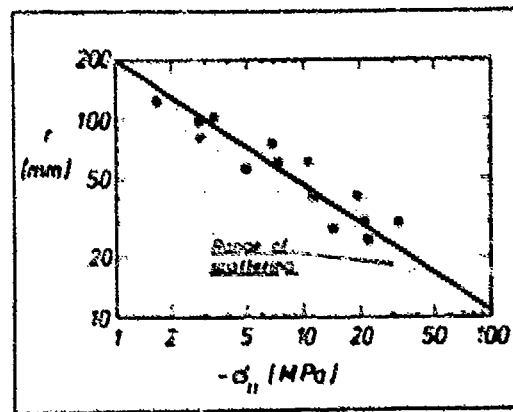
Fig. 7: Stress amplitude σ_{11} of the primary longitudinal pulse as a function of the front radius r.
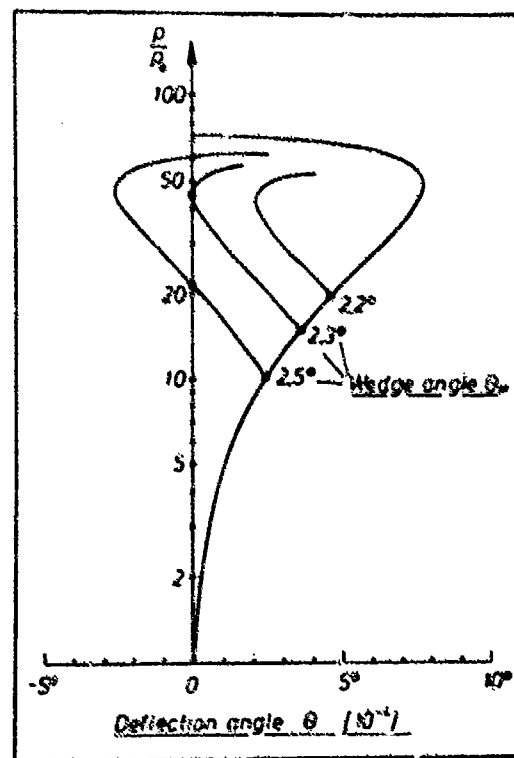
Fig. 8: Shock polar for the PMMA at a Mach number of $M_0 = 1.001$.
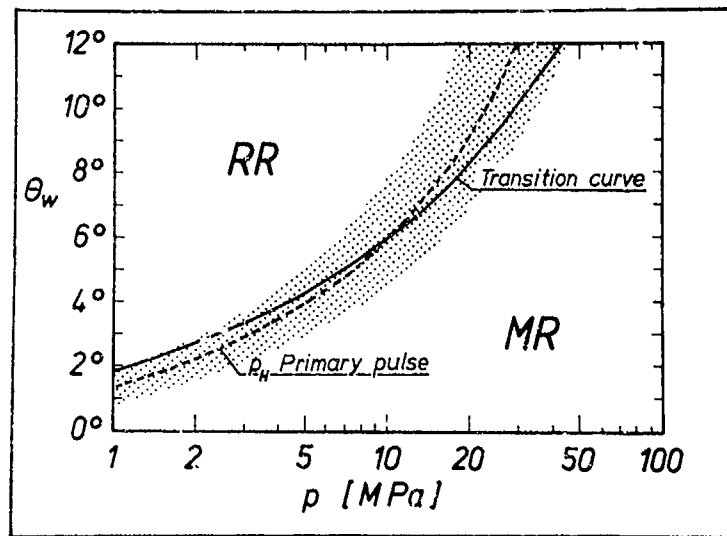
Fig. 9:
Comparison between the transition curve from regular (RR) to Mach reflection (MR) and the measured pressure of the primary longitudinal wave pulse.
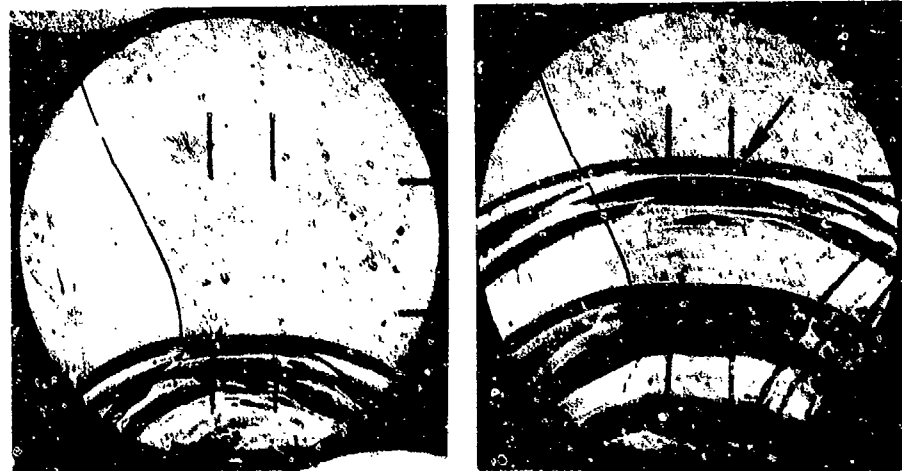
Fig. 10a and b: Shadowgraphs of the transition from regular reflection to Mach reflection; arrow indicates Mach stem.
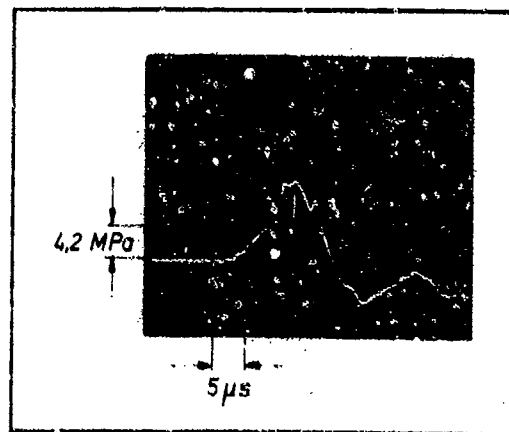
Fig. 11a: Pressure record in 120 mm distance from a single explosive.
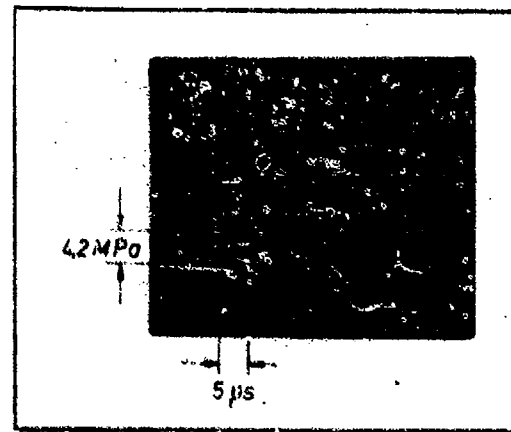
Fig. 11b: Pressure record caused by the Mach stem in 120 mm distance from two explosives.

SHOCK WAVE ASPECTS OF DYNAMIC POWDER COMPACTION

N.W.Page
Department of Mechanical Engineering
University of Queensland, St.Lucia,Q.4067 Australia

A shock wave analysis is applied to dynamic powder compaction initiated by a piston impacting onto powder contained in a die. The shock wave equations directly relate the pressure and particle velocity in this method of compaction. However, some measure of independent control over these quantities is shown to be possible by exploiting multiple shock reflections in the powder, but higher piston energy is needed to achieve this control. For a powder described by the Kawakita equation of state it is also shown that shock reflection at powder/surface interfaces is dominated by the geometrical mean impedance of the powder (based on incident and reflected states) in relation to the impedance of the reflecting surface.

1. INTRODUCTION

There are many methods available to consolidate metal powders into solid forms[1]. A dynamic method which lends itself to fundamental studies of the compaction mechanism is one in which a high speed piston is impacted onto the powder using an apparatus like that shown in Fig.1. High pressure gas from the reservoir is used to accelerate the piston down the launch tube. When the piston impacts onto the powder, two stress waves are generated – one propagating back along the piston and one in the powder causing compression. During this process the powder can be treated as a continuum and the wave propagating through it can be treated as a plane shock wave like that experienced in any other compressible substance[3]. For simplicity, the subsequent wave motion will be described in terms of the simplest compaction geometry, one in which the powder is compressed into a cylindrical billet. In this case the shock wave in the powder can be repeatedly reflected between the back of the die and the front of the piston (Fig.2). This process can occur many times so that very high pressures can be built up in the powder with correspondingly high compression. The basic method of operation has been described previously [3].

This paper describes a study of this method of dynamic powder compaction from the point of view of how the operational parameters, such as piston material, piston velocity and other material choices influence the compaction process. Unlike conventional quasi-static compaction, there is a direct connection between pressure and powder velocity during this dynamic compaction; a shock wave processes the powder to a higher pressure state with corresponding particle velocity. Previous workers [4], [5] have concentrated on tailoring the method to maximize compaction pressures and densities in very simple compact shapes in which powder velocity effects were relatively unimportant. However there are many applications in industry involving powder compaction in complex dies containing changes of cross-section. In applications like these, powder velocity is important in determining the uniformity of compact properties in the vicinity of changes in die geometry. The problem is particularly severe in dynamic compaction since partial reflection of the incident shock wave from, for example, reductions in die section, would momentarily cause very large velocity differences across the powder cross-section. In this work then, ways of independently controlling pressure and particle velocity are investigated. Significant features in this problem are the strength of the primary shock, the reflections that occur at the die and piston faces and the total time available for compaction. These will now be treated in turn.

2. PRIMARY SHOCK STRENGTH

Following Raybould[3], the one-dimensional momentum and mass continuity equations can be applied to the waves initiated on piston impact. Assuming the pressure in the powder ahead of the shock is zero, the pressure behind the primary shock in the powder is given in implicit form by

$$P_2 = \rho_1 \rho_2 (u_{p1} - P_2/\rho_p c_p)^2/(\rho_2 - \rho_1) \qquad (1)$$

where P is the pressure, ρ the apparent density, u the particle velocity, c the sound speed and the subscripts according to the notation shown in Fig.2 with p referring to the piston quantities. An equation of state is also needed to link the pressure and density. A number of such relations have been reported[4]. That due to Kawakita is valid for the loading phase of quasi-statically compacted metal powders[3],[7] and can be written as

$$\rho/\rho_0 = (1+bP)/(1+abP) \qquad (2)$$

where ρ_0 is the initial bulk density, a is the ratio of the initial free density of the powder to that of the solid from which it is made and b is an empirical constant representing the powder stiffness. For the present purposes it will be assumed that this equation is also valid for dynamic compaction. Equations 1 and 2 lead to a cubic equation in P_2 which generally yields 3 real solutions. One is negative and hence physically unrealizable, one is a "strong" shock solution with pressures well beyond those observed and the third is a "weak" shock solution with pressures consistent with observed behaviour. It will be this third solution which will be used in the subsequent discussion.

In equation 1, the second term in the bracket represents the velocity of the material in the piston measured with respect to that in its unstressed state. In general this is much smaller than u_{p1} and consequently, the pressure generated on impact (P_2) has an almost quadratic dependence on the impact velocity. This is shown in Fig.3 for the particular cases of steel and PVC pistons, both impacting onto iron powder. The curves in Fig.3 were calculated using values for a and b taken from Ref.3.

The physical properties of the piston material also affect the strength of the primary shock. PVC and steel have strongly contrasting properties in this context (Table 1) and hence are useful for comparative purposes here. The impedance shown in Table 1 is the acoustic impedance (ρc) which would approximate the shock impedance at stress levels below the yield strength.

It can be seen from equation 1 that the strength of the shock generated on impact depends on the impedance of the piston material. There is about a 20 fold difference in the impedances of PVC and steel shown in Table 1. Comparing the results in Fig.3 generated by pistons made from these two materials impacting at the same velocity, this difference in impedance is seen to cause about a 50% difference in P_2. However, when the results for the two pistons are compared with the same energy and compaction time, the lighter PVC is superior despite the higher impedance of the steel piston. Thus, if the highest peak pressures are required, it is best to operate with a light piston at high speed even though such a piston might not have a particularly high impedance.

The particle velocity behind the primary shock is high and using the same approach as for equation 1, can be shown to be given by

$$u_2 = [P_2(\rho_2 - \rho_1)/\rho_1 \rho_2]^{1/2} \qquad (3)$$

This together with equation 2 yields an expression for the velocity in terms of P_2. Fig.4 illustrates the relationship for the case of iron powder.

Clearly, the strategy of producing high primary shock strengths by using high piston impact velocities also produces high particle velocities. One approach to simultaneously achieving high pressures with low particle velocities is to use lower primary shock strengths and to exploit the multiple shock reflections that take place between the two powder boundaries.

3. REFLECTED SHOCK STRENGTH

(a) At the Die

For simplicity, the bottom of the die was assumed to be comprised of an infinitely long rod of the same section as the powder and made from linearly elastic material. Using a one-dimensional model for shock reflection from the powder/die interface, the momentum and mass continuity equations together with the equation of state give the pressure after reflection as

$$P_{rd} = [P_i + \rho_m c_m u_i]/[1 + \rho_m c_m / (\rho_d c_d)] \tag{4}$$

where $\rho_m c_m = \sqrt{\rho_i c_i \rho_r c_r}$ and the variables take their usual meanings. The subscripts i and r refer to the states behind the incident and reflected waves, m, the geometric mean, and d, the die. Again a cubic equation in the reflected shock strength ($P_{rd} = P_3$) is obtained if the densities and sound speeds are re-written in terms of the pressures from the equation of state. From equation 4, the strength of the reflected wave is seen be maximized by maximizing the impedance of the die compared with the geometric mean of that in the powder. Numerical results for P_3 are also shown in Fig.3 for the cases of steel and PVC pistons impacting onto iron powder. A considerable enhancement of pressure can be seen to be a result of this reflection.

A similar analysis shows that the particle velocity behind the reflected wave is given by

$$u_{rd} = P_r/\rho_d c_d \tag{5}$$

For a given die material then, the particle velocity depends on the strength of the incident wave. Also, the higher the impedance of the die material, the lower is the particle velocity behind the reflected shock.

(b) At the Piston

After reflection from the back of the die, pressures are very high but particle velocity small. This reflected wave is in turn reflected from the piston. Using the same method of analysis as in (a), the pressure developed at this reflection can be shown to be given by

$$P_{rp} = [P_i + \rho_m c_m (u_{p1} - u_i)]/[1 + \rho_m c_m / (\rho_p c_p)] \tag{6}$$

with the same notation as before. Once again, this equation reduces to a cubic in $P_{rp} = P_4$ if the densities and sound speeds are re-written in terms of pressure by means of equation 2.

In a similar way to that found above for reflection at the die base, equation 5 shows that the reflection at the piston face is controlled by the mean impedance of the powder compared with that of the piston material. The impedance of the piston material should be maximized to maximize the reflected wave strength. However, there is a conflict here in that, a piston material of low density is desirable to maximize piston velocity and hence primary shock strength for given reservoir pressure energy. But the sound speed and hence the impedance is typically low in low density materials leading to unfavourable reflection characteristics. If a low density piston material is used, the mean powder impedance could equal or exceed that of the piston in which case the denominator in equation 6 quickly grows so that the reflected

wave is of lower strength than the incident wave. The seriousness of this problem can be seen by comparing the impedances of possible piston materials shown in Table 1 with the impedance of iron powder. This, based on equation 2, is a linear function of pressure as shown in Fig.5. Considering a PVC piston, the powder would have a higher impedance than the piston at the relatively low pressure of about 150 MPa. For mean powder impedances higher than this, the particle velocity, given by

$$u_{rp} = u_{p1} - P_{rp}/\rho_p c_p \qquad (7)$$

is negative i.e. the unloading process has begun.

(c) Repeated reflection

In the absence attenuation or reflected waves from within the piston or the die, the reflection events described in (a) and (b) above would be repeated continuously. The use of this repeated reflection to control the pressure and particle velocities independently will be illustrated for the two contrasting cases of a PVC piston with an impact velocity of 260 m/s and a steel piston with an impact velocity of 120 m/s, both impacting onto iron powder. Pressures and velocities up to and including those at the first reflection from the face of the piston are shown in Table 2. During unloading, it was assumed that the powder would unload linearly and tangentially from the point of maximum pressure on the equation of state for loading. This was the basis for calculating the powder state 4 with the PVC piston, the only state in Table 2 affected by unloading. In this reflection event, the mean impedance of the powder is higher than that of the piston material and thus, the wave reflected back from the piston face is tensile – the unloading phase has commenced.

Of importance here is that the peak pressure developed over the time scale shown was about 860 MPa in both cases. With the high speed PVC piston this was achieved with just one reflection from the die base. In contrast, the shock wave originating from the slower steel piston required two reflections to reach this amplitude. In terms of the powder flow velocities, the important difference between these two cases is that this pressure was achieved with a much lower peak particle velocity (118 m/s) for the steel piston compared with that for the PVC piston (177 m/s).

4. COMPACTION TIME

So far attention has been fixed on wave motion in the powder only. There are also wave reflections in the piston and die. The most important of these is the wave system in the piston since it is the most difficult to control. On impact there is a compressive wave propagating back through the piston (Fig.2). This is reflected as a tensile wave from the free surface of the piston and contributes to the unloading process when it arrives back at the piston/powder interface. The time between piston impact and the arrival back at the interface of this unloading wave is a characteristic "compaction time". It is desirable to maximize the number of reflections producing increased compressive stress before the arrival of this unloading wave. At the very least, the compaction time should not be less than the time for the primary shock and the first reflected shock to pass through the powder. Applying one-dimensional shock wave analysis again, this translates into the requirement that

$$\frac{L}{x_1} > \frac{1}{2} c_p \left[\left\{ \frac{\rho_1(\rho_2-\rho_1)}{\rho_2 P_2} \right\}^{\frac{1}{2}} + \frac{\rho_1}{\rho_2} \left\{ \frac{\rho_2(\rho_3-\rho_2)}{\rho_3(P_3-P_2)} \right\}^{\frac{1}{2}} \right] \qquad (8)$$

where L is the piston length, x_1 the initial depth of the powder and the other symbols as defined previously. The minimum piston length required is therefore dependent on all the shock initiation and reflection events described above. However, for given powder and impact conditions, the wave speed through the piston determines the minimum piston length.

As in section 3(b), a conflict can be seen here in the ideal requirements for the piston. The large impedance necessary to maximize pressure gain by reflection requires a high sound speed and high density (Table 1). But a high sound speed means that the piston must be long to gain a satisfactory compaction time to take advantage of the favourable reflection character- istics. The longer the piston, the heavier it is and the lower is the impact velocity and hence primary shock strength for a given reservoir pressure. To achieve the necessary high pressures in the powder by means of repeated reflections, heavier pistons must have a higher kinetic energy on impact. This can best be illustrated by calculating the energy requirements for the two cases shown in Table 2. For the same compaction time, necessary to develop the same peak pressure, the ratio of steel piston length to that for PVC is 3.25. The kinetic energy on impact will be proportional to the product of density, length and the square of the velocity. Thus, for the cases shown in Table 2 the kinetic energy of the steel piston would need to be 3.91 times that of the PVC piston.

5. CONCLUSIONS

Very large pressures can be developed in powdered materials using a relatively light and simple apparatus employing the shock wave generated when a projectile (piston) impacts onto the powder. Further enhancement of the pressure can be achieved by utilizing reflections of the shock wave .

For powders conforming to the Kawakita equation of state, these shock reflections depend on the relative magnitudes of the impedance of the reflecting surface on the one hand, and the geometric mean powder impedance on the other. If the reflecting surface has a higher impedance, reflection causes further powder compression but if the reflecting surface impedance is lower, the reflected wave is an unloading wave.

The peak pressure and peak particle velocity can be independently controlled by appropriately exploiting the wave nature of the pressure build-up in the powder. The peak velocity can be minimized by tayloring the operation so that the peak pressure is built up by means of repeated shock reflections. The ability to take advantage of this mechanism is limited by the length of the piston. In practical terms this translates into a requirement for higher piston energies compared with those necessary for a light high speed piston producing the same peak pressure.

REFERENCES
1. BLAZYNSKI,T.Z. (Ed) "Explosive Welding, Forming and Compaction" Applied Science Pub. 1983.
2. SANO,Y. "A Continuum Approach to Dynamic Compaction of Metal Powder" Int.J.Powder Met.and Powder Tech. Vol.13, 1977, pp 81-98.
3. RAYBOULD,D. "The Dynamic Compaction of Aluminium and Iron Powder" Proc.15th Int.Machine Tool Design and Research Conf. Birmingham, 1974,MacMillan Lond. 1975, p.627.
4. RAYBOULD, D. "The Cold Welding of Powders by Dynamic Compaction" Int.J.Powder Met. and Powder Tech. Vol.16, 1980, pp.9-19.
5. RAYBOULD,D. "Wear-Resistant Al-Steel-Pb Admixed Alloys Produced by Dynamic Compaction" Powder Metallurgy Vol.25, 1982, pp.35-41.
6. RAMBERGER,R. and BURGER,A. "On the Application of the Heckel and Kawakita Equations to Powder Compaction" Powder Technol. Vol.43, 1985, pp.1-9.
7. KAWAKITA,K. and LUDDE, K-H. "Some Considerations on Powder Compression Equations" Powder Technol. Vol.4, 1970, pp.61-68.

TABLE 1	SOME PROPERTIES OF PISTON MATERIALS		
Material	Density (kg/m)	Sound Speed (m/s)	Impedance (kg/ms)
Polyvinylchloride (rigid) Steel	1390 7870	1590 5160	2.2×10^6 40.6×10^6

TABLE 2	CONDITIONS AFTER REPEATED SHOCK REFLECTIONS						
Piston	u_p (m/s)	P_2 (MPa)	u_2 (m/s)	P_3 (MPa)	u_3 (m/s)	P_4 (MPa)	u_4 (m/s)
PVC	260	184.1	176.6	858.3	21.12	596.7	-10.05
Steel	120	97.65	117.6	347.2	8.542	855.8	98.95
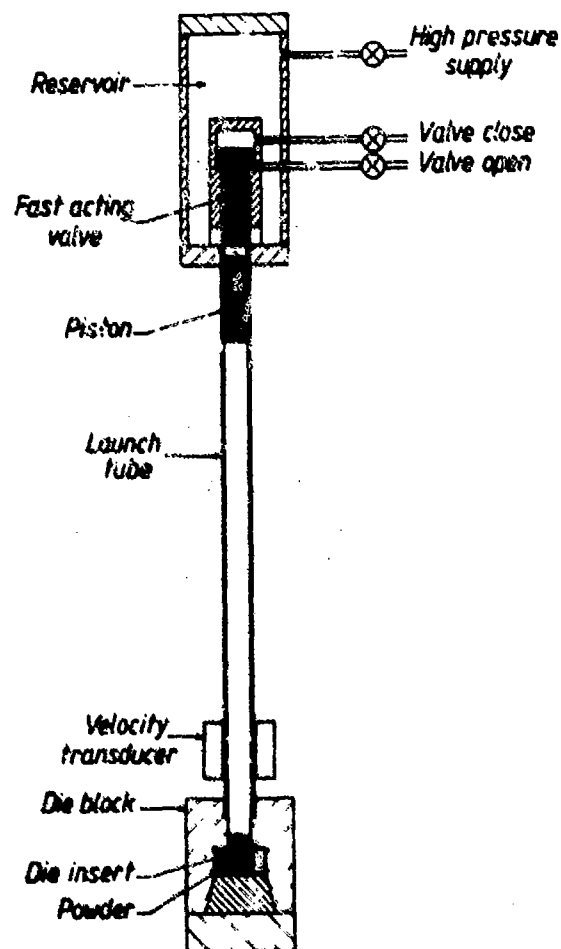
Fig.1   Compaction Apparatus
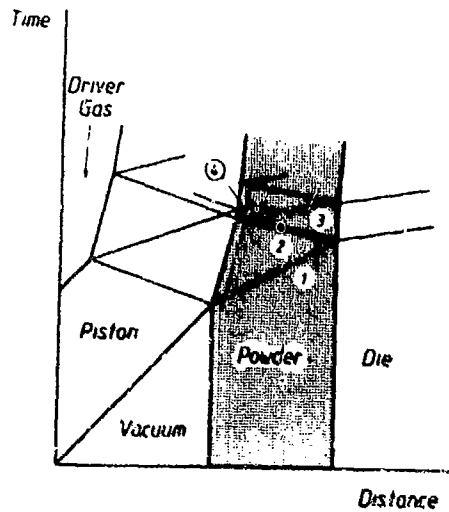
Fig.2　Wave Diagram
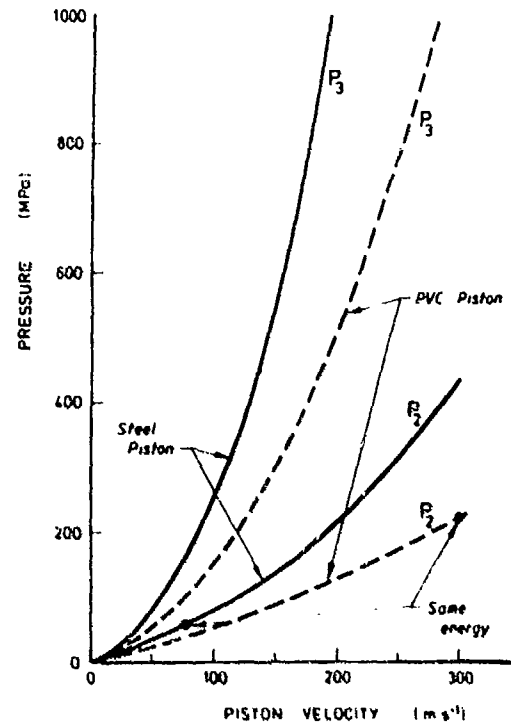
Fig.3　Relation between Piston Velocity and Shock Strength for Iron Powder and Steel Dies.
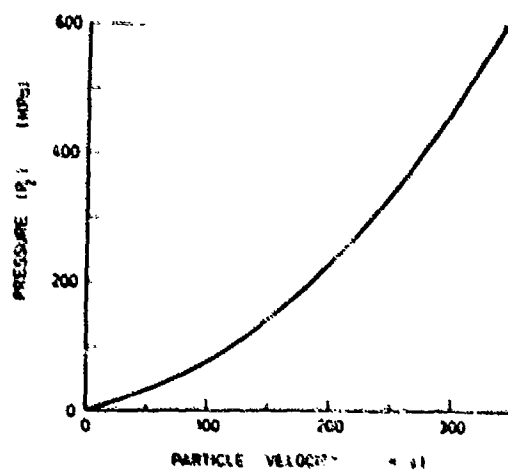
Fig.4　Relation between Particle Velocity and Primary Shock Strength for Iron Powder.
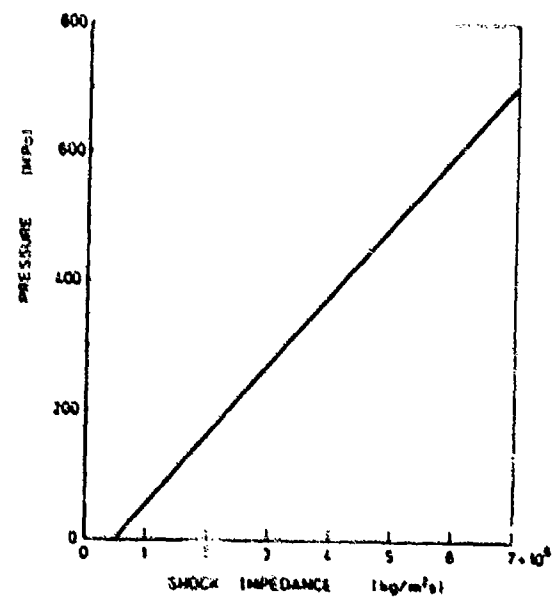
Fig.5　Variation of Shock Impedence with Pressure for Iron Powder.

MICROSCOPIC SIMULATIONS OF SHOCK PROPAGATION IN CONDENSED MEDIA:

COMPARISON BETWEEN REAL TIME AND FREQUENCY DOMAINS*

A. M. Karo, J. R. Hardy,** and M. H. Mehlman
Lawrence Livermore National Laboratory
Livermore, California 94550

**Behlen Laboratory of Physics, University of Nebraska
Lincoln, Nebraska 68588

Computer molecular dynamics (CMD) is now recognized as a
very powerful technique for examining the microscopic
details of a wide variety of chemical and physical
phenomena, including the shock-induced fast decomposition
processes that characterize the shock-initiation of
energetic materials. The purpose of the present paper is
to describe some results obtained by new methods of post
processing of CMD data. First we present a pictorial
history of a canonical system which is bonded with
identical potentials and has identical atomic masses. We
then present Fourier transforms of the energy components of
different units judiciously chosen to show the "frequency
fingerprint" of the shock impact and passage through
specific units of the system, including, e.g., the behavior
of spalled fragments.

To complement these studies, we also display the behavior
of our canonical system when defects (point or line) are
present. In these studies we monitor the motion of diatoms
above and below a line defect consisting of heavy masses.
The Fourier transform techniques provide optimum compromise
histories which present neither too much nor too little
detail.

1. INTRODUCTION

Of the three/four states of matter: solid, liquid and gas/plasma, the
last differs far more radically from the first two than the first two do from
each other. The primary difference, from which all others largely spring, is
that of density or volume/particle. While this is essentially unchanged at
the solid-liquid transition, at the liquid (or solid)-gas transition the
volume/particle ratio increases by many orders of magnitude (at least by 10^5
and often by far more). Consequently, the zero order theoretical approximation
is that of an assembly of largely non-interacting free particles (the "ideal
gas"). This has the consequence that workers dealing with shock phenomena in
gases recognize, either explicitly or implicitly, that there are fundamental
limitations on the continuum hydro-codes used to model hydrodynamic phenomena,
and that shock fronts are beyond those limits. As a consequence of this
realization, the shock is regarded as a discontinuity about which hydro-codes
can say essentially nothing and is simply modelled by imposing the Hugoniot
jump conditions across the shock front.

The recognition of this limitation stems from a proper understanding of gaseous behavior which acknowledges that thermodynamic concepts, such as pressure and temperature, can only be defined for regions large compared with the mean free path of molecules in the gaseous phase. Since shock fronts arise from non-linearities in the basic (Navier-Stokes) equations, they will automatically steepen until their width is at the mean free path limit. Thus the front is recognized as a special region whose full understanding can only be achieved by a detailed examination of the microscopic behavior of the molecules in the shock region. Specifically, it comes as no surprise that collisions between them can lead to bond rupture, even though the temperatures behind and in front of the shock are well below that required for thermal dissociation.

The study of shocks in condensed matter has suffered from the lack of any such clear-cut criterion. Thus, hydrocode studies of shock propagation in solids are carried through with the inclusion of a viscous (lossy) damping in the equations and typically give shock widths of millimeters and rise times of microseconds, both of which appear to agree with experiment. However, 0.5 mm/μsec = 5.0 Å/picosecond. Thus, if we have a front which is composed of a sequence of "steps" of width ∿ interatomic spacing, it will appear to show a microsecond rise time if it is examined by probes which are of millimeter dimensions; however, what these observations are actually reflecting are the natural time and frequency scales of interatomic motion.

Once this is realized it is apparent that the hydro-codes are being forced beyond the same natural limit as that for gaseous media; namely, the mean interatomic spacing which, in condensed materials, fills the same role as the mean free path in gases. The proper way to resolve this difficulty is to examine the propagating shock front at the microscopic (atomic) level; experimentally, this is beyond the limits of spatial and temporal resolution currently available simultaneously, although recent work has demonstrated that when both "windows" (limits) are reduced, the shock width shrinks in the manner we would predict. However, it is both easier and much cheaper to do a computer experiment using the techniques of computer molecular dynamics (CMD). These involve setting up in the computer the Newton's law equations of motion for an assembly of atoms bound in regular or irregular arrays and numerically integrating them to determine the system's temporal history, following initial impact loading.

Over the past ten years, we have carried out many such studies,[1] but most recently[2,3] we have been concerned with developing post-processing techniques that will enable us to present in a compact and manageable form the temporal histories of each simulation, without resorting to such broad averaging that the detailed behavior of the shock is lost or obscured. It is in the nature of the these simulations that they contain all possible information, and one can scan this by generating a movie of each history--however, this provides qualitative rather than quantitative insight.

In this paper we wish to present early results of applying two post-processing techniques both to one of our original canonical studies and to a related simulation designed to show the effects of lattice irregularities or defects.

2. NATURE OF THE SIMULATIONS

The techniques of CMD are now well documented by both others and ourselves.[1,4] The only novel features are the use of "neighborhood look-up"

procedures to keep track of the interatomic bonding, and the use of various post processing options such as Fourier transforms of the energy components of different units or regions of our assembly.

2a. STUDIES OF THE IDEAL SYSTEM

This consists of a regular two-dimensional array of atoms all identical and identically bonded to their first and second neighbors.* This array is shocked by bringing in with uniform velocity from the left a "plate" made up of an identical lattice. We then examine the temporal evolution of the system. In Fig. 1, we show selected stills from a movie history of the system which are of interest in their own right, since, in our original simulation, we had no provision for "look up" (a procedure which periodically updates the bonds retained); thus the configurations at later times, when radical particle rearrangements have taken place, were unrealistic.

We next proceeded first to tag the single atom indicated in Fig. 1 and then to tag the whole spall as a single unit. In Fig. 2, we show the energy flux into and out of the motion of the single tagged atom as the shock passes it, and the flux of energy into the spalled end as the spall developes. (A pointed end was chosen as displaying the most interesting behavior.)

These histories of energy flux permit general statements, but they also show that they are neither the clearest nor most compact presentations. Fairly clearly one has a number of sinusoidal, or near-sinusoidal, oscillations superposed. Given this situation in the temporal domain, the natural method of data reduction is that appropriate to signal processing: the Fast Fourier Transform (FFT). This provides a "fingerprint" identification of the various types of characteristic frequencies in any given atomic/molecular process.

These transforms are shown in Figs. 3 and 4 for the single atom and the spall. In order to retain sufficient temporal discrimination to display separately clearly distinct parts of the history (e.g., before and after spall), the temporal range was split into segments, and each was separately transformed. The most interesting feature is the rapid build up of higher frequency components in the spall motion as time proceeds.

2b. STUDIES ON IMPERFECT SYSTEMS

In view of the importance of the interactions of shocks with lattice irregularities or surfaces, processes which seem to provide the most efficient means of conversion of shock-energy into single atom/radical energy, we decided to examine the behavior of our canonical system when we introduced a line defect. We, therefore, set up the situation shown in Fig. 5 in which we have a line defect (for simplicity represented by heavy substitutional atoms of mass 100, a zero order approximation to a dislocation or twin boundary), and monitored two diatomic units situated such that one (the lower) is unshielded by the line defect and the other shielded. The shock was launched by the standard plate impact method. For brevity, we only show the transform (windowed as before) for both tagged diatoms in Fig. 6.

---

*We have the capability to study three-dimensional systems. In initial, survey types of calculations it is much more economical to restrict ourselves to two-dimensional systems. The addition of the third dimension introduces quantitative rather than qualitative changes.

It should be noted that the "shelter" is not particularly efficient: the reason for this is that the line of heavy atoms so distorts the shock front that considerable energy is projected diagonally upwards into the "sheltered" region. It is, however, apparent that the higher frequency components are suppressed in the sheltered region. Thus, it is evident that the shielding is most efficient for the higher frequency components of the motion.

3. CONCLUSIONS

The present rather preliminary studies clearly demonstrate the potential usefulness of the FFTs as a means of data reduction. The actual histories studied here have no very dramatic features, but they demonstrate clearly that high frequency molecular motions are readily excited by shock loading; however, such high frequency motions are more inhibited in their motion by heavy defects, or, probably, "soft" bonds.

REFERENCES

1. Karo, A. M and Hardy, J. R., "The Study of the Fast Shock-Induced Dissociation by Computer Molecular Dynamics," Proceedings of the NATO Advanced Study Institute on Fast Reactions in Energetic Systems (D. Reidel Publishing Co., Dordrecht-Holland, Boston, USA, 1981), p. 611.

2. Karo, A. M., Walker, F. E., DeBoni, T. M., and Hardy, R. J., "The Simulation of Shock-Induced Energy Flux in Molecular Solids," Progress in Aeronautics and Astronautics Vol. 94, 1985, p. 405.

3. Walker, F. E., Karo, A. M., and Hardy, J. R., "Non-Equilibrium Effects Seen in Molecular Dynamics Calculations of Shock Waves in Solids," Proceedings of the NATO Advanced Study Institute on Nonequilibrium Cooperative Phenomena in Physics and Related Fields (Plenum Press, 1983), p. 363.

4. MacDonald, R. A. and Tsai, D. H., "Molecular Dynamical Calculations of Energy Transport in Crystalline Solids," Physics Reports, Vol. 46, September 1978, p. 1.
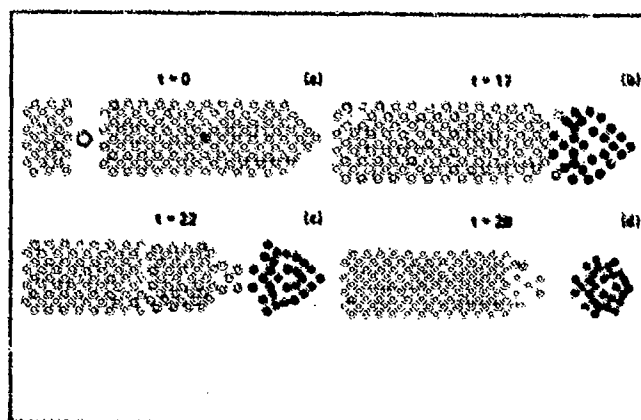
Figure 1. Configurations for a shocked monoatomic lattice (time in units of 10^{-14} s): a) t = 0 shows tagged atom; b) t = 17; c) t = 22; d) t = 28.
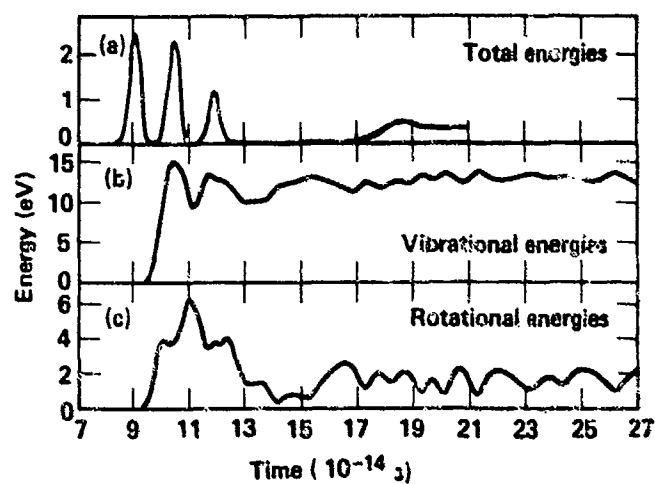
Figure 2. Histories of the vibrational energy: a) For the single tagged atom; b) For the spalled fragment; c) History of the rotational energy of the spalled unit.

Figure 3. Fast Fourier transforms (FFTs) for the vibrational energy of the atom tagged during the Fig. 2 run (time in units of 10^{-14} s): a) FFT, t = 0-10; b) FFT, t = 10-20.
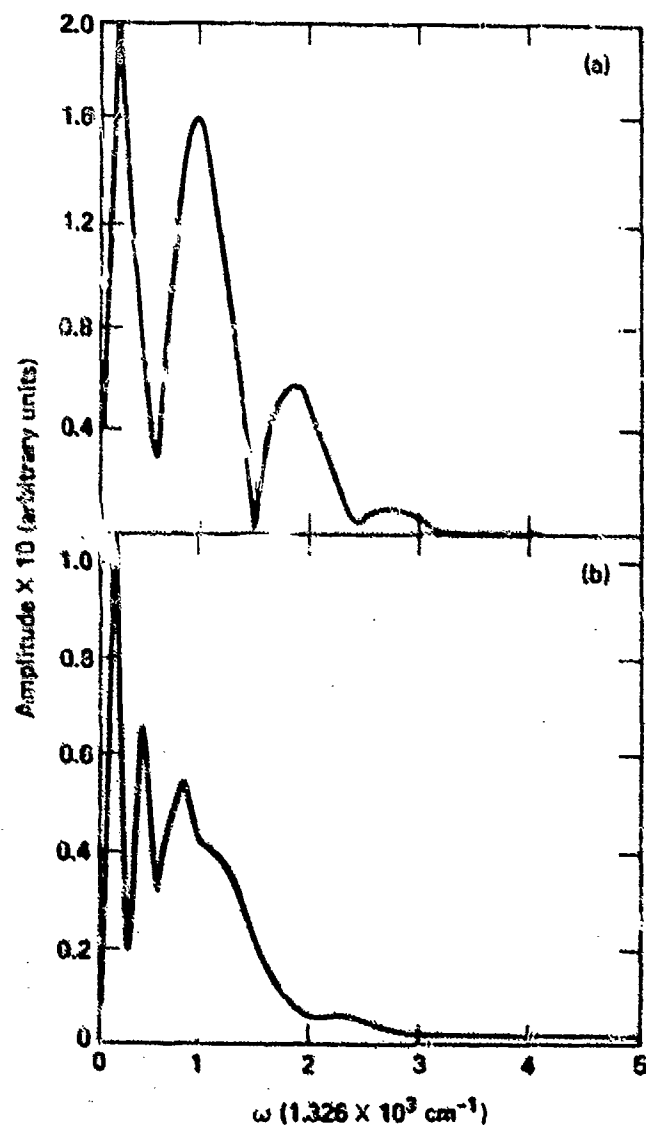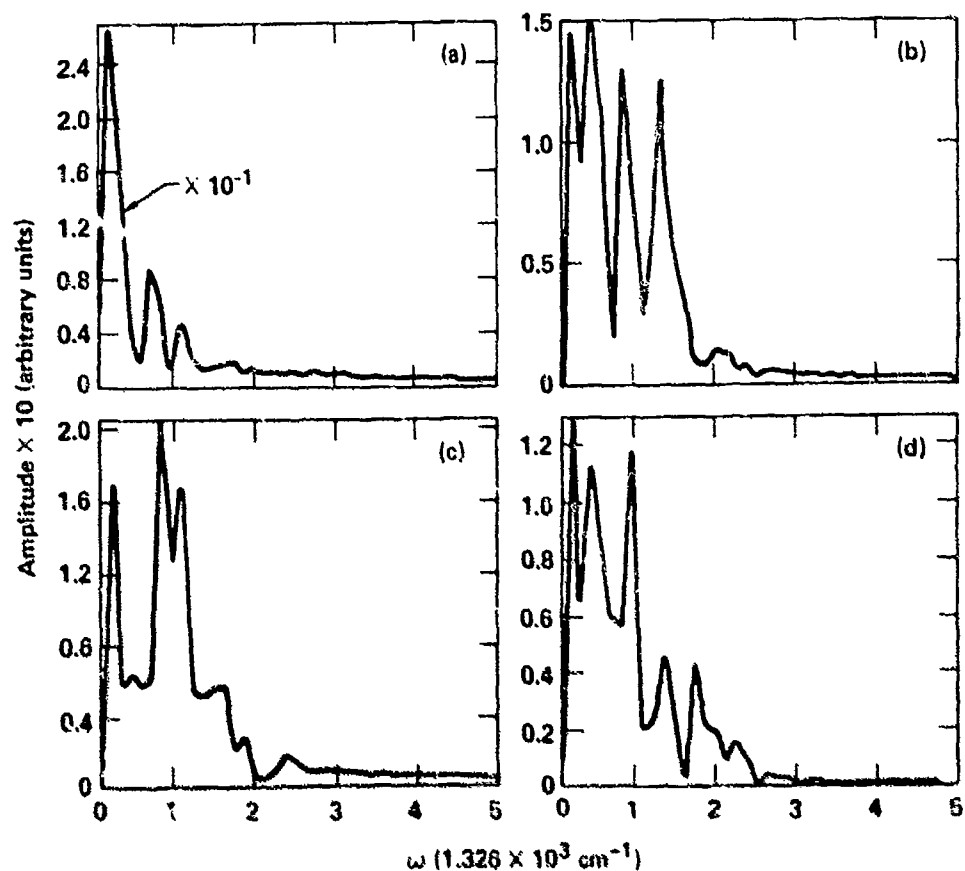
Figure 4. FFTs of the vibrational energy of the spalled fragment (time in units of 10^{-14} s): a) t = 7-17; b) t = 17-27; c) t = 28-38; d) t = 38-48. Note the build up of higher frequency components after spall.
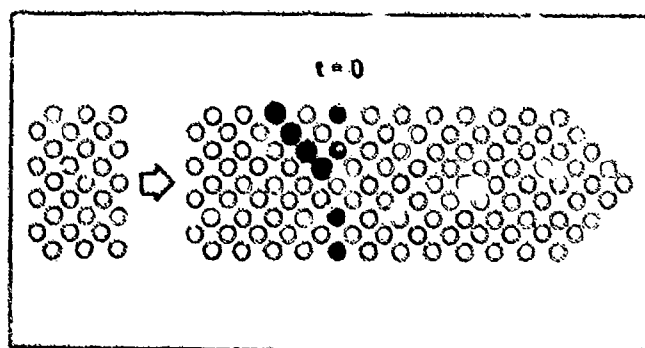
Figure 5. Initial configuration for the shock impact on an imperfect system showing the line defect (mass 100 atoms) and the two diatoms whose vibrational energy is tagged.
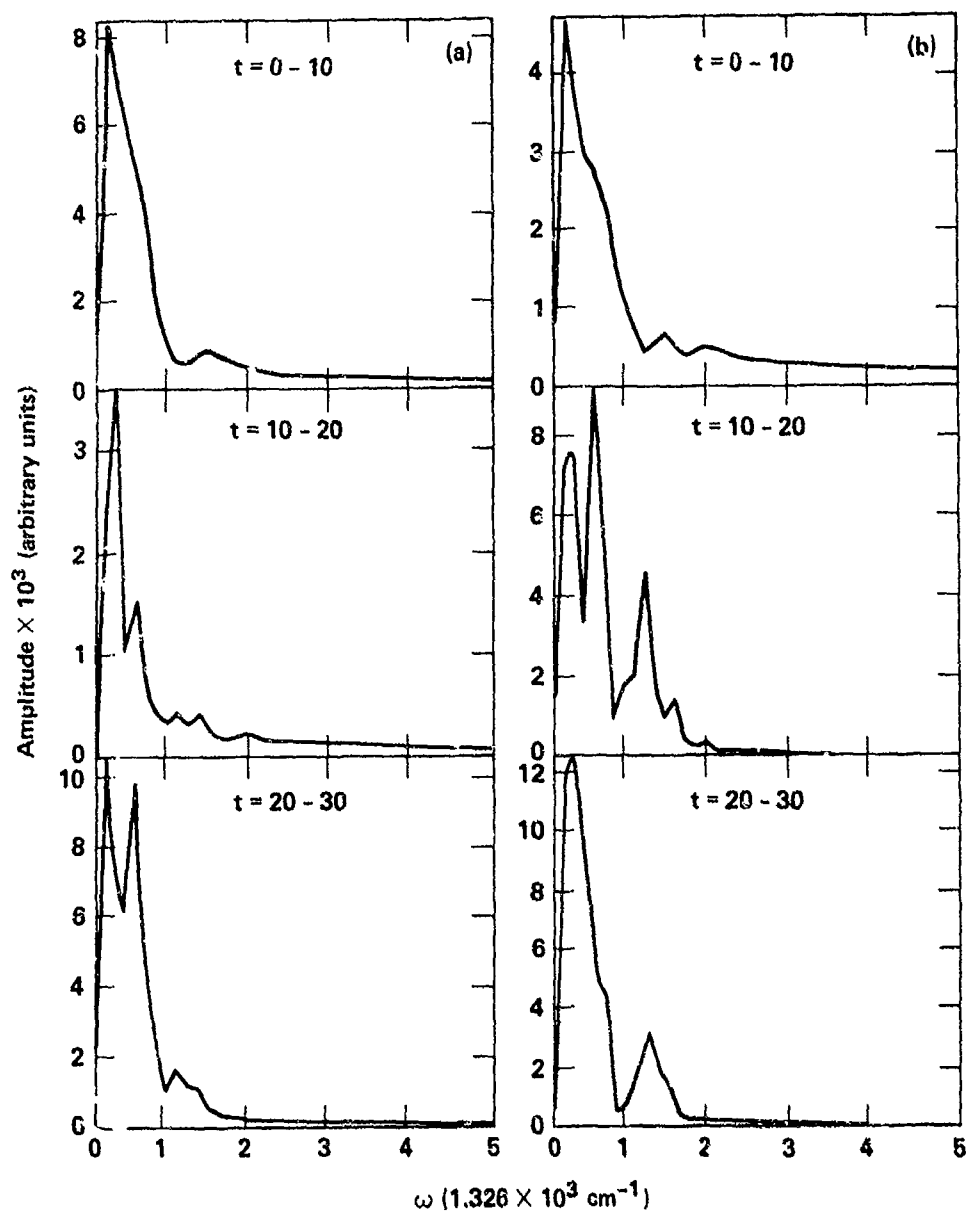
Figure 6.   FFTs of the diatom vibrational energies: a) "Sheltered" (upper) diatom; b) "Exposed" (lower) diatom.

SHOCK WAVE INTERACTION WITH NUCLEAR FUEL
BUNDLES IN GAS-LIQUID STRATIFIED FLOW
INSIDE PRESSURE TUBES

S.C. Sutradhar and J.S. Chang
Department of Engineering Physics
McMaster University
Hamilton, Ontario, Canada L8ᵃ 4M1

SUMMARY:

A theory is proposed to estimate the strengths of reflected and transmitted shock waves after an interaction with CANDU nuclear fuel bundles. The experimental results show good agreement with the theoretical analysis. For the type of fuel bundles considered here, the choking associated with the transmitted wave in the gas phase influences the strength of the wave downstream of the bundle. The experimental observations in a two-phase stratified system indicate a moderate increase in the strength of the reflected and transmitted waves in the phases.

INTRODUCTION:

The interaction of weak shock waves with the permeable materials in connection with the sound attenuating devices is gaining considerable attention in recent years. As the shock wave is allowed to be incident on the permeable materials, a reflected wave propagates upstream, and depending on the type of the permeable materials, a part of the wave transmits through them. Compressible flow through porous materials is investigated by Emanuel and Jones [1], and Beavers and Sparrow [2] for estimating the Mach numbers at different locations inside the porous materials. The reflection of the weak shock waves is dealt with by Beavers and Matta [3], using the shock wave speed upstream of the porous materials to evaluate the strength of the reflected shock waves. The flow through the porous fibrous materials with negligible inertia of the fluid has been discussed extensively by Collins [4] and Scheidegger [5]. For the high speed case, the flow inertia plays an important role and, the severe constrictions and the frictional losses offered by the passage result in the choking of the flow.

In CANDU-type nuclear reactors, the fuel bundles having definite number of fuel elements are placed inside the horizontal pressure tubes where the flow of coolant is allowed through these bundles. In the event of LOCA (Loss of Coolant Accident) weak shock waves may be generated inside the pressure tubes and these waves during their course of travel, will encounter with these fuel bundles. The flow stratification, which is an aftermath of a LOCA, has dominating influence in controlling the speed of the shock wave due to the compressibility effect of the gas phase [6,7]. The incompressibility of the liquid phase enhances the overpressure of the shock wave due to the reduction of compressible flow area, however the presence of the gas-liquid interface induces frictional loss to the system.

In this paper, the study of shock wave interaction with the nuclear fuel bundles in gas-liquid stratified flow inside the pressure tube has been conducted both experimentally and theoretically. The magnitude of overpressure in the two phase system is estimated assuming an adiabatic, but irreversible energy balance between a two phase system and to that of a single phase (gas) system. However at present only the experimental results for the pressure rise in a two phase system are provided and experimental and theoretical investigations in a gas phase system are presented. The porosity [1,2] of the fuel bundles, which determines the strength of the reflected and transmitted shock waves, is used as a resistance parameter [8] in the analysis. The equations obtained are solved using Newton-Raphson iterative method taking care of the effect of choking that occurs at higher incident pressure of the shock wave.

EXPERIMENTAL SET-UP:

A cylindrical aluminum shock tube 2.0 m long and 10.2 cm i.d., in which fuel bundles containing appropriate number of fuel elements can be placed inside it, is used. The weak shock waves (Mach Number = 1.15 ~ 1.3) are allowed to interact with these bundles and the incident and reflected shock waves in gas and liquid phases are measured at a distance about 10.0 cm upstream of the fuel bundle. The strength of the transmitted wave is measured 30.0 cm downstream of the fuel bundle.

Piezotype pressure transducers (Sundstand Data Control Inc. Model 211B5) are used to measure the over-pressures and these pressure signals are stored in a microcomputer through a Transient Memory (Kawasaki Electronica, TM 1410, 1 μsec per sample, 1 KW) and a homemade interface. Liquid levels inside the shock tube are measured using the ultrasonic liquid level metering technique as well as the mechanical type liquid level meter.

FORMULATION:

The mode of shock wave interaction with the fuel bundle is shown in Figure 1. The porosity, μ is defined as the ratio of the pore cross sectional area to the total cross sectional area normal to the flow. The resistance or blockage parameter, B estimated for different fuel bundles is presented in Figure 2. The strength of the wave reflected from an impermeable substance for a known strength of the incident shock wave is obtained using the principle of superposition of two shock waves moving in opposite direction as follows [9]:

$$\frac{p_c}{p_o} = \left[2 \left(\frac{p_1}{p_o} \right)^{(\gamma-1)/2\gamma} - 1 \right]^{2\gamma/(\gamma-1)} \tag{1}$$

where p_c is the pressure of the completely reflected wave, p_1 is the pressure of the incident wave, p_0 is the reference (atmospheric) pressure and γ is the ratio of specific heats of the gas under consideration. In the development of the present analytical model for weak shock waves, only mass and momentum balances with no heat transfer are considered. If p, ρ, u and W represent the pressure, density, particle velocity and shock wave velocity, respectively, then for the reflected wave, the conservation of mass and momentum respectively becomes:

$$\rho_1(W_2 + u_1) = \rho_2(W_2 + u_2) \tag{2}$$

$$p_1 + \rho_1(W_2 + u_1)^2 = p_2 + \rho_2(W_2 + u_2)^2 + B(p_c - p_2) \tag{3}$$

where the subscripts 1 and 2 are for incident and reflected waves respectively. The values of u_1 and ρ_1, which are the functions of the incident shock wave, may be obtained from the standard shock wave relations [11]. The equation (2) and (3) can be combined to find an implicit equation for the strength of the reflected wave as follows:

$$\frac{p_2}{p_o} = \frac{p_1}{p_o} + \frac{\rho_1}{p_o}(W_2 + u_1)^2 \left(1 - \frac{\rho_1}{\rho_2} \right) - B \left(\frac{p_2}{p_o} \right) \left(\frac{p_c}{p_2} - 1 \right) \tag{4}$$

If subscript 3 denotes the conditions pertaining to the transmitted wave, then the conservation of mass and momentum respectively becomes:

$$\rho_2 u_3 = \rho_3 u_3 \tag{5}$$

$$p_2 + \rho_2 u_2^2 = p_3 + \rho_3 u_3^2 + B(p_2 - p_o) \tag{6}$$

Combining equations (5) and (6), the strength of the transmitted wave is expressed as

$$\frac{p_3}{p_0} = \frac{p_2}{p_0} + \frac{p_2}{p_0}\left(1 - \frac{u_3}{u_2}\right)u_2^2 - B\left(\frac{p_2}{p_0} - 1\right) \tag{7}$$

where u_3 is evaluated corresponding to a pressure of p_3 using shock wave relation [11]. For the transmitted wave, the effect of choking which is an inevitable phenomenon for the transmitted wave having Mach numbers more than unity, is calculated using Fanno flow condition [11] through the passage. The wall friction factor f is estimated using the formula [12]:

$$\frac{1}{\sqrt{f}} = 2.0 \log_{10}(\mathrm{Re}\sqrt{f}) - 0.8 \tag{8}$$

As a first approximation, the bundle-shock tube assembly is considered a simple convergent nozzle with a finite exit length for the transmission of shock wave. Depending on the inlet Mach Number to the bundle, the transmitted wave strength is modified by the amount of frictional loss using the Fanno flow system as follows [11]:

$$f\frac{L_{max}}{D_h} = \int_M^1 \frac{2(1-M^2)}{\left(1+\frac{\gamma-1}{2}M^2\right)M^3}\,dM \tag{9}$$

where L_{max} is the length to point of sonic condition, D_h is the hydraulic diameter of the bundle system, M is the entrance Mach Number.

The propagation velocity of a shock wave is not influenced by the presence of a liquid phase in a stratified system, however, this liquid phase actually affects the magnitude of the overpressure of the wave travelling through the phases [7].

RESULTS AND DISCUSSION:

For 18-, 27- and 37-element bundles used in CANDU-type nuclear reactors, the respective porosity 0.24, 0.29 and 0.32 obtained from the physical measurements of the bundle elements are shown in Figure 2 along with the theoretical values of the bundle resistance B. The reflected shock wave strength as a function of the incident shock wave strength for various bundle porosities is shown in Figure 3. For a bundle having more pore area, the reflected wave is weaker than the reflected wave from a bundle having less pore area. The fuel bundle having 37-element (porosity - 0.32) has more flow area than compared to other type of bundles under consideration. The curve for completely reflected pressure wave is also drawn for the purpose of comparison. Except at low incident pressure ratios, the magnitude of the reflected pressure increases almost linearly with increasing incident shock wave strength. The strengths of the waves transmitting through the fuel bundles are presented in Figure 4 for various porosities. The discontinuities observed in Figure 4 are due to the effect of choking inside the passages. More the area reduction, weaker is the transmitted wave and faster is the choking effect. Beyond the choking range, the variation of transmitted wave strength is linearly proportional to the strength of incident shock waves. On either side of the choking region the experimental results agree quite well with the theoretical estimation of the pressure rise (Figure 4).

For a two-phase stratified system, the shock wave interaction with the fuel bundles has revealed the condition of enhanced strength of the reflected shock waves. In fact, the strength of the incident shock wave is found to be increasing due to the reduction in cross-sectional area of the compressible phase. This stronger wave when reflected by a fuel bundle shows a significant increase in the strength with the increase of liquid level. Although the presence of liquid does not change the effective flow area of the fuel bundle, however, it reduces the effective cross-sectional area of the compressible phase of the system. Hence, the increase in the strength of the shock wave may be attributed to the reduction of the area of the compressible phase. As shown in Figure 5, the non-linear increase in strength of the reflected waves at higher liquid levels is an indication of the effect of liquid level reducing the compressible flow area. However, the reduction in the flow area is observed to have

more and more predominant effect on the waves transmitting through the bundle as a result of the occurrence of choking inside the bundle. Figure 6 depicts the effect of choking on the transmitted wave where the shock strenght downstream of the bundle is observed to have diminishing strengths for higher liquid levels. The typical wave forms for the reflected and transmitted shock waves in the gas and liquid phases are presented respectively in Figures 7 and 8. The wave form for a reflected shock wave in the gas phase indicates a sharp jump in the overpressure, whereas that in the liquid phase shows a dispersive form of the pressure rise. The time-averaged magnitude of the overpressure is observed to be identical in both the phases. Now, considering the case of a transmitted wave form after the fuel bundle (Figure 8), the wave form in the gas phase exhibits a sharp rise of the overpressure and that in the liquid phase has a dispersive type of rise in overpressure.

CONCLUSION

A theoretical model, based on the single phase flow system, is developed to estimate the strength of the reflected and transmitted shock waves after its interaction with fuel bundles of known porosity. The occurrence of choking has an influence in the estimation of the transmitted wave strength. The reflected wave is not affected by the phenomenon of choking. For a two phase situation, the strength of the waves are found to be increasing with the increase of liquid level inside the pressure tube. The shock wave propagation speed which is strongly controlled by the gas phase compressibility, is not affected by the presence of the liquid phase in the system.

ACKNOWLEDGEMENTS

REFERENCES

1.   Emanuel, G. and Jones, J.P., "Compressible Flow Through a Porous Plate", Int. J. Heat Mass Transfer, vol. 11, 1968, pp. 827-836.

2.   Beavers, G.S. and Sparrow, E.M., "Compressible Gas Flow Through a Porous Material", Int. J. Heat Mass Transfer, vol. 14, 1971, pp. 1855-1859.

3.   Beavers, G.S. and Matta, R.K., "Reflection of Weak Shock Waves from Permeable Materials", AIAA Journal, vol. 10, 1972, pp. 959-961.

4.   Collins, R.E., "Flow of Fluids Through Porous Materials", Reinhold Publishing Corp., New York, 1961.

5.   Scheidegger, A.E., "The Physics of Flow Through Porous Media", University of Toronto Press, 1974.

6.   Morioka, S. and Matsui, G., "Pressure Wave Propagation Through a Separated Gas-Liquid Layer in a Duct", J. Fluid Mechanics, vol. 70, part 4, 1975.

7.   Sutradhar, S.C., Yoshida, H. and Chang, J.S., "Shock Wave Propagation in a Horizontal Stratified Gas-Liquid System in Straight and 'TEE' Tubes", Shock Tubes and Waves, Ed. R. Douglas and B.E. Milton, New South Wales University Press, 1983, pp. 435-444.

8. Yoshida, H., Tazawa, M. and Honma, H., "Reflection and Transmission of Weak Shock Waves Incident upon a Porous Material", 58th National Meeting of JSME, 1980, Hokkaido University, Japan.

9. Wade, J.H.T., private communication.

10. Liepmann, H.W. and Roshko, A., "Elements of Gas Dynamics", John Wiley and Sons, Inc., 1960.

11. Shapiro, A.H., "The Dynamics and Thermodynamics of Compressible Fluid Flow", Ronald Press Company, New York, 1953.

12. Rudinger, G., "Non-steady Duct Flow: Wave-diagram Analysis", Dover Publications, Inc., New York, 1969.
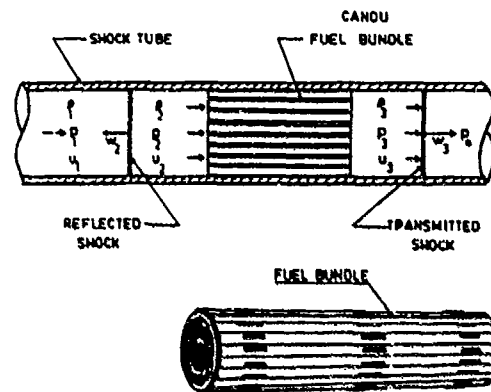
Fig.1: Schematic of shock wave interaction with fuel bundle.
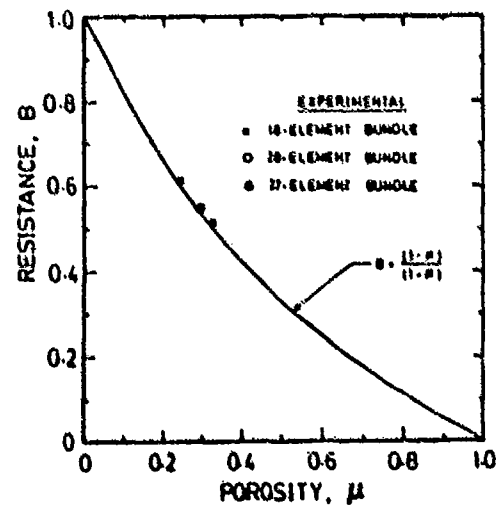
Fig.2: Porosity vs. Resistance for different fuel bundles.
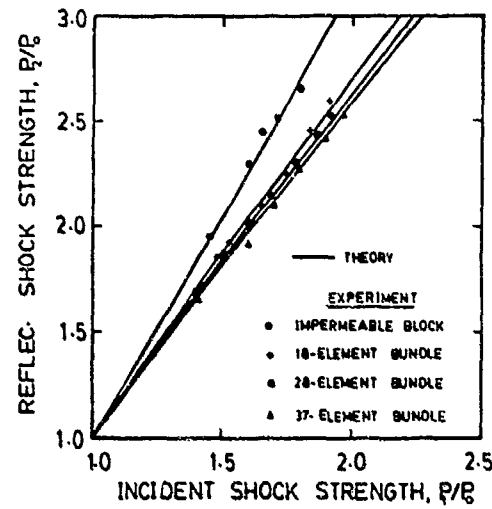
Fig.3: Reflected vs. inci-
dent shock strengths in
single (gas) phase.
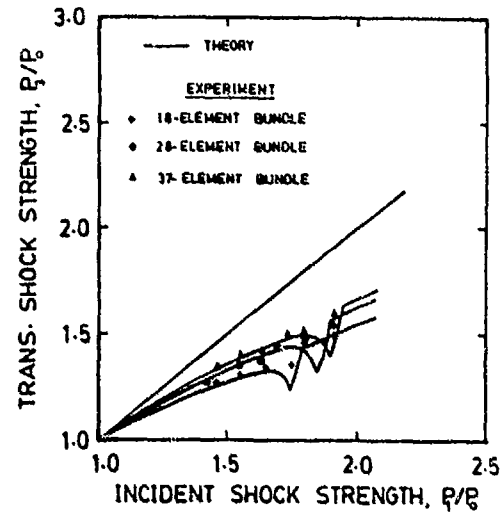
Fig.4: Transmitted vs. inci-
dent shock strengths in single
(gas) phase.
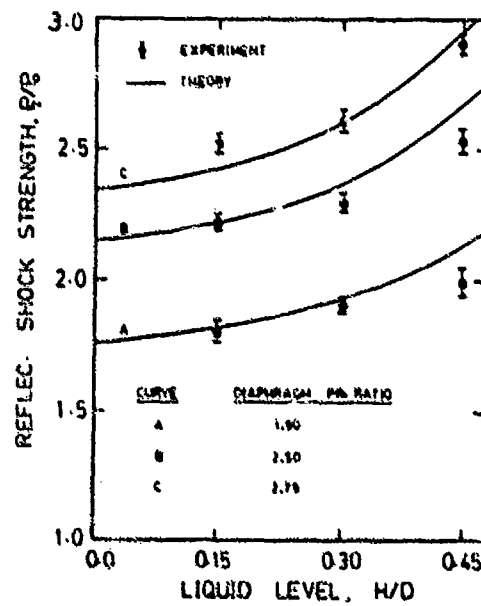
Fig.5: Two-phase reflected
shock strengths vs. liquid
levels for 37-element fuel
bundle.
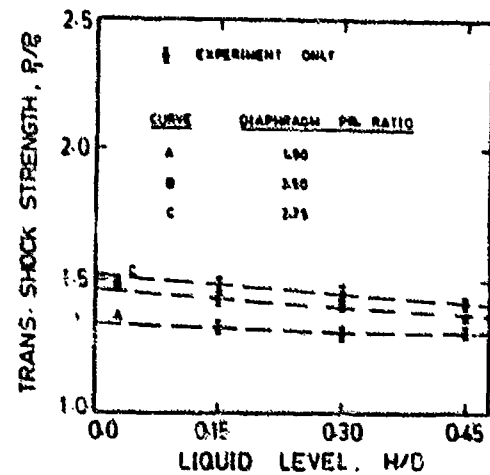
Fig.6: Two-phase transmitted
shock strengths vs. liquid
levels for 37-element fuel
bundle.

TIME (msec) ————→

(i)

TIME (msec) ————→

(ii)
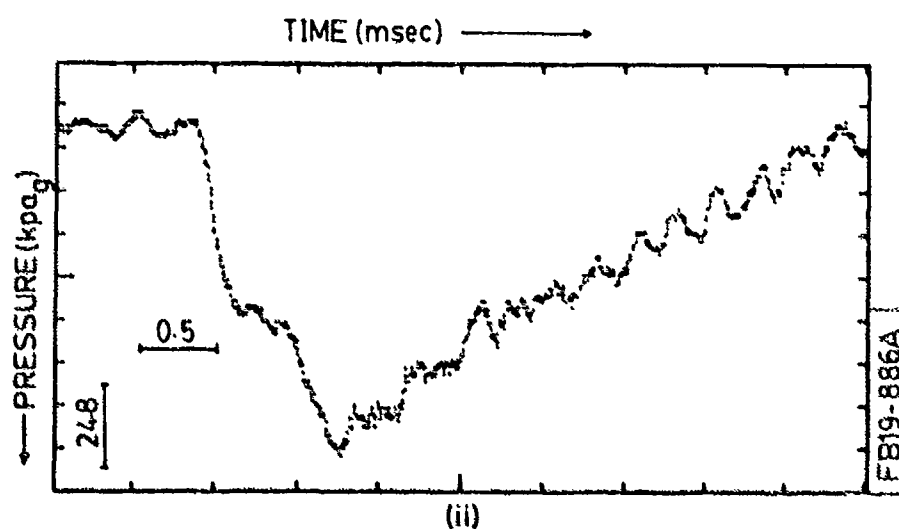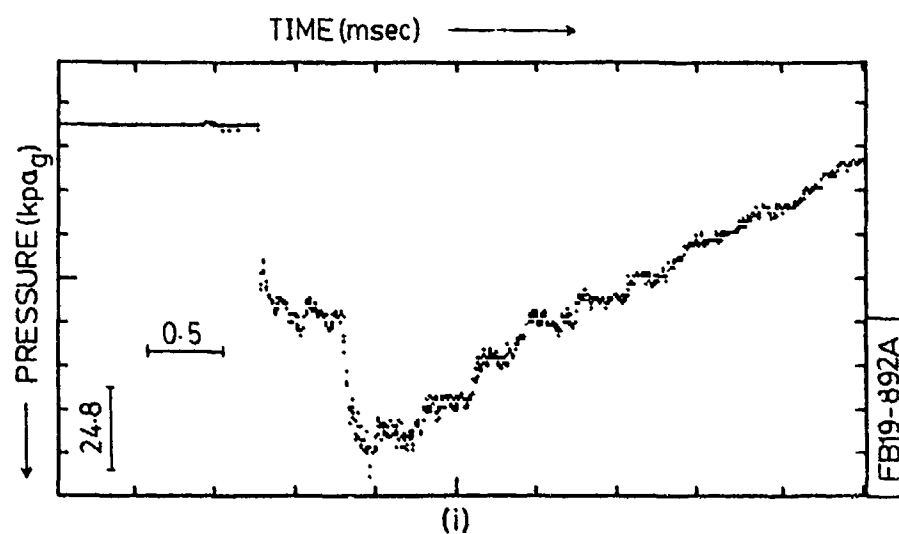
Fig.7: Pressure profiles for reflected shock waves for 37-element fuel bundle with diaphragm pressure ratio of 1.9 and liquid level of 30.0 mm; (i) Gas phase and (ii) Liquid phase.

TIME (msec) ────────▶

PRESSURE (kpa$_g$)

0.5

24.8

FB19-892B

(i)

TIME (msec) ────────▶

PRESSURE (kpa$_g$)

0.5

24.8

FB19-886B

(ii)
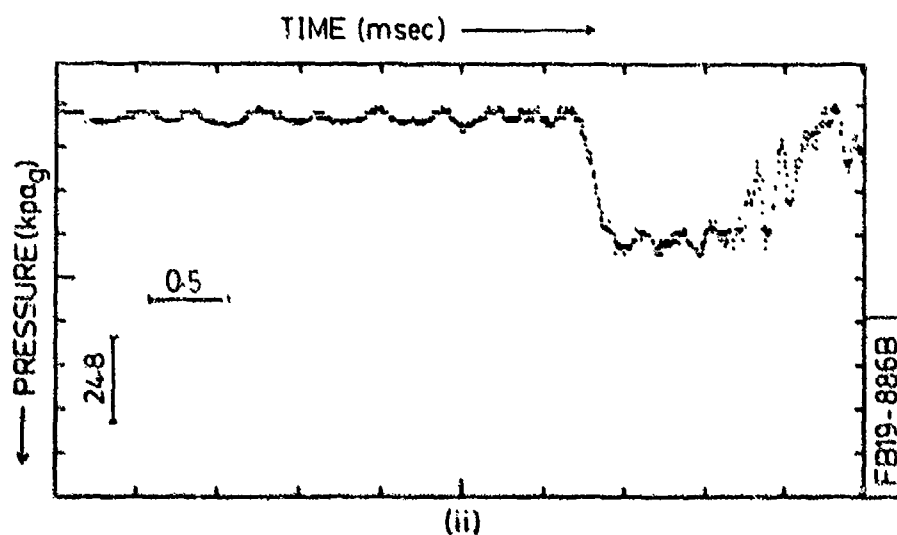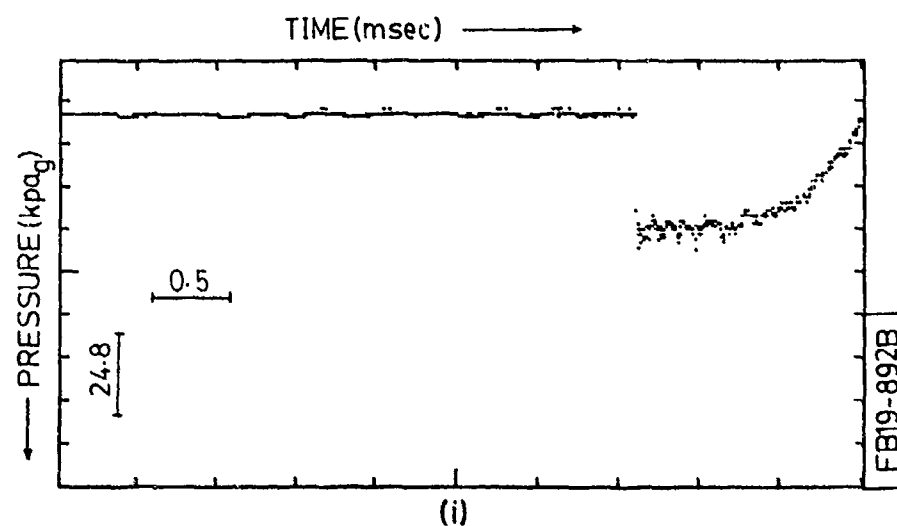
Fig.8:   Pressure profiles for transmitted shock waves for
37-element fuel bundle with diaphragm pressure ratio of 1.9 and
liquid level of 30.0 mm; (i) Gas phase and (ii) Liquid phase.

HIGH TEMPERATURE HEAT TRANSFER FOR GAS TURBINES USING SHOCK TUBES

Henry T. Nagamatsu* and Robert E. Duffy*
Department of Mechanical Engineering,
Aeronautical Engineering & Mechanics
Rensselaer Polytechnic Institute
Troy, New York 12180-3590

External local heat transfer rates were measured at the stagna-
tion region for circular cylinders, over flat plate with and
without pressure gradient, and in the junction region of flat
plate anc circular cylinder mounted normal to the plate over a
temperature range of 350° and 2500°K and various Reynolds and
Mach numbers anticipated in advanced gas turbines. Thin film
platinum heat gages were used to measure the local heat flux
for laminar, transition and turbulent boundary layers. Hot
wires were used to measure the turbulence level after the
incident and reflected shock waves in the test section. The
experimental heat flux data were correlated with the laminar
and turbulent theories and the transition phenomenon was examined.

INTRODUCTION

One of the critical problems for designing fuel efficient gas turbines[1-3]
with operating temperature as high as 2500°K and pressures of 40 atm is the
prediction of the external heat transfer rates to vanes and blades. The litera-
ture in the heat flux at very high temperatures and pressures for vanes and
blades is limited or not available. Thus, a research program was initiated
under the sponsorship of NSF and NASA at Rensselaer Polytechnic Institute using
the Low and High Pressure Shock Tubes[4,6] to obtain the heat transfer at the
stagnation region for circular cylinders, over flat plates with and without
pressure gradients, and in the junction region of flat plate and circular
cylinder mounted normal to the plate over a temperature range of 350° to 2500°K.
In addition, turbulence measurements were made in the shock induced flows to aid
in the interpretation of heat transfer results. The experimental heat transfer
data are correlated with the available laminar and turbulent boundary layer
theories.

EXPERIMENTAL APPARATUS AND INSTRUMENTATION

Two shock tubes, both having an internal diameter of 10.16 cm, have been
fabricated for investigating the heat transfer for gas turbine flow conditions
and the hypersonic flow phenomena in the nozzle attached to the high pressure
136 atm shock tube. The low pressure tube, rated at 6.8 atm, is used for
dynamic calibration of pressure and heat transfer gages and for those experi-
ments where the Reynolds number is low. The high pressure tube is used to
extend the operating Reynolds number range, and a 61 cm diameter conical nozzle,
housed in a 5.66 m³ dump tank, is connected to the end of the tube. Driver
length for both tubes is 4.57 m with nominal 18.3 m driven tube lengths.

Two different test sections are used for the heat transfer investigations. The one is the so-called circular test section at the end of the driven tube which was used to measure the stagnation region heat transfer for circular cylinders and the turbulence levels behind the incident and reflected shock waves. A smooth constant area transition is used to connect the 10.16 cm diameter shock tube to the square test section (9.02 cm × 9.02 cm) which houses the flat plate and is shown in Figs.1 and 2. The top and bottom walls are adjustable to produce the desired pressure gradient and the flow Mach number after the reflected shock wave over the flat plate to simulate the flows through gas turbine vanes and blades. Reflecting wedges, which act as orifices, are used to produce the desired flow Mach number after the reflected shock wave for the circular test section and for the square test section with parallel top and bottom walls.

The pressures in the test section after the incident and reflected shock waves are measured by Kistler pressure transducers, Fig.1. The speed of the incident and reflected shock waves is obtained by tracking their passage over the pressure gages. A time interval counter and oscilloscope are triggered by piezoelectric crystals placed 64 cm apart in front of the transition section. Tektronix oscilloscopes are used to record the pressure and heat transfer data on Polaroid films.

Thin film platinum heat gages are used to measure the local heat flux over flat plates and at the stagnation region for circular cylinders. They have a response of a few microseconds which makes them ideal for shock tube use[4-6]. A thorough discussion on how to make the heat gages is presented in Refs.4 and 5. The signal from the gage is amplified 100 times by a Tektronix Type 122 amplifier before being fed into an oscilloscope.

Various length flat plate models[6,7,8] were used to measure the heat flux with a width of 9.02 cm and thickness of 6.35 mm with rounded leading edge as shown in Fig.1. To investigate the heat flux at the junction region of a circular cylinder mounted normal to the flat plate, a flat plate was constructed with heat gages mounted on a rotating surface parallel and normal to the flow direction as shown in Fig.2. This configuration simulates the junction of vanes with the shroud in gas turbines where horseshoe occurs[9]. Circular cylinders with thin film platinum heat gage mounted at the stagnation region were constructed to measure the heat flux for various diameters at elevated temperatures[10,11].

DATA REDUCTION

The flow parameters of the heated gas generated by the incident and reflected shock waves in the shock tube is obtained in the following way[5]: The pressure is measured by the Kistler pressure transducers. The temperature is obtained from the strength of the incident and reflected shock waves and the temperature initially prevailing in the driven tube. The flow Mach number M_6 after the reflected shock wave and the flow velocity are determined from the open area of the shock reflection plate or the minimum area with the converging top and bottom walls, Fig.1. The length parameter used in the Reynolds number was the distance from the leading edge of the plate.

The purpose of the heat gage calibration procedure is to determine the heat gage constant β which is defined as

$$\beta = \frac{[(\rho c_p k)_b]^{1/2}}{a} \tag{1}$$

where ρ, C_p, and k are the density, specific heat, and thermal conductivity of the backing material and α is the thermal resistivity of platinum. The gage constants β are then used in the calculation of the heat transfer for each heat gage. The gage constant was obtained by the accurate evaluation of the initial voltage jump displaced on the oscilloscope trace when the incident shock wave passes over the heat gage and using Mirels theory[13] for laminar boundary layer, which was experimentally verified by Dillon and Nagamatsu[4].

The heat transfer data consists of a voltage trace for each gage which is recorded on film using an oscilloscope and the voltage traces on the photographs are digitized. The local heat transfer flux as a function of time is obtained from the following equation derived by Vidal[6]:

$$q(t) = \beta \frac{\sqrt{\pi}}{2I_0 R_0} \left\{ \frac{E(t)}{\sqrt{t}} + \frac{1}{\pi\sqrt{t}} \int_0^t \frac{[\sqrt{\tau} \cdot E(t)] - [\sqrt{t} \cdot E(\tau)]}{(t-\tau)^{3/2}} d\tau \right\} \qquad (2)$$

A computer program is then used to integrate this equation by using the digitized data.

EXPERIMENTAL RESULTS AND DISCUSSION

Heat Gage Traces for Laminar, Transition and Turbulent Boundary Layers

With the thin film platinum heat gages with a response time of a few microseconds[4,13], it is possible to determine the type of boundary layer from the oscilloscope traces. Heat gage signals were observed for laminar, transition, and turbulent boundary layers on the shock tube wall[4], flat plate[6,7,8], and over a $10°$ cone in hypersonic shock tunnel[13].

For a low Reynolds number with laminar boundary layer over the flat plate, Fig.2, a typical heat transfer variation with time after the incident shock wave is presented in Fig.3.[6] The flow Mach number behind the shock wave was 0.66 with a gas temperature of $378°K$ and unit Reynolds number Re/cm of 827. The experimental heat flux results agree well with Mirels[12] prediction of heat transfer behind a moving shock wave.

Flat Plate Heat Transfer with and without Pressure Gradient

The heat transfer results for laminar and turbulent boundary layers over a flat plate with parallel top and bottom walls, Fig.1, are presented in Fig.4a for a gas temperature of $425°K$, Mach number of 0.12 after the reflected shock wave and wall-to-gas temperature ratio of 0.70.[7] A laminar boundary layer was observed for the tests in which the unit Reynolds number Re/cm varies from 434 to 1710 and the heat flux results agree reasonably well with the laminar boundary layer theory of Pohlhausen. For tests in which the unit Reynolds number was greater than 2.65×10^4 a turbulent boundary layer was observed. The corresponding heat transfer results agree quite well with the turbulent boundary layer theory of von Kármán[14].

The Stanton numbers over the flat plate in the square test section with parallel top and bottom walls, Fig.1, for a gas temperature of $1000°K$, flow Mach number of 0.12, and wall-to-gas temperature ratio of 0.33 are presented in Fig.4b.[7] At low unit Reynolds numbers the Stanton numbers are close to the laminar predictions, but at higher unit Reynolds numbers of 2.09×10 the Stanton numbers are slightly greater than for the turbulent prediction which indicates that the turbulent boundary was not fully developed.

With the top and bottom walls convergent, Fig.1, to produce a flow Mach number after the reflected shock wave of 0.10 and an accelerating flow over the flat plate, the local heat transfer rates were measured for various Reynolds numbers[6]. For a Reynolds number of 4.37×10^7 over the first cm and a

temperature of 408°K the Nusselt numbers along the plate agree reasonably well
with the laminar theory, Fig.5a.

A flow Mach number after the reflected shock wave of 0.15 was produced and
heat transfer rates were obtained over the flat plate for a temperature range of
969° to 2575°K.[5] The heat transfer results for the highest temperature are
presented in Fig.5b for a Reynolds number of 1.15×10^4 over the initial cm of
the plate and wall temperature ratio of 0.11.

HEAT TRANSFER IN THE JUNCTION BETWEEN A RIGHT CIRCULAR CYLINDER AND FLAT PLATE

External heat transfer rates were measured on a flat plate in the junction
region of a circular cylinder mounted normal to the plate, Fig.2, at a location
90° from the stagnation point. This configuration simulated the junction of the
shroud with gas turbine vanes. Heat transfer rates are presented for laminar,
transition and turbulent boundary layers for a Mach number of 0.14 with gas
temperature of approximately 417°K over a flat plate at room temperature[8].

The Stanton number variations with Reynolds number for heat gage located at
$y/D = 0.2$ in the vertical plane from the junction region are presented in Fig.6a.
In this figure the analytical predictions for laminar and turbulent boundary
layers are presented to correlate with the experimental heat flux data[8]. The
cylinder caused a very large increase in the heat flux at low Reynolds number.
At this location the effects of horseshoe vortex[9] are very large since the
vortex decreases the boundary layer thickness in the junction region. In
Fig.6b the normalized heat transfer data for the heat gages located along the
line perpendicular to the flow direction are presented. The normalizing factor
for each heat gage is a curve-fit to the turbulent heat transfer rate without
the cylinder. For low Reynolds numbers the heat transfer rates with the
cylinder were increased by a factor of 4, 3, and 2.5 for the heat gages located
at $y/D = 0.2$, 0.4, and 0.6, respectively.

Stagnation Point Heat Transfer

Experiments have been conducted in the low pressure and high pressure shock
tubes at low and moderate temperatures to measure the stagnation point heat
transfer for cylinders of various diameters. The results[10] for a flow static
temperature 406°K and flow Mach number of 0.15 are shown in Fig.7a. The results
compare favorably with Eckert's laminar stagnation point heat transfer theory
applied to a cylinder and a cylindrical capped flat plate. Later measurements
of the turbulent intensity of the flow[6] show that the higher measured heat
transfer rates are predominantly attributable to turbulence effects. Measure-
ments taken of the stagnation point heat transfer[11] at a flow static temperature
and Mach number of 1044°K and 0.15, respectively, are shown in Fig.7b. At this
higher temperature the data show a continuous, but well behaved, departure from
Eckert's theory.

Turbulence Measurements in Shock Tube Flows

Turbulence intensity, length scale and Reynolds number all affect heat
transfer. Measurements were made in a low pressure shock tube in the incident
and reflected system. Fluctuating hot-wire output voltages were recorded,
digitized, filtered, corrected for finite wire aspect-ratio effects, and
analyzed to predict mass flux and total temperature intensities. An assumption
of constant pressure allowed the mass flux intensity to be separated into
velocity and density fluctuations.

For a flow Mach number of 0.15 and a flow static temperature of 406°K
measured mass flux intensities are between 0.6% and 1.5% in the incident region
and between 2% and 6% in the reflection region. The effect of flow Reynolds
numbers on these intensities is shown in Fig.8.

A question of considerable recent interest deals with amplification of turbulence across a shock wave. Measurements in the incident and reflected regions are used to determine such amplification. The amplification of mass flux and total temperature intensities across the reflected shock decrease with increasing incident Reynolds numbers, as seen in Fig. 9.

CONCLUSIONS

The shock tube is a good technique for producing short duration high enthalpy flows for advanced gas turbine conditions. Thin film platinum heat gages with fast response time are ideal for local heat transfer measurements and for detecting the transition of laminar boundary layer in the shock tube.

At low temperatures the heat transfer results agree with the laminar theory with constant flow properties for steady condition and with Mirels' theory after the incident shock wave. Heat transfer data were obtained for transition and turbulent boundary layers at higher Reynolds numbers. Heat transfer data were obtained for gas temperatures up to 2575°K. In the junction region of a flat plate and a circular cylinder the heat transfer was drastically increased due to the horseshoe vortex.

Stagnation point heat transfer for circular cylinders agreed reasonably well with the laminar theory at low temperatures corrected for the turbulence level, but at a temperature of 1044°K the heat flux data departed from Eckert's theory. The turbulence levels after the incident and reflected shock waves were approximately 1.5 and 6%, respectively, for moderate shock strengths, and the amplification of mass flux and total temperature intensities across the reflected shock wave decrease with increasing Reynolds numbers.

REFERENCES

1. Fink, D.E., "Power Plants of Next Century Studied," Aviation Week and Space Technology, 116, 26 (June 1982).

2. Graham, R.W., "Fundamental Mechanisms that Influence the Estimate of Heat Transfer to Gas Turbine Blades," NASA TM 79128, 1979.

3. Kercher, D.M., Sheer, R.E. and So, R.M.C., "Short Duration Heat Transfer Studies at High Freestream Temperatures," ASME 82-GT-129, 1982.

4. Dillon, R.E. and Nagamatsu, H.T., "Heat Transfer Rate for Laminar Transition and Turbulent Boundary Layer and Transition Phenomenon on Shock Tube Wall," AIAA Journal, 22, 8, 1524-1528 (1984).

5. Pedrosa, A.C.F. and Nagamatsu, H.T., "Convective Heat Transfer on Flat Plate at Very High Temperature and Pressure Gradient," ASME 83 GT-113, 1983.

6. Vidal, R.J., "Model Instrumentation Techniques for Heat Transfer and Force Measurements in a Hypersonic Shock Tunnel," Cornell Aeronautical Laboratory, Report No. AD-917-A-1, February 1956.

7. Brostmeyer, J.D. and Nagamatsu, H.T., "Flat Plate Heat Transfer for Laminar, Transition, and Turbulent Boundary Layers Using a Shock Tube," AIAA Paper No. 84-1726, June 1984.

8. Nagamatsu, H.T. and Hinckel, J.N., "Heat Transfer Investigation in the Junction Region of Circular Cylinder Normal to a Flat Plate at 90° Location," ASME 84-WA/HT-70, 1984.

9. Gaugler, R.E. and Russel, L.M., "Streamline Flow Visualization Study of a Horseshoe Vortex in a Large-Scale, Two-Dimensional Turbine Stator Cascade," ASME 80-GT-4, 1980.

10. Zaffuts, P.J., "Low Temperature Stagnation Point Heat Transfer at M = 0.15 and 0.45," Master's Project, Rensselaer Polytechnic Institute, Troy, New York, August 1983.

11. Dales, K.G., "Stagnation Point Heat Transfer at a Flow Mach Number of 0.15 and Static Temperature of 1800°R," Master's Project, Rensselaer Polytechnic Institute, Troy, New York, March 1985.

12. Mirels, H., "Laminar Boundary Layer Behind a Shock Wave Advancing Into Stationary Fluid," NACA TN 3401, 1955.

13. Nagamatsu, H.T., Graber, A.C. and Sheer, R.E., "Roughness, Bluntness and Angle of Attack Effects on Hypersonic Boundary Layer Transition," Journal of Fluid Mechanics, 24, 1-31 (1966).

14. von Kármán, T., "The Analogy Between Fluid Friction and Heat Transfer," Trans. ASME, 61, 705-710 (1939).

15. Trollier, J.W. and Duffy, R.E., "Turbulence Measurements in Shock Induced Flows," AIAA Paper No. 84-0632, 1984; also AIAA Journal (August/September 1985).
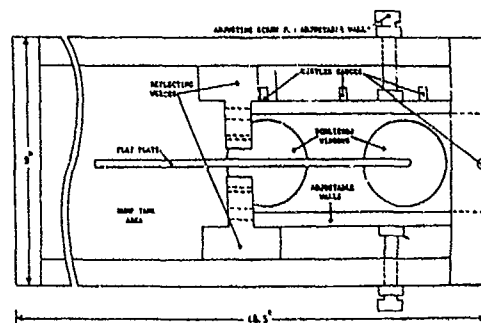
Fig.1   Square Test Section
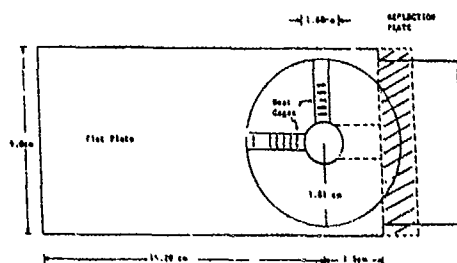
Fig.2   Flat Plate with Cylinder
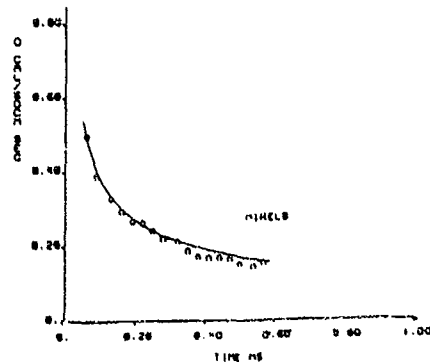
Fig.3   Heat Flux After Shock Wave
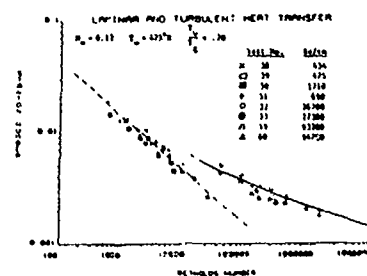
Fig.4a   Heat Transfer for Laminar and Turbulent Boundary Layer
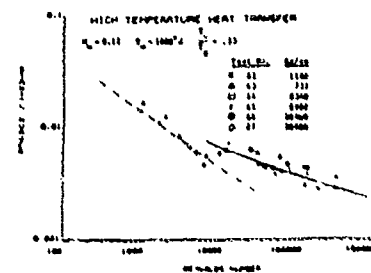
Fig.4b   Heat Flux for High Temperature

.Fig.5a Converging Wall - Laminar
Heat Transfer, T_∞ = 408°K,
M_∞ = .10

Fig.6b Normalized Heat Flux for
Heat Gages Located 90°
Location from the Stagna-
tion Point

.Fig.5b High Temperature Converging
Wall Heat Transfer,
T_∞ = 2575°K, M_∞ = .15

(a) M_∞ = 0.15

Fig.7a Stagnation Point Heat
Transfer Results for a Flow
Static Temperature of 406°R

Fig.6a Heat Transfer in Junction
Region with and without
Cylinder, y/D = 0.2

Fig.7b Heat Transfer Data:
M_∞ = 0.15, T_∞ = 1044°K
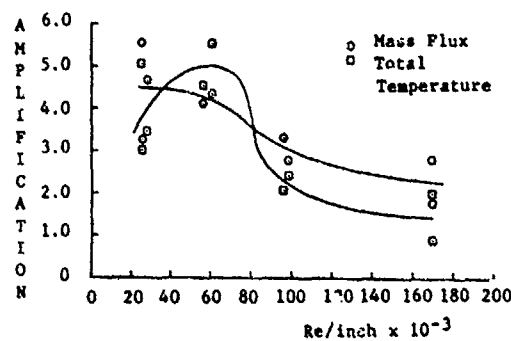
a) Incident Region
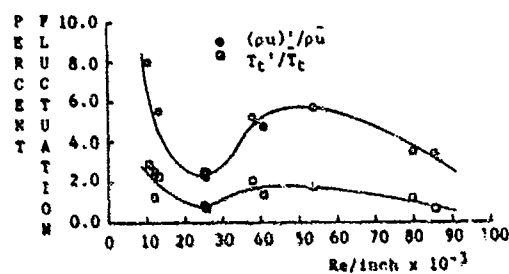
b) Reflected Region

Fig.8 Mass Flux and Total Temperature
Fluctuations Versus Reynolds
Numbers Per Inch. $M_\infty = 0.15$,
$T_\infty = 406^\circ K$
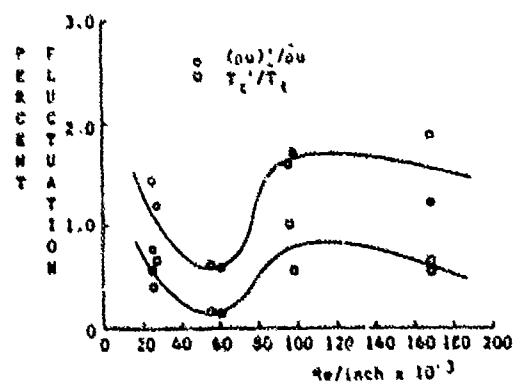
Fig.9 Amplification of Turbulence Ratio
of RMS Mass Flux and Total Temper-
ature Across a Reflected Shock Wave

MAGNETOHYDRODYNAMIC CONTROL OF BLAST ENERGY

A FEASIBILITY EXPERIMENT

C. A. ANDRADE

Benet Weapons Laboratory, AMCCOM, Department
of the Army, Watervliet Arsenal, Watervliet, N.Y. 12189

Magnetohydrodynamic experiments suggest that power can
be extracted at a gun muzzle from residual propellant
energy dissipated when the projectile achieves launch
velocity. For conceptual feasibility, it must be shown
that the insufficiently ionized propellant gases can be
enhanced by electronic seeding to requisite levels for
MHD power generation. Thus, a primary objective is to
show that the shock layer and seeded propellant driver
gases can be decelerated by post muzzle pulsed magnetic
flux. Procedure consisted of firing a 7.62 mm
projectile through a one inch diameter channel designed
so that magnetic flux could interact with the hot
propellant gas expansion and the incipient shock
structure emerging at the muzzle. Cartridges were
seeded with potassium carbonate (K_2CO_3) up to 13% of
full charge. Magnetic flux density was varied to a
maximum of 4 teslas transverse to the flow at interaction,
50 mm forward of the muzzle.

The present experimental results show that the shock wave
is transmitted through the interaction region with decreasing
velocity as the magnetic flux density is increased, a
result expected from shock tube literature. A 4%
decrease, from the zero flux (baseline) shock velocity
of 1850 m/s, was measured at nearly 2 T without the K_2CO_3
additive. However, the shock velocity drops to 20% of
baseline with increasing amounts of K_2CO_3 added at the
same flux density, an apparent threshold value of about
1.5 T. At 0.4 gm of additive the measured shock velocity
decrease was 50% and 60% of baseline, respectively, at 2
and 4 teslas.

I. INTRODUCTION

Shock tubes have played a prominent role in characterizing the electrical
conductivity of gases at elevated temperatures.[1-5] When the conductivity is
known, the interaction of flowing electrically conducting gas, with magnetic
flux applied perpendicular to the flow direction, may in reciprocal fashion be
used to characterize the propagation of shock waves through the region of
magnetohydrodynamic interaction.[1,6-9] This corollary effect occurs because
the reflection and transmission properties of sufficiently strong shock waves,
within the flux boundaries, reveal the presence and magnitude of shock induced
conductivity according to the Lorentz force law. These properties can therefore
be observed, mechanically, through the deceleration of shock waves that
propagate through the interaction region [6] and/or, electrically, by the
extraction of power to an external load.[10,11] Thus, a second corollary:

The associated shock wave strength reduction transmitted through the interaction region implies reduction in the shock overpressures. In turn, this suggests the possible application of post gun muzzle MHD as a large caliber weapon silencer. The concept can work in two modes. The first is by MHD shock attenuation, in which case the free-field shock overpressure reduction does not depend on power extraction. The second is accomplished by MHD power extraction, in which case the modes are coupled.

II. PRELIMINARY FLOW FIELD INVESTIGATION. ZERO FLUX.

A small scale test bed was chosen in order to advantageously use the available flow field database published by the Abteilung Für Ballistik.[12-14] The AFB Group measured the transient properties of propellant gas expanding at the muzzle of a 7.62 mm caliber rifle. The standard NATO 7.62 MM M14 rifle used in the present experiment was modified by truncating the barrel to the same length reported by the AFB, namely 451.5 mm. Compare properties on Table I.

Initial baseline tests were conducted at the Ballistics Research Laboratory.[15] The purpose of these tests was to determine the muzzle exit flow temperature by acoustic thermometry[16] and to study the flow through a 25 mm diameter channel designed to simulate the MHD channel of subsequent tests.

(a)   BARE MUZZLE FLOW

Considering first the bare muzzle, Figure 1 is a shadowgraph of the precursor shock wave and flow field formed by the column of air initially in the barrel ahead of the bullet. A simple one-dimensional unsteady flow calculation predicts that the initial velocity of the precursor shock wave at the muzzle is 1040 m/s. The jet boundary attached at the muzzle is clearly visible on the shadowgraph and so is the barrel shock which intercepts the normal inner shock wave (Mach disc) downstream. Measurements of the maximum distances of the two shock discontinuities from the muzzle were compared to the AFB shock trajectory data to within six calibers, thus suggesting that the projectile base exits the muzzle within 0.1 ms following the shadowgraph event. Coincident with the bullet's exit, propellant gases expand through the annulus between the muzzle and boattail. The expansion drives an initially cylindrical shock wave which is analysed at its vertex by 1-D unsteady flow.

This calculation is summarized on Table II. The procedure is to assume the rifle (cannon) is an open-end shock tube with gas velocity in the driver section equal to the projectile muzzle velocity. Then, using data from Table I, iteratively solve the resulting cannon uncorking (brust pressure) equation by simultaneous use of the NASA Thermochemical Equilibrium Program.[17] The iteration is satisfied by logic that requires temperature in region 3, upstream of the contact surface, to be 1700 degrees K according to the maximum AFB observations in the primary flash region.[12] The shock layer plasma properties listed on Table II were calculated with a subroutine that follows the methods, and is verified by the data, of Lamb and Lin.[3] For the 1-D unsteady, shock tube method described, we note the following:

(i)   The imparted velocity (2442 m/s) and temperature (1700°K) in the hot propellant side of the contact surface are in close agreement with the AFB measurements taken at about 60 μs and in the range 25 < z < 75 mm.

(ii)   The calculated propellant gas temperature at region 4 (T = 2642°K) is less than the published[18] propellant (WC846) flame temperature (T = 2855°K).

(iii)   These calculations are consistent with the BRL temperature measurement of 2100°K at the muzzle.[15]

A numerical simulation of the time-dependent, axisymmetric, inviscid, muzzle expansion flow was carried out using the single fluid Godunov technique as implemented by Taylor and Lin[19] and adapted for use at the Benet Weapons Laboratory by Dillon.[20] Shown on Figure 2 are histories of select flow quantities on a plane at z = 40.96 mm forward of the muzzle and at three values of the radius R from the axis of symmetry. The sharp rise in temperature at R =

4.10 mm is attributed to the projectile base shock wave since the propellant gas is expanding about the projectile base. The peak temperatures and velocities are, again, consistent with measured data.[12,13] Present effort consists of preparing a grid to simulate the channel flow.

(b) CHANNEL FLOW

The muzzle device shown on Figure 3 is the simulated MHD channel used at the BRL to study the magnet-free flow.[15] The device is a circular cylinder concentric with the barrel axis. Its inside diameter is 25.4 mm and its flow-through length is 223 mm. Eight PCB gauges were used to measure pressure and shock time-of-arrival. For the blast overpressure measurements, six Kistler gauges are positioned in a circular array 229 mm from the muzzle, on a plane containing the axis, and at angles of 15, 30, 60, 90 and 120 degrees from the line of fire. Figures 4 and 5 are shadowgraphs of the blast field emerging from the simulated MHD channel. The blast wave diffracting about the channel at the early time shows no evidence of a precursor wave. (Compare the wave intensities of Figures 1, 4 and 5.) Indeed, the measurements[15] show that the precursor is overtaken within the channel at $z = 168$ mm and $t = 0.87E^{-4}$s, at which point the precursor shock velocity is near sonic. This is shown on Figure 6 which displays the blast and precursor wave trajectories deduced from these measurements. It is of interest to note that the propellant driven incident shock wave moves at constant velocity over most of the short channel length and, in particular, over that section of the channel where subsequent MHD tests apply. Properly timed, MHD interaction should initiate while the incident shock wave is moving over the projectile, still within the non uniform field of the precursor. Figure 7 is an artists' conception of the flow field with wave interactions between the channel and projectile surfaces.[15]

III. THE MAGNETOHYDRODYNAMIC EXPERIMENTS

Figure 8 is a photograph of the MHD channel, with pulse coils[21] mounted diametrically opposite as shown. The coils are powered by a 50 kJ, 10 kV MAXWELL capacitor bank,[22] providing a maximum central field of ten Tesla (at 11 kA) perpendicular to the flow direction. Six KSP blast overpressure gauges were used in the same configuration described above for the short channel. In the MHD experiments the channel was constructed of G 10 tubing lined by a stainless steel section 381 mm long. The inside diameter is 25 mm. The M14 barrel was replaced by a thick walled barrel, again, modified to the ABF length. This provided pressure instrumentation at the chamber and port positions in-bore. The channel was instrumented with shock time-of-arrival pressure gauges at $z =$ 131.9 and at 208.1 mm. The mean location between these is at 170 mm from the muzzle and at 120 mm from the central field axis. This axis coincides with a diameter of the channel, 50 mm from the muzzle. The magnetic flux density is deduced from current measured by a Rogowski coil. A maximum experimental value of 4 T was obtained for the superposition field of both coils on the central field axis. Events were monitored by Nicolet digital recording oscilloscopes. Projectile velocity was measured by a break-light device. Cartridges were charged with the standard 2.98 grams of WC846 propellant and K2CO3 was tamped onto the charge in amounts up to 13.4% of full charge.

Procedure consisted of charging the bank, then firing the projectile. A signal near peak chamber pressure triggered the monitors and bank. Figure 9 shows time-of-arrival and current measurement for the 4 T shot. It is assumed the transmitted shock travels unattenuated from the interaction section. The measured shock velocity allows an estimate of time upstream at the central field location so that the value of current, corrected for its delay setting, may be read at the earlier time. The greater the shock arrival interval between the two transducers the greater the shock attenuation due to Lorentz forces at the upstream interaction section. Figure 10 presents the measurements of shock attenuation in the MHD channel. These data show that the shock wave is

transmitted through the interaction region with decreasing velocity as the magnetic flux density is increased, a result expected from shock tube literature.

Figure 11 shows a comparison of the baseline (flux-free) external blast overpressure measurements for the two flow channels used in these tests. These data show that fo. baseline cartridges, i.e. without the K2CO3 and free of magnetic flux, the greater external shock overpressure attenuation is obtained with the long channel used for the MHD tests. Thus, the lower set of data represents the baseline for comparison against rounds fired with the alkali electron donor for MHD interaction. A single baseline (round 108) was selected for comparison to MHD firings at several values of the magnetic flux density, shown on Figure 12. Thus, the maximum blast overpressure attenuation increased with increasing magnetic flux density, at 0.4 g of additive. At 4 T the gain incresed from 15% at the foremost gauge to 22% at the 60 degree gauge.

IV.   PRELIMINARY ANALYSIS

From our channel flow perspective (Figures 6 and 7) and measurements of the interaction (Figure 9) a procedure is being developed that may explain the apparent shock attenuation process observed on Figure 10. The electrical conductivity of the propellant gas shock layer downstream of the projectile base shock was evaluated using the NASA program. The composition used was an approximation for typical nitrocellulose base propellants[18], the major species consisting of H_2O, CO_2, CO N2 and H2; and with K2 and K at a total mole fraction of 12%. Conditions for the calculation [12-14] were u1 = 2435 m/s, p1 = 0.3 MN/m^2, T1 = 1736°K; the molecular weight, 31 g/mol, the ratio of specific heats (GAMMA) was 1.233 and the sonic velocity, 757 m/s. The result: v = u1 - u2 = 2012 m/s, p2 = 3.5 MN/m^2, T2 = 3316°K, GAMMA2 = 1.145 and the electrical conductivity is 51 mho/m. The flow stagnates and proceeds, in Newtonian approximation, to sonic condition at the projectile's edge and further expansion over the boattail. Isentropic expansion to 0.35 MN/m^2 yields the corresponding temperature of 2477°K. The same composition yields 10.3 mho/m at the final state. This result is not unlike data published in the MHD literature for seeded combustion plasma.

If propellant magnetoplasma in the annulus of interaction is characterized by 10 mho/m, with magnetic and dynamic pressures at 6.4 and 1.06 MN/m^2, respectively, then the estimated magnetic Reynolds number and interaction parameter are $R_m = \mu_0 \sigma$ v $l = \mu_0$ x 10 x 2000 x 0.025 = 0.63 E-3 and S = 6.4 x R_m/1.06 = 0.38 E-2. These need a combined multiplication approaching 200 for choked flow during the interaction[6] and for the possible consideration of power extraction.[10] A major portion of that can be accomplished with a large caliber device which will increase the interaction length. A larger field could be applied, possibly self-excited, using saddle coils.

V.   CONCLUDING REMARKS

(i) Electrical Conductivity: Seeding is required. Propellant gases are not ionized to the extent required for MHD electrical generation. Seeding the propellant charge and/or injecting the expansion gases with CS2SO4 would double the electrical conductivity obtained with K2CO3 at the same flow conditions observed in the present tests.

(ii) Power extraction with the present test device is not possible because of the short (1 inch) magnetic interaction length.

(iii)The effect of magnetic interaction on the blast wave inside the channel is to dissipate its energy and delay propagation, followed by redistribution of energy in the external flow field.

(iv) Free-field overpressures are delayed in time and reduced in strength by MHD interaction within the device.

(v) The primary objective was accomplished experimentally; effort continues toward predicting the observations analytically.

VI.   REFERENCES

1. Lin, S.C., Dissertation, Cornell U., 1952
2. Lin, S.C. Resler, E.L., and Kantrowitz, A.R., JAP 26, 1955, p. 95
3. Lamb, L. and Lin, S.C., JAP 28(7), 1957, p. 754
4. Lin, S.C., AVCO Everett Research Report 33, 1958
5. Greene, E.F., and Toennies, P.J., "Chemical Reactions in Shock Waves," Academic Press Inc., 1965, p. 168
6. Patrick, R.M., and Brogan, T.R., J. Fluid Mech., 5, Feb 1959, p. 298
7. Bout, D.A., Post, R.S. and Presby, H., Phys of Fluids 13, 1970, p. 1399
8. Zaytsev, S.G., et.al., "Study of Ionizing Flow Through a Transverse Magnetic Field," in Shock Tubes, Proc. of the 7th Int'l Shock Tube Symp., Ed., I.I. Glass, June 1969, p. 538
9. Oliver, T.F., et.al., AIAA Journal 19, June 1981, p. 699
10. Nagamatsu, H.T. and Sheer, R.E., Jr., Phys. of Fluids 4, 1961, p. 1073; also AIAA-85-0999, June 1985
11. Borghi, C.A. and Veefkind, A., AIAA Journal, Vol 22, March 1984, p. 348
12. Klingenberg, G. and Mach, H., Combustion and Flame, Vol 27, 1976, p. 163
13. Klingenberg, G. and Schroder, G.A., Op. Cit., Vol 27, 1976, p. 177
14. Klingenberg, G., Combustion and Flame, Vol 29, 1977, p. 289
15. Bundy, M.L. and Schmidt, E.M., Army Ballistic Research Laboratory, ARBRL-MR-03340, March 1984
16. Schmidt, E.M., et.al., AIAA Journal, Vol 15, Feb 1977, p. 222
17. Gordon, S. and McBride, B.J., NASA SP-273, 1971
18. Stiefel, L., Army ARDC, Dover, N.J. ARSCD-TR-80005, June 1980
19. Taylor, T.D. and Lin, T.C., AIAA 80-0273, Jan 1980
20. Dillon, R.E., Jr., and Nagamatsu, H.T., AIAA-84-1642, June 1984
21. Bitter Coils, designed and built by Electromagnetic Launch Research Inc., Cambridge, MA
22. MAXWELL bank, courtesy of Dr. P.J. Kemmey, ARDC, Dover, NJ

TABLE I.   BALLISTIC PROPERTIES OF THE MODIFIED 7.62 MM RIFLE

EXPERIMENT:	PRESENT	AFB
Modified barrel length, mm	451.5	451.5
Muzzle velocity, m/s	815.0	800.0
Projectile length, mm	28.0	28.0
Projectile weight, g	2.98	2.94
Propellant composition	WC 846	K 503
Propellant GAMMA	1.23	1.265
Chamber pressure, MPa	370	370
Muzzle pressure, MPa	59.0- 72.0	67.0

TABLE II.   THERMOCHEMICAL EVALUATION OF THE 7.62 MM GUN MUZZLE FLOW

Initial values (AFB)	p41	u4 (m/s)	T3 (°K)	GAMMA4		
	670	800	1700	1.265		

Final values	M1	u1 (m/s)	v (m/s)	T4 (°K)	T2 (°K)	p21
	8.168	2827	2442	2642	3300	81.7

Plasma	σ (mho/m)	e/cc	$\mathcal{N}(s^{-1})$	$\mathcal{N}_{e-1}(s^{-1})$	$Q(\pi a_0^2)$	Sum
	0.02	3.6 E12	5.6 E12	1.3 E9	9.87	0.9995
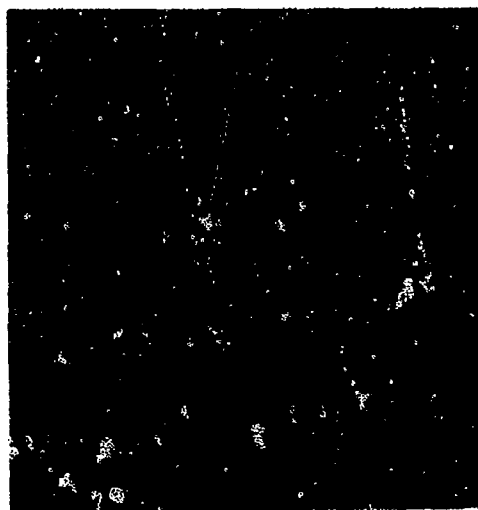
FIG. 1.   7.62 MM GUN PRECURSOR WAVE
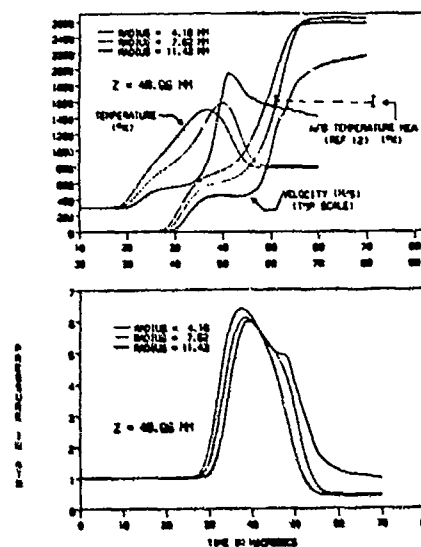
FIG. 2.   THE 7.62 MM MODIFIED M14 MUZZLE FLOW SIMULATION

FIG. 3.   SIMULATED MHD CHANNEL
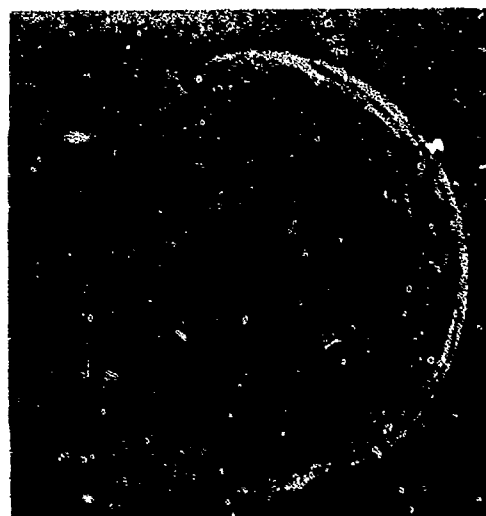
FIG. 4.   BLAST AT EARLY TIME

FIG. 5.   BLAST AT GAUGES
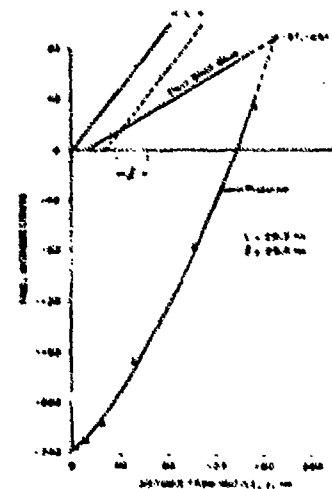
FIG. 6.   CHANNEL SHOCK TRAJECTORIES
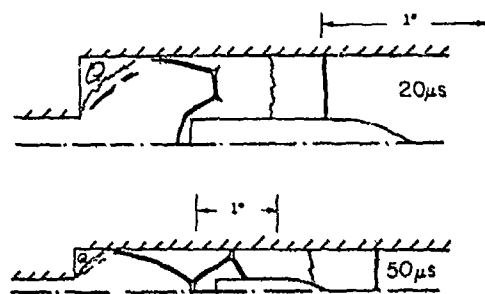
Figure 7. Conceptual View of the Flow Development in the Channel after Shot Ejection.

FIG. 8. MHD CHANNEL W/PULSE COILS
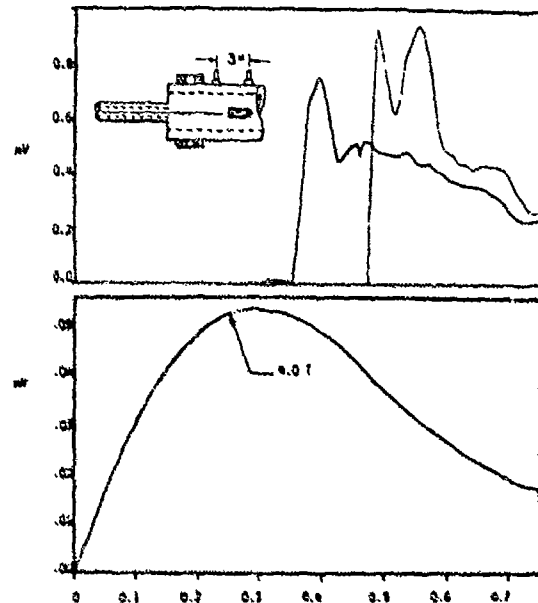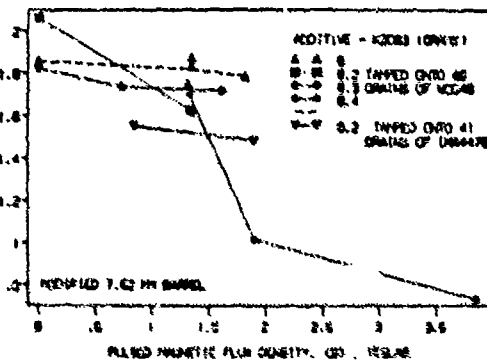
FIG. 10. SHOCK ATTENUATION IN THE MHD CHANNEL

Figure 9.

FIG. 11. THE 7.62 MM GUN BLAST OVERPRESSURE AFTER FLOW THROUGH POST MUZZLE CHANNELS.
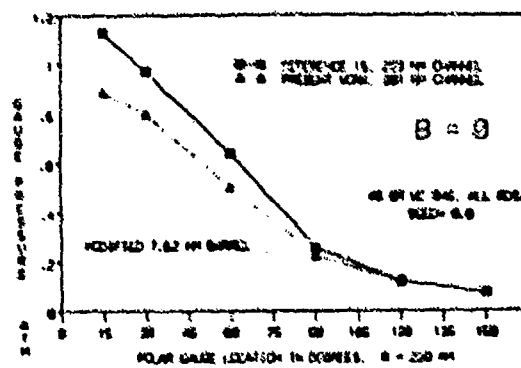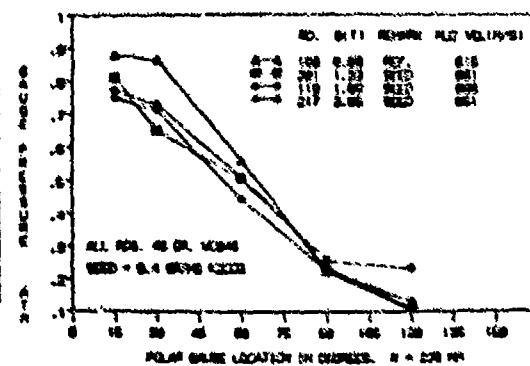
FIG. 12. THE ADAPTED 7.62 MM GUN BLAST OVERPRESSURE REDUCTION

Reference Matter

Previous Proceedings in This Series

Proceedings of the First Shock Tube Symposium, Feb. 26–27, 1957, ..eld at M.I.T., sponsored by Air Force Special Weapons Center. Headquarters, Air Force Special Weapons Center, Air Research and Development Command, Kirtland Air Force Base, New Mexico, SWR-TM-57-2, Ad No. 467201.

Proceedings of the Second Shock Tube Symposium, Mar. 5–6, 1958, sponsored by Air Force Special Weapons Center. Headquarters, Air Force Special Weapons Center, Air Research and Development Command, Kirtland Air Force Base, New Mexico, SWR-TM-58-3, Ad No. 211239.

Proceedings of the Third Shock Tube Symposium, Mar. 10–12, 1959, held at Fort Monroe, Virginia, sponsored by Air Force Special Weapons Center. Headquarters, Air Force Special Weapons Center, Air Research and Development, Kirtland Air Force Base, New Mexico, SWR-TM-59-2, Ad No. 230333.

Proceedings of the Fourth Shock Tube Symposium, Apr. 18–20, 1961, BRL Report No. 1160, February 1962, Ad No. 274039.

Proceedings of the Fifth International Shock Tube Symposium, published by the U.S. Naval Ordnance Laboratory, White Oaks, Silver Spring, Maryland, May 1966, Ad No. 484600.

High Temperature and Short Duration Flows. Proceedings of the Sixth International Shock Tube Symposium, R. J. Emrich, O. Laporte, and H. Reichenbach, eds., The Physics of Fluids Supplement I, 1969.

Shock Tubes. Proceedings of the Seventh International Shock Tube Symposium, I. I. Glass, ed., University of Toronto Press, Toronto, 1970.

Shock Tube Research. Proceedings of the Eighth International Shock Tube Symposium, J. L. Stollery, A. G. Gaydon, and P. R. Owen, eds., Chapman and Hall, London, 1971.

Recent Developments in Shock Tube Research. Proceedings of the Ninth International Shock Tube Symposium, D. Bershader and W. Griffith, eds., Stanford University Press, Stanford, California, 1973.

Modern Developments in Shock Tube Research. Proceedings of the Tenth International Shock Tube Symposium, G. Kamimoto, ed., Shock Tube Research Society, Japan, 1975.

Shock Tube and Shock Wave Research. Proceedings of the Eleventh International Symposium on Shock Tubes and Waves, R. Ahlborn, A. Hertzberg, and D. Russell, eds., University of Washington Press, Seattle, 1978.

Shock Tubes and Waves. Proceedings of the Twelfth International Symposium on Shock Tubes and Waves, A. Lifshitz and J. Rom, eds., The Magnes Press, The Hebrew University, Jerusalem, 1980.

Shock Tubes and Waves. Proceedings of the Thirteenth International Symposium on Shock Tubes and Waves, C. E. Treanor and J. G. Hall, eds., State University of New York Press, Albany, 1982.

Shock Tubes and Waves. Proceedings of the Fourteenth International Symposium on Shock Tubes and Waves, D. Bershader and R. Hanson, eds., Sydney Shock Tube Symposium Publishers, Sydney, 1984 (distrib. by New South Wales University Press).

Author Index